20th International Workshop on Atmospheric Icing of Structures (IWAIS 2024)

(June 18-21, 2024, Narvik, Norway)

Proceedings

Organized by

UiT-The Arctic University of Norway, Norway

Co-organized by

Faculty of Engineering Science & Technology, UiT

Arctic Technology & Icing Research Group (arcICE)

Sponsored by

STATNETT, Norway

NORCONSULT, Norway

LAKI POWER, Iceland

NORDKRAFT, Norway

The Research Council of Norway (RCN), Norway

IWAIS 2024

20th International Workshop on Atmospheric Icing of Structures

Narvik, Norway   June 18-21, 2024

Proceedings

Organized by

UiT-The Arctic University of Norway, Norway

Co-organized by

Arctic Technology & Icing Research Group (arcICE)

Sponsored by

The Research Council of Norway (RCN), Norway

STATNETT, Norway

NORCONSULT, Norway

CIGRE, France

LAKI Power, Iceland

NORDKRAFT, Norway

FORWARD

On behalf of the Organizing Committee, I am honored to welcome you to the 20th International Workshop on Atmospheric Icing of Structures (IWAIS 2024), which is organized by UiT- The Arctic University of Norway, and Co-organized by Arctic Technology & Icing Research Group (arcICE) at Faculty of Engineering Science & Technology, UiT. IWAIS 2024 will be held in Narvik, Norway, from 18-21 June 2024. The conference is sponsored by The Research Council of Norway (RCN) and leading industries of Norway and Iceland.

Human activities are increasingly extending in the ice prone cold regions, where atmospheric icing on structures can affect its design and safety. Atmospheric icing on structures is an area of concern from operational, maintenance, safety, and financial perspectives. Therefore, there is a growing need to improve knowledge and strengthen expertise about atmospheric icing on structures. The *International Workshop on Atmospheric Icing of Structures* (IWAIS) have been one of the most important scientific forums for disseminating research results about atmospheric icing and its effects on structures. Norway has a long-standing commitment to IWAIS and is hosting this event after 40 years as previously Norway hosted this in 1984 at Trondheim. We are very proudly happy to host this event in Narvik, Norway.

IWAIS gathers a vibrant community of researchers, consultants and utility stakeholders who are eager to innovate, share and implement effective solutions to mitigate icing on structures. I am sure that all the participants of IWAIS 2024 will have a wonderful and fruitful time at the conference, and that our oversea guests will enjoy their stay in Narvik in this beautiful June with an unforgettable experience of mid-night sun.

I warmly welcome all the participants of IWAIS 2024.

Sincerely,

Prof. Muhammad Shakeel Virk
Chairman of IWAIS 2024

CONFERENCE CHAIRMAN

Muhammad Shakeel Virk   UiT-The Arctic University of Norway, Norway

CONFERENCE VICE-CHAIRS

Bjørn Egil Nygaard   Norconsult, Norway

LOCAL EXECUTIVE COMMITTEE (LEC)

Muhammad Shakeel Virk	UiT-The Arctic University of Norway, Norway
Jan-Arne Pettersen	UiT-The Arctic University of Norway, Norway
Margrethe Grundstad Olsen	UiT-The Arctic University of Norway, Norway
Wenche L. Berg Kvernelv	UiT-The Arctic University of Norway, Norway

LOCAL ADVISORY COMMITTEE (LAC)

Hassan Abbas Khawaja	UiT-The Arctic University of Norway, Norway
Svein-Erik Sveen	UiT-The Arctic University of Norway, Norway
Xingbo Han	UiT-The Arctic University of Norway, Norway
Arefeh Lotfi	UiT-The Arctic University of Norway, Norway
Svein Magnus Fikke	

TECHNICAL COMMITTEE (ITC)

Arne Erik Holdø	László E. Kollár
Arefeh Lotfi	Mingfeng Huang
Adeel Yousuf	Manaf Muhammed
Boris Adum	Omar Badran
Fanghui Yin	Pavlo Sokolov
Gelareh Momen	Richard Hann
Hu Qin	Shahab Farokhi
Hu Hui	Timo Karlsson
Igor Gutman	Xingbo Han
Jia Yi Jin	Zaid Ayaz Janjua

INTERNATIONAL ADVISORY COMMITTEE (IAC)

TABLE OF CONTENTS

Keynote Speech 1：
Impact of Icing on Power Networks and Mitigation Options
Professor. Masoud Farzaneh, Canada

Keynote Speech 2：
State of the Art and Consideration on Ice Disaster Prevention in Power Grids
Professor Xingliang Jiang, China

Keynote Speech 3：
Role of Icing in a Warming World
Dr. Emilie Claussen Iversen, Norway

Technical Sessions

Icing on Overhead Power Lines

Experimental Modelling of Icing

Anti Icing Coatings

Mesoscale Modelling of Ice

Ice Mitigation

Ice Detection & Mitigation

Aircraft Icing

Field Study of Icing

Icing on Wind Turbines

Droplets & Ice Physics

Icing on Transport Infrastructure

General Topics

Overhead Line Conductor Icing - A Case Study of the Application of Numerical Weather Modelling in a Low Ice Environment

Laura Hume-Wright[1], Stuart Flint[2], Philip G Sansom[1], Karen Walter[1], David Borrie[2], Phil Hodge[1]

[1] *UK Met Office, FitzRoy Road, Exeter EX1 3PB, United Kingdom*
[2] *Scottish &Southern Electricity Networks -Transmission, United Kingdom*

laura.hume-wright@metoffice.gov.uk, stuart.flint@sse.com

Abstract— **While Scotland and the UK are typically considered a "low ice environment", the estimation of extreme return values of ice accretion on overhead powerlines remains a requirement of engineering standards for the design of electricity transmission infrastructure. Current practice is based on the BS EN 1993-3-1:2006 map of radial ice thickness, produced in the 1980s, and processed using the requirements of BS EN50341-2-9 technical standard. These methods predict ice values that should lead to widespread failures within the existing network that have not been observed. It is thus widely considered by the UK electricity transmission industry that the current approach leads to the costly over-engineering of electricity transmission infrastructure. Furthermore, in the UK there is little data available for the validation of ice load models.**

This project seeks to address these concerns by updating the current UK ice map over Scotland using modern numerical weather prediction model data and ice load estimation methods, with validation against the available observations at each step of the modelling chain.

Wet snow and in-cloud rime ice accretion models were developed following Makkonen (2000), ISO 12494 (2001), and Nygaard (2019), with input historical meteorological data provided by the Met Office Euro4 hindcast. Corrections were applied to the wind speed data to account for the effects of elevation, orographic roughness, and land use. The ice accretion models were run for two conductor heights and three diameters, to produce an 8 km x 8 km gridded 35-year timeseries of wet snow and in-cloud rime icing loads across Scotland. Extreme Value Analysis (EVA) was applied to annual ice load maxima using the Gumbel distribution specified by the engineering standards, and the Generalized Extreme Value (GEV) distribution, to produce maps of 3, 50, 150, and 500-year return values.

Map validation was provided in three stages; the verification of meteorological parameters against the available Met Office observations network data showed the climatology was captured well. Second, an observations-forced model showed those model data would not be responsible for any bias. Third, the modelled ice loads were compared to information discovered in the literature on icing events at the Deadwater Fell test site.

Results showed that the 50-year return values of wet snow loads at the two modelled heights were comparable with previous studies and the current standards, however 50-year return values of in-cloud rime ice loads were lower than expected. Further, the Gumbel distribution was a poor fit compared to the GEV distribution.

The work has highlighted many areas for further development and the challenges in modelling ice loads on overhead power lines, especially with limited icing observations. Furthermore, additional challenges were identified when reviewing how these values might be applied using the existing BS EN50341-2-9 framework.

Keywords – ***Overhead powerlines, numerical weather prediction, ice modelling, observations, low ice environment***

I. INTRODUCTION

While the practice of modelling snow and ice loads on overhead powerlines is examined extensively in the technical standards [1] and literature, and has achieved a high level of development and sophistication, its use in low ice environments such as the UK is less frequent and with less opportunity for validation.

The inclusion of snow and ice loads on overhead powerlines is a requirement of their design following BS EN 50341-1 [2] and its UK National Normative Aspects (NNA) in BS EN 50341-2-9 [3]. Current practice bases these calculations on the UK ice map [4] developed by the Met Office in the 1980s. Its predicted ice levels have not been observed in the historical record, suggesting there are costly over-estimations of ice loads within the design process. Further, the map and the NNA operate with ice loads measured by radial ice thickness, r_0 [millimetres], rather than $kg.m^{-1}$, adding complexity to the use of modern maps within the guidance of the standard.

This project uses modern numerical weather prediction (NWP) models and recent snow and ice accretion standards and literature to update the UK ice map to current practice while remaining within the framework required by the UK NNA.

II. METEOROLOGICAL MODELLING

Maps of gridded estimates of extreme ice loads were calculated by a model chain of meteorological modelling, ice accretion models, and extreme value analysis.

A. Meteorological variables

Meteorological variables were extracted from the Euro4 Hindcast dataset, which was generated from 2014 to 2015 using the Euro4 model, a part of the Met Office Unified Model which was the operational forecast suite of the time (Fig. 1).

The Euro4 model was initialised by each day of the ERA-Interim global reanalysis [5] 18Z run without assimilation of observations data, and run freely to T+30 hours (each 24 hour period to T+30 was used). The ERA-interim analysis was reconfigured using the Global model which provided the boundary and initial conditions for an intermediate 12km domain before downscaling further to the 4.4km grid over Europe. By initialising the Euro4 model every 24 hours with the downscaled ERA-interim analysis, a consistent hourly

hindcast from 1979 to June 2015 covering all of Europe at 4.4km resolution was produced.
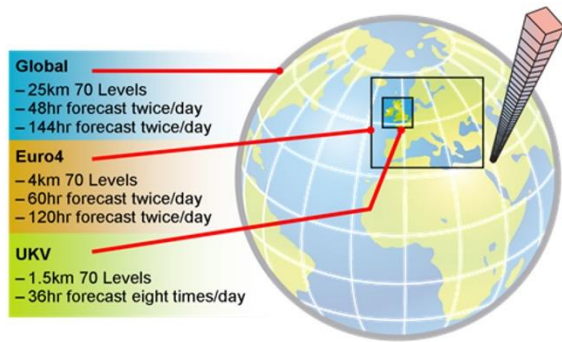
Fig. 1 Configuration of the Met Office Unified Model operational forecast suite in 2014.

B. Wind speed correction

Described by [6], the Unified Model employed parameterizations to correct for the effects of unresolved local terrain, including the use of an 'effective orographic roughness length' to represent the drag exerted on the near-surface flow. While the correction improved the modelling of the synoptic-scale weather, in regions of complex terrain such as Scotland the enhanced roughness caused an excessive reduction in the near-surface wind speed.

Developed following [7], the wind downscaling module within the Improver post-processing suite [8] provides tools to mitigate this impact, as well as other corrections that account for the impacts of differences between model orography and actual terrain elevations.

Experiments were conducted to identify the optimal combination of corrections specific to Scotland, with the result that only the roughness correction was applied. The selection was a compromise of delivering better verifying wind speeds in valleys where overhead line assets are more likely to occur at the cost of under-estimated, but plausible, wind speeds on high altitude terrain less suitable for grid infrastructure.

III. SNOW AND ICE MODELS

Being most recurrent in Scotland in the historical record, wet snow and in-cloud rime were modelled (following [1], [9] [10] [11]) to provide two sets of maps. For each icing mode, for each hour in the historical period, the scheme depicted in Fig. 2, assessed whether ice accretion or shedding occurred.
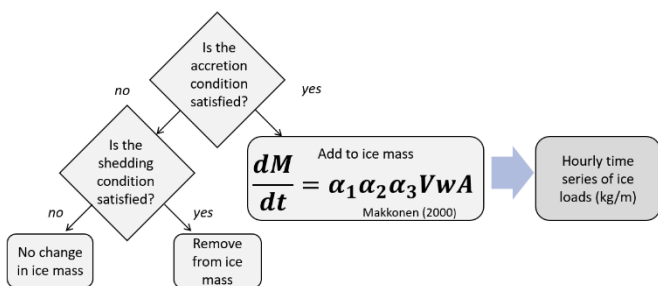
Fig. 2 Hourly scheme for the accretion or shedding criteria in both wet snow and in-cloud rime time series models.

The first phase of modelling used the BETA_SRU scheme [10] for the evaluation of wet snow sticking efficiency, β (or α_2). Unexpected high values of snow loads were generated at 33m

height above ground level and the persistence of snow loads in above-zero temperatures was deemed unphysical in specific accretion events. In a second phase of modelling the BETA_U scheme was used, and snow shedding was adapted, which solved these issues.

In the first phase both models were run for conductor diameters 14mm and 40mm, and hindcast model level heights above surface 13m and 33m, so that no vertical interpolation was necessary. In the second phase only the wet snow model was re-run, but with the inclusion of a 27mm conductor to assess non-linearity of snow load with conductor diameter.

Due to the data processing time and compute resource required, the ice accretion models were run at alternate model grid points (thereby 8.8km grid spacing) covering the domain of interest over Scotland at 890 locations plus 12 Met Office ground station locations and the Deadwater Fell test site for model validation.

IV. MODEL VALIDATION

Compared to regions at higher latitudes or continental land masses, the UK may be considered a low ice environment. The phenomenon of overhead line icing is less frequent, and consequently there have been few formal measurement campaigns. It was a particular challenge of the task that quantitative observations for the validation of model outputs were available only as annual summary values at the Deadwater Fell test site, reported in the literature [12]. Therefore, model validation was provided in three stages:

C. Input meteorological variables

Verification of four modelled meteorological variables (air temperature, precipitation, wind speed, and relative humidity) was conducted against standard observations at 39 Met Office ground weather stations across Scotland, which provided insight into the performance of the NWP model at a variety of locations and terrain altitudes representing overhead line networks.

Important variables specific to snow and ice accretion modelling are not recorded at standard weather stations in the UK and were not verified; particularly the in-cloud rime model's liquid water content (LWC), median volume droplet diameter (MVD), and droplet concentration (Nc).

1) Air Temperature: The overall mean bias of modelled air temperature at 1.5m height was -0.6 ± 1.2°C, but of greater relevance to the formation of ice was the comparison of quantile distributions spanning 0°C. At higher altitude sites (above 270m) the lower quantiles of modelled distributions showed a positive temperature bias. On lower ground the model was cooler, inferring a slightly greater frequency of freezing hours than were observed.

2) Precipitation: The overall bias of annual mean precipitation at 34 locations (since 5 high altitude sites were not equipped with rain gauges) was +271 ± 98mm. While the model's moderate over-estimation may partly be the result of unheated rain gauges failing to adequately measure frozen precipitation, an over-estimation in bins of 5mm per hour and above was also common.

3) Wind Speed: The 13m model level values of corrected wind speed were compared to standard 10m observations by cup anemometers. While sites below 270m elevation were a

mix of small over- and under-estimations, wind speeds at all sites at higher altitude were under-estimated. The application of the roughness correction improved the overall mean bias at 39 sites from -1.0 ± 2.3m/s to -0.4 ± 1.9m/s, without degrading the model performance at lower altitude sites.

4) Relative humidity: The overall mean bias in modelled relative humidity was +3.4 ± 3.4% but, like temperature, the greater relevance was the tail of the sites' quantile distributions approaching 100%, where cloud formation and precipitation become marginal. Akin to precipitation, generally the model over-predicted wetness in the upper tail of the distributions, except under-predictions at two small island sites in maritime environments where high wetness is expected, and two high altitude sites.

D. Observations-forced snow/ice models

The four modelled meteorological variables were further verified at nine weather station locations by modelling snow and rime loads at 13m height with modelled values replaced with observations where available, and comparing the resulting icing event maximum loads to purely modelled values. Events where any hour's observation was not available were discarded since those hours would be inappropriately zero-biased.

At all stations, for both wet snow and rime models, the comparisons were remarkable by their equality. Over the nine stations, for 14mm and 40mm conductors, the average maximum observations-forced wet snow event was 3.2 kg.m^{-1} and the average model bias was +2.3% ± 1.9%.

The maximum observations-forced rime event was 0.11 kg.m^{-1}, and were generally 2 orders of magnitude lower than wet snow. The average model bias was +3.9% ± 6.5%, the greatest being 17.2% at a site with very low ice loads.

E. Reported observations at Deadwater Fell test site

While numerical data of meteorological variables or individual icing events were not available from any UK test sites, sufficient information from Deadwater Fell was reported in the literature to provide indicative guidance on the current models' performance. Seasonal observed ice load maxima were reported by [12], which are compared to the wet snow model in TABLE I.

TABLE I. MODELLED MAXIMUM WET SNOW LOADS COMPARED TO SEASONAL OBSERVED MAXIMA AT DEADWATER FELL TEST SITE

Winter season	Observed ice load, kg/m	13m, modelled		33m, modelled	
		14mm	40mm	14mm	40mm
Feb-95	5.6	0.1	0.3	0.8	1.6
Jan-96	4.4	0.1	0.2	0.1	0.3
2005/06	1.4	0.2	0.5	0.7	1.6
2006/07	2.6	0.2	0.4	0.4	1.0
2007/08	0.8	0.3	0.8	0.9	1.7
2008/09	0.9	0.2	0.6	0.5	1.0
2009/10	3.0	0.2	0.6	0.8	1.8
2010/11	3.8	0.1	0.3	0.6	1.2
Period maximum, kg/m:		1.2	2.2	4.1	6.3

The maximum values recorded throughout the 35 year modelled period are also presented. Since the specifics (e.g.

line height and diameter) of the test site equipment were not available a precise comparison could not be made, but the period maximum observed and modelled values were similar.

Numerous examples of individual icing events presented in graphical format as line tension (in kilonewtons, kN) were also discovered in the literature, though as supplementary information was not available these could not be converted into ice mass and could be used only as indicators of icing events.

One such example provided by [13] of an event at Deadwater Fell in January 2008 is presented in Fig. 3, showing rime loads of similar order as wet snow. The comparable modelled temperature, and wet snow and rime masses for the period are presented in Fig. 4. The temperature trace bears good resemblance to the observed values, and occurrences of both the wet snow and the two rime icing periods were captured by the model – albeit as an incorrect order of magnitude for the latter.
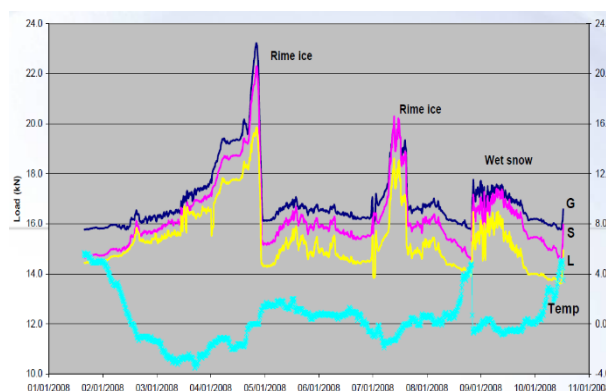
Fig. 3 Observed temperature and line tension (kN) due to rime ice and wet snow at Deadwater Fell in January 2008, reported by [13]
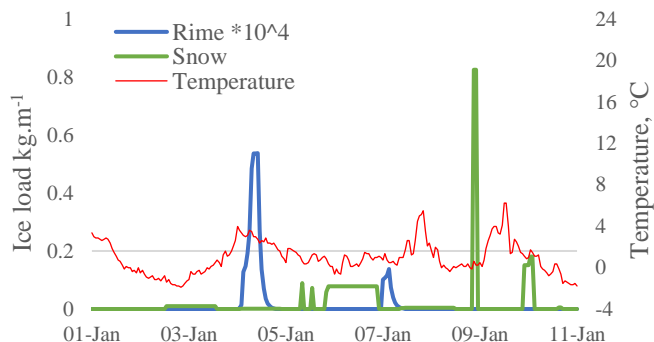
Fig. 4 Modelled temperature, rime and wet snow loads for the event presented in Fig. 3.

In other similar cases, [14] [15], the models demonstrated similar levels of capability in capturing most icing events. The study also provided diagnosis of the implausible persistence of wet snow events that led to revision of the shedding scheme in the second phase of modelling.

V. EXTREME VALUE ANALYSIS

For rime ice and wet snow loads individually, the 3, 50, 150, and 500-year extreme return levels were generated, with their associated mean, 83.4, and 97.5 percentiles to account for the uncertainty in the estimation. The UK standards recommend use of the Gumbel distribution, but model checking showed clearly that this fitted the data poorly, systematically

underestimating the ice load return levels. An alternative analysis was based on a Generalized Extreme Value (GEV) distribution that provided a better fit to the simulated ice loads, and more reliable estimation of 50-year return values. Examples of each type at the Leuchars weather station are presented in Fig. 5, which was representative of each of the weather stations tested.
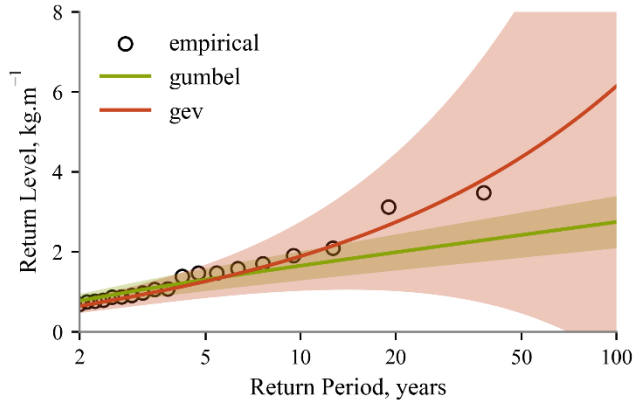
Fig. 7 Fitted return level plots of wet snow accretion modelled at the Leuchars weather station by Gumbel and Generalized Extreme Value distributions, with 95% confidence intervals shaded.

VI. MODEL OUTPUTS

Maps of snow and rime loads were provided for each of the model configurations described in section III. Fig. 6 presents a comparison of the rime and wet snow 50-year Return Levels on a 14mm conductor at 13m height, showing the sparse distribution of rime loads of the same order as wet snow. Fig. 7 shows a comparison of 50-year Return Levels calculated using the Gumbel and GEV distributions, for wet snow loads on a 27mm conductor at 33m height. The plots show the higher values estimated by the GEV.

The geographic distribution of modelled wet snow loads indicates an increase over the western mountains of the Scottish mainland from lower values over the Outer and Inner Hebrides, and the Orkney and Shetland Islands. A region of high values sits to the south east of the Cairngorm mountains.

VII. ADAPTION TO BRITISH STANDARDS

To prepare this study's estimated ice loads [kg.m^{-1}] for the BS EN 50341-2-9 [3] framework in radial ice [mm] required the reversal of the standard's formulae to deliver a single normalised ice map similar to the UK ice map [4], on which subsequent calculations would be based. The exercise produced much wider than expected variation in the normalised values of radial ice at each point. The average standard deviation of combinations of line height and diameter was 31%.

A review of the formulae used, identified two potential causes for the variation observed. Firstly, a linear equation was used to adjust for conductor diameter, despite the relationship between conductor diameter and ice load being non-linear. Secondly no differentiation was made by the standard in adjusting for site altitude and in adjusting for height above ground, instead a single wire altitude was used. This initial exercise indicates that a change in methodology to calculating ice values requires a reflective change in approach by the standard.
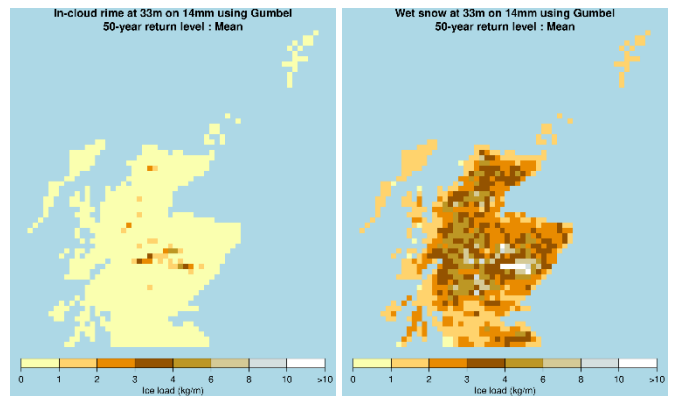
Fig. 6 Comparison of the spatial distribution of modelled rime [left] and wet snow [right] loads on a 14mm conductor at 33m height.
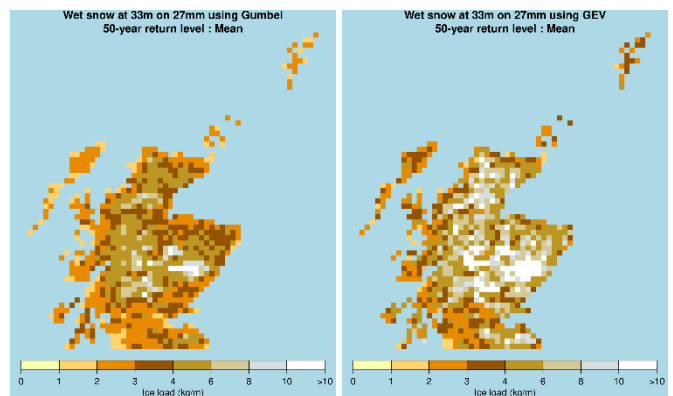
Fig. 6 Comparison of return levels of wet snow loads on a 27mm conductor at 33m height using Gumbel [left] and Generalized Extreme Value [right] distributions.

This conclusion was reinforced by a further complexity encountered. The mechanisms within the standard for changing return periods are based on the Gumbel distribution and were found to be incompatible with the GEV datasets.

VIII. DISCUSSION

With little data available for the verification of ice loads, validation of the models depended on verification of the meteorological dataset, with heavy reliance on the validity of the empirical ice models discovered in the literature.

A. Meteorological model

The verification against the Met Office observations network showed only small to moderate biases, suggesting the model was successful in capturing the general long-term climatology with no anomalous behaviours at any sites. The observations-forced model verification showed those parameters would not be responsible for ice load biases.

However, being a low ice environment, the meteorological variables relating specifically to icing are not measured at standard UK weather stations, and are a lower priority in operational forecast model development. Such variables could only be assessed qualitatively in reference to the literature.

B. Wet snow accretion model

The modelled 50-year Return Levels of wet snow are comparable with previous studies, and long-term readings at the Deadwater Fell test site. The western edge of the region of higher snow loads sits over the mainland mountains, rather than the islands of the Inner Hebrides as in the current UK ice

map. Its spatial distribution bears close similarity to snowfall days data produced by the UK National Climate Information Centre [16].

C. In-cloud rime accretion model

The 50-year Return Levels of in-cloud rime were lower than expected, resulting in only a sparse distribution of ice loads similar to wet snow. Nygaard [12] suggests rime and snow would be of similar order at Deadwater Fell, but here modelled rime was an order of magnitude lower than snow.

The reason for this needs further investigation, though standard meteorological variables were excluded as a cause. Other possible reasons include the 4km model resolution being insufficient, as found with [12], or the under-prediction of cloud liquid water content. The empirical evaluation of collision efficiency parameter (α_1) carried high uncertainty since cloud parameters were not verified and a sensitivity analysis was not conducted.

Nonetheless, value may be identified in the rime ice maps to highlight areas associated with a high risk of rime icing.

D. Extreme Value Analysis

The standards require expected 50-year return levels for ice loads based on fitting a Gumbel distribution to annual maximum ice loads. For many other industries and countries higher quantiles of the fitted probability distribution are required to account for the uncertainty in the estimation, and so 83.4, and 97.5 percentiles were also provided.

Though UK standards suggest estimation based on the Gumbel distribution, model checking clearly showed a poor fit, with ice load return levels systematically underestimated. The alternative GEV distribution provided a much better fit to the simulated ice loads, and more reliable estimation of 50-year return values. However, unlike the Gumbel, at long return periods the GEV values become physically implausible, indicating uncertainty with the wet snow model.

E. Application of results in engineering design

Initial work in applying the ice values to existing UK standards found that the current standard's formulae were overly simplistic and produced results that diverged notably from the values produced by this study. Likewise, the standard being based on the Gumbel distribution was not readily compatible with the GEV values. Further work is required to enable adoption of these values with the existing framework and ultimately, a fundamental revision to the standard may be required.

F. Further development of models

The greatest need for further development is in real world observations for model verification. While the spatial distribution and magnitude of wet snow loads fit with previous studies and operational experience, ice load data of real individual icing events were not available for model testing. This would include the need for weather variables specific to precipitation and cloud physics.

Being a distinct mode of ice accretion, it is not assumed that the spatial distribution of in-cloud rime would match wet snow. Following previous studies a high resolution weather model or sensitivity analysis of unknown variables may provide insights into the low values produced.

The analysis did not account for climate change since the current standards do not require it. Accounting for climate change and other large scale weather patterns, such as an increased prevalence of glaze ice in the UK is possible.

IX. CONCLUSIONS

Icing on overhead powerlines in the UK is a less severe phenomenon than colder climates, but remains an important consideration in the design of new infrastructure required by UK standards. While typical ice loads are lower, the unavailability of observations data for model tuning and verification, and the lower prioritisation for study thus leads to significantly greater uncertainty in modelled extreme ice loads. The uncertainty limits the cost savings that modern modelling techniques may offer over current methods developed in the 1980s, and remains a hinderance to the acceptance of modern methods in technical standards.

REFERENCES

[1] International Organization for Standardization, "ISO 12494," *Atmospheric icing of structures,* 2017.

[2] British Standards Institute, "BS EN50341-1," *Overhead electrical lines exceeding AC 1 kV,* 2012.

[3] British Standards Institute, "BS EN50341-2-9," *Overhead electrical lines exceeding AC 1 kV National Normative Aspects (NNA) for Great Britain and Northern Ireland,* 2017.

[4] British Standards Institute, "BS EN 1993-3-1:2006," *Eurocode 3. Design of steel structures. Towers, masts and chimneys. Towers and masts ,* 2008.

[5] D. P. Dee, S. Uppala, A. Simmons, P. Berrisford, P. Poli, S. Kobayashi, U. Andrae, M. Balmaseda, G. Balsamo, P. Bauer, P. Bechtold, A. Beljaars, L. van de Berg and J. Bidlot, "The ERA-Interim reanalysis: configuration and performance of the data assimilation system," *Qart. J. R. Meteorol. Soc.,* no. 656, pp. 553-597, Apr 2011.

[6] J. Standen, C. Wilson, S. Vosper and P. Clark, "Prediction of local wind climatology from Met Office models: Virtual Met Mast techniques," *Wind Energy,* pp. 20(3), 411–430, 2016.

[7] T. Howard and P. Clark, "Correction and downscaling of NWP wind speed forecasts," *Meteorological Applications,* p. 14 105–116, 2007.

[8] Met Office, "IMPROVER: Integrated Model post-PROcessing and VERification (Revision f5e46c1e)," 2019. [Online]. Available: https://improver.readthedocs.io/en/latest/about.html.

[9] L. Makkonen, "Models for the growth of rime, glaze, icicles and wet snow on structures," *Phil. Trans. R. Soc.,* p. 358, 2000.

[10] B. Nygaard, H. Ágústsson and K. Somfalvi-Tóth, "Modeling Wet Snow Accretion on Power Lines: Improvements to Previous Methods Using 50 Years of Observations," *J App Met Clim,* no. 52(10), p. 2189–2203, 2013.

[11] B. Nygaard, L. Carlshem, J. Bartsch, L. Lee and H. Ágústsson, "Development of a 50-year return value ice load map for Sweden," in *Proceedings – Int. Workshop on Atmospheric Icing of Structures (IWAIS)*, Reykjavík, 2019.

[12] B. Nygaard, I. Seierstad and A. Veal, "A new snow and ice load map for mechanical design of power lines in Great Britain," *Cold Reg. Sci. Technol.,* pp. 108, 28-35, 2014.

[13] B. Wareing, "Relation between test span measured ice loads and conductor size," in *IWAIS*, Uppsala, Sweden, 2015.

[14] S. Fikke, G. Ronsten, A. Heimo and e. al., "COST-727: Atmospheric Icing on Structures Measurements and Data Collection on Icing: State of the Art," MeteoSwiss, 2006.

[15] R. Cattin, D. Silke, B. Nygaard, K. Säntti and B. Wareing, "COST-727 ACTION: Measurements and Simulations," MeteoSwiss, 2008.

[16] Met Office, "Days of sleet/snow falling. Annual average 1981-2010," 2023. [Online]. Available: https://www.metoffice.gov.uk/research/climate/maps-and-data/uk-climate-averages/gcj8ds2s3.

Comparison of different methodologies for the identification of wet-snow conditions for snow sleeves forecast accretion on the Italian overhead transmission lines

Riccardo Bonanno[1], Matteo Lacavalla[1], Bruno Vitali[1]

[1] RSE SpA – Ricerca sul Sistema Energetico, Milan, Italy

riccardo.bonanno@rse-web.it, matteo.lacavalla@rse-web.it, bruno.vitali@rse-web.it

Abstract— **Wet snow is a critical atmospheric phenomenon that has a significant impact on the overhead power lines in Italy during the winter season. This particular type of snow is characterized by flakes with a high liquid content, which have the ability to adhere to the conductors of the power lines. As a result, heavy snow sleeves form on the conductors, leading to numerous electrical failures and significant structural damage to the lines. In order to enhance the resilience of the Italian electricity system, a forecasting and warning system called Wet-snow Overload aLert and Forecasting (WOLF) has been implemented. This forecasting tool serves as an information system able to predict the occurrence of wet snow overload on the overhead power lines across Italy.**

The purpose of this study is to explore an alternative method for identifying wet snowfalls that can complement the current Thermal Window method (TW) used in the operational system. The Thermal Window method relies on a specific temperature range (-1°C - +1.5°C), which has been determined based on various experimental case studies conducted at the snow sleeves monitoring facility in Vinadio, located in the Western Italian Alps at an altitude of 950 m agl. In contrast, the alternative method is based on the fraction of Frozen Precipitation (FP), which refers to the proportion of solid precipitation content compared to the total content (solid + liquid). This variable can be derived from the outputs of the meteorological model currently employed in the WOLF system, using the mixing ratios of the solid and liquid fractions of hydrometeors. To better understand the physical processes of snow in the complex orographic region of the study, high spatial resolution (1 km) test simulations were conducted on an area centered on Vinadio. The WRF-ARW model, with the same operational configuration as the WOLF forecasting tool, was utilized for these simulations. Similar to the operational tool, the meteorological outputs were used to feed the Makkonen wet snow accretion model (ISO 12494:2017), which describes the growth of a cylindrical sleeve on a typical High Voltage (HV) overhead conductor. In Vinadio, the Wet-snow Ice Laboratory Detection station (WILD) provides measurements of the snow sleeve mass on High Voltage (HV) overhead conductors, along with the main weather parameters involved during the snow accretion.

The comparison between the modeled and measured snow mass at the Vinadio station for various wet-snow case studies indicates that the FP method is more effective in predicting the timing of wet snow events and the alternation of wet and dry snow precipitation during an ongoing event. On the other hand, the thermal window method generally exhibits less accuracy in determining the timing of wet snow conditions and often leads to imprecise estimations of the sleeve load.

Simulations with different meteorological drivers (i.e., the ECMWF Integrated Forecasting System (IFS) and the Global Forecast System (GFS)) were also carried out in order to analyze the differences in performance of the meteorological predictions for the most significant wet snow events occurred in the recent years.

Keywords— *wet-snow, slow sleeves, overhead power lines, thermal window, hydrometeors*

I. INTRODUCTION

Wet snowfall prediction is still one of the most complex challenges from a modeling/prediction perspective. Wet snowfalls are characterized by a high adhesion capacity of snowflakes to conductors due to the presence of liquid water in the snowflake (Liquid Water Content, LWC). The snowflake can increase its liquid fraction, either because of its formation in clouds in the presence of supercooled liquid water or because it encounters warmer layers along its falling path. This study aims to investigate a new methodology for identifying wet snowfall that can be an alternative or complementary to the Thermal Window (TW) methodology currently used in the Wet-snow Overload aLert and Forecasting system (WOLF). According to the TW methodology, wet snow occurs when 2m air temperature T2m falls within a certain range (typically between -1°C and +1.5°C), which has been established based on some experimental case studies at the Wet-snow Ice Laboratory Detection station (WILD) in Vinadio at an altitude of 950 m a.s.l.. The new method, on the other hand, is based on the fraction of Frozen Precipitation or Snow Ratio (SR) that is, the fraction of solid precipitation content to total content (solid + liquid). This variable can also be derived from the meteorological models currently used in RSE from the mixing ratio of the solid and liquid fractions of hydrometeors. More precisely, the SR is defined in Equation 1 [1] as:

$$SR = \frac{Q_{graup} + Q_{snow}}{Q_{graup} + Q_{snow} + Q_{rain}} \qquad (1)$$

where Q_{graup} represents the graupel mixing ratio (kg kg⁻¹), Q_{snow} is the snow mixing ratio and Q_{rain} is the mixing ratio of the liquid part of the precipitation. The SR value has a direct influence on the sticking coefficient of the snowflake. The maximum adhesion of the snowflake on the surface conductor usually occurs within a specific range of SR values. In contrast, a snowflake that is too dry will hardly be able to stick to the surface of the conductor. Several formulations can be found in the literature defining the optimal range of the SR [2]. Admirat

[3] proposed SR values in the range of 0.7 to 0.98; Sakamoto [4] proposed a wider range between 0.5 and 0.98. For this study, we considered a wider SR range (0.5 <SR < 0.98) by analyzing some of the most significant case studies of wet snowfall that occurred in recent years at the WILD station.

A comparison with two different wet snow identification methodologies, namely, the thermal window (TW) and the Snow Ratio (SR), is carried out. The newest version of WRF-ARW [5] (v 4.5) was used, and a comparison of the forecasting performance obtained with different model drivers (IFS and GFS) and with different types of microphysics was performed.

II. Analysis of wet snow events on Vinadio with different forecast drivers and different types of microphysics

In Table I, the snow sleeve masses measured in the two Vinadio case studies analyzed in this study are shown.

TABLE I. List of wet (w) snowfall case studies analyzed at the Vinadio WILD station with their respective sleeve masses at the end of the event.

Case study	Event Type	Sleeve mass at the end of the event
01/12/2019	Wet-snow	3.2 kg/m
28/02/2016	Wet-snow	10 kg/m

The Snow Ratio (SR) and 2m temperature, the two variables involved in the proposed methodologies for wet snow identification, are both direct outputs of the WRF-ARW model used for the 1 km high-resolution simulations. In the following table (Table II), different definitions of wet snow and dry snow conditions based on the two methodologies are illustrated. The 2m temperature range for the maintenance and shedding of snow sleeves is also defined on the basis of experimental evidence from different case studies at the WILD station. Similarly, reasonable values for the SR range for the same conditions were also derived.

TABLE III. SR and t2m values associated with different wet and dry snow conditions for the two different methodologies (SR and FT) in the presence of precipitation.

Condition	SR	TW
Dry-snow	SR > 0.98	T2m < -1.0°C
Wet-snow	$0.5 \leqslant SR \leqslant 0.98$	$-1.0° \text{ C} \leqslant T2m \leqslant 1.5°C$
Maintenance	$0.1 \leqslant SR < 0.5$	$1.5° \text{ C} \leqslant T2m \leqslant 2.0°C$
Shedding(Rain)	SR<0.1	T2m >2.0°C

As mentioned before, the performances of different meteorological drivers (IFS ECMWF and GFS) in reproducing temperature and precipitation conditions are investigated for the two wet snow events mentioned above. The newest version of the WRF-ARW model (v 4.5) was used and properly configured to perform simulations at 1 km spatial resolution considering the same physical parametrization used in the WOLF operational setting. In this high-resolution

configuration, some parameters of the model namelist are properly set to avoid numerical instability during simulations that may occur in simulations covering territories with very complex orography, such as the Alpine region. Owing to these high-resolution simulations, the representative point of the WILD station with a similar orography is very close to the actual position (lat=44.31, lon=7.18).

Because of the complex orography in the analyzed domain and the strong difference in resolution between the drivers and the 1 km target grid, nesting was necessary to allow a gradual transition of initial and boundary conditions from the lower resolution of the meteorological driver (9 km for IFS, 25 km for GFS) to the finer resolution of the target grid. In Fig. 1, the nesting configurations used for the scale transition from the respective drivers to the finer 1-km grid are shown. For the IFS ECMWF driver, an intermediate grid at 3 km was sufficient, while for the GFS driver, two intermediate grids at 9 and 3 km were necessary.
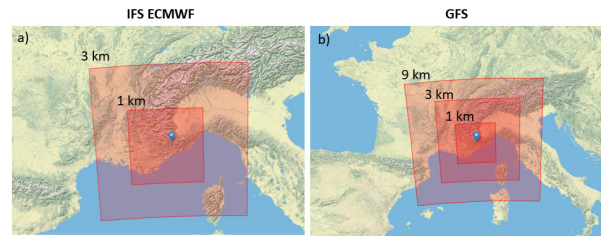
Fig. 1 Nesting configuration of the WRF-ARW model simulations with two different model drivers, IFS ECMWF (a) and GFS (b).

Three types of microphysics schemes were also tested in the simulations: the classical Thompson scheme [6], which is usually the most suitable for simulating snow events; the Thompson Aerosol Aware [7], which is a variant of the former that also considers the presence of aerosols; and the Morrison scheme [8]. The latter, coupled with the planetary boundary layer scheme of Mellor-Yamada-Janjic (MYJ), is also considered in some studies [9] to perform well in the simulation of snow events.

A. Case Study of December 1st, 2019

In this case study, an Atlantic trough approaches the western Mediterranean Sea, as evidenced by the synoptic maps of geopotential height and temperature at 500 hPa derived from the ERA5 reanalysis [10] (Fig. 2, a). This low-pressure system results in a moist and warm southwesterly flow in the upper atmosphere over northern Italy, while in the lower part (850 hPa,), a colder air layer lies in the Po Valley region (Fig. 2, b). The southwesterly flow conveys convective cells originating over the Ligurian Sea across the northwestern Italian Alps, resulting in a "mixed" type of precipitation in these regions, partly advective and partly convective. As evidence of this, in Fig. 3, a lightning map related to the central hours of December 1st, 2019 is shown. Convective systems can be clearly observed over the French coast and the southwestern Alps. In this case study, a snow sleeve mass of approximately 3.2 kg/m was measured at the end of the event, and an accumulated precipitation of 46.4 mm was recorded at the WILD station.
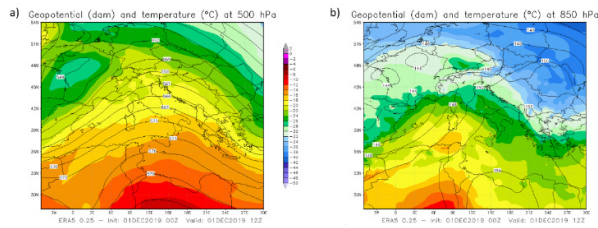
Fig. 2 Geopotential and temperature at isobaric levels of 500 (, panel a) and 850 hPa (, panel b) over the Mediterranean region from the ERA5 reanalysis for the December 1st 2019 case study.
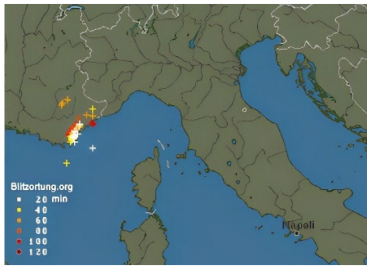
Fig. 3 Lightning map related to 18 UTC on December 1st 2019. Image from https://www.blitzortung.org/.

Fig. 4 shows the 24-hr accumulated precipitation on December 1st, 2019, over the 1 km domain predicted by the WRF-ARW model driven by the IFS ECMWF (a, hereinafter referred to as WRF-IFS) and by the GFS (b, hereinafter referred to as WRF-GFS). According to the figure, the WRF-IFS accumulated precipitation appears to be overestimated with respect to that of the WRF-GFS. In both simulations, the peaks of very intense precipitation associated with convective cells moving from the French coast toward the southwestern Alps can be observed, with the most intense peaks occurring in the WRF-IFS.
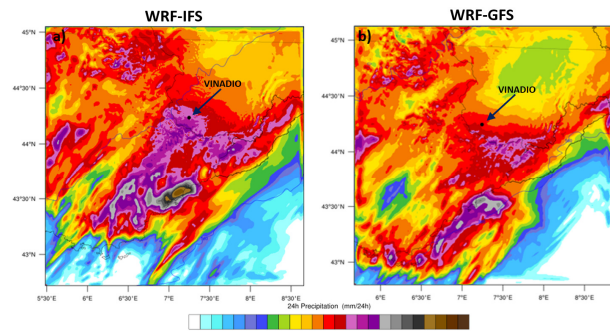
Fig. 4 24-hr accumulated precipitation on December 1st 2019, predicted by the WRF-IFS (a) and WRF-GFS (b). The black dot indicates the WILD station in Vinadio.

To better investigate the performance of the forecasts of the two different drivers, Fig. 6 can be analyzed. Time series of 2m temperature and accumulated and hourly precipitation are shown. From the analysis of Fig. 5, the WRF-IFS better describes the temporal distribution of precipitation during the day than does the WRF-GFS simulation, except in the final phase of the event where a noticeable deviation from the observation occurs, which is probably associated with a wrongly predicted convective event that did not actually occur. In this partially convective environment, an inaccurate location for the prediction of convective clusters can result in major deviations in precipitation values from those observed.

As far as temperature is concerned, the WRF-IFS predictions show the best agreement with the observations compared with those from the WRF-GFS simulation, especially in the early phase of the event. From a meteorological point of view, therefore, the WRF-IFS is the one resulting in the best forecast of temperature and precipitation.
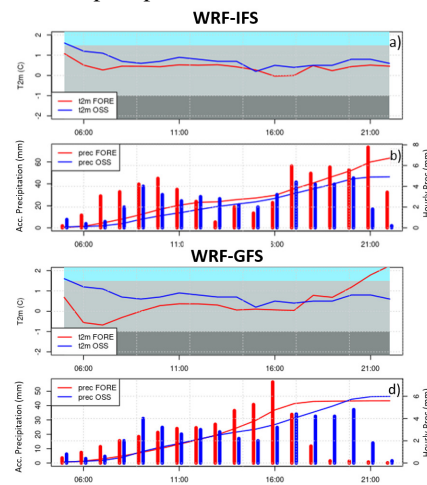
Fig. 5 2m temperature (a, c) and accumulated and hourly precipitation (c, d) for the December 1st 2019 event for the WRF-IFS (a, b) and WRF-GFS (c, d) runs. The red lines show the forecast time series, while the blue lines show the observations. In panel (c), the histograms indicate the hourly precipitation (mm), and the continuous lines indicate the 24-hr accumulated precipitation.

To investigate the performance of the WRF-IFS model in terms of snow sleeve mass forecasting, Fig. 6 can be analyzed, where time series of 2m temperature, Snow Ratio SR, precipitation, and snow sleeve mass are shown. The snow sleeve mass is calculated using the Makkonen model [11] considering the two wet/snow identification criteria based on the SR and TW and considering a typical high-voltage aluminum reference conductor with a 31.5 mm diameter.
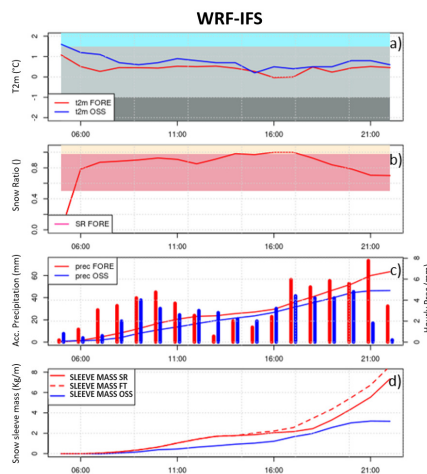
Fig. 6 2m temperature (a), Snow Ratio SR (b), precipitation (c) and snow sleeve mass (d) for the December 1st 2019 event in the WRF-IFS run. The red lines show the forecast time series, while the blue lines show the observations. The dashed red line in the snow sleeve mass panel indicates the TW method estimate, and the continuous red line indicates the SR method estimate. The pink band in figure (b) indicates the typical range of SR values for wet snow (0.5<SR<0.98), and the yellow band refers to the SR range related to

dry snow (SR≥0.98). In panel (c), the histograms indicate the hourly precipitation (mm), and the continuous lines indicate the 24-hr accumulated precipitation.

From the analysis of Fig. 6, the snow sleeve mass is found to be incorrectly estimated in both simulations. Both SR and TW methods overestimate the sleeve mass, but TW to a greater extent than SR method. The SR method predicts a dry snow condition that slows the growth of the snow sleeve, making the estimation closer to the observations. As far as the WRF-GFS simulation is concerned, the final snow mass is similar to the observation, but there is a large deviation between the observed and the predicted curve in the final part of the event. The snow mass simulations with the WRF-IFS run slightly deviated from the observed curve during the day and diverged only at the end of the event due to the final overestimation of precipitation mentioned above.

In this partially convective environment, it is interesting to draw attention to the vertical profile of the SR instead of considering only its surface values. From the maps shown in Fig. 7, and in particular from the vertical cross section (b), some regions of the upper atmosphere above the Vinadio station with SR values far lower than 1 can be observed. In this case, despite temperatures far below 0°C, some water can be observed in the clouds, probably because of supercooled liquid water associated with convective cells carried by the southwestern moist and warm flow associated with the Atlantic trough.
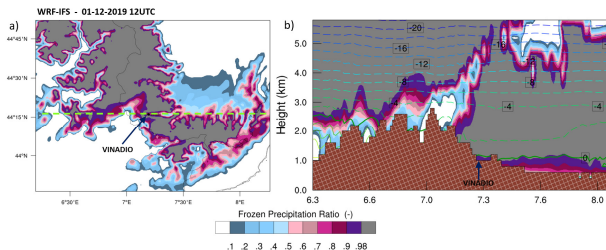
Fig. 7 Snow Ratio (SR) map (a) and W-E cross section of the SR variable and temperature (°C) (b) at the representative point at the Vinadio station (WILD) from the WRF-IFS simulation. The map refers to 12 UTC on December 1st 2019.

Considering the simulations carried out with the different types of microphysics mentioned above, the Thompson Aerosol Aware is the one that leads to the best estimation of snow sleeve mass compared to the other microphysics (not shown for brevity). In fact, this simulation predicts a time window with SR values lower than 0.5 in the central part of the event, temporarily interrupting the growth of the snow sleeve (maintenance phase) and allowing a better agreement of the estimated snow sleeve mass with the observation with respect to the classical Thompson microphysics (Fig. 6, a). Only in the final part of the event, the precipitation, and consequently, the snow mass was still strongly overestimated.
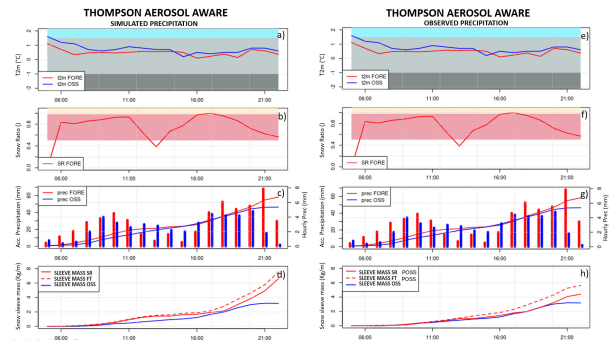
Fig. 8 Same as Fig. 6; (a), (b), (c), and (d) refer to the WRF-IFS simulations with Thompson Aerosol Aware microphysics; and (e), (f), (g), and (h) refer to the same run but with the snow sleeve mass modeled with the observed precipitation.

By trying to remove the error in precipitation prediction when simulating the snow sleeve mass with the observed precipitation, the improvement in the prediction of snow sleeve mass for this event is even more evident. The overestimation remains only in the final part of the day, probably related to an incorrect prediction of SR values. In the final part of the event, in fact, the SR values drop significantly but not enough to fall below the 0.5 threshold, which would have allowed the interruption of the growth of the snow sleeve and his maintenance of mass values more comparable with the observation.

B. *Case Study of February 28th 2016*

This case study is the most important in terms of the sleeve mass reached in the historical time series of measurements at the WILDstation, for which the sleeve mass was approximately 10 kg/m at the end of the event and for which the cumulative precipitation between 12UTC on February 28th and 12UTC on February 29th was approximately 80 mm. In Fig. 9, the geopotential height and temperature at 500 and 850 hPa are shown. This event was the result of a rather classic weather configuration, with a low-pressure system located over the western Mediterranean Sea (Fig. 9, a). This configuration conveys southerly flow over Northern Italy, gradually replacing the colder air masses stationed over the Po valley region (Fig. 9, b).
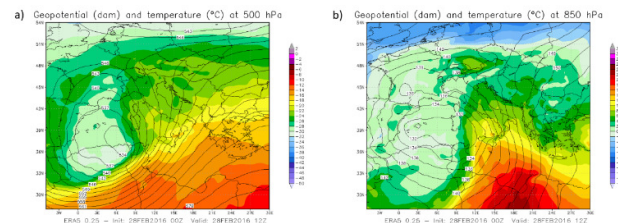
Fig. 9 Geopotential and temperature at isobaric levels of 500 (a) and 850 hPa (b) over the Mediterranean area from the ERA5 reanalysis for the case study of February 28th 2016.

Examining the accumulated precipitation resulting from the WRF simulations with the two different drivers IFS and GFS (Fig. 10), we can see that both runs predicted similar patterns, with comparable spatial distribution of precipitation. If we focus instead on the very narrow valley where Vinadio is located., the WRF-IFS simulation leads to the best estimate of precipitation (approximately 80 mm/24 hr), while the WRF-GFS simulation leads to an underestimation

(approximately 60 mm/24 hr). Because of the lower precipitation estimation performance in this case study, the WRF-GFS run was excluded from the computation of snow sleeve mass with the Makkonen model.
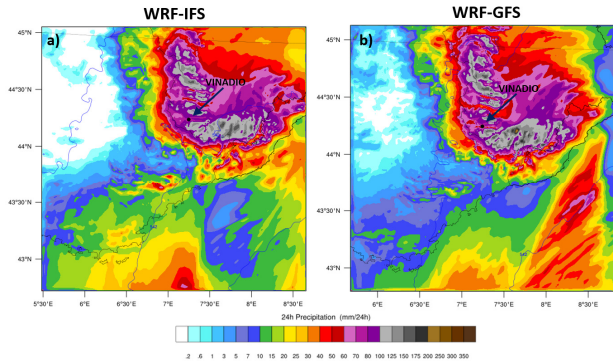
Fig. 10 As in Fig. 4 but for the case study of February 28th 2016.

Fig. 11 shows the performance of the WRF-IFS run in estimating the snow sleeve mass. The predicted precipitation is in phase with the observed precipitation, whereas the 2m temperature is not in full agreement with observations.
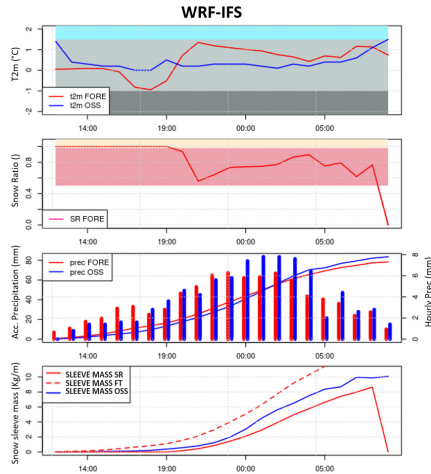
Fig. 11 As in Fig. 6 but for the case study of February 28th 2016.

WRF-IFS run with the SR method succeeded in achieving a snow sleeve mass comparable to that of the observation, with a slight underestimation (approximately 8 kg/m vs 10 kg/m measured). The TW method, on the other hand, leads to a strong overestimation of the sleeve mass, which reaches values of approximately 15 kg/m (not shown in the figure). The better performance of the SR method lies in the timing of snow sleeve formation, which is more accurate than that of the TW method, which instead anticipates sleeve formation by several hours, thus leading to a strong overestimation of the predicted mass.

Considering the SR map (Fig. 12, a) in the study domain and its vertical profile (Fig. 12, b), we can observe some differences with respect to the previous case study. SR values lower than 1 are distributed across the alpine valley at altitudes with positive temperatures, whereas SR values higher than 0.98 (gray areas) are located at high altitudes in the alpine region with negative temperatures. This is confirmed by the SR cross section (Fig. 12, b), in which SR values lower than 1 are concentrated only in the lower troposphere below the 0°C

isotherm. The differences in SR distribution over the alpine domain and in the vertical profile with respect to the previous case study are related to the absence of convective clouds (and consequently of supercooled liquid water) in this type of event.
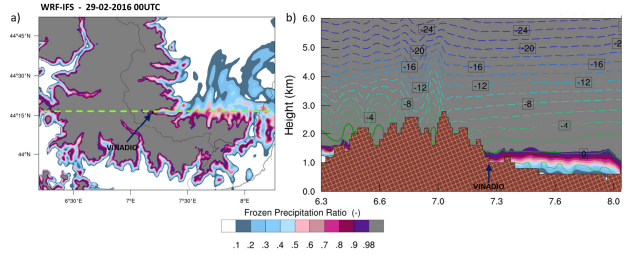
Fig. 12 As in Fig. 7 but for the February 28th 2016 case study.

The last part of this study is related to the impact of different types of microphysics on the simulated temperature and precipitation and, consequently, on the prediction of the snow sleeve mass. As in the previous case study, three different model simulations were carried out, leaving the model physics unchanged but changing only the microphysics options. Comparing the different simulations (not shown for brevity), Morrison microphysics (Fig. 13) leads to a better prediction of temperature than does both Thompson microphysics, especially in the early part of the event. However, for precipitation, Morrison microphysics leads to a slight overestimation, which results in a very good agreement between the simulated snow sleeve mass and the observation using the SR methodology. On the contrary, for all three microphysics, the TW method strongly overestimates the sleeve mass at the end of the event.
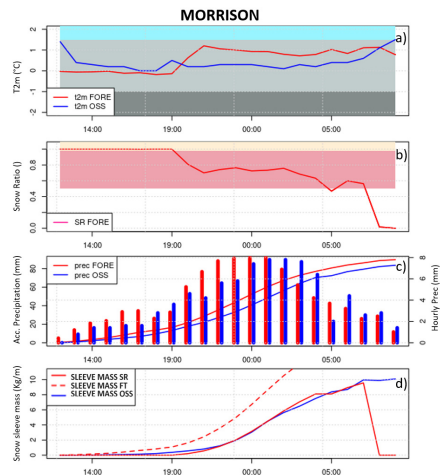
Fig. 13 Same as in Fig. 6 but for the case study of February 28th 2016, using Morrison microphysics.

III. CONCLUSIONS

In this study, the two most significant wet snow events that occurred at the WILD station in Vinadio were analyzed, considering 1 km simulation with the most recent version of the WRF-ARW model, comparing simulations with different model drivers (IFS and GFS) and with three different types of microphysics. These analyses showed good performance with the simulations driven by the IFS driver in the forecasting of

the meteorological variables of temperature and precipitation and in the estimation of snow sleeve mass; these findings were more evident in the second case study (February 28th 2016) and less evident in the first case study (December 1st 2019). In fact, the first case is more complex to simulate because of its mixed characteristics (convective and advective), with wet snow phases alternating with some dry time windows and with probable phases of very wet snow (SR <0.5) in which snow sleeve accretion did not occur. The analyses performed on these case studies also show the general advantage of the SR-based methodology respect to the TW-based methodology in estimating snow sleeve mass. From the microphysics point of view, which method performs better in estimating sleeve load is generally not so evident. In the first case study, the Thompson Aerosol Aware microphysics is the one that allows the best estimation of the snow sleeve mass for the most part of the event and is able to simulate a wet phase of the snowfall (SR < 0.5) in the central hours of the day, which has contributed to a better alignment of the predicted snow sleeve mass with the measurements. However, such microphysics did not help to smooth out the overestimation of the sleeve mass at the end of the event, even if the error in the precipitation estimation was removed by reconstructing the sleeve mass with the observed precipitation. In the second case study, instead, the Morrison microphysics appears to have an advantage over the other methods because of the better description of the temperature in the early phase of the event.

References

[1]   J. A. Milbrandt, A. Glazer and D. Jacob, "Predicting the Snow-to-Liquid Ratio of Surface Precipitation Using a Bulk Microphysics Scheme," *Mon. Wea. Rev.,* vol. 140, p. 2461–2476, 2012.

[2]   B. E. K. Nygaard, H. Ágústsson and Somfalvi-Toth, "Modeling Wet Snow Accretion on Power Lines: Improvements to Previous Methods Using 50 Years of Observations," *Journal of Applied Meteorology and Climatology,* pp. 2189-2203, 2013.

[3]   P. Admirat, "Wet snow accretion on overhead lines," *Atmospheric Icing of Power Networks ,* p. 119–169, 2008.

[4]   Y. Sakamoto, "Snow accretion on overhead wires," *Philos. Trans. Roy. Soc. London,* p. 2941–2970, 2000.

[5]   W. Skamarock, J. Klemp and J. Dudhia, "A Description of the Advanced Research WRF Version 3," *Tech. Note NCAR/TN-475+STR,* 2008.

[6]   G. Thompson, P. R. Field, R. M. Rasmussen and W. D. Hall, "Explicit forecasts of winter precipitation using an improved bulk microphysics scheme. Part II: Implementation of a new snow parameterization.," *Mon. Wea. Rev.,* vol. 136, p. 5095–5115, 2008.

[7]   G. Thompson and T. Eidhammer, "A Study of Aerosol Impacts on Clouds and Precipitation Development in a Large Winter Cyclone," *Journal of the Atmospheric Sciences,* vol. 71, no. 10, p. 3636–3658, 2014.

[8]   H. Morrison, J. A. Curry and V. I. Khvorostyanov, "A new double-moment microphysics scheme for application in cloud and climate models. Part I: Description.," *J. Atmos. Sci.,* vol. 62, p. 1665–1677, 2005.

[9]   P. Ghafarian, "Impact of physical parameterizations on simulation of the Caspian Sea lake-effect snow," *Dynamics of Atmospheres and Oceans,* vol. 94, 2021.

[10]   H. Hersbach, B. Bell, P. Berrisford, S. Hirahara, A. Horányi, J. Muñoz-Sabater, J. Nicolas, C. Peubey, R. Radu, D. Schepers, A. Simmons, C. Soci, S. Abdalla, X. Abellan, G. Balsamo, P. Bechtold, G. Biavati, J. Bidlot, M. Bonavita and al., "The ERA5 global reanalysis," *Q. J. Roy. Meteor. Soc.,* vol. 146, p. 1999–2049, 2020.

[11]   L. Makkonen, "Models for the growth of rime, glaze, icicles and wet snow on structures," *Philosophical Transactions of the Royal Society ,* vol. 358, pp. 2913-2939, 2000.

Research on the Suppression of De-icing Jumps on Transmission Lines under Strong Winds by Spacer Bars

Xinbo Huang[1], Shuai Wang[1], Yongcan Zhu[1], Yupeng Liu[1], Yiran Zhang[1]

[1] Xi'An Polytechnic University, China

huangxb1975@163.com, 3811019514@qq.com

Abstract— **In overhead transmission lines, the impact effect from the shedding of ice cover can lead to a dynamic response of the transmission line, which is further exacerbated by strong wind action. This not only shortens the interphase distance and increases the risk of electrical accidents, but also leads to wire breakage due to the increase in dynamic tension beyond the design tensile strength. By establishing a finite element model of the "conductor-spacer bar" de-icing response, the effect of the spacer bar on the de-icing bouncing of transmission lines under strong winds is investigated and analysed under different influencing factors. The results show that the strong wind will make the ice-covered conductor de-icing accompanied by obvious lateral displacement, resulting in a higher risk of flashover, the addition of interphase spacer bars for the conductor de-icing under strong winds bouncing transverse, longitudinal displacement have obvious inhibitory effect, which in the conductor stalls in the vicinity of the installation of spacer bars has the best effect, and can effectively avoid the occurrence of flashover accidents.**

Keywords— *Transmission lines; strong winds; de-icing; spacer bars; Deicing jump suppression*

I. INTRODUCTION

As a common failure cause of overhead lines in winter, snow and ice cover seriously threatens the safe and stable operation of the power system[1]. As one of the important ice-covering accidents of transmission lines, deicing jump can lead to serious accidents such as interphase or ground flashover, line break and hardware damage. Under the influence of different factors such as rising temperature, natural wind or man-made vibration and knock, large pieces of ice and snow covering on power lines fall off, causing severe vibration of the ground line and large displacement, which can lead to reduced safety gap and induce electrical accidents such as interphase and ground discharge[2]. In addition, the deicing of ice-covered lines will become more complicated under the influence of strong winds, which will narrow the conductor spacing and lead to discharge accidents. Therefore, it is of great significance to study the effect of spacer on deicing jump suppression of transmission lines under strong wind.

Many scholars at home and abroad have carried out a large number of theoretical and numerical simulation studies on the deicing of lines. Janez[3] used numerical simulation to study the static and dynamic response of snow load shedding of lines, and found that deicing oscillation could easily induce insufficient phase spacing of lines, and proposed the installation of interphase insulation rods and other suppression measures to control dance. By establishing a split line model,

Kollar[4]-[5] analyzed the dynamic response of sub-line deicing to split lines, and studied the influence of different deicing amounts, interphase spacing and number of split lines on the vibration response of lines. Niu Biao et.[6] built a finite element model based on actual lines and studied the inhibition effect of interphase spacer on deicing jump. Huang Zenghao et.[7] analyzed the dynamic response of deicing jump of a 500kV compact line conductor through simulation and proposed an optimization method. Yang Bin[8] established a continuous transmission tower line system model to analyze the deicing jump height, yaw and suspension point stress of the conductor under the most severe working conditions. At the same time, a mechanical model of semi-rigid interphase spacer was also established to compare the difference in the control effect of different spacer models on deicing jump response, and the optimal spacer layout scheme was obtained. Yang Chunxia[9] used the finite element model to build the insulator string-line system, and analyzed the dynamic response of deicing jump of non-uniform ice-covered lines under different ice-covering characteristics and line parameters. Zhu Yongcan[10] established a finite element model of deicing response under strong winds, and analyzed the displacement, unbalanced dynamic tension and minimum distance between phases at the maximum arc of deicing transmission line under different wind speeds and wind attack angles.

At present, studies on the use of spacers to inhibit the deicing jump of conductors have been relatively mature, but there are still relatively few studies considering the effect of spacers on deicing jump of conductors under strong winds. In order to further explore the effect of spacers on deicing jump of conductors under strong winds, this paper establishes a finite element model of "conductor-spacer bar" deicing response, respectively comparing the displacement of the midpoint of conductors during deicing. The effect of spacer on deicing of line under strong wind was evaluated.

II. SIMULATION MODEL OF ICE-COVERED LINE

A. Finite element model

In order to analyze the effect of installing spacer bars to inhibit line deicing bounce under strong wind, the finite element model of "conductor-spacer bar" deicing response was constructed in this paper, as shown in Figure 1. In order to simplify the analysis, only two lines arranged up and down were modeled. The transmission line model selected was LGJ-630/45, the cross-sectional area of the lines was 666.55mm^2, the diameter of the lines was 33.6mm, the elastic modulus was 6.3×1010Pa, and the single-gear distance was 400m.
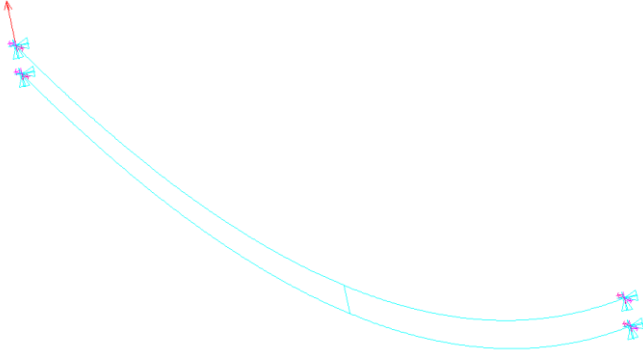
Fig. 1   Transmission line model

B. Ice and wind load simulation

For the calculation of icing load, the thickness, density and topography of ice covering at different locations of transmission lines may be different under the influence of micro-topography and micro-climate when the external temperature is low or during rain and snow. However, in order to facilitate calculation, it is generally believed that the ice cover is evenly distributed on the overhead line, and the cross section of the ice cover and the transmission line is shown in Figure 2.
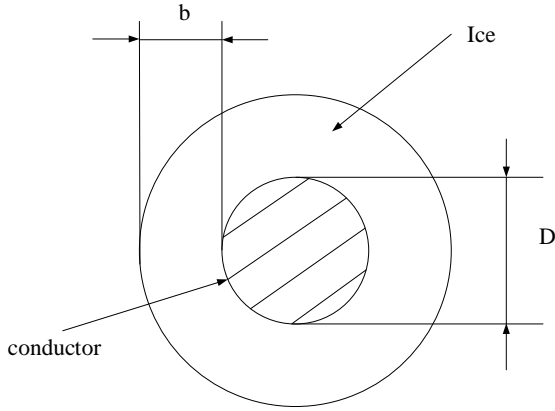
Fig. 2   Ice covering section

According to the model shown in Figure 2, an equally spaced concentrated force can be used in the finite element model to calculate the ice load M on each node.

$$\begin{cases} m = \rho\pi b(D+b) \\ M = mgL/n \end{cases} \tag{1}$$

Where m is the mass of the ice covering on the line in unit length, kg/m; ρ is the ice covering density, 900kg/m^3; D is the outer diameter of the conductor, mm; b is the ice thickness, mm; L is the length of the line, m; n indicates the number of divided units.

As for the calculation of wind load, due to the irregular shape of the ice cover, the strong wind will produce lift and resistance on the ice cover line, and when the ice cover line rotates, the wind attack Angle will change, and the wind load will also change. In this paper, the D-shaped ice cover shape is selected for research, and the cross-section of the wind ice cover line is shown in Figure 3.
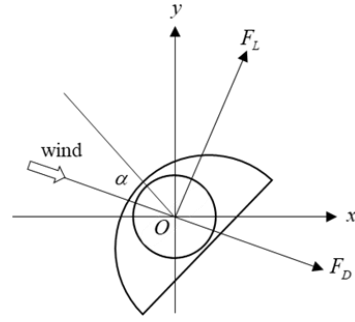
Fig. 3   Section diagram of D-shaped ice-covered line ansmission line model

The calculation formula of wind load F D and lift load F L per unit length (L=1m) of ice-covered transmission line is as follows:

$$\begin{cases} F_D = 0.5C_D\rho V^2 d \\ F_L = 0.5C_L\rho V^2 d \end{cases} \tag{2}$$

Where, F_D is the resistance of the ice-covered line, N; F_L is the lift force of the ice-covered line, N; C_D and C_L is the resistance and lift coefficient of the ice-covered line respectively; ρ is the air density, kg/m^3; V is the air flow velocity, m/s; d is the windward length, m.

III. ANALYSIS OF DEICING JUMP OF ICE-COVERED LINE UNDER STRONG WIND

Under the action of ice, the downward force on the line increases, and the downward shift occurs at the sag position of the line. When the line is deiced, under the action of the line tension, the line quickly bounces back, and its bounce direction, displacement and speed are affected by the initial factors. Under the influence of strong wind, the airflow resistance and lift force on the ice-covered line are very different, resulting in a large difference between the position of the line before and after deicing and the conditions of no wind, such as elastic potential energy, resulting in different operation risks.

A. Time history curve

Strong wind usually means that the instantaneous wind speed reaches 10m/s. This paper focuses on the analysis of the wind speed above 10m/s. During the setting and simulation process, the sudden change of the wind attack Angle caused by the continuous torsion of the line is not considered, that is, the Angle of the incoming wind and the vertical line direction remains unchanged before and after deicing. The maximum displacement change in deicing response of transmission lines with uniform ice cover and no height difference usually occurs at the midpoint of deicing gear (the maximum sag of deicing gear), so this paper only analyzes the deicing time history curve at the midpoint of deicing gear. Under the condition that the equivalent ice thickness is 15mm, the wind speed is 0 m/s and 15m /s, and the initial wind attack Angle α=0°, 120°, 240°, the displacement time history curve of the deicing middle point of the D-type ice-covered line is shown in Figure 4.

13
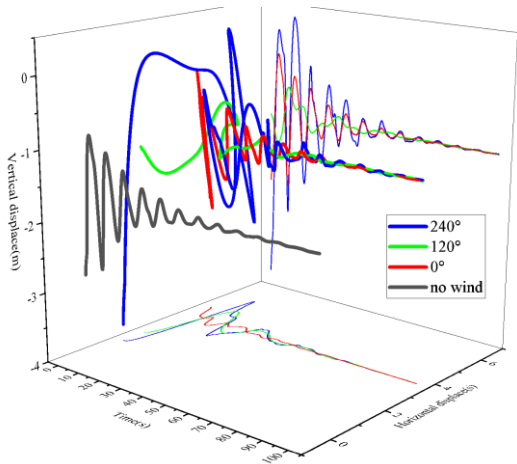
Fig. 4 The displacement time history curve of the deicing midpoint of the ice-covered conductor

As can be seen from Figure 4, there is no lateral displacement when there is no wind, and the maximum vertical displacement is 2m. Under the influence of strong wind, when the wind attack Angle is 0°, 120° and 240°, the maximum lateral displacement is 1.12m, 2.71m and 4.37m respectively, and the maximum longitudinal ice jump displacement is 2.03m, 0.9m and 4.07m respectively. Strong wind will affect the longitudinal displacement amplitude and increase the transverse displacement amplitude, and different wind attack Angle conditions will significantly change the peak displacement at the midpoint of the deicing line and the time history curve of lateral swing and longitudinal jump. Due to the small lift load on the line after deicing, the longitudinal displacement value of strong wind is very close to that of no wind at the steady-state moment after deicing, and the strong wind condition only affects the longitudinal displacement variation trend before it reaches a stable state during deicing.

B. Comparison of line displacement between wind-free deicing and strong wind deicing

If there is no wind with ice or wind with ice, simulation is carried out, and the change trajectory of the deicing midpoint of the ice-covered line is obtained when the plane of the line section is located is shown in Figure 5.
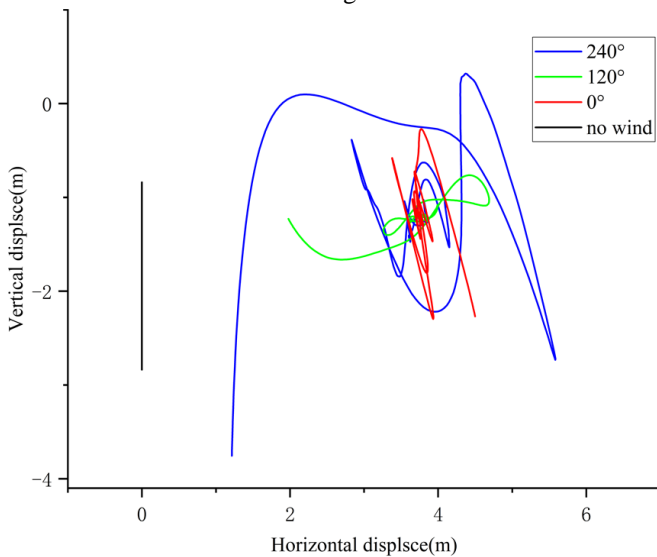
Fig. 5 Deicing oscillation curve at deicing midpoint of ice-covered line

As shown in Figure 5, it can be seen from the curve change trajectory that the deicing response of the transmission line under the action of strong wind is a round-trip bounce process with significant upward deviation compared with the position under the condition of no ice wind. When the wind attack Angle is 0°, the lateral displacement changes less and the longitudinal displacement changes more during deicing bounce. When the wind attack Angle is 120°, the change of longitudinal displacement during deicing bounce is less than that at no wind, and the change of lateral displacement is larger. When the wind attack Angle is 240°, the transverse and longitudinal displacements during the deicing bounce will be greatly displacements, which will lead to reduced line spacing and failure.

IV. ANALYSIS OF RESTRAINING EFFECT OF SPACER BAR ON DEICING JUMP OF CONDUCTOR UNDER STRONG WIND

A. Time history comparison of spacer bar displacement is applied

Spacer bars, as a common anti-dance device, connects lines of different phases. By using spacer bar from non-deicing phase line, it exerts a strong pull on the bounce of deicing phase line and has a certain inhibition effect on the bounce of deicing phase line. Since when the initial wind attack Angle is 240°, the deicing spring displacement of the line under strong wind is the largest, a spacer bar is applied to suppress this situation, and a spacer bar is applied at the midpoint of deicing for simulation. The deicing of the line with spacer bar and without spacer bar under strong wind is shown in Figure 6.
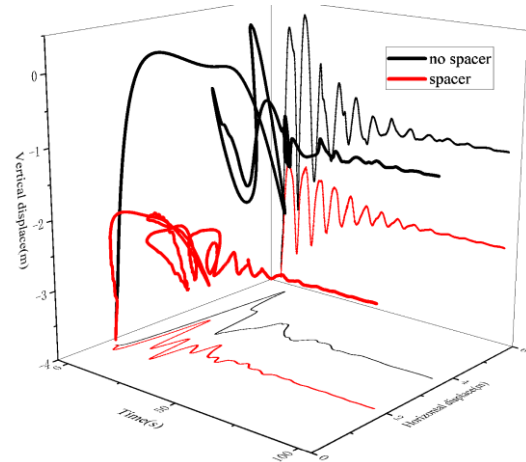
Fig. 6 Comparison diagram of deicing jump displacement time history of applying spacer bar

As can be seen from Figure 6, the maximum lateral displacement and vertical displacement of deicing without spacer bars are 4.37m and 4.07m, respectively, and the maximum lateral displacement and longitudinal ice jump displacement with spacer bars are 2.3m and 1.89m respectively. Spacer bar can inhibit both lateral and longitudinal displacements of line deicing jump under strong wind. At the steady state time after deicing, the offset of the line is less after the spacer bar is applied.

B. Spacer bar suppression effect added at different positions

Generally, the more spacer bars are, the better the inhibition effect on the deicing jump of the power line is, but the greater the amount of on-site engineering is. In order to study the

inhibitory effect of installing a small number of spacer bars at different positions on the ice falling off, based on the above finite element model, only one spacer bar was installed at 1/8, 1/5, 1/3 and 1/2 of the conductor, and the transverse displacement time history curve of the conductor's midpoint bouncing after the ice falling off was obtained, as shown in Figure 7.
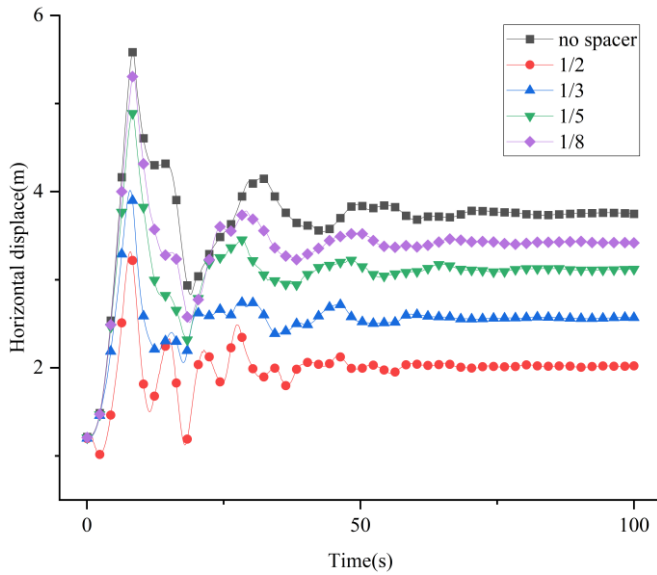
Fig. 7 Lateral deicing displacement of spacer bars are applied at different positions

As can be seen from Figure 7, the lateral deicing displacements of 1/8, 1/5, 1/3, 1/2 and no spacer bar of the line are 4.11m, 3.68m, 2.81m, 2.3m and 4.37m respectively. When spacer bars are applied at different positions, the lateral displacement of the line deicing bounce is inhibited to different degrees, and the inhibition effect is stronger as the spacer bars are applied closer to the midpoint. The longitudinal displacement time history curve of the midpoint of the line bouncing off the ice is shown in Figure 8.
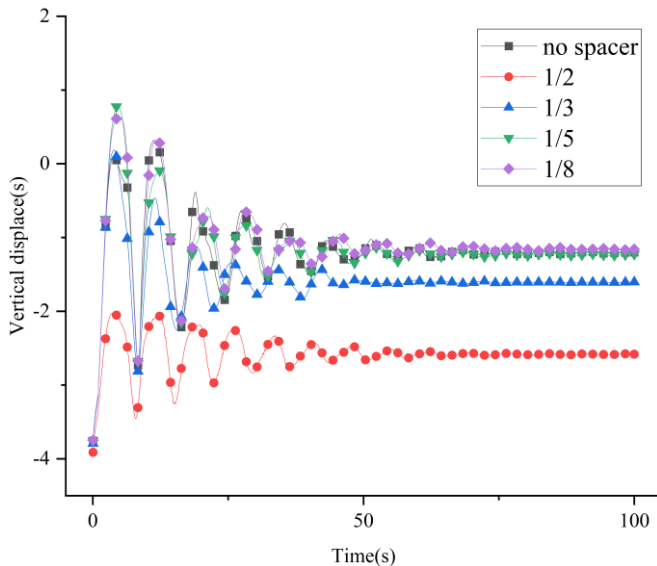
Fig. 8 Longitudinal deicing displacement of spacer bars are applied at different positions

As can be seen from FIG.8, the longitudinal deicing displacements of 1/8, 1/5, 1/3, 1/2 of the line and without spacer bars are 4.37m, 4.57m, 3.98m, 1.89m and 4.07m

respectively. When spacer bars are applied at different positions, the longitudinal displacement of deicing bounce of the line changes to different degrees. When spacer bars are applied far from the midpoint of the line (1/8 and 1/5), the spacer bars have no inhibiting effect on the amplitude of deicing bounce, but lead to the increase of the longitudinal displacement of the midpoint of the deicing line, which may affect the stability of the transmission line. The spacer bar applied at 1/2 and 1/3 of the transmission line has a good inhibition effect on the deicing bounce, especially at 1/2 the inhibition effect is the best, which can reduce the bounce amplitude by about 50%.

V. CONCLUSIONS

The deicing bounce of ice-covered transmission line under strong wind seriously affects the safe and stable operation of power system. In this paper, the finite element model of "conductor-spacer bar" deicing response is established, and the restraining effect of spacer bar on deicing bounce is analyzed. The conclusions are as follows:

1) The strong wind will make the ice-covered conductor de-icing accompanied by obvious lateral displacement, resulting in a higher risk of flashover.

2) The addition of interphase spacer under the action of strong wind can obviously restrain the lateral and longitudinal bounce displacement of line deicing.

3) The effect of spacer bar applied at different positions is different, and the effect of spacer bar installed near the conductor stop is the best, which can effectively avoid flashover accident.

REFERENCES

[1]   HUANG Xinbo, CAO Wen. Review of the disaster mechanism of transmission lines[J]. Journal of Xi'an Polytechnic University, 2017,31(05):589-605.

[2]   Zhou Zandong，Gong Hao，Wu Nian. Fault diagnosis of transmission line icing based on decision tree [J]. High Voltage Apparatus. 2019, 55(01): 165-169+177.

[3]   Janez J,Mohamed TAH,Ghyslaine M. Numerical modelling of snow shedding effects on a 110kV overhead power line in Slovenia[J]. Proceedings of the Eleventh (2001) International off shoreand Polar Engineering conference , 2001, 1: 690-694.

[4]   Kollar,L.E.,Farzaneh,M, Dyke,P.V. Modeling ice shedding propagation on transmission lines with or without interphase spacers[J]. IEEE Transactions on Power Delivery, 2013, 28(1): 261-267.

[5]   Kollar,L.E.,Farzaneh, M. Modeling sudden ice shedding from conductor bundles [J]. IEEE Trans actions on Power Delivery, 2013, 28(2): 604-611.

[6]   Niu Biao, Wang Chunwei, Liang Wei. Applied research on deicing jump fault preventive measures of 220 kv double circuit transmission lines[J]. Shanxi Electric Power.2020, (4): 46-48.

[7]   Huang Zenghao, Yang Qi, Li Hao, et al. Study on the influence of interphase spacer on ice-shedding jump of compact transmission lines [J/OL]. Power System Technology: 1-10[2023-10-12].

[8]   Yang Bin. Research on dynamic response of transmission lines after ice-shedding by parametric finite element method [D]. Huazhong University Of Science And Technology. 2016.

[9]   Yang Chunxia, He Wenqi, Liu Huicong, et al. Dynamic response characteristic of ice-shedding on multi-span transmission line under non-uniform icing[J/OL]. Industrial Construction: 1-10[2023-10-13].

[10]   ZHU Yongcan, XIE Songlin et al. Research of the ice-shedding response of transmission lines under strong winds. [J/OL]. Power System Technology: 1-8[2024-04-03].

Selecting Effective Countermeasures Against Snow Damage on Single-Conductor Lines Considering Meteorological and Structural Characteristics

Hisato Matsumiya[1,2], Soichiro Sugimoto[1], Mitsuharu Nomura[1], Teruo Aso[1],

Hiroki Matsushima[1], Saki Taruishi[1], Yuki Okazaki[1]

[1] *Central Research Institute of Electric Power Industry, Japan*
[2] *Kyoto University, Japan*

hisato-m@criepi.denken.or.jp, soichiro@criepi.denken.or.jp, nomuharu@criepi.denken.or.jp, ab-aso@criepi.denken.or.jp, m-hiroki@criepi.denken.or.jp, taruishi@criepi.denken.or.jp, okazaki3940@criepi.denken.or.jp

Abstract— **Wet snow accretion on overhead lines often causes large-scale damage. Excessive snow accretion often forms cylindrical sleeves around conductors, which can develop via two mechanisms: snow sliding along the wire strands or wire rotation due to snow's weight. In Japan, snow-resistant (SR) rings, counterweights, and interphase spacers are commonly employed to mitigate snow damage on single-conductor transmission lines. In this study, we investigated the effectiveness of these countermeasures under different meteorological and structural conditions. While the presence of counterweights significantly reduced snow accretion, it was concurrently observed to increase the occurrence of galloping. In contrast, lines equipped with interphase spacers suppressed galloping amplitudes effectively compared to those with counterweights. Additionally, under wet snow conditions, when the accreted snow was more likely to melt owing to air heat transfer and solar radiation and slide along the wire strand, SR rings facilitated snow shedding from the conductor. The effectiveness of SR rings was further enhanced when wire rotation was minimised using counterweights. However, SR rings proved to be entirely ineffective in dry snow conditions with calm to weak winds. In conclusion, the efficacy of these countermeasures was observed to be strongly influenced by meteorological conditions and structural features of transmission lines. Based on the observation data and its analysis, we proposed a method for selecting suitable countermeasure devices for single-conductor lines.**

Keywords— **overhead transmission lines, wet and dry snow accretion, galloping, field observations, countermeasures**

I. INTRODUCTION

Snow accretion on overhead transmission lines can cause significant damage and widespread power outages. Snow accretion can be categorised into two classes based on meteorological conditions: wet and dry [1], [2]. Wet snowflakes, occurring at temperatures around 0 °C with high relative humidity, contain liquid water and are more prone to adhere to conductors. Wet snow accretion is further characterised by its persistence in the presence of strong winds, whereas dry snow accretion occurs only in calm to weak winds. Consequently, wet snow accretion can induce galloping, i.e., substantial vertical oscillations, in strong wind conditions, leading to the risk of interphase short circuits [3].

Excessive snow accretion often creates cylindrical sleeves around conductors, which can develop via two mechanisms: snow sliding along the wire strands or wire rotation owing to the snow weight. In Japan, snow-resistant (SR) rings, counterweights, and interphase spacers are commonly used to mitigate snow damage in single-conductor transmission lines. SR rings are plastic rings that prevent snow from sliding along twisted strands. Counterweights are eccentric weights designed to inhibit conductor rotation. Interphase spacers not only prevent short circuits during galloping or ice shedding but also suppress conductor rotation, thereby reducing excessive cylindrical snow accretion.

To develop an estimation method for the amount of snow accretion and galloping amplitude and identify appropriate countermeasures for snow damage, the Central Research Institute of Electric Power Industry (CRIEPI) conducted field observations at multiple sites beginning in 2007, encompassing dry snowfall under calm to weak winds and wet snowfall in strong winds [4]–[6]. In particular, the Kushiro test line was constructed in 2013 in Kushiro City, Hokkaido, Japan to enable field observations of galloping in overhead lines and wet snow accretion on conductors and insulators [7].

This study evaluates the effectiveness of different countermeasures on single conductors based on extensive and long-term observations across various meteorological conditions.

II. OVERVIEW OF FIELD OBSERVATION FACILITIES

We collected data obtained from field observation systems for snow damage installed by CRIEPI in snowfall locations throughout Japan to investigate the actual conditions of snow damage and compare and validate the effectiveness of different countermeasures. In addition, observation data collected by electric power companies were centrally aggregated and analysed. Fig. 1 depicts the locations and panoramic views of the observation points, excluding those without notable observations, and Table 1 outlines the details of the observation facilities and countermeasures adopted at each location. Some of the installed countermeasures are illustrated in Fig. 2. The SR rings, counterweights and interphase spacers are explained in Section I. The spiral rods are originally intended as a countermeasure against wind-induced noise; however, some power companies install them to prevent accreted snow from sliding towards the wire strands, expecting an effect similar to that of SR rings. Polytetrafluoroethylene (PTFE) tape is used as a countermeasure to reduce the adhesive force of snow on the wire surface, thereby facilitating early snow shedding. Loose spacers are devices used to control galloping in multi-bundled
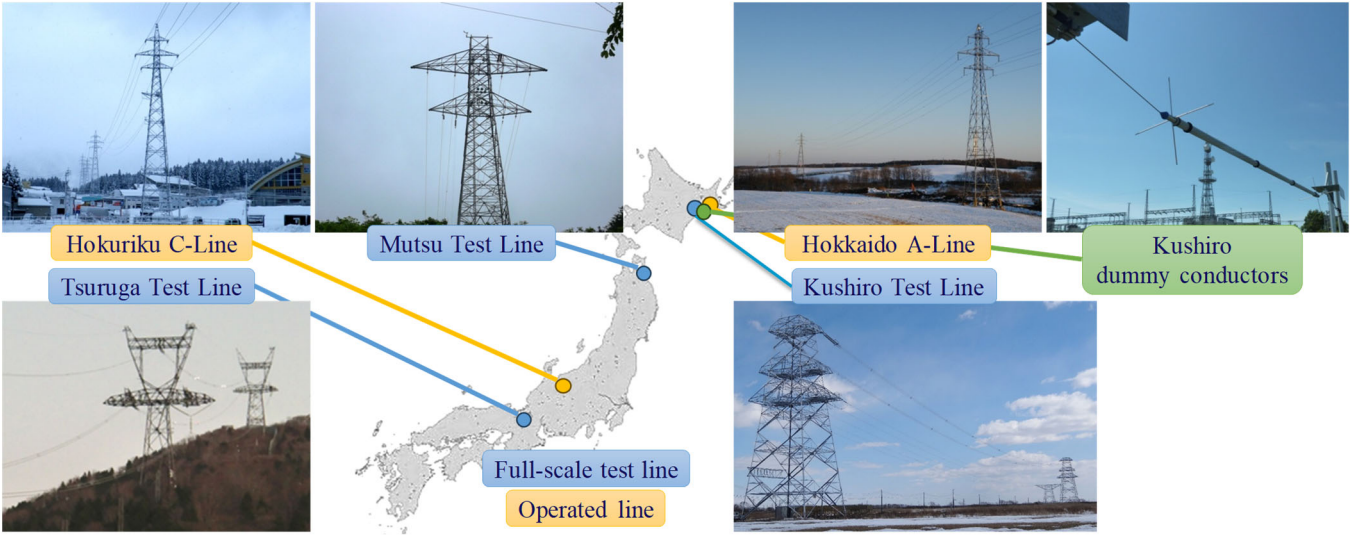
Fig.1 Field observation sites for snow damage data.

TABLE I. SPECIFICATIONS OF THE FACILITIES AND THE COUNTERMEASURES INSTALLED AT EACH OBSERVATION SITE

Observation site (specification[*1])	Main type of snow accretion	SR rings	Counter weights	Interphase spacers	Loose spacers	Others
Hokkaido A-Line (Single: ACSR240mm^2)	Wet snow, moderate to strong wind	○	○	○		
Kushiro dummy conductors (ACSR240, 410, 810mm^2)		○	○[*2]			
Kushiro test line (Single: ACSR240mm^2, 4-bundled: ACSR410mm^2)		○	○		○	
Mutsu test line (Single: ACSR160mm^2)		○		○		PTFE Tape
Hokuriku C-Line (Single: ACSR330mm^2)	Dry and wet snow, calm to weak wind	○				Spiral rods
Tsuruta test line (4-bundled: ACSR410mm^2)	(In-cloud icing)	○			○	

*1: ACSR denotes the Aluminium Conductor Steel Reinforced wire, the number indicates the nominal cross-sectional area.

*2: Characteristics are simulated based on the configuration of torsional rigidity of the conductor model.
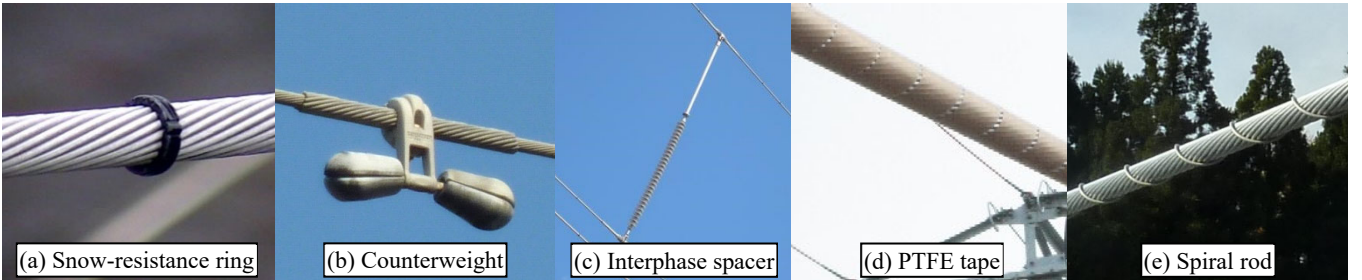
Fig. 2 Countermeasures installed in single-conductor lines.

conductor lines. This study discusses countermeasures for single-conductor lines; detailed discussions on loose spacers at the Tsuruga test line can be found in [6].

III. OBSERVATIONS IN HOKKAIDO A-LINE

The Hokkaido A-Line is a 66-kV single-conductor transmission line in eastern Hokkaido. Data on 21 wet snow accretion events on this line were recorded during the winter seasons in 2008–2015, with the majority occurring in strong winds with speeds exceeding 8 m/s [5]. Fig. 3 depicts the temperature and relative humidity corresponding to increasing snow accretion amount. Fig. 3 also presents the discrimination line between rain and other precipitation particle types and that between snow and other precipitation particle types. These discrimination lines were obtained using precipitation-type clarification analysis [8]. The type of precipitation was analysed using meteorological surface data (including precipitation particle types) from the past 40 years collected by a weather station located in eastern Hokkaido. A previous study proposed that wet snowflakes, which contain moderate

amounts of liquid water and easily accrete to the conductors, are frequently observed in the central zone between the two discrimination lines [9]. Based on this precipitation classification method, all events observed at this site were determined to be wet snow accretion events.

Fig. 4 compares the maximum amount of snow accretion in each event for lines with three different combinations of countermeasures: only SR rings (i.e., Ring), SR rings and counterweights (i.e., Ring+CW), and SR rings and interphase spacers (i.e., Ring+SP). The amount of snow accretion was significantly reduced in lines with both counterweights and interphase spacers, which suppressed the rotation of the conductor compared to the other lines. Limiting the rotation of the conductor constrained snow accretion in only one direction (windward side of the conductor), thereby promoting snow shedding during accretion.

However, suppressing conductor rotation also increased the incidence of galloping. This was attributed to the development of sharp snow shapes (i.e., triangular and crescent-shaped accretions) due to snow accretion in a single direction. Fig. 5

compares the vertical amplitudes (in 10-minute) of the "Ring" line and the "Ring+SP" line with that of the "Ring+CW" line. The oscillation amplitude of the line with counterweights was larger than those without them (i.e. "Ring" line). Furthermore, the maximum galloping amplitude of the line with interphase spacers was suppressed by approximately 40 % compared to the line with counterweights.

IV. OBSERVATIONS IN KUSHIRO DUMMY CONDUCTORS

CRIEPI uses a unique dummy conductor supported by wire ropes to collect snow accretion data efficiently [4], [7]. This dummy conductor is an observational instrument that replicates snow accretion while the conductor is rotating, mimicking actual power lines, by adjusting torsional rigidity using wire ropes placed at both ends. Prior to the construction of the Kushiro test line, preliminary observations were recorded using 12 dummy conductors during the winter seasons in 2011–2015 [4]. The setup allowed the simulation of snow accretion characteristics of lines with a span length of approximately 300 m and three different conductor sizes, comparing the amounts of snow accretion with and without SR rings. Furthermore, for ACSR240mm² conductors, the torsional rigidity was set for a span length of approximately 90 m to simulate snow-accretion characteristics of spans with counterweights installed. Fig. 6 compares the maximum snow accretion amounts of the "Ring", "CW", and "Ring+CW" conductors with those of the non-countermeasure conductor during each event. Although the effectiveness of SR rings alone was observed to be limited, snow accretion was reduced when countermeasures to suppress rotation were also adopted. Furthermore, it was evident that combining SR rings with rotation suppression countermeasures yielded better results than simply suppressing rotation.

Fig. 7 describes the snow accretion process magnified near the SR ring in the "Ring+CW" conductor. On the left side of the ring, the accreted snow gradually moved downward along the twisted portion of the wire. However, snow was not dislocated on the right side of the ring because of its blocking effect. Consequently, the accreted snow was segmented at the ring, promoting snow shedding. Conversely, when rotation was not suppressed, the wire rotated before the effect of snow sliding became apparent, leading to the formation of cylindrical snow around the wire, which inhibited the effectiveness of the SR rings.

V. OBSERVATIONS IN KUSHIRO TEST LINE

Snow accretion data have been recorded at the Kushiro test line since winter 2014 [7]. To date, several wet snow accretion events have been observed, including galloping and snow shedding. The effects of current-generated heat (DC: 150 A) on the development of snow accretion were investigated for two single-conductor lines. Fig. 8 compares the maximum snow accretion amount of the "Ring" and "Ring+CW" lines with those of the non-countermeasure line during each event. Fig. 8 presents the results observed during the winters in 2014–2018, with most events involving wet snow accretion at moderate wind speeds (3–8 m/s). The effects of SR rings under current-generated heat were compared with those of a non-countermeasure line with a passing current. The heat generated by the electric current in the conductor was observed to accelerate the effect of the SR rings. This was attributed to the facilitation of sliding of accreted snow along
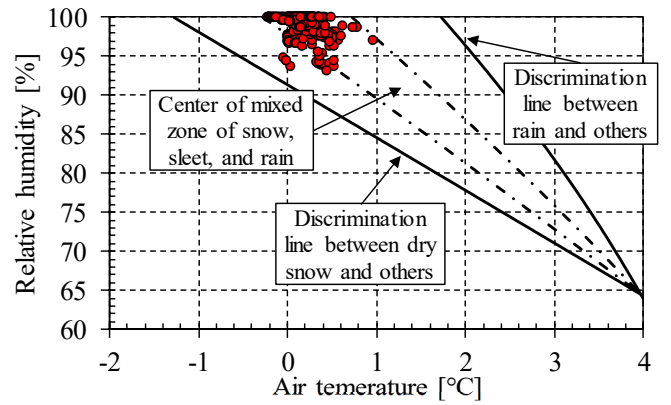
Fig. 3 Temperature and relative humidity corresponding to increasing snow accretion amount (Hokkaido A-Line).
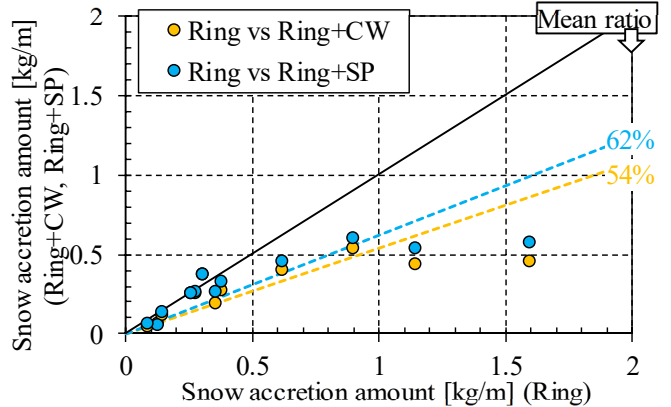
Fig. 4 Comparison of maximum snow accretion amounts during each event (Hokkaido A-Line).
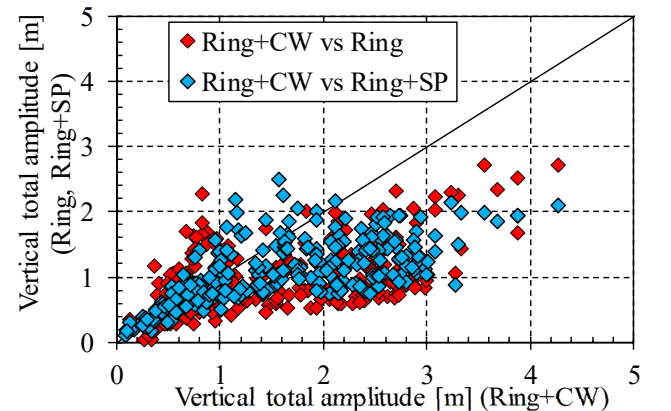
Fig. 5 Comparison of vertical total amplitude for each 10-minute statistical value (Hokkaido A-Line).
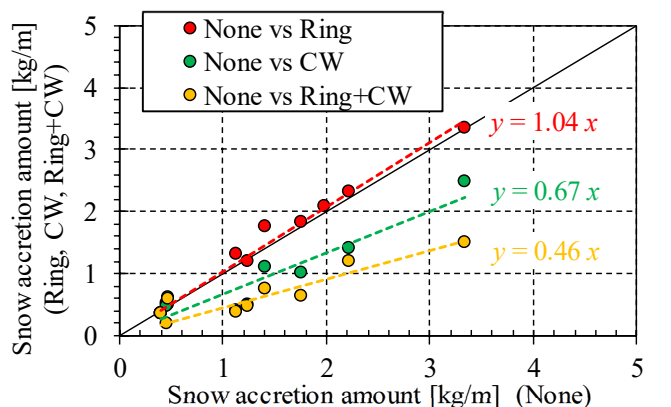
Fig. 6 Comparison of maximum snow accretion amount during each event (Kushiro dummy conductors).

the strand on the wire surface due to the melting of the accreted snow; promoting snow shedding in the presence of SR rings. Even when the SR rings were used alone without a passing current, they were observed to be more effective than dummy conductors. This was attributed to the resistance to conductor rotation near the support points (tower) and the inclination of the conductor, which facilitates the sliding of the accreted snow along the line. Notwithstanding some aberrations, the use of both SR rings and counterweights yielded a significant improvement in general.

VI. OBSERVATIONS IN HOKURIKU C-LINE

The Hokuriku C-Line is a 66-kV single-conductor transmission line located in the mountainous regions of central Japan along the Sea of Japan coast. Here, 20 snow accretion events were observed during the winter seasons in 2008–2015, with the majority occurring in calm to weak wind speeds (< 3 m/s). Approximately equal incidence of wet and dry snow accretion was observed. Fig. 9 compares the maximum snow accretion amounts of the "Ring" and "Spiral rod" lines with those of the non-countermeasure line during each event. Although the highest amount of snow accretion was observed to decrease, the effects of the SR rings and spiral rods were not evident in many cases. This was attributed to snow accretion on the top surfaces of the conductors at weak wind speeds, which increased accretion without applying a sliding force (gravity) to the snow mass. Moreover, most of the accretion was of the dry type. Even in cases of wet snow accretion, the wind speeds were very weak, reducing the likelihood of the snow melting during accretion. Consequently, the accreted snow did not slide along twisted portions of the wire strand, reducing the effectiveness of the countermeasures.

VII. OBSERVATIONS IN MUTSU TEST LINE

The Mutsu Test Line is a full-scale test line established by Tohoku Electric Power Co., Inc. Here, observations were recorded from 1981 to the present date [10]. At this site, wet snow accretion occasionally occurred under moderate to strong wind conditions. Fig. 10 compares the maximum snow accretion amounts of the "Ring", "Ring+CW", "Ring+SP", and "Ring+CW+PTFE" lines with those of the non-countermeasure line during each event. Fig. 10 presents the comparison results obtained by classifying the wind speeds into two categories: moderate wind (3–8 m/s) and strong wind (>8 m/s). First, the greatest reduction in snow accretion was achieved when PTFE tape was used in combination with SR rings and counterweights. Furthermore, in all lines equipped with SR rings, greater effectiveness was observed under stronger wind conditions. This was attributed to increased melting of snow in the presence of stronger winds under wet snow conditions, i.e., when the temperature is slightly above 0 °C, which accentuated the effects of SR rings. It is noteworthy that although only one interphase spacer was installed at the centre of the span, three counterweights were installed on it, making it less prone to conductor rotation and thereby reducing the effectiveness of interphase spacers.

VIII. EFFECTIVE METHOD FOR SELECTING COUNTERMEASURES

Fig. 11 presents a selection flowchart for the three most commonly used countermeasures for heavy snow accretion and galloping in Japan. Interphase spacers are the simplest countermeasure to suppress both snow accretion amount and
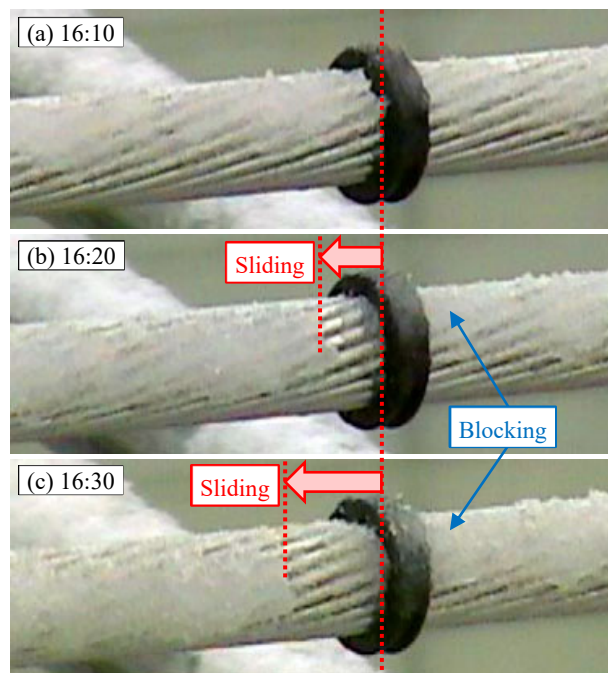
Fig. 7 Snow accretion process around the SR ring.

galloping amplitude in single-conductor lines. However, in
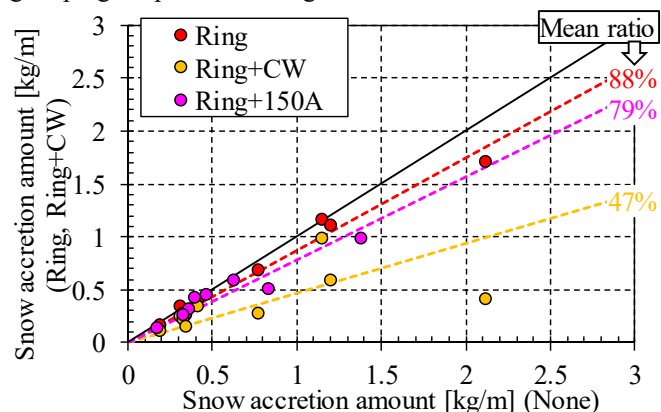
Fig. 8 Comparison of maximum snow accretion amount during each event (Kushiro test line).
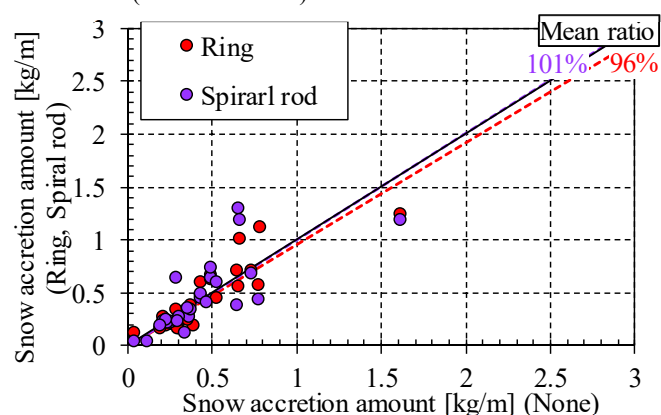
Fig. 9 Comparison of maximum snow accretion amount during each event (Hokuriku C-Line).

low wind speeds where galloping is not prominent, counterweights are preferable to suppress snow accretion considering the cost. By contrast, when snow accretion is low and galloping is common, installing counterweights is not preferable because they might increase the incidence of

(a) moderate wind (3-8m/s) (b) strong wind (over 8 m/s)
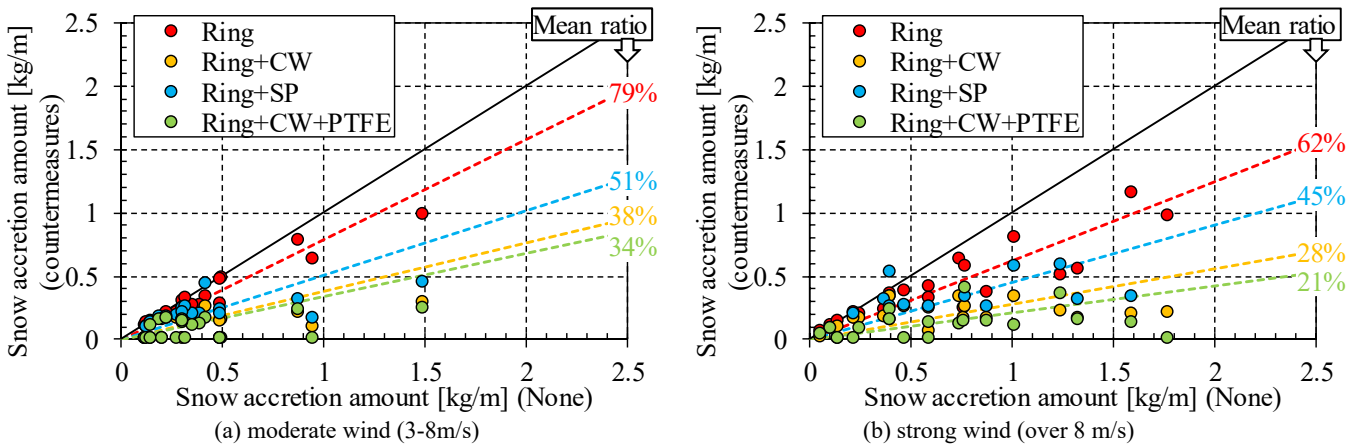
Fig. 10 Comparison of maximum snow accretion amount during each event (Mutsu test line).
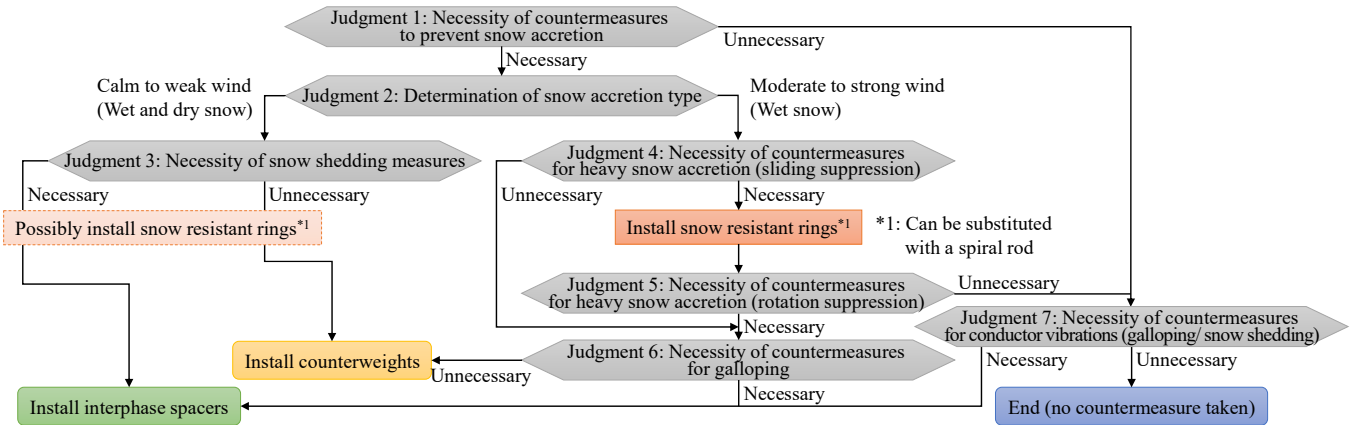
Fig. 11 Flowchart for selecting appropriate snow damage countermeasures for single-conductor lines.

galloping. In this case, galloping is suppressed simply by not using counterweights, even without installing interphase spacers. Furthermore, SR rings should be installed in wet snowfall conditions under moderate to strong winds. In cases wherein the span is short or the conductor size is large, the SR rings can be effective enough without installing counterweights or interphase spacers owing to the large torsional rigidity of the conductor. Thus, the proposed selection method avoids the need for excessive mitigation strategies by identifying appropriate countermeasures.

IX. CONCLUSIONS

The efficacy of countermeasures is strongly influenced by meteorological conditions and structural features (torsional rigidity) of transmission lines. The basic methodology proposed in this study enabled the selection of suitable countermeasures for single conductor lines based on specific weather and structural conditions of each facility.

ACKNOWLEDGMENTS

REFERENCES

[1] Y. Sakamoto, "Snow accretion on overhead wires," *Philos Trans Royal Soc A*, vol. 358, pp. 2941–2970, Nov. 2000.

[2] G. Wakahama, S. Kuroiwa, and K. Goto, "Snow accretion on electric wires and its prevention," *J Glaciol.*, vol. 19, pp. 657, 1977.

[3] M. Farzaneh and W. A. Chisholm, "Techniques for Protecting Overhead Lines in Winter Conditions," *Springer Nature Switzerland*, Aug. 2022.

[4] M. Shimizu, H. Matsumiya, S. Sugimoto, T. Ishikawa, A. Hashimoto, M. Nomura, T. Nishihara, and H. Hirakuchi, "Report on 10 Years Research of Snow Damage of Overhead Transmission Facilities (Part 1): Development of Practical Measures on Heavily Accreted Snow and Galloping (in Japanese)," *CRIEPI Research Report*, N16010, 2017.

[5] H. Matsumiya, H. Ichikawa, T. Aso, M. Shugo, T. Nishihara, M. Shimizu, and S. Sugimoto, "Field observation of wet snow accretion and galloping on a single conductor transmission line," *Proc. Int. Workshop Atm. Icing Struct,* Reykjavik, Iceland, 2019.

[6] H. Matsumiya, T. Yukino, M. Shimizu, and T. Nishihara, "Field observation of galloping on four-bundled conductors and verification of countermeasure effect of loose spacers," *J. Wind. Eng. Ind. Aerodyn.*, Vol. 220, 2022.

[7] H. Matsumiya, H. Matsushima, T. Aso, T. Nishihara, and S. Sugimoto, "Field observations of wet snow accretion on overhead transmission lines at the Kushiro test line," *Cold Regions Science and Technology*, Vol. 213, 103905, 2023.

[8] T. Matsuo, Y. Sasyo, and Y. Sato, "Relationship between types of precipitation on the ground and surface meteorological elements," *J Meteorol Soc Jpn.*, vol. 59, pp. 462–476, 1981.

[9] S. Sugimoto, T. Aso, and M. Saiki, "Proposal of a type classification method for snow accretion on overhead transmission line using meteorological data," *CRIEPI Research Report*, N11059, 2012. [in Japanese]

[10] H. Sugiura, I. Nakayama, T. Yamashita, and S. Sugawara, "Effective verification of various anti snow devices (in Japanese)," *Annual Meeting Record, I.E.E. Japan*, 7-096, pp. 146-147, 2012.

On-site cable ice shedding experiment and observation of an atmospheric icing event

Harri Juttula[1], Jussi Suopajärvi[2], Eero Molkoselkä[1], Ville Kaikkonen[1], Anssi Mäkynen[1]

[1] University of Oulu, Finland
[2] Lapland University of Applied Sciences, Finland

harri.juttula@oulu.fi

Abstract—**An 85 meters long steel was installed on top of the Olos fell in northern Finland to observe both ice shedding due to controlled impacts and rime ice growth due to cloud droplets. A custom ice dropper was designed and installed on the cable. Ice dropper design was based on sudden release of additional tension due to forced bending of the cable. A cloud droplet sensor (ICEMET) and weather station were installed on site to monitor the liquid water content (LWC), temperature and wind conditions during the field tests. Additionally, a commercial load sensor was attached to the cable and a camera was installed to provide live feed from the weather and ice conditions on the site. A series of remotely operated tests with the ice dropper were performed during the test period when significant amount of ice was observed on the cable. The ice dropper provided mixed results with some events removing successfully up to 30 kg of ice with clear visual evidence. Change in the ice mass was estimated by using a linear regression model based on a physical simulation of the cable created with COMSOL Multiphysics software. Simulation model of the cable related the cable tension to the physical properties of the cable, point load from the ice dropper, additional ice load and thermal expansion and drag forces due to temperature and wind. A total of eight ice dropper tests were analysed with the numerical model. Between two individual ice dropping events ICEMET detected a long period of up to 0.2 g/m³ liquid water content in the air which was visually confirmed by poor visibility in the surveillance camera images and increase of cable tension and diameter of ice layer.**

Keywords— ***Icing, de-icing, ice shedding, liquid water content, transmission lines***

I. Introduction

Atmospheric icing poses significant threats to transmission lines in cold climates with long periods of freezing conditions. Unattended, excessive icing can lead to transmission line failures, power outages and economic losses. Icing on wires and poles can cause mechanical overloads when the ice load exceeds the maximum designed load capacity of the structures. Ice increases the sagging of cables and under wind loads galloping of heavy ice covered wires can cause uneven loads on structures or risk their mechanical stability. Uneven ice accumulation or melting can cause asymmetrical loads and swinging, slipping of wires and increased wear and collision of wires.

Icing of transmission lines occurs typically between 0 °C to -15 °C when they are exposed to freezing rain, wet snow or cloud and fog droplets. Depending on the exact temperature and wind conditions and the source of water, ice typically forms frost, rime, glaze or mixed rime ice. Rime forms when small supercooled fog or cloud droplets in 10 – 40 µm range collide with the transmission lines and freeze on the surface. Mixed rime and glaze forms due to freezing rain and large water droplets [1].

Anti-icing and de-icing of transmission lines is time and labour intensive work. Over the year several methods to solve the icing problem have been developed and tested. An overview of the work is given in a recent review of anti- and de-icing methods [2]. De-icing methods include for example manual striking or scraping of the cable with insulated object or manually operated or robotic ice scraping pulleys [3,4], melting of ice using resistive losses [5] or using electromagnetic forces generated by currents to knock adjacent cables together [6].

In this work the aim was to design and test a remotely operated mechanical de-icing device attached to a real cable in freezing field conditions. Weather conditions were monitored during the test campaign and atmospheric icing event due to cloud droplets was observed.

II. Methods

A. Olos test site

A test site for ice dropper was setup on top of the Olos fell in Northern Finland. A steel cable was installed between the roofs of two cargo containers with support points of the cable being 85.32 meters apart and other end of the cable being 3.79 meters higher. Distances were acquired with laser rangefinder. The cable that was used goes by the tradename Sustrong and it consists of 30 aluminium and 7 steel wires with a 14.8 mm outer diameter and an average density of 0.486 kg/m.

A prototype ice dropper unit was installed on the cable 32.5 meters away from the lower support point. Tension of the cable due to cable's own mass and accumulated ice load was measured with a commercial load cell. A cloud droplet measurement sensor, and weather station measuring temperature and both wind speed and direction were installed on the roof of the upper cargo container approximately 2 meters above the endpoint of the cable. Additionally, a surveillance camera was installed on the roof to monitor the ice conditions on the cable and other instruments.

B. Ice dropper

A custom ice dropper device was built during the project to test ice shedding capabilities of sudden release of tension from the cable. Basic working principle of the ice dropper is shown in Fig. 1. The cable goes through three guides where the middle guide can be pulled down during reload cycle. During the reload the cable bends between the guides increasing the tension in the cable. When the middle guide is pulled to its extreme position, the clamps holding the guide are release the mechanism and the tension is instantly released. Mechanical trajectory of the clamps was designed to automatically release

and reattach themselves to the pulling mechanism. Distances from the outer cable guides were 90.

Reloading mechanisms was operated with a 12 V electric motor over remote ethernet connection. Both tensioning and resetting phases require approximately 2.5 minutes while the motor is operated with 10 A and 4.5 A currents respectively. A full cycle requires approximately 7 Wh energy input. Total mass of the ice dropper was 47.25 kilograms. Total cross-sectional area of the plexiglass housing was 0.8 m^2. On the test site the ice dropper was powered and controlled with external power and ethernet cables connected to it.
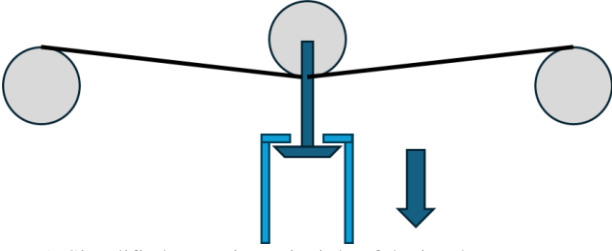
Figure 1. Simplified operating principle of the ice dropper prototype. Cable goes through three wire guides and the cable can be tensioned by pulling the middle guide downwards with a remotely operated electric motor. Tension is instantly released by releasing the clamps pulling the guide.

C. Tension model

A physical simulation model of the cable setup was created with COMSOL Multiphysics software in order to analyse the load cell data. Physical model was created with the truss interface of the structural mechanics package of the software. The cable was modelled as a freely hanging wire pinned from both ends under the influence of gravity, drag force due to wind and thermal expansion. Linear density 0.486 kg/m, Young's modulus of 66 GPa, Poisson's ratio of 0.3 and coefficient of thermal expansion of $17.8 * 10^{-6}$ K^{-1} were taken from the cable's datasheet. Ice dropper was introduced as a point load on the cable. Additional ice load on cable was taken into account as mass per unit length. Effective increase of cable diameter was solved for drag force calculation by assuming a constant rime ice density of 0.3 g/cm^3. Drag force acting on cable and ice dropper was calculated according to

$$F_d = \frac{1}{2} C_d \rho v^2 A.$$

Here C_d is the drag coefficient, ρ is the density of air, v is the flow speed and A is reference area. For the cable we used C_d of 1.1 and diameter of the cable for reference area resulting in drag force in N/m units. Drag force acting on the ice dropper was calculated assuming it to be a plate with cross sectional area of 0.8 m^2 and drag coefficient of 1.2. Resulting force was calculated only perpendicular to the cable and gravity. COMSOL model was compared against an analytical solution of a catenary [IRVINE] without point load of the ice dropper and drag forces. On average the COMSOL model produced 10 percent higher tension than the analytical solution with similar trend as with increased ice load as shown in Fig. 2. COMSOL model was chosen instead of the analytical solution due to its ability to easily incorporate point loads, drag forces and thermal expansion of the cable. Drag forces were solved only for wind perpendicular to the cable and ice dropper and its effect was small under 10 m/s wind speeds. Figure 3 shows that thermal expansion of the cable had a major effect on the

tension when temperature was varied to match the winter conditions on Olos.

The COMSOL model was run by varying the input parameters λ (additional ice load in N/m), v (wind speed in m/s) and T (temperature in °C) in the typical range of the conditions in Olos. For each run the cable tension was recorded at the location corresponding to the load cell. The resulting simulation dataset was used to create a linear regression model to retrieve the ice load on the cable as:

$$\lambda_{ice} = c_1 + c_2 F_T + c_3 T + c_4 |v_\perp|.$$

Here F_T is the tension in kN, T is temperature, $v_\perp$ is the wind perpendicular to the cable and coefficients are $c_1 = -19.64$, $c_2 = 3.11$, $c_3 = 0.13$ and $c_4 = -0.02$.

Simulations and later measurement data showed that the cable tension has only limited capability to predict the absolute value of the ice load on the cable. This is due to the fact that tension is very sensitive to the initial length of the cable and geometry. This was observed when the tension values of the COMSOL model was calculated with different initial values within the uncertainty of the initial geometry of the installation location. Small changes in initial length of the cable were observed to change the absolute value of tension by 30%. Fortunately, the change of tension due to ice load on cable seemed to be independent of the initial cable length both in COMSOL model and in analytical solution.
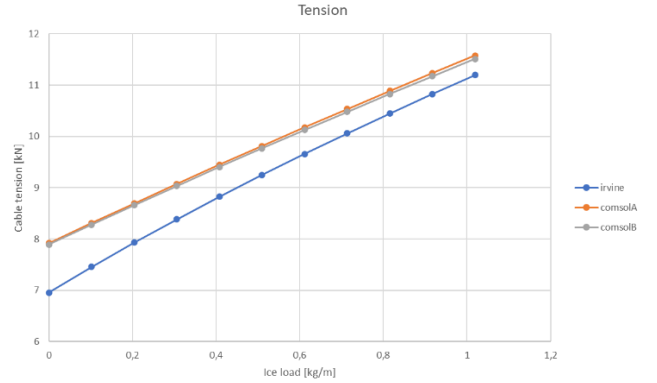
Figure 2. Comparison of Numerical COMSOL model and the analytical solution of a hanging wire without point load due to the ice dropper. Numerical model is on average 10 percent higher than the analytical solution while the response to ice load is similar.
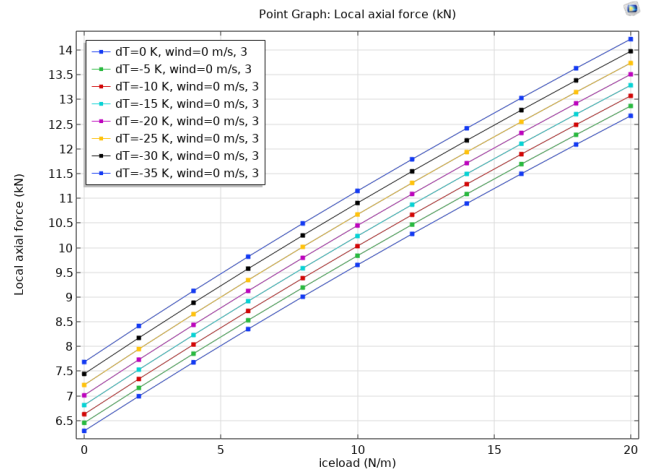
Figure 3. Effect of thermal expansion on the cable tension in the numerical model. Temperature is given as difference in K to reference temperature 0 °C.

D. Cloud droplet detector

The icing condition evaluation method (ICEMET) sensor is a novel holographic cloud particle imaging instrument. The ICEMET-sensor is designed for operation in harsh icing conditions with a 500 W heating capacity to protect it from icing. The sensor rotates freely to align itself correctly according to the wind direction. It can measure objects captured in the hologram with diameters ranging from 5 μm up to 1 mm, covering well the 10 to 30 μm diameter cloud droplet size range which significantly influences cloud ice formation on structures. The sensor system provides individual cloud particle information, as well as parameters such as liquid water content (LWC) and median volume diameter (MVD).

The holographic measurement relies on in-line holographic imaging using a point light source. The device captures 2048 x 2048 pixel holograms with a Sony IMX264 grayscale image detector with a global shutter. The holograms are exposed with a 660 nm laser diode (Ushio Opto Semiconductors Inc.) which is controlled by an in-house-built laser driver that produces 15 ns long pulses. The short laser pulse length effectively freezes the moment of the droplets in the holograms. The system has been tested up to wind speeds of 40 m/s. The maximum sampling rate of the system is 6 Hz, limited by the USB2-connection bandwidth of the slip-ring of the sensor. Typically, sampling rates from 0.25 Hz to 1 Hz have been used in field measurements. [8]

The holograms captured using the ICEMET sensor undergo analysis using a software called ICEMET-Server. This analysis software is built with C++, utilizing the OpenCV library, and is GPU-accelerated. Most of the algorithms developed for the software are based on the ideas described by Fugal et al. [9, 10].

III. Experiments

A. Ice dropper launch tests

Ice dropper was tested in field on the Olos site between 13.12.2021 and 9.3.2022 in winter conditions. Ice dropper was remotely controlled when sufficient ice accretion was observed from the surveillance camera feed. During the winter ice shedding experiments were performed on 24 individual dates. Each experiment consisted of 2 to 12 successive reload and launch cycles of the ice dropper with a total of 108 launches. In challenging and remote environment most tests lacked either weather or tension data or both due to technical problems. In these cases the launch tests were only accompanied with images from surveillance camera images before and after tests but in most cases they were unusable due to the fact that ice covered cable was indistinguishable from snowy background.

Data from successful launch dates with both weather and tension data are collected in Table 1 which includes a total of 28 launches on 8 different days with wide range of weather conditions. Visually the launches caused typically a whiff of snow and ice separating from the cable.

Before and after images of three launches are shown in Figures 4, 5 and 6 when the visibility and lighting were suitable for visual inspection. Images show that the ice dropper was not able to fully clear the cable on these tests. On

4th and 23rd of Feb the cable can't be distinguished from the background snow in before images but after dropper launches the cable is partially cleaned of ice and can be observed against background. On 15th of Feb visibility and lighting conditions are optimal and the frozen cable is visible against the shadows on the ground. 15th of February represents the most extreme ice load on the cable that was observed during the experiment campaign. While the ice dropper wasn't able to fully clear the cable of ice, large chunks of ice were observed to shed and based on the tension change largest amount of ice relative to the cable mass was removed.

TABLE I. Ice dropper test launches and removed ice load.

Date	Launches	T [C]	v [m/s]	Δλ [N/m]	Δm/m$_0$ [%]
23.12.21	6	-17	9	0	0
12.1.22	6	-3.5	13.5	1.6	33.6
4.2.22	4	-18.5	8	0.7	14.7
15.2.22	4	-11	2	2.9	60.8
16.2.22	3	-11.6	3	0	0
18.2.22	3	-7.9	12	0.25	5.2
21.2.22	3	-13.3	3.4	2	41.9
23.2.22	3	-17	5	1.2	25.2

Figure 4. Before and after images from series of 4 succesive ice dropper launches on 4th of February. Ice is partially removed and the cable is exposed.

Figure 5. Before and after images from series of 4 succesive ice dropper launches on 15th of February. Cable is not exposed but large chunks of ice was shed.

Figure 6. Before and after images from series of 4 succesive ice dropper launches on 23rd of February. Ice is partially removed and the cable is exposed.

According to the load cell tension data, typically the first of the consecutive launches had the most significant ice shedding effect while the latter launches in series had only minor effect or no effect on the ice load. Figure 7 shows examples of the loadcell raw data with one minute interval and the cable tension averaged over 10 minute interval during successful and failed ice shedding tests. Start time of the experiment is marked with dashed line and the reloading of the ice dropper can be seen as spikes in the raw data followed by a large drop of tension after the first launch on 15th of Feb. While no drop of load is observed in 16th of Feb, the ice dropper activity is seen in the raw data.

Long term suitability of a mechanical ice dropper in fixed position might be an issue. Total of 108 reload and launch cycles of the ice dropper were conducted during test campaing and a visible signs of wear was observable when the cable was inspected after removing it from the test site. Wear can be seen in Figure 8.
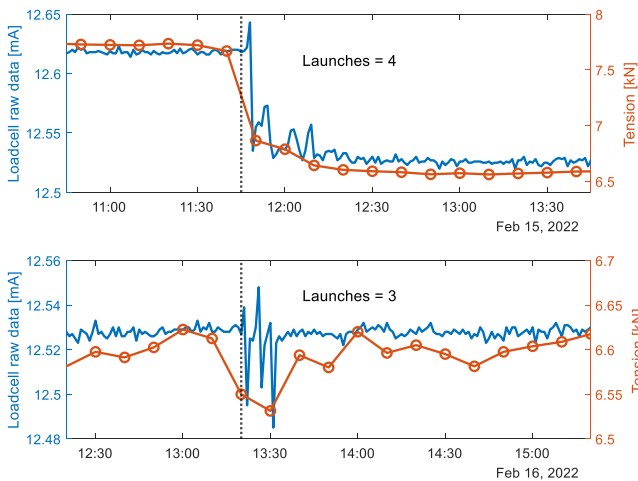
Figure 7. Load cell raw data and tension on 15th and 16th of February ice dropper launches. Reload and launch cycle is clearly seen in the raw data with one minute logging interval. Signigicant amount of ice was observed to shed on the 15th of Feb.

Figure 8. Scratches on the cable after test campaing.

B. Cloud droplet and icing event observation

Between the launcher tests on 21st and 23rd of February 2022 all sensors were operational during an atmospheric icing event. During this event temperature was below freezing point and the ICEMET sensor detected significant amount of atmospheric LWC. Average temperature during the continuous LWC period was -15.3 °C while the wind was 3.3 m/s nearly perpendicular to the cable. Formation of ice load on the cable was observed independently from the cable tension data and also visually confirmed from the surveillance camera images. Figure 9 shows the diameter of the ice covered cable, ice load estimated with the COMSOL model and the measured LWC and MVD values during the event.
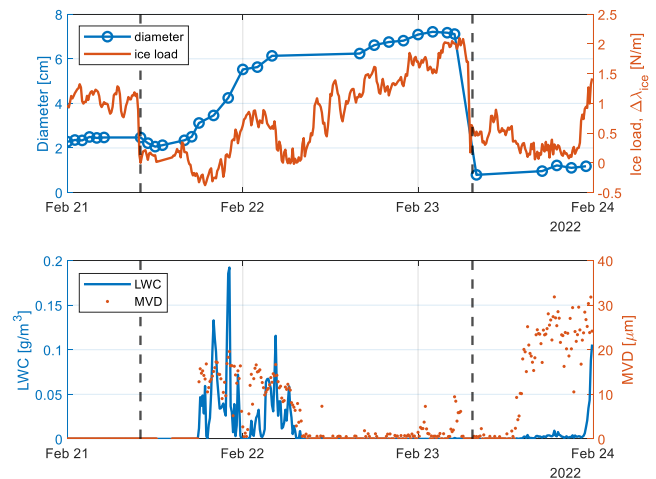
Figure 9. Evolution of ice layer diameter and ice load between two ice dropper launches (dashed lines) and the detected atmospheric icing event with up to 0.2 g/m³ LWC.

Visibility of the site in the surveillance camera images severely degrades on the evening of Feb 21st and the ICEMET sensor detects liquid water content on the air for several hours. Detected LWC and MVD values shown in Fig. 9 are averaged over ten minute periods. Detection of LWC is accompanied by a rapid increase in the diameter of the ice layer on the cable. Diameters were measured from the surveillance camera images with one hour intervals when allowed by visibility during the event. Diameter was determined from an approximately 5 meter long section of the cable closest to the camera. Sobel edge detection algorithm was used to detect the edges of the ice covered cable in the images and the results of edge detection were manually inspected and confirmed. Width of the ice layer was measured independently for each vertical pixel row in the region of interest and the effect of perspective was eliminated by normalizing the width against images of clean cable. Ice mass was then calculated by assuming a spanwise perfectly cylindrical ice layer over the cable. Temperature and wind conditions during the event result in rime ice with density of 0.1 g/m³ according to the ISO standard [1]. Image based estimate of the ice mass provided a peak value of ice load of 16 N/m after the event. Visually estimated ice load is larger than ice load solved from the tension measurement. This may indicate that the assumptions about the uniformity of the ice layer in image based estimation method overestimate the total volume of ice. Another possibility for the discrepancy is that the physical model doesn't include the supporting structures and fixing point and

their behaviour under tension and variable temperature conditions.

IV. Conclusion

A prototype ice dropper was built and tested in challenging field conditions. Tension of the cable was measured during the tests and the atmospheric icing conditions were monitored using a novel holographic cloud droplet sensor. The prototype ice dropper was based on the idea of delivering kinetic energy on the cable by sudden release of additional tension introduced by the ice dropper unit. The ice dropper showed limited success on removing the ice. Cable tension and visual observation indicated that the ice dropper was more successful on the cases where the amount of ice on the cable was high. However, large ice loads on the cable were rare during the measurement campaign and the amount of ice seen in Fig. 5 represents the most extreme case. Signs of wear were observed after the campaign on the cable.

References

[1] ISO12494:2017", Atmospheric icing of structures, Mar. 2017

[2] Zhang, Zhijin, Hang Zhang, Song Yue, and Wenhui Zeng. 2023. "A Review of Icing and Anti-Icing Technology for Transmission Lines" Energies 16, no. 2: 601

[3] C. Liu, J. Qin, Y. Hao, G. Li and Y. Chen, "Research on Verification Test of Tension Stringing for UHV Transmission Line Project," 2020 IEEE Sustainable Power and Energy Conference (iSPEC), Chengdu, China, 2020, pp. 1766-1771

[4] Montambault, Serge and Nicolas Pouliot. "The HQ LineROVer: contributing to innovation in transmission line maintenance." 2003 IEEE 10th International Conference on Transmission and Distribution Construction, Operation and Live-Line Maintenance, 2003. 2003 IEEE ESMO. (2003): 33-40.

[5] Pascal. P.H.,et.al. "Determination of Current Required to De-Ice Transmission Line Conductors", IWAIS XI, Montréal, June 2005.

[6] M. Landry, R. Beauchemin, A. Venne, De-icing EHV overhead transmission lines using electromagnetic forces generated by moderate short-circuit currents in: 2000 IEEE ESMO - 2000 IEEE 9th International Conference on Transmission and Distribution Construction, Operation and Live-Line Maintenance Proceedings. ESMO 2000 Proceedings. Global ESMO 2000. The Pow, 2000, pp. 94–100.

[7] Irvine, Max. *Cable Structures*. New York: Dover, 1992.

[8] Kaikkonen, V. A., Molkoselkä, E. O., & Mäkynen, A. J. (2020). A rotating holographic imager for stationary cloud droplet and ice crystal measurements. Optical Review, 27, 205-216.]

[9] Molkoselkä, E. O., Kaikkonen, V. A., & Mäkynen, A. J. (2020). Measuring atmospheric icing rate in mixed-phase clouds using filtered particle data. *IEEE Transactions on Instrumentation and Measurement*, *70*, 1-8.

[10] Fugal, J. P., Schulz, T. J., & Shaw, R. A. (2009). Practical methods for automated reconstruction and characterization of particles in digital in-line holograms. *Measurement Science and Technology*, *20*(7), 075501.

Study on the Rime Accretion on Energized Conductor under Different Electric Field Strengths

Tianqi Yu[a], Liming Wang[a], Fanghui Yin[a,*], and Masoud Farzaneh[b]

[a] Shenzhen International Graduate School, Tsinghua University, China
[b] Department of Applied Sciences, University of Quebec at Chicoutimi, Canada
[*] AndyYinEE@gmail.com

Abstract: Establishing a comprehensive conductor icing model helps to understand the icing mechanism and has important theoretical and practical value for predicting transmission line icing and formulating de-icing strategies. This paper additionally introduces the electric field around the conductor during steady-state simulation, and takes into account the dielectrophoretic force and electric field force on the particles during transient simulation. Based on the calculation results of local collision efficiency and the Bain-Gayet ice density formula, the expression for calculating the thickness of ice accretion is derived. High-order polynomials were selected to fit the icing-shaped boundary, and the differences in ice accretion characteristics of conductors after 30 minutes of icing were iteratively calculated. The simulation and experimental results show that as the electric field strength increases, the icing shape first expands outward and then contracts inward, and the icing amount and ice density both increase and then decrease. The simulation model can well match the experimental results.
Keywords: Rime accretion, Energized conductor, Electric field

1. Introduction

For artificial systems such as power systems, atmospheric icing is a serious threat, with the icing problem of transmission line conductors being particularly prominent [1]. The icing of transmission lines can cause mechanical and electrical accidents, and many countries such as the United States and Canada face serious icing threats to their transmission lines. In 1961, Norway experienced severe conductor icing, with the maximum cross-sectional diameter of the elliptical icing on the line reaching 1.4m and the amount of icing reaching 300kg/m [2].

It is essential to establish an icing growth model that includes different environmental parameters, analyze the influencing factors of icing, and ultimately achieve the prediction of conductor icing. Imai is the first to research the glaze icing process of conductors, believing that there is always a layer of water film on the surface of the icing, and the freezing amount of surface water is directly related to the icing growth [3]. Goodwin researched dry-growth icing and obtained an expression for the influencing factors of icing thickness through a series of theoretical deductions [4]. Makkonen model is a numerical model based on the conductor icing mechanism, which puts forward reasonable fluid mechanics and heat transfer explanations for conductor icing, and discusses in detail the collision, capture, and freezing process of supercooled water droplets and the conductor [5]. However, most current conductor icing models are based on the condition that the conductor is not energized, and the predicted icing amount and shape of the model differ greatly from the actual icing situation on the transmission line. Lozowski conducted wind tunnel tests to investigate the icing on the surface of non-rotating, unheated conductors to validate their proposed time-varying glaze icing model [6-7].

In this article, in addition to the airflow field considered in previous icing models, the simulation of the electric field is also introduced in the steady-state field simulation around the icing conductor. Based on this, a DC transmission line rime icing simulation model is iteratively established. The influence of electric field strength on icing characteristics under three different working conditions is analyzed in detail, and experiments with the same simulation conditions are conducted in an artificial climate chamber to verify the correctness of the proposed icing model.

2. Modelling of Rime Icing under DC Electric Field

2.1. Modelling Process

This article uses finite element simulation software to write corresponding control scripts, which can achieve the modeling of rime icing under the expected time under the DC electric field. The modeling process is shown in Figure 1.

Firstly, set the initial conditions for simulation, such as temperature, liquid water content, and other parameters. Secondly, set the boundary conditions of the physical field, such as inlet wind velocity, outlet pressure, and other parameters, conduct DC corona simulation, steady-state flow field and electric field simulation, and transient particle field simulation, and calculate the collision efficiency based on the simulated water droplet trajectory. Thirdly, the amount of icing on the surface microelements is obtained from the local collision efficiency, and the ice density on the surface microelements is calculated from the velocity of water droplets colliding with the icing surface. The combination of collision efficiency and ice density can obtain the icing growth thickness on the surface microelements. Finally, after each iteration, determine whether the input icing time has been reached. If the time is not reached, the grid and boundary conditions need to be updated based on the new icing shape, and the previous steps need to be repeated.

1
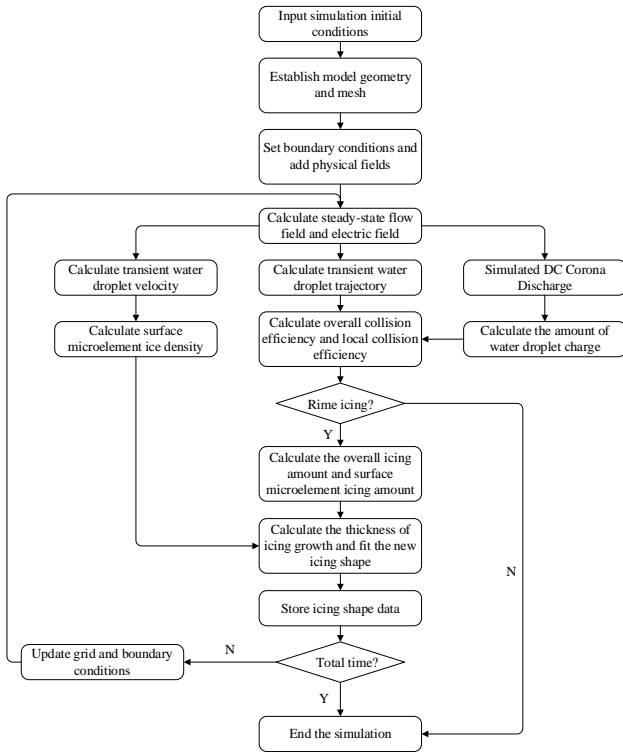
Fig. 1. *Simulation process of proposed rime icing model*

2.2. Simulation of Water Droplet Collision Efficiency

The icing load on the conductor is generated by the freezing of water droplets after colliding with the conductor. To quantitatively analyze the collision between water droplets and the conductor, the calculation of collision efficiency is important. The definition of overall collision efficiency is shown in Figure 2, which is numerically equal to the ratio of the initial distance of the envelope trajectory of water droplets to the diameter of the cylindrical conductor,

$$\eta = \frac{y_1 - y_2}{D} \tag{1}$$

where y_1 is the initial upper boundary of the envelope of the colliding droplets, and y_2 is the corresponding initial lower boundary.
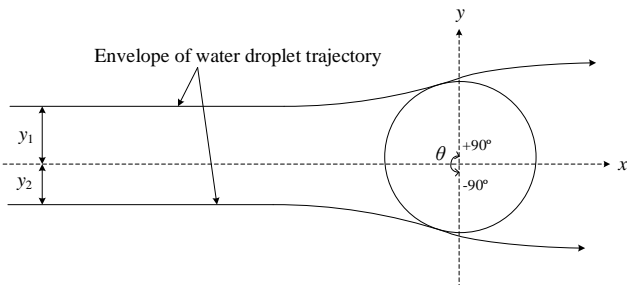
Fig. 2. *Definition of overall collision efficiency*

To obtain the shape of the icing, it is also necessary to calculate the Local Collison Efficiency (LCE), as shown in Figure 3, defined by adjacent particle trajectories:

$$\beta(\theta) = \frac{dy}{dl} \tag{2}$$

where dy is the difference in the longitudinal coordinates of adjacent particle trajectories at the starting position, and dl is the arc length of the corresponding particle along the icing surface.
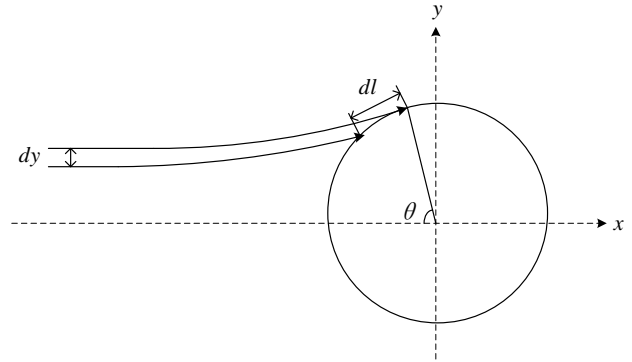
Fig. 3. *Definition of local collision efficiency*

When analysing the force on water droplets near the conductor, the force on the water droplet is a combination of drag force, buoyancy, gravity, dielectrophoretic force, and electric field force. The position of the water droplet is calculated by the motion equation. Assuming that the mass of water droplets near the conductor remains constant, according to Newton's second law, the vector equation describing the motion of water droplets is:

$$m_d \frac{dV}{dt} = F_d + F_{gb} + F_{dep} + F_e \tag{2}$$

where m_d is the mass of the water droplet, F_d is the drag force, F_{gb} is the buoyancy and gravity, F_{dep} is the dielectrophoretic force, and F_e is the electric field force. This equation is solved using the higher-order Runge Kutta algorithm to obtain the velocity and position of water droplets at different times.

The formula used to analyse the force on water droplets is as follows:

$$\begin{cases} F_d = \frac{1}{2}\rho C_D A |V - u|(V - u) \\ F_{gb} = (\rho_d - \rho)V_d g \\ F_{dep} = 2\pi a^3 \varepsilon_0 \varepsilon_1 (\frac{\varepsilon_2 - \varepsilon_1}{\varepsilon_2 + 2\varepsilon_1})\nabla |E|^2 \\ F_e = qE \end{cases} \tag{3}$$

where $A = \pi a^2$ is the cross-sectional area of the water droplet, V is the droplet velocity, and C_D is the dimensionless resistance coefficient, ρ_d is the density of water droplets, V_d is the volume of water droplets, and g is the acceleration of gravity, ε_0 is the vacuum dielectric constant, and q is the water droplet charge calculated based on the field induced charge formula.
y.

2.3. Calculation of the Growth Thickness of Rime Icing

When the number of released water droplets is sufficiently dense, the icing surface is divided into a series of microelements by the water droplets, as shown in Figure 4. The local icing amount on each surface microelement can be calculated by the local collision coefficient:

$$m_i = \beta_i V_\infty \omega l_i \Delta t \tag{14}$$

2
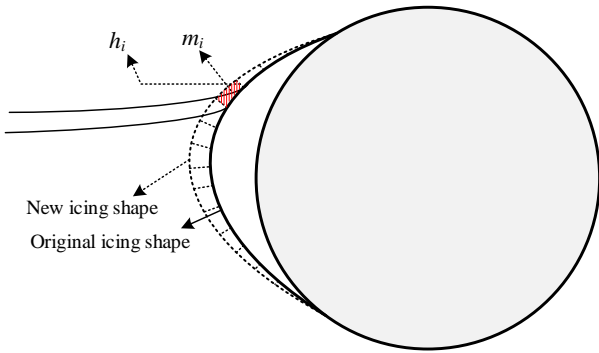
Fig. 4. *Ice growth on surface micro elements*

where m_i is the icing on the i-th segment of the element, β_i is the local collision coefficient on the i-th segment of the element, and V_∞ is the inlet wind speed, ω is the liquid water content in the air, l_i is the arc length of the i-th segment element, Δt is the time step of the iteration. In theory, the shorter the step size, the higher the calculation accuracy. However, considering the calculation cost comprehensively, the iteration is usually carried out in steps of 1 minute or 2 minutes.

3. Comparison of Simulation and Experimental results

The icing experiment is conducted in the small artificial climate laboratory. The relevant parameters for the energized icing test of three sets of parameters are shown in Table 1.

Table 1 Test parameters for icing of energized conductors

Wind velocity (m/s)	MVD (μm)	Conductor diameter (cm)	Ambient temperature (°C)	LWC (g/m³)
1.5	62.2	3.0	-8.0	1.2

The experimental and simulation results of the rime icing shape under the first set of working conditions are shown in Figure 5. When the electric field strength on the surface of the conductor is lower than 15kV/cm, no corona discharge has occurred, or the phenomenon of corona discharge is not obvious. Due to the attraction of dielectrophoretic force, the local collision efficiency of water droplets increases, and the icing shape expands towards the front of the conductor. The simulated icing shape and experimental icing shape are very consistent, and the maximum thickness deviation does not exceed 7%. When the surface field strength of the conductor is higher than 20kV/cm, there is a significant DC corona discharge. Due to the repulsion of the electric field force, the local collision efficiency of water droplets decreases, and the icing shape actually contracts inward. It is worth noting that there is a certain deviation between the simulation results and the experimental results at this time, with a maximum thickness deviation of 18.7%. This is because the reduction of icing under high electric field strength is caused by a combination of many factors. In addition to the water droplet charging factor considered in this article, the ionizing wind generated by corona discharge and the bombardment of ions on the tip of the icing can also lead to the reduction of icing.

(a)

(b)

(c)

(d)

3

(e)

(f)
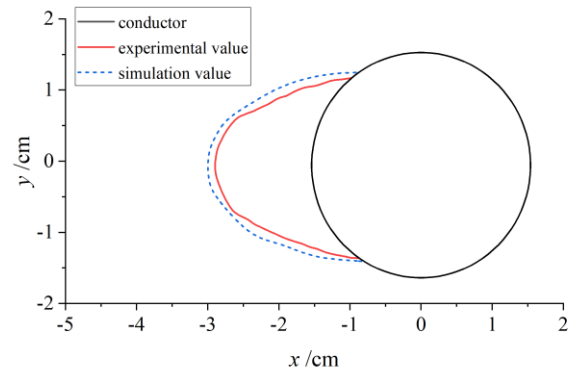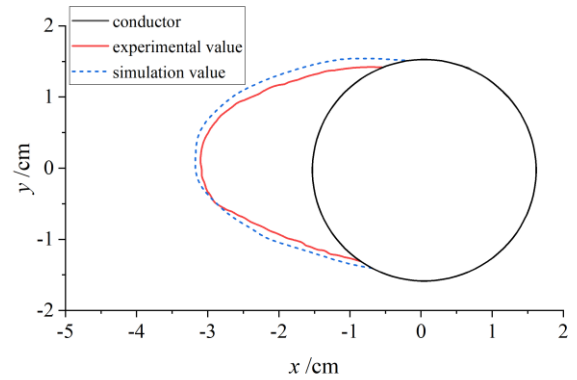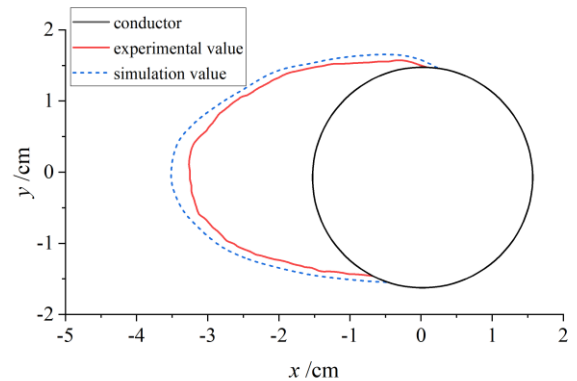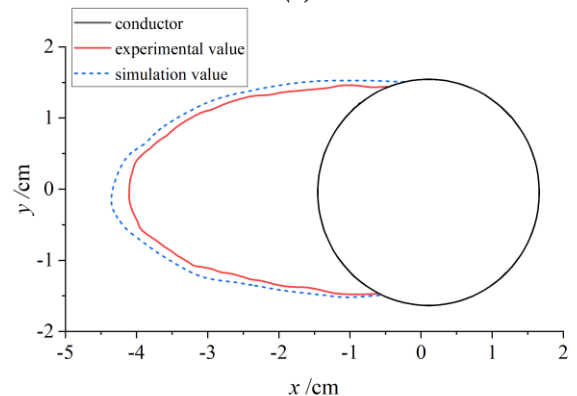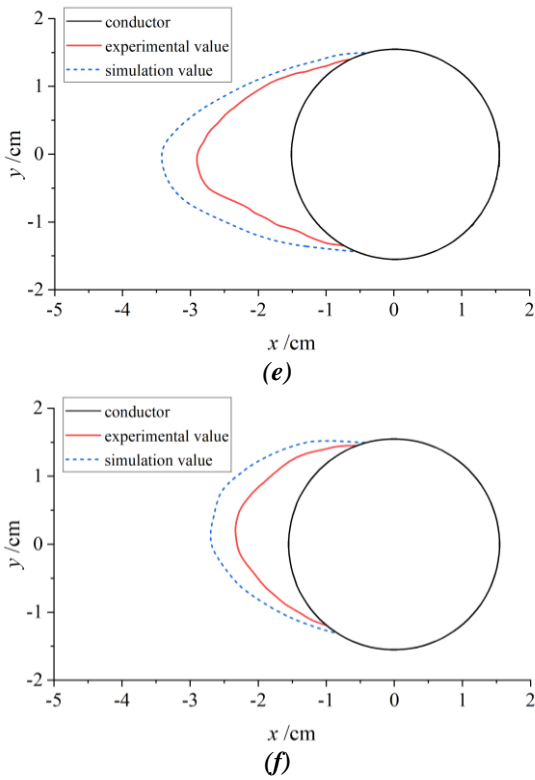
Fig. 5. *Comparison of icing shape between experiments and simulations under the first group of icing conditions (a) E_s = 0 kV/cm, (b) E_s = 5 kV/cm, (c) E_s = 10 kV/cm, (d) E_s = 15 kV/cm, (e) E_s = 20 kV/cm, (f) E_s = 25 kV/cm*

(a)

(b)
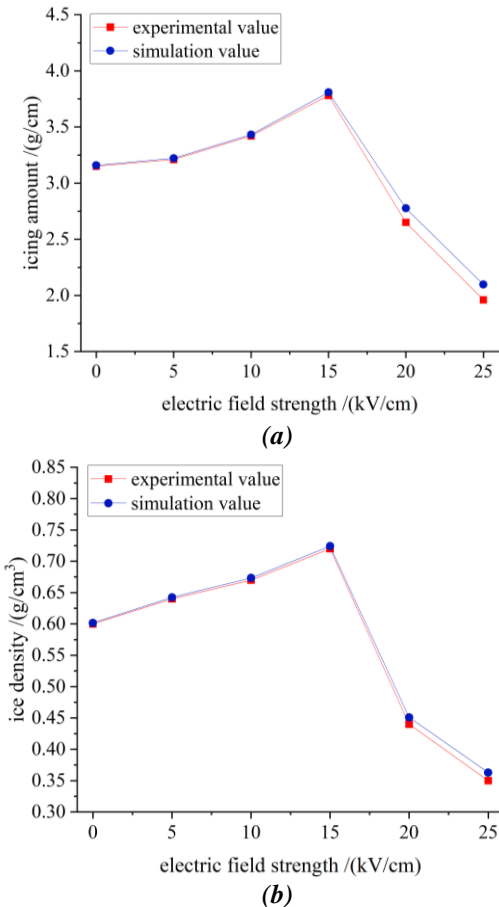
Fig. 16. *Comparison of icing amount and ice density between experiments and simulations under the first group of icing conditions (a) icing amount, (b) ice density*

The experimental and simulation results of icing amount and ice density under the first set of operating conditions are shown in Figure 6. As the electric field strength increases, both the amount of icing and the ice density show a trend of first increasing and then decreasing, but the reasons are different: the change in icing amount is caused by the overall collision efficiency change caused by particle force, while the change in ice density is caused by the change in Macklin parameters. The simulation model can effectively predict the amount and density of icing, even under an electric field strength of 25kV/cm, the simulation and experimental values of icing are 2.09g/cm and 1.96g/cm respectively, with a relative error of 6.6%. The simulation and experimental values of ice density are 0.363 g/cm^3 and 0.351g/cm^3 respectively, with a relative error of 3.4%.

4. Conclusion

To study the impact of an energized conductor on icing, this paper uses finite element simulation software to simulate the flow field, electric field, and particle field based on the simulation and experimental results of DC corona discharge. A rime icing model under DC electric field is established, and the correctness of the model is verified through high-voltage conductor icing experiments in the artificial climate chamber. The main conclusions of this paper are as follows:

(1) Based on the electric field-induced charge theory of particles, a formula for calculating the charge of water droplets near the conductor at any time is given. The calculation of the electric field is introduced into the simulation model, and the effects of dielectric electrophoresis force and electric field force are additionally considered when simulating the trajectory of water droplets, thereby calculating the collision efficiency of water droplets near the conductor.

(2) Based on the finite element software simulation method, the high-order polynomial is used to fit the ice shape, and a rime icing model for energized conductors is established through iteration. The model is validated using the same experimental conditions in the artificial climate chamber. The simulation and experimental results show that as the electric field strength increases, the icing shape first expands outward and then contracts inward, and the icing amount and ice density both increase and then decrease. The simulation model can well match the experimental results.

The above conclusions help to strengthen the understanding of the icing mechanism of energized conductors and provide theoretical references for the icing design of high-voltage transmission lines.

5. Acknowledgments

6. References

[1] Farzaneh, Masoud, ed. *Atmospheric icing of power networks*. Springer Science & Business Media, 2008.
[2] Ervik, et al. "Development of a Mathematical Model to Estimate Ice Loading on Transmission Lines by Use of General Climatological Data." *Power Apparatus and Systems, IEEE Transactions on* (1982).

4

[3] Imai I. Studies on ice accretion. *Researches on Snow and Ice* 3.1(1953): 35-44.

[4] Goodwin, E. J. I., et al. "Predicting ice and snow loads for transmission line design." *Proceedings of the 1st International Workshop on Atmospheric Icing of Structures, NH, USA*. 1983.

[5] Makkonen, Lasse. "Modeling power line icing in freezing precipitation." *Atmospheric research* 46.1-2 (1998): 131-142.

[6] Lozowski, E. P. , J. R. Stallabrass , and P. F. A. Hearty . "The Icing of an Unheated, Nonrotating Cylinder. Part I: A Simulation Model." *Journal of Applied Meteorology* 22.12(1983):2053-2062.

[7] Lozowski, E. P. , J. R. Stallabrass , and P. F. Hearty . "The Icing of an Unheated, Nonrotating Cylinder. Part II. Icing Wind Tunnel Experiments." *Journal of Applied Meteorology* 22.12(2010):2063-2074.

[14] Farzaneh, M. , and J. L. Laforte . "Ice Accretion on Conductors Energized by AC or DC : A Laboratory Investigation of Ice Treeing." International Society of Offshore and Polar Engineers(1994).

[15] Yin, F. , M. Farzaneh , and X. Jiang . "Influence of AC electric field on conductor icing." *IEEE Transactions on Dielectrics and Electrical Insulation* 23.4(2016):2134-2144.

[16] Farzaneh, et al. "Corona Investigation of an Energized Conductor under Various Weather Conditions." *IEEE Transactions on Dielectrics & Electrical Insulation A Publication of the IEEE Dielectrics & Electrical Insulation Society* (2017).

[17] List, Roland. "General heat and mass exchange of spherical hailstones." *Journal of Atmospheric Sciences* 20.3 (1963): 189-197.

[18] Bain, M. , and J. F. Gayet . "Contribution to the modelling of the ice accretion process: ice density variation with the impacted surface angle." *Annals of Glaciology* 4(1983):19-23.

5

Method for Measuring Ice Thickness and Density of Conductor Based on Its Capacitance Effect

Lina Dong[1], Zhijin Zhang[1], Hualong Zheng[1], Yunxuan Jiang[2]

[1] *Xuefeng Mountain Energy Equipment Safety National Field Scientific Observation and Research Station of Chongqing University/Chongqing/China*
[2] *Chongqing De-icing Group Technology Co. Ltd./Chongqing/China*

31790865@qq.com, zhangzhijing@cqu.edu.cn, hualong.zheng@cqu.edu.cn, 3121043930@qq.com

Abstract—**Ice-covering of conductors seriously endangers the safe operation of power grid. The measurement of ice thickness as well as its density is the basic basis of ice disaster prevention and emergency treatment of power grid. At present, the measurement methods based on wire tension and insulator string inclination or video image are widely used at home and abroad, which cannot accurately measure the actual ice thickness of the wire, let alone the density of the ice. Based on the dielectric characteristics of ice, this paper obtained the variation law of ice capacitance with ice thickness and density through artificial simulation and field test. According to the law that ice thickness of cylindrical wire decreases with the increase of wire diameter, a method for monitoring ice thickness and ice density of wire based on cylindrical array ice capacitor was proposed. Theoretical analysis and test results show that, Ice capacitance increases steadily with the increase of ice thickness and density, and the change of capacitance can accurately characterize the ice thickness and ice density. Therefore, the proposed method of monitoring ice thickness and ice density of wire based on ice capacitance on cylindrical array can solve the international problem of ice accurate measurement.**

Keywords—*Ice Accurate Measurement ； Ice Thickness; Ice Density; Ice Capacitance; Nature Field*

I. INTRODUCTION

As the global climate warms, less water vapor reaches the clouds. Although there are extreme cold days in winter, there is less snow. But ice is becoming more frequent. Under the condition of inversion layer, the ice crystals in the cloud melt during the falling process and turn into supercooling water when falling to the near ground, and the supercooling water falls on the low-temperature structure such as the wire, which quickly releases latent heat and turns into solid ice, forming the structural ice covering. China is one of the most serious ice-covered countries in the world, especially the distribution of micro-topography and micro-climate ice-covered is extremely random. Since the large-scale ice disaster in southern China in 2008, China has carried out a lot of research in the field of power grid anti-icing and ice monitoring, but because of the freezing problem of various sensors under ice conditions, ice monitoring has been a scientific problem and the key to the international solution. At present, it is widely used in power grid to estimate the equivalent ice thickness indirectly based on the variation of the tension of the ice-covered wire and the inclination of the insulator string, which has serious problems such as low accuracy and poor reliability, and can not effectively guide the implementation of various anti-ice and disaster reduction technologies and methods in power grid. Exploring new ice monitoring technology to improve the accuracy of ice monitoring has important

theoretical significance and engineering application value for effective ice prevention and disaster reduction of power grid.

II. TEST SITE AND METHOD

The experimental research of this paper was carried out in the large multi-functional artificial climate Chamber of Chongqing University, the National Field Scientific Observation and Research Station of Xuefeng Mountain Energy Equipment Safety in Hunan Province, and the Wulong Energy Equipment Safety Field Scientific Observation and Research Station, as shown in Fig. 1. Experiments on ice capacitance effect of structures are carried out, aiming to find out the main physical quantities affecting the change of ice capacitance and their relationship with the change of ice capacitance by analyzing the experimental data.

(a) Artificial climate chamber   (b) Wulong field station

(c) Xuefeng Mountain field station

Fig. 1   Test facilities and field sites

A. Manual Simulation

In the artificial climate chamber, the method of box ice covering and cylindrical distributed electrode is adopted, as shown in Fig. 2.

(a) Box ice covering

(b)Cylindrical distributed electrode icing

Fig. 2 Artificial climate chamber ice covering

B. Field Test

During the icing season, natural icing experiments were carried out at Xuefengshan Energy Equipment Safety National Field Scientific Observation and Research Station and Wulong Energy Equipment Safety Field Scientific observation and research Station with cylindrical array. In this paper, a four-cylinder array with different diameters is used, each cylinder is evenly arranged with three electrodes, and the cylinder is rotated at a constant speed of 3rps to make it evenly coated with ice in order to accurately measure the change of its capacitance with the ice thickness.

(a) Cylinder and electrode structure

(b) Ice coating of cylindrical electrode
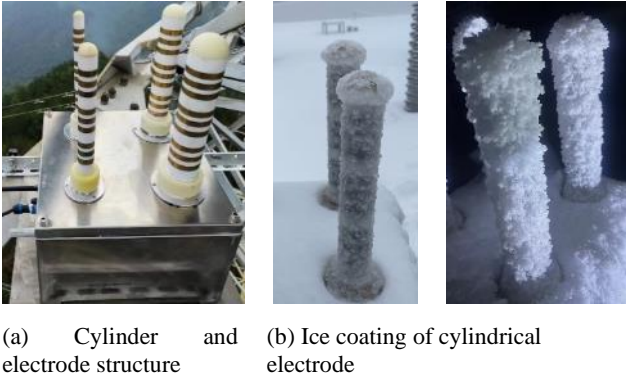
Fig. 3 Iced cylindrical electrode array at Xuefeng Mountain field station

III. DIELECTRIC PROPERTIES OF ICE AND INFLUENCING FACTORS OF ICE CAPACITANCE

A. Dielectric Properties of Ice

Ice is a good insulator in low temperature freezing conditions, and its dielectric properties are good, but its dielectric properties change significantly with the change of temperature and density, etc. The equivalent circuit of ice is shown in Fig. 4.
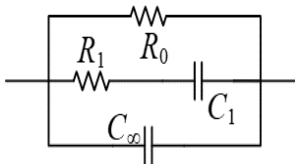
Fig. 4 equivalent circuit of Ice

In Fig. 4, C_1、 C_∞ are the capacitance of ice under low frequency and high frequency excitation respectively, F; R_0、 R_1 are the resistance of low frequency and high frequency respectively, Ω. As shown in Figure 4, the equivalent circuit complex impedance (Z) of ice is:

$$\frac{1}{Z} = \frac{1}{R_0} + \frac{1}{R_1 + 1/j\omega C_1} + j\omega C_\infty \qquad (1)$$

where: $j=\sqrt{-1}$；ω is the angular frequency of the applied voltage signal, Hz. According to the Debye Relaxation Equation, the complex form of the relative dielectric constant of ice (ε) can be obtained as:

$$\varepsilon = \varepsilon_\infty + \frac{\varepsilon_s - \varepsilon_\infty}{1 + j\omega\tau} = \varepsilon' + j\varepsilon'' \qquad (2)$$

where : $\varepsilon_s = \frac{L}{\varepsilon_0 A}(C_1 + C_\infty)$, $\varepsilon_\infty = \frac{LC_\infty}{\varepsilon_0 A}$,

$\varepsilon' = \varepsilon_\infty + \frac{\varepsilon_s - \varepsilon_\infty}{1 + \omega^2\tau^2}$, $\varepsilon'' = \frac{(\varepsilon_s - \varepsilon_\infty)\omega\tau}{1 + \omega^2\tau^2}$; ε' is the real part of the relative dielectric constant；ε'' is the virtual part of the relative dielectric constant, representing the dielectric loss； ε_s is the static relative dielectric constant；ε_∞ is the relative dielectric constant of high frequency and is generally considered to be temperature independent； $\tau=R_1C_1$ is the relaxation time of the dielectric； L is the thickness of the square block ice，A is the surface area of the square block ice.

In this paper, the power frequency is used to measure the ice capacitance, and the power frequency is low, so the complex characteristics presented in the high frequency condition can be ignored. Therefore, according to the Debye relaxation equation, under the power frequency condition measured in this paper, applicable $L \geq 2\varepsilon_0\varepsilon A\omega R_1$, capacitance of ice (C_1)and dielectric constant of ice (ε)can be obtained as：

$$\varepsilon = \frac{LC_1}{\varepsilon_0 A(1+\omega^2 R_1^2 C_1^2)} \qquad (3)$$

$$C_1 = \frac{L \pm \sqrt{L^2 - 4\varepsilon_0^2\varepsilon^2 A^2\omega^2 R_1^2}}{2\varepsilon_0\varepsilon A\omega^2 R_1^2} \qquad (4)$$

B. Factors Affecting Ice Capacitance

As can be seen from equation (4), the main factors affecting the capacitance of the ice sheet include ice thickness, ice density, ambient temperature and the content of conductive impurities in the ice sheet. In this paper, a lot of experiments and tests have been carried out in field stations and artificial climate chambers, and the factors affecting the capacitance of ice sheets and their laws have been obtained. Through the fitting relation between capacitance and ice thickness and ice density $d = f(C)$、 $\rho = g(C)$(d is the thickness of ice，mm; C is the capacitance of ice，μF； ρ is the density of ice，g/cm³）。

1) *The Effect of Ice Thickness:*A four-cylinder array was used to measure the effect of ice thickness and cylinder diameter on capacitance at Xuefeng Mountain Field station, and the test results are shown in Fig. 5.
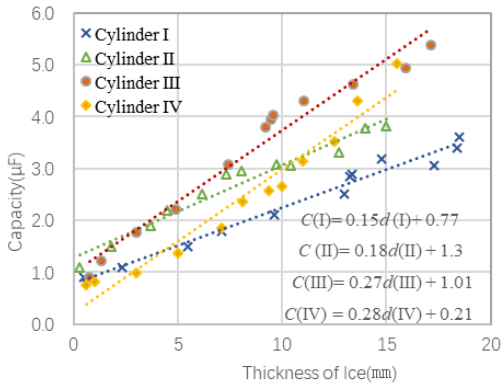
Fig. 5 Capacitance characteristics of natural ice covering cylindrical array at Xuefeng Mountain field station
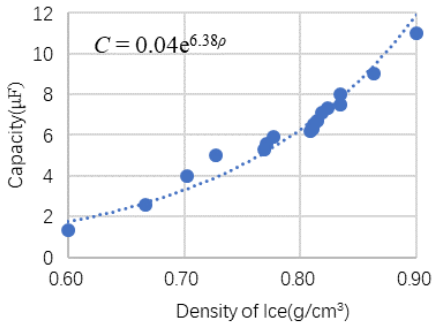
Fig. 6 Variation of capacitance and density of ice

It can be seen from the test results and analysis in Fig. 5 that the measured ice capacitance increases basically in a linear relationship with the increase of ice thickness, all satisfied $C=\gamma d+\beta$ (C is the total capacitance of the electrode group on the cylinder；γ is coefficient，which is related to the diameter of the cylinder；d is the thickness of ice；β is an additional factor brought about by measurement and other factors，which is negligible）；Therefore，the ice capacitance on the cylindrical electrode can be expressed as：$C=\gamma d$。

2) *Influence of Overlying Water Density:* The density of ice has a significant effect on its capacitance, and the test results and analysis in Fig. 6 show that when the density of ice is between 0.60 and 0.90 g/cm3, as the density of ice increases, its capacitance basically increases in accordance with the exponential law, meeting the law of $C=a*e^{b}$。It can be seen that the higher the density, the greater the capacitance value. Therefore, the density of ice can also be obtained by measuring the change law of its capacitance.

3) *The Effect of Ambient Temperature:* Ambient temperature affects the freezing form of ice. The test results and analysis in Fig. 7-9 show that when the ambient temperature is below 0℃ and the ice is frozen, the measured capacitance of ice decreases linearly with the decrease of ambient temperature.
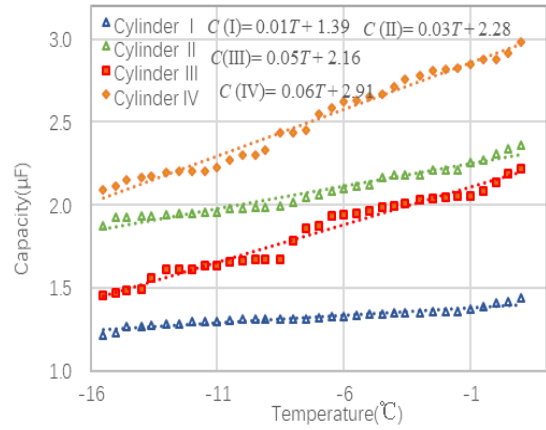
Fig. 7 Natural ice capacitance changes with ambient temperature at Xuefeng Mountain field station
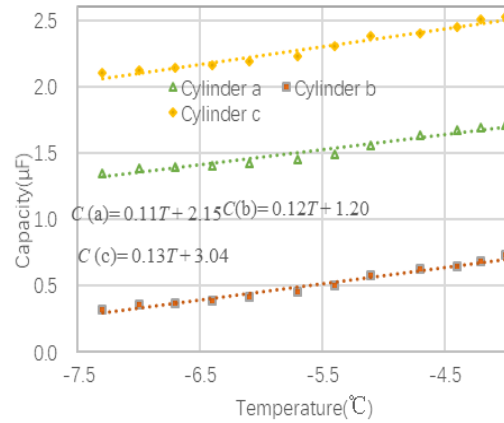
Fig. 8 Natural ice capacitance changes with ambient temperature at Wulong Mountain field station
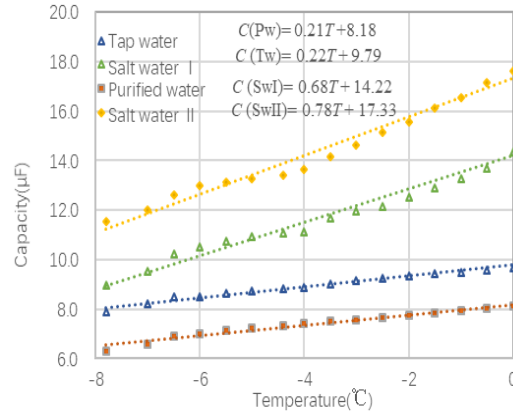
Fig. 9 The change of box ice capacitance with ambient temperature in artificial climate chamber

4) *The effect of ice temperature:* In the experiment, a digital thermometer probe was placed in the ice covering device under the same conditions to monitor the ice temperature after the ice covering of four different electrical conductivity. The test results in Fig. 10 show that when the condensation point is below 0℃, the measured capacitance changes greatly. Then, the capacitance of the ice decreases exponentially with the decrease of temperature until it becomes stable.

33
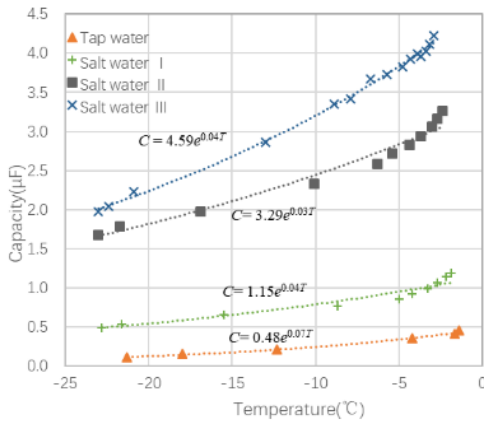
Fig. 10 Effect of ice temperature on ice capacitance

IV. CONCLUSION AND DISCUSSION

A. Ice is a kind of dielectric, and the capacitance of ice varies with its dielectric constant. The main factors affecting the dielectric properties of ice and the capacitance of ice are the thickness of ice, the density of ice, the conductivity of ice water and the ambient temperature.

B. Ice thickness and density covered on various structures can be measured by measuring ice capacitance, ice water conductivity and ambient temperature.

C. Ice capacitance-based measurement is a feasible method that can accurately measure ice cover. Research on ice capacitance-based measurement methods can be carried out in the future, and devices for measuring ice cover thickness and density based on ice capacitance-based measurement can be developed to solve the international problems that have been plaguing ice cover measurement.

REFERENCES

[1] Xingliang Jiang, Zhijin Zhang, Lichun Shu. *Atmospheric ice and defense [M]*. 2020.

[2] Harris P, Harris D. *The great ice storm of 1998[J]*. Countryside and Small Stock Journal, 1998, 82(3): 26.

[3] Farzaneh M, Baker T, Bernstorf A, et al. *Insulator icing test methods and procedures a position paper prepared by the IEEE Task Force on insulator icing test methods [J]*. IEEE Transactions on Power Delivery, 2003, 18(4): 1503-1515.

[4] Gyakum J R, Roebber P J. *The 1998 Ice Storm-Analysis of a Planetary-Scale Event[J]*. Monthly Weather Review, 2001, 129(12): 2983-2997.

[5] Peng F. *Dynamic characteristics of overhead transmission lines following ice shedding based on Lagrange equation[C]*//International Power, Electronics and Materials Engineering Conference. Paris, France: Atlantis Press, 2015: 241-246.

[6] Sijian Zhang, Zhiyun Lin, Gangfeng Yan. *Ice thickness measurement method for overhead transmission lines based on capacitance sensor[J]*. Automation of Electric Power Systems, 2011, 35(17): 99-102.

[7] YinKe Dou, Xiaomin Chang, Zhuo Dun, et al. *Application of capacitive sensing ice thickness monitoring system in Antarctic sea ice monitoring [J]*. Mathematics in Practice and Theory, 2014, 44(04): 197-204.

[8] Elzaidi A, Masek V, Bruneau S. *Water and Ice Detection in Marine Icing by Capacitive Sensor Array and the Artificial Neural Network Model[C]*//2019 IEEE 10th Annual Information Technology, Electronics and Mobile Communication Conference. IEEE, 2019: 94-97.

[9] Homola M C, Nicklasson P J, Sundsb P A. *Ice Sensors for Wind Turbines[J]*. Cold Regions Science and Technology, 2006, 46(2): 125-131.

[10] Andersson O. *Dielectric Relaxation of the Amorphous Ices[J]*. Journal of Physics: Condensed Matter, 2008, 20(24): 244115.

[11] Zhu Y C, Huang X B, Tian Y, et al. *Experimental Study on the Icing Dielectric Constant for the Capacitive Icing Sensor[J]*. Sensors, 2018, 18(10): 3325.

[12] Mughal U N, Virk M S, Mustafa M Y. *Dielectric Based Sensing of Atmospheric Ice[C]*. AIP Conference Proceedings. AIP, 2013, 1570(1): 212-220.

[13] Owusu K. *Capacitive Probe for Ice Detection and Accretion Rate Measurement: Proof, of Concept[J]*. Renewable Energy, 2013, 50(3): 196-205. Artemov V, Volkov A. Water and ice dielectric spectra scaling at 0℃[J]. Ferroelectrics, 2014, 466(1): 158-65.

[14] Flatscher M, Neumayer M, Bretterklieber T. *Field sensor analysis for electrical impedance spectroscopy based ice detection[C]*//2017 IEEE SENSORS. IEEE, 2017: 1-3.

[15] Vakilian M, Majlis B Y. *Study of interdigitated electrode sensor for lab-on-chip applications[C] //* Proceedings of 2014 IEEE International Conference on Semiconductor Electronics. Kuala Lumpur, Malaysia: IEEE, 2014: 201-204.

[16] Ling Chen. *Research on ice-covered growth model and ice-covered parameter prediction method of rotating cylinder [D]*. Chongqing University,2011.

[17] Lijun Chen, Qian Wu, Mei Shi, Ying Wang. *Review on the development of line icing detection technology[J]*. Control and Instruments in Chemical Industry,2011,02:129-133.

[18] Xingliang Jiang, Wenxuan Zhou, Lina Dong et al. *Ice covering measurement method based on rotating cylindrical three-electrode array[J]*. Transactions of China Electrotechnical Society, 2024,5:1524-1535.

Artificial snow laboratory for indoor snow-phobicity testing

G. Santucci de Magistris[1], M. Balordi[1], F. Pini[1], A. Casali[2]

[1] RSE - Ricerca sul Sistema Energetico spa, Milano, Italy
[2] Università degli Studi di Parma, Dipartimento di Scienze Chimiche, della Vita e della Sostenibilità Ambientale

giorgio.santucci@rse-web.it, marcella.balordi@rse-web.it, francesco.pini@rse-web.it, alessandro.casali@unipr.it

Abstract— **Ice and snow accumulation poses a significant threat to the reliability of the electrical system. For Italian transmission and distribution system the main issue is represented by wet snowfall events, occurring at temperatures close to 0°C, with snow density reaching up to 300 Kg/m³. Ice-phobic and snow-phobic coatings are one of the most promising ways for hindering ice and snow accumulation.**

Many studies report of icing and freezing phenomena and many methods have been developed over time to assess ice-phobic performances of coatings, mainly measuring ice adhesion (eg. shear stress testing, centrifuge testing etc.) and freezing delay. Many mechanisms have been consequently proposed to explain ice-phobic properties of tested coatings, according to their chemical composition and mechanical properties.

On the other hand, snow offers a considerable complexity and factors such as crystal structure, density, and liquid water content (LWC) can vary sharply with weather conditions. These properties have significant implications on the adhesion of snow on surfaces and inferring snow-phobicity of coatings from their ice-phobic performances can be misleading. For practical reasons it is somehow difficult to deal with snow for indoor performance testing and the tests are commonly delegated to outdoor activities. Outdoor testing of coatings is however affected by external uncontrollable factors such as the occurrence of snowfall events and their intensity, the presence of wind, air humidity and the presence of condensed water on surfaces.

To overcome these problems and to achieve a stricter measurement of the snow-phobic properties of coatings, RSE has recently put into operation the first artificial snow laboratory in Italy. This facility is capable of simulating snowfall with controllable flow, and to produce both dry and wet snow, with an LWC up to about 35%. The snow production is performed inside a cold chamber with settable air flow and temperature, down to -10°C, and measured relative humidity.

For the testing of snow-phobic coatings deposed on segments of conductors and ground wires, the laboratory is equipped with a custom-made apparatus capable of slowly rotating them, allowing the growth of artificial snow sleeves. The process, reproducing the sleeve accretion on overhead lines (OHL), is monitored through a camera and quantified with load cells that record the weight of the accumulated snow over time. It is thus possible to measure the snow-phobic behavior of coatings, in terms of delaying the formation of the snow sleeve and/or facilitating an earlier detachment. The laboratory is also equipped with a universal tensile strength machine to develop shear stress test with snow on flat surfaces.

All depicted tests can be performed with varying snow properties and environmental conditions of cold chamber, to assess the performances of coatings under different simulated snowfall scenarios.

The artificial snow laboratory is thus a valuable tool for the measurement of snow-phobic properties of surfaces and for a deeper comprehension of adhesion and detachment mechanisms, helping to provide valuable hints for further research and development.

Keywords— ***wet snow, overhead lines, indoor snow testing, snow-phobicity***

I. INTRODUCTION

During winter season several areas in Italy, mainly in Alpine and Apennine ridges, experience outages due to ice and snow accumulation. Italian OHLs of transmission and distribution are mainly threatened by wet snowfalls, occurring when air temperature is above 0°C and with a high relative humidity.

As the development of ice-phobic materials is pursued to deal with icing phenomena and is commonly regarded as a promising solution, many methods have been developed over time to measure ice adhesion for assessing their performances. On the other hand, snow offers a considerable complexity as, for instance, snowflakes have different adhesive properties to surfaces based on their LWC: the sticking efficiency on conductors, which is the tendency of snowflakes to stick to a cylindric surface after impact, is reported to rapidly increase with increasing LWC [1]. Snow, and in particular wet snow, is also hard to consistently recreate and to handle on a laboratory scale. Few works thus deal with the adhesion of snow to surfaces [2] and with the measurement of snow-phobic performances.

To achieve a rigorous testing of snow-phobic performances, a dedicated artificial snow laboratory (snow-lab) has been developed and is operational in the RSE facilities in Italy. The snow production machine of the snow-lab can produce snowfalls with different LWC inside a temperature-controlled chamber. The snowfalls can be used to test coating performances on OHL components directly under a snow flux or to measure the adhesion of snow samples to flat surfaces, by means of a dedicated strength testing machine for tensile and compression tests.

For a reliable snow-phobicity testing on OHL components, since comparisons among coated and uncoated surfaces should be made, a homogeneous snow flow must be ensured on all the OHL components under test. Since an effect of snow-phobic coatings can be observed in a delayed accretion or in an earlier shedding of the snow sleeve with respect to an uncoated, it can only be quantified if a reasonably comparable growth rate on all the segments is achieved.

A thorough setup process has thus been performed in the artificial snow-lab to seek the operating parameters to reliably reproduce snow with the required LWC meanwhile ensuring a homogeneous accretion rate of the sleeves on OHL components. Three different snowfall scenarios differing in

the LWC of the snowflakes, in the snow flux and in the environmental parameters of cold chamber, are reproduced to mimic both dry and wet snow.

In this paper the main results of activities held in snow-lab, related to snow sleeve growth on conductors, are presented and discussed, with reference to a proposed cylindric accretion model [3]. Results obtained on coated samples for snow-phobicity assessment are also presented and their evaluation is briefly discussed.

II. Snow-lab description and experimental setting

The testing area of the snow-lab is a 8 m^2 cold chamber (fig. 1-A) in which snow is produced by a snow machine. Briefly, snow is obtained by scraping, with metallic teeth, the ice layer which is continuously formed on the surface of a refrigerated rotating drum. The LWC of produced snow is controlled mainly acting on drum speed and temperature. The snow machine (fig. 1-B) is fed with liquid softened water collected in a basin placed in contact with the drum. Air blades fed with compressed air, located below the drum, can be activated to allow the detachment of the snow from the teeth.

The snow machine is attached to the ceiling of the cold chamber and snow falls from a height of about 1.8 m. An electromechanical linear conveyor can move back and forth the snow machine on a 2 m length rail: as the drum is 1 m in width, the snow-covered area can reach about 2 m^2.
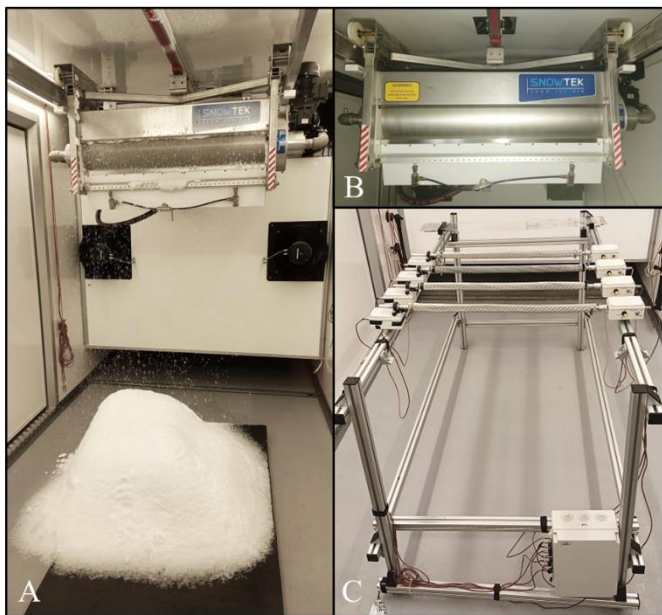
Fig. 1 A: view of the cold chamber with snow in production; B: detail of the snow machine; C: apparatus for components testing, with attached 31.5 mm diam. and 72 cm long aluminum conductors.

The maximum rate of snow production is 18 Kg×h^{-1}, corresponding to a precipitation flux of about 18 mmeq×m^{-2}×h^{-1} and the lowest settable temperature of the air in the cold chamber is -10°C.

By varying the operating parameters of snow machine and cold chamber conditions different types of snowfall events can be simulated. Snow with LWC up to about 35% and a corresponding density of about 300 Kg×m^{-3} can be produced.

Snow-chamber is equipped with temperature probes (PT100 resistance thermometer) for the continuous measurement of temperature in 9 different spots of the snow chamber and with a hygrometer for relative humidity (RH%) measurement. A high-resolution camera is used to periodically record images inside the cold chamber.

For snow-phobicity testing on components of OHL, a home-made exposure apparatus (fig. 1-C) has been developed and is operational inside the cold chamber. The apparatus consists of a modular aluminum frame on which it is possible to attach segments of conductors and ground wires, up to 2 m in length and with different diameters. In both the attachment points of the apparatus are located load cells (sensitivity: 1g, max load: 10 Kg) for the real-time measurement of the weight of segments. A dimmable 12V motor, placed in one of the two attaching points, allows to slowly rotate the segments up to about 1,5 rpm: during artificial snowfall events, rotation is imposed to allow the regular growth of snow sleeves on their surfaces. The apparatus is equipped with 8 load cells and 4 motors and can thus host 4 segments at the same time.

LWC measurements on produced snow are performed with a calorimetric method [4]: when hot water, at temperature T_1, is added to wet snow (an ice-water mixture at 0°C), the heat lost by the mass of hot water is equal to the heat absorbed by the ice fraction melting added to heat needed to bring the whole mass of water from 0°C to the final temperature T_2. LWC, expressed as mass fraction, is given by:

$$LWC = 1 - \frac{c_{P,w}}{L_f}\left[\frac{m_w}{m_{sn}}(T_1 - T_2) - T_2\right] \qquad (1)$$

where, $C_{p,w}$ is water specific heat at constant pressure, L_f is the ice melting latent heat, m_w is the mass of hot water; m_{sn} is the mass of snow. A centesimal thermometer is used for temperature measurements and a dewar vessel is used as a container: a correction is applied considering the heat exchanged by the container when varying in temperature, assessed with the method reported in [5]. Snow density is measured by weighing a container of known volume when filled with the produced snow. LWC and density are checked periodically during tests, sampling in different spots of the deposed snowpack.

III. Snow sleeves accretion on conductors

Target of the setup stage is to achieve a homogenous growth rate on 4 conductor segments simultaneously under 3 distinct snowfall scenarios. Snowfalls with about 0% (dry snow), 15% and 35% of LWC in the snowflakes, respectively named G0, G15 and G35, are reproduced.

Stranded aluminum conductors with a diameter of 31.5 mm and a length of 72 cm are used. Segments are obtained from the respective ACSR (aluminium-conductor steel-reinforced) cable. The internal steel strands and an inner layer of aluminum strands are removed and replaced with a rigid aluminum pipe of 1.5 cm diameter. Consequently, the conductors are only composed of the two outer concentric layers (24 and 18 wires respectively) of 3 mm diameter strands. This adaptation is required to properly accommodate the segments to the attaching points of the components testing apparatus. The configuration of the apparatus is chosen with the segments exposed in the transversal direction respect to the direction of movement of the snow machine. The height of

apparatus is set to 1 m from the floor and snowflakes thus collide with conductors with a 0.8 m fall height.

The testing facilities effectively allow to grow cylindrical snow sleeves - on the segments.

The setup activities allowed to find out the parameters of snow machine, cold chamber, and exposure apparatus to be set. Relevant parameters of snow machine are reported in Table I., together with cold chamber environmental parameters and with the measured properties of snow produced.

TABLE I. SNOW LABORATORY SETTINGS FOR HOMOGENEOUS GROWTH ON CONDUCTOR SEGMENTS WITH DRY (G0), 15% LWC (G15) AND 35% (G35) LWC SNOWFALLS

	G0	G15	G35
Snow production rate (Kg×h^{-1})	16.4	13.9	17.0
Surface covered (m^2)	1.1	1.8	1.8
Snow deposition rate (Kg×m^{-2}×h^{-1})	14.9	7.7	9.4
Rotation speed of segments (rpm)	1	1	1
Snow LWC – average (%)	1.6	14.3	34.8
Snow density – average (Kg×m^{-3})	122	216	417
Cold chamber T – average (°C)	-1	-0.5	-0.5
Relative humidity - average (%)	65	70	68

Setup tests were prolonged until at least a detachment of one snow sleeve was observed (for snowfall scenarios G0 and G15) or until 6 hours (for G35).

LWC and density measured on the snow, reported the graph of Fig. 2, were found to be substantially steady during testing periods under snowfalls G0, G15 and G35.
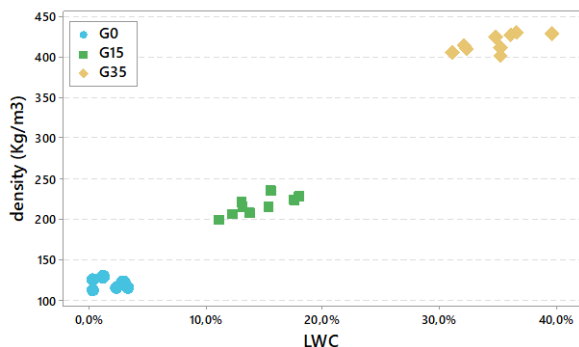
Fig. 2   LWC and density measured on snow during G0, G15 and G35 testing

A homogeneous accretion rate of the snow sleeves is achieved on all 4 segments under the 3 snowfall events, as can be observed in the graphs of Fig. 3 reporting their mass over time.

The trend of mass versus time curves found is in agreement with snow accretion models [3] and outdoor observations [6]. As expected, the observed rate of mass accretion increases with the increasing of the diameter of snow sleeve, as newly deposed layers of snow intercept more and more snow.
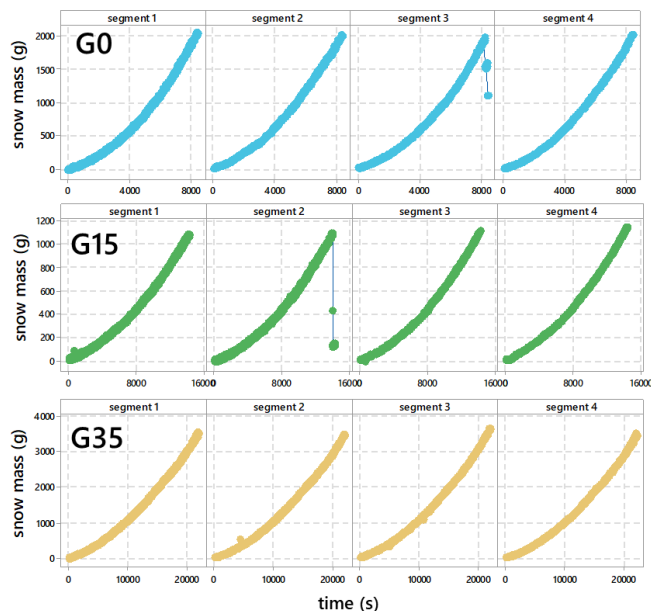
Fig. 3   snow masses accreted over time on the 4 segments under the three snowing conditions G0, G15 and G35. The shedding occurred in G0 (segment 3) and in G15 (segment 2) is visible

The mass accretion rates in the three scenarios are shown in Fig. 4 where is plotted the average mass of the snow sleeves against the snow deposed in the testing area in Kg×m^{-2} (approximately equivalent to mmeq).
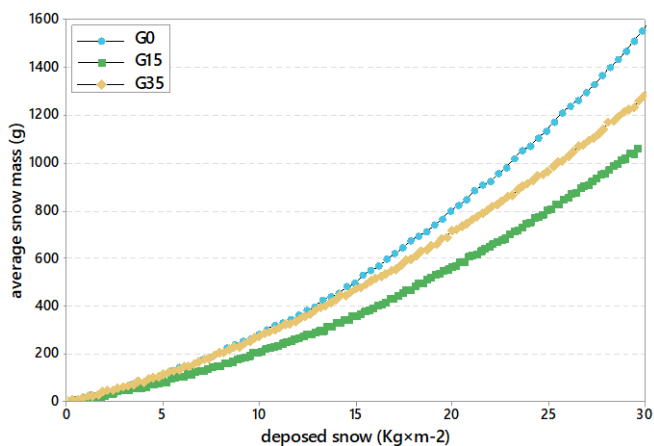
Fig. 4 accretion of snow sleeves in the different scenarios

Snow sleeve accretion rates for the three scenarios, in decreasing order are G0>G35>G15. The higher mass accretion rate observed under dry snowfall G0 is unexpected since higher sticking efficiency is reported for wet snow [1]. It must be however considered that different settings of snow machine are required to produce dry and wet snow: specifically, air blade activation is required to detach wet snow from the drum (while is not required for dry snow) leading to different impact speed on conductors. As tests are performed separately under the three snowfall scenarios, this is not expected to a critical issue for snow-phobic testing.

A comparison is performed also in terms of diameters of the snow sleeves. From the averages data of snow mass recorded (M), the snow sleeve diameter (D) is calculated at each time interval (i), according to [3], with the following equation:

$$D_i = \sqrt{\left[\frac{4(M_i - M_{i-1})}{\pi \rho_s} + D_{i-1}^2\right]} \qquad (2)$$

and using as ρ_s the average of the snow density measured. The diameters are also estimated from the images acquired at regular time intervals during accretion tests, visually measuring 3 distinct points on the segment for each image. A further comparison can be thus done, in the graphs of Fig. 5, between experimental data and data from model.
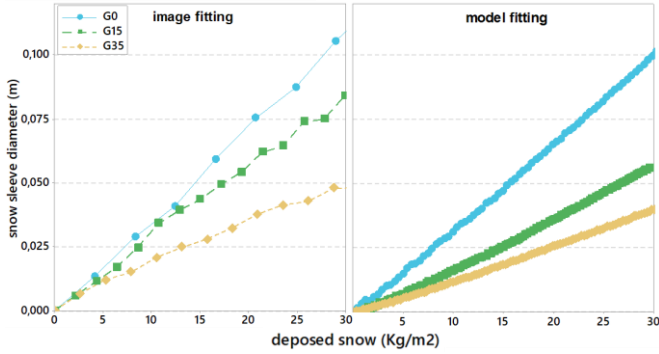
Fig. 5 left: results of diameter estimation based on image processing; right: results based on calculation according to equation 2

A linear accretion of the snow sleeve is observed if diameter is considered. Both data from images and from model agree that diameter accretion rate is, in decreasing order, G0>G15>G35, which is consistent with the increase of density of involved snow. Calculated and measured diameters are similar for the three scenarios, indicating a good consistency between theoretical and experimental data. Slightly lower diameters are however systematically calculated with the model. Possibly, the stacking of the snowflakes on the conductors under rotation is not as efficient as on a flat steady surface. This is suggested by camera images: in Fig. 6 the snow sleeves of present a jagged profile, with presence of local deposits of snowflakes and empty valleys. As a result, lower snow densities on the segments are expected and thus larger diameters are measured.

For diameter measurement, it should also be noticed that a degree of asymmetry is observed in the form of the snow sleeves, not reaching a perfect cylindric shape. This is likely due to a spatially unbalanced production rate of snow machine. The asymmetry, based on the difference in cell load readings between the two attachment points of each segment, is calculated in about 15% in G0, 10% in G15 and about 6% in G35 testing.
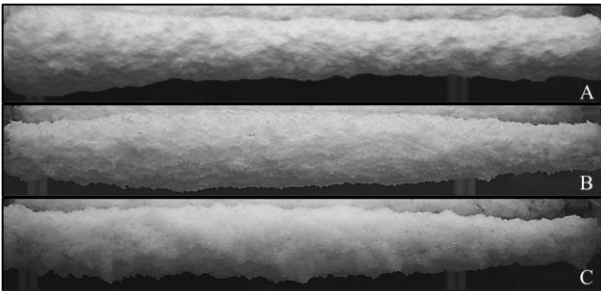
Fig. 6 camera images of snow sleeves on segments under G0 (A), G15 (B), G35 (C) snowfall scenarios

IV. SNOW-PHOBICITY TESTING AND EVALUATION

An example of testing on snow-phobic coatings is reported to briefly discuss the assessment of snow-phobic properties based on the snow-lab results.

The coatings under test, described elsewhere [7], and denoted as sample 1 and 2 are directly deposed on 31.5 mm diameter ACSR segments. Tests in snow-lab are performed simultaneously on both the coated segments, with two uncoated segments as reference. Test duration is set to 5 hours with the above-mentioned setup under snowfall G15. Snow masses on the segments over time are reported in Fig. 7.
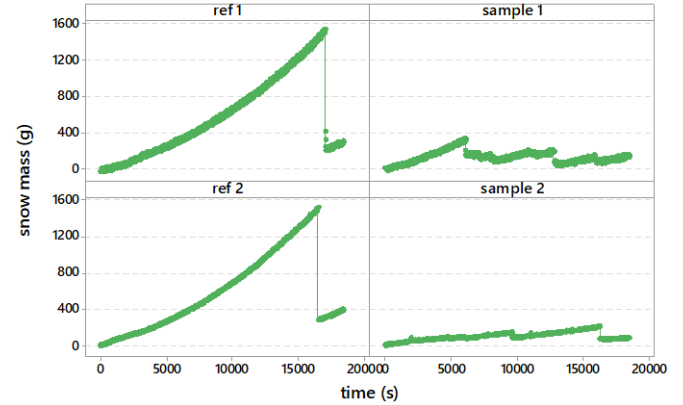
Fig. 7 snow masses of coated (sample) and uncoated (ref) ACSR segments under G15 testing up to 5 hours

The reduced snow load on samples is clearly visible in the graph, especially by the comparison with snow loads on the references. The experimental system is thus proven to be capable of evidencing differences in snow accumulation trends among segments treated with different coatings.

For a numerical quantification of snow-phobic properties, several parameters describing data results can be used, and some of them are listed below:

- average snow mass during test: M_A
- maximum snow mass: M_{max}
- snow mass at time i (hours): M_i
- shedding number during test: S_N
- average snow mass at shedding: M_{AS}

The parameters, calculated for the test hereby presented are reported in Table II.

TABLE II. PARAMETERS DESCRIBING DATA RESULTS OF THE SNOW-PHOBICITY TEST

	M_A	M_{max}	M_1	M_2	M_3	M_4	M_5	S_N	M_{AS}
Ref 1	566	1530	149	413	750	1160	250	1	1530
Smp 1	129	339	160	123	190	71	132	6	207
Smp 2	102	217	70	101	108	168	78	4	136
Ref 2	581	1520	172	428	779	1230	375	1	1520

Data generated during tests can however account for different snow-phobic behaviour of tested components, such as the hindering of snow sleeve accretion or the complete or partial shedding from the segments, that may not be fully witnessed by listed parameters. Specific performance

indicators should be developed and applied for snow-phobicity results.

V. Conclusions

A dedicated snow-lab is operational for snow adhesion testing on surfaces and for snow-phobicity assessment of coatings directly deposed on OHL components. For OHL testing an experimental setup has been developed to consistently depose snowflakes on ACSR segments. A homogenous growth of snow sleeve has been observed on 4 different segments under 3 distinct snowfall scenarios, ensuring a reliable snow-phobicity assessment. The experimental accretion rate of diameters of snow sleeves on segments has been found to be basically in agreement with a commonly accepted cylindrical accretion model.

Testing on segments treated with snow-phobic coatings has shown that, based on the comparison with untread segments, the proposed experimental setting is able to clearly point out snow-phobic properties, in terms of snow sleeve accretion delay and early shedding.

As few tests on snow-phobicity are reported and a lack of common practices and performance indicators is experienced in this field, snow-lab can be a useful source of experimental data for evaluation of snow-phobic performances.

References

[1] B. E. Kringlebotn Nygaard, H. Ágústsson, e K. Somfalvi-Tóth, «Modeling Wet Snow Accretion on Power Lines: Improvements to Previous Methods Using 50 Years of Observations», *Journal of Applied Meteorology and Climatology*, vol. 52, fasc. 10, pp. 2189–2203, ott. 2013, doi: 10.1175/JAMC-D-12-0332.1.

[2] R. Hefny, L. E. Kollár, M. Farzaneh, e C. Peyrard, «Adhesion of Wet Snow to Different Cable Surfaces», p. 8.

[3] L. Makkonen, «Estimation of wet snow accretion on structures», *Cold Regions Science and Technology*, vol. 17, fasc. 1, pp. 83–88, set. 1989, doi: 10.1016/S0165-232X(89)80018-7.

[4] K. Kawashima, T. Endo, e Y. Takeuchi, «A portable calorimeter for measuring liquid-water content of wet snow», *Ann. Glaciol.*, vol. 26, pp. 103–106, 1998, doi: 10.3189/1998AoG26-1-103-106.

[5] D. Fasani, F. Cernuschi, e L. P. M. Colombo, «Calorimetric determination of wet snow liquid water content: The effect of test conditions on the calorimeter constant and its impact on the measurement uncertainty», *Cold Regions Science and Technology*, vol. 214, p. 103959, ott. 2023, doi: 10.1016/j.coldregions.2023.103959.

[6] Y. Sakamoto, «Snow accretion on overhead wires», *Philosophical Transactions of the Royal Society of London. Series A: Mathematical, Physical and Engineering Sciences*, vol. 358, fasc. 1776, pp. 2941–2970, 2000.

[7] M. Balordi, G. Santucci de Magistris, e F. Pini, «Investigation on snowphobic and icephobic behavior of superhydrophobic surfaces», *IWAIS proceedings*, 2024.

Research progress of electromagnetic pulse de-icing technology for overhead ground wire

Qin Hu[1], Zhengfei Lei[1], Xingliang Jiang[1], Lichun Shu[1], Jun Ma[2]

[1] *Xuefeng Mountain Energy Equipment Safety National Observation and Research Station of Chongqing University, Chongqing 400044, China*
[2] *Chongqing Water Resources and Electric Engineering College, Chongqing 402160, China*

huqin@cqu.edu.cn, 463020434@qq.com, xljiang@cqu.edu.cn, lcshu@cqu.edu.cn, 19307088@qq.com

Abstract— **Icing has become a serious natural disaster that threatens the safety of the power system. Since it is difficult to short-circuit and melt icing on overhead ground wires, it is more serious and more likely to cause harm than transmission lines. Considering that electromagnetic pulse de-icing technology has the advantages of low energy consumption and fast de-icing speed, this paper designs and develops an overhead ground wire flat plate integrated electromagnetic pulse de-icing actuator based on the principle of electromagnetic pulse de-icing technology, and the parameters of the actuator are analyzed Optimization includes the number of coil turns, multiplier material and thickness, capacitor voltage and actuator weight and center of gravity. Ground wire de-icing tests in natural environments were conducted under optimal parameters of the de-icing actuator to verify the de-icing effect. The results show that the flat-plate integrated electromagnetic pulse de-icing actuator has a good de-icing effect on mixed rime, has high de-icing efficiency and has good application prospects.**

Keywords— *De-icing; Electromagnetic pulse; Actuator parameter optimization; Acceleration and pulse current; Natural tests*

I. INTRODUCTION

Since the 1950s, there have been thousands of ice disaster accidents recorded [1]. In particular, the large-scale and long-term rare freezing weather that occurred in many provinces in southern China in early 2008 caused a large number of accidents. Accidents such as the collapse of transmission towers and broken conductors have led to widespread power supply interruptions and even system breakdown, seriously affecting people's normal lives, causing extremely serious damage to the power system, and causing hundreds of billions of losses to the national economy. Huge losses [2-4]. After the ice disaster, various power grid companies and scientific research institutions have invested great enthusiasm in scientific research on the ice coating problem of the power grid, and have achieved many results in the mechanism of ice coating, the establishment of ice coating prediction models and the research and development of ice melting technology [5]. At present, the main de-icing method for the power grid is DC short-circuit ice melting. However, if the current ice melting solution is used for the ground wire, the ground wire needs to be modified. On the one hand, it increases the labor cost, and on the other hand, it will affect the lightning protection performance of the ground wire. Therefore, the icing situation of power lines is more serious than that of transmission conductors. Currently, various anti-icing technologies for ground wires, such as mechanical vibration de-icing and electric thermal anti-icing, generally consume large amounts of energy and have low safety. There is no safe, effective, and simple technology [6]. Electromagnetic pulse de-icing technology has the advantages of low energy consumption, high efficiency, and fast de-icing speed [7]. However, the current main research directions are aimed at de-icing surface-shaped structures such as aircraft wings and fan blades, and the technology has not yet been developed. mature, so there is an urgent need for an electromagnetic pulse de-icing technology for ground wires.

II. PRINCIPLE AND INFLUENCING FACTORS OF GROUND WIRE ELECTROMAGNETIC PULSE DE-ICING

A. Principle of electromagnetic pulse de-icing

The electromagnetic pulse de-icing method is essentially a mechanical de-icing method. The energy storage capacitor releases energy to the pulse coil at the moment of discharge, and an instantaneously changing magnetic field is generated in the coil. This magnetic field interacts electromagnetically with the metal surface in the target object. Eddy currents are induced inside the metal, which eventually generates high-amplitude, short-term electromagnetic force on the target. Under the action of the instantaneous electromagnetic force, the ice layer is destroyed and falls off, achieving the purpose of de-icing the target.

When the ground wire is used as the target object, because its main structure is a steel strand, its conductivity and stress area are small [8], and the eddy current generated by the overall structure of the metal structure is relatively smaller, so the pulse effect generated is less effective. Therefore, in the ground line electromagnetic pulse de-icing scheme, it is necessary to install a metal structure on the ground line as an eddy current multiplier. The pulse current generates a large eddy current on the multiplier, thereby generating a large pulse force for de-icing. The principle diagram of ground wire electromagnetic pulse de-icing is shown in Fig. 1.
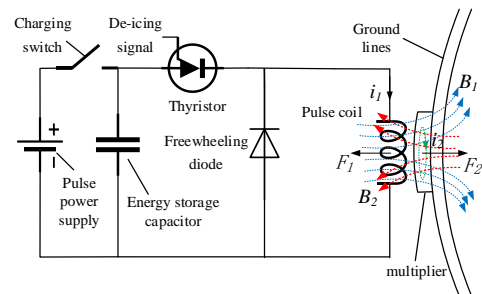
Fig. 1 Ground wire electromagnetic pulse de-icing principle

When the ice on the ground reaches a certain level and needs to be removed, the pulse power supply receives the

action command from the server and sends a charging signal to the charging switch such as a relay to charge the energy storage capacitor. After charging is completed, a de-icing signal is sent to the thyristor to turn it on, the pulse coil is discharged, and the pulse current i_1 is passed through the pulse coil to generate a transient magnetic field B_1. According to the law of electromagnetic induction and Lenz's law, the induced eddy current i_2 will be generated on the ground wire and the metal multiplier, which will excite the reverse magnetic field B_2, thereby generating the electromagnetic pulse force F_2 and causing the ice layer on the ground wire to fall off.

B. Factors affecting electromagnetic pulse de-icing

The electromagnetic pulse de-icing actuator circuit is equivalent to an RLC circuit as shown in Fig. 2. Ignore the nonlinear characteristics of circuit devices and consider the influence of freewheeling diodes.
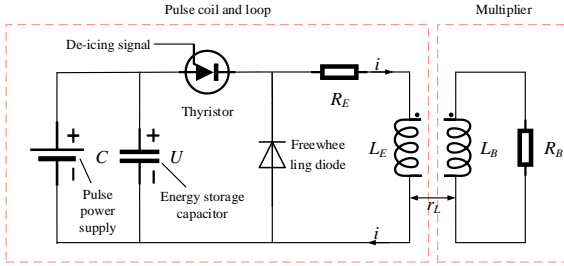
Fig. 2   Electromagnetic pulse de-icing actuator equivalent circuit

The system is in an under-damped state, and its current comprehensive expression is [9]:

$$i = \begin{cases} I_m e^{-\alpha t}\sin(\omega t) & 0 \le t \le t_{i,\max} \\ i_{\max} e^{-\frac{R_E}{L_E}(t - t_{i,\max})} & t \ge t_{i,\max} \end{cases} \quad (1)$$

where the parameters are detailed in the reference [9].

Calculate the induced electromotive force E and induced eddy current i_2 on the multiplier according to the law of electromagnetic induction, and further calculate the electromagnetic pulse force:

$$F(t) = \oint i_2(t)B_1(t)dl = 2\pi r_L |Z| e^{j\varphi} e^{-2\alpha t}\sin(\omega t - \frac{\pi}{2} - \varphi)\sin(\omega t) \quad (2)$$

where the r_L is the distance between the coil and the multiplier, Z is the equivalent impedance of the multiplier, and φ is the impedance angle of the multiplier.

It can be seen from equation (2) that the electromagnetic pulse force of the de-icing actuator is related to the multiplier and coil parameters. In order to achieve the best de-icing effect of the electromagnetic pulse de-icing actuator, this paper analyzes the de-icing actuator coil, multiplier and overall parameters. Optimization is carried out, mainly studying the effects of the number of coil turns, multiplier material and thickness, distance between multiplier and coil, capacitor voltage, actuator weight and center of gravity on the actuator effect.

C. Actuator effect evaluation indexs

Generally, the icing situation is eccentric icing, that is, the ground line and the center of the icing circle are offset. Since the lower half of the ice layer is subject to greater inertial force, it is enough to analyze the stress of the lower half. The

following is The stress situation of the half part is shown in Fig. 3.
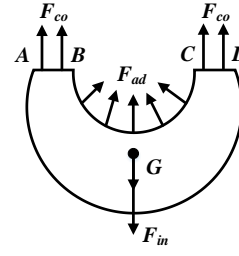
Fig. 3   Schematic diagram of the force on the lower half of uneven icing

At this time, the direction is downward. The stress analysis can be expressed by the equation (3):

$$F_{in} + G \ge F_{co} + F_{ad} \quad (3)$$

The critical condition for eccentric ice shedding, that is, the critical acceleration is [10]:

$$a_{vm} = \frac{8\left[\left(\sqrt{D^2 - 4e^2} - D_w\right)\tau_{co} + D_w\tau_{ad}\right]}{\rho_{ice}\left(2\pi D^2 - 2D^2\arccos(2e/D) + 4e\sqrt{D^2 - 4e^2} - \pi D_w^2\right)} - g \quad (4)$$

where the parameters are detailed in the reference [10].

When the eccentricity e=0 in equation (4), it is a special case of uniform ice coating. It can be seen from equation (4) that the critical acceleration value of ice shedding has nothing to do with the ice length L of the ground line. Under the action of the ground wire electromagnetic pulse de-icing actuator, when the peak acceleration at any point on the ground wire is greater than the critical acceleration, the ice covering there will be peeled off and removed. Therefore, the peak acceleration at various locations under the action of the actuator can be used as an evaluation index for effect and parameter optimization.

At the same time, pulse current can indirectly reflect the size and impulse of electromagnetic pulse force, and the test measurement method is simpler and more accurate than electromagnetic pulse force. Therefore, pulse current can also be used as one of the parameter optimization evaluation indicators.

III. DE-ICING ACTUATOR PARAMETER OPTIMIZATION AND EXPERIMENTAL RESEARCH

A. Test products, test platforms and test methods

1) Test products structural design
This paper designs the structural form of the flat plate pulse coil and corresponding de-icing actuator, as shown in Fig. 4.
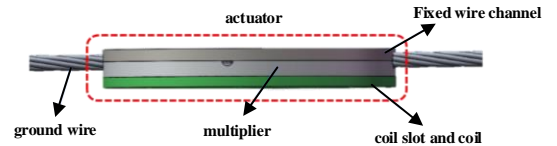
Fig. 4   Structural diagram of flat plate de-icing actuator

The flat plate de-icing actuator is composed of a circular flat plate pulse coil and coil plate, a metal multiplier plate, fixed wire trough, etc. From bottom to top are the circular flat plate pulse coil and coil plate, the metal multiplier plate, the

ground wire, and finally the fixed wire trough. The metal multiplier and fixed wire trough fix the flat plate de-icing actuator to the ground wire as a whole through screws. superior. The pulse coil is connected to the discharge circuit through the coil slot outlet.

This paper uses the overhead ground wire of the Xuefeng Mountain National Station of Chongqing University as a prototype to design a scaled-down experimental model. The specific parameters of the experimental ground wire are shown in Table 1.

Table 1 Short size test ground wire parameters

type	length (m)	Cross-sectional area (mm²)	external diameter (mm)	mass per unit length (kg/km)	Elastic Modulus (Gpa)
LH$_A$J50	4.6	50.14	9.06	137.1	59

2) *Test Platforms*

The overall layout of the test is shown in Fig 5. Both ends of the test ground wire are fixed on fixed suspension brackets with the height of 1 m. The screws on both sides can flexibly adjust the length of the ground wire and the tension of the ground wire. In the test, four acceleration sensors were used to measure the vibration acceleration of the ground wire at positions 45 cm, 90 cm, 135 cm and 180 cm away from the flat plate de-icing actuator, the Rogowski coil was used to measure the pulse current, and the displacement sensor was used to measure the vibration displacement of the ground wire. The tension sensor measures the tension at both ends of the ground wire. At the same time, the camera is used to record the test process, and an oscilloscope and digital display are used to collect test data.
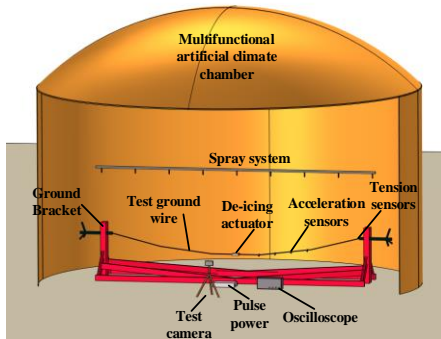
Fig. 5 Overall layout diagram of the testing device

Xuefeng Mountain Energy Equipment Safety National Observation and Research Station of Chongqing University is located in Huaihua, Hunan Province. The station is the only national-level field scientific observation platform in the field of energy and power. The overall picture is shown in Fig. 6.

Fig. 6 Overview of Natural Icing Environment

This National station has typical micro-topography and microclimate characteristics, and is an excellent natural ice-covering test site for domestic and foreign research on energy equipment ice-covering defense technology.

3) *Test methods*

This experiment is divided into two parts. Relying on the established test platforms, electromagnetic pulse tests were first conducted on the un-iced ground wires, and the parameters of the flat-plate de-icing actuator were optimized using effect evaluation indicators. Secondly, the natural environment de-icing test of the test wire was carried out at the Xuefeng Mountain National Station of Chongqing University. Appropriate actuator parameters were selected for the de-icing experiment and the ground wire de-icing length was recorded.

B. De-icing actuator parameter optimization test

According to the un-iced ground wire test method, the electromagnetic pulse test was carried out by changing the number of coil turns, multiplier material and thickness, capacitor voltage, actuator weight and center of gravity. Measure the ground vibration acceleration waveforms at different locations, conduct three electromagnetic pulse tests under each parameter, take the acceleration peak value, and calculate the average value.

1) *Coil turns*

The test was conducted by changing the number of turns of the pulse coil while ensuring that the pulse voltage was 1200 V, the thickness of the aluminum multiplier was 1.5 mm, and the conditions remained unchanged. The peak acceleration and pulse current test results are shown in Fig. 7 and Fig. 8.
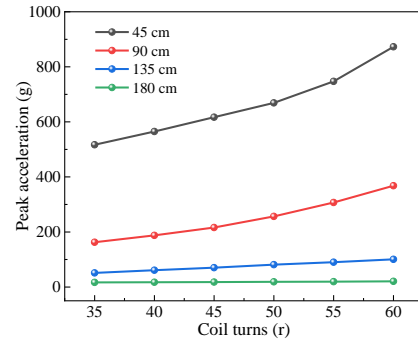
Fig. 7 Peak acceleration of different coil turns
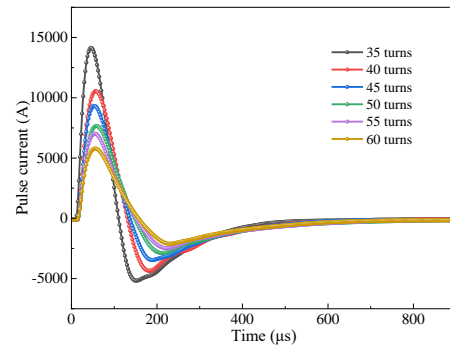
Fig. 8 Pulse current waveforms with different coil turns

It can be seen from Fig. 7 that as the number of turns of the pulse coil increases, the peak acceleration values of the four points measured by the test ground wire increase. And the

point closer to the actuator, such as 45 cm, has a greater change in peak acceleration, and the point farther away from the actuator, such as 180 cm, has a smaller change in peak acceleration. It can be seen from Fig. 8 that the pulse current waveform is high amplitude and short time, and as the number of pulse coil turns increases, the pulse current peak value decreases, but the pulse width increases. This is because the increase in the number of turns of the pulse coil leads to an increase in the equivalent inductance and equivalent resistance of the pulse coil, which increases the overall inductance and resistance of the actuator and reduces the peak value of the pulse current. However, the eddy current caused by the increase in the number of turns is greater. The pulse width increases.

Therefore, it is concluded that in order to improve the effect of the flat actuator, the number of turns of the pulse coil in the actuator can be increased, but at the same time, problems such as winding difficulties, inter-turn insulation and increase in overall volume caused by the increase in the number of turns need to be considered.

2) *Multiplier material and thickness*

The test was conducted by changing the thickness of aluminum multiplier and iron multiplier while ensuring that the pulse voltage was 1200 V, the number of turns of the pulse coil was 35, and the conditions remained unchanged. The peak acceleration test results are shown in Fig. 9 and Fig. 10.
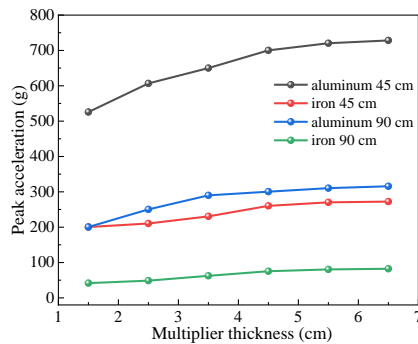
Fig. 9   Peak acceleration for different multiplier materials and thicknesses
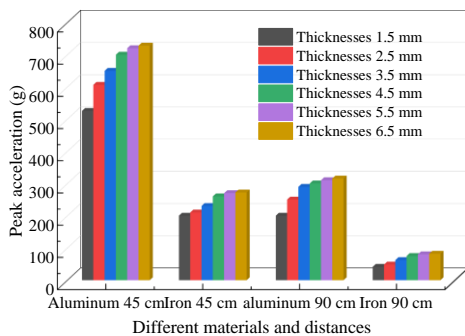
Fig. 10 The relationship between peak acceleration at different materials and distances and multiplier thicknesses

It can be seen from Fig. 9 and Fig. 10 that at the same measurement point, the larger the thickness of the iron or aluminum multiplier, the slower the peak acceleration increases. This is due to the high frequency of the pulse current and the skin effect needs to be considered. When the thickness of the multiplier of different materials is smaller than the trend When the skin depth increases, the peak acceleration increases sharply as the thickness increases. When the multiplier thickness of different materials is greater than the skin depth, as the thickness increases, the increase in peak acceleration slows down significantly and remains basically unchanged.

Under the same conditions, the peak acceleration value of the aluminum multiplier at each acceleration measurement point and at different thicknesses is greater than that of the iron multiplier. Therefore, under the action of the actuator, the electrical conductivity is better than the magnetic conductivity.

Therefore, it is concluded that in order to improve the effect of the flat actuator, the multiplier can be made of materials with good conductivity, and the thickness of the multiplier can be appropriately increased, but at the same time, issues such as the increase in skin depth and overall volume need to be considered.

3) *Capacitor voltage*

The voltage on the energy storage capacitor is related to the energy released by the flat-plate de-icing actuator. Ensure that the number of turns of the pulse coil is 45 and the thickness of the aluminum multiplier is 1.5 mm. Under the same conditions, change the pulse voltage and ensure energy storage every time. The capacitors are fully charged for testing. The peak acceleration and pulse current test results are shown in Fig. 11 and Fig. 12.
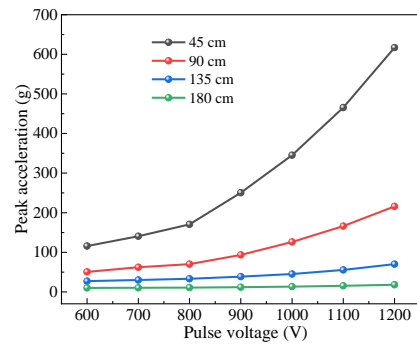
Fig. 11   Peak acceleration of different pulse voltages
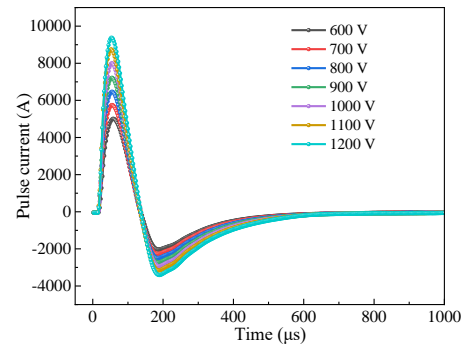
Fig. 12   Pulse current waveforms with different pulse voltages

It can be seen from Fig. 11 that as the pulse voltage increases, the peak acceleration values of the four points measured on the test ground wire increase. As the pulse voltage increases, the peak acceleration change pattern at each point satisfies the capacitance energy formula and presents a quadratic function image. It can be seen from Fig. 12 that as the pulse voltage increases, the pulse current waveform increases, the pulse current peak value increases, and the pulse width barely changes, resulting in an increase in both pulse

43

force and impulse. This is because when the number of turns of the pulse coil, the thickness of the multiplier, and the distance between the multiplier and the coil remain unchanged, increasing the pulse voltage stimulates a larger induced magnetic field, but the range of the induced eddy current does not change much, so only the amplitude increases but the pulse width almost no change at all.

Therefore, it is concluded that in order to improve the effect of the flat-panel actuator, the pulse voltage of the energy storage capacitor in the actuator can be increased, but at the same time, issues such as the withstand voltage insulation parameters of related components and the difficulty in energy extraction caused by the increase in pulse voltage need to be considered.

4) *Actuator weight and center of gravity*

This paper uses the special electroplated weight for testing to simulate the change in the weight of the actuator, and the hanging weight is located directly below the actuator. While ensuring that the pulse voltage is 1200 V, the number of turns of the pulse coil is 45, the thickness of the aluminum multiplier is 1.5 mm, and the center of gravity of the hanging weight is 20 cm away from the coil slot, the hanging weight and the weight of the hanging weight are changed as follows: The experiment was carried out by changing the center of gravity of the hanging weight under the same condition of 3 kg. The peak acceleration test results are shown in Fig. 13 and Fig. 14.
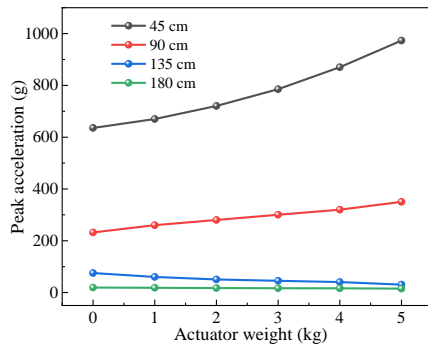
Fig. 13   Peak acceleration of different actuator weight
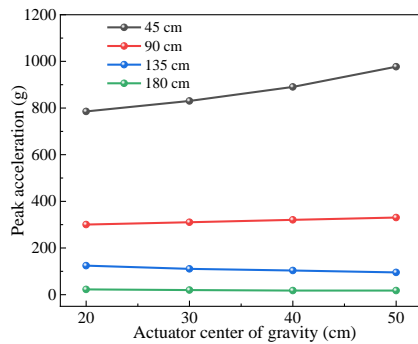
Fig. 14   Peak acceleration of different actuator center of gravity

It can be seen from Fig. 13 and Fig. 14 that as the hanging weight increases, the peak acceleration of the near point increases significantly, and the peak acceleration of the measurement point far away from the actuator shows the slowly decreasing and unchanged trend. That is, the heavier the weight is and the center of gravity is vertically downward, the peak acceleration at the near point will increase, but at the same time, the electromagnetic pulse force or acceleration propagates on the ground line and attenuates more seriously, and attenuates to 0 faster.

Therefore, it is concluded that in order to improve the effect of the flat actuator, the vertical downward distance of the center of gravity of the hanging weight can be appropriately increased, but at the same time, the problem of faster attenuation needs to be balanced and the shaking caused by the center of gravity being too low and the insulation from the wires need to be considered. Issues such as safe distance.

C. *Ground wire natural environment de-icing test*

According to the experimental results of the un-iced ground wire, it can be seen that the parameter optimization results are that the pulse voltage is 1200 V, the number of coil turns is 60 turns, and the thickness of the aluminum multiplier is 4.5 mm. Considering that the de-icing effect is greatly attenuated due to the length of the lead, this paper uses the pulse coil And the coil slot, multiplier, fixed wire slot, energy storage capacitor and control circuit are integrated together to develop the flat plate integrated de-icing actuators, and the length of the discharge lead is shortened as much as possible. The final weight of the flat plate integrated de-icing actuator is 3 kg, and the center of gravity is 22 cm. The flat plate integrated de-icing actuator is shown in Fig. 15.
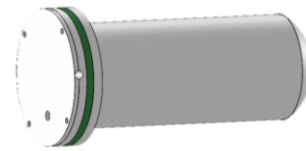
Fig. 15   Schematic diagram of flat plate integrated electromagnetic pulse de-icing actuator

Natural environment de-icing test was conducted based on the parameter optimization results of the flat plate integrated de-icing actuator. The test ground line of the Xuefeng Mountain National Station of Chongqing University was 85 m horizontally long, with the height difference of 4.38 m. The tension at both end points was measured by the tension sensor to be 6060 N. and 5905 N, with the property line facing 73 ° East. Because the icing on the windward side of the field station test ground wire is more obvious, use the vernier caliper to measure the lateral icing thickness of the test ground wire, and take 3 to 5 locations on the test ground wire to calculate the average thickness. The final icing is mixed rime, and the icing thickness is 30 mm. The de-icing test process diagram is shown in Fig. 16.

(a) Before de-icing test

(b) During the first de-icing test

(c) During the second de-icing test
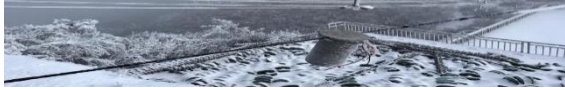
(d) After de-icing test

Fig. 16   De-icing actuator natural environment mixed rime de-icing test process

After 9 independent de-icing operations, the final de-icing length of the flat plate integrated de-icing actuator was 3.5 m, proving that the flat plate integrated de-icing actuator has a better de-icing effect on natural mixed rime icing.

IV. CONCLUSIONS

For the uniced ground wire, the peak acceleration increases with the increase in the number of coil turns, conductivity of the multiplier material, multiplier thickness, and capacitor voltage. At the same time, the heavier the weight of the actuator and the farther the center of gravity is away from the ground line and vertically downward, the closer to the flat plate integrated actuator the greater the peak acceleration will be, but the attenuation becomes faster, resulting in poorer far-point effect.

Under the conditions of pulse voltage of 1200 V, coil number of 60 turns, an aluminum multiplier thickness of 4.5 mm, flat plate integrated de-icing actuator weighing 3 kg, and the center of gravity of 22 cm, natural environment de-icing tests were conducted at the test site. The test wire length is 85 m, the icing is mixed rime, and the thickness is 30 mm. The final de-icing length of the flat plate integrated actuator is 3.5 m after 9 independent de-icing tests.

The flat plate integrated actuator developed in this paper using the overhead ground wire electromagnetic pulse de-icing method has a better de-icing effect on mixed rime and has higher de-icing efficiency. In the future, we can continue to study the effects of different icing types and different ground wire parameters on the de-icing effect. At the same time, in-depth research is needed on the application of long span distances and operating ground wires, as well as the reliability and practicality of de-icing actuators in extreme climates.

REFERENCES

[1] Bo Z Q, Lin X N, Wang Q P, et al. Developments of power system protection and control[J]. Protection and Control of Modern Power Systems, 2016, 1(1): 1-8.

[2] Fu P, Farzaneh M. Simulation of the ice accretion process on a transmission line cable with differential twisting[J]. Canadian Journal of Civil Engineering, 2007, 34(2): 147-155.

[3] Lu J, Guo J, Hu J, et al. Analysis of ice disasters on ultra-high-voltage direct-current transmission lines[J]. Natural hazards, 2017, 86(1): 203-217.

[4] Laforte J L, Allaire M A, Laflamme J. State-of-the-art on power line de-icing[J]. Atmospheric Research, 1998, 46(1): 143-158.

[5] X Jiang, Z Zhang, Q Hu, et al. Thinkings on the Restrike of Ice and Snow Disaster to the Power Grid[J]. High Voltage Engineering, 2018, 44(2): 463-469.

[6] Y Wang, H Miao, S Mo, et al. Summary of research on anti-ice, ice melting and de-icing of high voltage overhead transmission lines[J]. Power System Protection and Control, 2020, 48(18): 178-187.

[7] Laforte J L, Allaire M andre, Laforte C. Demonstration of the Feasibility of a New Mechanical Method of Cable De-Icing[C]//Proceedings 11th International Workshop on Atmospheric Icing of Structures. Montreal, 2005: 347-352.

[8] Egbert R I, Schrag R L, Bernhart W D, et al. An investigation of power line de-icing by electro-impulse methods[J]. IEEE Transactions on Power Delivery, 1989, 4(3): 1855-1861.

[9] Q Li, C Zhu, T Bai. Simplification of de-icing excitation and influential factors of the electro-impulse de-icing system[J]. Acta Aeronautica et Astronautica Sinica, 2012, 25(8):1384-1393.

[10] K Ji. Dynamic Response of Iced Overhead Electric Transmission Lines following Shock Loads[D]. North China Electric Power University (Beijing), 2016.

Study of wind speed and direction measurement method in icing conditions

Hongmei Zhang[1], Xingliang Jiang[1], Lie Ma[1], Qin Hu[1], Zhijin Zhang[1]

[1] State Key Laboratory of Power Transmission Equipment & System Security and New Technology, Chongqing University, Shapingba District, Chongqing 400044, China

zhm3120@163.com, jiangxingliang@cqu.edu.cn, malie17@outlook.com, huqin@cqu.edu.cn, zhangzhijing@cqu.edu.cn

Abstract— **The wind has a significant impact on the surface icing of power equipment in icing conditions, which is an important meteorological parameter to study the equipment icing mechanism and ice melting technology. To measure the wind speed and direction of natural wind accurately, a wind speed and direction measurement method is proposed based on the principle of wind pressure difference. According to the surface pressure distribution curve of subcritical flow around the cylinder, the circumferential array distribution of six cylindrical pipes is designed. The dynamic pressure of six cylindrical pipe orifices is measured by six high-precision differential pressure sensors, and the maximum value and the maximum value of the adjacent pipe are selected to calculate the wind speed and direction. In addition, based on the analysis of the anemometer affected by ice cover and the establishment of an electric heating deicing heat transfer model, The cylinder is tightly wound with a soft carbon fiber heating element and heated together with the anemometer to ensure the stable operation of the anemometer in the icing environment. Field tests were conducted to verify the effectiveness of the presented method under normal temperature and icing environment.**

Keywords— ***Wind speed and direction; Wind pressure difference; Anemometer; Carbon fiber heating; Icing***

I. INTRODUCTION

The wind is a natural phenomenon superimposed by many small-scale pulsations which change randomly in time and space. It is also a vector on large-scale regular airflow, mainly including wind speed and wind direction angle [1]. In icing weather, wind has a significant impact on the surface icing of power equipment such as transmission lines, and it is an important meteorological parameter to study the equipment icing mechanism and ice melting technology[2].

However, common anemometers are affected in the ice-covered environment, unable to measure or have low accuracy. Mechanical anemometers such as the cup anemometer are prone to icing and wind damage , and depositing ice on the rotor will gradually slow down its speed which can lead to wrong wind speed readings[3-4]. Non rotational wind measuring instruments such as ultrasonic anemometers still have limitations in being unable to be used or measuring accurately in icing environments due to their own characteristics[5]. The wind parameter measurement technology based on the pitot tube principle is widely used in high wind speed measurement, which has the advantages of simple structure, convenient manufacture, low price, large measurement range, high accuracy and good resolution[6-7]. The existing method based on the pitot tube can only measure the directional wind direction, not the natural instantaneous wind[8]. The measurement of transient wind is of great significance to improve the utilization efficiency of wind energy and monitor the icing environmental parameters of transmission lines[9].

To measure the wind speed and direction of natural wind accurately in icing conditions, A measurement method based on pitot tube array has been proposed in this research. According to the theoretical knowledge of pitot tube and cylinder flow, a six pitot tube circumferential array was established to measure dynamic wind pressure and calculate the wind speed and direction. A carbon fiber composite heating element was designed based on critical anti icing conditions. The measurement results of the anemometer, ultrasonic anemometer, and three cup anemometer are compared to verify the correctness of the method and the effectiveness of the anemometer.

II. PRINCIPLE OF PITOT TUBE WIND SPEED MEASUREMENT

A. Principle of Single Pitot Tube Wind Speed Measurement

The pitot tube anemometer consists of the pitot tubes, measuring sensor, and PVC hose. The pitot tube was invented by French engineer Henri Pitot in the early 18th century. When measuring the flow rate, the hemispherical head of the pitot tube is aligned with the inflow flow, and the small hole in the centre of the pressure head feels the total pressure of the inflow flow, which is transmitted to the pressure gauge through the back sleeve. The basic structure of a hydrostatic tube is that the front end of the cylindrical tube is spherical, and a row of holes are vertically distributed on the wall of the tube to detect the hydrostatic pressure of the fluid [6].The measuring principle is to measure the wind speed indirectly through a pitot tube. The schematic diagram is shown in Figure 1.
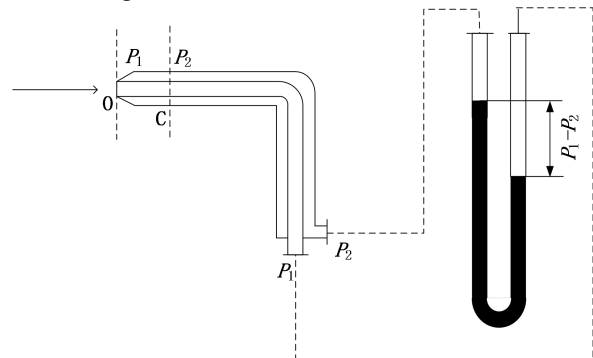
Fig. 1   Schematic diagram of pitot tube wind speed sensor

According to the Bernoulli equation, the formula is as follows:

$$P_1 = P_{dynamic} + P_2 \tag{1}$$

Where P_1、$P_{dynamic}$ and P_2 are total pressure, dynamic pressure, and static pressure respectively, in Pa.

The dynamic pressure is directly proportional to the square of the velocity, so after the total pressure and static pressure are measured, the wind speed can be calculated with the following formula:

$$V = \sqrt{\frac{2(P_1 + P_2)}{\rho}} \qquad (2)$$

Where V is the wind speed in m/s; ρ is the air density in kg/m³.

B. Principle of Flow Around the Cylinder

When the ideal fluid flows in parallel around the fluid without circulation, the velocity distribution on the cylinder surface is as follows:

$$V_r = 0 \qquad (3)$$

$$V_\delta = -2V_\infty \sin\theta \qquad (4)$$

Where θ is the wind direction value.

When the ideal fluid flows in parallel around the fluid without circulation, the pressure P at any point on the cylinder surface can be obtained from the following Bernoulli equation:

$$\frac{P}{\rho g} + \frac{V^2}{2g} = \frac{P_\infty}{\rho g} + \frac{V_\infty}{2g} \qquad (5)$$

Where P_∞ is the pressure of the fluid at infinity; V_∞ is the velocity of a fluid at infinity.

In engineering, it is customary to use a dimensionless pressure coefficient to express the pressure at any point of the liquid acting on the object. And the theoretical pressure coefficient of the flow around the cylinder is as follows[10]:

$$C_P = \frac{P - P_\infty}{\frac{1}{2}\rho V_\infty^2} = 1 - 4\sin^2\theta \qquad (6)$$
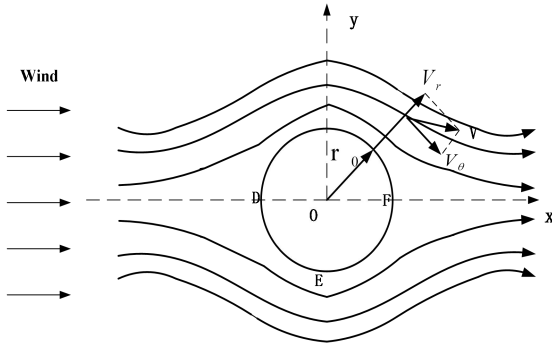
Fig. 2   Flow of uniform flow around a cylinder

As shown in Figure 2, at infinity on the left, $C_p = 0$, is the atmospheric pressure. When the fluid flows to the cylinder, due to the conversion of kinetic energy, the pressure increases gradually and reaches the maximum at D point, $C_p = 1$. From point D to point E, the pressure decreases gradually, and the minimum value is at point E, $C_p = -3$. From E to F, the pressure increases gradually. At point F, the flow velocity equals zero and the pressure returns to the maximum value, $C_p = 1$. At infinity on the right, the pressure drops back to P_∞, $C_p = 0$. When the ideal fluid flows around the cylinder, the pressure coefficient curve of the cylinder surface is shown in Figure 3.
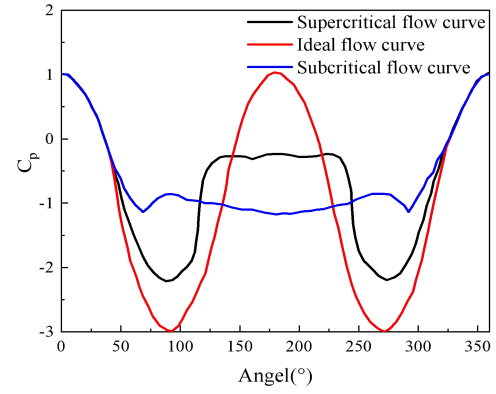
Fig. 3   Pressure coefficient of cylindrical surface

Different Reynolds number Re corresponds to different flow states around the cylinder. When $150 \sim 300 < Re < 1.9 \times 10^5$, the separation point between the boundary layer and the surface is on the upstream surface, and the angle between the separation point and the incoming flow is about 85°, called subcritical state, in which the pressure drop is dominant in the flow resistance around the cylinder. When $Re > 1.9 \times 10^5$, the laminar flow in the boundary layer gradually develops into turbulence. When $Re > 6.7 \times 10^5$, the boundary layer changes from laminar flow to turbulent flow before separation, and the separation point moves back to the back of the cylinder. The angle between the separation point and the incoming flow is about 135°, called the supercritical state. When different fluids flow around the cylinder, the pressure coefficient curve of the cylinder surface is shown in Figure 3.

According to the Reynolds number formula, when the wind speed range is within 5 m/s-40 m/s, Re is 4285-34280, which belongs to subcritical flow. That is to say, in the natural environment, most of the flow around a circular cylinder belongs to a subcritical flow. It can be seen from Fig. 3 that between 0-60° The pressure curve of subcritical flow is consistent with the ideal curve in the range of $0 \sim 60°$ The surface pressure distribution of subcritical flow around a cylinder can be calculated by the ideal cylinder flow formula.

C. Principle of Wind Speed and Direction Measurement with Multi Pitot Tubes
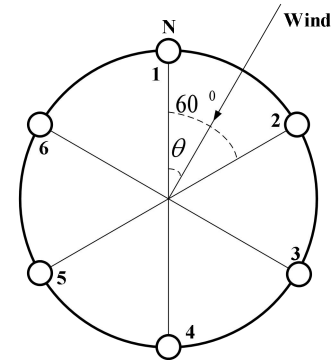
Fig. 4   Arrangement of 6 pitot tubes

In this paper, the measured wind speed range is within 0-30 m/s, and the fluid is subcritical flow by Reynolds number formula. Considering that the structure of the anemometer is symmetrical and the algorithm is simple, the number of anemometers divided into a circle array should be divisible by 360. The pressure curve of subcritical flow in the range is

consistent with the ideal curve between 0°- 60° , so six pitot tubes can be used, and the angle between adjacent pitot tubes is 60 degrees. The actual wind speed and direction can be inferred from the pressure distribution of six pitot tubes. The arrangement of pitot tubes on the cylindrical surface is shown in Figure 4. Six holes are arrayed at the position 20 mm away from the upper cover plate of the barrel, and the horizontal angle difference of each hole is 60°, Each hole is connected with the differential pressure sensor, and the air pressure of each hole is set as P_1, P_2, P_3, P_4, P_5, P_6. The air pressure of each hole can be obtained by the sensor. Therefore, the angle between the pipe at which the maximum wind pressure value P_i is located and the wind speed is set as θ, then the angle between the second-largest wind pressure $P_j$and the wind speed is (60°-θ）, There are:

$$P_i = P \cdot C_P(\theta) \qquad (7)$$

$$P_j = P \cdot C_P(60° - \theta) \qquad (8)$$

Where $C_p(\theta)$ is the fitting curve of the surface pressure of the cylinder within 60 ° angle range.The maximum dynamic pressure value P and wind direction angle θ can be calculated by equation (7) and equation (8), and the value of P is brought into equation (2) to calculate the value of wind speed.

III. DESIGN OF ANTI-ICING ANEMOMETER SYSTEM

A. Structural design of anemometer

The system structure of the anemometer is shown in Figure 5. The open ends of the six wind speed tubes are placed on the protruding position of the cylinder, and the position should meet the equation (9) to reduce the influence of flow disturbance near the end of the cylinder. The lower hose connects the middle wind pressure channel to the pressure sensor to detect the pressure difference. The microcontroller is used to read the differential pressure data to calculate the results, and the results are transmitted to the upper computer. The circuit board is placed in a container under the cylinder, and the ports provide power and communication functions.

$$\frac{1}{10}H < L < \frac{9}{10}H \qquad (9)$$

Where H is the total length of the cylinder, in m; L is the length from the center of the pipe to the upper-end plate of the cylinder, in m.
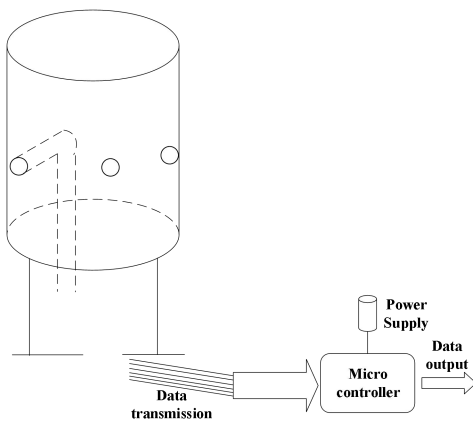
Fig. 5   Structural block diagram of anemometer systems

B. Structural design of carbon fiber heating element

Considering anemometer affected by ice cover, and the establishment of electric heating deicing model by carbon fiber in Figure 6. The carbon fiber composite shall have at least three layers: insulation and heat conduction layer, heating layer and heat insulation layer.The insulation and heat conduction layer adopts high temperature resistant adhesive tape, which can fix and protect the carbon fiber heating wire and insulation, so as to prevent the carbon fiber tow from contacting and conducting electricity with the heated equipment.The heating layer adopts carbon fiber tow of model T300 1K, which is assembled and fixed on the braided board to form flexible carbon fiber tow clusters. The insulation layer is made of PVC transparent soft glass, which can prevent heat radiation to the environment and increase the safety performance of carbon fiber.Thickness in total is less than 2mm, very soft.
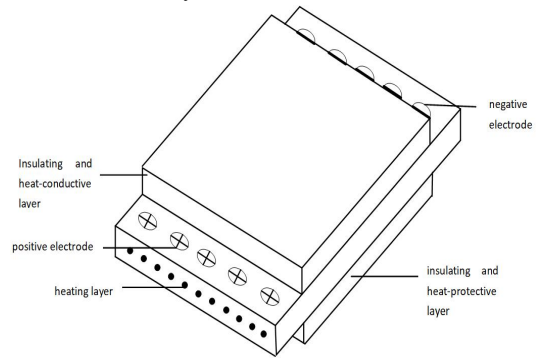
Fig. 6   Carbon fiber structure design drawing

IV. TEST AND ANALYSIS

In order to verify the measurement performance of anemometer, it is tested in normal temperature and iced natural environment respectively was carried out in Xuefengshan Energy Equipment Safety Field Scientific Observation and Research Station of Chongqing University (referred to as Xuefengshan Field Station, as shown in Figure 7). In normal temperature weather, observe at the same time with other anemometers to compare and analyze the wind speed and direction data. The icing and melting tests are carried out under different icing conditions to test the anti icing effect of the anemometer and verify the measurement accuracy of the anemometer under icing conditions.

Fig. 7   Xuefeng Mountain Test Station

A. Test on natural wind environment

To verify the effectiveness of the anemometer proposed in this paper, the wind speed data collected by different types of anemometers in the same period are compared and analyzed. As the starting wind speed of the three-cup anemometer is large, the data group with the wind direction within 110 ~ 150° and higher wind speed are selected. And the measured data of the pressure anemometer designed in this paper are compared with the three-cup wind speed data, as shown in Figure 8.
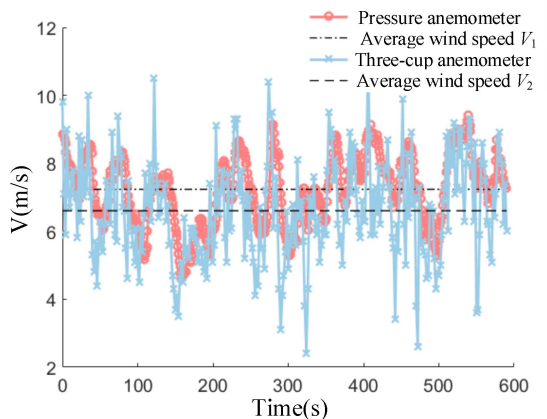
Fig. 8   Compared with the three-cup anemometer

The average wind speed V_1 of the pressure anemometer is 7.2355 m/s, the pulsating intensity is 1.0837 m²/s², and the mean square deviation of the pulsating wind speed is 1.0410 m/s, which is also called pulsating wind speed. The results show that the average wind speed of the three-cup type is 6.6034 m/s, the fluctuating intensity is 2.2201 m²/s², and the mean square deviation of fluctuating wind speed is 1.4900 m/s. At the same time, the deviation of average wind speed is 9.572%.

It can be found that the average wind speed measured by the three-cup anemometer is small in the time interval of 600 s, and the average wind speed measured by the two instruments represents an approximately stationary random process. Even the instantaneous wind speed can ensure that the overall trend of the two is similar. But at the same time, there are still differences in the measured values between the two devices. The fluctuating wind speed of the three-cup anemometer is larger, and it is easier to have extreme values. The wind speed of the anemometer is more stable. The main factor is that the wind cup has inertial mass and mechanical friction, and it has measurement delay and error, so it can not be used as a reference for standard wind speed. The test shows that the anemometer has a reference value in measuring instantaneous wind speed.

FRT environmental monitoring system is used in Xuefeng mountain to automatically measure wind speed, wind direction, and other basic meteorological elements. The principle of measuring wind speed and direction is ultrasonic propagation, and the accuracy of wind speed is high ± 3 m/s wind direction accuracy ± 3°, and the sampling period is 1 min. The ultrasonic anemometer and the pressure anemometer are set up on the same horizontal plane, 2 m away from the ground, with an interval of 2.5 m. The wind speed of the pressure anemometer designed in this paper is compared with the wind speed data measured by the ultrasonic anemometer, as shown in Figure 9 and Figure 10 .
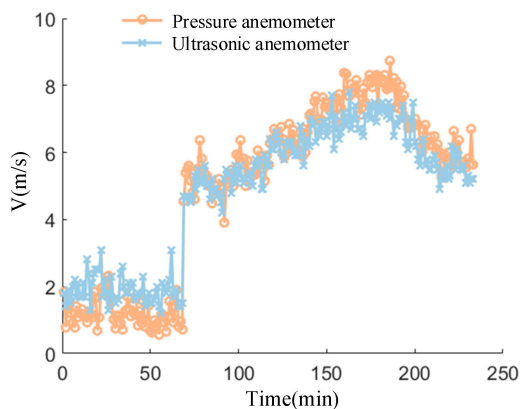
Fig. 9   Comparison with wind speed measured by ultrasonic anemometer
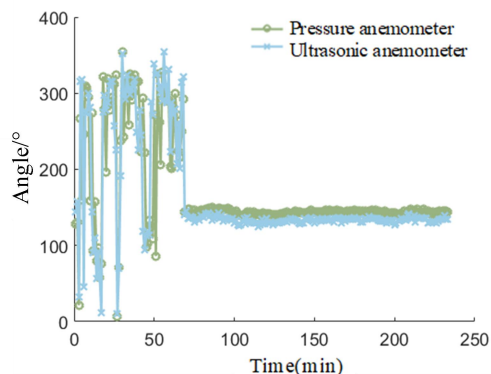
Fig. 10   Comparison with wind direction measured by ultrasonic anemometer

It can be found that compared with the measurement of wind pressure anemometer and ultrasonic anemometer, the overall trend is the same, and the wind speed within 1 minute is relatively stable. The wind speed and direction at low wind speed are basically consistent with that at high wind speed. At low wind speed, the relative error of wind pressure measurement is larger than that of ultrasonic measurement. With the increase of wind speed, the measurement accuracy is significantly improved. The wind direction fluctuates greatly at low wind speed. The wind angle measured by wind pressure type and ultrasonic type are disordered, which is similar to the disorder of wind direction. At high wind speed, the wind direction measured by the two methods is roughly similar, and the wind pressure type is about 5 ° greater than that of ultrasonic.

B. Test on natural wind environment

The standard pitot tube has a resolution of 1 Pa, which results in significant measurement errors at low wind speeds and can only be measured in the direction of incoming flow. Due to the influence of low temperature in an ice covered environment, the pitot tube experiences abnormal differential pressure measurements on the windward side, making it unable to measure wind speed.

When the snow and ice are light, the ultrasonic wave invades from the edge first, which is easy to block the wind, resulting in data error. When the icing is serious, the ultrasonic instrument as a whole, including the measuring probe, is blocked by ice and snow. When rain and snow fall

Fig. 11 Ultrasonic in icing environment

on the transmitting surface of the anemometer, the ultrasonic emission will be affected, resulting in the failure of the ultrasonic receiving transducer to receive the signal, as show in Figure 11.

The outside of the wind pressure anemometer is heated with composite heating material made of carbon fiber. The heating voltage is 220 V and the power is 65 W to prevent pipe orifice blockage. The heating material has good resistance stability, good heating uniformity and rapid heating. Ice-coated heating of anemometer is shown in Figure 12 and Figure 13. It can be found that the initial stage

    (a) Initial   (b)2min   (c)Melting completely
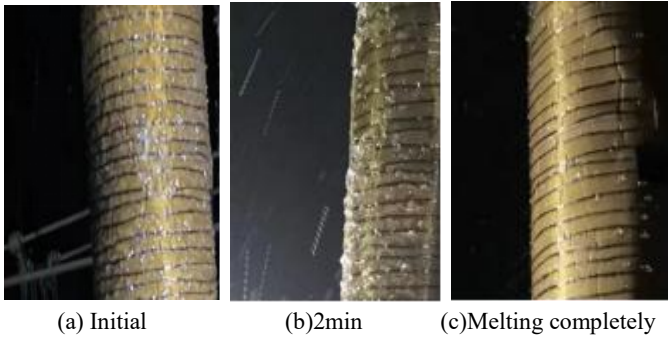
Fig. 12 Ice melting process (The average icing thickness of the cylinder is 1.6 mm)

    (a) Initial   (b)2min   (c)Melting completely
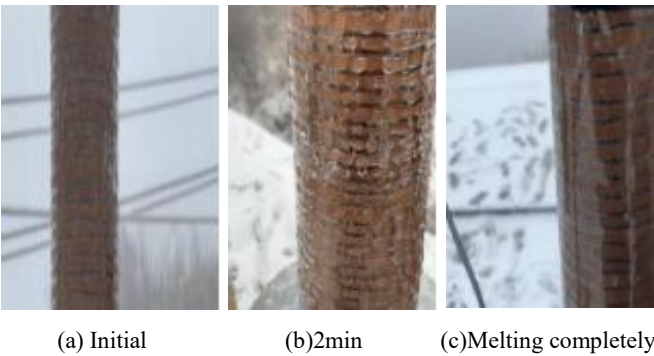
Fig. 13 Ice melting process (The average icing thickness of the cylinder is 2.1 mm)

is from the initial temperature of the ice layer to the freezing temperature, i.e. 0 ℃. The second stage is that the ice at 0 ℃ continues to absorb heat and change into 0 ℃ water. Water at 0 ℃ no longer absorbs the heat of hot water, but directly flows down from the edge of the instrument surface and falls off from the instrument surface. With the increase of icing thickness, the ice can be removed completely, but the time is prolonged.The results indicate that the anti icing process of carbon fiber composite materials generates Joule heat through the current of the fiber bundle, which diffuses and

transfers heat to the surface of the anemometer, and also prevents the freezing of liquid water.

V. Conclusions

(1) According to the principle of pitot tube wind speed measurement and the principle of flow around a cylinder, a wind speed and direction meter is designed. The wind speed and direction meter is composed of six wind speed tubes and a cylinder. The wind pressure in the wind speed tube is transmitted to the pressure sensor through the hose to detect the pressure difference.

(2) In the natural environment, the measurement results of the pressure anemometer designed, three-cup anemometer, and ultrasonic anemometer are compared. The results show that the anemometer designed has the advantages of fast response, high precision, large range, intelligence, and long working time.

(3) The cylinder is tightly wound with a soft carbon fiber heating element and heated together with the anemometer. The icing test shows that the anemometer will not be iced when heated, so as to ensure the normal operation of the instrument and the continuous measurement of wind speed and direction.

References

[1] Rong, K., Tian, L., Luo, J., and Wang, L. Study on wind-induced fatigue performance of large-span transmission tower-line system considering the combined distribution probability of wind direction and speed.Engineering Failure Analysis. 156 (2024): 107785.

[2] Yang, G., Jiang, X., Liao, Y., Li, T., Deng, Y., Wang, M., and Zhang, Z. Research on load transfer melt-icing technology of transmission lines: Its critical melt-icing thickness and experimental validation. Electric Power Systems Research, 221(2023) , 109409.

[3] Alfonso-Corcuera, D., Vega, E., Ogueta-Gutiérrez, M., Alcala-Gonzalez, D., and Pindado, S. Effect of ice/dirt on cup anemometer rotors. Flow Measurement and Instrumentation, 89 (2023), 102267.

[4] Ramos-Cenzano, A., Lopez-Nunez, E., Alfonso-Corcuera, D., Ogueta-Gutierrez, M., & Pindado, S.. On cup anemometer performance at high altitude above ground. Flow Measurement and Instrumentation, 79 (2021), 101956.

[5] Streichenberger, B., Chakir, R., Jouy, B., & Waeytens, J. Simulation and Validation of CFD turbulent airflow at pedestrian level using 3D ultrasonic anemometer in the controlled urban area "Sense-City". Journal of Wind Engineering and Industrial Aerodynamics, 219(2021), 104801.

[6] Liu X, Bian Z Q, Li S K. Standard pitot tube calibration coefficient measurement and uncertainty evaluation analysis[J]. Electronic measurement technology. 2020,43(14):50-54. (in Chinese)

[7] Leoni, A., Barile, G., Muttillo, M., Pantoli, L., Stornelli, V., Ferri, G., ... & Vita, L. D. A spherical directional anemometer sensor system. In Proceedings, Vol. 1, No. 4, p. 388. MDPI, 2017.

[8] Chevula, S., Sanz-Andres, Á., & Franchini, S. Estimation of the correction term of pitot tube measurements in unsteady (gusty) flows. Flow Measurement and Instrumentation, 46(2015), 179-188.

[9] Aboshosha, H., Elawady, A., El Ansary, A., & El Damatty, A. Review on dynamic and quasi-static buffeting response of transmission lines under synoptic and non-synoptic winds. Engineering Structures, 112(2016), 23-46.

[10] Liu C, Zhao Z, Du L D, et al.Method of Measuring Two-dimensional Wind Based on Diametrical Pressure Differences Developed by Flow Around Cylinder,Journal of Electronics & Information Technology. 39(3)(2017) 737-742.(in Chinese)

Icing Observed and Analysed in Correspondence with Helicopter Flight Campaigns in Norway in 2023

Eirik Mikal Samuelsen[1,2] and Kristoffer Kvist[2,3]

[1] The Norwegian Meteorological Institute (MET)
[2] The Arctic University of Norway (UiT)
[3]Norwegian Air Ambulance Foundation (SNLA)

eiriks@met.no, kristoffer.kvist@uit.no

Abstract— **Supercooled liquid water inside a cloud may freeze upon contact with objects like helicopters or fixed-winged aircraft. Large amounts of liquid water in sub-freezing conditions may therefore lead to hazardous ice build-up on various parts of the aircraft. In a worst-case scenario, the rotor blade of a helicopter or the wings of a fixed-wing aircraft may be completely iced-up, hampering the lift, which may lead to fatalities. Forecasting icing conditions is therefore a critical task for weather agencies worldwide. Icing forecasts are regularly issued by the Norwegian Meteorological Institute (MET Norway) as either direct model output from an atmospheric icing model or icing-warning bulletins provided by operational weather-aviation forecasters. However, due to the lack of numerous accurate icing or liquid-water content observations, there is only limited knowledge about the quality of the icing predictions. During the winter months of 2023, Airbus helicopters initiated two flight campaigns in Norway in cooperation with the Norwegian Air Ambulance Foundation (NAAF) and MET Norway. In these campaigns, liquid-water content, temperature, and droplet sizes were recorded in conjunction with camera surveillance of the ice build-up. In this study, the observations from the campaign are analysed and compared with numerical weather prediction output of the same parameters. Furthermore, the weather situations during the campaigns are scrutinised. Interestingly, in a situation with a thick cloud with frontal precipitation, only little water was present. On the other hand, in a relatively thin orographically-induced lenticularis cloud vast amounts of water existed, leading to severe icing on the helicopter.**

The results illustrate that the current icing predictions provide fairly accurate results for the cases analysed. However, increasing the horizontal and vertical model resolution further improves the model accuracy. Nevertheless, the results may be different in other weather situations not analysed in the current study.

*Keywords— **Aircraft icing, NWP, In situ LWC measurements, HARMONIE-AROME***

I.   INTRODUCTION

Atmospheric icing occurs when supercooled cloud droplets collide with objects like helicopters or fixed-wing aircraft. The rate of ice accumulation depends on the geometrical properties of the iced object [1-3] and several meteorological variables[4], the most important of the latter being the cloud liquid water content (LWC).

The icing forecasts issued by the Norwegian Meteorological Institute are based on meteorological data from the numerical weather prediction (NWP) model HARMONIE-AROME [5]. At the Norwegian Meteorological Institute the two HARMONIE-AROME models: Arome Arctic (AA) [6, 7], with a northern domain, and MEPS [5, 8], with a more southern domain, are run operationally eight times a day with a prognosis length of each run of 66 hours. In this study, only the control member of the ensemble system MEPS is applied. The time step of these models is 75 seconds, but data are only stored every hour. AA and MEPS are spectral models, using grids with 2.5 km resolution in the horizontal dimensions and with terrain following pressure-based hybrid sigma-coordinates [9-11] discretized on 65 levels in the vertical. The lowermost vertical layer is approximately 12 meters above the terrain while the top layer is at 10 hPa [12]. Most layers are located in the lower part of the atmosphere, i.e. 27 model levels within approximately the lowest 2000 meters. The boundary conditions of both model domains are based on relaxation [13] towards data from the High Resolution (HRES) operational system [14-16] of The European Centre for Medium-Range Weather Forecasts (ECMWF-IFS) with a horizontal grid spacing of 9 km. Global prediction data is further incorporated into AA and MEPS by spectral mixing [17, 18] of large-scale information from ECMWF-IFS using a wave number and coordinate-dependent weight function. Observational data are utilized by three-dimensional variational data assimilation of observations into the model background [8, 19]. Even at 2.5 km horizontal grid spacing, many important meteorological effects are not resolved e. g. turbulence, shallow convection, and cloud microphysics which are parametrized as described in [5] and references therein.

Apart from parametrized non-resolved physical processes, a deficit of discrete models is their inherent restriction in topographical representation. In mountainous regions exposed to humid marine air, such as the vast shoreline of western Norway, orographic lifting is a typical origin of cloud formation, and orographic effects are known to cause large gradients in cloud cover and precipitation amounts [20]. Furthermore, the boundary layer structure governing the transport properties of the lower atmosphere is highly influenced by complex terrain formations [21, 22]. Due to the inferior increase of computations with reduced horizontal grid spacing [23-25], the literature investigating the sensitivity of the cloud liquid water content (LWC) in mesoscale forecast models to horizontal grid spacing is sparse, motivating the case-based sensitivity experiments presented below.

For the presented cases we analyse the cloud origin and its relation to icing intensity, as multiple competing microphysical processes [26, 27] decide the amount of liquid

water creation and its persistence. As an example of the conflicting arguments that this multi-process complexity can lead to, former literature has argued that large areas of supercooled liquid water often accompany frontal precipitation and hence icing, and that dry weather conditions, as a consequence hereof, provide less icing [28]. On the other hand, cloud ice crystals grow at the expense of water droplets, causing frozen precipitation to drain the cloud free of water unless new droplets are formed through lifting and adiabatic cooling to compensate for the loss of liquid water [26].

In the following sections, the objective of the current study is specified and several case studies of data from cloud water collection experiments are presented. The collected data are compared to the forecast output of MEPS and AA in operational configuration. In addition, AROME has been run with a 300-meter horizontal grid spacing to investigate the forecast sensitivity of LWC to the horizontal grid spacing. Analyses of the weather situations during the data collection accompany the findings, to explore if certain situations are characteristic of high and low forecast accuracy.

II. OBJECTIVE

The object of the study is twofold. Firstly, to get more information about the model quality of the icing forecast, the liquid water content of both the operational models and experimental model setups with higher spatial resolution, i.e. shorter grid spacing, is compared with in situ measurements. Secondly, we seek to improve the understanding of the weather situations in which icing may arise, by analysing the weather situations in four cases where icing was encountered.

Fig. 1.   Iced windshield wiper after encountering severe icing near Alta on the 19th of April. Photo by Eirik Mikal Samuelsen.

III. SPECIFICATION OF MODEL OUTPUT DATA

The reported data were collected in the winter and spring of 2023 when the operational models (AA and MEPS) were running version CY43h2.2. In addition to the operational models, high-resolution AROME models with 300 m horizontal grid spacing have been run. These models are labeled AN-300m (AROME Nordland 300 m) and ATF-300m (AROME Troms Finnmark 300 m) for the cases of Brønnøysund and Alta respectively. The domain of AN-300m is a 600 x 900 grid centered at 11.5° E and 65.9° N,

with an initial time of the 28th of February 2023 0000 UTC. The domain of ATF-300m is a 540 x 1458 grid centered at 16.75° E 68.95° N, with an initial time of the 18th and 19th of March 2023 0000 UTC for cases 3 and 4 (see section V), respectively. The prognosis length of AN/ATF-300m is 36 hours in reported runs. For these hectometric-scale models, the atmosphere is divided vertically into 90 layers with 32 layers below 2000 meters. The lowermost layer is located approximately 5 meters above the terrain while the top layer is still at 10 hPa. The model version applied is CY43.h2.1. The time step for both domains is 5 seconds. For these runs, no direct data assimilation is applied. They are initialized with a cold start using ECMWF IFS HRES fields both initially and at the boundaries of the domains.

IV. METHODS

A. Data Collection

During the winter and spring of 2023, Airbus Helicopter initiated two flight campaigns in Norway. Airbus-H145 flew in the area around Brønnøysund airport (65.46° N, 12.22° E) in February and March. This helicopter does not have deicing equipment, restricting the amount of time it may fly in icing conditions. The larger helicopter H175 which is equipped with deicing flew in late April with a base at Alta airport (69.98° N, 23.37° E). Both the Airbus-H145 and Airbus-H175 were equipped with temperature sensors and a single-photodetector array cloud droplet probe (CDP) [29] for in situ measurements of cloud LWC. The CDP projects a collimated laser beam onto a linear array of 64 photodetectors.   The cloud-droplet size distribution is determined by monitoring the shadowing of photodetectors by cloud droplets. The CDP used in the relevant experiments measures the droplet counts in 30 equally sized bins covering the range 2-50 μm. It is assumed that the contribution to the total cloud LWC from droplets with diameters outside this range is neglectable. Given the relative air speed of the CDP, the LWC can be derived from the droplet-size spectrum.

B. Numerical Weather Prediction Model Data

Section V shows the CDP-measured LWC compared with the output of data from several NWP models (see sections I and III). The output data at the relevant temporal and spatial position of the helicopter is obtained by 4D linear interpolation. To interpolate in the vertical direction, the temporal-spatial dependent pressures of the model layers, $p_k(x, y, t)$, were calculated using

$$p_k(x, y, t) = a_{p,k} + b_k \cdot p_s(x, y, t),$$

where k indexes vertical layers $a_{p,k}$ and b_k are predefined constants of the vertical layers and p_s is the surface pressure. The surface pressure of the temporal-spatial position of the helicopter is determined from 3D linear interpolation. Having determined $p_k(x, y, t)$, interpolation in the vertical is accomplished using the onboard pressure measurement of the helicopter.

V. RESULTS AND DISCUSSION

Even though numerous data-collection flights were completed during the campaign period, only four cases of particular interest are presented here. These include two flights of the H145-campaign that occurred on the 28th of

February 2023, and the 1st of March 2023, and two flights of the H175-campaign that occurred on the 18th of April 2023 and the 19th of April 2023. Cases 1, 2, and 4 (see below) are the three cases with the largest ice accumulation measured during the campaigns in Alta and Brønnøysund. Despite the low observed LWC, case 3 is interesting as the measured icing was significantly lower than the model predictions.

A. Case 1. H145. 28 February 2023

The weather is characterized by a relatively thin stratocumulus layer along the coast, with gravity waves in the form of so-called mountain waves in the lee of both the Lofoten peninsula and over the land areas of Nordland. The large-scale wind is coming from the north-northwest with up to 25-30 KT in the Brønnøysund area and the air masses are quite cold with a temperature of around – 9 °C at around 850 hPa according to the operational MEPS model. The measured LWC and the interpolated model data are shown in Fig. 2 revealing a strong temporal and spatial correlation between all tested models and the measured data, but with the models generally underestimating LWC. The ice build-up during the flight demanded the helicopter to occasionally fly out of the clouds and into warmer and drier conditions for ice mitigation, as apparent in Fig 2.
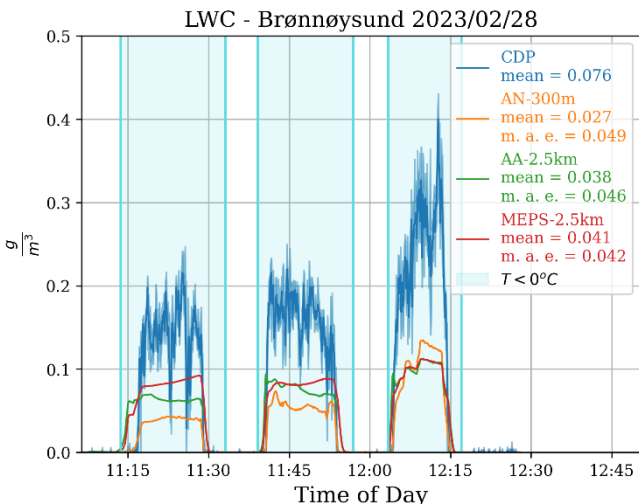
Fig. 2.   In situ measurements of cloud LWC compared to NWP models of differing domain and grid spacing. This data was collected using an Airbus H145.

B. Case 2. H145. 01 March 2023

The next day the weather is still characterized by stratocumulus clouds, west-northwesterly flow up to 30-35 KT in the Brønnøysund area, and mountain waves above the land areas. However, tendencies of more convective clouds offshore are apparent (Fig. 3), and radar echoes indicated tendencies of showers embedded in the stratocumulus layer (not shown). On the other hand, the air masses are much warmer than the day before illustrated by a temperature at 850 hPa of –2 to –3 °C. Due to the relatively high temperatures only little ice build-up on the critical parts of the helicopter (e.g. rotor) was observed.

The result of Fig. 4 indicates a good temporal-spatial correlation between measured data and model data of each of the tested models. The 300 m model does however manage to resolve details not apparent in the coarser models, especially in the first part of the flight (9:00-9:40). These
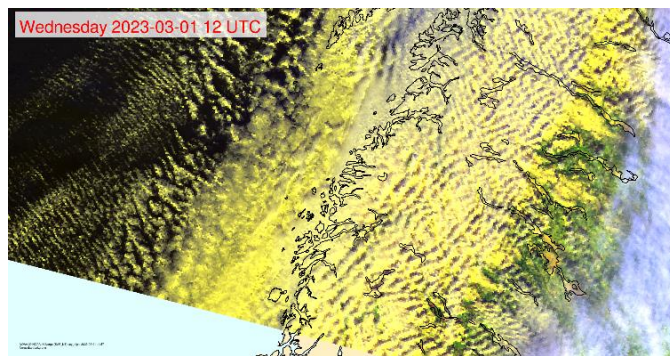
Fig. 3.   Satellite image 1st of March , visible channel. Source: NOAA/MET Norway.

differences are believed to be caused by the poor representation of the topography of the operational models. Specifically, we
suspect that the differences between the operational and high-resolution (AN-300m) models are due to different predictions of the mountain waves and sheltering effect caused by the mountains on an island (Vega) positioned up-wind relative to the flight route. In the operational models, the 800-meter-tall mountains of this island only rise 200 meters above sea level. This is substantiated by Fig. 5 showing a large discrepancy in the spatial distribution of liquid water between AN-300m and AA-2.5km.
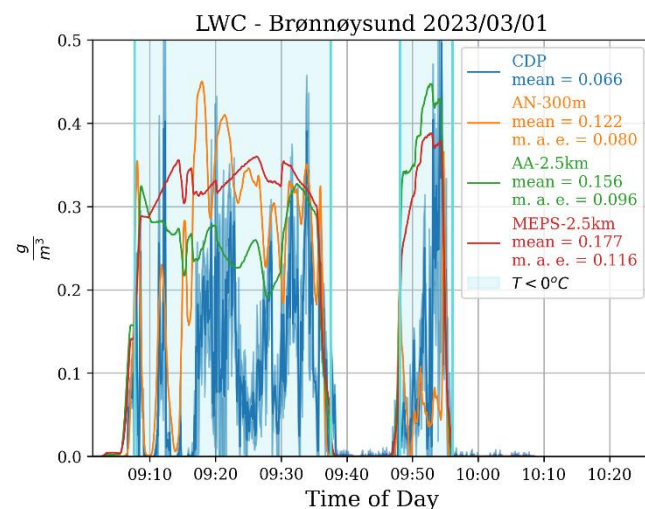
Fig. 4.   In situ measurements of cloud LWC compared to NWP models of differing domain and grid spacing. This data was collected using an Airbus-H145.

C. Case 3. H175. 18 April 2023

During the afternoon and evening of the 18th of April 2023, a frontal system is approaching from the west providing a relatively thick cloud layer with precipitation in the Alta region (not shown). The wind at 700 hPa or approximately 10.000 FT is around 35-40 KT from the west in the relevant area. The temperature at 5000 FT is around +2 °C, and at 700 hPa the temperature is –7 °C. As seen in Fig. 6 the measured LWC is highly localized with a detail not caught in the NWP models, such that the integral LWC of the operational models is higher than that of the measured. The localized pockets of LWC resulting in the peaks of LWC as measured by the CDP in Fig. 6 are likely to stem from orographically
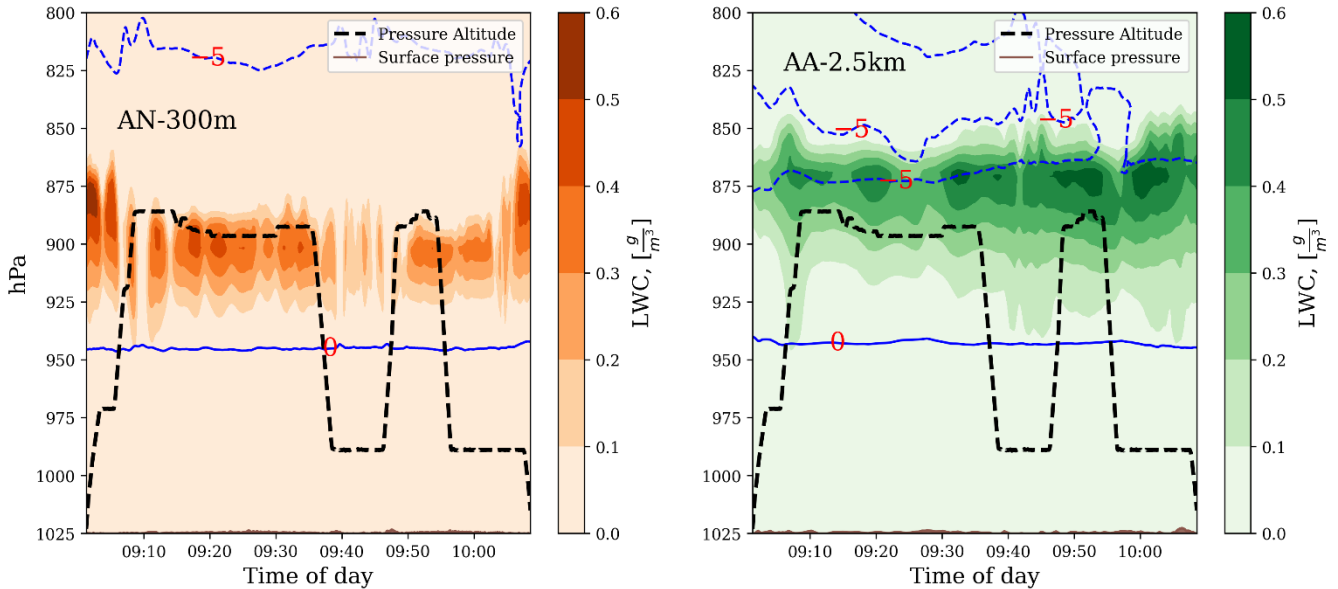
Fig. 5. Cross sections of the LWC interpolated to the temporal and spatial position of the helicopter of the ATF-300m and the operational AA-2.5km models respectively. The blue lines indicate temperature contours of 0 ºC and –5 ºC. The model surface height is barely visible as most of the flight route was over the ocean.

induced positive vertical velocities causing cooling and thus droplet production. None of the models are able to reproduce the variation in LWC observed by the helicopter, but the mean absolute error in the 300 m model is lower than that of the operational models. The observed ice accumulation was minuscule.

Fig. 6. In situ measurements of cloud LWC compared to NWP models of differing domain and grid spacing. This data was collected using an Airbus-H175.

D. Case 4. H175. 19 April 2023

The day after the frontal system has passed, there are strong winds from the west with up to 50 KT at 700 hPa or 10.000 FT. The temperatures aloft are a bit colder than the day before with around –9 ºC at 10.000 FT and around –4 ºC to –2 ºC at 5.000 FT. The weather is characterized by stratocumulus clouds with patches of precipitation in the mountain areas. The satellite image (Fig 7) reveals quite characteristic mountain wave features with relatively long wavelengths compared to the mountain waves of case 1 and case 2 (Fig. 2). The mountain waves are characterized by large spatial variation in both vertical velocities and horizontal velocities providing turbulence.

As indicated in Fig. 8 and Fig. 9 the helicopter encountered severe icing on this flight. The operational models underestimate the amount of cloud LWC whereas the high-resolution model (ATF-300) predicts this metric at high

Fig. 7. Satellite image, 19th of April, visible channel. Source: NOAA/MET Norway.

accuracy. The large accuracy of the high-resolution model as compared to the operational models is attributed to the significant increase in topography representation accuracy when decreasing horizontal grid spacing from 2.5 km to 300 m leading to an increased accuracy in the representation of the lee waves. A striking result is the large vertical distance between the maxima in LWC predicted by ATF-300m and AA-2.5km in this case. As seen in Fig. 8 the highest LWC in the vertical profile is indeed underestimated by AA-2.5km, but the primary difference between the two models is that the high-resolution model predicts the highest LWC to be at a higher altitude than AA-2.5km and additionally predicts the regions of high LWC to have a larger vertical extend. The same trend was observed for MEPS-2.5km (not shown).
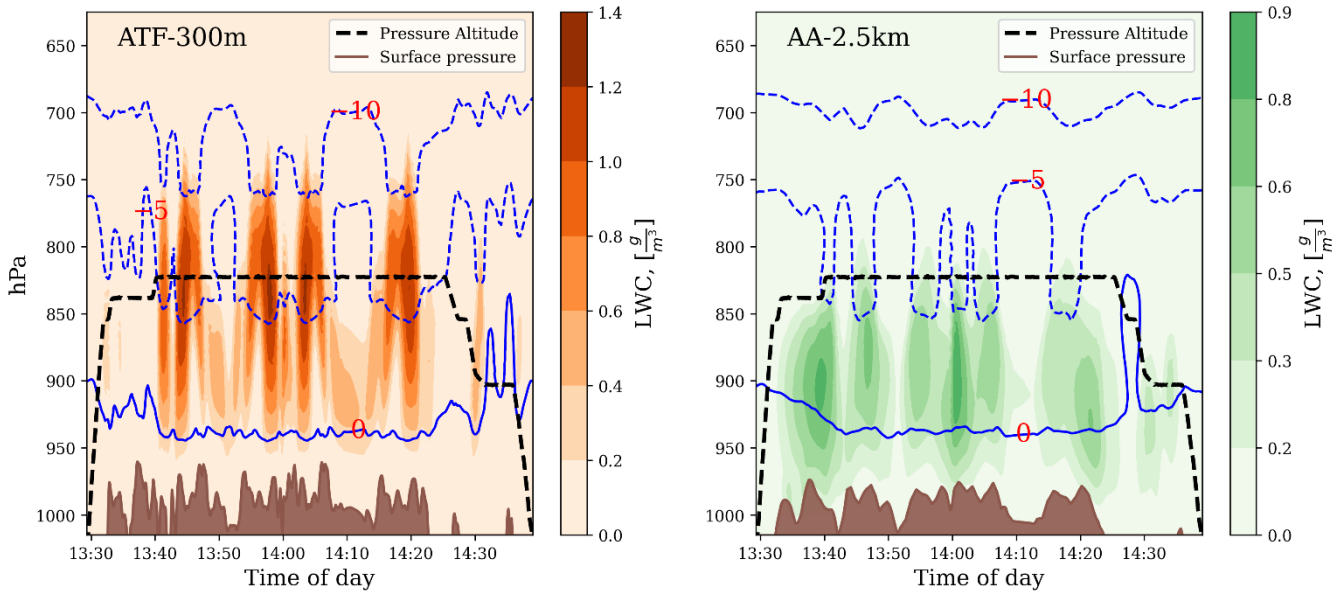
Fig. 8.   Cross sections of the LWC interpolated to the temporal and spatial position of the helicopter of the ATF-300m and the operational AA-2.5km models respectively. The blue lines indicate temperature contours of 0 ºC, –5 ºC, and –10 ºC. The brown shading shows the model surface height of the route of flight and thus depends on spatial resolution.

VI.   CONCLUSIONS

In general, there is a good correlation between the observed LWC and the LWC predicted by the operational models as well as the experimental high-resolution models. Earlier findings pinpoint that the operational models underestimate the cloud water due to too soon glaciation of the clouds [30]. This effect is not found to contribute significantly to the deviation of the output LWC of the operational models from the observed LWC in any of the
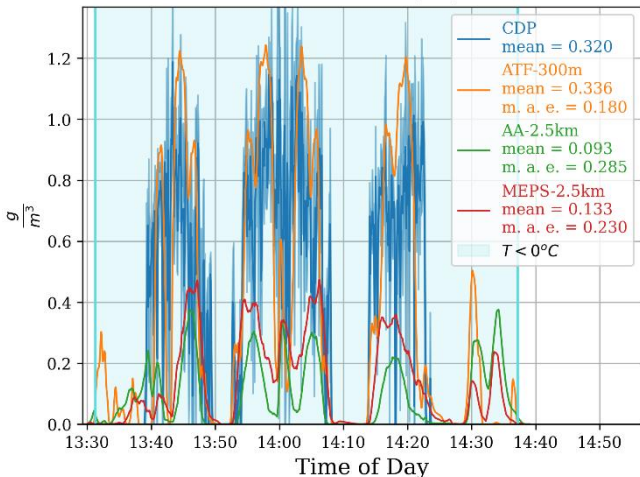
Fig. 9.   In situ measurements of cloud LWC compared to NWP models of differing domain and grid spacing. This data was collected using an Airbus-H175.

four reported cases. The improved prediction accuracy of the LWC and its spatial distribution in ATF/AN-300m highlights the importance of resolving the topography when modeling icing as LWC is sensitive to e.g. mountain waves and downstream effects. It is interesting to notice the strong

effect of the relatively small mountains on the island Vega close to Brønnøysund on both the observed and modelled cloud water. The fact that the effect of these mountains does not occur directly over the mountains themselves illustrates the importance of having a dynamical NWP model with high enough resolution to resolve the topographical downstream effects when forecasting icing.

Another interesting finding in this study is the relatively high amount of cloud water observed in weather situations not connected to frontal systems. In three of the cases, there were stratocumulus clouds combined with embedded showers and mountain waves, the latter of which provided the main forcing of the creation of the observed cloud water. In the case from the 18th of April 2023 with a frontal system approaching, a lower LWC was observed than in the other three cases presented. Even though studies have illustrated that icing mainly occurs close to frontal systems [28], other forcing mechanisms might be more important in Northern Norway than in e.g. the USA. For the Alta case of the 19th of April 2023 it is striking that LWC amounts up to 1.2 g/m³ are measured in a relatively thin stratocumulus lenticularis cloud resulting in severe icing of the helicopter. As to the authors' knowledge, this is the first time a severe icing case is documented to be so directly linked to mountain-wave generation in Norway.

The fact that the highest values of LWC in case 4 are located at higher altitudes both in the observations and ATF/AN-300m as compared to the operational 2.5km models, aligns with previous studies suggesting an underestimation of the altitude of moderate and severe icing conditions in the operational AROME icing model when compared to pilot reports [30, 31]. This substantiates the belief that a more accurate prediction of LWC can be achieved by a better topographic representation and that the increased accuracy is correlated with the improved representation of mountain waves in high-resolution models. These findings motivate further investigations of the correlation between LWC and mountain wave prediction accuracy and the spatial model resolution, to explore the operational value of hectometric models in aviation forecasting.

REFERENCES

[1] S. Rydblom and B. Thörnberg, "Measurement of atmospheric icing and droplets," *IEEE Transactions on instrumentation and measurement,* vol. 69, no. 8, pp. 5799-5809, 2020.

[2] E. W. Brouwers, J. L. Palacios, E. C. Smith, and A. A. Peterson, "The experimental investigation of a rotor hover icing model with shedding," in *American Helicopter Society 66th Annual Forum,* 2010, pp. 1863-1875.

[3] Y. Cao and K. Chen, "Helicopter icing," *The Aeronautical Journal,* vol. 114, no. 1152, pp. 83-90, 2010.

[4] Y. Cao, W. Tan, and Z. Wu, "Aircraft icing: An ongoing threat to aviation safety," *Aerospace science and technology,* vol. 75, pp. 353-385, 2018.

[5] L. Bengtsson *et al.*, "The HARMONIE–AROME model configuration in the ALADIN–HIRLAM NWP system," *Monthly Weather Review,* vol. 145, no. 5, pp. 1919-1935, 2017.

[6] M. Müller, Y. Batrak, J. Kristiansen, M. A. Køltzow, G. Noer, and A. Korosov, "Characteristics of a convective-scale weather forecasting system for the European Arctic," *Monthly Weather Review,* vol. 145, no. 12, pp. 4771-4787, 2017.

[7] M. Køltzow, B. Casati, E. Bazile, T. Haiden, and T. Valkonen, "An NWP model intercomparison of surface weather parameters in the European Arctic during the year of polar prediction special observing period Northern Hemisphere 1," *Weather and Forecasting,* vol. 34, no. 4, pp. 959-983, 2019.

[8] M. Müller *et al.*, "AROME-MetCoOp: A Nordic convective-scale operational weather prediction model," *Weather and Forecasting,* vol. 32, no. 2, pp. 609-627, 2017.

[9] A. J. Simmons and D. M. Burridge, "An energy and angular-momentum conserving vertical finite-difference scheme and hybrid vertical coordinates," *Monthly Weather Review,* vol. 109, no. 4, pp. 758-766, 1981.

[10] R. Bubnová, G. Hello, P. Bénard, and J.-F. Geleyn, "Integration of the fully elastic equations cast in the hydrostatic pressure terrain-following coordinate in the framework of the ARPEGE/Aladin NWP system," *Monthly weather review,* vol. 123, no. 2, pp. 515-535, 1995.

[11] R. Laprise, "The Euler equations of motion with hydrostatic pressure as an independent variable," *Monthly weather review,* vol. 120, no. 1, pp. 197-207, 1992.

[12] K. Hämäläinen, A. Hirsikko, A. Leskinen, M. Komppula, E. J. O'Connor, and S. Niemelä, "Evaluating atmospheric icing forecasts with ground‑based ceilometer profiles," *Meteorological Applications,* vol. 27, no. 6, p. e1964, 2020.

[13] H. Davies, "A lateral boundary formulation for multi‑level prediction models," *Quarterly Journal of the Royal Meteorological Society,* vol. 102, no. 432, pp. 405-418, 1976.

[14] F. Molteni, R. Buizza, T. N. Palmer, and T. Petroliagis, "The ECMWF ensemble prediction system: Methodology and validation," *Quarterly journal of the royal meteorological society,* vol. 122, no. 529, pp. 73-119, 1996.

[15] S. Malardel and N. P. Wedi, "How does subgrid‑scale parametrization influence nonlinear spectral energy fluxes in global NWP models?," *Journal of Geophysical Research: Atmospheres,* vol. 121, no. 10, pp. 5395-5410, 2016.

[16] E. Hólm, R. Forbes, S. Lang, L. Magnusson, and S. Malardel, "New model cycle brings higher resolution," *ECMWF Newsletter,* vol. 147, pp. 14-19, 2016.

[17] V. Guidard and C. Fischer, "Introducing the coupling information in a limited‑area variational assimilation," *Quarterly Journal of the Royal Meteorological Society: A journal of the atmospheric sciences, applied meteorology and physical oceanography,* vol. 134, no. 632, pp. 723-735, 2008.

[18] N. Gustafsson and P. Dahlgren, "Assimilating host model information into a limited area model," 2012.

[19] L. Berre, "Estimation of synoptic and mesoscale forecast error covariances in a limited-area model," *Monthly weather review,* vol. 128, no. 3, pp. 644-667, 2000.

[20] G. H. Roe, "Orographic precipitation," *Annu. Rev. Earth Planet. Sci.,* vol. 33, pp. 645-671, 2005.

[21] M. W. Rotach and D. Zardi, "On the boundary‑layer structure over highly complex terrain: Key findings from MAP," *Quarterly Journal of the Royal Meteorological Society: A journal of the atmospheric sciences, applied meteorology and physical oceanography,* vol. 133, no. 625, pp. 937-948, 2007.

[22] M. W. Rotach, M. Andretta, P. Calanca, A. P. Weigel, and A. Weiss, "Boundary layer characteristics and turbulent exchange mechanisms in highly complex terrain," *Acta Geophysica,* vol. 56, pp. 194-219, 2008.

[23] M. A. Tolstykh, "The response of a variable resolution semi‑Lagrangian NWP model to changes in horizontal interpolation," *Quarterly Journal of the Royal Meteorological Society,* vol. 122, no. 531, pp. 765-778, 1996.

[24] F. X. Giraldo and T. E. Rosmond, "A scalable spectral element Eulerian atmospheric model (SEE-AM) for NWP: Dynamical core tests," *Monthly Weather Review,* vol. 132, no. 1, pp. 133-153, 2004.

[25] F. X. Giraldo and N. R. L. M. CA, "Advanced Numerical Methods for NWP Models," 2003.

[26] H. R. Pruppacher, J. D. Klett, and P. K. Wang, "Microphysics of clouds and precipitation," ed: Taylor & Francis, 1998.

[27] J. Pinty and P. Jabouille, "A mixed-phase cloud parameterization for use in mesoscale non-hydrostatic model: simulations of a squall line 590 and of orographic precipitations," in *Conf. on Cloud Physics*, 1998, pp. 217-220.

[28] B. C. Bernstein, T. A. Omeron, F. McDonough, and M. K. Politovich, "The Relationship between Aircraft Icing and Synoptic-Scale Weather Conditions," (in English), *Weather and Forecasting,* vol. 12, no. 4, pp. 742-762, 01 Dec. 1997 1997, doi: https://doi.org/10.1175/1520-0434(1997)012<0742:TRBAIA>2.0.CO;2.

[29] D. Baumgardner, H. Jonsson, W. Dawson, D. O'Connor, and R. Newton, "The cloud, aerosol and precipitation spectrometer: a new instrument for cloud investigations," *Atmospheric research,* vol. 59, pp. 251-264, 2001.

[30] B. J. K. Engdahl, T. Carlsen, M. Køltzow, and T. Storelvmo, "The ability of the ICE-T microphysics scheme in HARMONIE-AROME to predict aircraft icing," *Weather and Forecasting,* vol. 37, no. 2, pp. 205-217, 2022.

[31] M. Køltzow, M. Hallerstig, R. Graversen, M. Jonassen, and S. Mayer, "Verification metrics and diagnostics appropriate for the (maritime) Arctic," in "MET reports," 2020. [Online]. Available: https://www.met.no/publikasjoner/met-report/met-report-2020/_/attachment/download/71e9166b-8e61-4587-8029-53986486fc57:7f0848b8ce6c3f72fd1afc4fcda61b78902c9c2e/METNO-report02-2020-Alertness.pdf

Development of an Experimental Method for Wet Snow Accretion of a Model Conductor

Saki Taruishi[1], Hisato Matsumiya[1,2], Yuki Okazaki[1], Hiroki Matsushima[1], Teruo Aso[1], Mitsuharu Nomura[1]

[1] Central Research Institute of Electric Power Industry, Japan
[2] Kyoto University, Japan

taruishi@criepi.denken.or.jp, hisato-m@criepi.denken.or.jp, okazaki3940@criepi.denken.or.jp, m-hiroki@criepi.denken.or.jp,
ab-aso@criepi.denken.or.jp, nomuharu@criepi.denken.or.jp

Abstract— **This study developed an experimental method for snow accretion experiments on a model conductor to investigate the fundamental snow accretion characteristics of conductors** and **aerodynamic characteristics of snow-accreted conductors. An experiment on a model conductor with typical structural characteristics used in Japan was conducted to investigate the snow accretion phenomenon on conductors. Data on snow accretion amount, shape, angle, and height were collected using this method. The aerodynamic coefficients derived from the experiment were compared with the conventional values in Japan, which were obtained from wind tunnel tests of model conductors with model triangle snow accretions. The relationship between the observed aerodynamic coefficients and snow shape showed some similarity to conventional values. Further research should include experiments with various snow accretion characteristics and improvements in measurement accuracy.**

Keywords— **Snow accretion, Conductor, Experiment, Galloping**

I. INTRODUCTION

Galloping of transmission lines is a self-excited vibration caused by ice and snow accretion, as well as strong winds. Countermeasure devices are often installed on transmission lines to mitigate the risk of severe electrical accidents caused by galloping. Accurate estimation of the amplitudes of transmission line galloping is important for identifying which lines require galloping countermeasures. Numerical simulations, such as the finite element method or energy method, are widely used for the estimations. They require appropriate structural and aerodynamic force models to achieve accurate results.

Particularly, the characteristics of ice and snow accretion, including the amount, shape, angle, and height, have a significant impact on aerodynamic forces, and consequently, galloping amplitudes. However, due to various uncertainties surrounding the actual characteristics of ice and snow accretion on transmission lines, the aerodynamic coefficients used in these simulations often rely on wind tunnel tests of model conductors with artificial snow accretions.

For example, the authors and Japanese transmission system operators (TSO) have assumed that snow accretion on conductors forms a triangular shape, based on empirical knowledge obtained from field observations or patrolling of actual transmission lines. Fig. 1 shows a photograph of wet snow accretion [1]. The cross-section of snow accretion appears triangular in shape. Therefore, the authors measured the aerodynamic coefficients of model conductors with model triangular snow accretions (see Fig. 2) and have been applying these coefficients to their simulations, as reported in [2], and

Fig. 1 Example of photograph of wet snow accretion just before snow shedding.
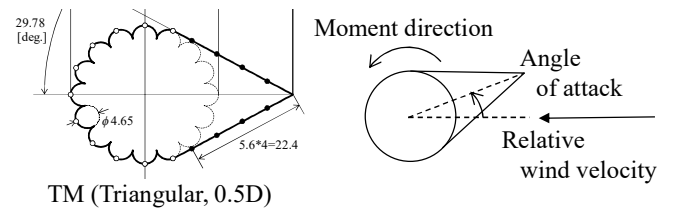
(a) Measurement model and definition of directions
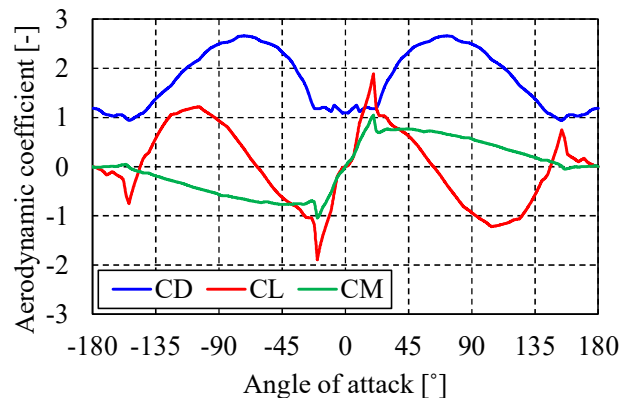
(b) Examples of measured aerodynamic coefficients

Fig. 2 Measurement of aerodynamic coefficients of a model conductor with model triangular snow accretion.

in various cases to date. In addition to the authors' findings, various field observations have shown shapes such as triangles, crescents, circles, and airfoil-like forms as examples of ice and snow accretion on transmission lines [3].

To improve the quantitative validity of the simulations, it is important to verify these empirical aerodynamic coefficients and apply more realistic values if needed. Therefore, it is crucial to clarify the fundamental characteristics of ice and snow accretion on conductors, as well as the aerodynamic characteristics of conductors with ice and snow.

Accordingly, this study aims to develop an experimental method for simulating snow accretion on a model conductor. First, a model conductor and measurement system for obtaining the shape of snow accretion and the loads acting on the snow-accreted conductor were developed. Next, fundamental snow accretion characteristics were measured using a snow accretion experiment. Finally, the aerodynamic coefficients calculated based on the experimental results were compared with those of conductors with model triangular snow accretions.

II. EXPERIMENTAL METHOD

A. Experimental Model

Figs. 3 and 4 show the schematics of the experimental model and photographs of the experimental model and measurement equipment, respectively. Table. I shows the properties of the model conductor.

The model conductor was set at a height of 300 mm from the floor via the support parts on both edges and the aluminum frame rack (see Fig. 4(a) and 5(a)). The model conductor was made from an aluminum shaft and the outermost layer of an actual ACSR240mm^2 conductor (ACSR: aluminum conductor steel reinforced). The support part consists of a load cell, angle indicator, strong and weak springs, stoppers, a rubber belt, and brackets to connect these parts (see Figs. 3(b), 4(b), and (c)).

The torsional stiffness of the model conductor is determined using springs and stoppers. The stoppers could be adjusted to angles ranging from 0 ° to 90 ° relative to the horizontal plane. The torsional stiffness is determined only by the strong spring when the stoppers are installed at a position of 0 ° because the rubber belt does not work. In this study, the springs were selected so that the torsional stiffness of the model conductor is 0.034 Nm/rad. This value is based on the mid-span value of a single ACSR240mm^2 conductor with a span of 300 m, equipped with counterweights that are frequently used as heavy snow countermeasure devices in Japan. This is one of the typical conditions applied in Japanese transmission lines.

The support part has a mechanism that allows the modelling of the case in which the torsional stiffness changes during snow accretion owing to the action of some countermeasure devices, although it was not applied in this study. By installing stoppers at a position greater than 0°, the torsional stiffness was determined by the connection spring of the two springs when the rotational angle of the model conductor was smaller than the installation angle of the stoppers. Once it exceeds the position of the stoppers, the torsional stiffness increases because only the strong springs work.

B. Experimental conditions

The snow accretion experiment was conducted at the Shinjo branch of the snow and ice research center of the national research institute for earth science and disaster prevention in Japan. The experimental methods employed for wet snow production and snow supply to the wind tunnels are based on methods applied in previous studies. They are as follows: [4].

First, artificial snow particles were created using a snowfall machine in a room with a temperature of -10 °C. Next, snow blocks were made from the artificial snow particles and placed overnight in a room at a temperature of 1.0 °C for moistening. The wet snow particles were then supplied to the model conductor set in the wind tunnel by shaving snow blocks at a constant speed, using wire meshes above the wind tunnel.

The experiment consisted of repetitions of a cycle, which involved a 4-min snow supply and 1-min interval. The snow supply at a wind speed of 5 m/s and snowfall density of approximately 50 mm/h lasts 4 min, followed by a 1-min interval without snowfall. During this interval, the wind speed gradually decreased to 0 m/s and remained at 0 m/s for approximately 20 s. Subsequently, the wind speed was gradually increased to 5 m/s. This 5-min cycle was repeated 23 times. Throughout the entire experiment, the temperature in the wind tunnel was maintained at 1.8 °C. Measurement items described in Section C are measured during the experiment.

(a)   Overview

(b)   Enlarged view of the support part
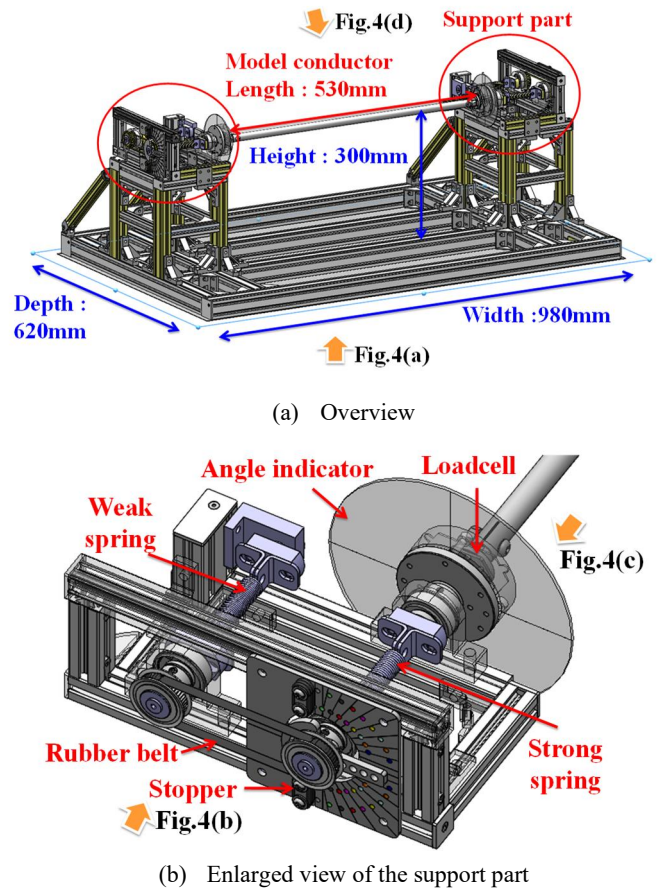
Fig. 3   Schematic of the experimental model.
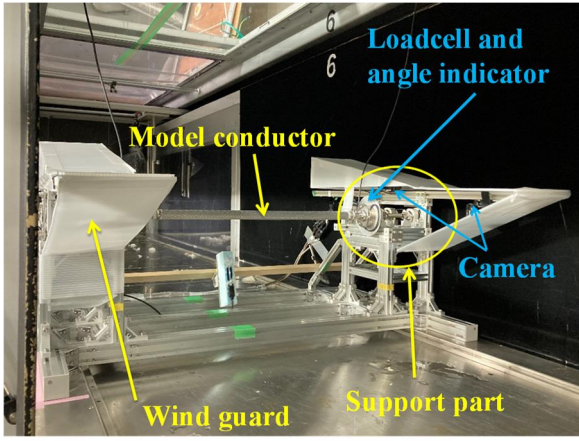
(a) Overview
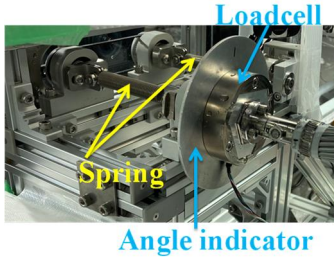
(b) Support part
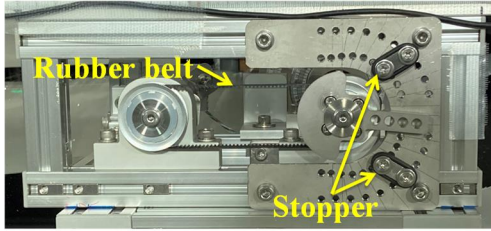
(c) Stopper
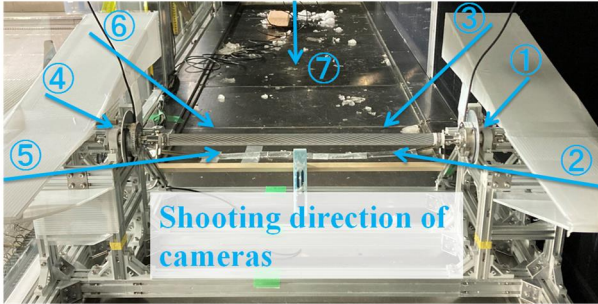
(d) Overhead view

Fig. 4 Photographs of the experimental model and measurement equipment.

TABLE I. Properties of the model conductor

Conductor type	ACSR240mm^2
Length	530 mm
Diameter	22.4 mm
Weight	0.76 kg
Torsional stiffness	0.034 Nm/rad
Stopper angle	0°
Spring material	Stainless steel

C. Measurement Method

Table II shows the list of measurement items. The loads in the three directions and moments around each axis were measured using load cells on both edges of the model conductor at a sampling rate of 1200 Hz during the experiment (see Fig. 4(b)). The rotation angles of the model conductor were measured using angle indicators and cameras 1 and 4 (see Fig. 4(b) and (d)). Fig. 5 shows examples of photographs captured by the cameras. Photographs of the model conductor were captured using the other cameras. The outline of the snow accretion on the model conductor was identified by the reflection of the laser light (see Fig. 4(d) and 5(b)), which was generated by sheet lasers installed on the windward and leeward sides of the model conductor.

Load cells with small rated values were chosen to precisely measure the loads generated by snow accretion, even if they are small. However, the load cells rotated together with the model conductor because their rated value was lower than the weight of the model conductor. Therefore, the vertical and horizontal forces acting on the model conductor must be derived from the 1-s average values of the measured loads, combined with the rotation angles obtained by reading the scale manually once every second (see Fig. 5(a)).

Table III shows the evaluation variables and items. These values were derived for each cycle. The amount of snow accretion in a certain cycle was calculated by averaging the vertical force over a 20-s no-wind period in that cycle. The snow accretion shape was derived by image analysis of photographs taken during the no-wind period. Consequently, the snow accretion angle was calculated from the snow accretion shape data. The drag and lift coefficients were calculated from the averaged horizontal and vertical forces over a 60 s data at the end of the snow supply period of the cycle. The additional rotation of the model conductor caused by the aerodynamic moment was considered in the calculation.

(a) Camera 4

(b) Camera 5

Fig. 5 Examples of photographs taken by cameras.

TABLE II. LIST OF MEASUREMENT ITEMS

Measurement item	Equipment	Measurement point
Load in three direction and moment around each axis	2 loadcells	Both edges of the model conductor
Rotational angle	2 cameras 2 angle indicators	Both edges of the model conductor
Photograph of the model conductor	5 cameras 2 sheet lasers	Centre of the model conductor

TABLE III. LIST OF EVALUATION VARIABLES AND ITEMS

Variable or item	Calculation method
Snow accretion amount	Averaging vertical forces during no-wind period
Snow accretion shape	Image analysis of photographs of the model conductor during no-wind period
Snow accretion angle	Calculate from the data of snow accretion shapes
Drag coefficient	Calculate from the average horizontal force during snow supply period
Lift coefficient	Calculate from the average vertical force during snow supply period

III. EXPERIMENTAL RESULTS

A. Fundamental snow accretion characteristics of model conductor

Figs. 6, 7, and 8 show the snow accretion amount, rotation angle, snow accretion shape, snow accretion angle, and height for each cycle. These results were obtained from data for the no-wind period. The missing values of cycle 8 in Fig. 6 were caused by the measurement error of Camera 4.

The rotation angle of the model conductor increased with increasing snow accretion. The amount of snow accretion increased rapidly from cycle 1 to cycle 4. The snow accretion shape is rounder than triangular at first and gradually become close to triangular shape. The snow accretion height increased to approximately 0.75D (where D is the diameter of the model conductor), and the snow accretion angle gradually decreased because of the increased snow accretion amount.

Subsequently, snow accretion characteristics showed only small changes from cycle 5 to cycle 11. The amount of snow accretion increased rapidly from cycle 12 to cycle 15. The snow accretion shape broadened primarily on the lower side of the accreted snow. The snow accretion height increased to 0.9D.

The snow accretion characteristics only exhibit small changes from cycle 16 to cycle 23, continuing until the end of the experiment. After 23 experimental cycles, the model conductor rotated only by approximately 10°. According to the snow accretion shapes, the tip of the snow accretion melts slightly because of the heat supplied by the wind. Consequently, the snow accretion height decreased to 0.8D.
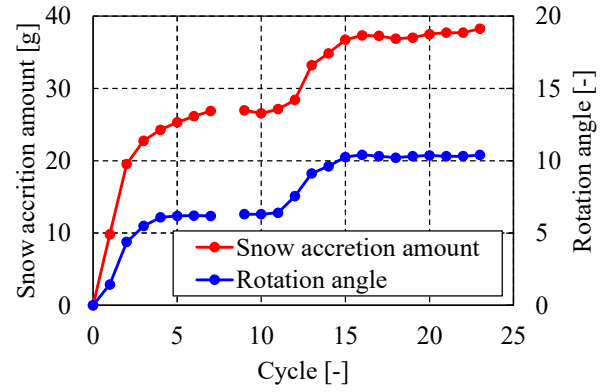
Fig. 6 Snow accretion amount and rotation angle of each cycle.
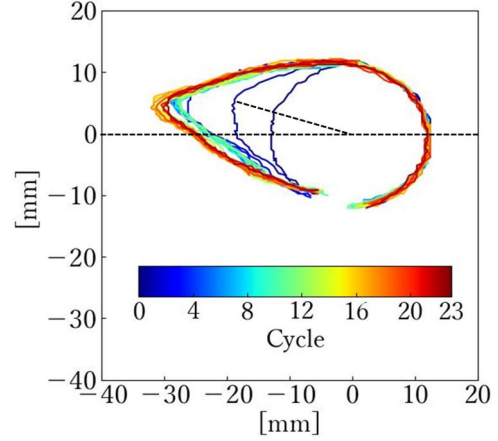
Fig. 7 Snow accretion shape of each cycle.
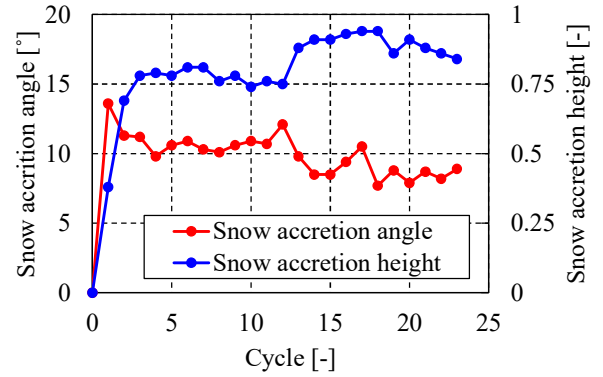
Fig. 8 Snow accretion angle and height of each cycle.

B. Comparison of aerodynamic coefficients with conventional values.

Fig. 9 shows a comparison between the experimental results and conventional aerodynamic coefficients. For example, "Triangle 1.0D" in the legend indicates the measurement results of the model conductor with a model triangular snow accretion, as reported in [2]. These are referred to as "conventional values" in the following part. Fig. 10 shows the relationship between snow accretion height and aerodynamic coefficients.

The angle of attack in this experiment was approximately 15° for all cycles. The drag coefficients varied from approximately 1.0 to 1.5. The conventional values,

approximately 1.2, are included in this range. The drag coefficient has only a weak correlation with the snow accretion height. Therefore, the drag coefficient might not have started to increase in this range of angles of attack, which corresponds to the tendency of the conventional values. The variation in the drag coefficients appears to be caused not only by the snow accretion characteristics but also by the measurement accuracy.

The lift coefficients varied from 0 to 1.0. They increased with the increasing snow accretion height, corresponding to the conventional values. However, the lift coefficient values were smaller than the conventional values. This may have been caused by the snow shape in the experiment, which was not completely triangular.

These results indicate that the snow accretion characteristics in the experiment were similar to those of the triangular snow accretion model to a certain extent. According to Fig. 2(b), the aerodynamic moment at an angle of attack of approximately 15° acts in the opposite direction to the moment generated by snow accretion. Therefore, the snow accretion characteristics in the experiment did not change for a long time because of the valence of snow accretion and aerodynamic moments. To investigate a wider angle of attack, other experiments should be conducted under conditions with fewer aerodynamic moments.
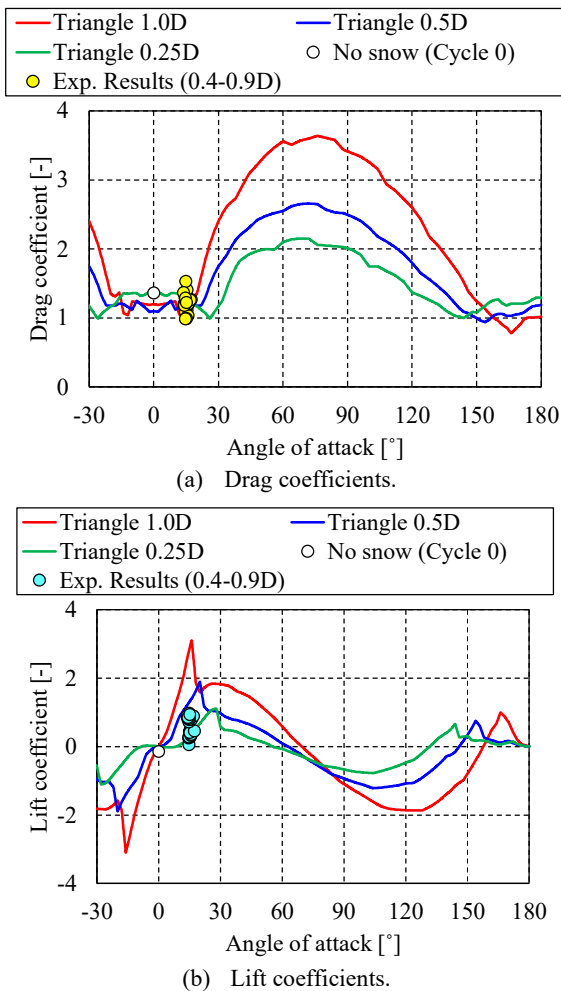
(a) Drag coefficients.

(b) Lift coefficients.

Fig. 9 Comparison of the experimental results and conventional aerodynamic coefficients.
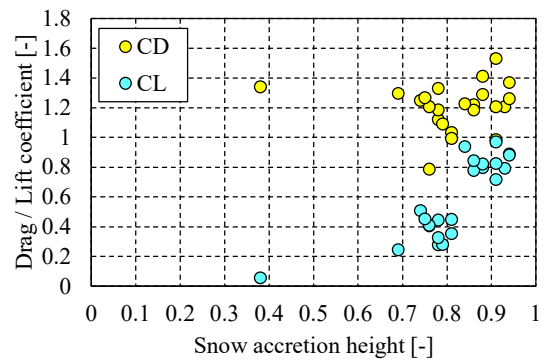
Fig. 10 Relationship between the snow accretion height and aerodynamic coefficients.

IV. CONCLUSIONS

An experimental method for snow accretion experiments using a model conductor was developed to investigate fundamental snow accretion characteristics such as the amount, shape, angle, and height of snow accretion. Additionally, the aerodynamic coefficients of the model conductor were derived from experimental results. They were compared with the conventional values obtained from wind tunnel tests of model conductors with model triangular snow accretions. The relationship between the aerodynamic coefficients and snow shape observed in the experiment corresponded to conventional values to a certain extent. For further investigation, additional experiments under conditions with a wider range of snow accretion characteristics and improved measurement accuracy are required.

REFERENCES

[1] H. Matsumiya, S. Taruishi, H. Matsushima and T. Aso, "Comparison of observed and simulated galloping responses of a four-bundled conductor under wet snow accretion," *Proceedings of the International Symposium of Dynamics and Aerodynamics of Cables*, pp. 85-98, 2023.

[2] H. Matsumiya, T. Nishihara, M. Shimizu, "Aerodynamic characteristics of ice and snow accreted conductors of overhead transmission lines," *Proceedings of the 13th International Conference on Wind Engineering*, 2011.

[3] CIGRE, "State of the art of conductor galloping," CIGRE Tech. Broc., No. 322, TF B2.11.O6., 2007.

[4] K. Yamamoto, H. Matsumiya, K. Sato, M. Nemoto, K. Togashi, H. Matsushima, T. Sumita and S. Sugimoto, "Evaluation for characteristics of wet snow accretion on transmission lines – Establishment of an experimental method using a vertical plate," *Cold Regions and Science Technology*, Volume 174, 103014, 2020.

DC Flashover Characteristics of Iced-covered Post Insulator in Cold Environment

Zhijin Zhang, Yuanpeng Zhang, Xingliang Jiang, Yutai Li, Guolin Yang

Xuefeng Mountain Energy Equipment Safety National Observation and Research Station, Chongqing University, Chongqing, China

zhangzhijing@cqu.edu.cn, 314957555@qq.com, xljiang@cqu.edu.cn, liyt@cqu.edu.cn, yanggl@cqu.edu.cn

Abstract— **Icing will lead to a significant decline in the insulation performance of post insulators, which seriously threatens the safe operation of power systems. At present, the research on the flashover characteristics of insulator icing is mainly based on artificial icing, which is quite different from natural icing. Therefore, this paper conducts an experimental study on the natural icing DC flashover characteristics of post insulators at the Xuefeng Mountain Energy Equipment Safety National Field Scientific Observation and Research Station of Chongqing University. The results show that the DC icing flashover voltage of the post insulator decreases with the increase of the salt density before icing and the deepening of the icing degree in a negative power exponential function. The range of the characteristic index a value of the pollution influence is 0.356 ~ 0.377, with an average value of 0.369. The range of the characteristic index c value of the influence of the ice thickness of the rotating conductor on the icing flashover voltage is 0.247 ~ 0.295, with an average value of 0.263. The DC icing flashover voltage U_{50} of the post insulator decreases in a negative power exponential function with the increase of the icing stress product (ISP), which is: $U_{50}=3005.5\ (ISP)^{-0.374}$.**

Keywords— *Post insulator, Natural icing, Direct current, Flashover characteristics, icing stress product.*

I. Introduction

Icing will lead to a significant decrease in the electrical performance of insulators, which will seriously endanger the safe operation of the power system [1-3]. In order to do a good job in the prevention of ice and snow disasters and reduce the huge losses caused by ice disasters, scholars in various countries have conducted a lot of research on the flashover characteristics of ice-covered insulators. The results show that the flashover voltage of insulators is significantly reduced when they are iced, and it is related to the degree of icing and pollution [4-5]. Among the icing types of insulators, it is divided into white frost, rime, mixed rime and glaze, among which the rime is the most harmful to the electrical performance of insulators. When the icicle bridging of insulator glaze icing reaches more than 2/3 of the insulator string, the external insulation characteristics decrease the most seriously, and the flashover voltage is also the lowest. The flashover voltage is also related to the icing water conductivity and string length of the insulator, and decreases with the increase of the icing water conductivity and the decrease of the string length [6-7]. The icing flashover voltage of the insulator is also related to its icing degree. When the icing degree of the insulator is deeper and the amount of icing is larger, the insulator is more likely to form a water flow channel during ice melting, resulting in a larger leakage current, so flashover accidents are more likely to occur [8-10].

Compared with the suspension insulator, the shed spacing of the station post insulator is shorter under the same voltage level, which is about half of the suspension insulator [11]. Therefore, under the same icing conditions, the shed of the station post insulator is easier to bridge, resulting in flashover accidents. Therefore, in moderate and severe icing areas, compared with the suspension insulators used in transmission lines, the phenomenon of icicle bridging of station post insulators is more common and faster, which leads to a significant decrease in the insulation level of post insulators, and the resulting insulation problems are more serious. At present, there are many researches on the icing flashover characteristics of suspension insulators for transmission lines at home and abroad. As an indispensable part of the power system, the research on the icing flashover characteristics of post insulators is also important. Most of the existing studies on the icing flashover characteristics of insulators are based on artificial icing, while there are few studies on the icing DC flashover characteristics of post insulators in natural environment.

Therefore, this paper takes the National Field Scientific Observation and Research Station of Xuefeng Mountain Energy Equipment Safety of Chongqing University as the test platform, and conducts experimental research on DC flashover characteristics of iced post insulators in natural environment. Finally, the natural icing DC flashover characteristics of post insulators are obtained, which provides a reference for the design and selection of external insulation of post insulators in converter stations and substations in icing areas, and has great practical engineering significance for ensuring the safe and reliable operation of power grids.

II. Test Equipment, Test Samples and Test Methods

A. Test Equipment and Test Samples

In this paper, the natural icing DC flashover test of post insulators is carried out by means of the National Field Scientific Observation and Research Station of Xuefeng Mountain Energy Equipment Safety of Chongqing University. The altitude of the test station is 1500 m, and the annual icing period can reach more than 10 times, which is concentrated from the end of November to the middle of February of the following year. The test station is located in a subtropical monsoon climate. It is cold in winter and has sufficient precipitation. The changing climatic conditions can form glaze, rime, mixed rime and other icing types. The six-element meteorological instrument equipped in the station can observe the changes of icing environmental conditions at any time. The ±800 kV DC power supply can provide sufficient test voltage for the DC icing flashover test of the post insulator.

The physical diagram of the post insulator used in this paper is shown in Fig.1. The structural parameters are shown in Table I, where H is the structural height; P is the extension of the shed; L is the creepage distance; S is the surface area.

Fig.1 Insulator physical diagram

TABLE I. INSULATOR PARAMETERS

H/mm	P/mm	L/mm	S/cm^2
1500	67/52	5027	24966

B. Test Methods

In this paper, before the test, the test insulator is washed and dried with water with low conductivity in the room, and then the insulator is polluted by the solid coating method. The salt density used in the test was 0.03,0.05,0.10,0.15 mg/cm^2, respectively, to simulate different degrees of contamination of insulators. The ratio of salt density to ash density in the test was 1:6, NaCl was used to simulate the soluble conductive substances in the contamination, and diatomite was used to simulate the insoluble substances. After the post insulator is smeared, wait for the environment to cool down. When the ambient temperature drops below 0 °C, the insulator is placed in an outdoor open place. In order to prevent the pollution loss of the subsequent post insulator during the icing process, this paper sprays low conductivity fog water on the surface of the insulator with a kettle before the icing of the insulator, until the surface is covered with a thin layer of ice to fix the pollution, and then wait for its natural icing. At the same time, a steel rotating conductor with a length of 500 mm, a diameter of 28 mm, and a uniform rotation speed of 1 r/min is placed next to the insulator, and the icing degree is measured by the icing thickness of the rotating conductor. Before the DC ice flashover test, the icing mass of the insulator is measured by the sensor, and then the ice melting water collector is placed at the bottom of the post insulator to collect the ice melting water during the pressurization process, and then the conductivity is measured and the temperature is recorded.

C. The Way of Applying Voltage and Data Processing

In this paper, the DC voltage applied in the test is negative, and the icing insulator is pressurized by uniform pressure method. In the process of pressurization, it is first pressurized to 75% of the expected flashover voltage U_y of the insulator, and then pressurized at a rate of $2\% U_y$ until the insulator is completely flashover. According to the above pressure method, more than 10 effective ice lightning voltages are obtained, and then the 50% ice lightning voltage U_{50} and relative standard deviation value σ are calculated according to formula (1) and formula (2).

$$U_{50} = \frac{\sum_{j=1}^{N} U_f(j)}{N} \tag{1}$$

$$\sigma = \sqrt{\frac{\sum_{j=1}^{N} \left[U_f(j) - U_{50} \right]^2}{N - 1}} \times \frac{100\%}{U_{50}} \tag{2}$$

In the above formula, U_{50} is the insulator 50 % icing flashover voltage, kV; $U_f(j)$ is the jth icing flashover voltage of insulator, kV; σ is the relative standard deviation of the test results, %.

III. DC FLASHOVER CHARACTERISTICS OF NATURAL ICING

In order to explore the natural icing DC flashover characteristics of the post insulator, the DC flashover test of the post insulator shown in Fig.1 is carried out according to the above test method. Because the glaze has the greatest damage to the external insulation strength of the insulator, this paper uses glaze icing to carry out DC flashover test. The test results are shown in Table 2, where SDD is the salt density of the insulator before icing, mg/cm^2; d is the icing thickness of rotating conductor, mm; W is the icing mass of insulator, kg; U_{50} is 50% flashover voltage of iced insulator, kV; σ is the relative standard deviation of DC flashover test results, %.

TABLE II. DC ICE FLASHOVER TEST RESULTS OF POST INSULATOR

SDD/mg/cm^2	d/mm	W/kg	U_{50}/kV	σ/%
0.03	3	2.65	246.3	5.4
	6	3.89	210.8	4.8
	9	5.22	186.5	5.8
0.05	3	2.77	216.8	3.4
	6	4.09	184.7	6.4
	9	5.18	163.1	1.8
0.10	3	2.48	166.9	4.2
	6	4.18	140.8	6.7
	9	5.33	125.2	2.6
0.15	3	2.41	135.2	3.3
	6	4.06	111.3	6.3
	9	5.16	97.3	6.9

A. The Effect of Salt Density Before Icing

The existing research shows that the relationship between the icing flashover voltage of the insulator and the salt density before icing can be expressed by formula (3) [12].

$$U_{50} = A_s \times (SDD)^{-a} \tag{3}$$

In formula (3), A_s is the coefficient related to insulator structure type, icing state and so on. And a is the characteristic index of the effect of SDD on 50 % DC flashover voltage of iced insulators.
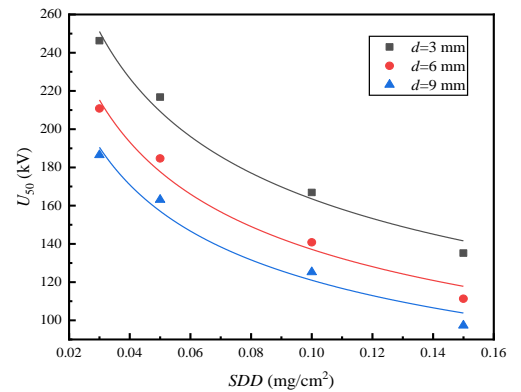
Fig. 2 Relationship between insulator icing flashover voltage U_{50} and SDD

TABLE III. FITTING PARAMETERS A_s, a, R^2

d/mm	Fitting Parameters		
	A_s	a	R^2
3	72.06	0.356	0.982
6	57.88	0.375	0.979
9	50.77	0.377	0.976

TABLE IV. FITTING PARAMETERS A_d, c, R^2

SDD/mg/cm²	Fitting Parameters		
	A_d	c	R^2
0.03	324.25	0.247	0.994
0.05	287.27	0.253	0.995
0.10	222.07	0.258	0.998
0.15	187.38	0.295	0.998

The test results in Table II are fitted according to formula (3), and the relationship between the DC icing flashover voltage of the post insulator and the salt density before icing can be obtained. The fitting results are shown in Fig.2 and Table III.

It can be seen from Fig.2 that under the same icing degree, the icing flashover voltage U_{50} of the insulator decreases with the increase of the salt density SDD in a negative power exponential function. Taking d=3 mm as an example, when the salt density of the insulator is 0.03, 0.05, 0.10 and 0.15 mg/cm², the icing flashover voltage is 246.3, 216.8, 166.9 and 135.2 kV, respectively. Compared with the salt density of 0.03 mg/cm², when the salt density is 0.05, 0.10 and 0.15 mg/cm², the icing flashover voltage of the insulator decreases by 12.0%, 32.2% and 45.1%, respectively.

From Table II, it can be seen that the coefficient A_s value related to insulator structure type and icing state decreases with the deepening of icing degree, ranging from 50.77 to 72.06; the value of the pollution influence characteristic index a does not change much with the deepening of the icing degree, ranging from 0.356 to 0.377, with an average of 0.369, indicating that the influence of pollution on the icing flashover voltage of the insulator under each icing degree is basically unchanged.

B. The Effect of Icing Degree

The existing research shows that the icing thickness of the rotating conductor can be used to measure the icing degree of the insulator. According to Reference [13], the relationship between the icing flashover voltage U_{50} of the insulator and the icing thickness d of the rotating conductor can be expressed by formula (4).

$$U_{50} = A_d \times d^{-c} \qquad (4)$$

In formula (4), A_d is the coefficient related to the insulator structure type and salt deposit density before icing; c is the characteristic index of the influence of ice thickness of rotating conductor on 50% DC flashover voltage.

Fig. 3 Relationship between U_{50} and d of insulator icing flashover voltage

The test results in Table II are fitted according to formula (4), and the relationship between the DC icing flashover voltage of the post insulator and the ice thickness of the rotating conductor can be obtained. The fitting results are shown in Figure 3 and Table IV.

It can be seen from Fig.3 that under the same salt density, the icing flashover voltage U_{50} of the insulator decreases with the increase of the ice thickness d of the rotating conductor in a negative power exponential function.

Taking the salt density of 0.05 mg/cm² as an example, when the icing thickness d of the rotating conductor is 3 mm, 6 mm and 9 mm, the icing flashover voltage of the insulator is 216.8 kV, 184.7 kV and 163.1 kV respectively, that is, compared with d of 3 mm, when d is 6 mm and 9 mm, the icing flashover voltage of the insulator decreases by 14.8% and 24.8% respectively.

It can be seen from Table IV that the coefficient A_d related to the insulator structure type and the salt density before icing decreases with the increase of salt density, ranging from 187.38 to 324.25. The characteristic index c value of the influence of the icing thickness of the rotating conductor on the icing flashover voltage does not change much with the increase of the salt density, ranging from 0.247 to 0.295, with an average value of 0.263, indicating that the influence of the icing thickness of the rotating conductor on the icing flashover voltage of the insulator is basically unchanged under various pollution levels.

C. The Effect of Icing Stress Product

It can be seen from the above analysis that the icing flashover voltage of the insulator will not only be affected by the degree of insulator contamination, but also by the amount of icing on the insulator. Under the combined action of the two, the external insulation performance of the insulator is greatly reduced, which seriously endangers the safe operation of the power system.

In order to reflect the influence of insulator pollution degree and icing amount on the electrical characteristics of insulators at the same time, scholars have obtained a parameter that can reflect the combined effect of the two and is suitable for engineering practice after a lot of experiments and research, that is, the icing stress product ISP [14].

The definition of the icing stress product ISP is the product of the icing mass w per unit arc distance and the icing water conductivity γ_{20} at 20 °C, that is, $ISP = \gamma_{20} \cdot w$. The dimensions of w, γ_{20} and ISP are g/cm, μS/cm and g·μS·cm⁻², respectively. The icing stress product ISP comprehensively characterizes the influence of the pollution degree of the insulator and the amount of icing on the icing flashover voltage of the insulator, which is conducive to the analysis of the flashover characteristics of the natural icing of the insulator. The test results of the icing stress product ISP and the icing flashover

voltage U_{50} of the post insulator in this paper are shown in Table V.

TABLE V. ICING FLASHOVER VOLTAGE U_{50} OF INSULATOR AND ISP

SDD/ mg/cm²	W/ kg	w/ g/cm	γ_{20}/ μS/cm	ISP/ g·μS·cm⁻²	U_{50}/ kV
	2.65	5.27	136	716.7	246.3
0.03	3.89	7.74	151	1168.7	210.8
	5.22	10.38	165	1712.7	186.5
	2.77	5.51	256	1410.6	216.8
0.05	4.09	8.14	262	2132.7	184.7
	5.18	10.30	249	2564.7	163.1
	2.48	4.93	448	2208.6	166.9
0.10	4.18	8.32	488	4060.2	140.8
	5.33	10.60	472	5003.2	125.2
	2.41	4.79	671	3214.1	135.2
0.15	4.06	8.08	697	5631.8	111.3
	5.16	10.26	746	7654.0	97.3

The existing research shows that the relationship between the icing flashover voltage U_{50} of insulators and ISP can be expressed by formula (5) [15].

$$U_{50} = A_{\mathrm{ISP}} \times (ISP)^{-p} \qquad (5)$$

In formula (5), A_{ISP} is the coefficient related to insulator structure type, material and so on. And p is the characteristic index of the influence of insulator pollution degree and icing amount on insulator icing flashover voltage.

The test results in Table V are fitted according to formula (5), and the relationship between the DC icing flashover voltage of the post insulator and the pollution ice parameters can be obtained. The fitting results are shown in Figure 4.
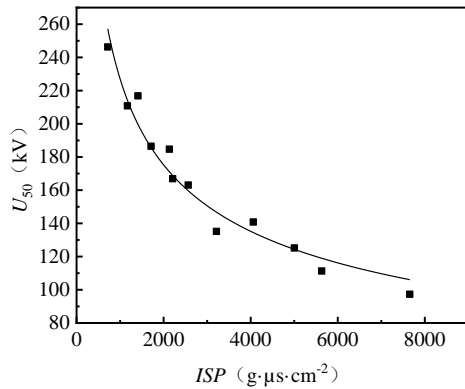
Fig. 4 Relationship between U_{50} and ISP

From Fig. 4, it can be seen that with the increase of the icing stress product ISP, the icing flashover voltage U_{50} of the post insulator gradually decreases. According to the fitting results of Fig.4, the specific relationship between the icing flashover voltage U_{50} of the insulator and the icing stress product ISP is shown in formula (6).

$$U_{50} = 3005.5(ISP)^{-0.374} \qquad (6)$$

From the formula (6), it can be seen that there is a good negative power exponential function relationship between the icing flashover voltage U_{50} of the post insulator and the icing stress product ISP, that is, the icing flashover voltage U_{50} of the insulator decreases with the increase of the icing stress product ISP in a negative power exponential function relationship.

For example, when the ISP is 716.7, 1712.7, 2564.7 and 5631.8 g·μS·cm⁻², the icing flashover voltage of the insulator is 246.3, 186.5, 163.1 and 111.3 kV, respectively. Compared with the ISP of 716.7 g·μS·cm⁻², when the ISP is 1712.7, 2564.7 and 5631.8 g·μS·cm⁻², the icing flashover voltage of the insulator decreases by 24.3%, 33.8% and 54.8%, respectively.

IV. CONCLUSIONS

In this paper, the DC flashover characteristics of natural icing on post insulators are studied. The effects of the degree of contamination before icing, the degree of icing and the icing stress product ISP on the icing flashover voltage of insulators are analyzed. The conclusions are as follows:

i. The DC icing flashover voltage U_{50} of the insulator decreases with the increase of the salt deposit density SDD before icing in a negative power exponential function, and the average value of the pollution influence characteristic index a is 0.369.

ii. The DC icing flashover voltage U_{50} of the insulator decreases in a negative power exponential function with the increase of the ice thickness d of the rotating conductor. The average value of the characteristic index c of the influence of the ice thickness of the rotating conductor on the icing flashover voltage is 0.263.

iii. The DC icing flashover voltage U_{50} of the insulator decreases in a negative power exponential function with the increase of the icing stress product ISP. The relationship is as follows: $U_{50}=3005.5(ISP)^{-0.374}$.

REFERENCES

[1] X. Jiang, S. Wang, Z. Zhang, S. Xie and Y. Wang, "Study on AC Flashover Performance and Discharge Process of Polluted and Iced IEC Standard Suspension Insulator String," *IEEE Transactions on Power Delivery*, vol. 22, no. 1, pp. 472-480, Jan. 2007.

[2] L. Chen, X. Shi, B. Peng and J. Sun, "Dynamic Simulation of Power Systems Considering Transmission Lines Icing and Insulators Flashover in Extreme Weather," *IEEE Access*, vol. 10, pp. 39656-39664, 2022.

[3] X. Jiang, S. Zhao, J. Hu, Z. Zhang and L. Shu, "Study of DC flashover performance of ice-covered insulators at high altitude," *IEEE Transactions on Dielectrics and Electrical Insulation*, vol. 20, no. 2, pp. 391-400, April 2013.

[4] H. Yang et al., "Characterization of pre-flashover behavior based on leakage current along suspension insulator strings covered with ice," *IEEE Transactions on Dielectrics and Electrical Insulation*, vol. 22, no. 2, pp. 941-950, April 2015.

[5] M. Farzaneh, J. Zhang and C. Volat, "Effect of insulator diameter on AC flashover voltage of an ice-covered insulator string," *IEEE Transactions on Dielectrics and Electrical Insulation*, vol. 13, no. 2, pp. 264-271, April 2006.

[6] X. Jiang, S. Zhao, J. Hu, Z. Zhang and L. Shu, "Study of DC flashover performance of ice-covered insulators at high altitude," *IEEE*

Transactions on Dielectrics and Electrical Insulation, vol. 20, no. 2, pp. 391-400, April 2013.

[7] P. Li, J. Fan, W. Li, Z. Su and J. Zhou, "Flashover Performance of HVDC Iced Insulator Strings," *IEEE Transactions on Dielectrics and Electrical Insulation*, vol. 14, no. 6, pp. 1334-1338, December 2007.

[8] L. C. Phan and H. Matsuo, "Minimum Flashover Voltage of Iced Insulators," *IEEE Transactions on Electrical Insulation*, vol. EI-18, no. 6, pp. 605-618, Dec. 1983.

[9] Y. Liu, M. Farzaneh and B. X. Du, "Nonlinear characteristics of leakage current for flashover monitoring of ice-covered suspension insulators," *IEEE Transactions on Dielectrics and Electrical Insulation*, vol. 23, no. 3, pp. 1242-1250, June 2016.

[10] Z. Li, Q. Zhang, F. Liu, H. Jia, L. Cheng and H. Xi, "Discharge Propagation Along the Air Gap on an Ice-Covered Insulator String," *IEEE Transactions on Plasma Science*, vol. 39, no. 11, pp. 2238-2239, Nov. 2011.

[11] M. Farzaneh et al., "Selection of station insulators with respect to ice and snow-part I: technical context and environmental exposure," *IEEE Transactions on Power Delivery*, vol. 20, no. 1, pp. 264-270, Jan. 2005.

[12] X. Jiang, L. Chen, Z. Zhang, C. Sun and J. Hu, "Equivalence of Influence of Pollution Simulating Methods on DC Flashover Stress of Ice-Covered Insulators," *IEEE Transactions on Power Delivery*, vol. 25, no. 4, pp. 2113-2120, Oct. 2010.

[13] J. Hu, C. Sun, X. Jiang, Z. Zhang and L. Shu, "Flashover Performance of Pre-contaminated and Ice-covered Composite Insulators to be Used in 1000 kV UHV AC Transmission Lines," *IEEE Transactions on Dielectrics and Electrical Insulation*, vol. 14, no. 6, pp. 1347-1356, December 2007.

[14] M. Farzaneh, "Insulator flashover under icing conditions," *IEEE Transactions on Dielectrics and Electrical Insulation*, vol. 21, no. 5, pp. 1997-2011, Oct. 2014.

[15] S. Taheri, M. Farzaneh and I. Fofana, "Empirical flashover model of EHV post insulators based on ISP parameter in cold environments," *IEEE Transactions on Dielectrics and Electrical Insulation*, vol. 23, no. 1, pp. 403-409, February 2016.

An Investigation of Spray Icing by Urea-doped Water on a Flat Specimen in Laboratory Experiments

Toshihiro Ozeki[1], Takatoshi Matsuzawa[2], Yuka Nakamura[1], Satoru Adachi[3],

Taiki Tokudome[4], Hayato Arakawa[3], Akihisa Konno[4]

[1] Hokkaido University of Education Sapporo, Japan
[2] National Maritime Research Institute, Japan
[3] Snow and Ice Research Centre, National Institute of Earth Science and Disaster Resilience, Japan
[4] Kogakuin University, Japan

ozeki.toshihiro@s.hokkyodai.ac.jp, zawa@m.mpat.go.jp, d10203s1@stu.hokkyodai.ac.jp, stradc@bosai.go.jp,
taiki.tokudome@gmail.com, h.arak@bosai.go.jp, konno@researchers.jp

Abstract—**In this study, laboratory experiments on spray icing were carried out using simple-shaped test specimens that resembles a member of a ship's superstructure with the goal of predicting the amount of icing on individual vessels.**

The spray icing experiment was conducted in an ice tank. As the use of salt water was prohibited in the ship model ice tank, experiments on the spray icing were conducted by spraying approximately 20 ‰ urea-doped water to grow wet ice. The air temperature in the cold room was maintained at approximately –10 °C. The icing experiments were conducted with different combinations of specimen angle and spray particle size. The wind velocity near the center of the specimen was approximately 10 m/s. Each experiment was conducted for 30 minutes, and at the end of the test, the icing weight was measured every 20 cm width and 23 cm height. In the early stages of icing, due to the hydrophobic feature of marine paint, the pieces of the spray ice often exfoliated and slid down the surface as slush. Because the specimens were installed on the floor, debris was often deposited at the lower end. A comparison of the amount of ice per specimen area for each test showed that although a peak of icing was observed at the centerline of the spray, the amount of icing was higher at the downwind edge. On the other hand, a peak in the amount of spray impinging on the specimen was observed at the centerline of the spray. Therefore, it was found that the impinging spray water flowed downwind and froze.

Keywords— ***Spray icing, Urea-doped water, Marine icing, Low temperature laboratory experiment***

I. INTRODUCTION

In recent years, the summer sea ice extent in the Arctic Ocean has been decreasing year by year, and the use of Arctic shipping routes is expected to increase. The use of large vessels with low ice class will increase near future, and the estimation of ship icing is one of the most important factors for the operational safety of Arctic shipping routes.

Several researchers have simulated seawater spray icing growth. Reference [1] developed a theoretical model of salt entrapment in spray ice. He assumed an analogy with sponginess of freshwater ice in wet growth. Reference [2] reviewed computer simulations of marine ice accretion and discussed the U. S. Coast Guard's Cutter Midgett model and a three-dimensional time-dependent vessel-icing model. Reference [3] applied a time-dependence model, MARICE, to the prediction of marine icing. MARICE calculated the turbulent airflow, trajectories of the droplets around the complete geometry of the structure, and heat transfer from the structure. Reference [4] and [5] studied the water breakup

phenomena of wave impact sea spray and developed a three-dimensional model for calculating the movement of a cloud of wave-impact sea spray over a Medium-sized Fishing Vessel (MFV). The results of spray impingement on the front side of the superstructure showed that 70 % of the droplets are smaller than 2 mm and 30 % are between 2 and 4 mm.

Because the phenomenon of sea spray icing is complex and the growth of icing varies depending on the shape of the ship and its superstructure, the practical risk of icing has been evaluated based on a relatively simple empirical equation PR [6] as following,

$$PR = \frac{V_a(T_f - T_a)}{1 + 0.4(T_w - T_f)}, \qquad (1)$$

where PR is the predictor relating to icing rate, T_f is freezing point of seawater [°C], T_a is air temperature [°C], T_w is sea temperature [°C], V_a is wind speed [m s^{-1}]. The factor used to estimate the severity of potential spray icing is derived from a simplified heat balance of the icing surface, which do not consider the characteristics of individual ships or the availability of anti-icing measures.

Although the PR values are useful for evaluating the safety of icing during navigation, more information is needed to use them in ship design and operational planning.

In this study, laboratory experiments on spray icing were carried out using simple-shaped test specimens that resembles a member of a ship's superstructure with the goal of predicting
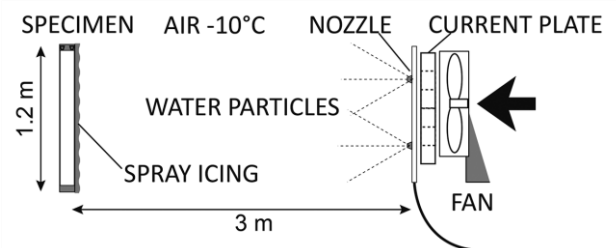
Fig. 1   A schematic view of experimental setting.

the amount of icing on individual vessels. The results for the flat-plate and cylindrical specimens are presented in this paper.

II. METHOD OF LABORATORY EXPERIMENTS

A. Equipment for spray icing experiments

The experimental apparatus (Fig. 1) was set up on an ice tank (20 m in length × 6 m in width × 1.8 m in depth) at the Technical Research Center of Japan Marine United Inc. The use of salt water is not permitted in this facility. The model ice for the ice tank test is made with urea-doped water so that brine is contained inside the ice. Therefore, we studied the icing characteristics of urea-doped water droplet icing including brine using a simple-shaped specimen.

Two fan-shaped nozzles (VE115-31 or VE115-59, Ikeuchi) and four fan-shaped nozzles (VP115-04, Ikeuchi) were installed on both sides of the fan, so that the sprayed water droplets were supplied to the specimen by the wind. The room temperature in the cold room was controlled at -10 ℃, and urea water with a concentration of about 20 ‰ was sprayed to grow brine-containing ice on the specimen.

In this study, PVC cylindrical specimens were tested at different diameters of 520 mm, 165 mm or 60 mm and a height

Fig. 2 Cylindrical and flat-plate specimens. Diameters of cylindrical specimens are 520 mm, 165 mm, or 60 mm.
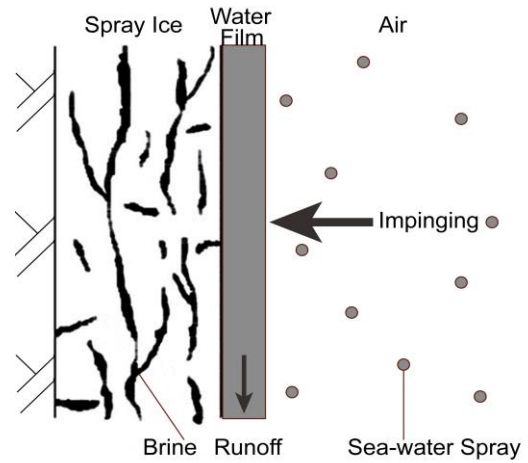
Fig. 3 A schematic vertical cross section of wet growth by sea-water spray.

of 1.2 m (Fig. 2). Experiments on flat plate (1000 mm in length × 918 mm in height) were carried out as well. The flat-plate specimen, painted with blue marine paint, was fixed on a dolly facing the wind direction. Fig. 2 shows the 0 ° angle directly into the wind. Further experiments were conducted at angles of 15 °, 30 °, and 45 ° to the leeward side. The distribution of wind velocity and droplet impact around the specimen was measured separately prior to each icing experiment. Spray particle counter (SPC-S7, Niigata Denki) was used to measure the particle size distribution of the droplets.

B. Visualization of brine structure in urea-doped spray ice using X-ray CT and MRI

Recently, X-ray computerized tomography (CT) has been used to measure the three-dimensional distribution of brine inside the sea ice nondestructively (e.g. [7], [8]). Nuclear magnetic resonance (NMR) is compatible with brine and has been applied to the measurement of sea ice [9]. In addition, magnetic resonance imaging (MRI) can acquire contrasting images in brine and ice mixtures (e.g. [10]-[12]). Reference [13] measured the three-dimensional microstructure of sea-water spray ice using the MRI technique and confirmed the presence of such a channelized network of brine in natural sea-water spray ice samples (Fig. 3). In this study, X-ray CT and MRI system set up in a cold room was used to visualize the brine in sodium chloride ice.

We used a μCT 35 system (SCANCO Medical) with a resolution of 1.75–72 μm for the X-ray CT. Meanwhile MRI was performed using a yokeless magnet with a field strength of 1.04 T [14]. A three-dimensional single spin-echo (3D-SE) sequence (image matrix = 256^3, voxel size = $(100 \ \mu m)^3$) was used for 3D high-resolution imaging. Each X-ray CT data and MRI data was analyzed using ImageJ that was an open source image processing software.

III. EXPERIMENTAL RESULTS

A. Observation of spray ice and brine distribution

The icing test on the cylindrical specimens was conducted eighteen times with different specimen diameters, wind speeds and spray particle sizes. The test conditions and test numbers for small particles (VE115-31) and very small particles (VP115-04) are given in Table 1. In this experiment,
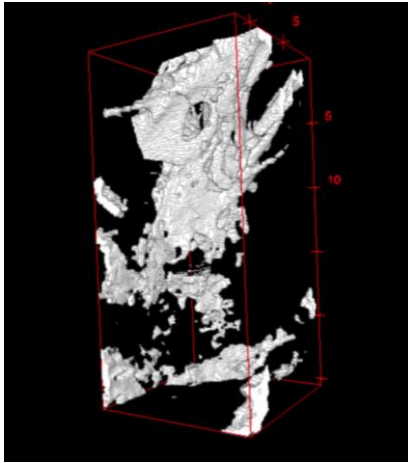
Fig. 4 Surface rendering of 3D X-ray image of brine distribution in spray ice created from 20‰ urea-doped spray water.

1 cm   -10 °C
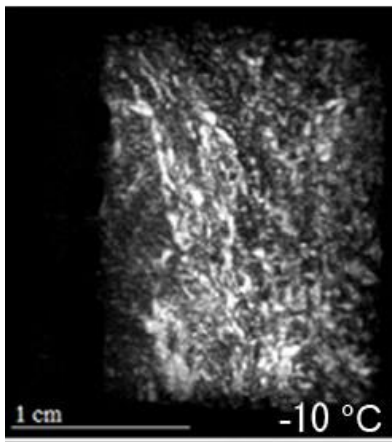
Fig. 5 3D MRI image of brine distribution in spray ice created from 30‰ sodium chloride spray water (MIP view).

the wind speed was about 10 m/s (high speed) or 7.5 m/s (middle speed) near the center of the specimen. The spraying was supplied continuously. The tests were conducted for 30 minutes each (20 minutes for #HS520 test), and the ice weight were measured at the end of each test at each one sixth height. The icing test on the flat plate specimen was conducted 9 times

TABLE I. SPECIMEN DIAMETER AND SPRAY PARTICLE DIAMETER (SMALL DROPLET AND VERY SMALL DROPLET)

Diameter	VE115-31		VP115-04	
[mm]	10 m/s	7.5 m/s	10 m/s	7.5 m/s
60	#HS60	#MS60	#HV60	#MV60
165	#HS165	#MS165	#HV165	#MV165
520	#HS520	#MS520	#HV520	#MV520

TABLE II. NOZZLE MODEL NUMBER FOR FLAT PLATE AND CORRESPONDING CYLINDRICAL SPECIMENS.

Diameter	VE115-31	VE115-59
[mm]	10 m/s	10 m/s
Flat plate	#HSFlat	#HLFlat
60	#HS60	#HL60
165	#HS165	#HL165
520	#HS520	#HL520

with small particles (VE115-31) and large particles (VE115-59) for 30 minutes each, and the wind speed was about 10 m/s near the center of the specimen. The ice weight was measured at the end of each test at each one forth height. The test conditions for the flat plate (0 °) and corresponding cylindrical specimens test numbers are given in Table 2.

Spray particles impinging on the cylinder formed a water film, and part of the water froze into spongy ice as it flowed down the PVC surface. In the early stage, part of the spray ice peeled off and slide down the surface as slush. The spray ice was spongy and had a milky white color. This is consistent with the characteristics of ice containing brine. Therefore, urea-doped spray ice was expected to contain a high amount of brine.

Fig. 4 shows a 3D X-ray image of brine network of spray ice created from 20‰ urea-doped water spray. We used surface rendering to visualize the brine pockets and channels. We have confirmed that the urea-doped spray ice contains a high amount of brine, the bright regions in the figure. A vertically converging drainage channel was observed in the brine distribution in the spray ice.

Fig. 5 shows 3D MRI image of brine distribution in spray ice created from 30‰ sodium chloride spray water [15]. Since the NMR signal from the ice was negligible as compared to that from the brine, the brine drainage channels appeared as bright regions. Fig. 3 is a picture visualized using the maximum intensity projection method (MIP view) from 3D MRI data. Brine drainage channels appear vertically in the sodium chloride spray ice. Structurally, urea-doped spray ice and sodium chloride spray ice were found to have very similar brine channels.

TABLE III. AMOUNT OF SPRAY WATER IMPINGING ON THE SPECIMEN AND AMOUNT OF ICING

Specimen	X: Spray Rate [kg m^{-2} min^{-1}]	Y: Ice Accretion [kg m^{-2} min^{-1}]	Y/X
#HS520	1.04	0.50	0.48
#MS520	0.64	0.31	0.48
#HV520	0.86	0.46	0.53
#MV520	0.85	0.39	0.46
#HS165	1.37	0.65	0.47
#MS165	1.01	0.57	0.56
#HV165	1.11	0.71	0.64
#MV165	1.18	0.58	0.49
#HS60	1.51	1.11	0.74
#MS60	1.16	1.09	0.94
#HV60	1.57	1.13	0.72
#MV60	no data	0.97	N/A

TABLE IV. SPRAY ICING RATIO (ICING/IMPINGING SPRAY WATER) ON THE FLAT PLATE SPECIMEN AND CYLINDRICAL SPECIMENS. WIND SPEED 10 M/S IN CENTER OF SPECIMENS.

Diameter	VE115-31 Small particles	VE115-59 Large particles
Flat plate	0.34 (#HSFlat)	0.27 (#HLFlat)
60 mm Φ	0.74 (#HS60)	1.01 (#HL60)
165 mm Φ	0.47 (#HS165)	0.51 (#HL165)
520 mm Φ	0.48 (#HS520)	N/A (#HL520)

B. Spray icing ratio

Table 3 shows the amount of spray water impinging on the specimen per unit time and unit area (X), and the amount of icing per unit time and unit area (Y); the projected area of the side surface of the specimen was used to calculate per unit area. Since the wind speed, projected area, and droplet particle size of each test were different, a direct comparison of the above values does not reveal a relationship. Therefore, the spray icing ratio Y/X, which represents the freezing rate relative to the impinging urea-doped water, was calculated. In both experiments on cylindrical specimens with diameters of 165 mm Φ and 520 mm Φ, approximately half of the impinging spray was frozen under these conditions, and there was no significant difference in the amount of ice formed over the entire sample per unit area. On the other hand, in the cylindrical specimen with a diameter of 60 mm Φ, Y/X was clearly larger than 50%, and the small particle test at 7.5 m/s (#MS60) showed a high value of 94%.

Fig. 7 A measurement of the distribution of urea-doped spray water.

Fig. 8 Amount of spray water [g] divided 60 area.

Fig. 6 Spray icing ratio as a function or the cylindrical specimen diameter. The flat plate is shown as equivalent to 1000 mm [16].

Table 4 shows the spray icing ratio for the flat plate specimen. The spray icing ratio for cylindrical specimens under the same test conditions was shown in the table. The small particle nozzle VE115-31 and the larger particle nozzle VE115-59 were used, however the heavier particles fell before they reached the specimens, and SPC measurements showed little difference in the particle size distributions of the two nozzles. The flat plate tended to have lower icing ratio than the cylindrical specimens. Moreover, the distribution of spray icing was concentrated on the edges.

Fig. 6 shows the spray icing ratio as a function of cylindrical specimen diameter. The flat plate (0 °) does not correspond to a diameter, thus is plotted for a width of 1000 mm, which corresponds to the width of the flat plate. The spray icing ratio tended to decrease as the diameter increased. The coefficient of determination for the logarithmic approximation is 0.77, which is in good agreement [16].

C. Result of flat-plane specimen

Fig. 7 shows a measurement of the distribution of urea-doped spray water. An array of 5 columns (A to E in Fig. 7) and 12 rows was constructed using high absorbent polymer sheets and the weight of spray water impinging on each sheet

Fig. 9 An experiment of urea-doped spray icing.

Fig. 10 Amount of Icing [g] divided 20 area.

was measured. Fig. 8 shows an example of the distribution of the amount of spray water impinging on the specimen divided 60 area. Fig. 9 shows an experiment of urea-doped spray ice. Fig. 10 shows an example of the distribution of the amount of icing divided 20 area. Each experiment was conducted for 30 minutes, and at the end of the test, the icing weight was measured every 20 cm width and 23 cm height. In the early stages of icing, due to the hydrophobic feature of marine paint, the pieces of the spray ice often exfoliated and slid down the surface as slush. Because the specimens were installed on the floor, debris was often deposited at the lower end.

Fig. 11 shows the amount of spray that impinges the A to E columns per minute when a large-diameter nozzle was used. In this experiment, a full cone nozzle (JJXP 60, Ikeuchi) was used except at 45°. Each line in Fig. 11 indicates the angle of the specimen from the wind direction. The line of 0° resulted in large values in column B, the center of the spray, while columns D and E had less impinging spray because they were out of the fan width. In contrast, when the specimen was installed diagonally to the leeward side, the peak value decreased, and the number of particles impinging columns D and E increased. A similar trend was observed for impinging spray water with small particle nozzles, with a smaller difference in spray volume from columns A to E at 45° (Fig. 12). It is also characteristic that the amount of impinging spray at 15° was higher than that at 0°. On the other hand, the amount of icing was higher at column A (Figs. 13 and 14). This may be the result of film water flowing downwind and froze. The amount of ice accretion at 15° and 30° tended to be larger than that at 0°.

IV. DISCUSSION

A. Comparison of spray icing increasing rate

Reference [16] obtained the projection area of ice accretion from graphic data set of each experiment. To compare the growth rate of icing on each test, the cross-sectional area of ice accretion was calculated every 5 minutes and divided by the spray rate (kg m^{-2} min^{-1}) for each test was plotted in Fig. 15. In all times, the cross-section increased linearly with time. The increasing rate was greater for the 520 mm diameter cylinder and smaller for the 165 mm cylinder.

The increasing rate of the spray icing cross-sectional area was greater for the 520 mm Φ cylinder than for the 165mmΦ cylinder. On the other hand, the ratio of the amount of spray water impinging on the specimen (X) and the amount of spray icing (Y) was not significantly different between the spray icing ratio for 165 mmΦ and 520 mmΦ, with Y/X clearly larger for the 60 mmΦ cylinder. The difference between these two results is due to the difference in the horizontal cross-sectional shape of the spray icing.

B. Comparison of cross-sectional shapes of spray ice in cylindrical specimens with different diameters

Fig. 16 shows horizontal cross-sectional photographs of spray icing on 60 mm Φ, 165 mm Φ, and 520 mm Φ cylindrical specimens. The 520 mm Φ sample was thickest at
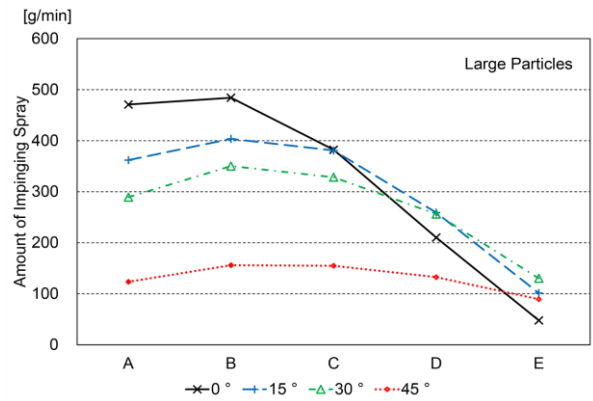
Fig. 11 Amount of spray water [g/min] on columns A to E using large diameter nozzle.
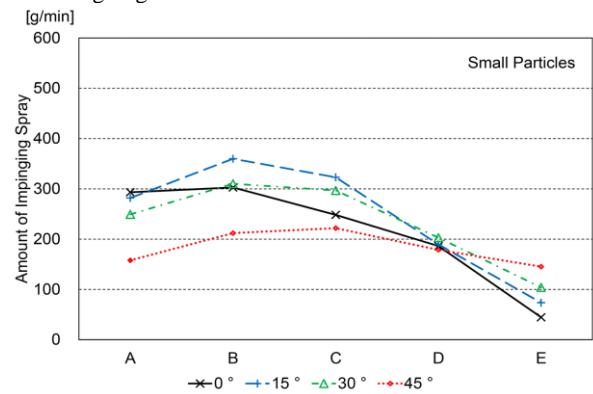
Fig. 12 Amount of spray water [g/min] on columns A to E using small diameter nozzles.
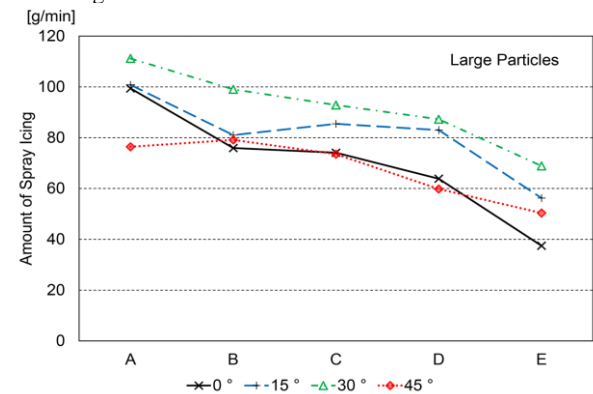
Fig. 13 Amount of spray icing [g/min] on columns A to E using large diameter nozzle.
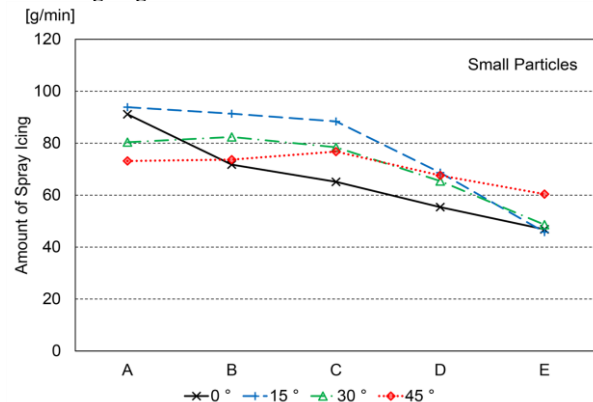
Fig. 14 Amount of spray icing [g/min] on columns A to E using small diameter nozzles.
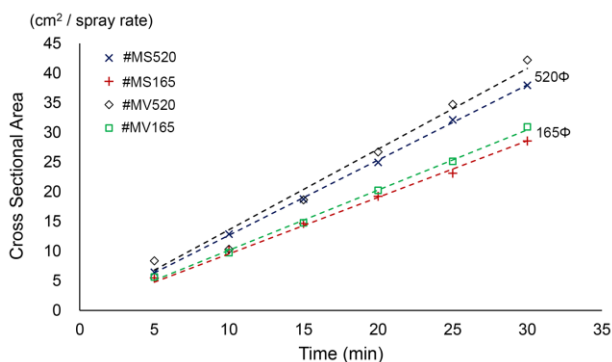
Fig. 15 Time series of cross-sectional area of ice accretion divided by the spray rate (kg m^{-2} min^{-1}) every 5 minutes [16].

the stagnation point on the windward front and became thinner toward the sides, while the 60 mm Φ sample had a shape where the edges protruded toward the sides. This is an expected result based on the trajectories of the streamlines and droplet particles. However, it is noteworthy that a change was observed between Φ165 mm and Φ60 mm. As a result, in the case of a thin cylinder, the icing grows significantly laterally, and its projected area become larger than the original projected area, which suggests that the amount of spray impinging the specimen was larger than the original.

V. CONCLUSIONS

Urea-doped spray icing experiment were conducted using a simple model of superstructure members. Spray icing experiments were conducted with different cylindrical specimen diameters, wind speeds and spray particle sizes. After each test, ice weight and salinity were measured at each one-sixth height. In all tests of 165 mm Φ and 520mm Φ in diameter, approximately half of the impinging spray has frozen. On the other hand, in the tests using 60 mm Φ cylindrical specimen, frozen ratio was clearly larger than 50%. This result suggests that the effect of diameter on the icing rate per impinging water varies between diameters of 60 mm Φ and 165 mm Φ. The amount of icing weight per unit time unit cross section increased with decreasing diameter. On the other hand, the graphical data analysis indicated the increasing rate in icing cross sectional area for cylinders with larger diameters was greater than for cylinders with smaller diameters. This result suggests that the horizontal cross-section of the icing

growing on the specimen deviates from an elliptical shape as the diameter decreases.

Spray icing experiments using flat-plane specimen were conducted with different setting angle from 0 ° to 45 ° to the leeward side. The flat-plate specimen was fixed on a dolly. A comparison of the amount of ice per specimen area for each test showed that although a peak of icing was observed at the centerline of the spray, the amount of icing was higher at the end of the flat plane specimen. On the other hand, a peak in the amount of spray impinging on the specimen was observed at the centerline of the spray. This tendency indicated that the impinging spray water flowed downwind and froze.

The experimental data will be useful for improving the PR equation by weighting the icing index according to the geometry of the object. Furthermore, as the development of icing is caused by the flight, collision, and freezing of wave spray particles, the icing index will be improved by estimating the trajectory of spray particles around the hull of a ship using CFD analysis.

REFERENCES

[1] L. Makkonen, "Salinity and growth rate of ice formed by sea spray," *Cold Reg. Sci. Tech.*, vol. 14, pp. 163–171, 1987.

[2] E.P. Lozowski, K. Szilder and L. Makkonen, "Computer simulation of marine ice accretion," *Phil. Trans. R. Soc. Lond.*, vol. A358, pp. 2811–2845, 2000.

[3] A. Kulyakhtin and A. Tsarau, "A time-dependent model of marine icing with application of computational fluid dynamics," *Cold Reg. Sci. Tech.*, vol. 104-105, pp. 33-44, 2014: doi.org/10.1016/j.coldregions.2014.05.001.

[4] S.R. Dehghani, Y.S. Muzychka and G.F. Naterer, "Water breakup phenomena in wave-impact sea spray on a vessel," *Ocean Eng*, vol. 134, pp. 50-61, 2017: doi.org/10.1016/j.oceaneng.2017.02.013.

[5] S.R. Dehghani, G.F. Naterer and Y.S. Muzychka, "3-D trajectory analysis of wave-impact sea spray over a marine vessel," *Cold Reg. Sci. Tech.*, vol. 146, pp. 72-80, 2018: doi.org/10.1016/j.coldregions.2017.11.016.
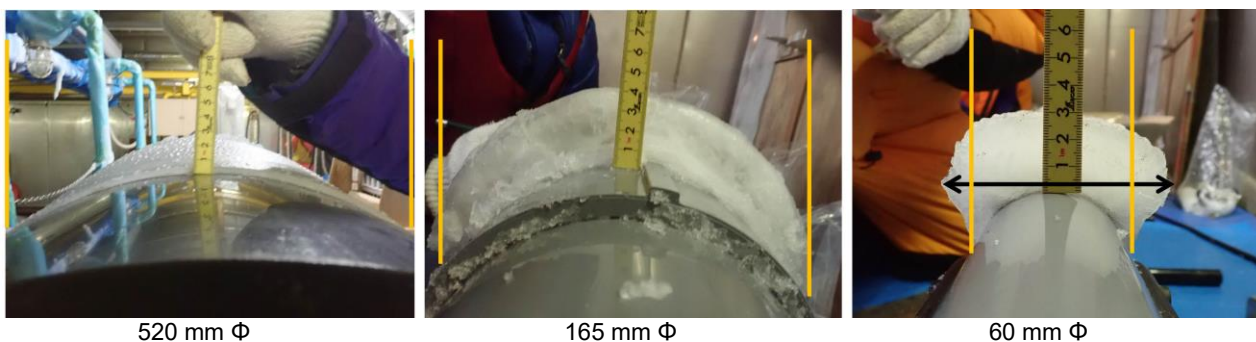
Fig. 16 Horizontal cross-sectional photographs of spray icing on 520 mm Φ, 165 mm Φ, and 60 mm Φ cylinders. The yellow reference line represents the icing contact point. The black double arrow line of 60 mm Φ represents the width of icing, which is larger than the diameter of the cylinder [16].

[6] J.E. Overland, "Prediction of Vessel Ising for Near-Freezing Sea Temperature," *Weather and Forecasting*, vol. 5, pp. 62-77, 1990.

[7] T. Kawamura, "Observations of the internal structure of sea ice by X ray computed tomography," *J. Geophys. Res.*, vol. 93(C3), pp. 2343–2350, 1988: doi:10.1029/jc093ic03p02343.

[8] R.W. Obbard, G. Troderman and I. Baker, "Imaging brine and air inclusions in sea ice using micro-X-ray computed tomography," *J. Glaciol.*, vol. 55, pp. 1113–1115: doi.org/10.3189/002214309790794814

[9] P.T. Calaghan, R. Dykstra, C.D. Eccles, T.G. Haskell and J.D. Seymour, "A nuclear magnetic resonance study of Antarctic sea ice brine diffusivity," *Cold Reg Sci Tech.*, vol. 29, pp. 153–171, 1999: doi.org/10.1016/S0165-232X(99)00024-5.

[10] W.A. Edelstein and E.M. Schulson, "NMR imaging of salt-water ice," *J. Glaciol.*, vol. 37, pp. 177–180, 1991: doi.org/10.3189/S0022143000042933.

[11] H. Eicken, C. Bock, R. Wittig, H. Miller and H.O. Poertner, "Magnetic resonance imaging of sea-ice pore fluids: methods and thermal evolution of pore microstructure," *Cold Reg. Sci. Technol.*, vol 31, pp. 207–225, 2000: doi.org/10.1016/S0165-232X(00)00016-1.

[12] M.I. Menzel, S. Han, S. Stapf and B. Blümich,"NMR characterization of the pore structure and anisotropic self-diffusion in salt water ice," *J. Magn. Reson.*, vol. 143, pp. 376–381, 2000: doi.org/10.1006/jmre.1999.1999.

[13] T. Ozeki, K. Kose, T. Haishi, S. Nakatsubo and Y. Matsuda, "Network images of drainage channels in sea spray icing by MR microscopy," *Mag. Res. Imag.*, vol. 23, pp. 333-335, 2005.

[14] S. Adachi, T. Ozeki, R. Shigeki, S. Handa, K. Kose, T. Haishi, M. Aoki, "Development of a compact magnetic resonance imaging system for a cold room," *Rev. Sci. Instrum.*, vol. 80, Article 054701: doi.org/10.1063/1.3129362.

[15] T. Ozeki, S. Adachi, T. Sakamoto and K. Kose, "Field observation of sea-spray icing in Hokkaido, Japan," in *Proc of Int. Symposium on Seasonal Snow and Ice*, Int. Glaciol. Society, 62A154, 2012.

[16] T. Ozeki, T. Matsuzawa, S. Nomura, S. Adachi, T. Tokudome, and A. Konno, "Laboratory experiments on spray icing with urea-doped water using flat and cylindrical specimens," *Okhotsk Sea and Polar Oceans Res.,* vol. 8, pp. 17-23, 2024.

Experimental study of superhydrophobic coating effects on dynamic ice accretion ice accretion process along S-1223 airfoil

Manaf Muhammed[1], Anvesh Dhulipalla[2], Harsha Sista[2], Kiran Digavalli[2], Muhammed Shakeel Virk[1], Hassan Abbas Khawaja[1], Hui Hu[2]

[1]Arctic Technology & Icing Research Group, UiT – The Arctic University of Norway, Narvik, 8514, Norway
[2] Dept. of Aerospace Engineering, Iowa State University, Ames, IA, USA

manaf.muhammed@uit.no, muhammad.s.virk@uit.no, hassan.a.khawaja@uit.no

Abstract— **Ice accretion on can be considered as a major threat for the operation of UAVs in the ice prone region, leading to loss of control and catastrophic failures. Active ice mitigation techniques are not suitable for UAV's due to availability of limited power. Superhydrophobic coatings can be considered as a promising passive ice mitigation technique for UAVs featuring exceptional capability to repel water, low power consumption, and lightweight properties. The effect of superhydrophobic coating on the ice accretion behaviour of a UAV wing with high lift airfoil S1223 is studied. High speed images of the ice accretion and force measurements were done to study the dynamic ice accretion process. For airfoils with high camber the application of superhydrophobic coatings can lead to rough ice structures close to the leading edge and can lead to more aerodynamic penalties.**

Keywords— *UAV, ice accretion, superhydrophobic coating, S-1223, icing wind tunnel.*

I. INTRODUCTION

This Atmospheric Icing can be considered as a significant threat on the performance of UAVs. Ice can accumulate on the body, wing and propeller of UAV [1]. Atmospheric icing occurs when super cooled water droplets impinge on the surface of the aircraft and then freezes. Ice accretion on the aircraft can alter its weight, which in turn changes center of gravity and thus causing a deterioration of the performance and stability of aircraft [2-4]. The ice mitigation methods can be classified in two categories: active and passive methods. When the active methods rely on an external system, passive methods take advantage of the physical properties of wing or/and propeller surfaces to eliminate or prevent ice formation and accretion without additional power input. Most of the active systems developed for icing mitigation are thermal systems that remove ice buildup by applying heat to wings. It should be noted that, this massive heating for operation would not be applicable to UAS due to the limited payload and excess power**.** In 2023 Müller developed an electro thermal ice protection system for UAV propeller and was tested at $-5^{o}C$ and $-15^{o}C$ icing condition. The amount of power required for anti-icing increased from 90 W to 200 W, when the temperature is lowered from $5^{o}C$ to $-15^{o}C$. Such high-power requirements can drain the battery in seconds and leading to the failure of mission. Therefore, passive methods are more appropriate for UAV deicing considering the power constrains. Superhydrophobic coatings can be considered as a promising passive ice mitigation technique for UAVs

featuring exceptional capability to repel water, low power consumption, and lightweight properties [5].

The self-cleaning property of the lotus leaf and duck feathers inspired the development of super hydrophobic coatings, on which water droplets bead up with a very large contact angle (i.e., > 150◦) and drip off rapidly when the surface is slightly inclined. These coatings reduce the ice adhesion strength on the surface and thus preventing the ice accumulation. The various methodologies adopted for the fabrication of superhydrophobic coatings are discussed in detail by Zhang et.al [6] and Chauhan [7]. Numerous studies related to different types of superhydrophobic coatings and the applicability of the same as an aircraft anti-icing material is done by Bhushan et al. [8-11]and Farzaneh et al. [12-17].

Wang in 2010 [18] studied the ice accretion on aluminum surface with super hydrophobic coatings by conducting experiments in a climatic chamber with a working temperature of $-6^{o}C$. The studies are done with a focus of anti-icing on transmission line, but the insights of such studies are useful in proposing ice mitigation techniques for UAVs. The experiments were conducted on 3 different aluminum surfaces: a hydrophilic surface, a hydrophobic surface and a superhydrophobic surface. During the initial spraying of super cooled water only few areas of the superhydrophobic sample were covered by water droplets, whereas the hydrophobic surface is partially, and hydrophilic surface is fully covered with water droplets. With increase in spraying time the water droplets transformed into ice and is observed that no new ice crystals appeared for the superhydrophobic surfaces with time, the ice start accumulating only on the surfaces initially covered by droplets. Ice started accumulating on more surfaces of hydrophobic surface with time and ice covers the entire hydrophilic surface within a comparatively shorter time.

The use of superhydrophobic coatings as an anti-icing technique for UAVs were also studied by few researchers. Liu in 2017 [19] conducted experimental investigations to understand the effect of surface wettability on the dynamic ice accretion over a UAV propeller. The experiments were conducted for glaze ice conditions at the Iowa State University Icing Research Tunnel (ISU-IRT) for a hydrophilic and superhydrophobic surfaces. The ice accretion on the superhydrophobic surfaces is observed to be much less than the same on hydrophilic surfaces, but still considerable icicle structures were observed along the leading edge of the superhydrophobic propeller. This can be attributed to the fact of low or no shear stress near the stagnation line and thus not

able to overcome the capillary forces. Further accumulation of ice occurs over the initial ice surface as it is no longer hydrophobic. It could be interesting to note the capability of superhydrophobic coating to prevent any ice accretion on the surface of propeller due to water runback. The performance degradation of propeller due to ice accretion is also measured during this study. The performance penalties were observed to be less for superhydrophobic surfaces, reduction of the thrust loss (~70% less) and a reduction in power consumption (~75% less) is observed.

Han [20] in 2022 conducted experimental studies on UAV propeller to compare the effectiveness of three different anti-icing coatings: superhydrophobic coating (SHS), Slippery Liquid-Infused Porous Surfaces coating (SLIPS) coating and Stress Localized anti-icing Coating (SLS). SLS and SLIPS attempt to diminish the ice's adhesion force; hence, the ice sheds more quickly. SHS prevents the droplet from adhering to the surface, causing it to fall away. The experimental results demonstrate that both low-adhesion coatings are significantly successful at preventing icing, while the superhydrophobic surface's anti-icing performance is quite subpar. The various challenges related to the durability of superhydrophobic coatings as an ice mitigation technique for UAV is discussed in [6].

The studies related to use of superhydrophobic coatings in UAVs were focused on the rotary wing UAVs. Ice mitigation in such cases happens mainly due to the repulsion of droplets from the surface due to centrifugal forces due to propeller rotation. In case of manned aircraft, the droplets are transported away from the surface by the action of shear force. In case of fixed wing UAVs, the centrifugal effects are absent, and the shear forces are smaller due to low operating velocities. Thus, it is interesting to study the capability of super hydrophobic coatings as an anti-icing technique for small and medium scaled fixed wing UAVs. Most high lift airfoils are characterized by high camber, such high cambers can affect the water transport behaviour on the airfoil surface. Thus, the study focuses on the effectiveness of superhydrophobic coatings as a anti icing technique for UAVs operating at low Reynolds number with highly cambered airfoils.

II. Experimental Methodology

This experimental study was performed in an Icing Research Tunnel available at Aerospace Engineering Department of Iowa State University (ISU-IRT). A schematic of the ISU-IRT icing tunnel is shown in Fig. 1. The ISU-IRT has a test section of 2.0 m in length $\times$ 0.4m in width $\times$ 0.4m in height with four optically transparent side walls. It has the capacity to generate a maximum wind speed of 60 m/s and an airflow temperature down to -25 ∘C. An array of 8 pneumatic atomizer/spray nozzles are installed at the entrance of the contraction section of ISU-IRT to inject micro-sized water droplets (10 ~100 μm in size), which can be sufficiently cooled down to the air temperature during the flight along with the airflow before impacting on the model. By manipulating the water flow rate through the spray nozzles, the liquid water content (LWC) in ISU-IRT could be adjusted in the range from LWC=0.1 g/m^3 to 5.0 1 g/m^3. In summary, ISU-IRT can be used to simulate atmospheric icing phenomena over a range of icing conditions (i.e., from dry rime to extremely wet glaze ice conditions). Further information about ISU-IRT is available in Waldman and Hu [21]. The operating conditions

for the experimental studies were selected according to the FAR 25 Appendix C icing envelope and it listed in *TABLE 1*.

The experiments were performed on a UAV wing with s1223 airfoil having a chord length of 20 cm and wingspan of 40 cm. Uncoated (clean) and coated models are tested in these experiments. The wing model is made of a hard plastic material (VeroWhitePlus, RGD835 by Stratasys, Inc.), and was manufactured using a rapid prototyping machine (3D printer). The surface of the wing model was coated with several layers of spray-on sandable primer. The primed surfaces were then wet-sanded using a series of progressively finer sandpapers (up to 2000 grit) to achieve a very smooth, glossy finish with a characteristic roughness over the propeller surface being about 25μm. Then, a readily available all-weather protective spray-on enamel (Rustoleum, Flat Protective Enamel, white) was coated onto the primed surface. The sanded primer layers would provide a strong adhesion of the enamel onto the propeller surface. Then the surface of the wing was treated with a spray-on superhydrophobic coating (Rust-Oleum™ NeverWet™).

III. Results and Discussion

The experiments were initially performed on the clean wing without any super hydrophobic coating at glaze ice conditions. The ice accretion process is captured using a high-speed camera as a function of time. The lift and drag forces were also measured as a function of time. The wing is coated with the superhydrophobic coating, and the icing tunnel experiments are performed for the same experimental conditions as of clean wings to understand the effect of super hydrophobic coatings on ice accretion.

document must be in Times New Roman. Type 3 fonts must not be used. Other font types may be used if needed for special purposes. The recommended font size are summarized in Table I.

A. High Speed Images

The high-speed images for ice accretion on a clean wing at different time instants is shown in Fig. 3. It can be observed from the images that the thickness of ice along the leading edge increases with time. It could be interesting to note that the extent of ice accretion on the wing surface remains same with time and no considerable runback is observed. As the time increases more droplets of water are impinging on the airfoil surface and ice keeps on accumulating on the top of already accumulated ice. Thus, the leading edge of the airfoil is contaminated with more rough ice structures with time. Fig. 4 shows the ice accretion on the wings coated with superhydrophobic coatings. The behaviour of ice formation with time is similar to what is observed for clean wings, but the extend of ice on the airfoil surface is considerably less in this case. The formation of ice is limited to areas very close to the leading edge and the runback is considerably reduced. Because the water droplets are not spreading on the wing surface, the droplets start freezing on the portion very close to leading edge and thus creating more rough structures close to the leading edge. The effect of this change in ice accumulation behaviour on the coated and non-coated models are reflected on the aerodynamic forces. The effect of ice accretion on the aerodynamic forces on the clean and coated models is

discussed below. Further a comparison is also made between
the variation of forces in the clean and coated cases.

TABLE 1. TEST MATRIX

No	Airfoil	T^{oC}_{∞}	LWC (g/m^3)	MVD (μm)	V_{∞} (m/s)	AOA	Time (S)	Ice Type
1	Clean S1223	-5	2	20	20	0	463	Glaze
2	Coated S1223	-5	2	20	20	0	463	Glaze
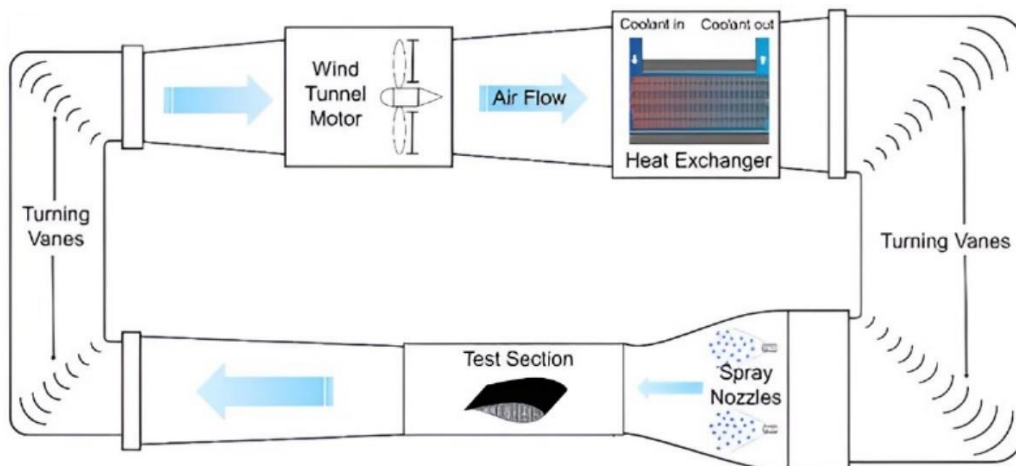
Fig. 1: Schematic of Icing Research Tunnel available at Aerospace Engineering Department of Iowa State University (ISU-IRT)
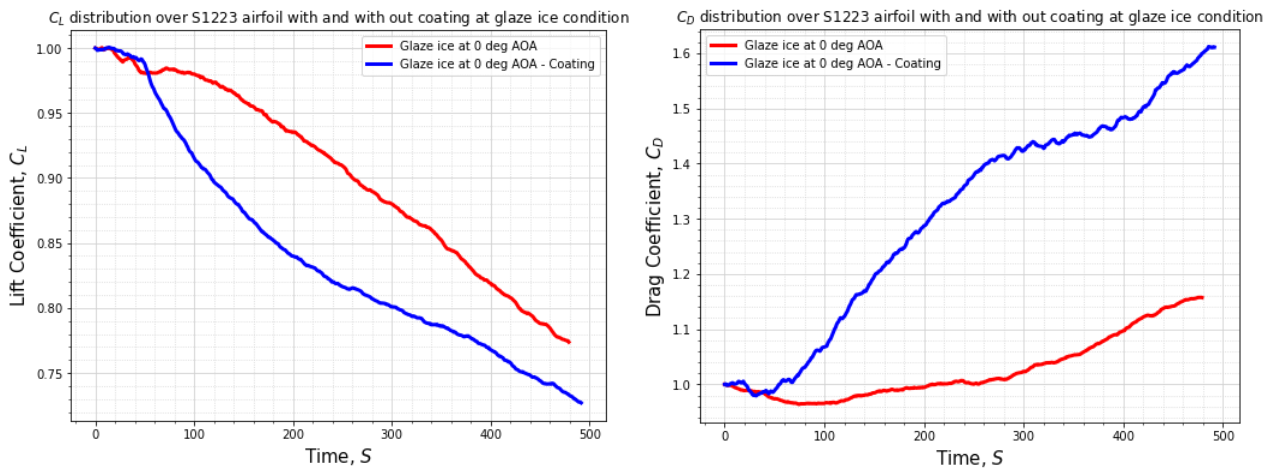
Fig. 2: C_L(left) and C_D (right) distribution over clean and coated S1223 airfoil wing at rime ice condition.

Fig. 3: Ice accretion on the surface of clean UAV wing at glaze ice condition (0,100,200,300,400,460 seconds).
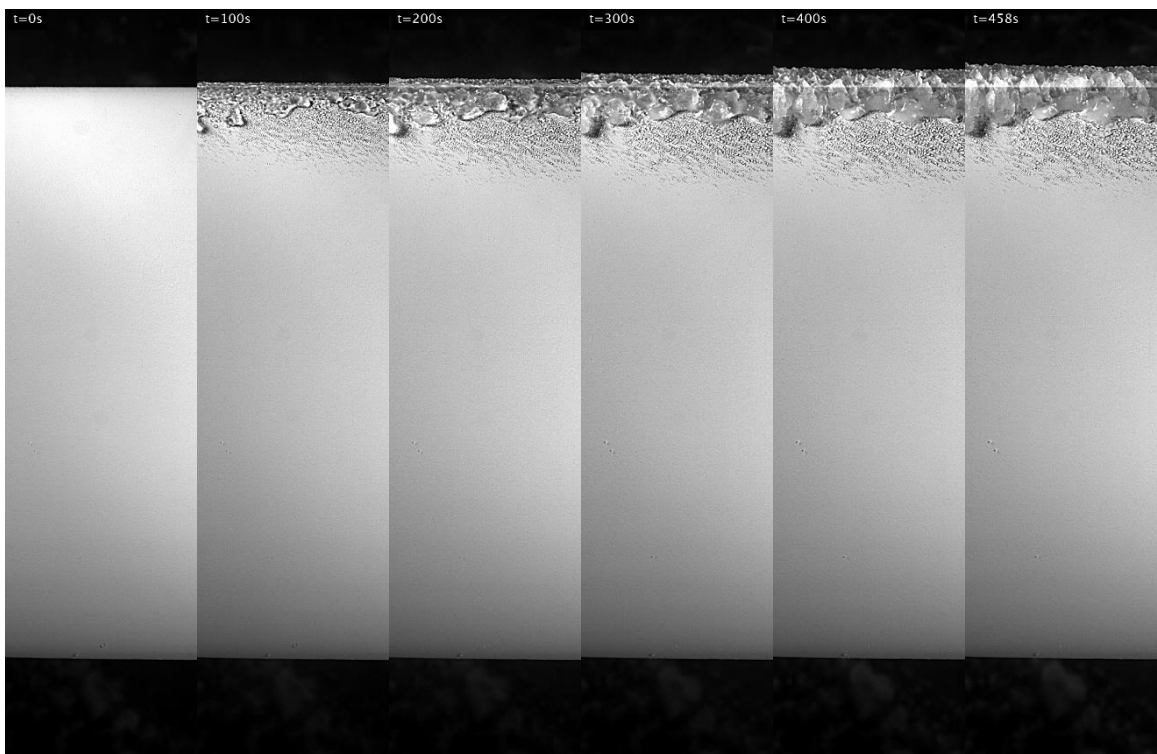
Fig. 4: Ice accretion on the surface of coated UAV wing at glaze ice condition (0,100,200,300,400,460 seconds).

B. Force Measurements/

Aerodynamic force measurements were made for both the coated and uncoated cases, the coefficient of lift (C_L) and coefficient of drag (C_D) are measured as a function of time. The coefficients are normalized by their value at no ice condition. For glaze ice condition, the lift decreases and drag increases with time for both the coated and uncoated cases as shown in Fig. 2. On comparing the lift coefficient of coated and uncoated case, it can be observed that the rate of decrease of lift is more for the coated case than the uncoated case. Also, the drag increases suddenly for the coated wing case as compared to the uncoated case. These observations are not expected as the purpose of applying superhydrophobic coating is to reduce the intensity of icing. But this can be explained with the help of high-speed images. It can be observed from the high-speed images that the accumulation of ice near the leading edge leads to the formation of large rough ice structures near the leading edge and this can lead to flow separation which can lead to increase in drag and decrease of lift.

IV. CONCLUSION

The influence of superhydrophobic coating on the ice accretion behaviour of a high camber UAV airfoil is studied. At glaze ice conditions the coated airfoils lead to agglomeration of water droplets near the leading edge of the airfoil and thus leading to the formation of rough ice structures close to the leading-edge area. Thus, the lift decreases and drag increases at a higher rate than the non-coated ones. Thus, for airfoils with high camber the application of superhydrophobic coatings can lead to rough ice structures close to the leading edge and can lead to more aerodynamic penalties at glaze ice conditions.

REFERENCES

[1] Hann, R., *Atmospheric Ice Accretions, Aerodynamic Icing Penalties, and Ice Protection Systems on Unmanned Aerial Vehicles.* PhD Thesis, Norwegian University of Science and Technology., 2020.

[2] Bragg, M.B., A.P. Broeren, and L.A. Blumenthal, *Iced-airfoil aerodynamics.* Progress in Aerospace Sciences, 2005. **41**(5): p. 323-362.

[3] Muhammed, M. and M.S. Virk, *Ice Accretion on Fixed-Wing Unmanned Aerial Vehicle—A Review Study.* Drones, 2022. **6**(4): p. 86.

[4] Muhammed, M. and M.S. Virk, *Ice Accretion on Rotary-Wing Unmanned Aerial Vehicles—A Review Study.* Aerospace, 2023. **10**(3): p. 261.

[5] Huang, X., et al., *A survey of icephobic coatings and their potential use in a hybrid coating/active ice protection system for aerospace applications.* Progress in Aerospace Sciences, 2019. **105**: p. 74-97.

[6] Zhang, Z., J. Ou, and W. Li, *Perspective Chapter: Challenges in the Durability of Superhydrophobic Coatings Pertinent to Unmanned Aerial Vehicle (UAV) Icing Mitigation.* Superhydrophobic Coating-Recent Advances in Theory and Applications, 2024.

[7] Chauhan, K.V., M.K. Desai, and A.C. Patel, *Recent progress in the development and anti-icing applications of superhydrophobic coatings.* Materials Today: Proceedings, 2022. **62**: p. 3922-3928.

[8] Bhushan, B. and Y. Chae Jung, *Wetting study of patterned surfaces for superhydrophobicity.* Ultramicroscopy, 2007. **107**(10-11): p. 1033-41.

[9] Michael, N. and B. Bhushan, *Hierarchical roughness makes superhydrophobic states stable.* Microelectronic Engineering, 2007. **84**(3): p. 382-386.

[10] Nosonovsky, M. and B. Bhushan, *Roughness-induced superhydrophobicity: a way to design non-adhesive surfaces.* Journal of Physics: Condensed Matter, 2008. **20**(22): p. 225009.

[11] Nosonovsky, M. and B. Bhushan, *Patterned Nonadhesive Surfaces: Superhydrophobicity and Wetting Regime Transitions.* Langmuir, 2008. **24**(4): p. 1525-1533.

[12] Farhadi, S., M. Farzaneh, and S.A. Kulinich, *Anti-icing performance of superhydrophobic surfaces.* Applied Surface Science, 2011. **257**(14): p. 6264-6269.

[13] Farzaneh, M., *Atmospheric Icing of Power Networks.* 2008: Springer, Dordrecht.

[14] Farzaneh, M. and C. Ryerson, *Anti-icing and deicing techniques.* Cold Regions Science and Technology, 2011. **65**: p. 1–4.

[15] Kulinich, S. and M. Farzaneh, *How Wetting Hysteresis Influences Ice Adhesion Strength on Superhydrophobic Surfaces.* Langmuir : the ACS journal of surfaces and colloids, 2009. **25**: p. 8854-6.

[16] Kulinich, S.A. and M. Farzaneh, *Ice adhesion on super-hydrophobic surfaces.* Applied Surface Science, 2009. **255**(18): p. 8153-8157.

[17] Kulinich, S.A. and M. Farzaneh, *Effect of contact angle hysteresis on water droplet evaporation from super-hydrophobic surfaces.* Applied Surface Science, 2009. **255**(7): p. 4056-4060.

[18] Wang, F., et al., *Ice accretion on superhydrophobic aluminum surfaces under low-temperature conditions.* Cold Regions Science and Technology, 2010. **62**: p. 29-33.

[19] Liu, Y., et al., *An experimental study of surface wettability effects on dynamic ice accretion process over an UAS propeller model.* Aerospace Science and Technology, 2018. **73**: p. 164-172.

[20] Han, N., H. Hu, and H. Hu. *An Experimental Investigation to Assess the Effectiveness of Various Anti-Icing Coatings for UAV Propeller Icing Mitigation.* in *AIAA AVIATION 2022 Forum.* 2022.

[21] Waldman, R.M. and H. Hu, *High-Speed Imaging to Quantify Transient Ice Accretion Process over an Airfoil.* Journal of Aircraft, 2016. **53**(2): p. 369-377.

A thorough understanding of the relationship between physiochemical properties of Ionic Liquids and anti-icing behaviour of coatings

Saba Goharshenas Moghadam[1], Gelareh Momen[1], Ehsan Bakhshandeh[1], Reza Jafari[1]

[1] *Department of Applied Sciences, University of Quebec in Chicoutimi (UQAC), 555, boul. de l'Université, Chicoutimi, Quebec G7H 2B1, Canada*
sgoharshen@etu.uqac.ca, Gelareh_Momen@uqac.ca, Ebakhshand@etu.uqac.ca, Reza_Jafari@uqac.ca

Abstract— **Formation of ice poses challenges to infrastructure and daily activities. Ionic liquids (ILs), characterized by low freezing temperatures, offer a unique avenue for dynamic melting at the interface. In meeting the growing need for long-lasting anti-icing solutions, ILs exhibit great promise by imparting dynamic properties to interfaces. Despite their potential, the investigation of anti-icing characteristics across different ILs remains limited, and the coating-oriented development of these materials is still in its emerging stages. Hence, this study explores the relationship between the anti-icing behaviour and physicochemical properties of two imidazolium-based ILs, incorporated into Sylgard 184 silicon elastomer coatings to provide insights for further advancements. Differential scanning calorimetry, centrifugal adhesion and push-off testing were employed to distinguish between the two ILs concerning, ice formation temperature and adhesion strength, respectively. The formation of a non-frozen interfacial quasi-liquid layer- (QLL) through ionic hydrogen bonds with water molecules contributed to the reduction in ice adhesion strength, as verified by Solid-state NMR spectroscopy. The study suggests that the anions of ILs play a minor yet distinct role in their icephobic properties. Evaluating the anti-icing performance of room temperature ionic liquids (RT-ILs) emphasizes the significance of considering various physicochemical characteristics such as solubility/miscibility in water, geometric structure, and mobility on effectiveness of ILs in subzero temperatures.**

Keywords— ***Ionic liquid, Icephobicity, Ice adhesion strength, Ionic hydrogen bonds, Quasi-liquid layer.***

I. INTRODUCTION

Icings are a common natural occurrence in cold climates, significantly impacting human activities and vulnerable infrastructure [1,2]. An alternative approach to replacing active systems involves developing ice-resistant coatings as a passive solution [3]. Over the decades, significant efforts have been devoted to developing and creating passive anti-icing surfaces, such as superhydrophobic surfaces (SHSs) and slippery liquid-infused porous surfaces (SLIPS) [4,5]. Despite notable advancements in ice-repellent surfaces and coatings, it remains essential to establish the underlying fundamentals that may be lacking. Presently, anti-icing surfaces are primarily constructed from a static perspective, achieved through modifications in surface chemistry and physics or adjustments in substrate properties. However, structures and properties at the ice-substrate interface are influenced by factors such as time, temperature, and external stimuli [6]. Furthermore, the limited durability of SHSs and SLIPS, has

constrained their practical applications in combating surface icing. Consequently, the inability to adapt to environmental fluctuations and susceptibility to damage has prompted researchers to concentrate on enabling dynamic alterations in the chemical and physical states of the ice–substrate interface to enhance anti-icing capabilities [7,8]. This significant transition from static to dynamic anti-icing surfaces has encouraged researchers to develop dynamic anti-icing surfaces by integrating innovative agents that facilitate dynamic interface melting, addressing challenges posed by harsh environmental conditions [6]. Introducing dynamic properties at the ice-substrate interface offers the opportunity to manipulate interface interactions and reduce ice adhesion strength. However, the development of an ideal anti-icing, anti-frosting coating still faces several challenges. ILs hold promise as potential candidates for inducing dynamic interface melting. ILs with exceptionally low freezing temperatures could initiate dynamic interface melting and form a thicker interfacial liquid layer [9,10].

The lack of extensive research on how various types of ILs and their physical and chemical characteristics affect their performance in sub-zero conditions, particularly in coatings, offers an intriguing opportunity for thorough exploration. This area holds significant promise for tailoring ILs to meet specific application requirements. In this study, we undertake an exploration of the effects of two distinct RT-ILs on ice nucleation and adhesion strength within coatings using Sylgard 184 silicone elastomer, a commonly employed industrial coating material. Our objective is to uncover a systematic understanding of how IL mobility and physicochemical properties influence their effectiveness in mitigating ice formation.

II. MATERIALS & METHODS

Sylgard 184 silicone served as the foundational material for the developed coatings, with both the base and curing agent sourced from Dow Corning. Two ILs were utilized in formulating the pair of IL-containing coatings. The first, 1-ethyl-3-methylimidazolium bis(trifluoromethanesulfonyl)imide (EMIM TFSI), with a melting point of -15 °C and designated as ILI, was procured from TCI America™. The second, 1-butyl-3-methylimidazolium tetrafluoroborate (BMIMBF4), with a melting point of -71 °C and identified as ILB, was obtained from Sigma-Aldrich (USA).

The IL-containing coatings were prepared by adding ILs (either ILI or ILB or both) to the base Sylgard 184 at weight

ratio of 1:10 (IL: Sylgard 184). In a clean beaker, the mixture was vigorously agitated for five minutes. The curing agent was then added (10%) and the full mixture was stirred for 10 min. The coatings were then applied on cleaned aluminium substrates using a film applicator. The IL-containing specimens were left for about 3 h at 120 °C. According to the type of ILs that were included, the samples were given labels. CILI, CILB and CILIB are PDMS-based coatings containing ILI, ILB and equal amount of both ILs, respectively.

A. Surface characterization

The distribution regularity of the ILs components, particularly F, S, and B on the surface of coatings were acquired by Scanning electron microscope (SEM) images (JSM-6480 LV SEM instrument manufactured by JEOL Japan) and Energy-dispersive X-ray (EDX) elemental mappings (e-beam voltage= 15 keV).

Surface roughness and the 3D profiles of the surfaces before and after 10 icing/de-icing cycles were examined using a confocal laser microscopy profiler (with magnification of 50x, Profil3D, Filmetrics, USA).

B. Icephobicity characterization

Using differential scanning calorimetry (DSC) with a TA instrument DSC 250 in the heating range of 40 ± 0.05 to -40 °C at a heating rate of 5 °C.min-1, the impact of ILs on the thermal behaviour and ice nucleation temperature of the coatings was investigated. A 5 mg deionized water droplet was deposited into a Tzero aluminium pan for each sample. It should be noted that before that the pans were each coated with a thin layer of the designed coating.

The ice adhesion strengths of the coatings were measured at -10°C using a push-off test. Deionized water was poured into a 1-cm-diameter cylindrical column and placed on the surface of the samples. The coatings were then left in a cold chamber overnight at -10.0 ± 0.2°C to completely freeze and form an ice cylinder. The working principle of the home-made push-off setup is illustrated in Fig. 1a. Samples were secured on the holder using vacuum, and the force meter probe moved towards the cylindrical column at a rate of 0.05 mm/s, applying force until the frozen cylinder detached from the sample surface. The ice adhesion strength was determined by dividing the maximum force during ice detachment by the cross-sectional area of the ice-surface interface. Additionally, the endurance of the surfaces through repeated icing/de-icing cycles was evaluated by conducting the push-off test 10 times.

For the ice centrifugal adhesion test, samples measuring 2.5 cm × 3.5 cm were prepared. These samples were coated with ice by spraying supercooled water microdroplets inside a climatic chamber set at a temperature of -8°C for approximately 35 minutes, simulating icing conditions akin to freezing drizzle, resulting in an ice accumulation of around 5.5 ± 0.5 g. The samples were then transferred to a cold room at a temperature of -10°C ± 0.2°C and securely installed at the end of a beam. They were subjected to controlled rotation at a specific frequency, as depicted in Fig. 2b. Subsequently, the adhesion strength was calculated by dividing the force applied by the area covered by the ice.
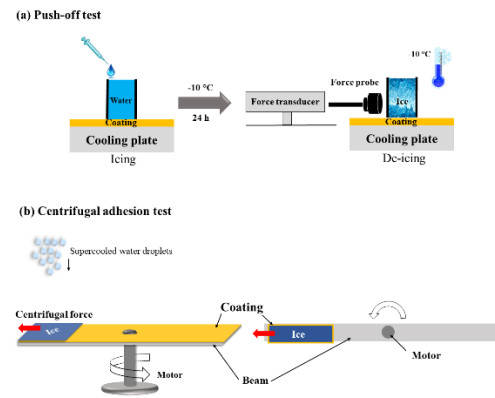
Fig. 1 Schematic of the designed (a) push-off and (b) centrifugal set up for measuring ice adhesion strength.

C. Solid-state NMR spectroscopy

In order to verify the presence of the nonfrozen quasi-liquid layer (QLL) existing at the interface between bulk water and coatings, both lacking and containing ILs, solid-state NMR spectroscopy was employed. All solid-state NMR (SS-NMR) experiments were firstly conducted at a temperature of 276 K using a 400 MHz wide-bore Bruker Avance III-HD spectrometer (Milton, Canada) operating at 400.03 MHz for 1H. Subsequently, the temperature was reduced to 268 K and maintained for a duration of 3 h before acquiring additional spectra. Sequentially, spectra were collected every 3 h, with a decrement of 5 K for each subsequent temperature point, until there was no longer any liquid water detectable by NMR. To enable quantitative analysis of the 1H signal in bulk water, the recycling delay was set to 5 s, ensuring complete signal relaxation. T2 measurements and 1H spectra were obtained using the Hahn echo experiment and subsequently processed using Bruker TopSpin software.

III. RESULTS & DISCUSSION

D. Surface topography

To further evaluate the presence of ILs components, either cation or anion, on the surfaces of coatings, SEM-EDX (elemental mapping mode for F, S, and B) was utilized. According to Fig.2a, b and c, peaks and maps of F, S components for the CILI coating and also elemental mapping of B (in the form of $B(OH)_3$, See Supporting information) for the CILB sample were further complemented the FTIR and XPS results on the surface chemistry [11]. The created heterogeneous surface allowed 3D profilometry to also shed light on the surface topography and structures. Fig.3 (a-d) illustrates various obtained surface structures due to incorporation of ILs. As demonstrated by 3D profile maps of samples containing ILs, either ILI or ILB and the reference PDMS, the surface roughness (Sq, root mean square roughness parameter) increased from 5.68 nm ± 1.36 for the Sylgard 184 to 29.27 nm ± 5.43, 82.65 ± 6.72 and 47.27 ± 4.33 for the samples CILI, CILB and CILIB, respectively. This difference likely stems from an immiscibility between ILs and PDMS at molecular scale and migration of ILs to the surface. However, this situation did not cause any significant phase separation. It is worth mentioning that more immiscibility of ILB in Sylgard 184 compared to ILI resulted in higher Sq.
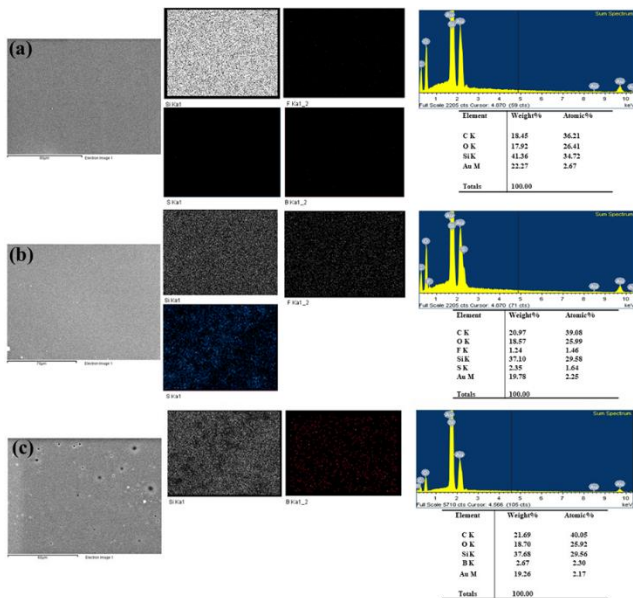
Fig. 2 The EDX mapping of the produced samples; (a) Sylgard 184, (b) CILI, and (c) CILB with the distribution of Si, F, S, and B elements over the surface.
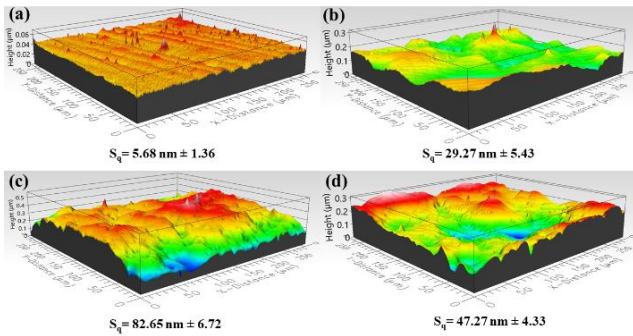
Fig. 3 The 3D profile and roughness value of the designed samples; (a) Sylgard 184, (b) CILI, (c) CILB, and (d) CILIB.

E. Ice formation temperature

We evaluated the influence of ILs on the ice nucleation temperature (INtemp, $\pm 0.05°C$) of coatings Utilizing DSC. As illustrated in Fig. 4a, a notable decrease in the average INtemp was observed, showing a significant drop from -15.8°C for Sylgard 184 to -21.8°C for CILIB. The reduced INtemp of IL-containing coatings stemmed from the diffusion of ILs into water molecules, thereby lowering the freezing temperature [9]. The geometric structure and steric configuration of ILs play pivotal roles in influencing the characteristics of hydrogen bonds, which may differ from conventional H-bonds. Consequently, the formation of ionic hydrogen bond networks between water and ILs constrains the mobility and rearrangement of water molecules.

Moreover, the creation of ice nuclei from bound water necessitates more energy compared to unbound water, thus introducing a higher energetic barrier for nucleation. Consequently, heterogeneous ice nucleation can be inhibited and initiated at lower temperatures [12]. Consequently, ILI in Sylgard 184 exhibited superior performance in depressing

INtemp due to the greater availability of sites on the surface of CILI for donating hydrogen bonds (Fig. 4b).
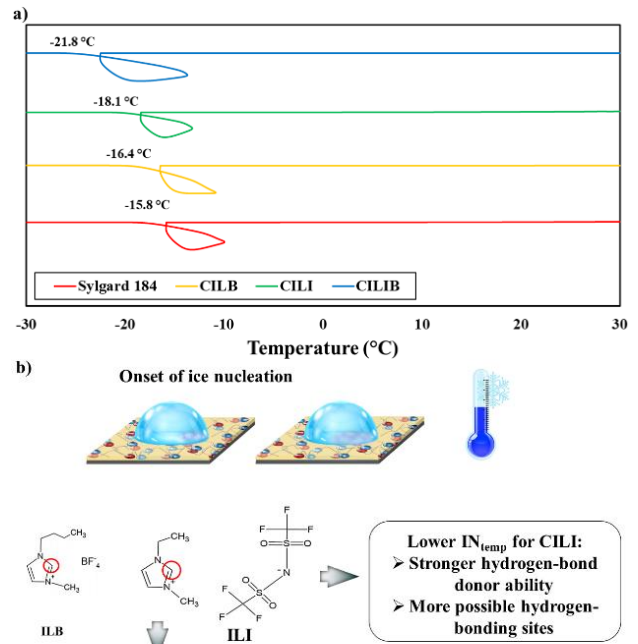
Fig. 4 a) Delayed ice nucleation of water and on the surface of PDMS-based coatings containing ILs, b) Schematic of the effective parameters of ILs structures on ice nucleation temperature.

F. Ice adhesion strength

In this investigation, we employed two distinct methods, the push-off and centrifugal adhesion test, specifically developed by our research team. Fig.5 illustrates the impact of ILs on the ice adhesion strength of PDMS-based coatings, demonstrating a significant reduction to values below 60 kPa compared to Sylgard 184. Specifically, the ice adhesion strength of IL-containing coatings measured through the push-off test was quantified at 58.3 kPa for CILI, 81.1 kPa for CILB, and 54 kPa for CILIB.

Moreover, ILs have the capability to diffuse into water droplets, resulting in lower freezing temperatures and an extended liquid state. Subsequently, the diffused ILs are expelled by the unfrozen liquid phase, creating an interfacial liquid layer enriched with ions [9]. Additionally, ionic hydrogen bonds between water molecules and ILs contribute to the formation of the QLL at the ice-surface interface.
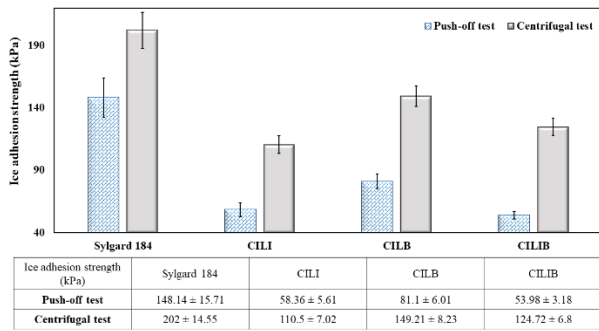
Fig. 5 Ice adhesion strength (kPa) of coatings, obtained using Push-off and Centrifugal tests.

Ice adhesion strength (kPa)	Sylgard 184	CILI	CILB	CILIB
Push-off test	148.14 ± 15.71	58.36 ± 5.61	81.1 ± 6.01	53.98 ± 3.18
Centrifugal test	202 ± 14.55	110.5 ± 7.02	149.21 ± 8.23	124.72 ± 6.8

G. Quasi liquid-like layer characterization

To confirm the presence of the non-frozen QLL at the interface between bulk water and coatings, particularly those containing ILs, solid-state NMR spectroscopy was employed.
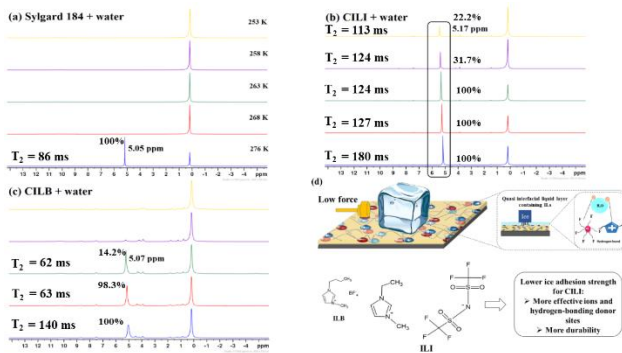
Fig. 6 ^{1}H spectra and T2 relaxation time of (a) Sylgard 184+water, (b) CILI+water, and (c) CILB+water between 276 K (blue) and 253 K (yellow), obtained by SS-NMR spectroscopy. (d) Schematic of lowering ice adhesion strength in presence of ILs through formation of QLL at interface.

Based on Fig. 6 (a-c), the 1H spectra of Sylgard 184 + water, CILI + water, and CILB + water samples were initially recorded at 276 K to assess the properties of bulk water before freezing onset. A notable observation is the increase in water 1H chemical shifts of the coatings as temperature decreases. This behaviour corresponds with previous studies on supercooled water, attributed to strengthened hydrogen bonds at lower temperatures, consequently impacting the shielding and deshielding of water protons [13].

This significant finding confirms the presence of nonfrozen water even at temperatures as low as -20 °C. This nonfrozen water layer acts as a self-lubricating interface, contributing to the low ice adhesion strength observed on IL-containing coating surfaces. It's noteworthy that as temperature drops below 0 °C, the signal intensity of nonfrozen water (indicating the amount of nonfrozen water) sharply decreases for Sylgard 184. Upon reaching a critical level of subcooling, the nonfrozen water may substantially decrease and eventually freeze completely, leading to a sudden and significant increase in ice adhesion strength on CILB.

However, the persistence of this signal for CILI at 253 K confirms the thicker QLL due to its stronger hydrogen-

bonding ability (Fig.6d) [14]. The rise in viscosity due to hydrogen bonding can be estimated by performing 1H T2 relaxation measurements, as the T2 relaxation time inversely correlates with viscosity. Intriguingly, the results obtained in Table 3 unveiled a greater hydrogen-bond accepting capacity of ILB towards locally bound water at the interface up to 263 K. Furthermore, alongside the persistence of the water 1H signal at 253 K, the decrease in T2 relaxation time for CILI further validated the stronger hydrogen-bond donor ability of ILI towards local interfacial water [15].

IV. CONCLUSION

Our research is centred on developing innovative coatings that integrate novel room temperature ILs renowned for their exceptional anti-icing properties. Employing analytical SEM/EDX analysis, we have validated the presence of these ILs on coating surfaces, facilitating the formation of ionic hydrogen bonds with water molecules. Our investigations have underscored the capacity of IL-containing coatings to reduce ice nucleation temperatures, as evidenced by DSC results. By either impeding ice nucleation or promoting ice melting, these coatings generate an unfrozen QLL at low temperatures. This liquid layer, confirmed by solid-state NMR spectroscopy, promotes interfacial slippage and diminishes ice adhesion strength, thereby enhancing anti-icing properties. Comparing the anti-icing behaviour of various room temperature ILs highlights the significance of considering their diverse physicochemical characteristics, including solubility/miscibility in water, geometric structure, and mobility, in subzero temperatures. Nevertheless, steric hindrance and intramolecular interactions influence IL mobility and the total number of effective ions within a matrix. Hence, the miscibility of ILs with the matrix should also be considered, as hydrophobic ILs may exhibit differing anti-icing behaviour in a hydrophilic matrix.

V. REFERENCES

[1] Z. Wang, Recent progress on ultrasonic de-icing technique used for wind power generation, high-voltage transmission line and aircraft, Energy Build. 140 (2017) 42–49.

[2] R. Carriveau, A. Edrisy, P. Cadieux, R. Mailloux, Ice adhesion issues in renewable energy infrastructure, J. *Adhes. Sci. Technol*. 26 (2012) 447–461.

[3] A. Azimi Yancheshme, G. Momen, R. Jafari Aminabadi, Mechanisms of ice formation and propagation on superhydrophobic surfaces: A review, *Adv. Colloid Interface Sci*. 279 (2020) 102155.

[4] A.M. Emelyanenko, L.B. Boinovich, A.A. Bezdomnikov, E. V. Chulkova, K.A. Emelyanenko, Reinforced Superhydrophobic Coating on Silicone Rubber for Longstanding Anti-Icing Performance in Severe Conditions, *ACS Appl. Mater. Interfaces*. 9 (2017) 24210–24219.

[5] C. Tao, X. Li, B. Liu, K. Zhang, Y. Zhao, K. Zhu, X. Yuan, Highly icephobic properties on slippery surfaces formed from polysiloxane and fluorinated POSS, *Prog. Org. Coatings*. 103 (2017) 48–59.

[6] F. Wang, Y. Zhuo, Z. He, S. Xiao, J. He, Z. Zhang, Dynamic Anti-Icing Surfaces (DAIS), *Adv. Sci*. 8 (2021) 1–26.

[7] S.A. Kulinich, S. Farhadi, K. Nose, X.W. Du, Superhydrophobic surfaces: Are they really ice-repellent?, *Langmuir*. 27 (2011) 25–29.

[8] J.S. Wexler, I. Jacobi, H.A. Stone, Shear-driven failure of liquid-infused surfaces, *Phys. Rev. Lett*. 114 (2015).

[9] Y. Zhuo, S. Xiao, V. Håkonsen, J. He, Z. Zhang, Anti-icing Ionogel Surfaces: Inhibiting Ice Nucleation, Growth, and Adhesion, *ACS Mater. Lett*. 2 (2020) 616–623.

[10] C. Austen Angell, Y. Ansari, Z. Zhao, Ionic Liquids: Past, present and future, *Faraday Discuss*. 154 (2012) 9–27.

[11] Y.H. Yeong, A. Milionis, E. Loth, J. Sokhey, Self-lubricating icephobic elastomer coating (SLIC) for ultralow ice adhesion with enhanced durability, *Cold Reg. Sci. Technol*. 148 (2018) 29–37.

[12] S. and J.W. KunDong, Understanding the Hydrogen Bonds in Ionic Liquids and their Roles in Properties and Reactions, *Chem. Commun*., 2016,52, 6744-6764. 52 (2016) 6744–6764.

[13] D. Chen, M.D. Gelenter, M. Hong, R.E. Cohen, G.H. McKinley, Icephobic surfaces induced by interfacial nonfrozen water, *ACS Appl. Mater. Interfaces*. 9 (2017) 4202–4214.

[14] D. MacFarlane, M. Kar, J. Pringle, Fundamentals of Ionic Liquids From Chemistry to Applications, First, *WILEY-VCH Verlag GmbH & Co. KGaA*, Weinheim, 2017.

[15] Li K, Xu S, Chen J, Zhang Q, Zhang Y, Cui D, Zhou X, Wang J, Song Y. Viscosity of interfacial water regulates ice nucleation. *Applied Physics Letters*. 2014 Mar 10;104(10).

Effect of frosting on ice-adhesion strength of anti-icing slippery surfaces

Huiying Xiang[1], Lijun Yang[1*], Xu Dai[1], Tao Zhu[1], Xujiang Hua[1], Yingying Zhao[1], Yuan Yuan[1],

[1]*Chongqing University, China*

20200901052@cqu.edu.cn, yljcqu@cqu.edu.cn, xudai@cqu.edu.cn, davezhu@cqu.edu.cn, 20230901040@stu.cqu.edu.cn,

20193002@cqu.edu.cn, yuany@cqu.edu.cn,

Abstract—**The icing of outdoor equipment, such as transmission lines and buildings, has brought huge economic losses and social impacts. Different anti-icing surfaces have been widely reported. Herein, the effect of frosting on the ice-adhesion strength of different anti-icing surfaces was studied. Micron-scale superhydrophobic (SHP), nano-scale SHP and slippery liquid infused porous surfaces (SLIPS) were prepared. The results show that the SLIPS has the lowest ice adhesion strength (4.2 kPa), which is 2% and 20% of those of the micron-scale SHP and nano-scale SHP, respectively. The ice-adhesion strength of micron-sized SHP and nano-sized SHP increases with the increase of frosting time, especially the micron-sized SHP increases faster. This is because the extension of frosting time increases the water vapor entering the structure and increases the interlocking. Surprisingly, the ice-adhesion strength of the SLIPS tends to decrease slowly with time. When the SLPS was frosted for 60 min, its ice-adhesion strength was 3.8 kPa. This is because the loose frost layer between the ice and the substrate reduces the adhesion of the ice. Therefore, SLIPS can maintain extremely low ice adhesion strength in frosting environment and has great potential application.**

Keywords— ***Ice adhesion strength, slippery surface, frosting***

I. INTRODUCTION

Water droplets will inevitably freeze on the surface of outdoor equipment, so de-icing is very necessary. Reducing the ice adhesion on the substrate surface is one of the most promising strategies for creating anti-icing surfaces. Ice adhesion strength is the most critical factor in evaluating surface ice adhesion. The anti-icing surface is divided into the following categories by ice adhesion strength : Low ice adhesion surface is usually defined as ice adhesion strength less than 60 kPa [1]. When the adhesion strength of ice is less than 20 kPa [2], it is defined as a surface with extremely low ice adhesion strength. The ice formed on the surface can fall off by natural vibration, its own weight or natural wind [3]. When the ice adhesion strength is less than 10 kPa, it is defined as an ultra-low ice adhesion surface [4], and the surface can realize the ice sample with a size of $1 \times 1 \times 1 \text{ m}^3$ falling through its own weight.

In the past few decades, research on low ice adhesion surfaces has been increasing. Among them, the slippery surface can achieve ultra-low ice adhesion strength. In 2014, the study [5] proved for the first time that the ice formed on the slippery surface can be blown away by the wind in a wind tunnel that controls the temperature and wind speed, and can maintain a low ice adhesion strength even when the temperature is reduced to -53 °C. Since then, many literatures have reported the low ice adhesion strength of slippery surface [6-8]. The ice adhesion strength of slippery surface is related to

the characteristics of matrix and lubricating oil. Kripa K. Varanasi et al. [9] reported that the ice adhesion strength of slippery surface with thermodynamic stability decreases with the increase of texture (micro-pillar) density. The frozen FIB / SEM imaging shows that the ice partially penetrates into the space between the columns, resulting in the column edge acting as a stress concentrator and a crack initiation site. The number of crack initiation points increases with the increase of texture density, thus reducing the ice adhesion strength. In addition, our previous work also confirmed that the slippery surface prepared by the matrix with pore structure showed a lower ice adhesion strength value than the matrix with pore structure [10]. Anti-icing super-lubrication surfaces are commonly used in frost or glaze icing environments. The humidity is often above 90%, which causes its anti-adhesion strength to be particularly heavy at low temperature and high humidity, which has not been studied.

In this study, the effect of frosting time on the ice adhesion strength of super-lubricated anti-icing surfaces was studied. Untreated Al and superhydrophobic surfaces were used for comparison. At the same time, the mechanism of low ice adhesion on the anti-icing surface was revealed from the perspective of intermolecular forces.

II. EXPERIMENT

A. Material

Oxalic acid ($H_2C_2O_4$), phosphoric acid (H_3PO_4), and anhydrous ethanol were purchased from Chuandong Chemical Co., Ltd, China. Aluminum plate (1061Al) was provided by Dongguan Chaomei Aluminum Products Co., Ltd. Dimethyl silicone oil (200 cSt) and Hexadecyltrimethoxysilane (OTS) were purchased from Aladdin Reagent Co., Ltd. Sodium hydroxide (NaOH) and ethylene glycol are provided by Chengdu Kelon Chemical Co., Ltd. Deionized water was used in the experiment.

B. Preparation

The preparation of super-lubrication samples includes pretreatment, anodization and post-treatment.

1) Pretreatment: The aluminum plate with a size of 20 mm × 25 mm × 1 mm was ultrasonically cleaned in ethanol and deionized water for 3 min, respectively. The cleaned plate was put into NaOH solution (1 mol / L) to remove the oxide layer on the surface.

2) Anodic Oxidation: The prepared sample was used as the anode and the stainless steel sheet was used as the cathode. The cathode and anode are connected to the DC power supply through a wire, and then placed in the electrolyte with a certain

oxidation current and oxidation time to prepare anodic aluminum oxide (AAO). The pore structure was prepared by two-step anodization. Firstly, the electrode was oxidized in $H_2C_2O_4$ electrolyte for 10 min, and the current density was 0.08 A / cm^2. Then it was further oxidized in 0.3 mol/L H_3PO_4 electrolyte for 10 min, and the current density was constant at 0.14 A/cm^2. 30 % ethylene glycol was added to the phosphoric acid solution, and the aluminum ion concentration was maintained at 712 mg/L. The prepared anodic aluminum oxide (AAO) was ultrasonically cleaned in ethanol for 5 min, and then dried in a drying oven at 75 °C.

3) *Post Treatment:* The surface of the treated sample was modified by OTS to improve the affinity of the lubricating oil to the surface. Specifically, the samples were immersed in 2 wt. % OTS solution for 30 min, and then taken out and dried in a drying oven at 110 °C for 60 min. By injecting lubricating oil into the modified sample to prepare SLIPSs, the penetration depth of the lubricating oil in the pore structure is controlled by the force balance between the capillary force and the pressure generated by the air trapped in the nanopore [11]. Therefore, vacuum impregnation is used to achieve as complete perfusion as possible [12, 13]. Specifically, the modified sample was placed in a vacuum container for 5 h to completely remove the air. The silicone oil was injected into the container through the inlet valve of the vacuum container and the sample was immersed for 12 hours. Silicone oil is slowly injected into the porous structure of the sample. Then, the sample is taken out of the vacuum chamber, and the atmospheric pressure further pushes the lubricating oil into the structure. Finally, SLIPSSs were successfully prepared by tilting the sample 90° to remove excess lubricating oil on the surface.

The untreated surface, etched surface, and AAO were used as contrast samples. The etched surface was prepared by placing the cleaned Al in a HCl solution (5 wt. %) for 5 min at room temperature. The etched surface and AAO were modified by OTS to obtain etched-SHP and AAO-SHP.

C. Characterization

The ice adhesion strength was measured by horizontal shear test. Specifically, the sample adheres to the cooling platform. A hollow cylindrical mold with an inner diameter of 14.2 mm was placed on the surface of the sample. Water (~1 mL) is added to the cylindrical mold to form ice (known as mold ice). Considering that the measured icing adhesion strength is affected by the test parameters (such as temperature, ice balance time, etc.), the air chamber temperature and relative humidity are maintained at − 15 ℃ and 40 %, respectively, and the freezing time of water is maintained at 30 min. After the ice is generated, the force sensor (Edberg, SH-100N, China) gently pushes the cylindrical mold until the mold is separated from the sample surface. The change of probe distance and probe impact velocity will affect the result of ice bonding strength. In this study, the loading rate and the distance between the probe and the sample surface were constant at 3 mm and 1 mm / s, respectively. The maximum force was recorded and the ice adhesion strength was calculated. Measure the sample three times to take the average.

III. RESULT AND DISCUSSION

A. Ice Adhesion Strength:

The ice adhesion strength of different types of aluminum surfaces is shown in Fig.1.The surface has frosted for 10 min during the cooling process. The hydrophilic untreated Al showed a great ice adhesion strength of 262.1 kPa. The ice adhesion strength of etched-SHP is 208.5 kPa, which is close to that of the untreated surface, indicating that the superhydrophobic surface with micron-scale structure fails to significantly reduce the ice adhesion strength. The AAO-SHP with nano-scale structure has a lower ice adhesion strength (22.0 kPa), but still exceeds the upper limit of very low ice adhesion strength (20 kPa). The ice adhesion strength of SLIPS is 4.2 kPa, which is about 1 % of that of untreated Al, indicating that it is easy to achieve automatic de-icing under wind or gravity, and is also significantly lower than the test values of anti-icing materials in most literatures.
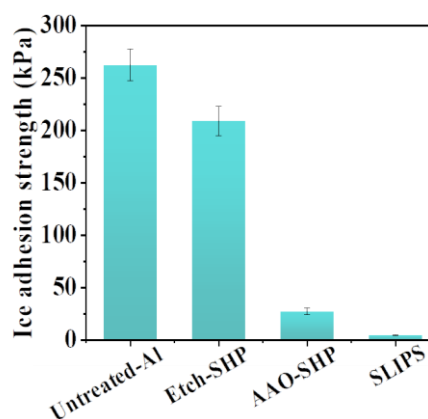
Fig. 1 Ice adhesion strength of different aluminum surfaces.

Frosting has a significant effect on the ice adhesion strength of the anti-icing surface[10, 14].Therefore, the ice adhesion strength after frosting is a key parameter to characterize the anti-icing performance of the surface. As shown in Figure 2, the ice adhesion strength of SHPs increases with the increase of frosting time, especially the etched-SHP value. When the frosting increased to 60 min, the ice adhesion strength of the etched-SHP increased from 107.5 kPa to 280.4 kPa, an increase of 1.6 times, and exceeded the untreated surface. Under high humidity environment, the micro-nano structure of the superhydrophobic surface is interlocked with ice, resulting in high ice adhesion strength. Moreover, the longer the frosting time is, the more serious the interlocking effect is. However, the ice adhesion strength of SLIPS did not change significantly, or even decreased slightly. It can be seen from the enlarged figure that the ice adhesion strength of SLIPS decreased from the initial 6.0 kPa to 4.2 kPa after 10 min of frosting, and then decreased slowly, which was due to the weaker adhesion between the loose frost layer and the oil film on the slippery surface. In the actual measurement, when the sample is cooled to the specified temperature and remains constant, it has been frosted for a period of time, which is also in line with the actual working conditions. In order to maintain unity, the test of ice adhesion strength in this subject was measured after frosting for 10 min (placed for 10 min).
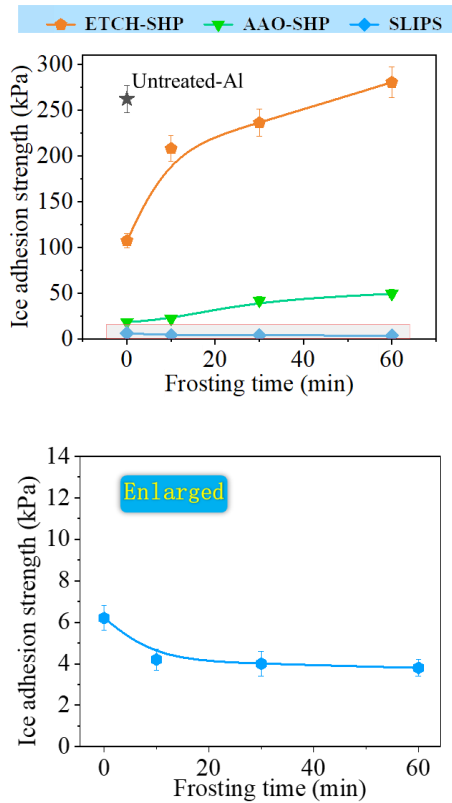
Fig. 2 Variation of ice adhesion strength on different aluminum surfaces with frosting time.

The horizontal shear test of ice adhesion strength can be carried out on a refrigeration platform or in a refrigerator. Here, the ice adhesion strength of SLIPS on the refrigeration platform and in the refrigerator was measured. As shown in Fig.3, since SLIPS is not easy to frost in an air-cooled refrigerator, its ice adhesion strength is 6.1 kPa, which is slightly higher than the value of the refrigeration platform. In order to maintain unity, the ice adhesion strength test in this topic is carried out on the refrigeration platform.
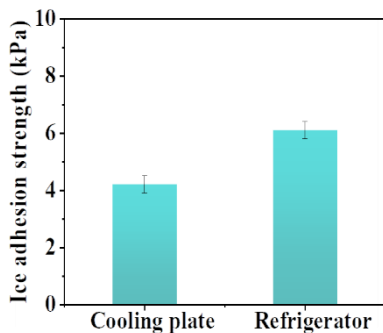
Fig. 3 Ice adhesion strength of SLIPS tested on the Peltier cooling plate and in the refrigerator.

B. Low Ice Adhesion Mechanism

The ice adhesion strength value mainly depends on the sample surface type and frosting condition. The anti-icing mechanism is studied from these two aspects, as shown in Fig.4. Due to its hydrophilicity, the untreated Al has a strong hydrogen bond interaction with water molecules, resulting in a high ice adhesion strength. In comparison, etched-SHP and AAO-SHP have weaker hydrogen bond interaction (parallel orientation) with ice due to their lower interfacial energy, and the micro-nano structure also reduces the contact area with ice, resulting in lower ice adhesion. For etched-SHP, the air cushion in the micron-scale rough structure is unstable at low temperature, resulting in a large contact area between the ice and the substrate, which makes the ice adhesion strength higher than that of AAO-SHP. In the frosting environment, water vapor enters the interior of the structure, and the microstructure is interlocked with the ice, thus the ice adhesion strength is greatly increased. The nano-scale structure of AAO-SHP has a certain effect of inhibiting condensation and frosting, but with the increase of frosting time, water vapor will still gradually condense in the structure, and pore icing will occur, and the ice adhesion strength will also increase slowly.

For SLIPS, the stable lubricating film on the surface prevents direct contact between water and the substrate. When the ice is removed from the sample surface, the fracture occurs at the weak interface between the ice and the oil layer [15]. The lubricating film is firmly attached to the surface nanostructure by capillary force and van der Waals force, and the oil molecules interact strongly with the nanostructure. When in contact with water/ice, oil molecules are inflexible and cannot re-orientate to form strong hydrogen bonds with water molecules, which makes the lubricating oil layer and ice have a small hydrogen bond interaction (parallel orientation) [16], resulting in ultra-low ice adhesion strength. According to the thermodynamic state of water droplets on SLIPS (the lubricating oil is immersed in the matrix and the water is in contact with the top of the matrix), the condensate water in the high humidity environment nucleates at the top of the structure and is lifted up by the matrix and oil layer after growing up. Therefore, in a frosting environment, the lubricating oil film can prevent water vapor from frosting inside the pores, which makes the de-icing fracture still occur at the interface between the ice and the oil film. It is worth noting that the loose frost layer has a weaker binding force with the film, and the slippery surface after frosting has a lower ice adhesion strength. In summary, even in the frost environment, the stable lubricating oil film on the slippery surface still gives it ultra-low ice adhesion strength.

IV. Conclusions

In this study, Effect of frosting on ice-adhesion strength of anti-icing slippery surfaces was studied. The main conclusions are as follows: (1) Compared with other types of Al surfaces, SLIPS has a lower ice adhesion strength, which is about 2% of that of untreated Al. (2) The de-icing fracture of the slippery surface occurs at the ice/oil interface, which has a small hydrogen bond interaction. (3) Since the lubricating oil film prevents the nucleation of condensation droplets inside the matrix structure, SLIPS can still maintain super ice adhesion strength after frosting.
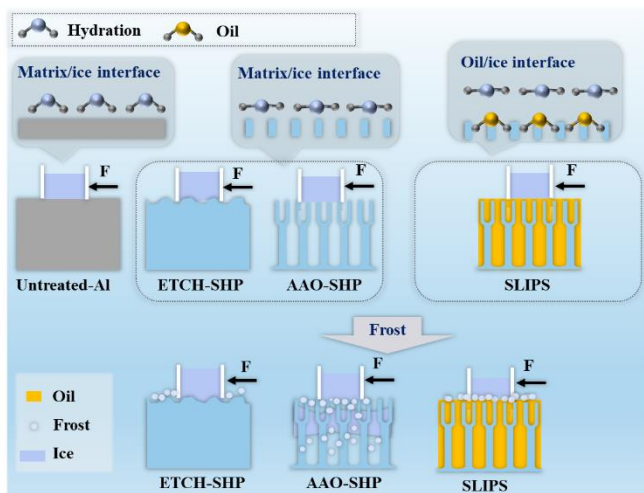
Fig. 4 Mechanism of ice adhesion strength on different aluminum surfaces.

REFERENCES

[1] Z. He, E. T. Vågenes, C. Delabahan, J. He, Z. Zhang, "Room Temperature Characteristics of Polymer-Based Low Ice Adhesion Surfaces," Scientific Reports, Vol. 7, pp. 42181, 2017.

[2] J. H. Kim, M. J. Kim, B. Lee, J. M. Chun, V. Patil, Y.-S. Kim, "Durable ice-lubricating surfaces based on polydimethylsiloxane embedded silicone oil infused silica aerogel," Appl. Surf. Sci., Vol. 512, pp. 145728, 2020.

[3] D. L. Beemer, W. Wang, A. K. Kota, "Durable gels with ultra-low adhesion to ice," J. Mater. Chem. A, Vol. 4, pp. 18253-18258, 2016.

[4] Z. He, S. Xiao, H. Gao, J. He, Z. Zhang, "Multiscale crack initiator promoted super-low ice adhesion surfaces," Soft Matter, Vol. 13, pp. 6562-6568, 2017.

[5] R. Dou, J. Chen, Y. Zhang, X. Wang, D. Cui, Y. Song, L. Jiang, J. Wang, "Anti-icing coating with an aqueous lubricating layer," ACS Appl. Mater. Interfaces, Vol. 6, pp. 6998-7003, 2014.

[6] L. Zhou, A. Liu, J. Tang, Y. Han, J. Kang, Y. Li, S. Kuai, X. Xue, N. Chen, H. Liu, "Robust and durable self-lubricated surface by facile fabrication for anti-icing/deicing," J. Appl. Phys., Vol. 134, 2023.

[7] T. Inoue, A. Koyama, D. Kowalski, C. Zhu, Y. Aoki, H. Habazaki, "Fluorine-Free Slippery Liquid-Infused Porous Surfaces Prepared Using Hierarchically Porous Aluminum," Phys. Status Solidi A, Vol. 217, pp. 1900836, 2020.

[8] W. Pan, Q. Wang, J. Ma, W. Xu, J. Sun, X. Liu, J. Song, "Solid-Like Slippery Coating with Highly Comprehensive Performance," Adv. Funct. Mater., Vol. 33, 2023.

[9] S. B. Subramanyam, K. Rykaczewski, K. K. Varanasi, "Ice Adhesion on Lubricant-Impregnated Textured Surfaces," Langmuir, Vol. 29, pp. 13414-13418, 2013.

[10] Y. Yuan, H. Xiang, G. Liu, L. Wang, H. Liu, R. Liao, "Self-repairing performance of slippery liquid infused porous surfaces for durable anti-icing," Adv. Mater. Interfaces, Vol. 9, pp. 2101968, 2022.

[11] H. Cho, T. Kim, S. Kim, "Tunable thickness and uniform drop deposition of graphene oxide on porous anodic aluminum oxide and a reliable thickness measurement technique," Surf. Topogr., Vol. 9, pp. 025026, 2021.

[12] Z. Yang, X. He, J. Chang, X. Bai, P. Cao, C. Yuan, "Fabrication of biomimetic slippery liquid-infused porous surface on 5086 aluminum alloy with excellent antifouling performance," Surf. Interface Anal., Vol. 53, pp. 147-155, 2020.

[13] D. Wu, D. Zhang, Y. Ye, L. Ma, B. Minhas, B. Liu, H. A. Terryn, J. M. C. Mol, X. Li, "Durable lubricant-infused anodic aluminum oxide surfaces with high-aspect-ratio nanochannels," Chem. Eng. J., Vol. 368, pp. 138-147, 2019.

[14] S. Bengaluru Subramanyam, V. Kondrashov, J. Ruhe, K. K. Varanasi, "Low ice adhesion on nano-textured superhydrophobic surfaces under supersaturated conditions," ACS Appl. Mater. Interfaces, Vol. 8, pp. 12583-12587, 2016.

[15] M. Jin, Y. Shen, X. Luo, J. Tao, Y. Xie, H. Chen, Y. Wu, "A combination structure of microblock and nanohair fabricated by chemical etching for excellent water repellency and icephobicity," Appl. Surf. Sci., Vol. 455, pp. 883-890, 2018.

[16] C. Zhang, S. Adera, J. Aizenberg, Z. Chen, "Why Are Water Droplets Highly Mobile on Nanostructured Oil-Impregnated Surfaces?," ACS Appl. Mater. Interfaces, Vol. 13, pp. 15901-15909, 2021.

Investigation on snowphobic and icephobic behavior of superhydrophobic surfaces

M. Balordi[1], G. Santucci de Magistris[1], F. Pini[1]
[1] RSE, Ricerca sul Sistema Energetico, Piacenza, Italy

marcella.balordi@rse-web.it, giorgio.santucci@rse-web.it, francesco.pini@rse-web.it

Abstract—**One way to mitigate the atmospheric icing phenomena on metallic surfaces is to lower their wettability with hydrophobic coatings and superhydrophobics (SHPs) are considered promising candidates. A debate on ice-phobic properties of SHP surfaces is however underway in the last years, as many studies disagree on the effectiveness of SHP in all surrounding conditions. Different theories have also been proposed to explain ice adhesion reduction of SHPs. On contrary, just few works deal with the performances of SHPs in reducing snow adhesion, and the related mechanisms are still to be comprehended.**

Here we present several SHP coatings on aluminun alloy, obtained with a three-step process that envelope chemical etching, hydrothermal treatment and dip coating in a fluorinated alkyl silane (FAS). By varying the applied conditions different hierarchical roughness are obtained. SEM and profilometer measurements are carried out to evaluate the morphologies. Hydrophobicity is measured with static and dynamic contact angles and ice-phobicity is assessed with shear stress tests.

In general, by increasing the roughness with harsher etching conditions the ice-phobicity of surfaces get worse while no effect is found on the wettability. Which means that, although all the samples exhibit SHP behavior, only some of them resulted ice-phobic. To study the relationship between the ice-phobic and snow-phobic properties, two selected samples with different ice-phobicity, were tested in the artificial snow laboratory. Snowfalls were simulated on treated segments of conductors, compared with a bare specimen, to study their performances in delaying the formation and/or triggering an earlier detachment of the snow sleeve.

This work aims to shed some light on the role of the superhydrophobicity towards anti-snow and anti-icing applications.

Keywords— *superhydrophobic; icephobic; snowphobix; snow-test; chemical etching*

I. INTRODUCTION

Superhydrophobic coatings are characterized by a static contact angle (SCA) higher than 150° and a Roll-Off angle (RA) of less than 5°. These unique characteristics grant surfaces a complete repulsion towards water. These coatings find applications in several fields, such as self-cleaning materials, anticorrosive coatings or industrial uses as oil-water separation [1]. Over the last few decades, the SHPs have been largely researched for their potential as anti-icing coatings. Due to their exceptionally low surface energy, they can reduce the adhesive force between ice and surfaces as well as hindering ice nucleation. However, despite these premises, there is ongoing debate regarding the actual efficiency and durability of SHPs as anti-icing materials [2]. SHPs can lose their anti-icing properties under specific climatic conditions.

High humidity and low temperatures can lead to the formation of a thin layer of condensed water on superhydrophobic surfaces, drastically reducing the water repulsion [3]. When this phenomenon occurs, SHP surfaces become wettable, transitioning from a Cassie-Baxter to a Wenzel state, exposing a large surface area to icing. Consequently, ice can strongly adhere to the surface. Therefore, in some cases, hydrophobic materials with a smooth surface may exhibit a better icephobic behavior than SHPs.

While the anti-icing behavior of these materials has been intensively debated, their interaction with snow has not been thoroughly researched yet. Nevertheless, among atmospheric icing phenomena, the formation of snow sleeves on overhead conductors and ground wires poses one of the most significant challenges to the resilience of the Italian power line system.

Ice and snow greatly differ in mechanical and physical properties and the effectiveness of coatings in repelling ice or snow can vary significantly.

In this work we present several hydrophobic and superhydrophobic aluminium alloy coated samples. These samples have all been obtained with a three-step treatment: the first being an acid etching, followed by a hydrothermal treatment and, lastly, the deposition of a FAS layer (fluorinated alkyl silane). Depending on the type of etching treatment, some of them showed a very pronounced roughness, while others have smoother surfaces. All the so-obtained samples exhibit very high static contact angle and, in some cases, very low roll-off angle. The samples were tested as anti-icing coatings: the best ones are the highly hydrophobic coatings: they can reduce the ice adhesion up to 22 times. Instead, superhydrophobics exhibit a more fluctuating icephobic behavior.

The two most promising coatings according to wettability and ice adhesion testing, were applied to 75 cm long span Aluminium conductor steel-reinforced cables (ACSR) and their snowphobic performances were studied under simulated snowfall in an artificial snow laboratory. The weight of the snow sleeve accreted on the conductors, kept under slow rotation during tests, was measured and compared with that on a reference untreated ACSR conductor, providing the evidence of the actual snowphobicity of the coatings.

This work aims to explore the relationship among wettability, icephobicity and snowphobicity, and to rationalize the key factors determining the effectiveness of the coatings in real conditions.

II. Experimental

A. Materials and samples preparation

Flat plates (20×70×2 mm) and bars (12mm diameter×100mm length) of aluminum alloy (6082) and ACSR conductors (3,4 cm diameter×75 cm lenghts) were used as substrates. Dynasylan® SIVO CLEAR EC coating was purchased from EVONIK and was used as received (FAS). HCl (36%) Hexane (95%) and acetone (> 99.5%) were purchased from Sigma Aldrich.

All the aluminum alloy specimens were cleaned with basic soap, rinsed in ultrasonic bath for 10 min with acetone and dried under nitrogen flux.

In general, a three-step process was carried out to prepare the samples:

1. immersion in HCl at different concentrations and times;
2. boiling in hot demineralised water;
3. dip-coating with FAS coating (dipping–withdrawing speed: 0.7 mm/s, permanence time: 120 s).

The coatings were finally cured at 120°C for 1 hour. Different concentrations of acidic solution, immersion and boiling times were tested, as indicated in the table below.

TABLE 1. SAMPLES PREPARATION.

Sample	Concentration of HCl (M)	immersion time (min)	boiling time (min)
1	0,5	30	0
2	0,5	15	0
3	0,5	15	5
4	0,5	30	30
5	0,5	15	30
6	0,5	30	5
7	3	30	0
8	3	15	0
9	3	30	30
10	3	30	5
11	3	15	30
12	3	15	5

B. Methods

The static water contact angle (SCA) measurements were carried out with a Kruss DSA 30 Drop Shape Analyzer using the sessile drop method, using a 2 µl volume of water, at 20 °C. The measurements were replicated at least 5 times for each sample. The roll-off angles (RA) were performed with the tilting table method using 20 µL of water at 23 °C ± 2. At least 3 measures were done for each sample.

The surface morphologies were examined using a field emission scanning electron microscope (FE-SEM) (Tescan)

A Taylor Hobson mechanical profilometer was used to measure surface roughness, data were averaged over at least 5 runs for each sample.

Ice adhesion was evaluated by shear stress analysis, performed with a home-made apparatus installed on the electromechanical tensile testing system INSTRON 4507

following the previously described method [4]. Shear stresses were calculated as the average of 10 tests on each sample. Results are reported in terms of Adhesion Reduction Factor (ARF), the ratio between the shear stress of bare and coated samples: the higher the ARF, the more icephobic the sample.

Snowphobicity tests were carried out in an artificial snow laboratory, maintained at temperatures near 0 °C. The ACSR conductors, both coated and bare, were slowly rotated (1 rpm) under a flux of artificial snow for 5 hours, to induce the growth of the snow sleeve. The weight of the snow sleeve grown on the samples and on the reference was recorded throughout the duration of the snowfalls. Three snowing conditions have been used for the tests resulting in the hereafter named "dry" (LWC ≃ 5%), "hybrid" (LWC from 10 to 15%) and "wet" (LWC ≃ 35%) snow. The Snow Reduction Factor (SRF), defined as the ratio between the weight of the snow on the reference and on the sample at a given testing time, was chosen, similarly to ARF, to evaluate the capacity of the coatings to reduce the formation of the snow sleeve. The higher the SRF, the more snowphobic the sample.

III. RESULTS AND DISCUSSION

The morphology of treated and untreated specimens was analysed by FE-SEM microscopy. Etching in HCl 3M gives rise to uniform micro-roughened structures even after a short immersion time (15 minutes), on the contrary substrates treated with 0,5M HCl exhibit a gently etched surface even after 30 minutes of treatment (Figure 1 a and b, respectively).
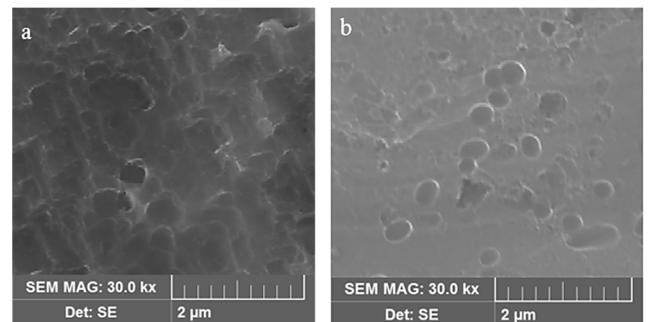
Figure 1. SEM images (secondary electrons) of Al alloy etched in HCl 3M (a) and in HCl 0,5M (b) for 15 minutes and 30 minutes, respectively.
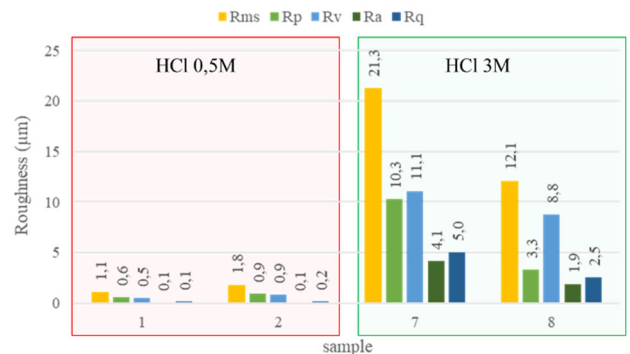
Figure 2. Roughness parameters of Al alloy etched in HCl 0,5M and HCl 3M for different times.

In general, roughness measurements show a remarkable increase of all the main parameters (Ra, Rq, Rp, Rv, Rz and

Rms) at the increase of the concentration and immersion time in the acidic solution (Figure 2) thus confirming the SEM observations. All the considered roughness parameters are highly correlated with each other.

The boiling process gives rise to the growth of a pseudo-boehmite acicular nanostructure, as previously reported [4]. Different boiling times had no significant effect on the morphological structure, both short and prolonged treatments resulted in the growth of a homogeneous oxide layer (Figure 3). However, it is possible to observe that the acicular nanostructures formed on sample treated for 30 minutes report higher aspect ratios than those formed iafter only 5 minutes of treatment.
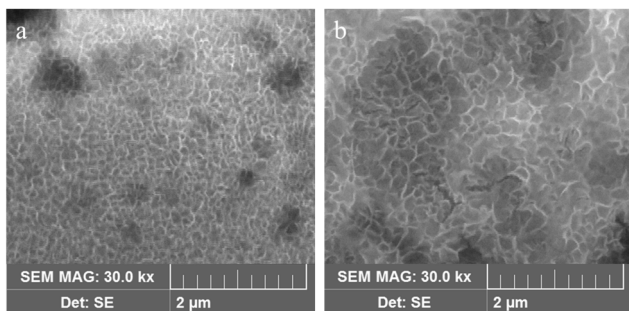
Figure 3. SEM images of Al alloy after 5 minutes (a) and 30 minutes (b) of treatment in boiling water.

The formation of this peculiar oxide layer on top of an etched surface imparts a hierarchical micro-nano roughness which is a crucial parameter to achieve superhydrophobic surfaces (SHP).

The wettability properties of the coated samples are depicted in Figure 4. Samples without boiling treatment evidence hydrophobic (HP) properties (samples 1, 2, 7 and 8). Etching in 0,5M HCl gives rise to SHP surfaces (SCA >150°and RA <5°) only for samples boiled for 30 minutes (samples 4 and 5), while a 5-minute treatment in hot water results in high hydrophobic surfaces (HHP) in Wenzel's regime (SCA >150° and RA>5°, samples 3 and 6) [5]. In contrast, the immersion in 3M HCl lead to superhydrophobic behaviour for both boiling times (samples 9, 10, 11, 12).
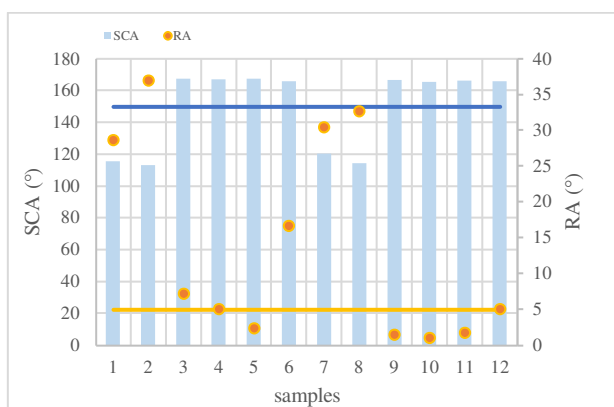
Figure 4. Wettability of the prepared samples. Blu and orange lines indicate the WCA and RA thresholds required to achieve superhydrophobicity.

All the so-prepared samples evidence ice adhesion reduction, however, important differences in their icephobic

behaviour are evidenced in Table 2. HP samples exhibit the lowest ARFs (maximum value about 2), which is only to be attributed to the low surface energy coating. SHPs display a complex behaviour: those treated with 0,5M HCl have very high ARF (>10), while those immersed in 3M HCl demonstrate lower ARF, ranging from 4,5 to 7,9. All the high-hydrophobic coatings (HHP) exhibit very promising icephobicity, with ARF values reaching up 22.

TABLE 2. HYDROPHOBIC BEHAVIOUR AND ADHESION REDUCTION FACTOR.

Sample	ARF	Hydrophobic behaviour	Sample	ARF	Hydrophobic behaviour
1	1,2	HP	4	13,3	SHP
2	1,4		5	13,5	
7	1,2		9	4,5	
8	2,1		10	4,8	
3	11,8	HHP	11	7,0	
6	**22,5**		12	7,9	

The icephobic behavior of the samples can be put in perspective considering both the SCA and the roughness values: in general, ARFs increase at the increase of SCAs and the decrease of roughness parameters (Figure 5; Rms was chosen as roughness parameter). Results indicate that a remarkable hydrophobicity is needed to achieve icephobicity whereas the roughness, which is needed to impart the hydrophobic regime itself, can conversely promote ice adhesion. In this work a balance in the roughness parameters was found for samples from 3 to 6.
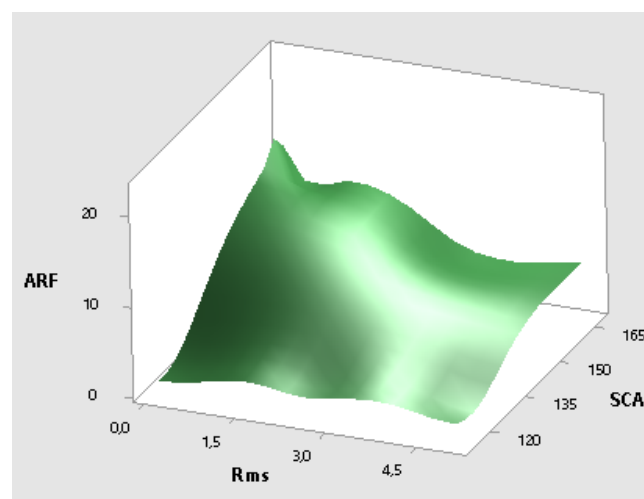
Figure 5. Surface plot of ARF vs SCA and Rms. The Rms was chosen as representative among the roughness parameters, that are correlated with each other's.

To assess the snowphobic performances and to understand the relationship between icephobicity and snowphobicity, the samples 6 (HHP) and 10 (SHP) were selected to be tested, under artificial snowfall. Sample 6 represents the best icephobic sample with high hydrophobic behaviour, whereas sample 10 is a superhydrophobic surface with medium-low icephobicity (ARF 4,5). SRF was calculated after 1 hour, 2,5 hours and 4 hours. The SRF of the average weight grown

during the entire snowfall was calculated as well. The SRF at the end of the experiment (5 hours) is not representative because in some cases the snow sleeves on the reference detached due to its excessive weight after about 4,5 hours.

TABLE 3. SNOW REDUCTION FACTO FOR HHP AND SHP SAMPLES UNDER DIFFERENT ARTIFICIAL SNOW FALLS.

SRF	dry snow		hybrid snow		wet snow	
	HHP	SHP	HHP	SHP	HHP	SHP
SRF_{1h}	1,1	2,9	1,1	2,6	1,1	1,7
$SRF_{2,5h}$	0,8	8,3	5,3	4,4	1,0	1,6
SRF_{4h}	1,5	3,1	12,8	7,2	1,0	2,6
SRF_{ave}	1,2	2,9	4,5	5,7	1,0	2,1

As reported in Table 3, the HHP and SHP samples performed differently depending on the snow LWC content. In the dry-snow test, HHP does not significantly mitigate the snow accumulation (maximum SRF 1,5) whereas SHP exhibit a good snowphobicity, with a maximum SRF of 8,3 after 2,5 hours and a 3-fold average snow reduction accumulation in respect to the reference.

In the hybrid-snow test, both HHP and SHP show the best anti-snow behavior, reducing average snow accumulation by 4,5 and 5,7 times, respectively. During the test, several events of snow detachment were observed on both HHP and SHP samples, particularly after 4 hours the SRF of HHP was about 13. Thus, SHP and HHP surfaces exhibit low adhesion to hybrid snow.

In the wet-snow test, HHP does not show any mitigation in snow accretion, while SHP decreases snow accumulation by a factor of 2 during the whole snowfall.

Overall, it is important to emphasize that SHP performs more consistently across all test conditions and demonstrates a significant SRF even from the first hours of the snowfall, as showed in Figure 6.
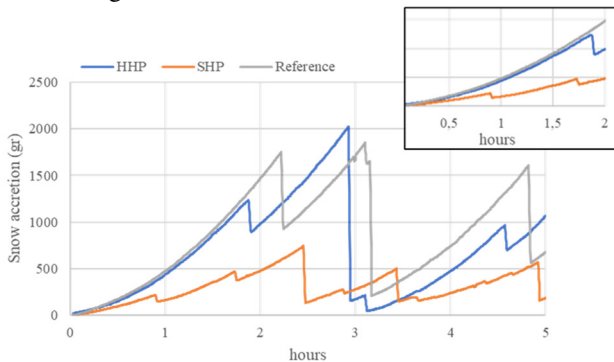
Figure 6. Snow accretion on HHP, SHP and reference during a dry-snow test. The delay in snow accretion at the beginning of the experiment for SHP is clearly visible in the inset.

This suggest a mechanism whereby there is initially a delay in the formation of the first snow layer on the surface, followed by an early detachment of the snow sleeve.

In contrast, HHP only exhibit interesting snowphobicity properties only under hybrid-snow conditions. Moreover, it does not mitigate the snow growth at the onset of the event, indicating that, in this case, the snowphobicity is more about causing an earlier detachment rather than delaying the formation of the initial layer.

IV. CONCLUSIONS

In this work we prepared several surfaces, with SCA values ranging from 116° to 167°, RA values from 1° to 37° and different roughness values.

We assessed the icephobic properties of the samples and a relationship among icephobicity, static contact angle and roughness have been here proposed.

The best icephobic sample (sample 6) has high hydrophobic behavior but is not superhydrophobic. High value of SCA is a key factor to obtain anti-icing surfaces, while the role of roll-off angle is not completely understood and seems not to be essential. Moreover, the samples evidenced good anti-icing properties only when roughness parameters are kept as low as possible. Thus, the roughest SHPs are not very effective as icephobic surfaces.

Snowphobicity was assessed on the most icephobic (sample 6, HHP) and on the most superhydrophobic (sample 10, SHP) samples in the artificial snow laboratory. Three different snow falls ranging from dry snow to a LWC about 35% were tested. The formation and detachment of the snow-sleeve on the coated samples were compared to those on a untreated reference sample, indicating different snowphobic behaviour depending on the coating and on the type of snow. Unexpectedly, considering ice adhesion results, the SHP sample exhibited the best snowphobicity, mitigating the snow sleeve in every tested condition and decreasing the 5 hours averaged SRF up to 5,7 times.

The HHP, which is the best anti-icing coating, displayed a good anti-snow behavior only under hybrid snowfall, whereas it didn't significantly reduce sleeve accretion under wet and dry snow conditions.

These results demonstrate that the key parameters for achieving anti-icing and anti-snow surfaces are different. On one hand, a material with high static contact angle is necessary to reduce both snow and ice accretion on the surface; on the other hand, having low-roughness surfaces is crucial for anti-icing but seems to be of a lesser importance when aiming at snowphobicity. Instead, from preliminary data, it seems that roll-off angles could play a role towards snowphobic properties, whereas it does not seem to be a key factor in reducing ice adhesion.

This work sheds some light on the role of superhydrophobicity on icephobic and snowphobic properties of surfaces, however further studies are needed to delve deeper into these aspects.

REFERENCES

[1] J. T. Simpson et. al., "Superhydrophobic materials and coatings: a review". Rep. Prog. Phys., 2015, vol 78.

[2] W. Li, Y. Zhan, S. Yu, "Applications of superhydrophobic coatings in anti-icing: Theory, mechanisms, impact factors, challenges and perspectives", Progress in Organic Coatings, 2021, vol 152.

[3]   N. Cohen, A. Dotan, H. Dodiuk, S. Kenig, "Superhydrophobic Coatings and Their Durability" Materials and Manufacturing Processes, 2016, vol 31.

[4]   M. Balordi. A. Cammi, G. Santucci de Magistris, C. Chmelli, "Role of micrometric roughness on anti-ice properties and durability of hierarchical super-hydrophobic aluminum surfaces", Surface & Coatings Technology, 2019, vol 374, pp 549-556.

[5]   R. Wenzel, "Resistance of solid surfaces to wetting by water", Ind. Eng. Chem, 1936, 28, 988-994.

Electromechanical de-icing systems: Influence of coatings on fracture mechanisms

G. Gastaldo[1], V. Pommier-Budinger[1], M.Budinger[2], G. Hernández Rodríguez[3], Anna Maria Coclite[3]

[1] Fédération ENAC ISAE-SUPAERO ONERA, University of Toulouse, 31400 Toulouse, France

[2] Institut Clément Ader (ICA), University of Toulouse, INSA, ISAE-SUPAERO, MINES ALBI, UPS, CNRS, 31055 Toulouse, France

[3] Institute of Solid State Physics, NAWI Graz, Graz University of Technology, 8010 Graz, Austria

Abstract- **Ice accretion negatively impacts aviation by causing performance losses and compromising the safety of passengers. To overcome these issues, ice protection systems (IPS) are used. In recent years, electromechanical resonant de-icing systems have gained interest due to their potential in terms of weight and energy savings. They rely on piezoelectric transducers that are bonded or embedded inside the aircraft's skin. The transducers excite the structure at its resonant frequency, creating high stress in the ice that leads to its failure and eventual delamination. The purpose of this study is to investigate the effect of coatings on resonant ice protection systems. Coatings can alter the interfacial properties, typically reducing the shear strength or the toughness, and can potentially change the fracture mechanism and help to achieve more effective fracture propagation. The study first qualitatively examines the critical properties on a bare sample and a coated sample equipped with piezoelectric actuators. The study also investigates fracture mechanisms for various ice block sizes, which are known to impact de-icing mechanisms. The analysis reveals the fracture mechanisms involved, and the changes induced by the use of coatings.**

Keywords - **Electromechanical de-icing, Coatings, Fracture mechanisms, Shear Strength, Toughness**

1 INTRODUCTION

Ice accretion negatively impacts aviation and many other systems operating in cold climates. In the case of aircraft icing, supercooled water droplets that are suspended in clouds can impact on the aircraft's surfaces and freeze. The resulting ice alters the aerodynamic properties of the wing, leading to severe performance degradation and safety threats. [1] Such problems are overcome by using ice protection systems (IPS), which traditionally rely on chemical, thermal, and mechanical approaches. They can be classified as active or passive ice protection systems. Active ice protection systems are generally thermal or mechanical. Among the mechanical systems, resonant de-icing systems have gained interest due to their potential for weight and energy savings. Electromechanical transducers are bonded or embedded into the aircraft skin, and they vibrate the structure at one of its resonant frequencies, thus creating high stresses in the ice that lead to failure and eventual delamination [2].

Passive systems often rely on the surface chemistry. In general, superhydrophobic and hydrophobic surfaces are characterized by a lower water adhesion, which reduces water accumulation prior to freezing. Also, it is possible to apply icephobic coatings, for which ice adhesion is low. This means that when ice forms on the surface, lower shear forces are required to remove it [3]. In some cases, superhydrophobic surfaces have also shown low ice adhesion behavior [4]. Recently, hybrid solutions using both active and passive anti-icing systems have been investigated as they could improve the effectiveness of active anti-icing systems or reduce the energy consumption of existing systems. In [5], the use of a superhydrophobic coating coupled with an electrothermal ice protection system reduced the consumed energy by around 50 %. Antonini et al. [6] evaluated the influence of superhydrophobic coatings on the energy reduction of an electrothermal anti-icing system. They tested in an icing wind tunnel three airfoils with different wettability properties: a hydrophilic untreated aluminum prototype, a poly(methyl methacrylate) (PMMA) coated surface and a superhydrophobic Teflon-coated aluminum surface. The use of a superhydrophobic coating in various icing conditions was found to reduce the heating power required to protect the leading edge from ice formation (up to 80% of power savings). There was also a significant reduction or elimination of runback ice. Strobl et al. [7] developed a hybrid system for ice protection that utilizes heating elements on the stagnation area, piezoelectric actuators, and a hydrophobic coating applied to the entire surface. The hybrid system was

tested in an icing wind tunnel, and the required total power density is 2.74 kW/m^2 compared to a strictly thermal ice protection power density of between 16.4 and 62 kW/m^2. However, the paper does not analyze the contribution of the hydrophobic coating to the decrease in power density. In this paper, the effect of coatings on the ice fracture mechanisms is evaluated using electromechanical ice protection systems and some considerations on the de-icing effectiveness are done.

2 COATINGS EFFECT ON THE DE-ICING CAPABILITIES OF RESONANT ICE PROTECTION SYSTEMS

2.1 Principles of resonant ice protection systems

Resonant de-icing systems apply vibrations to the structure to create high-level stresses within the ice, leading to fractures and ice shedding. Two types of fracture can be generated: cohesive fractures (or bulk fractures) occurring within the ice block, and adhesive fractures, which occur at the interface between the ice and the substrate.
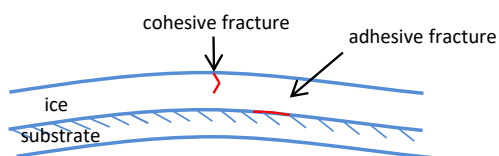
Figure 1: Cohesive and adhesive failure [8].

In the de-icing process, cohesive fractures may not always occur. If they do occur without adhesive fractures, the ice may still stick to the surface it has accreted on, making ice shedding impossible. Therefore, adhesive fractures are necessary for ice debonding.

Cohesive fractures occur when the tensile stress in the bulk ice exceeds its tensile strength ($\sigma_I \geq \sigma_c$). Two different mechanisms can generate adhesive fractures. Golovin et al. [9] found that the adhesive fracture mechanism depends on the ice block size. For small bonded lengths, fracture occurs when the average shear stress at the interface exceeds the shear strength ($\tau_{xy} \geq \tau_c$) while for long ice blocks, the fracture is dominated by the critical energy release rate ($G \geq G_c$). To accurately evaluate these criteria, it is essential to pay close attention to the critical properties of the ice or the interface between the ice layer and the substrate. The upcoming part will analyze the criteria.

2.2 Tensile stress criterion

The cohesive stress condition is based on the characteristic value of the ice tensile strength σ_c. Rankine theory specifies that cohesive fractures appear in brittle material if:

$$\sigma_I \geq \sigma_c \tag{1}$$

where σ_I represents the tensile stress in the ice.

2.3 Shear stress criterion

The adhesive stress condition is based on the characteristic value of the shear strength τ_c of the studied interface. For the following studies in this paper, it is assumed that complete delamination occurs when the following condition is met:

$$min(\tau_{xy}) \geq \tau_c \tag{2}$$

where $min(\tau_{xy})$ represents the minimum shear stress over the interface.

2.4 Energy release rate criterion

The energy condition relies on the critical energy release rate (or toughness) value G_c. This criterion was first introduced by Griffith, who stated that fracture occurs when the energy stored in the structure exceeds the energy required to create a new crack, which is a property of said structure [10]. In the case of a multi-material system, the critical value is dependent on the studied interface (in our case the interface between the substrate and the ice). The energy release rate is given by:

$$G = -\frac{1}{b}\frac{dU}{da} \tag{3}$$

where dU is the differential decrease in potential energy, da is the differential increase in crack length, and b is the specimen width. The fracture propagates if the released energy is equal to or greater than the critical value of G, thus expressed as $G \geq G_c$.

2.5 Fracture mechanisms and interest in coatings

Budinger et al. [11] studied two modes for fracture propagation in resonant de-icing systems: flexural and extensional modes. Flexural modes are characterized by a significant out-of-plane displacement, while extensional modes vibrate mainly in the in-plane direction.
Gastaldo et al. [8] investigated the mechanisms of fracture initiation and propagation in resonant de-icing systems as a function of ice block size. The study was performed on an uncoated titanium plate that had accumulated ice on its upper surface. It revealed that the fracture mechanism changes depending on the amount of ice

coverage. When ice covers most of the surface, cohesive cracks appear first, and the adhesive fracture initiates from there and extends to the sides. However, when the ice surface is smaller, no cohesive fracture occurs, and the adhesive fracture starts from the sides.

The method for analyzing the fracture mechanisms used in [8] involves comparing the amplitudes required to initiate a fracture by exceeding the critical stress value and the amplitude required to initiate propagation by exceeding the critical energy release rate. It is based on numerical finite element simulations. Modal analyses are used to obtain stress and elastic strain energy distributions for the resonance mode of interest. The amplitude required to initiate a cohesive fracture is defined by (4):

$$x_{r\sigma} = \frac{\sigma_c}{\sigma_{mod}} x_{mod} \qquad (4)$$

with σ_c the tensile strength of ice, σ_{mod} and x_{mod} respectively the modal tensile stress and the modal displacement.

Similarly, the amplitude required to initiate an adhesive fracture based on the adhesive stress criterion is defined by (5):

$$x_{r\tau} = \frac{\tau_c}{\min(\tau_{mod})} x_{mod} \qquad (5)$$

with τ_c the shear strength of ice, τ_{mod} and x_{mod} respectively the modal shear stress and the modal displacement. Finally, the amplitude required to initiate fracture propagation based on an energy release rate criterion is defined by (6):

$$x_{rG} = \sqrt{\frac{G_c}{G_{mod}}} x_{mod} \qquad (6)$$

with G_c the fracture toughness and G_{mod} and x_{mod} respectively the modal energy release rate and the modal displacement. In the case of flexural mode, x_{mod} is the out-of-plane maximum displacement.

Fractures are easier to generate when the amplitude is smaller. For example, if $x_{rG} < x_{r\sigma}$ or $x_{rG} < x_{r\tau}$, the de-icing mechanism is said to be energy release rate-dominant, otherwise it is said to be stress-dominant. A low ice adhesion or a low toughness coating would reduce the critical properties τ_c and G_c, thus leading to smaller amplitudes $x_{r\tau}$ and x_{rG}. Therefore, for the same ice coverage of the bare substrate, alternative fracture mechanisms may be achievable.

In the following sections, the study focuses on the comparison between uncoated and coated samples, and the effect on both the fracture mechanism and the de-icing effectiveness is evaluated.

3 COATING CHARACTERIZATION

The objective of this section is to have further information on the critical energy release rate at the interface between the ice layer and the substrate. This is achieved by implementing a hybrid numerical/experimental method. The experiments are performed on 130x50x1 mm^3 aluminum plates. One sample is left uncoated, while the other is coated with an icephobic gradient polymer coating deposited via initiated chemical vapor deposition (iCVD)[12]. The plates are equipped with two soft piezo-ceramics (PIC 255, 50x22x0.5 mm^3).

3.1 Numerical results

The curve in Figure 2 is obtained numerically by computing the key performance indicator $KPI_{3adh} = \frac{G_{adhi}}{X^2}$ found in [11] for the first flexural mode. In this case, G_{adhi} is the value of the energy release rate for the i step of adhesive propagation, while X is the displacement needed to initiate the crack. Note that, as the quality factor of the two plates is close (Q_m=37 and Q_m=38), the displacement X is assumed to be the same for the two samples, which allows comparing the value of G and computing a reduction factor. The samples are modeled in a 3D finite element analysis with a uniform 3 mm-thick layer of ice on top. Two separate models are considered to retrieve all quantities in this study. The first model assumes a pristine ice block, and it is used to calculate the stored elastic energy U_0. The second model includes a cohesive crack at the point where the maximum tensile stress is found, which also corresponds to the point where the maximum displacement is located. The energy release rate is then computed as defined in [13]. The adhesive crack is propagated and the elastic strain energy of the structure is retrieved for each propagation step i. The energy release rate value is then computed using the formula (7):

$$G_i = -\frac{1}{b}\frac{\delta U}{\delta a} = \frac{1}{b}\frac{U_0 - U_{i+1}}{a_i} \qquad (7)$$

where b is the width of the plate, U_0 represents the stored elastic energy for the for a pristine ice block state, while U_i represents the stored elastic energy at each step i of the adhesive propagation once the cohesive crack is formed. The length of the adhesive crack is represented by a_i. Once all the parameters are obtained, the ratio $\frac{G}{X^2}$ versus the crack percentage is plotted as seen in Figure 2. The crack percentage is computed as the crack length over the total length of the plate.

3.2 Experimental results

The points on the curve of (Figure 2) are obtained experimentally by testing the two samples with a 3 mm-thick

ice layer formed on top using the first flexural mode. Once the tests are performed, the extent of the crack is measured and reported on the numerical plots. It is possible to notice in Figure 2 that, for the considered samples, the generated fracture is more extensive in the case of the iCVD-coated sample. The critical energy release rate value G_c cannot be measured exactly, but from the curve it is possible to obtain an average toughness reduction factor around 1.6. In the following part, a usual value of G_c=1 J/m^2 is considered for the bare aluminum substrate, while a G_c=0.625 J/m^2 is adopted for the iCVD-coated plate based on the toughness reduction factor.
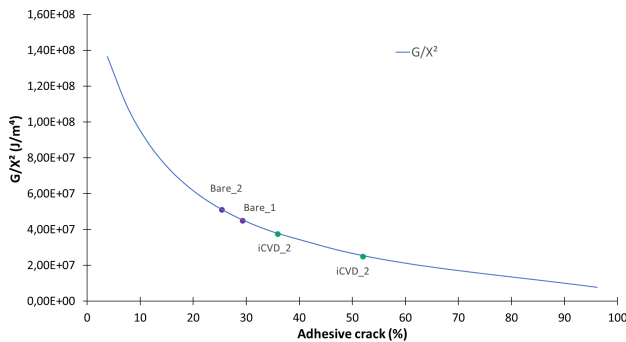
Figure 2: $\frac{G}{X^2}$ numerical curve and experimental values obtained for the bare aluminum and the iCVD-coated aluminum samples.

4   FRACTURE MECHANISMS EVALUATION

Numerical calculations are used to determine the amplitudes required to initiate a fracture for the three fracture mechanisms (initiation of fractures by tensile strength, shear strength or energy release rate) when exciting the first flexural mode. The critical properties are kept the same for the two stress-dominated mechanisms (σ_c=3 MPa, τ_c=1 MPa), while the toughness is varied to verify its effect on the fracture mechanism. Figure 3a shows the plotted curves for G_c=1 J/m^2. It can be observed that adhesive initiation becomes more favorable than the creation of cohesive cracks when approximately 78% of the sample's surface is covered with ice. Assuming a lower interfacial toughness (G_c=0.625 J/m^2), adhesive initiation becomes the dominant mechanism when 82% of the surface is covered with ice (see figure 3b).

The fracture mechanisms have been experimentally verified through testing samples with a 100%, 80% and 60% ice coverage and a 3 mm ice thickness. After the ice layer is formed, a low-voltage sweep (20 Vpk) is performed to identify the resonant frequency, which is then excited at 200 Vpk. Each test is repeated at least twice. Figure 4 shows that both the bare and coated plates (figures 4a and 4b respectively) experience cohesive fracture at the antinode when covered with 100% ice. However, when

covered with ice on 80% of their surface, two different fracture mechanisms are observed. The bare sample still exhibits cohesive fracture at the center of the ice layer (figure 4c), while the iCVD-coated sample shows adhesive propagation from the lower edge of the ice layer towards the center (figure 4d). For 60% ice coverage, the fracture mechanism changes from cohesive to adhesive for both samples (figures 4e and 4f). The difference in fracture mechanism for the samples covered with ice on 80% of their surface is attributed to the different interfacial properties. As previously mentioned, it is due to the fact that the toughness at the interface between the iCVD-coated sample is lower than that of the bare sample.

It is important to consider the effectiveness of de-icing. The first flexural mode typically only propagates the fracture without complete delamination from the sample. While the icephobic coating may improve propagation or alter the fracture mechanism, it does not lead to ice detachment. The properties of the interface are altered, but there is no significant improvement in de-icing. As shown in Figure 2, the energy release rate of the flexural mode decreases significantly as the fracture propagates. It may be advantageous to use modes, such as extensional modes, for which the trend of the energy release rate is more stable and the contribution of the coating is more evident [11, 14].

5   CONCLUSIONS

The study compares the interfacial toughness and the de-icing capabilities of two different samples equipped with an electromechanical de-icing system: a bare aluminum sample and an icephobic sample coated with a gradient polymer coating via initiated chemical vapor deposition. The interfacial toughness is verified qualitatively through a hybrid experimental and numerical study. The plates are excited at the resonant frequency of the first flexural mode. The extent of adhesive fracture propagation is measured and reported on the $\frac{G}{X^2}$ plot obtained numerically, providing information on the G_c of the two interfaces. The results indicate that the coated surface has lower interfacial toughness. Based on this information, numerical calculations are performed to determine the curves required to trigger different fracture mechanisms in relation to the amount of the sample's surface covered with ice using two different values of G_c. A lower value of toughness implies a change in the fracture mechanism from cohesive to adhesive for a greater amount of ice. The numerical results are then experimentally validated through testing of the two samples with varying degrees of ice coverage: 100%, 80%, and 60%. The sur-

(a) $G_c = 1$ J/m^2

(b) $G_c = 0.625$ J/m^2
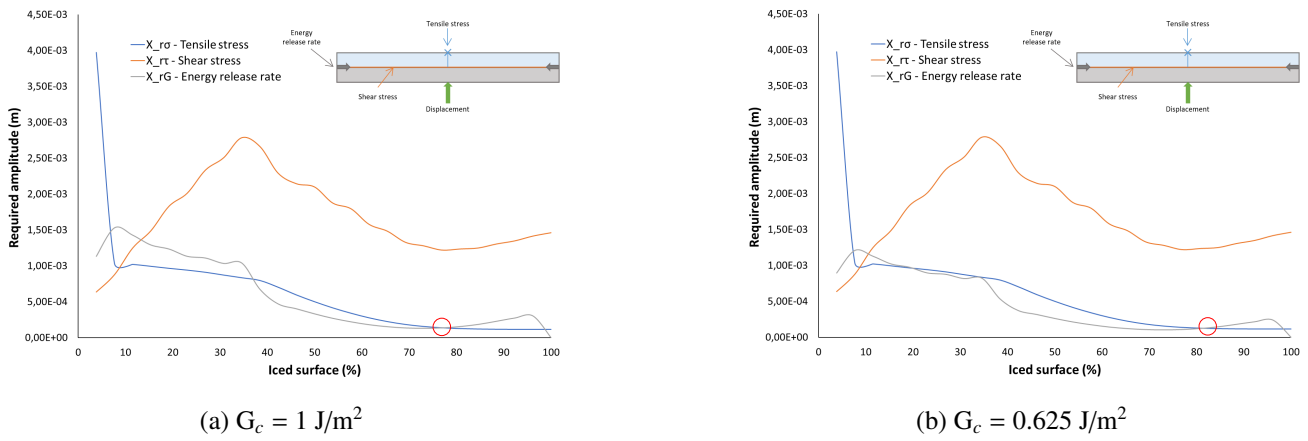
Figure 3: The amplitudes necessary to initiate fracture for the three fracture mechanisms when exciting the first flexural mode.

(a) Bare sample 100% ice: Cohesive crack

(b) Coated sample 100% ice: Cohesive crack

(c) Bare sample 80% ice: Cohesive crack

(d) Coated sample 80% ice: Adhesive crack

(e) Bare sample 60% ice: Adhesive crack

(f) Coated sample 60% ice: Adhesive crack
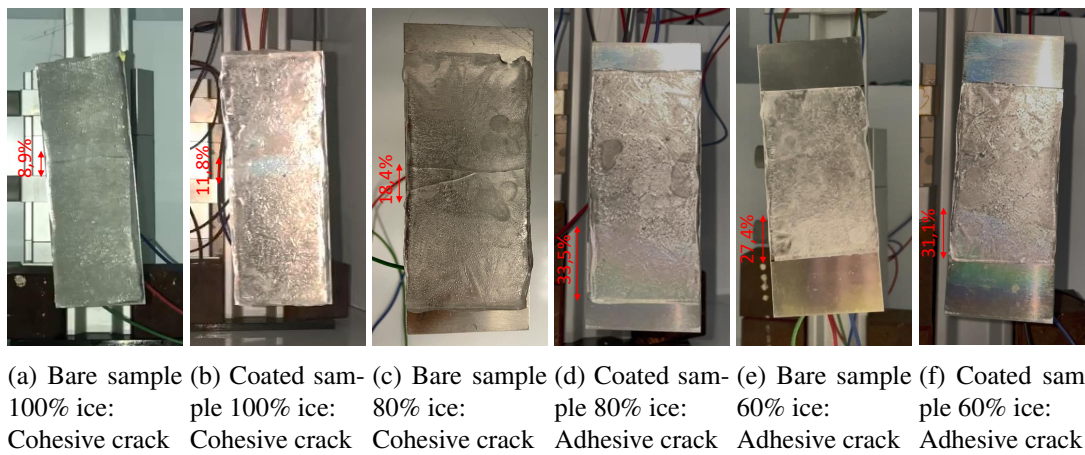
Figure 4: Fracture mechanism depending on the ice length for the first flexural mode (200Vpk de-icing).

face coated with an icephobic coating shows a change in fracture mechanism when 80% of the surface is covered with ice. This confirms the influence of coatings on de-icing mechanisms.

6   ACKNOWLEDGMENTS

REFERENCES

[1] Y. Cao, W. Tan, Z. Wu, Aircraft icing: An ongoing threat to aviation safety, Aerospace science and technology 75 (2018) 353–385.

[2] V. Pommier-Budinger, M. Budinger, P. Rouset, F. Dezitter, F. Huet, M. Wetterwald, E. Bonaccurso, Electromechanical resonant ice protection systems: initiation of fractures with piezoelectric actuators, AIAA Journal 56 (11) (2018) 4400–4411.

[3] C. Laforte, J. Laforte, J. Carrière, How a solid coating can reduce the adhesion of ice on a structure, in: Proceedings of the international workshop on atmospheric icing of structures (IWAIS), Vol. 6, 2002.

[4] L. Cao, A. K. Jones, V. K. Sikka, J. Wu, D. Gao, Anti-icing superhydrophobic coatings, Langmuir 25 (21) (2009) 12444–12448.

[5] Y. Ibrahim, R. Kempers, A. Amirfazli, 3d printed electro-thermal anti-or de-icing system for composite panels, Cold Regions Science and Technology 166 (2019) 102844.

[6] C. Antonini, M. Innocenti, T. Horn, M. Marengo, A. Amirfazli, Understanding the effect of super-hydrophobic coatings on energy reduction in anti-icing systems, Cold regions science and technology 67 (1-2) (2011) 58–67.

[7] T. Strobl, S. Storm, M. Kolb, J. Haag, M. Hornung, Development of a hybrid ice protection system based on nanostructured hydrophobic surfaces, in: 29th Congress of the International Council of the Aeronautical Sciences, 2014, pp. 1–12.

[8] G. Gastaldo, V. Palanque, M. Budinger, V. Pommier-Budinger, Stress and energy release rate influence on ice shedding with resonant electro-mechanical de-icing systems, in: ICAS 2022-33rd Congress of the International Council of the Aeronautical Sciences, 2022.

[9] K. Golovin, A. Dhyani, M. Thouless, A. Tuteja, Low–interfacial toughness materials for effective large-scale deicing, Science 364 (6438) (2019) 371–375.

[10] A. A. Griffith, Vi. the phenomena of rupture and flow in solids, Philosophical transactions of the royal society of london. Series A, containing papers of a mathematical or physical character 221 (582-593) (1921) 163–198.

[11] M. Budinger, V. Pommier-Budinger, A. Reysset, V. Palanque, Electromechanical resonant ice protection systems: energetic and power considerations, AIAA Journal 59 (7) (2021) 2590–2602.

[12] G. Hernandez Rodriguez, M. Fratschko, L. Stendardo, C. Antonini, R. Resel, A. M. Coclite, Icephobic gradient polymer coatings deposited via icvd: A novel approach for icing control and mitigation, ACS Applied Materials & Interfaces (2024).

[13] V. Palanque, A. Marbœuf, M. Budinger, V. Pommier-Budinger, L. Bennani, Improving mechanical ice protection systems with substrate thickness and topology optimization, In preparation (2021).

[14] G. Gastaldo, M. Budinger, Y. Rafik, V. Pommier-Budinger, V. Palanque, A. Yaich, Full instantaneous de-icing using extensional modes: The role of architectured and multilayered materials in modes decoupling, Ultrasonics (2024) 107264.

Thermally Sprayed Coatings on Concrete for Icephobic Protection in Sea Water Environments

Betül Aktas[1], Magdalena Rajczakowska[2], Niklas Kandelin[1], Andrzej Cwirzen[2], Heli Koivuluoto[1]

[1]*Tampere University, Faculty of Engineering and Natural Sciences, Materials Science and Environmental Engineering, Korkeakoulunkatu 6, 33720 Tampere, Finland*
[2]*Luleå University of Technology, Department of Civil, Environmental and Natural Resources Engineering, 97187 Luleå, Sweden*

betul.aktas@tuni.fi, magdalena.rajczakowska@ltu.se, niklas.kandelin@tuni.fi, andrzej.cwirzen@ltu.se, heli.koivuluoto@tuni.fi

Abstract— The growing demand for renewable energy has increased the use of offshore wind turbines, requiring sturdy infrastructure. However, environmental challenges impact not only the turbine components but also the foundations in the water. Different foundation structures exist for varying sea-bed conditions, each with material durability pros and cons. Concrete, a common choice for shallow shores, contributes significantly to the industry's carbon footprint. Eco-friendly concrete alternatives aim to reduce environmental impact but may lead to variable performance. This study explores thermally sprayed coatings on eco-friendly concrete surfaces to enhance icephobic performance in seawater conditions, crucial for offshore wind turbine foundations. Multilayered coating system is created using flame spraying of PE and electric arc spraying of Zn. Extensive testing, including simulated seawater conditions, evaluates coating efficacy in solving ice-related challenges. The findings offer valuable insights into the performance of thermally sprayed coatings, providing innovative solutions for marine environments.

Keywords— *thermal spraying, icephobic coating, sea water, ice adhesion*

I. INTRODUCTION

The global demand for renewable energy sources continues to escalate [1], [2], urging the exploration and implementation of innovative offshore energy solutions. Among these, offshore wind farms stand out as promising contributors to sustainable energy production. With their potential to harness vast wind resources from large oceanic territories, offshore wind farms offer clean energy generation [3]. However, the efficacy and environmental sustainability of such structures determined by structural integrity and ecological footprint.

Offshore wind turbines rely on concrete foundations (gravity type) to secure stability in shallow waters [4]. While concrete structures provide robust support, they pose significant environmental challenges, primarily due to their substantial carbon footprint [5]. The production of concrete contributes significantly to greenhouse gas emissions, thereby undermining the ecological benefits of renewable energy generation of offshore windfarms. Therefore, eco-friendly concrete is designed to reduce the carbon footprint of concrete [6]. However, reducing the carbon footprint comes at a price. Eco-friendly concrete can be susceptible to environmental factors [6]. In the case of offshore wind farms, the harsh marine environment presents additional impact on concrete foundations. Exposure to seawater intensifies concerns of corrosion, water intrusion, and the formation of ice on a cold climate region, which can lead to issues lowering the performance of these structures [7], [8], [9]. Despite

advancements in eco-friendly concrete formulations, the susceptibility of such materials to environmental stressors remains a pressing issue.

The icing problem itself has been studied over the years for different structures and several approaches have been developed: active and passive. Active solutions involve methods where external energy is applied to prevent or remove ice formation, such as by using heaters [10], [11], [12] or deicing fluids [13], [14]. These methods require ongoing power input and maintenance. In contrast, passive solutions employ materials or designs that naturally mitigate icing, like anti-icing or icephobic coatings. Passive solutions tend to be more sustainable and cost-effective in the long term, as they operate without continuous energy consumption. Icephobicity is correlated with low ice adhesion strength, however it has not been fully standardized yet. It is widely accepted that ice adhesion strength lower than 100 kPa indicates icephobicity [15], [16], [17]. Icephobic coatings can be produced by variety of methods including thermal spraying [16], [17], [18].

Icing in marine environment differs from atmospheric icing. The formation of ice, consequently the ice type is different as well as the water salinity. Sea water differs from fresh water in terms of freezing characteristics as salts inside the water change the freezing temperature and other characteristics [19]. Sea water involves various dissolved ions, mostly chloride and sodium. Phase diagram of pure water changes vastly with the addition of NaCl, as freezing point decreases and different compounds form [20]. Phase diagram of water and NaCl is given in Figure 1. According to the phase diagram, in order to achieve full solidification of saline water, the temperature has to be lower than the eutectic temperature (21.1 $^\circ C$).
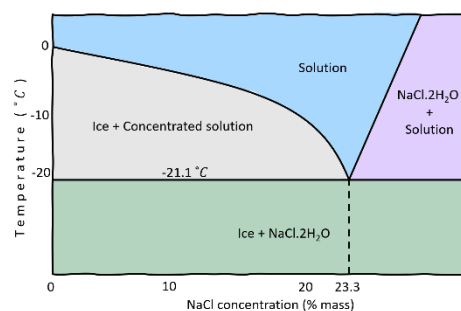
Figure 1 A part of the water-NaCl phase diagram showing the eutectic temperature at -21 $^\circ C$. (Modified from [20].)

In this research, multilayered coating system was developed to protect eco-friendly concrete from icing and

corrosion. The coating was composed of icephobic outer layer and anti-corrosive bond layer on concrete surface. Based on the previous studies [16], [21], polyethylene (PE) was selected as icephobic layer material and produced by flame spraying. However, considering the challenges related to adhesion of PE coating on concrete substrate and to corrosion protection, zinc (Zn) bond layer was produced by electric arc spraying. It is well-established that Zn exhibits corrosion resistance [22], [23], [24], [25], [26]. Multilayered coatings were characterized and tested for ice adhesion strength. Water with different salinities was employed for icing tests. Since the current testing equipment requires specific sample size, coatings on stainless steel (SS) substrates were tested under icing conditions.

II. EXPERIMENTAL PROCEDURE

A. Concrete

Concrete was produced using 50% Ground granulated blast furnace slag (GGBS) (Merit, Merox, Sweden) as a partial replacement for Portland cement, ensuring both high strength and reduced environmental impact. The water-to-binder (w/b) ratio was set at 0.42, with a binder content of 400 kg/m³. The fillers used were quartz Norquartz 45 (Sibelco Nordic, Norway) and fine sand B15 (Baskarpsand AB, Sweden). In addition, the aggregate, which was provided by Jehander Heidelberg Cement Group, had a particle size range of 0-8 mm. The concrete was mixed using a 75-liter rotating pan mixer, model Zyklos-ZZ75HE. After casting, the specimens were submerged in water for a curing period of 28 days, and the compressive strength measured at that time reached 80 MPa.

B. Coating production

Coatings on concrete were produced in two steps. First, the bond layer was produced manually by electric arc spraying (Smart Arc PPG Electric Arc Gun, Oerlikon Metco, Pfäffikon, Schwyz, Switzerland) of Zn wires (Vertic Zinc Wire Oy, Finland) on concrete that was grit-blasted with fine glass balls (40-70 µm). Then, icephobic coating was produced by flame spraying of polyethylene (PE) powder (Plascoat Systems Limited, Zuidland, The Netherlands). For flame spraying, CastoDyne DS 800 gun (Castolin Eutectic, Dällikon, Switzerland) was used. The speed of the gun was 750 mm/s, and the distance of the gun from the substrate was 300 mm. Oxygen and acetylene gases were used to obtain the flame. The pressures for the combustion gases were 4.0 bar and 0.7 bar, respectively. 6 layers of PE coating were deposited on bond layer and smoothened by post heating. The same spraying procedure was repeated with stainless steel substrates to be able to test the coating material with the current testing set-up. Electric arc spraying of Zn on SS was done with a robot by using the gun speed of 900 mm/s, gun distance of 150 mm, and process parameters as; current of 200 A, voltage of 30 V, and air pressure of 2.5 bar.

C. Surface characterization

Surface textures were analyzed by optical profilometer (Alicona Infinite Focus G5, Alicona Imaging GmbH, Graz, Austria) over 8 mm x 8 mm area. Areal roughness value, Sa, was obtained over the same areal measurement by using Surface Texture Measurement module in MeasureSuite software (Alicona Imaging GmbH, Graz, Austria).

Wetting properties were analyzed with a droplet shape analyzer (DSA, DSA100, KRÜSS Scientific, Hamburg, Germany) by measuring the static contact angles. Measurements were done in a temperature and humidity-controlled room (+23 ºC and 50 ± 2 % humidity) by following the standard sessile-drop method. 9 droplets per sample were measured by placing 5 µL ultra-high pure water droplet (MilliQ, Millipore Corporation, Burlington, MA, USA) on the sample surface. The results are presented as averages of 9 measurements with their standard deviations.

D. Saline water molded ice adhesion testing

PE coatings on Zn bond-coated SS and on SS substrates were tested under saline icing conditions. Five samples for each type of substrates were tested Results are presented as an average of five measurements with their standard deviations. Testing was carried out in Ice Laboratory at Tampere University. 0.1 wt % NaCl and 1 wt % NaCl water solutions were prepared and poured into 3D-printed 10 x 23 x 23 mm (H x W x D) PET-G molds to obtain ice cubes on the sample surfaces at -25 °C. Samples stayed in the cold conditions about an hour prior to pushing test. Pushing type ice adhesion test was carried out also in the same cold conditions. Test set-up is given in Figure 2. Knowing the force required to detach the ice, F, and the ice coverage area, A, ice adhesion strength, τ was calculated for each sample using the equation 1.

$$\tau = F/A \qquad \text{(EQ. 1)}$$

The same ice molding and ice adhesion testing was done with pure water for comparison. For pure water, three samples per substrate type were tested.
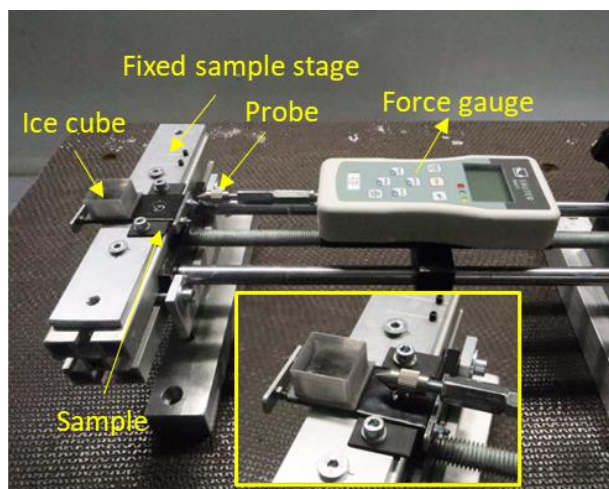
Figure 2 Pushing test set-up at Tampere University, Ice Laboratory.

III. RESULTS AND DISCUSSION

Digital camera images of flame sprayed PE coatings on concrete and SS substrate are presented in Figure 3 and schematics are provided next to the corresponding images. As it is clearly shown in the images, coatings on concrete and SS are visually identical. As the main idea is to evaluate the outermost icephobic layer under icing conditions, testing was done with the coatings on SS substrates. However, to examine effects of bond layer on the final surface quality, coating systems on SS were produced with and without the bond layer.

Figure 3 Digital images of coatings on concrete and SS substrates together with their schematics of the structure.

Wetting properties of the coating surfaces were analyzed by measuring static contact angles (CA). The result is given in Table 1.

Table 1 Results of contact angle (CA) measurements for each sample.

Sample	CA (°)
SS // Zn // PE	94 ± 3.6
SS // PE	90 ± 4.6
Concrete // Zn // PE	96 ± 3.2
Concrete	50 ± 10.4

Contact angle measurements revealed the hydrophobic behavior of PE coating, which is in the line with the previous studies by Koivuluoto et al. [16] and Donadei et al. [21]. Having a bond layer promoted hydrophobicity even further. Flame sprayed PE coating on SS without a bond layer recorded CA of 90° ± 4.6 whereas PE coating on bond layered SS had CA of 94° ± 3.6. Coated concrete sample achieved a similar level of hydrophobicity (96° ± 3.2), indicating identical surface properties of the coating on different substrates. As comparison, bare concrete sample had the CA of 50° ± 10.4, which was showing that water spreads on the surface, indicating hydrophilic behavior. The surface wettability results proved that flame sprayed PE coating improved hydrophobicity.

Figure 4 shows the textures of different samples and corresponding surface roughness, Sa, values. Similar to the wetting results, having the bond layer slightly affected the surface roughness values. The PE surface without the bond layer (SS // PE) had the smoothest surface with the Sa value of 1.89 µm. Introducing the bond layer changed the areal roughness value to 2.48 µm, as it is shown for SS // Zn // PE. However, this difference was small compared to the areal roughness of reference concrete, which was 22.55 µm. Coating on concrete reduced the areal roughness value to 2.19 µm. Surface wettability and roughness values showed similar results for PE surfaces with and without bond layer, on SS and on concrete. Therefore, it can be concluded that surface properties of PE coating are not affected by the substrate type.
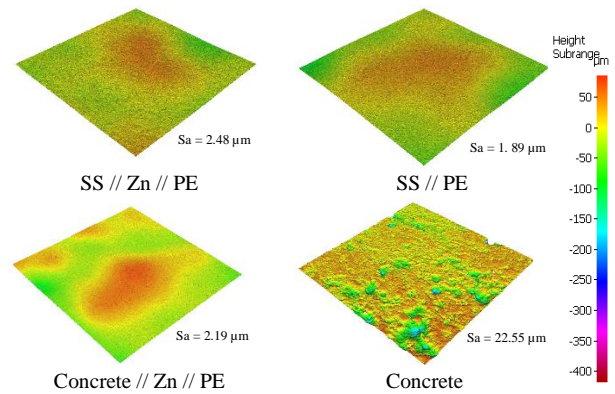
Figure 4 Surface textures of PE coating on SS substrate, PE coating with bond layer on SS substrate, and concrete with duplex coating system and reference concrete. Sa values are given next to the corresponding images.

Flame sprayed PE coating has shown low ice adhesion strength in the previous studies [16], [21]; in which wind tunnel assisted ice accretion was employed by using pure water at $-10°C$. However, in our current research, ice was created by molding of water with different salinities at $-25°C$. The result is given in Figure 5 for PE coating with and without the bond layer and for the bare concrete. PE coating on Zn bond layer (SS//Zn//PE) had the pure water ice adhesion strength of 95 kPa, similarly, without the bond layer, the similar PE coating (SS//PE) had the ice adhesion strength of 93 kPa. The slight difference between these samples lies within the standard deviation.
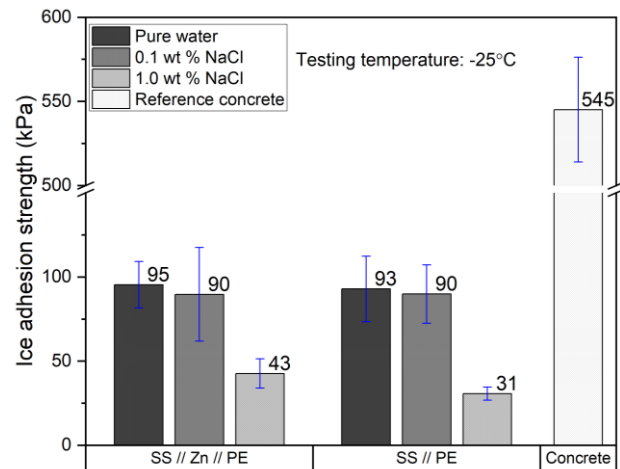
Figure 5 Ice adhesion strengths of SS // Zn // PE and SS // PE with different salinity level of water. Ice adhesion strength of concrete is also presented as a reference.

Saline water ice adhesion strength results were different than pure water ice adhesion strength, even the ice itself had different visual features (Figure 6). Results showed that the increase in the salinity level of water causes a decrease in ice adhesion strength. In the case of 0.1 wt % NaCl solution, ice adhesion strengths of both PE coatings with and without the bond layer were slightly less than pure water ice adhesion strengths of the parallel samples. Both PE coatings with and without the bond layer had the ice adhesion strength of 90 kPa. Ice adhesion strengths of samples with 1.0 wt % NaCl solution were significantly lower, as higher salinity resulted in brine

formation at the interface which decreased the ice adhesion strength [27]. PE without the bond layer (SS//PE) achieved lower saline water ice adhesion strength (31 kPa) than PE with the bond layer (SS//Zn//PE) (43 kPa). The slight difference might be caused by the higher roughness of SS//Zn//PE (Figure 4) On the other hand, the concrete sample had extremely high ice adhesion strength (545 kPa). The testing of concrete was done with different salinities of water but reported as an average of those values as in each test the ice failed cohesively and got stuck in the surface groves of concrete. Moreover, the concrete samples had different thickness which affected where the ice was pushed from. All in all, the reference value was provided for a rough comparison. These results showed that flame sprayed PE coating is a suitable material for concrete protection against icing in marine conditions.
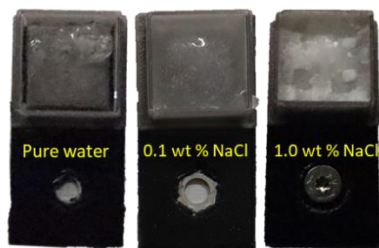
Figure 6 Molded ice with different salinity. Higher salinity resulted in less transparent ice.

IV. CONCLUSIONS

Addressing the negative environmental effects posed by producing concrete foundations of offshore wind farms requires innovative solutions that balance structural integrity with ecological sustainability. Ecological concrete could overcome the problems regarding the carbon footprint but leads to reduced performance. This study proposes a multilayered coating system incorporating icephobic and anti-corrosive layers to mitigate the impact of icing and salty conditions on eco-friendly concrete. Through testing and characterization, the effectiveness of the coating in reducing ice adhesion strength was demonstrated, offering a potential solution towards improving the resilience of the material systems in harsh marine environments. Further research is required to replicate the marine environment better, to study corrosion effect on concrete and ice friction on the coatings.

REFERENCES

[1] "Clean sources of generation are set to cover all of the world's additional electricity demand over the next three years." Accessed: Mar. 28, 2024. [Online]. Available: https://www.iea.org/news/clean-sources-of-generation-are-set-to-cover-all-of-the-world-s-additional-electricity-demand-over-the-next-three-years

[2] "Renewable energy will produce 35% of global electricity by 2025." Accessed: Mar. 28, 2024. [Online]. Available: https://www.weforum.org/agenda/2023/03/electricity-generation-renewables-power-iea/

[3] "Offshore renewable energy." Accessed: Mar. 28, 2024. [Online]. Available: https://energy.ec.europa.eu/topics/renewable-energy/offshore-renewable-energy_en#offshore-wind-energy

[4] C. Lavanya and N. D. Kumar, "Foundation Types for Land and Offshore Sustainable Wind Energy Turbine Towers," in *E3S Web of Conferences*, EDP Sciences, Aug. 2020. doi: 10.1051/e3sconf/202018401094.

[5] J. Watts, "Concrete: the most destructive material on Earth," 2019. Accessed: Mar. 27, 2024. [Online]. Available: https://www.theguardian.com/cities/2019/feb/25/concrete-the-most-destructive-material-on-earth

[6] A. Kothari, K. Habermehl-Cwirzen, H. Hedlund, and A. Cwirzen, "A Review of the Mechanical Properties and Durability of Ecological Concretes in a Cold Climate in Comparison to Standard Ordinary Portland Cement-Based Concrete," *Materials 2020, Vol. 13, Page 3467*, vol. 13, no. 16, p. 3467, Aug. 2020, doi: 10.3390/MA13163467.

[7] E. M. Schulson, "Ice Damage to Concrete," 1998. [Online]. Available: http://www.crrel.usace.army.mil

[8] S. W. Tang, Y. Yao, C. Andrade, and Z. J. Li, "Recent durability studies on concrete structure," *Cem Concr Res*, vol. 78, pp. 143–154, Dec. 2015, doi: 10.1016/J.CEMCONRES.2015.05.021.

[9] M. G. Stewart and D. V. Rosowsky, "Time-dependent reliability of deteriorating reinforced concrete bridge decks," *Structural Safety*, vol. 20, no. 1, pp. 91–109, 1998, doi: 10.1016/S0167-4730(97)00021-0.

[10] O. Parent and A. Ilinca, "Anti-icing and de-icing techniques for wind turbines: Critical review," *Cold Reg Sci Technol*, vol. 65, no. 1, pp. 88–96, Jan. 2011, doi: 10.1016/J.COLDREGIONS.2010.01.005.

[11] J. Yang *et al.*, "Prefabricated Flexible Conductive Composite Overlay for Active Deicing and Snow Melting," *Journal of Materials in Civil Engineering*, vol. 30, no. 11, p. 04018283, Aug. 2018, doi: 10.1061/(ASCE)MT.1943-5533.0002473.

[12] H. Wei, Z. Ma, L. Han, B. Jiang, and S. Han, "Durability of Conductive Ethylene–Propylene–Diene Monomer Rubber Composite with Active Deicing and Snow Melting under Vehicle Load," *Journal of Materials in Civil Engineering*, vol. 34, no. 5, p. 04022055, Feb. 2022, doi: 10.1061/(ASCE)MT.1943-5533.0004192.

[13] D. M. Ramakrishna and T. Viraraghavan, "Environmental impact of chemical deicers - A review," *Water Air Soil Pollut*, vol. 166, no. 1–4, pp. 49–63, Sep. 2005, doi: 10.1007/S11270-005-8265-9/METRICS.

[14] E. Huttunen-Saarivirta, V. T. Kuokkala, J. Kokkonen, and H. Paajanen, "Corrosion effects of runway de-icing chemicals on aircraft alloys and coatings," *Mater Chem Phys*, vol. 126, no. 1–2, pp. 138–151, Mar. 2011, doi: 10.1016/J.MATCHEMPHYS.2010.11.049.

[15] V. Hejazi, K. Sobolev, and M. Nosonovsky, "From superhydrophobicity to icephobicity: forces and interaction analysis," *Scientific Reports 2013 3:1*, vol. 3, no. 1, pp. 1–6, Jul. 2013, doi: 10.1038/srep02194.

[16] H. Koivuluoto, E. Hartikainen, and H. Niemelä-Anttonen, "Thermally sprayed coatings: Novel surface engineering strategy towards icephobic solutions," *Materials*, vol. 13, no. 6, Mar. 2020, doi: 10.3390/ma13061434.

[17] R. Khammas and H. Koivuluoto, "Durable Icephobic Slippery Liquid-Infused Porous Surfaces (SLIPS) Using Flame- and Cold-Spraying," *Sustainability*, vol. 14, no. 14, p. 8422, Jul. 2022, doi: 10.3390/su14148422.

[18] H. Koivuluoto, C. Stenroos, M. Kylmälahti, M. Apostol, J. Kiilakoski, and P. Vuoristo, "Anti-icing Behavior of Thermally Sprayed Polymer Coatings," *Journal of Thermal Spray Technology*, vol. 26, no. 1–2, pp. 150–160, Jan. 2017, doi: 10.1007/S11666-016-0501-X/FIGURES/8.

[19] D. Saha, S. R. Dehghani, K. Pope, and Y. Muzychka, "Temperature distribution during solidification of saline and fresh water droplets after striking a super-cooled surface," *Arctic Technology Conference 2016*, 2016, doi: 10.4043/27421-MS.

[20] A. A. C. Bode *et al.*, "Sodium Chloride Dihydrate Crystals: Morphology, Nucleation, Growth, and Inhibition," *Cryst Growth Des*, vol. 15, no. 7, pp. 3166–3174, Jul. 2015, doi: 10.1021/ACS.CGD.5B00061/SUPPL_FILE/CG5B00061_SI_002.CIF.

[21] V. Donadei, H. Koivuluoto, E. Sarlin, and P. Vuoristo, "Icephobic Behaviour and Thermal Stability of Flame-Sprayed Polyethylene Coating: The Effect of Process Parameters," *Journal of Thermal Spray Technology*, vol. 29, no. 1–2, pp. 241–254, Jan. 2020, doi: 10.1007/s11666-019-00947-0.

[22] H. Koivuluoto, "Corrosion resistance of cold-sprayed coatings," in *Cold-Spray Coatings: Recent Trends and Future perspectives*, Springer International Publishing, 2017, pp. 373–392. doi: 10.1007/978-3-319-67183-3_13/FIGURES/15.

[23] G. Jiang, G. Liu, T. Shang, and W. Qiu, "Corrosion Properties of Steel Sheet with Zinc-Base Alloy Coatings," *Minerals, Metals and Materials Series*, pp. 949–957, 2019, doi: 10.1007/978-3-030-05861-6_93/COVER.

[24] O. Dolgikh *et al.*, "Corrosion protection of steel cut-edges by hot-dip galvanized Al(Zn,Mg) coatings in 1 wt% NaCl: Part I. Experimental study," *Materials and Corrosion*, vol. 70, no. 5, pp. 768–779, May 2019, doi: 10.1002/MACO.201810209.

[25] W. Chen *et al.*, "Friction and anti-corrosion characteristics of arc sprayed Al+Zn coatings on steel structures prepared in atmospheric environment," *Journal of Materials Research and Technology*, vol. 15, pp. 6562–6573, Nov. 2021, doi: 10.1016/J.JMRT.2021.11.084.

[26] C. Senderowski, W. Rejmer, N. Vigilianska, and A. Jeznach, "Changes in Corrosion Behaviour of Zinc and Aluminium Coatings with Increasing Seawater Acidification," *Materials 2024, Vol. 17, Page 536*, vol. 17, no. 3, p. 536, Jan. 2024, doi: 10.3390/MA17030536.

[27] W. Luo, K. Alasvand Zarasvand, Z. Azimi Dijvejin, A. V. Nadaraja, and K. Golovin, "Influence of Salinity on Surface Ice Adhesion Strength," *Adv Mater Interfaces*, Jan. 2023, doi: 10.1002/ADMI.202300606.

Superhydrophobic coatings for aeronautical applications

Filomena Piscitelli

Italian Aerospace Research Centre – CIRA via Maiorise, 81043 Capua, Italy

f.piscitelli@cira.it

Abstract— **In this work, the main properties of a superhydrophobic coating's (SHC) family were presented. The Icing Wind Tunnel test campaigns performed on two test articles speech in favour of the utility of using the SHCs as passive Ice Protection Systems (IPS) in a temperature range of -3 to -12°C. These findings lay the foundations for the next steps in designing new coatings which could widen the range of conditions in which these coatings effort beneficial effects in reducing the accreted ice.**

Keywords— ***Superhydrophobic coatings, icephobic coatings, passive Ice Protection Systems, Icing Wind Tunnel tests, ice accretion, low wettability.***

I. Introduction

Aircraft icing has been widely recognized as a severe weather hazard to flight safety in cold climates, since the ice accretion on aircraft surfaces alters the flight aerodynamics, reducing lift and increasing weight and drag, thus leading to dangerous stall conditions with a temporary or permanent loss of control of the aircraft. Currently, to hinder the ice accretion dangers, active Ice Protection Systems (IPS) requiring energy are being employed, either to prevent icing (anti-icing) or to remove it (de-icing). The use of these active IPS, which can be thermal, electro-mechanic, electro-thermal, pneumatic, or a glycol-based fluid type, leads to an increase in construction complexity, weight, manufacturing, and management costs together with an increase of the on-board power consumption, and then of the CO_2 emissions [1]-[6]. Conversely, it would be highly desirable and advantageous if surfaces could passively reduce or delay the ice accretion and/or facilitate the ice removal. In this contest, superhydrophobic coatings (SHC) owing to their extraordinary water repellence, and not requiring additional energy consumption, can be viewed as excellent candidates as passive IPS [2],[7]. While active methods rely on energy input from an external system for the anti-/de-icing operations, passive methods take advantage of the physical properties of the airframe surfaces, such as the surface wettability, to prevent, delay, or reduce the ice formation and accretion [8],[9]. The combination of active and passive IPSs could be seen as a strategic instrument to assure high efficiency in a wide range of environmental conditions at reduced power consumption, so reducing the CO_2 emissions for more sustainable and efficient solutions for flight safety. Additionally, passive IPS can be highly helpful during take-off operations, since according to the Federal Aviation Administration regulation, the active IPSs cannot be activated until the aircraft reaches 400 feet above the take-off surface to avoid engine thrust reduction [10].

In this contest the Italian Aerospace Research Centre (CIRA) has been developing SHCs having water contact angles ranging between 157 and 169° and low Surface Free Energy. They were applied on two test articles, i.e., two NACA 0015 wing profiles and a nacelle lip-skin, and then tested in the CIRA Icing Wind Tunnel. Starting from results of both IWT test campaigns, some considerations have been formulated, useful to design new coating's formulations to be combined with active IPS.

II. Materials and methods

A. Coating's formulation

Nanostructured multilayer coatings developed at CIRA [11],[12] were applied with an aerograph using de-humified air at 3 bars. After application, each coating's layer was cured at 80 °C. The coating's formulations were tailored and optimized to the specific material's substrate and application, and, although little differences, the main coating's characteristics, such as the wettability and the Surface Free Energy (SFE), functional to the ice reduction, did not change.

B. Substrate pre-treatment

It was found that a substrate's sponge-like morphology guarantees a good adhesion of the coating on the substrates. On metallic surfaces the sponge-like morphology was achieved through the sand blasting process [13]; on composites surfaces, several methods were employed to achieve a good adhesion, among which the shot peened and the laser texturing [14]. After pre-treatment, surfaces were cleaned with Metaflex, bi-distilled water, isopropyl alcohol and ethyl alcohol.

C. Coating's characterization

After curing, the coatings were characterized in terms of:

1) roughness, using a SAMA SA6260 surface roughness meter, according to the ISO 4288 [15];

2) wettability as contact angle (CA) measurements, performed at 23°C in compliance with the ASTM D7490–13 [16] standard, with 3μL of water (H_2O), diiodomethane (CH_2I_2), and formamide ($HCONH2$);

3) SFE, assessed using the method described in [13] starting from the CAs measurements;

4) optical microscopy images, acquired with a microscope USB Dino-Lite AM4815ZTL;

5) coating's thickness measured according to ISO 2360 [17] using the Defelsko PosiTector 6000 FSN2, manufactured by DeFelsko Corporation, Ogdensburg, NY, USA.

6) coating's immersion tests performed at room temperature in two distinct aqueous solutions: a) 5 wt% NaCl in water and b) 0.1M NaOH [18] on stainless-steel flat samples.

D. IWT test facility

Icing wind tunnel (IWT) tests were performed in the CIRA IWT facility, which is a closed-loop circuit, refrigerated wind tunnel with three interchangeable test sections and one open jet configuration, whose main mission is to perform icing tests. The cloud generation for icing conditions simulation is carried out by the spray bar system, which is able to generate water droplets with diameters (median volumetric diameter—MVD) and concentrations (liquid water content—LWC) covering nearly all the envelope as prescribed by the CS-25 Appendix C for both continuous and intermittent cloud conditions.

E. IWT test articles and test conditions

1) Two wing profiles NACA0015 manufactured with a 3D printing machine, having a length of 135 mm and a chord of 100 mm made of acrylonitrile butadiene styrene (ABS). Two coating's formulations were applied on one-half of the test article as A1 and A2, leaving the other parts uncoated as reference (AR). The two samples were mounted with the two reference sides in opposite positions, as shown in Figure 1b, in order to minimize the effect of a possible cloud inhomogeneity. These tests were performed in the framework of the SMOS (SMart On-board Systems) project funded by The Italian Ministry for Education, University and Research (MIUR) through the National Aerospace Research Program (PRORA) D.M. 305/98 art. 4 comma 1 [19].

They were tested in the IWT test conditions detailed in TABLE I.

TABLE I. IWT TEST CONDITIONS FOR NACA0015 PROFILES.

TEST ID	Static T [°C]	V [m/s]	Altitude [m]	Static T [°C]	LWC [g/m3]	Exposure Time [s]
1	−22.98	94.9	3001	−22.98	0.602	79
2	−22.95	94.5	83	−22.95	0.553	77
3	−5.97	95.0	3002	−5.97	0.307	137
4	−3.10	50.0	3001	−3.10	0.297	227
5	−12.18	50.0	3000	−12.18	0.298	228
6	−7.96	95.0	3007	−7.96	0.293	72

2) A nacelle lip-skin belonging to the M28 PZL vehicle, with dimensions of 50 cm × 50 cm × 20 cm and made of stainless-steel (the piccolo tube anti-icing (PTAI)) and composite (the back side), in the framework of SAT-AM (More Affordable Small Aircraft Manufacturing) project Clean Sky JTICS2- 2015-CPW02-AIR-02-07 [20]. The reference vehicle was the M28 designed and manufactured by Consortium Partner Polskie Zakłady Lotnicze (PZL), Mielec (PL). It is a commuter category 19 passenger, twin-engine high-wing cantilever monoplane, suited for passenger and/or cargo transportation and certified under EU CS-23 and USA FAR 23 requirements. The test article was tested in the uncoated and coated configurations in the IWT test conditions detailed in TABLE II.

TABLE II. IWT TEST CONDITIONS FOR THE NACELLE LIP-SKIN.

TEST ID	T [°C]	v [m/s]	LWC [g/m3]	Exposure Time [s]
1	−5	70	0.3	140
2	−5	70	1	140
3	−12	70	0.3	140
4	−12	70	0.3	420
5	−5	95	0.3	140

III. RESULTS AND DISCUSSION

The developed coating's family was applied to several substrates made of ABS, carbon fibres/epoxy resins composites, with or without the application of a commercial aeronautical paint as reference, aluminium or stainless-steel surfaces. Roughness of substrates before the application of the coating ranged between 1 and 4 μm, which changes significantly after the coating's application according to the specific applied coating's formulation. The wettability of reference samples fell in the range 44-80°, becoming 155-169° after the application of the coating (see Fig. 1 as example). The SFE varied consequently from 35-50 mN/m for references and 0.05-2 mN/m for coated samples. Depending on the coating's formulation, the coating's thicknesses measured after the 80°C curing were 40-200 μm (see Fig. 2 as example). An example of sponge-like morphology achieved though the sand blasting on stainless-steel samples before and after the application of the SHC is shown in Fig. 3.
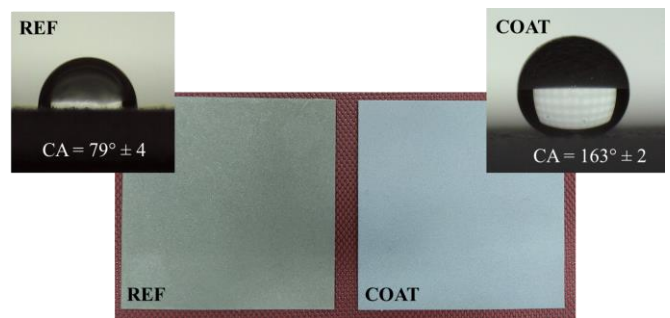
Fig. 1 Stainless steel 1.4301 flat samples before (REF) and after (COAT) the application of the SHC.

Fig. 2 Step followed for the measurements of the coating's thickness.

REF   COAT

20x   20x

a)   c)

80x   80x

b)   d)
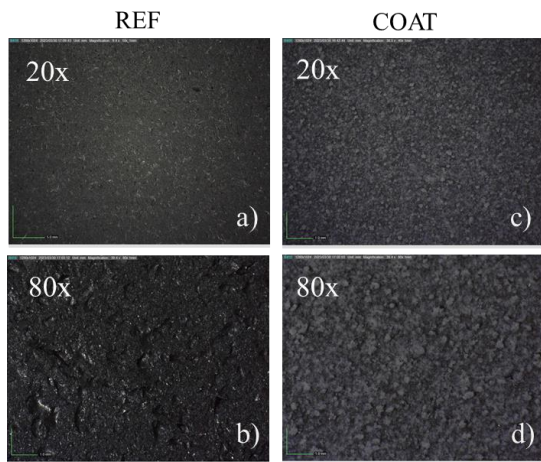
Fig. 3 Optical microscope images of reference (a, b) and coated (c, d) samples.

After 8 days in NaCl   After Cleaning

(a)   (b)

(c)   (d)
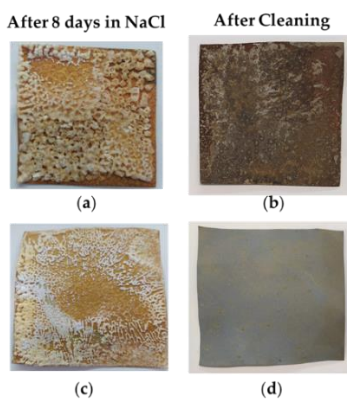
Fig. 4 Pictures of Reference (R) sample after 8 days in NaCl (a) and after cleaning (b), and of Coated (C) sample after 8 days in NaCl (c) and after cleaning (d).
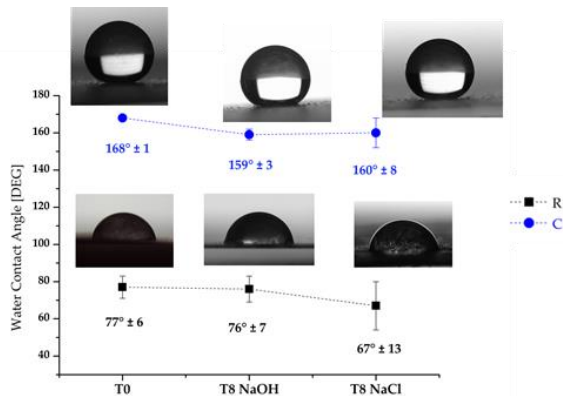
Fig. 5 Water contact angle at T=0 and after 8-days immersion in NaOH or NaCl for Reference (R) and Coated (C).

Main results of the coating's immersion tests shown in Fig. 4 and in Fig. 5 give evidence that the SHC passed the immersion tests since the surface retained its superhydrophobic properties even after an 8-day immersion in NaCl and NaOH solutions (see CA in Fig. 5). Additionally, it was found that the SHC notably reduced the corrosion extent, particularly in the challenging NaCl environment [22].

IWT test campaigns performed on the two wing profiles show that in rime ice conditions (test 1 and 2 in Fig. 6), the ice thickness t_{ice} measured at the stagnation point on A1 and

A2 was similar to or higher than those measured on AR; whereas in glaze ice conditions, in test 3 and test 6 of Fig. 6, the t_{ice} measured on A1 was reduced by −12 and −34%, respectively, with respect to the AR site; lower differences were observed in all other cases (data not shown for brevity [19]). The length of the compact ice L_{ci} measured starting from the impingement point is the second parameters describing the effect of the superhydrophobic surfaces on the ice accretion. As well as the t_{ice} measured on the impingement point, also the L_{ci} measured on the A1 site in test 1 and test 2 was +5% and −5%, respectively, compared to those measured on the AR. In both tests, L_{ci} on the A2 site was higher than the AR (+39 and +22%, respectively). A different scenario was observed in glaze ice conditions (tests 3, 4, and 6) and in test 5 (Fig. 6), for which L_{ci} measured on A1 and A2 was considerably lower than those measured on the AR (from −12 to −100%). Fig. 7 reports the difference of L_{ci} (ΔL_{ci}) measured on coated and reference surfaces as a function of the temperature, highlighting that L_{ci} measured on coated surfaces decreases as the temperature increases. So, the low wettability is helpful in reducing the accreted ice in a temperature range between -3 and -12°C, where the water droplets slip away before freezing. At lower temperatures, i.e. -20°C, the water droplets froze immediately after impacting to the surface.
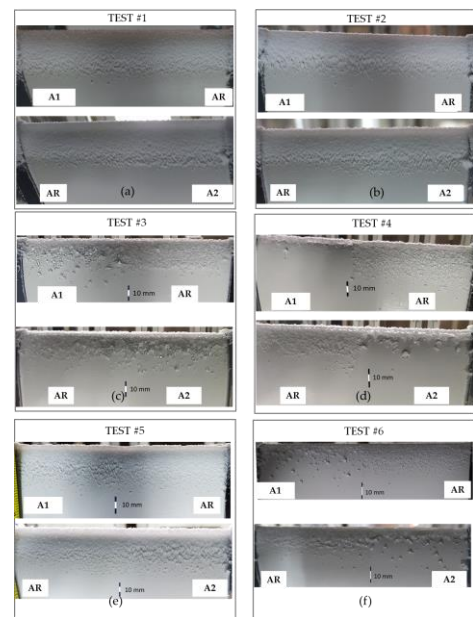
Fig. 6 Pictures of the ice accreted on the two wing profiles during the IWT tests. A1 and A2 are the coated parts, AR the reference side.
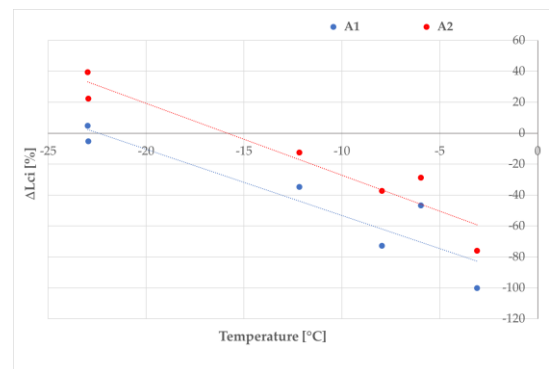
Fig. 7 Percentage variation in Lci of coated surfaces with respect to the references as a function of the tests' temperature.
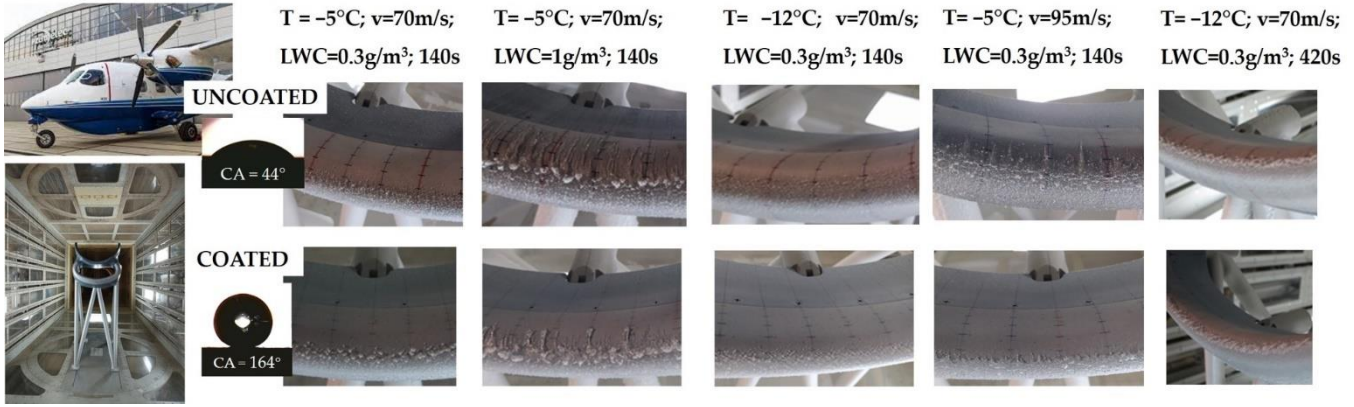
Fig. 8. IWT test carried out on the nacelle lip-skin.

IWT test results performed on the nacelle lip-skin are shown in Fig. 8 along with the pictures of the test article and the water droplets as a measure of the wettability of surface before (44°) and after (164°) the application of the SHC. Fig. 9 shows the percentage variation of t_{ice} and L_{ci} measured on coated test article with respect to the reference. Across the entire spectrum of test conditions investigated a reduction of t_{ice} was observed. The maximum t_{ice} reduction, i.e., −49% was recorded during the tests at −12 °C, matching to an increase in the impingement length of 0.5%. Significant t_{ice} reduction was measured at 95 m/s and at 420 s of exposure time, respectively, as −27% and −14%, respectively. L_{ci} reductions were −9.6% and −7.6%, respectively. At higher LWC a moderate reduction in the t_{ice}, i.e., −8%, matched to an increase in L_{ci}, i.e., 3.7% was observed. Nevertheless, the relevant finding at a higher LWC is the reduced length and number of the ice rivulets observed for the coated configuration.

After the two IWT test campaigns, the superhydrophobicity of surfaces was preserved.

Starting from the IWT tests' results, some consideration can be gathered. First, in the temperature range between -3°C and -12°C the low wettability of the SHC reduces the permanence time of water droplets on surfaces and then the probability of icing on the coated surfaces with respect to the uncoated ones. Second, at temperatures of -23°C the SHCs are not able to reduce the accreted ice, since the water droplets immediately froze after impacting to the surface, regardless the surface properties. These findings agree with Veronesi et al.[23] which tested slippery liquid-infuse (SLIPS) coatings in IWT in different conditions but same velocity, 50 m/s, to obtain glaze and rime regimes. Tested coatings displayed a decrease in ice accretion with respect to the uncoated surface in glaze conditions. In rime ice conditions not much improvement was observed compared with the reference. Good results in IWT tests performed on hydrophobic coatings at -8°C and 50 m/S was achieved also by Rivero et al. [24]. Differently, authors in [25] demonstrated that under both rime and glaze conditions the mass of ice accreted on all quasicrystals hydrophobic and superhydrophobic coatings was less than ice on standard metals.

Lastly, lesson learnt form the IWT results is that the thickness and the impingement length of the accreted ice largely depending on the geometrical configuration of the test article. As a consequence, it was found that the ice thickness variations observed in the first test campaign for tests carried out at temperatures ranging between −3 °C and −12 °C varied from −3% to −34% and from +5% to −5% for A1 and A2 coated configurations, respectively, whereas in the second test campaign the ice thickness reduction is more pronounced, ranging between −8% and −49%. The impingement length reduction with respect to the uncoated surfaces in the first test campaign ranged between −35% and −100% for A1, and −12% and −76% for A2, which becomes less pronounced in the second one, ranging between +3.7% and −10%.
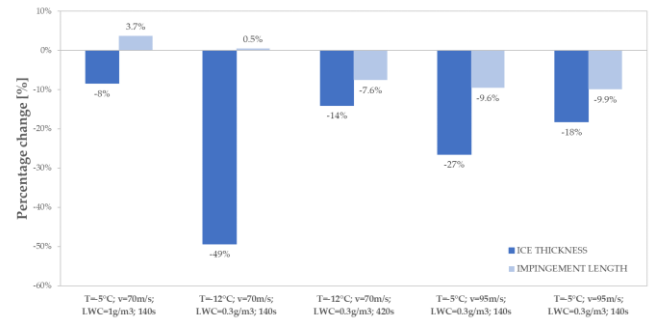
Fig. 9 Percentage variation of ice thickness (t_{ice}) and impingement length (L_{ci}) measured at investigated test conditions.

IV. CONCLUSIONS

The Italian Aerospace Research Centre (CIRA) has been developing SHCs having water contact angles ranging between 157 and 169° and low SFE. They were applied on two test articles, i.e., a NACA 0015 and a nacelle lip-skin, and then tested in the CIRA IWT, highlighting that the application of the SHCs reduces the accreted ice in temperatures ranging from -3°C to -12°C, velocities between 50 and 95m/s, and LWC ranging from 0.3 and 1g/m³.

In order to widen the beneficial effects of the coatings in reducing the accreted ice, next steps will be focused on the development of surfaces at low wettability and SFE, with low roughness, able to allow to the ice frozen on surfaces at temperatures lower than -12°C, to slip away by means of the aerodynamic forces. Ice adhesion measurements will be carried out on samples with similar surface chemistry but different roughness in order to correlate ice adhesion strength and roughness. This study will be preliminary for an optimized design of the aeronautical surfaces to be combined with active IPS for an energy-saving hybrid IPS.

References

[1] C. Antonini, M. Innocenti, T. Horn, M. Marengo et al., *Understanding the Effect of Superhydrophobic Coatings on Energy Reduction in Anti-icing System*. Cold Reg. Sci. Technol. 2011, 67, 58-67.

[2] G. Fortin, M. Adomou, J. Perron, *Experimental Study of Hybrid Anti-icing Systems Combining Thermoelectric and Hydrophobic Coatings*, SAE Technical Paper 2011-38-0003, 2011, doi:https://doi.org/10.4271/2011-38-0003.

[3] D. Mangini, C. Antonini, M. Marengo, A. Amirfazli *Runback Ice Formation Mechanism on Hydrophilic and Superhydrophobic Surfaces*. Cold Reg. Sci. Technol. 2015, 109, 53-60.

[4] T. Strobl, S. Storm, M. Kolb, J. Haag et al., *Development of a Hybrid Ice Protection System Based on Nanostructured Hydrophobic Surfaces*, in 29th Congress on International Council of Aeronautical Sciences, St. Petersburg, Russia, September, 2014, 7-12.

[5] F. Piscitelli, S. Ameduri, R. Volponi, L. Pellone et al., *Effect of Surface Modification on the Hybrid Ice Protection Systems Performances*, SAE Technical Paper 2023-01-1452, 2023, doi:10.4271/2023-01-1452.

[6] X. Huang, N. Tepylo, V. Pommier-Budinger, M. Budinger, E. Bonaccurso, P. Villedieu, L. Bennani *A survey of icephobic coatings and their potential use in a hybrid coating/active ice protection system for aerospace applications.* Prog. Aerosp. Sci. 105, 74–97, 2019.

[7] G. Fortin *Super-Hydrophobic Coatings as a Part of the Aircraft Ice Protection System*, SAE Technical Paper 2017-01-2139, 2017, https://doi.org/10.4271/2017-01-2139.

[8] D. Abhishek, et al. *Surface design strategies for mitigating ice and snow accretion*. Matter 5.5 (2022): 1423-1454.

[9] L. Zhou; X. Yi; Q. Liu *A Review of Icing Research and Development of Icing Mitigation Techniques for Fixed-Wing UAVs*. Drones 2023, 7, 709. https://doi.org/10.3390/drones7120709.

[10] FA Regulation. *Airworthiness Standard: Transport Category Airplanes Part 25 Appendix C Federal Aviation Administration*, Atlantic City International Airport, NJ 08405; 1982.

[11] F. Piscitelli, *Rivestimento Superidrofobico e Ghiacciofobico Di Un Substrato, Metodo per Il Suo Ottenimento e Substrato Così Rivestito*, Italian Patent N. IT102021000032444, December 23, 2021.

[12] F. Piscitelli, *Substrate Superhydrophobic and Icephobic Coating, Method for Obtaining It and Substrate Thus Coated*, International Patent Application N° PCT/IB2022/062672 2022, December 22, 2022.

[13] F. Piscitelli; A.Chiariello; D. Dabkowsk; G. Corraro; F. Marra; L. Di Palma, *Superhydrophobic Coatings as Anti-Icing Systems for Small Aircraft.* Aerospace 2020, 7, 2. https://doi.org/10.3390/aerospace7010002.

[14] F. Piscitelli; R. De Palo; A. Volpe *Enhancing Coating Adhesion on Fibre-Reinforced Composite by Femtosecond Laser Texturing*. Coatings 2023, 13, 928. https://doi.org/10.3390/coatings13050928.

[15] *ISO 4288*; Geometrical Product Specifications (GPS)–Surface Texture: Profile Method–Rules and Procedures for the Assessment of Surface Texture. International Organization for Standardization: Geneva, Switzerland, 1996.

[16] *D7490-13*; Standard Test Method for Measurement of the Surface Tension of Solid Coatings, Substrates and Pigments using Contact Angle Measurements. American Society for Testing and Materials: West Conshohocken, PA, USA, 2013.

[17] *ISO 2360:2017*; Non-Conductive Coatings on Non-Magnetic Electrically Conductive Base Metals—Measurement of Coating Thickness—Amplitude-Sensitive Eddy-Current Method. International Organization for Standardization: Geneva, Switzerland, 2003.

[18] H. Sojoudi; M. Wang; N.D. Boscher; G.H. McKinley; K.K. Gleason, *Durable and Scalable Icephobic Surfaces: Similarities and Distinctions from Superhydrophobic Surfaces.* Soft Matter 2016, 12, 1938–1963.

[19] F. Piscitelli *Characterization in Relevant Icing Conditions of Two Superhydrophobic Coatings.* Appl. Sci. 2022, 12, 3705. https://doi.org/10.3390/app12083705.

[20] F. Piscitelli; S. Palazzo; F. De Nicola *Icing Wind Tunnel Test Campaign on a Nacelle Lip-Skin to Assess the Effect of a Superhydrophobic Coating on Ice Accretion*. Appl. Sci. 2023, 13, 5183. https://doi.org/10.3390/app13085183

[21] H. Memon; J. Wang; X. Hou. *Interdependence of Surface Roughness on Icephobic Performance: A Review*. Materials 2023, 16, 4607. https://doi.org/10.3390/ma16134607.

[22] F. Piscitelli; A. Volpe *Superhydrophobic Coatings for Corrosion Protection of Stainless Steel.* Aerospace 2024, 11, 3. https://doi.org/10.3390/aerospace11010003.

[23] F. Veronesi; G. Boveri; J. Mora; A. Corozzi; M. Raimondo, *Icephobic Properties of Anti-Wetting Coatings for Aeronautical Applications*. Surf. Coat. Technol. 2021, 421, 127363.

[24] Rivero, P.J.; Rodriguez, R.J.; Larumbe, S.; Monteserín, M.; Martín, F.; García, A.; Acosta, C.; Clemente, M.J.; García, P.; Mora, J.; et al. Evaluation of Functionalized Coatings for the Prevention of Ice Accretion by Using Icing Wind Tunnel Tests. Coatings 2020, 10, 636. https://doi.org/10.3390/coatings10070636.

[25] A. Vicente; P.J. Rivero; N. Rehfeld; A. Stake; P. García et al. *Icephobic Coating Based on Novel SLIPS Made of Infused PTFE Fibers for Aerospace Application* Polymers 2024, 16, 571. https://doi.org/10.3390/polym16050571.

Anti-icing Elastomeric Coatings: Striking the Hydrophobicity-Elasticity Balance

A. Casali[1,2], P. Pelagatti[1], M. Balordi[2], G. Santucci de Magistris[2], F. Pini[2]

[1]Università degli Studi di Parma

[2] RSE, Ricerca sul Sistema Energetico, Piacenza, Italy

alessandro.casali@unipr.it, paolo.pelagatti@unipr.it, marcella.balordi@rse-web.it, giorgio.santucci@rse-web.it, francesco.pini@rse-web.it

Abstract— Atmospheric ice formation is a well-known problem in the aviation, shipbuilding, automotive, construction, and energy fields. The accumulation of snow and ice on electrical system components, such as conductor cables and guard ropes, can lead to structures becoming damaged or broken, with great social, environmental, and economic impact.

Different studies have been conducted to mitigate this phenomenon. Among these, great interest is attributed to the icephobic coatings, "passive" systems capable of impeding the formation or facilitating the detachment of ice and snow from surfaces, without involving extra energy sources. Our focus is on both superhydrophobic and elastomeric coatings. Superhydrophobics materials can minimize ice adhesion thanks to the low surface energy, moreover, their peculiar wettability causes a delaying in ice accretion. Elastomeric materials, thanks to a low Young's modulus (YM), exploit the structural flexibility at the ice-surface interface to promote snow or ice detachment mechanisms. Although the combination of superhydrophobic and elastomeric properties in a singular material can lead to a strong enhancement of icephobicity, the increase of the hydrophobicity sometimes reduces the elastic properties of the elastomer.

The aim of this work is to study how the anti-icing properties of an elastomer change by simultaneously varying the hydrophobicity and YM. Starting from polydimethylsiloxane (PDMS), we prepared several hydrophobic and superhydrophobic elastomeric coatings through the dispersion of different percentages of super hydrophobic filler (PVDF) within the rubbery matrix.

The morphology of the material was studied by SEM while wettability was evaluated through measurements of static contact angle, roll-off and droplet freezing temperature. Hardness and Young's modulus were calculated, and anti-icing properties were estimated through shear stress measurements.

In general, increasing the percentage of fillers within the elastomeric matrix significantly increases hydrophobicity of the material, however at the expense of its physical properties, leading to hardening and fragmentation.

This suggests that, to achieve coatings with better anti-icing properties, low YM is prioritized over high hydrophobicity. The goal is to find the right conditions to effectively combining elasticity with superhydrophobicity.

Keywords— Atmospheric icing, Eletrical system components, Anti-icing coatings, Elastomeric coatings, Hydrophobicity, Polydimethyilsiloxane, Superhydrophobic fillers

1. Introduction

Atmospheric icing[1,2,3] is a world-renowned problem that manifests itself with the accumulation of snow and ice on surfaces. When events of this type affect the components of the electrical system, such as conductor cables and guard ropes, they can lead to damage or breakage of structures, with a great social, environmental, and economic impact[4]. To date,

there are several approaches[5] to deal with this problem and among them the use of *anti-icing coatings*[6,7,8] seems to be a good compromise between versatility and applicability. By exploiting their chemical-physical properties, these surfaces can promote the detachment of ice or prevent its growth without involving the use of extra energy sources.

Different strategies for obtaining anti-icing surfaces are known in the literature and the creation of *superhydrophobic surfaces*[9,10,11] is certainly a widely explored solution that allows, owing to their low surface energies and micro-nano structure, to delay the nucleation time of the droplet and favouring ice detachment[12,13].

Although they are promising materials, superhydrophobic surfaces are difficult to prepare and apply on a large scale. Moreover, they tend to deteriorate over time due to the abrasive effect of ice during its [14]. In addition, they suffer from the effect of condensation which leads, at low temperatures, to the creation of an "aqueous film" on the surface and inside the roughness, worsening the wettability properties by favouring the adhesion of the ice.

These limitations induced us to study alternative anti-icing materials, such as *elastomeric coatings*[14,15,16]. Thanks to their elastic behaviour, elastomers can deform reversibly, facilitating the early detachment of ice or snow from the surface, according to the mechanism depicted in Figure 1[17]. The best anti-icing properties are expected for those materials featured by low Young's modulus (YM).
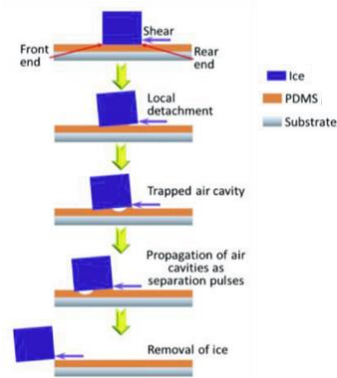
Fig 1. Description of the ice-elastomer interface following the application of a shear stress. As can be seen in the sequence, the elastomer reversibly modifies its structure by incorporating air at the interface with the ice. This makes it possible to reduce the stress required for detachment.

This class of materials is particularly resistant to stress, and it is possible to modulate their chemical-physical properties by varying parameters such as the degree of crosslinking or the cross-linking conditions[18,19]. Moreover, a chemical modification of the material can be easily done by introducing

functional groups or fillers capable of conferring specific properties to the final material[20]. In literature, composite materials deriving from the addition of hydrophobic fillers to elastomeric matrices are reported.[21] However, it is known that to obtain the desired properties at the surface level, the addition of high percentages of fillers is necessary and this leads to a decrease of elasticity or breakage of the material.

The aim of this work is to evaluate the relative importance of elasticity and hydrophobicity over the anti-icing properties of materials obtained combining a commercial elastomer with a superhydrophobic filler.

Several anti-icing coatings were prepared from *polydimethylsiloxane* (PDMS), using the commercial formulation Sylgard 184[®22] and adding increasing percentages of hydrophobic *polyvinylidenefluoride* (PVDF) filler. The chemical and physical properties of the materials have been thoroughly characterized and the anti-icing properties evaluated by shear stress tests.

2. EXPERIMENTAL

2.1 *Materials and samples preparation*

The commercial formulation Sylgard 184[®] was purchased from Dow Chemical[®] and consists of a two-component kit in which there is a part A (prepolymer) and a part B (cross-linking agent) that can be mixed in different weight ratios. *Polyvinylidenefluoride* (PVDF) was purchased from Alfa Aesar[®] and is a fine white powder consisting of microparticles with an average diameter of around 350 nm.

The anti-ice coatings were prepared on 50x50 mm Anticorodal6082 sheets washed and sonicated with acetone. The mixture was prepared maintaining the *standard* 10:1 ratio and varying the percentage by weight of PVDF. The tape casting method was used for the deposition. The coatings were cured in hoven for 60 min at 100°C, cooled at room temperature and stored in a dryer. Below is a summary of the different samples prepared (Tab. 1).

Table 1. Samples preparation. Curing temperature: 100°C, Curing time: 60 min

Sample	Part A/Part B Sylgard184 ratio	Concentration of PVDF (wt%)
Ref	10:1	0
1	10:1	20
2	10:1	30
3	10:1	50
4	10:1	60

2.2 *Methods*

The coatings were previously metallized and then analysed through FESEM Mira 3 (Tescan).

The surfaces were characterized by FTIR spectroscopy using Bruker Alpha 1 equipped with ATR platinum Diamond using a resolution of 4 cm^{-1} and a scan time of 1 min (24 scans/min) for samples and background. Spectra were recorded in the range of 4000-400 cm^{-1}.

Wettability measurements were collected using Kruss DSA 30 tensiometer maintaining a temperature of 23 °C ± 2 and a relative humidity of 30%. For low temperature static contact angle measurements, the temperature was set at -2°C ± 0.3°C, droplet volume of 15 μL was used for the calculation of the static contact angle (SCA) and averaged over at least 5 measurements for each sample. Roll-off angles (RA) and contact angle hysteresis (CAH) were measured using internal tilting table device with a droplet volume of 25 μL, tilting rate of 30°/min and taking at least 3 measurements for each sample. Ice nucleation temperature (T_n) was measured in an environmental chamber. The sample was placed inside the chamber on the Peltier cell and five 10 μL water droplets were deposited on the surface at 20°C. Then the temperature was decreased with a cooling rate of 6 °C/min. The test finished when all the five droplets reached the freezing point, and the T_n is the result of the average of these five values.

The Shore A hardness manual tester has been calibrated by adjusting the hardness of the spring using materials certified by the ASTM-D2240 standard. The bulk samples analysed were at least 6 mm thick, and the measurements were made by performing at least 5 repeats at 6 mm from the edge and 6 mm from each other. The spring was indented on the surface of the sample for a minimum of 15 seconds and a maximum of 30 seconds to allow the value to stabilize. The resulting hardness values are expressed as dimensionless values on a scale from 0 to 100.

The anti-icing properties were estimated by measuring the shear stress (kPa) through Push-Test using a homemade device already described in a previous work[11]. For each type of coating, three different sample were prepared, and 4 tests were carried out on each one for a total of 12 tests.

3. RESULTS AND DISCUSSION

PVDF powder is a commercially available filler that can impart hydrophobicity when added to a polymer matrix. Normally, the addition of fillers leads to a variation in the chemical-physical properties of the materials, but only high concentrations lead to a visible effect at the surface level as shown in Figure 2.
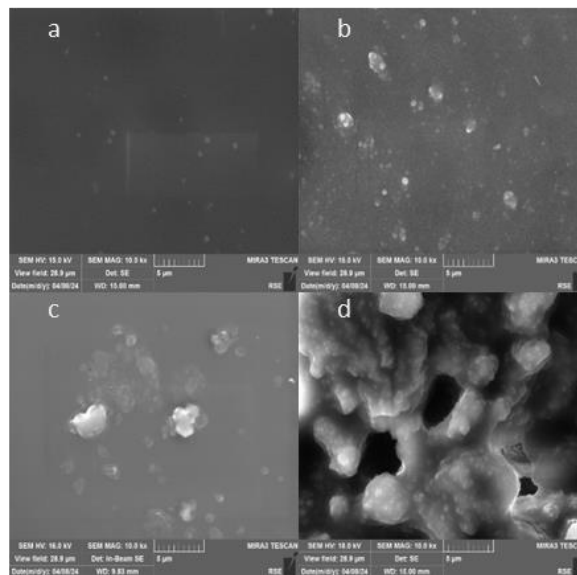
Fig. 2 FSEM pictures of coatings. 2a Sample 1 (20% PVDF), 2b Sample 2 (30% PVDF); 2c Sample 3 (50% PVDF); 2d Sample 4 (60% PVDF).

In samples **1** and **2** (fig.2a and b, respectively) the PVDF is uniformly distributed within the polymer matrix, although

areas where the filler tends to form aggregates that protrude on the surface are visible.

Increasing the percentage of fillers increases the size of the clusters, which tend to aggregate completely and emerge on the surface, as can be seen for the samples **3** and **4** containing a higher concentration of PVDF (Fig.2c, 2d).

The FTIR spectra of the samples and **ref** are reported in Fig. 3. Sample **1** and **2**, with lower content in PVDF, do not evidence any signals different from those of the reference.
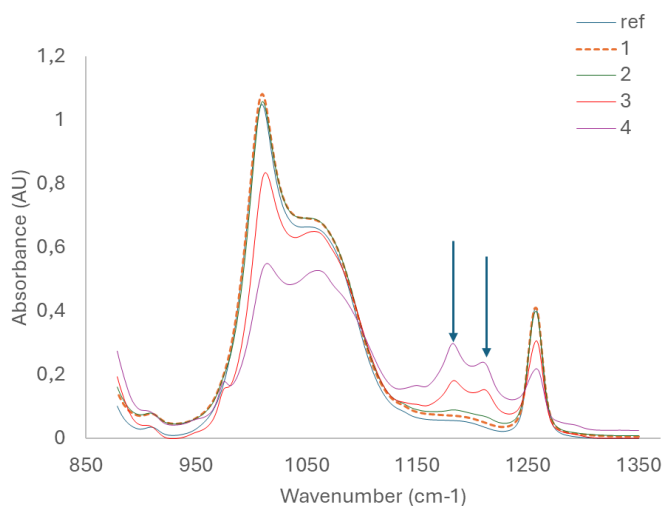
Fig. 3 FTIR spectrum in the range 850 – 1350 cm^{-1}. The arrows indicate the rising of PVDF two signals around 1182 and 1210 cm^{-1}. The decreasing of Si-CH$_3$ (around 1250 cm^{-1}) and Si-O-Si signals (range 1000- 1100 cm-1) of PDMS are also evident.

On the contrary, for samples **3** and **4** the typical signals at 1182 and 1210 cm^{-1}, related to the stretching of the bond CF$_2$ of the filler, increases.

Through wettability measurements it is possible to observe the surface effect of PVDF (Table 2). PDMS is already intrinsically hydrophobic with SCA values above 90°, but following the addition of the filler we can see an increase in the SCA value and an improvement in the dynamic properties with a lowering of the RA and CAH values. The effect is more pronounced for samples **3** and **4**, whereas for samples **1** and **2**, where the percentage of PVDF is lower, the effect is less pronounced, and the values are more like those of **ref**.

Table 2. Wettability measurements. SCA: static contact angle, RA: Roll-off angle, CAH: contact angle hysteresis, l.t SCA: low temperature static contact angle, T$_n$: ice nucleation temperature.

Sample	SCA (°)	RA (°)	CAH (°)	l.t. SCA (°)	Tn (°C)
Ref	104,9 ± 1,4	61,4 ± 5,0	53,6 ± 2,3	86,1 ± 3,0	-6 ± 0,4
1	111,1 ± 2,0	44,7 ± 1,8	37,8 ± 2,9	97,2 ± 3,4	-5,1 ± 0,8
2	125,1 ± 1,9	44,4 ± 1,2	35,9 ± 1,1	103,7 ± 8,3	-5,5 ± 0,2
3	140,7 ± 0,6	17,4 ± 1,3	29,1 ± 3,0	120,3 ± 4,9	-2,9 ± 0,8
4	149,0 ± 1,4	13,3 ± 1,1	23,7 ± 1,1	130,2 ± 5,8	-2,8 ± 0,3

To understand the wettability behaviour of the samples at low temperature, the SCAs were also collected at -2°C. As can be seen in Table 2, there is a decrease of the contact angle due to the formation of a condensation layer on the surface, enabling interaction between the droplet and the surface. The ice nucleation temperature was also measured and none of the samples exhibit a decrease in value compared to **ref** (Table 2). For samples **1** and **2**, where the filler has not fully surfaced, both the T$_n$ and the l.t. SCA are comparable to those of the reference, while for samples **3** and **4**, the T$_n$ is higher than that of the reference. This is likely due to the presence of numerous large clusters of PVDF on the surface, which act as nucleation centres for ice.

The presence of increasing amounts of fillers leads to an overall worsening of the elastic properties of the material with an increase in hardness and Young's modulus obtained empirically through the Gent[23] equation (Table 3).

TABLE 3. HARDNESS SHORE A MEASUREMENTS. THE YM IS CALCULATED USING AN EMPIRICAL FORMULA

Sample	Hardness Shore A	YM Gent function (MPa)
Ref	48,3 ± 0,8	2,30 ± 0,07
1	60,5 ± 1,3	3,68 ± 0,18
2	63,3 ± 0,6	4,70 ± 0,27
3	72,6 ± 1,5	6,25 ± 0,46
4	75,3 ± 1,8	7,16 ± 0,67

The high amount of PVDF required to affect the wettability of the elastomer blocks the sliding of the chains, leading to a material that fragments when subjected to stress. This has effect on the anti-icing properties of the coatings, which depends more on the elasticity than on the hydrophobicity of the material (Figure 4).

Sample	Shear stress (kPa)
Ref	96,8 ± 9,2
1	142,7 ±33,3
2	202,3 ± 66,2
3	466,6 ± 63,9
4	609,8 ± 105,4
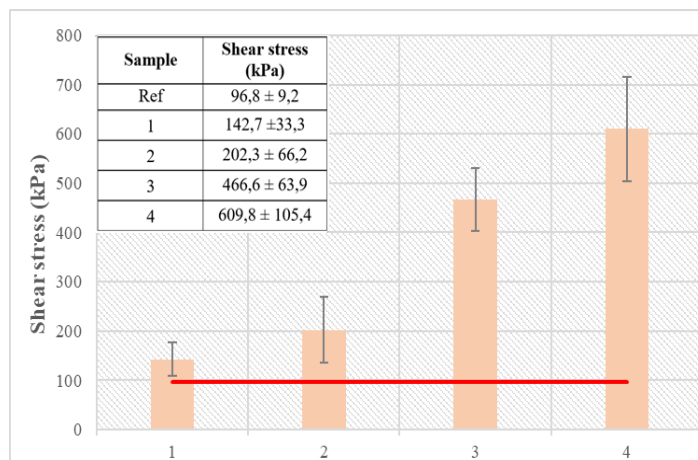
Fig. 4 Shear stress values of the samples compared with **ref** (red bar).

4. CONCLUSIONS

In the present work, some elastomers have been prepared by modulating the elastic and hydrophobic properties, through the addition of a superhydrophobic filler. The addition of PVDF has led to the achievement of surfaces with high hydrophobicity, but at the same time the elastic properties of the elastomers have drastically worsened, due to the presence of solid clusters that block the sliding of the polymer chains. It was observed that as the hydrophobicity of the samples increased, a worsening of the elasticity was followed by the concomitant loss of the anti-icing properties.

It has therefore been shown that the elastic properties play the major role in determining the anti-icing properties of the material. This work paves the way for further development of effective anti-icing materials based on the right compromise between hydrophobicity and elasticity.

REFERENCES

[1] M. Farzaneh, Atmospheric Icing of Power Networks. Springer, 2008.

[2] M. Farzaneh, "Overview of impact & Mitigation of Icing on Power Network Equipment",INMR, 2019.

[3] CIGRE SCB2 WG16.03, Guidelines for meteorological icing models, statistical methods and topographical effects. CIGRE Technical Brochure TB291, 2006.

[4] P. Bonelli, and M. Lacavalla. "Experimental activity and investigation of wet-snow accretion on overhead power lines in Italy." In Proc. 13th International Workshop on Atmospheric Icing of Structures, Andermatt. 2009.

[5] CIGRE SCB2 WG2.44, Coatings for protecting overhead power network equipment in winter conditions. CIGRE Technical Brochure TB631, 2015.

[6] P. Irajizad, S.Nazifi, H.Ghasemi, Icephobic surfaces: Definition and figures of merit, Advances in Colloid and Interface Science, Volume 269, 2019, Pages 203-218. https://doi.org/10.1016/j.cis.2019.04.005.

[7] R. Menini, and M. Farzaneh (2011) Advanced Icephobic Coatings, Journal of Adhesion Science and Technology, 25:9, 971-992.

[8] R. Menini, Z. Ghalmi, M. Farzaneh, Highly resistant icephobic coatings on aluminum alloys, Cold Regions Science and Technology, Volume 65, Issue 1, 2011, Pages 65-69.

[9] M. Reyssat, J. M. Yeomans and D. Quéré, Impalement of fakir drops, Europhysics Letters Association, Volume 81, Number 2, 2008 EPL 81 26006 [10] W. Li, Y. Zhan, S. Yu, Applications of superhydrophobic coatings in anti-icing: Theory, mechanisms, impact factors, challenges and perspectives, Progress in Organic Coatings, Volume 152, 2021, 106117.

[11] M. Balordi, F. Pini, G. Santucci de Magistris, Superhydrophobic ice-phobic zinc surfaces, Surfaces and Interfaces, Volume 30, 2022, 101855.

[12] N. Wang, D. Xiong, Y. Deng, Y. Shi, and K. Wang, ACS Appl. Mater. Interfaces 2015, 7, 11, 6260–6272, March 6, 2015.

[13] C. Liu, Q. Liu, R. Jin, Z. Lin, H. Qiu, Y. Xu, Mechanism analysis and durability evaluation of anti-icing property of superhydrophobic surface, International Journal of Heat and Mass Transfer, Volume 156, 2020, 119768.

[14] S. A. Kulinich, S. Farhadi, K. Nose, and X. W. Du, Langmuir 2011, 27, 1, 25–29, December 8, 2010, https://doi.org/10.1021/la104277q

[15] T .Vasileiou, TM. Schutzius, D. Poulikakos, Imparting Icephobicity with Substrate Flexibility. Langmuir. 2017 Jul 11; 33(27): 6708-6718.

[16] A. M. Emelyanenko, L. B. Boinovich, A. A. Bezdomnikov, E. V. Chulkova, and K. A. Emelyanenko, Reinforced Superhydrophobic Coating on Silicone Rubber for Longstanding Anti-Icing Performance in Severe Conditions, ACS Appl. Mater. Interfaces 2017, 9, 28, 24210–24219, June 28, 2017.

[17] D. L. Beemer, W. Wang, e A. K. Kota, «Durable gels with ultra-low adhesion to ice», J. Mater. Chem. A, vol. 4, n. 47, pag. 18253–18258, 2016,.

[18] D Johnston, D. K. McCluskey, C. K. L. Tan, and M. C. Tracey, Mechanical characterization of bulk Sylgard 184 for microfluidics and microengineering, J. Micromech. Microeng. 24 035017, 2014.

[19] J. Vaicekauskaite, P. Mazurek, S. Vudayagiri, and A. L. Skov (2019). Silicone elastomer map: design the ideal elastomer. In Y. Bar-Cohen, & I. A. Anderson (Eds.), Proceedings of SPIE: Electroactive Polymer Actuators and Devices (EAPAD) XXI (Vol. 10966). [1096625] SPIE - International Society for Optical Engineering. Proceedings of SPIE, the International Society for Optical Engineering.

[20] M. Yu, L. Liang, Y. Zhang, and Z. Wang, Fabrication of a durable anti-icing composite coating based on polyurethane elastomer and silica nanoparticles, Mater. Res. Express 9 055504, 2022.

[21] Zhao, Z., Li, X., Li, W. *et al.* Progress in mechanism design of functional composites for anti-ice/deicing materials. *Surf. Sci. Tech.* **2**, 2 (2024).

[22] Sylgard 184 technical data sheet: https://www.dow.com/content/dam/dcc/documents/en-us/productdatasheet/11/11-31/11-3184-sylgard-184-elastomer.pdf.

[23] A. N. Gent (1958), On the relation between indentation hardness and Young's modulus, Institution of Rubber Industry -- Transactions, 34, pp. 46–57. doi:10.5254/1.3542351.

Thermal-vibration-assisted Deicing Based on Superhydrophobic Coatings

Bo Wang[1], Xueqin Zhang[1], Shirui Xu[1], Bingkun Li[1], Zheng Gao[1], Song Xiao[1], Yujun Guo[1], Wenfu Wei[1], Guoqiang Gao[1], Guangning Wu[1]

[1] School of Electrical Engineering, Southwest Jiaotong University, Chengdu, China

billionwang@my.swjtu.edu.cn, xq_zhang@swjtu.edu.cn, shiruixu@my.swjtu.edu.cn

Abstract— **Electrical equipment used in outdoor environments is often exposed to interface icing. The overall quality of the equipment changes and the physical and chemical properties of the surface change as a result of icing, and this problem seriously affects the operational efficiency and safety of the equipment. Current de-icing methods are unsatisfactory in terms of efficiency, energy savings, and environmental friendliness. The lightweight and multifunctional nature of superhydrophobic coatings can give the equipment a functional surface, which has great potential for equipment protection. However, current superhydrophobic materials are still not able to keep liquids from freezing on their surfaces for long periods. Considering that coating application scenarios are accompanied by Joule heat and vibrations with different frequencies. Helpful in both preventing icing and shedding. The superhydrophobic coating with high thermal conductivity and low ice adhesive force is designed to be ice-free for a long period under the conditions of heat and vibration generated in the operation of electrical equipment. Provides a new idea for the application of superhydrophobic coating in the protection of electrical equipment.**

Keywords— ***Electrical equipment, superhydrophobic, thermal, vibration***

I. Introduction

Ice cover is a common low-temperature phase change phenomenon in nature. On the power, transportation and other equipment caused great inconvenience. In serious cases, it threatens the safe and stable operation of equipment and causes great damage to people's lives and property错误!未找到引用源。_错误!未找到引用源。 4]. In wind power generation, ice-covered wind turbine blades reduce the efficiency of power generation and shorten the life of the equipment错误!未找到引用源。 -6]. In power transmission, ice-covered insulators, towers, and lines often cause flashovers due to insulation degradation. Problems such as reduced equipment quality, fallen towers, and broken lines错误!未找到引用源。 -8]. On electrified railways at the power end. Ice-covered arch networks are obstructed by flow and trains cannot run normally[9]. Current de-icing methods include physical de-icing and chemical de-icing in various forms[10-12]. Physical de-icing involves using manpower or heat to cause the ice to fall and melt. It is very inefficient and consumes a lot of manpower and energy[13]. Chemical de-icing mainly uses salt to lower the freezing point. However, it pollutes the surface, soil, and groundwater to varying degrees and is currently banned in many areas错误!未找到引用源。.

Superhydrophobic materials, as multifunctional extreme wetting materials, are of increasing interest to the majority of scientists. Its ultra-high interfacial contact angle and ultra-low rolling angle greatly reduce surface water accumulation and solid-liquid contact area. The resulting anti-icing and self-cleaning properties are exactly the characteristics needed for outdoor equipment[15-19]. However, according to current research. Superhydrophobic materials can only delay icing and reduce ice adhesion. It is not possible to make the interface permanently ice-free under adverse conditions[20-22].

In response to the above situation. Consider and exploit the vibration and Joule heat generated in the operation of the equipment[23-24]. This paper investigates a combined heat and vibration-assisted anti-icing and de-icing approach based on superhydrophobic coatings.

II. Experiment

SiO$_2$ Modification: SiO$_2$ (Macklin, 99.5%, 20±5 nm) and ethanol (Quanwangda Chemical Technology Co., LTD, Guangdong, 99.7%) were mixed and stirred at the ratio of 3 g:100 ml for 10 min, followed by 30 min of ultrasound. 1H,1H,2H,2H-perfluorodecyltrimethoxy silane (PTS) (Macklin, 97%) and SiO2 were added to the SiO$_2$ dispersion at the ratio of 1:3 in a 60 °C water bath and stirred for 3 h. The precipitate was collected by centrifugation at 8000 rpm for 15 min. The collected SiO$_2$-F is placed in a vacuum oven to dry at 120 °C and ground into powder.

h-BN Stripping: h-BN (Macklin, 99.5%, 1 μm) and iso-propanol: After ultrasonic treatment for 24 h and centrifugation for 2000 rpm, the unstripped boron nitride precipitate was removed for 15 min. Then the supernatant was centrifuged for 8000 rpm and 30 min to collect boron nitride nanosheets of a certain thickness. The boron nitride was cleaned with deionized water and the supernatant was neutral, then it was placed in a vacuum oven to dry at 120 °C and ground into powder.

Preparation of the Solutions: (Take S30 as an example) 0.194 g SiO$_2$ and 30 ml tetrahydrofuran (THF) (Macklin, 99%) were mixed and stirred for 10 min and then ultrasonic for 30 min. 0.67 g Polydimethylsiloxane (PDMS) and 30 ml THF were mixed for 30 min. Mix SiO$_2$ dispersion with PDMS/THF solution. Add curing agent (curing agent: PDMS = 1:10) and stir for 10 min.

Spraying Process: The slides and silicone rubber sheets were wiped and dried with absolute ethanol. Adjust the parameters of the spray gun to spray the solution evenly on the surface of the slide and the silicone rubber sheet. After spraying, the samples were placed in an oven and dried and cured at 120 °C for 2 h.

Characterizations of Materials and Coating: The contact Angle was measured by a contact Angle measuring instrument (Lukes Scientific Instruments, Shanghai, DSAHT17C), and the rolling Angle was measured by adjusting the horizontal Angle of the optical platform.

Flashover Experiments: In the experiment, a 220 V, 50 Hz power supply was boosted and rectified by a high-voltage DC generator. The current was controlled within 5 mV by a current-limiting resistor. The voltage range could be

controlled from 0 to 120 kV. The sample was placed between the plate–plate electrodes. The pressure was slowly increased until a flashover occurred.

Ice-covering and de-icing tests: Droplet freezing time is carried out using a specimen in a thermostat, to which a quantitative amount of deionized water is added, and the freezing time of the droplets on the surface is recorded using an optical microscope. The icing of real insulators is carried out using an icing system in an artificial climate chamber, where insulators are iced at -2°C, and de-icing is carried out using a shaking table and a heating table.

III. RESULT &DISSCUSSION

The prepared coatings and filled phases were analyzed by XRD and the results are shown in Fig. 1 and Fig. 2. XRD tests were carried out on the filler phase, matrix, and SiO_2/PDMS composite coating, and according to Fig. 1, it can be seen that: SiO2 is an amorphous gas phase, with bun peaks appearing at $2\theta=15°-30°$. PDMS has two bun peaks appearing at $2\theta=10°-30°$, which partially overlap with those of the gas-phase SiO2, and according to the comparison of the peak strengths at $2\theta=15°-30°$, it was found that PDMS's crystallinity (polymer crystallinity is the regular arrangement of molecular chains) is slightly weaker. In the composite coating, when the volume fraction of SiO_2 is lower than 35 vol.%, the bun peak is covered by PDMS, and when the volume fraction of SiO_2 is lower than 35 vol.%, the diffraction peaks begin to appear, and at the same time, the peaks of PDMS at $2\theta=10°\sim15°$ still exist, which proves that the filling of SiO_2 does not have a more obvious effect on the crystallinity of PDMS, and the crystallinity of PDMS is not significantly influenced by SiO_2, and it is only in the case of the filler with the volume fractions of 30 vol.% and 35 vol.%, that the crystallinity of PDMS is slightly weaker than that of PDMS. 30 vol.% and 35 vol.% had a slight effect on the crystallinity of PDMS.
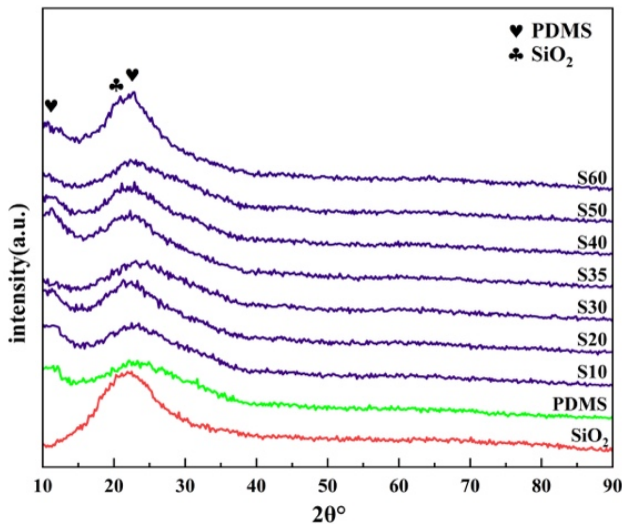
Fig. 1 XRD patterns of the filled phase, matrix, and SiO_2/PDMS composite coating

XRD tests were carried out on the filled phase, matrix, and SiO_2@BN/PDMS composite coatings, and according to Fig.2, it can be seen that h-BN is the crystalline phase, and a fine sharp peak appears at $2\theta=27°$. In the composite coating, the characteristic peaks were enhanced with the increase of the filling ratio of h-BN, while the bun peaks of PDMS did not

change because of the filling ratio of h-BN, which proved that both filling ratios did not significantly change the molecular chain arrangement of PDMS, and only had a slight effect on the crystallinity of PDMS when h-BN: SiO_2 was 7.
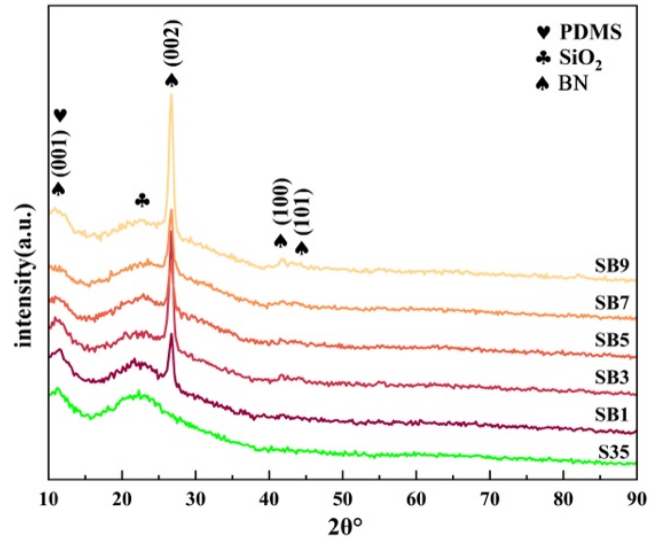
Fig. 2 XRD patterns of filler phase, matrix, and SiO_2@/PDMS composite coating.

A series of wettability tests were conducted to characterize the superhydrophobicity of the prepared coatings, and the results are shown in Figure 3. To coat different surfaces in the electrical equipment, the prepared superhydrophobic coatings were applied on hydrophilic surfaces represented by slides, hydrophobic surfaces represented by silicone rubber sheets, and metallic surfaces represented by brass sheets. It can be seen that the superhydrophobic coatings in which small volume fillings (volume fraction not exceeding 35 vol.%) occur exhibit a positive correlation of increasing hydrophobicity with increasing volume fraction of fillings on all three coated substrate surfaces. The reason for this is, on the one hand, that the increase in the volume of filled nanoparticles directly leads to an increase in the roughness of the coating surface, an increase in the volume of air "trapped" by the coating surface, and an increase in the lifting force of static droplets on the surface.
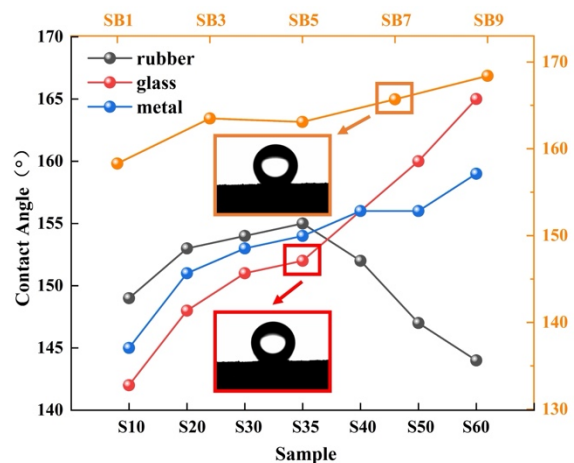
Fig. 3 Polt of contact angle relation with volume fraction of filled phase for superhydrophobic coatings on different substrates.

The direct relationship between the volume fraction of the filled phase and the surface roughness can be seen in the microscopic by the change in roughness photographed by the surface profiler in Figure 4. Macroscopically it is directly manifested in the increase of static droplet contact angle. As the volume fraction of the filler phase increases, the coating on the hydrophobic surface substrate builds up, which causes the coating to crack during the curing process as seen in Fig. 4. This phenomenon results in a surface roughness that is too large for the droplet scale, and also results in the inability to travel on the surface to "trap" air to form air pockets that can lift the droplets, which in the macroscopic view shows a direct relationship between static droplet contact angle and surface roughness. Macroscopically, the contact angle of static droplets decreases and hydrophobicity is weakened. On the other hand, due to the increase in the volume fraction of the filled phase, the nanomaterials, although modified with low surface energy, are broken up and agglomerated on the coated surface as the space is reduced. This leads to an unavoidable decrease in the effective surface roughness as shown in Fig. 4, which further leads to a decrease in the droplet contact angle.
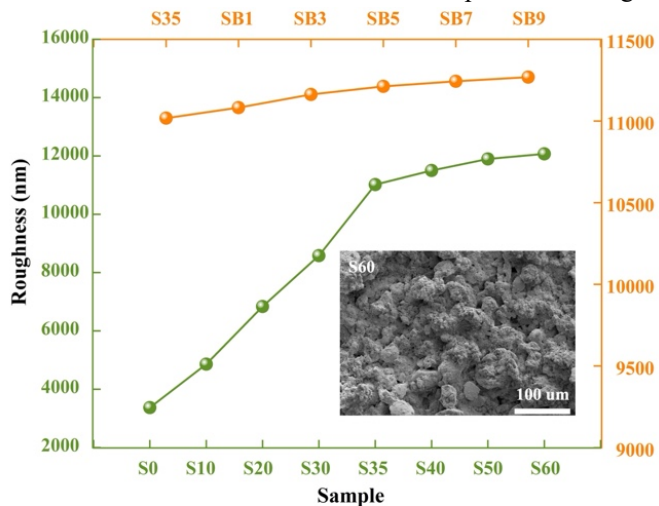
Fig. 4 Polt of surface roughness of superhydrophobic coatings as a function of loading (inside agglomeration occurring at large volume loadings)
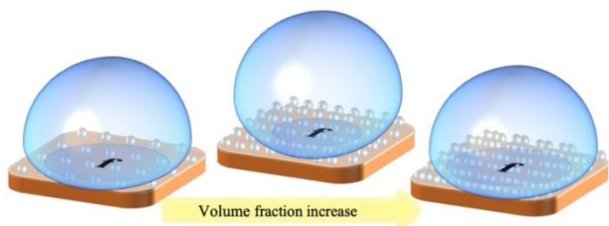
Fig.5 Schematic diagram of the variation of droplet morphology with loading on the surface of superhydrophobic coatings

Dynamic contact angle tests were performed on the above coatings and the results are shown in Table 1.

TABLE I. NUMERICAL VALUES OF DYNAMIC CONTACT ANGLE OF SUPERHYDROPHOBIC SPECIMENS

Sample	滚动角	前进角	后退角	弛豫角
PDMS	> 20°	102°	54°	48°
S10	12°	131°	12°	20°
S35	4°	159°	154°	5°
S60	4°	149°	142°	7°
SB1	3°	161°	158°	3°
SB3	4°	164°	161°	3°
SB5	3°	165°	161°	4°
SB7	3°	166°	160°	6°
SB9	4°	165°	162°	3°

Considering the stability of curing after spraying, surface roughness, and hydrophobicity, the optimal filling volume of SiO_2/PDMS superhydrophobic coating on the surface of electrical equipment is 35 vol.%, and the optimal filling ratio of SiO_2@BN/PDMS superhydrophobic coating is BN: SiO_2 is 7.

In addition, the electrical properties of the coating were tested for flashover voltage, and the results are shown in Fig. 6, which shows that the intensity of the flashover voltage along the surface increases with the increase of the volume fraction of SiO_2, but the dispersion of the flashover voltage increases significantly when the volume fraction exceeds 30 vol.%. This is due to the decrease in the adhesion between the coating and the substrate, and the flashover will lead to obvious discharge traces on the coating, which will lead to the back of the discharge path appearing to follow the phenomenon, leading to the reduction of the subsequent discharge voltage. After adding h-BN as a modified material, the stability of the coating is improved, and at the same time, the interface trap depth and trap density are increased, and the conductivity of the coating is reduced, which makes the flashover voltage of the coating increase, and the dispersion of the flashover voltage is reduced. This is of great significance for the stable operation of electrical equipment.
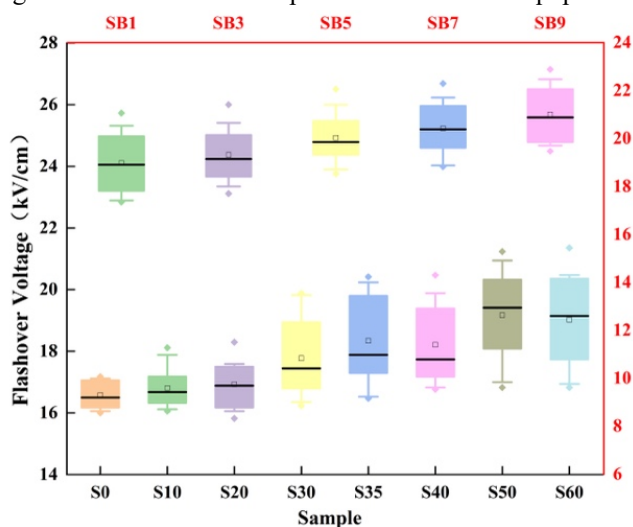
Fig.6 Box-plot of flashover voltage for different coatings

After ensuring the electrical properties of the coatings, the adhesion of the coatings to the surface-covered ice was tested, and the results are shown in Fig. 7. The adhesion of the coating to ice decreased extremely rapidly with the increase of the monolithic filled phase loading, from 5.8 N /cm2 for S0 to 0.7 N /cm^2 for S20, and 20 vol.% resulted in an 88% decrease in the surface ice adhesion. This is due to the elevated surface roughness of the coating due to SiO$_2$ filling, which decreases the contact area of ice with the coating. Afterward, as the volume fraction of the coating increases, the tested ice adhesion tends to be saturated by the force between the filled phase and the substrate due to the high filler loading of the coating, which causes agglomeration of SiO$_2$ and a decrease in the stability of the coating. With the introduction of h-BN, both coating stability and roughness were improved, resulting in a further decrease in the ice adhesion of the coatings, exhibiting the lowest coating adhesion on the SB7 specimen. This degree of surface adhesion allows the surface ice cover to come off easily with the assistance of vibration.
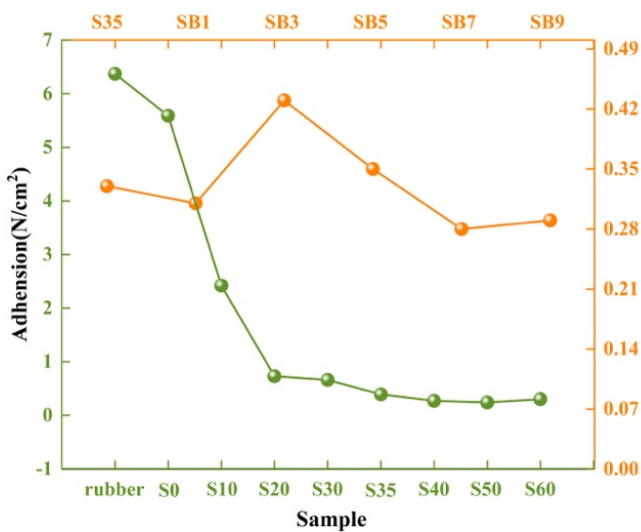
Fig.7   Box-plot of adhesion force for different coatings

Regarding thermally assisted deicing, a coating with high thermal conductivity is required for heat transfer. In the absence of SiO$_2$ filling, the thermal conductivity of the coating is significantly lower than that of silicone rubber. With the introduction of SiO$_2$ in the coating, the thermal conductivity of the coating is increased and maintained near 0.35 W/mk at loadings ranging from 10 vol.% to 35 vol.%, and there are three intermediate variables: 1. Elevation of the coating roughness leads to a decrease in the base area of the coating and the hot electrode, which results in a decrease in the thermal conduction; 2. The gradual formation of a thermally conductive network by SiO$_2$ enhances the thermal conductivity of the coating; 3. The increase in the SiO$_2$-PDMS interface leads to a decrease in thermal conductivity. The coupling of the three factors puts the coating at a level where there is no significant change in the integrated thermal conductivity. Later, with the increase of SiO$_2$ loading, the thermal resistance of the SiO$_2$-PDMS interface plays a dominant role in the coupled thermal conductivity of the coating, leading to a decrease in thermal conductivity. After the introduction of h-BN, its intrinsic thermal conductivity is much larger than that of SiO$_2$ and PDMS, resulting in a significant increase in the thermal conductivity of the coating

occurs with the increase in the loading of h-BN. This makes it easier for the heat from the coating matrix to be conducted to the coating-ice interface for interfacial ice melting to occur.
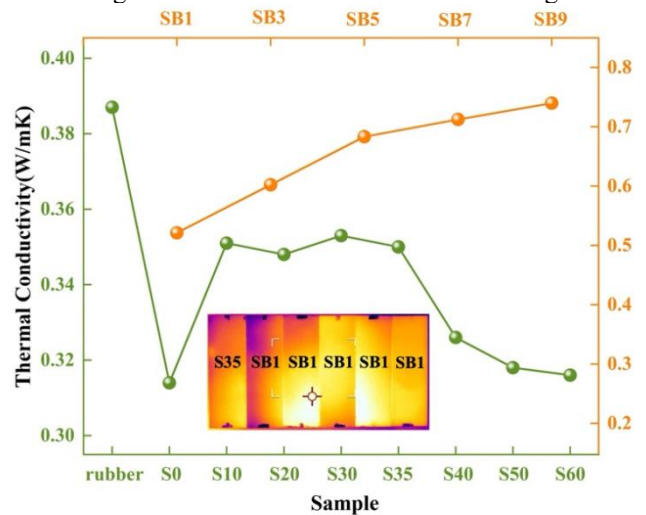
Fig.8   Box-plot of thermal conductivity for different coatings

IV. CONCLUSIONS

The following conclusions were obtained by analyzing the data on the coating's wettability, electrical properties, ice adhesion, and thermal conductivity:

1. superhydrophobic coatings with ultra-low ice adhesion and thermal conductivity are good aids for vibration-assisted de-icing but are not conducive to thermal de-icing at the interface. the introduction of h-BN has resulted in improved stability of the coatings, improved thermal conductivity, and electrical properties.

2. The high loading of the coating causes agglomeration of the coating, at which time the high surface roughness is not favorable to the superhydrophobic performance of the coating. The introduction of a multiscale filling ratio will improve this problem.

3. The influence of loadings on the thermal conductivity of superhydrophobic coatings needs to be considered from various perspectives due to the changes in the surface roughness of the coatings, the formation of thermal conductive networks, and the relationship between interfacial thermal resistance.

REFERENCES

[1]   Z.Y. Liu, Y.Y. Hu, X.L. Jiang, et al. Influence of positive DC electric field on rime icing on the insulator and its experimental verification in the natural environment. High Voltage, 2023, 8(5): 954－9666.

[2]   C.Y. Zong, Y.Y. Hu, X.L. Jiang, et al. AC flashover characteristics and arc development process of glaze ice-covered insulators in natural environment. Int. J. Electr. Power Energy Syst, 2022, 135, 107559.

[3]   M. Farzaneh. Insulator flashover under icing conditions. IEEE Trans. Dielectr. Electr. Insul, 2014, 21(5), 1997－2011.

[4]   M. Farzaneh. Ice accretions on high-voltage conductors and insulators and related phenomena. Phil. Trans. A Math. Phys. Eng. Sci, 2016, 358(1776), 2971－3005.

[5]   R. Patrice, L. Jean, R. Jean, et al. Definition of an ice index for wind turbines in cold climate. Cold Regions Science and Technology. 2023, 213, 103930.

[6]   G.Q. Jiang, R.X. Yue, Q. He, et al. Imbalanced learning for wind turbine blade icing detection via spatio-temporal attention model with a self-adaptive weight loss function[J]. Expert Systems With Applications, 2023, 229.

[7] W. Huang, B. Hu, S. Mohammad, et al. Preventive Scheduling for Reducing the Impact of Glaze Icing on Transmission Lines. IEEE Transactions on Power Systems, 2022, 1297-1310.

[8] L. Yang, Z.Q. Chen, Y. P. Hao, et al. Experimental study on ice monitoring method for 10 kV transmission line with tangent tower in alpine landform. High Voltage, 2023, 9(1): 182-194.

[9] Y.B. Wang, Y.M. Xu, F. Su, et al. Damage accumulation model of ice detach behavior in ultrasonic de-icing technology. Renewable Energy, 2020, 1396-1405.

[10] K. Adelya, B. Baglan, S. Fail, et al. A Mini-Review on Recent Developments in Anti-Icing Methods[J]. Polymers, 2021, 13(23): 4149-4149.

[11] Y.F. Niu, Y.K. Sun, X.F. Tao, et al. Superhydrophobic-electrothermal laser-induced graphene for effectively anti-icing and de-icing. Composites Communications, 2024, 101830.

[12] P. Srinivas Verma Dr, et al. A Review on Current Methods of De-Icing and an Idea for Designing an Autonomous Robot for De-Icing. International Journal of Engineering Technology, 2018, 7.1.8:182-182.

[13] Y. Wang, G. Zhang, Z. Tian, et al. An Online Thermal Deicing Method for Urban Rail Transit Catenary. IEEE Transactions on Transportation Electrification, 2021, 7.2: 870-882.

[14] T. Xie, J.K. Dong, H.W. Chen, et al. Experimental investigation of deicing characteristics using hot air as heat source. Applied Thermal Engineering, 2016, 107: 681-688.

[15] M.M. Liu, Y.Y. Hou, T.J. Chen, et al. Research progress on basic theory and preparation technology of superhydrophobic anti-icing materials. Materials Protection, 2023, 56(5): 40-62.

[16] G. Prasad, G. Vidya, J.B.R. Rosei, et al. Bioinspired Superhydrophobic Material with Nafion Polymer for Anti-Icing Coating on Aluminium Alloy Surface. Theoretical Foundations of Chemical Engineering, 2024, 57(6): 1572-1584.

[17] Z.Y. Liu ,Y.W. Zhang ,Y. Li, et al. Superhydrophobic coating for blade surface ice-phobic properties of wind turbines: A review. Progress in Organic Coatings, 2024, 108-145.

[18] A. Allahdini, R. Jafari ,G. Momen. Transparent non-fluorinated superhydrophobic coating with enhanced anti-icing performance. Progress in Organic Coatings, 2022, 106758.

[19] H.Y. Yong, Z.I. Li, X.B. Huang, et al. Superhydrophobic Materials: Versatility and Translational Applications. Advanced Materials Interfaces, 2022, 9, 2200435.

[20] J. Jiang, Y. Shen, Y. Xu, et al. An energy-free strategy to elevate anti-icing performance of superhydrophobic materials through interfacial airflow manipulation. Nature communications, 2024, 15(1): 777-777.

[21] H. He, Z.G. Guo, Superhydrophobic materials used for anti-icing Theory, application, and development. iScience, 2021, 24, 103357.

[22] W. Huang, J.X. Huang, Z.G. Guo, et al. Icephobic/anti-icing properties of superhydrophobic surfaces. Advances in Colloid and Interface Science, 2022, 102658.

[23] S. Li, J. Li. Condition monitoring and diagnosis of power equipment: review and prospective. High Voltage, 2017, 2(2): 82-91.

[24] E. A. Grin'. The Possibilities of Fracture Mechanics as Applied to Problems of Strength, Service Life, and Substantiation of Safe Operation of Heat-Generating and Mechanical Equipment. Thermal engineering, 2013, 60(1): 24-31.

Centrifugal ice adhesion testing combined with heating as de-icing method

Niklas Kandelin[1], Betül Aktaş[1], Ruqaya Khammas[1], Heli Koivuluoto[1]

[1] *Tampere University, Faculty of Engineering and Natural Sciences, Materials Science and Environmental Engineering, Tampere, Finland*

niklas.kandelin@tuni.fi, betul.aktas@tuni.fi, ruqaya.khammas@tuni.fi, heli.koivuluoto@tuni.fi

Abstract— **Heating is used as a de-icing method in different applications, e.g., in blades of the wind turbines and wings of the airplanes. In many cases, de-icing needs to be done quickly and easily because stopping operation or needs for external maintenance caused by icing increase costs and service time as well as weaken safety issues. Ice on the critical surfaces needs to be removed by using external energy or motion. However, more passive solutions are under development. For this, surface engineering can offer surface and coating solutions, which have icephobic properties and can be used to weaken an ice adhesion between ice and surface. Additionally, one interesting solution is to combine heating as de-icing together with icephobic coatings as anti-icing to achieve multifunctional performance for icing protection systems.**

In this research, we focus on the development of centrifugal ice adhesion testing (CAT) combined with heating (H) of the tested surface during testing. This way, the icing properties of different materials and coatings were evaluated to understand the combined influence of heating and surface material on ice removal. In centrifugal ice adhesion testing, ice was accreted on the sample surfaces (area ~30 x 30 mm) in an icing wind tunnel. Different ice types i.e., glaze, mixed glaze and rime ice, can be accreted. Ice adhesion can act as an indicator for icephobicity of the surfaces. If the ice adhesion value is low, the surface is icephobic. Because heating is used as de-icing method and can be combined with the icephobic coatings, we developed the ice adhesion testing to analyze this multifunctional behavior.

Electrical heating setup for the CAT was designed to evaluate heating effect on ice adhesion. Samples with accreted ice were placed on the heated sample holder for CAT testing (H-CAT). These H-CAT results were compared to CAT results for investigating heat and material influence separately. Several bulk materials and icephobic coatings were studied in order find out suitable heating concept for different materials and coatings.

Keywords— *Anti icing, De-icing, Coating, Icing wind tunnel, Wind power, Aviation*

I. INTRODUCTION

The formation of ice on surfaces has significant implications for daily life and a variety of industries, including aviation [1–3], energy production and transmission infrastructures [4–10], and marine [11,12]. Among the structures that are most affected by icing are transmission lines [4,5,10], aircrafts [1–3], wind turbines [6–9], and ships [12], as mentioned in various studies. The problem is particularly severe in regions with consistently low temperatures, where ice formation can be a daily occurrence, leading to significant disruptions to daily activities and posing safety hazards [13]. Ice formation occurs due to a combination of different factors, including temperature, humidity, liquid water content and wind speed [14]. Depending on these factors different ice types are formed in the atmosphere: in-cloud icing and precipitation icing. In-cloud icing occurs when supercooled water droplets within a cloud encounters a surface of an object, resulting in the formation of ice. This leads to the formation of either glaze ice or rime ice [10]. Glaze ice is transparent and dense, while rime ice is rough and milky-white. Precipitation icing occurs when a surface of an object encounters falling precipitation, such as freezing rain, snow, or sleet. Freezing rain can form glaze ice on exposed surfaces, while snow or sleet can accumulate and freeze. Both in-cloud and precipitation icing can pose risks and impact the performance of structures [13].

Various methods have been developed to address the challenges posed by ice formation on surfaces. These methods can be broadly categorized into two types: active and passive methods [7]. Active methods involve the use of an external source such as electrical heating [7,15,16], vibration [17] or deicing liquids [18] to remove ice from surfaces. Different testing methods can be found in the literature depending on the de-icing source. One testing method is recording the time required to remove the ice under a certain external effect and to compare different surfaces and external sources [16,19,20]. Another approach is determining the power input to remove the ice [21]. Temperature can also be recorded at the time that the ice detaches from the surface to compare different materials and methods [22]. While active methods are generally more effective, they can be expensive and energy intensive. On the other hand, passive methods, which rely on specialized coatings or component designs to prevent ice formation, are often more cost-effective and environmentally friendly [7]. The main idea behind the passive methods is having low ice adhesion strength to obtain anti-icing and/or icephobic surfaces.

However, passive methods, anti-icing or icephobic surfaces, may not be effective or sufficient in extreme weather conditions. Therefore, combination of active and passive methods would merge the advantages of both methods and help to disregard negative sides of them. However, that would need a different testing set-up that also combines two methods. To address this challenge, we have developed a new testing setup that combines testing of both passive and active methods to provide a comprehensive and quantitative assessment of ice adhesion strength of different icephobic surfaces by centrifugal ice adhesion testing under heating as deicing approach. By combining these two approaches, our testing method enables us to evaluate the performance of ice prevention and removal strategies more effectively than using either method alone.

II. EXPERIMENTAL PROCEDURE

Ice adhesion measurements were done using an Icing Wind Tunnel (IWiT) and Centrifugal Ice Adhesion Test (CAT) at Tampere University, Ice Laboratory. Using IWiT ice was accreted from supercooled water droplets which hit the sample at a speed of 25 m/s in a cold room, where the temperature was set as -10°C (humidity 75-85 %). This method of ice accretion resembled atmospheric icing. IWiT can be used to create rime ice, mixed glaze ice and glaze ice. In the present study, for CAT and HCAT tests mixed glaze ice was used. Average water droplet diameter was 25 µm and it was measured using HiWatch HR2 particle measurement camera designed for cold conditions, which can be seen in Figure 1. Ion exchanged water with Purity II, purified with Milli-DI Water Purification System (MilliporeSigma, The United States) was used in IWiT. [23, 24]

Figure 1. HiWatch HR2 diagnostic camera in water droplet measurement position under IWiT at Tampere University, Ice Laboratory.

Samples were attached to 34 cm aluminum CAT-bars for ice accretion. The iced area was controlled by masking the rest of the sample and the CAT-bars. The iced area for CAT experiments was 30 x 30 mm, and for heat plate test the whole sample (120 x 40 mm) was covered with the ice. Samples were placed in the cold room at least one hour before ice accretion to endure that their temperature was the as the environment during the ice accretion. Iced samples for heat plate and CAT are shown in Figure **2**.

Figure 2. Heat plate samples on the left and samples for CAT testing with the masks after ice accretion on the right.

The ice used for the experiments was mixed glaze ice, accreted on the cleaned samples using the IWiT at -10°C. Thickness of the accreted ice was ~10 mm. After ice accretion the samples were left to freeze for 16 h at -10°C. CAT and H-CAT was performed on four parallel samples of each sample type.

A. Centrifugal ice adhesion test (CAT)

Centrifugal ice adhesion test was performed by rotating the samples at an increasing rotational speed (300 rpm/s) until the ice was detached from the sample (Figure 3). An acceleration sensor attached to the dome was recording the speed at the moment of ice detachment, and the angular velocity ω can be calculated from RPM value using Equation 1:

$$\omega = RPM * 2 * \frac{\pi}{60} \qquad (1)$$

Angular velocity ω is then used in Equation 2 to calculate the force using mass m and radius of rotation r, which was 17 cm for this setting.

$$F = mr\omega^2 \qquad (2)$$

The force can be converted to shear stress, which is the value of ice adhesion, dividing the force by the iced area on the sample, using the Equation 3:

$$\tau = \frac{F}{A} \qquad (3)$$

where τ is the shear stress and A is the area of ice. [23]

Figure 3. Centrifugal ice adhesion tester (CAT) at Tampere University, Ice Laboratory.

The mass of the ice was determined by measuring the weight of the sample with ice before CAT, and then measuring the weight of the sample after CAT. This was done using EJ-610 scale (A&D Company, Limited, Tokyo, Japan) in the cold room.

B. Heating plate tests

A test using a heating plate was designed to evaluate the effectiveness of heating as a de-icing method for different materials. In this testing, a plate of 20 x 30 cm was heated to the chosen temperature and set at an angle of 45°. Samples were placed on the heated plate and kept there until the ice fell off. Heating plate with the samples is shown in Figure **4**. The time to de-ice the surface was measured and the de-icing times can be compared. Testing was done in the cold conditions (-10 °C).
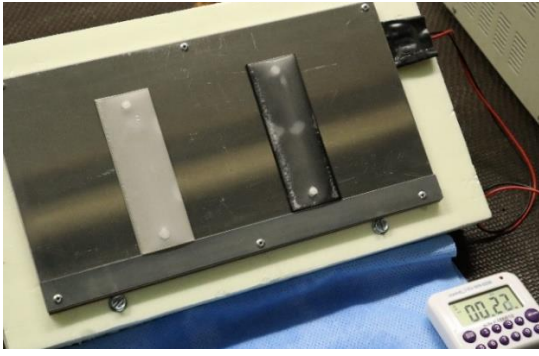
Figure 4. De-icing testing set up for heating plate tested with an uncoated sample and a coated sample.

C. Heated CAT (H-CAT)

Combining heating with the centrifugal ice adhesion test was done by installing a small heating plate on the tip of CAT-bar to where the sample was attached before the rotation. The plate was kept at a constant temperature using a PS3005 DC power supply (ELFA, Sweden).

The power supply was connected to the heating plate using a slip ring, enabling continuous heating during the rotation. The slip ring and modified sample holder are presented in Figure 5.
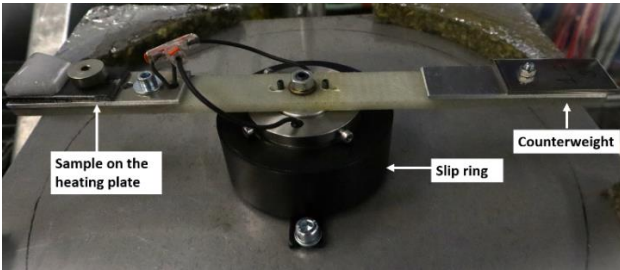
Figure 5. H-CAT set up for centrifugal ice adhesion measurement with heating.

Usage of slip ring changed the CAT operation slightly. Instead of each sample having its own bar for ice accretion and attaching to the CAT, samples needed to be removed from the bars that they are attached to during icing procedure and fixed with a specific H-CAT bar. Therefore, they were all rotated on the same bar, which was fitted with the heating plate and slip ring. This required specific caution and handling the samples was kept to a minimum. The samples were placed in the H-CAT using tweezers. The temperature of the heating plate was monitored between sample removal to ensure the consistency of the heating for each sample.

The heating plate temperature was set to 10°C. Before rotation, the samples were placed on the heating plate for 20 s to ensure that all samples were exposed to the heating for the same time, and that the heat would have enough time to affect the sample. This time was chosen through preliminary tests using the heating plate.

D. Materials

Testing of the system was done using samples with three different aluminum alloys: aluminum 2017, aluminum 6082, and aluminum 7075. These alloys were chosen because they are commonly used for vehicles, aviation and other applications that are exposed to icing [24][25]. In addition,

aluminum has high thermal conductivity, which is useful for de-icing with heating.

Each Al alloy was tested with three surface types: 1) original sample surface as received from manufacturer (AR), 2) polished sample surface (P), and 3) sample surface coated with flame sprayed polyethylene (PE). This amounted to a total of nine different sample materials (Table 1).

Table 1. Tested sample materials and surface types.

Surface type		
Flame-sprayed polyethylene coating (PE)	**Original surface (AR)**	**Polished surface (P)**
AL2017-PE	AL2017-AR	AL2017-P
AL6082-PE	AL6082-AR	AL6082-P
AL7075-PE	AL7075-AR	AL7075-P

Flame sprayed polyethylene was chosen for the comparison because of its known low ice adhesion [23]. The samples were coated using CastroDyne DS 8000 (Castolin Eutectic, Dällikon, Switzerland) flame spray gun using oxygen and acetylene gases. Process parameters were as following pressures for oxygen and acetylene of 4,0 bar and 0,7 bar, respectively, spray distance of 325 mm, step size of 5 mm and traverse speed of the spray gun as 750 mm/s. Polyethylene powder was LDPE from Plascoat Systems Limited (Zuidland, The Netherlands) with an average particle diameter of 300 µm. The powder feeder was manufactured by Oerlikon Metco (Wohlen, Switzerland) and compressed air was used as the carrier gas. Before coating, the aluminum substrate was grit-blasted with Al_2O_3 grits with a grit size of Mesh 40 for better adhesion. Substrate was preheated prior spraying, and the coating was sprayed layer by layer with continuous three layers first followed by another three layers.

III. RESULTS AND DISCUSSION

In the heating plate tests, when comparing coated and uncoated materials it was noted that the uncoated materials were significantly faster to de-ice even though their ice adhesion values were much higher. This was because of the much lower heat conductivity of the coating and the increase in sample thickness compared to non-coated samples. These observations led to the idea to combine CAT and heating plate into a single testing method (Heated CAT, H-CAT), to evaluate the effectiveness of combining coatings with low ice adhesion with heating as de-icing.

Figure 6 shows a comparison of ice adhesion strengths for different surface types measured with CAT and HCAT. In this, average of all Al alloys was gathered to evaluate an effect of heating on the ice adhesion of different surface finishing. Thermal conductivities for the aluminum alloys are $134 \frac{W}{mK}$ for 2017, $170 \frac{W}{mK}$ for 6082 and $130 \frac{W}{mK}$ for 7075 [24]. Thermal conductivity is an important factor in the de-icing by heating [26]. It was clearly noted that heating had the high influence on ice adhesions by lowering them with all surface types. Ice adhesion values for PE surfaces were 80 kPa (CAT) and 41 kPa (H-CAT). As-received aluminum surfaces had ice adhesions as 296 kPa (CAT) and 61 kPa (H-CAT) whereas values for polished aluminum surfaces were 156 kPa (CAT) and 100 kPa (H-CAT).
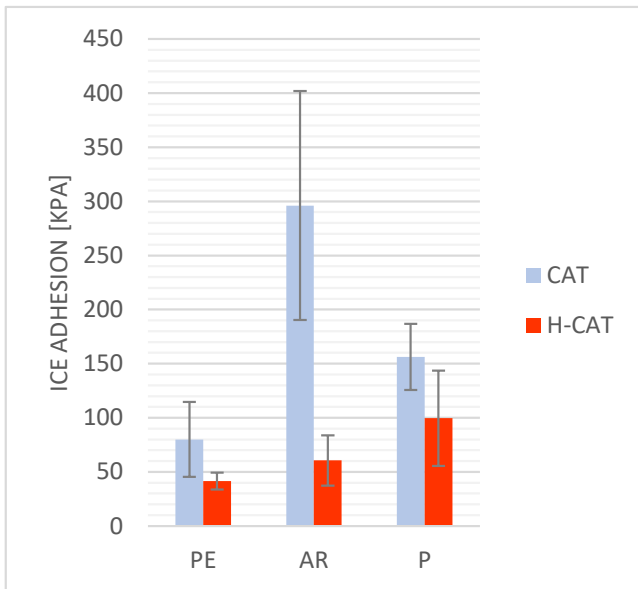
Figure 6. Comparison of CAT and H-CAT for different surface types. PE=Flame sprayed polyethylene, AR=As received Al surface, P=Polished Al surface.

Ice adhesion of as received Al surface was lowered 80 %, ice adhesion of PE surface was lowered 48 %, and ice adhesion of polished Al surface was lowered 36 %.

The highest effect of heating was seen with as-received aluminum surfaces (AR). It is known that aluminum has high ice adhesion [24]. and therefore, de-icing is usually needed. In the current research, heating procedure (temperature) was the same for each sample and it was selected based on the preliminary tests for aluminum.

In this work, heating affected the most on as-received aluminum surfaces because their area for conducting heat was large and their ice adhesion were the highest at the starting point. This indicated that with the high thermal conductivity materials, heating worked well as de-icing especially when there was higher contact area (as received versus polished aluminum surface). Polishing reduced the surface roughness, reducing the surface area. On the other hand, polymer coating acted as an insulator when heating was applied but it had higher icephobicity compared to aluminum and therefore, the lowest ice adhesions were gained with the combination of icephobic surface and heating as de-icing. [27][28]

Ice adhesion of polished aluminum surfaces tested with H-CAT had also higher standard deviation than measured for other surfaces with H-CAT. This could be due to the polishing procedure, which can leave discrepancies to the surface even done with automated polishing machine. On the other hand, ice adhesion of as-received aluminum surfaces measured with CAT also had a high standard deviation, because after the manufacturing process surfaces can have differences in the surface roughness, which can result in a lot of divergence between individual sample surfaces. Surface finishing and surface quality had high effect on icing behavior and ice adhesion, and it should be considered while designing and testing the surfaces.

Figure 7 shows ice adhesions measured with CAT and H-CAT for all different samples separately. For polyethylene surfaces, the ice adhesion decrement was 60 % on 2017, 43 % on 6082, and 36 % on 7075 Al substrates. For as-received surfaces, the decrement was 79 % with 2017, 87 % with 6082 and 65 % with 7075 Al alloy. For polished surfaces, the decrement was 59 % with 2017, 26 % with 6082 and 23 % with 7075 Al alloy.
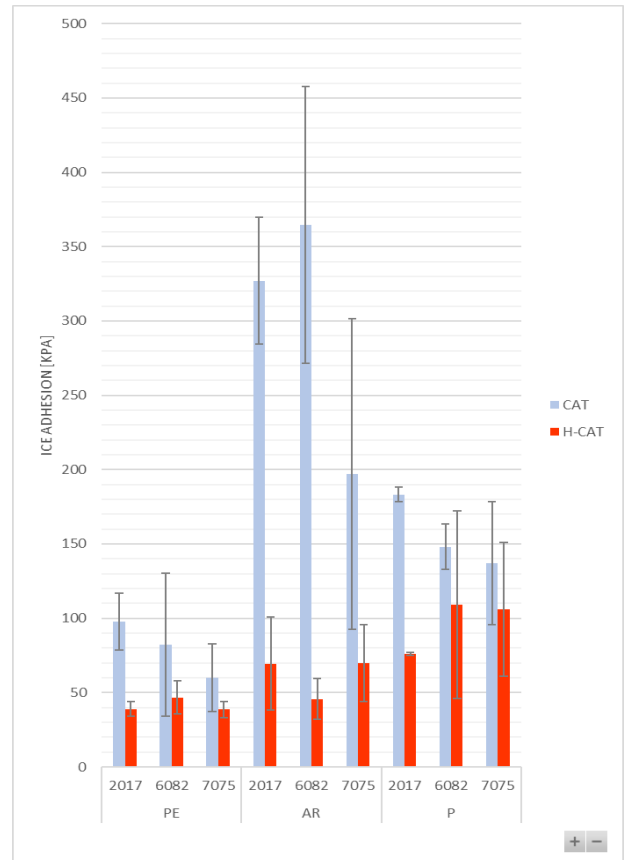
Figure 7. Comparison of CAT and H-CAT for all aluminum types and surface types.

All individual surface types showed the effect of heating during H-CAT testing. However, the effect of different thermal conductivities of different aluminums was not distinctive in Figure 7. Thermal conductivity was highest for the aluminum 6082 alloy ($170 \frac{W}{mK}$), and very similar for 2017 and 7075, $134 \frac{W}{mK}$ and $130 \frac{W}{mK}$ respectively, but the effect of heating was not remarkably higher for this alloy [25]. Only the original, as-received surface type samples showed this difference and were most affected by the heating. Thermal conductivity for PE coating was only $0{,}3175 \frac{W}{mK}$, which was very low in comparison to aluminum alloys [29]. The PE layer was significantly thinner than the aluminum substrate, so its thermal conductivity had smaller effect. Modified surfaces (P and PE) had more variables in their preparation, such as polishing procedure and coating process, that can affect the ice adhesion.

IV.   CONCLUSIONS

This study focused on combining two different testing methods of icing research. As a complex phenomenon, icing research needs variety of testing methods. Because ice prevention can be done many different ways, testing can be challenging. A testing method to test a passive anti-icing (coating) and an active de-icing (heating) can increase

understanding in the synergies of combined ice prevention methods.

The experiments were performed with the H-CAT method to demonstrate the effectiveness of the device in measuring combined effect of heating and icephobic coating. The heating during rotation in centrifugal ice adhesion testing lowered the ice adhesion of the samples, as was expected. The effect of heating was the highest on as-received (unmodified) Al alloy surfaces. Polyethylene coated samples were affected by the heating more than the polished samples. The percentual decrease was smallest for polished samples. Even though the polyethylene coating hinders the effect of the heating de-icing as it works as an insulator, heat effects it more than the polished samples. The ice adhesion of coated surfaces in H-CAT was still lower than non-coated surfaces, suggesting that the combination of heating and icephobic coating was still better for ice prevention. The coating thickness was smaller than the substrate thickness, so the significance of the PE coating for the overall thermal conductivity was smaller.

The H-CAT testing can be still improved in future research. A constant heat monitoring of the heat plate during rotation would improve the reliability of the measurements. Testing different materials with different thermal conductivities is also important to expand understanding of both the testing method and ice prevention. Icing tests for coatings containing additives to increase thermal conductivity are also suggested in future.

REFERENCES

[1] Y. Boluk, *Adhesion of freezing precipitates to aircraft surfaces,* Optima Specialty Chemicals & Technology Inc., Montreal, 1996

[2] Y. Cao, Z. Wu, Y. Su, & Z. Xu, "Aircraft flight characteristics in icing conditions." *Progress in Aerospace Sciences*, vol 74, pp. 62–80, 2015.

[3] Y. Cao, W. Tan, & Z. Wu, "Aircraft icing: An ongoing threat to aviation safety." *Aerospace science and technology*, vol 75, pp. 353–385, 2018.

[4] J. L. Laforte, M. A. Allaire, & J. Laflamme, "State-of-the-art on power line de-icing." *Atmospheric research*, vol 46, pp. 143–158, 1998.

[5] M. Tomaszewski, B. Ruszczak, P. Michalski, & S. Zator, "The study of weather conditions favourable to the accretion of icing that pose a threat to transmission power lines." *International Journal of Critical Infrastructure Protection*, vol 25, 139–151. 2019.

[6] T. Laakso, E. Peltola, B. Tammelin, "Wind turbines in icing environment: Improvement of tools for siting, certification and operation: new icetools." *Ilmatieteen laitos. Raportteja* No. 2005:6

[7] O. Parent, & A. Ilinca, "Anti-icing and de-icing techniques for wind turbines: Critical review." *Cold regions science and technology,* vol 65, 88–96 2011.

[8] N. Dalili, A. Edrisy, & R. Carriveau, "A review of surface engineering issues critical to wind turbine performance." *Renewable & Sustainable Energy Reviews*, vol 13(2), 428–438, 2009

[9] A. G. Kraj, & E. L Bibeau, "Phases of icing on wind turbine blades characterized by ice accumulation." *Renewable energy* 35, 966–972, 2010.

[10] M. Farzaneh, *Atmospheric Icing of Power Networks*. 1st ed., Dordrecht: Springer Netherlands, 2008.

[11] T. Rashid, H. A. Khawaja, & K. Edvardsen, "Review of marine icing and anti-/de-icing systems." *Journal of Marine Engineering and Technology,* vol 15, pp. 79–87, 2016.

[12] A. R. Dehghani-Sanij, S. R. Dehghani, G. F. Naterer, & Y. S. Muzychka, "Sea spray icing phenomena on marine vessels and offshore structures: Review and formulation."*Ocean Engineering,* vol 132, pp. 25–39, 2017.

[13] S. M. Fikke, J. E. Kristjánsson, & B. E. Kringlebotn Nygaard, "Modern meteorology and atmospheric icing." *Atmospheric Icing of Power Networks,* pp.1–29, 2008.

[14] J. W. Elliott, & F. T. Smith, "Ice formation on a smooth or rough cold surface due to the impact of a supercooled water droplet." *Journal of engineering mathematics*, vol 102, pp. 35–64, 2017.

[15] J. Yang, Z. Xingyi, L. Lihan, L. Hongwei, Z. Peiting, C. Zhihao, S. Aiwu, & D. Yong, "Prefabricated Flexible Conductive Composite Overlay for Active Deicing and Snow Melting." *Journal of materials in civil engineering* 30, no. 11, 2018.

[16] H. Wei, Z. Ma, L. Han, B. Jiang, & S. Han, "Durability of Conductive Ethylene–Propylene–Diene Monomer Rubber Composite with Active Deicing and Snow Melting under Vehicle Load." *Journal of Materials in Civil Engineering 34*, 2022.

[17] T. Bai, C. Zhu, B. Miao, K. Li, & C. Zhu, "Vibration de-icing method with piezoelectric actuators." *Journal of Vibroengineering,* vol 17, pp. 61–73, 2015.

[18] E. Huttunen-Saarivirta, V. T. Kuokkala, J. Kokkonen, & H. Paajanen, "Corrosion effects of runway de-icing chemicals on aircraft alloys and coatings." *Materials Chemistry and Physics*, vol. 126, no. 1, pp. 138–51, 2011.

[19] Q. Wu, Z. Zhimeng, L. Pengfei, R. Xuetan, W. Xikui, Z. Fei, & W. Shanlin, "Fluorine-Modified CNT@epoxy Electrothermal Coating for Long-Term Anti-Icing at Low Pulse Voltage." *Colloids and surfaces. A, Physicochemical and engineering aspects* 666, 2023.

[20] T. Xiang, C. Xuxin, L. Zhong, T. Wei, C. Jun, S. Yizhou, L. Bokai, X. Yannan, & Z. Shihong. "Stable Photothermal Solid Slippery Surface with Enhanced Anti-Icing and de-Icing Properties." *Applied surface science,* vol 624, 2023.

[21] L. Shen, D. Li, Y. Shang, & J. Wang, "Deicing behavior and residue characteristic on cold surface excited by ultrasonic vibration." *International Journal of Refrigeration,* vol 149, pp. 168–180, 2023.

[22] J. Zhao, W. Xuancang, X. Lei, R. Junru, C. Yangsen, & T. Yuan, "Concrete Pavement with Microwave Heating Enhancement Functional Layer for Efficient De-Icing: Design and Case Study." *Cold regions science and technology,* vol 210, 2023.

[23] H. Koivuluoto, C. Stenroos, M. Kylmälahti, M. Apostol, J. Kiilakoski, P. Vuoristo, "Anti-icing Behavior of Thermally Sprayed Polymer Coatings. *Journal of Thermal Spray Technology*, vol 26 (1-2), pp. 150-160, 2017.

[24] H. Koivuluoto, E. Hartikainen, & H. Niemelä-Anttonen, "Thermally Sprayed Coatings: Novel Surface Engineering Strategy Towards Icephobic Solutions." *Materials*, *13*(6), 1434-. 2020.

[25] (2024) Aerospace metals website [Online] available: https://aerospacemetals.com/, cited April 19th 2024.

[26] Y. Zhu, X. Huang, J. Jia, Y. Tian, L. Zhao, Y. Zhang, "Experimental study on the thermal conductivity for transmission line icing." *Cold regions science and technology*, vol 129, pp. 96–103. 2016.

[27] Z. He, H. Xie, M. I. Jamil, T. Li, & Q. Zhang, "Electro‑/Photo‑Thermal Promoted Anti‑Icing Materials: A New Strategy Combined with Passive Anti‑Icing and Active De‑Icing." *Advanced Materials Interfaces*, vol 9(16). 2022.

[28] Z. Zhao, H. Chen, X. Liu, H. Liu, & D. Zhang, "Development of high-efficient synthetic electric heating coating for anti-icing/de-icing." *Surface & Coatings Technology*, vol 349, pp. 340–346. 2018.

[29] (2024) Designer Data [Online] Available: https://designerdata.nl/materials/plastics/thermo-plastics/low-density-polyethylene, cited April 19th 2024.

Ice penetration test: Raman spectroscopy insight and benefits

Mario Marchetti[1], Claire Charpentier[2], Jean-Denis Brassard[2], Luc Capobianco[3], Gelareh Momen[2]

[1] *UMR MCD / University of Gustave Eiffel-Cerema, Marne La Vallée, France*
[2] *Anti-icing Materials International Laboratory / Université du Québec à Chicoutimi, Canada*
[3] *Aéroports de Paris, Laboratoire ADP, Orly, France*

claire.charpentier1@uqac.ca, Jean-Denis1_Brassard@uqac.ca, mario.marchetti@univ-eiffel.fr, Luc.CAPOBIANCO@adp.fr, Gelareh.Momen@uqac.ca

Abstract— **Winter maintenance of transportation infrastructures do rely on a set of procedures, protocols, staff organizations and weather services. Certain infrastructures, such as airports, present specific challenges. Chloride chemicals are prohibited due to corrosion risks on aluminium alloys, and extremely low temperatures must be considered. To address these constraints, standardized tests have been developed within the framework of the SAE to evaluate the performance of chemicals either used in de-icing or anti-icing procedures. One such test is the ice penetration test AS-6211 from the G-12 SAE committee, offering a quantitative assessment of a chemical's ability to penetrate a layer of ice over time.**

While this test has proven relevant for evaluating and classifying chemicals, it does have limitations. The use of rhodamine or fluorescein introduces subjectivity into the determination of penetration depth. Furthermore, as the amount of ice melt increases, the dilution of the chemical reduces its efficiency over time However, without a quantitative assessment of concentration, determining a threshold below which the chemical becomes inefficient is challenging. But without any quantitative appreciation of the concentration, it is difficult to appreciate a concentration threshold below which the chemical is no longer efficient. Performing the test at negative temperatures increases the likelihood of ice occurrence, but the inability to observe a liquid-to-solid phase transition poses a limitation. It is difficult to appreciate a concentration threshold below which the chemical is no longer efficient without a quantitative assessment of concentration.

The Anti-icing Materials International Laboratory (AMIL) at the University of Quebec in Chicoutimi possesses an extensive experience in characterizing these chemicals, specifically runway anti-icing fluids and aircraft de-icing fluids, and in implementing the AS-6211 test. Recently, AMIL has explored the benefits of integrating Raman spectroscopy into these tests to overcome the aforementioned limitations.

To achieve this, an experimental approach was developed based on the AS-6211 test, incorporating continuous spectroscopic measurements at depths of 2, 4, 8, and 10 mm below the ice surface within a glass tube after the application of the de-icing chemical. Raman measurements enabled the detection of when the chemical reached each selected depth and its concentration. By considering the time of acquisition for each Raman spectrum, it becomes possible to elaborate on ice melting kinetics. This methodology demonstrates the extent to which chemical dilution may begin to limit its ability to melt residual ice, leading to the detection of a phase transition from liquid to solid when dilution reaches a critical threshold.

Keywords— ***Runway de-icing product, Raman spectroscopy, ice, ice penetration, characterization***

I. Introduction

Winter maintenance of transportation infrastructures do rely on a set of procedures, protocols, staff organizations and weather services. Among the existing procedures, some are dedicated to the spreading of de-icers either in the form of dry salts, of brine, or as a mixture of both. They aim at avoiding ice occurrence of circulated surfaces, and snow accumulation, and therefore maintain a proper grip level. Theses de-icers are mainly chloride salts for roads and highways. But certain infrastructures, such as airports, present specific challenges. Thus, chloride chemicals are prohibited due to corrosion risks on aluminium alloys, and extremely low temperatures to which both the infrastructures than for aircrafts might be submitted to must be considered. To address these constraints, standardized tests have been developed within the framework of the SAE to evaluate the performance of chemicals either used in de-icing or anti-icing procedures. One such test is the ice penetration test AS-6211 [1] from the G-12 SAE committee, offering a quantitative assessment of a chemical's ability to penetrate a layer of ice over time.

The Anti-icing Materials International Laboratory (AMIL) at the University of Quebec in Chicoutimi possesses an extensive experience in characterizing these chemicals, specifically runway anti-icing fluids and aircraft de-icing fluids, and in implementing the AS-6211 test. Recently, AMIL has explored the benefits of integrating Raman spectroscopy into these tests to overcome the aforementioned limitations. This approach was implemented in the mid 2000 and has proven its ability to both identify water solid-liquid phase transition [2], along with the one to quantify both the freezing point and the concentration in anti-icing products [3].

To achieve this implementation, a cooperation between AMIL, UMR MCD and Aéroports de Paris has been elaborated based on the competences and knowledge of each. An experimental approach was then jointly developed based on the AS-6211 test, incorporating continuous spectroscopic measurements at depths of 2, 4, 8, and 10 mm below the ice surface within a glass tube after the application of the de-icing chemical. Raman spectra were collected since these measurements enabled the detection of when the chemical reached each selected depth and its concentration. By considering the time of acquisition for each Raman spectrum, it becomes possible to elaborate on ice melting kinetics. This methodology demonstrates the extent to which chemical dilution may begin to limit its ability to melt residual ice, leading to the detection of a phase transition from liquid to solid when dilution reaches a critical threshold.

II. Materials and methods

Materials, experimental set ups, staff and scientific instrumentation were collectively brought by AMIL, UMR MCD and Aéroports de Paris.

A. Ice and anti-icing materials

In this first feasibility approach, a potassium formate (KFo) anti-icing salt worldwide used on airport platforms facing. To be compliant with the AS-6211 test, a KFo brine was elaborated at a concentration close to saturation with dry salt and distilled water.

A glass tube containing water was placed into a climatic chamber 24 h prior to perform the test o generate 0.5 mL of ice

B. Climatic chamber

Tests were conducted in a refrigerated chamber of 2 m x 2 m x 9.1 m, where it is possible to simulate precipitations such as freezing rain and ice pellets, that can be applied to medium- and large-scale structures such as cables, bridge sections, aircraft, and even drones. The climatic chamber temperature, which can be controlled between +10°C and -35°C, was set to -5°C.

C. Raman spectrometer

The Raman spectrometer consisted in a i-Raman Plus portable spectrometer from BWTek, operating with a 785 nm laser wavelength with a 340 mW output power. The Raman signal is collected by means of a Raman BAC 102 probe using a confocal lens, providing a contactless measurement with a distance of roughly 5 mm. The spectrometer is operated through the BWSpec 4.11 software, allowing a control of both the laser power, the integration time and the acquisition frequency. The characteristics of spectroscopic measurements are summarized in Table 1. One a Raman spectrum is collected, a few milliseconds were allocated to the system before triggering the next acquisition. As a consequence, a spectrum was collected nearly every 10 s.

TABLE I. Spectroscopic measurements characteristics

Spectrometer Characteristics	Value
laser power (mW) (and %)	340 (100 %)
integration time (s)	10
number of accumulated spectra	1

D. Experimental set up and protocol

The AS-6211 ice penetration process with implementation of a Raman spectrometer consisted in placing the Raman probe against the glass tube first 2 mm below the interface between ice and air before the application of the anti-icing fluid, see Fig. 1.
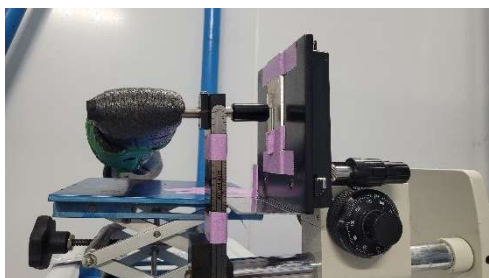
Fig. 1 Experimental set up of the ice penetration test including a Raman probe in a climatic chamber at -5°C.

Then, once the melting has started, the probe is moved of 2 mm towards the bottom of the tube each time the interface between the fluid and the ice has reached the zone where the spectroscopic measurement is performed. Therefore, each time the anti-icing fluid is detected, 2 mm of ice have been melted as illustrated in Fig. 2. Test lasted till the detection of the brine occurred once the Raman probe was located 10 mm below its initial position, measured with a metallic ruler, as indicated in Fig. 1.
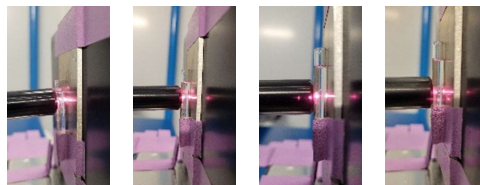
Fig. 2 Evolution of the BAC 102 Raman probe position during the ice penetration test.

III. Results and discussion

At the end of this ice penetration test, over 810 Raman spectra were collected, and the experiment lasted nearly 15 minutes. Spectroscopic data was pre-processed to remove cosmic ray peaks, fluorescence, and was normalized with respect to each spectrum area, as indicated in Fig. 3. A peak characteristic of intense and sharp formate one in the 1350 cm^{-1} spectral range can be observed
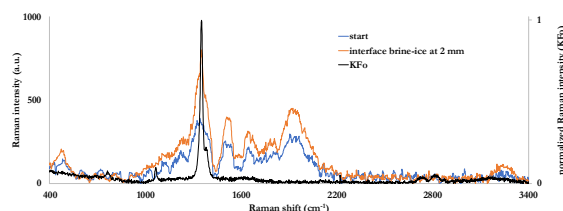
Fig. 3 Raman spectra of during the ice penetration on the first 2 mm at the beginning (blue line) and once the interface ice-brine reached 2 mm (orange line), with the 1350 cm-1 peak due to formate.

As expected, the Raman signature of the interface at 2 mm does present a peak of the formate, indicating the penetration of the brine into a 2 mm thick full layer. It took 400 s for the initial KFo to melt this layer of ise. But Raman spectra were accurately investigated before the interface was reached. Results are presented in Fig. 4. It appears that the brine was detected thanks to the KFo peak at 1350 cm^{-1} after 120 s. This means that the ice penetration test based on the visual detection of the ice-brine interface, included when using a color indicator, underestimates the capacity of an anti-icing to penetrate ice.
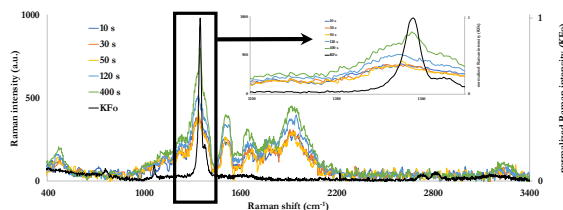
Fig. 4 Raman spectra collected during the ice penetration test on the first 2 mm indicating brine is detected at 2 mm before the ice

is fully melted, thanks to the presence of the 1350 cm^{-1} peak due to formate detected as soon at 120 s.

The same analysis was conducted for the other 2 mm-thick ice layers, with times offsets, illustrated in Table 3 and in Fig. 5. It appears that above a 6 mm-ice thickness, there is no longer any significant difference between the detection of penetrated ice by the anti-icing fluid using a visual detection and a spectroscopic one. This can be attributed to the dilution of anti-icing fluid by melted ice. Nevertheless, a 6 mm thickness can already be considered as an important layer and as a serious threat for runway grip during winter. Also, the thinner the ice layer, the greater the ice penetration and the easier its removal using an ice scraper mounted on a vehicle.

TABLE 2. ELAPSED TIME FOR ICE PENETRATION BASED ON VISUAL AND SPECTROSCOPIC DETECTION

Ice Layer Thickness	Elapsed Time by Visual Detection	Elapsed Time by Spectroscopic Detection
2	400	120
4	720	630
6	1320	1180
8	3620	3420
10	8120	7990
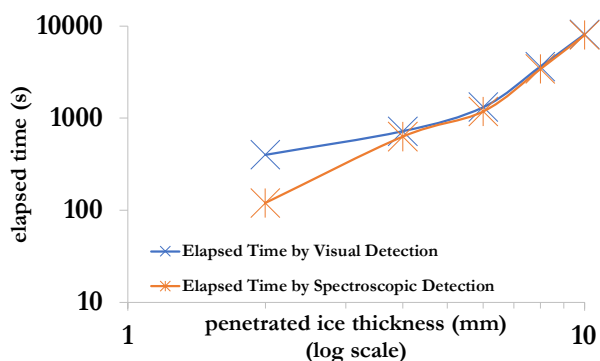
Fig. 5   Ice penetration elapsed time as a function of ice thickness.

IV. CONCLUSIONS

Runway anti-icing fluids and aircraft de-icing fluids are submitted to a series of standardized tests prior to their use into winter maintenance protocols and procedures on airports. Among these tests, the AS-6211 one from the G-12 SAE committee is offering a quantitative assessment of a chemical's ability to penetrate a layer of ice over time. So far, the result was obtained through a visual inspection using a ruler and a color indicator. Raman spectroscopy was recently implemented to identify to what extent it could provide new insights on the performance of these anti-icing fluids. Spectroscopic measurements confirmed results obtained using the current AS-6211 protocol, in particular the efficiency decrease as the amount of melted ice increases and the anti-icing fluids is progressively diluted. But it also revealed that the fluid significantly penetrated the ice layer without any visual detection, significantly improving the ice penetration performance at the very beginning of the test. Once the first 4 mm of ice are melted, both the spectroscopic approach and the conventional are providing results within the same order of magnitude. Such results do confirm the benefits of the spectroscopic approach in the characterization SAE tests of winter maintenance chemicals for airports.

REFERENCES

[1] AS6211 Ice Penetration Test Method for AMS1431 and AMS1435 Runway Deicing/Anti-icing Products, Aerospace Standard AS6211, SAE International, 2021.

[2] I. Durickovic, P. Bourson, M. Marchetti, R. Claverie, J.-M. Chassot, M. Fontana. *Water-ice phase transition probed by Raman spectroscopy*. Journal of Raman Spectroscopy, 201142, 6, pp. 1408–1412.

[3] M. Marchetti, P. Bourson, M. D. Fontana, C. Jobard, B. Saintot, G. Casteran. *Spectroscopic and chemiometrics supported studies on discrimination, phase transition and concentration identifications of 1,2-propylene glycol solutions, and of a mixture of potassium acetate with 1,3-propanediol solutions as anti-icing fluids*. Cold Regions Science and Technology, 142, (2017), pp. 34–41. https://doi.org/10.1016/j.coldregions.2017.07.009.

Determination of Ice Adhesive Properties for Icephobic Substrates and their Application within Cohesive Zone Models

Pau Riera[1,2], Solène Delran[2], Valérie Pommier-Budinger[2], Ian Roberts[1]

[1] *AeroTex UK LLP, Farnborough, United Kingdom*
[2] *ISAE-SUPAERO, University of Toulouse, Toulouse, France*

pau.riera-i-portillo@isae-supaero.fr, solene.delran@isae-supaero.fr, valerie.budinger@isae-supaero.fr, ian.roberts@aerotex.co.uk

Abstract— **Hybrid ice protection systems combining icephobic coatings with electro-expulsive actuators exhibit potential to significantly reduce power requirements compared to conventional systems. Numerical modelling of these systems is hindered by the lack of both experimental data and clear simulation guidelines to reproduce adhesive de-icing from an icephobic coating. The critical energy release in mode I (tension) of an ice/substrate interface for several coated samples is characterized by means of a previously developed framework and used in a finite element analysis via a Cohesive Zone Model. The presence of a coating is implicitly considered through the computed fracture parameters. Simulation results are validated with the experimentally observed delamination, demonstrating strong agreement. The icephobic performance of the samples is assessed and compared.**

Keywords— ***Electro-expulsive ice protection system, icephobic coating, ice failure modelling, cohesive zone model, ice fracture energy in mode I.***

I. Introduction

Current requirements in the aerospace industry are shifting the focus from anti-icing to de-icing with ultra-low power ice protection systems (IPS) driven by the requirements from novel concepts such as air-taxis and drones. Within the context of transitioning to More Electric Aircraft (MEA), the need to optimise power consumption has become a primary concern. Mechanical IPS offer a significant reduction in power consumption compared to bleed-air or electro-thermal systems while maintaining the same advantages [1]. These systems could further benefit from the presence of low ice adhesion coatings. Some icephobic coatings have shown improved de-icing performance by achieving ice adhesion strengths up to several orders of magnitude lower than those with metallic substrates such as aluminium or titanium. Hybrid IPS composed of electro-expulsive actuators and icephobic coatings show promise in addressing these applications where little electrical power is available [2]. Presently, the development of icephobic coatings faces several challenges such as the complex interaction of ice with surfaces [4]-[7] and the limited durability that most show against environmental agents [8]-[10]. On the other hand, the design of hybrid systems would benefit from their numerical modelling as well as the resulting ice shedding by improving their exploitability and significantly reduce testing costs, often associated with testing facilities.

A substantial part of the modelling is the ability to correctly predict adhesion failure of the ice from the underlying substrate. While delamination in composite materials has been widely studied, characterising the failure between ice and a substrate is challenging due to variability in the ice structure with temperature, freezing fraction and other environmental factors, in addition to the nature of the substrate itself [10]-[12]. Experimental testing with icephobic coatings is scarce in the literature and ice adhesion characterisation is a challenging task due to the lack of experimentally derived fracture parameters under relevant loading conditions. Reported data is limited to providing ice adhesion strength to coated substrates [12]-[14], which provides a short-ranged scope within a wider context of ice failure analysis. Furthermore, given the significant scatter of measurements found in the literature, it is essential that the failure mechanism to be modelled mirrors the system under assessment.

The Cohesive Zone Model (CZM) has proven to be a powerful and versatile tool to model ice delamination alongside finite element models [15]-[18]. While standard CZM formulations used in composite material modelling rely on specific interfacial parameters to be determined by means of specialized testing configurations, these are generally infeasible for use in ice/substrate interfaces. To address this issue, a rational complementary framework was developed in [19], where a quasi-static pushing test rig is used on an iced plate in combination with the Virtual Crack Closure Technique (VCCT) to assess the critical energy release rate in tension of the ice/substrate interface. The test rig is designed to produce ice delamination representative of an electro-expulsive system, as an impulse produces adhesive delamination as well as cohesive fracture within the ice itself [20]. Furthermore, no current guidelines exist for the integration of icephobic-coated substrates within a CZM, especially given that the average thickness of an icephobic coating lies within the microscopic scale, well below meshing capabilities in macroscopic models.

The work presented in this paper will build upon and extend the progress in [19] through describing improvements to the experimental methodology to better determine critical parameters employed in the CZM. Ice adhesive fracture propagation for a series of aluminium plates with and without icephobic coatings and its modelling using finite elements and a CZM approach are presented. The critical energy release rate in mode I (tension) derived from the testing and posterior VCCT analysis is then implemented into a finite element analysis employing the CZM and the ability of this approach

to predict the adhesive failure behaviour when icephobic coatings are present is demonstrated and validated.

The considered coatings consist of state-of-the-art concepts based on gradient vertical polymers, patterned hydrophobic/hydrophilic coatings with patterning parallel and perpendicular to the cohesive crack propagation direction, and a hydrophobic silicone-epoxy coating. By applying the experimental and analysis process to both conventional aluminium surfaces and those with icephobic coatings, the relative performance of the surfaces and their integration into a Cohesive Zone Model to a design hybrid de-icing system is discussed.

II. THE COHESIVE ZONE MODEL

The CZM is a phenomenological approach predominantly employed in composite material modelling to forecast the onset and progression of delamination between two adherents [21], [22]. This technique operates under the assumption that within a fractured interface, the material's failure process is confined to a narrow region ahead of the crack tip, while the remainder of the body adheres to conventional laws of deformation and stays undamaged. Previous concerns regarding theoretical stress singularities at the crack tip are therefore alleviated, as adhesive failure is continuously modelled. However, cohesive zone models necessitate a priori understanding of the physical system being modelled, as the crack propagation path must be explicitly outlined.

Typically coupled with finite elements, the CZM employs a distinct formulation compared to conventional elements. Instead of complying with classical mechanics, the constitutive equation is based on a function describing the relationship between the traction experienced by the two crack faces and their relative displacement. The traction-displacement (or cohesive) law relates the boundary traction σ with the separation $\delta = u_n^+ - u_n^-$ of the crack faces conforming the adherents, in the case of adhesion modelling. Depending on the materials' interface, the shape and size of the cohesive law may vary widely, but a common approach for brittle materials is the so-called bi-linear softening law [23], [24]. The bi-linear law assumes that the plastic region ahead of the crack tip is small enough for the damage to be highly localized. In a single-mode loading scenario, fracture onset and propagation using this formulation is determined by a combination of three out of four parameters: the linear stiffness K, the peak stress σ_c, the failure displacement δ_f and/or the critical energy release rate G_c (area under the curve), as seen in Fig. 1.
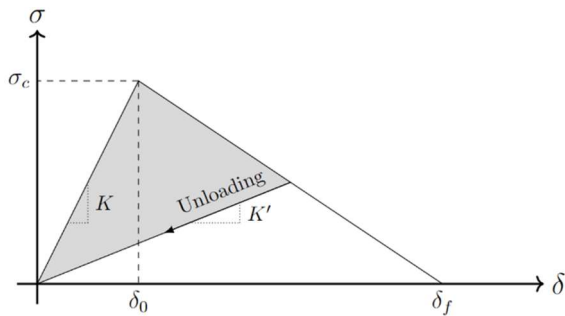
Fig. 1 Bi-linear traction-displacement law.

Under more realistic mixed-mode delamination conditions, that is a combination of mode I, II and/or III, fracture initiation and propagation criteria need to be established. Every fracture mode has its corresponding bi-linear law, but crack onset and progression are realistically achieved much earlier than reaching the critical traction and displacement separately for each mode function. A quadratic law is a common choice as a fracture initiation criterion

$$\sqrt{\left(\frac{\sigma_z}{\sigma_c}\right)^2 + \left(\frac{\tau_{zx}}{\tau_c}\right)^2 + \left(\frac{\tau_{yz}}{\tau_c}\right)^2} = 1, \qquad (1)$$

for the normal stress σ_z and the shear stresses τ_{zx} and τ_{yz}, associated, respectively, to modes I (tensile), II and III (sliding and tearing shear, respectively). The parameters σ_c and τ_c represent, respectively, the peak stresses (or tractions) in shear and tension. For a uniform, isotropic interface, it is assumed that delamination mechanisms in mode II and III are identical, thus leading to the selection of the same variables. In addition, the power law is typically utilized to forecast fracture propagation in mixed-mode delamination conditions

$$\left(\frac{G_I}{G_{Ic}}\right)^\alpha + \left(\frac{G_{II}}{G_{IIc}}\right)^\beta = 1, \qquad (2)$$

with α and β usually ranging between 1 and 2 and being material dependent. In this study, $\alpha = \beta = 1$ for simplicity. Furthermore, the magnitudes G_{Ic} and G_{IIc} represent the critical energy release rates for mode I and mode II-III, respectively.

III. METHODOLOGY

A. Fracture energy retrieval

In this paper, the critical energy release rate in mode I, G_{Ic}, for coated plates is obtained using the framework described in [19], where experimental and simulation results are combined to determine the appropriate value. A quasi-static pushing test rig (see Fig. 3) is used on a clamped iced plate to determine the delamination length for a given deflection of the plate due to the action of an actuator, based on a displacement-driven electrical cylinder. All coated and uncoated samples have a substrate of 1-mm thick aluminium 6082 and a width of 40 mm. The length between the clamps is 130 mm except for the patterned coatings that have a plate length of 110 mm.
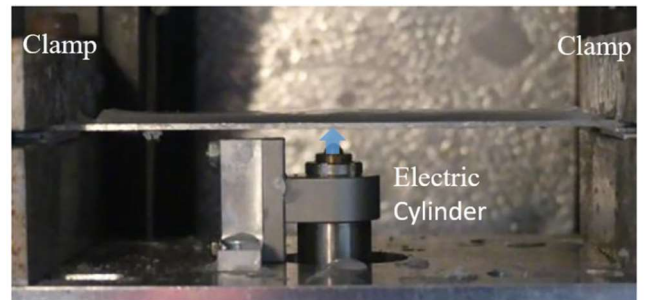
Fig. 2 Flexural test rig with an iced plate.

The first coated sample employs a novel method involving the manufacturing of icephobic coatings. By using initiated chemical vapor deposition, a gradient polymeric coating 300 μm-thick is applied onto the aluminium plate. This polymer is formed from two distinct compounds: a monomer exhibiting encouraging icephobic properties located at the top section of the structure, and a monomer with high adhesion to the substrate, located consequently in the bottom section of the

structure [25]. This approach thereby mitigates concerns regarding durability and erosion. This sample is referred to as 'Gradient'. The second sample is coated using the off-the-shelf boat bottom paint Wearlon Super F-6M [26]. This a water-based silicone-epoxy coating with highly hydrophobic and low surface tension properties. This sample is referred to as 'F-6M'. Finally, the last batch of samples utilises the concept of discontinuity-enhanced icephobicity, by which ice nucleation and propagation are regulated to ensure lower ice adhesion to the substrate [27], [28]. Using hydrophilic patterns embedded in a hydrophobic surface, spatial control over ice nucleation can be achieved. The substrate is made from epoxy resin, and the patterns use the PHEMA polymer. Due to the radial nature of the test rig, two different patterns were designed to exploit this behaviour to promote delamination in a radial manner (see Fig. 3), while an unpatterned sample serves for comparison. These are referred to as 'Pattern' A to C as shown in Fig. 3.
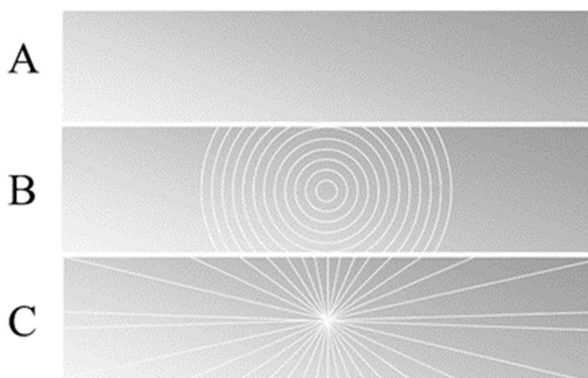
Fig. 3 All samples are coated with hydrophobic polymers. Samples B and C have different patterns of hydrophilic epoxy.

A test with this setup begins with ice accretion onto the plate inside a freezing chamber at -20°C. The presence of a hydrophobic coating makes the process of ice accretion especially challenging. Since spraying or direct water deposition are not viable options, a pressure-sensitive adhesive is used to delimit a contained region (see Fig. 5) where 10 ml of water are poured using a syringe to create a uniform, 3 mm-thick structure of ice. Following ice accretion, the actuator initiates a gradual upward motion at a rate of 0.1 mm/s. The loading rate is deliberately set to ensure quasi-static conditions, while also being large enough to disregard any creep effects. As the iced plate deflects, tensile stress accumulates on the upper surface of the ice, leading to the formation of a cohesive crack across the plate width that rapidly propagates through the ice thickness until reaching the ice/substrate interface. At this point, delamination begins and extends with increasing load. Generally, adhesive crack propagation occurs abruptly, rather than progressively. Therefore, instead of gradually increasing, delamination advances in sudden bursts upon reaching specific plate deflections. In this work, the vertical displacement for which the adhesive crack suddenly propagates is considered, as opposed to [19], where a fixed deflection value is taken for all measurements. Finally, the measured delaminated length and the vertical displacement of the plate are used as input parameters to a VCCT analysis, providing G_{Ic} as an output. The VCCT model, similarly to [19], is only comprised of a plate with ice, both parts being modelled as elastic materials.

In the case of the ice, the material density used is 900 kg/m^3, the Young's modulus is 9 GPa, and the Poisson's ratio, 0.33. Given the thin nature of the coatings, which makes meshing and any consequent calculations extremely computationally expensive, their presence is hereby accounted for implicitly. As a consequence, only the adhesive properties of the ice/coating interface may be inferred, assuming that the coating does not contribute to the total mass or stiffness of the system.

Fig. 4 Confined region using a pressure-sensitive adhesive to prevent water from slipping.

B. Cohesive zone numerical model

A quasi-static, three-dimensional numerical model using finite elements coupled with CZM is implemented to reproduce the experimental results. The model is built on the commercial software LS-DYNA, based on a nonlinear explicit solver suitable to integrate a CZM analysis. The bi-linear traction-displacement formulation is implemented through a tiebreak contact between the upper-most layer of elements corresponding to the plate and the bottom-most layer of ice elements.

Similarly to [19], a quarter model with an artificially pre-cracked central face in the ice is used, where the ice elements are unconstrained. In addition, the row of ice elements closest to the clamp is tied to the plate by sharing nodes to avoid stress concentrations from overtaking unrealistic adhesive failure from the borders. A representation of the model is shown in Fig. 5, where the ice is meshed in blue, the plate sample is grey, and the tip of the actuator is a black sphere. As stated earlier, the coating is not explicitly considered in this model. Instead, the fracture parameters of the coating are used in the tiebreak contact to account for its presence. The employed elements are fully integrated hexahedrons and the material models for the ice and the plate are the same as previously used in the VCCT analysis.
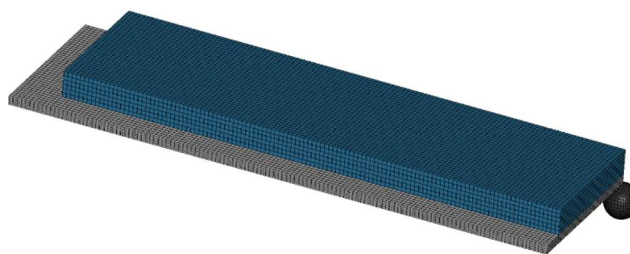
Fig. 5 Quartered finite element model of the iced plate.

The CZM formulation in the tiebreak contact is implemented using two bi-linear laws, for modes I and II-III, respectively. Both can be defined using the critical energy release in mode I obtained from the VCCT analysis. Given the tensile nature of the test rig, mode II fracture does not impact

the results significantly. Therefore, the values for G_{IIc} are chosen appropriately as function of those in mode I for shear not to have influence. The linear stiffness is a numerical construct that need to be large enough for the interface not to contribute significantly to the global compliance. Following [24], the values $K_I = K_{II} = 1.5 \cdot 10^5$ N/mm^3 are chosen. Finally, the peak stresses can be related to the ice adhesion strength. All numerical studies in the literature use peak stresses corresponding to measures of force averaged by the surface of the interface. On the other hand, some authors agree on employing measures based on stress distributions close to the fracture zone instead [28]-[30]. Here, an alternative approach is taken to ensure the mesh size is compliant with accurate results. In [24], it is recommended to use, for a mode I bi-linear law,

$$\sigma_c = \min \left\{ \sigma^0, \sqrt{\frac{E G_{Ic}}{3h}} \right\} \qquad (3)$$

where σ^0 represents the experimentally measured value, E is the Young's modulus of the adherend, and h is the mesh size of the elements conforming the interface. The same foundations apply for the function for mode II-III. This approach ensures that at least three elements are within the cohesive zone length, a small area ahead of the crack tip where the fracture mechanism is concentrated. In the case of the 130 mm-long plates, $h = 0.5$ mm, whereas $h = 0.42$ mm for the model with 110 mm-long plates, so that the overall number of elements is constant.

IV. RESULTS

A. Experimental testing

A set of between six to ten experiments were performed using the aforementioned procedure for each of the samples. Adhesive crack propagation was shown to be abrupt for all samples but the F-6M one, where gradual delamination is observed. A vertical displacement of 0.55 mm was measured as the required deflection for a plate to abruptly propagate an adhesive crack. This result has shown consistency throughout experiments and different samples. The result of a test for an F-6M is portrayed in Fig. 6, where the delaminated ice is spotted by having higher opacity around the central part of the plate.
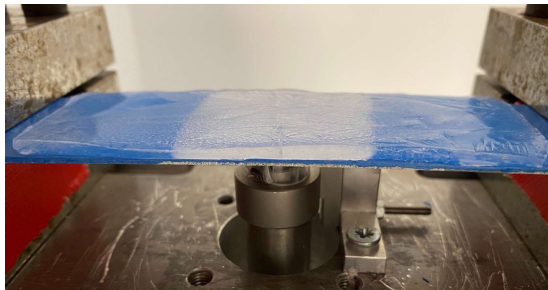
Fig. 6 Tested F-6M sample, with a total delamination length of 40 mm.

Furthermore, Fig. 7 displays the adhesive performance of all coated samples as well as a bare aluminium plate. The normalised fracture energy G_{Ic} with respect to be the bare plate from the VCCT analysis is represented alongside the mean relative crack length obtained experimentally (shown as the percentage of delaminated length from the total interfacial length) for every sample, each with the standard deviation of the results. In the case of the bare aluminium plate, the computed fracture energies range from 0.2 to about 0.5 J/m^2, in line with similarly reported values in aluminium substrates [31]-[33]. As observed, the best performance is demonstrated by the F-6M coated plate, displaying the lowest fracture energy and largest delamination length, implying less ice adhesion. Furthermore, data from the uncoated and gradient polymer coated samples are very similar, suggesting little to no effect from the coating in lowering ice adhesion. This may be explained by the fact that none of the coated plates are polished, and given the low coating thickness, the ice may be experiencing interlocking with the surface finish. In addition, during the experiments, easy detachment of the whole ice structure was observed while removing the bounding adhesive shown in Fig. 4 from these samples, implying that the gradient polymer may be more effective in applications dominated by shear stress. On the other hand, the patterned coatings appear on the other end of the spectrum. While the crack lengths in patterns A and B are close to other measures, the shorter samples induce more curvature on the central part of the plates for equal deflections due to the actuator, promoting delamination. Therefore, the computed fracture energy values are larger.
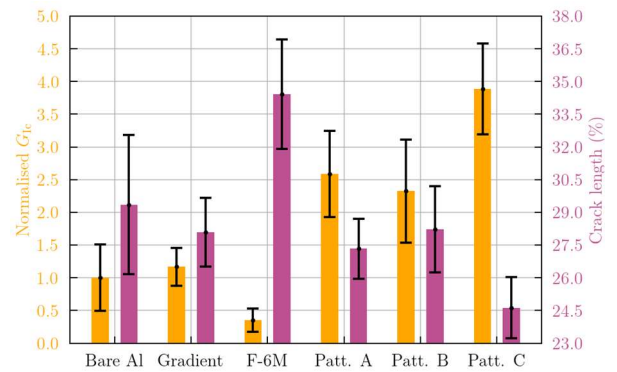
Fig. 7 Mean and standard deviation of the measurements for each coating.

Finally, an aspect of primary concern regarding icephobic coatings is their erosion resistance against environmental agents as well as durability. During the tests it was noted that the gradient and patterned coatings did substantially degrade after ten to twenty testing cycles each, with visible scratches and decreased performance.

B. Cohesive zone model analysis

The previously presented data in Fig. 7 can be readily used in a CZM analysis to assess the validity of the results and their subsequent implementation in delamination simulations. For a complete set of fracture parameters in a CZM analysis, G_{IIc} and the peak tractions in mode I and II-III, σ_c and τ_c are needed. As mentioned above, the primary mechanical stress induced in the ice/substrate interface is tension, where shear does not play a significant role. Consequently, G_{IIc} may take an arbitrarily large value that guarantees no ice adhesion failure will occur in mode II-III. Taking the mean values from Fig. 7 for the two extreme cases, the F-6M and Pattern C, as well as the bare aluminium as an intermediate case, Fig. 8 presents the simulated crack length as a function of the ratio G_{IIc}/G_{Ic}. For the simulations, the corresponding peak stress for

shear and tension is computed using (3), where the cohesive zone length approximation is always used due to the relatively low energy values. The plot displays an asymptotic behaviour that gets more prominent for lower values of G_{Ic}, as is the case with the F-6M coating. Nonetheless, it shows that a ratio G_{IIc}/G_{Ic} of 2 or above is generally a good approximation to have a similar value in crack length as the one experimentally retrieved. Going higher in G_{IIc} does not significantly impact the final delamination length.
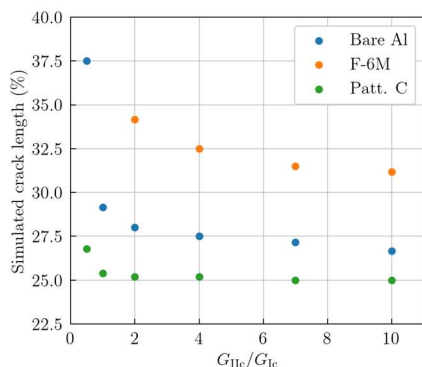
Fig. 8 Simulated crack length as a function of G_{IIc}/G_{Ic}.

Finally, using the mean values from Fig. 7 and $G_{IIc} = 2G_{Ic}$, a CZM analysis is performed for each sample. The simulated delamination for the whole interface between the ice and a plate coated with F-6M can be seen in Fig. 9. In the figure, the interfacial damage in the tiebreak contact is fringed from 0 (no damage) to 1 (complete damage, i.e. delaminated), and may be visually compared to Fig. 6. The resulting delamination lengths are reported in Fig. 10, where they are compared with the experimentally measured ones, showing an overall good agreement. The closest match corresponds to the F-6M coating, with a relative error of around 0.73%, whereas the bare aluminium has the greatest difference between simulated and measured adhesive crack length, having a relative error of 4.61%. These values fall well within the experimental scatter and therefore demonstrate that the approach used is a valid one.
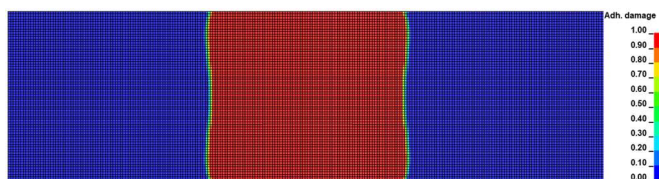
Fig. 9 Simulated adhesive damage in the ice/substrate interface in the case of an F-6M sample.
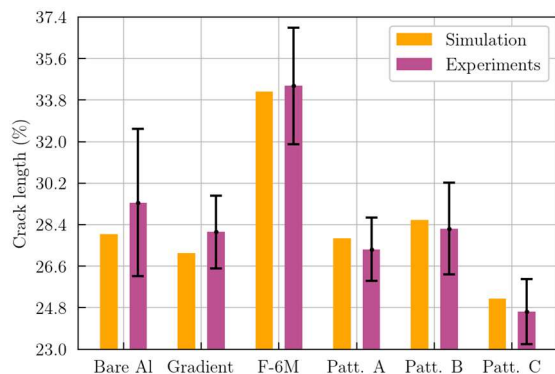
Fig. 10 Comparison between the simulated delamination length and the experimentally measured one.

V. Conclusions

In this paper, an existing methodology that computes the critical energy release rate in mode I of fracture for an ice/substrate interface is used and improved for its application on icephobic-coated surfaces. The determination of fracture parameters is paramount to ensure a proper and accurate modelling of ice delamination, but the literature is lacking the required parameters to enable such modelling.

Four different kinds of substrates are considered in this work: a bare aluminium plate, a state-of-the-art icephobic coating based on a gradient polymer, a hydrophobic boat bottom paint, and three different hydrophilic patterns embedded on a hydrophobic epoxy polymer. Each coating is tested using the improved procedure, showing controllable, repeatable, and consistent results throughout many repetitions. The patterned coatings displayed the lowest adhesive crack propagation, implying a lower performance with a G_{Ic} four-fold that of bare aluminium. On the other hand, the Wearlon F-6M exhibited the best performance overall, experiencing a reduction in critical energy release rate of 65% with respect to a bare aluminium substrate.

The value of G_{Ic} for each sample is then used in a CZM analysis, where the presence of a coating is accounted for implicitly via the adhesive parameters on an ice/aluminium interface. For a mixed-mode CZM, the parameter G_{IIc} is shown not to be significant due to the tensile nature of the test rig. The peak stresses can be readily computed using the fracture energies. The simulated delamination is shown to be in good agreement with the measurements for each coating, being 4.61% the largest error between both, in the case of the bare aluminium.

References

[1] Z. Goraj, 'An Overview of the De-Icing and Anti-icing Technologies with Prospects for the Future', presented at the 24th International Congress of the Aeronautical Sciences, Yokohama, Japan, 2004.

[2] X. Huang *et al.*, 'A survey of icephobic coatings and their potential use in a hybrid coating/active ice protection system for aerospace applications', *Progress in Aerospace Sciences*, vol. 105, pp. 74–97, Feb. 2019,

[3] I. A. Ryzhkin and V. F. Petrenko, 'Physical Mechanisms Responsible for Ice Adhesion', *J. Phys. Chem. B*, vol. 101, no. 32, pp. 6267–6270, Aug. 1997,

[4] M. Huré, P. Olivier, and J. Garcia, 'Effect of Cassie-Baxter versus Wenzel states on ice adhesion: A fracture toughness approach', *Cold Regions Science and Technology*, vol. 194, p. 103440, Feb. 2022,

[5] T. M. Schutzius *et al.*, 'Physics of Icing and Rational Design of Surfaces with Extraordinary Icephobicity', *Langmuir*, vol. 31, no. 17, pp. 4807–4821, May 2015,

[6] A. Elzaabalawy and S. A. Meguid, 'Advances in the development of superhydrophobic and icephobic surfaces', *Int J Mech Mater Des*, vol. 18, no. 3, pp. 509–547, Sep. 2022,

[7] G. Fortin, 'Considerations on the Use of Hydrophobic, Superhydrophobic or Icephobic Coatings as a Part of the Aircraft Ice Protection System', in *SAE Technical Papers*, Montreal, Canada, Sep. 2013.

[8] N. Rehfeld, B. Speckmann, C. Schreiner, and V. Stenzel, 'Assessment of Icephobic Coatings—How Can We Monitor Performance Durability?', *Coatings*, vol. 11, no. 6, p. 614, May 2021,

[9] A. Nistal, B. Sierra-Martín, and A. Fernández-Barbero, 'On the Durability of Icephobic Coatings: A Review', *Materials*, vol. 17, no. 1, Art. no. 1, Jan. 2024,

[10] Ml. A. Pervier and D. W. Hammond, 'Measurement of the fracture energy in mode I of atmospheric ice accreted on different materials using a blister test', *Engineering Fracture Mechanics*, vol. 214, pp. 223–232, Jun. 2019,

[11] A. Marbœuf, L. Bennani, M. Budinger, and V. Pommier-Budinger, 'Electromechanical resonant ice protection systems: numerical

investigation through a phase-field mixed adhesive/brittle fracture model', *Engineering Fracture Mechanics*, vol. 230, p. 106926, May 2020,

[12] N. Rehfeld *et al.*, 'Round-Robin Study for Ice Adhesion Tests', *Aerospace*, vol. 11, no. 2, Art. no. 2, Feb. 2024,

[13] H. Koivuluoto, C. Stenroos, R. Ruohomaa, G. Bolelli, L. Lusvarghi, and P. Vuoristo, 'Research on icing behavior and ice adhesion testing of icephobic surfaces', presented at the 16th International Workshop on Atmospheric Icing of Structures, Uppsala, Sweden, 2015, pp. 183–188.

[14] C. Laforte and A. Beisswenger, 'Icephobic Material Centrifuge Adhesion Test', presented at the 11th International Workshop on Atmospheric Icing of Structures, Montreal, Canada, 2005.

[15] Y. Chen, W. Wenhao, W. Dong, M. Li, and L. Lei, 'Numerical Study on the Adhesion Strength Between Ice and Aluminium Based on a Cohesive Zone Model', in *Volume 1A: Aircraft Engine; Fans and Blowers*, Düsseldorf, Germany: American Society of Mechanical Engineers, Jun. 2014.

[16] R. Milanese, R. Scigliano, V. De Simone, and V. Carandente, 'Ice release phenomena modelled by Finite Element models', in *AIAA Modeling and Simulation Technologies Conference*, San Diego, California, USA: American Institute of Aeronautics and Astronautics, Jan. 2016.

[17] L. Fu, Y. Chen, M. Xu, X. Wu, and W. Dong, 'Numerical Simulation of Ice Shedding From a Spinning Cone by Using Coupled CZM and XFEM', in *Volume 7A: Structures and Dynamics*, Seoul, South Korea: American Society of Mechanical Engineers, Jun. 2016.

[18] M. Riahi, D. Marceau, and J. Perron, 'Three-dimensional model of interface between ice and aluminium', in *8e Colloque national en calcul des structures*, Giens, France: CSMA, May 2007.

[19] P. Riera, J. R. Pothin, V. Pommier-Budinger, M. Budinger, I. Roberts, and F. Lachaud, 'A Complementary Framework to Predict Ice Adhesion Failure', presented at the International Conference on Icing of Aircraft, Engines, and Structures, Vienna, Austria, Jun. 2023, pp. 2023-01–1456.

[20] V. Pommier-Budinger *et al.*, 'Electromechanical Resonant Ice Protection Systems: Initiation of Fractures with Piezoelectric Actuators', *AIAA Journal*, vol. 56, no. 11, pp. 4400–4411, Nov. 2018,

[21] D. S. Dugdale, 'Yielding of steel sheets containing slits', *Journal of the Mechanics and Physics of Solids*, vol. 8, no. 2, pp. 100–104, 1960.

[22] G. I. Barenblatt, 'The mathematical theory of equilibirum cracks in brittle fracture', *Advances in Applied Mathematics,* vol. 7, pp. 55–129, 1962.

[23] P. P. Camanho, C. G. Davila, and M. F. De Moura, 'Numerical Simulation of Mixed-Mode Progressive Delamination in Composite Materials', *Journal of Composite Materials*, vol. 37, no. 16, pp. 1415–1438, Aug. 2003,

[24] A. Turon, C. G. Davila, P. P. Camanho, and J. Costa, 'An Engineering Solution for using Coarse Meshes in the Simulation of Delamination with Cohesive Zone Models', *Engineering Fracture Mechanics*, vol. 74, no. 10, pp. 1665–1682, Jul. 2007.

[25] G. Hernández Rodríguez, M. Fratschko, L. Stendardo, C. Antonini, R. Resel, and A. M. Coclite, 'Icephobic Gradient Polymer Coatings Deposited via iCVD: A Novel Approach for Icing Control and Mitigation', *ACS Appl Mater Interfaces*, vol. 16, no. 9, pp. 11901–11913, Mar. 2024,

[26] 'Data Sheet for Wearlon Super F-6M - Wearlon Water-Based Industrial Coatings'.

[27] Y. Liu, Y. Wu, S. Liu, and F. Zhou, 'Material Strategies for Ice Accretion Prevention and Easy Removal', *ACS Materials Lett.*, vol. 4, no. 2, pp. 246–262, Feb. 2022,

[28] X. Zhou, Y. Sun, and J. Liu, 'Designing Anti-Icing Surfaces by Controlling Ice Formation', *Advanced Materials Interfaces*, vol. 8, no. 17, p. 2100327, 2021,

[29] M. L. A. Pervier, B. Gurrutxaga Lerma, E. Piles Moncholi, and D. W. Hammond, 'A new test apparatus to measure the adhesive shear strength of impact ice on titanium 6Al-4V alloy', *Engineering Fracture Mechanics*, vol. 214, pp. 212–222, Jun. 2019,

[30] L. Stendardo *et al.*, 'Reframing ice adhesion mechanisms on a solid surface', *Applied Surface Science*, vol. 641, p. 158462, Dec. 2023,

[31] L. Stendardo, G. Gastaldo, M. Budinger, C. Antonini, V. Pommier-Budinger, and A. C. O. Patiño, 'Dynamic and Static Test Methods: Quantifying the Shear Strength at the Interface of Iced Substrates', presented at the International Conference on Icing of Aircraft, Engines, and Structures, Vienna, Austria, Jun. 2023.

[32] Y. Wei, R. M. Adamson, and J. P. Dempsey, 'Ice/metal interfaces: fracture energy and fractography', *Journal of Materials Science*, vol. 31, no. 4, pp. 943–947, Feb. 1996,

[33] E. H. Andrews and N. A. Lockington, 'The cohesive and adhesive strength of ice', *J Mater Sci*, vol. 18, no. 5, pp. 1455–1465, May 1983,

[34] M. Budinger, V. Pommier-Budinger, L. Bennani, P. Rouset, E. Bonaccurso, and F. Dezitter, 'Electromechanical Resonant Ice Protection Systems: Analysis of Fracture Propagation Mechanisms', *AIAA Journal*, vol. 56, no. 11, pp. 4412–4422, Nov. 2018,

Assessment of aircraft anti-icing ethylene glycol-based fluid ethylene glycol-based performance using thermography approach

Benaissa Sanae, Derek Harvey[1], Hassan Abbas Khawaja[2], Gelareh Momen[1]

[1] University of Quebec at Chicoutimi, Quebec, Canada
[2] UiT-The Arctic University of Norway, Tromsø, Norway

sbenaissa2@etu.uqac.ca, d2harvey@uqac.ca, hassan.a.khawaja@uit.no, Gelareh_Momen@uqac.ca

Abstract— **Protecting the aircraft surfaces from ground icing in cold weather conditions before takeoff via anti-icing fluids is crucial for flight safety. These fluids offer a specific protection time evaluated through outdoor endurance time testing. As outdoor conditions are difficult to standardize and repeat, there is interest in developing interior tests under simulated snow conditions. This study investigates the impact of snow type on snow-fluid interactions which govern fluid failure mechanisms. Natural snow is compared to fresh and aged artificial snow for ethylene glycol-based anti-icing fluids. Infrared and visual cameras are utilized to monitor a small test plate measuring six by eight centimetres, with a depth of 6 millimetres. This plate serves as the deposition site for snow at regular intervals, adjusted based on the precipitation rate at the center of the plate. The snow is distributed onto the plate via a specially designed deposition system, ensuring a consistent volume over a constant area. Thermography is used to study temperature drops and the rebalancing process under simulated snow precipitations. This work presents two test methodologies: the first considers a single snow deposition for each fluid at different concentrations. The second aims to study fluid saturation by simulating different snow intensities. The snow mass is calculated based on the density measured by the Schnee- und Lawinenforschung (SLF) snow sensor and the known deposited snow volume. The average deposited snow mass is then used to determine the time interval for snow deposition to simulate representative natural precipitation rates. Infrared (IR) thermography results for each snow type (natural, fresh artificial snow, aged artificial snow) are considered. Snow types are characterized by density and liquid water content (LWC). Results show that ethylene-based fluids experienced significant temperature drops and have a characteristic temperature rebalancing process related to the fluid's thermal and diffusion properties. Furthermore, the relationship between the deposited snow mass and the temperature gradient remains consistent irrespective of the snow type as long as the snow mass does not almost reach the saturation threshold. The impact of different snow types is studied and compared for both test procedures to evaluate possible sources of discrepancies between outdoor and indoor fluid snow precipitation endurance testing. This study revealed how the temperature changes, fluid saturation, and failure stages are reached for each studied anti-icing fluid with snow precipitation rate and snow types.**

Keywords— ***Aircraft anti-icing fluid, Endurance time, Infrared thermography, Natural snow, Artificial snow***

I. Introduction

Aircraft icing is one of the leading external causes of flight accidents [1, 2]. Several studies proved that aircraft icing has a fatal effect on flight safety [1, 3-5]. Winter operations for aircraft on the ground are based on aircraft anti-icing mechanisms that protect surfaces from precipitations such as snow and freezing rain, which is paramount as these elements can adhere to critical surfaces. Using liquid glycol products is the primary method of anti-icing the aircraft on the ground [6]. These fluids provide a specific endurance time for which they can protect the surface, beyond which the security of the surface is compromised. The industry standards SAE AS6285 and SAE ARP5485B introduced in these papers give the methods and procedures for adequate anti-icing of aircraft on the ground [7, 8]. The performance of these products is determined by their ability to postpone the formation of freezing and frozen contaminations. Their efficiency depends on their composition and meteorological conditions, such as temperature and precipitation type and intensity [9]. Studying the interaction between snow and the anti-icing fluid is crucial to deepening our understanding of failure mechanisms in evaluating the performance of anti-icing fluids. The fundamental principle of anti-icing fluids is to lower the freezing point of water, hence the interest of studying these fluids using infrared thermography. This paper will present the temperature gradient measurement after a precise snow mass deposition. Focusing on thermographic analysis, it delves into the interaction between ethylene glycol-based fluids and diverse snow types within a small-scale experimental setup. Thermography methodologies use infrared imaging technology to capture temperature variations in time within an area. This study can contribute to the field's understanding by clarifying the influencing parameters and offering valuable insights into this interaction. To fulfill this, our research team has developed a specific setup, which is presented in the following section.

II. Materials and methods

1) Presentation of the experimental setup

A small-scale experimental setup has been developed, including a newly developed snow deposition system called "snow dropper" and an aluminum test plate with a thickness of 12mm to ensure thermal stability during tests. The plate has 4 compartments of 80mm x 60mm x 6mm (L x W x H). Aluminum was chosen to prevent corrosion. A funnel with an outlet diameter of 8 mm is added to the setup to manage the deposition area. Fig. 1 presents this setup.
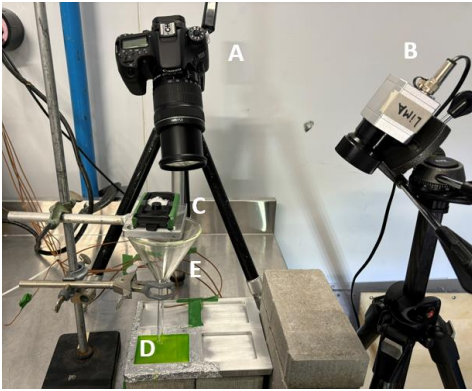
Fig. 1. Experimental setup. (A) Visual camera (B) Infrared camera (C) Snow deposition system (E) Funnel (D) Test plate.

The snow dropper allows the deposition of a precise volume of snow at a precise location. The deposited mass is estimated from the snow density measured by the snow sensor from FPGA Company GmbH (website as ref). The snow is sifted before measuring the density of the snow.
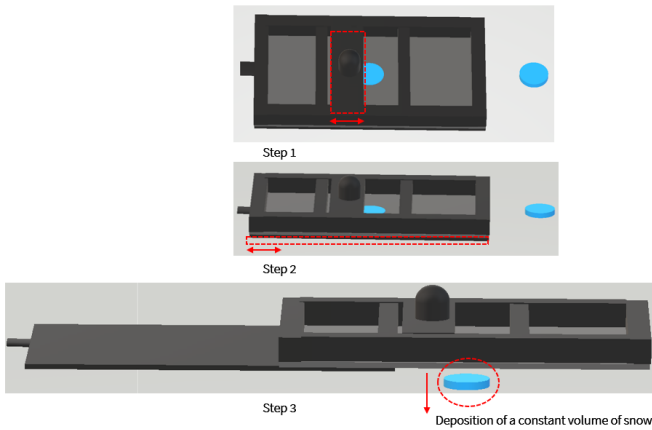
Fig. 2. The snow deposition system.

The deposition process of this system is based on three main steps (Fig. 2):

- Snow filling (Step 1): The first step involves sifting snow, filling it in the deposition volume, and ensuring it is correctly filled. The volume is equal to 13.17mm³.
- Levelling the snow volume (Step 2): The snow volume is levelled by moving the upper bar to remove any excess snow.
- Snow deposition (Step 3): The third step involves depositing the snow by removing the lower plate to allow the snow volume to fall.

These three steps ensure a precise and controlled snow deposition process for subsequent tests and measurements. The deposition area depends on the funnel height relative to the fluid level. Several trials were conducted to determine the optimal height, which was 2.3cm, resulting in an area of around 8-9mm. Artificial snow tends to densify over time, so density is measured on each testing day with the SLF snow sensor from FPGA Company GmBH. The mass of deposited snow is evaluated every test day by conducting multiple depositions and then calculating the average of each deposition. The snow morphology was investigated by taking pictures of natural and artificial snow using a Canon EOS70D camera with the EFS 18-135 mm macro 0.39/1.3ft lens.

An infrared camera (Optris Pi450i) and its corresponding software (Optris PIX Connect) are used to visualize the fluid-snow interaction thermally. The goal is to quantify the temperature drop when snow comes into contact with the anti-icing fluid, the snow melting, and the thermal re-equilibration of the environment. A visual camera, Canon EOS70D with EF-S lens, is also set up to capture video of visually observable phenomena and compare it with the data from the infrared camera.

The studied fluids are based on ethylene glycol, a green commercial anti-icing fluid Type IV and a clear reference fluid manufactured in AMIL laboratory which is a simple dilution of a pure ethylene glycol. Both fluids are studies are specific concentrations: 50%, 37.5% and 25% in volumetric concentration relative to the active component, ethylene glycol. The most concentrated solution is 50% because the commercial anti-icing fluid used in winter operations is at this concentration. This range of concentrations allows us to observe the effects of different fluid concentrations on the temperature drop.

The first type of test in our controlled environment is the single snow deposition test. In this test, a single snow deposition is performed on a 2.6mm thick layer of the studied fluid on a horizontal test plate. Three repetitions are conducted for each sample, ensuring the reliability of our measurements and aiming to measure the minimum temperature drop. The second type of test is intensity-based, where the snow is deposited in successive snow drops with time intervals between each snow drop. The time interval is defined based on the deposition area and the mass of deposited snow to achieve a targeted intensity. This test procedure aims to simulate different snowfall intensities on a small surface to thermally evaluate the failure of the anti-icing fluid. These tests were conducted in the cold chamber at an ambient temperature of -5°C in the anti-icing materials international laboratory (AMIL).

2) The study of morphology of natural snow and artificial snow

This research also delved into the morphology of natural and artificial snow. Photographs were captured of natural snowflakes collected during snowfall and artificial snowflakes produced in the AMIL laboratory.
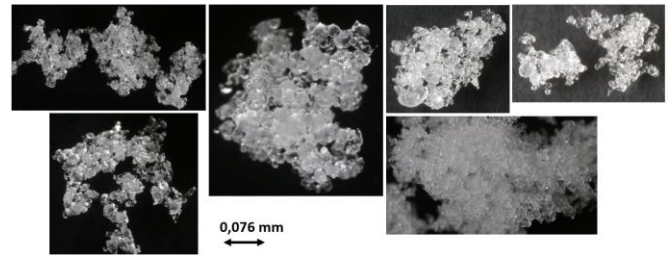
Fig. 3. Artificial snow crystals.
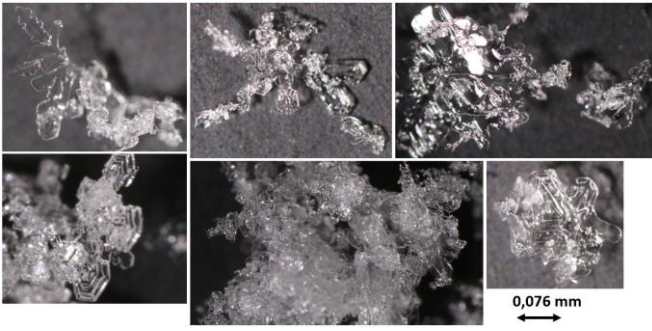
Fig. 4. Natural snow crystals.

Fig. 3 displays the artificial snow crystals we produced in AMIL, characterized by tiny frozen droplets and a 141.64 kg/m^3 density. In contrast, Fig. 4 showcases natural snow with a 53.55 kg/m^3 density collected during snowfalls with an air temperature of 0°C. This snow exhibits a crystalline structure with symmetrical and patterned shapes such as dendrites, hexagonal plates, and stellar forms [10, 11]. These distinct morphological differences highlight the unique characteristics of natural and artificial snow depending on the formation process. These pictures show the remarkable differences between them. Since the snow crystal formation mechanisms depend on environmental and meteorological conditions, they influence growth rates and generate various snowflake characteristics and morphologies [12].

The natural snow formation starts when the ice nucleation of water droplets begins in the clouds at higher altitudes when the temperatures decrease. The freezing of supercooled water droplets (liquid water at sub-zero temperatures) occurs due to the presence of ice nucleators. Ice nucleation is an exothermic process that releases energy to the surroundings. Ice nucleator defines a nucleus with an ice-like structure called a nascent snow crystal. The ice nucleators help water molecules to get into an ice crystal lattice. They also control the nucleation temperature, even though the nucleation mechanisms of ice nucleators are still unknown. They can be inorganic or organic materials. Many organic ice nucleators exist, commonly proteinaceous, including many microorganisms such as bacteria, birch pollen, and fungi. They provide higher ice-nucleating activity compared to inorganic particles. The ice-nucleating activity demonstrates the capacity to induce the crystallization of supercooled water [13], [14], [15]. The nascent snow crystal grows into more giant snowflakes by accumulating water vapour from supersaturated air [13]. The released energy allows the evaporation of encircling water droplets to get enough water molecules for snow crystal growth, in other words, to get the necessary supersaturated water vapour phase.

AMIL laboratory produces artificial snow in a cold chamber between -20°C and -25°C using fine spray hydraulic nozzles that spray supercooled water droplets which have mean volumetric diameter of approximately 25 µm. The sprayed water transforms into snow when it contacts a with a solid surface (the ground).

III. THE IR THERMOGRAPHY RESULTS OF ANTI-ICING FLUIDS BASED ON ETHYLENE GLYCOL WITH DIFFERENT TYPES OF SNOW

This section presents the study of the IR thermography results of anti-icing fluids conducted in this paper.

Thermography methodology is used to investigate anti-icing fluids' effectiveness when subjected to various snow types. It allows one to examine the temperature changes within the fluid-snow system to understand the fluid's ability to facilitate snow melting.

A. The single snow deposition tests results

This test was conducted for two different productions of artificial snow. The temperature gradient after snow deposition was measured for each studied fluid and each test was repeated three times for each snow production. Both reference and industrial fluids were used with 50%, 37.5%, and 25% dilutions. Fig. 5 shows an example of the IR images of snow deposition on anti-icing fluid type IV, ethylene glycol-based (concentration of 50%). Upon contact with the fluid, a noticeable a temperature decline occurs with temperature gradient of -10.26°C due to an ensuing endothermic reaction and subsequent equilibration and melting processes until a new equilibrium state is achieved.
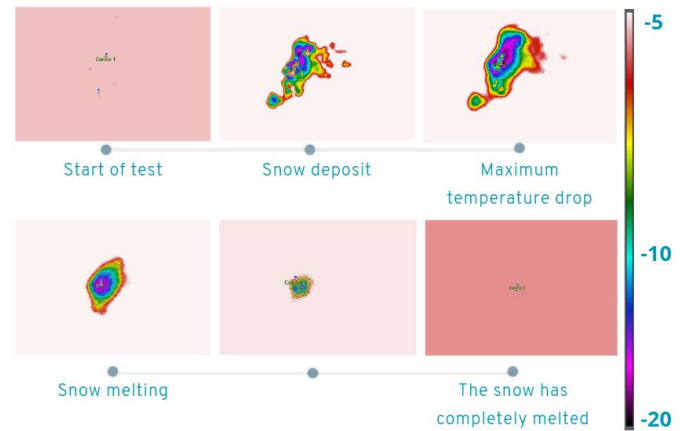
Fig. 5. IR images of the fluid Type IV based on ethylene glycol.

The temperature drop is the decrease of the minimal measured temperature in the measuring area. The gradient temperature represents the temperature change rate over a given space and time interval. The temperature gradient is calculated by dividing the temperature difference between the initial temperature before the snow deposition and the minimal temperature reached during the temperature drop. The obtained results in this section are presented in Fig. 6 and Fig. 7.
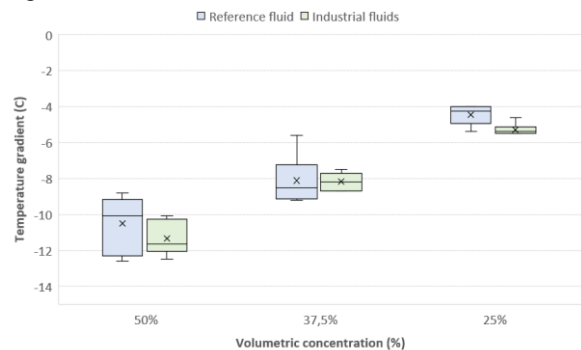
Fig. 6. Boxplot of temperature gradient for different concentrations depending on the type of fluid.
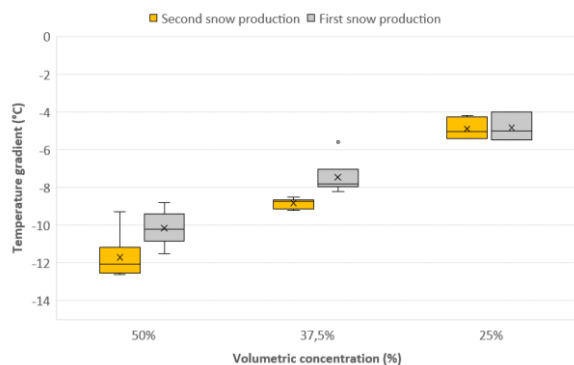
Fig. 7. Boxplot of temperature gradient for different concentrations depending on the snow type.

Fig. 6 and Fig. 7 show that the lower the concentration of ethylene glycol in the solution, the smaller the temperature gradient observed, which is expected because fewer active elements are responsible for the decrease in temperature. In other words, the effectiveness of the anti-icing fluid in reducing temperature is directly related to the concentration of ethylene glycol present in the solution.

The average mass of snow deposited per deposition from the first snow production is 8.56mg, and that of the second production is 9.67mg. The second production has a higher average mass of snow deposited per deposition, which explains why the temperature gradient obtained for the second snow production was slightly different than that of the first, as presented in Fig. 7. In addition, the temperature gradient difference for the 25% concentration is nearly similar regardless of the snow production. Indeed, at this lower concentration, both deposit masses appear to result in approaching the fluid to its saturation locally, where only a portion of the deposited snow is transformed into water. Conversely, the 50% and 37.5% concentrations are not saturated (100% snow mass is converted to water), and the temperature gradient varies accordingly. The difference in the deposited mass is due to the snow used since the mass depends on the density of the studied snow. The new snow deposition system is based on constant volume, which presents a technical limitation. The obtained results show how the ethylene glycol concentration in each tested sample affects the thermal behaviour and effectiveness of the sample by measuring the temperature drop and the temperature gradient upon snow deposition to quantify the temperature changes and asses the sample performance at different concentrations.

TABLE I. A COMPARATIVE ANALYSIS OF SINGLE DEPOSITION TESTS WITH NATURAL AND ARTIFICIAL SNOW

Volumetric Concentration	Temperature gradient (°C)	Average snow mass per deposition (mg)	Type of snow
50 %	-12	4	Artificial snow
50 %	-12.7	4.09	Natural snow
37.5 %	-9.2	4	Artificial snow
37.5 %	-9.3	5.52	Natural snow

Single deposition tests were conducted using both natural and artificial snow, where only the reference fluid was used for two concentrations, 50% and 37.5%. Table I shows that the temperature gradient obtained for identical concentrations remains consistent due to the proximity of the average snow mass per deposition. These preliminary results reaffirm a recurring trend observed in the previous experiments, indicating a significant correlation between the temperature gradient and the quantity of deposited snow, irrespective of its type (morphology).

B. Snow intensity tests

The snow precipitation rate (snow intensity) used for these tests was 30 $g/dm^2/h$. The tests lasted one hour and fifty minutes, with snow being deposited every two minutes. The fluids used were the reference and industrial, with a 50% volume concentration of ethylene glycol.

Figures Fig. **8** and Fig. **9** present the minimum temperature recorded of two zones: a reference zone defined away from the deposition zone and a specific measurement zone where the snow was deposed.
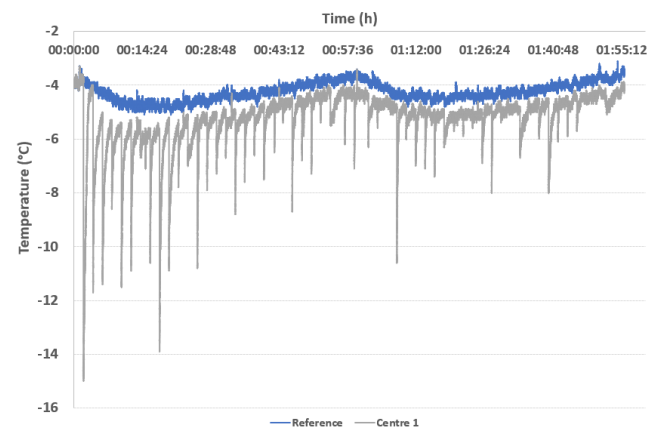
Fig. 8. The temperature over time for the intensity rate test at 30 $g/dm^2/h$ for the industrial fluid at 50%.
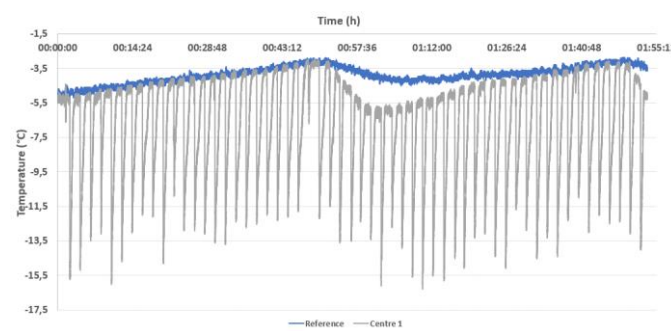
Fig. 9. The temperature over time for the intensity rate test at 30 $g/dm^2/h$ for the reference fluid at 50%.
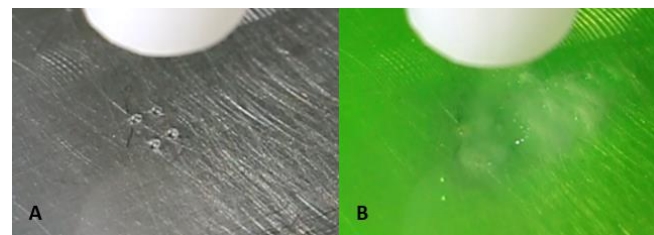
Fig. 10. Visual images at the end of the intensity test (A) for the reference fluid - (B) for the industrial fluid.

135
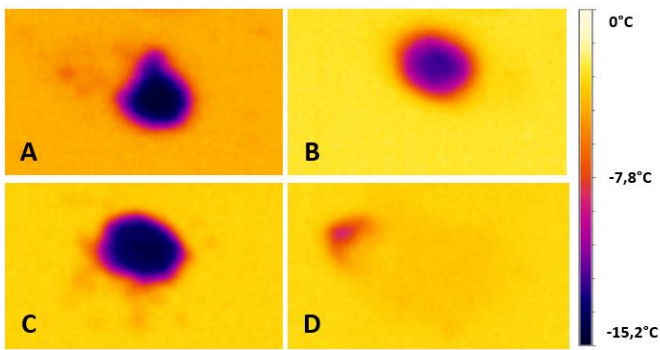
Fig. 11. Infrared images (A) First snowdrop in the reference fluid 50%- (B) Last snowdrop in the reference fluid 50%- (C) First snowdrop in the industrial fluid 50%- (D) Last snowdrop in the industrial fluid 50%.

Fig. 8 and Fig. 9 show notably that the temperature drop of industrial fluids decreases after several depositions, while the reference fluid's temperature drop varies more or less around the same values. Indeed, this is due to each fluid's viscosity. The industrial fluid is viscous (measured viscosity equal to 39.300cP), while the reference fluid has a viscosity similar to water since it contains no additives. The visual images in Fig. 10 confirm this: snow is observed on the industrial fluid, while no accumulation occurs in the reference fluid. The infrared pictures in Fig. 11 for each fluid's last snowdrop clearly show the industrial fluid's thermal failure being saturated. In contrast, the reference fluid is still able to perform thermally. The industrial fluid, which is thicker and where diffusion mechanisms take longer than in the reference fluid, decreases its ability to provide energy to the snow after successive depositions since it approaches saturation, where it can no longer perform (decline in local concentration of ethylene glycol).

When snow interacts with a solution that reduces the freezing point of water, the temperature of the solution decreases in proportion to the quantity of snow introduced. This phase change from solid to liquid, composed of a solid fraction and a liquid fraction of melted snow, necessitates energy, decreasing the solution's temperature. As the snow melts, the solution becomes more diluted locally, and diffusion equalizes the concentration to match the surrounding solution. Eventually, the temperature reduction stabilizes once a specific amount of snow is deposited, dictated by the concentration of the solution and its viscosity, impacting the diffusion mechanisms and leaving solid snow behind. This indicates saturation, suggesting that the solution has reached its melting point based on its local concentration, and snow accumulation begins, ultimately leading to the solution's inefficacy.

IV. CONCLUSIONS

This paper investigates the relationship between the concentration of ethylene glycol in a solution, the observed temperature gradient, and the effectiveness of anti-icing fluid. It also analyses the impact of the average mass of snow deposited per deposition on the temperature gradient obtained. The following points conclude the funding in this work:

- The study of natural and artificial snow morphology shows significant differences in morphology and density. Artificial snow crystals appear composed of

frozen droplets, resulting in a higher density than natural snow, which exhibits a more intricate and symmetrical crystalline structure.

- For a given snow production, a consistent temperature drop is observed for both fluids at identical concentrations when a specific volume of snow is deposed. However, variations in snow density measurements between snow productions reveal that denser snow leads to a greater mass from the constant volume deposition approach which increases the temperature drop. This is true as long as the fluid is not saturated; at saturation the temperature drop becomes constant and the fraction of snow remaining solid increases leading to accumulation. However, fluid saturation occurs at lower concentrations, even in small deposit masses, which keeps the gradient unchanged.

- Consequently, if two snow productions exhibit different densities, the experiment would showcase varying gradients, as the snow deposition system controls volume deposition rather than mass.

- The viscosity of anti-icing fluids plays a significant role in determining the failure mechanism, as it affects diffusion rates, which are slower in thicker industrial fluids than the reference fluid. Consequently, the industrial fluid's capacity to supply energy to the snow diminishes with successive depositions, reducing its temperature drop. This decline occurs as the fluid nears saturation, where it becomes unable to function effectively due to a decrease in the local concentration of ethylene glycol. Higher viscosity correlates with lower diffusion rates due to reduced molecular mobility. As the snow melts, localized dilution of the fluid occurs, accelerating saturation and snow accumulation since diffusion from higher concentration regions is too slow.

REFERENCES

[1] W. T. Yihua Cao, Zhenlong Wu, "Aircraft icing: An ongoing threat to aviation safety," *Aerospace Science and Technology,* p. 28, 2018.

[2] Y. Cao, Z. Wu, Y. Su, and Z. Xu, "Aircraft flight characteristics in icing conditions," *Progress in Aerospace Sciences,* vol. 74, pp. 62-80, 2015.

[3] J. MCLEAN, J, "Determining the effects of weather in aircraft accident investigations," in *24th aerospace sciences meeting*, 1986, p. 323.

[4] M. Elshamy, "Effect of atmospheric processes on launch decisions," *Journal of Spacecraft and Rockets,* vol. 32, no. 5, pp. 801-805, 1995.

[5] L. Chang, "Aircraft icing and aviation safety. Aeronaut," *Sci. Technol,* vol. 5, pp. 12-14, 2010.

[6] E. Villeneuve, C. Charpentier, J.-D. Brassard, G. Momen, and A. Lacroix, "Aircraft Anti-Icing Fluids Endurance Under Natural and Artificial Snow: a Comparative Study," *International Review of Aerospace Engineering (IREASE),* vol. 15, no. 1, pp. 1-11, 2022.

[7] *AS6285, Aircraft Ground Deicing/Anti-Icing Processes*, Aerospace Standard AS6285, revision A, SAE International, 2018.

[8] S. o. A. E. G12. *Guide to Aircraft Ground Deicing*, 2022, p. 400.

[9] M. S. Switzenbaum and et al., "Best management practices for airport deicing stormwater," (in eng), *Chemosphere,* vol. 43, no. 8, p. 1051, 2001.

[10] W. Shimada and K. Ohtake, "Three-Dimensional Morphology of Natural Snow Crystals," *Crystal Growth & Design,* vol. 16, no. 10, pp. 5603-5605, 2016, doi: 10.1021/acs.cgd.6b01263.

[11] W. A. Bentley and W. J. Humphreys, "Snow Crystals," *Nature,* vol. 129, no. 3265, pp. 778-779, 1932/05/01 1932, doi: 10.1038/129778a0.

[12] Libbrecht and K. G, "The physics of snow crystals," *Reports on Progress in Physics,* vol. 68, pp. 855-895, 2005-04-01 2005, doi: 10.1088/0034-4885/68/4/R03.

[13] B. Mohammadian, N. Namdari, A. H. Abou Yassine, J. Heil, R. Rizvi, and H. Sojoudi, "Interfacial phenomena in snow from its formation to accumulation and shedding," *Advances in Colloid and Interface Science,* vol. 294, p. 102480, 2021, doi: 10.1016/j.cis.2021.102480.

[14] K. E. Zachariassen and E. Kristiansen, "Ice Nucleation and Antinucleation in Nature," (in eng), *Cryobiology,* vol. 41, no. 4, p. 257, 2000.

[15] M. Joly and et al., "Ice nucleation activity of bacteria isolated from cloud water," (in eng), *Atmospheric Environment,* vol. 70, p. 392, 2013.

Effect of anodic oxidation process on porous structure of anti-icing slippery conductor

Yuan Yuan[1*], Huiying Xiang[1], Yingying Zhao[1], Tao Zhu[1], Xu Dai[1], Xujiang Hua[1],

[1]Chongqing University, China

yuany@cqu.edu.cn, 20200901052@cqu.edu.cn, 20193002@cqu.edu.cn, davezhu@cqu.edu.cn, xudai@cqu.edu.cn, 20230901040@stu.cqu.edu.cn

Abstract— **The icing disaster of transmission lines seriously threatens the safe operation of power system. Slippery liquid infused porous surface (SLIPS) exhibits excellent anti-icing performance. However, there is no systematic study on the preparation of SLIPSs on transmission lines. Herein, a porous substrate was prepared on the surface of aluminium conductor by two-step anodization, and the effect of anodization process on the porous structure was studied. The results show uniform nanopore structure can be prepared by using an annular cathode plate. Meanwhile, the electrolyte temperature should be lower than 15 ℃ and the chloride ion concentration in phosphoric acid should be lower than 8 mg/L. The slippery conductor with the optimal structure can significantly reduce the ice-adhesion strength, which is 2% of the untreated conductor. Therefore, this research lays a foundation for the application of SLIPS in transmission lines.**

Keywords—***Aluminum conductor, Super lubrication, Anodic oxidation, anti-icing***

I. INTRODUCTION

The icing disaster of transmission lines seriously threatens the safe operation of the power grid. In particular, the icing of overhead aluminum conductor will bring excessive or uneven loads, and then lead to accidents such as conductor galloping, wire breakage, and tower collapse. DC ice-melting technology is mainly used in engineering practice. However, this operation requires power outages and a potential incentive for ice-shedding jumps of conductors. In addition, the cost of DC ice melting device is high, which is not suitable for the ice melting demand of medium and low voltage transmission lines and distribution networks. Therefore, the development of persistent anti-icing surfaces that can be applied in low temperature and high humidity environments has important theoretical value and engineering practical significance for improving the safe operation of transmission lines and ensuring new energy transmission channels.

In 2011, Joanna Aizenberg et al.reported a new anti-icing strategy [1] to create a self-healing, smooth liquid-injected porous surface (super-lubricated surface, SLIPS) with special liquid repellency, ice repellency and pressure stability. In 2012, the team demonstrated for the first time the anti-icing performance of a super-lubricated surface. The super-lubricated surface prepared on the aluminum surface not only suppresses the accumulation of ice/frost by effectively removing condensed water, but also exhibits low ice adhesion [2]. The lubricating oil in the super-lubricated surface replaces the air in the microstructure and forms a uniform oil film on the surface. Its anti-icing advantages are: inhibiting the condensation of water vapor in the structure [3], excellent water droplet mobility [4] and low ice adhesion strength [5].

Slippery surfaces are almost all prepared and studied on flat surfaces with small sizes ($< 70 \times 30 \times 2$ mm^3). However, the transmission aluminum conductor is a complex spiral structure composed of several aluminum single wires, and it has a large volume. The conductor diameter range is 4 ~ 51 mm, and the experimental length is generally 0.4 m or more. Therefore, the precise control of the micro-nano structure on the surface of aluminum conductor will face problems such as uneven oxide film, local corrosion, and sharp rise in electrolyte temperature. In this study, the precise construction of the dendritic pore structure from the flat plate to the complex spiral structure surface of the aluminum conductor was realized by regulating the anodic oxidation process. Aiming at the complex structure and large size of aluminum conductor, the effects of cathode and anode configuration, electrolyte temperature and chloride ion concentration in electrolyte on the growth of pore structure were studied.

II. EXPERIMENT

A. Material

The model of aluminum conductor is JL/LB20A-240/30, which is purchased from Henan Tongda Cable Co., Ltd. This type of aluminum conductor is made of 24 aluminum monofilaments with a diameter of 3.60 mm and 7 aluminum-clad steel cores with a diameter of 2.40 mm, with an overall diameter of 21.6 mm. Oxalic acid ($H_2C_2O_4$), phosphoric acid (H_3PO_4), and anhydrous ethanol were purchased from China Chuandong Chemical Co., Ltd. Dimethyl silicone oil (200 cSt) and hexadecyltrimethoxysilane (OTS) were purchased from Aladdin Reagent Co., Ltd. Sodium hydroxide (NaOH) and ethylene glycol are provided by Chengdu Kelon Chemical Co., Ltd. Pure water was used in the experiment.

B. Preparation

The anodizing device of aluminum conductor is composed of electrolytic cell, annular cathode, circulating cooling system and DC power supply (100 A / 200 V). The cell cavity size is $60 \times 34 \times 40$ cm^3. The annular cathode is composed of six stainless steel plates with a size of 50×7 cm^2, and the overall diameter of the cathode is 20 cm. The electrolyte was circulatingly cooled by an industrial chiller to maintain a constant temperature during the anodic oxidation process. The cleaned conductor and the annular cathode are placed in an electrolytic cell containing an electrolyte. One end of the aluminum conductor is wound with an aluminum wire and connected to the anode output line of the DC power supply, and the annular cathode is connected to the cathode line of the DC power supply. Aluminum conductor was anodized with a certain current density and oxidation time. Aluminum

conductors with dendritic pore structure were prepared by two-step anodic oxidation method in oxalic acid and phosphoric acid electrolyte, respectively. The aluminum ion concentration in the phosphoric acid electrolyte was controlled in the range of 800 ~ 900 mg / L, and 30 % ethylene glycol was added. The electrolyte concentrations of oxalic acid and phosphoric acid were both 0.3 mol/L. The temperature of oxalic acid electrolyte was controlled at 15 °C, and the temperature of phosphoric acid electrolyte was controlled at 15 ~ 41 °C. The chloride ion concentration in the electrolyte is controlled in the range of 1 ~ 20 mg/L. The anodic oxidation parameters are as follows: the current density of oxalic acid electrolyte in the first step is 50 A/m, and the time is 15 min; the current density of the second step phosphoric acid electrolyte is 70 A/m, and the oxidation time is 20 min. In addition, the sample prepared by the plate cathode was used as a comparison sample. The aluminum conductor prepared by anodic oxidation is recorded as AAO wire.

The AAO conductor is modified with low surface energy. In detail, the sample was immersed in 2 wt. % modifier-ethanol solution for 30 min, and the sample was taken out and placed in a drying oven at 110 °C for 60 min. The super-lubricated surface was prepared by injecting lubricating oil into the modified sample. Then, the vacuum impregnation method was used to achieve the full injection of the nanoporous structure as much as possible [6]. Finally, the super-lubricated surface is prepared by placing the sample vertically to remove the excess lubricating oil on the surface.

C. Characterization

The morphology of the samples was characterized by a field emission scanning electron microscope system (SEM, Zeiss Auriga, Germany) equipped with an energy dispersive spectrometer (EDS) probe. The concentration of chloride ions in the solution was sent to Shanghai Microspectral Detection Technology Group Co., Ltd.for testing. The test equipment was an ion chromatograph (Thermofisher, AQ-1100, USA).

The ice adhesion strength of aluminum strand was tested. Considering the complex macroscopic shape of aluminum strand, a special ice adhesion strength mold was designed. The mold is made of polyethylene with a size of $60 \times 45 \times 20$ mm^3. There are arc-shaped grooves on both sides of the mold, and the diameter of the groove is the same as the outer diameter of the aluminum strand. The mold was placed in a refrigerator (-20 °C). The aluminum strand is placed on the mold with water to make the aluminum strand in contact with water. The freezing time of water is about 1.0 h. The tensile method was used to test the ice adhesion strength. The maximum tensile force was recorded, and the ice adhesion strength was calculated by dividing the force by the contact area. Each sample was tested three times and averaged.

III. RESULT AND DISCUSSION

Aiming at the problem that the complex structure and large size of aluminum conductor have great influence on the preparation process, the effects of cathode and anode configuration scheme, electrolyte temperature and chloride ion concentration in electrolyte on the growth of pore structure were studied.

Firstly, aiming at the complex structure of aluminum conductor, the influence of cathode and anode configuration on the construction of pore structure was studied. The electrolyte temperature was controlled at 15 °C, and the concentration of chloride ion in the electrolyte was controlled within 8 mg / L. When using a cathode similar to the plate sample, that is, the plate cathode is configured on both sides of the anode aluminum conductor, the macro and micro morphology of the Y-AAO aluminum conductor is shown in Figure 1, and the alumina conductor is extremely uneven on the macro. The area 1 is yellow, while the area 2 is white. From the microscopic morphology, it can be seen that the yellow area is uneven nano-holes, some of the holes collapse, and the white area is nano-fiber-like. Due to the different distance from the flat cathode at different positions on the spiral aluminum conductor, the electric field distribution is not uniform, which makes the local area dissolve and form an uneven oxide film layer.
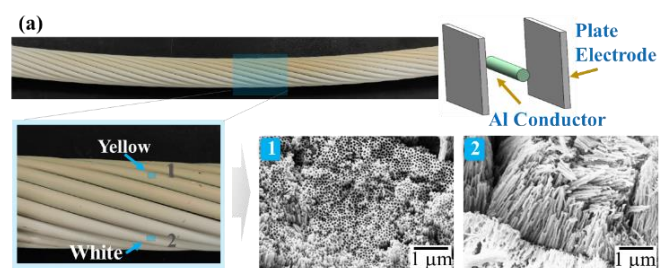
Fig. 1 Macro and micro morphology of Y-AAO conductor and plate electrode.

In order to apply a uniform electric field on the outer surface of the cylindrical aluminum conductor, an annular cathode plate coaxial with it was designed. As shown in Fig. 2, the anode aluminum conductor is located at the axis of the annular cathode plate. The uniform white oxide film was obtained on the anodic alumina conductor, and the nanopores with complete pore walls were distributed in different regions (marked as 1) on the aluminum conductor. When the annular electrode with the same shape as the cylindrical aluminum conductor is used, the uniform electric field distribution is generated because the various positions of the aluminum conductor are facing the cathode and the distance is close. Therefore, the coaxial configuration of cathode and anode during anodic oxidation is conducive to the uniform construction of complete pore structure.

Fig. 2 Macro and micro morphology of Y-AAO conductor and ring electrode.

Secondly, aiming at the thermal effect caused by the large size of aluminum conductor, the influence of phosphoric acid electrolyte temperature on the pore structure construction was

studied. The anode and cathode were coaxially configured, and the chloride ion concentration in the electrolyte was controlled within the range of 8 mg / L. When no cooling measures are taken, the temperature of the electrolyte rises to 41 ℃ after anodic oxidation, and the macro and micro morphology of the prepared Y-AAO conductor is shown in Fig. 3. Although the alumina strands show a uniform oxide film layer on the macro level, from the microscopic morphology, the pore structure of the oxidized surface undergoes a transitional dissolution and forms a piled fibrous shape (zone 1). The heat generated by the electrolyte increases the ion activity and accelerates the dissolution of the oxide film, resulting in a damaged pore structure in each area of the aluminum conductor surface, which is equivalent to a uniform accelerated corrosion.
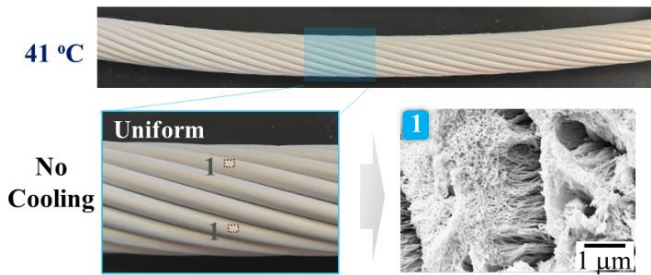
Fig. 3 Macro and micro morphology of Y-AAO conductor in H_3PO_4 electrolyte at 41 ℃

In order to remove the large amount of heat generated during anodic oxidation, a cooling and circulation device is used to maintain the electrolyte temperature in an appropriate range. As shown in Fig. 4, the electrolyte is cyclically stirred by an acid pump, and the solution is cooled by the heat exchanger in the cooling equipment outside the tank and sent back to the tank through the infusion pipeline. The infusion pipe in the groove opens a jet hole in the direction of the aluminum conductor. During anodic oxidation, the cooled electrolyte flows towards the aluminum conductor to take away the heat from the surface. The electrolyte temperature was controlled to 25 and 15 ℃ by cooling and circulating devices, respectively. At 25 ℃, the hole wall of the oxidized surface still breaks (Region 1), and the surface profile is uneven. This indicates that the temperature of the electrolyte is still high so that the dissolution rate of the oxide film is greater than the growth rate. At 15 ℃, the different regions (2) on the surface of the oxidized Y-AAO conductor showed uniform and flat nanopores. Therefore, a complete nanopore structure of the pore wall can be obtained by using a cooling and circulation device and controlling the electrolyte temperature below 15 ℃.
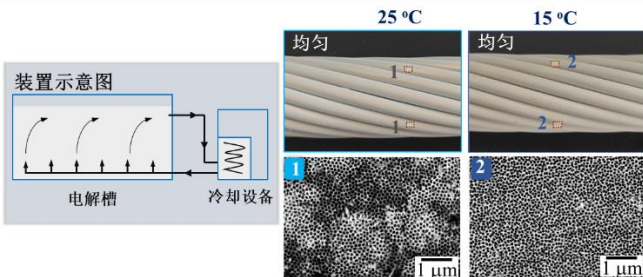
Fig. 4 Macro and micro morphology of Y-AAO conductor in H_3PO_4 electrolyte at 25 and 15 ℃

The impurity anions in the electrolyte have a great influence on the quality of the anodic oxide film, especially the chloride ions will make the oxide film rough, loose and even local corrosion. In order to adapt to the industrial production of large-size aluminum conductors, the frequent replacement of unqualified electrolyte should be avoided, which requires strict control of the chloride ion composition in the solution. Therefore, for the large size of aluminum conductor, the effect of chloride ion concentration in the electrolyte on the pore structure construction of the matrix surface was studied.

The effect of chloride ion concentration in phosphoric acid electrolyte on the dendritic pore structure was studied. The macro and micro morphology of Y-AAO conductor under different chloride ion concentrations in phosphoric acid electrolyte is shown in Figure 5. The concentration of chloride ion in oxalic acid electrolyte was controlled in the range of 8 mg / L, and the electrolyte temperature was controlled at 15 ℃. When the concentration of phosphate chloride ion is less than 8 mg / L, there are no obvious defects in each part of the anodic oxide film (Region 1), and the pore structure on the microstructure is uniform and flat. When the chloride ion concentration is greater than 8 mg / L, white bulges gradually appear on the surface of the aluminum conductor, and the number increases with the increase of chloride ion concentration. The microstructure of the bulge shows an expansive nanopore wall (Region 3), which is due to the local volume expansion caused by the chemical reaction between excess chloride ion and aluminum phosphate. Larger nanopores appear near the bulge (Region 2), indicating that the upper pores formed in the first step are completely dissolved, exposing the lower pore structure prepared by the phosphoric acid electrolyte. This is also because of the uneven accelerated dissolution around the aggregation of chloride ions. However, the area 1 far away from the bulge is distributed with uniform and flat nanopores, which indicates that the chloride ion in the phosphoric acid electrolyte has concentration corrosion on the surface of the aluminum conductor. Therefore, the chloride ion concentration in the phosphoric acid electrolyte should be controlled within the range of 8 mg / L.
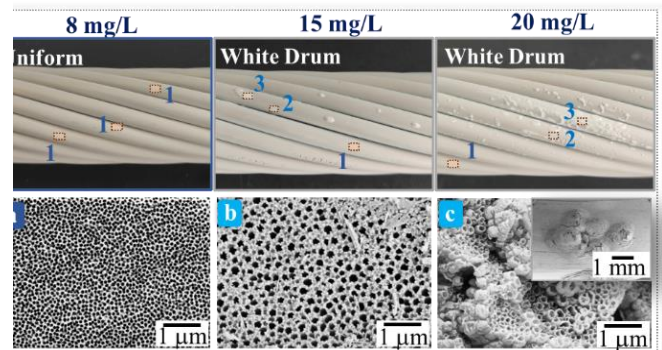
Fig. 6 Macro and micro morphology of Y-AAO conductor under different chloride ion concentrations in H_3PO_4 electrolyte.

The adhesion strength of super-lubricated aluminum conductor ice is shown in Fig. 7, and the tensile ice adhesion strength of untreated stranded conductor is the highest, which

is 283.5 kPa. After the modification of AAO aluminum conductor, the ice adhesion strength decreased to 28.5 kPa. Because the lubricating oil film prevents the contact between ice and the substrate, the ice adhesion strength of SLIPS aluminum conductor is only 6.7 kPa, which is about 2 % of the untreated conductor. This indicates that the super-lubricated aluminum strand with the optimal pore structure achieves ultra-low ice adhesion strength.
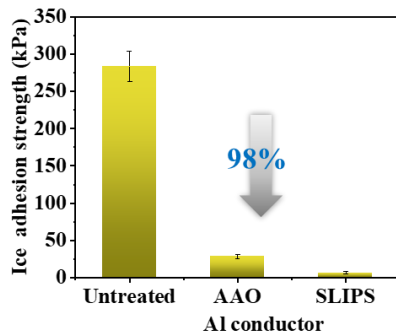
Fig. 7 Ice adhesion strength of different Al conductors.

IV. CONCLUSIONS

In this study, the effect of anodic oxidation process on porous structure of anti-icing slippery conductor was studied. The main conclusions are as follows: (1) Due to the complex structure and large size effect of aluminum conductor, the shape of cathode plate, the temperature and composition of electrolyte are the key factors to construct dendritic pore structure on the surface of aluminum conductor during anodic oxidation. (2) Excessively high temperature will accelerate the dissolution of the pore structure in various regions of the surface, that is, uniform corrosion occurs, while excessive chloride ion concentration will cause local dissolution of the surface pore structure, that is, concentration corrosion occurs. (3) In order to prepare a uniform film on the aluminum conductor, an annular electrode should be used to make the anode and cathode coaxially configured. The electrolyte temperature should be lower than 15 °C, and the chloride ion concentration should be lower than 8 mg / L. (5) The ultra-low ice adhesion strength of 6.7 kPa was obtained for the super-lubricated aluminum strand with the optimal pore structure.

REFERENCES

[1] T. S. Wong, S. H. Kang, S. K. Tang, E. J. Smythe, B. D. Hatton, A. Grinthal, J. Aizenberg, "Bioinspired self-repairing slippery surfaces with pressure-stable omniphobicity," Nature, Vol. 477, pp. 443-447, 2011.

[2] P. Kim, T.-S. Wong, J. Alvarenga, M. J.Kreder, W. E.Adorno-Martinez, J. Aizenberg, "Liquid-infused nanostructured surfaces with extreme anti-ice andanti-frost performance," ACS Nano, Vol. 6, pp. 6569-6577, 2012.

[3] S. Anand, A. T. Paxson, R. Dhiman, J. D. Smith, K. K. Varanasi, "Enhanced condensation on lubricant-impregnated nanotextured surfaces," ACS Nano, Vol. 6, pp. 10122–10129, 2012.

[4] G. Y. Liu, Y. Yuan, R. J. Liao, L. Wang, X. Gao, "Fabrication of a porous slippery icephobic surface and effect of lubricant viscosity on anti-icing properties and durability," Coatings, Vol. 10, pp. 1-10, 2020.

[5] Y. Liu, S. Gao, J. Liu, Q. Zhang, "Biomimetic slippery liquid-infused porous surfaces fabricated by porous fluorinated polyurethane films for anti-icing property," Prog. Org. Coat., Vol. 179, pp. 107524, 2023.

[6] Z. Yang, X. He, J. Chang, X. Bai, P. Cao, C. Yuan, "Fabrication of biomimetic slippery liquid‐infused porous surface on 5086 aluminum alloy with excellent antifouling performance," Surf. Interface Anal., Vol. 53, pp. 147-155, 2020.

Development of ice load maps for Türkiye

Bjørn Egil Nygaard[1], Kristian Ingvaldsen[1], Sigmund Guttu[1], Umit Cetinkaya[2], Arda Atatüzün[3]

[1] Kjeller Vindteknikk, Norconsult, Norway
[2] TEİAŞ, Türkiye
[3] Eltemtek, Türkiye

bjorn.egil.nygaard@norconsult.com, kristian.ingvaldsen@norconsult.com, sigmund.guttu@norconsult.com,
umit.cetinkaya@teias.gov.tr, arda.atatuzun@eltemtek.com.tr

Abstract—**Atmospheric icing has caused numerous mechanical as well as electrical faults on the transmission grid in Türkiye during the last decades. Ice loads and the combination of ice and wind have frequently exceeded the design values in many regions, particularly in the high-altitude sections of mountain crossing transmission lines. The development of the icing maps presented in this paper has therefore had the goal of providing updated ice and wind loads for design and route selection of electricity transmission and distribution lines and will replace the existing ice load map developed in the 1970s.**

The ice loads are modelled based on a state-of-the-art ice accretion model, with meteorological input from a 40-year high-resolution hindcast dataset. Characteristic values for ice loads are calculated through traditional extreme value analysis methods and made available as digital maps.

The modelled weather and icing data have been validated against measurement data from meteorological weather stations as well as known icing events on transmission lines documented through images and sensor data by the Turkish Electricity Transmission Corporation (TEİAS) during the 2022-23 winter season. The validation study suggested that the model captures rime icing and wet snow icing well, however, at least two events of soft rime related to freezing radiation fog were missed by the model.

Keywords— ***OHL design, ice load map, hindcast data, icing model.***

I. Introduction

With rich moisture transports from both the Black Sea to the north and the Mediterranean to the south, and with an average elevation of more than 1000 m, many parts of Türkiye are frequently exposed to atmospheric icing during the winter. High-altitude hydroelectric power plants, mostly located in the eastern part of the country, constitute a significant part of the electricity generation, and require transmission grid to be built at elevations exceeding 1500 m. In such areas many towers and line sections are exposed to rime icing, which has led to numerous faults during the last decades, including cascading tower collapses [1]. An example of a recent rime icing event in the mountainous parts of north-eastern Türkiye is shown in Fig. 1. This is a typical condition in Türkiye, where a transmission line crosses a mountain peak or ridge and locally becomes exposed to low clouds containing supercooled droplets combined with strong winds leading to severe rime icing.

Low-pressure systems and associated frontal precipitation have also led to significant wet snow icing and subsequent tower collapses in low-altitude coastal regions. One example of the latter is shown in Fig. 2 where a cylindrical wet snow sleeve has formed on a shield wire during a wide-spread wet

snow event in the Marmara region in December 2016. Several transmission lines were affected in the same region and numerous faults due to wet snow and wind loads were registered on the transmission lines.

Fig. 1   Rime icing on the 170 kV line in the North-east region, December 2022.

Fig. 2   Wet snow sleeve on a 170 kV line in the Marmara region, December 2016.

Problems with ice loads were evident even from the very beginning of the operation of the 420 kV transmission grid in Türkiye. The 420 kV grid was put in operation in 1974, and 117 towers were destroyed due to icing and wind during the first five years in operation [1].

The great number mechanical failures related to icing and wind clearly indicates that the design practice used in the past has limitations when it comes to resilience against severe ice loads and the combination of ice and wind. The goal of developing the icing maps presented in this paper has been to

improve future security of electric supply by providing updated ice and wind loads for design and route selection of transmission and distribution lines. The updated maps provide all necessary data for OHL-design according to international standards such as EN 50341-1 and IEC 60826.

II. DATA AND METHODOLOGY

The methodology used to develop the icing maps is similar to the one described in [2], and consists of the following steps:

1. Generation of a meteorological high-resolution database (hindcast data) covering the entire country.
2. Run an ice accretion model using the hindcast data as input.
3. Apply statistical methods for estimation of extreme values for every grid point of the model domain.

A. Hindcast data

The atmospheric hindcast data is prepared with the Weather Research and Forecasting (WRF) model version WRF-ARW 4.1.2. It is a state-of-the-art mesoscale atmospheric model, used both for operational forecasting and for hindcasting [3]. The model used in this study has been updated with regards to parameterization of melting snow as described in [4].

A long-term hindcast simulation is produced by simulating the period 1982 – 2023 for a domain extending across the entire country (Fig. 3) at 4 km x 4 km horizontal grid spacing, corresponding to 160 000 grid points horizontally.

The high-resolution hindcast is produced with the same model setup, but at a horizontal grid spacing of 1 km x 1 km for the three sub-domains shown in Fig. 4, corresponding to more than 1,2 million grid points. The simulation covers two years (winter season only), which were selected based on a set of criteria, such as storm frequency, distribution of wind speed and direction, measured ice loads etc.

All simulations are initiated and forced on the lateral boundaries by the ECMWF–ERA5 dataset [5]. The Thompson-Eidhammer aerosol aware microphysics scheme [6] is used for parameterization of the cloud and precipitation processes but with modifications to the melting layer parameterization according to [4].

The land-use and terrain information used as input are from the U.S. Geological Survey (USGS) dataset based on advanced very high-resolution radiometer (AVHRR). The topographic data are from a global elevation model (GEM) called Global Multi-resolution Terrain Elevation Data (GMTED2010) with a horizontal grid spacing of 30 arc seconds (approximately 1km). For the 1 km simulation, the CORINE[1] land-use dataset was applied.
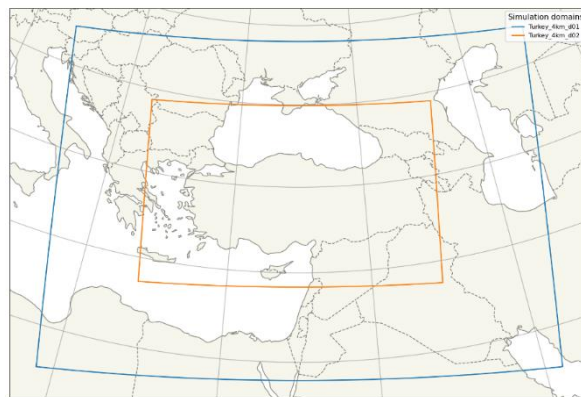
Fig. 3 WRF domains for the long-term hindcast simulation. The outer domain (blue) has a grid spacing of 12 km x 12 km, and the inner domain (orange) has a grid spacing of 4 km x 4 km.
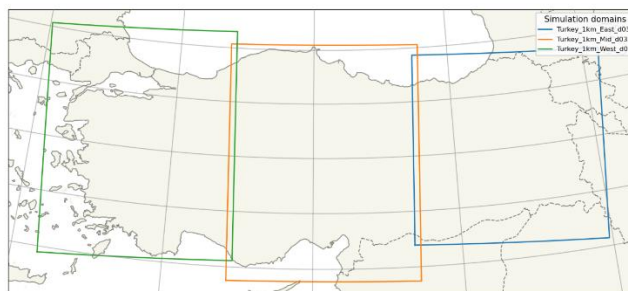
Fig. 4 WRF domains for the high-resolution hindcast simulation. All the three subdomains (green, orange and blue) have grid spacings of 1 km x 1 km.

Before calculating the ice loads, key variables such as cloud liquid water content, wind speed and wind direction were statistically downscaled by combining the high-resolution and the long-term hindcast datasets. The statistical downscaling follows the procedure described in [2].

B. Calculations of ice loads

An ice accretion model is applied to calculate hourly values of accumulated ice loads using the statistically downscaled hindcast dataset as input. The model accounts for all icing types and allows for addition of dry snow accretion under certain conditions. The ice accretion models follow the descriptions in [2]. Conductor diameter is assumed to be 30 mm and the average conductor height above ground to be 15 m in both simulations. The line direction is assumed to be perpendicular to the wind direction (omnidirectional), thus the resulting ice loads can be considered as worst-case with regards to icing wind direction.

Since wet snow occurs within a narrow range of atmospheric conditions, the phenomenon is quite rare and even 40 years of data can be too short for statistical analyses of extreme values. To cope with this problem, an ensemble approach has been used to expand the statistical basis and hence obtain more robust extreme value estimates. The ensemble consists of 40 different model runs, where the temperature in each run is perturbed stepwise by 0.1 °C within

---

[1] https://land.copernicus.eu/pan-european/corine-land-cover

the interval of $\pm 2\,°C$ from the original model temperature. See [2] and [7] for further details.

C. Extreme value analysis

Extreme values of rime icing are estimated by fitting a generalised extreme value distribution (GEV) to the annual maximum rime ice loads. This is done for each grid point individually, using the scikit-extremes package in python. 50-year ice loads are derived from the fitted distribution, and the procedure is repeated for each of the model grid points.

Due to the rarity of wet snow events, annual maxima may not be the optimal selection of bulk maxima for extreme value analysis. The peaks-over-threshold (POT) extreme value analysis is better suited for wet snow as all icing events are treated individually, and several events from the same year can be included in the analysis. The 50-year return values for wet snow are found through the following steps:

- Identify all icing events with the corresponding maximum value (peaks) from each of the 40 ensemble members.
- Combine peaks from all ensemble members to one joint distribution (pooling)
- Define the threshold for the POT analysis.
- Fit a generalised pareto distribution to the values exceeding the threshold.
- Derive a 50-year return value from the fitted distribution.

III. RESULTS

A. Icing maps

The final icing map in Fig. 5 shows 50-year values of ice load divided into loading zones according to the intervals given in Table 1. The map is based on separate extreme value calculations for rime ice and wet snow and the highest value among the two in each grid point is used as a basis to draw the map.

It can be noted that relatively high ice loads are found at low elevations along the northern coast towards the Black Sea, mainly caused by wet snow accretion in this precipitation rich area. Along the southern and western coast towards the Mediterranean Sea, the modelled ice loads are small (loading zone I), mainly because of the warm climate and rarely any snowfall at all.

Qualitatively, the map corresponds reasonably well with the old icing map of Türkiye, but the local variation is much more evident, and the values are higher in most, but not all regions. Furthermore, the map indicates extreme icing conditions in some mountainous regions exposed to moist air from either the Black Sea or from the Mediterranean Sea. The model data suggests 50-year ice loads exceeding 50 kg/m several places. Few of these areas coincide with existing transmission lines, but according to [1], icing diameters as large as 45 cm (corresponding to ~75 kg/m at density of 500 kg/m³) have been measured in the past.
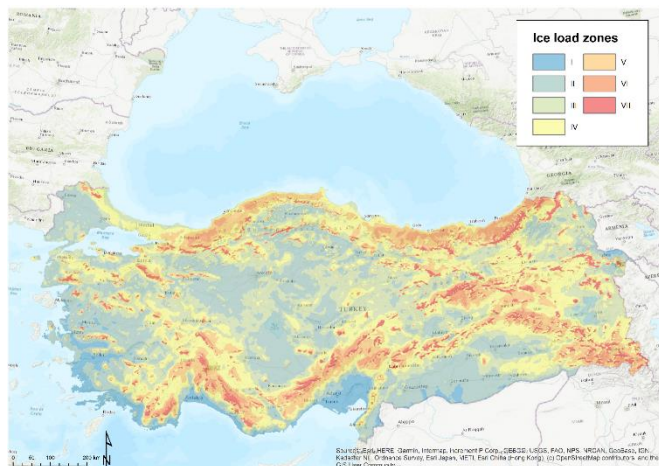
Fig. 5   Ice load map for Türkiye, divided into ice load zones.

TABLE I. DEFINITION OF ICE LOAD ZONES USED IN THE ICING MAP

Zone	Range (kg/m)
I	<0.5
II	0.5 – 1.5
III	1.5 – 2.2
IV	2.2 – 4.0
V	4.0 – 6.6
VI	6.6 – 17.0
VII	>17.0

There are fundamental differences between the different types of atmospheric icing that is important to take into account when using the icing values in OHL design. In order to separate the areas where rime icing (hard rime) is the predominant icing type, a separate map layer has been developed, as shown in Fig. 6. The map indicates the areas where rime icing is the predominant icing type. In other areas, precipitation icing is assumed to be predominant, mostly in the form of wet snow icing in this case. For rime icing areas there are two aspects to consider:

- The rime ice loads (kg/m) can be considered independent on conductor diameter. This effect is supported by both theoretical studies ([8] and [9]), field measurements [10] as well as observations from transmission lines in Türkiye [1]. This means that the thinner shield wires should be designed to withstand the same ice load as the phase conductors in rime areas.
- The average ice density of rime ice in exposed areas is higher than the average wet snow density. The values proposed by EN 50341-1 are 700 kg/m3 for hard rime and 500 kg/m3 for wet snow. The different densities can be considered when converting between ice mass and ice diameters (for calculation of wind load on iced lines)

For convenience, a separate icing map showing the radial ice thickness values corresponding to the characteristic ice loads has been created (not shown here). Outside rime areas the radial ice thickness from the map can be used directly for

both phase conductors and shield wires, independent on the line diameter.
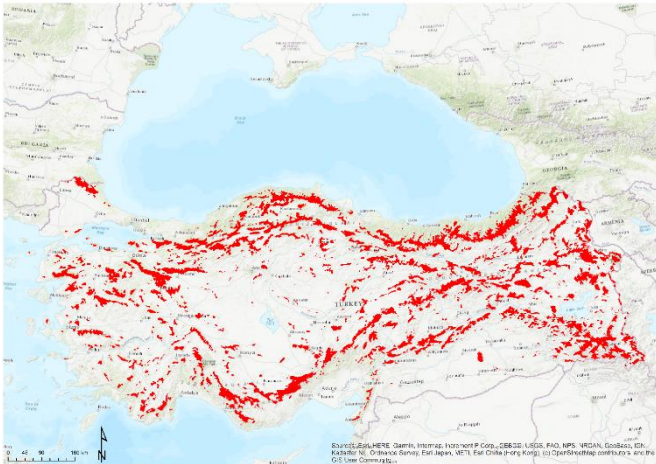
Fig. 6   Ice type classification map. Areas with rime ice as predominant icing type are shown in red.

IV. DISCUSSION

A. Validation

Very little historical quantitative information on ice loads or ice thicknesses have been available for validation of the model data. However, before the winter 2022/2023 ice monitoring test stations were installed at a few locations, and all raw data have been available for model validation. Additionally, local staff of TEİAS have documented icing events in a systematic manner throughout the same winter season, and a list of approximately 35 icing observations was prepared for comparison with the model data. It should be noted that combinations of the same WRF setup and ice accretion models have been validated earlier in [2] and [7].

The winter season of 2022/2023 turned out to be relatively calm with only a few icing events, and most of them relatively small in magnitude. Two of the events captures by the monitoring stations are shown in Fig. 7 and Fig. 8. Both events were classified as rime icing, and both events were captured reasonably well by the model. The modelled ice loads corresponding to picture a) and b) of Fig. 7 were 0,0 and 0,76 kg/m. The modelled ice loads corresponding to picture a) and b) of Fig. 8. were 1,2 and 2,4 kg/m.
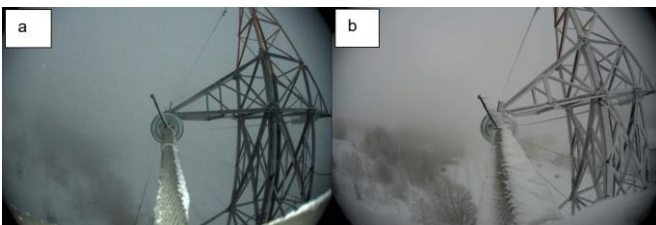
Fig. 7   Screenshots from the LAKI Power monitoring station on the 170 kV transmission line in the Marmara region. The pictures were captured 2023.02.05 18:40 [1c] and 2023.02.06 10:15 [2c].
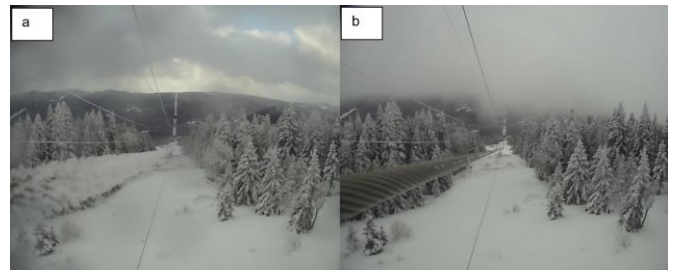
Fig. 8   Screenshots from the OTLM monitoring station on the 170 kV transmission line in the East Black Sea region. The pictures were captured 2023.02.13 06:00 [1e] and 2023.02.15 09:00 [2e].

The icing observations collected from OHLs during the winter 2022/2023 contain information about the time and date of the event, coordinates, line type and pictures showing the accumulated ice. All events have been simulated with the ice accretion model to evaluate whether the model is capable of capturing the timing and location of each event (and to some degree the severity, even though the magnitudes of the ice loads are unknown). Some observations are results of the same weather event (e.g. a low-pressure system that has a similar impact on the weather across a large area and/or period of time), but have been analysed separately nonetheless.

General findings are that the model seems to capture wet snow events as well as typical in-cloud icing (hard rime) events, however, the hindcast dataset seems to miss at least one major fog event in central Türkiye that led to rime ice accumulation on several different lines in the period between January 5th and January 9th, 2023, as well as a smaller but similar event from December 23rd to December 24th, 2023. The general weather conditions suggest widespread radiation fog, which is typically associated with cold surface temperatures and low wind speeds during high-pressure situations. The radiation fog during these particular events seems to be completely absent in the WRF hindcast data, likely due to lacking moisture in the ERA5 reanalysis data that serves as input to WRF. However, due to the low wind speeds associated with radiation fog, the icing events that are missing in the model from this period (and area) are generally not severe. The absence of such fog layers in the global model will severely limit the high-resolution model's possibilities to develop radiation fog as observed in the inland areas. A possible future solution to the problem could be to parameterize the fog conditions in a similar manner as in [9].

The comparison to the observations can be summarized as follows.

Positives:
- The model is able to capture traditional wet snow and in-cloud icing events well.
- The wet-bulb temperature sensitivity runs help capture icing events that otherwise would have been missed doe to small errors in the modelled temperatures.
- The events that are completely missed by the model are typically not severe.

Negatives:
- At least two widespread radiation fog events are completely absent in the WRF hindcast dataset, leading to missed icing events at several lines.

V. Conclusions

A detailed ice load map for Türkiye is produced based on high-resolution meteorological hindcast data and state-of-the-art methods for time dependant modelling of atmospheric icing. The icing maps are given as both ice load (kg/m) as well as radial ice thickness (mm), and a separate map layer is produced to distinguish the rime icing from other icing types when the maps are used for planning and design of OHLs.

The map corresponds well with the general experiences related to icing and failures due to icing on the existing power grid. Compared to the old map providing design ice loads, the new map is much more detailed, with higher variation on a local scale, and yields significantly higher values in many regions.

The validation study suggested that the model captures traditional rime icing and wet snow icing well, however, at least two events related to freezing radiation fog were found to be absent in the model, likely due to lacking low-level moisture in the reanalysis data. Although such events are typically associated with low-intensity icing (due to low wind speeds), they can be relatively widespread and impact a large number of lines/towers.

Further validation and calibration of the model require continued collection of icing measurements from sensors and monitoring stations. Therefore, for the future winter seasons, additional monitoring stations will be installed, along with the establishment of an operational icing forecasting system. Designing OHLs according to validated ice and wind load maps is crucial for sustainable operation.

References

[1] F. Iliceto, M. Babalioglu and D. F., " Report of failures due to ice, wind and large birds experienced on the 420kV lines of Turkey," *Cigre Symposium 22. Vol. 81. ,* pp. Paper 111-15, 1981.

[2] B. E. Nygaard, K. Ingvaldsen and Ø. Welgaard, "Development of Ice Load Maps for Structural Design," in *IWAIS*, Montreal, 2022.

[3] W. C. Skamarock, J. B. Klemp, J. Dudhia, D. O. Gill, Z. B. J. Liu and X. Y. Huang, "A description of the advanced research WRF model version 4.," *Atmospheric Research,* 2019.

[4] E. C. Iversen, G. Thompson and B. E. Nygaard, "Improvements to melting snow behavior in a bulk microphysics scheme," *J. Atmos. Res.,* vol. 253, p. 105471, 2021.

[5] H. Hersbach, "The ERA5 Atmospheric Reanalysis," in *AGUFM, NG33D-01.*, 2016.

[6] G. Thompson and T. Eidhammer, "A study of aerosol impacts on clouds and precipitation development in a large winter cyclone.," *Journal of the atmospheric sciences,* vol. 71(10, pp. 3636-3658., 2014.

[7] E. Thorsteins, B. E. Nygaard, K. Ingvaldsen and Á. J. Eliasson, "Wet snow icing modeling and comparison with field data," in *International Workshop on Atmospheric Icing of Structures (IWAIS)*, 2022.

[8] L. Makkonen, "The effect of conductor diameter on ice load as determined by a numerical icing model," in *3rd International Workshop on Atmospheric Icing of Structures. ,* 1986.

[9] M. S. Virk, "Ice accretion on circular cylinder in relation to its diameter," *Wind Engineering 41.1,* pp. 55-61., 2017.

[10] Á. J. Eliasson, P. T. Gunnlaugsson and E. Thorsteins, "Ice accumulation at measuring site Hallormsstadahals.," in *13th IWAIS*, Andermatt, 2009.

[11] B. N. H. Deloux, "Ice loads on overhead lines due to freezing radiation fog events in plains," *Cold Regions Science and Technology,* vol. 153, pp. 120-129, 2018.

Developing an ice load map for overhead lines in Sweden

Sigmund Guttu[1], Bjørn Egil Nygaard[1], Hanna Sabelström[2], Josefin Masreliez[3], Johan Bartsch[3], Jörgen Martinsson[3]

[1] Kjeller Vindteknikk, Norconsult, Norway
[2] Kjeller Vindteknikk, Norconsult, Sweden
[3] Svenska kraftnät, Sweden

sigmund.guttu@norconsult.com, bjorn.egil.nygaard@norconsult.com, hanna.sabelstrom@norconsult.com ,
josefin.masreliez@svk.se, johan.bartsch@svk.se, jorgen.martinsson@svk.se

Abstract— **This paper presents the development of a climatological ice load map for overhead transmission lines in Sweden. The map is made for responsible authorities in Sweden who need to take extreme ice loads into account when planning and designing the electrical power grid.**

The ice load map is based upon the ERA5 reanalysis dataset dynamically downscaled for a 33-years long period applying the Weather Research and Forecasting model (WRF) over a region covering Sweden. The meteorological data are then processed by ice accretion models to produce hourly values of accumulated ice loads. An extreme value analysis on the icing time series is then performed to yield extreme ice loads with a 50-year return period. The final climatological ice load map is based on the maximum of the rime ice and wet snow 50-year value in every model grid point.

The results show that rime icing combined with dry snow accumulation is the most frequent icing type in Mid- and Northern Sweden. Over Southern Sweden, the ice loads are significantly lower and wet snow is the predominant icing type. Due to lack of measurements, the results are not validated quantitatively, but the overall results are in line with experiences from local operators.

Keywords— ***ice load map, hindcast data, icing model, dry snow***

I. INTRODUCTION

Icing on overhead lines is a common issue in many European countries subject to harsh winter climate. Historically, there are few problems with icing on the transmission lines in Sweden, but somewhat more frequent on the distribution lines, particularly in northern parts of the country. Typically rime ice is observed at high elevations and wet snow in lower terrain, but common for many of the observed events is the combination of rime ice or wet snow with dry snow accretion during extended periods of low temperatures, heavy precipitation, and low wind speeds.

The ice load values used in the design of the Swedish transmission grid is currently under revision by the national transmission system operator, Svenska kraftnät. A first version of a Swedish icing map was generated using similar methodology as in this paper, as presented in [1]. However, experiences and analyses have indicated that the ice loads were underestimated in some regions, and that the underestimation was related to insufficient treatment of combination of icing types, such as dry snow and rime icing. Lately, in the Icebox research project [2] the ice accretion models have been further developed and validated against observations to produce a revised ice load map for Norway [3].

In this study, we use a state-of-the-art numerical weather model together with updated ice accretion models to generate a climatological ice load map for Sweden. The maps presented here show the large-scale variation in ice loads and local assessments particularly in complex terrain needs site-specific analyses when designing the power grid.

II. DATA AND METHODOLOGY

A. Hindcast data

The Weather Research and Forecasting (WRF) model have been used to produce the hindcast data. WRF is a state-of-the-art meso-scale numerical weather prediction system, aiming at both operational forecasting and atmospheric research needs.

A long-term dataset with 3 km × 3 km horizontal resolution (WRF3km) covering Scandinavia and Finland (Fig.1) are prepared by the version WRF-ARW 4.1.2 [4]. The simulation is forced on the lateral boundaries by the ECMWF-ERA5 over a 33-year period from 1989 to 2022.

A high-resolution hindcast with 1 km × 1 km horizontal resolution (WRF1km) covering Sweden with five overlapping domains (Fig.1) is prepared by WRF-ARW 3.2.1 [5]. The simulations have applied FNL as meteorological forcing, starting in October 2009 covering a 2-year period for Southern Sweden and a 1.5-year period for Northern Sweden.

Both hindcast datasets have 32 vertical layers, where the four lowermost levels are below 200m agl.. The NOAA dataset is used as geographical input, but the landuse data is updated to CORINE in WRF3km while the surface roughness and landuse data are update to Lantmäteriets GSD database in WRF1km. Cloud and precipitation processes are represented by the Thompson-Eidhammer aerosol aware microphysics scheme [6] with modifications to the melting layer parametrization [7]. Other relevant parametrization schemes are listed in Table 1.

A long-term high-resolution dataset for wind is produced by adjusting the WRF3km data applying the fine scale features of WRF1km. The adjustment is based on a statistical downscaling involving a sector-wise quantile regression model linking the wind field from the two WRF datasets. The methodology is described in detail in [8].
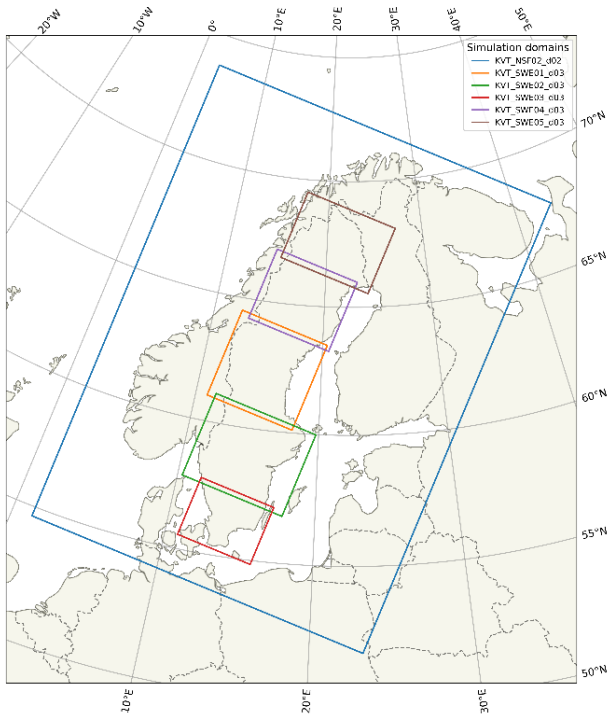
Fig. 1 WRF domains for the long-term hindcast simulation (WRF3km, in blue) and the short-term hindcast (WRF1km, other colours)

TABLE I. PARAMETERIZATION SCHEMES USED IN THE WRF SIMULATIONS

Type of input/scheme	WRF3km	WRF1km
Boundary layer	MYNN 2.5 [9]	YSU [10]
Surface layer	MYNN [9]	MM5 [11]
Radiation	RRTMG [12]	Dudhia [13]
Land surface	Noah [14] *	

*except for the northernmost domain in WRF1km, where a 5-layer thermal diffusion scheme [15] was used.

B. Calculations of ice loads

An ice accretion model is applied to calculate hourly values of accumulated ice loads using the WRF datasets as meteorological input. Two separate simulations are performed, one including rime ice and one including wet snow, both allowing for dry snow accumulation under certain conditions. Conductor diameter is assumed to be 30 mm and the average conductor height above ground to be 15 m in both simulations.

The rime ice accretion model is described in [16] and [17]. In addition to rime icing (in-cloud), the model includes freezing drizzle and freezing rain. The time integration of hourly icing rates is calculated based on the statistically downscaled wind field and cloud liquid water content from WRF3km. Other input parameters are temperature, humidity, pressure, rain water content and incoming short-wave radiation, all from WRF3km. The droplet size distribution referred to as the "Langmuir J" distribution was chosen based on experiences from similar studies [18]. The rime ice calculations are carried out for four discrete line directions, in

order to quantify the effect of the orientation of a power line relative to the icing wind direction.

The wet snow accretion model used is based on the one presented in [19]. Further improvements have been carried out by comparing the model with observed wet snow load in Iceland [20]. They include:

- The cloud liquid water content should be included in the estimation of the liquid fraction of the snowflakes to avoid overestimated icing rates at exposed sites.
- A reduction factor is introduced for the sticking efficiency, depending on the amount of graupel during wet snow events.
- Allowance for dry snow accretion on already existing wet snow at low wind speed.
- Precipitation intensity limit for the initiation of wet snow icing, calculated from the energy balance at the cylinder surface.

The input parameters for the wet snow accretion modelling are precipitation, wind, temperature and humidity and these are extracted from WRF3km. The line direction is assumed perpendicular to the wind direction (omnidirectional).

Since wet snow only occur within a very narrow range of atmospheric conditions, an ensemble approach has been used to expand the statistical basis and hence obtain a more robust extreme value analysis. The ensemble consists of 40 different model runs, where the temperature in each run is perturbed stepwise by 0.1 °C within the interval of ± 2 °C from the original model temperature.

Experiences in Sweden have shown that combinations of rime icing and dry snow accumulation is crucial to the extreme value distribution in Mid and North Sweden. To account for this, the accretion model includes accumulation of dry snow particles under certain conditions. Studies have shown that dry snow particles tend to bounce off overhead power lines at wind speeds exceeding 2 – 3 m/s [21]. Our ice accretion model applies a simplified approach assuming a linear reduction of dry snow accumulation from 1 m/s to 5 m/s, where no dry snow accretion occurs. Another precondition for dry snow accumulation is that the conductor is already covered by ice due to riming or wet snow accretion (dry snow particles tend to bounce off bare conductors, even at lower wind speeds than 2-3 m/s).

C. Extreme value analysis

Rime ice extreme values is most commonly estimated by fitting the yearly maxima of the time series in each grid point to a generalized extreme value distribution (GEV). Since large part of Southern Sweden is relatively flat, rime icing is not a common phenomenon and GEV is therefore not an appropriate method. To account for a small number of possible rime icing events, the statistical method Peaks-Over-Threshold (POT) [22] is used to estimate extreme values from the modelled rime ice time series. The method takes all independent occurrences of modelled rime ice loads that exceed a certain threshold value and fit them to a generalized Pareto distribution using the method of maximum likelihood. This approach is repeated for all four line directions. The final

rime ice map is the maximum 50-year extreme value of the four directional dependent extreme values in each grid cell.

The method of POT is also used for calculating wet snow extreme values. This approach is well suited for wet snow since wet snow events are rare and POT allows for several events from the same year. The calculations of 50-year return values for wet snow are summarized as follows:

- Identify all icing events with the corresponding maximum value (peaks) from each of the 40 ensemble members.
- Combine peaks from all ensemble members to one joint distribution (pooling).
- Define the threshold for the POT analysis.
- Fit a generalised pareto distribution to the values exceeding the threshold.
- Derive a 50-year return value from the fitted distribution.

D. Calculation of final icing maps

To produce one ice load map for designing overhead power lines in Sweden, we combine the rime ice and wet snow maps. The wet snow map is re-gridded to 1 km × 1 km horizontal resolution. The maximum of the two maps in each grid cell constitutes the final ice load maps. A smoothed contour map is produced to be able to be incorporated in the Swedish design codes (not shown in this paper).

In certain exposed hilly or mountainous regions where pure rime ice may be the predominant icing type, the probability for simultaneous extreme wind is higher. To account for this in the structural design, the combination factor needs to be adjusted in such regions. This is also reflected in the design codes such as EN-50341, where combinations factors for wind and ice depend on the icing types. We solve this by calculating a so-called "rime-risk" map, where pure rime icing is separated from rime icing including dry snow. In our study, we apply a simplified approach where rime ice is considered predominant in regions where density exceeds 400 kg/m^3 and ice load exceeds 60 N/m.

III. RESULTS

Fig. 2 shows the final ice load map for Sweden given in N/m. In Southern Sweden, the ice loads are generally below 20 N/m, but with higher loads in elevated regions, where 80 N/m is exceeded locally. In the middle part of the country, the ice loads range from below 20 N/m in the lowland to above 80 N/m at high elevations. In Northern parts, the overall ice loads are above 40 N/m except for the coastal region and some local areas shielded by high elevation regions. The ice loads exceed 80 N/m and even 200 N/m in the mountainous region towards the Norwegian border.

In most parts of Southern Sweden and also in the low elevation regions in the middle part of Sweden, wet snow is the predominant icing type. These are typically regions with relatively low ice loads. To the contrary, in high elevation regions and in the entire Northern Sweden, the wet snow values are below 40 N/m over large regions while the rime ice exceeds 40 N/m in most places.

The rime ice loads are substantially higher than in the previous version of the revised icing map [1], where large parts of Northern Sweden had values below 20 N/m. The main reason is that the model now includes dry snow accretion on wires already covered by rime ice. Experiences have indicated that such conditions are typical for extreme icing in Mid and Northern Sweden. Fig.3 shows an example of an icing event associated with a line failure near Slagnäs in Northern Sweden in January 1951. The presence of dry snow is clearly seen, and is supported by very low measured ice densities, typically in the range 100 to 200 kg/m^3. Observations of the same event showed ice loads on the order of 100 N/m, which are in line with the 50-year values shown in the revised ice load map in Fig.2.
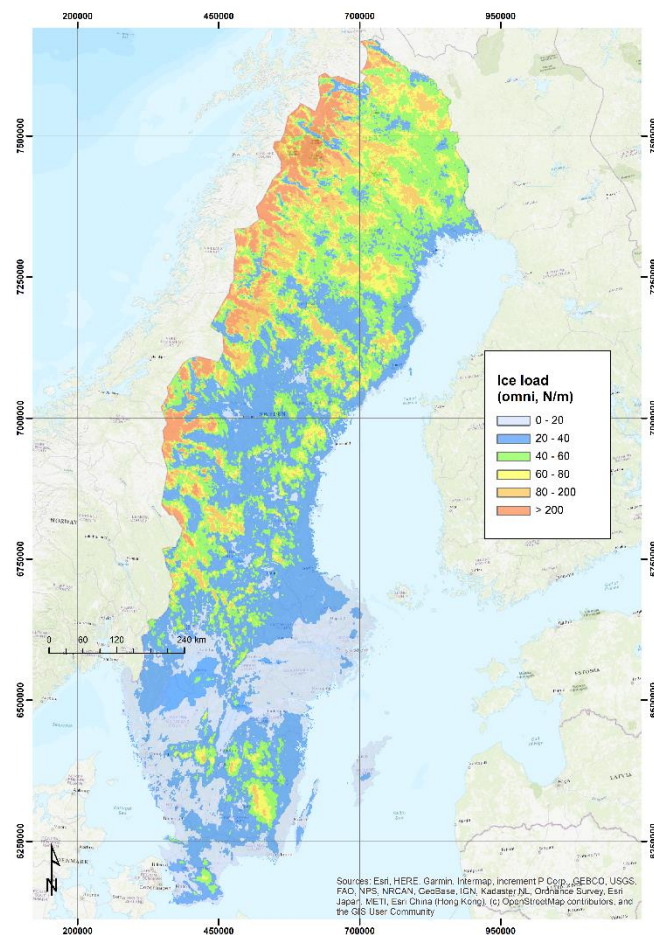
Fig. 2 Ice load map for Sweden. The map represents the maximum of wet snow and rime ice.

Fig. 3 Picture demonstrating an icing event including dry snow in January 1951 in near Slagnäs, Northern Sweden. Provided by Svenska kraftnät.

Due to the nature of both precipitation and rime icing, the ice loads depend strongly on terrain height. For practical use of the icing map, it would be useful to separate the height dependence from the map to obtain reference ice loads, in a similar manner as is commonly done in design codes for other climatic actions, such as e.g. wind loads. We attempted this approach by smoothing the original ice load map (Fig.2) and estimating a general relationship between icing and terrain height. Unfortunately, such a function was not possible to establish, even on regional scale. It demonstrates that the icing variability is highly complex and are influenced by other factors than height only, for example distance from coast, local exposure/sheltering, effect of lakes and rivers etc.

To take into account the combined effect of wind and icing in regions where pure rime icing is the predominant icing type, a "rime risk" map is shown in Fig.4. The map shows that areas with local elevation maxima have an increased risk of pure rime icing. Such places are more exposed to strong winds, favouring pure rime icing and preventing the mixed icing type including dry snow. The map further demonstrates that in Sweden, pure rime icing is mostly an issue in mountainous regions.
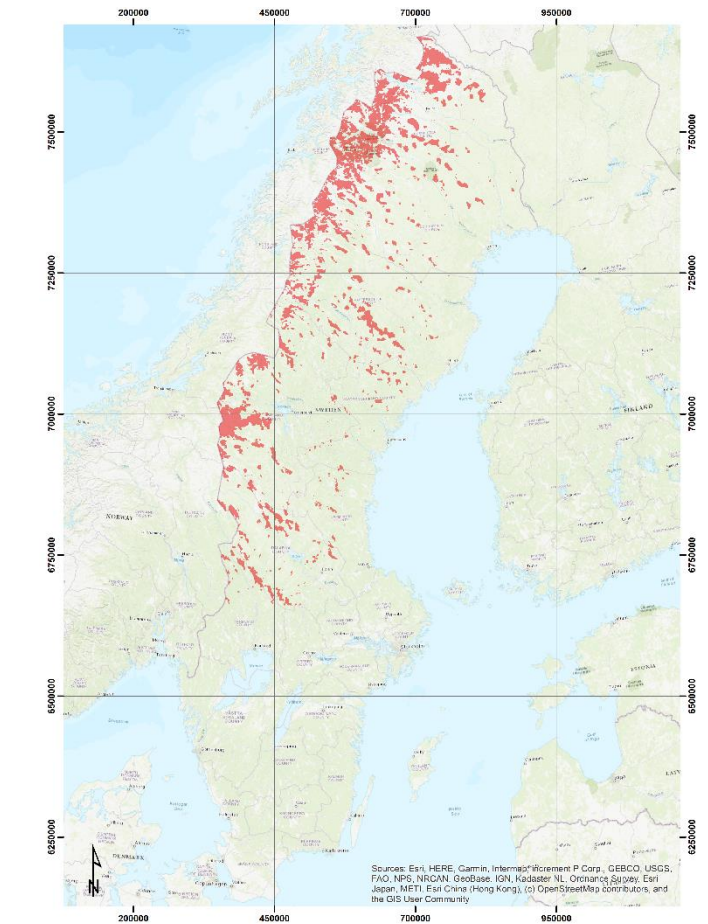
Fig. 4 Rime risk map illustrating regions where pure rime icing is the predominant icing type.

IV. Conclusions

A revised ice load map for Sweden is produced using a numerical weather prediction model and state-of-the-art ice accretion models. Due to lack of systematic measurements, a proper verification has not been performed, but the overall magnitudes compare well with operational experiences. Furthermore, by including dry snow in the simulation of rime icing, the predominant icing type in Northern Sweden is suggested to be rime icing surrounded by dry snow, also in agreement with experiences and documented historical heavy icing events in this region. Pure rime icing is most relevant in the mountainous region.

The ice loads are designed in such a way that they can be incorporated in the national design practise of Sweden.

.

References

[1] B. E. Nygaard, L. Carlshem, J. Bartsch, L. Lee and H. Ágústsson, "evelopment of a 50-year return value ice load map for Sweden," in IWAIS, Reykjavik, 2019

[2] "Icebox project:," Statnett SF, [Online]. Available: https://www.statnett.no/en/about-statnett/innovation-and-technology-development/our-prioritised-projects/icebox/

[3] B. E. Nygaard, K. Ingvaldsen and Ø. Welgaard, "Development of Ice Load Maps for Structural Design," in IWAIS, Montreal, 2022.

[4] W. C. Skamarock, J. B. Klemp, J. Dudhia, D O. Gill, Z. B. J. Liu and X. Y. Huang, "A description of the advanced research WRF model version 4.," Atmospheric Research, 2019

[5] W. C. Skamarock, J. B. Klemp, J. Dudhia, D O. Gill, D. Barker, M. G. Duda, X. Y. Huang, W. Wang, J. G. Powers, "A Description of the Advanced Research WRF Version 3.," Atmospheric Research, 2008

[6] G. Thompson and T. Eidhammer, "A study of aerosol impacts on clouds and precipitation development in a large winter cyclone.," Journal of the atmospheric sciences, vol. 71(10, pp. 3636-3658., 2014.

[7] E. C. Iversen, G. Thompson and B. E. Nygaard, "Improvements to melting snow behavior in a bulk microphysics scheme," J. Atmos. Res., vol. 253, p. 105471, 2021

[8] S. Liléo, E. Berge, O. Undheim, R. Klinkert and R. Bredesen, "Long term correction of wind measurements. State-of-the-art, guidlines and future work.," Elforsk report, no. 13:18, 2013.

[9] M. Nakanishi and H. Niino, "Development of an improved turbulence closure model for the atmospheric boundary layer.," Journal of the Meteorological Society of Japan., vol. 87, pp. 895-912., 2009.

[10] S. Y. Hong, Y. Noh and J. Dudhia, "A new vertical diffusion package with an explicit treatment of entrainment processes," Mon. Weather Rev, vol. 134, pp. 2318- 2341, 2006

[11] G. A. Grell, J. Dudhia and D.R. Stauffer, "A description of the fifth-generation Penn State/NCAR mesoscale model (MM5)," NCAR technical note, NCAR/TN–398 + STR, 122, 1995

[12] M. Iacono, E. Mlawer, S. Clough and J. Morcrette, "Impact of an improved longwave radiation model, RRTM, on the energy budget and thermodynamic properties of the NCAR community climate model, CCM3.," Journal of Geophysical Research, 2000.

[13] J. Dudhia, "Numerical study of convection observed during the Winter Monsoon Experiment using a mesoscale two-dimensional model," J. Atmos. Res., vol. 46, pp. 3077-3107

[14] K. Mitchell, "The Community Noah Land-Surface Model (LSM)," NOAA, Boulder, 2005.

[15] J. Dudhia, "A multi-layer soil temperature model for MM5," in Proc. 6h PSU/NCAR Mesoscale Model Users Workshop, Boulder, CO, USA, 1996

[16] ISO 12494, "Atmospheric icing of structures, first edition," 2001.

[17] L. Makkonen, "Models for the growth of rime, glaze, icicles and wet snow on structures," Philosophical Transactions of the Royal Society of London. Series A: Mathematical, Physical and Engineering Sciences, Vols. 358(1776),, pp. 2913-2939, 2000.

[18] P. Sokolov and M. S. Virk, "Droplet distribution spectrum effects on dry ice growth on cylinders.," Cold Regions Science and Technology, vol. 160, pp. 80-88., 2019.

[19] B. E. Nygaard, H. Ágústsson and K. SomfalviTóth, "Modeling wet snow accretion on power lines: improvements to previous methods using 50 years of observations," Journal of Applied Meteorology and Climatology, pp. 2189-2, 2013.

[20] Á. Elíasson, G. Hannesson and E. Thorsteinson, "Wet snow icing—Analysis of field measurements 1999–2016," in International Workshop on Atmospheric Icing of Structures, 2017.

[21] M. Roberge, "The Physics of Wet Snow Accreted on an Overhead Wire," Structural Engineering Series, Vols. 2005-03, 2005.

[22] S. Coles, "An introduction to statistical modeling for extreme values," Springer, 2001.

The effect of spatial resolution on the in-cloud atmospheric icing conditions in numerical weather model at the Fargernes mountain, Norway

Yngve Birkelund[1], Pravin Punde[1], Jonas Mundheim Strand[1,2]

[1] UiT The Arctic University of Norway, Norway
[2] Kjeller Vindteknikk, Norway

yngve.birkelund@uit.no, pravin.b.punde@uit.no, jonas.m.strand@uit.no

Abstract— **Atmospheric icing poses significant risks to infrastructure, aviation, and the energy section. Numerical weather models, as the Weather Research and Forecasting model (WRF), can be used to describe the atmospheric conditions relevant for atmospheric icing. In this study, we will focus on the Fagernes mountain meteorological icing measurement site where the WRF model is set up using ERA5 input data, Thompsons microphysics scheme to describe the different hydrometeors, and the Yonsei University (YSU) planetary boundary scheme with increasing spatial resolutions from 9, 3 and 1 km resolution. The final high-resolution model is using a Large Eddy Simulation (LES) for planetary boundary layer option in WRF with 91 m horizontal resolution in the model, in which a 10 m digital elevation model of Norway is used as model input.**

Using supercooled liquid water content, we have shown that the increased resolution from 9 to 1 km clearly changes the atmospheric conditions in the numerical model at the Fagernes mountain icing rig site. The main reason for this change seems to be that higher resolution models provides a better representation of the true terrain. Since the icing rig is located on a mountain top, the model height of the site does increase as the model spatial resolution increases.

Introducing the high-resolution LES model, both the mountain height the surrounding terrain is clearly closer to the real terrain at the measurement site. The LES model provides very good results for studying single or short time icing events and allows for a better understanding of the local terrain effects when in comes to atmospheric icing. The increased computational cost of the LES model makes it difficult use for larger areas and/or for long time simulations.

Keywords— ***WRF, numerical weather models, large eddies simulations, icing measurements.***

I. Introduction

Numerical weather prediction models (NWP) describe the physical weather parameters in the atmosphere, at the surface and in the soil. The physical relationship for the parameters is given as mathematical equations that are solved numerically, or in cases where meteorological processes are small scale or complex, solved using different parameterizations. For atmospheric icing, some of the important weather parameters are temperature, liquid water content and wind speeds.

With an established mathematical model of the atmosphere, the NWP model need to be initialized with information about the terrain at the place under study as well as the current state of atmosphere. Measurement from both ground stations, satellites and radiosondes are collected, and in most cases shared between meteorological organizations, to create a global coverage of standardized measurements of the current weather. After initialization, the NWP model can be used to estimate the historical, current or future state of the atmosphere, or at any place around the globe. The numerical model is based on Examples of operational weather forecast services are the Integrated Forecasting System (IFS) from the European Centre for Medium-Range Weather Forecast (ECMWF) and the Global Forecast System (GFS) from the NOAA Environmental Modeling Center in US, both models are updated four times a day with a horizontal resolution/ forecast length of 15days/9km and 16days/13km, respectively.

The Weather and Research Forecasting model (WRF) is an open community model by the National Center for Atmospheric Research [1]. This model can be configured with several different physical schemes options, and both research and industry users have been using this for a wide range of applications as e.g. wind resource assessment [2,3], wildfire tracking [4] and icing [5,6].

II. Method

A. Fagernes mountain icing measurement station

The icing measurement station is at the Fagernes mountain in Northern Norway as shown in Fig. 1. The location is at 1013 m asl, at latitude 68.4206N and longitude 17.4851E, with steep dropoff to sea-level at the fjords Beisfjorden to the south and Rombaken to the north. The city of Narvik is located nearby to the west, and several mountain peaks nearby to the east. Note that a power line (black line) passes close to this location, and also telecommunication masts and ski lift are in within a 100 meters distance. Earlier winters has shown that all this infrastructure is prone to icing, and we will look on a measured icing event during November 29.-30. 2022.

The location is above the Arctic circle, and in a coastal region with open ocean to west, a complex terrain with several fjords and mountains for several kilometres in all directions, and flat and in-land climate further to the east. Low pressure systems typically bring precipitation from the ocean during winter season, while easterly wind is cold and dry.

Measurements every 10 min are used for this station, and in this paper we will focus on temperature, relative humidity, pressure, wind speed and icing rates on a standard cylinder.

Fig. 1 Location of measurement mast (orange marker) and nearby terrain features. Map from: www.norgeskart.no

B. WRF setup

WRF version 4.4 was configured with physics schemes as shown in Table 1. The model was initialized with hourly ERA5 data from ECMWF, and run from 28.10.2022 12:00 to 31.10.2022 00:00 to cover an icing event captured at the icing measurement station.

The nesting ability of WRF was used for domains of size 103x103 cells with increasing horizontal resolution of 9, 3, 1 km for domain 01-03, respectively, shown in Fig. 2, with terrain data from Global Multi-resolution Terrain Elevation (GMTED) at 30 arcsec. Due to the complex terrain in the region, the number of vertical levels was set to 121 and the timesteps for the numerical simulation was set to 3*DX to avoid CFL-errors. The final high-resolution simulation in domain 04 consisted of 199x199 cells with 90,9 m horizontal resolution, shown in Fig. 3. using a 10m resolution digital elevation model from the Norwegian Mapping Authority [13] and converted to WRF format.
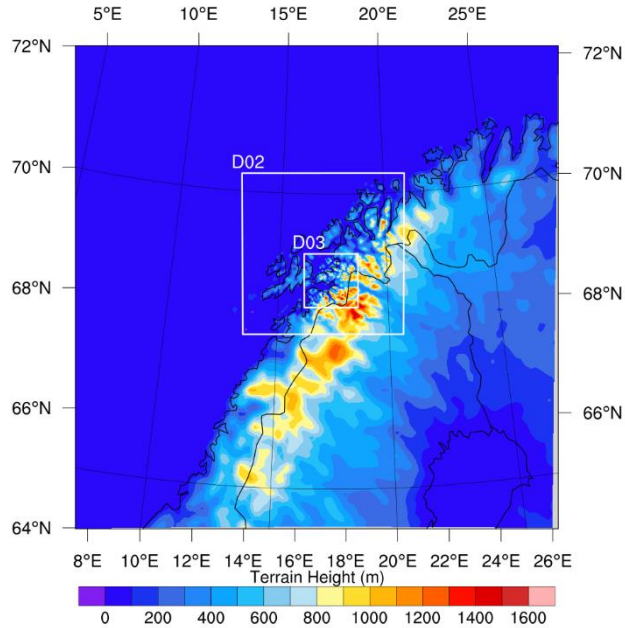
Fig. 2 WRF domains D01 (large plot), D02 and D03. Color code within each domain corresponds to its model terrain heights.
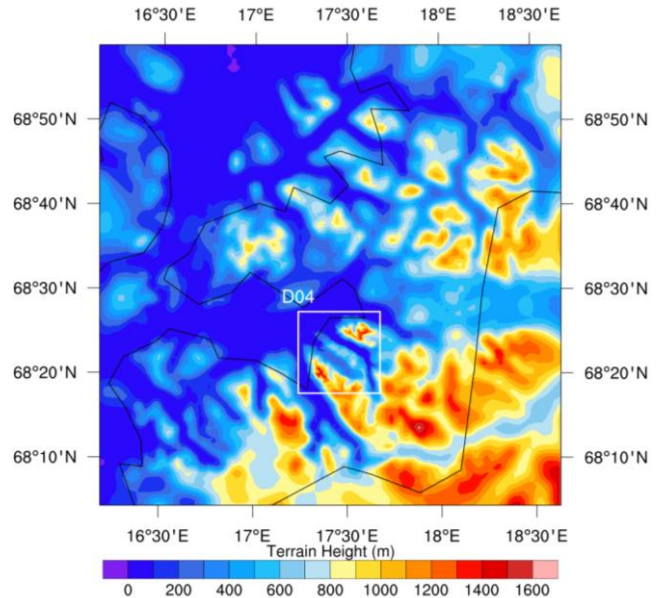
Fig. 3 Location and terrain of D03 and D04 (LES) in WRF. Black lines show global sea-land mask and the border between Norway and Sweden.

TABLE I. WRF CONFIGURATION

Physics	Scheme (opt)	Domains	Reference
Microphysics	Thomson (8)	01-04	[7]
Long/shortwave radiation	RRTMG (4)	01-04	[8]
Cumulus	Kain-Fritsch (1)	01-03	[9]
Planetary boundary layer	YSU (1)	01-03	[10]
	LES (0)	04	
Surface physics	MM5 (1)	01-04	[11]
Land-surface	Noah (2)	01-04	[12]

C. WRF simulations and post-processing

Simulations were run on the Fram supercomputer through the Sigma2 national e-infrastructure in Norway. The first 3 domains was run without feedback between the domains, and the LES domain was run using this NDOWN option with D03 as input. Dynamic options includes: w_damping=1, diff_opt=2 and epssm=0.1. For the LES simulation epssm was increased to 0.8, and mix_isotropic=1 was applied.

To allow for a direct comparison of results from all domains, the WRF outputs are interpolated to the exact location of the measurement mast using wrf-python scripts.

The icing rate is calculated using Makkonens model for a cylinder [14]

$$\frac{dM}{dt} = \alpha_1 \alpha_2 \alpha_3 \omega v A . \quad (1)$$

Here M is the ice mass, ω mass concentration of hydrometeors (typically supercooled liquid water content), v the wind velocity and A the cross-section of the cylinder. The α- terms are for collision, sticking and accretion efficiency, respectively. More details about measurement, calculation of these parameters and the WRF icing rate can be found in the companion papers [15,16].

III. RESULTS

A. Terrain heights and model resolution

The true terrain is shown in Fig. 4 a) together with the WRF model terrains in Fig. 4 b)-d) all for the inner domain. This region covers an area of 18x18 km, and the terrain is highly complex with several steep cliffs, narrow fjords and sharp mountain peaks.

When using a model with 3km resolution the terrain is clearly smoothed so that both lower terrain features as fjords as well as mountain peaks have disappeared within this region. A model resolution of 1km, as in the case of D03 in Fig. 4 c), gives a better resemblance to the valleys/fjords but still the height of the measurement station is more than 200 meter too low compared to its true height. The height difference is connected to the narrow mountain ridge the station is located on.

The high-resolution LES model shown in Fig. 4 d), on the other hand, clearly shows all peaks and fjords, and the height difference at the measurement rig is less than 10 meters.

B. Icing event time series

Fig. 5 shows the time series of measurements and WRF results at the measurement station during the period Nov 29th at 00:00 to Nov. 31st, 2022. Note that color code for the model output are the same in all plots in this figure, although the legend is only shown in second and fourth plot to avoid masking the data.

The measured temperature (T) shown in upper row of Fig. 5 starts at 0°C, drops down to -5°C during the first day before it rises again. The model outputs all follow the same time dependency, but with different levels for each domain. The D01 has temperature approx. +4°C compared to the measurements, while D02-D04 are approx. +2, 0, -1°C, respectively. These temperature level differences have a direct and strong connection to the model terrain heights, which increases as the resolution increases.

Fig. 4 Terrain heights using a) Digital elevation model of Norway - 10 m resolution, b) WRF D02 - 3 km, c) WRF D03 – 1 km, d) WRF D04 – 90,9m. Green colorscale shows height above sea level, contour lines are shown every 200 m from 100 masl to 1500 masl. Red markers give location of the measurement mast, and its corresponding model height is shown in the text box

Fig. 5 Measurement (black lines) and model result from D01 (red), D02 (orange), D03 (blue), D04 (green). Temperature, relative humidity, pressure, and wind speed in row 1-4, respectively

Relative humidity (RH) during this event, shown in second row of Fig. 5, have measurement in the range from 85% to 99%, with its lowest values in the middle of the event from 29.10 18:00 – 30.10 06:00. The model results are mostly in the same range, but some deviations are clearly visible. First, the modelled RH varies up-and-down several time during this event, most notably for the D04 case where the drop in RH can be down to 40% for single time steps. Second, during the last day the model tends to decrease RH while the measurements show a slowly increasing trend.

The pressure results, shown in third row of Fig. 5, shows a very good fit between the measurements and the D04 model result. This is expected as the model height is almost the same as the true terrain height for this domain, while the D01-D03 results shows higher pressure directly related to their respective model height at this spot.

The last row of Fig. 5 shows the wind speed results. The measurement in this event stops around 11:00 this first day, a disturbing but not uncommon problem during icing events. The anemometer is heated, but the misfunction was probably a result of strong cooling from the combination of temperature and wind. While working, the measurements are close to the D03 and D04 results, while both D01 and D02 shows lower wind speeds. Results from D04 have clearly higher wind speeds compared to the other domains, but, as in the case of RH model results, the variation is very large as the wind speed jumps between 20-50 m/s. The road authorities have measurements at Gratangsfjellet (334 masl, 68.67N, 17.90E) which shows wind gust of 33 m/s at these times.

The ice load measurement is shown in Fig. 6 as a red line. Measurements are saved every minute, and the data has high variation with a build up of ice on the cylinder starting from approximately 10:00 the first day. This matches well with the sharp increase in wind speed shown in Fig. 5. To reduce noise, the ice load time series was filtered with a low pass Chebyshev filter of 8th order with cut-off frequency $f_c = 0.8 \frac{fs}{2} \frac{1}{60}$, and the resulting hourly icing load is shown as the light green line in Fig. 6. From this a first order difference is used to create an estimate of the icing rate, shown as black line in Fig. 6.

Going from ice load measurement to icing rate is a difficult task, as it is difficult to distinguish between e.g. measurement noise, ice accretion and ice shredding on the cylinder. As the temperature during this event is below zero, no melting are expected but the ice/snow build up on the cylinder is most likely falling of piecewise during the ice accretion phase.

Fig. 7. show the icing rate results using the WRF model for domain D01-D04. In the lowest resolution domains, D01 and D02, produce almost no icing, while both D03 and D04 give icing rates that confirms the icing event. Note that both these domain give quite high icing from 03:00-15:00 the second day, while the ice load measurement only shows small loads (red line, 1 min measurements in Fig 6). In addition, the average level of icing rates during the first day indicates that the D03 results are below the measurement results, while the D04 results are above and at two points all the way up to 1600 g/h.
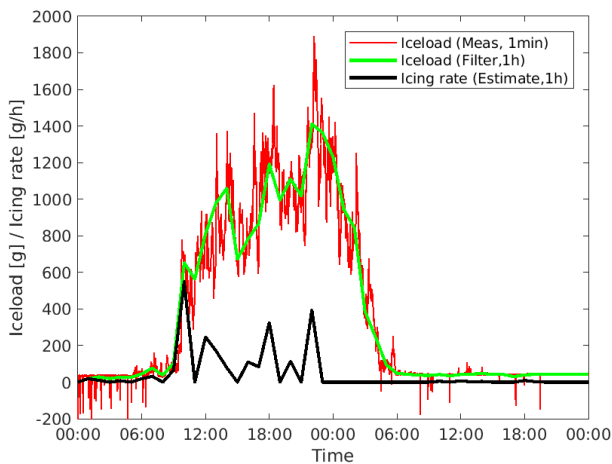
Fig. 6 Ice load measurements and estimated icing rate.
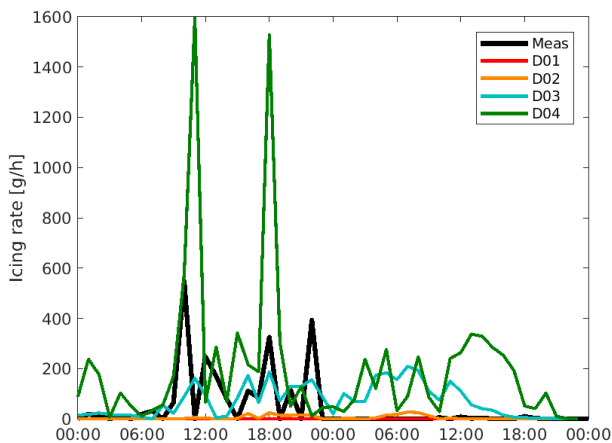
Fig. 7. Icing rate results from ice load measurement and WRF modelling using domain D01-D04.

C. Liquid water content during icing event

The upper row of Fig. 8 shows the horizontal wind speed, wind direction and liquid water content (LWC) contour lines from WRF domain D03 and D04, to the left and right, respectively. Results are from the lowest model layer, at approximately 20magl, from 29.10.2022 at 11:00 in the beginning of the measured icing event.

Starting with the wind results from D03, the main wind direction is from the north. The mountains north of the measurement station provides some shadowing effects so that lower-level terrain as e.g. the fjord experience lower wind speeds. Further inland, the wind tends to turn to the east. This is particularly the case along fjords going in this direction. Wind speeds and directions in D04 is much more complex, as LES captures smaller structures so that wind follows the terrain, changes directions several places, and we typically find much higher wind speeds over mountains. Results from other nearby output times, not shown, further elaborate the difference between D03 and LES (D04), as time steps in D03 typically have similar results while LES results may change significantly for our time step during rough weather events.

The LWC in these results clearly indicates that mountain areas, where temperature drops, are prone to icing at this time. In D03 we find LWC above 1 g/kg at some spots, while the D04 icing rates could be twice as high. Looking near the measurement station, shown as yellow circle in these plots, we find that the whole mountain is within a 1g/kg level, and also a nearby 1.5g/kg contour line.

The low row of Fig. 8 shows a vertical cross section along the south-north line crossing the measurement station. The terrain height is shown with brown region below, and the dotted temperature lines in D03 gives a freezing temperature level at 0°C around 500 masl. Below this line no icing would normally occur. The mountains do create some movement of air vertically, as also can be seen on the temperature isobars. When going LES and D04, the high wind speed can be seen over a large vertical distance, and we also find strong variations spatially both for temperature, wind and LWC. At this instant, our results indicate heavy icing potential from the measurement station and all the way up to 3000 masl.

IV. CONCLUSIONS

We have shown that the horizontal resolution in the weather model has a strong impact on the estimated icing rate, and we have identified two important reasons for this: 1) A higher resolution in the model is better able to reproduce the true terrain features, and 2) LES modelling allows for capturing high wind events which may produce short time icing conditions with extreme high icing rates.

Some concerns and limitations: a) High resolutions and extreme weather conditions means that we need high computation power as well as analysing output with high temporal resolution. b) The WRF output in this paper are instantaneous values and does not include averaging as in the measurement cases c) Our results are only for a single station, for a short event, and finding should thus only be read as indication of trends when moving into LES modelling for icing.
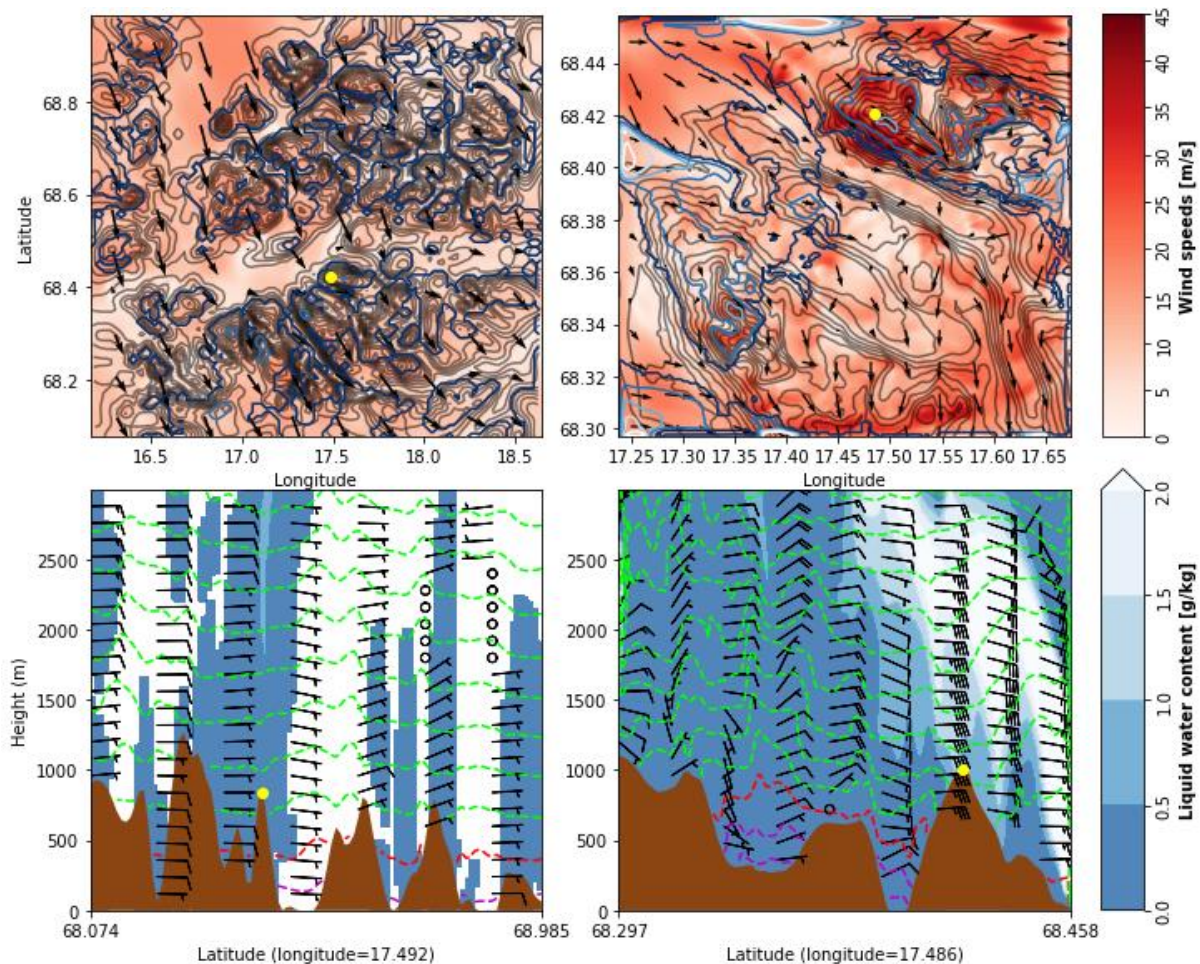
Fig. 8. Liquid water content (blue/filled contour) and wind speeds (red filled contour) from WRF. Upper row lowest horizontal model plan (~20 magl), lower row cross section plan south-north through model station (yellow circle). Left: D03, right: D04. Temperature contours: 0°C (red dotted line), +2 increase (dotted magenta line), -2 decrease (dotted cyan line). Wind direction shown with quiver and barbs.

REFERENCES

[1] Skamarock, W. C., Klemp, J. B., Dudhia, J., Gill, D. O., Liu, Z., Berner, J., Wang, W., Powers, J.G., Duda, M.G., Barker, D. and Huang, X. (2021). "A Description of the Advanced Research WRF Model Version 4.3" (No. NCAR/TN-556+STR)

[2] Hahmann, A.N., Sïle, T., Witha, B., Davis, N.N., Dörenkämper, M., Ezber, Y., García-Bustamante, E., González-Rouco, F., Navarro, J., Olsen, B.T. and Söderberg, S. (2020). "The making of the New European Wind Atlas-Part1 Model sensitivity", Geoscientific Model Development, 13(10), pp 5053-5078.

[3] Anacona, H.W., Mattar, C., Alonso-de-Linaje, N.G., Sepúlveda, H.H. and Crisóstomo, J. (2023). "Wind simulations over western Patagonia using the Weather Research and Forecasting model and reanalysis" Atmosphere 14, no. 7: 1062.

[4] A. Bakhshaii and E.A. Johnson. 2019. "A review of a new generation of wildfire–atmosphere modeling", Canadian Journal of Forest Research. 49(6): 565-574.

[5] Kringlebotn Nygaard, B. E., J. E. Kristjánsson, and L. Makkonen, 2011: Prediction of In-Cloud Icing Conditions at Ground Level Using the WRF Model. J. Appl. Meteor. Climatol., 50, pp 2445–2459

[6] Federico, S., Díaz-Fernández, J., Quitián-Hernández, L., Bolgiani, P., Santos-Muñoz, D., García Gago, Á., Fernández-González, S., Valero, F., Merino, A., García-Ortega, E., Sánchez, J.L., Sastre, M., Martín, M.L. (2020) "Mountain Waves Analysis in the Vicinity of the Madrid-Barajas Airport Using the WRF Model", Advances in Meteorology

[7] Thompson, G., P. R. Field, R. M. Rasmussen, and W. D. Hall, (2008) Explicit Forecasts of Winter Precipitation Using an Improved Bulk Microphysics Scheme. Part II: Implementation of a New Snow Parameterization. Mon. Wea. Rev., 136, 5095–5115,

[8] Iacono, M. J., J. S. Delamere, E. J. Mlawer, M. W. Shephard, S. A. Clough, and W. D. Collins (2008), Radiative forcing by long-lived greenhouse gases: Calculations with the AER radiative transfer models, J. Geophys. Res., 113, D13103

[9] Kain, J. S., 2004: The Kain–Fritsch Convective Parameterization: An Update. J. Appl. Meteor. Climatol., 43, 170–181

[10] Hong, S., Y. Noh, and J. Dudhia, 2006: A New Vertical Diffusion Package with an Explicit Treatment of Entrainment Processes. Mon. Wea. Rev., 134, 2318–2341

[11] Jiménez, P. A., J. Dudhia, J. F. González-Rouco, J. Navarro, J. P. Montávez, and E. García-Bustamante, 2012: A Revised Scheme for the WRF Surface Layer Formulation. Mon. Wea. Rev., 140, 898–918

[12] Tewari, M., Chen, F., Wang, W., Dudhia, J., LeMone, MA., Mitchell, K., Ek, M. Gayno, G., Wegiel,J. Cuenca, R.H., 2004. Implementation and verification of the unified Noah land surface model in the WRF model, 20th Conf. on Weather Analysing and Forecasting, 2165–2170

[13] (2023) The Norwegian Mapping Authority website [Online] https://hoydedata.no/

[14] Makkonen, L., 2000: "Models for the Growth of Rime, Glaze, Icicles and Wet Snow on Structures". Philosophical Transactions: Mathematical, Physical and Engineering Sciences, 358(1776), 2913–2939.

[15] Punde, P., Birkelund, Y., Virk, M.S., Han, X. 2024: "In-Cloud Icing - A case study at Fagernesfjellet, Norway using Weather Research and Forecasting model and observations", IWAIS 2024

[16] Strand, J.S., Birkelund, Y., Punde, P., 2024: "Atmospheric In-cloud Icing Using WRF for an Alpine Wind Power Plant in Norway", IWAIS 2024

In-Cloud Icing - A case study at Fagernesfjellet, Norway using Weather Research and Forecasting model and observations.

Pravin Punde[1], Yngve Birkelund[1], Muhammad Shakil Virk[1], Xingbo Han[1]

[1] UiT The Arctic University of Norway

pravin.b.punde@uit.no, yngve.birkelund@uit.no, muhammad.s.virk@uit.no, xingbo.han@uit.no

Abstract— **Atmospheric icing poses significant challenges to infrastructure integrity and transportation safety, especially in mountainous regions such as Fagernesfjellet, Norway. This paper presents a comprehensive case study of in-cloud icing over Fagernesfjellet, leveraging hindcast data obtained through dynamic downscaling with the Weather Research and Forecasting (WRF) model alongside observational data. Spanning from October 1, 2022, to December 31, 2022, the study focuses on evaluating the performance of microphysical schemes in predicting icing rates, liquid water content and other hydrometeors. Various statistical analyses are employed to assess model accuracy and validate against field measurements. The findings highlight the proficiency of the WRF model in simulating in-cloud icing, with the Thompson scheme exhibiting better performance in replicating low icing rates threshold compared to alternative schemes while Morrison for high icing rates threshold. This study underscores the critical role of model physics selection in accurately assessing in-cloud icing conditions, offering valuable insights for icing prediction and infrastructure resilience efforts. Additionally, we utilize NEWA data to analyse icing climate from 2005 to 2018, and further validate WRF results against NORA3 data over a three-month simulation period.**

Keywords— *ice accretion, NWP model for icing, ice load, microphysics, in- Cloud Icing, atmospheric icing, icing, WRF*

I. INTRODUCTION

In-cloud icing, occurring when unheated structures encounter liquid cloud droplets at temperatures below freezing, is particularly prevalent in exposed mountainous regions where cloud bases often descend below peak elevations. This phenomenon, lasting days or even weeks in some areas, poses significant risks to infrastructure integrity, including power lines, wind turbines, and telecommunication towers[1]. Ski lifts, measurement masts, and buildings are also susceptible, with instances of ice accumulation exceeding 300 kg/m² reported [2]. Reliable long-term icing data is scarce, but crucial for assessing icing climatology, especially in Nordic regions where potential wind farm sites are frequently subject to in-cloud icing [3]. The impact on wind power production can be substantial, emphasizing the need for robust modelling tools to evaluate icing frequency and intensity. In-cloud icing also poses safety hazards for small aircraft, necessitating further attention and mitigation strategies [4].

Utilizing the Weather Research and Forecasting (WRF) model, our research focuses on investigating in-cloud icing phenomena at Fagernesfjellet. Our aim was twofold: to analyse the specific in-cloud icing conditions experienced at Fagernesfjellet and to evaluate the effectiveness of various microphysics schemes within the WRF model. To establish a climatological perspective, we integrated data from the New European Wind Atlas (NEWA) [5]. Furthermore, we validated the WRF model outcomes through comparison with both observational data and the NORA3 dataset [6].

II. DATA AND METHODS

A. Study Area

Fagernesfjellet (68.4206° N 17.4851° E), located on Norway's western coast, is 1013 meters above sea level and lies to the east of the Ofotfjorden and northwest of the Beisfjorden. This region has a diverse and complex mountainous topography, which is distinguished by its proximity to the Arctic Circle and location near the Swedish national border. Fagernesfjellet faces the open sea to the south, spreading southwest and westward. The air masses that sweep across this area are moist, owing to the Gulf Stream currents running through the North Atlantic Ocean, which contribute to atmospheric ice occurrences during the winter. With air temperatures ranging from -21°C to 0°C, conditions are favourable for atmospheric icing, which shapes the region's peculiar environment [7].

Fagernesfjellet test site was established in October 2022. In addition to measuring wind speed, wind direction, and air temperature, it provides ice load on a cylinder with minute resolution.

Fig. 1 Location of the Fagernesfjellet test site [8]

B. Datasets

The NEWA dataset, developed in collaboration with the Technical University of Denmark (DTU) and other European institutions, provides comprehensive wind resource information tailored specifically for Europe. With a spatial resolution of 3 km, NEWA offers detailed data on icing, winds, and related parameters spanning from 2005 to 2018. In

our study, we utilized NEWA data to analyse the climatology of icing, precipitation, wind, and temperature at 2 meters above the ground (T2m) over our study location. The dataset, available at half-hourly resolution, includes icing loads measured at heights ranging from 50 to 500 meters, with our analysis focusing on the lowest level. We converted icing loads to the number of icing days and precipitation to annual values, while dividing wind speed data into seasonal categories (winter, spring, summer, autumn) to identify prevailing wind directions during specific seasons. T2m data was retained in its original temporal resolution for further analysis.

The NORA3 dataset is a high-resolution, nonhydrostatic hindcast covering the North Sea, Norwegian Sea, Barents Sea, and the Scandinavian Peninsula. Spanning from 1995 to 2020, NORA3 provides a detailed three-dimensional representation of the atmosphere. Utilizing a horizontal resolution of 3 km, NORA3 incorporates surface analysis and boundary conditions from ERA5, a global reanalysis dataset. In our analysis, we utilized NORA3 data for T2m, relative humidity (RH), wind speed, and direction, retaining these variables in their native temporal resolution. We compared NORA3 data with observations and outputs from the Weather Research and Forecasting (WRF) model to assess its performance.

C. Model Configuration

We employed the fully compressible nonhydrostatic Advanced WRF model (Version 4.4) [9] for simulating october 1st, 2022 to December 31st, 2022. The model utilized terrain-following coordinates with a constant pressure top surface. The model configuration leveraged the Global Multi-resolution Terrain Elevation Data 2010 (GMTED 2010) with horizontal resolution 30 arc-seconds (1km) is used as terrain input data.

We configured WRF with one-way nested domains: a 9 km outer domain (D01) and a 3 km second domain (D02) and 1 km 3rd domain (D03). All three domains spanned from the surface up to 50 hPa with 51 vertical levels. The domain setup can be seen in fig. 2.
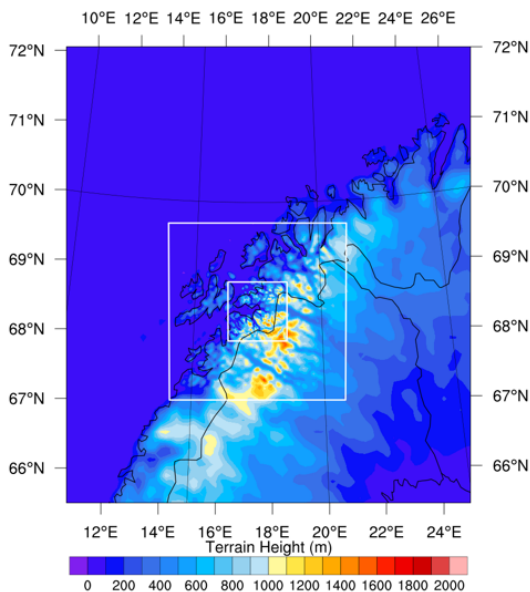
Fig. 2   WRF Domain setup. Colours represents terrain heights within the domain.

A. Initial and Boundary Conditions

Initial and lateral boundary conditions, along with sea surface temperature data, were obtained from the European Centre for Medium-Range Weather Forecasts Atmospheric Reanalysis of the Global Climate (ERA5) [10].

B. Parameterization Schemes

TABLE I.   WRF Model Setup

Initial, lateral boundary condition	ECMWF Atmospheric Reanalysis of the Global Climate (ERA5) (0.25º)
Domain extends	9ºE – 27ºE, 65ºN –72ºN
Radiation schemes (Shortwave, Longwave)	Rapid Radiative Transfer Model for global circulation models (RRTMG) [11]
Planetary boundary layer Scheme	YSU [12]
Land surface scheme	Noah land surface model scheme[13]

A detailed breakdown of the various parameterization schemes employed in the model simulations is provided in Table I. Here, we'll highlight a microphysics choices.

The Thompson scheme [14] scheme explicitly predicts the mixing ratios of various hydrometeors, including cloud water, rain, graupel, cloud ice, and snow. It utilizes a double-moment approach for cloud ice, predicting both the mass and number concentration of ice particles. Milbrandt-Yau 2-Moment Scheme (Milbrandt) [15] scheme predicts both the mass mixing ratio and the number concentration for all six hydrometeor species: cloud water, rain, cloud ice, snow, graupel, and hail. Morrison Double-Moment scheme [16] predicts the mass mixing ratio and number concentration of major hydrometeors that influence precipitation, including ice, snow, rain, and graupel. WRF Single-Moment 6-class (WSM6) [17] forecasts simply the mass mixing ratio for different hydrometeors to maximize computing efficiency. WRF Double-Moment 7-class (WDM7) [18] is a variation of WSM6 that adds graupel as a separate category and provides double-moment prediction for warm rain processes (cloud water and rain).

D. Ice accretion model

The International Organization for Standardization (ISO) established a model for ice accretion known as the Makkonen model [19]. Ice accumulation principles are modeled using a Standard Reference Collector, a cylindrical device with a rotating circular cross-section. Typically 30 mm in diameter and 1 meter in length, it can be shortened to 500 mm for scenarios with significant ice buildup [2] .This collector serves as the basis for ice accretion rate calculations. The model's calculations estimate the ice accretion rate using

$$\frac{dM}{dt} = \alpha_1 . \alpha_2 . \alpha_3 . v . A . LWC \qquad (1)$$

Where $\frac{dM}{dt}$ is the ice accretion mass (*kg/s*), α_1= collision efficiency, α_2= sticking efficiency, α_3= freezing efficiency, v = wind speed(*m/s*), A = Area of cross section(*m²*), *LWC*= liquid water content (*kg/ m²*).

Ice accumulation rate (dM/dt) depends on collision efficiency (α1), sticking efficiency (α2), freezing efficiency (α3), wind speed (v), object's cross-sectional area (A), and

liquid water content (LWC) in the air. Collision efficiency (α1) reflects droplets hitting the object, while sticking efficiency (α2) determines how many sticks, and freezing efficiency (α3) influences ice growth. Higher wind speed (v) increases droplet contact, and the object's cross-sectional area (A) affects the available surface for ice accumulation. LWC dictates the available water to freeze. [20] proposed the Median Volume Diameter method for collision efficiency, simplifying calculations while maintaining accuracy. This approximation offers a valuable tool for practical applications, as supported by [21].

The MVD can be calculated as follows.

$$MVD = \frac{(3.672+\mu)}{\lambda} \qquad (2)$$

Where μ = shape parameter depends on droplet number concentration N_c (cm^{-3})

μ can be calculated as

$$\mu = \min\left(\frac{1000}{N_c} + 2, 15\right) \qquad (3)$$

also λ can be calculated using.

$$\lambda = \left[\frac{\pi}{6}\rho_w\left(\frac{\Gamma(4+\mu)}{\Gamma(1+\mu)}\right)\left(\frac{N_c}{LWC}\right)\right]^{\frac{1}{3}} \qquad (4)$$

Where ρ_w = density of water (kg/m^2)

α_1 can be caculated using MVD

$$\alpha_1 = A - 0.028 - C(B - 0.0454) \qquad (5)$$

Where,

$$A = 1.066K^{-0.00616} \exp(-1.103K^{-0.688})$$
$$B = 3.641K^{-0.498} \exp(-1.497K^{-0.694})$$
$$C = 0.00637(\phi - 100)^{0.381}$$

Where K = Droplet Inertia Parameter, ϕ = Langmuir parameter [22], they can be calculated using

$$K = \frac{\rho_w MVD^2 v}{9\mu D}$$

$$\phi = \frac{\rho_a MVD v}{u}$$

Where D is the cylinder diameter, R_e= Reynolds number

ρ_a= Air density(kg/m^3), u = dynamic viscosity($kg/m.s$), v = free stream velocity(m/s).

B. Model verification.

To evaluate the model simulations, a range of statistical metrics were calculated for WRF and NORA3, including mean bias, root-mean-square error (RMSE), Bias(B), and the Pearson correlation coefficient (PCC). These metrics provide essential quantitative insights into the performance and accuracy of the model simulations.

$$RMSE = \sqrt{\frac{\sum_{i=1}^{n}(x_i - o_i)^2}{n}} \qquad (6)$$

x_i and o_i are the model and observed variable for i^{th} point.

n is the total number of points.

$$B = \frac{1}{n}\sum_{i=1}^{n}(x_i - o_i) \qquad (7)$$

$$PCC = \frac{COV(x_i, o_i)}{\sigma x_i \sigma o_i} \qquad (8)$$

$COV(x_i, o_i)$ is the covariance between x_i and O_i (model and observed variables, respectively) Here σx_i and σo_i are the standard deviation of variable for model and observation, respectively.

Probability of Detection (POD) and False Alarm Ratio (FAR) are essential metrics used to assess the performance of predictive models in accurately predicting weather events. The POD measures the percentage of observed events that were correctly predicted by the model, providing a straightforward indication of predictive accuracy. On the other hand, the FAR evaluates the model's tendency to incorrectly forecast events that do not occur, offering insights into potential false predictions.

POD is computed by dividing the total number of observed events correctly identified by the model, known as "hits," by the total number of observed events. With a scale ranging from 0 to 1, a POD score of 1 signifies perfect accuracy [23].

$$POD = \frac{H}{M+H} \qquad (9)$$

FAR is calculated by dividing the number of false alarms by the total number of forecasted events. With a scale ranging from 0 to 1, a FAR score of 0 indicates perfect accuracy, meaning no false alarms were raised by the model. Essentially, the FAR provides a straightforward measure of the model's tendency to predict an event when none actually occurred, offering valuable insight into its reliability and performance.[23]

$$FAR = \frac{F}{F+H} \qquad (10)$$

III. RESULTS AND DISCUSSION

A. *Icing, precipitation, temperature and wind climatology*

The location at Fagernesfjellet, as indicated by data from NEWA, experiences an annual occurrence of icing days ranging between 125 and 175 within the period from 2005 to 2018; can be seen in fig. 3. While there appears to be a decreasing trend in icing days over this timeframe, it is not deemed statistically significant. Despite this, the region remains susceptible to icing events, underscoring its vulnerability to atmospheric icing phenomena.
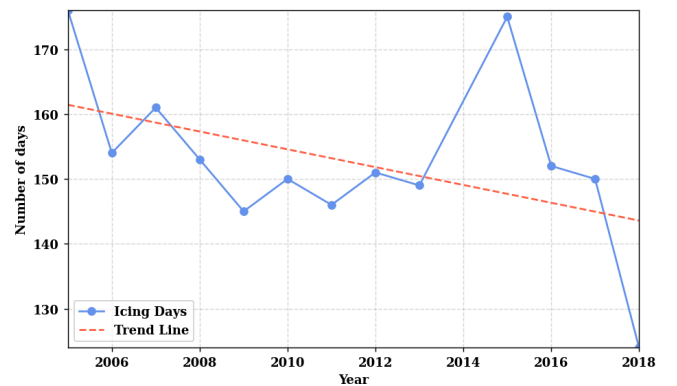
Fig. 3 Number of Icing days climatology at Fagernesfjellet between years 2005-2018.
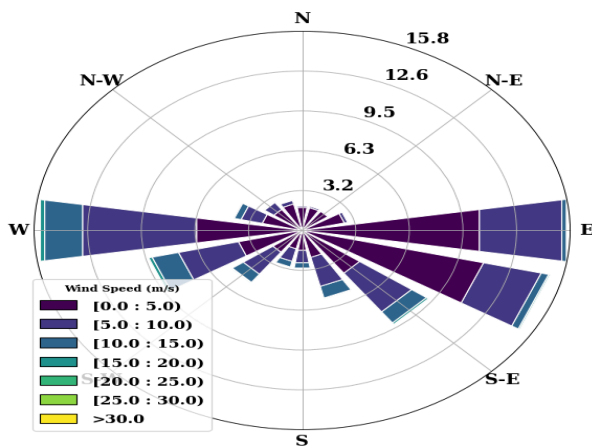
Fig. 4 Wind climatology at Fagernesfjellet between years 2005-2018.

B. *Comparative Analysis of Meteorological Parameters from Observations, NORA3, and WRF for October-December 2022*

Fig. 6 T2m at Fagernesfjellet between Oct-Dec 2022 from Observations, NORA3, WRF.

In addition to icing events, the total precipitation climatology reveals that Fagernesfjellet receives an annual precipitation range of 1280 to 2200 millimetres (not shown in figure). Notably, there is also a trend of decreasing total precipitation over time, although, similar to the number of icing days trend, this decrease is not statistically significant. This data further underscores the area's susceptibility to both icing and precipitation occurrences, highlighting the importance of continued monitoring and assessment of icing patterns in the region.

Annually the prevailing wind directions are west, east, and south-east. The annual maximum wind speed observed was around 16 m/s as shown in fig. 4. During the winter season (DJF) (not shown in figure), the prevailing wind direction is predominantly from the east to southeast, reaching maximum speeds of approximately 23 m/s. Conversely, in the transition months of spring (MAM) (not shown in figure), the wind direction shifts to east-southeast to west-southwest, with peak speeds reaching around 17 m/s from the west. Throughout the summer season (JJA) (not shown in figure), winds primarily originate from the west, with maximum wind speeds peaking at approximately 23 m/s. As autumn arrives (SON) (not shown in figure), the dominant wind patterns feature westerly and east-south-easterly directions, with peak wind speeds again reaching around 23 m/s from the west. The T2m climatology reveals a broad range of temperature values, spanning from -21°C during winter to 25°C on summer days, as shown in fig. 5.

The fig. 6 depicts the observed and simulated T2m at Fagernesfjellet. Throughout the three-month period, temperatures fluctuate between 10°C and -15°C. Both models effectively capture these temperature variations, albeit displaying slightly warmer surface temperatures compared to observations. Notably, the WRF results closely align with the observed temperatures. Regarding RH, both models accurately capture the RH variations, albeit exhibiting higher RH values compared to observations. However, the disparity between WRF and observations is less pronounced compared to NORA3, fig. 7 reports the Relative Humidity Comparison. The prevailing wind direction during the study period was south-southeast, with the wind rose from WRF closely resembling observations compared to NORA3. Additionally, while the observed wind maxima were 20.7, WRF and NORA3 depict 25.2 and 18.3, respectively, as illustrated in the fig. 8.
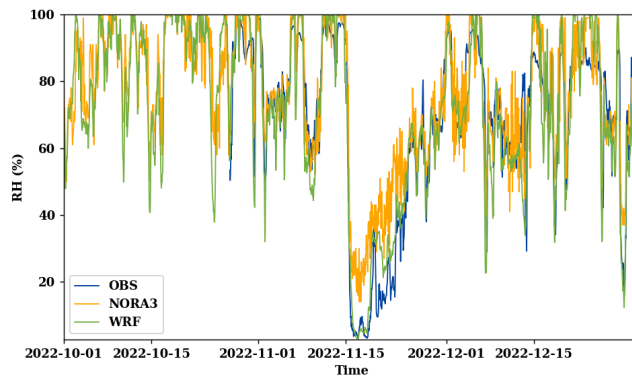
Fig. 7 Relative Humidity Comparison at Fagernesfjellet during Oct-Dec 2022: Observations vs. NORA3 vs. WRF.

During the three-month period, statistical analysis reveals notable performance metrics for T2m, RH, and wind speed for both WRF and NORA3 models. In terms of T2m, WRF demonstrates a high correlation of 0.97, with NORA3 closely trailing at 0.94. The RMSE for WRF stands at 1.68°C, whereas NORA3 exhibits a slightly higher RMSE of 2.31°C. The B in T2m is 1.12°C for WRF and 1.44°C for NORA3. Similarly, for RH, both models show commendable correlation coefficients, with WRF at 0.90 and NORA3 at 0.91. The RMSE for RH is 11.35% for WRF and 11.74% for NORA3, with biases of -1.09% and 4.81%, respectively.

Fig. 5 T2m climatology at Fagernesfjellet between years 2005- 2018 from Observations, NORA3, WRF.

Regarding wind speed, WRF achieves a correlation of 0.66, while NORA3 registers 0.58. WRF's RMSE for wind speed is 3.74, slightly higher than NORA3's 3.56. The bias for wind speed is minimal for WRF (0.06) but slightly negative for NORA3 (-0.84). These findings are summarized in the table II.
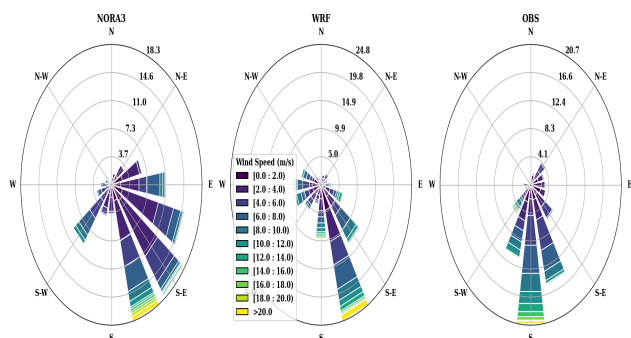
Fig. 8 Comparison of Wind Roses at Fagernesfjellet from Observations, NORA3, and WRF during Oct-Dec 2022

C. *Case study of icing event 28.10.2022 to 3.11.2022*

During the period from October 28, 2022, to November 3, 2022, we observed several icing episodes of notable intensity. To analyse these events, we employed various microphysics schemes while maintaining consistency in all other model physics settings. Observation data provided detailed icing load information on a minute-by-minute basis, which we converted into icing rates. For our analysis, we focused on instances with positive icing rates, aggregating these into hourly mean values. In contrast, the WRF model generated icing rates every 10 minutes, which we similarly consolidated into hourly means. The peak icing rate recorded during this event reached 400 g/hr, as per observational data, with the most significant icing occurring on October 28 and October 30.

TABLE III. CORRELATION, BIAS AND RMSE FOR WRF AND NORA3

Metric	WRF -TMP	NORA3-TMP
Correlation	0.97	0.94
RMSE	1.68	2.31
Bias	1.12	1.44
	WRF-RH	NORA3-RH
Correlation	0.90	0.91
RMSE	11.35	11.74
Bias	-1.09	4.81
	WRF -WS	NORA3 -WS
Correlation	0.66	0.58
RMSE	3.74	3.56
Bias	0.06	-0.84

The icing event coincided with distinct low-pressure systems situated over the Norwegian Sea and Russia. A notable synoptic condition on October 29, 2022, at 06 UTC, highlighted these phenomena: a low-pressure area was located in the Norwegian Sea, north of Norway, and another over Russia, moving towards Scandinavia. Fig. 9 shows the three hourly accumulated precipitation and Sea level pressure on

29.10.2022, 06 UTC. These conditions fostered strong winds in northern Norway, with maximum speeds observed between 35-40 knots. The interaction between these winds and the prevailing sea-level pressure is depicted in the fig. 10, illustrating the dynamic atmospheric conditions that might have contributed to the observed icing episodes.
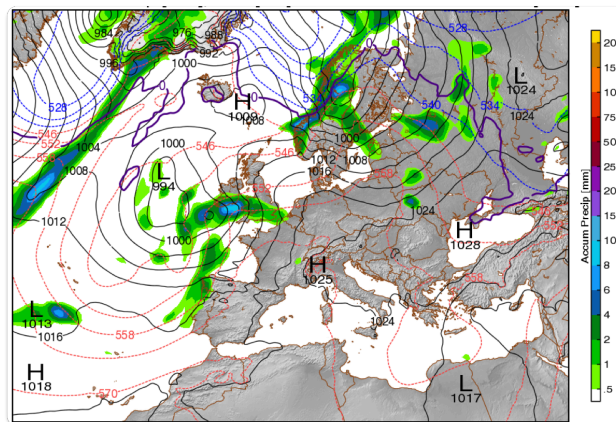
Fig. 9 Three hourly accumulated precipitation and Sea level pressure on 29.10.2022, 06 UTC from MERRA2 [24]
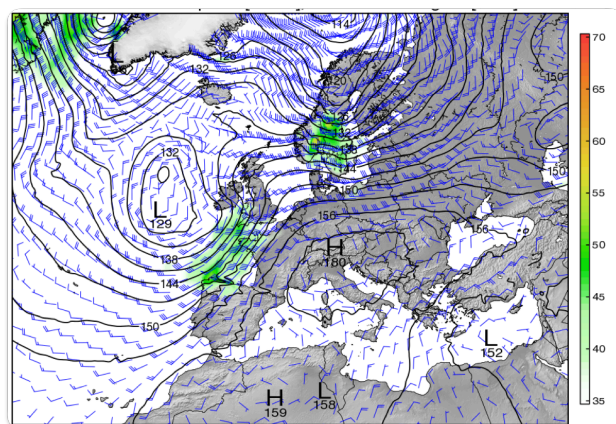
Fig. 10 850 hpa wind speed (knots) and barbs on 29.10.2022, 06 UTC from MERRA2 [24]

The LWC is a crucial parameter for understanding icing conditions. On October 29, 2022, at 06:00 UTC, the model indicates a significant presence of LWC in the lower levels, as depicted in the fig. 11(The cross section was taken along a line as shown by arrow in fig. 1). Observations reveal LWC values exceeding 0.5 g/kg at the summit of Fagernesfjellet. Moreover, a substantial amount of LWC extends up to a height of 1.5 km during this specific time interval.

In addition, the fig. 11 illustrates a notably higher concentration of LWC on the Fagernesfjellet summit compared to surrounding mountain, suggesting a possible influence of orographic lifting. At the mountain peak, the temperature hovered around zero degrees celsius, while the RH reached 99%, as evident from the figure.

Between October 28th and 30th, 2022, Fagernesfjellet experienced its highest icing rates, with observations reporting a maximum of around 400 g/hr. Various microphysics schemes generally agree with the observations but show some overestimates and underestimates. The WDM7 and Morrison schemes recorded the highest icing rates, reaching up to 420 g/hr. However, there are discrepancies in the timing of icing

rate occurrences between the actual observations and different microphysics schemes, which can be seen fig. 12.
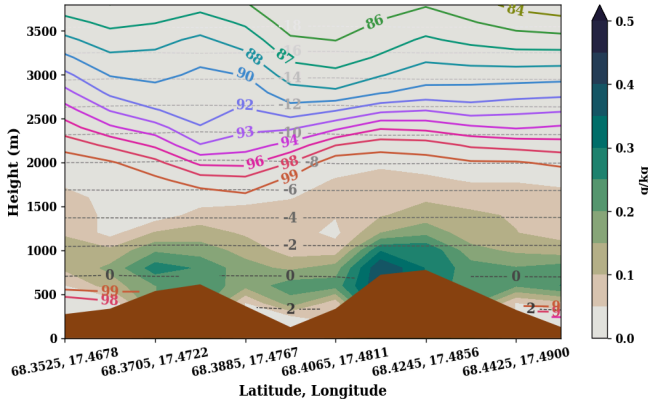
Fig. 11 Cross-sectional representation of RH, Temperature, and LWC on October 29, 2022, at 06:00 UTC from WRF.

We conducted an analysis of the Probability of Detection (POD) and False Alarm Ratio (FAR) for the icing rates. When the icing rate threshold was set at 10 g/hr, the microphysics schemes exhibited varying performance metrics. The Thompson scheme showed the highest Probability of Detection (POD) at 0.81, indicating its superior ability to accurately detect icing rates at lower thresholds. Following closely, the WSM6, Thompson, and Morrison schemes all displayed strong performance, with POD values of 0.78 each. Conversely, the WDM7 scheme showed a relatively lower POD of 0.78 and a False Alarm Ratio (FAR) of 0.50, suggesting a higher rate of false alarms compared to other schemes.
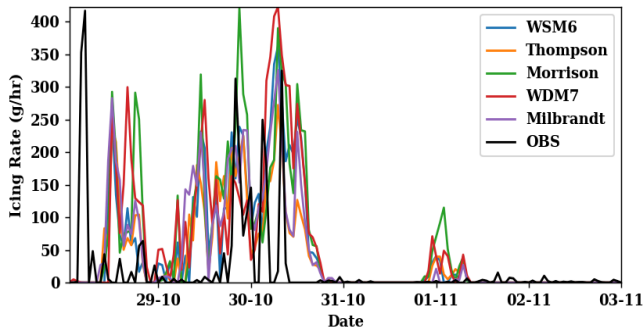
Fig. 12 Comparison of icing rates from various microphysics schemes in WRF and observations during the period from October 28, 2022, to November 3, 2022, at Fagernesfjellet.

When the icing rate threshold was increased to 50 g/hr, the performance metrics of the microphysics schemes shifted. The Morrison scheme exhibited the highest POD at 0.42, indicating its ability to accurately detect icing events at higher thresholds. The WSM6 and Thompson schemes also showed strong performance, with POD values of 0.28 each. However, the WDM7 scheme displayed a POD of 0.00, suggesting a failure to detect any icing events at the higher threshold. Additionally, the FAR values for all schemes decreased compared to the 10 g/hr threshold, indicating a reduction in false alarms. These results highlight the impact of threshold

selection on the performance of microphysics schemes in detecting icing events. Details about it can be seen in table III.

TABLE IV. POD AND FAR FOR DIFFERENT MICROPHYSICS SCHEMES FOR THE ICING EVENT

Microphysics	POD	FAR
Threshold 10 g/hr		
WSM6	0.78	0.41
Thompson	0.81	0.42
Morrison	0.78	0.47
WDM7	0.78	0.50
Milbrandt	0.78	0.39
Threshold 50 g/hr		
WSM6	0.28	0.87
Thompson	0.28	0.77
Morrison	0.42	0.82
WDM7	0.00	1.00
Milbrandt	0.28	0.85

By qualitatively analysing the hydrometeor evolution in the lower atmosphere across various microphysics schemes, distinct characteristics emerge (not shown in figure). Notably, Milbrandt and Thompson schemes exhibit higher LWC, while Morrison scheme portrays the highest snow water content and WDM7 the lowest. Regarding rainwater mixing ratio, WDM7 tops the list, whereas Milbrandt records the lowest values. WDM7 also predicts the highest ice mixing ratio, followed by WSM, with other schemes showing negligible amounts. Graupel content is notably higher in the Milbrandt scheme. In summary, LWC, rainwater, and snow emerge as the dominant hydrometeors across the analysed schemes. The sample distribution of hydrometeors at lowest level from Thompson scheme is shown in fig. 13.
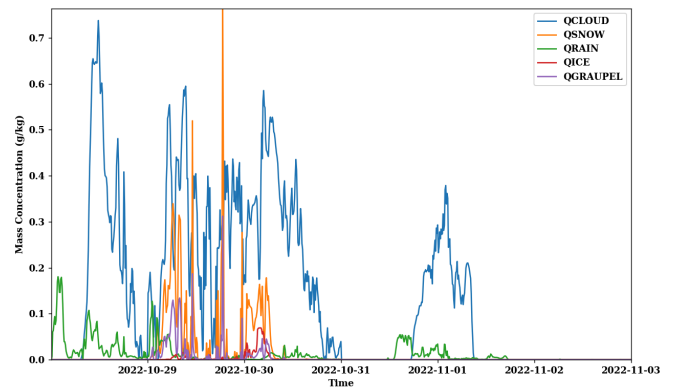
Fig. 13 Comparison of different hydrometeors from Thompson microphysics schemes in WRF during the period from October 28, 2022, to November 3, 2022, at Fagernesfjellet

IV. CONCLUSIONS

The climatological analysis of weather parameters at Fagernesfjellet underscores the region's susceptibility to atmospheric icing and precipitation events. According to data

from NEWA, the area experiences an annual occurrence of icing days ranging from 125 to 175 within the period from 2005 to 2018. Although a decreasing trend in icing days is observed over this timeframe, it is not statistically significant, emphasizing the persistent vulnerability to icing phenomena in the region. Concurrently, Fagernesfjellet receives an annual precipitation range of 1280 to 2200 millimetres, with a decreasing trend in total precipitation over time. Despite the lack of statistical significance in these trends, the findings highlight the area's continued susceptibility to both icing and precipitation occurrences.

Furthermore, the analysis of meteorological parameters from observations, NORA3, and WRF models for October to December 2022 provides valuable insights into model performance and atmospheric conditions. Both models effectively capture temperature variations, albeit exhibiting slightly warmer surface temperatures compared to observations. WRF results closely align with observed temperatures, while discrepancies in relative humidity are less pronounced in WRF compared to NORA3. Additionally, WRF demonstrates higher correlation coefficients and lower biases for temperature, relative humidity, and wind speed compared to NORA3.

During a notable icing event from October 28 to November 3, 2022, several episodes of significant icing were observed at Fagernesfjellet. The comparison of icing rates from various microphysics schemes in WRF and observations highlights some discrepancies in the timing and magnitude of icing events. Analysis of the POD and FAR for different microphysics schemes further underscores the impact of threshold selection on the detection of icing events. Notably, the Thompson scheme exhibits slightly better performance at lower icing rate thresholds, while the Morrison scheme shows better performance at higher thresholds.

Overall, these findings emphasize the importance of selection of microphysics and model physics significantly influences the determination of icing conditions, underscoring its importance in accurately assessing weather phenomena.

REFERENCES

[1] Thorkildson, R., K. Jones, and M. Emery, *In-cloud icing in the Columbia basin.* Mon. Wea. Rev., 2009. **137**: p. 4369-4381.

[2] Fikke, S.M., J.E. Kristjánsson, and B.E. Kringlebotn Nygaard, *Modern Meteorology and Atmospheric Icing*. Dordrecht: Springer Netherlands: Dordrecht. p. 1-29.

[3] Kjersem, H.A., *Estimation of production losses due to icing on wind turbines at Kvitfjell wind farm.* 2019, Norwegian University of Life Sciences, Ås.

[4] Gent, R.W., N.P. Dart, and J.T. Cansdale, *Aircraft icing.* Philos. Trans. Math. Phys. Eng. Sci., 2000. **358**: p. 2873-2911.

[5] Hahmann, A.N., et al., *The making of the New European Wind Atlas – Part 1: Model sensitivity.* Geosci. Model Dev., 2020. **13**(10): p. 5053-5078.

[6] Solbrekke, I.M., A. Sorteberg, and H. Haakenstad, The 3 km Norwegian reanalysis (NORA3) – a validation of offshore wind resources in the North Sea and the Norwegian Sea. Wind Energ. Sci., 2021. **6**(6): p. 1501-1519.

[7] Rashid, T., et al., *A Field Study of Atmospheric Icing Analysis in a Complex Terrain of the High North.* The International Journal of Ocean and Climate Systems, 2014. **5**(4): p. 189-197.

[8] Norgeskart available: https://www.norgeskart.no/

[9] Skamarock, W.C., et al., *A description of the advanced research WRF version 3.* NCAR technical note, 2008. **475**: p. 113.

[10] Hersbach, H., et al., *The ERA5 global reanalysis.* Quarterly Journal of the Royal Meteorological Society, 2020. **146**(730): p. 1999-2049.

[11] Iacono, M.J., et al., *Radiative forcing by long‑lived greenhouse gases: Calculations with the AER radiative transfer models.* Journal of Geophysical Research: Atmospheres, 2008. **113**(D13).

[12] Hong, S.Y., *A new stable boundary‑layer mixing scheme and its impact on the simulated East Asian summer monsoon.* Quarterly Journal of the Royal Meteorological Society, 2010. **136**(651): p. 1481-1496.

[13] Chen, F. and J. Dudhia, Coupling an advanced land surface–hydrology model with the Penn State–NCAR MM5 modeling system. Part I: Model implementation and sensitivity. Monthly weather review, 2001. **129**(4): p. 569-585.

[14] Thompson, G., et al., *Explicit Forecasts of Winter Precipitation Using an Improved Bulk Microphysics Scheme. Part II: Implementation of a New Snow Parameterization.* Monthly weather review, 2008. **136**(12): p. 5095-5115.

[15] Milbrandt, J.A. and M.K. Yau, *A multimoment bulk microphysics parameterization. Part I: Analysis of the role of the spectral shape parameter.* Journal of the atmospheric sciences, 2005. **62**(9): p. 3051-3064.

[16] Morrison, H., J.A. Curry, and V.I. Khvorostyanov, *A new double-moment microphysics parameterization for application in cloud and climate models. part I: Description.* Journal of the atmospheric sciences, 2005. **62**(6): p. 1665-1677.

[17] Hong, S.Y. and J.-O.J. Lim, *The WRF Single-Moment 6-Class Microphysics Scheme (WSM6).* Asia-pacific Journal of Atmospheric Sciences, 2006. **42**: p. 129-151.

[18] Bae, S.Y., S.-Y. Hong, and W.-K. Tao, *Development of a single-moment cloud microphysics scheme with prognostic hail for the Weather Research and Forecasting (WRF) model.* Asia-Pacific Journal of Atmospheric Sciences, 2019. **55**: p. 233-245.

[19] Foder, M.H. *ISO 12494" Atmospheric Icing of Structures" and How to Use It.* in *ISOPE International Ocean and Polar Engineering Conference.* 2001. ISOPE.

[20] Finstad, K.J., E.P. Lozowski, and L. Makkonen, *On the median volume diameter approximation for droplet collision efficiency.* Journal of the atmospheric sciences, 1988. **45**(24): p. 4008-4012.

[21] Thornes, J.E. and D.B. Stephenson, *How to judge the quality and value of weather forecast products.* Meteorological Applications, 2001. **8**(3): p. 307-314.

[22] Global Modelling and assimilation office, 2024.

Online: https://gmao.gsfc.nasa.gov/

Atmospheric In-cloud Icing Using WRF for an Alpine Wind Power Plant in Norway

Jonas Mundheim Strand[1,2], Yngve Birkelund[1], Pravin Punde[1]

[1] *University of Tromsø - The Arctic University of Norway*
[2] *Kjeller Vindteknikk (part of Norconsult), Norway*

Jonas.mundheim.strand@norconsult.com, yngve.birkelund@uit.no, pravin.b.punde@uit.no,

Abstract— **Troms Kraft have identified a location in Kvænangen, Norway, for a new wind power plant with promising wind resources. However, the site is in an arctic climate with mountainous terrain exposed to severe icing conditions.**

Assessments of icing conditions at proposed locations for new wind power plants in areas exposed to icing is crucial to identifying icing related challenges. This paper investigates atmospheric in-cloud icing and thereby identifying conditions affecting the wind turbines at the proposed site. Meteorological parameters are provided from simulations using the Weather Research and Forecasting (WRF) model. Modelled parameters are applied to calculate estimates of the expected annual hours with ice accretion rate exceeding threshold values 10 g/h and 50 g/h for suggested turbine locations. This is done by applying the Makkonen ice accretion model. The WRF model has been run for the whole of 2022.

It is found that model terrain elevation is strongly connected to the calculated ice accretion rate. Because of this, a method for adjusting the icing estimations to differences between model and actual terrain height is conducted.

Analysis of wind patterns at times with modelled meteorological icing shows that ice accretion normally accumulates during winds coming from north-westerly directions. Case studies shows that icing conditions with north-westerly winds induce an increased LWC as a result of orographic lifting.

Keywords— ***In-cloud icing, WRF, Orographic lifting, Norway, Wind power, Arctic***

I. INTRODUCTION

Wind power production in arctic regions face significant challenges related to atmospheric icing. Accumulation of ice, most frequently caused by in-cloud icing, on structures like turbine blades and power lines can result in severe damage. Ice accretion on turbine blades can adversely impact the aerodynamics of the blade and reduce the turbines production [1]. A combination of imbalances in ice mass and aerodynamics may cause vibrations increasing the risk of mechanical failure [2]. Accumulation of ice on the turbines may exert serious safety hazards for people and infrastructure in case of ice shedding [3].

Early assessments of the icing conditions at specific locations becomes increasingly important as a part of the developing process of a new wind power plant. In the search for great wind resources energy companies look to construct in mountainous areas. This also results in an increased exposure to severe icing which will affect both power production and maintenance costs [4][5][6].

Detailed information regarding the icing conditions can be utilized to compare estimated production loss due to icing between prospected sites. This can prove to be essential when assessing turbine placements and evaluate locations for construction. Local meteorological patterns found from conditional analysis could be useful for forecasting icing events [7].

II. METHOD

A. Data

The site of interest in this paper is located south of Kvænangsbotn, in Kvænangen municipality, Troms County. The suggested wind turbines are located in mountainous terrain with topography varying from 700 – 900 meters above sea level surrounded by complex terrain in all directions. The site is placed at the top of a steep terrain elevation from Sørfjorden (0 masl) to the north of the site, meaning all winds blowing from N-NW directions will be orographically lifted before reaching the site. In south/south-east and easterly directions the terrain can be described as relatively flat and in-land climate. Low pressure systems typically bring precipitation from the ocean during winter season, while easterly wind is cold and dry.

All data in this study is retrieved from simulation done by Weather Research and Forecasting model, version 4.3. WRF is a three-dimensional, fully compressible, nonhydrostatic state of the art numerical weather prediction model designed for different mesoscale applications. The model is developed by National Centre of Atmospheric Research (NCAR) and is used for both research and forecast purposes [8].

The WRF model has been run for the whole of 2022 with three one-way nesting domains d01, d02 and d03 with grid spacing 9km, 3km and 1km (Fig. 1). All domains are configured with a vertical structure of 51 terrain following sigma levels with 50 hPa as upper boundary layer. The simulation is initiated and forced on the lateral boundaries by the ECMWF-ERA5 dataset [9]. Global Multi-resolution Terrain Elevation Data 2010 (GMTED 2010) with horizontal resolution 30 arc-seconds (1km) is used as terrain input data. Parameterization schemes used are listed in Table I.

TABLE I. PARAMETERIZATION SCHEMES USED IN THE WRF SIMULATION

Type of scheme	WRF variable name	Scheme
Microphysics	mp_physics	Thompson [10]
Planetary boundary	bl_pbl_physics	YSU [11]
Shortwave radiation	ra_sw_physics	RRTMG [12]
Longwave radiation	ra_lw_physics	RRTMG [12]
Land surface	sf_surface_physics	Unified Noah [13]
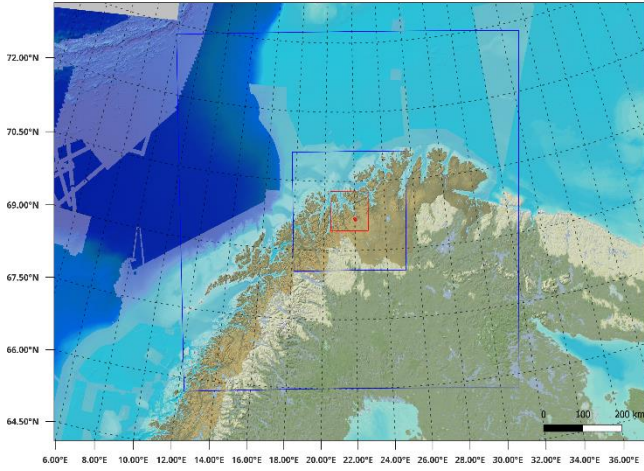
Fig. 1 Domain configuration of nested domains used in the WRF simulation. d01 (outer square), d02 (middle square) and d03 (inner red square). The site of interest is marked in red within d03.

B. Theoretical calculations

The ice accretion rate is calculated using the output data from WRF-d03 as input in the Makkonen model described in [14] on a standard reference collector (SRC) with dimensions 30mm diameter and 1m length. This follows the equation

$$\frac{dM}{dt} = \alpha_1 \alpha_2 \alpha_3 v A (LWC)$$

The accreted ice mass (*dM/dt*) [*kg/s*], is a function of the collision efficiency, α_1, the sticking efficiency (mainly for wet snow), α_2, the freezing efficiency (determines "dry and "wet" growth for rime), α_3, the wind speed (perpendicular to accreting object), v [*m/s*], the cross-sectional area of object, A [*m²*], and the liquid water content, LWC [*kg/m³*]. All the terms α_1, α_2 and α_3 are correction factors with a value in the range 0 to 1.

In this study $\alpha_1 = \alpha_2 = 1$ giving an assumption of dry ice growth, hence all impinging droplets will freeze on impact with the SRC. α_1 and MVD is calculated from the following equations [15]

$$MVD = \frac{(3.672 + \mu)}{\lambda}$$

Where μ is the shape parameter, diagnosed by the pre-specified droplet concentration number, N_c [m^{-3}]. $N_c = 100$ cm^{-3} is used in the calculations for this paper.

$$\mu = \min\left(\frac{1000}{N_c} + 2, 15\right)$$

And λ is found using gamma distribution, with ρ_w as the density of water [kg/m^3]

$$\lambda = \left[\frac{\pi}{6}\rho_w \left(\frac{\Gamma(4+\mu)}{\Gamma(1+\mu)}\right)\left(\frac{N_c}{LWC}\right)\right]^{\frac{1}{3}}$$

The MVD can then be used to calculate the collision efficiency from

$$\alpha_1 = A - 0.028 - C(B - 0.0454)$$

Where

$$A = 1.066 K^{-0.00616} \exp(-1.103 K^{-0.688})$$

$$B = 3.641 K^{-0.498} \exp(-1.497 K^{-0.694})$$

$$C = 0.00637(\phi - 100)^{0.381}$$

And the dimensionless parameters, droplet inertia parameter, K, and Langmuir parameter, ϕ

$$K = \frac{\rho_w MVD^2 v}{9uD}$$

$$\phi = \frac{Re^2}{K}$$

$$Re = \frac{\rho_a MVDv}{u}$$

Where D is the diameter of the cylinder and Re is the Reynolds number given by air density, ρ_a [kg/m^3], dynamic viscosity of air, u [*kg/m s*] and the free stream velocity, v [*m/s*].

Icing intensity, I [g/h], is then used to calculate annual hours with hourly average ice accretion rate exceeding a threshold value of 10 g/h, known as the industry limit [16]. Moreover, atmospheric in-cloud icing occurs for temperatures less than 0 °C. Therefore, only hourly average values with a threshold value of $T < 0°C$ are included.

It is found that model terrain elevation is strongly connected to the calculated ice accretion rate. Because of this, a method for adjusting the icing estimations to differences between model and actual terrain height is conducted. This method is described in [17].

III. RESULTS

A. WRF model terrain height

A closer look at the WRF-d03 models' terrain representation is depicted in Fig. 2. Limitations regarding representation of the terrain in the model will affect the output data at the site, and the influence of terrain and especially local terrain features as nearby mountains in westerly directions is not accurately represented which is important when describing the icing potential. This misrepresentation of steep elevation changes and actual elevation, in combination with the wind direction of the site, may influence the model icing results. The magnitude of this relation in the represented case will remain unknow as no actual observations at the site is available for comparison.
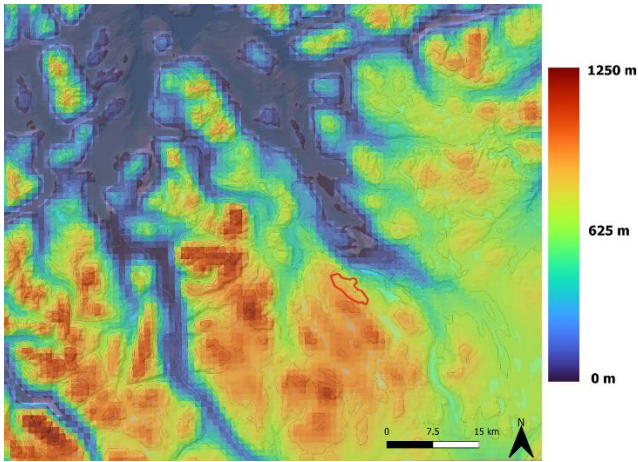
Fig. 2   Terrain height for WRF model domain - d03.

B. Icing conditions analysis

A wind rose representing wind directions and wind speeds during hours when icing intensity exceeds 10 g/h for a suggested turbine location within the site is shown in Fig. 3.

The results show that ice accretion mainly forms with winds blowing from NW directions for both threshold values. This is a strong indication of winds following the fjord resulting in orographically lifting of air before reaching the site. Due to the location characteristics at the top of a hill, the site is likely for NW winds to experience a much higher LWC than surrounding areas. This effect will intensify the icing at the site.

C. Icing event

Through investigations of hourly averaged ice accretion rate for the whole of 2022 we can identify icing events. This paper will further inspect an event in January characterized by winds blowing from north-west which is the direction most common for ice accretion at the site.

Fig. 4 shows a timeseries plot for the hourly averaged values for ice accretion rate, temperature, wind speed and MVD during an icing event starting at hour 03:00 on the 20th
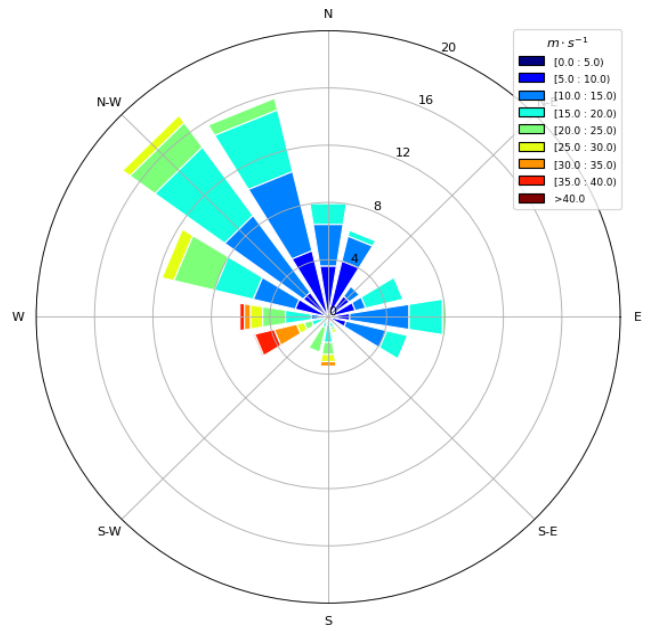
Fig. 3   Wind rose during times when icing intensity exceeds 10 g/h at height 174 m.a.s.

and ending 00:00 in the 21st. Throughout the event we identify a sustained icing event marked by large fluctuations in the estimated icing intensity. The temperature is well below freezing for the whole period and incidents with no-icing cannot be explained by positive temperatures in the model.

Investigating the results, we find increasing ice accretion rate with higher values for MVD and wind speeds. As expected, there is a prominent relation to warmer temperatures and high MVD, however, for the specific case at time 20:00 (20.01) we can observe an interesting high MVD during lower temperatures. The cause of this spike in MVD is not investigated but a relation between MVD and wind speeds seems to be present. This could be a result of increased terrain-induced vertical atmospheric-motions as the main forcing for production of LWC for higher wind speeds.

Usually, temperatures this low seem to inflict less icing than depicted in the graphical representation. Inspecting characteristics in the air masses before reaching the turbine could help explain this.
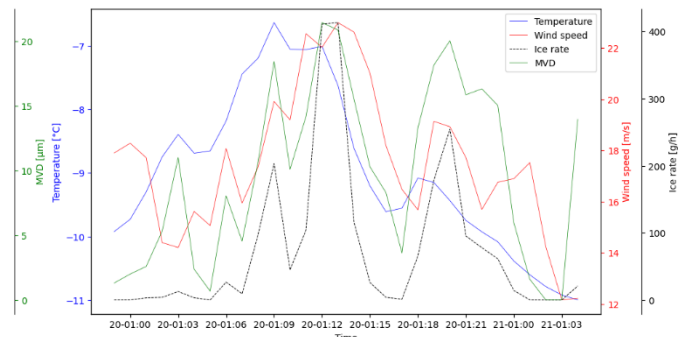
Fig. 4   Timeseries for period from 00:00 at the 20.01.2022 to 04:00 at the 21.01.2022. Hourly averaged values at height 174 m.a.s. for; ice accretion rate (dashed line), temperature (blue), MVD (green) and wind speed (red).

Fig. 5 displays a wind rose showing the direction of the wind during meteorological icing for the period 20th to 21st. This clearly shows a main direction of winds blowing from north-westerly directions, which is the same direction as the yearly overall main direction during ice accretion (Fig. 3).

Fig. 6 shows LWC at height 174 m.a.s marked by purple colour-bar over model-terrain, equal to as presented in (Fig. 2). The direction of the wind in the model is illustrated by arrows. The representation of the conditions depicted illustrates the specific conditions during the icing event at which the ice accretion rate is at its peak, 13:00 on the 20th of January.

For the represented geographical area there is a clear wind direction coming from NW. This evidently force winds to follow the fjord in direction toward the site of interest, marked in red ellipse. Identifying areas with high LWC there seems to be a prominent relation to higher LWC located over higher terrain elevation that is first faced by the winds.

Fig. 7 shows a vertical cross section with stating point in the green dot following the line to the end point in the red dot marked in (Fig. 6).

The wind direction is parallel to the line, meaning that the direction of the wind in (Fig. 7) flows directly from left to right relative to the figure. In the figure the white dashed lines represent temperature $[°C]$, purple lines RH $[\%]$, and the colour-bar LWC $[kg/kg]$. The model terrain is illustrated by the brown filled sections. The total length of the cross section is 40 km where the site is located 1 km before the highest peak.

Orographic lifting due to winds forcing air to follow the terrain will cool the air and condensation of water vapour will increase the LWC. The figure shows how LWC is consequently increasing with its maximum value located at and around the top of the mountain. The site located near the top at the windward side will experience a higher LWC compared to surrounding areas during north-westerly winds.
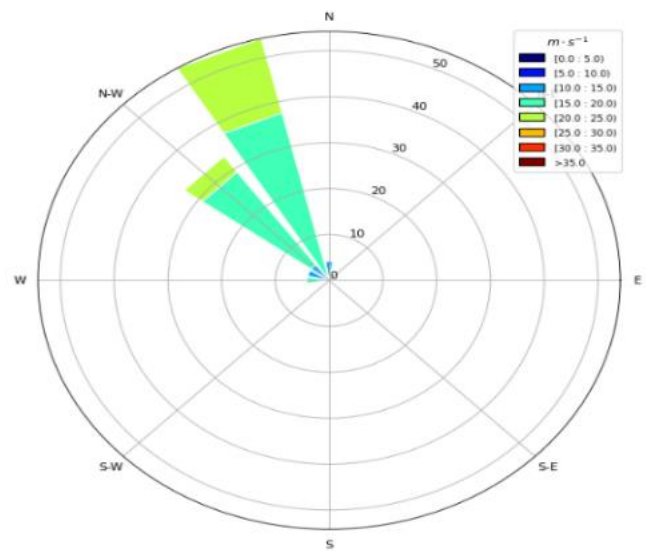
Fig. 5 Wind rose for hourly averaged values at times where icing intensity exceeds 0 g/h at height 174 m.a.s.

Orographic lifting might be the most significant reason for a relatively high LWC observed at the site when seen in relation to relatively low temperatures.
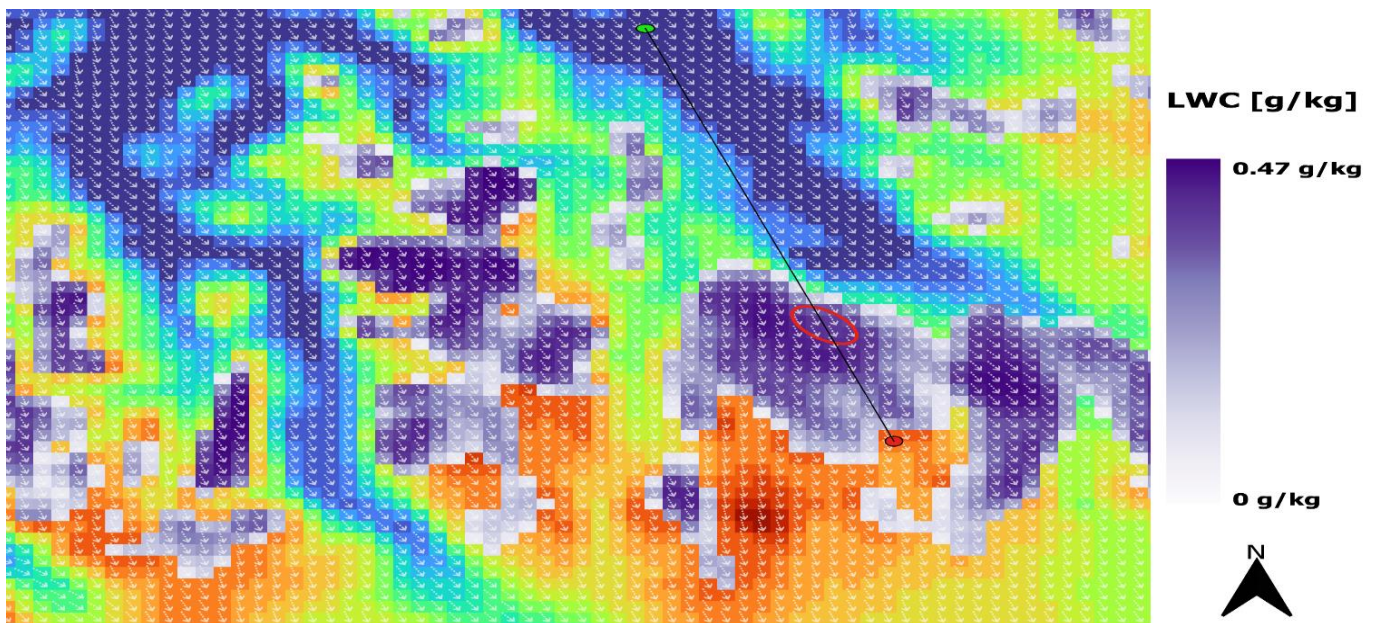
Fig. 6 Overview of the LWC from layer 174 m.a.s over model terrain extracted from model domain 3 at timestamp 13:00 on the 20.01.2022. The direction of the wind at the same layer-height for each grid cell is marked by the arrows. The green dot marks the starting point and the red dot the ending point for the vertical cross-section shown in Fig. 7. The red ellipse illustrated the approximate location of the suggested site.
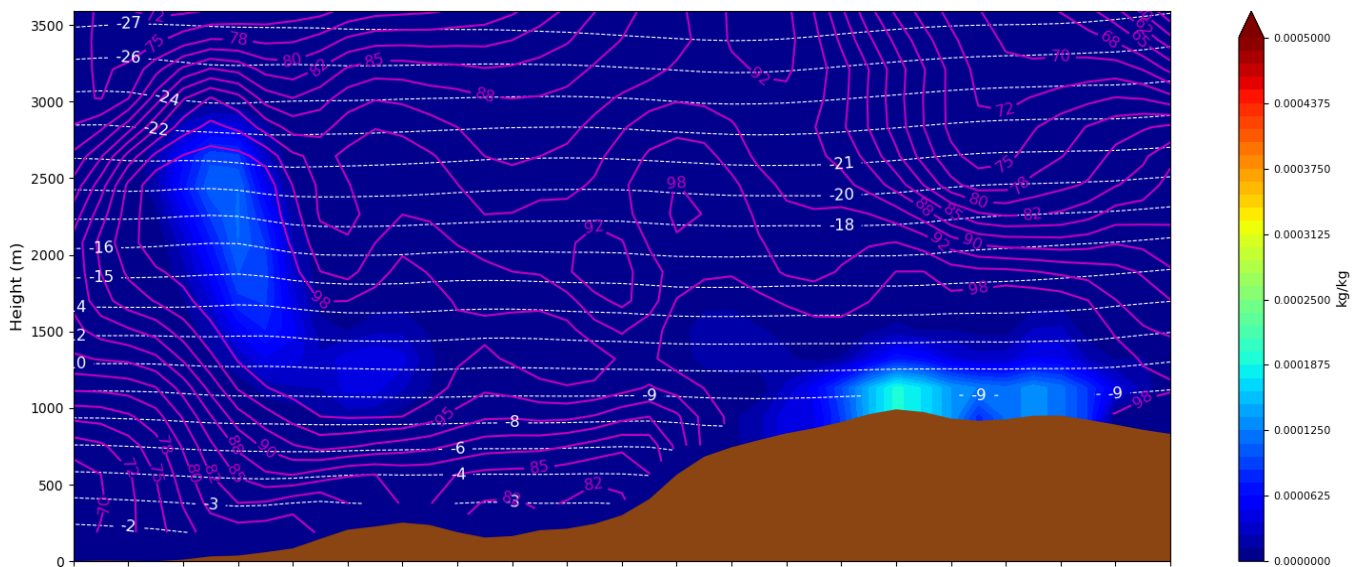
Fig. 7 Vertical cross-section with horizontal length 40km with start and end point as illustrated in Figure 4.29. The models vertical height is represented in meters above sea level and model terrain is marked in brown. The vertical cross-section shows temperature [°C] (white),relative humidity [%] (purple) and LWC [kg/kg] (colour-bar).

IV. CONCLUSIONS

There are no available measurements from the proposed site, and the analysis used output data from the NWP model WRF with a horizontal resolution of 1 km. The time-period considered covered the year of 2022.

The modelled ice accretion shows that the turbine located at the highest terrain elevation has the highest number of yearly icing hours, with 948 hours for icing rates above 10 g/h. The turbine located at lowest elevation has the lowest number of total annual hours, with 385 hours for icing rates exceeding 10 g/h. This shows large deviations in estimated icing intensity within the site. Model terrain elevation is found to be strongly connected to the ice accretion rate. Because of this, a method for adjusting the icing estimations to differences between model and actual terrain height is conducted. This aims to provide more accurate results.

Analysis of wind patterns at times with meteorological icing, shows that ice accretion normally accumulates during winds coming from north-westerly directions. The case studies shows that icing conditions with north-westerly winds induce an increased LWC because of orographic lifting. This is the main cause for ice accretion at the site.

REFERENCES

[1] Hochart, C., et al., *Wind turbine performance under icing conditions.* Wind Energy: An International Journal for Progress and Applications in Wind Power Conversion Technology, 2008. 11(4): p. 319-333.

[2] Homola, M.C., *Atmospheric icing on wind turbines: Modeling and consequences for energy production.* 2011

[3] Seifert, H., *Technical requirements for rotor blades operating in cold climate.* DEWI-Magazin, 2005

[4] Contreras Montoya, L.T., S. Lain, and A. Ilinca, *A review on the estimation of power loss due to icing in wind turbines.* Energies, 2022. 15(3): p. 1083

[5] Ebrahimi, A., *Atmospheric icing effects of S816 airfoil on a 600 kW wind turbine's performance.* Scientia Iranica, 2018. 25(5): p. 2693-2705

[6] Homola, M.C., et al., *Performance losses due to ice accretion for a 5 MW wind turbine.* Wind Energy, 2012. 15(3): p. 379-389

[7] Thorsson, P., S. Söderberg, and H. Bergström, *Modelling atmospheric icing: A comparison between icing calculated with measured meteorological data and NWP data.* Cold regions science and technology, 2015. 119: p. 124-131

[8] W. C. Skamarock, J. B. Klemp, J. Dudhia, D. O. Gill, Z. B. J. Liu and X. Y. Huang, *A description of the advanced research WRF model version 4.*, Atmospheric Research, 2019.

[9] H. Hersbach, *The ERA5 Atmospheric Reanalysis*, in AGUFM, NG33D-01., 2016

[10] Thompson, G., et al., *Explicit forecasts of winter precipitation using an improved bulk microphysics scheme. Part II: Implementation of a new snow parameterization.* Monthly weather review, 2008. 136(12): p. 5095-5115

[11] Dudhia, J., *WRF physics options.* NCAR WRF basic tutorial, 2010. 26: p. 30

[12] Iacono, M.J., et al., *Radiative forcing by long-lived greenhouse gases: Calculations with the AER radiative transfer models.* Journal of Geophysical Research: Atmospheres, 2008. 113(D13

[13] Mukul Tewari, N., et al. *Implementation and verification of the unified NOAH land surface model in the WRF model (Formerly Paper Number 17.5).* in *Proceedings of the 20th conference on weather analysis and forecasting/16th conference on numerical weather prediction*, Seattle, WA, USA. 2004

[14] ISO 12494, *Atmospheric icing of structures, first edition,* 2001

[15] Thompson, G., Nygaard, B. E., Makkonen, L., & Dierer, S. (2009). *Using the Weather Research and Forecasting (WRF) model to predict ground/structural icing.* 13th International Workshop on Atmospheric Icing on Structures, METEOTEST, Andermatt, Switzerland

[16] Hämäläinen, K. and S. Niemelä, *Production of a numerical icing atlas for Finland.* Wind Energy, 2017. 20(1): p. 171-189

[17] Strand, J.M, *Atmospheric in-cloud icing using WRF for an alpine wind power plant in Kvænangen,* Master's thesis, University of Tromsø – The Arctic University of Norway, 2023

The impact of saddle-type micro-terrain on transmission line icing

Hongxia Wang[1], Hualong Zheng[2], Yizhang Wang[2], Meng Li[1], Zhijin Zhang[2], Qin Hu[2], Xingliang Jiang[2]

[1] State Grid Xinjiang Electric Power Research Institute, Urumqi 830013, China
[2] Xuefeng Mountain Energy Equipment Safety National Observation and Research Station, Chongqing University, Chongqing 400044, China

wanghongxiaab@163.com, hualong.zheng@cqu.edu.cn, 765390461@qq.com, 297910523@qq.com

Abstract— **China possesses diverse and intricate topography, with widespread micro-terrain regions that can influence local meteorological elements such as wind speed and temperature. One of the impacts of micro-terrain on the safe operation of transmission lines, especially for those located in mountainous areas, is conductor icing. To reveal the influence of micro-terrain on transmission line icing, this paper focuses on one of the most common micro-terrains, saddle-type, which is widely distributed in mountainous and hilly areas. The disturbance effects of typical saddle terrain on airflow are analyzed using computational fluid dynamics (CFD) simulations. By comparing wind fields with various saddles of different widths assembled by twin Gaussian-shaped hills, it was discovered that the acceleration effect of saddle terrain on wind speed is primarily determined by the saddle slope, and dominates the entire saddle region when the saddle slope exceeds 35%. Wind accelerations at the hill crest are more pronounced, influencing a region above 30% of the hill height, whereas the speed-up effect is well restrained within the saddle. Above the saddle center, wind velocity is less affected and thus has minor influence on icing process. The results suggest that when transmission lines span over the hill peaks, the saddle effect is insignificant. Only the wind acceleration at the crest needs to be considered. However if a multi-span crossing is planned across the saddle region, a wind acceleration ratio of 1.1 may be considered too conservative, and thus underestimates the icing on transmission line conductors.**

Keywords—***wind speed-up, saddle-type micro-terrain, transmission line icing***

I. Introduction

Ice accumulation severely affects the operational safety of power grids in winter months. Ice accretion on transmission lines not only increases the static load on a tower-line system but also leads to an significant increase on the wind load due to the enlarged icy surface. Icing-induced loads can affect sag distances, potentially leading to phase-to-phase and phase-to-earth flashovers, and once exceeding a critical threshold, catastrophic failures, such as tower collapses and conductor breakages could be incurred [1]. In the strategic planning of transmission line routes, there is a concerted effort to avoid regions prone to significant ice accumulation [2]. However, it is acknowledged that certain areas, for instance valleys, gorges, ridges, or areas adjacent to bodies of water, may have local climatic conditions markedly different from the surrounding region, owing to their unique topographical characteristics, and thus lead to intensified ice accretion on a smaller scale.[3] Given the widespread distribution of these micro-topographical regions, it is, in fact, difficult, if not impossible, to completely bypass the areas of minute meteorological phenomena.

Extensive research has been undertaken to develop numerical models aimed at predicting ice thickness on transmission lines, encompassing empirical [4] and semi-empirical models [5], alongside theoretical analyses [6] of the physical phenomena underlying ice accretion. It has been recognized that temperature, wind velocity and direction are the most influential meteorological factors reflecting icing intensity in the physical processes of liquid water droplets, driven by the air flow, interact with the conductors, and the phase transition of water. Therefore, to understand the complex influence of microtopography on power transmission lines, it is critical to first characterize the airflow perturbations induced by topography features.

In China, mountainous regions encompass two-thirds of the nation's total area. The influence of orography, such as hills and cliffs, on wind patterns is also a primary concern in overhead transmission line (OHL) design criteria for assessing the impact of natural wind forces. IEC 60826 [2] provides a guideline to calculate the wind speed up effects due to local topography for hills or ridges. Similarly, corrections for wind velocity over hills are also presented in civil engineering codes of practice, for instance, in [7]. However, current standards primarily offer a basic correction for simple topography in a 2D format. The saddle-type micro-terrain is in principle of a 3D feature (i.e. saddle region is perpendicular to the wind direction) has yet to be extensively discussed.

To the best of the author's knowledge, there is not a universal criteria to define an area of saddle-type micro-terrain, but it is normally recognised as a depression in a mountain range. An example is given in Fig.1. But it is necessary to maintain that different shapes of saddle-type micro-topography were also proposed in literatures[8]. The aim of this work is to analyse the wind speed-up effects in saddle-type micro-terrain and thus contribute to the understanding of the consequent impacts on transmission line ice accretion. Rougher than performing exhaustive research on different types of saddle-type microtopography, this work intends to focuses on the type characterized by two low hills, representing typical orography in hilly areas. CFD simulations were performed to analyse the wind speed-up effect induced by saddles of different size, which is further characterised as saddle slope. The results reveal the impact of saddle-type micro-terrain on wind velocities and thus the protential influence on conductor icing, contribute to a better understanding and assessment on transmission line icing over micro-terrain areas
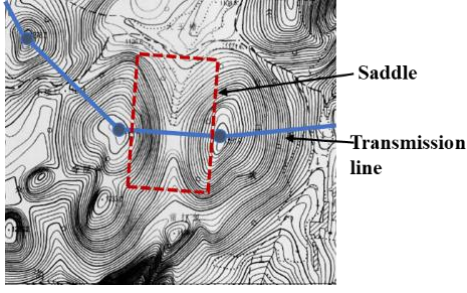
Fig. 1 An example of transmission line through saddle-type micro-terrain. In particular, the transmission line spans over the two hill peaks above the saddle highlighted by red dashed box.

II. SIMULATION METHOD

A. Terrain Geometry

To mimic a saddle-type microtopography, two hills of Gaussian shape were assumed to form an idealised situation. The distance between the twin-hill peaks define the width of the saddle W, and the depth of the saddle is equal to the hill height H as can be seen in Fig.2. The analytic form of the Gaussian shape hill is given by:

$$Z(x, y) = H * e^{-\frac{x^2 + y^2}{2\sigma^2}} \quad (1)$$

$$\sigma = \frac{W}{6} \quad (2)$$

where Z is the altitude above the x-y indexed ground plane. The hill shape factor σ is determined by W.

B. Governing equations

The physical process is modelled with three fundamental equations in computational fluid dynamics simulations, i.e. mass conservation, momentum conservation, and energy conservation. When the temperature variation is negligible, the energy equation can be omitted.

$$\frac{\partial \rho}{\partial t} + \frac{\partial (\rho \bar{u}_i)}{\partial x_i} = 0 \quad (3)$$

$$\frac{\partial (\rho u_i)}{\partial t} + \frac{\partial (\rho u_i u_j)}{\partial x_j} = -\frac{\partial p}{\partial x_i} + \frac{\partial}{\partial x_j}(\mu \frac{\partial u_i}{\partial x_j}) + S_i \quad (4)$$

where t is time; u represents the partial velocity of the fluid along the coordinate axis in the three-dimensional coordinate axis; ρ is the fluid density.

A set of Navier-Stokes (N-S) equations derived from the momentum equation is applied. The N-S equation reflects the basic mechanical laws of viscous fluid flow, and can be solved directly to reproduce the entire turbulent flow process.
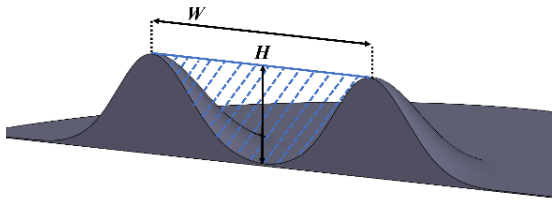
Fig. 2 Cross-section view of the idealised terrain geometry mimicking a saddle-type micro-terrain. The area of interest is indicated by the dashed region.

$$\frac{\partial u_i}{\partial t} + u_j \frac{\partial u_i}{\partial x_j} = f_i - \frac{1}{\rho}\frac{\partial p}{\partial x_i} + \frac{\mu}{\rho}\frac{\partial^2 u_i}{\partial x_j^2} \quad (3)$$

where ρ represents the density of the fluid. u, v, w are the velocity components of the fluid at point (x, y, z) at time t. p represents the pressure. f represents the volume force. μ is the dynamic viscosity.

The shear stress transport (SST) formulation was adopted, using a $k - \varepsilon$ formulation in the domain adjacent to the boundary layer and a $k - \omega$ formulation to the boundary layer. It combines the advantages of the two models and has obvious advantages for separated flows [9-11].

The solution utilizes a pressure-based steady-state solver, employing the SIMPLEC algorithm for pressure coupling. The momentum equation and turbulence model's nonlinear convection terms are discretized with a second-order upwind scheme. The convergence criterion for all variables, including the continuity equation, is established at 10^-5. Once the residuals and observation point values converge to their respective specified values, the computation is considered complete.

C. Boundary conditions

To avoid potential biases in the results from varying wind speed profile and terrain parameters, and to simplify the understanding of wind acceleration effects, this study employs a uniformly distributed longitudinal wind profile as the inlet condition. At the velocity inlet, wind speed is fixed, and both turbulent kinetic energy and its dissipation rate are determined and set according to the formula below [12-14].

$$k = \frac{u_*^2}{\sqrt{C_\mu}}\sqrt{C_1 \, ln(\frac{z+z_0}{z_0}) + C_2} \quad (6)$$

$$\omega = \frac{u_*}{k\sqrt{C_u}}\frac{1}{z + z_0} \quad (7)$$

where, z is the height from the ground, u_z is the average wind speed at height z; u^* is the friction speed; z_0 is the aerodynamic roughness length; C_μ is the turbulence model constant; C_1 and C_2 are constants.

The outlet adopts a pressure outlet, the side and top surfaces adopt symmetric boundary conditions, the bottom adopts no-slip boundary conditions, and the roughness height K_s is 0.352.

D. Computational domain
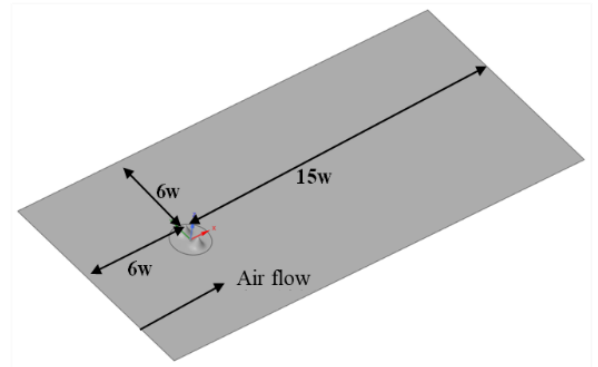
Fig. 3 Computational domain.

In order to avoid the impact of the size of the computational domain boundary on the flow within the domain, the the regulations outlined in the "Standards for Wind Tunnel Test Methods in Construction Engineering" [15] should be adhered to. The optimal blocking ratio for the mountain in the boundary layer numerical simulation should not exceed 5%. Therefore, the distances from the domain edges to the mountain front, mountain sides, and the top were set at 6W, 6W, and 15W, respectively.

III. RESULTS AND DISCUSSION

To quantitively analysis the wind speed-up effect induced by the twin-hill assembled saddle, the hill shapes under different parameters were subsequently converted into the saddle slopes (i) to unify the influencing variables. At the same time, two dimensionless numbers, the acceleration ratio of wind speed (S) and the relative height (Z), were used to measure the acceleration effect across saddles of various sizes.

$$i = \frac{H}{W/2} \times 100\% \qquad (8)$$

$$S = \frac{U(z)}{U_0} \qquad (9)$$

$$Z = \frac{z}{H} \qquad (10)$$

where, $U(z)$ is the steady-state wind speed in m/s when the height is z, U_0 is the inlet wind speed, z is the actual height, and H is the mountain height i.e. 100 m.

The independence of the acceleration effect on the inlet wind speed is first examined. The wind velocity typically considered for the transmission line icing studies is below 35 m/s. Therefore, a range of seven different inlet flow rates from 5 m/s to 35 m/s in intervals of 5 m/s was adopted in the simulation model. Probes were applied within the saddle region to compare the wind speed at the same location across different inlet flow rates. The results suggest that despite some small variations indeed exist, the wind speed at the same location is generally proportional to the inlet flow rate within the studied range of wind speeds. An example ($W = 300$ m, $H = 100$ m) of the acceleration ratios along a straight line connecting the two hill peaks (which can be regarded as the primary spatial locations for transmission lines) is presented in Fig.4.

A typical wind speed-up effect across the saddle region can be seen in Fig.5a, where the acceleration ratios are represented as a surface plot at the cross-section of the saddle-
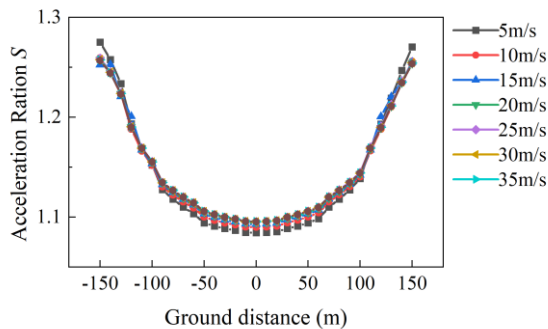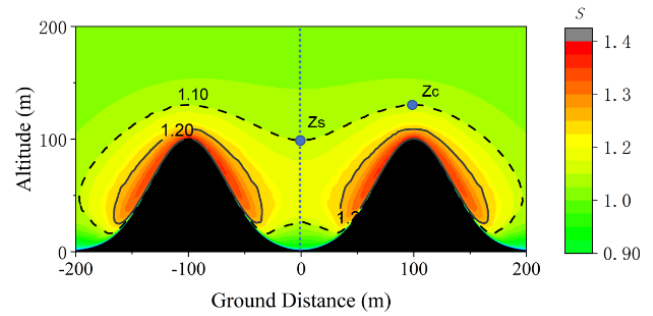
(a) $i = 100\%$
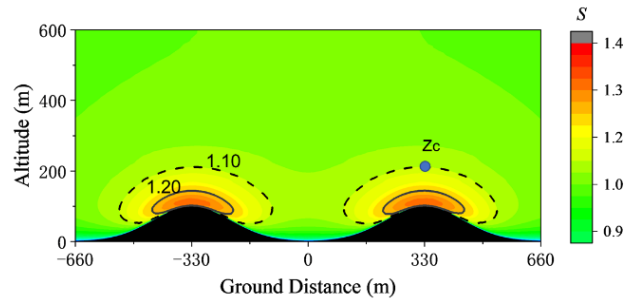
(b) $i = 30\%$

Fig. 5 Acceleration ratio S at the cross-section of the saddle-type microtopography of two slopes. A black contour line is given at $S = 1.2$, and a brown contour line is given at $S = 1.1$. Zs indicates the altitude above which the S drops below 1.1 at the vertical middle axle of the saddle, and similarly Zc is the height of $S = 1.1$ up the hill peak.

type micro-terrain. Two contour lines are marked at $S = 1.1$ and $S = 1.2$ for the illustrated saddle with a slope of $i = 100\%$. The speed-up effect is more pronounced adjacent to the hill. Nevertheless, the saddle region is of the primary research interest, where S is generally above 1.1. It needs to be pointed out that the decelerated region at the saddle bottom is also related to the adopted boundary conditions. Since the near-surface layers were not a primary concern in this study, the impact of different surface conditions was not further discussed in this work.

With a gentle slope of 30%, as shown in Fig.5b, wind acceleration becomes inconspicuous across the saddle region, but extends to enlarged regions above the hill crests.

To characterise the influence of saddle-type micro-terrain on wind acceleration, a group of simulation geometries with 12 different saddle widths W ranging from 60 m to 1400 m , all at a height of $H = 100$ m, were utilized. Thus, the wind acceleration characteristics in the saddle region can be compared across saddle slopes ranging from 14% to 333%. Fig. 6 illustrates the variations in acceleration ratio S along the vertical central axis of the saddle region (i.e. the dotted line in Fig. 5a). It can be seen that, with a gentle slope below 30%, the acceleration ratios at the saddle centre are generally below 1.1. With slopes exceeding 35%, the speed-up effect becomes obvious at the saddle centre. In the meanwhile, the location of maximum S shifts to the bottom of the saddle as the saddle slope increases.

Fig. 4 Acceleration ratios along a straight line connecting the two hill peaks of $W = 300$ m and $H = 100$ m under different inlet flow rates.
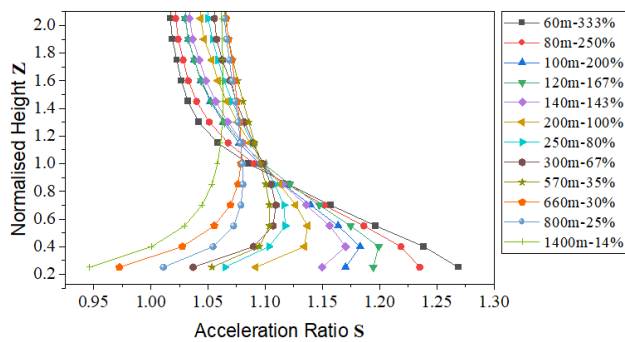
Fig. 6 Speed-up effects at the vertical middle axis of the saddle. Lines were named in a format of "*W-i*".
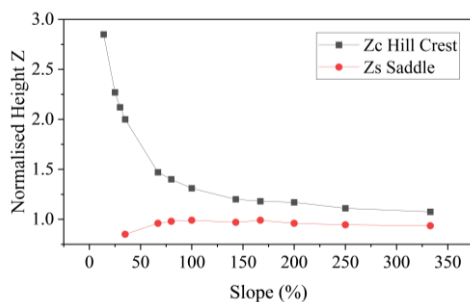
Fig. 7 Critical heights Zc and Zs plotted against saddle slopes

Currently, a 10% increase in the wind velocity compared to that of flat terrain is recommended for overhead transmission line design [16] in mountainous areas when meteorological data is not available. Therefore it is of the primary concern for this work to identify the speed-up regions exceeding a acceleration ratio of 1.1. The two critical heights Zc and Zs as indicated in Fig. 5 are further plotted against the saddle slope in Fig.7.

It can be seen from Fig. 7 that as the saddle slope increases, the critical height *Zc* decreases exponentially, while Zs shows minimal variation with values around $Z = 1$. From a practical point of view, the slope of two-hills shaped saddles are commonly below 100%, above which a slope would be regarded as a vertical plane in geographical significance. This indicates that the wind speed-up effect is more pronounced at low hill crests, with a significant acceleration region that is 30% higher than the hill heights. And the acceleration region only retained to the near surface region of Z<1.3 for precipitous hills or spurs.

In the planning of an overhead transmission line, it commonly spans over the low hill peaks. Therefore, the height of conductors can be roughly regarded as above $Z = 1$. According to Fig. 7, *Zs* are generally around $Z = 1$, meaning that wind acceleration regions are restrained in the saddle. Therefore, it is less likely to affect the wind load or impact the subsequent icing process of transmission lines. Consequently, the influence of saddle-type micro-terrain on transmission line icing only needs to be considered when there are multiple spans across the saddle region.

IV. CONCLUSIONS

The phenomenon of increased ice accumulation on transmission lines across micro-terrain regions has drawn increasing attention to power grid. It is of practical importance to establish criteria for assessing the impact of various micro-topography on transmission line icing. This work focuses on the saddle-type micro-terrain which is prevalently found in hilly terrains. Based on simulation studies using the idealized geometry of twin axisymmetric gaussian hills, it suggests that the twin-hills have limited effect on wind acceleration above the saddle region, and thus may not substantially influence the ice accretion on conductors for a single-span transmission line across the saddle. Nevertheless, for multiple spans through a saddle, the generally accepted wind speed-up ratio of 1.1 for mountainous areas appear to be conservative. The effect of wind speed-up within the saddle region increase with the saddle slope.

REFERENCES

[1] X. Jiang, Z. Zhang, Q. Hu, J. Hu, and L. Shu, *"Thinkings on the Restrike of Ice and Snow Disaster to the Power Grid,"* Gaodianya Jishu/High Voltage Engineering, vol. 44, no. 2, pp. 463-469, 2018, doi: 10.13336/j.1003-6520.hve.20180131017.

[2] IEC 60826-2017: *Overhead transmission lines-design criteria*, IEC, 2017.

[3] S. Wang and J. Li, *The influence of microtopography and micrometeorology on power transmission lines.* Beijing: China Electric Power Press (in Chinese), 1999.

[4] E. Sundin and L. Makkonen, "*Ice Loads on a Lattice Tower Estimated by Weather Station Data %J Journal of Applied Meteorology,*" (in English), vol. 37, no. 5, pp. 523-529, 01 May. 1998 1998.

[5] K. F. Jones, "*A simple model for freezing rain ice loads," Atmospheric Research*, vol. 46, no. 1, pp. 87-97, 1998/04/01/ 1998, doi: https://doi.org/10.1016/S0169-8095(97)00053-7.

[6] L. Makkonen, "*Models for the Growth of Rime, Glaze, Icicles and Wet Snow on Structures,*" Philosophical Transactions: Mathematical, Physical and Engineering Sciences, vol. 358, no. 1776, pp. 2913-2939, 2000. [Online]. Available: www.jstor.org/stable/2666835.

[7] H. Gulvanessian, "EN1991 Eurocode 1: Actions on structures," *Proceedings of the Institution of Civil Engineers - Civil Engineering*, vol. 144, no. 6, pp. 14-22, 2001, doi: 10.1680/cien.2001.144.6.14.

[8] JIANG Xingliang；WU Jianguo；DENG Ying；HU Jianlin；REN Xiaodong；, " *Research on Uneven Icing of Lines in Adjacent Towers Under Pass Micro-topography*," Proceedings of the Chinese society for electrical engineering, vol. 44, no. 06, pp. 2462-2475, 2024, doi: 10.13334/j.0258-8013.pcsee.223299.

[9] D. Adanta, I. R. Fattah, N. M. J. J. o. M. S. Muhammad, and Engineering, "*Comparison of standard k-epsilon and SST k-omega turbulence model for breastshot waterwheel simulation*," 2020.

[10] A. Hellsten, "*Some improvements in Menter's k-omega SST turbulence model," in 29th AIAA, Fluid Dynamics Conference*, 1998, p. 2554.

[11] Y. Yin et al., "*Research on turbulence model for simulation of wind flow in mountain areas of micro-topography,*" in Journal of Physics: Conference Series, 2023, vol. 2441, no. 1: IOP Publishing, p. 012012.

[12] Duan,J. "*Field measurement research on near-ground wind characteristics and wind effects of super high-rise buildings in strong wind processes in urban areas,* " South China University of Technology, PhD dissertation.

[13] Y. Yang, M. Gu, and X. Jin, "*New inflow boundary conditions for modeling the neutral equilibrium atmospheric boundary layer in SST k-ω model,*" 2009.

[14] Y. Yang, Z. Xie, M. J. W. Gu, and S. A. I. Journal, "*Consistent inflow boundary conditions for modelling the neutral equilibrium atmospheric boundary layer for the SST k-ω model,*" vol. 24, no. 5, pp. 465-480, 2017.

[15] " *Standard for wind tunnel test methods for construction engineering* ".JGJ/T 338-2014.2014.

[16] "*Design specifications for 110kV~750kV overhead transmission lines* ".GB 50545-2010.2010.

Icing Process Simulation on a Real Transmission Conductor Based on WRF

Zidi Zhu[1], Changzheng Chi[1], Mingfeng Huang[1], Muhammad Shakeel Virk[2], Rong Bian[3], Keji Chen[3]

[1] *College of Civil Engineering and Architecture, Zhejiang University, Hangzhou, China*

[2] *Institute of Industrial Technology, Faculty of Engineering Science & Technology, UiT – the Arctic University of Norway, Narvik, Norway*

[3] *Economic Research Institute of State Grid Zhejiang Electric Power Co., Ltd., Hangzhou, China*

mfhuang@zju.edu.cn

Abstract— **Ice accretion on conductors is a severe natural disaster of electrical power transmission lines in mountainous regions. In this study, the on-site disaster situation involving an interphase flashover accident on a transmission line in the mountainous regions of Zhejiang Province is investigated. Utilizing the Weather Research and Forecasting (WRF) model, the meteorological conditions at the accident site concurrent with the incident are reconstructed. Based on the reconstructed meteorological parameters, a numerical simulation method for ice accretion on the conductor of transmission lines considering time-varying meteorological parameters and topographic factors is proposed by utilizing the finite element software FENSAP-ICE. The numerical simulation results indicate that the ice thickness on the transmission line conductors during the accident reached 19.55 mm, which belongs to the rapid ice accretion and ice-shedding accident in non-traditional ice-prone areas.**

Keywords— ***Ice accretion; WRF; Meteorological parameters, Micro-meteorology, Micro-topography***

I. Introduction

In recent years, the frequent icing incidents on transmission lines have potentially led to widespread power outages and tower collapses, which poses a significant threat to the safety and reliability of power grids. Researchers and institutions globally have extensively investigated icing through various methods, such as on-site ice observation measurements[1]-[2], artificial icing experiments[3], and numerical simulation analysis[4]-[5]. Compared with on-site measurements and artificial experiments, numerical simulation analysis provides a more convenient method for predicting ice accretion and determining ice-shedding jump height on transmission conductors, which plays a crucial role in guiding effective prevention of icing-related disasters in power grids.

Icing on transmission lines often occurs in remote and harsh regions where accessibility is limited. Manual inspections are challenging and imprecise, making it difficult to accurately reflect the actual icing conditions. Consequently, predicting transmission line icing has become increasingly crucial. Most researches predominantly employ either single mechanistic models [6]-[8] or statistical empirical models [9]-[10] for predicting ice accretion on transmission conductors. Mechanistic models consider the physical processes of supercooled water droplet collision and freezing, accounting for various icing factors. However, they overlook the cumulative effects of meteorological conditions, yielding better results only for short-term icing forecasts. On the other hand, statistical empirical models establish the correlation between meteorological conditions and conductor icing mass and thickness using statistical methods. However, these models disregard the physical processes of conductor icing and are applicable only to specific regions under specific conditions.

Existing studies indicate that the ice accretion and ice-shedding processes on mountainous transmission conductor are significantly influenced by micro-topography and meteorological conditions. It is a temporal process that constantly evolves. Most existing studies rely on meteorological data collected from nearby monitoring stations for simulating ice growth.[11]. However, mountainous areas, where transmission lines are usually located, face challenges due to sparse monitoring station coverage, inadequate historical records, and low data quality. Consequently, the Weather Research and Forecasting (WRF) model is employed to reassess meteorological conditions in the icing area, obtaining high-quality and high-resolution meteorological parameters. A numerical simulation framework is proposed for icing processes on conductors considering time-varying meteorological variables. This method was also used to retrospectively analyse a real ice accident in Zhejiang Province.

II. Meteorological Analysis of Transmission Conductor Ice Accretion

A. Ice Accident Report

On December 2, 2022, a few transmission lines in a mountainous regions of Zhejiang Province suffered a severe ice accretion and ice-shedding jumping, leading to a interphase flashover accident. After measuring the residual ice, it was determined that the ice accretion on the transmission lines was a mixture of rime and glaze ice, with diameters approximately 80 mm (see Fig.1). According to meteorological records from the transmission line, Zhejiang Province experienced a severe temperature drop starting from November 30, accompanied by light rain and even sleet, with humidity exceeding 95%. On December 2, influenced by warm and moist air currents, the temperature rapidly increased, resulting in large-scale ice-shedding from the conductors. The temperature recorded by the nearby micrometeorological monitoring device at Tower 13# on the transmission line is shown in Fig. 2.

Fig. 1 The residual ice after ice-shedding.
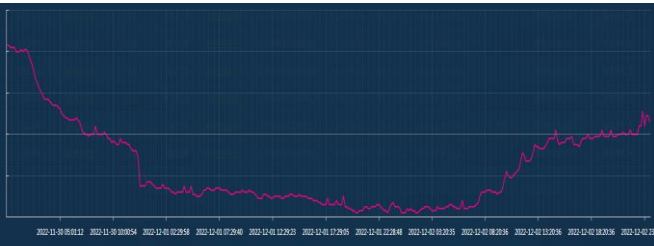
Fig. 2 The temperature recorded by the micrometeorological monitoring device.

For 500 kV overhead transmission lines, the return period of design ice thickness should be 50a[12]. According to the analysis of the provincial power grid ice-covered area zoning conducted by State Grid Zhejiang Electric Power Co., Ltd., when the altitude is between 400 and 600 meters (approximately 530 meters at the accident site), the design ice thickness is 15 mm, following the guidelines for the moderate ice zone. However, based on the estimation from ice blocks falling at the accident site, considering on-site temperature, time to flashover and melting losses, the maximum ice cover thickness for the conductor may reach approximately 20 mm, significantly exceeding the design ice thickness for this region. In view of this, the numerical simulation method is employed to reproduce the ice accretion process during the accident, aiming to analyse the meteorological conditions associated with severe ice cover accidents in non-traditional ice-prone areas.

B. Regional Climate Simulation

To address the lack of observation data such as precipitation and wind environment during the ice accretion period, a regional climate simulation utilizing the Weather Research and Forecasting (WRF) mesoscale meteorological model is conducted to derive the icing climate parameters specific to the accident area, obtaining all necessary meteorological elements for numerical ice simulation.

The WRF Model is a state-of-the-art mesoscale numerical weather prediction system. By leveraging global meteorological databases and data assimilation techniques provided by meteorological agencies worldwide, the WRF model can be applied to simulate local-scale weather phenomena at different time scales, as well as atmospheric emission modeling. Currently, the WRF model finds extensive use in operational meteorological forecasting and scientific research across the mesoscale domain. Notable applications include simulating typhoon processes [13]-[15], regional precipitation modeling [16]-[17], and air pollution forecasting [18]-[19].

In this paper, WRF3.7 is used for meteorological simulation of the ice accretion region, and the initial atmospheric conditions and boundary conditions of the grid calculation domain are provided by the global meteorological reanalysis data FNL (with a horizontal grid point accuracy of 1°×1°, updated every six hours) published by the U.S. Environmental Prediction Center. The topographic and geomorphological subsurface information of the calculation domain is obtained from the MODIS land use data provided by NASA and the SRTM elevation data formed by joint surveying with the Department of Defense's National Mapping Agency (NIMA). Since the accident site is located in the microtopography region of the pass, the land use data with an accuracy of 15 seconds (about 500m) and elevation data with an accuracy of 3 seconds (about 100m) are selected.

In this study, the 6-layer one-way nesting scheme is used to simulate the meteorological conditions of the accident area for up to 48 hours. The simulation period spans from 12:00 on November 30, 2022, to 12:00 on December 2, 2022. The simulation employed physics options and grid parameters as detailed in Tables I and Tables II, and the simulated computational domain is illustrated in Fig. 3.

TABLE I. PHYSICS OPTIONS

Physics Options	Scheme
Microphysics	WSM6
Shortwave & longwave radiation	Dudhia scheme and RRTM scheme
Land surface	Noah
Surface layer	Revised MM5 Monin-Obukhov
Planetary boundary layer	YSU
Cumulus parameterization	Kain-Fritsch

TABLE II. GRID PARAMETERS

Domain	Horizontal Grid(km)	The First Layer Vertical Grid(m)	Grid Number (x × y × z)	Domain Area (km × km)	Time Integration Step (s)
d01	36	26	247 × 158 × 36	8892×4108	180
d02	12	26	421 × 298 × 36	5052×3576	60
d03	4	26	604 × 433 × 36	2416×1732	20
d04	1.333	26	589 × 418 × 71	785×557	6.67
d05	0.444	23	577 × 406 × 71	256×180	2.22
d06	0.148	23	565 × 394 × 71	84×58	0.74
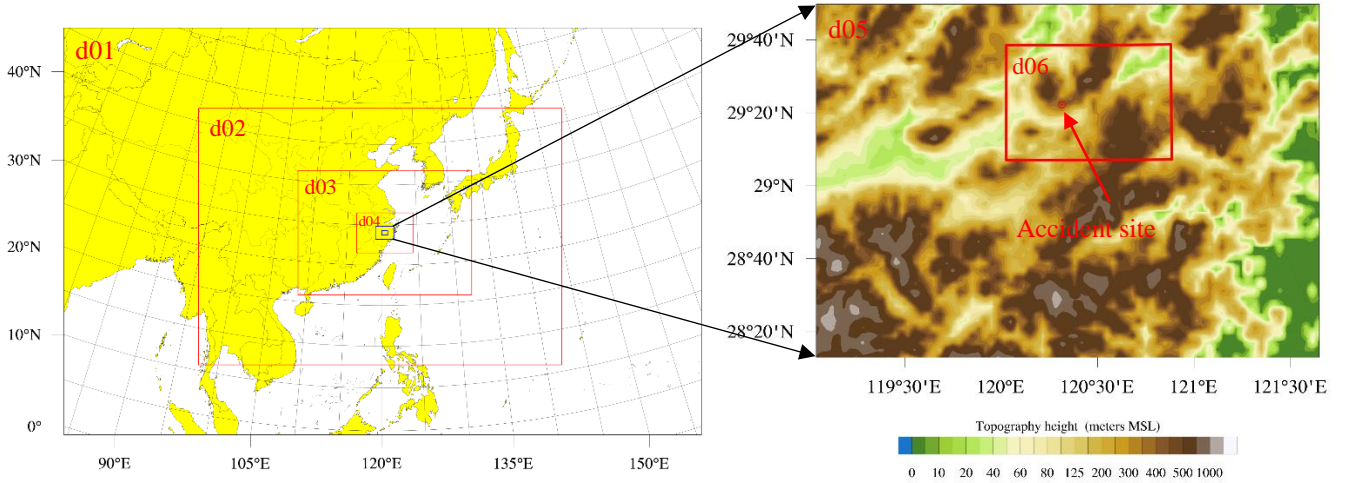
Fig. 3   Meteorological condition simulation domain.

Utilizing the Advanced Research WRF (ARW) core solver, the main meteorological conditions in the target area during the ice accretion period are calculated as shown in Fig. 4, including wind speed (V), temperature (T), and liquid water content (LWC). As can be seen from Fig. 4, the temperature obtained through WRF simulation are slightly lower than the observed data. This discrepancy may be attributed to the actual accident location being situated in a mountain pass terrain. Overall, the simulated data aligns with the observed data in terms of the trend of variation.
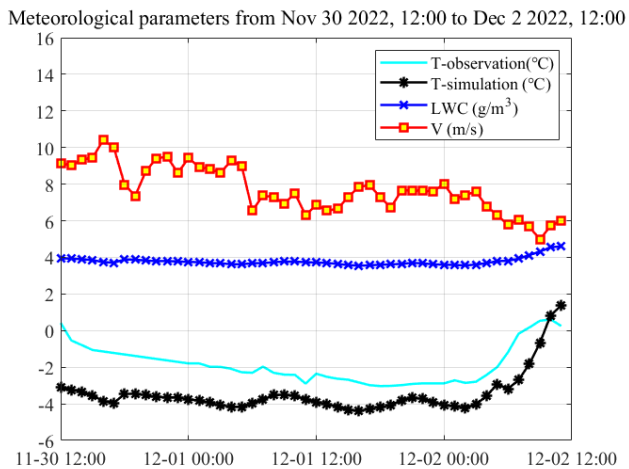
Fig. 4   WRF-based regional meteorological simulation results.

III. NUMERICAL SIMULATION METHOD OF ICE ACCRETION

Transmission lines usually build in complex geographical terrains, where micro-meteorological conditions vary spatially and temporally. Therefore, it is essential to take into account the cumulative effects of meteorological factors in ice accretion prediction.

A. Numerical simulation model

The essence of conductor ice accretion is actually the physical process where supercooled water droplets collide with the surface of the conductor when the temperature is below $0°C$, leading to freezing and ice formation. Additionally, transmission lines usually build in complex geographical terrains, where micro-meteorological conditions vary spatially and temporally. It is essential to take into account the cumulative effects of meteorological factors in ice accretion prediction. Based on Euler's gas-liquid two-phase flow calculation method and the thermodynamic model of water droplet freezing, a numerical simulation model of transmission conductor ice accretion considering time-varying meteorological parameters was established in reference [20]. Four parameters are selected to investigate the ice accretion effect on transmission conductors, including wind speed (V), temperature (T), liquid water content (LWC) and the median volume diameter of water droplets (MVD). Based on the FLUENT software and MULTI-FLUENTDROPICE multi-time-step solver from FENSAP-ICE software, the multi-time-step calculations for conductor ice accretion is performed. Following each time step, the icing boundary is updated based on the computed ice growth results, and the updated grid is outputted for the subsequent ice

accretion computations. Based on the regional meteorological parameters obtained by the WRF model, the computational process is illustrated in Fig. 5.
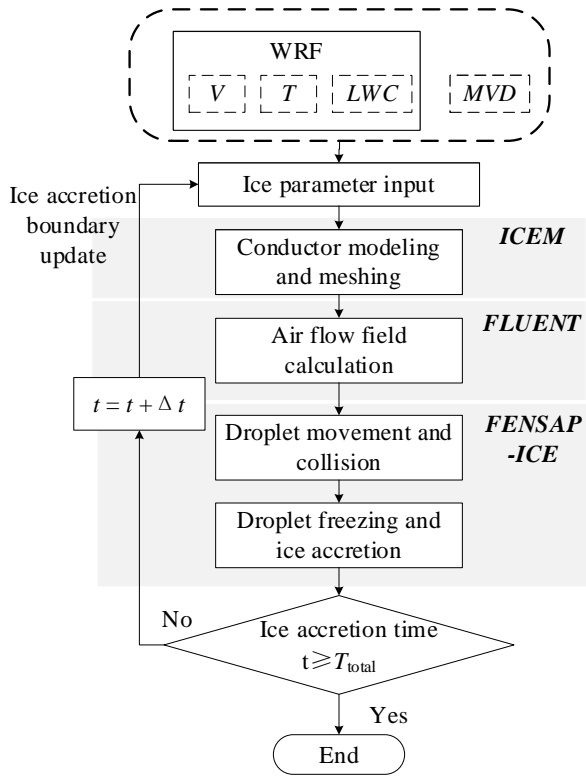
Fig. 5 Flow chart of numerical simulation of conductor icing process.

B. A real ice accretion process simulation on transmission conductor

A four-bundled conductor is used for numerical simulations with the meteorological conditions according to Fig. 4. In addition to the three parameters of *V*, *T* and *LWC*, the simulation of ice accretion on conductors also requires the parameter *MVD*, which is challenging to obtain via meteorological monitoring or WRF simulations. Fortunately, scholars have noted that the *MVD* of rime ice is generally less than 50 μm, while the *MVD* of glaze ice is generally greater than 500 μm[21]. Considering the mixed-type ice accretion observed at the accident site, we have accordingly set the *MVD* at 50 μm. To balance computational efficiency and accuracy, the ice accretion simulation working conditions are set according to the meteorological conditions, as shown in Table III.

The cumulative effects of meteorological factors is accounted for and the conditions are periodically updated. The conductor diameter *D* = 34.32mm. Since the substantial torsional rigidity of the four-bundled conductor, the torsional effect of the conductor is disregarded. The simulation time is 48 hours, that is, from 12:00 on November 30, 2022 to 12:00 on December 2, 2022.

TABLE III. ICE ACCRETION PARAMETERS UNDER DIFFERENT WORKING CONDITIONS

Time	*V* (m/s)	*T* (°C)	*LWC* (g/m³)	*MVD* (μm)	*Duration* (hours)
Nov 30 12:00 —15:00	9.6	-3.2	3.8	50	3
Nov 30 15:00 —18:00		-3.8			3
Nov 30 18:00 — Dec 1 00:00	8.8	-3.6	3.9		6
Dec 1 00:00 — 06:00		-4.0	4.0		6
Dec 1 06:00 — 11:00	7.3	-3.7	3.7		5
Dec 1 11:00 — Dec 2 04:00		-3.8	3.6		17
Dec 2 04:00 — 08:00	5.9	-3.1	3.8		4
Dec 2 08:00 — 12:00		-0.5	4.4		4

To ensure computational efficiency and accuracy, a quadrilateral structured grid with higher quality and clear boundary conditions is adopted. The fluid region is adequately large, especially the distance from the conductor center to the domain outlet, which is set to 30*D*, allowing sufficient development of wake flow and vortex shedding within the computational domain. Grid points farther away from the conductor surface gradually diffuse with a coefficient of 1.05. For near-wall grids, the boundary layer mesh is utilized, with the first layer grid set at 0.001*D*. To fully account for the three-dimensional effects of turbulent flow, the domain is extended into 30*D* with a vertical grid scale of 0.1*D*. After each ice accretion growth calculation step, an automatic grid displacement technique is applied to replace the volume grids covered by accumulated ice. When temperature adjustments are necessary, the current ice shape is exported, and manual grid redivision is performed. Fig. 6 illustrates the grid during the third manual division, showing effective mesh refinement near the wall.
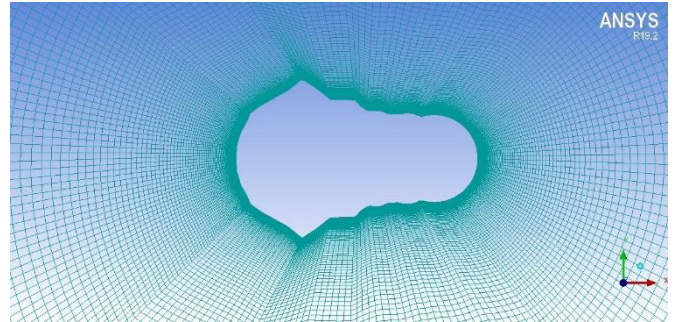
Fig. 6 Grid refinement of near-wall area.

The results of conductor ice accretion considering the cumulative effects of meteorological parameters from 12:00 on November 30, 2022, to 12:00 on December 2, 2022, are depicted in Fig. 7. From the figure, it is evident that the maximum ice thickness on one side of the conductor can reach 72.44mm. Based on the constant ice mass principle, the ice covering shape is equivalent to circular uniform. The equivalent ice thickness can be calculated using the formula:

$$b = \frac{\sqrt{\dfrac{4\rho S}{0.9\pi} + D^2} - D}{2}$$

where: b represents the equivalent ice thickness. D is the conductor diameter. S is the area of ice accretion. ρ is the ice density (taken as 900 kg/m³).

The equivalent ice thickness of the conductor within 48 hours can be calculated from the above formula as 19.55mm, which closely aligns with the estimated maximum ice thickness reported in the accident analysis. It can be inferred that the accident belongs to the rapid ice accretion accident in non-heavy ice area caused by sudden temperature decreasing in mountainous pass terrain. Consequently, this transmission line qualifies as a non-traditional ice-prone line, necessitating enhanced monitoring and early preventive measures in anticipation of potential extreme cold weather events.
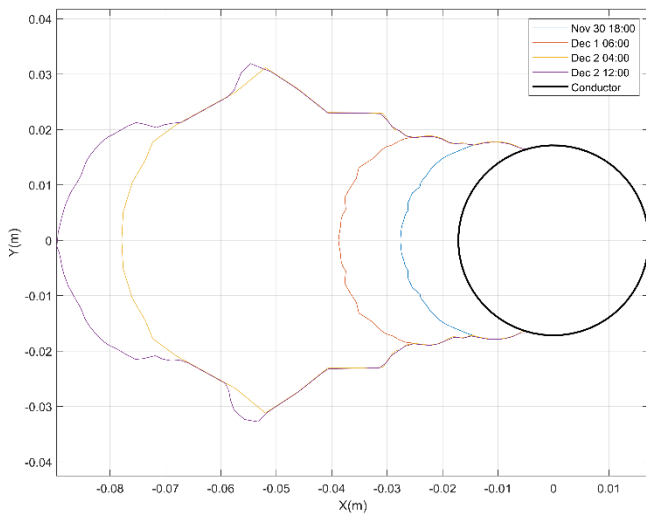
Fig. 7 Ice accretion pattern of 48h.

ACKNOWLEDGMENT

REFERENCES

[1] E. J. Goodwin, J. D. Mozer, A. M. Digioia and B. A. Power, "Predicting Ice and Snow Loads for Transmission Line Design," in *Proceedings of the First IWAIS*, 1983.

[2] K. F. Jones, "A simple model for freezing rain ice loads," *Atmospheric Research*, vol. 46, no. 1-2, pp. 87-97, 1998.

[3] W. Xiong, H. J. Yuan, and L. You, "Prediction method of icing thickness of transmission line based on MEAO," *Cluster Computing*, vol. 21, no. 1, pp. 845-853, 2018.

[4] X. B. Huang, H. B. Li, Y. C. Zhu, Y. X. Wang, X. X. Zheng and Y. G. Wang, "Short-term Forecast for Transmission Line Lcing by Time Series Analysis and Kalman Filtering," *High Voltage Engineering*, vol. 43, no. 06, pp. 1943-1949, 2017. (In Chinese)

[5] D. Dai, X. T. Huang, Z. Dai, Y. B. Hao, L. C. Li and C. Fu, "Regression Model for Transmission Lines Icing Based on Support Vector Machine," *High Voltage Engineering*, vol. 39, no. 11, pp. 2822-2828, 2013. (In Chinese)

[6] L. Makkonen, "Modeling of Ice Accretion on Wires," J*ournal of Applied Meteorology*, vol. 23, no. 6, pp. 929-939, 1984.

[7] L. Makkonen, "Models for the growth of rime, glaze, icicles and wet snow on structures," *Philosophical Transactions of the Royal Society of London. Series A: Mathematical, Physical and Engineering Sciences*, vol. 358, no. 1776, pp. 2913-2939, 2000.

[8] X. L. Jiang, F. Y. Jiang, Q. L. Wang, B. Luo and X. B. Han," Prediction of Rime Accretion on Transmission Line Based on Optimal Time Step Model," *Transactions of China Electrotechnical Society*, vol. 33, no. 18, pp. 4408-4418, 2018. (In Chinese)

[9] M. Farzaneh, K. Savadjiev, "Statistical analysis of field data for precipitation icing accretion on overhead power lines," *IEEE Transactions on Power Delivery*, vol. 20, no.2, pp. 1080-1087, 2005.

[10] X. Wu, P. J. Sun, Y. Liu and X. P. Jin," An Icing Conductor Meteorological Model Based on Estimating the Visibility in Fog Condition," *Journal of Applied Meteorological Science*, vol. 23, no. 06, pp. 755-762, 2012. (In Chinese)

[11] P. Thorsson, S. Söderberg and H. Bergström, "Modelling atmospheric icing: A comparison between icing calculated with measured meteorological data and NWP data," *Cold Regions Science and Technology*, vol. 119, pp. 124-131, 2015.

[12] *Code for design of 110kV ~ 750kV overhead transmission line*, National Standard of the People's Republic of China, 2010

[13] M. F. Huang, Y. F. Wang, W. J. Lou and S. Y. Cao., "Multi-scale simulation of time-varying wind fields for Hangzhou Jiubao Bridge during Typhoon Chan-hom," *Journal of Wind Engineering and Industrial Aerodynamics*, vol. 179, pp. 419-437, 2018.

[14] H. Fu, Y. Q. Wang, "Effect of uncertainties in sea surface temperature dataset on the simulation of typhoon Nangka (2015)," *Atmospheric Science Letters*, vol. 19, no. 1, e797, 2018.

[15] T. Takemi, T. Yoshida, S. Yamasaki and K. Hase, "Quantitative Estimation of Strong Winds in an Urban District during Typhoon Jebi (2018) by Merging Mesoscale Meteorological and Large-Eddy Simulations," *SOLA*, vol. 15, pp. 22-27, 2019.

[16] T. M. Hamill, "Performance of operational model precipitation forecast guidance during 2013 Colorado Front-Range floods," *Monthly Weather Review*, vol. 142, no. 8, pp. 2609-2618, 2014.

[17] J. P. Evans, M. Ekström, F. Ji, "Evaluating the performance of a WRF physics ensemble over South-East Australia," *Climate Dynamics*, vol. 39, pp. 1241-1258, 2012.

[18] U. Im, K. Markakis, A. Unal, T. Kindap, A. Poupkou, S. Incecik, O. Yenigun, D. Melas, C. Theodosi and N. Mihalopoulos , "Study of a winter PM episode in Istanbul using the high resolution WRF/CMAQ modeling system," *Atmospheric Environment*, vol. 44, no. 26, pp. 3085-3094, 2010.

[19] K. W. Appel, S. J. Roselle, R. C. Gilliam and J. E. Pleim, "Sensitivity of the Community Multiscale Air Quality (CMAQ) model v4.7 results for the eastern United States to MM5 and WRF meteorological drivers," *Geoscientific Model Development*, vol. 3, no. 1, pp. 169-188, 2010.

[20] Q. Wang, W. J. Lou, H. W. Xu and L. Q. Wang, "Numerical simulation of icing on transmission conductors considering time-varying meteorological parameters," *Journal of Harbin Institute of Technology*, vol. 54, no. 11, pp. 11-21, 2022.

[21] Z. Feng, "Prediction and Monitoring of Power Lines Icing Thickness and Experimental Study on Icing Bond Strength," M. Eng. thesis, Zhejiang University, Hangzhou, China, Jul. 2020. (In Chinese)

An updated CLIWAC model to investigate wet snow sleeve events on overhead lines in Italy by the end of the Century

P. Faggian[1], A. Trevisiol[1], G. Decimi[1]

[1] Ricerca sul Sistema Energetico RSE S.p.A., Milan - Italy

paola.faggian@rse-web.it, arianna.trevisiol@rse-web.it, goffredo.decimi@rse-web.it

Abstract— **An updated version of the CLImate Wet snow sleeve ACcretion model CLIWAC is presented. The novelty lies in: refining wet snow thermal range and the criteria to distribute daily cumulative precipitation on an hourly scale; taking into account the sleeve accretion in dry snow conditions and partial shedding and melting; using wind data instead of parametrized wind values.**

The comparison between the new estimates of Wet Snow Load (*WSL*) with the observations, acquired by the Wet snow Ice Laboratory Detection at Vinadio (Italy), showed better performance than previous results. In addition, the analysis of the new CLIWAC results, inferred from the MERIDA OI reanalysis, about the reconstruction of some Italian severe wet snow events in relation with the recorded failures in the energy supply, gave better results than before.

On the basis of daily data provided by 12 high-resolution (~12 km spatial resolution) Euro-CORDEX simulations, realized under the two emission pathways RCP8.5 and RCP4.5, CLIWAC was used to elaborate future projections of *WSL* on high voltage conductors (ACSR - d 31.5 mm) over Italy by 2100. To overcome the concept of "return time", obsolete in a climate change context, the two frequency indices *WSLD* (Wet Snow Load Days) and *WSLF* (Wet Snow Load Frequency) were also estimated to elaborate future scenarios at short-, medium and long-term to investigate the probability of *WSL* exceeding some infrastructural thresholds from 1 kg/m to 18 kg/m. Weighted ensemble scenarios were computed, and the statistical significance of the projected variations was investigated through the Wilcoxon test and the agreement among the models.

The results highlight a general reduction in intensity and frequency of the extreme wet snow episodes, especially in RCP8.5, as rainfalls will prevail over snowfalls due to global warming, except for high Alpine altitudes, so far spared by this kind of events.

Keywords— ***CLIWAC model, wet snow sleeve on overhead lines, regional climate models, climate extreme indices, Energy System resilience***

I. Introduction

Climate variability and change pose increasingly significant challenges to societies worldwide. Human influence on the climate system is unequivocal, and recent anthropogenic emissions of greenhouse gases are the highest in history [1]. WMO confirmed that 2023 was the warmest year on record, with the global average near-surface temperature at $1.45 \pm 0.12\,°C$ above the pre-industrial baseline. Moreover, it was the warmest ten-year period on record [2]. Over the last decade, European surface temperatures were more than 2 °C warmer than pre-industrial levels,[3]. The last bulletin of Copernicus[1] highlights that February 2024 was the warmest February on record globally, and recent climate changes have had widespread impacts on human and natural systems. In order to undertake efficient adaptation actions to withstand climate change impacts, climate information plays a crucial role in national development planning, for managing development opportunities and risks.

Heavy snowfalls represent one of the most serious hazards for electric grids because they trigger the formation of sleeves on overhead power lines whose loads may cause outages and sometimes prolonged disruptions of the energy supply. Hence stakeholders ask for information about future climate scenarios in planning actions to strength the resilience of the electric network against wet snow impacts.

The present study aims to improve on previous estimates [4] about the effects of climate change on the snow loads on overhead power lines, through an updated version of CLIWAC to assess future wet snow scenarios from state-of-art regional climatic simulations.

The datasets used and the methodology adopted to elaborate climate future projections are mentioned in Section II; main results are discussed in Section III and some conclusions are drawn in Section IV.

II. Data set, CLIWAC model, and Methodology

A. Variables and datasets

Hindcast and future projections of wet snow load (*WSL*) have been computed through an updated version of CLIWAC whose input consists of daily minimum T_n and maximum T_x temperature [°C], cumulated precipitation P [mm/d], and wind speed V [m/s]. These data have been inferred from 12 high-resolution (~12 km) region climate model (Table I) developed in the framework of the European Project Euro-CORDEX (https://euro-cordex.net/) by considering simulations realized under the Representative Concentration Pathways RCP8.5 and RCP4.5 representing respectively a pessimistic "*business as usual*" emission pathway, i.e. without reduction of green-house gas (GHG) and with partial reduction of GHG.

In addition, the meteorological data from the reanalysis dataset MERIDA OI, at 4-km spatial resolution covering the period 1990-2020 over Italy [5] (http://merida.rse-web.it; Optimal Interpolation version for temperature) have been also retrieved, in order to:

---

[1] https://climate.copernicus.eu/climate-bulletins

- remap climate model data from 12 km to 4 km and reconstruct the reference climatology;
- remove systematic temperature biases in climate model simulations to better identify the wet/dry snow thermal condition: T_n was bias-corrected (T_nAdj) at seasonal scale by using the Equidistant Quantile Mapping Technique. Then, T_x was bias-corrected according to the expression: $T_xAdj = T_nAdj + DTRAdj$, where $DTRAdj$ is the Diurnal Temperature Range bias-corrected at seasonal scale, too. Instead, P and V were used as raw data to maintain the temporal correlation between meteorological data, even if P bias may exceed 100% of the signal in cold months [6] and there is a great uncertainty about V values due to the great spread among the model (not shown).
- validate the new CLIWAC model.

TABLE I. LIST OF EURO-CORDEX SIMULATIONS. THE NAME IDENTIFIES THE GLOBAL CIRCULATION MODEL AND THE REGIONAL CLIMATE MODEL

Id	Climate model Simulation
1	ICHEC-EC-EARTH_CLMcom-CCLM4-8-17
2	ICHEC-EC-EARTH_KNMI-RACMO22E
3	ICHEC-EC-EARTH_SMHI-RCA4
4	MOHC-HadGEM2-ES_KNMI-RACMO22E
5	MOHC-HadGEM2-ES_SMHI-RCA4
6	MPI-M-MPI-ESM-LR_SMHI-RCA4
7	CNRM-CERFACS-CNRM-CM5_KNMI-RACMO22E
8	CNRM-CERFACS-CNRM-CM5_CLMcom-CCLM4-8-17
9	CNRM-CERFACS-CNRM-CM5_SMHI-RCA4
10	IPSL-IPSL-CM5A-MR_SMHI-RCA4
11	MOHC-HadGEM2-ES_CLMcom-CCLM4-8-17
12	MPI_M-MPI-ESM-LR_CLMcom-CCLM4-8-17

B. The upgraded CLIWAC model

The new version of CLIWAC have been achieved by modifying the wet snow thermal range, hourly precipitation distribution, sleeve accretion in dry snow conditions, partial shedding and melting, and wind contribution, in order to improve the reconstruction of the sleeve accretion events recorded at the WILD station [2], in comparison with the previous version of CLIWAC, as discussed in Section III.

It might be useful to recall here the characteristics of Makkonen model [7][8][9]. The resulting wet snow load at time i, L_i [kg/m][3] is the vectorial sum of the two components: M_i (linear mass component), and Wf_i (horizontal wind force acting on the iced conductor per length unit), which express the contributions to sleeve growth due to precipitation flow and wind action on the conductor, respectively:

$$L_i = \sqrt{M_i^2 + Wf_i^2}$$

The sleeve accretion is typically cylindrical and M_i [kg/m], at time i, is described by the equation:

$$M_i = M_{i-1} + I_i\, D_{i-1}\, \Delta t$$

where:
- M_{i-1} is the sleeve mass at time i-1
- $I_i = \beta\sqrt{V_i^2 + v_s^2}\, w_i$ is the flux [kg/(m²·s)], i.e. the intensity of snow deposition around the cable, assuming a wind velocity orthogonal to it, where:

  β = is the sticking efficiency;

  V_i is the wind speed [m/s];

  v_s is the snowflake terminal velocity [m/s];

  $w_i = P_i / v_s$ is the mass concentration of snow in the air;

  P_i = total precipitation at time i
- D_{i-1} is the sleeve diameter at the previous time step i-1, whose evolution is described by:

  $D_i = \sqrt{4 \cdot \frac{M_i - M_{i-1}}{\pi \rho_s} + D_{i-1}^2}$, where:

  ρ_s [kg/m³] is the snow density;

  $D_0 = 0.0315$ m is the high voltage cable diameter at the first timestep;
- Δt is the time step, assumed equal to 1 hour in this study.

The wind action component Wf_i is described by the formula:

$$Wf_i = 0.5/g \cdot \rho_{air} \cdot V_i^2 \cdot D_i$$

where:
- $g = 9,8$ m/s² is the gravitation acceleration;
- ρ_{air} is the density of the air [kg/m³].

To investigate future wet snow load scenarios, CLIWAC model was developed by adapting the hourly accretion model to handle daily meteorological data, with the following approximations, similarly to old version:
- hourly temperature T_i is inferred from a sinusoidal-like evolution reconstructed between minimum T_n (imposed to 5:00 a.m.) and maximum T_x (at 2:00 p.m.) with continuity among consecutive days;
- ρ_{air} ranges between 1.170 kg/m³ and 1.274 kg/m³ depending on orographic height z, considering that 1.219 kg/m³ is the typical value of air density when air humidity is $\sim$ 80% as in the case of wet snow conditions.

The variations from the old version are listed here:
- wet snow accretion happens when temperature is between - 0.5° C (instead of - 1.0° C) and 1.5° C and it is a rainy day, with daily cumulated precipitation $P > 1$ mm/d (instead of 0 mm/d);
- dry snow accretion (not considered in the previous version) happens when $T_i < $ - 0.5° C, $P > 1$ mm/d, and a sleeve is already grown at the previous time step;
- P is only evenly distributed during the hours of wet and dry snow conditions (instead of all 24 hours);
- V_i is equal to the daily V (instead of being parametrized between 1 and 1.5 m/s in 3 altimetric classes depending on model grid orography);
- v_s is fixed to 1.7 m/s and 1.1 m/s in wet and dry snow conditions respectively;
- referring also to [9], β and ρ_s are defined as follow.

  In wet snow conditions:

---

[2] The Wet snow Ice Laboratory Detection (WILD), sited at Vinadio (CN - Italy) at 960 m a.s.l. (44,298° N, 7,152° E) since the winter 2013-2014, is an open-air laboratory to measure the wet snow load on some high voltage conductors, integrated with a weather station.

[3] For simplicity, it is expressed in kilogram-force per meter of cable, as it is used by the TSO.

$$\begin{cases} \beta = 1 & ; \ \rho_s = 300 + 20 \cdot V_i \text{ for } V_i < 1 \\ \beta = 1/\sqrt{V_i}; \ \rho_s = 300 + 20 \cdot V_i \text{ for } 1 \le V_i < 10 \\ \beta = 0.3 & ; \ \rho_s = 500 \text{ for } 10 < V_i \end{cases}$$

In dry snow conditions:

$\beta = 0.3$; $\quad \rho_s = 200$.

Spontaneous/stochastic ice shedding is difficult to simulate, but in the new CLIWAC model a partial shedding has been modelled by considering:

1) with precipitation (P > 1 mm/d):
- $M_i = 85\% \ M_{i-1}$, if $0.5°$ C $< T_i \le 1.5°$ C and T_i is rising with a gradient $\Delta T > 0.25°$ C/h;
- $M_i = 60\% \ M_{i-1}$, if $1.5°$ C $< T_i \le 2.5°$ C, for maximum 24 consecutive hours, after which $M_i = 0$.

2) without precipitation (P ≤ 1 mm/d):
- $M_i = M_{i-1}$, if $T_i < -0.5°$ C (instead of - 1.0° C) for maximum 24 consecutive hours, after which $M_i = 0$;
- $M_i = 60\% \ M_{i-1}$, if $-0.5°$ C $< T_i \le 2.5°$ C, for maximum 24 consecutive hours, after which $M_i = 0$.

A total melting occurs if $T_i > 2.5°$ C.

Finally, as in the old version, a total breaking is described if M_i exceeds 20 kg/m or after a 3-days sleeve accretion, considering that no historical events recorded in WILD station lasted more than 3 days.

C. Methodology

The daily maximum wet snow load (hereafter *WSL*) values computed by CLIWAC were stored to study the climatology from 1990 to 2020 from MERIDA OI data, and to investigate the climate evolution from 1990 to 2100 from the regional models (Table I). The analysis periods were split into five 20-year time frames: the reference period 2001-2020 (REF), and four future scenarios 2021-2040, 2041-2060, 2061-2080, 2081-2100. The period 1990-2000 (VER) was also considered to characterize the climatological variations in the recent past. The climate scenarios were calculated at annual and seasonal scale neglecting summer, as wet snow events are very rare in Italy during warm months.

The WSL extreme values have been analysed by estimating three indices, already defined in [4]:

1) *WSL95*, i.e. the 95th percentile of *WSL* at annual/seasonal scale, computed filtering out the values lower than 0.05 kg/m. *WSL95* was computed, instead of mean values because *WSL* values, averaged over a twenty-year period, are very small, due to the very small temporal and spatial scale of the events. Moreover, as *WSL95* describes highest values, it is of most interest in investigating risks for overhead lines outages.

2) *WSLD* (*WSL* Days): the number of days on which the *WSL* exceeds the infrastructural damage thresholds 1, 2, 4, 6, 8, 10, 12, 14, 16, 18 kg/m on an annual scale in each analysis period.

3) *WSLF* (*WSL* Frequency): the number of years in which *WSL* exceeds the aforementioned thresholds, divided by the number of years of each time frame (20 years in this case).

To improve the accuracy of the future projections, among various model atmospheric approaches, referring to [10], a weighted ensemble mean (hereafter simply ensemble) has been considered with weights decreasing exponentially with

respect to the *WSL* absolute bias between the model results and MERIDA estimate in the REF scenario, normalised with respect to the mean absolute bias of the *N* models:

$$p_{ens} = \sum_{i=1}^{N} a_i \cdot e^{-\left(\frac{b_i}{B}\right)^2} \cdot p_i$$

where:

p_{ens}: weighted ensemble mean projection for a given grid point

p_i: projection of the model *i* for the same grid point

a_i: normalisation coefficient

b_i: *WSL* bias between model *i* and MERIDA in REF

B: mean value of the absolute bias of the models.

The assessment about the future climate projections is carried out in term of anomalies (i.e. differences between future and reference scenarios) inferred from the weighted ensemble mean. The climate change signal was considered robust if 9 out of 12 models (75% model agreement) gave the same sign of anomalies.

III. RESULTS

The performances of the new CLIWAC were first tested by comparing the outputs of the updated version, applied to the average daily meteorological variables recorded at the WILD station, with the wet snow loads measured at Vinadio. Then CLIWAC results, inferred from the MERIDA OI reanalysis at daily scale have been analysed by considering the *WSL* spatial patterns together with the location of faulted high voltage lines recorded during some serious wet snow events over Italy (*A.*). The historical climatology in REF and the future scenarios of *WSL95*, *WSLD* and *WSLF* are discussed in paragraph *B.*, *C.*, and *D.* respectively.

A. Validation of the new CLIWAC model

The updated CLIWAC model shows better performances in the description of the phenomena. Such an example in Fig. 1 are reported the hourly diagrams of *T*, *P* and *L* in two wet snow episodes registered at WILD and calculated by the old CLIWAC on the left and by the new code on the right. The Fig. 1 shows the improvements in describing the shedding of the sleeve on 2015-02-21, and in evaluating the load on 2018-01-08 underestimated in the old version.

The improvement is also noticeable in Fig. 2 which depicts the faulted high voltage lines and the new *WSL* fields over Italy for the two severe episodes occurred in Emilia-Romagna region on 2015-01-06 and in Abruzzo region on 2017-03-05: now the recorded outages are better explained by the increased weight of the loads.

B. Analysis of WSL95

WSL95 historical variations were first calculated by using both reanalysis and model data. Fig. 3 shows the annual *WSL95* reconstructions inferred from MERIDA in VER (left) and REF (centre), and the ensemble values in REF (right). Compared to previous results [4], the updated *WSL95* values are higher and, therefore, more consistent with observations. In addition to the effect of the new parameterisations, the new, more satisfying results also depend on having imposed a threshold 0.05 kg/m, which removed small unrealistic values

in the cumulative distribution function from which *WSL95* was computed.
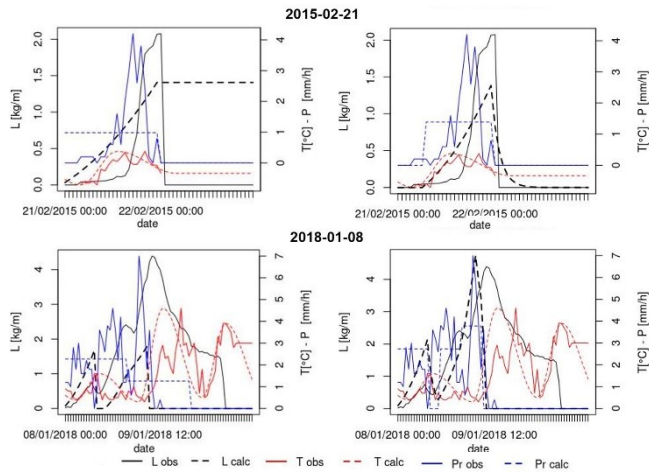
Fig. 1 Hourly *T*, *P* and *L* registered (continuous line) at WILD and calculated (dashed lines) by the old CLIWAC (left) and by the new CLIWAC (right) on 2015-02-21 (top) and 2018-01-08 (bottom).
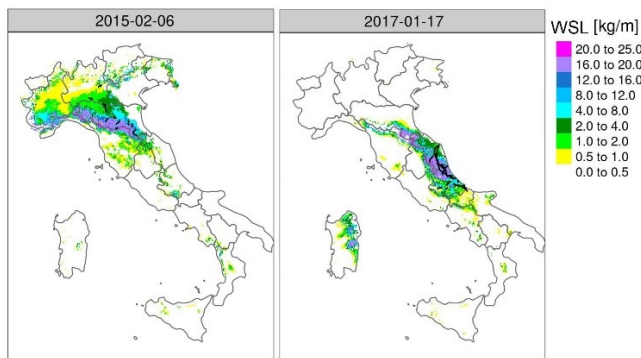
Fig. 2 *WSL* maps and high voltage lines failures (black lines) for the events recorded in Italy on 2015-01-06 (left) and 2017-03-05 (right).

Confirming the previous results [4], the new estimates highlight a significant ($p < 0.05$ from Wilcoxon test) positive trend of *WSL95* over most of Italy in the recent past (REF) compared to the more distant period (VER), in particular over the Apennine ridges, due to more abundant precipitation and an increase of minimum temperature in the last decades. The ensamble scenario in REF is characterised by comparable or slightly lower values than those described by the reanalysis and reproduces the complex spatial pattern in a completely satisfactory manner (Fig. 3).
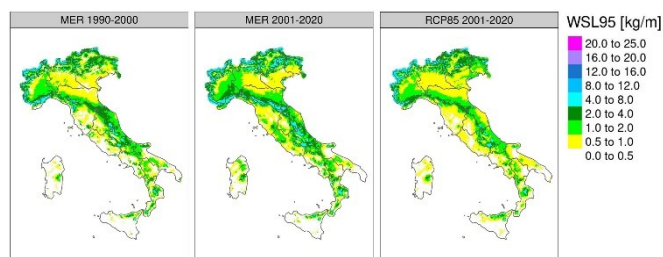
Fig. 3 Annual climatology of *WSL95* in the past: MERIDA OI in VER = 1990–2000 (left); MERIDA OI in REF = 2001–2020 (centre); ensemble in RCP8.5 in REF (right).

About future projections, very small decreases (within 0.5 kg/m) are inferred at short term (not shown). The decrease is accentuated in the second half of the Century at the lower-middle elevations (above 2 kg/m), whereas the events are expected to increase locally over high alpine regions (within 1 kg/m). Fig. 4 represent the *WSL95* evolution under the RCP8.5 hypothesis, but very similar results are inferred in RCP4.5. The noteworthy differences concern the scenario 2081-2100 in which the downward trend of *WSL* is slightly reduced (about 1 kg/m) on the Apennines and Alps. These long-term differences may be explained by the lower warming and more intense precipitations expected in RCP4.5 configuration compared with RCP8.5 [6].
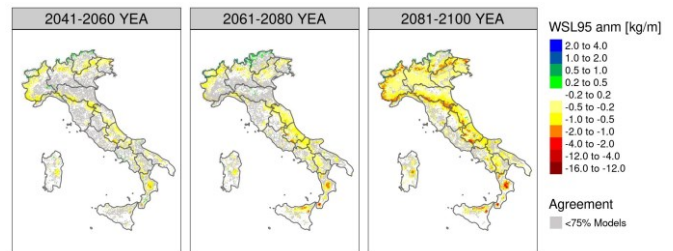
Fig. 4 Annual anomalies of *WSL95* for the ensemble mean in RCP85, from left to right: 2041-2060; 2061-2080; 2081-2100 scenarios. The grey colour represents areas where the agreement among models in the sign of anomaly is lower than 75%.

C. Analysis of WSLD

As mentioned above, *WSLD* index points out the number of occurrences of wet snow events exceeding some infrastructural damage thresholds. The maximum annual values of *WSLDmax = max (WSLD$_i$,)* ($1y \leq i \leq 20y$) are here discussed to investigate the trend of serious wet snow events.

In REF, the highest values of *WSLDmax* characterize the Alpine region (by about 50 to 100 days at level 1 kg/m), as expected and in close agreement with MERIDA field. The first row of Fig. 5 represents *WSLDmax* for the multi model ensemble under RCP8.5 hypothesis for the threshold levels = 1, 4, and 10 kg/m. The future anomalies at medium- and long-term (2nd and 3rd row of Fig. 5, respectively) indicate that, where the agreement among the model is > 75%, the *WSLDmax* trend is negative (blue colours) everywhere and becomes more pronounced along the Century, with reductions for each threshold level. The positive trend (red colours) affects only few points over the Alps in the future. Analogous results are found in RCP4.5 hypothesis with smaller anomalies (1-2 days, not shown).

D. Analysis of WSLF

According to its definition, the *WSLF* represents the relative frequency of wet snow events above the thresholds of interest, therefore *WSLF* fields can be considered probability maps of exceedance of some threshold values in a year.

Fig. 6 represents the *WSLF* values for the ensemble mean under RCP8.5 hypothesis for the threshold levels as in Fig. 5. In REF (1st row of Fig. 6), the probability of occurrence of low *WSL* is very high over Northern Italy and Apennine regions. Regarding more serious levels (≥ 10 kg/m), the frequency continues to be high only for high-altitude regions in close agreement with MERIDA results and confirming the Italian critical areas highlighted in the previous work [4].
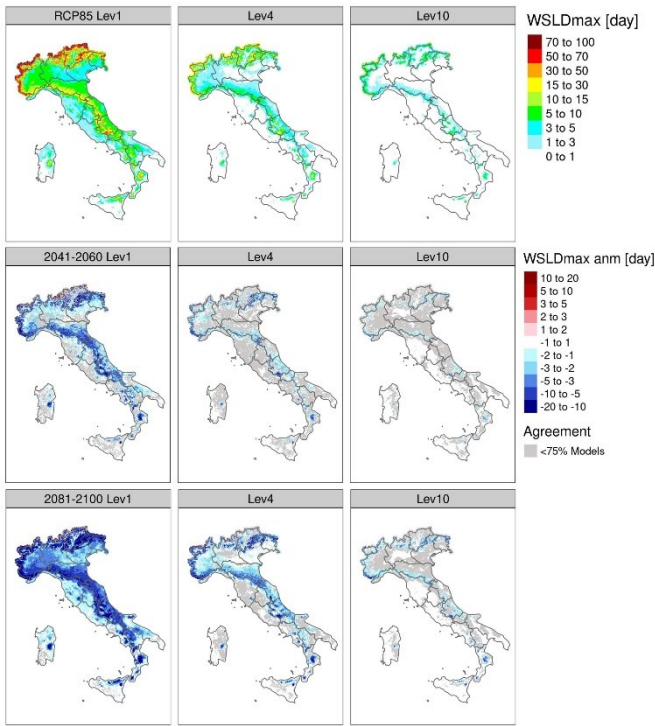
Fig. 5 *WSLDmax* ensemble mean in RCP85 in REF (1st row) and corresponding anomalies [day] in 2041-2060 (2nd row) and 2081-2100 (3rd row). The grey colour represents areas where the agreement among models in the sign of anomaly is lower than 75%.
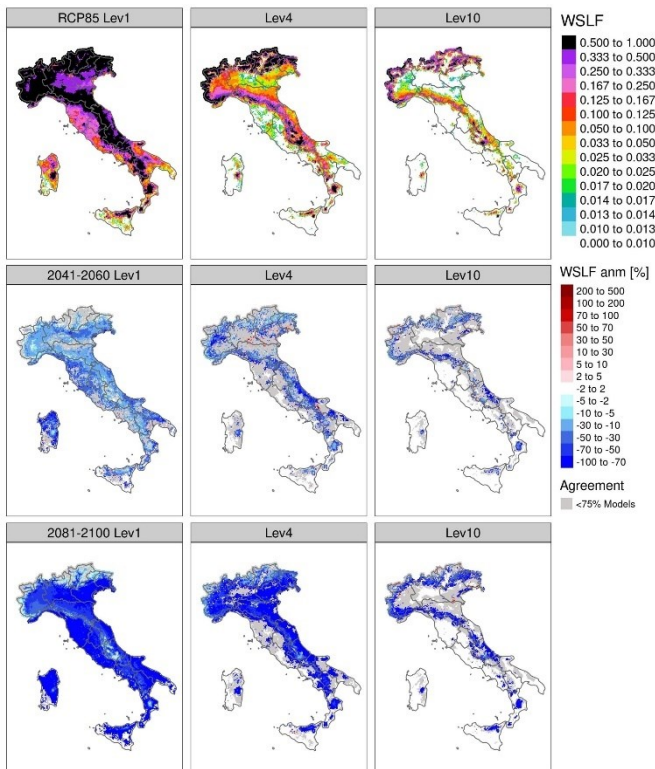
Fig. 6 *WSLF* ensemble mean in RCP85 in REF (top) and corresponding percentage anomalies [%] in 2041-2060 (2nd row) and 2081-2100 (3rd row). The grey colour represents areas where the agreement among models in the sign of anomaly is lower than 75%.

In the future a decrease of *WSLF* is projected elsewhere from medium- to long-term (2nd and 3rd row of Fig. 6, respectively). The confidence in the results decreases at low-medium altitude, where the topographic features such as elevation and terrain shading may be described in different way by the different climatic models (grey areas Fig. 6) and, therefore there is more uncertainty in the results. A slight increase of the *WSLF* is expected strictly in some locations.

Analogous results are found in RCP4.5 scenarios (not shown for the sake of brevity).

IV. CONCLUSIONS

Following the methodology developed in [4] and by applying an updated CLIWAC model, a new investigation of wet snow sleeves on overhead lines in Italy by the end of the Century has been carry out.

Wet snow events are related to topographic features. However, their frequency is projected to decrease in general from short- to long-term, as shown through the analysis of *WSLD* and *WSLF* indices, because rainfalls will prevail over snowfalls due to global warming. The *WSL95* analysis also highlights a general decrease in the intensity of extreme wet snow loads, except for the higher Alpine regions so far spared because of their historical cold temperatures. This negative trend is expected to be more pronounced in RCP8.5 than in the RCP4.5 pathway. Unlike previous results, the Apennine region will also be characterized by a reduction of the events.

The methodology developed and the results could directly impact on the decision-making process of electric user to cope with climate change impacts, and on the revision of Eurocodes.

REFERENCES

[1] IPCC, 2021: The Physical Science Basis. Contribution of Working Group I to the Sixth Assessment Report of the Intergovernmental Panel on Climate Change. Cambridge University Press, Cambridge, United Kingdom and New York, NY, USA. https://doi.org/10.1017/9781009157896, 2391 pp.

[2] World Meteorological Organization 2024: State of the Global Climate 2023. https://wmo.int/publication-series/state-of-global-climate-2023

[3] European Environmental Agency, 2023. Trends and projections in Europe 2023. DOI 10.2800/595102

[4] P. Faggian, A. Trevisiol, G. Decimi, Future projections of wet snow frequency and wet snow load on overhead high voltage conductors over Italy, Cold Regions Science and Technology, vol. 217, 103980, 2024.https://doi.org/10.1016/j.coldregions.2023.103980.

[5] Bonanno, R., Lacavalla, M., Sperati, S., 2019. A new high-resolution Meteorological Reanalysis Italian Dataset: MERIDA. Q. J. R. Meteorol. Soc. https://doi.org/ 10.1002/qj.3530.

[6] Faggian, P., 2021. Future Precipitation scenarios over Italy. Water MDPI J 13 (1335), 1–17.

[7] Makkonen, L., 1989. Estimation of wet snow accretion on structures. Cold Reg. Sci. Technol. 17 (1), 83–88.

[8] Makkonen, L., Wichura, B., 2010. Simulating wet snow loads on power line cables by a simple model. Cold Reg. Sci. Technol. 61 (2–3), 73–81. https://doi.org/10.1016/j. coldregions.2010.01.008.

[9] Nygaard, B.E., ´Agústsson, H., Somfalvi-T´oth, K., 2013. Modeling Wet Snow Accretion on Power Lines: Improvements to previous Methods using 50 years of Observations. J. Appl. Meteorol. Climatol. 52, 2189–2203. https://doi.org/10.1175/JAMC-D-12- 0332.1.

[10] E. C. Massoud, V. Espinoza, B. Guan, D. E. Waliser, «Global Climate Model Ensemble Approaches for Future Projections of Atmospheric Rivers,» *Earth's Future,* vol. 7, p. 1136–1151, 2019. https://doi.org/10.1029/2019EF001249

Thermal de-icing technology based on the Peltier effect of thermoelectric material

Li Wang[1], Qin Hu[1], Huang Wang[1], Lichun Shu[1], Xingliang Jiang[1]

[1] *Xuefeng Mountain Energy Equipment Safety National Observation and Research Station of Chongqing University*

first.wangli@cqu.edu.cn, second.huqin@cqu.edu.cn, third.wanghuan@stu.cqu.edu.cn

Abstract— **Snow and ice cover can seriously threaten the safety as well as stable operation of energy equipment. While thermal ice melting technology as one of the most effective de-icing methods, the traditional heating element produces heat on both sides, melting the ice layer while also heating the substrate material, which not only causes heat loss to the substrate material, but also increases the energy consumption of the system. In order to solve the above problems, the de-icing technology based on the Palladium effect of thermoelectric materials is proposed. The thermoelectric material, which produces heat on one side, is used as the heating element to limit the bidirectional flow of heat and reduce power consumption; the thermoelectric analogy method is used to establish the system thermal circuit model, simplify the thermal calculation, and analyze the influence of the temperature difference between the hot and cold ends and the power supply current on the efficiency of the heating element in terms of heat production.**

Keywords—***Thermal deicing; Heating elements; Energy consumption; Heat production efficiency; Thermoelectric materials***

I. Introduction

Icing is one of the most common physical phenomena in nature and is affected by multiple meteorological and environmental factors such as altitude, temperature, liquid water content, median droplet diameter, and air pressure. The prevalence of icing can limit the performance and functionality of modern mechanical and energy equipment such as wind turbines [1][2], photovoltaic arrays [3][4], and airplanes [5][6].

Thermal ice melting technology is one of the most effective de-icing technologies, using the Joule effect, microwave, infrared, hot air [7]-[10] and other pathways to heat the surface of the structure, melting the ice layer, to achieve the effect of melting the ice, but there are also significant limitations. STOECKER W G F et al. [11] studied the heating of refrigeration equipment to defrost and freeze, and found that 70% of the heat flux is used to heat the equipment itself, and only 30% of the of the heat was used to melt the ice, resulting in significant heat loss. Literature [12] found that the use of Joule heat effect to achieve the deicing effect requires a great energy input. Dutta P K et al [13] experimentally proved that the heating time and the number of cycles cause thermal damage to the composites and even reduces the mechanical strength. Zhu R et al [14] verified that the stiffness of the fiber reinforced composites decreases with the increase of the temperature, and the in-situ bending properties are also altered.

To solve the problem of high energy consumption caused by double-sided heating of traditional heating elements and thermal damage to the substrate material caused by long-term heating. This paper adopts the thermoelectric material as the heating element, utilizes its advantages of single-sided heating

and heating efficiency higher than 1, reduces the power consumption of the system, and solves the problem of thermal damage of the substrate material. The thermoelectric analogy method is used to establish the thermal circuit model of the thermal de-icing system, simplify the heat transfer calculation, and analyze the effect of different temperature differences and power supply current on the heat production efficiency of the thermoelectric element.

II. Methods and Models

A. Problem formulation

Energy equipment such as wind turbine blades and airplanes have different shapes, resulting in different curvatures of icing surfaces for different equipment. The thermal analysis of ice melting process for icing surfaces with different curvatures is unfavorable to the design of thermal deicing system. The article adopts the idea of micro-element control body in the integral to deal with complex shapes, and simplifies the icing surfaces with different curvatures into a unified flat plate model, which is shown in Fig. 1:
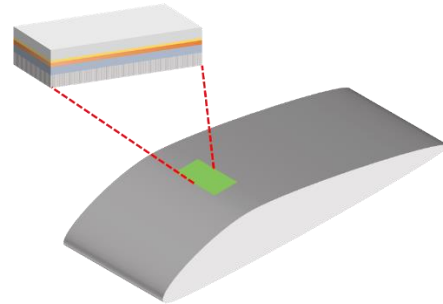
Fig. 1   Simplified model

When the thickness of the ice cover on the surface of the energy equipment structure reaches the threshold set by the system [15], the thermal de-icing system is activated, the electric current is converted to Joule heat through the heating elements, and the heat flux is conducted in both directions towards the ice and the substrate material. In the direction of the ice layer, the heat flow is conducted to the ice layer through the heat-conducting resin and skin, and part of the heat is used to melt the ice layer and form a water film at the interface between the flat plate and the ice layer; the rest of the heat spreads to the inside of the ice layer and is transferred to the contact surface between the air and the ice layer, and the heat is exchanged with the external environment through convection and radiation. In the direction of the substrate, the heat flow passes through the heat insulation material to the substrate, and since the heat insulation material is usually chosen to have a low thermal conductivity, the heat flowing into the substrate material is very little, and it can be ignored

that the substrate material produces heat exchange with the external environment. Ice melting heat transfer process is shown in Fig. 2:
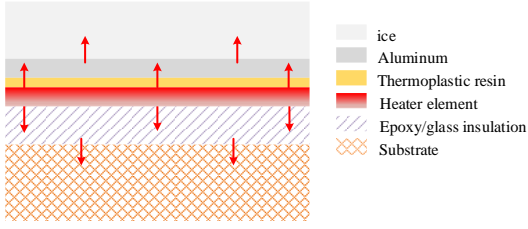
Fig. 2　Ice melting heat transfer process

From the above thermal analysis, it can be seen that the bidirectional flow of heat flux is one of the reasons for the high energy consumption of electro-thermal deicing. To make the heat flow generated by the electric heating element diffuse only to the inside of the ice layer, this paper solves the problem by utilizing the characteristics of thermoelectric materials to produce heat on one side.

B. *Thermal circuit model of thermoelectric heating elements*

Considering the periodic distribution of thermocouples in the thermoelectric device, the article performs physical model as well as thermal analysis for a single thermoelectric unit. Fig. 3 shows that the thermoelectric unit is connected to the current, the electrons and holes in the electric field force upward movement, the top produces a high temperature T_1, the heat flow through the copper electrodes and alumina ceramic substrate conduction to the hot end of the upper surface of the substrate, the temperature of T_h; the bottom produces a low temperature T_2, the heat flow transfer to the cold end of the substrate lower surface, the temperature of T_c. Inside the thermoelectric unite, heat is transferred from the top to the bottom by conduction in response to a temperature gradient. Since the total resistance of the thermoelectric unite is R, the Joule heat generated by the current per unit time is I^2R.Literature [16] shows that the Joule heat transferred to the hot and cold ends is $0.5I^2R$, respectively. In addition, the hot end can dissipate the heat to the environment by natural convection. Therefore, the exothermic quantity q₁ and absorptive quantity q_2 are jointly determined by the Peltier effect, Fourier effect, Joule effect and ambient heat dissipation. From the above thermal analysis, the equilibrium equations are established at the hot and cold ends, and the exothermic quantity q₁ and the absorptive quantity q₂ are expressed as [17]:

$$q_1 = \pi_{NP}I + \frac{1}{2}I^2R_{N/P} - \lambda_{N/P}(T_1 - T_2) \quad (1)$$

$$q_2 = \pi_{NP}I - \frac{1}{2}I^2R_{N/P} - \lambda_{N/P}(T_1 - T_2)$$

Which，$R_{N/P} = \frac{L_N}{A_N}\rho_N + \frac{L_P}{A_P}\rho_P$；$\lambda_{N/P} = \frac{L_N}{A_N}\lambda_N + \frac{L_P}{A_P}\lambda_P$；

Where, $\pi_{P/N}$ is the Peltier coefficient; $\lambda_{N/P}$ is the Thermoelectric unit thermal conductivity; $L_{N/P}$ is the Thermoelectric unit arm length; $\rho_{N/P}$ is the Thermoelectric unit resistivity; $A_{N/P}$ is the Thermoelectric unit cross-sectional area; and the subscripts N/P denote N-type and P-type semiconductors;
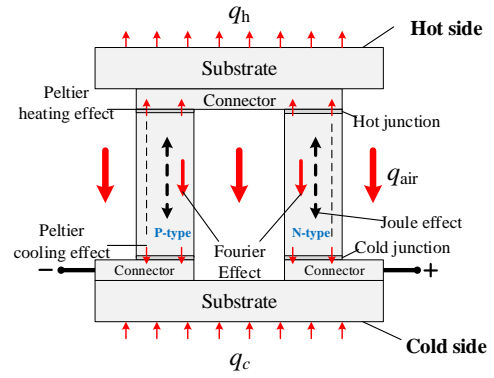
Fig. 3　Thermal analysis of thermoelectric unit

Since the article focuses on the Peltier effect of thermoelectric materials, the influence of material properties on the thermoelectric effect is not concerned for the time being. Therefore, including copper electrodes, semiconductors can be simplified as a heat flux of q_1, q_2 "black box", ignoring the heat loss of the air sandwich between the electrode and the semiconductor, the substrate, N/P-type semiconductor, the air gap between the upper and lower substrate heat conduction problem is simplified as a thermal network model, the three-dimensional mathematical model is simplified to zero-dimensional. The thermal network model is shown in Fig. 4:
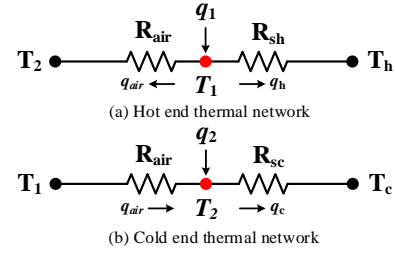
Fig. 4　Thermal network of thermoelectric unit

The heating capacity q_h and cooling capacity q_c of the thermoelectric unit cold and hot substrates are [18]:

$$q_h = q_1 - q_{air} = q_c + p \quad (2)$$
$$q_c = q_2 - q_{air}$$

where q_{air} denotes the heat flow conducted by the air gap between the substrates; p is the input power supply power;

The heat flow at the hot and cold ends can be expressed in terms of the thermal resistance of the substrate:

$$q_h = \frac{T_1 - T_h}{R_{sh}} \quad (3)$$

$$q_c = \frac{T_c - T_2}{R_{sc}}$$

The heat flow q_{air} conducted in the air gap is denoted:

$$q_{air} = \frac{T_1 - T_2}{R_{air}} \quad (4)$$

Which，

$$R_{air} = \frac{1}{K_{air}} = \frac{1}{h_{air}A_{sub}(1-F)}$$

where F is denoted as the fill factor, $F = \frac{A_{N/P}}{A_{sub}}$, A_{sub} is expressed as substrate surface area; $A_{N/P}$ semiconductor cross sectional area;

Associative Eq. (1)-(2), Hot and Cold end node temperatures T_1 and T_2 are:

$$T_1 = \frac{(R_s R_{N/P} I^2 + T_c + T_h)(R_s \lambda_{N/P} + \frac{R_s}{R_{air}}) + \frac{1}{2} R_s R_{N/P} I^2 + T_h + R_s \pi I}{2(R_s \lambda_{N/P} + \frac{R_s}{R_{air}}) + 1}$$

$$T_2 = \frac{(R_s R_{N/P} I^2 + T_c + T_h)(R_s \lambda_{N/P} + \frac{R_s}{R_{air}}) + \frac{1}{2} R_s R_{N/P} I^2 + T_c - R_s \pi I}{2(R_s \lambda_{N/P} + \frac{R_s}{R_{air}}) + 1} \quad (5)$$

Derived from Eq. (3):

$$q_h = \frac{(R_s R_{N/P} I^2 + T_c - T_h)(\lambda_{N/P} + \frac{1}{R_{air}}) + \frac{1}{2} R_{N/P} I^2 + \pi I}{2(R_s \lambda_{N/P} + \frac{R_s}{R_{air}}) + 1}$$

$$q_c = \frac{(T_c - T_h - R_s R_{N/P} I^2)(\lambda_{N/P} + \frac{1}{R_{air}}) - \frac{1}{2} R_{N/P} I^2 - \pi I}{2(R_s \lambda_{N/P} + \frac{R_s}{R_{air}}) + 1} \quad (6)$$

C. Thermal circuit model of deicing system

To simplify the thermal deicing model, the article gives the following simplification conditions: 1) convective heat transfer occurs only at the contact surface between the material and the natural environment, ignoring the contact resistance between the materials; 2) each layer of the material is approximately regarded as a flat plate, ignoring the air gaps between the layers; 3) the ambient temperature is a constant; the heat transfer coefficient of the material does not change as the temperature increases, and the material isotropic.

Ice melting occurs at the contact surface between the material and the ice, so the temperature difference between the surface of the ice and the environment is small, and thermal convection and thermal radiation can be neglected [15]. Assuming that the thickness of the ice layer is th_{ice}, the thickness of the melted ice is L_{water}, and the thickness of the un-melted ice layer is $th_{ice} - L_{water}$, the deicing thermal network is shown in Fig. 5:
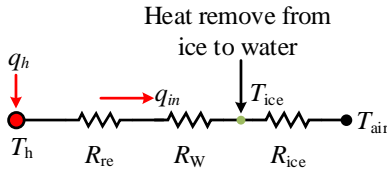
Fig. 5   Resistance network for representing deicing heat flux

The thermal resistance of the ice layer is:

$$R_{ice} = \frac{th_{ice} - L_{water}}{k_{ice} A_c} \quad (7)$$

The hydrothermal resistance is:

$$R_{ice} = \frac{L_{water}}{k_{ice} A_c} \quad (8)$$

The ice sheet conduction heat flux q_{in} is:

$$q_{in} = \frac{T_{ice} - T_{air}}{R_{ice}} \quad (9)$$

The heat flux q_h conducted by the heating element in the direction of the ice is:

$$q_h = q_{in} + A_c h_{fs} \frac{dth_{ice}}{dt} \quad (10)$$

The heating element surface temperature T_h is:

$$T_h = q_{in}(R_{re} + R_p + R_w) + T_{ice} \quad (11)$$

Associate Eq (9)-(11) (9)-(11), the ice melting power q_h is:

$$q_h = \frac{\left(\frac{T_{ice} - T_{air}}{R_{ice}} + A_c h_{fs} \frac{dth_{ice}}{dt}\right)(R_{re} + R_p + R_w) + T_{ice} - T_{air}}{R_{ins} + R_{su} + \left(\frac{1}{R_{con,a}} + \frac{1}{R_{rad}}\right)^{-1}} + \frac{T_{ice} - T_{air}}{R_{ice}} + A_c h_{fs} \frac{dth_{ice}}{dt} \quad (12)$$

Where, $\frac{dth_{ice}}{dt}$ is the rate at which the ice sheet is melting;

III. SIMULATION AND EXPERIMENTATION

Commercial thermoelectric sheets are usually made of Bi_2Te_3 and consist of multiple thermoelectric unite of P-N type semiconductors connected in series to achieve higher cooling power. But the physical process and performance parameters are basically the same. The article in order to verify the effectiveness of the Peltier effect deicing method based on thermoelectric materials, using a combination of finite element and thermal circuit analysis to analyze a single thermoelectric unit, the specific parameters are shown in TABLE. I:

TABLE. II PARAMETERS OF THERMOELECTRIC UNIT

Name	Parameters
Sizes	1mm*1.2mm*1.7mm
Pitch	0.7 mm
Heat capacity	154.4 J/(kg*K)
Conductivity	1.1e5 S/m
Seebeck coefficient	2e-4 V/K
Thermal conductivity	1.6 W/(m*K)

The calculations were performed using a three-dimensional simplified model as shown in Fig. 6. The model is divided into five layers, from top to bottom: ice, metal skin, thermal silicon, thermoelectric unit, and base material.
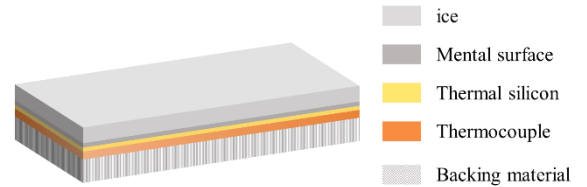
Fig. 6   Three-dimensional simplified model

The dimensions of the length×width×height of the computational model shown in Fig. 6 are 1.2 mm ×1 mm ×21.1 mm. The material parameters and thicknesses of each layer are shown in TABLE. II where d indicates the thickness of the material layer, k indicates the thermal conductivity, and c_p indicates the specific heat capacity. Simulate the natural environment of the mildly ice-covered area, the ambient temperature is 268.15K, assuming that the initial thickness of the ice layer is 5mm, although with the melting process of the accumulated ice, the ice layer will form a layer of water film on the surface of the substrate material, and the thickness of its thickness is with the melting process of the ice to change the coefficient of thermal conductivity.

TABLE 2. PHYSICAL PARAMETERS OF LAYERS

Layers	d(mm)	k (w/m*K)	c_p (J/kg*K)
Backing material	10	0.2	962.9
Thermocouple	3.9	1.6	154.4
Thermal silicon	0.2	13.5	0.94
Aluminum	2	115.087	1088.5
ice	5	2.22	200
Water	---	0.5538	4186.553

A. Simulation results and discussion

1) Comparison of Finite Elements analysis and Thermal Circuits

To verify the reliability of the calculation results of the thermal circuit model, the electric power, temperature difference and hot end temperature are compared with the finite element model calculation results, as shown in Fig. 7 and Fig. 8; due to the simplification of the parameter calculation of the thermal circuit model and the simulation conditions, although there will be a certain degree of error, and the maximum errors of the electric power, temperature difference and hot end temperature are 5.094%, 2.660% and 3.120%, respectively, The calculated values and finite element values basically match.
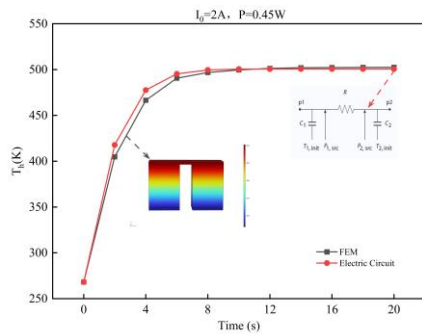
Fig. 7 Temperature comparison between FEM and Electric Circuit
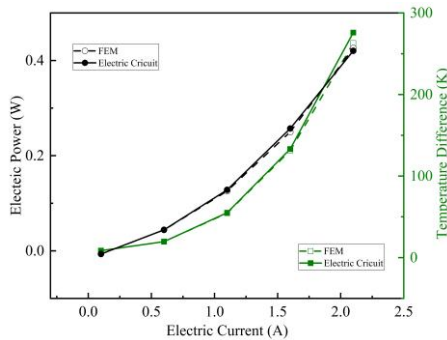
Fig. 8 Electric power and Temperature difference comparison between FEM and Electric Circuit

2）Heat production efficiency (HCOP)

Fig. 9 shows the relationship between the input electrical energy and the amount of heat released when the current is 2A. From the figure, it can be seen that the released heat, input electrical energy and time show a linear relationship. However, with the change of time and the enhancement of carrier migration motion, the system releases heat gradually larger than the input electric energy, showing excellent thermal effect.
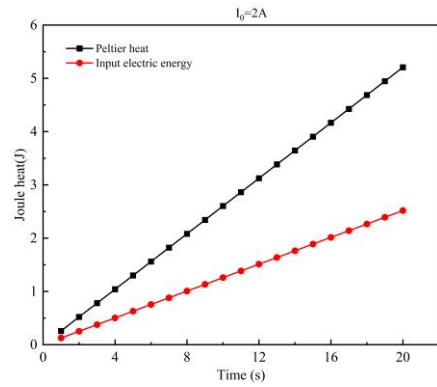
Fig. 9 Comparison of Thermal and Electric energy, I_0=2A
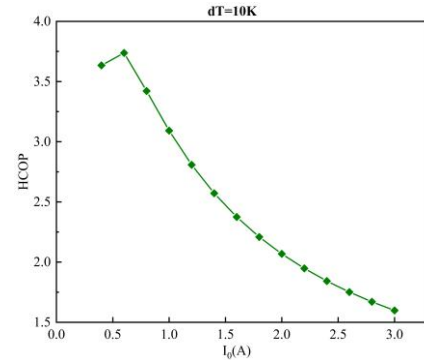
Fig. 10 Thermocouple heat efficiency for various Current, dT=10K

Fig. 10 shows the relationship between the HCOP and current for a temperature difference of 10 K between the hot and cold ends of the thermocouple. As shown by the figure, the HCOP of the thermoelectric material is not linearly related to the current. The system reaches a maximum thermal efficiency of 3.7375 when the current is equal to 0.6 A. Due to the existence of the Thomson effect of the thermoelectric material, when the current exceeds the threshold, the HCOP decreases with the gradual increase of the current, and eventually it will be less than 1. Therefore, the optimal current needs to be calculated in the engineering design of the thermoelectric de-icing system.
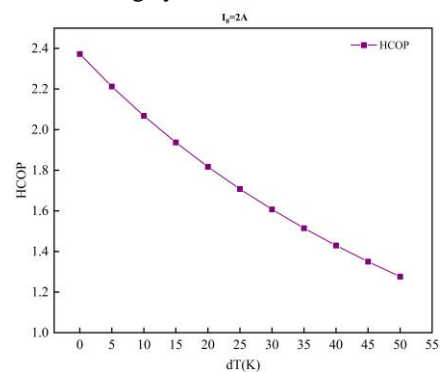
Fig.11 Thermocouple heat efficiency for temperature difference, I_0=2A

Fig. 11 shows the relationship between temperature difference and thermal efficiency at an input current of 2A. As can be seen from the figure, the thermal efficiency is maximum when the temperature difference dT is 0. As the temperature difference increases, the thermal efficiency decreases, while the decrease slows down. When the temperature difference is greater than 70K, the thermal

efficiency HCOP will be lower than 1. Therefore, the engineering application try to maintain a lower temperature difference between the two ends of the thermocouple, which can maintain a high thermal efficiency. In the de-icing system, the cold end is fixed on the surface of the material, preventing the heat from flowing into the equipment, while the hot end is covered by the ice, the heat released is basically used to melt the ice, while the ice-covered ambient temperature is maintained at 0°C or below, the thermocouple will not produce a very high temperature difference between the two ends of the thermocouple can be maintained at a very high thermal efficiency.

B. Experimental results and discussion

To verify the feasibility of the de-icing method proposed in the article, an artificial climate chamber at Chongqing University was utilized, as shown in Fig. 12(a), where the internal temperature was adjustable in the range of -1.1 ℃ to -36 ℃. An ICE standard nozzle was mounted at the top of the chamber to provide the overcooled water droplets by pressurized air atomizing the water stream. The thermoelectric module measures 40 mm ×40 mm ×3.9 mm, as shown in Fig. 12(b), is made of Bi_2Te_3 and consists of 127 pairs of thermoelectric units connected in series.

(a) Artificial climate laboratory (b) Thermoelectric modules
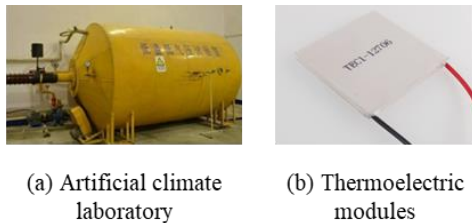
Fig.12   Equipment

The deicing prototype is shown in Fig. 13, where the semiconductor sheet is embedded in an epoxy resin plate through a groove, and a metal mask is fixed to the surface of the thermoelectric module, and the thermal contact is altered by thermally conductive silicone grease.

Metal-skin: Al
Thermal Grease
Semiconductor plate
Epoxy resin
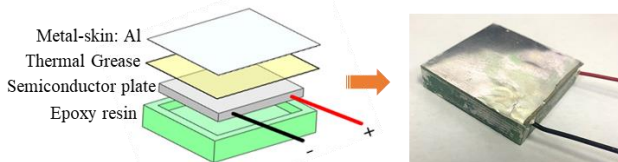
Fig. 13   Thermoelectric de-icing panel

The experimental test device is shown in Fig. 14, divided into two modules of data acquisition and temperature control, utilizing the temperature sensor PT100 to collect data with an accuracy of 0.15 K. The temperature control module includes two parts of heating and power supply, both of which are connected through a temperature control switch to achieve the purpose of temperature control. The data acquisition module contains two parts, the data logger and computer, the logger acquisition interval is 1s, and it is connected to the computer through RS485 communication.
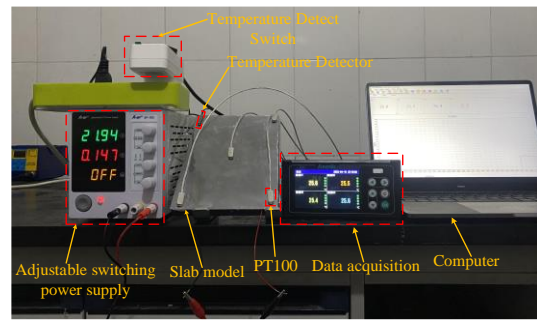
Fig. 14   Experiment Apparatuses

1) Plate deicing test

Fig. 15 shows the effect of de-icing of a thermoelectric sheet flat plate. The thickness of the flat plate covered with ice is 5.23 mm, as shown in Fig. 15(a); the thermoelectric sheet de-icing prototype is fixed on a bracket with an angle of 120 ° to the horizontal plane, as shown in Fig. 15(b); after connecting to the DC power supply, the ice layer melts, and eventually the ice layer slips under the action of its own gravity, but the power cord is also iced up in a low-temperature environment, and it cannot generate heat for melting, which results in the ice layer hanging on the surface of the flat plate, as shown in Fig. 15(c) shows, and the feasibility of the de-icing method based on the semiconductor thermoelectric effect is also verified.

Fig. 15   Flat plate de-icing effect show
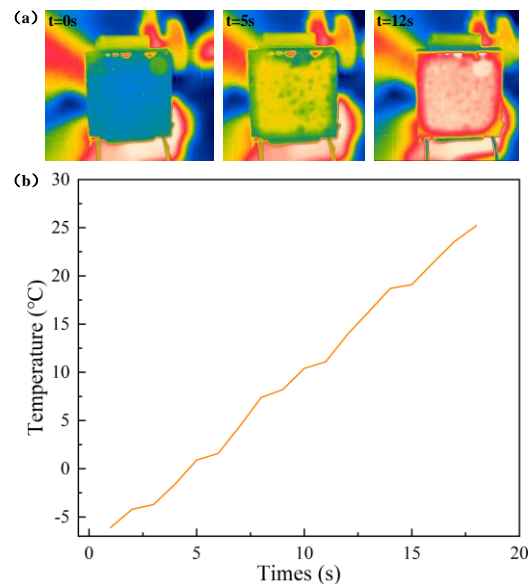
Fig.16   Thermal response

Figure 16(a) captures the temperature rise process of the de-icing plate using an infrared imager, demonstrating the temperature change of the plate at 0s, 5s, and 12s, with the interface color evolving from blue to yellow, and finally to red, while the color change represents the melting process, indicating that the melting of the ice layer occurs at the contact surface between the metal skin and the ice layer in 0-5s, and

when the time reaches 12s, the melting has spread to the inside of the ice layer. Fig. 16(b) is the temperature data collected by using the temperature sensor PT100, the semiconductor sheet in the access to the current, the temperature in 20s from -6.1 ℃ rose rapidly to about 25 ℃, which shows that the semiconductor sheet has a rapid thermal response ability, can be used as a heat pulse of the heat making device.

IV. CONCLUSION

To simplify the heat transfer calculation, the thermoelectric analog method is used to establish a heat path model for a single Peltier Pellets, and compared with the finite element model, the computational errors of the hot end temperature, temperature difference, and electric power are 5.094%, 2.660%, and 3.120%, respectively, and the computational results basically coincide with each other.

In this study, this paper utilizes the Peltier effect of thermoelectric materials to avoid the bidirectional diffusion of heat flux, to improve the heating efficiency of the heating element to greater than 1, and also to avoid thermal damage to the substrate material by long-term heating. Flat plate experiments carried out in the artificial climate chamber of Chongqing University verified that the thermoelectric material has a fast thermal response and can be used as a heat generation device to achieve the goal of thermal deicing rather than thermal ice melting.

REFERENCES

[1] Lehtomäki V, Task I E A W. Wind energy in cold climates available technologies-report[R]. Task 19, Tech. Rep., IEA 2018. 2018. Available online: ashx, 2016.

[2] Pedersen M C, Sørensen H. Towards a CFD model for prediction of wind turbine power losses due to icing in cold climate[C]//16th International Symposium on Transport Phenomena and Dynamics of Rotating Machinery. 2016.

[3] Li Z, Jianbo C, Shunchao W, et al. An Experimental Study of Influencing Factors on the Snow Removing Time for Self-Heating Snow Removed Photovoltaic Panels[J]. International Journal of Green Energy, 2022, 19(8): 904-917.

[4] Rahmatmand A, Harrison S J, Oosthuizen P H. An experimental investigation of snow removal from photovoltaic solar panels by electrical heating[J]. Solar Energy, 2018, 171: 811-826.

[5] Cao Y, Tan W, Wu Z. Aircraft icing: An ongoing threat to aviation safety[J]. Aerospace science and technology, 2018, 75: 353-385.

[6] Li L, Khodakarami S, Yan X, et al. Enabling Renewable Energy Technologies in Harsh Climates with Ultra‐Efficient Electro‐Thermal Desnowing, Defrosting, and Deicing[J]. Advanced Functional Materials, 2022: 2201521.

[7] Peng C, Hu Y, You Z, et al. Preparation and anti-icing performance of acrylic superhydrophobic asphalt pavement coating with microwave heating function[J]. Construction and Building Materials, 2022, 344: 128289

[8] Sollén S, Kumar Eppanapelli L, Casselgren J, et al. Experimental Investigation of an Infrared Deicing System for Wind Power Application in a Cold Climate[J]. Journal of Cold Regions Engineering, 2022, 36(4): 04022008.

[9] Li L, Liu Y, Tian L, et al. An experimental study on a hot-air-based anti-/de-icing system for aero-engine inlet guide vanes[J]. Applied Thermal Engineering, 2020, 167: 114778.

[10] STOECKER W G F, LUX JR J J, KOOY R J. Energy considerations in hot-gas defrosting of industrial refrigeration coils[J]. ASHRAE transactions, 1983, 89: 549-573.

[11] Atmospheric icing of power networks[M]. Springer Science & Business Media, 2008.

[12] Atmospheric icing of power networks[M]. Springer Science & Business Media, 2008.

[13] Dutta P K, Ryerson C C, Pergantis C. Thermal deicing of polymer composite helicopter blades[J]. Materials for Space Applications, 2005, 851: 563.

[14] Zhu R, Li X, Wu C, et al. The In-Situ Mechanical Properties of Carbon Fiber/Epoxy Composite under the Electric-Current Loading[J]. Polymers, 2022, 14(20): 4452.

[15] Shu L, Qiu G, Hu Q, et al. Numerical and experimental investigation of threshold de-icing heat flux of wind turbine[J]. Journal of Wind Engineering and Industrial Aerodynamics, 2018, 174: 296-302.

[16] Ioffe A F, Stil'Bans L S, Iordanishvili E K, et al. Semiconductor thermoelements and thermoelectric cooling[J]. Physics Today, 1959, 12(5): 42.

[17] Lee H S. Thermal design: heat sinks, thermoelectrics, heat pipes, compact heat exchangers, and solar cells[M]. John Wiley & Sons, 2022.

[18] Holman J P. Heat transfer[M]. McGraw Hill, 1986.

Towards an aerospace standard for assessing the performance of runway de-icing products

Jean-Denis Brassard[1], Gelareh Momen[1]

[1] Anti-Icing Materials International Laboratory, Université du Québec à Chicoutimi, Canada

jdbrassa@uqac.ca , gmomen@uqac.ca

Abstract—**Northern airports heavily rely on the application of thousands of tons of deicing products during winter to maintain runways in an acceptable and, consequently, safe condition. Two primary standards delineate the requirements for airport runway deicing products: AMS1431 for solids and AMS1435 for liquids. These standards, derived from those governing aircraft products, mandate an evaluation of corrosion resistance and environmental impact. The sole cold-related criterion pertains to the freezing point, stipulating that the freezing point of the product, diluted 1:1 by weight with ASTM D1193, Type IV water, should be reported and must be lower than +6 °F (-14.5 °C), determined in accordance with ASTM D1177. In addition to these, three supplementary standards assess the de-icing performance of products: AS6211 Ice Penetration Test Method, AS6172 Ice Undercutting Test Method, and AS6170 Ice Melting Test Method. While these standards provide information on product performance, they are not mandatory and do not propose minimum requirements. The standards state that the product, when used according to the manufacturer's recommendation, should effectively remove accumulated frozen deposits of frost and ice from airport aprons (ramps), taxiways, and runways. The product's effectiveness is to be tested in accordance with AIR6170 for ice melting, AIR6172 for ice undercutting, and AIR6211 for ice penetration. Acceptance criteria will be mutually agreed upon by the purchaser and vendor. The Runway Deicing Product Performance Working Group (RDP2), under the auspices of the Society of Automotive Engineers (SAE), is actively involved in developing laboratory tests to assess the performance of deicing products. This collaborative initiative aims to culminate in the creation of an Aerospace Informational Report (AIR) that will serve as a crucial tool in informed decision-making within airport operations. Simultaneously, it will empower manufacturers to offer improved and more efficient deicing solutions. This research's objective is to outline the main criteria considered in establishing this document. RDP will be utilized under calibrated simulated icing conditions in the laboratory. The comprehensive evaluation includes the meticulous identification of contaminants, distinguishing between solid, liquid, brine, and ice forms. The main criteria involve visual and tactile assessments, employing a thermal camera to evaluate phase changes and Raman spectroscopy to assess the concentration of the remaining chemical. A crucial aspect of this undertaking is the evaluation of anti-icing performance, particularly when the product is applied preventively. Additionally, the assessment involves a rigorous examination of frictional properties, with a specific focus on delineating the impact of a given product on friction evolution. Friction will be evaluated using the British Pendulum Tester under the aforementioned conditions. This multifaceted approach underscores RDP2's dedication to establishing robust testing protocols that significantly contribute to the advancement of deicing technology in the aviation industry.**

Keywords—***winter, airport, runway deicing products, anti-icing and standard***

I. INTRODUCTION

As the winter months approach, northern airports gear up for the challenges that come with snow and ice. With thousands of flights taking off and landing each day, it is imperative that runway conditions remain safe for aircraft operations and passenger safety [1]. This is where deicing products come into play [2]. Deicing products are essential for maintaining optimal runway performance during the winter season in cold climate regions. They help mitigate the inherent dangers associated with reduced skid resistance caused by wintry precipitation [3, 4]. Snow and ice accumulation significantly heighten the risk of runway excursions and accidents, making it critical to apply deicing measures effectively [1, 5]. While deicing products are necessary for maintaining safe runway conditions, their usage can have environmental implications [6]. These products contain chemicals that can harm aquatic life and vegetation. Therefore, airports must take measures to ensure that they are using deicing products responsibly.

Airport runway deicing products are essential for maintaining safe and efficient air travel during cold weather conditions. To ensure the quality and effectiveness of these products, two primary standards have been established: AMS1431 for solids and AMS1435 for liquids [2]. These standards outline the necessary specifications that deicing products must meet in order to be approved for use on airport runways. In order to comply with these standards, deicing products must undergo a thorough evaluation process that includes a range of assessments. These assessments include tests for corrosion and environmental impact, as well as evaluations of the product's performance under different weather conditions. This rigorous testing ensures that only the highest quality deicing products are used on airport runways.

One of the most important criteria for deicing product compatibility is the freezing point. This criterion specifies that the product's freezing point, when diluted 1:1 by weight with ASTM D1193, Type IV water, must be below +6 °F (-14.5 °C) as determined in accordance with ASTM D1177 protocols [2]. This is crucial because if the deicing product freezes at the ground operation temperature, it will not be effective in melting ice and snow on the runway [7, 8].

In addition to the freezing point, there are other important factors that must be considered when evaluating deicing products. For example, the products must be safe for use around aircraft and must not cause damage or corrosion to the runway surface. They must also be environmentally friendly and not have any negative impacts on the surrounding ecosystem.

Overall, the AMS1431 and AMS1435 standards ensure that airport runway deicing products meet the requirements and

safety standards. By adhering to these standards, airports can maintain safe and efficient operations during cold weather conditions, ensuring that passengers and crew can travel safely and on time [9].

Deicing products are essential for maintaining safe and efficient airport operations during the winter months. However, their effectiveness can vary greatly depending on the type of product and the conditions in which they are used. To ensure that deicing products are up to the task, several standards have been established to evaluate their performance [1, 7, 8, 10].

The AS6211 Ice Penetration Test Method [11], AS6172 Ice Undercutting Test Method [12], and AS6170 Ice Melting Test Method [13] are three additional standards that are commonly employed to evaluate the effectiveness of deicing products. These standards provide valuable insights into product efficacy, but they currently lack mandatory status or propose minimum requirements.

According to the guidelines, deicing products should effectively eliminate accumulated frozen deposits of frost and ice from airport aprons, taxiways, and runways, as per the manufacturer's recommendations.

The establishment of acceptance criteria is contingent upon mutual agreement between the purchaser and the vendor. This means that both parties must agree on the standards that will be used to evaluate the product's performance. This ensures that both parties have a clear understanding of what is expected and can work together to achieve the desired results.

Overall, the use of these standards is essential for ensuring that deicing products are effective and safe for use in airport operations. By following these guidelines, airport operators can maintain safe and efficient operations during the winter months, even in the face of challenging weather conditions.

The Runway Deicing Product Performance Working Group (RDP2), under the supports of the Society of Automotive Engineers (SAE), is presently engaged in the development of laboratory tests aimed at ascertaining the performance of deicing products. This concerted effort is intended to culminate in the formulation of an Aerospace Informational Report (AIR). The resultant AIR is envisioned to serve as a pivotal tool, facilitating informed decision-making within airport operations while concurrently empowering manufacturers to proffer enhanced and more efficacious deicing solutions.

The aim of this paper is to present the main criteria that will be considered in the establishment of this document. RDP will be evaluated primarily under calibrated simulated icing conditions in the laboratory. The overarching criteria governing this comprehensive evaluation encompasses the meticulous identification of contaminants, distinguishing between solid, liquid, brine, and ice forms. The main criteria will be based visual, tactile but also using thermal camera to assess phase change. A critical dimension of this undertaking involves the evaluation of anti-icing performance, specifically when the product is preventively applied. Furthermore, the assessment involves a rigorous examination of frictional properties, with a keen focus on delineating the impact of a given product on the evolution of friction. The friction will be evaluated using the British Pendulum Tester under the aforementioned conditions.

This multifaceted approach underscores the commitment of the RDP2 in establishing robust testing protocols that

contribute to the advancement of deicing technology in the aviation industry.

II. METHODOLOGY

The proposed methodology consists of six criteria based on the WG discussions.

A. Current Aerospace Standard tests

-1. AS6211-Ice Penetration

The first assessment involves conducting the ice penetration test method in accordance with AS6211 [11]. This test provides insight into the depth, measured in millimetres that the Runway Deicing Product (RDP) penetrates into ice per minute. The ice is generated by introducing 0.5 ml of ASTM D1193 type IV water into a micro centrifuge glass tube, followed by an initial measurement (M1). Subsequently, 25 μl of dyed RDP is introduced into the tube. The utilization of rhodamine B as a dyeing agent does not impact the performance of the RDP and facilitates precise penetration determination. After intervals of 5, 10, and 30 minutes, a second measurement (M2) is taken. The depth of ice penetration, in millimetres, is calculated by subtracting M1 from M2. This testing protocol is repeated four times for each product.

-2. AS6172 Ice Undercutting

The second evaluation involves conducting the ice undercutting test method as prescribed by AS6172 [REF]. This test assesses the area that the Runway Deicing Product (RDP) can undercut, measured in square millimetres per minute, from a substrate. Initially, a Petri dish, lined with a 120-grit silicon carbide abrasive paper, is filled with 60 ml of ASTM D1193 type IV water and positioned in a cold chamber at -10 °C. Following a minimum incubation period of 8 hours, 3 mm cavities are created using a 70 °C aluminum rod, and any resulting melted ice is extracted using a syringe. After an additional 2-hour period, 25 μl of dyed RDP is applied to the cavities. Subsequently, at 5, 10, and 30-minute intervals, two measurements are recorded, denoted as M1 and M2. The undercut area is determined by subtracting the initial area from the total undercut area, calculated using the average of M1 and M2.

-3. AS6170 Ice Melting

The third evaluation entails conducting the ice melting test method as outlined in AS6170 [REF], providing insight into the ice melting capabilities of Runway Deicing Products (RDP) in terms of grams per minute. Initially, a Petri dish is filled with 60 ml of ASTM D1193 type IV water and placed within a cold chamber at -10 °C. Following a minimum incubation period of 8 hours, the Petri dish, along with the formed ice, is weighed utilizing a calibrated 2-digit weighing instrument. Subsequently, 5 g of RDP is evenly distributed onto the ice sample. After the duration of 5 minutes, the brine, comprising a mixture of RDP and melted ice, is eliminated by tilting the dish and utilizing compressed air. The Petri dish is then reweighed, accounting for any remaining ice. The quantity of melted ice is determined by the difference between the final and initial masses. This process is iterated at intervals of 10 and 30 minutes, each conducted for three repetitions.

B. Anti-icing protection time test

The anti-icing protection time test (IPT) of a product is the time it resists weathering by preventing ice formation while keeping the surface wet [10]. Since the RDP dissolution reaction is endothermic, it is possible to determine the protection time of products by analysing the temperatures measured on the surface of product samples in real time. This protection time is estimated by IR thermography, using an Optris PI450, by exposing a concrete sample, previously coated with a fixed, low amount of product, to freezing drizzle precipitation under controlled conditions in a climatic chamber. The cold chamber temperature is maintained at -5°C and the precipitation intensity is maintained at 8.5 g/dm²·h. These conditions are representative of those found in natural environments. Infrared video recording is used to repeatedly determine the time it takes for ice to start to form over the protected area. This time is considered critical because ice formation can compromise safety by making the concrete surface more slippery. For reproducibility, the test is repeated three times for each product. The products can then be compared to determine which are the most effective. The figure below shows examples of the type of images obtained with the IR camera.
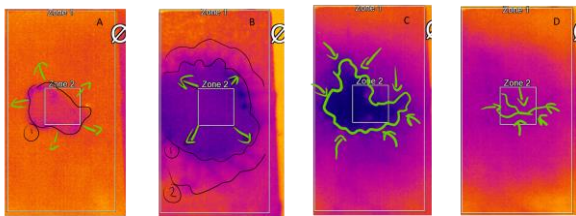
Fig. 1 Examples of IPT IR images: A - RDP diluted with water, temperature drops and areas expand, B - RDP at maximum dilution, ice begins to form around the edge, C - Ice forms on RDP toward the center, D - Ice completely formed.

C. Friction testing

Under the same icing conditions presented in the previous test, i.e. freezing drizzle, the effect of the products on skid resistance is evaluated under anti-icing conditions (SKID A) (when applied before precipitation) and under deicing conditions (SKID D) (when applied after icing) using the British Pendulum Tester in accordance with ASTM E303 [1]. For anti-icing, RDP is applied to the dry substrate surface with a syringe at three equidistant positions 1 ml each for a total of 3 ml. Precipitation is then initiated for a period of 10 minutes. After a waiting period of 20 minutes, the BPN reading is taken. For deicing, the substrate is precipitated for 10 minutes, then the product is placed on ice with a syringe at three equidistant positions 1 ml each for a total of 3 ml. After a waiting period of 20 minutes, the slip reading is taken. Each condition is repeated five times. When a measurement is taken, it is repeated 5 times on the same sample.

D. Performance Evaluation Criteria

To standardize the comparison of Runway Deicing Product (RDP) performance, a relative rating system out of 1 has been devised. This rating is determined by comparing each product's performance to the best values obtained in each category, with a ratio of 1 assigned to the best-performing product. A higher ratio indicates closer alignment with optimal performance, enabling manufacturers and airports to gauge product effectiveness and explore potential alternatives.

Additionally, for Ice Melting (IM), Ice Prevention (IP), and Ice Uncertainty (IU) parameters, consistent product conditions were maintained, with ratings averaged across four criteria: temperatures of -2°C and -10°C, and duration of 5 and 30 minutes. These criteria include IPT (Anti-icing Protection Time) for resistance against freezing drizzle precipitation, SKID A (Surface Skid Resistance after anti-icing treatment), and SKID D (Surface Skid Resistance after deicing treatment), facilitating comprehensive assessment of product efficacy in varying conditions.

E. Products Evaluated

Three reference products were evaluated in this article to demonstrate the potential of the method. These products are non-commercial and based on water freezing point depressants. The first product is potassium acetate (KAC) at 50% w/w in water with a freezing point of approximately -50°C. The second is potassium formate (KFO) at 50% w/w in water with a freezing point of about -50°C. The third is a mixture of 25% w/w propylene glycol, 25% w/w potassium acetate and the balance water. The freezing point is -35°C.

III. RESULTS

All of the results obtained with these products have been validated individually in other presentations, working groups, or scientific articles. In the context of this article, the results have been simplified, as the primary goal is to present a procedure for final integration into a standard. The main results are presented in a single figure. The choice of this type of graph makes it possible to quickly determine which product is the most effective among the six selected criteria. A Spyder chart is chosen for comparing results due to its ability to visually represent multiple variables simultaneously, facilitating quick and comprehensive comparisons across different parameters. Its radial layout and proportional axes allow for easy identification of strengths and weaknesses across various data points, aiding in decision-making processes. The most stable product is KFO. However, it is outperformed by KAC in almost all categories except SKID - deicing. Knowing that liquid products are rarely used alone for deicing, we could choose KAC despite its poor performance in this condition. Finally, the HYBRID could still be considered, as it offers average characteristics in all conditions.
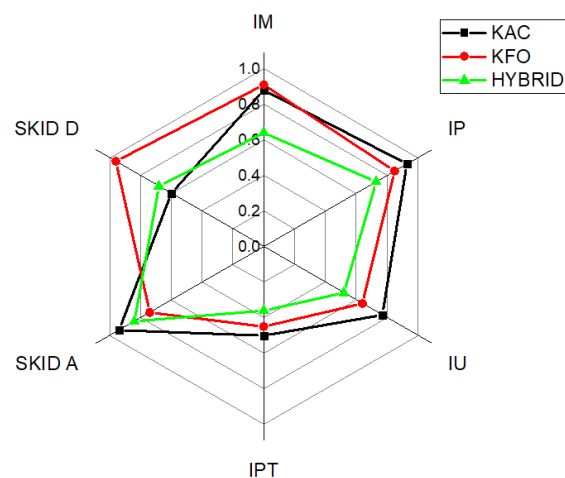
Fig. 2 - Main results obtained by the three RDPs in the 6-test procedure proposed for the standard.

The preliminary results presented relate only to the study of winter performance. To assist airports in their decision-making process, certain other criteria have already been evaluated in the AMS 1431 and 1435 standards. These include environmental impacts such as biodegradation rates, or even better, corrosion rates on aircraft carbon brakes. The could be added as pass/fail criteria

Performing these more detailed analyses on RDPs is beneficial to all parties involved. On the one hand, manufacturers will be able to know the performance of their products and thus propose more effective ones, using part of the tests carried out during the development phases. On the other hand, it will provide airports with the tools they need to select a product. Airports could impose such a procedure directly in the tendering process and ensure quality products.

IV. CONCLUSIONS

An aerospace standard to evaluate the performance of RDPs is currently being developed by SAE G12's RDP2WG. The standard will include tests to evaluate various aspects of product performance, such as deicing, anti-icing and slip performance. The manner in which the results are presented will allow for quick visualization and informed decision-making in product selection. The proposed standard will allow for the addition of several criteria related to the environment or aircraft brake degradation to assist airports in their improvement process. Lastly, the working group is dedicated to formulating a standardized method for determining the optimal application rate of deicing agents.

ACKNOWLEDGMENT

REFERENCES

[1] J.-D. Brassard, A. Beaulieu, M. M. Tremblay, and G. Momen, "Assessment of Runway Surface Conditions by British Pendulum Testing under the Global Reporting Format Winter Conditions," *Applied Sciences,* vol. 12, no. 19, p. 9646, 2022.

[2] *AMS1435 Fluid, Generic, Deicing/Anti-icing Runways and Taxiways*, Aerospace Material Specification AMS 1435, revision C, SAE International, June 2012 2012. [Online]. Available: http://www.sea.org

[3] Y. Niu, S. Zhang, G. Tian, H. Zhu, and W. Zhou, "Estimation for Runway Friction Coefficient Based on Multi-Sensor Information Fusion and Model Correlation," *Sensors,* vol. 20, no. 14, p. 3886, 2020.

[4] J. Procházka and M. Kameník, "Contaminated Runway Operations-Adverse weather," *MAD-Magazine of Aviation Development,* vol. 1, no. 4, pp. 3-7, 2013.

[5] Boeing. "Statistical Summary of Commercial Jet Airplane Accidents." https://www.boeing.com/resources/boeingdotcom/company/about_bca/pdf/statsum.pdf (accessed 2022-01-19, 2022).

[6] H. Lissner, M. Wehrer, M. Jartun, and K. U. Totsche, "Degradation of deicing chemicals affects the natural redox system in airfield soils," *Environmental Science and Pollution Research,* vol. 21, no. 15, pp. 9036-9053, 2014/08/01 2014, doi: 10.1007/s11356-013-2096-9.

[7] C. Charpentier, J.-D. Brassard, G. Momen, and J. Perron, "Development of a dynamic ice penetration model for runway de-icing products through performance experimental characterization," *Cold Regions Science and Technology,* p. 103932, 2023.

[8] C. Charpentier, J.-D. Brassard, M.-M. Tremblay, and G. Momen, "A Refined Procedure for Evaluating the Airport Runway De-icing Products Performance."

[9] *Advisory Circular (AC) No. 300-019: Global Reporting Format (GRF) for Runway Surface Conditions,* O. Transport Canada: Ottawa, Canada, 2021.

[10] J.-D. Brassard, C. Laforte, M. M. Tremblay, and C. Volat, "Runway Deicing Product Anti/Deicing Performance Assessment: Review and Future Directions," 2019. [Online]. Available: https://doi.org/10.4271/2019-01-1974.

[11] *AS6211 Ice Penetration Test Method for AMS1431 and AMS1435 Runway Deicing/Anti-icing Products*, Aerospace Standard AS6211, SAE International, 2021.

[12] *AS6172 Ice Undercutting Test Method for AMS1431 and AMS1435 Runway Deicing/Anti-icing Products*, Aerospace Standard AS6172, SAE International, 2021.

[13] *AS6170 Ice Melting Test Method for AMS1431 and AMS1435 Runway Deicing/Anti-icing Products*, Aerospace Standard AS6170, SAE International, 2021.

Optimizing Gridded Heater Arrangements in Anti-/De-icing Systems through Multiphysics Thermal Simulation

Adeel Yousuf, Hassan Abbas Khawaja, Muhammad Shakeel Virk

UiT – The Arctic University of Norway

yousuf.adeel@uit.no, hassan.a.khawaja@uit.no, muhammad.s.virk@uit.no

Abstract— **The electro-thermal system in anti-/de-icing systems, known for its reliability, is often favoured despite its notable drawback—high power consumption. Seeking to mitigate this issue, the adoption of a gridded heated surface emerges as a promising avenue for energy optimization. In this study, a finite difference method is employed to meticulously examine heat transfer across a selected surface with defined material properties. The simulation specifically investigates heat conduction under various boundary conditions, considering scenarios where a cold surface is either partially or fully heated in the presence of an ice cover. The discourse in this paper delves into the examination of different geometries of heating elements, assessing their impact on critical parameters such as overall power consumption, heating time, performance, efficiency and other relevant factors. By systematically analysing these variables, the study aims to offer insights into the efficacy of gridded heated surfaces as an energy-efficient alternative within electro-thermal systems. This research contributes to the ongoing quest for more sustainable and resource-conscious solutions, offering a nuanced understanding of how gridded heaters can optimize energy usage while maintaining the robustness associated with electro-thermal heating techniques in anti-/de-icing systems.**

Keywords— ***Finite difference, heat transfer, ice protection, system design, electrothermal***

I. Introduction

Ice accretion in the cold regions impacts onshore [1, 2], offshore [3, 4] and airborne structures [5, 6] rigorously, which necessitates the requirement of heating systems to allow for proper functioning of machines, stability of structures, and ventilation [7]. In Arctic regions, heating systems are part of common household necessities like car to commercial jetliners to avoid icing problems. A range of techniques exist that convert an available source of energy into thermal energy based upon the application, e.g.: photothermal, electrothermal, geothermal and thermochemical. Electrothermal heating among them is widely used for its efficiency, system portability, reliability, and safety – as no combustion or gas leakage risk is involved.

A conceptual idea to design an economical ice protection system was presented by Yousuf et al. [8] in which basic idea is to use active infrared thermography for ice detection purpose and gridded heaters for ice mitigation. Before moving on for system design implementation phase, preliminary heat transfer simulations are carried out to lay a foundation for an energy efficient heating strategy. Literature review was conducted in this domain to study about thermal analysis for different surfaces and aerofoil structures. Khawaja et al. [9] and Taimur et al. [10] performed dedicated research on

simulation leading to experimental verification for thermal signature of fresh water and saline ice cube. Mohseni et al. [11] made a comparative numerical heat transfer study for two different patterns of anti-icing heating elements (wires) that were embedded in polymer composite of aerofoil. Zhu et al. [12] assessed the performance of electrothermal de-icing system using 2D numerical approach; they simulated ice-water phase transition process via enthalpy method and studied AUX method for conductive heat transfer. Bennani et al. [13] conducted a detailed numerical study coupling unsteady ice accretion, heat conduction via electrothermal system, melting of ice, and boundary-layer flow.

Current paper is an extension of previous research conducted by Khawaja et al. [14-17] presents a 2D conductive numerical heat transfer simulation over a supposed aluminium surface holding heating elements from the perspective of heat flow and energy conservation. It is postulated that a gridded heated surface can offer a better optimization instead of a large heating surface. Two different test cases are presented in order to assess the proposition.

II. Numerical Study Of Conductive Heat Transfer

Temperature is a measure of heat energy and the variation of temperature (distribution of heat energy) in a given region of space over the transition of time is expressed by partial differential equation. This partial differential heat equation in 2-D in terms of diffusion coefficient (α) is expressed as:

$$\frac{\partial T}{\partial t} = \alpha \left(\frac{\partial^2 T}{\partial x^2} + \frac{\partial^2 T}{\partial y^2} \right); \begin{cases} t \geq 0 \\ 0 \leq x \leq L \\ 0 \leq y \leq W \end{cases}$$

where T is the temperature, t is time, (x, y) are spatial dimensions for length (L) and width (W), and α is the diffusion coefficient which is a material property.

The solution for this transient heat equation can be obtained for a finite time if initial conditions (at $t = 0$) and boundary conditions at $(x, y) = (0,0)$ and $(x, y) = (L, W)$ are known. To solve this partial differential equation is discretized using Finite Difference Method. Since the heat equation involves both first and second derivatives, it can be solved by Forward Time Centred Space (FTCS) discretization [18]. FTCS is employed for the purpose of this study by using forward difference for (time) transient term and central difference for spatial terms, i.e.:

$$\frac{T_{i,j}^{t+1} - T_{i,j}^t}{\Delta t} = \alpha \left(\frac{T_{i+1,j}^t - 2T_{i,j}^t + T_{i-1,j}^t}{(\Delta x)^2} + \frac{T_{i,j+1}^t - 2T_{i,j}^t + T_{i,j-1}^t}{(\Delta y)^2} \right)$$

where: subscript i, j denote computational points in spatial domain (x, y). $(\Delta x, \Delta y)$ formulate the mesh spacing, and Δt is the time step for simulation.

The solution for FTCS methodology resembles to that of a parabolic differential equation, that can become unstable for certain values of $\alpha, \Delta x, \Delta t$. Collecting these terms in above heat equation solution gives: $c_x = \alpha \frac{\Delta t}{\Delta x^2}; c_y = \alpha \frac{\Delta t}{\Delta y^2}$. These values (cx, cy) related to mesh sizing or mesh quality are called Courant numbers, and the stability criteria is defined as Courant–Friedrichs–Lewy (CFL condition) [19]. As per this criteria, they should be limited by a maximum value (typically less than 1) [20]. For this study, the values of $\alpha, \Delta x$, and Δt were chosen so that the Courant number was about 0.1.

III. SIMULATION SETUP

To study the conductive heat transfer over a surface from the perspective of heat flow and energy conservation, it is postulated that a gridded heated surface can offer a better optimization. To assess this conjecture a two-dimensional aluminium surface (100cm×50cm) subjected to icing and then de-icing, is simulated in MATLAB® and its heat transfer pattern is studied. For this purpose, two cases are chosen to analyse qualitatively: (i) comparison of a single heat source and gridded heaters (ii) comparison of heaters geometry. The simulations run for 500 sec and heater(s) turn on at t=5s. Assumed constant values related to mesh sizing and initial & boundary conditions are tabulated below in TABLE I and brief case description is given in TABLE II.

Some assumptions have been made while running the simulation:

a) Heat transfer is occurring only through conduction.
b) No heat loss is taking place via any face of rectangular sheet.
c) Heaters turn ON as a step function.
d) Presence of ice is simulated as a surface region with 253K (-20°C) temperature and its thickness is neglected so as to consider a 2D scenario.

TABLE I. DIFFERENT PARAMETERS CONSIDERED DURING MATLAB SIMULATION FOR HEAT TRANSFER

Constant Parameters	
Diffusion Constant (α)	0.1 cm^{2}s^{-1}
Time Step (Δt)	1 s
Spatial Domain Step ($\Delta x, \Delta y$)	(1s, 1s)
Initial Conditions	
Metal Sheet Temp.	255 K (-18°C)
Boundary Conditions	
Ambient Air Temp. (all 4 sides)	258 K (-15°C)
Other Constants	
Heater Temp	400 K (673°C)
Heater Turn ON Instant	t = 5s (& onwards)
Aluminum Specific Heat	0.90 J/(g.°C)$^{-1}$

With the conditions described in Table-I, the same heating pattern is obtained in all test cases for the first 4 secs when the heaters are off. So, they are separately shown in Figure-1. The

rectangular contour in the centre of the upper plot is iced region at 253K and surrounding zone describes metal temperature at 255K. In the elapsed time till 4s, heat diffuses from hot region (sheet) to the cold region (ice block) which appears as a thermal gradient shaded according to colour bar and chosen palette. Similarly, the contours on the outer border describe heat flow from boundary (hot air) towards metal sheet (cold zone).

IV. SIMULATION RESULTS

A. Case-1: Heaters Quantity

Conventional approach for commercial anti-icing and de-icing systems is to use a single heating element that spans across the target surface, for instance in case of leading edge of aileron for conduction. To assess the concept of gridded heaters for a rectangular sheet, a case of two heaters spanning across its length is compared to a matrix of 18 heaters (3×6). Two heaters are considered instead of single heater so that heat transfer can be studied better visually because otherwise single heater would maintain 400K temperature on a larger area of the sheet for whole duration when it turns on.

TABLE II. TEST CASES CONSIDERED TO ANALYSE GRIDDED HEATERS CONCEPT

194
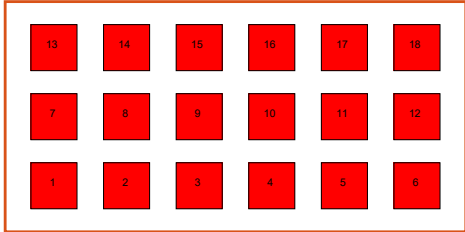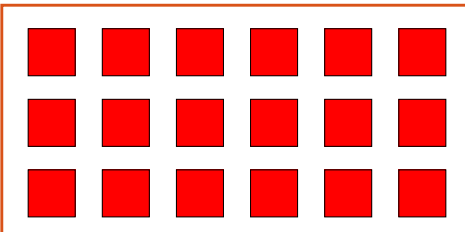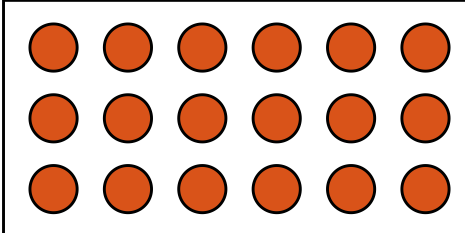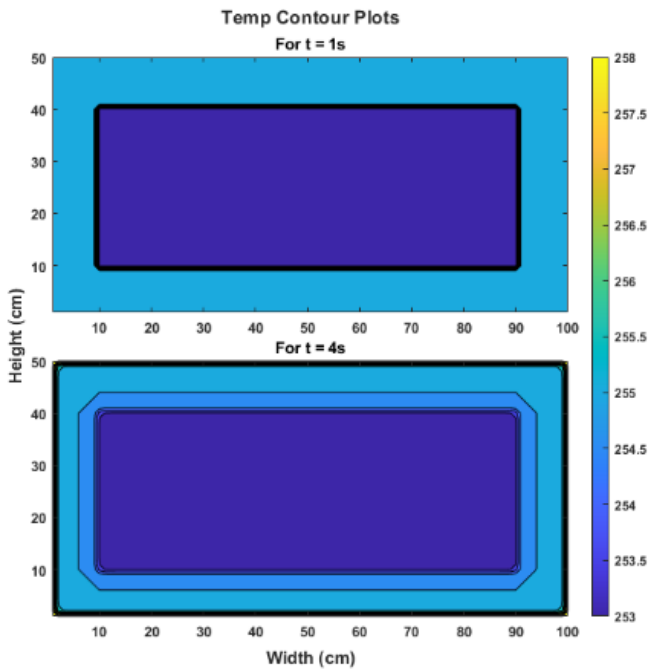
Fig. 1   Thermal contour plots for t = 1s and t = 4s.

Figure 1 shows the heating pattern for the two spanning heaters and Figure 2 shows its corresponding gridded heaters concept. Although the two heaters maintain the temperature across the covered area, the gaps in between the heaters exhibit low temperature zones till at least $t = 150s$.

B. Case-2: Heaters Geometry

In this case 18 square and circular heating elements are simulated with dimensions 10 cm length and 10 cm diameter respectively. Horizontal and vertical spacing between heaters is set as 5.6cm and 5cm respectively, and same values are considered for horizontal and vertical border margins as well. Figure 3 and Figure 4 below describe the heating patterns for square and circular heaters in which it is quite evident that former ones reach thermal equilibrium at much greater rate than the latter case, i.e., square heaters achieved it at around 150s and after that the temperature transition is almost at steady state. Cold temperature zones are present between heaters in both the cases till at least 80s however due to less area occupied by a circle ($(5 \times 5)\pi = 78.5$ cm^2) than a square ($10 \times 10 = 100$ cm^2), circular heaters have to work more. In other words, if pulse heating is to be used then on-time for circular heaters will be more than square ones. Some interesting and opposing patterns are observed in both the cases, for example at t = 80s: in case of square heaters the centre of aluminium sheet will acquire equilibrium late as compared to the left/right sides. This pattern is totally opposite in case of circular heaters.
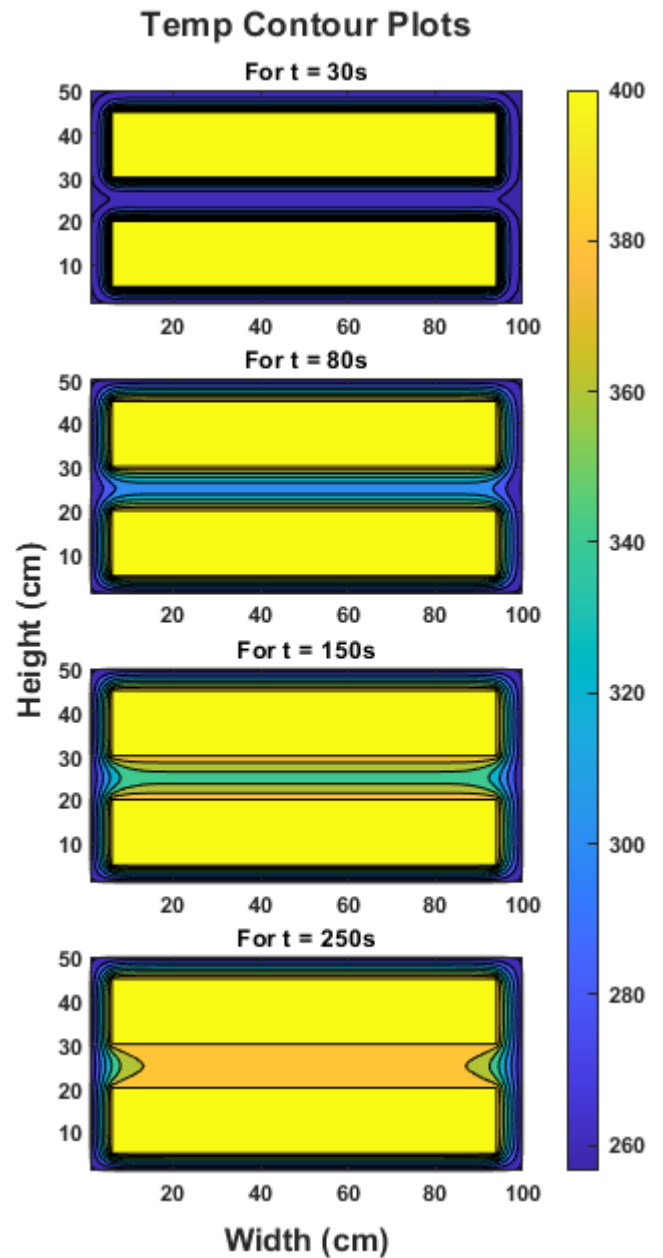
Fig. 2   Heating pattern for the case of heaters spanning across the sheet.

It can also be observed at later time instants: t = 150s and 250s that temperature evolution follows the order: centre – (then) left/right – (then) centre left/centre right of the sheet. The contours around the border attain almost similar pattern throughout the simulation for both geometries as fixed boundary conditions for atmospheric temperature are assumed.

Temp Contour Plots
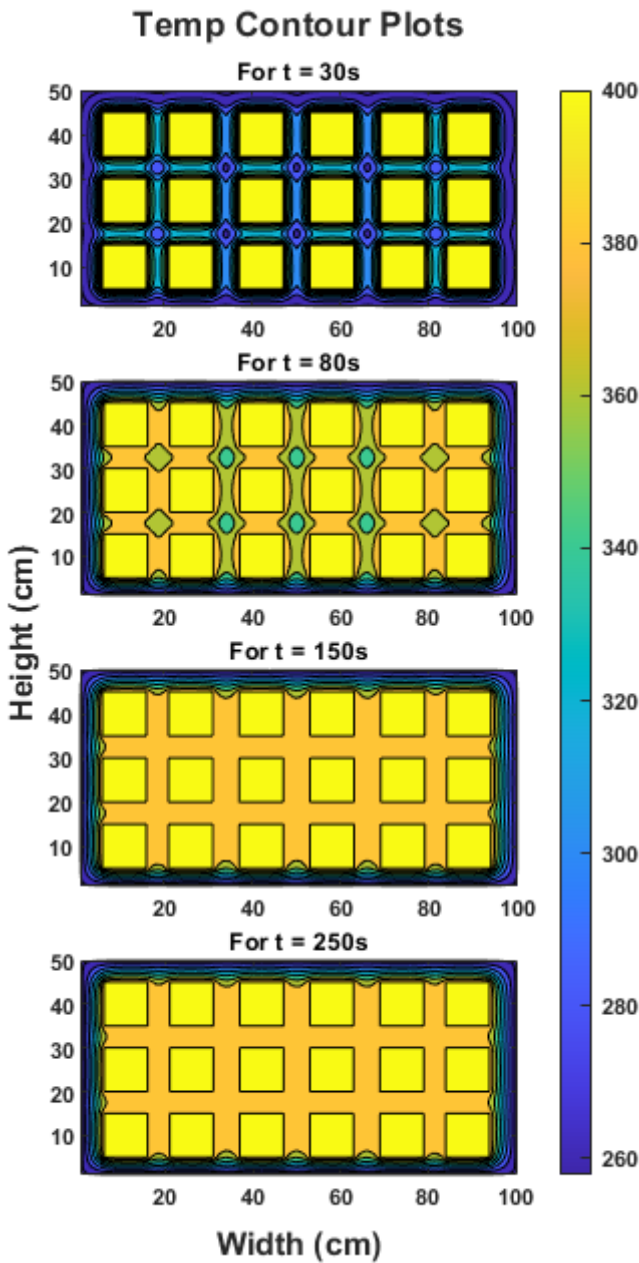
Fig. 3   Heating pattern for square heaters.

Fig. 4   Heating pattern for circular heaters.

V. CONCLUSION

Despite the evident disadvantage of high-power consumption of electrothermal heating systems in general, their comparatively high efficiency, safety, reduced weight, and possibility to implant or embed in different materials still makes them a choice for certain applications. This study presents the concept of a gridded heated surface created through small heaters against a conventional approach in which whole surface is heated by large heater. Two dimensional simulations for conductive heat transfer are carried out in MATLAB using finite difference method. Two test cases are considered concerning the overall concept of gridded heaters and their geometry. Results suggest that gridded heaters allow the thermal equilibrium to be reached earlier and consume low power per unit mass. They also allow more control to the user for heating a specific portion of target surface. In case of geometrical shape, heat transfer for square and circular heaters revealed opposite patterns: for square heaters thermal gradient is established from lateral sides towards the centre, whereas for circular heaters its direction is from the centre and lateral sides of sheet towards their in-between space. Nonetheless overall heat transfer rate is high for square heaters but the expense of more power per unit mass. Selection of suitable heating elements may depend upon various factors, such as financial/maintenance cost, application, and shape of target surface. So, the study does not intend to reject one geometry for the other for any general case study. The simulation work is a preliminary step towards the development of actual hardware setup for an energy optimized ice protection system.

196

REFERENCES

[1] A. Lotfi and M. S. Virk, "Railway operations in icing conditions: a review of issues and mitigation methods," Public Transport, 2023.

[2] H. A. Khawaja, H. Xue, H.-K. Eidesen, Z. Andleeb, and M. Moatamedi, "Ice shedding from wind turbines," in Multiphysics of Wind Turbines in Extreme Loaded Conditions (Multiphysics: Advances and Applications): Academic Press, 2024, ch. 6, pp. 139-168.

[3] K. Wei, Y. Yang, H. Zuo, and D. Zhong, "A review on ice detection technology and ice elimination technology for wind turbine," (in English), Wind Energy, vol. 23, no. 3, pp. 433-457, 2020.

[4] T. Rashid, H. A. Khawaja, and K. Edvardsen, "Review of marine icing and anti-/de-icing systems," Journal of Marine Engineering & Technology, vol. 15, no. 2, pp. 79-87, 2016.

[5] A. Samad, E. Villeneuve, C. Blackburn, F. Morency, and C. Volat, "An experimental investigation of the convective heat transfer on a small helicopter rotor with anti-icing and de-icing test setups," Aerospace, vol. 8, no. 4, 2021.

[6] A. Shinkafi and C. Lawson, "Enhanced method of conceptual sizing of aircraft electro-thermal de-icing system," International Journal of Aerospace and Mechanical Engineering, vol. 8, no. 6, 2014.

[7] A. Yousuf, H. Khawaja, and M. S. Virk, "A review of infrared thermography applications for ice detection and mitigation," Cold Regions Science and Technology, vol. 218, no. 104058, 2024.

[8] A. Yousuf, H. A. Khawaja, and M. S. Virk, "Conceptual design of cost-effective ice detection system based on infrared thermography," Cold Regions Science and Technology, vol. 215, no. 103941, 2023.

[9] H. Khawaja, T. Rashid, O. Eiksund, E. Brodal, and K. Edvardsen, "Multiphysics simulation of infrared signature of an ice cube," The International Journal of Multiphysics, vol. 10, no. 3, pp. 291-302, 2106.

[10] T. Rashid, H. A. Khawaja, and K. Edvardsen, "Determination of Thermal Properties of Fresh Water and Sea Water Ice using Multiphysics Analysis," The International Journal of Multiphysics, vol. 10, no. 3, pp. 277-290, 2016.

[11] M. Mohseni and A. Amirfazli, "A novel electro-thermal anti-icing system for fiber-reinforced polymer composite airfoils," Cold Regions Science and Technology, vol. 87, pp. 47-58, 2013.

[12] C.-X. Zhu, Y. Wang, N. Zhao, C.-L. Zhu, and C.-Y. Liu, "Numerical simulation and experimental verification of the airfoil electrothermal deicing system performance," Journal of the Chinese Institute of Engineers, vol. 44, no. 7, pp. 608-617, 2021.

[13] L. Bennani, P. Trontin, and E. Radenac, "Numerical simulation of an electrothermal ice protection system in anti-icing and deicing mode," Aerospace, vol. 10, no. 1, 2023.

[14] A. N. Leyli, H. Khawaja, M. Moatamedi, and B. Alzahabi, "Multiphysics Study of Forced Convection Conjugate Heat Transfer (CHT) Problem," The International Journal of Multiphysics, vol. 13, no. 3, pp. 215-229, 2019.

[15] T. Rashid, H. Lang, M. Taimur, N. Chiodarelli, M. Volder, K. Edvardsen, H. A. Khawaja, "Roll to Roll coating of carbon nanotube films for electro thermal heating," Cold Regions Science and Technology, vol. 182: no. 103210, 2021.

[16] A. N. Leyli, Z. Andleeb, H. Khawaja, R. Messahel, R. Kanna, M. Moatamedi. Conjugate Heat Transfer Model Based on SIMPLE and Coupled Energy and Heat Equations. The International Journal of Multiphysics, vol. 15, no. 1, pp. 29-47, 2021.

[17] T. Rashid, H. A. Khawaja, K. Edvardsen, "Measuring Thickness of Marine Ice Using IR Thermography," Cold Regions Science and Technology, vol. 158, pp. 221 – 229, 2018.

[18] H. Khawaja, "Applicability extent of 2-D heat equation for numerical analysis of a multiphysics problem," in 11th International Conference on Mathematical Problems in Engineering, Aerospace and Sciences, La Rochelle, France, 2016, vol. 1798, no. 1, 2017.

[19] R. Courant, K. Friedrichs, and H. Lewy, "Über die partiellen Differenzengleichungen der mathematischen Physik," Mathematische Annalen, 1928.

[20] H. Khawaja, "Solution of Pure Scattering Radiation Transport Equation (RTE) Using Finite Difference Method (FDM)," in Image Analysis (SCIA 2017), vol. 10269, P. Sharma and F. Bianchi Eds.: Springer, Cham, 2017.

Effect of safflower oil on large-scale deicing performance of polyurethane coatings

Tao Zhu[1], Yuan Yuan[1*], Xingde Wei[1], Linbo Song[1], Xujiang Hua[1], Huiying Xiang[1], Xu Dai[2]

[1] *College of Materials Science and Engineering, Chongqing University, Chongqing 400044, China*
[2] *State Key Laboratory of Power Transmission Equipment & System Security and New Technology, Chongqing University, Chongqing 400044, China*

davezhu@cqu.edu.cn, yuany@cqu.edu.cn, 202209021042@stu.cqu.edu.cn, 202109021149t@cqu.edu.cn, 20230901040@stu.cqu.edu.cn, 20200901052@cqu.edu.cn, xudai@cqu.edu.cn

Abstract— **Ice covering on surfaces such as aircraft and wind turbine blades interferes with stable operation and even causes major safety incidents. Potentially applicable icephobic materials like superhydrophobic and super-lubricated coatings are believed to be passive anti-icing technologies. However, the deicing force of icephobic coatings generally increases with the increase in the icing area, constraining their applications. A low-interfacial toughness material has gained wide attention for breaking the limitation of deicing force being restricted by the icing area. Herein, polyurethane coatings were prepared by drop coating a well-stirred mixed solution of polyurethane and safflower oil onto an aluminum plate. The added safflower oil adjusts the interfacial toughness of polyurethane. There exists a critical length of strength-controlled to toughness-controlled transition in the deicing force of polyurethane coatings. Beyond the critical length, the deicing force remains constant. Furthermore, the deicing force and interfacial toughness of the polyurethane coatings exhibit a tendency of first decreasing and then increasing with the growth of safflower oil content. The difference is that the critical length is slowly increasing while the ice adhesion strength is gradually decreasing. Adding 15% safflower oil has the lowest deicing force and interfacial toughness, which is conducive to large-scale deicing. The low-interfacial toughness polyurethane coatings have the potential for effective large-scale deicing and show promise for applications.**

Keywords— *Polyurethane; Coating; Safflower oil; Large-scale; Deicing*

I. INTRODUCTION

As a natural disaster, the icing often occurs, threatening the safe operation of aircraft and wind turbines. The ice layer will change the aerodynamic characteristics of the surface, affecting the stability and maneuverability of the aircraft, posing significant safety hazards [1]. For the wind turbines, the ice covering can lead to power loss, mechanical failures and security risks caused by falling ice [2,3]. Therefore, the research on anti-icing/deicing technology for aircraft and wind turbine blades is urgently needed.

The traditional deicing technologies, such as mechanical deicing, electrothermal deicing and gas-thermal deicing, offer good efficiency and are widely applied. However, the deicing technologies require complex equipment and a large amount of investment [4]. At this time, the passive anti-icing technologies based on coatings without energy consumption have received widespread attention. The most typical ones are the hydrophobic and superhydrophobic coatings that utilize excellent hydrophobicity for anti-icing/deicing [5,6]. In combination with a micro-nano rough structure and low surface energy substances, a large number of air cushions are formed on the surface of the superhydrophobic coatings. This effectively retards the freezing of water droplets and reduces the ice adhesion strength [6]. The superhydrophobic coatings may face the defect of anti-icing failure in low temperature and high humidity environments [7,8]. In addition, there are super-lubricated coatings that achieve ultra-low ice adhesion strength by utilizing a layer of lubricant to cause slippage [9]. The lubricant on the surface also reduces the nucleation temperature of water droplets and delays icing [10]. Besides, the poor durability of super-lubricated coatings limits their application [11,12]. On the other hand, the deicing force of superhydrophobic and super-lubricated coatings tends to increase as the icing area expands. This is not conducive to timely deicing of large ice-covered areas on the surface of aircraft and wind turbine blades. In this case, the low-interfacial toughness coatings have shown excellent large-scale deicing performance [13–15]. The deicing force of low-interfacial toughness coatings remains almost constant as the icing area increases [13]. Along with this, the ice adhesion strength gradually decreases, which facilitates efficient large-scale deicing [14,15]. It has been reported that polyurethane, which is commonly used for anti-erosion of wind turbine blades, exhibits low ice adhesion strength and can be employed as a favorable candidate for anti-icing or deicing coatings [16,17]. The great resilience and weather resistance also provide polyurethane with the possibility to realize large-scale deicing. Therefore, as a potential low-interfacial toughness material, the large-scale deicing performance of the polyurethane coatings deserves to be investigated.

In this study, polyurethane coatings with low interfacial toughness were prepared on aluminum plates using drop coating. Different contents of safflower oil were added to modulate the interfacial toughness of the polyurethane. The effect of safflower oil content on the large-scale deicing performance of the polyurethane coatings was evaluated by microscopic characteristics, wettability, deicing force and ice adhesion strength.

II. MATERIALS AND METHODS

A. Materials

Aluminum plates (1060) were provided by Shenzhen Hongnian Metal Materials Co., Ltd. Polyurethane (VytaFlex 40) was purchased from Beijing Angelcrete Art Landscaping Co., Ltd. Safflower oil was supplied by Heowns Biochem Co., Ltd. Ethyl acetate was obtained from Chengdu Kelong

Chemical Co., Ltd. Anhydrous ethanol was bought from Chongqing Chuandong Chemical (Group) Co., Ltd.

B. Preparation

First, the 1060 aluminum plates were cleaned with anhydrous ethanol. The aluminum plates were placed in an oven at 70 °C for drying. Then, 5 g of polyurethane A component was added to a beaker. Sequentially, 5 g of polyurethane B component, a certain amount of safflower oil and an appropriate amount of ethyl acetate were added. The solution of 100 mg/ml was formulated by stirring for 2–3 min. The well-mixed solution was poured onto the aluminum plates by drop coating. Finally, the aluminum plates were subjected to an oven at 70 °C overnight. Among them, different masses of safflower oil were added to prepare polyurethane coatings with safflower oil content of 0%, 5%, 10%, 15% and 20%.

C. Characterization

The microscopic morphology and elemental composition of the samples were characterized by scanning electron microscopy (SEM, Zeiss Auriga) and energy dispersive spectroscopy (EDS). The contact angle (CA) and contact angle hysteresis (CAH) of the samples were determined using a water contact angle meter (SINDIN SDC-100). The volume of the test water droplets was approximately 3 μL. Five positions were measured and averaged. The deicing force was measured on the sample surface using a semiconductor cooling platform [6]. The sample was placed horizontally on the cooling plate. The rectangular molds of different sizes were placed on the sample surface. The width and height of the molds were 1 cm. The lengths were 0.5, 1, 2, 4, 6, 8, 10, 12.5, 15, 17.5, 20 and 25 cm [15]. The mold was filled with tap water. The temperature of the cooling plate was set to –10 °C and held for about 60 min to ensure that the water inside the mold was completely frozen. The mold was pushed away from the sample surface by a moving guide controlled by a stepper motor. The peak deicing force was recorded by a force transducer. The speed of the moving guide was 74 μm/s [13]. In addition, the ice adhesion strength was calculated from the peak force and the ice area.

III. RESULTS AND DISCUSSION

A. Microscopic Morphology

The microscopic morphology of the polyurethane coatings with different contents of safflower oil is shown in Fig. 1. It can be found that the surface of all the samples is relatively smooth. With the increase of safflower oil content, a small number of protrusions and holes appear on the surface of the polyurethane coatings. This is due to the fact that the safflower oil hinders the crosslinking of the polyurethane and interferes with the curing process of the polyurethane coating to a certain extent. At the same time, a large amount of safflower oil will also plasticize the polyurethane (lowering the elastic modulus) to achieve modulation of the interfacial toughness. Moreover, the more uniform surface of the film also means that the safflower oil is successfully blended with the polyurethane.

B. Elemental Composition

The elemental distribution of the polyurethane coating with 15% safflower oil content is presented in Fig. 2. There

are homogeneous C, N, O and Al elements distributed on the surface. Among them, the C element has a high percentage of 61.6%, which is mainly derived from polyurethane and safflower oil. The Al element is originated from the substrate material. In addition, the detected N and O elements prove the presence of urethane chain segments. These indicate the successful preparation of polyurethane coatings with added safflower oil.
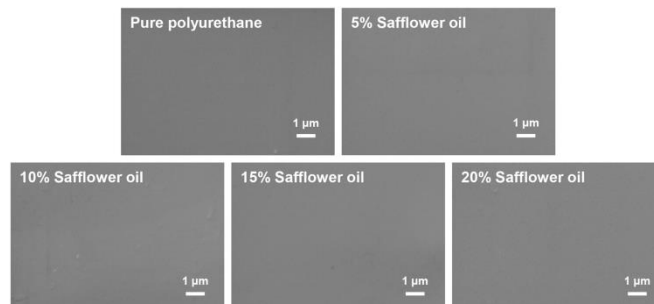
Fig. 1 Microscopic morphology of polyurethane coatings.
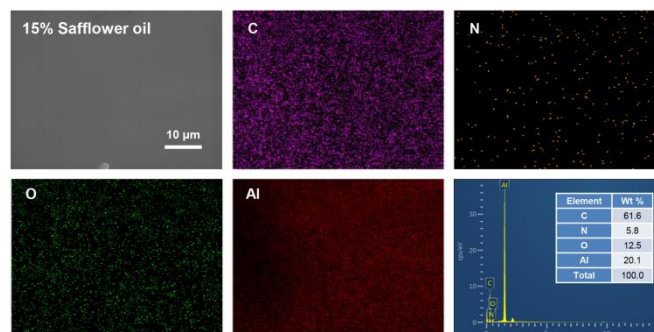
Fig. 2 Elemental composition of polyurethane coating with 15% safflower oil content.

C. Wettability

The contact angle and contact angle hysteresis of the polyurethane coatings are displayed in Fig. 3. There is a significant effect of safflower oil on the wettability of the polyurethane coatings. The contact angle of the polyurethane coatings decreases with the increase of safflower oil content. The contact angle is reduced from 87.6° to 75.1°. This is attributed to the hydrophilic safflower oil spreading on the surface of polyurethane. Furthermore, the contact angle hysteresis of the polyurethane coatings with added safflower oil decreases dramatically compared to the pure polyurethane (44.5°). The contact angle hysteresis of the polyurethane coatings with different safflower oil contents is about 30°. This suggests that safflower oil can enhance the dynamic anti-wettability of polyurethane. Therefore, the polyurethane coatings can provide good icephobicity under the sliding action of safflower oil.

D. Large-scale Deicing Performance

The variation of deicing force of the polyurethane coatings with length is shown in Fig. 4. The deicing force of the pure polyurethane increases linearly with increasing length. This implies that the deicing force of the pure polyurethane is mainly controlled by the strength [13]. For the polyurethane coating with safflower oil content of 5%, the deicing force exhibits an increasing trend. This suggests that the less safflower oil has a limited effect on the deicing force of the polyurethane. When the safflower oil content reaches 10%,

the deicing force curve of the polyurethane coating presents a significant transition (critical length). As the length is smaller than the critical length, the deicing force of the polyurethane coatings is dominated by the strength, which gradually increases. After the length exceeds the critical length, the deicing force of the polyurethane coatings is governed by the interfacial toughness, which remains almost constant. This indicates that the addition of appropriate safflower oil can effectively regulate the interfacial toughness of the polyurethane to realize large-scale deicing. It can be inferred that with the increase of ice-covered area, the ice adhesion strength of the polyurethane coatings will gradually decrease, which is conducive to timely deicing [15]. To sum up, the polyurethane coatings prepared by adding safflower oil demonstrate good large-scale deicing performance.
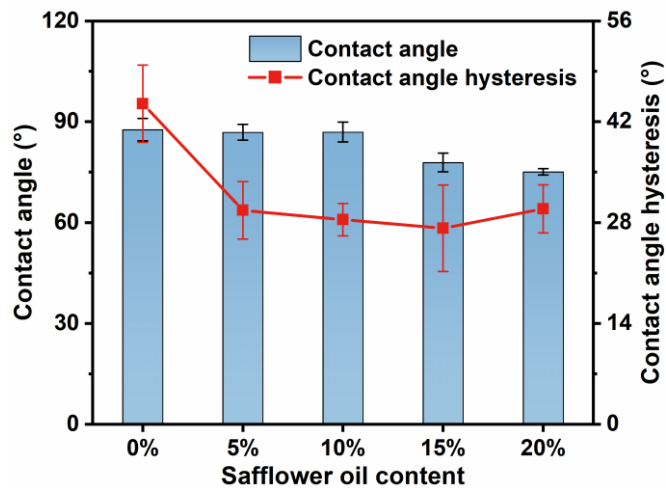
Fig. 3   Contact angle and contact angle hysteresis of polyurethane coatings.

The constant deicing force and critical length of the polyurethane coatings were extracted as displayed in Fig. 5. The deicing force of the pure polyurethane and polyurethane coating with 5% safflower oil shows no observed transition from strength control to toughness control (Fig. 4). Therefore, the critical length is more than 25 cm and there is no constant deicing force [15]. A critical length emerges for the polyurethane coatings with safflower oil content above 10%. This indicates that the safflower oil can offer the potential for large-scale deicing of polyurethane. The constant deicing force of the polyurethane coatings first decreases and then increases as the safflower oil content is further increased. Unusually, the critical length of the polyurethane coatings exhibits a gradually increasing trend. From the critical length (7.2 cm), the polyurethane coating with 10% safflower oil has the fastest rate of transition from strength to toughness. However, for ultra-large aircraft or wind turbine blades, the constant deicing force has a more pronounced influence on the deicing efficiency. Whereas, the polyurethane coating with 15% safflower oil possesses the lowest constant deicing force (116.1 N/cm). As a result, the polyurethane coating with 15% safflower oil demonstrates the best large-scale deicing performance compared to the other polyurethane coatings.

In addition to constant deicing force and critical length, ice adhesion strength is also critical for deicing [6,9,13,14]. The ice adhesion strength of the polyurethane coatings is shown in Fig. 6. It is clearly seen that the ice adhesion strength of the polyurethane coatings gradually decreases with the increase of safflower oil content. In this case, the ice adhesion strength of the pure polyurethane is as high as 283.8 kPa. In contrast, the ice adhesion strength of the polyurethane coatings with the addition of safflower oil decreases significantly. The ice adhesion strength of the polyurethane coatings with 10, 15 and 20% safflower oil is 180.2, 120.0 and 105.5 kPa, respectively, which is about two times lower than that of the pure polyurethane. This is attributed to the plasticizing effect brought about by safflower oil reducing the elastic modulus [13-15]. Additionally, the added safflower oil forms a lubricant layer on the surface, which can remarkably reduce the ice adhesion strength [9,10]. Therefore, the safflower oil also enhances the icephobicity of polyurethane. On the other hand, it is important to point out that an excessive amount of safflower oil (20% content) can degrade durability by deteriorating mechanical properties [10-12]. Combined with the constant deicing force (Figs. 4 and 5) and ice adhesion strength (Fig. 6), it can be found that the polyurethane coating with 15% safflower oil has good large-scale deicing performance and icephobicity, which has potential applications. In conclusion, large-scale deicing can be realized by modulating the interfacial toughness of polyurethane with appropriate addition of safflower oil.
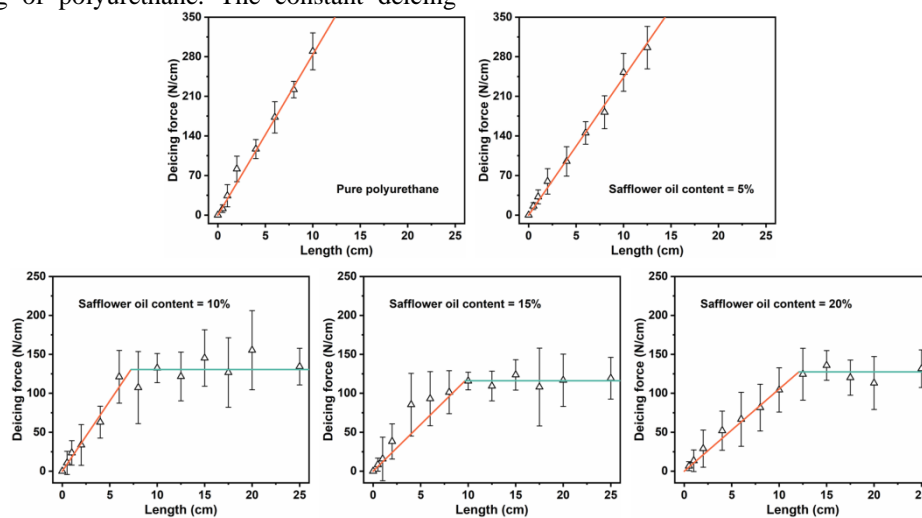
Fig. 4   Variation of deicing force with length for polyurethane coatings.
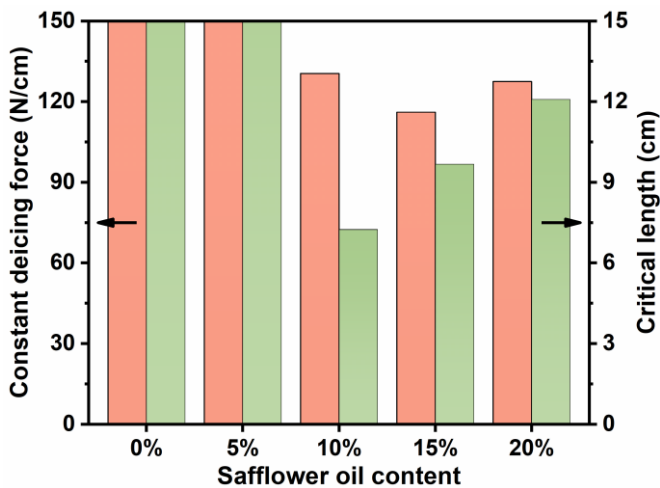
Fig. 5 Constant deicing force and critical length of polyurethane coatings.
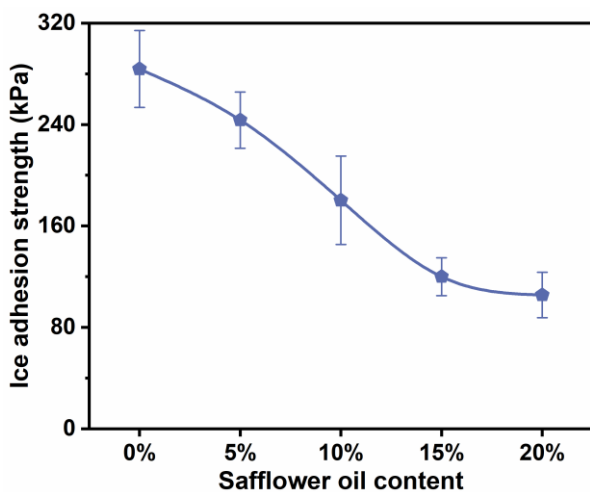
Fig. 6 Ice adhesion strength of polyurethane coatings.

IV. CONCLUSIONS

Polyurethane coatings were prepared by drop coating on aluminum plates. The effect of safflower oil on the large-scale deicing performance of the polyurethane coatings was investigated. Unlike the pure polyurethane where the deicing force increased linearly, there was a constant deicing force controlled by the interfacial toughness of the polyurethane coatings as the icing area expanded. Also, the polyurethane coatings with added safflower oil exhibited lower deicing force and ice adhesion strength than the pure polyurethane. This is due to the plasticizing and slip effect of safflower oil. The constant deicing force of the polyurethane coatings increased and then decreased with increasing safflower oil content. In particular, the polyurethane coating with 15% safflower oil combined good large-area deicing performance and icephobicity. The constant deicing force, critical length and ice adhesion strength were 116.1 N/cm, 9.7 cm and 120.0 kPa, respectively. The large-scale deicing property of polyurethane can be regulated by the simple addition of safflower oil, which has certain reference value for the preparation of low-interfacial toughness coatings.

REFERENCES

[1] Y. H. Cao, W. Y. Tan, and Z. L. Wu, "Aircraft icing: An ongoing threat to aviation safety," Aerosp. Sci. Technol., vol. 75, pp. 353–385, Apr. 2018.

[2] L. Y. Gao and J. R. Hong, "Wind turbine performance in natural icing environments: A field characterization," Cold Reg. Sci. Tech., vol. 181, pp. 103193, Jan. 2021.

[3] O. Fakorede, Z. Feger, H. Ibrahim, A. Ilinca, J. Perron, and C. Masson, "Ice protection systems for wind turbines in cold climate: characteristics, comparisons and analysis," Renew. Sust. Energ. Rev., vol. 65, pp. 662–675, Nov. 2016.

[4] E. Madi, K. Pope, and W. M. Huang, "A new method to limit thermal energy required to de-ice the leading edge of a cylindrical surface," Cold Reg. Sci. Tech., vol. 217, pp. 104045, Jan. 2024.

[5] L. Fan, B. Li, Y. Wang, J. H. He, J. Bai, T. Zhu, and Y. Yuan, "Superhydrophobic Epoxy/Fluorosilicone/PTFE Coatings Prepared by One-Step Spraying for Enhanced Anti-Icing Performance," Coatings, vol. 13, pp. 569, Mar. 2023.

[6] T. Zhu, Y. Yuan, H. Y. Xiang, G. Y. Liu, X. Dai, L. B. Song, and R. J. Liao, "A composite pore-structured superhydrophobic aluminum surface for durable anti-icing," J. Mater. Res. Technol-JMRT, vol. 27, pp. 8151–8163, Dec. 2023.

[7] K. K. Varanasi, T. Deng, J. D. Smith, M. Hsu, and N. Bhate, "Frost formation and ice adhesion on superhydrophobic surfaces," Appl. Phys. Lett., vol. 97, pp. 234102, Dec. 2010.

[8] J. Chen, J. Liu, M. He, K. Y. Li, D. P. Cui, Q. L. Zhang, X. P. Zeng, Y. F. Zhang, J. J. Wang, and Y. L. Song, "Superhydrophobic surfaces cannot reduce ice adhesion," Appl. Phys. Lett., vol. 101, pp. 111603, Sep. 2012.

[9] H. Y. Xiang, Y. Yuan, C. Zhang, X. Dai, T. Zhu, L. B. Song, Y. Gai, and R. J. Liao, "Key Factors Affecting Durable Anti-Icing of Slippery Surfaces: Pore Size and Porosity," ACS Appl. Mater. Interfaces, vol. 29, pp. 3599–3612, Dec. 2022.

[10] X. T. Zhou, Y. L. Sun, and J. Liu, "Designing Anti-Icing Surfaces by Controlling Ice Formation," Adv. Mater. Interfaces, vol. 8, pp. 2100327, Aug. 2021.

[11] P. Baumli, M. D'Acunzi, K. I. Hegner, A. Naga, W. S. Y. Wong, H. J. Butt, and D. Vollmer, "The challenge of lubricant-replenishment on lubricant-impregnated surfaces," Adv. Colloid Interface Sci., vol. 287, pp. 102329, Jan. 2021.

[12] W. H. Yao, L. Wu, L. D. Sun, B. Jiang, and F. S. Pan, "Recent developments in slippery liquid-infused porous surface," Prog. Org. Coat., vol. 166, pp. 106806, May. 2022.

[13] K. Golovin, A. Dhyani, M. D. Thouless, and A. Tuteja, "Low-interfacial toughness materials for effective large-scale deicing," Science, vol. 364, pp. 371–375, Apr. 2019.

[14] Y. D. Yu, L. Chen, D. Weng, Y. C. Hou, Z. B. Pang, Z. W. Zhan, and J. D. Wang, "Effect of Doping SiO2 Nanoparticles and Phenylmethyl Silicone Oil on the Large-Scale Deicing Property of PDMS Coatings," ACS Appl. Mater. Interfaces, vol. 14, pp. 48250–48261, Oct. 2022.

[15] T. Zhu, Y. Yuan, L. B. Song, X. D. Wei, H. Y. Xiang, X. Dai, X. J. Hua, and R. J. Liao, "A PDMS coating with excellent durability for large-scale deicing," J. Mater. Res. Technol-JMRT, vol. 29, pp. 4526–4536, Feb. 2024.

[16] Y. H. Ng, S. W. Tay, and L. Hong, "Ice-phobic polyurethane composite coating characterized by surface micro silicone loops with crumpling edges," Prog. Org. Coat., vol. 172, pp. 107058, Nov. 2022.

[17] H. Memon, D. S. A. De Focatiis, K. S. Choi, and X. H. Hou, "Durability enhancement of low ice adhesion polymeric coatings," Prog. Org. Coat., vol. 151, pp. 106033, Feb. 2021.

Impact of Deicer Reapplication Frequency on Runway Deicing Model

Aida Maroufkhani[1], François Morency[1], Gelareh Momen[2]

[1]*Département de génie mécanique, École de technologie supérieure, Montréal, Canada*
[2]*Département des sciences appliquées, Université du Québec à Chicoutimi, Chicoutimi, Canadae*

aida.maroufkhani.1@ens.etsmtl.ca, francois.morency@etsmtl.ca, gelareh.momen@uqac.ca

Abstract— **The deicing procedure is a critical winter maintenance task for airports, requiring the substantial use of deicing chemicals to melt ice and snow. Deicing models exist for road pavements and they help compute the appropriate deicer quantity and time for reapplication. The application of such models to runway could help achieve an enhanced melting rate for the runway. In this study, we propose a model designed for runway ice melting through the application of a chemical solution. Our model is proficient at analyzing the melting rate of deicing materials on the runway pavement. Hence, we can analyze the effects of frequency and quantity of deicer reapplications. Our model incorporates temperature and diffusive flux variations over time in the normal direction as key factors to predict melted ice mass. Additionally, it calculates the mass and heat transfer within three distinct regions, encompassing the liquid, mushy, and solid phases. The enthalpy method addresses the Stefan problem, wherein the solid, liquid, and interface regions utilize enthalpy to predict temperature changes considering the specific heat. The temporal and spatial evolution of deicer concentration is modeled using Fick's law. The variable melting point temperature stems from the dilution of the deicer within the solution. This paper contrasts temperature variations and melted ice mass results through the reapplication of varying deicer quantities at different time intervals and considering wind velocity. Additionally, we will compare the melting rates of two products for runway deicing — potassium acetate and potassium formate.**

Keywords— ***Runway Deicing, deicer reapplication, melting rate, deicing model***

I. INTRODUCTION

Deicing the runway stands out as a crucial task for the aviation industry during the winter months. Consequently, substantial quantities of deicer chemicals are employed to ensure the runway remains free from snow and ice, minimizing the risk of aircraft skidding. Optimizing the utilization of deicer chemicals can mitigate both the expenses associated with airport maintenance and environmental pollution [1]. Mathematical modeling of deicing applications offers a promising avenue for optimizing the usage of these chemicals. To date, researchers have devised mathematical models aimed at this optimization task for roads and runway [2-6]. These models typically rely on either statistical approaches or physical methodologies, with leveraging heat balance methods. The following paragraph presents five articles that utilize these models, focusing on analysing the heat and water balance specifically on road and runway surfaces.

Fujimoto et al. present a road freezing model that predicts road conditions in freezing temperatures, validated through field experiments. Considering heat, water, and salt balances, it offers a practical tool for winter maintenance[2]. Dan et al.

introduce a Water-Ice-Salt model, analysing the dynamics of road conditions and salt application rates, with insights into ecological implications [3]. Nuijten's study focuses on runway temperature prediction at Oslo Airport, demonstrating precise forecasting using meteorological data and a numerical model [4]. These zero-dimensional models, originating from Fujimoto et al.'s research, do not directly compute the melting rate; instead, they rely on experimental data. One notable source for experimental data for melting rate is the study by Kulyakthin and Klein-Paste, which employs calorimetry to measure melting rates and compares results across three deicers [5].

Precious articles investigate the frequency of deicer reapplication, predominantly through experimental approaches. One significant study by Hossein et al. conducted tests in authentic winter settings over two seasons. During each snow event, specific application rates of salts were applied to test sections, and their performance was monitored over time [6]. Another experimental study examining deicer application rates and comparing different deicers is conducted by Fischel [7].

In previous studies, the melting rate was determined through experimental data rather than numerical modelling. Therefore, there is still a need for a numerical model tailored to runway conditions capable of accurately calculating the melting rate. Such a model should ideally operate in at least one dimension to accurately predict the melting rate. In our prior publication[8], we presented a one-dimensional runway deicing model that integrates mass diffusion and heat transfer mechanisms. Mass diffusion addresses variations in solute concentration over space and time, with Fick's second law used to calculate concentration across all phases (liquid, mushy, solid). As melting occurs, the melting point temperature change at each location. The model determines the temperatures across all phases, the thickness of ice melted, and the concentration of the solution over time [8].

This article aims to examine the frequency of deicer reapplication on the runway using the deicing model introduced in our previous publication [8]. First, we define the problem and assumptions, followed by describing the mathematical model. Next, we introduce the numerical method, specifically the enthalpy method. In the results, we compare the melting rates of potassium acetate and potassium formate deicers. Additionally, for potassium acetate deicer we present temperature variations and ice melting amounts for various deicer reapplication frequencies under three conditions: reapplication at 30 minutes, every 20 minutes, and every 15 minutes, with a wind velocity of 1m/s.

II. MODELS AND METHODOLOGY

A. Problem Definition

When ice or snow covers the runway, a deicer solution is used to melt it away. This solution is sprayed onto the surface by a specialized vehicle, initiating the melting process because it has a lower freezing point than pure ice. In Figure 1, we see the initial conditions after the deicer solution has been applied to the ice layer on the runway surface. This figure shows three layers: the runway pavement, the iced surface layer, and the deicer solution layer. As time progresses, the presence of the deicer causes the ice to melt. Additionally, factors like wind, illustrated in the figure, influence the deicing process. The goal is to estimate the amount of ice melted and the temperature of both the ice and solution layers based on the mass and frequency of deicer application.
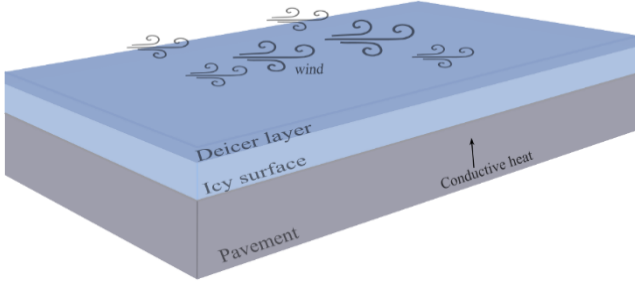
Figure 1 Schematic of the problem.

Melting occurs between the ice and the deicer solution layer. Therefore, the model analyses the heat and mass transfer specifically within these layers, with constant pavement and ambient temperatures assumed over time. Thus, the computational domain we consider extends from the top of the pavement to the surface of the solution. We will account for boundary conditions between the pavement and ice, as well as between the solution layer and the ambient environment.

B. Assumptions

Figure 2 depicts the 1D scheme utilized in the runway model along with the primary boundary conditions. There are three distinct phases present between the runway surface and the air. These encompass the simultaneous transition of the ice film (solid phase), the mushy zone (mixture of solid and liquid), and the solution (liquid phase).
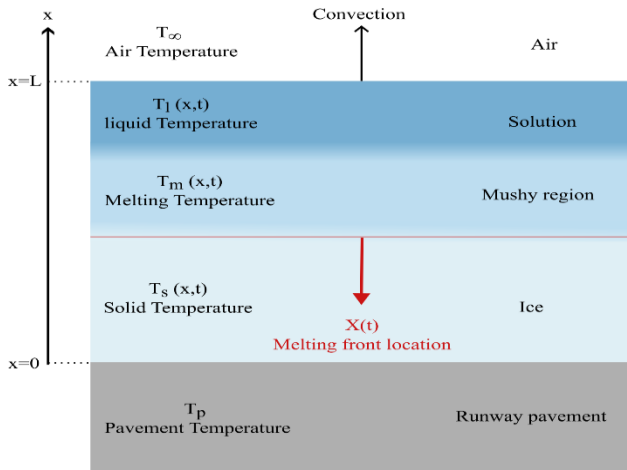
Figure 2 Computational domain in 1D.

Our domain spans from x=0, representing the end of the ice (where it contacts the pavement surface), to x=L, signifying the surface of the solution (the total length covered by the deicing solution and ice). Beginning with ice and concluding with the deicing solution, the domain encompasses three temperature layers, each corresponding to a specific layer. The melting point temperature is denoted as T_m, with the mushy region's temperature being equivalent to the melting temperature. We account for the concentration of deicer within each region ($C(x,t)$).

The model employs several assumptions to streamline the problem:

- Thermophysical parameters remain constant within solid and liquid regions and independent of temperature. These parameters include specific heat (c), thermal conductivity (k), diffusion coefficient (D), and thermal diffusivity ($\alpha = k/\rho c$). Density (ρ) is constant and equal in all regions.
- There exists a conductive flux at x=0 originating from the runway pavement (BC1).
- A convective flux exists at the surface of the deicing solution due to natural convection, with an imposed heat transfer coefficient (h) (which considers wind velocity) (BC2).
- The model operates in a 1D framework, thus examining heat conduction and mass diffusion solely along the vertical direction (x-axis).
- Consider the mushy region as the sharp melting front.

C. Mathematical Model

To tackle the phase change problem, we begin by applying the principles of energy and mass conservation. The energy conservation law, under the assumption of no sink or source heat, is given by:

$$\frac{\partial E}{\partial t} + \nabla \cdot q = 0 \qquad (1)$$

Here, E represents energy, t denotes time, and q signifies heat flux. To include the melting in the energy equation, we utilize the Stefan problem, a classical phase-change problem involving the conduction of heat during melting or solidification. The primary challenge in solving the Stefan problem lies in dealing with a moving front boundary between the solid and liquid region. Across this boundary, the heat flux undergoes discontinuity, necessitating a flux condition that relates the velocity of the front boundary to the jump of heat flux across the melting front.

Consequently, we have heat conduction equations within each phase:

$$\frac{dT}{dt} = \alpha_s \frac{d^2T}{dx^2} \text{ for } 0 < x < X(t) \text{ (solid phase)} \qquad (2)$$
$$t > 0$$

$$\frac{dT}{dt} = \alpha_l \frac{d^2T}{dx^2} \text{ for } X(t) < x < L \text{ (liquid phase)} \qquad (3)$$
$$t > 0$$

In these equations, T represents temperature, α_l denotes the thermal diffusivity in the liquid phase, and α_s represents the thermal diffusivity in the solid phase. Additionally, X(t) represents the position of the melting front, and L denotes the total thickness of the deicing solution and ice.

Additionally, at the interface between solid and liquid phases, we incorporate the Stefan condition for heat balance across the melting front:

$$\rho L_f \dot{X}(t) = -k_l \frac{dT}{dx}(X(t)^-, t) + k_s \frac{dT}{dx}(X(t)^+, t), t > 0 \tag{4}$$

where L_f is the latent heat of fusion, $\dot{X}(t)$ is the velocity of the melting front ($\frac{dX(t)}{dt}$), the value of $\frac{dT}{dx}(X, t)$ is $\frac{dT}{dx}(X(t)^{\mp}, t)$ when $x \to X(t)^{\mp}$ (two sides of melting front). The temperature of melting front location:

$$T(X(t), t) = T_m, \quad t > 0 \tag{5}$$

For the conservation of solute mass, we employ the mass-diffusion equation, which governs the solute mass balance utilizing Fick's law of diffusion. The equation for solute mass conservation is articulated as:

For the solid region

$$\frac{dC}{dt} = D_s \frac{d^2 C}{dx^2}, \quad 0 < x < X(t), t > 0 \tag{6}$$

For the liquid region

$$\frac{dC}{dt} = D_l \frac{d^2 C}{dx^2}, \quad X(t) < x < L, t > 0 \tag{7}$$

In these equations, C represents solute concentration, D_l denotes the diffusion coefficient in the liquid phase, and D_s represents the diffusion coefficient in the solid phase. The diffusion coefficient in the liquid D_l is determined using the equation Wike Chang [9]:

$$D_l = D_0 \frac{\eta}{\eta_0} \left(\frac{M_w}{M_0}\right)^{1/3} \left(\frac{C}{C_0}\right)^{-2/3} \tag{8}$$

D_0 is a reference diffusion coefficient, η is the viscosity of the solvent, η_0 is a reference viscosity, M_w is the molecular weight of the solvent M_0 is a reference molecular weight, C is the volume fraction of the solute in the solvent, C_0 is a reference volume fraction.

For melting to take place, the diffusion coefficient within the solid phase is needed for the deicer to penetrate the ice, as initially, the deicer concentration is zero within the solid region. This coefficient, which is approximately $D_s \approx 10^{-10} \frac{cm^2}{s}$, is inferred from literature [10].

D. Numerical Method

To tackle the two-phase Stefan problem, this paper utilizes the enthalpy method, known for its simplicity and versatility. It considers both material temperature and enthalpy, with enthalpy (E) representing heat per unit mass and linked to temperature through the liquid fraction (λ) [11]. The enthalpy method does not impose the Stefan condition (jump condition) on the solution; rather, it is naturally fulfilled.

The problem is explicitly solved with the finite difference method. In the enthalpy method, the mushy region is represented by a cell containing the melting front, comprising two parts: ice and solution. The position of the melting front is determined by the liquid fraction within the cell. When the cell is entirely liquid or solid, the liquid fraction is 1 or 0, respectively. In the case of a mushy cell, the liquid fraction is determined based on the enthalpy, which will be elaborated upon later.

The initial conditions are fully described in [8].

At t>0, the determination of thermal conductivity involves the following computation:

$$\frac{1}{k_j^n} = \frac{\lambda_j^n}{k_L} + \frac{1 - \lambda_j^n}{k_s} \tag{9}$$

The diffusion coefficient is calculated by equation 8 at each time and spatial step. The calculation of heat resistance and fluxes involves:

$$q_{j-1/2}^n = -\frac{T_j^n - T_{j-1}^n}{R_{j-1/2}}, j = 2, \dots, M$$

$$\text{with } R_{j-1/2} = \frac{1}{2} \Delta x \left(\frac{1}{k_{j-1}} + \frac{1}{k_j}\right) \tag{10}$$

The boundary condition at x=0 (BC1) is calculated at each time and spatial step considering conductive heat flux from the pavement. The boundary condition at x=L (BC2) imposes convective heat flux.

There is no mass flux occurring at boundaries x=0 and x=L. The mass resistance and mass fluxes are computed with:

$$J_{j-1/2}^n = -\frac{C_j^n - C_{j-1}^n}{R2_{j-1/2}}, j = 2, \dots, M$$

$$\text{with } R2_{j-1/2} = \frac{\frac{1}{2}\Delta x_{j-1}}{D_{j-1}} + \frac{\frac{1}{2}\Delta x_j}{D_j} \tag{11}$$

The explicit determination of the enthalpy approximation E_j^{n+1} of E occurs at time t_{n+1} using equation 12, which employs a first-order temporal Euler scheme.

$$E_j^{n+1} = E_j^n + \frac{\Delta t_n}{\Delta x_j}\left[q_{j-1/2}^n - q_{j+1/2}^n\right], j = 1, \dots, M \tag{12}$$

The explicit determination of the concentration approximation C_j^{n+1} of C takes place at time t_{n+1} using equation 13.

$$C_j^{n+1} = C_j^n + \frac{\Delta t_n}{\Delta x_j}\left[J_{j-1/2}^n - J_{j+1/2}^n\right], j = 1, \dots, M \tag{13}$$

Prior to the temperature updates, it's necessary to establish the local enthalpy in both the solid E_{solid} and in liquid E_{liquid} phases relative to the melting temperature of the pure material (water) T_{mpure}. In the scenario of pure water, where the melting temperature matches that of the pure material ($T_{m j} = T_{mpure}$), E_{Solid} equals to 0, and E_{liquid} equals to ρL_f. In the case of solution:

$$E_{Solid} = \rho c_s (T_{m j} - T_{mpure}) \tag{14}$$

$$E_{liquid} = \rho (c_l (T_{m j} - T_{mpure}) + L_f) \tag{15}$$

when the enthalpy is below E_{Solid} everything is in solid phase with the zero liquid fraction. Conversely, when the enthalpy exceeds E_{liquid} everything is liquid with a liquid fraction of one. In cases where the enthalpy falls between these two local enthalpies, a mushy region is present, and the liquid fraction needs to be determined accordingly using Equation 16

$$\lambda_j^n = \begin{cases} 0 & E_j^n \leq E_{Solid} \quad (solid) \\ \dfrac{E_j^n - E_{Solid}}{E_{liquid} - E_{Solid}} & E_{Solid} \leq E_j^n \leq E_{liquid} \quad (interface) \\ 1, & E_j^n \geq E_{liquid} \quad (liquid) \end{cases} \tag{16}$$

With the freezing fraction known, Equation 17 is utilized for the temperature updates.

$$T_j^n$$
$$= \begin{cases} T_{m\,j} + \dfrac{E_j^n}{\rho c_s}, & \lambda_j^n \leq 0 \quad (solid) \\ T_{m\,j}, & 0 \leq \lambda_j^n \leq 1 \quad (interface) \\ T_{m\,j} + \dfrac{E_j^n - \rho L_f}{\rho c_L}, & \lambda_j^n \geq 1 \quad (liquid) \end{cases} \quad (17)$$

To determine the freezing front location at each time t_n, when the mushy node is the M-th node, we utilize the following equation:

$$X^n = x_{m-\frac{1}{2}} + (1 - \lambda_m^n)\Delta x_m \quad (18)$$

The melting point is adjusted at every time step and spatial position according to the local concentration. In this study, to update the melting temperature, the liquidus temperature equation is employed [12]:

$$T_{m\,j} = T_{mpure} + (T_e - T_{mpure})(\frac{C_j}{C_e}) \quad (19)$$

Here, T_{mpure} represents the melting temperature of pure material, while C_e and T_e denote the eutectic concentration and temperature of the binary solution, respectively. The characteristics of the products and the values for the eutectic temperature and concentration are obtained from the research conducted by Melinder [13].

III. RESULTS

The dimensions of the runway at Aéroport de Montréal are 3650 meters in length and 60 meters in width. For the study purposes, we consider a smaller area measuring 1 meter in length and 1 meter in width. Initially, the temperatures of the pavement, air, ice, and deicer solution are set to -2°C. The initial thickness of the ice layer is 2.54 centimeters. To start, we apply 150 grams of solution with a concentration of 50%. The wind velocity is assumed to be 1 m s^{-1}. Based on article by Fujimoto et al.[2], the heat convection coefficient with a wind speed 1 (m s^{-1}) is h= 9.6 (W m^{-2} K^{-1}). We will analyze the results over a span of 60 minutes.

A. Melting Rate Comparison

The results presented here correspond to two products: Potassium Formate (KFO) and Potassium Acetate (KAC). The properties of the products and the initial values are the same as values presented in previous article [8].

Figure3 illustrates the melting rates of the potassium acetate (KAC) and potassium formate (KFO), over a 60-minute period. The melting rates, measured in kilogram per minute, are plotted on the y-axis, while time in minutes is represented on the x-axis. The blue line depicts the melting rate of potassium acetate, while the orange line represents the melting rate of potassium formate. As observed, both deicers exhibit a gradual decrease in melting rate over time. However, throughout the duration, KAC consistently demonstrates higher melting rates compared to KFO. The maximum discrepancy occurs at t=10, with KAC melting at around 7g/min more than KFO.

The accompanying table1 provides a detailed breakdown of the melting rates for potassium acetate (KAC) and potassium formate (KFO). The table1 lists the melting rates, measured in kg per minute, at various time intervals ranging from 1 to 60 minutes. Upon closer examination of the data, it becomes evident that KAC consistently exhibits higher melting rates compared to KFO across all time intervals.
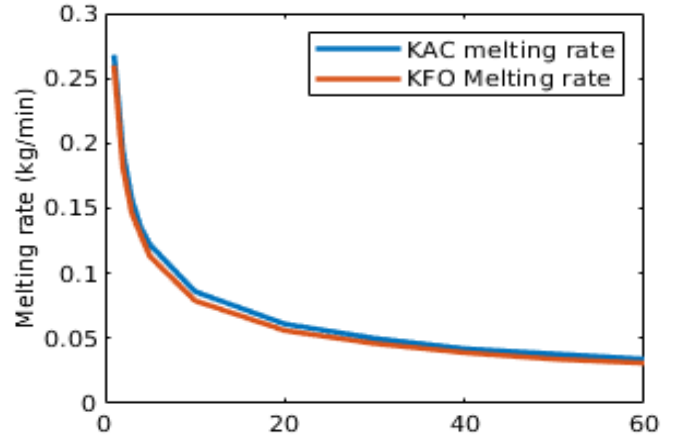
Figure 3 melting rate of KAC (blue line), and KFO (orange line) as a function of time

For instance, at the 60-minute mark, the melting rate for KAC is recorded at 0.034 kg/min, while KFO shows a slightly lower melting rate of 0.031 kg/min. This pattern persists throughout the observation period, indicating that potassium acetate is more effective in melting ice compared to potassium formate under the specified conditions. Thus, based on the higher melting rates observed for potassium acetate, it can be concluded that KAC is the better deicer option for this scenario.

TABLE 1 MELTING RATE KG/MIN OF TWO DEICERS KFO AND KAC

Time (min) / Deicer	1	10	20	30	40	50	60
KAC kg/min	0.268	0.086	0.061	0.050	0.042	0.038	0.034
KFO kg/min	0.260	0.079	0.056	0.046	0.039	0.034	0.031

In the subsequent section, our investigation into the frequency of deicer reapplication will focus on potassium acetate (KAC) as the chosen deicer.

B. Frequency of reapplication

We aim to investigate the frequency of reapplying 150 g/m^2 of deicer (KAC) solution. We will compare its effects on the thickness of ice melted and the temperature of the surface layer of the solution under three different conditions:

1. Reapplying 150 g/m^2 of solution at t=30min.
2. Reapplying 75 g/m^2 of solution every 20 minutes (at t=20 and t=40 minutes).
3. Reapplying 50 g/m^2 of solution every 15 minutes (at t=15, t=30, and t=45 minutes).

Figure 4 displays the melting front location over a span of 60 minutes. The blue line represents the scenario with no deicer reapplication, while the orange, purple, and green lines correspond to conditions 1, 2, and 3, respectively. It is evident that dividing the 150 grams of solution into smaller portions and applying them more frequently, results in a greater extent of ice melting. By the end of 60 minutes in condition 3, there is approximately 0.05 mm (equivalent to 52 grams) more ice melted compared to condition 1. The findings from the melted ice indicate that within one hour, only 0.24 cm of ice has melted, which falls short of our expectations for deicing a runway covered by 2.54 cm of ice. Several explanations are plausible. Firstly, certain physical phenomena, like radiation

heat or heat emanating from the deicer truck or airplane tires, is not have been accounted for in the model. Another possibility is that the deicer solution may not have been uniformly applied onto the ice surface in reality, potentially resulting in localized areas of increased melting where the solution infiltrated beneath the ice.
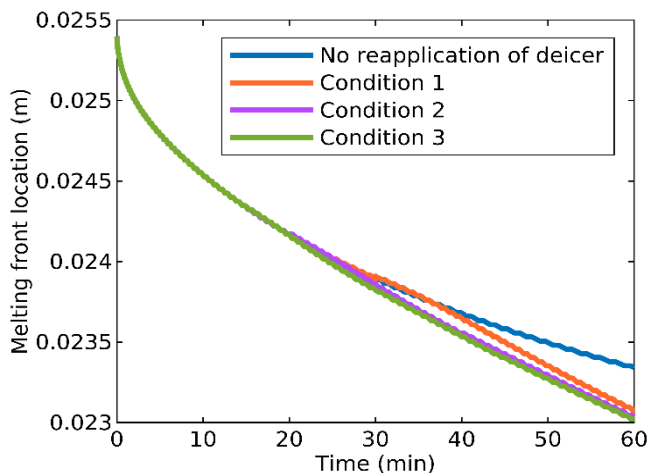
Figure 4 Melting front location over 60 minutes under different scenarios for deicer reapplication.

Figure 5 depicts surface temperatures (solid lines) and melting temperatures (dashed lines) for various conditions: no deicer reapplication (solid lines), and conditions 1, 2, and 3 (orange, purple, and green lines, respectively). Deicer application increases solution concentration, lowering melting temperatures accordingly. This leads to surface temperature reduction. However, abrupt drops followed by sharp increases occur upon deicer application because with passing time, the solution becomes more dilute, causing an increase in melting temperature. Despite these fluctuations, minimal concentration differences across scenarios result in consistent temperatures near -3.5°C by the observation's end in 60 minutes.
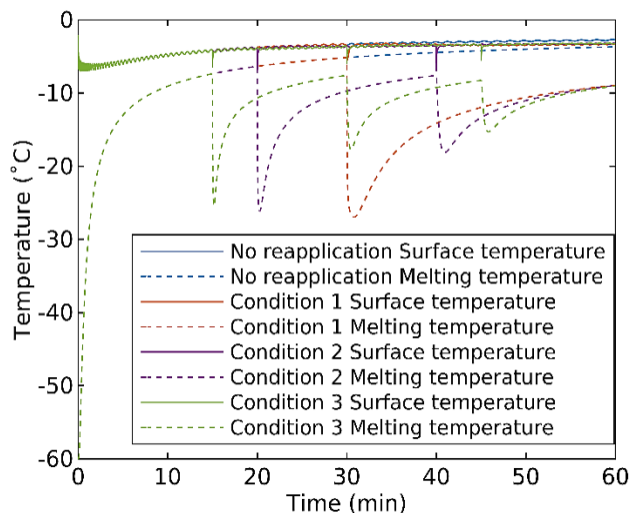
Figure 5 Surface temperature and melting temperature over 60 minutes under different deicer reapplication scenarios.

IV. CONCLUSION

This paper aims to investigate the impact of deicer reapplication frequency on runway conditions by utilizing a runway deicing model. The model, along with the numerical method employed, is introduced. Ice melting is addressed using the two-phase Stefan problem, with discretization achieved through the enthalpy method and finite difference method. Explicit solution is obtained using the first-order Euler scheme.

Subsequently, we constructed a runway model that reflects the physical attributes of the runway, taking into account factors such as wind velocity. The study examines the melting rates of two liquid deicers, potassium acetate (KAC) and potassium formate (KFO), and compares their efficacy in melting ice. Results indicate that potassium acetate is more effective for our scenario. Following this, we investigate the influence of deicer reapplication frequency (using KAC) on both ice melting mass and surface temperature.

The study contrasts the outcomes of three scenarios involving the reapplication of 150 grams of deicer. Findings indicate that when the deicer solution is divided and reapplied more frequently (at shorter time intervals), it leads to increased ice melting. Additionally, temperature results reveal that by the end of the 60-minute process, the surface temperature is around -3.5°C across all scenarios.

References

1. Klein-Paste, A., Runway Operability under Cold Weather Conditions. Tire-pavement friction creation by sand particles on iced pavements, and non-contacting detection of sand particles on pavements. 2007.
2. Fujimoto, A., et al., A road surface freezing model using heat, water and salt balance and its validation by field experiments. Cold Regions Science and Technology, 2014. **106-107**: p. 1-10.
3. Dan, H.-C., et al., Simulation and optimization of road deicing salt usage based on Water-Ice-Salt Model. Cold Regions Science and Technology, 2020. **169**: p. 102917.
4. Nuijten, A.D.W., Runway temperature prediction, a case study for Oslo Airport, Norway. Cold Regions Science and Technology, 2016. **125**: p. 72-84.
5. Kulyakthin, S. and A. Klein-Paste, Can calorimetry be used to measure the melting rate of deicers? Cold Regions Science and Technology, 2021. **181**: p. 103170.
6. Hossain, S.M.K., L. Fu, and C.-Y. Lu, Deicing Performance of Road Salt:Modeling and Applications. Transportation Research Record, 2014. **2440(1)**: p. 76-84.
7. Fischel, M., Evaluation of selected deicers based on a review of the literature. 2001.
8. Maroufkhani, A., et al., Effect of Variable Melting Temperature on the Enthalpy Model for Runway Deicing. 2023, SAE International.
9. Bird, R.B., W.E. Stewai, and E.N. Lightfoot, Phenomena Second Edition.
10. Dietrich, O., Diffusion Coefficients of Water. 2002.
11. Esen, A. and S. Kutluay, A numerical solution of the Stefan problem with a Neumann-type boundary condition by enthalpy method. Applied Mathematics and Computation, 2004. **148(2)**: p. 321-329.
12. Prakash, C. and V. Voller, On the numerical solution of continuum mixture model equations describing binary solid-liquid phase change. Numerical Heat Transfer, Part B: Fundamentals, 1989. **15(2)**: p. 171-189.
13. Melinder, Å., Thermophysical Properties of Aqueous Solutions Used as Secondary Working Fluids Doctoral Thesis By. 2007.

Improving the Carbon Fiber Epoxy Composite Using Graphene Nanoplates for De-icing Processes.

Belal Alemour [1], Mohd Roshdi Hassan [2], Omar Badran [3*]

1. *Department of Mechanical Engineering, Bahrain Polytechnic University, Isa Town, Bahrain.*
2. *Department of Mechanical and Manufacturing Engineering, Universiti Putra Malaysia, 43400 Serdang, Selangor, Malaysia.*
3. *Department of Mechanical Engineering, Al-Balqa Applied University, FET, Amman, Jordan.*
   * Guest Professor at arctic Technology & Icing Research Group (arcICE), Institute of Industrial Technology, Faculty of Engineering Science & Technology, UiT- The Arctic University of Norway.

belal.alemour@polytechnic.bh, ombad3209@uit.no, roshdi_hassan@upm.edu.my

Abstract__ **The electrical conductivity of Carbon Fiber Reinforced Epoxy Composite (CFRE) is poor and need more improvement to be used in more applications such as de-icing processes. Functionalized Graphene Nanoplates (FGNP) is used in present study to improve and enhance the electrical conductivity of CFRE by coating on its top surface. The results show that the electrical conductivity of CFRE is increased significantly by 11 times with a percentage of improvement of 1110 %. The effect of Joule heating in CFRE/FGNP specimen is also studied. The results show that the self-heating of CFRE is improved after coating it with FGNP. The self-heating of CFRE/FGNP specimen becomes more efficient and homogeneous, reaching elevated levels of temperature, more than CFRE neat at the same applied voltage. Tensile test is also performed by applying axial tensile load on the CFRE /FGNP specimen to investigate the effect of tensile load on its electrical conductivity. Therefore, it is found that the electrical resistivity of CFRE /FGNP is increased by increasing the applied tensile load.**

Key words__ **Electrical Conductivity, Carbon Fiber, Composite Material, Graphene, de-icing**

I. INTRODUCTION

Conductive composite materials are made by adding conductive fillers such as carbon-based materials like Graphene to a nonconductive matrix using certain techniques for creating composite materials having high electrical conductivity. These conductive composite materials can be utilized in many applications such as de-icing and lightning strike for aerospace technologies [1, 2].

Carbon Fiber reinforced composites (CFRE) are used nowadays in manufacturing of aircraft structures, due to their light weight and high strength. However, the electrical conductivity of CFRE is low, which means it cannot withstand the high currents from the lightning strike, also it is heat conductivity will not be sufficient for de-icing, eventually, CFRE can be damaged and need high-cost maintenance. Therefore, the electrical conductivity of CFRE must be improved, to withstand the lightning strikes and be useful for the de-icing process. So that, this conductive composite could be used as a heater for de-icing in the aircraft structure, to increase the performance of aircraft. Scientists have found out that thunderstorms are increasing significantly due to the global warming effect and the icing effect is becoming severe in cold regions. Trapp et al 2007, found that a doubling of greenhouse gases in the atmosphere would significantly increase the number of days that severe thunderstorm could occur in the southern and eastern United States [3]. The technology used by aircraft companies to protect the aircraft from lightning strikes is metal mesh, which made of aluminum or copper, this metal meshes are attached to the top surface of CFRE composite, to increase the electrical conductivity of the aircraft's structure. On the other hand, metal mesh increases the weight of aircraft and needs high-cost maintenance [4 - 9].

The researchers investigated high electrically conductive composite materials that can be attached to the aircraft's structure to replace the metal mesh due to their light weight and high electrical conductivity. These conductive composites contain conductive filler such as carbon-based materials like graphene and carbon nanotube [4, 14]. Imran et al, 2016, Bangwei et al, 2017, Kumar et al, 2018 prepared a coating made of graphene that is applied on the surface of carbon Fiber epoxy laminate to protect it from the lightning strike. Li et al, 2018, prepared a spray coating of carbon nanotubes and Graphene Nanoplates used to increase the electrical

conductivity of CFRPs, and the results showed more improvement in the electrical conductivity that can be used later for heating purposes [10 - 14]. Thermal conductivity of CFRE also can be improved using Graphene Nanoplates, because graphene has extremely high thermal conductivity, and this will enhance the self-heating of CFRE to reach higher temperatures at same applied voltage. Therefore, these conductive graphene composites can be used as a de-icing element heater in the aircrafts [13, 14].

The aim of this research is to develop a high electrical and thermal conductive carbon fiber reinforced epoxy composite material through the addition of Functionalized Graphene Nanoplates (FGNP). The results show that the electrical conductivity of CFRE is enhanced and increased significantly by about 11 times and with percentage of improvement of 1110 %. The self-heating of all specimens by the Joule effect was analyzed. It is found that the self-heating of CFRE has been enhanced and improved after coating or printing it with FGNP.

II. MATERIALS

Carbon fabric reinforced epoxy (HexPly 8552 prepregs), supplied by Hexcel Composites company has been used. The epoxy matrix is amine and thermoplastic toughened together and the carbon fabric is manufactured with T300 fiber.

In this research, functionalized graphene nanoplates (FGNP) shown in the Fig. 1, is used to coat the top surface of carbon fiber reinforced epoxy composite (CFRE). FGNP is prepared in the laboratory of chemistry department at faculty of science in University Putra Malaysia, using different processes. An experiment of 1 g of graphene nanoplates (GNPs) were mixed with 10 g of methacrylate and heated at 150 ^{o}C for 24 h. The GNPs functionalized with polymethyl methacrylate were decanted by filtration. Disperse 10 mg/ml GNPs functionalized with polymethyl methacrylate in a mixture of water, methanol, and polyvinyl alcohol at a mass ratio of 10:10:1.

Fig. 1 Functionalized graphene nanoplates (FGNP).

III. METHODOLOGY

A. Preparation CFRE and CFRE/FGNP Composites

In this research, two specimens are prepared for testing. The first specimen is CFRE neat, which is carbon fiber reinforced epoxy composite without FGNP, which will be considered a control sample. The second specimen is CFRE /FGNP-P, where FGNP is printed on the top surface of CFRE using inkjet printer. CFRE neat is fabricated as shown in Fig. 2 (a). The twelve layers of HexPly 8552 prepregs were stacked one after another to form CFRE laminate, then it is cured using hot press machine at 180 ^{o}C for two hours. Specimen CFRE /FGNP-P is fabricated as shown in Fig. 2 (b), where FGNP paste is printed on the top surface of CFRE laminate after curing.
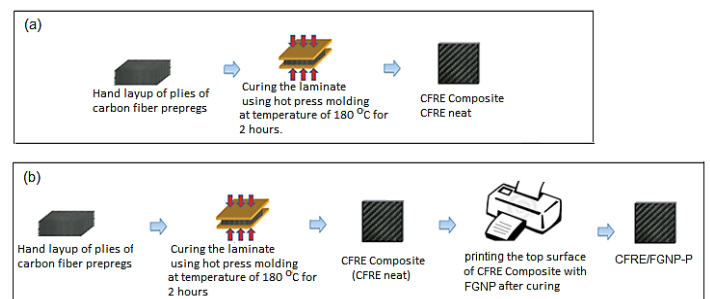
Fig. 2 Procedures of preparing the testing specimens: (a) CFRE neat (b) CFRE /FGNP-P

B. Electrical Conductivity Test

Four-point probe device is used to find the electrical conductivity value for the specimens. The specimens were cut into a proper dimension (1 cm x 1 cm x 0.2 cm) to be used in the testing device. Four-point probe device was used to measure the voltage (V) and the current (I). Then, the electrical resistance (R) of the specimens is determined from equation (1). Finally, the electrical conductivity (σ) can be found from the equation (2) [2, 14]:

$$R = \frac{V}{I} \qquad (1)$$

$$\sigma = \frac{RL}{A} \qquad (2)$$

Where L is the length of specimen, and A is the area of specimen.

C. Self-Heating Test by The Joule Effect

This test is performed to characterize the effect of self-heating caused by the transportation of electrical current in the specimens (i.e. CFRE neat, CFRE /FGNP-S and CFRE /FGNP-P). The test consists of the determination of the temperature reached as a function of the applied voltage. All specimens are prepared and cut to a certain dimension (20 mm x 20 mm x 2 mm), then four copper wires are attached to the top surface of each specimen, where two wires used for measuring the electrical current through the specimen, and

two wires for measuring the voltage across the specimen. Digital Infrared Thermometer is used to measure the temperature of each specimen due to self-heating [14].

D. Tensile Test

The tensile test is performed on CFRE /FGNP-P specimen, to study the effect of tensile applied load on the electrical conductivity of CFRE /FGNP-P specimen. In this test there is no failure to the specimen, only the specimen will be subjected to an axial tensile load in the elastic region, and there is two silver paste points at the specimen surface to measure the electrical resistance as shown in the Fig.3. The experiment was set up in accordance with American Society of Testing and Materials (ASTM) standards that best corresponded to the test specifications. The specimen is prepared and tested according to the ASTM D638 as shown in Fig. 3 [2, 14 – 15].
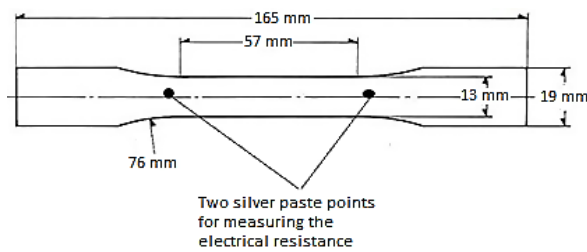
Fig. 3 CFRE /FGNP-P specimen prepared for tensile test according to the ASTM D638.

E. Morphological Characterization

The scanning electron microscopy (SEM) was used to characterize the top and side surfaces of three specimens (CFRE neat, CFRE /FGNP-S and CFRE /FGNP-P) to compare between them. Specimens were sputter-coated with gold to prevent electrical charging during the examination and obtain more clear images. An accelerating voltage of 20 kV was used to obtain the SEM images.

IV. RESULTS AND DISCUSSION

A. Electrical Conductivity

The electrical conductivity value is measured for specimens CFRE neat and CFRE/FGNP-P, respectively. From the results. As shown in Fig. 4, it is found that the electrical conductivity of CFRE is increased and enhanced significantly after coating it with FGNP by about 11 times with percentage of 1110 %. Specimen CFRE /FGNP-P has the electrical conductivity of 3.1 $\times 10^4$ (S/m), while the electrical conductivity of CFRE neat is 1.38 $\times 10^3$ (S/m). It is found that the electrical resistance of CFRE is decreased significantly after coating it with FGNP, which indicates that the electrical conductivity of CFRE is enhanced. For example, specimen

CFRE /FGNP-P has the lowest electrical resistance of 0.0169 (ohm), while CFRE neat has the highest electrical resistance of 0.36 (ohm).

Fig. 5 shows the electrical conductivity versus temperature for all specimens (CFRE neat, and CFRE /FGNP-P). It is observed that the electrical conductivity of all specimens' decreases so slightly with increasing temperature from -10 ºC to 27 ºC, however, this change is almost constant.
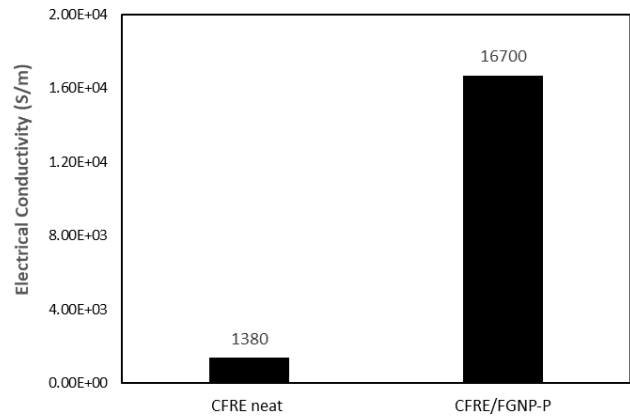
Fig. 4 Electrical conductivity average value comparisons for all specimens.
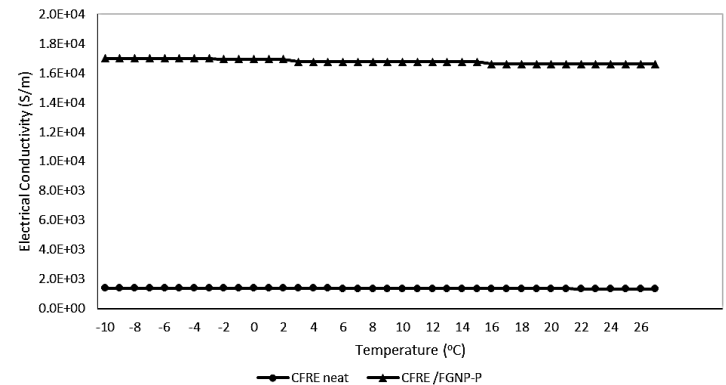
Fig. 5 Electrical conductivity versus Temperature comparisons for all specimens.

The electrical conductivity of all specimens in this study is compared with copper, aluminum and some previous studies as shown in Fig. 6. In this research, it is found that the electrical conductivity of CFRE has improved significantly after coating it with FGNP and reached 1.7 x 10^4 (S/m), but it is still lower than the electrical conductivity of copper and aluminum. By comparing this study with other previous studies that used CNT (Bekyarova, 2007 and Chu, 2015) as conductive filler, it is clear from Fig. 6 that FGNP improved the electrical conductivity of CFRE more than CNT. Bekyarova et al, 2007, used CNT to coat CFRE surface to enhance its electrical conductivity, their results showed that the electrical conductivity was improved to 1.3 x 10^4 (S/m)

[17]. While Chu et al, 2015 [18] reached a value of 8.3 x 10³ (S/m) by inserting CNT based Bucky paper to improve electrical conductivity of CFRE. Fig. 6 also shows the comparison of this study with other studies that used GNP (Zhang, 2013 and Li, 2018). Zhang et al 2013, obtained an electrical conductivity of 5.26 x 10³ (S/m) by coating the carbon fiber surface with GNP [19]. While another research by Li et al 2018, a GNP/CNT hybrid was used to coat the surface of CFRE. Finally, Raj et al 2023 prepared a composite material made of carbon fiber reinforced with peek materials, but the electrical conductivity obtained was exceedingly small if compared with the other studies. The electrical conductivity of CFRE was improved and reached 3.4 x 10³ (S/m) [20]. It is noticed that the electrical conductivity of CFRE has been improved after coating it with FGNP. Also, it is found that by increasing the percentage of FGNP content, the electrical resistance decreased significantly, which led to an increase in the value of electrical conductivity of CFRE several times. Therefore, the use of FGNP on CFRE has been proved to enhance the conductivity than other materials.
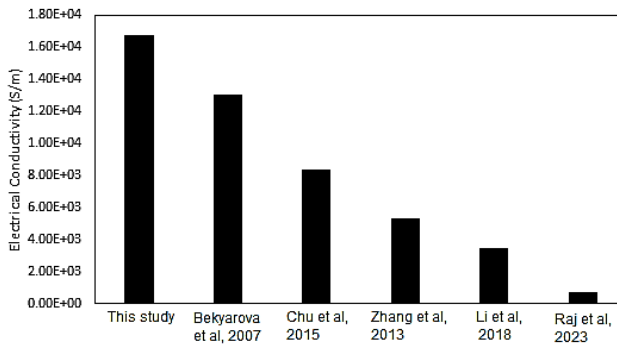
Fig. 6 Comparison of electrical conductivity results with previous studies

B. Self-Heating Test

In this test, the self-heating of all specimens by the Joule effect was analyzed. The aim of this test is to make sure that the self-heating of CFRE has been improved after coating it with FGNP. It is found that the self-heating of specimen CFRE /FGNP-P is more effective, more homogeneous, and reaching higher temperatures for their high thermal conductivity as shown in Fig. 7, also the value of applied voltage on the specimens is low, which reduces the energy consumption. The self-heating of CFRE /FGNP-P has been improved after coating it with FGNP. It was also confirmed that the self-heating is repetitive in several cycles, reaching the same temperature when the same voltage is applied.

Fig. 7 shows the temperature versus applied voltage graph for the studied specimens (CFRE neat, and CFRE /FGNP-P). It is observed that the temperature of the specimens increases by increasing the applied voltage, because more electrical current will pass through the specimen, for example at applied voltage

= 10 mV, the temperature of CFRE neat is reached to 64 ºC due to self-heating, but the temperatures of CFRE /FGNP-P reached to higher value at same applied voltage, where the temperature of CFRE /FGNP-P reached to 75 ºC, respectively. In addition to that, the addition of FGNP nanofiller induced an increase in the thermal conductivity of CFRE, that is directly proportional to the nanofiller content. When the FGNP content is increased, the thermal and electrical conductivities of the samples are increased and then the self-heating due to joule effect is enhanced, eventually, the samples temperatures reached higher levels due to such augmentations.
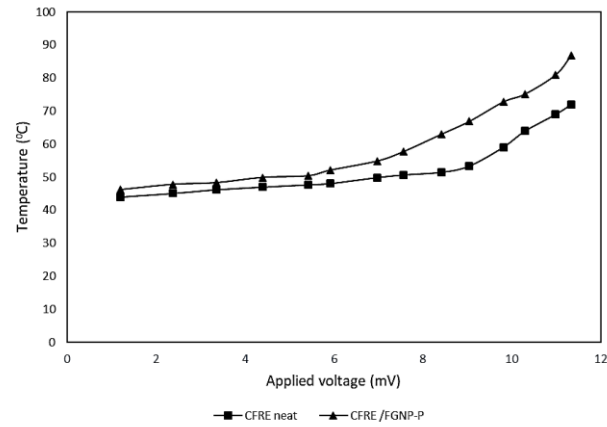
Fig. 7 Temperature vs. applied voltage curves of all specimens obtained from the Joule effect.
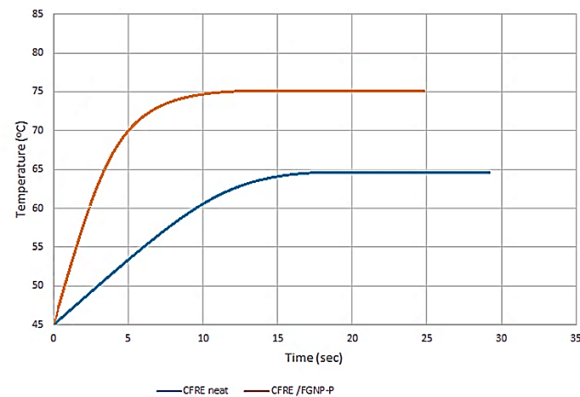
Fig. 8 Temperature vs. time of all specimens at applied voltage of 10 mV.

From Fig. 8, it is found that specimen CFRE neat took 17 seconds to reach the equilibrium temperature of 64 ºC, at applied voltage of 10 mV. While the time taken to reach the equilibrium temperature for specimens CFRE /FGNP-P is 10 seconds at the same applied voltage. It is found also that the time taken to reach temperature of 64 ºC for specimens CFRE /FGNP-P is 3.5 seconds at applied voltage 10 mV, which is 5-6 orders lower than time taken by specimen CFRE neat to reach the same temperature (17 seconds). This is due to the addition of FGNP to CFRE neat, which improved its thermal conductivity to higher values.

C. Tensile Test

The tensile test was conducted on CFRE /FGNP-P, to find the influence of tensile load on the electrical conductivity of CFRE /FGNP-P. Fig. 9, shows the electrical resistance vs applied tensile load curve of specimen CFRE /FGNP-P. This test is performed by applying axial tensile load on the specimen CFRE /FGNP-P, to find out how the change in electrical conductivity of CFRE /FGNP-P will be. It is found from Fig. 9, that the electrical resistivity of CFRE /FGNP-P is increased gradually by increasing the applied tensile load on the specimen; as the deformation increases in the specimen, the electrical resistivity of CFRE /FGNP-P also increases (decreasing the electrical conductivity); as the applied tensile load increase (the strain increases) , the FGNP layer is stretched anisotropically, causing FGNP particles move away from each other (breakdown of the FGNP layer as it is stretched), leading to the rapid increase in resistivity of specimen CFRE /FGNP-P.
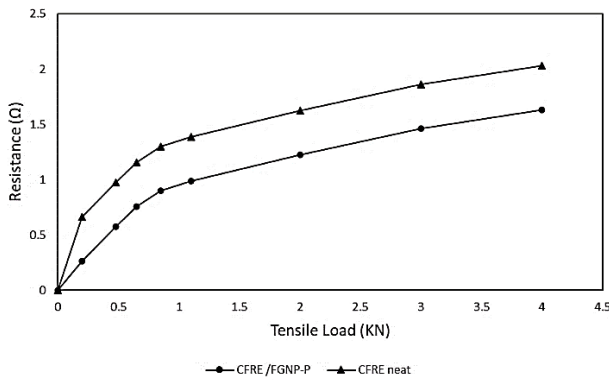
Fig. 9 Electrical resistance vs. tensile load curve of specimen CFRE /FGNP-P.

D. Material Characterization

 Fig.10 shows the characterization result of the top surface of two samples, CFRE neat and CFRE /FGNP-P using Scanning electron microscopy (SEM). Fig. 10-(a) shows the image of top surface of CFRE neat, which shows that there is no FGNP at top surface. While Fig. 10-(b) shows the FGNP coating over CFRE neat top surface. The image in Fig. 10-(c) shows the shape of FGNP sheets at magnification of 500 nm in the CFRE /FGNP-P sample, where the FGNP sheets are transparent and homogenous with less agglomeration. However, in Fig. 11 the images show the side view surface of CFRE /FGNP-P.

(a)

(b)

(c)
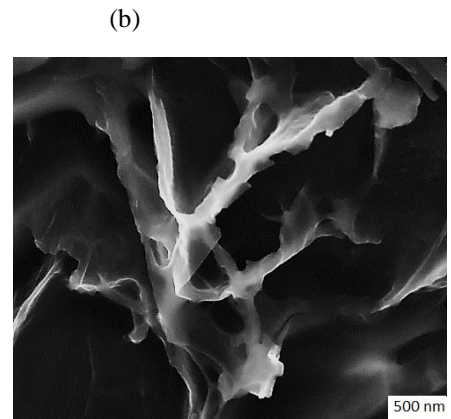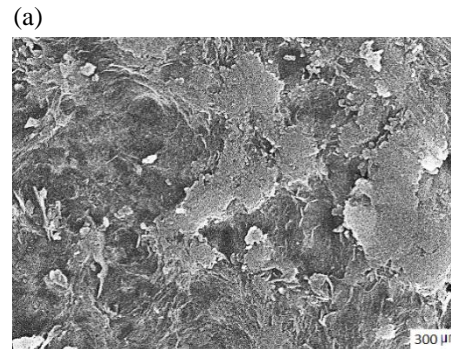
Fig. 10 (a) Top view image of CFRE neat surface (b) Top view image of CFRE /FGNP-S surface (c) Top view image of CFRE /FGNP-S surface at magnification of 500 nm.
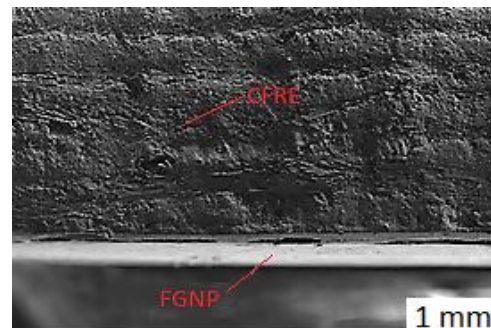
Fig. 11 Side view image of CFRE /FGNP-P, at magnification of 500 µm

V. CONCLUSION

The aim of this study is to develop a cheaper highly electrically conductive epoxy resins through the addition of functionalized graphene which, when combined with conductive carbon fiber, resulted in a highly conductive carbon fiber reinforced epoxy composite material capable of withstanding lightning strike and can be utilized for de-icing which has lighter weights than metallic compounds. Developing such a material would result in safer aircraft, less weight and cost savings from eliminating expensive metallic meshes and eliminating time associated with integrating them into the structure.

A functionalized graphene nanoplates (FGNP) is used to coat the top surface of CFRE to improve and enhance its electrical conductivity to be used for lightning strikes and de-icing in aviation applications. The electrical conductivity is measured for the specimens using a four-point probe device. The results show that the electrical conductivity of CFRE is enhanced and increased significantly when it is coated with FGNP. The results show that the specimen CFRE /FGNP-P has the highest electrical conductivity of 1.67 x10^4 (S/m), while CFRE neat has the lowest electrical conductivity of 1.38 x10^3 (S/m), which means that the electrical conductivity of CFRE neat is increased by about 1110 %.

The results showed that the self-heating of CFRE is enhanced and improved after coating it with FGNP. The self- heating of CFRE /FGNP-P is more effective and more homogenous, reaching higher temperatures, than CFRE neat. It was also confirmed that the self-heating is repetitive in several cycles, reaching the same temperature when the same voltage is applied.

The results also showed that the electrical resistivity of CFRE /FGNP-P is increased by increasing the applied tensile load on the specimen; as the deformation increases in the specimen, while the electrical conductivity decreased). When the applied tensile load increase (the strain increases), the FGNP layer is stretched anisotropically, causing FGNP particles move away from each other (breakdown of the FGNP layer as it is stretched), leading to the rapid increase in resistivity of specimen CFRE /FGNP-P and decrease in conductivity.

ACKNOWLEDGMENT

REFERENCES

[1] N. V. Nayak, "Composite materials in aerospace applications". International Journal of Scientific and Research Publications, 2014. 4(9), 1-10.

[2] B. Alemour, M. H. Yaacob, H. N. Lim, & M. R. Hassan, "Review of Electrical Properties of Graphene Conductive Composites". International Journal of Nanoelectronics & Materials, 2018, 11.4.

[3] R. Trapp, S.Noah, E.Harold, E.Michael, D.Eric, and S. Jeremy, "Changes in severe thunderstorm environment frequency during the 21st century caused by anthropogenically enhanced global radiative forcing". Proceedings of the National Academy of Sciences, 2007, 104.50: 19719-19723.

[4] B.Alemour , O.Badran, & M. R. Hassan, "A Review of using conductive composite materials in solving lightning strike and ice accumulation problems in aviation". Journal of Aerospace Technology and Management, 2019. 11.

[5] A.Katunin , K.Krukiewicz, R.Turczyn, P. Sul, & M. Bilewicz, "Electrically conductive carbon fiber-reinforced composite for aircraft lightning strike protection". In IOP Conference Series: Materials Science and Engineering, 2017. Vol. 201, No. 1, p. 012008. IOP Publishing.

[6] M. Gagné, & D. Therriault, "Lightning strike protection of composites". Progress in Aerospace Sciences,2014. 64, 1-16.

[7] L. M., Gammon, & A. Falcone, "Lightning strike damage in polymer composites". Advanced materials & processes,2003. 161(8), 61-62.

[8] J.Morgan, "Thermal Simulation and Testing of Expanded Metal Foils Used for Lightning Protection of Composite Aircraft Structures". SAE International Journal of Aerospace, 6(2013-01-2132), 371-377.

[9] I. M., Alarifi, W. S.Khan , M. M.Rahman, & R. Asmatulu, "Mitigation of Lightning Strikes on Composite Aircraft Via Micro and Nanoscale Materials". Advances in Nanotechnology, 2017. 39.

[10] L. R. Vishnyakov, L. N.Pereselentseva, & E.L. Vishnyakova, "Knitted Soldered Meshes and Nanostructured Carbon Particles for Lightning Protection of Composite Wind Turbine Blades". Powder Metallurgy and Metal Ceramics,2014. 53(5-6), 368-374.

[11] K. Imran, "Enhancement of electrical conductivity of carbon/epoxy composites by graphene and assessment of thermal and mechanical properties", (Doctoral dissertation, North Carolina Agricultural and Technical State University), 2016

[12] Z. Bangwei, S. A. Soltani, L. N. Le, & R. Asmatulu, "Fabrication and assessment of a thin flexible surface coating made of pristine graphene for lightning strike protection". Materials Science and Engineering: 2017, B, 216, 31-40.

[13] S. S. Kumar, M. N.Uddin, M. M.Rahman , & R. Asmatulu, "Introducing graphene thin films into carbon fiber composite structures for lightning strike protection". Polymer Composites.2019

[14] Y.Li, H.Zhang , Y. Liu, H.Wang , Z.Huang , T. Peijs , & E. Bilotti, "Synergistic effects of spray-coated hybrid carbon nanoparticles for enhanced electrical and thermal surface conductivity of CFRP laminates". Composites Part A: Applied Science and Manufacturing,2018. 105, 9-18.

[15] B. Alemour, M. H. Yaacob, H. N. Lim, O. Badran, & M. R. Hassan, "Improving the electrical conductivity of carbon fiber reinforced epoxy composite using reduced graphene oxide". Materials Research Express, 2019. 6(6), 065607.

[16] H. Ku, H.Wang , N. Pattarachaiyakoop , & M. Trada, "A review on the tensile properties of natural fiber reinforced polymer composites". Composites Part B: Engineering,2011. 42(4), 856-873.

[17] Anne Helmenstine. 2018. retrieved at: https://sciencenotes.org/author/azareal/

[18] E. Bekyarova , E. T. Thostenson, A.Yu , H. Kim, J. Gao, J. Tang, & R. C. Haddon, "Multiscale carbon nanotube− carbon fiber reinforcement for advanced epoxy composites". Langmuir,2007. 23(7), 3970-3974

[19] H. Chu, Z. Zhang, Y .Liu, & J. Leng , "Self-Response Multi-Functional Composite Material Base on Carbon Nanotube Paper Using Deicing, Flame Retardancy, Thermal Insulation, and Lightning-Strike Protection". SPIE Smart Structures and Materials+ Nondestructive Evaluation and Health Monitoring: International Society for Optics and Photonics; 2015. p. 94320S-94320S-94328.

[20] B. Zhang, V. R.Patlolla , D. Chiao, D. K.Kalla , H. Misak, & R. Asmatulu, Galvanic corrosion of Al/Cu meshes with carbon fibers and

graphene and ITO-based nanocomposite coatings as alternative approaches for lightning strikes. The International Journal of Advanced Manufacturing Technology, 2013. 67, 1317-1323.

[21] Y.Li, H.Zhang , Y. Liu, H.Wang , Z.Huang , T. Peijs , & E. Bilotti, "Synergistic effects of spray-coated hybrid carbon nanoparticles for enhanced electrical and thermal surface conductivity of CFRP laminates". Composites Part A: Applied Science and Manufacturing,2018. 105, 9-18.

The Influence of Ice-covered Shapes on DC High Current De-Icing Time for Single Conductor Transmission Lines

Heling Xie[1], Xingliang Jiang[1], Guolin Yang[1], Hu Qin[1], Zhijin Zhang[1], Lie Ma[1]

[1] Xuefeng Mountain Energy Equipment Safety National Observation and Research Station，Chongqing University, Chongqing 400044, China

20221101032@stu.cqu.edu.cn, xljiang@cqu.edu.cn, GL_Yang@cqu.edu.cn, huqin@cqu.edu.cn, zhangzhijin@cqu.edu.cn, malie17@outlook.com

Abstract— **High-current DC ice melting is an effective measure for preventing ice disasters on transmission lines. Under actual operational conditions, there is variable icing shape on individual conductors of transmission lines. Calculation and analysis of high-current DC ice melting time for single conductor circular ice and wing-shaped ice. The result show that the winged ice melting time is about 10% of the circular ice melting time. High-current DC ice melting experiments were conducted on two types of single conductor models, LGJ-300/50 and LGJ-400/35, at the Xuefeng Mountain Energy Equipment Safety National Observation and Research Station, Chongqing University. The experimental results show that the melting time of LGJ-300/50 conductor wing-shaped ice is 10.6% of the melting time of circular ice, and the melting time of LGJ-400/35 conductor wing-shaped ice is 8.3% of the melting time of circular ice. Based on the experiment data, advocating the inhibition of circular ice formation to promote wing-shaped ice growth can notably reduce the time and energy consumed in high-current DC ice melting.**

Keywords—***Transmission lines; Circular ice; Wing-shaped ice; Melting time; High-current DC***

I. INTRODUCTION

Deicing is the best way to cope with transmission line ice cover. Through the continuous efforts of scholars at home and abroad, dozens of de-icing methods for transmission lines have been researched and developed. According to its working principle, it can be divided into mechanical de-icing method, thermal ice melting method and passive de-icing method, etc. Despite the numerous de-icing methods, DC high current ice melting has proven to be the most widely used de-icing method([1-2]). However, its shortcomings are equally obvious, each time the ice melting requires line outages to access the ice melting equipment, long ice melting time and high energy consumption ([3-6]). Transmission line ice cover is closely related to the DC high current ice melting work, which determines the size of the ice melting current, but also determines the length of the ice melting time. Mastering the transmission line ice cover law is crucial for promoting the development of DC high current ice melting technology.

DC high current ice melting technology is still the preferred method of transmission line ice defense at this stage. Although researchers have gradually deepened the research on the process and mechanism of transmission line ice-covering, the DC high current ice melting technology is limited to determining the ice melting current and starting time, and optimizing the ice melting workflow. Can not be a good

solution to the problem of DC ice melting time is long, high energy consumption. Based on this, this paper takes the shape of transmission line single conductor ice cover as the main research body, analyzes the difference between wing-shaped ice and round ice melting time, and carries out field natural ice melting experimental research. Thus, it is proposed to change the shape of transmission line ice cover to reduce the time of transmission line DC high current ice melting to reduce the ice melting energy consumption method. The research results of this paper can provide reference for the researchers of transmission line de-icing work and power grid ice disaster defense.

II. CHARACTERISTICS OF ICE SHAPE DISTRIBUTION ON SINGLE CONDUCTOR OF TRANSMISSION LINES

As shown in Figure 1 for the field natural environment of the shape of the conductor ice cover with the development of ice cover changes. Transmission line ice cover by the air cooling water droplets encountered with the airflow movement of the conductor after the conductor surface frozen solidification. Therefore, the ice cover first occurs in the windward side of the wire, with the increase of the number of overcooling water droplets frozen, the ice cover on the surface of the wire gradually accumulates into the wing-shaped ice shown in Figure 1a.
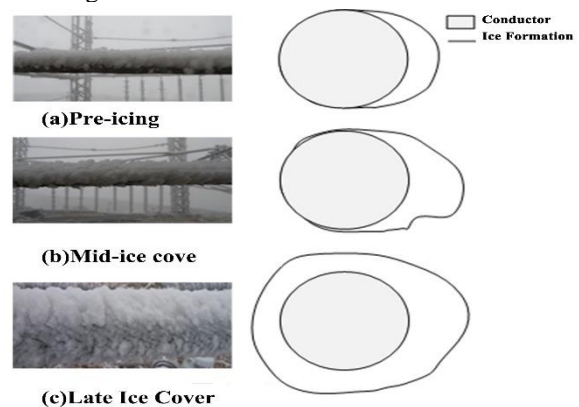
Fig.1 Improvement of ice shape on conductor

From the above analysis, it can be seen that the free torsion of the conductor driven by the ice layer is the root cause of the round shape of the conductor ice cover. The conductor itself has a certain degree of torsion resistance, characterized by torsional stiffness. The greater the torsional stiffness, the less likely to torsion of the conductor over ice, the more difficult

to form round ice. For aluminum stranded wire, the torsional stiffness is shown below.

$$\begin{cases} K = a\left(G_1 J_1 + G_2 J_2\right) \\ J_1 = \dfrac{\pi}{32} d^4 \\ J_2 = \dfrac{\pi}{32}\left(D^4 - d^4\right) \end{cases} \qquad (1)$$

Where K indicates the torsional stiffness of the wire, N·m²/rad; a is the winding twist coefficient; G_1 indicates the torsional modulus of elasticity of the steel core; G_2 indicates the torsional modulus of elasticity of the aluminum stranded layer; J_1 is the torsional polar moment of inertia of the steel core layer, m4; J_2 is the torsional polar moment of inertia of the aluminum stranded layer, m⁴; D is the diameter of the wire, m; d is the diameter of the steel core layer, m.

From Eq. (1), the torsional stiffness of the conductor is its inherent property. However, for the overhead single conductor fixed at both ends, the distribution of torsional stiffness along the wire is not uniform. The length of L on the conductor j torsional stiffness can be equated to the length of x_j of the conductor and the length of L-x_j of the conductor in parallel with the equivalent torsional stiffness $K(j)$ [13]:

$$K(j) = \frac{K}{x_j} + \frac{K}{L - x_j} = \frac{KL}{x_j\left(L - x_j\right)} \qquad (2)$$

Analysis of the formula (2) can be seen, the length of a certain length of overhead single conductor, the closer to the center of the conductor, the lower the equivalent torsional stiffness, and the closer to the two sides of the conductor suspension point, the higher the equivalent torsional stiffness of the conductor. Therefore, the transmission line ice, from the two ends of the wire suspension point, the closer to the center of the wire, the wire ice shape closer to the circle, and the closer to the two ends of the wire suspension point, the shape of the wire is closer to the wing shape.

III. ANALYSIS OF MELTING TIME OF SINGLE CONDUCTOR CIRCULAR ICE AND WINGED ICE

Single conductor round ice melting ice can be divided into three stages: the first is the conductor covered with ice adhesion failure stage. In the Joule heat effect produced by the large current, the wire and the ice layer temperature began to gradually increase. After a certain period of time, the outer surface of the wire and the inner surface temperature of the ice layer reached 0 ℃, between the wire and the ice layer to form a water film. At this time, the ice and the wire between the adhesion failure, then enter the second stage, that is, the ice rotation stage. Ice and wire adhesion failure, under the action of gravity to rotate, the thinner side of the ice cover is lighter, after the rotation is located above the wire. The water film formed in the first stage flows out of the micropores of the ice [30] and air flows in to fill the air gap between the wire and the ice. The final stage is the melting of the ice above the wire. The ice layer located directly above the conductor melts under the action of the current and the thickness of the ice layer gradually decreases until it is all melted and then the round ice falls off from the surface of the conductor, and the melting of ice ends.

The wing-shaped ice by the conductor does not twist when the overcooling water droplets in the conductor windward side of the accumulation, so its leeward side almost does not occur over ice. This paper considers the wing-shaped ice melting ice in the conductor ice-covered adhesion failure immediately after the end. And make the following provisions:

(1) The effect of ice surface roughness and ice ribs is not considered.

(2) In the process of melting ice by high current of conductor, the role of external mechanical force such as sunlight radiation and jumping of conductor off ice is ignored.

(3) Between the outer surface of the conductor and the inner surface of the wing-shaped ice due to the heating of the water film, the wing-shaped ice immediately detached from the conductor.

As shown in Figure 2 for the ice-covered single conductor round ice melting process heat balance diagram. The Joule heat generated by the current so that the outer surface of the wire and the inner surface of the ice layer produced a water film, the heat is mainly in the steel core (Φ_1), aluminum core (Φ_2) and the ice layer (Φ_4) between the transfer of the time required for:

$$t_s = \frac{\sum\limits_{k=1,2,4} C_{\Phi_k} \rho_{\Phi_k} V_{\Phi_k} \Delta T_{\Phi_k}}{I^2 r_T - h l_i (T_{i0} - T_a)} \qquad (3)$$

In the formula, t_s is the time for the formation of water film inside the round ice, and also the melting time of the wing-shaped ice, in the latter part of the text, without special explanation, t_s are expressed as the melting time of the wing-shaped ice, s; $C_{\Phi k}$ is the specific heat capacity of the Φ_k area, J/（kg.℃）; $\rho_{\Phi k}$ is the density of Φ_k, kg/m³; $V_{\Phi k}$ is the volume of the area Φ_k, m³; $\triangle T_{\Phi k}$ is the temperature rise of Φ_k area, ℃; I is the ice melting current, A; r_T is the resistivity of the wire when the temperature is T, Ω/m; h is the heat exchange coefficient of convective and radiative heat transfer between the outer surface of the ice sheet and the environment, W/(m².K); l_i is the surface area of the outer surface of the ice cover, m², T_{i0} is the temperature of the outer surface of the ice sheet when the temperature of the ice sheet is 0, ℃; T_a is the ambient temperature, ℃.
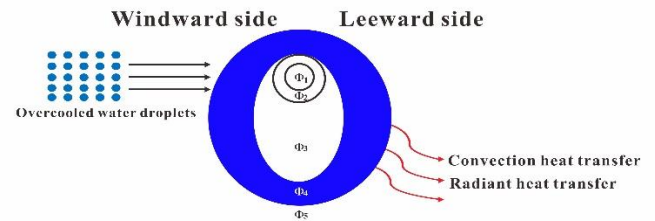
Fig.2 Sketch of heat balance about circular ice on transmission lines

The surface heat transfer coefficient can be obtained from equation (4):

$$h = (0.295 R_i)^{-0.534} U^{0.466} + 4.39 \times \left(1 + 0.01 T_a\right) \qquad (4)$$

Where R_i is the radius of the cylinder formed by the conductor and the ice layer after the conductor is covered with ice, m; U is the ambient wind speed, m/s.

The melting time of circular ice can be obtained from equation (5):

$$\begin{cases} t_j = A \cdot t_{jc} \\ t_{jc} = \dfrac{(\rho_i L_F V + \rho_i C_i\left(-T_i\right) V_i / 2)}{I^2 r_T - \pi\left(R_c + d\right) h\left(T_i - T_a\right)} \end{cases} \qquad (5)$$

Where: t_j is the melting time of circular ice, s; A is the correction coefficient, in this paper, according to the long-term field experimental data, A is taken as 1.2; t_{jc} is the preliminary formula for the melting time of circular ice [8-10]; ρ_i is the density of the ice layer, kg/m³; LF is the latent heat of melting of the ice, L_F=335 kJ/kg; V is the volume of the melted part of the ice layer, m³; V_i is the volume of the ice layer in the initial state, m³; V_c is the volume of the conductor, m³; C_i is the specific heat of ice, J/(kg·°C); T_i is the temperature of the leeward side of the ice-covered conductor at the initial moment, °C; R_c is the radius of the un-ice-covered conductor, m; and d is the thickness of the ice layer, m.

V is obtained from equation (6):

$$V = \pi\left(R_c + d/2\right) \times \frac{\left[\sqrt{R_i(R_c+d/2)} + \sqrt{R_c(R_c+d/2)}\right]}{2} - \pi R_c^2 \quad (6)$$

T_i as shown in the following equation:

$$\begin{cases} T_i = \dfrac{R_q h}{1 + R_q h} T_a \\ R_q = \dfrac{\ln\left(R_i / R_c\right)}{\pi \lambda_i} \end{cases} \quad (7)$$

R_q is the ice thermal resistance and λ_i is the ice thermal conductivity, 2.22W/(m·K).

From equation (3)~equation (7) to calculate the melting time of circular ice and wing-shaped ice of three kinds of conductors, LGJ-240/30, LGJ-300/50, LGJ-400/35, respectively, and the basic parameters of three kinds of conductors are shown in Table 1:

TABLE I. BASIC TECHNICAL PARAMETERS OF WIRE

Wire Model	(quantities/calibre)/mm		diameter	DC resistance
	Aluminum Stranded wire	Steel Core	(mm)	(Ω/km)
LGJ-240/30	24/3.6	7/2.4	21.60	0.1181
LGJ-300/50	26/3.83	7/2.98	24.26	0.0964
LGJ-400/35	48/3.22	7/2.5	26.82	0.07389

When calculating, the thickness of ice cover is 10mm, the ambient wind speed is 3m/s, and the ambient temperature is -5℃. Due to the different types of conductors with different current capacity, the current size is determined by the melting current density when melting ice. In this paper, three types of conductors were loaded with ice melting current according to the current density of 1.5A/mm2, 2A/mm2 and 3A/mm2, and the calculation results are shown in Table 2.

TABLE Ⅱ. MELT-ICING TIME OF DIFFERENT CONDUCTORS

d=10mm，v=3m/s, T_a=-5°C				
Wire Model	Ice melting current （A）	t_s(min)	t_j(min)	$\beta=t_s/t_j$(%)
LGJ-240/30	360	14.18	183.65	9.27
	480	7.98	95.12	10.06
	720	3.55	40.01	10.63
LGJ-300/50	450	12.96	158.63	9.80
	600	7.30	82.94	10.56
	900	3.24	35.10	11.08
LGJ-400/35	600	11.28	129.9	10.42
	800	6.35	68.73	11.08
	1200	2.82	29.30	11.55

With the same conductor type, the higher the ice melting current density, the shorter the melting time of circular ice. When the melting current density is increased from 1.5A/mm2 to 3A/mm2, the melting time of circular ice of the three conductors is 21.78%, 22.13% and 22.55% of the original, respectively. In the case of the same ice melting current density, the larger the conductor cross section, the shorter the conductor circular ice melting time. When the wire type is changed from LGJ-240/30 to LGJ-400/35, the latter's circular ice melting time under the three ice melting current densities is 70.73%, 72.26% and 73.25% of that of the former, respectively. It can be seen that under the same ice-covered environment, the melting current density has a greater influence on the melting time of circular ice than the type of conductor.

The variation rule of melting time of wing-shaped ice with melting current density and wire type is consistent with that of circular ice. However, numerically, the melting time of wing-shaped ice is much smaller than that of circular ice. Define β as the ratio of the melting time of the wing-shaped ice and the melting time of the circular variable of the transmission line. From the table, it can be seen that the maximum value of β is 11.55%, the minimum value is 9.27%, and the average value is 10.49%, i.e., the melting time of wing-shaped ice of a single conductor is about 10% of that of circular ice. In the case of the same type of conductor, β increases with the increase of ice melting current density, with the ice melting current density of 1.5A/mm2 as the benchmark, LGJ-240/35 conductor in the ice melting current of 2A/mm2 has the largest growth ratio of 8.52%. In the case of the same melting ice current density, β becomes larger as the cross-section of the conductor becomes larger, taking LGJ-240/35 conductor as the base, LGJ-300/50 conductor has the largest growth ratio at the melting ice current of 2A/mm2, which is 12.41%.

IV. SINGLE CONDUCTOR FIELD NATURAL ICE MELTING EXPERIMENT

This paper carries out the single conductor field natural environment high current heating ice melting experiment in "Xuefeng Mountain National Field Station". The experimental wiring is shown in Figure 5, LGJ-300/50 conductor and LGJ-400/35 conductor are set up between two freezing towers, the length of which is 100 m. On one side of the freezing towers, two conductors are connected with 300 mm2 yarn braided copper wires, and on the other side, two rectifiers are connected to the rectifier through 300 mm2 yarn braided copper wires. The current required for the experiment was provided by the high current generator through the rectifier, and its maximum output could reach 5000A to meet the requirements of ice melting. The ambient temperature and wind speed are obtained by the six elements of meteorological sensors arranged in the station as shown in Fig. 6, and the measurement range of ambient temperature is -50±0.2°C~+100±0.2°C, and the measurement range of wind speed is 0~60±0.3 m/s, which meets the demand of this experiment.

Measured before the experiment, the ice thickness of LGJ-300/50 conductor is 15.5mm, and the ice thickness of LGJ-400/35 conductor is 9.3mm. two types of conductors in the ice near the freezing rain tower side are wing-shaped, measure the length of the two conductor surfaces in the wing-shaped ice, the total length of the line of the wing-shaped ice on both sides

of the LGJ-400/35 conductor is 31.5m, and the length of the line of the wing-shaped ice on both sides of the LGJ-300/50 conductor is 25.7m. two conductors connected in series will pass the same size current with different melting current density. LGJ-400/35 wire on both sides of the wing-shaped ice line length is 31.5 m, LGJ-300/50 wire on both sides of the wing-shaped ice line length is 25.7 m. After the two wires are connected in series, they will pass the same size of current with different ice melting current density. During the experiment, the experimental circuit is loaded with 900A DC current, and the melting time of the circular ice and the wing-shaped ice of the conductor is recorded, and the ambient temperature and wind speed during the experiment are recorded in real time.
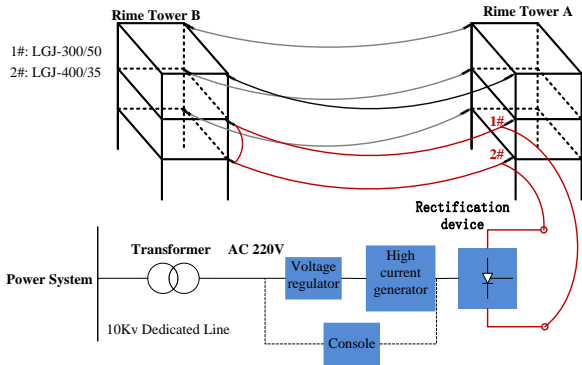
Fig.3 Layout of melt-icing experiment on natural environment

Fig.4 Six elements meteorological sensor

At the end of the experiment, the average value of ambient temperature during the experiment is -3.6℃, and the average value of wind speed is 2.8m/s. The average value of wire ice thickness, wire ice current, ambient temperature and wind speed during the experiment is substituted into Eqs. (3)~(7) to obtain the calculated value of two kinds of wire ice melting time, which will be analyzed in comparison with the experimental results.

The experimental and calculated values of this experiment are shown in Tables 3 and 4, where the meanings of the variables are the same as in the previous article, and the subscripts with the word "calculated" indicate that the value is calculated, and the word "real" indicates that the value is obtained from the experiment.

TABLE Ⅲ. MELT-ICING TIME BY SIMULATION AND EXPERIMENT OF LGJ-300/50

d=15.5mm，v=2.8m/s, T_a=-3.6°C, I=900A					
Count t_s (min)	Survey t_s (min)	Count t_j (min)	Survey t_j (min)	Count β (%)	Survey β (%)
4.52	4.75	48.23	44.86	9.4	10.6

TABLE Ⅳ. MELT-ICING TIME BY SIMULATION AND EXPERIMENT OF LGJ-400/35

d=9.3mm，v=2.8m/s, Ta=-3.6 ℃, I=900A					
Count t_s (min)	Survey t_s (min)	Count t_j (min)	Survey t_j (min)	Count β (%)	Survey β (%)
3.73	3.47	38.33	42.05	9.7	8.3

The computational errors for each value obtained according to equation (8) are shown in Table 5:

$$\text{Calculation error} = \frac{\left| \text{Experimental value-Calculated value} \right|}{\text{Experimental value}} \times 100\% \quad (8)$$

TABLE Ⅴ. ERR OF SIMULATION AND EXPERIMENT (%)

Wire model	t_s calculation error	t_j calculation error	B calculation error
LGJ-300/50	4.84	7.51	11.32
LGJ-400/35	7.49	8.84	16.87

As can be seen from Tables 3 to 5.

The wing-shaped ice melting time of LGJ-300/50 conductor is much smaller than the round ice melting time, and the wing-shaped ice melting time accounts for 10.6% of the round ice melting time in the experiment. The experimental value of the wing-shaped ice melting time is larger than the calculated value; the experimental value of the circular ice melting time is smaller than the calculated value; the ratio of the wing-shaped ice melting time to the circular ice melting time is larger in the experimental results than the calculated results. In terms of computational errors, the computational errors of the melting time of circular and winged ice of the conductor are less than 10%, the computational error of the β value is the largest, 11.32%, and the computational error of ts is the smallest, 4.84%.

The wing-shaped ice melting time of LGJ-400/35 conductor is much smaller than the round ice melting time, and the wing-shaped ice melting time accounts for 8.3% of the round ice melting time in the experiment. The experimental value of the wing-shaped ice melting time is smaller than the calculated value; the experimental value of the circular ice melting time is larger than the calculated value; on the ratio of the wing-shaped ice melting time to the circular ice melting time, the experimental results are smaller than the calculated results. In terms of computational errors, the computational errors of the melting time of circular ice and winged ice of the conductor are less than 10%, the computational error of the β value is the largest, 16.34%, and the computational error of ts is the smallest, 7.49%.

Both types of conductor calculation error is β is the largest, ts is the smallest because: β is a dimensionless ratio, the ratio of the term has its own error, once again calculated to make the error larger; according to this paper on the definition of ts, in the experiment, it is the transmission line wing-shaped ice occurred in the first time when the shedding of the value of the record, so it is more accurate.

To ts time after the wing-shaped ice and wire bonding failure did not directly detach from the wire, but the same as the circular ice rotation, until the back of the ice layer melted before finally detached from the wire surface. In order to further analyze the difference between the actual shedding time of the wing-shaped ice and the shedding time of the circular ice, the time and length of each shedding of the wing-

shaped ice of the two conductors were recorded from the first shedding of the wing-shaped ice of the conductor, until the wing-shaped ice was completely shed.

The results are shown in Fig. 4. From the figure, it can be seen that the wing-shaped ice shedding on the surface of LGJ-300/50 conductor occurred 4 times, and the maximum length of single shedding was 9.7m, and the last shedding occurred in the 15th.2 minutes after the start of ice melting, and the time of wing-shaped ice melting accounted for 33.88% of the melting time of the round ice.The wing-shaped ice shedding occurred 5 times on LGJ-400/35 conductor. The maximum length of a single dislodgement was 12.2 m, and all the winged ice on the conductor surface was dislodged at the 14.3th minute after the start of ice melting. The wing ice melting time accounted for 34.09% of the conductor circular ice melting time.
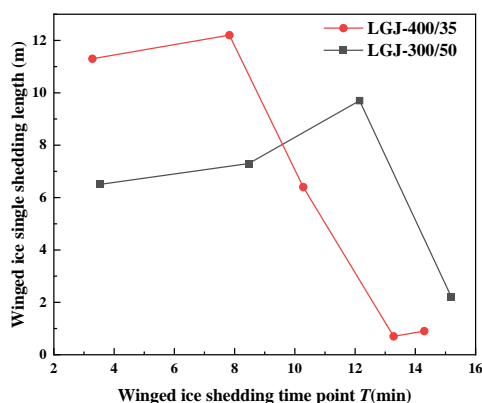
Fig.4 The length and time point when wing ice separate from conductor

V. Conclusions

(1) Under the wild natural environment, the transmission line single conductor ice cover quality increases, will drive the conductor around the center of the free torsion, the ice cover shape is ultimately presented as a circle. For overhead transmission lines fixed at both ends, the closer to the center of the wire, the lower the torsional stiffness of the wire, the easier it is to form a round ice, and the closer to the suspension point of both ends of the wire, the closer the shape of the wire ice is to the wing.

(2) Compared with circular ice, the melting process of winged ice is simpler and it can be detached from the conductor faster than circular ice. Calculations show that the melting time for single conductor winged ice is only about 10% of that for circular ice.

(3) Field natural experiments on single conductor high current DC ice melting were conducted at the Xuefengshan National Field Station. The error between the experimental results and the calculated results of the single-conductor ice-melting time is within 10%, and the ratio of the wing-shaped ice-melting time to the circular ice-melting time is 10.6% and 8.3%, respectively.

(4) During the experiment, it was found that some of the wing-shaped ice at both ends of the single conductor was also covered with ice on the leeward side of the conductor due to the torsion of the conductor, thus increasing the wing-shaped ice melting time. Taking the time node when all the wing-shaped ice of the conductor is completely detached as the melting time of wing-shaped ice, the melting time of the wing-shaped ice of the two conductors during the experiment is

33.88% and 34.09% of the melting time of the circular ice, respectively.

(5) According to the results of this paper, if we can promote the single conductor along the line does not generate circular ice but generates wing-shaped ice, the DC high-current ice melting time will be reduced by about 70% to 90%. In particular, all along the conductor to form a strict wing-shaped ice (conductor does not twist, no ice accumulation on the leeward side) is better.

References

[1] Lenhard Robertw. An Indirect Method for Estimating the Weight of Glaze on Wires[J]. Bulletin of the American Meteorological Society. 1955, 36(1): 1-5.

[2] KÁLMÁN T，FARZANEH M，MCCLURE G．Numerical analysis of the dynamic effects of shock-load-induced ice shedding on overhead ground wires[J]．Computers & Structures，2007，85(7-8)：375-384.

[3] KALMAN T ．Dynamic behavior of iced cables subjected to mechanical shocks[D]．Chicoutimi：Université du Québec à Chicoutimi，2007.

[4] LEBLOND A ，LAMARCHE B ，BOUCHARD D ，et al．Development of a portable de-icing device for overhead ground wires[C]// Proceedings of the 11th International Workshop on Atmospheric Icing of Structures ．Montreal ，Canada ：11th International Workshop on Atmospheric Icing of Structures，2005：399-404.

[5] Hu Qin, Jiang Tao, Jiang Xingliang, Shu Lichun, Chen Yu, Li Chao. Experimental study on Vibration Acceleration of Ground electromagnetic pulse deicing System [J]. Power System Technology,2022,46(11):4541-4548.

[6] Zhang Zhijin, Yang Shenghuan, Jiang Xingliang, Zhu Chengzhi, Liu Ye. Characteristics of water jet in Hot water deicing Process of Power Equipment [J]. High Voltage Engineering,2021,47(03):1012-1019.

[7] Jiang Xingliang, Bi Conglai, Wang Han, Yang Zhongyi, Han Xingbo. Effect of inverted T Arrangement on Icing and AC Flashover Characteristics of Insulator String [J]. Transactions of China Electrotechnical Society,2019,34(17):3713-3720.

[8] Huang Yafei, Jiang Xingliang, Ren Xiaodong, Li Zhiyu. Research on Prevention of snow and Ice Disaster of Transmission Lines by Eddy Current Self-heating Ring [J]. Transactions of China Electrotechnical Society,2021,36(10):2169-2177.

[9] Bi Conglai, Jiang Xingliang, Han Xingbo, Yang Zhongyi, Ren Xiaodong. Anti-icing Method Using Expanded Wire instead of Split Wire [J]. Transactions of China Electrotechnical Society,20,35(11):2469-2477.

[10] Han Xingbo, WU Haitao, Guo Sihua, JIANG Xingliang, WANG Yujie. Research on Diameter selection method of rotating multi-conductor for Measurement of Icy Environment [J]. Transactions of China Electrotechnical Society,2022,37(15):3973-3980.

[11] Xia Zhengchun. Research on galloping and ice-shedding of ul-tra-high-voltage transmission conductors[D]. Wuhan, China: Huazhong University of science and technology, 2008.

[12] MENG X, WANG L, HOU L, et al. Dynamic characteristic of ice-shedding on UHV overhead transmission lines[J]. Cold Regions Science and Technology, 2011, 66(1): 44-52.

[13] JIANG Xingliang, SUN Caixin, GU leguan, et al. Characteristics of traverse ice coating and Rime ice coating model in Three Gorges Area [J]. Journal of Chongqing University (Natural Science Edition), 1998, 21(02): 18-21.

A new deicing method based on shock wave generated by liquid-electric effect

Zhaoxia Peng[1,2], Guolin Yang[1,2], Zhongfeng Zhu,[1,2] Zhijin Zhang[1,2], Qin Hu[1,2], Xingliang Jiang[1,2], Yutai Li[1,2]*

1 Xuefeng Mountain Energy Equipment Safety National Observation and Research Station, Chongqing University, Chongqing 400044, China;
2 School of Electrical Engineering, Chongqing University, Chongqing 400044, China;

*Corresponding author: Yutai Li E-mail: liyt@cqu.edu.cn

Abstract— **The persistence of extreme weather in recent years has been a wake-up call for human society. There is no time to lose in addressing environmental issues. Wind power, as a clean energy source, has received great attention and has been widely used. However, the problem of wind turbine blade ice cover in cold winter is still difficult to solve. In this regard, we propose a novel mechanical de-icing method: the shock wave generated by the liquid electric effect is used to de-ice the blades. In this study, an experimental platform for the liquid-electric effect is constructed, and the feasibility of this new de-icing method is experimentally verified. The research results are expected to solve the icing problem of wind turbines under extreme low temperature environment and promote the sustainable development of human society.**

Keywords—***deicing; shock wave; liquid-electric effect***

I. INTRODUCTION

The continued high incidence of extreme weather in recent years has been a wake-up call for human society. The State of the Global Climate in 2022, published by the World Meteorological Organization (WMO), states that a succession of extreme weather events across the globe has affected the livelihoods of millions of people around the world and caused untold damage [1]. Between September 2020 and March 2023, the Earth's northern hemisphere experienced an extremely rare "triple" La Nina climate event [2] that resulted in colder winters and hotter summers. Climate change is the main cause of the frequent occurrence of extreme weather events, and in response to climate change, a number of countries and regions have proposed carbon neutral and net zero emission targets [3]. As a result, there has been a dramatic change in the energy sector, with clean energy getting more attention. Wind power is growing rapidly in volume as an important clean energy source [4-5]. However, wind resource-rich areas (e.g., mountains, oceans) where wind farms are built usually face extreme humidity and low temperatures in winter. Thus, the blades of wind turbines are at serious risk of icing [6], as shown in Fig. 1. Downtime due to blade icing can result in a reduction in wind power generation of up to 20% of annual output, resulting in significant economic and energy losses [7-8]. Hence, de-icing technology for wind turbines blades has attracted a lot of focus and there is an urgent need to find a solution to this thorny issue.

Many of the current de-icing methods used for wind turbine blades have been slow to spread in practice due to more or less insurmountable shortcomings. Thermal de-icing methods include electrothermal de-icing, aerothermal de-icing and microwave heating de-icing [9-11]. This type of method melts the overlying ice by heating the blades, which requires long-

term maintenance of the temperature of the blade surface above the melting point of the ice, and the problem lies in the excessive power loss in the process of melting the ice. Material de-icing methods include spraying antifreeze, applying photo-thermal coatings and hydrophobic coatings [12-14]. These material methods are more effective in laboratory environments and in the early stages of ice cover, but less effective in actual field applications in harsh and complex environments. The geometries and scales of droplets and mists are more varied in the field, and the blade surface is more susceptible to contact with supercooled, very small-scale droplets (micron diameter) and icing. Mechanical de-icing methods include electric pulse de-icing and pneumatic pulse de-icing [15-17], which have received much attention. They have the advantage of high energy efficiency. However, they require modifications to the outer surface structure of the wind turbine blade, filling it with specific coils or air pockets through which the mechanical pulse dynamics effect can be realized.

Figure 1. Ice cover on the blades of wind turbines in winter (Hunan Province, China).

We propose here a novel mechanical de-icing method: pulsed discharge in the liquid to generate shock waves for breaking up the ice cover on the blade surface. This method has never been proposed and experimented with before. As early as 1905, Swedbery noticed the strong shock wave when he applied a pulsed high voltage to the liquid and discharged it. After this, a great deal of research has been carried out on its mechanism and applications [18-21]. The key advantages of this method for de-icing are its high energy efficiency and the fact that it does not require modification of the outer surface structure of the blades. The method is expected to overcome the limitations of other existing de-icing methods and solve the problem of wind turbine blade ice-covering.

In this paper, a preliminary exploratory study of the proposed new de-icing method is carried out. Firstly, the structure of a de-icing device based on the generation of shock

waves by pulsed discharges in the liquid, which can be mounted on the inner surface of wind turbine blades, was designed. The liquid-phase discharges were then tested to see if the shock waves generated by the liquid-phase discharges could traverse to the outer surface of the blades. At last, de-icing experiments were conducted to verify the feasibility of the new method.

II. Experiment Setup

The de-icing device shown in Fig. 2(a) was designed for mounting on the inner surface of the blades of a wind turbine. The copper electrodes have a tip-tip structure to create an extremely inhomogeneous electric field to reduce the breakdown voltage. The gap between the two electrodes was set to 1 mm. The liquid dielectric for the discharge is selected as antifreeze (60% ethylene glycol + 40% water) with a freezing point of -45 ℃ to prevent liquid from freezing at low temperatures. The materials of the liquid containers were considered in two separate categories, hard copper and soft latex tubing. The material thickness of both types of liquid containers is 2 mm. In this study the insulated board (epoxy resin) with a thickness of about 2 mm was used to replace (or simulate) the actual wind turbine blades.
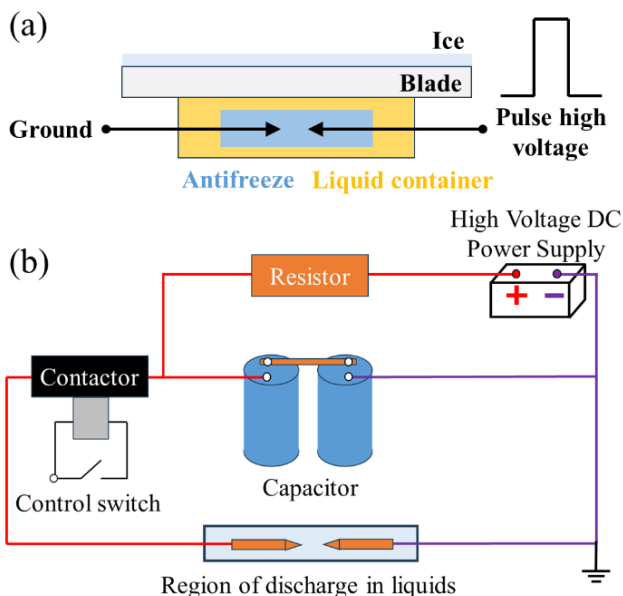
Figure 2. (a) De-icing device. (b) The circuit for generating high voltage pulses.

The circuit for generating high voltage pulses is shown in Figure 2(b). The high voltage DC power supply can output stable high voltage with an amplitude of 0-10 kV. The resistor has a resistance value of 1 kΩ to limit the charging rate of capacitors. Two capacitors are used in series, each with the capacitance of 400 μF and the voltage not exceeding 1.8 kV. The opening and closing of the high voltage DC contactor are controlled via a low voltage control switch. The voltage and current waveforms of the discharge were measured with Tektronix P6015A (75 MHz) and Rogowski coil, respectively. The measured voltage and current waveforms were captured with the oscilloscope Teledyne LeCroy HDO6104A with 10 GS/s sampling rate and 1 GHz bandwidth.

III. De-icing Experiments

Pulsed discharge experiments in antifreeze were carried out. The charging voltage of the capacitor bank is set at about 2 kV to ensure stable breakdown of the 1 mm liquid gap. Then the stored energy of the capacitor bank for each discharge experiment can be calculated as about 400 J by using Equation $W = \frac{1}{2} \cdot C \cdot U^2$. The measured voltage and current waveforms of the discharge are shown in Fig. 3. It can be seen that after the antifreeze is broken down, the voltage drops rapidly and the current rises rapidly. By multiplying the voltage and current waveforms and integrating the time, as shown in Equation $W_{\text{deposite}} = \int U \cdot I \mathrm{d}t$, the deposited energy of the pulsed discharge in liquid can be calculated as about 30 J. The energy injection efficiency is slightly less than 10%, possibly because the capacitors used are not dedicated pulse capacitors. This will not affect the subsequent deicing experiments.
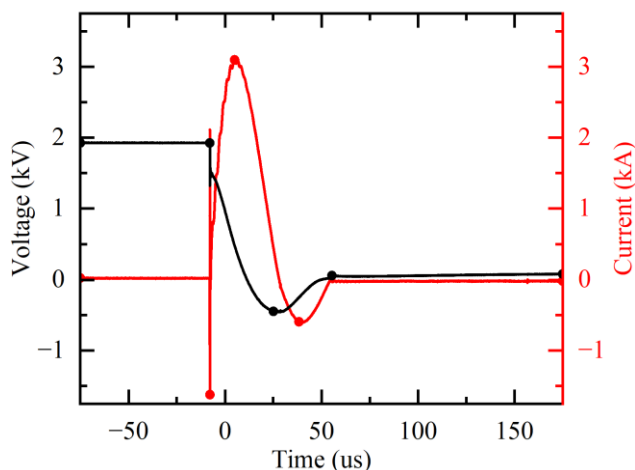
Figure 3. Discharge voltage and current waveforms.

Before carrying out the de-icing experiments, we need to first test whether the shock waves generated in the liquid by pulsed discharge can be transmitted to the outer surface of the blades. This will also determine which liquid container (hard copper or soft latex tubing) to select. As shown in Fig. 4(a), we preliminarily used screws to secure the de-icing device to the inside of the blade, while nails was arranged above the corresponding outer surface of the blade. Judgement of whether the shock wave can be transmitted to the outer surface of the blade is based on whether the nails can be bounced. De-icing experiments with shock waves generated by pulsed discharges were carried out in hard copper and in soft latex tubes, respectively. The results of the pulsed discharge experiments in the hard copper container were that the nails barely moved, which seems to indicate that it was difficult for the shock wave to be transmitted from within the hard copper to the outer surface of the blade. On the contrary, as shown in Fig. 4(b), the results of the pulsed discharge experiments in the soft latex tubes were better, and the nails was obviously jumped up by the shock, which seems to indicate that sufficient shock waves were successfully transmitted to the blade surface. Consequently, only soft latex tubes were chosen as the liquid container in the subsequent de-icing experiments in this paper.

In the large multi-purpose climate chamber constructed by our research group, the temperature was set to the range of -5 to -8 ℃ and the air humidity was elevated in order to achieve blade surface icing. The blade surface was covered with ice as

shown in Fig. 5(a), which was relatively uniform and about 1 cm thick. The de-icing experiments with the shock wave generated by the pulsed discharge in the antifreeze were performed several times consecutively. The results of these de-icing experiments were similar. When the discharge occurs in the antifreeze, the overlying ice is knocked away from the blade by the shock wave (as shown in Fig. 5(b)), but immediately falls back down to its original state by gravity (as shown in Fig. 5(c)). The experimental results illustrate the possibility that the ice covering the blades may be able to detach from the blades under the action of the discharge shock wave.
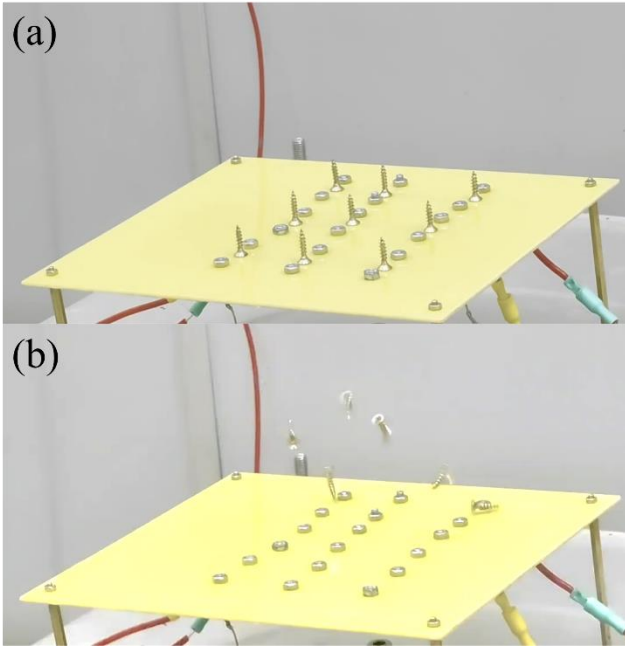
Figure 4. (a) The nails are placed on the blade before the discharge. (b) The nails are jumped up when the discharge occurs.
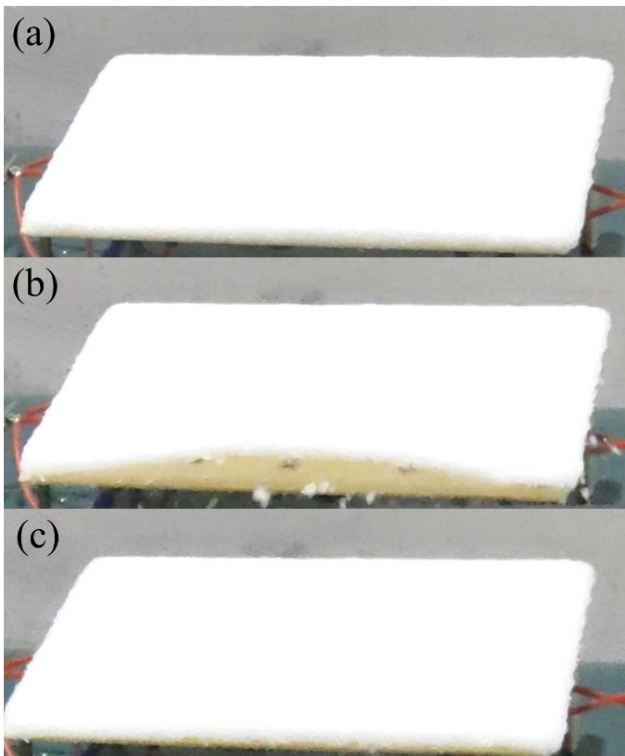
Figure 5. (a) Ice cover on blade before discharge. (b) Ice cover was knocked up during the discharge. (c) Ice cover on the blade after discharge.

Based on the above experimental results, we tentatively consider that this de-icing method is feasible, since the ice on the blades will not always be exactly perpendicular to the direction of gravity in an actual operating wind turbine. To confirm the conjecture, we arranged the blade in the same direction as gravity and conducted the de-icing experiment again. When only one discharge has occurred in the antifreeze, there is little difference from the frontal direction of the ice (Fig. 6(b)) from before the discharge (Fig. 6(a)). However, when viewed further from the side of the ice, the effect of de-icing became apparent, as shown in Fig. 6(c). Clearly the ice has mostly fallen off the surface of the blades. The ice didn't fall because it was supported by the table top. After two discharges occurred in the antifreeze, the ice was broken and essentially completely detached from the blade, as shown in Figure 6(d). The results of this set of de-icing experiments fully confirm the feasibility of the new de-icing method proposed in this paper.
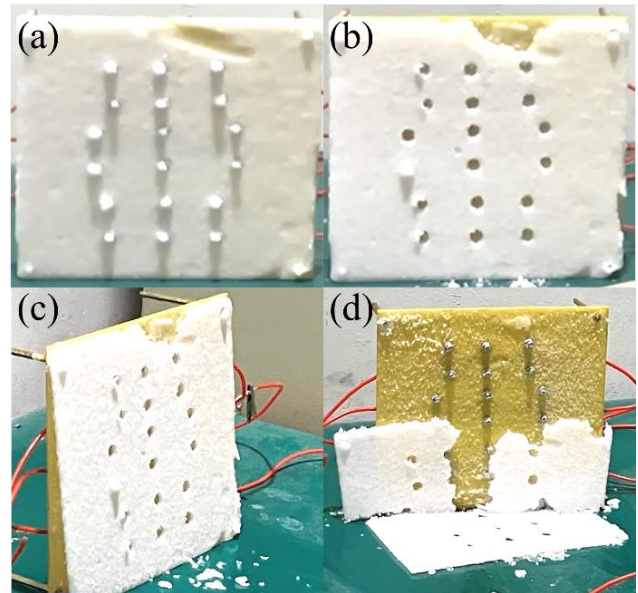
Figure 6. (a) Ice cover on blade before discharge. (b) Frontal view of ice when discharged once. (c) Side view of ice when discharged once. (d) Ice detaches from the blade when discharged twice.

IV. CONCLUSIONS

In summary, this paper presents a new de-icing method based on shock waves generated by liquid discharges. The liquid discharge structure arranged on the inner side of the blade is designed, and experiments were carried out to test the presence of shock waves at the outer surface of the blade and de-icing experiments were conducted. The experimental results show that the shock wave generated in the antifreeze can be transmitted to the outer surface of the blade, and the de-icing effect is good. This study provides a new idea for solving the icing problem of wind turbine blades, and it is also possible to extend the solution to the icing problem of other plate structures, such as aircraft wings. After that, the author will further study the basic scientific issues such as the deicing principle of this method.

REFERENCES

[1] World Meteorological Organization. State of the Global Climate in 2022.

See "https://public.wmo.int/en/our-mandate/climate/wmo-statement-state-of-global-climate".

[2] Iwakiri T, Imada Y, Takaya Y, et al. Triple-Dip La Niña in 2020-23: North Pacific Atmosphere Drives 2nd Year La Niña. *Geophysical Research Letters*. 50(22), e2023GL105763 (2023).

[3] Ma Jing, Kong Huiwen, Wang Jianxiao, et al. Carbon-neutral pathway to mitigating transport-power grid cross-sector effects. *Innovation*. 5(3), 100611 (2024).

[4] Lindroos TJ, Ikäheimo J. Profitability of demand side management systems under growing shares of wind and solar in power systems. *Energy Sources Part B-Economics Planning And Policy*. 19(1), 2331487 (2024).

[5] Sahi N Kubra Nur, Sutcu Muhammed. Probabilistic assessment of wind power plant energy potential through a copula-deep learning approach in decision trees. *Heliyon*. 10(7), e28270 (2024).

[6] Shu LC, Yu Z, Hu Q, et al. Numerical and Experimental Investigations of Deicing Performance for the Pneumatic Impulse Deicing Method. *Journal of marine science and engineering*. 11(7), 1371 (2023).

[7] Davis NN, Pinson P, Hahmann AN, et al. Identifying and characterizing the impact of turbine icing on wind farm power generation. *Wind Energy*. 19(8), 1503-1518 (2016).

[8] Zarasvand KA, Pope C, Nazari S, et al. Durable Metallic Surfaces Capable of Passive and Active De-Icing. *Advanced Engineering Materials*. 24(12), 2200573 (2022).

[9] Zhang ZJ, Yang SH, Jiang XL, et al. Hot Water Deicing Method for Insulators Part 2: Analysis of Ice Melting Process, Deicing Efficiency and Safety Distance. *Ieee Access*. 8, 130729-130739 (2020).

[10] Shu LC, Qiu G, Hu Q, et al. Numerical and experimental investigation of threshold de-icing heat flux of wind turbine. *Journal of wind engineering and industrial aerodynamics*. 174, 296-302 (2018).

[11] Vertuccio L, De Santis F, Pantani R, et al. Effective de-icing skin using graphene-based flexible heater. *Composites Part B-Engineering*. 162, 600-610 (2019).

[12] Tang BH, Wang Q, Han XC, et al. Fabrication of anti-icing/de-icing surfaces by femtosecond laser. *Frontiers in chemistry*. 10, 1073473 (2022).

[13] He ZW, Xie HM, Jamil MI, et al. Electro-/Photo-Thermal Promoted Anti-Icing Materials: A New Strategy Combined with Passive Anti-Icing and Active De-Icing. *Advanced Materials Interfaces*. 9(16), 22000275 (2022).

[14] Shi J, Ke SL, Wang F, et al. Recent advances in photothermal anti-/de-icing materials. *Chemical Engineering Journal*. 481, 148265 (2024).

[15] Jiang XL, Wang YY. Studies on the Electro-Impulse De-Icing System of Aircraft. *Aerospace*. 6(6), 67 (2019).

[16] Labeas GN, Diamantakos ID, Sunaric MM. Simulation of the electroimpulse de-icing process of aircraft wings. *Journal of aircraft*. 43(6), 1876-1885 (2006).

[17] Petrenko VF, Sullivan CR, Kozlyuk V, et al. Pulse electro-thermal de-icer (PETD). Cold Regions Science and Technology. 65, 70-78 (2011).

[18] Yi Liu, Zhiyuan Li, Xiandong Li, et al. Intensity improvement of shock waves induced by liquid electrical discharges. *Physics of Plasmas*. 24, 043510 (2017).

[19] Yifan Huang, Hui Yan, Bingzhe Wang, et al. The electro-acoustic transition process of pulsed corona discharge in conductive water. *Journal of Physics D-Applied Physics*. 47(25), 255204 (2014).

[20] Yuan Li, Linbo Li, Jiaye Wen, et al. Towards an improved understanding of nanosecond-pulse discharge initiation in water: from cavitation to electron multiplication. *Plasma Sources Science and Technology*. 29(7), 075005 (2020).

[21] Ying Sun, Timoshkin I V, Given M J, et al. Acoustic impulses generated by air-bubble stimulated underwater spark discharges. *IEEE Transactions on Dielectrics and Electrical Insulation*. 25(5), 1915-1923 (2018).

Site Experimental Study on Suspension-tension Arrangement for Preventing Transmission Lines from Icing Tripping

Xinliang Jiang[1], Lie Ma[a*], Hongmei Zhang[a], Heling Xie[a]

jiangxingliang@cqu.edu.cn, malie17@outlook.com, zhm3120@163.com,xhlstudy2014@163.com

Abstract— In cold regions and sometime in the temperate zone, one of the biggest problems on all level voltage transmission lines in winter is icing failure both at structures of tower and insulator strings. It is always to cause both structural damages and electrical short circuits. Through investigating all over China, it indicates that the suspension insulator string on support towers is much likely to flashover in icing condition. And the worst case is that, so far, there is still not a good way to prevent transmission lines from icing short circuit or icing flashover all over the world. Therefore, it is very important to research and take a reasonable arrangement mode for the insulator string of support towers in transmission lines. After a lot of experimental and theoretical analyses, we find that the suspension-tension arrangement has a very good performance in anti-pollution-flashover for transmission lines in icing regions because the icing flashover is always associated with pollution. Based on the experiment results carried at Xuefeng Mountain Natural Icing Station from December 2017 to February 2018, it is found that the suspension-tension arrangement can effectively enhance the flashover voltage of the same length contaminated insulator string in icing condition compared with normal suspension insulator string. And it is also found that there is a best mode for the vertical branch length and the lateral branch in the suspension-tension arrangement insulator strings.

KEYWORDS— *icing tripping; suspension-tension arrangement; flashover voltage; critical arc length*

I. INTRODUCTION

With the development of power electronics and control technology, the reliability of power supply in modern power grids is getting higher and higher, and the failure probability of internal equipment and control in power grids is getting lower and lower [1]. However, as the global warming and the frequency of extreme weather events increase [2], the potential for unpredictable extreme weather conditions and natural disasters in the wild natural environment and the possibility of large-scale power outages are increasing [3]. Icing and snowing in winter is one of the serious natural disasters faced by transmission lines [3-4], which can not only cause mechanical damage to transmission lines but also lead to external insulation flashover of the transmission line, resulting in a power grid tripping [5]. For example, in January 1998, a serious icing accident occurred in transmission lines, causing large-scale blackouts in the United States and Canada. In early 2008, an extremely serious icing disaster occurred in southern China that caused 13 major provinces' power outages [6]. For decades, the impact of ice and snow on the safety of power grids and its protection methods and measures have been paid much attention to by the whole world [7-12]. A variety of methods and technical measures are put forward to prevent tower collapse and transmission line breakage [13]. For example, since the large-scale ice disaster in China 2008, the DC ice-melting technology has been widely promoted, and thousands of ice-covered online monitoring devices based on the change of ice tension of transmission lines have been installed [14]. However, there is still no good method to prevent the external insulation flashover of transmission lines caused by icing [15].

In this paper, through a large number of on-site icing observations and insulator icing flashover experiments in the natural environment, a method of using the suspension-tension arrangement to prevent the flashover of transmission lines was proposed. Through experimental and theoretical analysis, it is found that the suspension-tension insulator arrangement can effectively improve the electrical

performance of the outer insulation of the transmission lines under freezing conditions. Therefore, it has a good application prospect for preventing the flashover trip of the transmission lines [7].

II. 2 TEST FACILITIES AND PROCEDURES

A. Specimens

In this paper, the sample is glass insulator LXP-210. The technical parameters and structure schematic diagram of LXP-210 are shown in Table 1 and Fig. 1. Among them, H is the structure height of the insulator, D is disk diameter, L is creeping distance.

Table 1 Test insulator technical parameters.

Insulator type	Material	H/mm	D/mm	L/mm
LXP-210	Glass	170	280	390
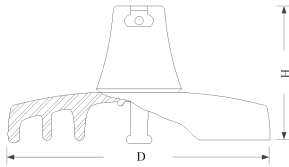
Fig. 1 Structure schematic diagram of LXP-210

B. Test Facilities

The experiment in this paper was carried out in the natural environment at the Xuefeng Mountain Natural Icing (Contamination) Station of Chongqing University (Fig. 2) from 12th January 2018 to 11th February 2018. The schematic diagram of test equipment is shown in Fig.3. The altitude of the station is 1500m. The ice age is from October to March of the next year, the maximum ice thickness reaches 500mm (27.3mm conductor). And the maximum wind speed is 35m/s. All of these conditions make the station an ideal place to do icing tests in the natural environment. There are two glaze tower squared 9m*9m*9m, equipped with a test section of conductor, which is 120m long .

Fig. 2. *Xuefeng Mountain Natural Icing (Contamination) Station of Chongqing University*
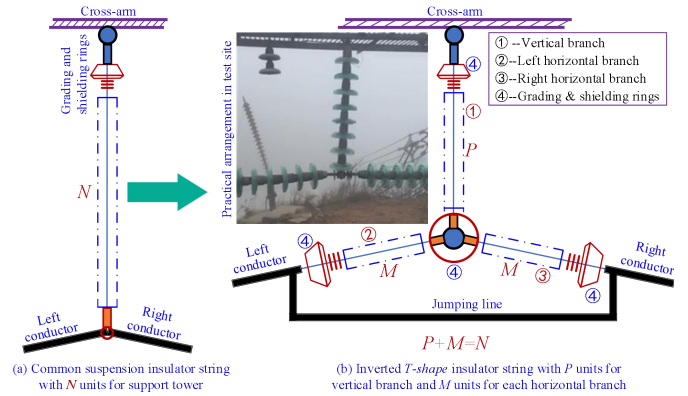
Fig. 3. *With suspension-tension arrangement insulator string replacing the suspension one*

The test was carried out on the left glaze tower. The arrangement of the test insulator string is inverted T-shape, which means, the N units of suspension insulator string in the conventional linear tower is divided into three branches, including a vertical branch (P units), a left lateral branch (M units) and a right lateral branch (M units). As shown in Fig. 3, it satisfies the condition ($P+M=N, M<P$), that is, increasing the M units of insulators to obtain the new arrangements (the increased insulator cost is relatively negligible compared to the annual ice flashover accident).

The schematic diagrams of AC and DC test equipment refer to the literature and respectively. The ±800kV/300mA DC or 500kV/2A AC test power supply is used in the test, which meets the requirements of the IEC standard for icing test power supply. In addition, the voltage divider ratio of the resistor divider is 2000:1.

C. Procedures

The sample is pre-contaminated in the room with

different ESDD and NSDD. After naturally dried, it is hung under the glaze tower in a suspension-tension arrangement. The maximum number of vertical branch insulator is 8 units, the maximum number of two lateral branches insulator is 5 units respectively.

III. RESULT AND DISCUSSION

Testing continuously for nearly a month, the 110kV insulator string test was completed under similar environmental conditions. Some data whose standard deviation is over 15% was discarded, and the remaining were those whose standard deviation was between 5% and 15%. The effective test results are shown in Fig. 4 and Fig. 5 (As it's easy to observe the relatively large standard deviation of test results test from the curve, the standard deviation of each test result is not shown in the plot.).

A. Flashover characteristics of common suspension insulator strings

The electrical characteristics of the insulator are influenced by the test site, environmental conditions and the test operator [24]. In order to compare the different electrical characteristics of different insulator arrangements, firstly, the flashover voltage of the suspension insulator string, which is used in the conventional linear tower under ice-covered conditions, is given, as shown in Fig. 4. It can be seen that under the critical icing condition, the pollution flashover voltage of the LXP-210 insulator gradually decreases with the increasing contamination degree. But the decreasing trend of this condition is less steep than that of non-icing conditions. The characteristic exponents that characterize the influence of pollution under critical icing conditions are only 0.11 (AC) and 0.24 (DC), which are obviously less than the normal AC/DC pollution characteristic exponents of about 0.30. Besides, under the same environmental conditions, the AC flashover voltage of the LXP-210 insulator is significantly different from the DC flashover voltage. For example, under the critical icing condition, when the NSDD is 0.12mg/cm^2, the DC flashover voltage (14.6kV) is reduced by 17.0% compared with AC flashover voltage (17.6kV).
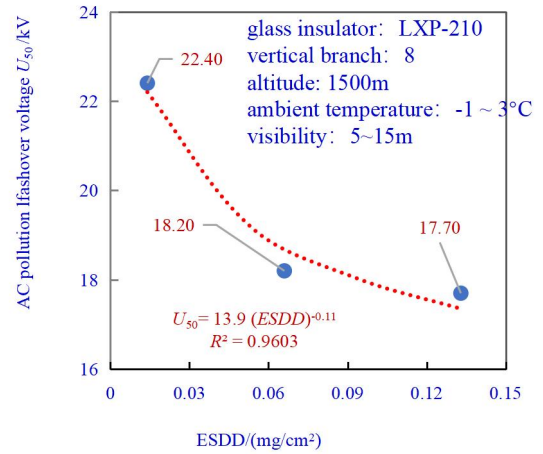
(a)
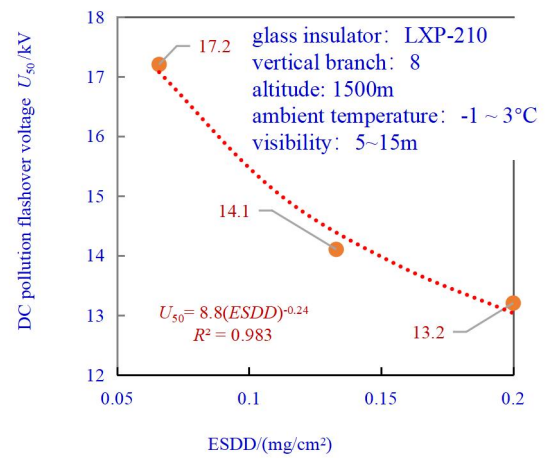
(b)

Fig. 4. *Pollution flashover voltage (kV/piece) of 110kV suspension insulator string in the critical ice-covered environment of Xuefeng Mountain station* **(a)** *AC,* **(b)** *DC*

B. Flashover characteristics of suspension-tension arrangement insulator strings

225

(a) ESDD/NSDD=0.066/0.398mg/cm2

(b) ESDD/NSDD=0.133/0.996mg/cm²

(c) ESDD/NSDD=0.20/1.2mg/cm²
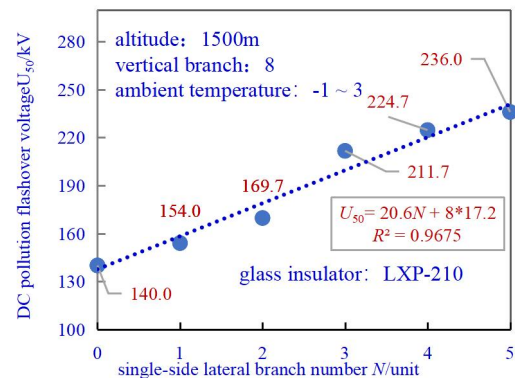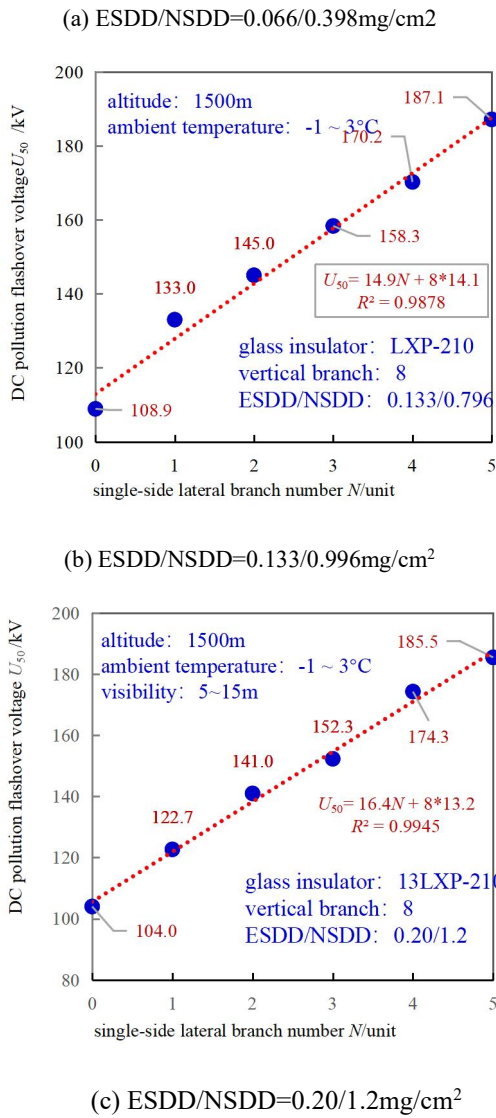
***Fig. 5.** AC and DC pollution flashover voltage of suspension-tension arrangement under critical ice conditions in the natural environment*

Table 2 Pollution flashover voltage of suspension-tension arrangement at the critical ice-covered condition

ESDD/NSDD (mg/cm²)	Average flashover voltage of vertical branch (kV/unit)		Average flashover voltage of lateral branch (kV/unit)	
	AC	DC	AC	DC
0.014/0.082	22.4	/	25.2	/
0.066/0.398	18.2	17.2	18.5	20.6
0.133/0.798	17.7	14.1	18.6	14.9
0.20/1.20	/	13.2	/	16.4

The conditions of the natural field station were harsh and difficult to control during the test. The range of ESDD was between 0.014 and 0.20 mg/cm², based on the test conditions at that time. In this test, the ratio of NSDD to ESDD is 6:1, and the test results are shown in Fig. 5.

It can be seen from Fig. 5 and Table 2 that:

Compared with the only one flashover path of common suspension insulator strings, there are two flashover paths of the suspension-tension insulator string. One path is along the vertical branch and the left lateral branch, and the other is along the vertical branch and the right lateral branch. The flashover voltage is nonlinear along the total path of the insulator string, but for the vertical branch (P) or lateral branch (M), the pollution flashover voltage under critical icing conditions is linear. For example, at severely polluted conditions, ESDD/NSDD is 0.133/0.798 mg/cm², the flashover voltages of the AC and DC are ($18.6M+17.7P$) and ($14.9M+14.1P$) respectively. So the flashover voltages of the whole insulator string are nonlinear. But for the vertical or lateral branches respectively, the flashover voltage is linear. Moreover, the lateral branch can increase flashover voltage relatively more than the vertical branch. Therefore, a longer length of the lateral branch should be adapted in the suspension-tension arrangement.

(2) The more serious the contamination is, the better anti-icing flashover effect the suspension-tension arrangement insulator has. On the unit number of the vertical branch insulators is 7~8, adding 1~5 units of insulators to each lateral branch, the average single unit flashover voltage of lateral branch insulator is higher than that of the vertical branch insulator. For example, when the ESDD/NSDD is 0.014/0.082 mg/cm², for common suspension insulator strings, the AC unit flashover voltage of the vertical branch is 22.4kV. But for suspension-tension arrangement insulator strings, the flashover voltage of the lateral branch is 25.2kV, which is increased by about 11.0%.

(3) The comparison of flashover characteristics between common suspension insulator strings and suspension-tension arrangement insulator strings is achieved through Fig. 4 and Fig. 5 (d), where the unit number of common suspension insulator strings is 8 units and the unit number of suspension-tension arrangement insulator strings is (7+i) units, where i is 0~4.

IV. Conclusion

Through experimental and theoretical analysis, the AC/DC contamination and icing flashover characteristics of the 110kV system suspension-tension arrangement insulator strings are studied. The impulse discharge performance and the development of relevant fittings are still in progress. The conclusions are as follows:

(i) The suspension-tension arrangement is a new type of arrangement for decreasing flashover tripping of transmission lines in ice-covered areas. The suspension-tension arrangement can significantly improve the ability of transmission lines to resist icing and flashover.

(ii) The structure of the inverted T-shaped arrangement can be optimized according to the icing and polluted environment. Generally, the length of the lateral branch can be increased as much as possible to make the length of the vertical branch less than or equal to the length of the critical flashover arc.

(iii) The reason why the inverted T-shaped arrangement improves the electrical characteristics is the shunting effect of the lateral branches, which can prevent the development of the local arc, control the length of the critical flashover arc, and improve the voltage at which the local arc develops into a critical flashover current.

References

[1] X. Jiang, and H. Yi, 'Ice Accretion on Transmission Lines and Protection' (*Beijing: China Electric Power Press*, 2002) (in Chinese).

[2] L. Chen, H. Zhang, Q. Wu and V. Terzija, "A Numerical Approach for Hybrid Simulation of Power System Dynamics Considering Extreme Icing Events," *IEEE Transactions on Smart Grid*, 2018, 9(05), pp. 5038-5046

[3] Bernstein A, Bienstock D, Hay D, et al. 'Power grid vulnerability to geographically correlated failures — Analysis and control implications' [C]// Infocom, IEEE. 2014:2634-2642

[4] Farzaneh M., and Chisholm W.: '50 years in icing performance of outdoor insulators', *IEEE Electrical Insulation Magazine*, 2014, 30, (1), pp. 14-24.

[5] Horwill C, Davidson C C, Granger M, et al. 'An Application of HVDC to the de-icing of Transmission Lines' [C]// Transmission & Distribution Conference & Exhibition. 2006:529-534.

[6] Q. Chen *et al.*, "Review on blackout process in China Southern area main power grid in 2008 snow disaster," *2009 IEEE Power & Energy Society General Meeting*, Calgary, 2009: 1-8.

[7] Farzaneh M, Chisholm W A. Effects of Ice and Snow on the Electrical Performance of Power Network Insulators[M]// Atmospheric Icing of Power Networks. 2008.

[8] Shu, Shang, Jiang, et al. Comparison between AC and DC flashover performance and discharge process of ice-covered insulators under the conditions of low air pressure and pollution[J]. Generation Transmission & Distribution Iet, 2012, 6(9):884-892.

[9] X. Jiang, Y. Wang, L. Shu, Z. Zhang, Q. Hu and Q. Wang, "Control scheme of the de-icing method by the transferred current of bundled conductors and its key parameters," *IET Generation, Transmission & Distribution*, 2015, 9, no. (15), pp. 2198-2205.

[10] M. Yan, *et al.*, "Enhancing the Transmission Grid Resilience in Ice Storms by Optimal Coordination of Power System Schedule With Pre-Positioning and Routing of Mobile DC De-Icing Devices," *IEEE Transactions on Power Systems*, 2019, 34(4), pp. 2663-2674.

[11] Z. Peter, C. Volat, M. Farzaneh and L. I. Kiss, "Numerical investigations of a new thermal de-icing method for overhead conductors based on high current impulses," *IET Generation, Transmission & Distribution*, 2008, 2(5), pp. 666-675

[12] R. Bernardo, J. Cardoso, R. Catalão and L. Ilharco, "Anti-ice and snow coating for EDP Distribuição's overhead lines," in *CIRED - Open Access Proceedings Journal*, 2017, 2017(1), pp. 33-36.

[13] Bothma J G . Transmission line tower collapse investigation: A case study[C]// Power Engineering Society Conference & Exposition in Africa. IEEE, 2013.

[14] Bin F , Lixing Z , Zhe T . The Study on Factors Influencing the Ice-Melting Performance of Transmission Line[C]// Fourth International Conference on Intelligent Systems Design & Engineering Applications. IEEE, 2014.

[15] Jiang X L, Zhang Z J, Hu Q., et al. Thinkings on the Restrike of Ice and Snow Disaster to the Power Grid[J]．High Voltage Engineering, 2018, 44(02): 463-469.

[16] J. Li, Z. Huang, X. Yan and Y. Wei, "An OH-PDMS-modified nano-silica/carbon hybrid coating for anti-icing of insulators part I: Fabrication and small-scale testing," *IEEE Transactions on Dielectrics and Electrical Insulation*, 2016, 23(2), pp. 935-942.

Experimental Investigation on Ice-Aluminum Interface Adhesion Strength Under Heating Conditions

Yusong Wang[1], Chengxiang Zhu[1], Chen Lei[1], Ke Xiong[1,2], Chunling Zhu[1,2,*]

[1] *College of Aerospace Engineering, Nanjing University of Aeronautics and Astronautics, Nanjing, 210016, China*
[2] *State Key Laboratory of Mechanics and Control of Mechanical Structures, Nanjing University of Aeronautics & Astronautics, Nanjing, 210016, China*

yswang1873@nuaa.edu.cn, cxzhu@nuaa.edu.cn, sx2101224@nuaa.edu.cn, kxiong@nuaa.edu.cn clzhu@nuaa.edu.cn

Abstract— **Accumulation of ice on airfoils and engines poses a serious threat to flight safety. The accurate measurement of adhesion strength between ice and substrate is crucial for the design of anti-icing/de-icing systems. In this study, a test bench for measuring adhesion strength is constructed and the effect of heating temperatures on adhesion strength at different initial substrate temperatures and heating powers is examined. A parameter, designated as AW, is introduced to evaluate the heating power in terms of energy consumption and adhesion strength. The results indicate that adhesion strength dMoreover, the adhesion strength decreases at a slower rate as the initial temperature decreases. Additionally, the temperature at which Weak Adhesion State (WAS) occurs during heating changes with the initial temperature. Higher power heating leads to a greater decrease in adhesion strength for the same temperature increase. The AW values demonstrate that moderate power heating is more advantageous for reducing adhesion strength with minimal energy consumption.**

Keywords—***Aircraft de-icing; Adhesion strength; Experimental setup; Freezing temperature; Heating power***

I. INTRODUCTION

When aircrafts encounter cold cloud conditions during flight, it can cause ice to accumulate on the surface, which in turn negatively affects the lift and increases drag, posing a significant threat to flight safety [1]. Therefore, there is a critical need to focus on effective anti-/de-icing systems in aircraft design. Presently, there are established anti-icing/de-icing systems such as the electrothermal system, electro-impulse system, and hot-air system [2-4]. Additionally, some newer technologies such as plasma jet, icephobic surfaces, and hybrid systems have shown significant development [5-7].

Regardless of the anti-icing/de-icing technology used, the primary challenge lies in the study of adhesion between ice and the aircraft surface. Consequently, ice adhesion has been extensively researched by the scientific community. Researchers have delved into adhesion mechanisms and Petrenko and Whitworth, for example, presented an explanation of the adhesion mechanism between ice and substrate from a molecular perspective [8]. The mechanisms were categorized into covalent or chemical bonds, Van der Waals forces, and ionic power. Knuth et al. interpreted ice adhesion mainly through a mechanical connection theory, suggesting that when ice made its way into a structure, like a

surface groove or hole, it formed an "anchor"-like structure connecting it to the substrate. Based on this theory, he proposed a mathematical model for predicting shear adhesion strength [9]. Derjagin put forth the electrostatic adhesion theory, suggesting that mutual attraction between the ice and the substrate was driven by electrostatic forces [10]. Guy Fortin also introduced an adhesion model based on this theory [11]. Frederic Guerin proposed the presence of a liquid-like layer (LLL) situated between the ice and the substrate, which possesses properties intermediate to those of ice and water. He formulated an equation to compute the adhesion strength, incorporating surface structure, surface energy, medium volume diameter (MVD), and other relevant factors [12].

Further studies have also been conducted to measure the adhesion strength between ice and the substrate through experimental means. The Centrifuge Adhesion Test (CAT) and the direct mechanical test are the two most commonly utilized testing methods. The Anti-Icing Materials International Laboratory (AMIL) first introduced the Centrifuge Adhesion Test (CAT) in 2005 to study the adhesion force, which leveraged centrifugal force to remove ice [13]. Due to its similar working principle, this method became a common choice for studying the adhesion of rotorcraft surfaces [14]. Kulinich evaluated the adhesion strength of superhydrophobic surfaces using this method [15]. Meanwhile, Brouwers et al. employed the Instrumented CAT (ICAT) to investigate ice adhesion, incorporating an airfoil and impact ice in the test [16]. In their study, the centrifugal force is augmented by the continuous accumulation of ice, which differs from the previous approach of increasing rotation speed. However, these methods based on centrifuge force unavoidably raise concerns about accurate capture at the moment of ice shedding and sample integrity. Apart from the CAT, the direct push/pull method has been widely used by researchers to assess adhesion strength. This method separates the ice and substrate interface by directly applying force to the ice sample. Adam J. utilized a push test to explore the relationship between water wettability and ice adhesion [17]. Ge pushed the ice with a needle to analyze the anti-icing properties of superhydrophobic surfaces[18]. Kevin investigated the forces that dislodge ice of various scales using the push method, and found a critical bonded length where a transition between strength-controlled and

toughness-controlled failure mode occurred [19]. More recently, Wang developed a new setup to measure the adhesive shear strength of impact ice on different substrates in icing wind [20]. Compared to the centrifugal method, the direct mechanical test is considered more cost-effective, time-efficient, and reliable. While centrifugal tests tend to provide more consistent results, many researchers prefer the direct push/pull methods due to their advantages.

Based on the aforementioned research, numerous scholars have carried out both theoretical and experimental analyses on ice adhesion. However, none of the mentioned studies have addressed the adhesion of ice under conditions of substrate heating. Considering the widespread use and promising potential of electrothermal anti/de-icing systems, it is essential to comprehensively investigate the adhesion properties of ice when the substrate is heated. To address this gap, Zhang conducted preliminary research on composite materials, examining the ice adhesion forces under various heating temperatures, heating voltages, and heating durations. Notably, the study did not involve an aluminum substrate [21]. It was observed that increased energy consumption led to a reduction in adhesion strength. Yet, from an energy-saving standpoint, finding a balance between energy consumption and adhesion strength degradation is crucial. This aspect remains unexplored at present.

This article presents the development of an experimental setup to assess the shear force between ice and aluminum substrates. A set of experiments is conducted to gauge shear adhesion strength under varying heating parameters. Furthermore, a dimensionless parameter is introduced to identify a balance between energy expenditure and reduction in adhesion strength.

II. EXPERIMENTAL SETUP

Conducting direct-force tests, particularly using the push method, is one of the most dependable techniques for assessing the adhesive strength between ice and substrate. We have developed an experimental apparatus based on this principle, illustrated in Fig. **1**.
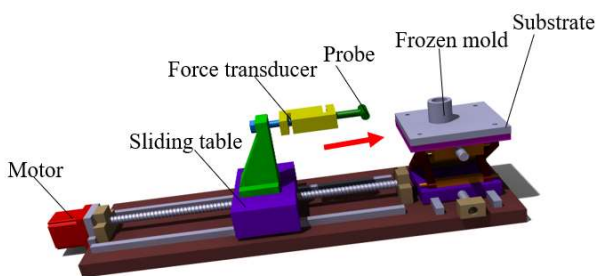
Fig. 1 The panorama of the experimental set-up

Initially, the ice is frozen within a mold on the aluminum plate. Afterward, the motor drives the sliding table towards the ice, causing the force transducer and the probe to push the mold and ice to slide. When the ice becomes detached from the substrate, the sensor reading represents the adhesion shear force. By dividing the adhesion force by the contact area between the ice and the aluminum plate, the shear strength can be calculated:

$$\tau = \frac{F}{A} \qquad (1)$$

Where τ is adhesion shear strength, F the adhesion shear force and A the contact area between ice and aluminum plate.

The heating system consists of a substrate surface, a heating layer, and an insulation laye, as shown in Fig. 2. The insulation layer is designed to prevent heat propagation in other directions. The heating layer is positioned between the substrate surface and insulation layer. The controller enables the adjustment of the heating temperature. Additionally, all substrate surfaces were sanded with 1000 grit sandpaper to ensure a uniform surface roughness.
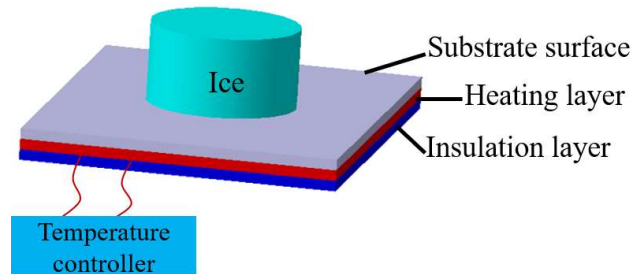
Fig. 2 Heating components

III. RESULTS AND DISCUSSION

A. Effect of freezing temperature on adhesion strength

The influence of various freezing temperatures on adhesion strength was initially investigated in unheated conditions. The results are shown in the Fig.3. With the increase in freezing temperature, the shear adhesion strength between the ice and the substrate first increases and then decreases, reaching a peak at approximately -11°C. The rate of reduction between -11°C and -3°C is higher than the rate of increase between -19°C and -11°C. When the temperature reaches approximately -3°C, the adhesion strength decreases to the lowest level. Hence, it is evident that freezing temperature significantly impacts adhesion strength. Consequently, when studying adhesion strength under heated conditions, the different initial freezing temperatures should be taken into consideration
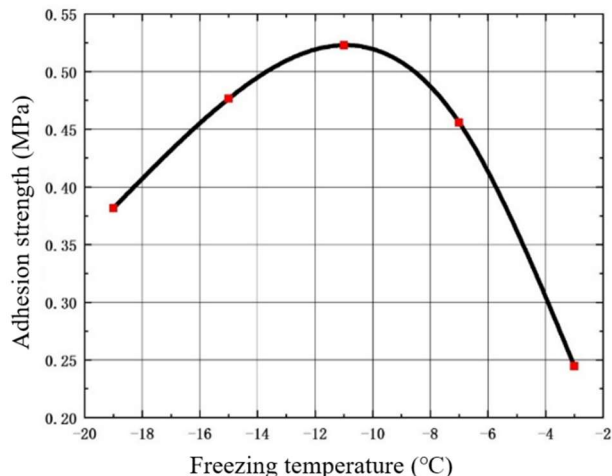
Fig.3 Adhesion strength at different freezing temperature without heating

B. Effect of heating temperature on adhesion strength

The substrate was then heated to varying temperatures. Due to the cold environment, maintaining a constant heating

temperature for the substrate was challenging. The final heating temperature was determined based on the sensor reading at the point of ice shedding. In Fig.4, the adhesion strength at different heating temperatures is displayed for a range of initial freezing temperatures (-19°C, -15°C, -11°C and -7°C). Clearly, regardless of the initial temperature, the adhesion strength decreased as the heating temperature increased. As the temperature rose, the chemical bonds formed by the molecules between the substrate and the ice layer began to degrade. Additionally, the heat led to partial melting of the ice layer embedded in the substrate microstructure, which weakened the mechanical interlocking effect between the ice and the substrate.
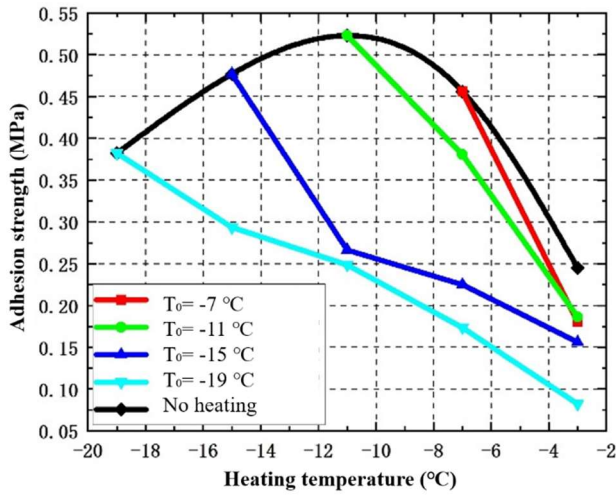
Fig.4 Adhesion strength at different heating temperatures for various initial freezing temperatures

To better describe the relative strength of adhesion, we define the adhesion state with adhesion strength less than 0.2 MPa as weak adhesion state (WAS). As depicted in Fig.4, when the initial freezing temperatures changed from -19°C to -15°C, and subsequently to -7°C, the temperature required for WAS varied from -8°C to -6°C, and then -3°C. It was evident that at lower initial temperatures, greater energy was needed to achieve the WAS, despite the lower adhesion strength without heating. Additionally, the findings indicated that it was unnecessary to heat the substrate above zero degrees when using an electric heating system, especially an electric-mechanical coupling system, for de-icing. Even at lower initial temperatures, heating the surface to -8°C was sufficient. The ice could be easily removed through aerodynamic or mechanical forces when the adhesion was in the WAS state.

C. Effect of heating power adhesion strength

To analyze the impact of heating rate on adhesion strength, we applied different power levels (10W, 30W, and 50W) to heat the substrate. Fig.5 presents the adhesion strength results at these power levels. While the different powers were not used on the same substrate, resulting in slight variations in initial adhesion strength. With the same temperature increase, higher heating power led to a greater decrease in adhesion strength, despite the shorter heating time. The slopes were -0.014 MPa/℃, -0.028MPa/℃, and -0.032MPa/℃ for 10W, 30W, and 50W respectively.
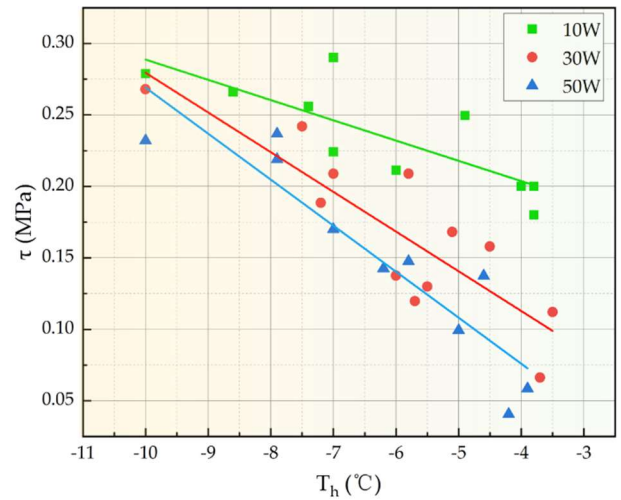
Fig.5 Adhesion strength at different heating temperature for various heating power

It was known that higher power would bring more energy consumption. Therefore, both the energy consumption and adhesion strength reduction should be taken into ac-count when selecting the heating power. A dimensionless parameter AW considering the above two factors was defined by equation (2), which characterized the adhesion weakening per unit of energy consumption.

$$AW = \frac{\tau_0 - \tau_h}{P \cdot t} \cdot V \qquad (2)$$

Where τ_0 and τ_h were the adhesion strength before and after heating respectively. P was the heating power. t was heating time. V was the volume of the ice sample, which could be easily calculated by the bottom area and height of cylindrical ice.

The data in Fig.6 showed the AW values at different heating power levels. Specifically, the AW values were reported at 2.94, 3.07, and 2.18 for 10W, 30W, and 50W respectively. The adhesion strength at 30W was the highest, followed by 10W and 50W. Although 50W resulted in a rapid decrease in adhesion strength, it was not efficient in terms of energy consumption. Therefore, in terms of energy optimization, a moderate power level, such as 30W, would be the preferred choice to reduce adhesion strength.
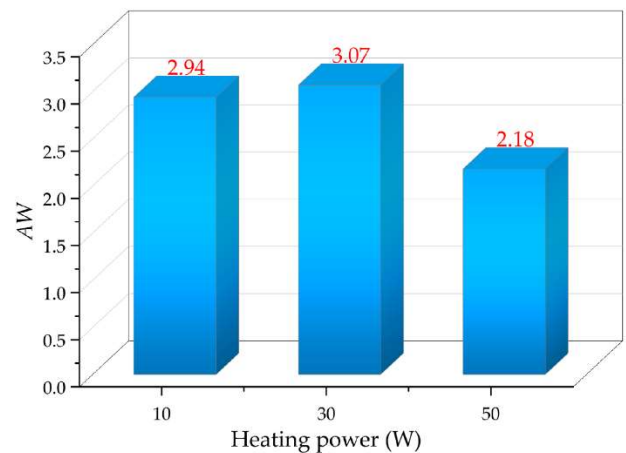
Fig.6 Values of AW at various heating power

IV. Conclusions

In the study, a high-precision adhesion test rig is employed to analyze adhesion strength under heating conditions. The research evaluates the impact of heating temperature on adhesion strength at various initial temperatures and heating power levels. The findings demonstrate a reduction in adhesion strength as heating temperature increases, with a more gradual decrease at lower initial temperatures. Additionally, the study introduces the concept of the weak adhesion state (WAS) to categorize adhesion and observes that the temperature of the WAS changes depending on the initial temperature. Moreover, higher heating power leads to a more pronounced weakening of adhesion strength at the same temperature rise. To account for energy consumption and adhesion weakening, the dimensionless parameter AW is introduced. The analysis indicates that choosing a moderate power level for heating can effectively reduce adhesion strength. These research findings can contribute to the development of energy-efficient and dependable electro-thermal or electro-mechanical hybrid de-icing systems to meet de-icing requirements.

Acknowledgment

References

[1] Cao, Y., Tan, W., Wu, Z. "Aircraft icing: An ongoing threat to aviation safety," *Aerospace Science and Technology* 2018, *75*, 353-385.

[2] Wang, Y., Guo, T., Li, K., Zhu, C., Du, Q. "Research on the dual-channel electro-impulse de-icing system of aircrafts," *Proceedings of the Institution of Mechanical Engineers, Part G: Journal of Aerospace Engineering* 2022, *236*, 2315-2326.

[3] Botura, Galdemir, Dave Sweet, and David Flosdorf. "Development and demonstration of low power electrothermal de-icing system," *43rd AIAA Aerospace Sciences Meeting and Exhibit.* 2005.

[4] Li, Linkai, et al. "An experimental study on a hot-air-based anti-/de-icing system for aero-engine inlet guide vanes," *Applied Thermal Engineering*, 167 (2020): 114778.

[5] Wang, Peng, et al. "A superhydrophobic/electrothermal synergistically anti-icing strategy based on graphene composite, " *Composites science and technology* 198 (2020): 108307.

[6] Ma, Liqun, et al. "Bio-inspired icephobic coatings for aircraft icing mitigation: A critical review," *Progress in Adhesion and Adhesives* 6 (2021): 171-201.

[7] Liu, Yang, et al. "An experimental study on the thermal characteristics of NS-DBD plasma actuation and application for aircraft icing mitigation," *Plasma Sources Science and Technology* 28.1 (2019): 014001.

[8] Petrenko, Victor F., and Robert W. Whitworth. *Physics of ice.* OUP Oxford, 1999.

[9] Knuth, Taylor Dayton. "Ice adhesion strength modeling based on surface morphology variations." Master Thesis, The Pennsylvania State University, Pennsylvania, USA, 2015.

[10] Deriagin, Boris Vladimirovich, N. A. Krotova, and Vol'demar Petrovich Smilga. *Adhesion of solids.* New York: Consultants Bureau, 1978.

[11] Fortin, Guy, and Jean Perron. "Ice adhesion models to predict shear stress at shedding." *Journal of adhesion science and technology* 26.4-5 (2012): 523-553.

[12] Guerin, Frederic, et al. "Analytical model based on experimental data of centrifuge ice adhesion tests with different substrates." *Cold Regions Science and Technology* 121 (2016): 93-99.

[13] Laforte, Caroline, and Arlene Beisswenger. "Icephobic material centrifuge adhesion test." *Proceedings of the 11th International Workshop on Atmospheric Icing of Structures,* IWAIS, Montreal, QC, Canada. 2005.

[14] Morelli, Myles, and Alberto Guardone. "A simulation framework for rotorcraft ice accretion and shedding." *Aerospace Science and Technology* 129 (2022): 107157.

[15] Kulinich, S. A., and M. Farzaneh. "On ice-releasing properties of rough hydrophobic coatings." *Cold Regions Science and Technology* 65.1 (2011): 60-64.

[16] Brouwers, Edward W., et al. "Ice adhesion strength measurements for rotor blade leading edge materials." *67th American Helicopter Society International Annual Forum 2011.* 2011.

[17] Meuler, Adam J., et al. "Relationships between water wettability and ice adhesion." *ACS applied materials & interfaces* 2.11 (2010): 3100-3110.

[18] Ge, Liang, et al. "Anti-icing property of superhydrophobic octadecyltrichlorosilane film and its ice adhesion strength." *Journal of Nanomaterials* 2013 (2013): 3-3.

[19] Golovin, Kevin, et al. "Low–interfacial toughness materials for effective large-scale deicing." *Science* 364.6438 (2019): 371-375.

[20] Wang, Yusong, et al. "Evaluation of the shear adhesion strength of impact ice by a new method." *Engineering Fracture Mechanics* 292 (2023): 109641.

[21] Zhang, Yishu, Long Chen, and Hui Liu. "Study on ice adhesion of composite anti-/deicing component under heating condition." *Advanced Composites Letters* 29 (2020): 2633366X20912440.

Mitigating icicles on superhydrophobic PDMS surfaces using femtosecond laser-processed surface molds

Toshimitsu Sakurai[1], Toshihiro Somekawa[2,3], Yuji Hirai[4], Hiroki Matsushita[1], Atsushi Nishimura[1]

[1] Civil Engineering Research Institute for Cold Region, Public Works Research Institute, Japan
[2] Institute for Laser Technology, Japan
[3] Institute of Laser Engineering, Osaka University, Japan
[4] Department of Applied Chemistry and Bioscience, Chitose Institute of Science and Technology, Japan

First author: sakurai@ceri.go.jp

Snow and ice that fall from highway structures can disrupt traffic, sometimes causing accidents. The shedding of icicles also causes damage to vehicles. Icicles often form at road tunnel mouths and on road information boards, bridges, and other structures when heat sources melt snow. Anti-icing coatings have been used for decades to prevent snow and ice from adhering to highway structures. However, the lifetime of these coatings is only a few years, and there is a need for long-life anti-icing materials. Here, we report on the performance of superhydrophobic polydimethylsiloxane (PDMS) prepared by femtosecond laser processing surface molds in terms of water repellency and icicle mitigation under freezing temperatures. PDMS is known to have a long lifetime in ambient air. Femtosecond laser pulses created a laser-induced periodic surface structure (LIPSS) on a stainless-steel surface. The structure was molded onto PDMS. The PDMS was found to exhibit super-hydrophobicity, with a water contact angle of about 161° and a water sliding angle of about 2.0°. Water-cooled droplets were added to the PDMS surface to examine the mitigation of water repellency and icicle formation. The water droplets were found to roll off the superhydrophobic PDMS immediately, and the surface was found to mitigate icicle formation. However, the fact that water-cooled droplets also froze on the surface and the edge of the superhydrophobic PDMS surface indicates that the superhydrophobic surface with LIPSS does not afford complete anti-icing.

Icicle formation mitigation, femtosecond laser processing, molding, superhydrophobic PDMS

I. INTRODUCTION

Large chunks of snow suddenly falling onto vehicles from highway structures such as bridge superstructures and road signposts can cause traffic accidents and other damage. In Japan, several mitigation techniques have been examined and have proven useful [1][2][3]. For instance, tilted plates are installed on road information signs to reduce the duration of snow accretion. However, these plates can be insufficient for the heavy snowfalls that often occur in Hokkaido (the northernmost island of Japan), with large chunks of snow and icicles dislodging from them when heat sources melt the snow. Therefore, comprehensive measures against such shedding of snow and icicles are still needed.

In recent decades in Hokkaido, coatings made of organic fluorine compounds that promote snow-sliding have been widely used [4][5], and it is known that the specific heat and thickness of the material are related to snow-sliding [4][6]. Coatings are widely used, but these need to be reapplied every few years, and this lack of durability means that they fail to reduce maintenance budgets for road structures. More importantly, the environmental impacts of organo-fluorine compounds with fluorocarbon chains have begun to be reported, including concerns about health hazards due to their tendency to bioaccumulate in human bodies, and the use of these compounds has been restricted in the United States since 2018 [7]. Therefore, there is an urgent need to develop materials that do not use organo-fluorine compounds and to develop more durable alternative technologies for snow and ice repellency.

II. RECENT PROGRESS ON SURFACE REPELLENCY FOR SNOW AND ICE

Lotus leaves and taro leaves have cell-derived surface microstructures on the scale of tens of micrometers. These are formed by the waxes of the leaves. Such microstructures are known to be water-repellent and self-cleaning, shedding dust and other particles with rain droplets [8]. They are known to be superhydrophobic due to the air pockets on the concave surfaces, a phenomenon that can be explained by the Cassie‐Baxter model [9].

It is possible to artificially create a superhydrophobic surface with multiple concavo-convex structures that are seen on lotus leaves and other materials. Onda *et al.* (1996) [10] showed that a superhydrophobic surface could be achieved through a simple method of forming a fractal structure of alkylketene dimers by melting and crystallizing a paper coating agent. Surface wettability is generally enhanced by surface irregularities, and the fractal structure lends superhydrophobicity to the surface. Efforts to control surface wettability, including through the use of fractal surfaces, have resulted in various methods for producing water-repellent surfaces, including those that exhibit anti-icing or icephobicity (e.g., [11][12][13][14][15]).

Among the surface modifications that have been reported are slippery liquid-infused porous surfaces (SLIPS), which improve liquid repellency by using organic fluorinated oil infused on the surface, without increasing the contact angle as in the case of superhydrophobicity using microstructures [16]. Similar infused oils, such as silicone oil, have been used on the surface of poly-dimethylsiloxane (PDMS) materials [17].

PDMS is a polysiloxane hybrid polymer that exhibits thermal stability, biocompatibility, corrosion resistance, flexibility, and permeability [18]. By itself, PDMS has the

issues of low elastic modulus and low strength, but these issues can be overcome by adding particles or reinforcing agents inside or on the surface of PDMS (e.g., [19][20][21][22][23][24][25]).

Laser processing is also used to produce surface modifications. Irradiating and scanning a metal surface with a picosecond to a femtosecond laser beam can generate laser-induced periodic surface structures (LIPSS) with a periodic length of about the laser wavelength on the metal [26][27]. Superhydrophobicity can be imparted under certain processing conditions, depending on the metal [28][29]. A recent review addressed the use of femtosecond pulsed lasers in surface processing [30], and another review addressed the use of laser processing directly on materials to generate an anti-icing effect [31]. For instance, an aluminum surface that was meshed by direct nanosecond laser writing and direct picosecond laser interference patterning methods was found to be superhydrophobic. Water droplets on the superhydrophobic aluminum surface delay ice formation [32]. Additionally, a study used LIPSS on metal iron surfaces fabricated by a picosecond laser using the dimple processing method, and that surface was used as a mold for imparting superhydrophobicity to PDMS [33].

When the technology is to be applied to highway infrastructure, then the ability to mass produce the materials should also be considered. The production rate per unit area depends on the speed at which the laser scans across the material surface. The scanning speed required to impart superhydrophobicity ranges from 1 ~ 5 mm/s [30]. Depending on the pitch spacing, generating a large area of superhydrophobic surface can take a significant amount of time. In contrast, a technique for transferring the structure of a mold to a material has been reported as a method for mass production (e.g., [34]). Thus, mass production by roll-to-roll nanoimprint lithography (e.g., [35]) will be possible if superhydrophobic materials can be produced by molding. As the above studies suggest, it will be possible to develop highly durable anti-icing materials if multiple concavo - convex structures like lotus leaf surfaces can be formed on PDMS surfaces.

Here, we report on the water repellency and icicle mitigation under freezing temperatures of superhydrophobic PDMS fabricated by using femtosecond laser-processed surface molds. It should be noted that superhydrophobic PDMS is intended for application to anti-icing materials for highway infrastructure, where icicles often form when heat sources melt snow, but it is not intended for aviation (e.g., [36]) nor as a material with low surface adhesion against ice (e.g., [12]).

III. EXPERIMENTS

A. Mold preparation using a femtosecond laser

The laser system we used is the Solstice Ace (Spectra-Physics), with a wavelength, pulse duration, repetition rate, and maximum pulse energy of 800 nm, 100 fs, 1 kHz, and 5 mJ, respectively. The laser output energy is tuneable using polarizers and waveplates. Figure 1 is a schematic of the femtosecond laser processing system. The system is equipped with an XYZ stage that is spatially controllable in increments

of 1 μm, and the irradiation position can be scanned automatically according to the program. A circularly polarized laser (lens focal length = 150 mm) was guided to the processing stage, where it irradiated a wave plate (λ/4).) The laser beam irradiated the processing stage at a scanning speed of 2.0 mm/s in the XY plane. The fluence (laser energy per unit area, J/cm^2) was calculated from the processing marks on the metal plate. The process of irradiating and scanning with a femtosecond laser is hereafter referred to as "laser processing".

Stainless steel sheets (SUS304, JIS G 4305, hereafter referred to as "SUS") were used for our molds. The size of the SUS for observation by scanning electron microscopy (SEM) was 20 mm × 20 mm × 2 mm, and the size of the SUS for the mold used to transfer the structure by laser processing was 100 mm × 100 mm × 2 mm. SEM (VE-9800, Keyence) was used to observe the surface properties after laser treatment. A contact angle meter (DMe-200, Kyowa Surfaces Co., Ltd.) was used to measure the water contact angle (WCA) for a droplet of distilled water of 2 to 3 μL (for high-performance liquid chromatography). The WCA was measured two or three times for each fluence.
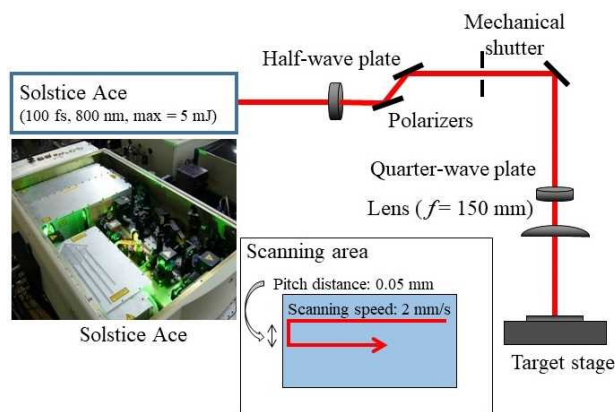
Figure 1. Schematic of femtosecond laser processing.

B. Molding, and the measurement of WCA and WSA

The PDMS used in the experiment was Silpot 184 (Sansyo Co., Ltd.). Carbon black (CB) of a few weight % (wt%) was added to the uncross-linked PDMS with the main solvent medium and the hardener at a ratio of 10:1. The uncross-linked PDMS was poured onto the laser-processed SUS mold and cross-linked at 60 °C for 12 hours using a vacuum oven at ambient pressure. We also made smoothed PDMS using a smoothed glass surface as a mold in the same manner. After thermal cross-linking, the PDMS was peeled off from the mold, and 3 μL of ultrapure water (25 °C, 18.2 MΩ·cm) was dropped onto the PDMS to measure the WCA and the water sliding angle (WSA) using an automatic contact angle meter (Drop Master, Kyowa Surface Science Co., Ltd.). The PDMS surface was observed using a field emission scanning electron microscope (FE-SEM, JSM-7800F, JEOL). Before the WCA and the WSA were measured, contaminants on the PDMS samples were washed out using ethanol and the samples were air-dried. The PDMS whose SUS surface was molded by laser processing will be referred to as "the Structure PDMS", and the PDMS whose surface was molded by using the smoothed glass will be referred to as "the Flat PDMS".

C. Icicle formation experiment and temperature ramping test

Figure 2 is a schematic of the icicle formation experiments. The temperature in the freezer (RRS-262NF, Remacom Co., Ltd.) was set to about –10 °C and tap water was dropped from above the sample using a rubber tube and snake nozzles (SN2-M-23, Fuso Seiki Co., Ltd.).
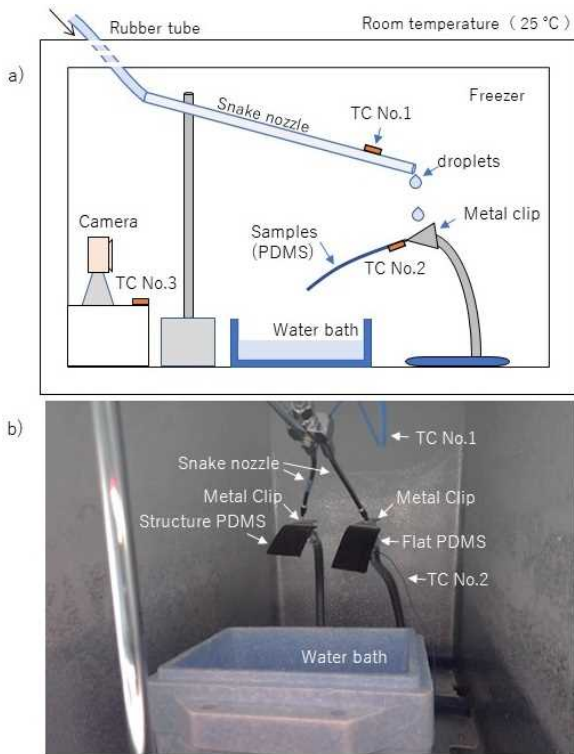
Figure 2. The setup of the icicle formation experiment. a) Schematic. b) An image taken by the camera set in the freezer. "TC" stands for "thermocouple". TC1, TC2, TC3 is attached on the snake nozzle, on the back side of the PDMS, and on the inner freezer, respectively.

The temperature of the droplets was monitored by a thermocouple at the nozzle tip, and the temperature at the nozzle tip was adjusted by the length of rubber tubing inserted into the freezer. Since the droplet temperature also depends on the flow rate, that rate was finetuned by the cock of the nozzle outflow. The flow rate of the droplets was set as $30 \sim 40$ drops per minute, measured by the number of drops per minute, with approximately 50 µL per drop as measured by the weight of 10 drops. The nozzle temperature and flow rate were balanced such that the water droplets formed ice on the surfaces or icicles at the sample edges.

The drops were placed on the metal clips shown in Figure 2. Note, that the impact of the drops on the PDMS was not considered (e.g., [37][38]) in this study because the drops were not directly placed on the PDMS. Thus, we imagine that the experimental setup reproduced the refreezing of water droplets from melting snow on highway infrastructure. The angle of the PDMS samples was approximately 50 degrees from horizontal at the metal clips.

To reproduce the melting icicles from materials on highway infrastructure, for a temperature ramping test, we opened the freezer cover and turned off the freezing, and the PDMS samples were irradiated by simulated solar light after the icicle formation experiment. We used a xenon lamp of 100 W with a spectral correction filter for the device (LAX-C100, Asahi

Spectra Co., Ltd.). The lamp irradiates the samples about a distance of 1 m. A two-dimensional area of the icicle was measured using Image J software after irradiating the simulated solar light device. Time-lapse images were taken at 1-minute intervals using a digital camera (Tough 3, Olympus Co., Ltd.).

IV. RESULTS AND DISCUSSION

A. Femtosecond laser-processed surface molds

Figure 3 shows examples of SEM images of the SUS surface fabricated by femtosecond laser processing at fluences of $0.6 \sim 24.0$ J/cm². The structures on the SUS surface became increasingly fine with increased laser fluences. At fluences of $0.6 \sim 1.3$ J/cm² structures of LIPSS were observed. Similar structures were obtained in previous studies (e.g., [28]).
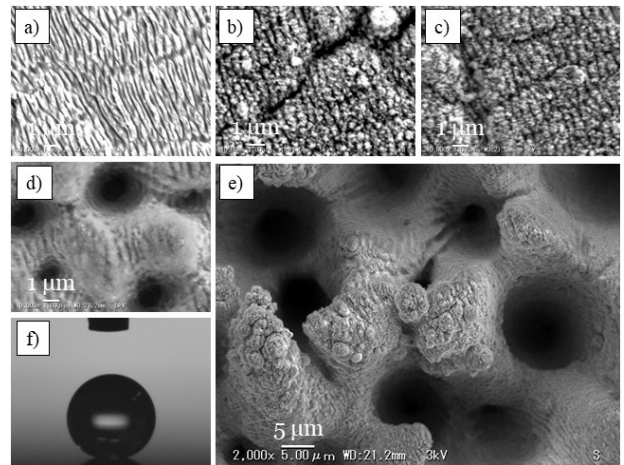
Figure 3. SEM images of the SUS surface. The laser fluences for the images are a) 0.6, b) 1.1, c) 1.3, d) 2.5, and e) 24.0 J/cm², and also photo of WCA measurements after laser processing of the surfaces at 24.0 J/cm² is shown f) when WCA is about 156 °. The figure d) and e) is modified from our previous study [41].

The relationship between laser fluence and WCA, the change in structure and WCA with increasing fluence has been known as a stepwise change in the SUS surface from flat to LIPSS, then to parabolic and LIPSS, then to columnar and LIPSS, and finally to rectangular and LIPSS, with increases in the laser fluence [39]. The phenomena of increased WCA due to structure changes may be attributable to the higher percentage of area occupied by air at the interface between the water droplet and the structure of the concave surfaces, as explained by the Cassie−Baxter model. At the laser fluence of 2.5 and 24.0 J/cm² in this study, the surface also showed a fractal-like structure (hereinafter referred to as a "microstructure") with a parabolic structure on the SUS surface and LIPSS formed on the surface (Figure 3d, e). Although the mechanism behind the generation of a parabolic shape on the SUS surface by femtosecond laser processing was not clarified in this study nor previous studies, the WCA was about 156° (Figure 3f), and water droplets rolled off immediately when the sample was tilted. Please note that the laser processing of metals other than SUS results in different shapes refer to the previous report for other metals [40].
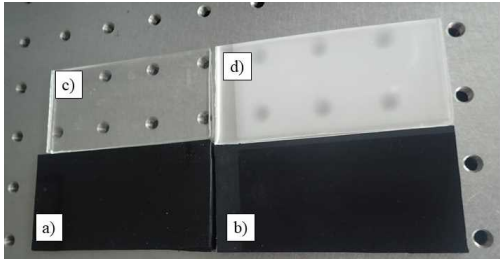
Figure 4. An image of the transferred PDMS samples. a) and b) PDMS with CB, c) and d) PDMS without CB. b) and d) The microstructures transferred to the PDMS. a) and c) The flat surface transferred to the PDMS. This figure is modified from our previous study [41].

Based on the above experiments, the laser processing conditions required for SUS surface modification are as follows: a scanning speed of 2.0 mm/s, a laser wavelength of 800 nm, a pulse duration of 100 fs, a repetition frequency of 1 kHz, and a laser fluence of 2.5 J/cm^2 or higher. Under these conditions, a 100 mm × 100 mm SUS plate was used for the laser processing of the mold.

B. *Transferring the structure to PDMS, and the WCA and WSA*

Figure 4 shows images of the Structure PDMS samples (Figure 4a, b) and the Flat PDMS samples (Figure 4c, d). In the case of PDMS without CB, the Structure PDMS with the
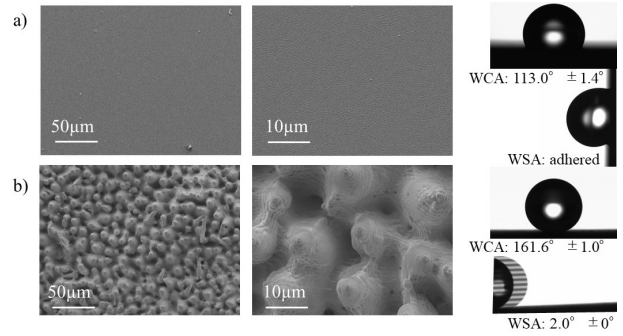
Figure 5. SEM images of the PDMS with CB. a) The Flat PDMS. b) The Structure PDMS. Scale bar in each image. The photo of WCA and WSA show in the right side of the figure.

transferred microstructure appears cloudy white while the Flat PDMS without a microstructure is transparent.

Figure 5 shows an example of an SEM image of the transferred PDMS containing 0.1 wt% CB. The Structure PDMS surface shows microstructures, i.e., parabolic shapes of about 10 μm, and the LIPSS structure confirms that the microstructure of the mold was also transferred to the PDMS. In contrast, the surface of the mold and the surface of the Flat PDMS are so smooth that no such microstructures can be seen in the SEM images.

The results of the WCA and the WSA, respectively, were measured with a contact angle meter. The WCA on the Flat PDMS is approximately 115°, and the WSA measurements
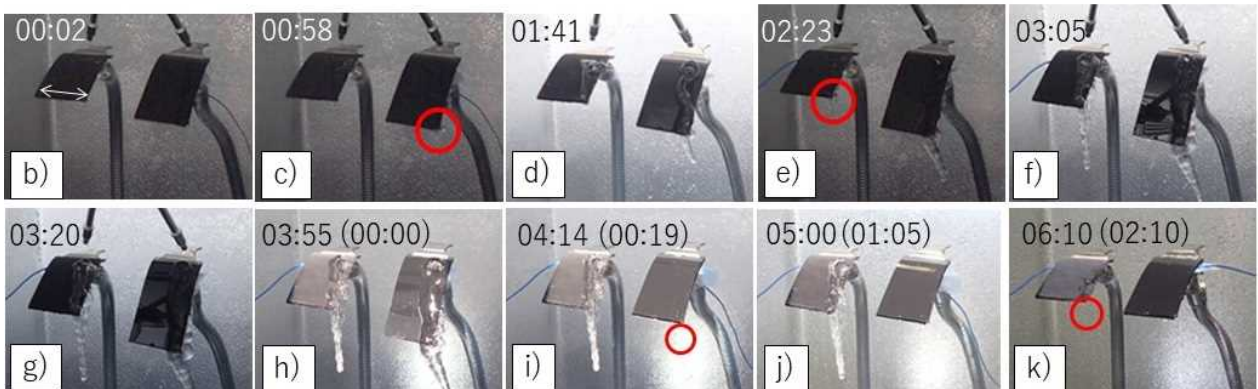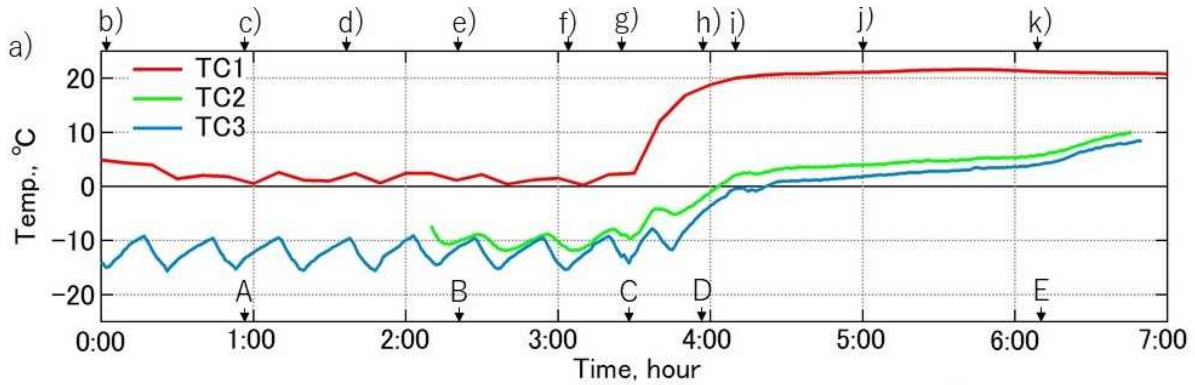
Figure 6. Results of the icicle experiment. a) Temporal changes in the temperature measurement by TC shown in Figure 2, respectively. b) to f) photos of the Structure PDMS (left) and the Flat PDMS (right) during the freezing experiment. g) to k) photos of the same sample during the temperature ramping experiment. Time stamp in parentheses are from begging of temperature ramping test. A: Icicle formed on the Flat PDMS, B: Icicle formed on the Structure PDMS, C: opened freezer cover, D: Freezing turned off and simulated solar light device turned on, E: icicle on the Structure PDMS shedding. The scale bar in the first photo of b) (arrow) is 40 mm.

show that the droplet adheres to the surface and does not slide even when the surface is tilted to a vertical angle. For the Structure PDMS containing 0.1 wt% of CB, which had microstructures transferred from the mold, the WCA was 161.6 ° ± 1.0° and the WSA was 2.0°. These results confirmed that the water droplets slid off immediately.

The WCA and WSA results indicate that the Structure PDMS can be given a superhydrophobic surface by transferring the microstructures from the mold surface to the Structure PDMS and that the CB content of the PDMS does not affect the wettability of the PDMS surface.

C. *Icicle formation on the PDMS samples*

Figure 6 shows the results of icicle formation on the PDMS in the freezer experiment and temperature ramping test after the icicle formations. The freezer temperature averaged about −11.1 ± 2 °C. Assuming the temperature of the thermocouple attached to the snake nozzle (TC1 in Figure 2) to be equal to the temperature of the water droplets, then the water temperature was 5 °C at the beginning of the experiment and gradually decreased to 1.5 ± 0.8 °C at 20 minutes into the experiment.

On the Flat PDMS, in the first 58 minutes of the experiment, ice gradually accreted on the PDMS, and the growth of icicles from the edge was observed (red circle in Figure 6c). On the other hand, on the Structure PDMS, in the time stamp of 2:23 (143 minutes), the icicle started to grow from the edge.

Milles *et al*. (2019) [32] show that water droplets on a superhydrophobic laser-processed surface turned to ice slowly due to the small contact area between the droplets and the surface. Our experimental results also show that the Structure PDMS with a superhydrophobic surface had slower ice growth than the Flat PDMS. The difference between the previous study and our experiment is that the water droplet is in a static or dynamic state, i.e., the previous study [32] is the former and our experiment is the latter. Please note that it is not clear when the icing on the PDMS is started and we could not identify the icing formation during the sliding of the water droplet on the PDMS in this experiment. Therefore, our icicle formation experiment only tells us that the icicle formation at the edges is clear and the icicle formation on the Structure PDMS is slower than the Flat PDMS.

D. *Icicle melting on the PDMS samples*

The result of the temperature ramping test with the simulated solar light device shows that the icicle on the Flat PDMS is shedding 19 minutes after the simulated solar light device was irradiated onto the PDMS samples (Figure 6i). More interestingly, the icicle on the Structure PDMS is shedding at 2:10 (130 minutes) after the simulated solar light is irradiated. The timing of ice shedding from the Structure PDMS is so late than we expected.

We conducted another experiment, which has been reported previously [41] in the same manner as the above experiment. Figure 7 shows that the ice surface appeared as cloudy white after peeling off from the Structure PDMS which is very similar to the surface of the Structure PDMS with the transferred microstructure without CB (Figure 4d). The accreted ice with cloudy white on its surface seems to be the
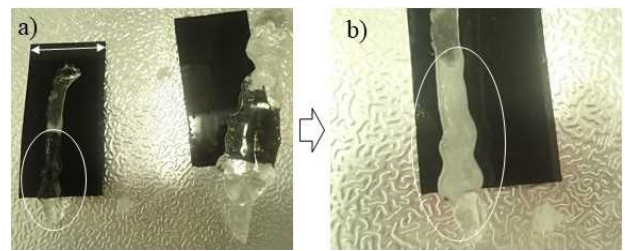
Figure 7. The photos of the interface between ice and the PDMS samples. a) photo of the adhered ice just after the experiment. The Structure PDMS (left), and the Flat PDMS (right). Adhered ice was already slide off from the Flat PDMS. The ice is transparent before peeing off from the Structure PDMS (white circle). b) photo of the adhered ice was peeled off from the Structure PDMS (white circle). The scale bar (arrow) is 40 mm. This figure is modified from our previous study [41].

microstructure of the Structure PDMS that is transferred to that ice surface. In other words, the ice on the Structure PDMS should have penetrated the microstructure grooves of the Structure PDMS and the ice is so-called "Wenzel ice" (e.g., [12]).

Figure 8 shows time variations in the two-dimensional icicle area after irradiating the simulated solar light onto the PDMS samples analyzed by Image J software. The icicle on the Flat PDMS was shedding 19 minutes after irradiating simulated solar light onto the samples as mentioned above. Simultaneously, the temperature of the thermocouple set at the back side of the PDMS (TC2 in Figure 6a) increases slightly higher than the melting temperature of ice, 0 °C. This is thought to be because the adhesion of the icicle and the Flat PDMS decreases due to the existence of the quasi-liquid layer of the interface between ice and the Flat PDMS.

The icicle on the Structure PDMS is shedding at 2:10 (130 minutes) after irradiating simulated solar light onto the samples despite the temperature of the PDMS being way higher than the melting temperature of ice.

The ice adhesion intensity to the Structure PDMS surface is not known from this study but previous studies show that the ice adhesion intensity to the superhydrophobic surface especially "Wenzel ice" is higher than to the smooth polymers [12][42][43][44].

Meanwhile, the quasi-liquid layer of the interface between Wenzel ice and the Structure PDMS should exist at the temperature condition in this study (e.g., Figure 6j). Note, the interface between Wenzel ice and the Structure PDMS should be 0 °C. The result of our experiment shows the ice on the Structure PDMS would not shed even if the temperature is way higher than the melting temperature of ice. Thus, the weak interaction force between ice and the Structure PDMS is probably not dominant for the adhesion but the mechanical force may occur between them. The result suggests that the thickness of the microstructure of Wenzel ice adhered to the Structure PDMS is much thicker compared to the thickness of the quasi-liquid layer itself [45][46]. Therefore, the ice shedding from the Structure PDMS is slow due to the ice adhering to the surface penetrating the microstructure grooves. The disappearance of the microstructure on the ice, the interface between ice and the Structure PDMS surface, causes ice shedding from the Structure PDMS (Figure 6k) when ice
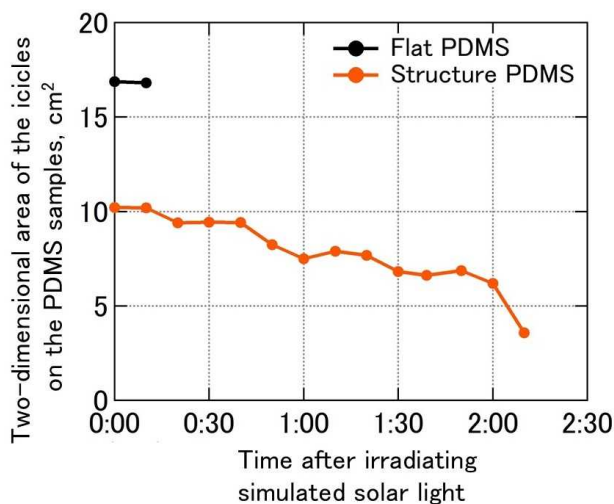
Figure 8. Two-dimensional area of the icicles on the Flat PDMS and the Structure PDMS after irradiating simulated solar light onto the PDMS samples.

is exposed above melting temperatures for long periods of at least 2 hours in this experiment.

The two-dimensional area of the ice measured just before shedding from the PDMS samples, in Figure 8, was 16.9 cm^2 on the Flat PDMS and 3.6 cm^2 on the Structure PDMS after 2 hours from the beginning of irradiating simulated solar light. The ratio of the Structure PDMS ice area to the Flat PDMS ice area is about 0.2, and we would like to conclude that the Structure PDMS affords a greater anti-icing effect than the Flat PDMS but the Structure PDMS does not afford complete anti-icing.

The shedding of ice from highway structures onto vehicles can cause traffic accidents. The Structure PDMS may be useful as a countermeasure to highway structures when the caught snow and ice on the structures is not shedding until they melt enough to a small size, which requires further investigations before implementation to the highway structures.

V. CONCLUSIONS

We reported the fabrication of a superhydrophobic PDMS using a stainless-steel mold that was processed by femtosecond laser irradiation. The surface that was transferred to the PDMS had a fractal-like microstructure like a lotus leaf and achieved a water contact angle of $161.6 \pm 1.0°$ and a water sliding angle of $2.0 \pm 0°$. Icicle formation experiments were conducted to suppress the generation of icicles on highway infrastructure. As a result, less ice adhered to the superhydrophobic PDMS than to the PDMS with a smoothed surface, indicating that the superhydrophobic PDMS is effective in slowing the formation of icicles. Additionally, from the temperature ramping test during the simulated solar light irradiation, the superhydrophobic PDMS adhered icicle, and the area of the icicle tended to decrease to the ratio of about 0.2, the superhydrophobic PDMS ice area to the flat PDMS ice area, which that the superhydrophobic PDMS affords anti-icing effect than the flat PDMS.

REFERENCES

[1] Takeuchi, M., "Snow accretion on traffic-control signs and its prevention", *seppyo*, 40(3), 15-25, 1978 (written in Japanese with English Abstract)

[2] Matsushita, H., Y. Ito, Y. Kajiya, "Meteorological conditions for accumulating and falling of snow cover on overhead traffic information sign", *International Workshops on Atmospheric Icing of Structures (IWAIS)*, 1-5, 2007

[3] Sakase, O., H. Matsushita, M. Matsuzawa, "Conditions for installation of snow accretion countermeasures on road information signs", *International Workshops on Atmospheric Icing of Structures (IWAIS)*, 1-5, 2011

[4] Yoshida, M. et al., "Investigation to prevent icing -adhesion of ice to various materials-", *Hokkaido Research Organization Reports*, No.292, 13-22, 1993

[5] Saito, H., K. Takai, G. Yamauchi, "Water-and ice-repellent coatings", Surface Coatings International, 80(4), 168-171, 1997

[6] Ito, T., M. Yuasa, T. Tomabechi, R. Imazu, "Characteristics of materials influencing the snow accreting property", *Journal of Snow Engineering of Japan*, 11(4), 3-10, 1995 (written in Japanese with English abstract)

[7] Environmental Protection Agency (EPA), "EPA delivers results on PFAS action plan" [Online], Available: https://www.epa.gov/newsreleases/epa-delivers-results-pfas-action-plan

[8] Barthlott, W., and C. Neinhuis, "Purity of the sacred lotus, or escape from contamination in biological surfaces", *Planta*, 202, 1-8, 1997

[9] Cassie, A.B.D., and S. Baxter, "Wettability of porous surface", *Transactions of the Faraday Society*, 40, 546-551, 1944

[10] Onda, T., S. Shibuichi, N. Satoh, and K. Tsujii, "Super-water-repellent fractal surfaces", Langmuir, 12(9), 2125-2127, 1996

[11] Sojoud, H., M. Wang, N.D. Boscher, G.H. Mckinley, and K.K. Gleason, "Durable and scalable icephobic surfaces: similarities and distinctions from superhydrophobic surface", *Soft Matter*, 12, 1938, 2016

[12] Kreder, M.J., J. Alvarenga, P. Kim, and J. Aizenberg, "Design of anti-icing surfaces: smooth, textured or slippery", *Nature Reviews Materials*, 1, 1-15, 2016

[13] Das, S., S. Kumar, S.K. Samal, S. Mohanty, and S.K. Nayak, "A review on superhydrophobic polymer nanocoatings: Recent development, application", *Industrial & Engineering Chemistry Research*, 57(8), 2727-2745, 2018

[14] Yanchesheme, A.A., G. Momen, and R.J. Aminabadi, "Mechanisms of ice formation and propagation on superhydrophobic surfaces: A review", *Advances in Colloid and Interface Science*, 279, 102155, 2020

[15] Shamshiri, M., R. Jafari, and G. Momen, "Potential use of smart coatings for icephobic applications: A review", *Surface & Coatings Technology*, 424, 127656, 2021

[16] Wong, T-S., S.H. Kang, S.K.Y. Tang, E.J. Smythe, B.D. Hatton, A. Grinthal, and J. Aizenberg, "Bioinspired self-repairing slippery surfaces with pressure-stable omniphobicity", *Nature*, 477, 443-447, 2011

[17] Urata, C., G.J. Dunderdale, M.W. England, and A. Hozumi, "Self-lubricating organogels (SLUG) with exceptional syneresis-induced anti-sticking properties against viscous emulsions and ices", *Journal of Materials Chemistry A*, 3, 12626-12630, 2015

[18] Ariati, R., F. Sales, A. Souza, R.A. Lima, and J. Ribeiro, "Polydimethylsiloxane composites characterization and its applications: A review", *Polymers*, 13, 4258, 2021

[19] Liu, X., Y. Xu, K. Ben, Z. Chen, Y. Wang, and Z. Guan, "Transparent, durable and thermally stable PDMS-derived superhydrophobic surfaces", *Applied Surface Science*, 339, 94-101, 2015

[20] Wang, Y., Huang, R.S. Gurney, and D. Liu, "Superhydrophobic and photocatalytic PDMS/TO₂ coatings with environmental stability and multifunctionality", *Colloids and Surface A: Physicochemical and Engineering Aspects*, 561(20), 101-108, 2019

[21] Peng, S., W. Meng, J-X. Guo, B. Wang, Z. Wang, N. Xu, X. Li, J. Wang, and J. Xu, "Photocatalytically stable superhydrophobic and translucent coatings generated from PDMS-Grafted-SiO₂/TiO₂@PDMS with multiple application", *Langmuir*, 35(7), 2760-2771, 2019

[22] Gong, X., and S. He, "Highly durable superhydrophobic polydimethylsiloxane/silica nanocomposite surface with good self-cleaning ability", *ACS Omega*, 5, 4100-4108, 2020

[23] Xue, C-H., Q-Q. Tian, S-T. Jia, L-L. Zhao, Y-R. Ding, H-G. Li, and Q-F. An, "The fabrication of mechanically durable and stretchable superhydrophobic PDMS/SiO₂ composite film", *RSC Advances*, 10, 19466-19473, 2020

[24] Sheshkar, N., G. Verma, C. Pandey, A.K. Sharma, A. Gupta, "Enhanced thermal and mechanical properties of hydrophobic graphite-embedded polydimethylsiloxane composite", *Journal of Polymer Research*, 28:403, 2021

[25] Zhang, B., J. Duan, Y. Huang, B. Hou, "Double layered superhydrophobic PDMS-Candle soot coating with durable corrosion resistance and thermal-mechanical robustness", *Journal of Materials Science & Technology*, 71, 1-11, 2021

[26] Birnbaum, M., "Semiconductor surface damage produced by ruby lasers", *Journal of Applied Physics*, 36(11), 3688, 1965

[27] Okamurao, K., M. Hashida, Y. Miyasaka, Y. Ikuta, S. Tokita, and S. Sakabe, "Laser fluence dependence of periodic grating structures formed on metal surfaces under femtosecond laser pulse irradiation", *Physical Review B*, 82, 165417, 2010

[28] Kietzig, A-M., S.G. Hatzikiriakos, and P. Englezos, "Patterned superhydrophobic metallic surfaces", *Langmuir*, 25(8), 4821-4827, 2009

[29] Skoulas, E., A. Manousaki, C. Fotakis, and E. Stratakis, "Biomimetic surface structuring using cylindrical vector femtosecond laser beams", *Scientific Reports*, 7, 45114, 2017

[30] Yong, J., W. Yang, X. Hou, and F. Chen, "Nature-inspired superwettability achieved by femtosecond laser – review article", *Ultrafast Science*, 9895418, 51, 2022

[31] Volpe, A., C. Gaudiuso, and A. Ancona, "Laser fabrication of anti-icing surfaces: A review", *Materials*, 13, 5692, 2020

[32] Milles, S., M. Soldera, B. Voisiat, and A.F. Lasagni, "Fabrication of superhydrophobic and ice-repellent surfaces on pure aluminium using single and multiscaled perodic textures", *Scientific Reports*, 9, 13944, 2019

[33] Cheng, L., Z. Minlin, F. Peixun, L. Jiangyou, G. Dingwei, and Z. Hongjun, "Picosecond laser fabrication of large-area surface micro-nano lotus-leaf structures and replication of superhydrophobic silicone rubber surfaces", *Chinese Journal of Lasers*, 41(9), 0903007, 1-8, 2014 (written in Chinese with English abstract)

[34] Wu, P.H., C.W. Cheng, C.P. Chang, T.M. Wu, and J.K. Wang, "Fabrication of large-area hydrophobic surfaces with femtosecond-laser-structured molds", *Journal of Micromechanics and Microengineering*, 21, 115032, 2011

[35] Kooy, N., K. Mohamed, L.T. Pin, and O.S. Guan, "A review of roll-to-roll nanoimprint lithography", *Nanoscale Research Letters*, 9, 320, 2014

[36] Lin, Y., H. Chen, G. Wang, and A. Liu, "Recent progress in preparation and anti-icing applications of superhydrophobic coatings", *Coatings*, 8, 208, 2018

[37] Aboud, D.G.K., and A-M. Kietzig, "On the oblique impact dynamics of drops on superhydrophobic surfaces. Part I: Sliding length and maximum spreading diameter", *Langmuir*, 34, 9879-9888, 2018

[38] Aboud, D.G.K., and A-M. Kietzig, "On the oblique impact dynamics of drops on superhydrophobic surfaces. Part II: Restitution coefficient and contact time", *Langmuir*, 34, 9889-9896, 2018

[39] Moradi, S., S. Kamal, P. Englezos, and S.G. Hatzikiriakos, "Femtosecond laser irradiation of metallic surfaces: effects of laser parameters on superhydrophobicity", *Nanotechnology*, 24, 415302, 2013

[40] Yong, J., W. Yang, X. Hou, and F. Chen, "Nature-inspired superwettability achieved by femtosecond laser – review article", *Ultrafast Science*, 9895418, 51, 2022

[41] Sakurai, T., T. Somekawa, Y. Hirai, H. Matsushita, Superhydrophobic PDMS fabricated with a femtosecond pulsed laser for inhibiting icicle formation, *Seppyo*, 85(6), 327 – 338, 2023 (written in Japanese with English abstract)

[42] Meuler, A.J., J.D. Smith, K.K. Varanasi, J.M. Mabry, G.H. McKinley, and R. E. Cohen, "Relationships between water wettability and ice adhesion", *ACS Applied Materials & Interfaces*, 2, 22, 3100-3110, 2010

[43] Varanasi, K.K., T. Deng, J.D. Smith, M. Hsu, and N. Bhate, "Frost formation and ice adhesion on superhydrophobic surfaces", *Applied Physics Letters*, 97, 234102, 2010

[44] Huré, M., P. Olivier, J. Garcia, "Effect of Cassie-Baxter versus Wenzel states on ice adhesion: a fracture toughness approach", *Cold Regions Science and Technology*, 194, 103440, 2022

[45] Furukawa, Y., and H. Nada, "Anisotropic surface melting of an ice crystal and its relationship to growth forms", *Journal of Physical Chemistry B*, 101, 32, 6167-6170, 1997

[46] Zeng, Q., and K. Li, "Quasi-liquid layer on ice and its effect on the confined freezing of porous materials", *Crystals*, 9(5), 250, 2019

Development of a Test Apparatus for the Measurement of Tensile Properties of Accreted Ice

Derek Harvey[1], Gelareh Momen[1]

[1] *Anti-icing Materials International Laboratory, Université du Québec à Chicoutimi, Canada*

derek_harvey@uqac.ca, gelareh_momen@uqac.ca

Abstract— **This work presents a new apparatus concept which allows testing tensile properties of atmospheric ice accretions. The apparatus is a machined cylinder where the central portion consists of a series of thin, disconnected slices. During icing, the assembly is aligned and maintained together by means of an internal tension rod and the cylinder is rotated by an electrical motor to achieve a uniform ice accumulation. After the desired ice thickness is obtained, the tension rod is removed and at this moment the ice is the only structural element keeping the cylinder together. Without any alteration, the test specimen is installed in a tensile test machine and tested to failure while remaining in the same controlled environment. Force and extensometer data acquisitioned during testing are used to produce stress versus strain curves from which the tensile modulus and tensile strength are determined. To demonstrate the test procedure, results are presented for atmospheric ice accreted from freezing drizzle in a cold room environment at different temperatures and precipitation intensities. The developed test method allows to study tensile stiffness and strength and their variability on unaltered iced specimens.**

Keywords— ***Ice, Accreted ice, Mechanical properties of ice, Tensile testing, Experimental methods***

I. Introduction

The mechanical properties of accreted ice are influenced by multiple factors such as ambient temperature, water droplet size and temperature, precipitation intensity, impact velocity, surrounding thermal exchanges, etc. [1, 2]. In practise, we define different types of accreted ice such as glaze, mixed and rime but even within these categories the properties of ice can vary significantly as a function of temperature, crystallite size and grain boundary density, internal defects, the porosity level and even the pore size and distribution [3, 4].

This variability poses a challenge to the development of accurate ice shedding predictive models. On rotating structures such as rotors, fans, and propellers, ice shedding will typically involve a combination of cohesive (through the volume) and adhesive (interfacial) failure. The cohesive and adhesive failure can occur simultaneously leading to partial shedding of the ice on the rotating structure. In other scenarios, cohesive fractures may appear earlier due to bending loads for example without immediate adhesive failure and ice detachment. The fractures create sites for future interfacial crack initiation and propagation. In both scenarios, accurate cohesive failure predictive models are a necessity to model ice shedding events.

Tensile testing has been used in the past to study accreted ice. Xian et al. [5] tested wind tunnel ice accumulations on solid aluminium rods. Finite element analysis was then used to determine the stiffness modulus of ice from experimental data of the ice-aluminium composite structure [6]. Mohamed and Farzaneh [7] also performed tensile tests on ice specimens accreted in an icing wind tunnel. Their approach consisted of machining dumbbell tensile test specimens from a bulk accumulation of ice realized on a rotating cylinder. Their study provided measurements of tensile strength but not the elastic modulus for various icing conditions and strain rates. The procedure is quite involved requiring to accumulate the ice, machine the specimens and bonding the ice to metallic caps for loading.

In this work, a new test apparatus concept is considered to study the tensile properties of accreted ice without the need of treating the specimen as a composite nor intensive manipulations of the ice prior to testing.

II. Materials and Methods

A. Design of the test apparatus

The new tensile test apparatus is designed to enable testing the tensile properties of ice accreted in varied types of simulated icing environments such as cold chamber freezing precipitations or icing clouds simulated in a wind tunnel. The concept is inspired by the rotating cylinder test used for measuring liquid water contents (LWC) in icing wind tunnels [8] and by collapsible or sacrificial tooling used to fabricate tubular structures. Here, the cylindrical structure over which ice is accreted is designed to have stiffness only during the ice accretion step and zero stiffness during the testing step to allow direct measurement ice properties.

The test apparatus concept is presented in Fig. 1. The central section of the cylinder has an outer diameter of 25.4 mm and measures 50 mm long. It is composed of 25 of 10 mm thick slices of aluminium 6061-T6. To either side of the central section are the gripping regions where the aluminium surface is knurled to increase adhesion to transfer the tensile loads through the ice and ensure that the specimen fails cohesively in the central portion. The end of the gripping regions includes a welded disk (55 mm in diameter) which acts as a shield to avoid ice from forming outside of the designated icing area and the extremities are pierced to allow pinned supports in the tensile tester.

The central and the gripping sections of the cylinder are hollowed to fit a tension rod prior and during ice accretion to keep the different components together and aligned. At one end of the tension rod, a flexible shaft coupling is fixed to connect to the output shaft of the electrical motor. The opposite end of the tension rod is threaded and a nut and washer are used to apply light compression to the central and gripping sections. Alignment of the components is ensured by using a V-block during assembly. Once ice has been accumulated, the tension rod is removed at which point the components are only held together by the ice.

Fig. 1 Multi-component cylinder used for fabricating tubular ice tensile specimens.

A simple support frame was designed and fabricated to allow icing of three cylinders simultaneously under freezing drizzle conditions reproduced in a cold chamber, Fig. 2. On the exterior side walls, three electrical motors (10W) are mounted and three sealed ball bearings are mounted on the opposing wall. On the motor side, insulation was applied to both sides of the wall to manage the heat generated by the motors during ice accretion. The cylinders are supported by the motors and bearings and are spaced 10 cm apart. An aluminium plate was welded to the top of the frame such that only the gripping and central regions of the cylinders are exposed to icing. The cylinders are rotated at a constant speed of 60 RPM during ice accretion phase.
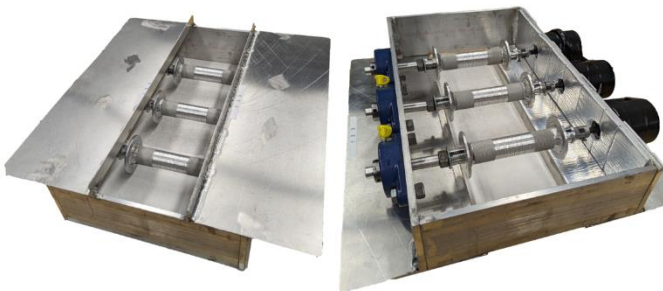
Fig. 2 Support frame used for ice accretion using freezing drizzle in a cold room environment

B. Experimental ice accretion procedure

For this test development work, all tests were performed using freezing drizzle precipitations simulated inside a cold chamber. The experimental setup is presented in Fig. 3. A single spray nozzle is installed on a linear motion guided rail. The spray nozzle receives distilled water cooled to 4°C from a tank pressurized at 70 psi. The water droplets produced have a median volume diameter (MVD) of 320 µm. The spray nozzle is installed at a height of 1.6 m above the cylinders. The nozzle sprays water only while travelling from one end to the other and spraying is paused for a specified amount at the travel limits. In this configuration, precipitation intensity is controlled by the travel speed (0.2 m/s, constant for all tests) and the pause duration.

Each test begins with a conditioning period where the test setup is exposed to the target test temperature for a minimum period of 12 hours prior to icing. Just before starting the precipitation, the electrical motors are powered and rotate at a constant speed of 60 RPM. Then, freezing precipitation is started at the target intensity until the targeted thickness of ice accumulated on the cylinder. For glaze and mixed ice, a thickness of 5.5 mm was targeted to remain within the maximum load capacity of the tensile test machine. In the present study, three icing conditions are presented at -5°C, -7.5°C and -10°C. The precipitation intensities were adjusted to obtain ice accretion rates to obtain uniform ice accumulations. After the targeted ice thickness is reached, precipitation is stopped and a minimum wait time of 2 hours was respected before manipulating the iced cylinders and testing. Then, each cylinder is removed from the fixture, weighted to determine the mass of ice, and the outer diameter of the ice is measured at the center and limits of the central section.

Fig. 3 Freezing drizzle icing experimental setup

C. Tensile test procedure and property calculations

Tensile tests are performed using a Texture Analyser TA.XTplus100C by Stable Micro Systems (Surrey, UK). The test machine has a small foot-print which allows to move the equipment inside the cold chamber prior to testing. This provides the advantage that the ice specimens remain in the same environment throughout the experimental procedure. The tensile machine is limited to forces up to 1 kN, with a force resolution of 0.1 g. All tests were performed using a constant cross-head displacement rate of 0.01 mm/s. An MTS

Systems Corporation (Eden Prairie, Minnesota, United States) extensometer model 632.11F-90 which has a gage length of 25 mm was used for strain measurements. Test data was logged at a rate of 25 hz. A representative example of a test specimen ready for testing is shown in Fig. 4.

The tension rod of the iced cylinder is removed just before being installed in the test machine by simply removing the retaining nut and washer and pulling out the cylinder from the rod. Pin supports are used to connect the specimen to the fixed base and moving cross-head of the test machine. The extensometer is equipped with knife edges and kept in place using spring attachments. All tests are performed by loading the specimen until failure occurs and the thickness of ice at the failure location is measured.

The applied tensile stress is calculated from the load cell data and experimental measurements by:

$$\sigma = \frac{F}{A} = \frac{4F}{\pi(d_{ext}^2 - d_{int}^2)} \qquad (1)$$

Where d_{ext} is the average diameter measured on the iced specimen and d_{int} is the diameter of the aluminium cylinder core before icing. For brittle material behaviour, the tensile strength is determined by the maximum load recorded and the cross-section area at the position of failure. The tensile modulus is calculated from the slope of the stress-strain function.
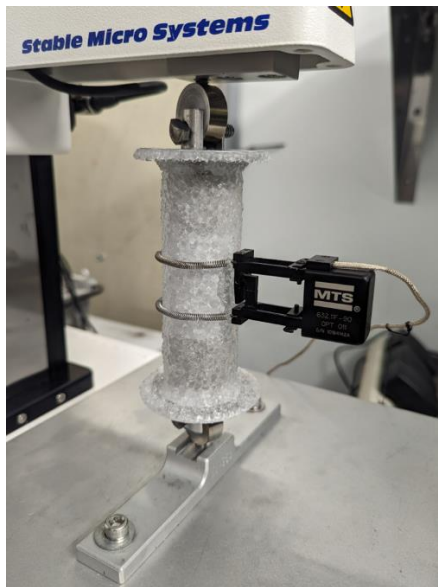
Fig. 4 Ice specimen ready for tensile testing. The example shows an ice specimen obtained at the -10°C condition.

III. EXPERIMENTAL RESULTS

A. *Ice characteristics and repeatability*

To evaluate the new apparatus and experimental procedure, ice accretions were performed at three different temperatures and at different ice accretion rates. The icing conditions and resulting average ice thicknesses are presented in Table 1. The average thickness and standard deviation are each calculated from the three measurements on each cylinder for the specific icing event. Representative images of the iced specimens are shown in Fig. 5. The first temperature tested was at -10°C, which was tested for two different accretion rates. For both conditions, the resulting ice has a bumpy-like surface which indicates that the ice is transitioning from glaze to rime. The

obtained ice coverage was uniform along the length of the cylinder. The second temperature tested was at -5°C. The precipitation rate used for the first trial produced poor uniformity of the ice diameter due to excessive liquid water during icing (Fig. 5). Reducing the intensity addressed the issue in the second trial. In both cases, the ice is transparent, typical of glaze ice. Finally, a single icing condition was tested at -7.5°C and the condition resulted in a very uniform glaze ice accumulation.

TABLE 1. ICING CONDITIONS AND AVERAGE ICE THICKNESS

Temperature	Accretion rate (mm/h)	Final avg. thickness (mm)
-5°C	1.8	4.60 ± 0.33
	1.5	5.20 ± 0.10
-7.5°C	2	5.55 ± 0.07
-10°C	4	5.54 ± 0.12
	4	5.80 ± 0.11
	2	5.82 ± 0.11
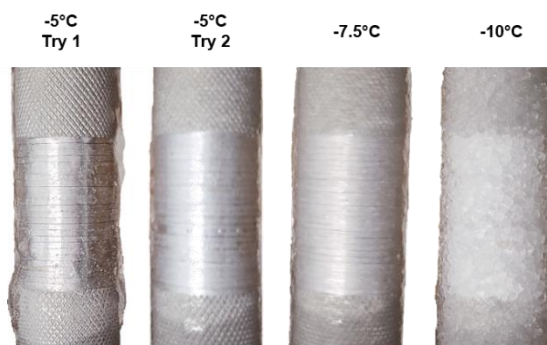
Fig. 5 Representative illustration of the iced cylinders after ice accretion. First try at -5°C illustrates non-uniform ice coverage due to excessive water.

B. *Stress and strain data*

The stress and strain data were calculated for each test from the load cell, extensometer and experimental dimensional measurements. Representative stress-time and stress-strain data are presented in Fig. 6 and Fig. 7.
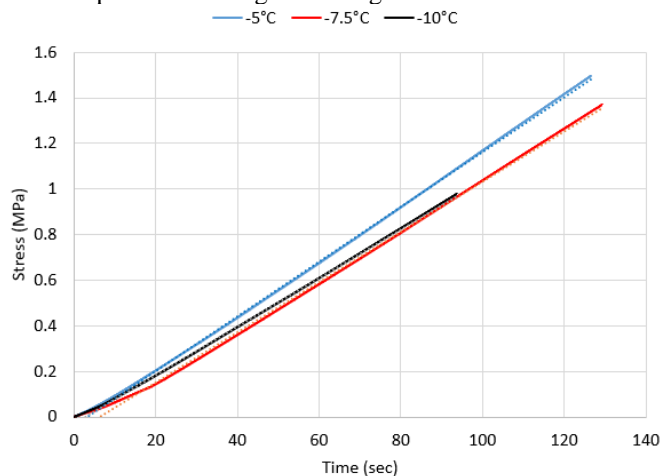
Fig. 6 Representative stress versus time graphs for each test temperature

All results obtained at the selected strain rate are typical of brittle material behaviour where there is no plastic

241

deformation. Stress increases linearly until sudden failure occurs. Force measurements were highly linear as a function of time with some data presenting a small toe region at the start of the test as shown through the stress versus time graphs.
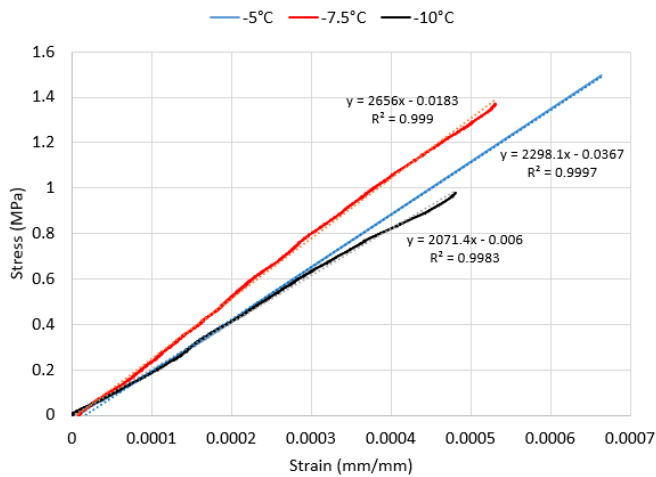
Fig. 7 Representative stress versus strain graphs for each test temperature

Strain measurements from the extensometer data had overall good linearity but some trials did present minor fluctuations which can be seen in the stress-strain curves presented in Fig. 7. Using an extensometer on ice poses challenges as the ice has low friction and the surface presents irregularities. Example of the fracture surfaces are presented in Fig. 8. All specimens presented a fracture plane perpendicular to the loading axis. Images highlight the quality of the ice forming around the central section and the absence of water infiltration between the sections.

The maximum stress and tensile modulus obtained at each test conditions are summarized in Fig. 9. Values are in good agreement with similar work reported in [5] and [7]. The plots are based on 6 data points at -5°C, 3 at -7.5°C and 9 at -10°C. Tensile strength had higher variability at -5°C compared to the lower temperature conditions. More repetitions should be performed for all cases to conclude but this may very well be a consequence of testing the material so close to its melting temperature. Stiffness modulus measurements have higher variability for the glaze ice conditions (-5°C and -7.5°C) then on the mixed ice condition. Both tensile strength and modulus appears to be reducing as the ice is transitioning from glaze to mixed. In the glaze region, results suggest the presence of an optimum as temperature is lowered compared to the fusion temperature.
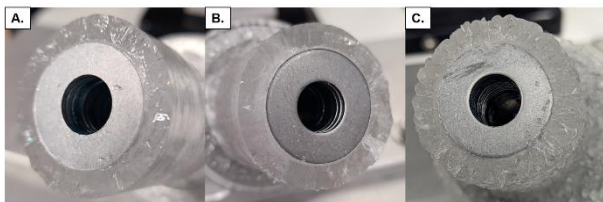
Fig. 8 Fracture surfaces after tensile failure for the three ice formation temperatures considered (A. -5°C glaze ice, B. -7.5°C glaze ice and C. -10°C mixed ice).
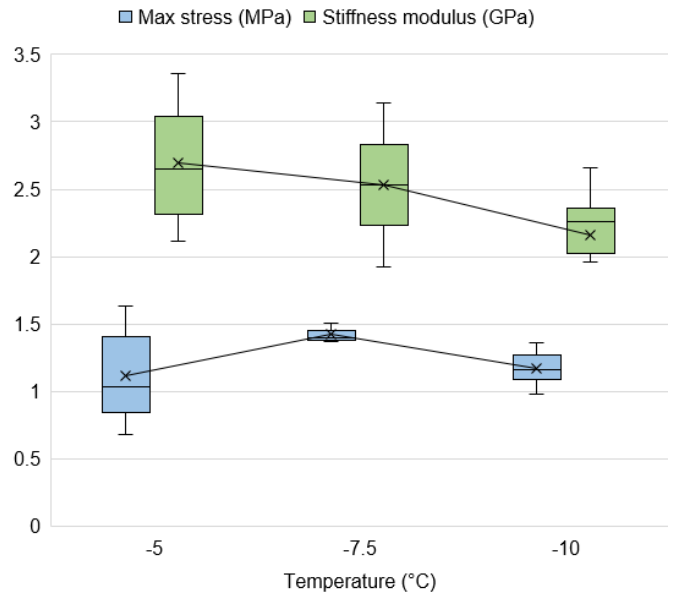
Fig. 9 Tensile strength and modulus data distribution

IV. DISCUSSION

The presented test apparatus is an interesting new tool to study tensile properties of atmospheric ice. In terms of icing conditions, the procedure can be applied to a broad variety of simulated natural icing conditions. The natural aspects of the ice such as its internal porosity and the roughness and irregularity of its surface are preserved while remaining adequate for property testing purposes. Additionally, the concept allows to measure the properties of the ice without requiring the need to treat the test article as a composite material or extensive modifications to produce the tensile specimen. Contrary to typical material characterization for design purposes, studying ice as it is formed with its imperfections is desirable to improve ice shedding predictions and better understand the variability range.

The apparatus used in this work is a first design iteration and could be improved by using higher grade materials and high precision machining. Heading into the first trials, it was unclear whether water infiltration between the mating surfaces would be a problem for glaze ice accretions. However, after multiple tests, observations support that the water does not infiltrate due to the centrifugal forces generated by the rotation, the thinness of the joints and early freezing of the surface which seals it.

The material strength results presented in this work are in good agreement with results reported in the literature for similar tests. However, there is limited information in the literature for elastic modulus of accreted ice and results are significantly different than the idealistic modulus of ice of 9 GPa. The most challenging aspect of the test procedure is the measurement of strain. As presented in Fig. 7, strain data calculated from the extensometer could present some irregularities. We believe this can be caused by low surface friction, the effects of the pressure applied by the contacting edges of the extensometer and the presence of surface irregularities. The high degree of linearity allows to have good confidence that the measurements are representative and in the right order of magnitude. However, the use of non-contact measurement methods such as 3D digital image correlation would improve the method and allow to confirm if slight

measurement errors are responsible for the variability obtained in the measured stiffness modulus. Another alternative would be to measure the displacements on an ice-free section of the tensile apparatus with a larger gage length.

V. Conclusions

A new apparatus concept is presented for studying tensile properties of atmospheric ice. The procedure presented in this work was tested for freezing precipitations simulated in a cold chamber but is perfectly suitable for ice accretions produced in an icing wind tunnel. The obtained tensile test specimen configuration is tubular and the structure over which ice was accreted provides no tensile stiffness during testing. The streamline approach allows to measure both tensile strength and elastic modulus experimentally without altering the ice or the need to consider a composite specimen. The new apparatus represents a useful addition to existing experimental tools for the study of tensile properties of accreted ice to support the advancements of predictive ice shedding models.

Acknowledgment

References

[1] Macklin, W.C., *The density and structure of ice formed by accretion.* Quarterly Journal of the Royal Meteorological Society, 1962. **88**(375): p. 30-50.

[2] Petrovik, J.J., *Review Mechanical properties of ice and snow.* Journal of Materials Science, 2003. **38**.

[3] Hobbs, P.V., *Ice Physics*. 1974. 837 p.

[4] Schulson, E., *The structure and mechanical behavior of ice.* JOM Journal of the Minerals, Metals and Materials Society, 1999. **51**(2): p. 21-27.

[5] Xian, X., et al., *An experimental evaluation of the tensile strength of impact ice.* Journal of Materials Science Letters, 1989. **8**(10): p. 1205-1208.

[6] Chu, M.L., R.J. Scavuzzo, and T.S. Srivatsan, *A combined analytical-experimental tensile test technique for brittle materials.* Experimental Techniques, 1992. **16**(1): p. 46-50.

[7] Mohamed, A.M.A. and M. Farzaneh, *An experimental study on the tensile properties of atmospheric ice.* Cold Regions Science and Technology, 2011. **68**(3): p. 91-98.

[8] Committee, A.-C.A.I.T., *Calibration and Acceptance of Icing Wind Tunnels*. 2015, SAE International.

Observation Research of Icing in High Altitude Typical Icing Area

Xu Zhang[1], Zhijin Zhang[1], Xingliang Jiang[1], Hang Zhang[1], Qin Hu[1], Hualong Zheng[1]

[1] *Xuefeng Mountain Energy Equipment Safety National Observation and Research Station, Chongqing University, Chongqing, China*

zhangxu@xz.sgcc.com.cn, zhangzhijing@cqu.edu.cn, xljiang@cqu.edu.cn, zhanghangelectr@foxmail.com, huqin@cqu.edu.cn, hualong.z@foxmail.com

Abstract— **At present, electrical power transmission lines all over the world suffer from icing events, which is a great threat to the safe and stable power system. More and more researchers have carried out icing research on transmission line conductors and insulators. However, many important transmission lines are located in complex terrain areas with mountains, canyons and hills, and their icing status is rarely reported. Based on this, according to the image, video and meteorological monitoring instruments installed along the transmission lines in the high-altitude areas, the paper observed the icing of conductors and insulators in the work site of the area during the icing period. Based on the analysis of the image and meteorological data, the internal relationship between the icing thickness and meteorological parameters in the high altitude typical icing area was obtained.**

Keywords—***Icing; High altitude; Transmission lines; Icing thickness; Meteorological parameters***

I. INTRODUCTION

Transmission line corridors are mostly built in high-altitude mountainous areas with diverse topography, and the icing has typical characteristics in high altitude, micro-topography and microclimate [1]. It is not uncommon for the transmission lines insulation performance to decline and even cause flashover broken down accidents caused by icing, resulting in huge losses [2].

The study found that transmission lines icing causes mechanical overload [3], uneven icing or de-icing at different times [4], icing conductors galloping [5], and insulators icing flashover [6] as the main causes of accidents. The factors affecting transmission lines icing mainly include meteorological conditions, geographical terrain, altitude, line trend, suspension height, external dimension, electric field, etc. [7].

Literature [8] proposed a preventive scheduling model, which can avoid the icing of transmission lines caused by mild icing disaster and effectively inhibit the icing growth that cannot be completely de-icing under strong storms. In literature [9], a dynamic dry growth icing model based on composite insulators was established considering the influence of icing shape and climate factors, and the observation was carried out in the test tower of the field test base. In literature [10], the loss of water film on insulator surface and water supply of icicles were considered, and the icicles growth equation was reconstructed according to water mass balance, and a complete wet growth icing model including icing accretion on insulator surface and icicles growth was established.

In the literature [11], three kinds of porcelain insulator strings were naturally icing with glaze and mixed rime at Xuefeng Mountain Natural Test Station. Combining with the meteorological data during the icing period, the icing growth rule was analysed, and the differences in icing morphology among the three kinds of insulator strings were studied. The results showed that the icing thickness would gradually increase but the trend would slow down. In literature [12], an experimental device was installed at a natural icing test site in Valin Mountain, Quebec, Canada, which was composed of two instrument test lines, meteorological instruments, a data acquisition and transmission system. The icing data collected at the test site was introduced and the processes of accretion stage, persistence stage and shedding stage were analysed.

In literature [13], icing mechanism of transmission lines with different diameters under four natural icing types were studied, and the freezing degree of transmission lines was characterized by the normalization method in which standard icing thickness replaced various icing forms, and a large number of field tests were conducted at natural icing observation stations to verify the effectiveness. Literature [14] studied the icing of bundle conductors, and found that when the two conductors are not on the same horizontal line, the windward conductor has no influence on the leeward conductor. When the angle between the two conductors is close to 0°, the leeward conductor has smaller droplet velocity, local collision efficiency and icing amount. Literature [15] studied the icing mechanism of transmission lines, analysed the factors affecting icing, and then established a pre-processing model of icing based on a big data platform to quantitatively analyse the factors affecting transmission lines icing. The results showed that five factors, including ambient temperature, relative humidity, wind speed, light intensity and load current, had the greatest affecting on icing of transmission lines. Literature [16] studied and considered the effects of wind speed, Median Volume Diameter (MVD) of water droplets, temperature, Liquid Water Content (LWC), wind direction angle and electric field strength on transmission lines icing characteristics, established a two-dimensional transmission line icing model to predict icing. The results showed that the greater the meteorological parameter of wind speed, the greater the MVD, the lower the temperature, the higher the LWC, then the greater the amount of icing.

However, in recent years, most of the research on transmission lines icing have been carried out in artificial climate laboratory, and its icing characteristics are different from the natural icing of working site, and there are few researches on the field related conditions of transmission line natural icing. Based on this, this paper carried out on-site observation of two 500kV transmission lines in high altitude

area, obtained data and statistical analysis, and obtained the relationship between the actual icing of transmission lines and temperature and wind speed.

II. TEST LINES OVERVIEW

In this paper, image, video and meteorological monitoring instruments installed along two 500kV transmission lines (line I and II) in high altitude areas are used to obtain icing data. As for images of transmission lines with the aid of image observation captured by drones, and statistical analysis is performed. Among them, the total length of the line I is 236.3km, using the 521 towers, the line II is 236.727km, using the 525 towers, the basic wind speed of the whole line design is 29 m/s, 31m/s, the design icing thickness is 15mm and 10mm, the ground conductor design icing thickness is 5mm higher than the transmission conductor, the wind speed design is 33m/s. Designed with insulation according to class C pollution area (creepage specific distance is 39mm/kV). The altitude of the lines is 2900m-5300m, the average altitude is about 4800 m, the terrain is alpine mountainous 31%, hills accounted for 36%, valleys accounted for 33%, the general elevation difference of 500 ~ 1200m, the maximum elevation difference of 1550m, belonging to the alpine mountains, valleys and hills areas mixed type landform.

Fig. 1. Topography of test transmission line

The terrain where the #036-#050 towers of these two lines are located fluctuates, with significant micro-topography and micro-meteorology. The weather is rain, snow, fog and so on all the year round. The work site environment of the lines is harsh, as shown in Fig. 1. Where #036-#047 is single-loop erection, where the left phase of the I conductor arrangement is phase B, the middle is phase C, the right is phase A, the left conductor of the II line is phase A, the middle is phase B, the

right is phase C, the transmission conductor type is JL/G1A-500/45, the ground conductor type is GJ-100, and the optical cable type is OPGW-120. The #048-#050 towers are double-loop erection, the transmission conductor type is L/G1A-520/35, the upper of I is phase C, the middle is phase A, the lower is phase B, the upper of II is phase B, the middle is phase A, the lower is phase C, the ground cable adopts the form of double optical, the optical cable type is OPGW-120. The form of insulator adopts porcelain insulator strings and composite insulator strings, in which the tensile string adopts porcelain insulators, and the overhang string and jumper string adopts composite insulators.

III. ANALYSIS OF ICING TEST DATA

In this paper, the #048-#050 towers of Line I and Line II were continuously observed for 15 days. During this period, icing covered the line for many days, accompanied by strong winds. The relative humidity is stable around 50%, and the average temperature (AT), average wind (AW) speed and equivalent icing thickness (EIT) are statistically analysed.

There was no icing covered on line I for 4 days, the average temperature was -8°C ~ 1°C, the average wind speed was between 4m/s - 17m/s, and the icing thickness was between 1.08mm and 5.47mm. The maximum icing thickness occurred on the 15th day, the thickness was 5.47mm, the average temperature was -7°C, and the average wind speed was 8m/s. The lowest temperature was -8°C on 14th day, with an average wind speed of 9m/s and a maximum equivalent icing thickness of 4.6mm. The maximum wind speed was 17 m/s on the 12th day, the average temperature was -3°C, and the icing thickness was 2.15mm. Specific data are shown in Table I:

TABLE II. STATISTICAL TABLE OF ICING DATA OF 500 kV LINE I

Number	AT(°C)	AW(m/s)	EIT(mm)
1	-5	7	2.71
2	-1	8	/
3	-4	11	1.92
4	-4	4	4.21
5	-6	7	3.96
6	-1	5	1.08
7	-1	5	/
8	-3	9	1.61
9	1	6	/
10	0	9	/
11	-3	8	1.47
12	-3	17	2.15
13	-6	9	3.12
14	-8	9	4.6
15	-7	8	5.47

The icing thickness of Line I is 1.1mm ~ 2.0mm for 4 days, and 2.1mm ~ 3mm, 3.1mm ~ 4.0mm, 4.1mm ~ 5.0mm have 2 days each, 5.1mm ~ 6.0mm have 1 day. The maximum and minimum values are 5.47mm and 1.08mm respectively. The average temperature is mainly based on -5°C ~ -1°C, 9 days, and -10°C ~ -6°C, 4 days, 0°C ~ 5°C, 2 days, the highest temperature is 1°C, the lowest temperature is -8°C. The average wind speed is mainly in the range of 6 m/s to 10 m/s for 10 days, and 0 m/s to 5 m/s for 3 days, 11 m/s to 15 m/s, 16 m/s to 20 m/s for 1 day, the minimum and maximum values are 4 m/s and 17 m/s, respectively. The statistics of average temperature, average wind speed and icing thickness of line I are shown in Fig. 2. It can be seen that the lower the temperature, the thicker the icing cover, and the icing thickness is negatively correlated with the temperature. The higher the wind speed, the greater the icing thickness, but it is not obvious.
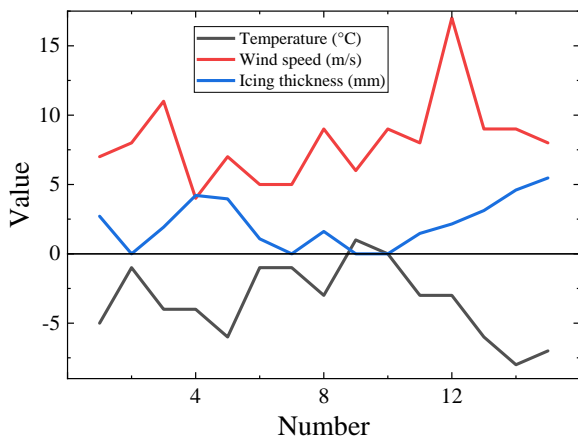
Fig. 2. Statistical of temperature, wind speed and icing thickness in line I

There was no icing on line II for only 1 day, and the average temperature was between -8°C and -1°C. The average wind speed is between 6 m/s -14 m/s, icing thickness between 1.1mm and 4.4mm. The maximum icing occurred on 4th day, with a maximum of 4.4mm, an average temperature of -6°C, and an average wind speed of 6m/s. The lowest temperature occurred on the 12th day, -8°C, the average wind speed was 12m/s, and the icing thickness was 3.7mm, which was relatively thick. The maximum wind speed appeared on the 3rd and 5th days, both of which were 14 m/s, the average temperature on the 3rd day was -4°C and the icing thickness was 2.2mm. The average temperature on the 5th day was -7°C and the icing thickness was 4.2mm. Specific data are shown in Table II:

TABLE II Statistical table of icing data of 500kV line II

Number	AT(°C)	AW(m/s)	EIT(mm)
1	-2	9	2.9
2	-1	10	/
3	-4	14	2.2
4	-6	6	4.4
5	-7	14	4.2
6	-2	9	1.4
7	-1	7	1.1
8	-3	11	1.8
9	-3	7	1.2
10	-5	8	1.2
11	-6	11	1.8
12	-8	12	3.7
13	-7	9	3.2
14	-5	11	2.8
15	-4	11	3

The icing thickness of line II is 1.1mm-2.0mm for 6 days. 2.1mm-3mm has 4 days, 3.1mm-4.0mm, 4.1mm-5.0mm has 2 days each, and the maximum and minimum values are 4.4mm and 1.1mm respectively. The average temperature is still mainly based in -5°C ~ -1°C, with 10 days, -10°C ~ -6°C, with 5 days, with the highest temperature -1°C and the lowest temperature -8°C. The average wind speed is mainly based on 6 m/s -10 m/s with 8 days and 11 m/s-15 m/s with 7 days. The maximum and minimum values are 14 m/s and 6 m/s respectively. The statistics of average temperature, average wind speed and icing thickness of line II are shown in Fig. 3. Similar conclusions can be drawn to I, the lower the temperature, the thicker the icing cover. The higher the wind speed, the thickness showed an increasing trend, which was still not obvious.
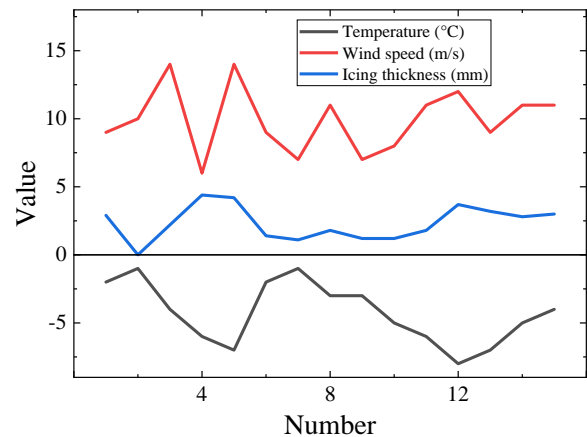
Fig. 3. Statistical of temperature, wind speed and icing thickness in line II

As can be seen from the data of line I and II as a whole, when the icing thickness is above 3mm, the average temperature is -6°C and below, and the average wind speed is mostly around 10m/s and above. When the icing thickness is below 3mm, the average temperature is -5°C and above, and the average wind speed is mostly around 10m/s and below. Because the temperature and wind speed data are average for the day, there may be large changes during the day. At the same time, the relative humidity of the site is also an important

factor affecting the icing. Although it is relatively stable at around 50%, it is also affected by rainfall during the observation period, and is not included in the research scope. There are other factors associated with icing, and the laws under natural icing are still complex. The icing site situation of the lines is shown in the Fig. 4.

(a) The icing of a tower on line I

(b) The icing of a tower on line II

Fig. 4. The icing site situation of the lines

IV. CONCLUSION

1) Natural icing observation data show that the average temperature is mainly -5°C ~ -1°C, and the average wind speed is mainly between 6m/s ~ 10m /s. The lower the temperature, the higher the wind speed, and the more severe of the transmission lines icing.

2) The icing thickness of the transmission lines is mainly 1.1mm ~ 2.0mm. In the few days when no icing was observed on the line, the temperature increased to 0°C or above, preventing icing from forming.

3) According to statistics, when the icing thickness is above 3mm, the average temperature is about -5°C and below, and the average wind speed is mostly about 10m/s and above.

REFERENCES

[1] Farzaneh, Masoud.; William A.; Chisholm. Insulators for Icing and polluted Environments. *M*.**2009**

[2] Barat, A.; Guo, Q.; Fan, F.; Guo, X.; Zhang, Q. Analysis and Design of Transmission Line Icing Monitoring System Based on Optical Fiber Sensing. *2022 IEEE 10th Joint International Information Technology and Artificial Intelligence Conference (ITAIC).* **2022**, pp. 1846-1849, doi: 10.1109/ITAIC54216.2022.9836838.

[3] Runhua, W. Analysis of the accident based on low temperature, snowstorm, ice, coagulation. *2008 China International Conference on Electricity Distribution.* **2008**, pp. 1-7, doi: 10.1109/CICED.2008.5211824.

[4] Kunpeng, J.; et al. Dynamic analysis and suppression method of bundled conductors following ice shedding. *2021 IEEE Sustainable Power and Energy Conference (iSPEC).* **2021**, pp. 1596-1601, doi: 10.1109/iSPEC53008.2021.9735610..

[5] Huang, Q.; Tan, Y.; Mao, X.; Zhu, S.; Zhou, X. Study on Melting Ice Current Characteristics under Low Temperature and High Wind Speed. *2021 IEEE 5th Conference on Energy Internet and Energy System Integration (EI2).* **2021**, pp. 4382-4385, doi: 10.1109/EI252483.2021.9713437.

[6] Lu, J.; Zeng, M.; Zeng, X.; Fang, Z.; Yuan, J. Analysis of Ice-Covering Characteristics of China Hunan Power Grid. in *IEEE Transactions on Industry Applications.* **2015** vol. 51, no. 3, pp. 1997-2002, May-June 2015, doi: 10.1109/TIA.2014.2365295.

[7] Zhang, Z.; Zhang, H.; Yue, S.; Zeng, W. A Review of Icing and Anti-Icing Technology for Transmission Lines. Energies, 2023, 16, 601. https://doi.org/10.3390/en16020601.

[8] W. Huang et al., "Preventive Scheduling for Reducing the Impact of Glaze Icing on Transmission Lines," in IEEE Transactions on Power Systems, vol. 37, no. 2, pp. 1297-1310, March 2022, doi: 10.1109/TPWRS.2021.3099978.

[9] Han, Xingbo, Xingliang Jiang, Zhongyi Yang, and Conglai Bi. 2018. "A Predictive Model for Dry-Growth Icing on Composite Insulators under Natural Conditions" Energies 11, no. 6: 1339. https://doi.org/10.3390/en11061339

[10] Jiang, X., Han, X., Hu, Y. and Yang, Z. (2018), Model for ice wet growth on composite insulator and its experimental validation. IET Gener. Transm. Distrib., 12: 556-563. https://doi.org/10.1049/iet-gtd.2017.0229

[11] Zhijin Zhang, Hang Zhang, Song Yue, Xu Zhang, Chang Li, Wenhui Zeng, Growth characteristics and influence analysis of insulator strings in natural icing, Electric Power Systems Research, Volume 228, 2024, 110097, ISSN 0378-7796, https://doi.org/10.1016/j.epsr.2023.110097.

[12] J. Druez and P. McComber. 1996. FIELD DATA ON POWER LINE ICING. Transactions of the Canadian Society for Mechanical Engineering. 20(3): 259-273. https://doi.org/10.1139/tcsme-1996-0015

[13] C. Fan, X. Jiang, Analysis of the Icing Accretion Performance of Conductors and Its Normalized Characterization Method of Icing Degree for Various Ice Types in Natural Environments. Energies 2018, 11, 2678. https://doi.org/10.3390/en11102678

[14] Q. He, J. Zhang, M. Deng, D. Du, M. Lasse, T. Mikko, Rime icing on bundled conductors, Cold Regions Science and Technology, Volume 158, 2019, Pages 230-236, ISSN 0165-232X, https://doi.org/10.1016/j.coldregions.2018.08.027.

[15] Li, L., Luo, D. & Yao, W. Analysis of transmission line icing prediction based on CNN and data mining technology. Soft Comput 26, 7865–7870 (2022). https://doi.org/10.1007/s00500-022-06812-7.

[16] F. Xu, D. Li, P. Gao, W. Zang, Z. Duan, J. Ou, Numerical simulation of two-dimensional transmission line icing and analysis of factors that influence icing, Journal of Fluids and Structures, Volume 118, 2023, 103858, ISSN 0889-9746, https://doi.org/10.1016/j.jfluidstructs.2023.103858.

Electrofreezing of Supercooled Aqueous Electrolyte Solutions under a Low Static Voltage

Yang Liu, Min Chen*

Department of Engineering Mechanics, Tsinghua University, Beijing 100084, China

mchen@tsinghua.edu.cn

Abstract— **We investigate the nucleation process of supercooled droplets of different aqueous electrolyte solutions under a small voltage ranging from -1V to 1V, measuring their nucleation temperature. Experiments reveal that the ice nucleation is hindered under the small voltage regardless of its direction, and the inhibition is prominently related to the ion types. A mechanism of the electric field effect on the ice nucleation of the solution is proposed based on the electric double layer theory, noting that the electric field inside the electric double layer elevates the energy required for heterogenous nucleation, thus impeding the nucleation. The electric intensity within the electric double layer is tuned by different effective aqueous radii of different ions, resulting the different changes of nucleation temperature of varied electrolyte solutions under the external voltage.**

Keywords— **electrofreezing, aqueous electrolyte solution, supercooled droplet, electric double layer, outer Helmholtz plane**

I. INTRODUCTION

Controlling the icing temperature of supercooled droplets is significant in various applications from ground and air transportation to powerline failure prevention.[1], [2], [3], [4], [5] In the maintenance of the powerline, mitigating the freezing of supercooled water condensed on the cable is crucial for the safety of the electric system and the reduction of maintenance costs.[2], [3] In the aviation industry, controlling droplet freezing on airfoils ensures safe transportation and facilitates anti-icing process.[1], [5] A promising approach to ice nucleation control is applying an electric field on the liquid, called electrofreezing.[6] It is reported in early experiments that an external electric field elevates the nucleation temperature of supercooled droplets, which is explained as the electric field facilitates a uniform direction of polar water molecules, and therefore the forming of the ice structure.[7], [8], [9] The droplet nucleation is easily affected by the magnitude and direction of the electric field. The critical magnitude of the electric field for promoting nucleation is around 10^9 V/m predicted by molecular dynamics simulation and the classical nucleation theory, which is much higher than that of 10^5 V/m in experiments.[8], [10], [11], [12] As for the direction of the electric field regarding the rest droplet, Ehre et al. reported an opposite effect on nucleation of surfaces carrying positive or negative charges, but others claim that no difference is observed when changing the field direction in other experiments.[11], [13], [14] In all, considering the complex effect of the electric field on supercooled water including humidity, water purity and the droplet shape, a widely accepted law of the electrofreezing effect on supercooled droplets is yet to be determined.[6]

In most real applications like anti-icing for transportation, water contains electrolyte ions dissolved from the environment, whose locally accumulation under electric field greatly influences the electrofreezing behavior of supercooled water, necessitating investigations of the electrofreezing of supercooled aqueous electrolyte solutions.[15], [16] Ma et al. have revealed the electrolyte ions in the physiological saline largely lower the critical electric field required to hinder liquid nucleation to 10^2 V/m.[17] Others like Javitt et al. complement that different ions may either hinder or facilitate the nucleation under a given electric field owing to their different spatial structures.[18] Although research has revealed the influence of the electric field on supercooled electrolyte solutions, how factors like ion types, the magnitude and direction of the electric field affects the nucleation of the solution remains valuable to be explored.

In this work, we investigate the nucleation process of supercooled aqueous electrolyte solutions when a low static voltage is perpendicularly applied to the drop by inserting an electrode inside, measuring the nucleation temperature of 0.1M LiCl, KCl and CsCl solutions under a voltage ranging from -1V to 1V. Results show that the ice nucleation is hindered under the 1V voltage regardless of its direction, and the inhibition is prominently related to the ion types. We therefore propose a mechanism of the electric field effect on the ice nucleation of the solution based on the electric double layer theory, noting that the impediment of ice nucleation correlates positively with the electric intensity within the electric double layer, which is tuned by different effective aqueous radii of different ions. We argue that the solution containing ions of smaller effective aqueous radii under a relatively large voltage regardless of its direction has a lower nucleation temperature.

II. METHOD

The experimental setup is shown in Figure I, where the droplet is placed on a horizontal multilayer pile of smooth platinum plate, copper plate and thermoelectric cooler (TEC1-12704). The droplet is isolated from the environment by a small PMMA hood, through which a platinum wire (Φ0.05) is perpendicularly inserted into the droplet as an electrode. A thermocouple (National Instrument) is buried in the middle of the copper padding for temperature measure. All of the platform is shielded in a large, thermal insulation cotton-covered PMMA hood with a nitrogen atmosphere to control humidity. A DC power supply (PS-6005D) exerts 1V voltage between the electrodes, and a programmable power supply (Keysight-N5767A) for the thermoelectric cooler is coded to generate a linearly decrease of the temperature inside the smaller hood.
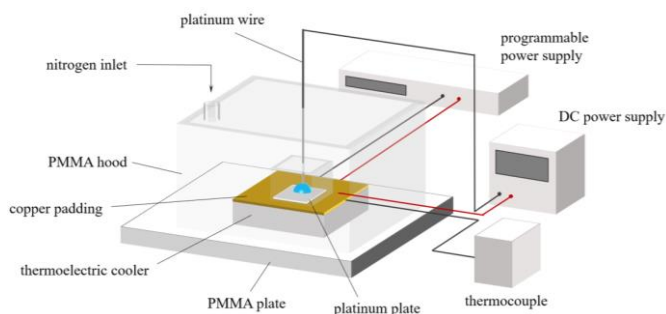
Fig. 1   The experimental setup.

Solutions of 0.1M LiCl, KCl and CsCl with a volume of 4μL are utilized for the experiment for simplicity. We observed similar contact angles of around 62° for solution droplets of different electrolytes on the platinum plate, which eliminates the impact of droplet shape on the nucleation in the experiments. We fix the distance between the electrodes (0.5mm), keeping consistent roughness of the platinum plate and the platinum wire at the center of the droplet. We do not observe a macroscopic current under 1V voltage that indicates electrolysis, a significant temperature difference at different points on the droplet (within $\pm 1°C$), nor the influence of the external electric field on thermocouple measure.

At the beginning of the experiment, the platinum plate and wire are cleaned by DI water, ethanol and DI water successively to exclude potential interference of previous experiments. The nitrogen gas is then infilled into the setup, creating an atmosphere without water vapor, after which the thermoelectric cooler starts operating until the ice nucleation. We define the "positive voltage" as when the platinum plate is the anode. The nucleation temperature is recognized through the recoalescence of droplets monitored by the thermocouple as shown in Figure II, which implies the freezing process of a 0.1M KCl droplet. A considerable temperature leap of approximately 7 ℃ occurs at the recoalescence when the droplet nucleates owing to the released latent heat, through which the nucleation temperature (the red dashed line) can be determined. After the nucleation, the surface temperature rises to the room temperature and the droplets is removed.
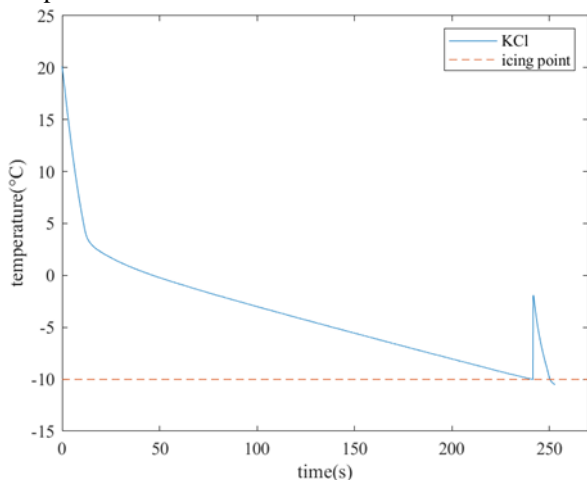
Fig. 2   The profile of the freezing process in the experiment. The blue curve in the figure denotes the droplet temperature measured by the thermocouple, and the red dashed line denotes the recognized nucleation temperature.

III. RESULTS

The nucleation temperatures of different electrolyte solutions under voltages ranging from -1V to 1V are plotted in Figure III, where each data point is the average of 5 repetitive experimental outcomes. Figure III shows that the nucleation temperature overall decreases when a small voltage is applied regardless of its direction, while a local increase exists for 0.1M KCl and LiCl solutions under a certain smaller positive voltage. Moreover, varied electrolyte solutions respond to the external voltage differently, where the 0.1M LiCl solution has the maximal decline of nucleation temperature under ±1V and the 0.1M CsCl the least.
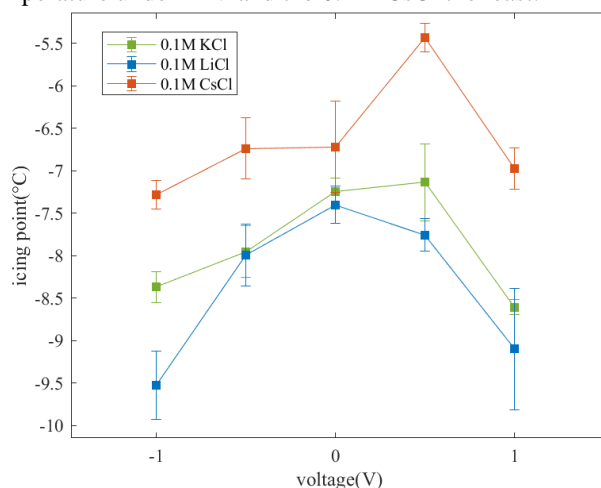
Fig. 3   Nucleation temperatures of different electrolyte solutions under voltages ranging from -1V to 1V. The squares and the error bars in the figure denote the average and the standard deviation of 5 repetitive outcomes in each data group.

The nucleation process is recorded utilizing the highspeed camera, shown as a series in Figure IV. The crystallization alters the refractivity of the droplet surface, through which one can determine from the figure that the initial nucleation occurs on the contact line between the liquid and platinum plate. The prevalence of the phenomenon matches that the possibility of heterogenous nucleation is much higher than that of homogenous nucleation, entailing a microscopic interfacial model for result analysis.
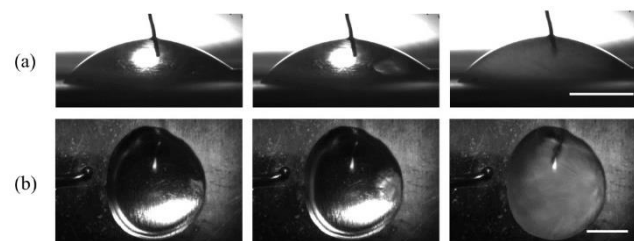
Fig. 4   Snapshots of a single nucleation process (a) from a side view and (b) from a vertical view. Image time, from left to right: before nucleation, initial nucleation occurring, after nucleation. The wire in the side-view image is the platinum electrode, and the wire in the vertical-view image is the thermocouple. All scale bars represent 1mm.

IV. DISCUSSION

When a voltage exists between the electrolyte solution and metal surface, charges in the metal and aqueous ions with opposite charges accumulate on the interface by electrostatic induction, forming the electric double layer. The classic Gouy-Chapman-Stern model of the electric double layer is

illustrated in Figure V.[19] In the region of electric double layer, a film of water molecules is adsorbed on the metal surface, constituting sites for heterogenous nucleation. This water layer is sandwiched by the metal surface and an aqueous ion layer (the Outer Helmholtz plane, OHP) if no specific adsorption happens, and the layer between the OHP and the metal surface accounts for most of the voltage drop.[19] The distance between the OHP and the metal surface (with an order of 1Å), which determines the inner electric intensity under a given voltage, has a positive correlation with the effective aqueous ion radius.[20], [21] In the experiment, the electric intensity within the OHP is estimated to be $\sim10^9 V/m$ under an external voltage of 1V, which is much larger than the critical electric intensity reported in previous experimental research that can influence the nucleation temperature, justifying that the change in nucleation temperature results from the manipulation of electric field within the OHP.[11], [12], [14]
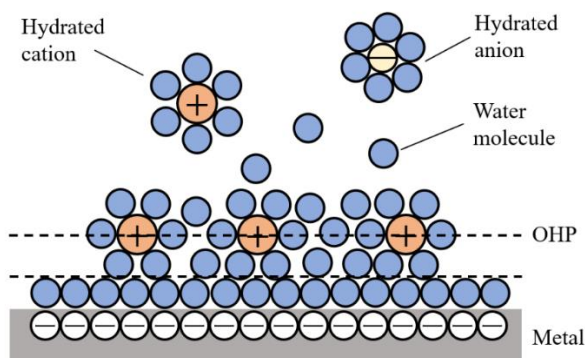
Fig. 5   Sketch of the Gouy-Chapman-Stern model of the electric double layer.

During the nucleation process, ice crystallization pushes the induced ions outward against the electric field within the OHP, i.e., the electric field within the OHP lifts the free energy required for nucleation of the droplet. Hence, the electric field within the OHP hinders nucleation in the electric double layer, and the impediment is positively correlated with the electric intensity regardless of its direction.

Previous study reveals that electric double layer forms spontaneously on the solution-metal interface without an external voltage.[21] Owing to electron mobility inside the metal, electrons accumulate on the metal side of the spontaneously-induced electric double layer, generating a $\sim0.1V$ voltage within the OHP from the solution to the metal.[22] When the external voltage is applied to the same direction with the spontaneous OHP voltage, the inner electric intensity is enhanced, further hindering the ice nucleation. In contrast, an external voltage of an opposite direction with the spontaneous OHP voltage would attenuate, or if exceeding the spontaneous OHP voltage, rebuild the electric field within the OHP, resulting the highest nucleation temperature under a certain positive voltage comparable to the spontaneous OHP voltage. In fact, the voltage corresponding to the maximal nucleation temperature matches in magnitude with the existing data of 0.1M NaCl and KCl solutions provided by

Grahame, where larger cations have much higher spontaneous OHP voltages.[23]

Since ions of different effective aqueous radii vary in the thickness of the electric double layer, the change of electric intensity within the OHP is ion-relevant under an identical external voltage.[21] The electric double layers of smaller ions like Li^+ are more susceptible to an external voltage, which results in a large increase of electric intensity within OHP and thus a considerable drop of the nucleation temperature as shown in Figure III.[24]

V. Conclusion

We experimentally investigate the nucleation process of supercooled droplets of different aqueous electrolyte solutions under a small voltage ranging from -1V to 1V, measuring their nucleation temperature. The solutions utilized are 0.1M LiCl, KCl and CsCl, and the volume of each droplet is 4μL.

Results show that the ice nucleation is hindered by 0.5-1℃ under the 1V voltage regardless of its direction, and has a positive correlation with the electric intensity. As for different ions, the inhibition of nucleation is stronger with the order of CsCl, KCl and LiCl. With the observation of heterogenous nucleation on the solution-electrode interface, a mechanism of the electric field effect on the ice nucleation of the solution based on the interfacial electric double layer theory is proposed. We argue that the electric field inside the electric double layer elevates the free energy gap needed for nucleation, since the ions are pushed outward against the electric field during the crystallization. When the external voltage is to the same direction with the spontaneous electric double layer formed by electrostatic induction, the electric intensity within the OHP is enhanced, further hindering the nucleation and lowering the nucleation temperature. If the outer voltage is against the spontaneous electric intensity, the nucleation temperature reaches the highest when the electric intensity is offset by the external voltage, and drops if the voltage continues increasing and reverse the electric double layer. Ions of smaller effective aqueous radii generate thinner electric double layers where the electric intensity changes more greatly under an external voltage, explaining the ascending order of nucleation inhibition strength of CsCl, KCl and LiCl.

In conclusion, judging from our mechanism of the electric field effect on the ice nucleation of the solution, we reveal that solutions of ions of smaller effective aqueous radii under a relatively large voltage regardless of its direction have lower nucleation temperatures. This exploratory research provides a guideline to control the freezing of supercooled aqueous electrolyte solutions, either to hinder the ice nucleation on structures such as transportation systems or to accelerate freeze drying.

References

[1] T. Cebeci and F. Kafyeke, "Aircraft Icing," *Annu. Rev. Fluid Mech.*, vol. 35, no. 1, pp. 11–21, 2003, doi: 10.1146/annurev.fluid.35.101101.161217.

[2] A. Lotfi and M. S. Virk, "Railway operations in icing conditions: a review of issues and mitigation methods," *Public Transp*, vol. 15, no. 3, pp. 747–765, Oct. 2023, doi: 10.1007/s12469-023-00327-6.

[3] C. Volat, M. Farzaneh, and A. Leblond, "De-icing/Anti-icing Techniques for Power Lines: Current Methods and Future Direction," 2005.

[4] O. Parent and A. Ilinca, "Anti-icing and de-icing techniques for wind turbines: Critical review," *Cold Regions Science and Technology*, vol. 65, no. 1, pp. 88–96, Jan. 2011, doi: 10.1016/j.coldregions.2010.01.005.

[5] D. De Pauw and A. Dolatabadi, "Effect of Superhydrophobic Coating on the Anti-Icing and Deicing of an Airfoil," *Journal of Aircraft*, vol. 54, no. 2, pp. 490–499, Mar. 2017, doi: 10.2514/1.C033828.

[6] P. V. Acharya and V. Bahadur, "Fundamental interfacial mechanisms underlying electrofreezing," *Adv. Colloid Interface Sci.*, vol. 251, pp. 26–43, Jan. 2018, doi: 10.1016/j.cis.2017.12.003.

[7] L. Dufour, "Uber das Gefrieren das Wassers and ubber die Bildung des Hagels," *Poggend. Ann. Phys.*, vol. 114, pp. 530–554, 1861.

[8] S. Wei, X. Xiaobin, Z. Hong, and X. Chuanxiang, "Effects of dipole polarization of water molecules on ice formation under an electrostatic field," *Cryobiology*, vol. 56, no. 1, pp. 93–9, Feb. 2008, doi: 10.1016/j.cryobiol.2007.10.173.

[9] R. W. Salt, "Effect of Electrostatic Field on Freezing of Supercooled Water and Insects," *Science*, vol. 133, no. 3451, pp. 458–9, Feb. 1961, doi: 10.1126/science.133.3451.458.

[10] J. Y. Yan and G. N. Patey, "Molecular dynamics simulations of ice nucleation by electric fields," *J. Phys. Chem. A*, vol. 116, no. 26, pp. 7057–64, Jul. 2012, doi: 10.1021/jp3039187.

[11] X.-X. Zhang, X.-H. Li, and M. Chen, "Role of the electric double layer in the ice nucleation of water droplets under an electric field," *Atmos. Res.*, vol. 178–179, pp. 150–154, 2016, doi: 10.1016/j.atmosres.2016.04.001.

[12] M. Orlowska, M. Havet, and A. Le-Bail, "Controlled ice nucleation under high voltage DC electrostatic field conditions," *Food Res. Int.*, vol. 42, no. 7, pp. 879–884, 2009, doi: 10.1016/j.foodres.2009.03.015.

[13] D. Ehre, E. Lavert, M. Lahav, and I. Lubomirsky, "Water freezes differently on positively and negatively charged surfaces of pyroelectric materials," *Science*, vol. 327, no. 5966, pp. 672–5, Feb. 2010, doi: 10.1126/science.1178085.

[14] K. Carpenter and V. Bahadur, "Electrofreezing of water droplets under electrowetting fields," *Langmuir*, vol. 31, no. 7, pp. 2243–8, Feb. 2015, doi: 10.1021/la504792n.

[15] S. Curland, L. Javitt, I. Weissbuch, D. Ehre, M. Lahav, and I. Lubomirsky, "Heterogeneous Electrofreezing Triggered by CO(2) on Pyroelectric Crystals: Qualitatively Different Icing on Hydrophilic and Hydrophobic Surfaces," *Angew Chem Int Ed Engl*, vol. 59, no. 36, pp. 15570–15574, Sep. 2020, doi: 10.1002/anie.202006433.

[16] S. Curland *et al.*, "Heterogeneous Electrofreezing of Super-Cooled Water on Surfaces of Pyroelectric Crystals is Triggered by Trigonal Planar Ions," *Angew Chem Int Ed Engl*, vol. 59, no. 36, pp. 15575–15579, Sep. 2020, doi: 10.1002/anie.202006435.

[17] Y. Ma, L. Zhong, H. Zhang, and C. Xu, "Effect of applied electric field on the formation and structure of ice in biomaterials during freezing," 2010.

[18] L. F. Javitt, I. Weissbuch, D. Ehre, I. Lubomirsky, and M. Lahav, "Biguanide, an Efficient Electrofreezing 'Ice-maker' Ion of Supercooled Water," *Crystal Growth & Design*, vol. 22, no. 1, pp. 43–47, 2021, doi: 10.1021/acs.cgd.1c01025.

[19] O. Stern, "The theory of the electrolytic double shift," *Z. Elektrochem. Angew. Phys. Chem.*, vol. 30, pp. 508–516, 1924.

[20] F. H. Stillinger and J. G. Kirkwood, "Theory of the Diffuse Double Layer," *The Journal of Chemical Physics*, vol. 33, no. 5, pp. 1282–1290, 1960, doi: 10.1063/1.1731401.

[21] M. A. Brown *et al.*, "Determination of Surface Potential and Electrical Double-Layer Structure at the Aqueous Electrolyte-Nanoparticle Interface," *Phys. Rev. X*, vol. 6, no. 1, 2016, doi: 10.1103/PhysRevX.6.011007.

[22] R. R. Kumal, T. E. Karam, and L. H. Haber, "Determination of the Surface Charge Density of Colloidal Gold Nanoparticles Using Second Harmonic Generation," *The Journal of Physical Chemistry C*, vol. 119, no. 28, pp. 16200–16207, 2015, doi: 10.1021/acs.jpcc.5b00568.

[23] D. C. Grahame, "The Electrical Double Layer and the Theory of Electrocapillarity.," *Chem. Rev.*, vol. 41, no. 3, pp. 441–501, Dec. 1947, doi: 10.1021/cr60130a002.

[24] J. G. Speight and N. A. Lange, Eds., *Lange's handbook of chemistry*, 16t. ed., 70th anniversary ed. in McGraw-Hill standard handbooks. New York: McGraw-Hill, 2005.

Studies on wettability and anti-icing performance of superhydrophobic Al conductors by the industrialized anodization

Xu Dai[1], Yuan Yuan[1]*, Jie Xiao[1], Huiying Xiang[1], Xujiang Hua[1], Tao Zhu[1], Ruijin Liao[1]*

[1] Chongqing university, China

xudai@cqu.edu.cn, yuany@cqu.edu.cn, 1226073385@qq.com, 20200901052@cqu.edu.cn, 20230901040@stu.cqu.edu.cn, davezhu@cqu.edu.cn, rjliao@cqu.edu.cn

Abstract—**Icing can cause significant economic damage to the power grid. Superhydrophobic surfaces have been widely studied as an economical anti icing strategy, but research on preparation and anti-icing properties of superhydrophobic aluminium conductors (especially the Aluminium conductors steel reinforce) is limited. In this study, industrialized anodization method was put forward to prepare porous superhydrophobic aluminium surfaces and aluminium conductors. Different anodization parameters were adopted to study the optimal wettability and anti-icing properties, including the hydrophobicity and ice adhesion. Here, the contact angle on the prepared superhydrophobic aluminium surface reaches 151°, the ice adhesion force reaches 5.5 kPa, showing 2.3 % that of the bare aluminium surface. Therefore, the industrialized superhydrophobic aluminium conductor shows potential application future.**

Keywords— ***superhydrophobic, aluminum stranded lines, industrialized anodization, anti-icing, wettability.***

I. INTRODUCTION

The safe operation of power lines is of practical importance. Sudden icing may lead to transmission line failures, even large-scale power outages, causing significant economic losses. [1] Since the 20th century, icing incidents on overhead transmission lines have occurred frequently in newspapers. Therefore, ice is always a serious natural disaster in the domestic and international power industry [2-4].

In high cold and humid climates, the cooled liquid on the surface of transmission lines can be prone to condensation, ice formation and accumulation [3, 5]. In addition, severe icing can even cause line breakage and tower collapse. [1] The miscellaneous power grid may be increasingly subjected to large-scale icing tests. Especially under the influence of micro terrain, if not prevented and controlled, ice disaster accidents in the power system will be inevitable [2]. Therefore, much research was reported on the de-icing and anti-icing technologies under different icing conditions to ensure transportation [4, 6].

Among many anti-icing technologies, superhydrophobic surface has gained much focus for the good anti-icing effect and convenient preparation. Lian et, al. reported the durable superhydrophobic Al surface by laser-etching technique to show the good wettability. However, laser-etching method could have technique difficulty and high energy consumption on the large-scale preparation of hundred meters of Aluminium conductor steel reinforce (ACSR). Recently, hydrophobic Al strands and ACSR conductors have been reported of good anti-icing properties by acid etching and hydrothermal treatment. Based on this, our group has also reported the superhydrophobic ACSRs with excellent anti-icing property by anodized method. In addition, hundred meters or kilometres ACSRs should processed the industrialized anodization to achieve the standardized and stable preparation of anti-icing transmission lines. However, the industrialized anodization is significantly different from the laboratory experiments. This requires further exploration of relevant preparation process parameters.

In this study, industrialized anodization method was put forward to prepare porous superhydrophobic aluminium conductors. Different anodization parameters (applied anodized voltages) were adopted to study the optimal wettability and anti-icing properties, including the hydrophobicity and ice adhesion. Here, when the applied voltage is 55 V, the contact angle on the prepared superhydrophobic aluminium surface reaches 151°, the ice adhesion force reaches 5.5 kPa, showing 2.3 % that of the bare aluminium surface. Therefore, the industrialized superhydrophobic aluminium conductor shows potential application future that continuous production of hundred meters or kilometres ACSRs.

II. EXPERIMENT

A. Materials

The treated ACSRs (JL/LB20A-120/20) were purchased from the Henan Tongda Cable Co., Ltd. Anhydrous ethanol were provided by Chengdu Kelong Chemical Co., Ltd, China. Oxalic acid ($H_2C_2O_4$) was provided by Tongliao Gemchemical Co., Ltd. Inner Mongolia Autonomous Region, China. FAS modification agents were provided by Shanghai Aladdin Reagent Co., Ltd. Pure water is produced by the water purifier.

B. industrialized anodization and modification

Considering the large-scale preparation of several hundred meters or even kilometers of Al conductors, industrialized anodization is a promising industrial surface treatment technology. Here, the industrial anodization of long lines is being carried out in the Zhong Run Surface Treatment Industrial Park, in Bishan district, Chongqing, China. The industrial preparation of long conductors adopts a fully automatic gantry anodizing production line, mainly including gantry crane, electrical control system, and anodizing related equipment, etc. The production process includes: degreasing, water washing, alkaline washing, water washing, acid washing neutralization, and water washing for pre-treatment;

Anodizing treatment; Water washing, ultrasonic cleaning, drying, and modification for post-processing. This production line system is a commonly used method for processing large aluminium materials, with a high degree of automation. It can modify and record various process parameters during the oxidation process to ensure anodized product quality, improve product consistency, and also facilitate the exploration of preparation parameters in the early stage.

In Fig. 1 a, 120/20 ACSRs (50 cm) were clamped tightly onto a Titanium fixture to confirm the stable load current. Fig. 2 b and c depicts the pre-treatments (water washing and acid washing neutralization) of the bare 120/20 ACSR. Fig. 2 d shows the anodization of the untreated 120/20 ACSR. Fig. 2 e shows the post-processing (ultrasonic cleaning) of the 120/20 ACSR. According to the preparation process parameters in the laboratory, the tentative oxidation time is 30 minutes, and the tentative anodization voltages on ACSRs are determined as 15V, 35V and 55 V. Here, these processed ACSRs are named as 15V, 35V and 55V, respectively. After the anodization, anodized ACSRs were completely dried with moisture in an oven, then soaked in 3 wt.% FAS solution for 5 hours, and thermally cured at 100 °C to obtain the final superhydrophobic lines.
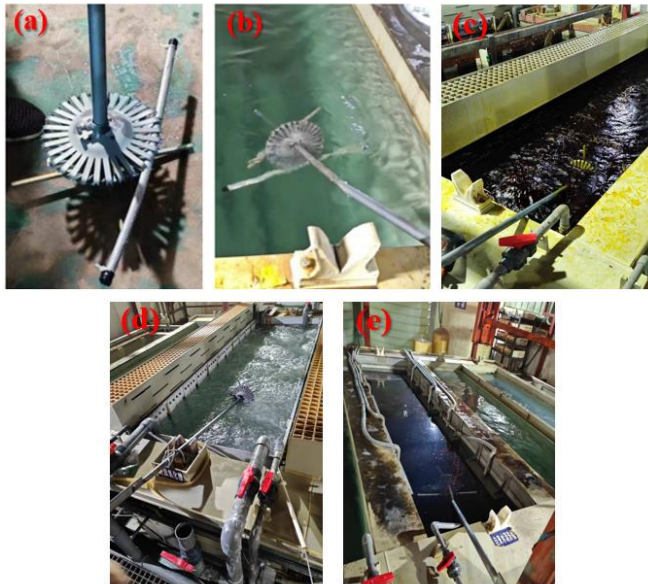
Fig. 1   Industrialized preparation of anodized ACSR for anti-icing application: (a) Anodized clamping hardware; (b, c) Pre-treatment process; (d) Anodization process; (e) Post treatment process.

C. Characterizations and performance testing

The morphology and structure of samples were characterized by a field emission scanning electron microscope system (SEM, Zeiss Auriga, Germany) equipped with an energy dispersive spectrometer (EDS).

Wettability (contact angle) can be measured by the contact angle testing instrument (SINDIN, SDC-100, China). For measuring the ice adhesion, a special PTFE cylindrical mold with 5 cm×2 cm×1.5 cm was used by filled with water, which has been reported in previous studies. It is cooled in the refrigerator at -10 °C until completely frozen. After being fully frozen, a digital thrust meter is used to push horizontally to obtain the peak thrust. The value of thrust is divided by the contact area (bottom area of the tube) to calculate the ice adhesion strength. The contact area has also been reported by previous studies. Each sample was tested three times and its average value was taken.

III. RESULTs AND DISCUSSION

Fig. 2 depicts the macroscopic and microscopic images of SLIPS sample. Fig. 2 (a) and (b) show micrographs of the surface of the industrialized anodized 120/20 ACSRs under different anodized voltages. From the macroscopic pictures, with the increase of applied anodized voltages, Al conductor shows a more prominent yellow luster. When the Al conductor applied on the low voltage (15 V), the whole appears pale white and dull. From the micro-morphology, ACSR of applied 55 V shows the significant honeycomb structure with the high porosity. The average diameter of nanopores can be calculated as ~ 50 nm, showing the small size of pore structure. In contrast, ACSRs with the applied voltages of 15 V and 35 V only show the no pores structure or fine pores structure. Micro structure could cause the difference of macroscopic view of Al conductors that larger pore size leads to the more obvious yellow glossiness.
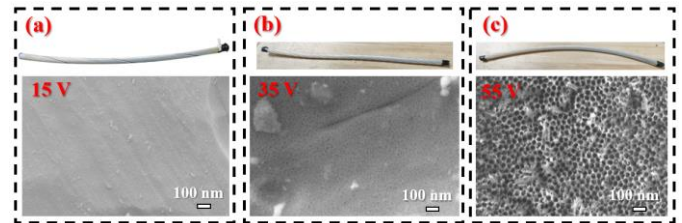
Fig. 2   Macroscopic and microscopic images of the industrialized anodized 120/20 ACSRs under different anodized voltages: (a) 15 V; (b) 35 V; (c) 55 V.

By fitting the droplets on the curved surface of the single strand from ACSRs, the contact angle results of the bare and industrialized anodized 120/20 ACSRs were provided in Fig.3. Bare specimen shows the low CA of about 76°. The CA of 15 V specimen is 104°, showing the poor hydrophobicity. This can be attributed to the relative flat surface and modification of low surface energy products. In addition, 35 V specimen has the CA of 122°, indicating the mediocre hydrophobicity. 55 V specimen shows the ideal contact angle of 151°, corresponding to the superhydrophobicity.
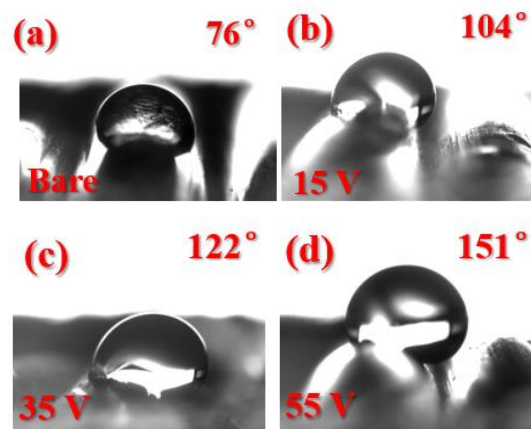
Fig. 3   Wettability of bare and industrialized anodized ACSRs: (a) Bare; (b) 15 V; (c) 35 V; (d) 55 V.

Ice adhesion is the important indicator to evaluate the anti-icing performance of hydrophobic samples. Fig. 4 shows the comparison in the ice adhesion strength of bare and industrialized anodized conductors. The ice adhesion of bare plate is 235.3 kPa, while all anodized specimens show the lower ice adhesion. 15 V, 35 V and 55 V specimens have the ice adhesion of 76.2, 35.5, and 5.5 kPa, respectively. It is worth noting that the ice adhesion strength of 55 V specimen is 2.3 % of that of the bare sample. This because the good superhydrophobicity can reduce the contact area between frozen water and solid phase structure. Similar results are also reported by other studies.
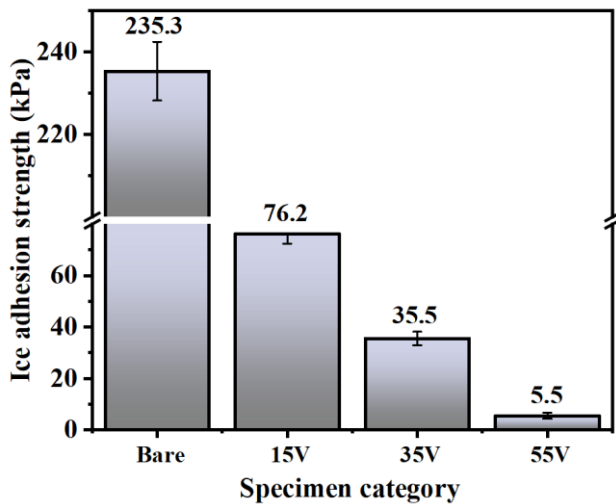
Fig. 4 Comparison of ice adhesion of the industrialized anodized 120/20 ACSRs

IV. Conclusions

In this study, industrialized anodization method was put forward to prepare porous superhydrophobic aluminium conductors. Here, when the applied voltage is 55 V, the contact angle on the prepared superhydrophobic aluminium surface reaches 151°, the ice adhesion force reaches 5.5 kPa, showing 2.3 % that of the bare aluminium surface. Therefore, the industrialized superhydrophobic aluminium conductor shows potential application future that continuous production of hundred meters or kilometres ACSRs.

References

[1] X. Jiang, C. Fan, and Y. Xie, "New Method of Preventing Ice Disaster in Power Grid Using Expanded Conductors in Heavy Icing Area", IET Generation, Transmission & Distribution, Vol. 13, pp. 536-542, 2019.

[2] J. Lu, M. Zeng, and Yuan, J., "Analysis of Ice-Covering Characteristics of China Hunan Power Grid", IEEE Transactions on Industry Applications, 2015, Vol. 51, pp. 1997-2002, 2015

[3] Z. Zhang, H. Zhang, and W. Zeng,, "A Review of Icing and Anti-Icing Technology for Transmission Lines", Energies, 2023.

[4] S. Fan, X. Jiang, L. Shu, P. He, P. Liu, and H. Nie, "Dc Ice-Melting Model for Elliptic Glaze Iced Conductor", IEEE Transactions on Power Delivery, Vol. 26, pp. 2697-2704, 2011.

[5] B. Li, J. Bai, J. He, X. Dai, and Y. Yuan, "A Review on Superhydrophobic Surface with Anti-Icing Properties in Overhead Transmission Lines", Coatings, 2023.

[6] M. Huneault, C. Langheit, J. Audet, and J. C. Richard, "A Dynamic Programming Methodology to Develop De-Icing Strategies During Ice Storms by Channeling Load Currents in Transmission Networks", IEEE Transactions on Power Delivery, Vol. 20, pp. 1604-1610, 2005.

[7] G. Y. Liu, Y. Yuan, R. J. Liao, L. Wang, X. Gao, "Fabrication of a porous slippery icephobic surface and effect of lubricant viscosity on anti-icing properties and durability," Coatings, Vol. 10, pp. 1-10, 2020.

[8] X. Dai, Y. Yuan, R. J. Liao, "Experimental Studies of a Novel Anti-Icing Aluminum Conductor with Excellent Durability and Improved Electrical Performance," IEEE Transactions on Power Delivery, Vol. 1, pp. 99, 2023.

Deformation and Fragmentation of an Ice Crystal after an Impact onto a Rigid Substrate

Ilia Roisman[1], Elmar Bonaccurso[2], Jeanette Hussong[1]

[1] *Institute of Fluid Mechanics and Aerodynamics, Technische Universität Darmstadt, Darmstadt 64287, Germany*
[2] *Airbus Group Innovations, Munich 81663, Germany*

roisman@sla.tu-darmstadt.de

Abstract—In this study, the collision of a spherical ice particle on a solid surface is modeled theoretically. An approximate, kinematically admissible flow field in the particle satisfies the continuity equation and the wall impenetrability conditions. The stress field is expressed from the momentum balance in the deforming particle, accounting for the plastic stresses and inertia in the flow. Moreover, this expression accounts for the dependence of the yield strength on the local rate of strain. Next, the failure strain allows us to determine the geometry of the fractured zone in the particle. Its size depends on the time, the particle impact velocity, and initial size.

The theory allows us to predict the collision duration, maximum spreading size, size of the fractured zone, and the size of the maximum crystal fragment. The theory is validated by comparison with the numerous experimental data from the literature.

Keywords—ice crystal, impact, particle deformation, ice accretion, fragmentation

I. Introduction

Impact, deformation and fragmentation of solid particles are determined by their material properties like density, yield strength, fracture toughness, elastic modulus and others. The impact outcome is also determined significantly by the behavior of the material in respect to fragmentation, namely whether it is plastic or brittle.

Several attempts have been made to formulate a universal scaling for the size distribution of the fragments after a particle impact. The log-normal distribution of the fragments has been employed for a random discrete particle fragmentation [1]. Further mathematical developments of these ideas, including the evolution of the distributions of the fragment sizes in time and in space during the fragmentation process, can be found in [2], [3].

The characteristic size of the fragments obtained by a fast deformation of plastic materials can be obtained from the balance of the kinetic energy of the fragment deformation and the energy required for the surface formation [4], [5]

$$\lambda_{\text{Grady}} \sim \left[\frac{K_c^2}{2\rho E \dot{\epsilon}^2} \right]^{1/3}, \qquad (1)$$

where K_c, ρ and E are the fracture toughness, density and elastic modulus of the material, respectively, and $\dot{\epsilon}$ is the strain-rate. An alternative scaling parameter has been provided earlier in [6]

$$\lambda_{\text{Mott}} \sim \left[\frac{Y}{\rho \gamma \dot{\epsilon}^2} \right]^{1/2}, \qquad (2)$$

where Y is the yield stress and γ is a fracture activation parameter.

The probability density of the particle sizes can be well described using chaotic disintegration theory [7] based on the results of percolation theory

$$p(d) = \frac{\chi b^{-(1+\theta)/\chi}}{\Gamma\left[(1+\theta)/\chi\right]} d^\theta \exp[-bd^\chi], \qquad (3)$$

which is analogous to the gamma function or Weibull distribution, depending on the parameters. Here the constants χ and θ, which depend on the probability of the voids in the material, are known form the percolation theory [8], [9].

Such distributions are well suited for the description of the various problems of penetration mechanics, for example for the description of the parameters of the debris cloud formed by an impact and penetration of a kinetic projectile into a metal target [5], [10].

The fragmentation process of brittle materials is governed by different length scales. The distributions of the fragment sizes of brittle materials often described in the literature by a power law [11]. The power law for the distributions of the fragment sizes has been found applicable for the numerous experiments on the impact of brittle particles and computations thereof [12]–[15].

Moreover, it has been shown [11] that the fragmentation of brittle materials is governed by the length scale associated with the balance of the elastic strain energy and the fracture energy, which yields

$$\lambda_{\text{elastic}} \sim \frac{\rho \Upsilon}{\Gamma}, \qquad (4)$$

where Υ is elastic strain energy and Γ is the fracture energy. This scale is a mechanical property of a material and does not depend on the particle impact velocity.

The finite size L of the primary particle is also an important parameter governing the scale $\lambda \sim L$ of the largest fragments [11].

Ice particles are usually considered as a quasi-brittle material [16], [17] for which the effect of a plastic flow is notable.
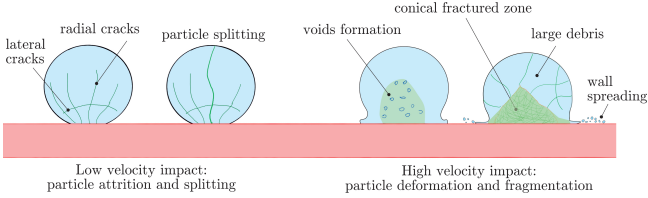
Fig. 1. Sketch of the typical phenomena of brittle particle impact, deformation and fragmentation.

Moreover, it is known that the yield stress Y of ice depends on the local strain-rate of the particle deformation [18]–[24].

Another important parameter characterizing the fragmentation of brittle materials is the failure strain ϵ_f. The failure strain $\epsilon_f \sim 10^{-2}$ of fast unilateral compression of ice has been estimated in experiments [23], [25].

The existence of several length scales and influencing factors makes it difficult to interpret experimental data for the distributions of the fragments sizes and their initial velocities following the impact of a brittle particle. It is important to identify the main physical players for a certain material and for a certain range of the conditions leading to breakup and fragmentation.

Typical phenomena of impact of ice or any brittle particle onto a dry rigid substrate is shown schematically in Fig. 1. At relatively small velocities the impact may cause the generation of radial and lateral cracks [26]. When the crack length [27] is comparable with the particle size, the particle breaks up. Experiments [28] show that the critical impact velocity associated with the particle breakup is proportional to $L^{-2/3}$, which is the result of the particle splitting by a radial crack.

In the case of high velocity particle impact its deformation is significant. Correspondingly, the strains in the neighborhood of the wall are large. As a result of the strong material deformation, at some time an array of voids appears in the deforming particle [29], [30]. These voids then expand and propagate into the particle material as cracks. Finally, all these cracks lead to the formation of the fractured zone of typical nearly conical shape (shown in the sketch in Fig. 1).

Outside the conical fractured zone the particle is fragmented into several large debris whose size is comparable with the particle size, as shown in Fig. 1. Finally, a radial stream of fine particles along the substrate is ejected from the region of the propagating contact line [24], [31].

In this paper the impact of an ice particle onto a solid dry smooth substrate is modeled theoretically. A model based on the theory of particle impact and deformation [32] has been developed, which allows prediction of the shape of the fractured region and the size of the maximum fragment. The aim of the theoretical model is not to accurately compute the distributions of the sizes of the particle fragments but rather to identify the correct length scales governing the process of the ice fragmentation and also to better understand the main mechanisms and characteristic regions of the related phenomena.

II. IMPACT, DEFORMATION AND FRACTURE OF A QUASI-BRITTLE SPHERICAL PARTICLE: A THEORETICAL MODEL

Ice is a semi-brittle material. This means that it behaves like a plastic material if the strains not exceed the failure strain. The model for a flow in a plastic spherical particle impacting onto a dry perfectly rigid smooth substrate has been developed in [32].
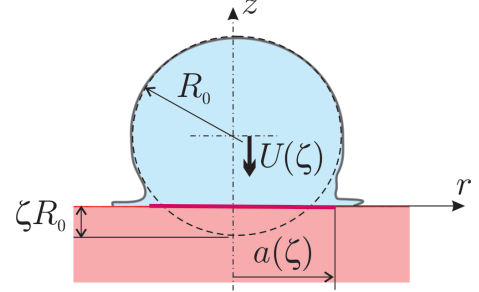
Fig. 2. Shape and kinematics of an impacting particle.

Consider a cylindrical coordinate system $\{r, \theta, z\}$, defined in Fig. 2, and the corresponding unit base vectors $\{\boldsymbol{e}_r, \boldsymbol{e}_\theta, \boldsymbol{e}_z\}$. Consider an initially spherical particle of the radius R_0 impacting onto a rigid substrate $z = 0$ with the impact velocity U_0. The particle dislodging during deformation is denoted ζR_0, where $\zeta(t)$ is a dimensionless particle dislodging. The instantaneous particle dislodging velocity is denoted $U(\zeta)$ and the impression radius is denoted $a(\zeta)$.

The dimensionless particle dislodging $\zeta(t)$ is related to the dislodging velocity as

$$R_0 \frac{\mathrm{d}\zeta}{\mathrm{d}t} = U. \tag{5}$$

A. Kinematics of the flow in the particle

The velocity field in the particle is approximated by a kinematically admissible incompressible irrotational flow associated with the uniform flow around a thin disk of radius a. This known velocity field $\boldsymbol{u}$ is given in the form

$$\boldsymbol{u} = \nabla\phi, \quad \phi = \frac{2aU}{\pi}\cos\eta\left[\sinh\xi\cot^{-1}(\sinh\xi) - 1\right] - Uz, \tag{6}$$

where ϕ is the velocity potential, ξ, η are dimensionless elliptic coordinates defined through

$$\xi + i\eta = \sinh^{-1}\left(\frac{z + ir}{a}\right). \tag{7}$$

Further details of the flow field in the particle can be found in [32].

The rate-of-strain tensor $\boldsymbol{E} = [(\boldsymbol{\nabla}\boldsymbol{u}) + (\boldsymbol{\nabla}\boldsymbol{u})^T]/2$ of the flow in the particle is the symmetric part of the velocity gradient. At the impact axis the expression for the rate-of-strain tensor can be simplified and derived explicitly

$$\boldsymbol{E} = \frac{2a^3 U}{\pi(a^2 + z^2)^2}(\boldsymbol{e}_r \otimes \boldsymbol{e}_r + \boldsymbol{e}_\theta \otimes \boldsymbol{e}_\theta - 2\boldsymbol{e}_z \otimes \boldsymbol{e}_z), \tag{8}$$
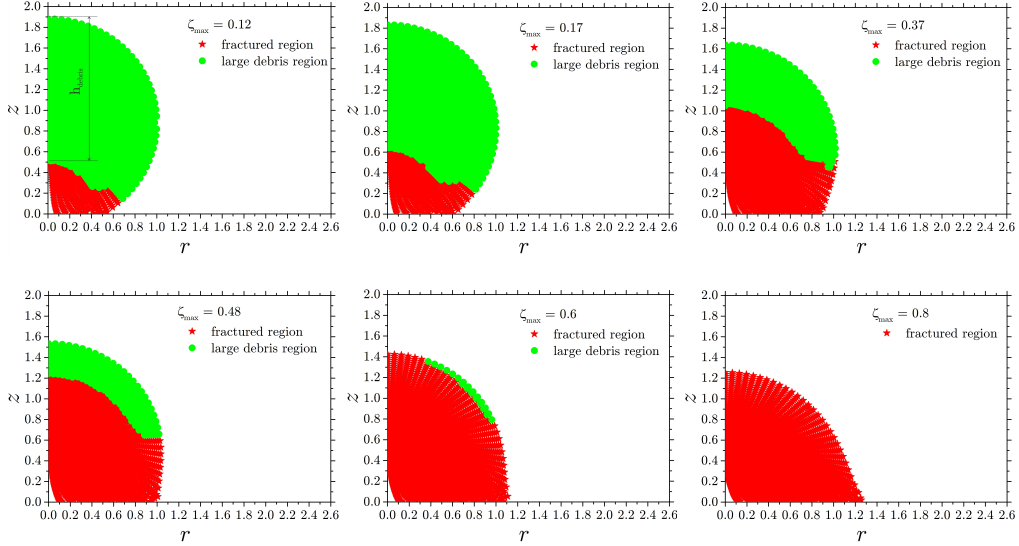
Fig. 3. Theoretical predictions of the particle shape and of the fractured zone determined by the failure strain $\epsilon = 0.025$ for various values of $\zeta_{\max}$. The ejected mass in the radial stream of fragments along the substrate is not considered in the model. The coordinates r and z are dimensionless, scaled by R_0.

where the symbol $\otimes$ denotes the usual tensor product.

Near the impact axis the particle material is compressed in the axial direction and is stretched in the radial direction. The radial stretching may lead to the appearance of voids and lacunae in the particle material. We define a characteristic rate of strain in the form $\dot{\epsilon} \equiv \sqrt{2/3}\sqrt{E_{zz}^2 + E_{zz}^2 + E_{zz}^2}$. This form at the particle axis is equal to the typical compression rate. This definition is a convenient choice, allowing to compare the results with the available data for uniaxial ice compression.

Finally, the typical strain in the particle can be computed in the Lagrangian form using the relation

$$\frac{\mathrm{d}\epsilon}{\mathrm{d}\zeta} = \frac{R_0}{U}\dot{\epsilon} \qquad (9)$$

which must be computed together with the equation of the particle motion

$$\frac{\mathrm{d}\boldsymbol{x}}{\mathrm{d}\boldsymbol{\zeta}} = \frac{R_0\boldsymbol{u}}{U}, \qquad (10)$$

where $\boldsymbol{x}$ is the radius vector of the material point and $\boldsymbol{u}/U$ is its dimensionless velocity.

In Fig. 3, the particle shapes are shown for various values of the dimensionless particle dislodging ζ. Moreover, the fractured region in the particle is determined by the material points at which the strain ϵ exceeds the failure strain. The measurements of the failure strain ϵ_f during the uniaxial compression of ice has been estimated in [23] for the range $0.005 < \epsilon_f < 0.05$. It almost does not depend on the strain rate but only on the sample size. In this study the mean value $\epsilon_f = 0.025$ has been chosen to estimate the shape of the fractured region and to estimate the size of the large particle debris.

B. Solution for the particle maximum deformation

The momentum balance equation accounts for the stresses associated with the inertial effects in the flow of the deforming particle and the plastic effects, characterized by the yield strength Y. The solution of the momentum balance equation yields [32] a system of the ordinary differential equations for the evolution of the particle velocity in time. The theory allows to predict the maximum value of the dimensionless particle deformation $\zeta_{\max}$. The value of $\zeta_{\max}$ depends on the initial particle diameter D_0 and impact velocity U_0. For engineering purposes, for example, for the computation of multiple impact of a cloud of polydisperse ice crystals leading to ice accretion, it is convenient to provide a correlation function for $\zeta_{\max}$. Computations [32] show that for the diameters $D_0 < 1$ mm, the value of $\zeta_{\max}$ is influenced mainly by the impact velocity and the effect of D_0 is negligibly small. The fit of the computations for $\zeta_{\max}$ yields

$$\zeta_{\max} \approx \left(0.58 + \left[\frac{D_0}{\delta}\right]^{0.77}\right)\left(\exp\left[\frac{U_0}{V}\right] - 1\right), \qquad (11)$$

where $\delta = 215$ mm and $V = 250$ m/s are the fitting parameters. The fitting is valid for $D_0 < 30$ mm and $U_0 < 160$ m/s.

III. SIZE OF THE PARTICLE FRAGMENTS

Fragments of the particle include the relatively large debris of size comparable with the initial particle diameter, and the fine particles, generated mainly in the fractured zone but in the debris region as well. This is why the distribution of the debris fragments and fine fragments have to be treated separately.

The experimental data for the maximum fragment size D_f scaled by the initial particle size D_0 is shown in Fig. 4 as a function of the theoretically predicted values of $\zeta_{\max}$.
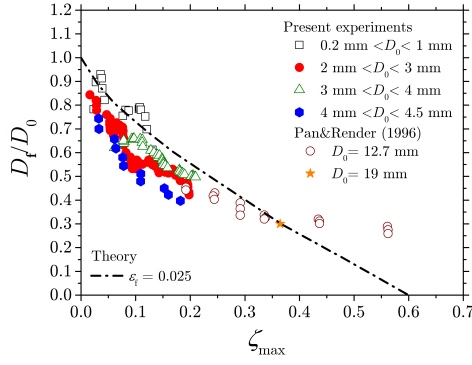
Fig. 4. Experimental data [33]–[35] for the maximum size of the ice particle fragment in comparison with the theoretical prediction for h_{debris}/D_0 with the failure strain $\epsilon_f = 0.025$. The particle shape before impact is nearly spherical. The data are smoothed using the moving average calculation.
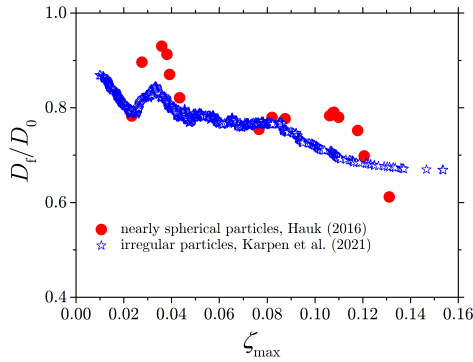
Fig. 5. Experimental data for the dimensionless size of the maximum fragment for sub-millimeter particles. Comparison of D_f/D_0 for the nearly spherical particles (the measurement results by Hauk (2016) obtained in the framework of the study [36]) and for irregular particles [37]. The data are smoothed using the moving average calculation.

A moving average is used to better quantify the correlation between the fragment sizes and ζ_{max}.

Additionally the height h_{debris} at the impact axis has been determined from the computations, as shown in Fig. 3. The values of D_f are comparable with h_{debris} for the range of the impact parameters corresponding to $\zeta_{\mathrm{max}} < 0.4$. This result indicates that in the range of parameters the large debris region break up by radial cracks, as shown in Fig. 1. For larger values of the maximum dimensionless particle dislodging $\zeta_{\mathrm{max}} > 0.4$ the maximum size of a fragment is not determined by the height of the large debris region. This is well illustrated in Fig. 3 for $\zeta_{\mathrm{max}} > 0.6$.

Moreover, in the range $\zeta_{\mathrm{max}} \gg 0.6$ the particle is fragmented completely (see Fig. 3 for $\zeta_{\mathrm{max}} > 0.8$). In these cases the maximum fragment size is determined by the physics of fragmentation of the material in the fractured region.

In Fig. 5 the experimental data for D_f/D_0 for nearly spherical particles are compared with the data for irregular particles [34]. The data are smoothed using the moving
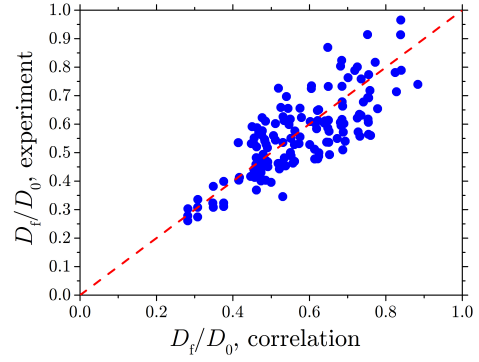
Fig. 6. Experimental data for the dimensionless size of the maximum fragment D_f/D_0 as a function of the empirical correlation (12). The dashed line corresponds to perfect agreement.

average calculation. Both data sets agree rather well, despite the fact that they have been obtained by different groups in the iCORE facility.

For the purposes of engineering approximation we provide here an empirical correlation for the maximum fragment size in the form

$$D_f/D_0 \approx 0.26 + 0.69 \exp\left(-6.11\zeta_{\mathrm{max}}\right), \quad \zeta_{\mathrm{max}} < 0.6, \quad (12)$$

where for the given particle diameter D_0 and impact velocity U_0 the value of ζ_{max} can be computed using the correlation (11) or obtained from the numerical solution of the equations for particle deformation. Certainly, this correlation is valid only for impact velocities exceeding the threshold velocity of particle breakup [28].

In Fig. 6 the experimental data for the dimensionless size of the maximum fragment, D_f/D_0, are compared with the empirical correlation (12). The dashed line corresponds to the perfect agreement. It should be noted that the scatter of the data is not a result of the low model precision. This scatter is physical, since the value of D_f can significantly vary for the same impact parameters.

IV. CONCLUSIONS

An approximate theoretical model [32] for the deformation of a spherical ice particle has been applied for the description of particle fragmentation. It has been further used for the estimation of the effective strain in the particle for various values of the dimensionless dislodging ζ. Next, the condition for a constant failure strain, typical of brittle materials and ice, has been applied for the description of the boundary between the fractured region in the particle and the outer region of large particle debris. The fractured zone has been observed in numerous experiments from the literature as a conical region with fine fragments.

Next, we have found that the dimensionless size of the largest fragment D_f, scaled by the initial particle size D_0, correlates rather well with the dimensionless particle dislodging ζ_{max}. This result confirms our assumption that the value

of the failure strain influences significantly the distribution of the particle fragmentation. This result is valid also for the fragmentation of larger ice spheres of sizes up to 19 mm, characterized in [35]. Moreover, in the range $\zeta_{\max} < 0$ the values of D_f/D_0 are comparable with the theoretically predicted height of the region of large particle debris.

Finally, a correlation for the value of the maximum fragment size D_f is proposed, which can be used for an engineering description of impacts of a cloud of polydisperse ice particles, relevant to the modeling of the ice accretion due to the ice crystal impact [38]–[40].

References

[1] A. N. Kolmogorov, "On the log-normal distribution of particles sizes during breakup process," *Dokl. Akad. Nauk. SSSR*, vol. 31, pp. 99–101, 1941.

[2] V. V. Yanovsky, A. V. Tur, and O. V. Kuklina, "Universal elements of fragmentation," *J. Exp. Theor. Phys.*, vol. 110, pp. 863–876, May 2010.

[3] M. Gorokhovski and M. Herrmann, "Modeling primary atomization," *Annu. Rev. Fluid Mech.*, vol. 40, pp. 343–366, 2008.

[4] D. Grady, "Local inertial effects in dynamic fragmentation," *Journal of Applied Physics*, vol. 53, no. 1, pp. 322–325, 1982.

[5] A. Yarin, I. Roisman, K. Weber, and V. Hohler, "Model for ballistic fragmentation and behind-armor debris," *International Journal of Impact Engineering*, vol. 24, no. 2, pp. 171–201, 2000.

[6] N. F. Mott, "Fragmentation of shell cases," *Proceedings of the Royal Society of London. Series A. Mathematical and physical sciences*, vol. 189, no. 1018, pp. 300–308, 1947.

[7] A. L. Yarin, *Free liquid jets and films: hydrodynamics and rheology*. Longman Publishing Group, 1993.

[8] D. Stauffer, "Scaling theory of percolation clusters," *Physics reports*, vol. 54, no. 1, pp. 1–74, 1979.

[9] D. Stauffer, *Introduction to percolation theory*. London: Taylor & Francis, 1985.

[10] A. L. Yarin, I. V. Roisman, and C. Tropea, *Collision phenomena in liquids and solids*. Cambridge University Press, 2017.

[11] D. Grady, "Fragment size distributions from the dynamic fragmentation of brittle solids," *I. J. Impact Eng.*, vol. 35, pp. 1557–1562, Dec. 2008.

[12] J. J. Gilvarry and B. H. Bergstrom, "Fracture of Brittle Solids. II. Distribution Function for Fragment Size in Single Fracture (Experimental)," *Journal of Applied Physics*, vol. 32, pp. 400–410, Mar. 1961.

[13] J. J. Gilvarry and B. H. Bergstrom, "Fracture of Brittle Solids. III. Experimental Results on the Distribution of Fragment Size in Single Fracture," *Journal of Applied Physics*, vol. 33, pp. 3211–3213, Nov. 1962.

[14] S. Wu, K. Chau, and T. Yu, "Crushing and fragmentation of brittle spheres under double impact test," *Powder Technology*, vol. 143-144, pp. 41–55, June 2004.

[15] G. Ma, Y. Zhang, W. Zhou, T.-T. Ng, Q. Wang, and X. Chen, "The effect of different fracture mechanisms on impact fragmentation of brittle heterogeneous solid," *International Journal of Impact Engineering*, vol. 113, pp. 132–143, 2018.

[16] M. Jirásek and Z. P. Bažant, "Particle model for quasibrittle fracture and application to sea ice," *Journal of engineering mechanics*, vol. 121, no. 9, pp. 1016–1025, 1995.

[17] Z. P. Bažant, "Scaling of dislocation-based strain-gradient plasticity," *Journal of the Mechanics and Physics of Solids*, vol. 50, no. 3, pp. 435–448, 2002.

[18] H. Kim and J. N. Keune, "Compressive strength of ice at impact strain rates," *Journal of materials science*, vol. 42, no. 8, pp. 2802–2806, 2007.

[19] S. J. Jones, "High strain-rate compression tests on ice," *The Journal of Physical Chemistry B*, vol. 101, no. 32, pp. 6099–6101, 1997.

[20] G. A. Kuehn, E. M. Schulson, D. E. Jones, and J. Zhang, "The compressive strength of ice cubes of different sizes," *ASME. J. Offshore Mech. Arct. Eng.*, vol. 115, no. 2, p. 142–148, 1993.

[21] L.-T. Shen, S.-D. Zhao, X.-N. Lu, and Y.-X. Shi, "Effects of temperature and strain rate on uniaxial compressive strength of naturally formed fresh-water ice," in *Proceedings of the seventh international conference on offshore mechanics and Arctic engineering*, (New York), p. 19–23, ASME, 1988.

[22] M. Mellor and D. M. Cole, "Deformation and failure of ice under constant stress or constant strain-rate," *Cold Regions Science and Technology*, vol. 5, no. 3, pp. 201–219, 1982.

[23] M. Shazly, V. Prakash, and B. A. Lerch, "High strain-rate behavior of ice under uniaxial compression," *International Journal of Solids and Structures*, vol. 46, no. 6, pp. 1499–1515, 2009.

[24] J. D. Tippmann, H. Kim, and J. D. Rhymer, "Experimentally validated strain rate dependent material model for spherical ice impact simulation," *International Journal of Impact Engineering*, vol. 57, pp. 43–54, 2013.

[25] M. Mellor and D. M. Cole, "Stress/strain/time relations for ice under uniaxial compression," *Cold Regions Science and Technology*, vol. 6, no. 3, pp. 207–230, 1983.

[26] I. Roisman and C. Tropea, "Impact of a crushing ice particle onto a dry solid wall," *Proceedings of the Royal Society A: Mathematical, Physical and Engineering Sciences*, vol. 471, no. 2183, p. 20150525, 2015.

[27] M. Ghadiri and Z. Zhang, "Impact attrition of particulate solids. part 1: A theoretical model of chipping," *Chemical Engineering Science*, vol. 57, no. 17, pp. 3659–3669, 2002.

[28] T. Hauk, E. Bonaccurso, I. Roisman, and C. Tropea, "Ice crystal impact onto a dry solid wall. particle fragmentation," *Proceedings of the Royal Society A: Mathematical, Physical and Engineering Sciences*, vol. 471, no. 2181, p. 20150399, 2015.

[29] F. Kun and H. J. Herrmann, "Transition from damage to fragmentation in collision of solids," *Phys. Rev. E*, vol. 59, pp. 2623–2632, Mar. 1999.

[30] H. A. Carmona, F. K. Wittel, F. Kun, and H. J. Herrmann, "Fragmentation processes in impact of spheres," *Phys. Rev. E*, vol. 77, p. 051302, May 2008.

[31] J. D. Rhymer, *Force criterion prediction of damage for carbon/epoxy composite panels impacted by high velocity ice*. University of California, San Diego, 2012.

[32] I. V. Roisman, "Hydrodynamic model of a collision of a spherical plastic ice particle with a perfectly rigid substrate," *I. J. Impact Eng.*, vol. 159, p. 104019, 2021.

[33] L. M. Reitter, M. Schremb, H. Lohmann, I. Roisman, J. Hussong, and C. Tropea, "MUSIC-haic_WP1_t11_tuda_01_ParticleImpactOnRigidColdSurface," Oct. 2021.

[34] N. Karpen, A. Cuco, D. Kuenstler, and E. Bonaccurso, "MUSIC-haic_WP1_T11_ACRT_01_ParticleImpactOnRigidSurface," Oct. 2021.

[35] H. Pan and P. Render, "Impact characteristics of hailstones simulating ingestion by turbofan aeroengines," *Journal of Propulsion and Power*, vol. 12, no. 3, pp. 457–462, 1996.

[36] T. Hauk, *Investigation of the impact and melting process of ice particles*. Phd thesis, Technische Universität Darmstadt, Darmstadt, Germany, 2016.

[37] N. Karpen, A. Cuco, D. Kuenstler, E. Bonaccurso, L. M. Reitter, I. V. Roisman, and C. Tropea, "Characterizing microscopic ice particle impacts onto a rigid surface: Wind tunnel setup and analysis," in *AIAA AVIATION 2021 FORUM*, p. 2671, 2021.

[38] D. Knezevici, D. Fuleki, T. Currie, and J. MacLeod, "Particle size effects on ice crystal accretion," in *4th AIAA Atmospheric and Space Environments Conference*, p. 3039, 2012.

[39] D. Kintea, I. Roisman, and C. Tropea, "Transport processes in a wet granular ice layer: Model for ice accretion and shedding," *International Journal of Heat and Mass Transfer*, vol. 97, pp. 461–472, 2016.

[40] P. Trontin and P. Villedieu, "A comprehensive accretion model for glaciated icing conditions," *International Journal of Multiphase Flow*, vol. 108, pp. 105–123, 2018.

Validation of ICE-T for icing forecasts for aircraft campaigns

Bjørg Jenny Kokkvoll Engdahl[1]

[1] *Norwegian Meteorological Institute, Norway*

bjorgjke@met.no

Abstract— **Atmospheric icing on aircraft is a major hazard for the aviation industry, and a challenge for weather services world wide to forecast correctly. A new modified cloud microphysics scheme, ICE-T, has been implemented into the MET-Norway operational weather forecast model HARMONIE-AROME, in order to better represent supercooled liquid water and hence forecasts of atmospheric icing. In April 2023 an aircraft measurement campaign was launched in Northern-Norway in order to test helicopter ability to fly through icing conditions. Simulations with both ICE-T and the default microphysics scheme, DEF, were carried out. The results from the simulations showed generally higher amounts of cloud liquid water (CLW) with ICE-T than DEF, yet both simulations seem to underestimate CLW for both days.**

Keywords— *numerical weather prediction, icing on aircraft, microphysics scheme, cloud liquid water content*

I. Introduction

Atmospheric icing on aircraft remains a major hazard for the aviation industry. Supercooled liquid droplets may freeze upon contact with aircraft and accumulate enough ice to change the aerodynamic flow around the structure and suppress lift. Many commercial aircraft have heated wings and instruments to avoid ice accretion, but smaller aircraft and unmanned aerial vehicles, which is a growing industry, often have insufficient equipment to sustain heavy icing. Hence, forecasting atmospheric icing is an important task for weather agencies world wide.

However, forecasting atmospheric icing is not a trivial task. Due to the complexity of clouds and their numerous physical internal processes, weather forecasting models struggle to represent supercooled liquid in an adequate way. The part of a numerical weather prediction (NWP) model responsible for the generation, evolution, and dissipation of clouds and supercooled liquid water, is called a microphysics scheme. Over the years, numerous different microphysics schemes have been developed, ranging from very simple schemes with only a few hydrometeor categories to sophisticated schemes with prognostic calculations of many different hydrometeor categories, processes and properties.

Many microphysics schemes have a tendency to produce ice hydrometeors at the expense of supercooled liquid water, often due to a too active Wegener-Bergeron-Findeisen effect, or too efficient collection-accretion of liquid water by solid hydrometeors. The HARMONIE-AROME NWP model ([1]) is the basis for the operational forecasting at many European weather agencies, including MET-Norway ([5]). Previous studies have found that HARMONIE-AROME also tends to glaciate the clouds prematurely. In order to remedy this model deficiency, Engdahl et al. 2020a[2] implemented elements from the Thompson ([6]) microphysics scheme into HARMONIE-AROME. The updated microphysics scheme, called ICE-T, has been validated both for ice loads on transmission lines ([3]) and atmospheric icing on aircraft, and satellite estimates of liquid- and ice-water content ([4]). Both studies have found that ICE-T produces more realistic amounts of supercooled liquid water. However, validation against in-situ measurements of cloud properties has not been carried out.

Recently, several aircraft campaigns have been launched in the Norwegian north territory. These campaigns provide unique observations for validation of microphysical properties. In the current study, ICE-T is validated against in-situ measurements of cloud liquid- and ice water content for the Airbus helicopter icing campaign in the vicinity of Alta. We will see how ICE-T performs in two very different weather situations.

II. Alta campaign

The Alta helicopter campaign was launched by Airbus in April 2023. The goal was to test the H175 helicopter's ability to fly through heavy icing conditions. The helicopter was equipped with instruments for measurements of in-cloud liquid water content, namely a cloud droplet probe (CDP). The CDP measures cloud particles in the range of 2 - 50um in diameter, which covers most of the droplet size distribution, while ice particles are usually larger. Therefore we can assume that the particles measured by the CDP are mainly liquid.

Several flights were carried out on April 18th and 19th (see Figure 1). During the afternoon of April 18 the wind in the Alta region was mainly westerly, with a frontal passage and some light rain. The operational forecast showed light to moderate icing in the area, however, only trace and light icing were observed. The CLW content was measured to be 0.4g/m³ at the most.

The next day, April 19, the weather had shifted to strong westerly winds, which lead to mountain waves and lenticularis clouds with high amounts of supercooled liquid. Two different flights were carried out, one in the morning and in the afternoon. The morning flight experienced heavy icing, with large pieces of ice attached to the helicopter after landing. Unfortunately, the CDP stopped working during the flight, so the highest amounts of supercooled liquid were not recorded. The weather conditions were similar in the afternoon, and this time the CDP worked throughout the flight. Once again the helicopter experienced heavy icing, and the CDP recorded liquid water content as high as 1.3g/m³. Large chunks of ice fell off the helicopter after landing. The operational forecast

only had moderate icing, while this was a clear case of severe icing. For this study we will focus on the afternoon flights both days.

III. SIMULATIONS

Two parallel simulations were carried out, one with the default ICE3 and OCND2 setup, while the other had the ICE-T microphysics active. Otherwise the configurations of the two simulations were the same and similar to the default setup. A detailed description of the modifications in the ICE-T scheme is found in Engdahl et al. 2020a, but some of the key differences include stricter conditions for ice nucleation, reduced efficiencies of solid hydrometeors collecting liquid hydrometeors, and a variable rain intercept parameter allowing for smaller raindrops. The cy46h1 version of HARMONIE-AROME was used, with a domain similar to the operational AROME-Arctic areas, covering northern parts of Scandinavia, Svalbard and the Barents Sea. No upper-air data assimilation was used in order to let the microphysics evolve undisturbed. Separate simulations were run for both days, starting at 0000UTC and running for 36h each, only hours after +12h were used, to allow for model spin-up.

IV. RESULTS

A. Cloud liquid water content at flight level

For the afternoon flight on April 18th, the simulations show relatively low values of liquid water content in the area of interest. Figure 2 shows the cloud liquid water content in the Alta region at model level 34, corresponding to ~700hPa and the approximate flight level for most of the flight. The simulated cloud liquid is mostly around 0.2 - 0.4g/m³ for both simulations, which is similar to the highest observed peaks. The ICE-T simulation has somewhat higher amounts of cloud liquid than DEF, yet the difference plot shows areas where DEF clearly has more CLW as well. This could mean that some of the difference is due to displacement in locations of the areas with the most CLW, rather than a general increase with ICE-T. This is confirmed by the domain average difference in CLW, which is only 0.002 g/m³.

The results from the next day, on the afternoon of April 19th, show a clear increase in cloud liquid water content with ICE-T active. The flight level was lower on that day, mostly at around 830hPa. Figure 3 shows cloud liquid water mass at model level 41 (~830hPa) for DEF and ICE-T and the difference between them. This is the approximate height the helicopter flew in and detected high contents of liquid water content. In contrast to the April 18th simulations, the clouds have a similar geographical distribution in both simulations, yet there is clearly more in ICE-T, and the differences are largest where the CLW content is highest. The differences are mostly between 0.1-0.2g/m³, but occasionally as high as 0.3g/m³. The absolute values are close to 1g/m³ in the areas with the highest CLW. The mean difference between the two simulations is 0.016 g/m³ for the entire domain.

B. Cross sections

Cross sections were made for both flights. The cross sections for each flight are shown in figure 1, marked with red lines. For the April 18 flight a cross section stretching from approximately Akkarfjord on Sørøya to Langfjorden outside of Alta. The vertical distribution of cloud liquid water for both

simulations is shown in figure 4. The distribution is similar between the two simulations with an exception of the location of the maximum cloud liquid water which is at slightly higher altitudes for ICE-T. There are only minor differences between the two plots, which can be explained by displacement in locations, and the total difference is small.

For the April 19th flight a cross section stretching from approximately Kvalsund to Alta was made following the red line in fig 2b. Although the cross section does not follow the flight track entirely, the variation in LWC over the area should be representative. The liquid water content of the cross section is shown in figure 3 for DEF, ICE-T, and the difference, respectively. As with the horizontal distribution, the LWC in the cross section is generally higher for ICE-T than DEF. Perhaps more interesting is that the differences are not largest where the highest amounts of LWC are found.

C. Comparison with observed LWC

Direct comparison (time and place) of observed and simulated cloud liquid water content is difficult due to differences in placement of the clouds. Instead, the frequency of observed and simulated CLWC is plotted in histograms in figures 6 (April 18th) and 7 (April 19th). The histograms of simulated values contains all values in an area of 20 grid boxes in each direction of Alta in the 5 model levels closest to the main flight levels (levels 32-36 for April 18th and levels 39-43 for April 19th). Both the observed and simulated values are filtered for values lower than 0.005g/m³ (common threshold for cloud/no-cloud). Keep in mind that the CDP has a much higher spatial and temporal resolution, and will therefore normally capture higher values than the simulations that give an average value over a 2.5x2.5km² grid box with hourly output.

There was relatively little CLWC observed on April 18th, so the distribution is skewed towards lower values, with the bulk being lower than 0.1g/m³. The values are even lower for the simulations, with few occurrences above 0.1 g/m³. The slightly higher values in ICE-T can be a benefit as the observations are generally higher.

The observed values from the afternoon flight of April 19th, tell a very different story compared to April 18th. Here, the bulk observations of cloud liquid water ranges from 0.6-1g/m³, with a peak between 0.7-0.8g/m³, which must be regarded as high and would give severe icing in the area. There are also quite a number of observed values above 1g/m³. Yet, again the simulated values of cloud liquid water is far lower than the observed, and the shape of the distributions do not match the observed, with a skew towards lower values. Only ICE-T has a small peak around 0.4g/m³, and has a handful of values above 0.8g/m³ which are not seen in DEF. The increased values in ICE-T compared to DEF, are more prominent in the April 19th simulation, yet remain far lower than the observed values. The title must use a font-size of 24 pt and be centred in a single column. It must present each word capitalized, except for connecting words.

V. CONCLUSIONS

In this study, simulations with a modified microphysics scheme, ICE-T, are compared with the default microphysics scheme, DEF, and measured values cloud liquid water, for

two different weather situations during a helicopter icing campaign around Alta, Norway. The first flight was carried out on April 18th 2023 and showed relatively low values of around 0.2-0.4g/m³, while the other was carried out the next day with high amounts of cloud liquid water and severe icing. The results from the simulations showed generally higher amounts of cloud liquid water with ICE-T than DEF, yet both simulations seem to underestimate CLW for both days. However, the differences between the simulations are larger on the second day, when heavy icing was experienced. This could indicate that ICE-T leads to higher values of CLW when it matters most, while not exaggerating in cases with lower amounts. However, more cases are needed in order to conclude on this, and it should be pointed out that both simulations were far away from the actual observed values.

REFERENCES

[1] L.Bengtsson, and co-authors, "The HARMONIE–AROME model configuration in the ALADIN–HIRLAM NWP system. " Mon. Wea. Rev., 145, 1919–1935, 2017

[2] B.J.K, Engdahl, G.Thompson, and L. Bengtsson, "Improving the representation of supercooled liquid water in the HARMONIE-AROME weather forecast model." Tellus, 72A, 1–18, 2020a

[3] B.J.K. Engdahl, B. E. K. Nygaard, V. Losnedal, G. Thompson, and L. Bengtsson, "Effects of the ICE-T microphysics scheme in HARMONIE-AROME on estimated ice loads on transmission lines." *Cold Reg. Sci. Technol.*,**179**,103139, 2020b

[4] B.J.K. Engdahl, T. Carlsen, M. Køltzow, and T. Storelvmo, "The Ability of the ICE-T Microphysics Scheme in HARMONIE-AROME to Predict Aircraft Icing."*Wea. Forecasting*,37, 205–217, 2022

[5] M.Müller, and co-authors, "AROME-MetCoOp: A Nordic convective-scale operational weather prediction model. " *Wea. Forecasting, 32, 609–627, 2017*

[6] G. Thompson, P. R. Field, R. M. Rasmussen, and W. D. Hall, "Explicit forecasts of winter precipitation using an improved bulk microphysics scheme. Part II: Implementation of a new snow parameterization." *Mon. Wea. Rev., 136, 5095–5115, 2008*
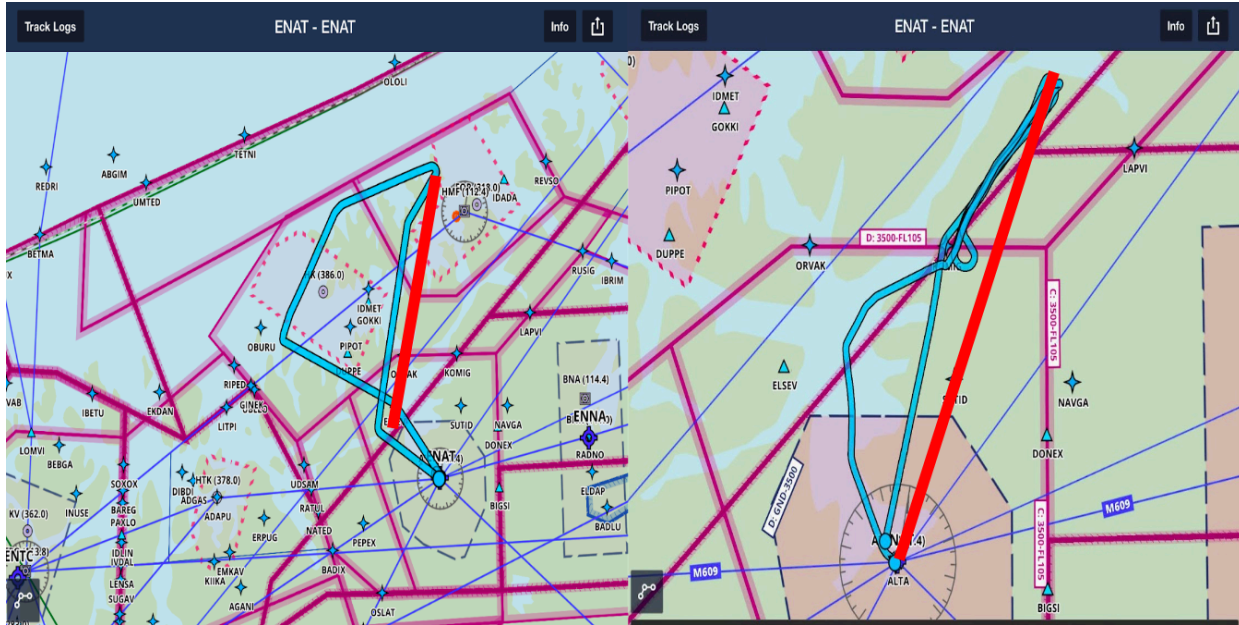
Figure 1: Flight tracks for the afternoon flights on April 18th (left) and April 19th (right). Flight tracks indicated by blue lines. Red lines mark the cross sections used in Figures 4 and 5.
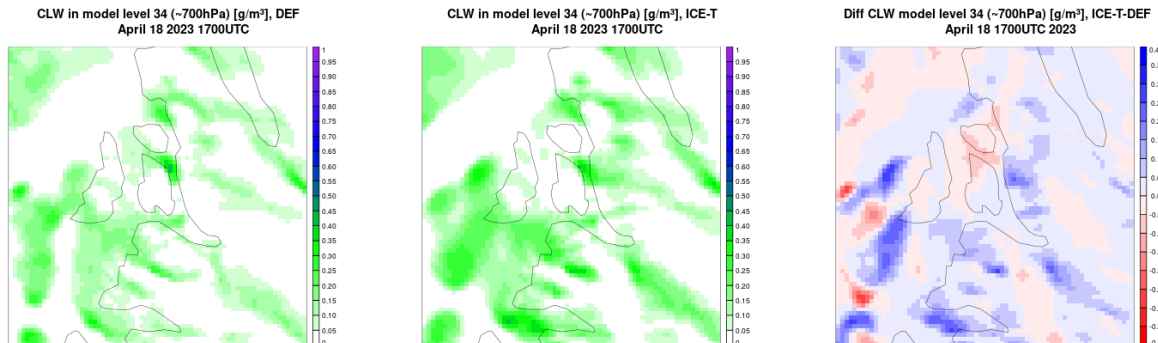
Figure 2: Cloud liquid water content over the Alta region in model level 34 (approx. 700hPa) for DEF, ICE-T and difference for April 18 1700 UTC.
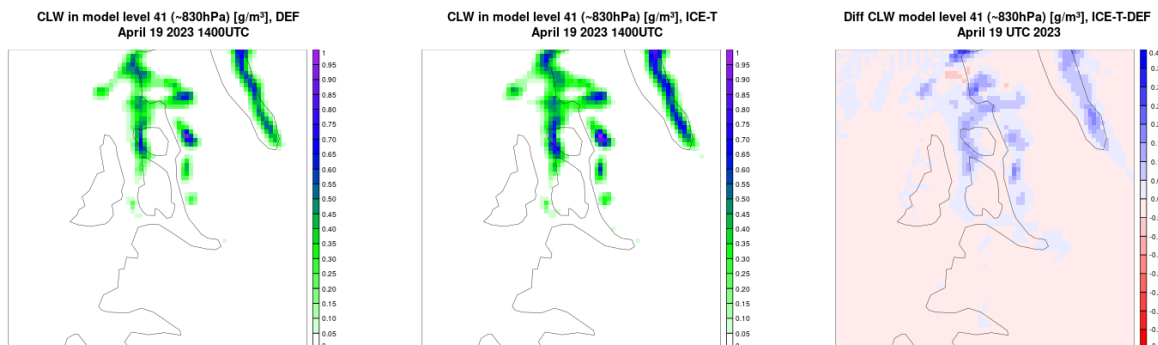
Figure 3: LWC over the Alta region in model level 40 (approx. 820hPa) for DEF, ICE-T and difference for April 19 1400 UTC.
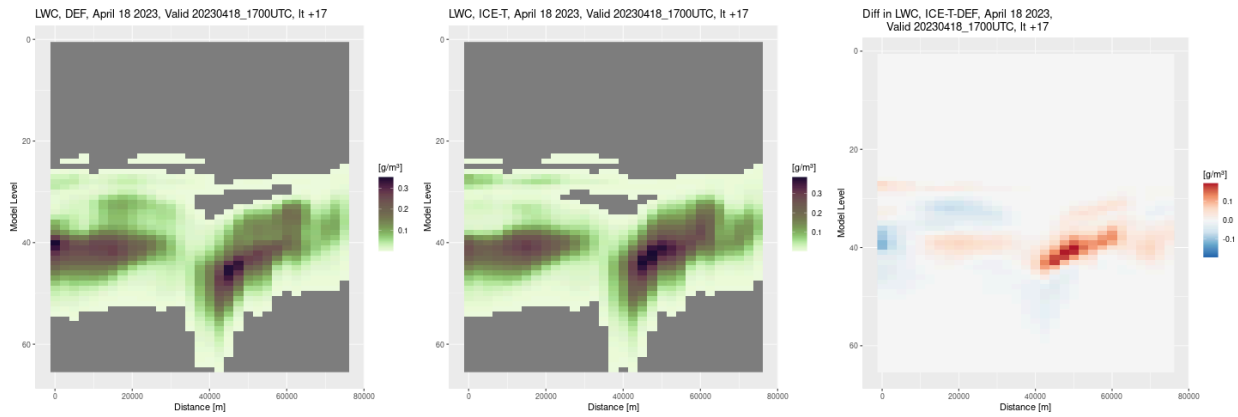
Figure 4: Cross sections of LWC on April 18 at 1700UTC for DEF, ICE-T and the difference between the two simulations.
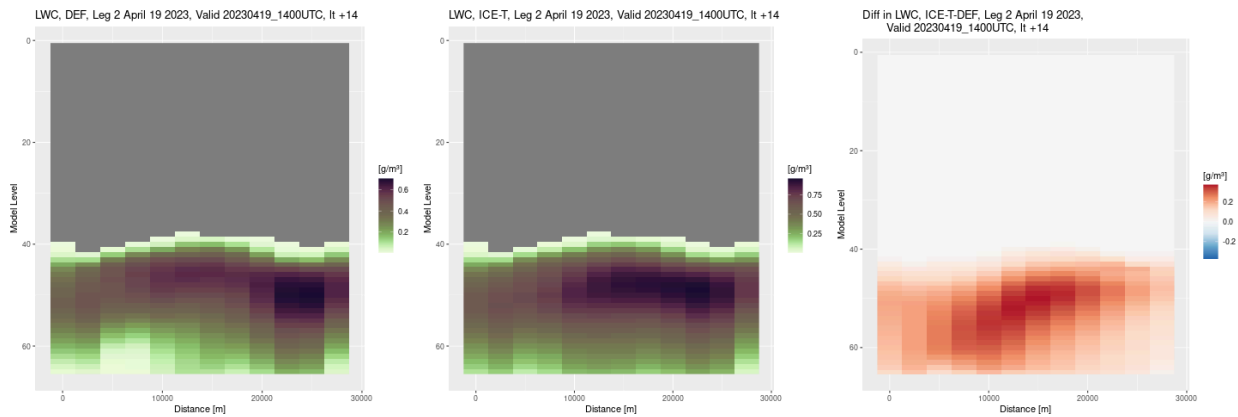
Figure 5: Cross sections of LWC on April 19 at 1400UTC for DEF, ICE-T and the difference between the two simulations.
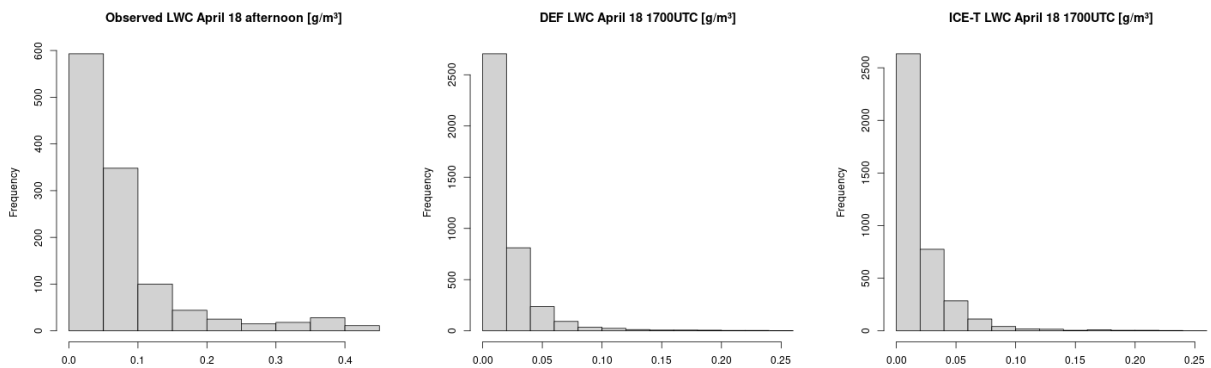
Figure 6: Histograms of observed CLWC (left) and simulated with default microphysics, DEF (middle), and ICE-T (right) for the afternoon flight on April 18th.
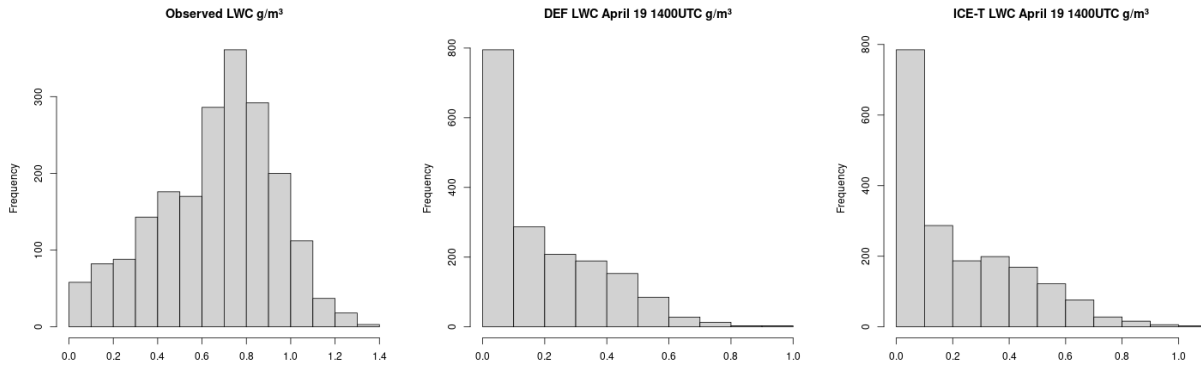
Figure 7: Histograms of observed CLWC (left) and simulated with default microphysics, DEF (middle), and ICE-T (right) for the afternoon flight on April 19th.

Numerical Simulation of Snow Accretion of Power Lines with Different Countermeasures for a January 2022 Event at Kushiro Test Line

Yuki Okazaki[1], Hisato Matsumiya[1,2]

[1] *Central Research Institute of Electric Power Industry (CRIEPI), Japan*
[2] *Department of Civil and Earth Resources Engineering, Kyoto University, Japan*

okazaki3940@criepi.denken.or.jp

Abstract— **In winter, excessive snow accretion on power lines can cause extensive damage to power transmission facilities. Thus, appropriate countermeasures are required to reduce snow accretion. Numerical simulation is an effective method to verify countermeasures against rare large-scale snow events that are seldom observed. This study presents the results of a replicated analysis of snow accretion on a wet snow event that occurred at the Kushiro test line in Japan in January 2022, using SNOVAL, a simulation code developed at the Central Research Institute of Electric Power Industry. To validate the precision of SNOVAL, the amount of snow accretion and rotation angle of various simplified conductors were calculated based on meteorological data from the Kushiro test line during this specific period. The simulation analysis successfully replicated the variations in the maximum snow accretion by approximately fourfold. The accretion shape and mass water content at the time when the snow accretion dropped from the transmission line were evaluated, revealing that the mass water content depended on the accretion shape. For the simplified conductors with low torsional stiffness, the snow landing shape developed into a cylindrical shape covering the entire circumference of the wire, and the mass water content exceeded 40% at the time of dropout. However, when the torsional stiffness was increased, the cross-sectional shape of snow accretion became flat and tended to reach a mass water content of approximately 20% owing to the large eccentric moment and small adhesion area. In addition, the same tendency was observed in the results for full-scale conductors, and it was concluded that the dropout property was affected by the shape of snow accretion owing to the torsional stiffness of the wire.**

Keywords—*countermeasures, field observations, numerical simulation, overhead transmission lines, wet snow accretion*

I. INTRODUCTION

Excessive snow accretion on power lines during winter can cause serious damage to power transmission facilities. Therefore, countermeasures are required to reduce the amount of snow on cables. To verify the effectiveness of various countermeasures, we developed SNOVAL [1], a simulation code for snow accretion on conductors, in addition to the full-scale observations of the Kushiro test line [2]. SNOVAL considers water content, falling speed of snowflakes, melting of snow accretion, and torsion of conductors. However, few large-scale snowfall observations have been made, and the accuracy of SNOVAL has not been verified. In this study, SNOVAL was used to reproduce a mid-wind and wet snow event that occurred on January 11 and 12, 2022 on the Kushiro test line. To understand the details of snow accretion events, we evaluated the accreted snow shape, mass water content, and characteristics of the snow body at the time of dropout.
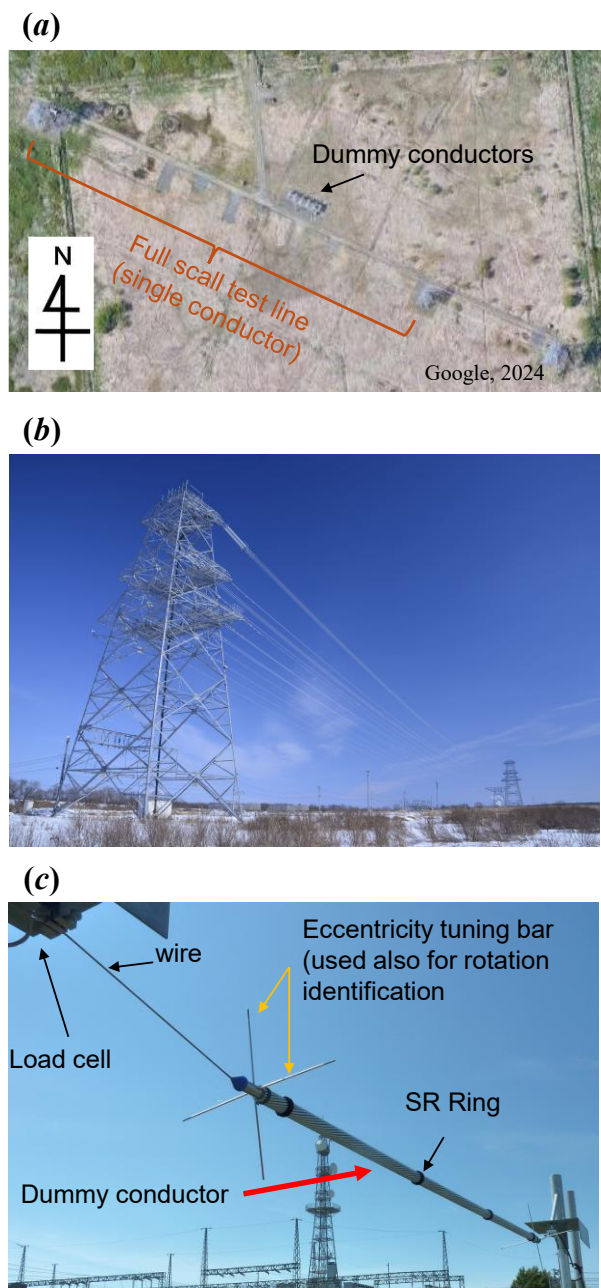
Fig. 1 Overview of the Kushiro test line: (*a*) satellite view, (*b*) full-scale test line, (*c*) dummy conductor.

The rest of this paper is organized as follows. Section 2 presents explanations of SNOVAL and the meteorological conditions of a large-scale event on the Kushiro test line on January 2022. Section 3 verifies SNOVAL and demonstrates the characteristics of accreted snow on short dummy conductors at the time of dropout. Section 4 presents the results of a replicated analysis of snow accretion and dropout situations for a full-scale conductor.

II. TARGET EVENT AND SIMULATION OVERVIEW

A. Wet-type event on the Kushiro test line in January 2022

The Kushiro test line is a full-scale test site located in eastern Hokkaido, Japan (Fig. 1). As Fig. 1(a, b) shows, a full-scale conductor (293 m in length) was installed in the west–northwest to east–southeast direction to evaluate the effectiveness of snow resistance (SR) rings and counterweights (CW), which are widely used in Japan for snow damage prevention. Various 2 m-long dummy conductors (i.e., supported wires whose torsional stiffness is replicated at the center of a full-scale conductor) (Fig. 1(c)), were installed to compare the effectiveness of different combinations of countermeasures. On January 11 and 12, 2022, a wet snow event occurred and resulted in the maximum snow accretion of 1.4 kg/m on a single ACSR240 conductor during a long period of precipitation in a positive temperature range < 1 °C. Figure 2 shows the meteorological data at 11 m above the ground. In this case, continuous snowfall in the subzero temperature range from approximately 18:00 on January 11 was observed, with positive temperatures from 22:30, followed by prolonged snowfall at temperatures below +1 °C and 98% relative humidity until 06:00. The wind speed gradually increased from 4 to 8 m/s.

B. Outline of simulation code: SNOVAL

SNOVAL treats a conductor as a smooth cylinder and calculates the snow thickness on a differential grid of the wire length and circumference of its cross-section, which is divided equally in the axial and circumferential directions, respectively. The vertical temperature distribution of snow falling from the sky was assumed to be linear from an altitude of 0 °C to the ground, which was set based on meso-objective analysis data from the Japan Meteorological Agency. The terminal velocity and mass water content of snowflakes falling under the meteorological conditions were calculated based on Matsuo and Sasyo [3]. In addition, the snow accretion increment was calculated based on the snowfall flux obtained from precipitation and wind speeds observed at the site. The impact rate was assumed to be one, and the snowfall rate was proportional to the cosine of the angle of impact with the snowfall target and inversely proportional to the 0.4 power of the wind speed. Snowflakes are compacted by wind, and snowpack density varies proportionally with wind speed [4]. The water content was calculated by assuming a cylindrical shape and considering the sensible heat to the outer surface of the snowpack based on the heat transfer coefficient of a cylinder equivalent to the outer circumference of the snowpack, and the latent heat due to evaporation and condensation on the outer surface of the snowpack. The average water content was calculated by assuming that meltwater in the snowmelt instantly permeated the inner area, which contained several voids, and homogenized the snowmelt.
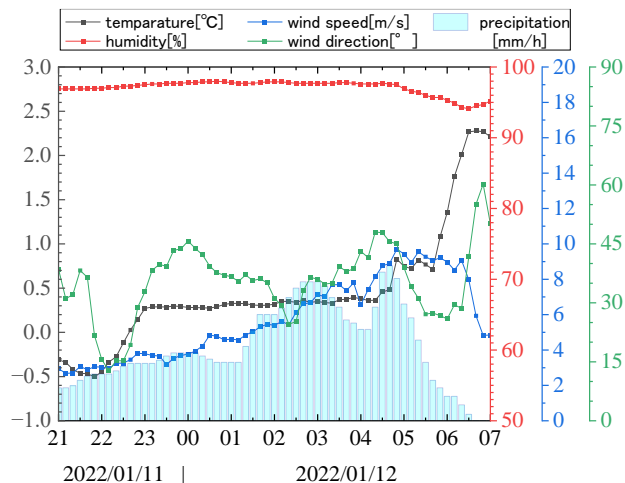
Fig. 2 Weather conditions 11 m above the ground on January 11 and 12, 2022: temperature, relative humidity, precipitation, wind speed, and direction (clockwise from north at 0°).

C. Calculation targets and conditions

This study first presents the results of a reproducible analysis of a 2 m-long dummy conductor [2] supported by a wire with torsional stiffness equivalent to that of the center of the ACSR240 transmission line installed on the Kushiro test line (293 m in diameter) to verify the accuracy of the SNOVAL. For accuracy verification, the amount of snow deposited and the angle of rotation of the sampler, which were calculated using 10 divisions in the wire axis direction, 720 divisions in the circumferential direction, and a time increment of 1 s, were compared with the observed data. In the case of a wet snow event with strong winds, the amount of snow deposition was considered to depend on the installation angle of the wire relative to the wind direction; thus, the reproducibility of snow deposition was also compared for two cases (Case +45 and Case -45) in which the installation orientation was changed by ±45°. In addition, the analysis was performed for two cases with different torsional stiffnesses, one of which was the ACSR810 wire, which had a thicker diameter and higher torsional stiffness. In addition, the analysis was performed for a hypothetical case in which a CW was installed (widely used in Japan to prevent snow damage by increasing torsional stiffness). The torsional stiffness of the wire used in each sampler was 8.5 and 11 times that of the wire used in ACSR240, respectively.

In addition, a reproduction analysis was performed for the ACSR240 full-scale test line for phases without countermeasures (Phase A) and with a CW (Phase C). CWs of 11 kg were installed in Phase C at approximately 40% and 70% of the location from the steel tower on the west side of Fig. 1(a). The analysis was performed with 100 divisions in the axial direction and 720 divisions in the circumferential direction, with a time step of 1 s.

267
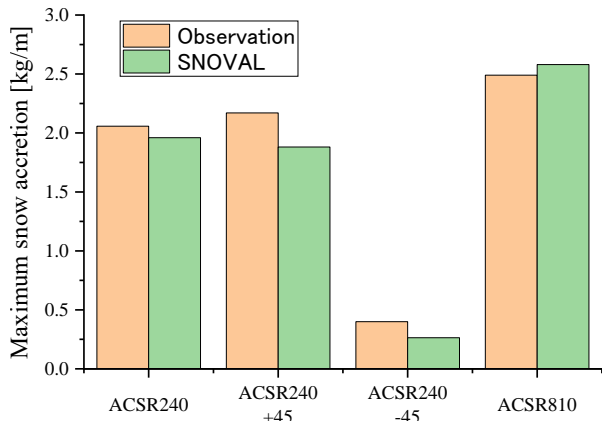
Fig. 3 Comparison of maximum snow accretion between that for observations and snow amount corresponding to the same time for SNOVAL.
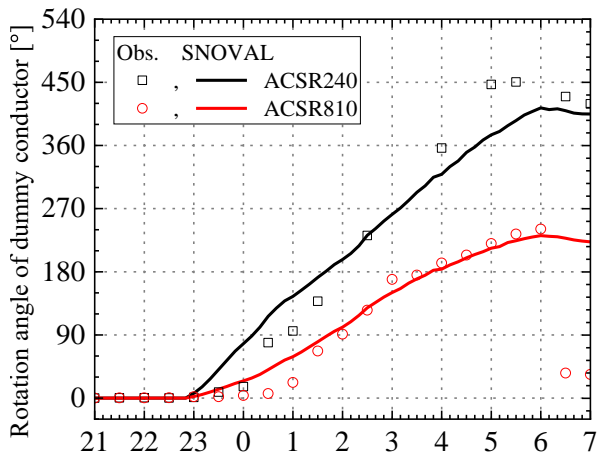
Fig. 4 Comparison of rotation angles of dummy conductors, ACSR240, and ACSR810, between for observation and for SNOVAL.

(*a*)

(*b*)

(*c*)

Fig. 5 (*a*) Results of replicated analysis for snow accretion and mass water content, (*b*) cross-sectional accretion shape for ACSR240 and 810, (*c*) snapshots of snow accretion of those dummy conductors.

III. RESULTS

A. Validation of SNOVAL with observation data

Figure 3 simultaneously compares the maximum snow amount on various types of wires and the replicated snow amount in SNOVAL. In this event, Case -45 had the lowest snow amount with respect to the installation angle of the wires, whereas Case +45 had approximately four times the maximum snowfall, indicating that SNOVAL replicated the large difference in snowfall with respect to the wire installation direction. In addition, ACSR810, which had high torsional stiffness, replicated the tendency of the maximum snow amount to be larger than that of ACSR240 owing to the larger wire diameter.

Figure 4 compares the rotation angles of the ACSR240 and ACSR810 conductors obtained from the eccentricity tuning bars and the replicated rotation amount in the SNOVAL. The larger the wire size, the higher the torsional stiffness, and the general trend was for ACSR810 to have a smaller sampler rotation angle. In addition, SNOVAL accurately replicated the rotation angle with an increase in the amount of snow. During this event, snow accretion for the ACSR810 conductor decreased at 06:00 on January 12, 2022, and the observed data exhibited a radical decrease in the rotation angle. In contrast, for ACSR240, snow accretion on the conductor occurred at 09:00.

B. Cross-sectional shape and mass water content of snow body at the time of dropout

Figure 5(*a*) compares the amount of snow and mass water content for the ACSR240 and ACSR810 conductors using SNOVAL during this specific period. However, the mass

water content of the two conductors did not differ significantly throughout the analysis period, because the area of the snow receiver was larger in proportion to the wire size. Figure 5(b) compares the replicated results of the cross-sectional snow shape of ACSR810 at 06:00 and 02:00; the time when the snow deposited on ACSR240 exceeded 360° in the sampler rotation angle at 06:00, and a cylindrical shape (cylindrical snow) covering the entire circumference of the wire was formed. In contrast, ACSR810, which had higher torsional rigidity than ACSR240, did not form a perfect snow cylinder simultaneously. In addition, the same trend was confirmed in the observed images, qualitatively confirming the validity of the replicated shape of the snow accretion.

Figure 6 shows the results of the reproduction analysis of the mass water content and snow accretion shape for the ACSR240 (CW) conductor compared to those of ACSR240. The results demonstrated that partial shedding occurred at 03:00, 04:00, and 06:00 and that the snow shape was not replicated by the observed data. Therefore, note that the shape of snow deposition differed to some extent from the results obtained from the observations. The time evolution of the snow amount using this conductor showed that the increment in the amount of snow accretion per hour was smaller than that of a normal sampler during the initial stage. This is believed to be because the torsional stiffness of the wire was 11 times higher than that of a normal sampler, resulting in a pointed snow shape in the upwind direction owing to the small torsional stiffness of the wire relative to the amount of snow in the early period. The sharp snow shape caused a temporary decrease in the snow adhesion rate, owing to the cosine law effect with the snowfall flux. However, as the snow cover increased and the rotation of the wire progressed, a wider snow cover surface was exposed to snow flux. Therefore, at 02:30, the rate of increase in snow cover was temporarily higher than that of the normal ACSR240 wire. However, because the center of gravity of the pointed snow shape was located away from the center of the wire, it eventually decreased earlier than that of the normal wire. Based on the SNOVAL analysis results, the water content of the snow landing body was approximately 15%–20%, indicating that a large eccentric moment caused snow accretion to drop out at a time when its water content was low.

IV. RESULTS FOR FULL-SCALE TEST LINE

As shown in Fig. 7, the observation results demonstrated that the amount of snowfall in the case of CW installation tended to be reduced compared to that without countermeasures because of the reduction in snow accretion rate. Moreover, the amount of snow deposited by CW installation tended to be lower than that without the countermeasure in the early stages of snow accretion owing to the snow deposition rate reduction effect. Therefore, the average mass water content increased during the same period. In the CW phase, the snowmelt began to fall off at approximately 03:00, and the average snowmelt rate did not exceed 0.5 kg/m during this event. The water content of the snowpack at the time of shedding was approximately 15%, which was consistent with the results of the snowpack sampler analysis corresponding to the CW phase. However, the amount of snow deposited in the no-countermeasure phase decreased from approximately 05:30, and the snow deposited continued to fall until approximately

(a)

(b)
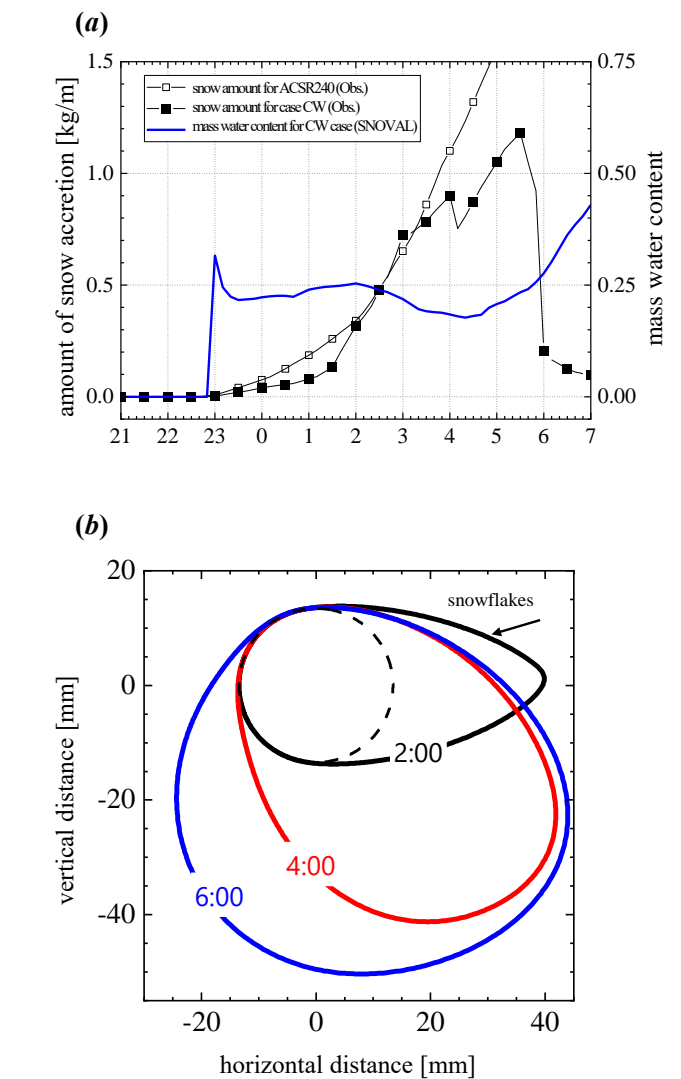
Fig. 6 Replicated analysis for dummy conductor of ACSR240(CW): (a) snow amount and mass water content, (b) cross-sectional shape of snow accretion.

09:00. After 08:30, the rate of decrease in snow deposition accelerated, indicating that snow deposited in the no-countermeasure phase fell off one after another in most the span. The mean mass water content at this time exceeded 40%, which was consistent with the mass water content of the dummy conductor that became a snow cylinder.

Figure 8 shows the shape of the snowfall at the start of the snowfall for Phases A and C. Torsional stiffness varied within the span. Because the torsional stiffness varied within the span, snow accretion shapes at 10% and 50% (center) from the west tower are shown for comparison. The snow accretion shape near the center of Phase A (Fig. 8(a)), was cylindrical, similar to the results of the snow accretion analysis, whereas the center of gravity of the snow accretion 10% from the support point was farther from the center of the wire. The torsional stiffness near the support point was higher than that at the center, and the snow accretion shape was similar to that of the CW equivalent of the simplified sampler at 06:00 (Fig. 6(b)). During Phase A, the snow-accretion body continued to decrease from 05:30 to 09:00. The snow-accretion body was
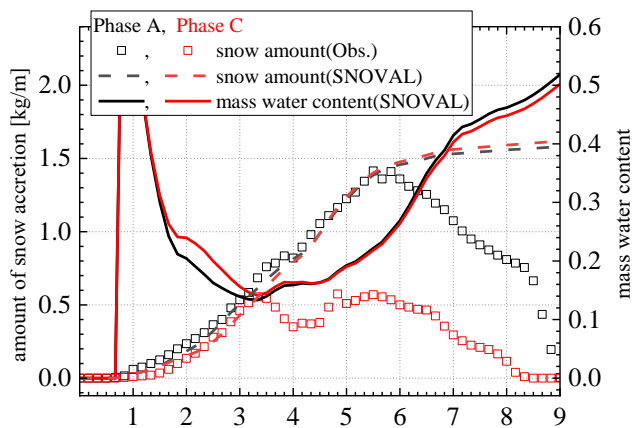
Fig. 7 Comparison of snow accretion amount for observation of full-scale conductor, mass water content for SNOVAL between ACSR240 without countermeasures (Phase A) and ACSR240 with CW (Phase C).

Fig. 8 Comparison of cross-sectional shape of reproductive snow accretion at 10% and 50% (center) position from the east side tower: (*a*) Phase A at 6:00, (*b*) Phase C at 3:00.

assumed to drop near the support point of the wire in the initial dropping stage when the moisture content reached approximately 20%. The snowdrops continued to fall between 09:00 and 09:30. As the snow deposit melted and the water content increased, the snow tube near the center of the span fell off. Figure 8(*b*) shows that the shape of the C-phase snow deposition was thinner and flatter near the ends. It was assumed that snowfall was less likely to receive a drag force from the wind near the end of the wire, and more likely to receive a drag force from the wind at the point where the torsional angle of the wire was larger near the center of the span.

V. CONCLUSIONS

We performed a replicated simulation of a wet snow event on a transmission line that occurred on the Kushiro test line in January 2022, using SNOVAL, a snow accretion simulation code developed at the Central Research Institute of Electric Power Industry. The snow accretion was compared when the maximum snow amount was observed for a simplified conductor that simulated the torsional stiffness near the center of a full-scale diameter interval using a wire. The amount of snow and the rotation angle was accurately produced. The snow accretion shape trend, which varied with the torsional stiffness of the wire, qualitatively agreed with the observed results. The ACSR240 conductor, which had the lowest torsional stiffness, was cylindrical, and snow accretion remained on the conductor until the mass water content reached approximately 40%. In contrast, ACSR810, which had a greater torsional stiffness than ACSR240, did not have a completely cylindrical shape, and snowdrops occurred at a mass water content of approximately 25%. For the CW conductor with higher torsional stiffness, the snow shape was flattened, resulting in a larger eccentric moment. Consequently, snowdrops occurred at a mass water content of approximately 15–20%. The SNOVAL analysis for a full-scale conductor without countermeasures and with CWs exhibited a similar trend with respect to mass water content during dropout.
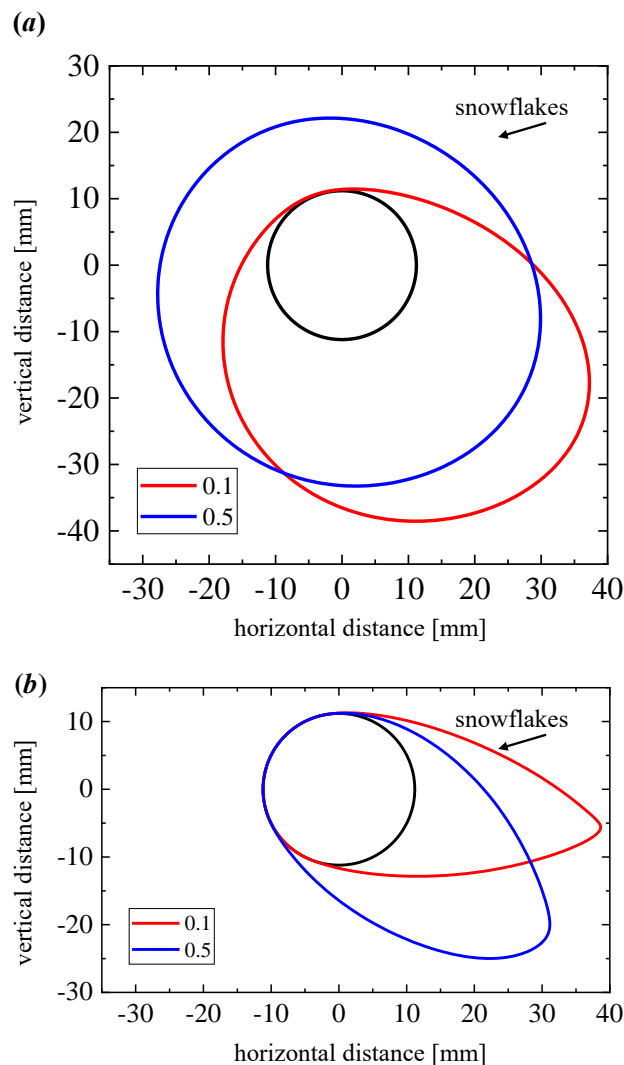
As shown, it was possible to estimate the characteristics of snow accretion during dropout using SNOVAL. It was necessary to compare the replicated characteristics and observational snapshots to understand dropout conditions.

REFERENCES

[1] Y. Eguchi, Y. Okazaki, H. Matsumiya, and S. Sugimoto, "Observational validation of a numerical model to simulate snow accretion on a transmission line conductor with moment of inertia and torsion compliance," Cold Reg. Sci. Technol., submitted.

[2] H. Matsumiya, H. Matsushima, T. Aso, T. Nishihara, and S. Sugimoto, "Field observations of snow damage to overhead transmission lines at the Kushiro test line," Cold Reg. Sci. Technol., Vol. 213, 103905, 2023.

[3] T. Matsuo and Y. Sasyo, "Melting of snowflakes below freezing level in the atmosphere," J. Meteor. Soc. Japan, 59, pp.10-25, 1981.

[4] K. Yamamoto, H. Matsumiya, K. Sato, M. Nemoto, K. Togashi, H. Matsushima, T. Sumita, and S. Sugimoto, "Evaluation for characteristics of wet snow accretion on transmission lines - Establishment of an experimental method using a vertical plate," Cold Reg. Sci. Technol., Vol. 174, 2020.

Numerical Modelling of Freezing of Aircraft Anti-icing Fluid

Igor A. Usachev[1], Dmitry Kolomenskiy[1], Oleg A. Rogozin[1], Viktor G. Grishaev[1], Alidad Amirfazli[2], Vladimir P. Drachev[1]

[1] *Skolkovo Institute of Science and Technology, Russia*
[2] *York University, Canada*

igor.usachev@skoltech.ru, d.kolomenskiy@skoltech.ru, o.rogozin@skoltech.ru, v.grishaev@skoltech.ru, alidad2@yorku.ca, v.drachev@skoltech.ru

Abstract— **The on-ground icing is a major concern for aircraft. Icing contamination reduces lift and increases drag forces. De/anti-icing fluid treatment is widely used to delay the onset of freezing. A fast and reliable method to predict de/anti-icing fluid performance is needed. Here a numerical model of fluid freezing (Type IV fluid) based on a simplified Navier-Stokes 2D equation coupled with diffusion equation, is proposed; its results were verified with experimental test data. The differences observed between experimental data and numerical results were of the order of 15% indicating a fairly good validation of the model.**

Keywords—*aircraft anti-icing fluids, endurance tests, fluid freezing, simulation, experiment validation*

I. INTRODUCTION

The on-ground icing is a major concern for aircraft. Icing contamination reduces lift and increases drag forces. That is why aircraft de/anti-icing fluids (AAFs) are widely used today. Such fluids form a protective film on critical aircraft surfaces delaying the onset of freezing. Endurance tests are used to examine the fluid performance.

The Water Spray Endurance Test (WSET) simulates freezing drizzle conditions: precipitation rate 5 g/dm²h, the air and surface temperatures fixed at –5℃, droplet average diameter 20 μm. The test is done in a cold chamber. The WSET procedure is as follows: a fluid is poured on tilted aluminium test plates (10×30 cm) lying on a chiller unit. After five minute settling time the water spray and stopwatch is turned on. An observer records the time when the ice front touches the failure zone, or the slush is formed at 10% of the plate's surface [1]. This characteristic time shall be greater than the expected critical value for the fluid.

The experimental study of fluid freezing is limited in the possible choice of test conditions; the test process is restricted to overall measurements of the ice front, time-consuming, and even subjective due to operator's observation requirements. Therefore, a mathematical model of the fluid freezing can be an alternative. Also, it can serve as a fast evaluation tool if it can be verified by the experimental data.

The Anti-icing Materials International Laboratory (AMIL) developed different models to simulate the freezing process of AAFs [2]–[4]. Their last model [4] has been successfully applied to both Newtonian and pseudo-plastic fluids. However, the model was validated only at one time point, which makes it impossible to estimate its ability to predict complete ice front propagation or icing kinetics. No information was provided to estimate minimum visible ice thickness. The key equation for understanding the freezing behaviour of fluids, the freezing fraction equation was not shown.

Our previous research [5] made it possible to record the complete icing kinetics during the WSET. Therefore, any freezing model can be verified throughout the entire duration of the test. We present here a model of the anti-icing fluid freezing during the WSET procedure and validate it with our experimental observations.

II. MODELLING

The proposed simulation is restricted to two dimensions. Figure 1 represents the numerical domain. The x-axis shows the distance along the plate (from plate top to bottom); the y-axis is the height normal to the plate. All distributions along the z-axis (plate width) are considered uniform and, therefore, can be omitted.
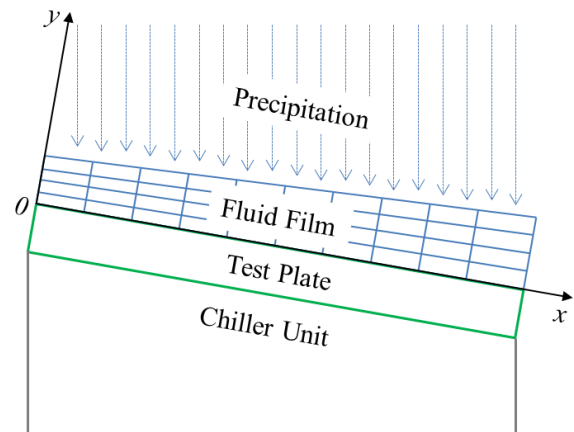
Fig. 1 Numerical domain for calculation

A. Governing Equations with Initial/Boundary Conditions

All the symbols used in the work are summarized in Table I.

1) *Velocity and Thickness Time Variation:* The Navier–Stokes equation reduced to the simplest form (the y component of velocity is zero, the x component of the velocity gradient is zero and the downstream pressure gradient is the thickness gradient) can represent the velocity distribution for a certain thickness gradient (Eq. 1). To obtain the full picture the mass balance equation (Eq. 2) is required.

TABLE I. NOMENCLATURE

Symbol	Description	Units
u	Horizontal component of the velocity	m/s
t	Time	s
μ	Fluid viscosity	Pa·s
ρ	Fluid density	kg/m³
x	Horizontal coordinate	m
y	Vertical coordinate	m
g	Gravitational acceleration	m/s²
θ	Plate tilt angle	°
h	Film thickness	m
m''	Precipitation rate	kg/m²s
ρ	Water density	kg/m³
C	Glycol volume concentration	-
D	Water diffusion coefficient	m²/s
H	Total enthalpy	J/kg
k	Thermal conductivity	W/mK
C_p	Specific heat	J/kgK
	Thermal diffusivity	m²/s
	Mass liquid fraction	-
L_f	Latent heat of freezing	J/kg
L_m	Latent heat of mixing	J/kg

$$\text{—} \quad \text{—} \quad \text{—} \qquad\qquad \text{—} \tag{1}$$

$$\text{—} \quad \text{—} \quad \int \text{—} \tag{2}$$

The initial conditions are zero velocity $\left(u|_{x,y,t=0} = 0\right)$ and uniform film thickness $\left(h|_{x,t=0} = h_0\right)$.

The boundary conditions for the velocity are the no-slip condition at the plate surface $\left(u|\quad 0\right)$ and a free surface condition at the air/fluid interface $\left(\frac{\partial u}{\partial x}\Big|\quad 0\right)$. A realistic assumption for the thickness is the zero height condition above the plate top $\left(h|_{x=0,t} = 0\right)$.

2) *Concentration Time Variation:* Anti-icing fluid can freeze at about –5°C only by reaching the required dilution with water (15% solute concentration for AAF Type IV). Therefore, the calculation of the concentration change is necessary to obtain icing kinetics. Based on the dimensional analysis, the following form of the diffusion equation (Eq. 3) was proposed [4]:

$$\text{—} \quad \text{—} \quad \text{—} \tag{3}$$

The simulation starts with a uniform solute concentration $\left(C|\qquad\right)$.

The boundary conditions are a zero porosity at the plate surface $\left(\text{—}|\quad = 0\right)$ and water flux at the air/fluid interface $\left(\text{—}|\qquad \text{—}C\right)$.

3) Enthalpy and Liquid Fraction Time Variation

Voller et al. [6] proposed the enthalpy method for convection/diffusion phase change. In our case, a specific form of the heat equation with latent heat source terms was developed (Eq. 4). Note, that there are two latent heat sources in WSET: the one is the latent heat of freezing and the other is the latent heat of mixing of glycol with water.

$$\text{—} \qquad \text{—} \qquad \text{—} \qquad \text{—} \tag{4}$$

The initial fluid temperature equals to the ambient temperature $\left(T|_{x,y,t=0} = 268K\right)$, the initial condition for the liquid fraction is 100% liquid $\left(\varphi|_{x,y,t=0} = 1\right)$.

At both boundaries we assume the ambient temperature conditions $\left(T|_{x,y=0,t} = T|_{x,y=h,t} = 268K\right)$. For the liquid fraction no phase change happens at the boundary $\left(\varphi|_{x,y=0,t} = \varphi|_{x,y=h,t} = 0\right)$.

The enthalpy equation has two unknowns (the total enthalpy and mass liquid fraction), so to solve it one more equation is required. From the total enthalpy definition, we derive the equation for the liquid fraction (Eq. 5):

$$\left(0 \quad n\left(1 \quad \text{———}\right)\right) \tag{5}$$

Note, that the liquid fraction shall change only when freezing conditions are met $\left(T < T_{cr}(C)\right)$. Here, the freezing point of the fluid is the function of its glycol content (Fig. 2) [7]. Here, the glycol concentration is assumed to be equal to the AAF concentration, which is reasonable in the considered temperature range (discussed with the manufacturer).
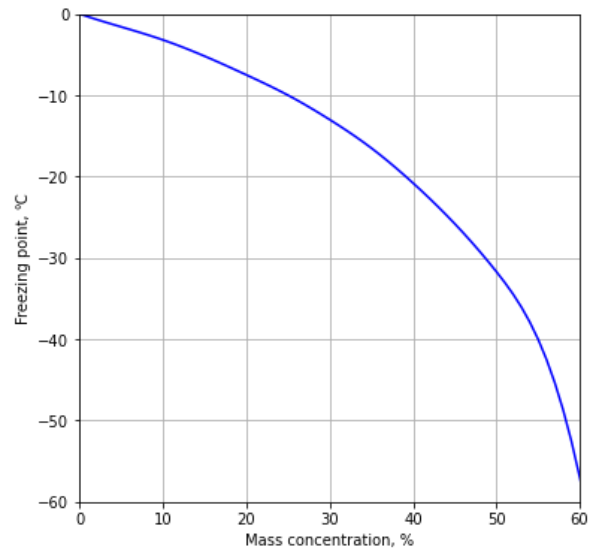
Fig. 2 Freezing point of aqueous solutions of propylene glycol

B. Discretization

The discretized form of governing equations was obtained by a finite difference method. Forward difference scheme was used for a first time and spatial derivative. The Crank–Nicolson method was implemented for a second spatial derivative. For instance, Eq. 6 shows the discrete diffusion equation for some time step at a node i, j. Here, i represents the position along x and j is the position along y-axis, $*$ represents a previous time step and ——— (a constant created to simplify the algebra).

$$(1 \quad r)C$$
$$(1 \quad r)C \tag{6}$$

———   ———

Eq. 7 demonstrates a discrete version of the integro-differential balance equation. All the notations remain the same.

$$-\left(\sum u \qquad \sum \qquad \right) \tag{7}$$

Final matrix equations were solved numerically in Python. Time step size was fixed at 1 s, the number of meshes was 30×20 in x, y-directions.

To consider the icing front propagation, liquid fraction for nodes at x step i was calculated only after complete freezing of the film layer at the previous x step $i - 1$.

C. Stable Layer Concept

The preliminary computation shows that the Type IV does not freeze completely by thickness during the WSET. The same was already observed for low diffusion fluids [3]. But during the test we notice complete surface icing. Therefore, this must be a certain minimum ice thickness (let us call it a stable layer) visible to the naked eye. To estimate the stable layer thickness, simple considerations must be taken. Calculated thickness of ice at the moment of first visible icing during the test can be approximated as the stable layer (Fig. 3).

III. Simulation Results

The proposed numerical model was tested for the SAE Type IV fluid "Defrost ECO 4" (JSC RCP Nordix). The obtained icing kinetics was compared with the WSET experimental results (Fig. 3). Variations are of the order of 15% which indicates fairly good validation of the model.

The model nicely captures the whole freezing curve. However, initial freezing happens faster than in experiments.

The developed model does not consider how icing nucleation occurs on the top of the plate. Therefore, the initial deviation shall increase exactly as we observe.
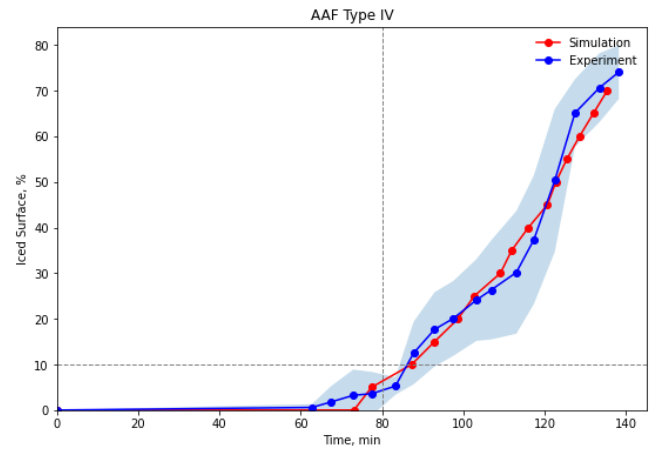
Fig. 3 Comparison of the calculated icing kinetics of the SAE Type IV fluid with the experimental observations. Solid lines and shaded areas show averaged values and standard deviations, respectively. Grey vertical dashed lines represent the minimum required endurance times for the fluids at 10% ice covering

IV. Conclusions

The numerical model of freezing of the anti-icing fluid is developed. The enthalpy equation with latent source terms is derived. The concept of a stable layer and sequential ice front propagation was proposed.

The simulation is validated on the icing kinetics of the SAE Type IV fluid on aluminium substrates. The model developed successfully predicts the fluid failure and icing kinetics during the WSET. The deviation from the experiment is less than 15%. The deviation is more in the beginning of the experiment because of the random nature of icing nucleation.

Next, the model shall be validated on the icing kinetics of the SAE Type I and II fluids.

References

[1] *Water Spray and High Humidity Endurance Test Methods forAMS1424 and AMS1428 Aircraft Deicing/Anti-icing Fluids (Aerospace Standard No. AS5901D)*, SAE International, 2019.

[2] P. Louchez, J-L Laforte, and G. Bouchard, "Experimental and Numerical Investigations of Deicing and Anti-Icing Fluid Performances under Various Precipitation Conditions," in *Proc. Subzero Engineering Conditions Conference and Exposition*, 1994.

[3] T.V.K. Tông, P.R. Louchez, and A. Zouzou, "Introductory analysis of draining and freezing of de-icing fluids," *Cold Regions Science and Technology*, vol. 25(3), pp. 207–214, Apr. 1997.

[4] A. Zouzou, P. Louchez, and S. Bernardin, "Modeling of the draining and freezing of aircraft de-icing and anti-icing fluids," in *Proc. 36th AIAA Aerospace Sciences Meeting and Exhibit*, 1998.

[5] V.G. Grishaev, I.A. Usachev, V.P. Drachev, R.K. Gattarov, N.I. Rudenko, A. Amirfazli, 43 I.S. Borodulin, I.K. Bakulin, M. V Makarov, I.S. Akhatov, "Ice imaging in aircraft anti-icing fluid films using polarized light," *Cold Regions Science and Technology*, vol. 194, article 103459, Feb. 2022.

[6]   V.R. Voller, M. Cross, and N. C. Markatos, "An enthalpy method for convection/diffusion phase change," *International Journal for Numerical Methods in Engineering,* vol. 24, pp. 271-284, 1987.

[7]   G. O. Curme, Jr. and F. P. Johnston, Eds., *Glycols American Chemical Society Monograph Series*, New York, USA: Reinhold Publishing Corporation, 1952.

Ice accretion on airfoils and engine nacelle based on Finite Area Method

Yinglin Yang[1], Shinan Chang[1*], Xiaowei Zhu[1], Haifeng Qi[1], Jingwu He[1]

[1]Beihang University, School of Aeronautic Science and Engineering, China

yangyl@buaa.edu.cn, sn_chang@buaa.edu.cn, xiaoweizhu@buaa.edu.cn, qhf@buaa.edu.cn, hejingwu@buaa.edu.cn

Abstract— **The results of the icing processing simulation were presented in this article. An improved droplet Eulerian two-phase flow solver was developed. To accurately simulate ice accretion, the thermodynamic process in the water film was developed based on the finite area method (FAM). All modules involved in this article were validated based on numerical or experimental results. Subsequently, the dynamic characteristics of the water film during the icing process on the GLC305 airfoil and engine nacelle were analyzed.**

Keywords— *Ice accretion, Runback water, Thermodynamic, Turbofan engine nacelle, Finite area method*

I. INTRODUCTION

Ice accretion on the aircraft poses a significant threat to flight safety[1–3]. When the aircraft flies through clouds containing supercooled water droplets, components such as the wings, tail, engine, and airspeed sensors are easy to ice accumulation[4]. Ice accretion not only damages the aerodynamic shape of the aircraft but also increases its weight. This can result in an increase in drag and a decrease in lift, thereby reducing aerodynamic performance and operational efficiency. Many theoretical, experimental, and numerical studies have been carried out to further understand the damage caused by aircraft icing[5–9]. Furthermore, a series of meteorological design specifications related to aircraft icing were summarized and issued.

Various approaches including experimental studies and computational simulations have been used to study aircraft ice accretion. Papadakis[10,11] conducted ice tests on the components such as the wings, and engines at NASA Glenn Wind Tunnel and recorded the ice shape on these components under different ice conditions. Mathematical methods, based on Euler-Euler or Euler-Lagrange models, also have been used to simulate the ice accretion process. These approaches have been widely implemented in the computation codes such as LEWICE[12], FENSAP-ICE[13], and IGLOO2D/3D[14].

This article used the finite area method to calculate the thermodynamic equilibrium equation of supercooled water droplets impacting on component surfaces and with this method, the icing process was also calculated. The ice accretion calculation results were compared with the experimental results to verify the accuracy of this method in predicting the ice accretion process. The mathematical models used in this article will be first presented in section II. Then the test cases of ice- accretion will be discussed in section III.

II. MATHEMATICAL MODEL INTRODUCTION

Based on the OpenFOAM v2106 library[15], a comprehensive methodology has been developed to simulate the three-dimensional ice accretion process, integrating an airflow calculation module, a droplet impingement calculation module, an ice accretion module, and a grid-regeneration module. The airflow is assumed to be steady, which is a standard way in many icing software[12–14]. The rhoSimpleFoam is used to solve the compressible Reynolds-averaged Navier-Stokes equations as follows:

$$\nabla \cdot \left(\rho_a \boldsymbol{u}_a \right) = 0 \tag{1}$$

$$\nabla \cdot \left(\rho_a \boldsymbol{u}_a \boldsymbol{u}_a \right) = -\nabla p + \nabla \cdot \tau \tag{2}$$

$$\nabla \cdot \left((\rho_a H_a + p)\boldsymbol{u}_a \right) = \nabla \cdot [k_a (\nabla T_a) + \boldsymbol{u}_a \cdot \tau] \tag{3}$$

where ρ_a and $\boldsymbol{u}_a$ represent air density and speed, respectively. τ is the stress tensor, and k is the air thermal conductivity. An ideal equation of state $p = \rho_a R T_a$ is used to close the conservation laws. The pressure-velocity coupling with the compressible SIMPLE method was used. For the turbulence model, the Menter's k − ω shear stress transport model is chosen considering the flow may be separated in this work.

A water droplet collection efficiency solver based on the Eulerian method was developed to predict the motion of super cold droplets. As introduced by Bourgault et al.[16], the droplets phase could be assumed to be a continuum flow and spherical particles for the small size(less than 50 μm). So the effect of the droplet phase on airflow was ignored[17], which means the air phase and droplet phase can be solved separately and coupled unidirectionally. Since the original Eulerian droplet method is not hyperbolic[18] the pressure term disappeared when the separated two phase model with the assumptions above. The Harten-Lax-van Leer-Contact (HLLC) scheme[18] is used by adding a vector term, $\nabla \cdot \left(\alpha \boldsymbol{g} d \right)$, in the Eulerian droplet momentum equation. The Eulerian method is calculated as follows:

$$\nabla \cdot \left(\alpha_n \boldsymbol{u}_d \right) = 0 \tag{4}$$

$$\nabla \cdot \left(\alpha_n \boldsymbol{u}_d \boldsymbol{u}_d + \alpha_n \boldsymbol{g} d \right) = \frac{C_D Re_r}{24K} \alpha_n \left(\boldsymbol{u}_a - \boldsymbol{u}_d \right) + \alpha_n \boldsymbol{g} + \boldsymbol{g} d \nabla \cdot \alpha_n \tag{5}$$

where ρ_d and $\boldsymbol{u}_d$ represent droplet density and speed, respectively. α_n represents the non-dimensionalized volumetric fraction of droplets, $\alpha_n = \alpha/\alpha_\infty = \alpha/(\mathrm{LWC}/\rho_d)$. α and α_∞ represent the volumetric fraction of droplets and the freestream volumetric fraction. The first term on Eq.(5)'s right-hand side is the drag force of airflow acting on droplets. Where K is the inertial parameter, $K = \rho_d d^2/18\mu$; d is the average diameter of the water droplet, which is

usually equal to the medium volume diameter (MVD) of droplets; μ is the dynamic viscosity of air. C_D is the drag coefficient for sphere droplets, and Re_r is the relative Reynolds number,

$$\mathrm{Re}_r = \frac{\rho_a d}{\mu}\left|\boldsymbol{u}_a - \boldsymbol{u}_d\right| \tag{6}$$

many previous studies on the drag coefficient are commonly used in modern icing solvers and the form in Beaugerdre et al.[16] is used in this study:

$$C_D = \begin{cases} \left(24/\mathrm{Re}_r\right)\left(1 + 0.15\mathrm{Re}_r^{0.687}\right), \ \mathrm{Re}_r \leq 1300 \\ 0.4 \qquad\qquad\qquad\qquad, \ \mathrm{Re}_r > 1300 \end{cases} \tag{7}$$

the second term on the right-hand side of Eq.(5) represents the gravity forces. Once impacting a surface, droplets are absorbed. The local collection efficiency β, which is one of the crucial parameters affecting icing calculation, is the ratio of the actual water that is collected in the local area to the maximum possible water that can be collected:

$$\beta = \alpha_n \cdot \frac{\boldsymbol{u}_d \cdot \boldsymbol{n}}{|\boldsymbol{u}_\infty|} \tag{8}$$

where $\boldsymbol{u}_d$ and $\boldsymbol{n}$ are the local droplet velocity vector and the normal vector to the impinging surface, respectively; $\boldsymbol{u}_\infty$ is the droplet velocity of freestream, and α_n is the non-dimensionalized volumetric fraction of droplets, as mentioned before.

The water flow impacting the surface can be evaluated and the icing process can be calculated. Water film may freeze, evaporate, and sublimate under the influence of airflow shear stress and the thermodynamic effects associated with both air flow heat transfer and droplet impingement. In this paper, the Shallow-Water Icing Model [19] was used to calculate heat and mass transfer while modifications are introduced to the momentum conservation equation. It is worth noting that the model was developed with the finite area method, which was first introduced by Tukovic and Jasak[20], and the detailed process was described by Rauter and Tukovic[21]. Several assumptions were made on the water film to derive the equations. Only the derivative in the normal direction was considered compared to the tangential direction as the film was thin enough and was only flowing parallel to the surface of the components which means the normal direction of film velocity was also ignored. The equation is as follows:

$$\rho_f\left[\frac{\partial h_f}{\partial t} + \nabla\cdot\left(\boldsymbol{u}_f h_f\right)\right] = u_\infty\cdot\mathrm{LWC}\cdot\beta - \dot{m}_{evap} - \dot{m}_{ice} \tag{9}$$

$$h_f\bar{\boldsymbol{u}}_f = -\frac{h_f^3}{3\mu_f}\left(\nabla_s p_f + \rho_f\mathbf{g}_s - \frac{3\tau_a}{2h_f}\right), \tag{10}$$

$$\rho_f\left[\frac{\partial h_f c_{p,f}\tilde{T}}{\partial t} + \nabla\cdot\left(\boldsymbol{u}_f h_f c_{p,f}\tilde{T}\right)\right] = \dot{Q}_{drop} + \dot{Q}_{ice} - \dot{Q}_{ev} - \dot{Q}_{conv} \tag{11}$$

Where $\tilde{T} = T_{surf} - T_{ref}$, and

$$\dot{Q}_{drop} = \left[c_{p,f}\left(T_a - \tilde{T}\right) + \frac{\|\boldsymbol{u}_d\|^2}{2}\right]u_\infty\cdot\mathrm{LWC}\cdot\beta \tag{12}$$

$$\dot{Q}_{ice} = \left(L_{fusion} - c_{p,ice}\tilde{T}\right)\dot{m}_{ice} \tag{13}$$

$$\dot{Q}_{ev} = 0.5\dot{m}_{evap}\left(L_{evap} + L_{sub}\right) \tag{14}$$

$$\dot{Q}_{cov} = k_h\left(\tilde{T} - T_{rec}\right) \tag{15}$$

Typically, there are three unknowns in the mass and energy equations, which are the thickness of the water film, the equilibrium temperature of the air, water film, ice and wall surface, and the icing quality. Therefore, the following compatibility relations are used to close the system: $h_f \geq 0, \ \dot{m}_{ice} \geq 0, \ h_f\tilde{T} \geq 0, \ \dot{m}_{ice}\tilde{T} \leq 0$.

After the icing processing was determined, the ice shape was updated with the ice thickness on the components' surface. The ice growing distances for each point on the icing surface at every time step were calculated with the growth rate of ice thickness combined with the ice growing direction:

$$d_{node} = \delta_{ice}\cdot\boldsymbol{n}_{node} \tag{16}$$

where the ice growing direction was calculated by the normal vectors of surrounding surfaces:

$$\boldsymbol{n}_{node} = \sum\frac{\boldsymbol{n}_i}{|\boldsymbol{n}_i|} \tag{17}$$

As part of the OpenFOAM package, the dynamic mesh library was also used. By solving the Laplace equation, the offset of all nodes in the flow field was given out.

III. ICE ACCRETION PREDICTION

A. GLC305 airfoil results

The icing test data of GLC305 airfoil released by NASA[22] is used to verify the icing calculation results. The computation conditions are depicted in Table 1, with the airfoil's chord length being 0.9144 m. A hexahedral grid is utilized, and the height of the first layer of the wall is $1e^{-6}$ m.

Table 1 Computation parameters for GLC305 airfoil

Case No.	U_∞ m/s	T_∞ K	AoA °	LWC g/m3	MVD μm	Time min
1	90	268.3	4	0.54	20	6
2	90	258.2	4	0.54	20	6
3	90	255.1	4	0.54	20	6

Fig.3 shows the comparison between the result of water collection coefficient calculated with the developed droplet solver and FENSAP in case 1. It can be seen from the diagram that the results of the developed droplet solver were slightly larger than the FENSAP results at the stagnation point, which may be caused by the artificial viscosity coefficient that FENSAP used. It can be clearly seen that the water collection coefficient was basically same. Therefore, the difference in the ice accretion results is mainly due to the model of the icing process and water film runback based on the FAM method used in this paper.
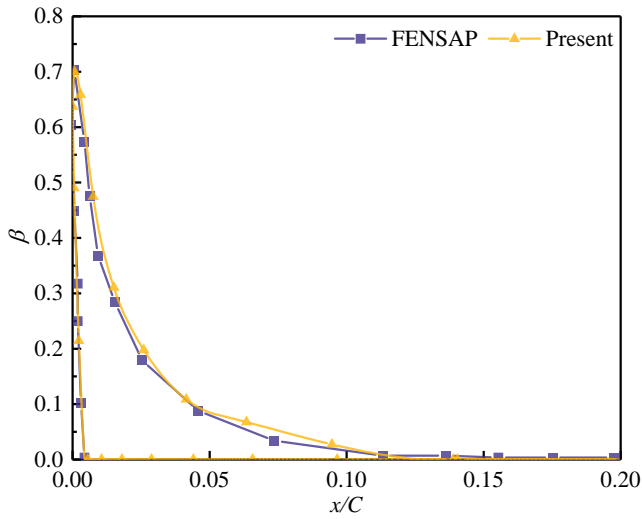
Fig. 1 Comparison of collection efficiency results for Case 1

Simulations were conducted at different temperatures: $T_\infty = 268.3$ K, 258.2 K, and 255.1 K, with a calculation time of 6 minutes. The results were compared and validated with data from Ref[22]. As a result, Fig. 2, Fig. 3, and Fig. 4 display the ice shapes on the airfoil of various cases.
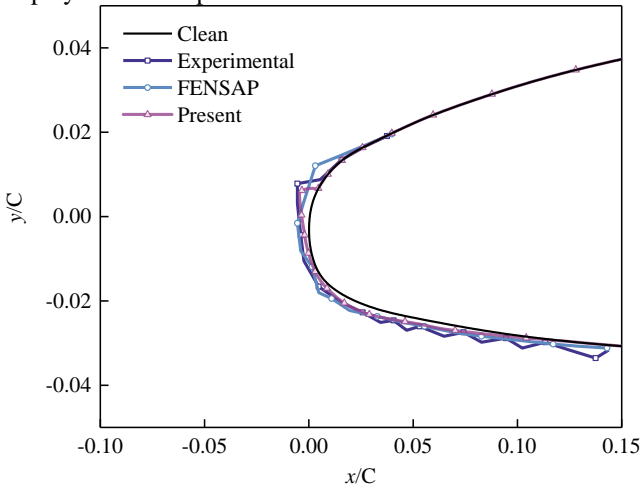
Fig. 2 Comparison of ice shapes for Case 1

It is obvious in Fig. 2 that the ice sharp results are close to the experimental results, and similar single-horn-shaped ice was correctly captured. Meanwhile, FENSAP is not able to calculate the ice shape, the ice coverage on the upper surface of the airfoil was too large.

The results of Case 2 and Case 3 are illustrated in Fig. 3 and Fig. 4. It is clear that the ice shape profile was in good agreement with the experimental results on the upper surface of the airfoil, but the lower part of the ice sharp was still larger than the experimental results. The main reason is that the heat transfer coefficient calculated in the air flow solver to the lower part is smaller.
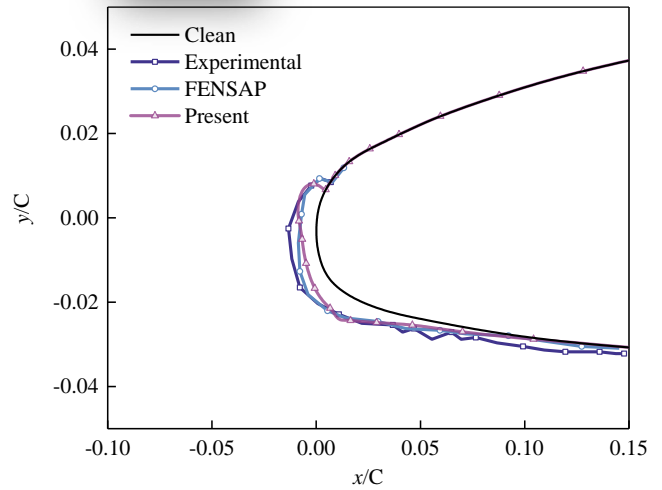
Fig. 3 Comparison of ice shapes for Case 2
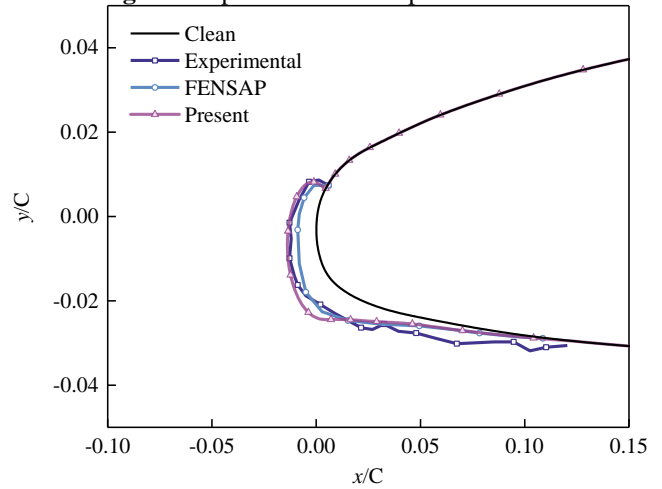
Fig. 4 Comparison of ice shapes for Case 3

B. Engine nacelle results

The developed three-dimensional ice accretion solvers were employed to conduct icing processing on a turbofan engine nacelle. The model of the nacelle and the computational domain were shown in Fig. 5. The locations of sections at 0°, 90°, and 180° were investigated at different times, and the computation parameters were listed in Table 2.

Table 2 Computation parameters for nacelle

Mass flow kg/s	U_∞ m/s	P_∞ Pa	T_∞ K	AoA °	LWC g/m3	MVD μm	Time min
200	120	84309	267.15	4	1	30	6
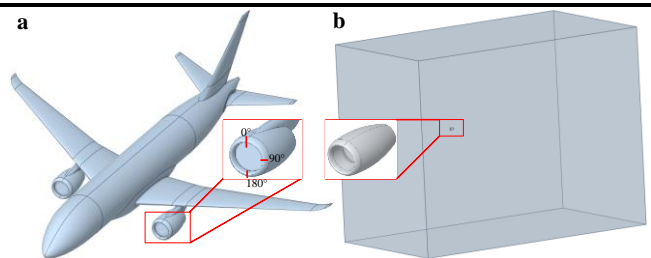
Fig. 5 The airplane with engine and the nacelle simulation domain

Fig. 6, Fig. 7, and Fig. 8 show the ice shape tracked at each specified time for the selected section, respectively. As

can be seen, the icing region is large and the ice limits on the surface move to the outer surface with the icing time. The impacting droplets are frozen directly and less unfrozen water flows backward. At the section of 0°, the ice area moved up to the outer surface as time passed. However, in the case of 90°, there seems fewer droplets would freeze here for water film turned up as the effect of airflow or they turned down for the gravity force. Besides, it is obvious that the ice grew downwards to the outer surface as time passed for the case of 180° as the result of the angle of attack of airflow.
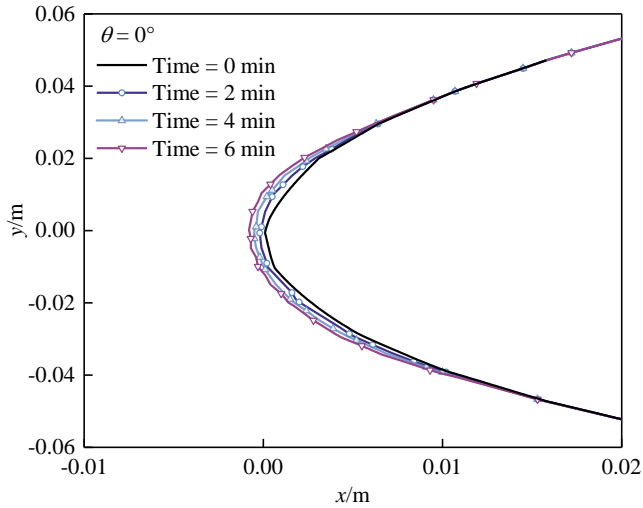
Fig. 6 Ice shapes at sections of 0° at different times
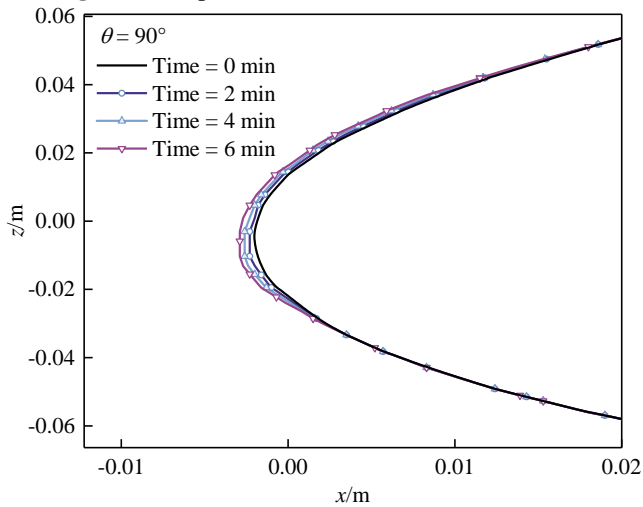
Fig. 7 Ice shapes at sections of 90° at different times
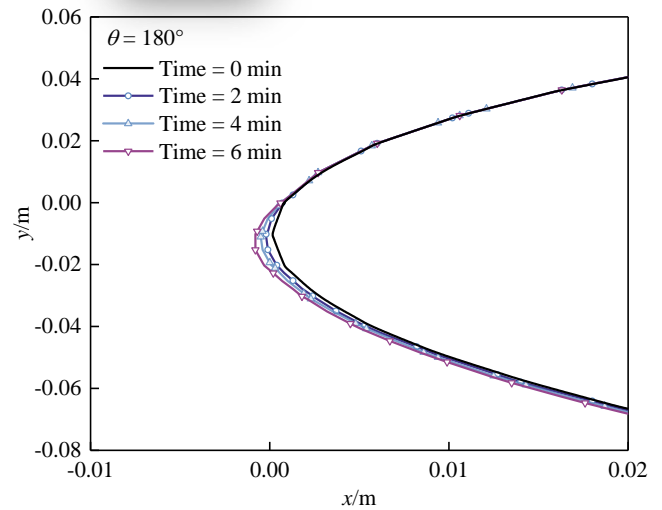
Fig. 8 Ice shapes at sections of 180° at different times

IV. CONCLUSION

This paper summarizes the research contributions of our research group on aircraft icing simulation. All cases use the developed solvers for simulation verification and the results are very satisfactory. The water collection efficiency results of the improved droplet solver are generally well-verified. For ice accretion, the calculation results based on the FAM method are highly satisfactory for both the GLC305 airfoil and engine nacelle cases.

REFERENCES

[1] Q. Su, S. Chang, Y. Zhao, H. Zheng, C. Dang, A review of loop heat pipes for aircraft anti-icing applications, Appl Therm Eng. 130 (2018) 528–540. https://doi.org/10.1016/j.applthermaleng.2017.11.030.

[2] H. Qi, S. Chang, Y. Yang, Numerical study of mixed phase ice accumulation in aero-engine inlet system, Appl Therm Eng. 231 (2023) 120909. https://doi.org/10.1016/j.applthermaleng.2023.120909.

[3] A. Lai, H. Cheng, M. Li, J. Pan, Ice particle distribution simulation in a transonic axial compressor based on Eulerian evaporation coupling model, P I Mech Eng G-j Aer. 237 (2023) 956–971. https://doi.org/10.1177/09544100221113215.

[4] R.J. Kind, M.G. Potapczuk, A. Feo, C. Golia, A.D. Shah, Experimental and computational simulation of in-flight icing phenomena, Prog Aerosp Sci. 34 (1998) 257–345. https://doi.org/10.1016/S0376-0421(98)80001-8.

[5] Y. Liu, T. Wang, Z. Song, M. Chen, Spreading and freezing of supercooled water droplets impacting an ice surface, Appl Surf Sci. 583 (2022) 152374. https://doi.org/10.1016/j.apsusc.2021.152374.

[6] W. Kong, L. Wang, P. Bian, H. Liu, Effect of surface wettability on impact-freezing of supercooled large water droplet, Exp Therm Fluid Sci. 130 (2022) 110508. https://doi.org/10.1016/j.expthermflusci.2021.110508.

[7] S. Chang, Y. Yang, Q. Shi, H. Qi, Experimental study of shear-driven water film with brightness-based laser-induced fluorescence technique, Int J Multiphas Flow. 166 (2023) 104514. https://doi.org/10.1016/j.ijmultiphaseflow.2023.104514.

[8] S. Chang, H. Qi, S. Zhou, Y. Yang, Experimental and numerical study on freezing process of water droplets under surfaces with different wettability, Appl Therm Eng. 219 (2023) 119516. https://doi.org/10.1016/j.applthermaleng.2022.119516.

[9] S. Chang, H. Qi, S. Zhou, Experimental Study on Freezing Characteristics of Water Droplets on Cold Surfaces, SSRN Journal.

(2022). https://doi.org/10.2139/ssrn.4071351.

[10] M. Papadakis, K.E. Hung, Experimental Investigation of Water Droplet Impingement on Airfoils, Finite Wings, and an S-Duct Engine Inlet, (2002).

[11] M. Papadakis, H.-W. Yeong, S.-C. Wong, S.-H. Wong, Comparis on of Experimental and Computational Ice Shapes for an Engine Inlet, in: AIAA Atmospheric and Space Environments Conferen ce, American Institute of Aeronautics and Astronautics, Toronto, Ontario, Canada, 2010. https://doi.org/10.2514/6.2010-7671.

[12] H. Vladimír, C. Zdeněk, In-flight Ice Accretion Prediction Code, INCAS BULLETIN. 2 (2010) 119–126. https://doi.org/10.13111/ 2066-8201.2010.2.4.16.

[13] F. Morency, H. Beaugendre, G. Baruzzi, W. Habashi, FENSAP-I CE - A comprehensive 3D simulation system for in-flight icing, in: 15th AIAA Computational Fluid Dynamics Conference, Ame rican Institute of Aeronautics and Astronautics, Anaheim,CA,U.S. A., 2001. https://doi.org/10.2514/6.2001-2566.

[14] P. Trontin, G. Blanchard, A. Kontogiannis, P. Villedieu, Descripti on and assessment of the new ONERA 2D icing suite IGLOO2 D, in: 9th AIAA Atmospheric and Space Environments Conferen ce, American Institute of Aeronautics and Astronautics, Denver, Colorado, 2017. https://doi.org/10.2514/6.2017-3417.

[15] H. Jasak, A. Jemcov, Z. Tukovic, OpenFOAM: A C++ Library f or Complex Physics Simulations, in: International workshop on c oupled methods in numerical dynamics, IUC Dubrovnik Croatia, 2007: pp. 1–20.

[16] Y. Bourgault, W. Habashi, J. Dompierre, Z. Boutanios, W. Di B artolomeo, Y. Bourgault, W. Habashi, J. Dompierre, Z. Boutanios, W. Di Bartolomeo, An Eulerian approach to supercooled drople ts impingement calculations, in: 35th Aerospace Sciences Meetin g and Exhibit, American Institute of Aeronautics and Astronautic s, Reno,NV,U.S.A., 1997. https://doi.org/10.2514/6.1997-176.

[17] S. Wirogo, S. Srirambhatla, An Eulerian Method to Calculate th e Collection Efficiency on two and Three Dimensional Bodies, i n: 41st Aerospace Sciences Meeting and Exhibit, American Instit ute of Aeronautics and Astronautics, Reno, Nevada, 2003. https:/ /doi.org/10.2514/6.2003-1073.

[18] S.K. Jung, R.S. Myong, A second-order positivity-preserving finit e volume upwind scheme for air-mixed droplet flow in atmosph eric icing, Computers & Fluids. 86 (2013) 459–469. https://doi.or g/10.1016/j.compfluid.2013.08.001.

[19] Y. Bourgault, H. Beaugendre, W.G. Habashi, Development of a Shallow-Water Icing Model in FENSAP-ICE, J Aircraft. 37 (200 0) 640–646. https://doi.org/10.2514/2.2646.

[20] Ž. Tuković, H. Jasak, A moving mesh finite volume interface tr acking method for surface tension dominated interfacial fluid flo w, Comput Fluids. 55 (2012) 70–84. https://doi.org/10.1016/j.com pfluid.2011.11.003.

[21] M. Rauter, Ž. Tuković, A finite area scheme for shallow granula r flows on three-dimensional surfaces, Computers & Fluids. 166 (2018) 184–199. https://doi.org/10.1016/j.compfluid.2018.02.017.

[22] W. Wright, Validation Results for LEWICE 3.0, in: 43rd AIAA Aerospace Sciences Meeting and Exhibit, American Institute of Aeronautics and Astronautics, Reno, Nevada, 2005. https://doi.org /10.2514/6.2005-1243.

UAV Icing: Experimental Analysis of Icing on a Rotor of a UAV

Nicolas C. Müller[1,2], Richard Hann[1,2]

[1] *Norwegian University of Science and Technology, NTNU, Trondheim, Norway*
[2] *UBIQ Aerospace AS, Trondheim, Norway*

nicolas.c.muller@ntnu.no, richard.hann@ntnu.no

Abstract— **Rotors are the most sensitive part of small multi-rotor uncrewed aerial vehicles (UAVs) to atmospheric in-flight icing. Ice accumulation on a rotor can reduce the ability of the rotor to produce lift and thrust and increase the required propulsion power. If the required propulsion power exceeds the capabilities of the powertrain, the UAV might lose its ability to maintain its altitude and stability, which can have catastrophic consequences. In this study, the performance of a UAV rotor is analysed in horizontal flight and vertical climb in icing conditions. An icing wind tunnel was used to test a 381 mm UAV rotor in icing conditions at two temperatures of −5 °C and −10 °C. The impact of icing on the propeller is examined by measuring and analysing the rotor's change in thrust and torque. A high-speed camera is used to record and observe the dynamic ice accretion, and a photogrammetry-based method is used to extract the ice shape at the end of the ice accretion process. This study reveals that the propeller responds differently to ice accretion in thrust and lift configurations. In the vertical lift configuration, the rotor's lift stayed constant in icing after an initial drop of 20%, while in the horizontal rotor configuration, the rotor's thrust declined continuously during the ice accretion process. The rotor's torque has increased linearly with the ice accretion time in both configurations. This is done to assess the influence of icing on the rotor of a multi-rotor UAV, to understand the risk of icing for a UAV. This data can be used to detect the existence of ice on the UAV based on its rotors, and to evaluate mitigation methods for icing on UAV rotors.**

Keywords— ***UAV, Propeller, Inflight-Icing, Rotor, Atmospheric Icing, Wind tunnel***

I. INTRODUCTION

The capabilities of uncrewed aerial vehicles (UAVs), also called remotely piloted vehicles (RPAS) or unmanned aerial systems (UAS) have developed a lot in the last few years, which has led to an increased use of UAVs in commercial and military applications [1,2]. With these increased applications, the operational availability of UAV services becomes more critical. One significant limitation to the use of UAVs is adverse weather. One especially critical adverse weather condition is atmospheric in-flight icing. [3] This describes the condition, in which liquid water exists in clouds at temperatures below the freezing point. When flying through those conditions, the droplets can freeze upon contact with the aircraft, leading to ice accumulations [3].

This ice accumulation can have severe implications on the aerodynamic performance of UAVs by increasing the drag and the weight of the UAV while at the same time reducing the maximum lift [4]. This can lead to the loss of control of the UAV. The ice accretion is especially critical for UAVs, as the ice accumulation is faster at the lower Reynolds numbers common with UAVs [5,6].

One part of a UAV that is especially sensitive to icing are the propellers or rotors of the UAV[7]. This sensitivity is due to their higher velocity through the air, and the smaller chord length, which enables a significantly faster ice accumulation compared to wing. This ice accumulation can lead to the loss of thrust within a minute [8]. For multi-rotor UAVs, this loss of thrust additionally leads to a loss of control since the thrust generated by the rotors is directly used to lift the UAV and control the UAV [9].

The flow conditions around the rotor of a multi-rotor UAV are dependent on the current flight state. Three different flight conditions for rotary wing aircraft can be identified: hover, stationary climb, and forward flight [10]. In hover, the forward flight velocity of the aircraft is zero, in which case, the flow of the air through the rotors is only the induced airflow generated by the rotors to create lift. In a stationary climb, an additional velocity component is created by the climbing speed of the UAV. This increases the airflow through the rotor. If the UAV is in forward flight, the airflow through the rotor has a component perpendicular to the rotation axis. This flow component leads to flow conditions, which change during the rotation of the rotor dependent on the position of the rotor blade relative to the direction of the flight of the UAV [11, 12].

The young field of icing on UAVs has initially focussed on icing analysing the ice accretion on the wings of UAVs[6]. It was observed that a reduction in the Reynolds number leads to an increase in the water collection efficiency on the wings, which increases the performance degradation of wings in icing conditions if the sizes of the test object decrease [13].

Experiments on the propellers of UAVs have shown that ice accretion on the propeller can lead to a very rapid decrease in its performance, especially in glaze icing conditions, which occur at high temperatures and are classified by complex ice shapes [14].

Research has shown that the degree of performance loss of UAV propellers in icing conditions strongly depends on the ice shedding. Ice shedding occurs when the ice breaks of the propeller due to centrifugal forces, which leads to a recovery of the performance. Ice shedding occurs after longer ice accretion at colder temperatures. and thus, the performance degradation on UAV propellers is more substantial at lower temperatures, as ice shedding occurs later and is more violent at those temperatures [15].

The performance degradation of the propeller is dependent on the liquid water content (LWC) and the mean volume diameter (MVD) of the droplets in the air. Both factors affect the ice thickness and the ice shapes.[16].

This paper aims to analyse the influence of the flight direction of the multi-rotor UAV on the ice accretion on the rotor. To evaluate the difference in the performance of the

rotor, the ice accretion on the rotor is tested both in horizontal flight conditions, in which the rotation axis is perpendicular to the airflow and in a vertical climb configuration, in which the rotation axis is aligned with the rotation of the rotor.

This work helps to define the influence of icing on small multi-rotor UAVs in different flight conditions. Understanding the ice accretion is important to evaluate the behaviour of UAV rotors in icing conditions and develop numerical methods to predict the ice accretion on the rotors of UAVs. Understanding the ice accretion on UAV rotors is a key step to developing UAVs that can operate in icing conditions, and expand the use of UAVs in cold climates.

II. METHODS

A. Icing wind tunnel

The experiments were performed at the VTT icing wind tunnel in Helsinki [17]. The tunnel can deliver wind speeds up to 50 m/s and temperatures down to −25 °C.

A Flight Stand 1580 dynamometer was used to measure thrust and lift of the propeller [18]. The force measurement unit was placed in the centre of the test section. It was mounted in two different orientations, as can be seen in Fig. 1. The orientations were used to emulate the conditions experienced in different flight situations of a multirotor UAV. The thrust position, with the rotation axis aligned with the flow is representative of a vertical climb of the UAV, and the lift configuration with the rotation axis perpendicular to the flow represents the horizontal flight of the UAV.
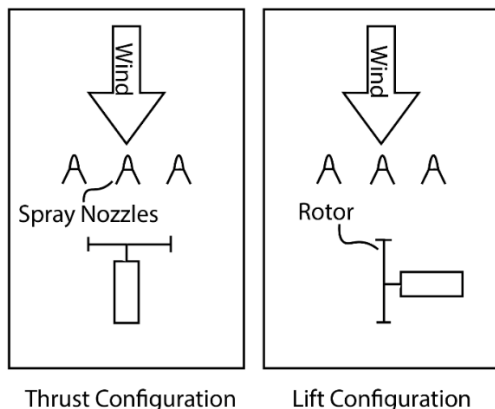
Fig. 1 The propeller test setup in the wind tunnel in the lift configuration.

A Phantom Veo710L high-speed camera was used to record phase-locked images of the rotor during the ice accretion process [19]. The camera was synchronised by a laser beam that was triggered by the rotating rotor blades passing through the beam. An Arduino Uno digitised this signal and to trigger the high-speed camera and 4 MultiLED QT lights that were used as illumination, which are also controlled by the Arduino.

The test was performed with constant rotation rate and constant thrust modes. Testing with a constant rotation rate enables easier comparison of the experiments with numerical simulations, while a constant thrust experiments are more consistent with real fighting conditions. Both modes were controlled by a custom JavaScript code running inside the RC-Benchmark software that controls the test stand.

After the experiment, for selected icing runs, a 3D scan of the ice shape was performed using photogrammetry based on the process indicated in [20]. For this, the propeller was removed from the test stand in the icing wind tunnel. The ice mass on the propeller was measured, after which the propeller was painted with white acrylic paint. The rotor was placed in a freezer at −20 °C for the paint to freeze. The propeller was now placed on a turntable, and 48 evenly spaced pictures were taken of the propeller with a Sony A6400 camera using a SEL5018 Lens. The images were loaded into the photogrammetry software Agisoft Metashape, and a 3D geometry was created. This 3D geometry was then analysed using Tecplot to extract the cross sections of the ice shape. Cross sections were extracted at 75% of the radius of the rotor to compare the results of different rotor tests.

B. Test Conditions

The experiment was performed at two different temperatures, −5 °C and −10 °C. In total 25 test runs were performed in horizontal and vertical configuration. Further variations were the used rotation rate and the LWC. Two LWCs were used, one at 0.6 g/m³ and one at 1.8 g/m³. The LWC was calibrated at the end of the wind tunnel at 25 m/s airspeed using a round cylinder [21]. The LWC was corrected by correlating the airspeed used for the calibration and the airspeed used for testing.

TABLE I. TEST CONDITIONS

Element	Range	Unit
Temperature	−5, −10	°C
MVD	22.7	µm
LWC	0.56, 1.80	g/m³
Velocity	6	m/s
Rotation Rate	4400-5000	rpm
Duration	120-240	s
Lift	10	N

C. Test objects.

The experiments were performed on a 15x5 rotor manufactured and sold by Mejzlik Propellers sro. [22]. The diameter of the rotor is 15 inches or 381 mm. The rotor is a representative rotor size for multirotor UAVs with a weight of about 3-5 kg.

III. RESULTS

Figure 2 shows the results of the tests performed at −5 °C. Three different test results are plotted. A constant rotation rate test at 5000 rpm in thrust and lift configuration, as well as a constant rotation test at 4400 rpm test in lift configuration. For both tests in lift configuration, the recorded thrust shows a slight decline from 11 N to 9 N, after which the measured thrust stays stable. The experiment in thrust configuration shows the same initial thrust decline, followed by a gradual reduction in thrust, which continues until the test stopped after 90 s. The recorded torque during all the experiments is increasing linearly during the initial ice accretion phase. The gradient of the torque increase is similar for both the 5000 rpm runs and lower for the 4400 rpm experiment. The test at 5000 rpm in thrust configuration was stopped after 80 s

because the current drawn by the motor exceeded the rating of the speed controller.
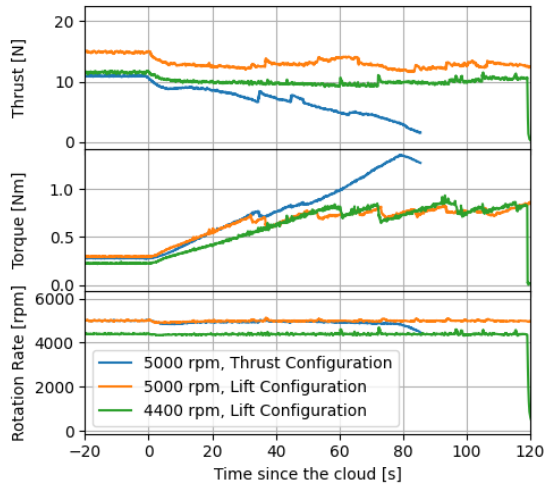
In Fig. 3, the thrust and torque development for the experiments performed at −10 °C are shown. Here, a constant rotation test in lift configuration is performed at 4400 rpm and in thrust configuration at 5000 rpm. A constant thrust test at 10 N of thrust in lift configuration is also shown.

Both the constant thrust run and the constant rotation rate run in the lift condition experiment show a constant thrust of 10 N during the experiment. The thrust configuration test shows a gradual decline in thrust, which is then followed by a sudden increase in thrust and subsequent decrease. The sudden thrust increases correlate to a visual loss of ice on the rotor (ice shedding), observed from high-speed camera footage. The constant thrust case shows a variation in the rotation rate, which correlates with the chances in the torque. The efficiency of the rotor in the thrust case decreased by 300%.

The torque increased at similar gradients for all the experiments, and after 50 seconds, all experiments showed frequent sudden reductions in the torque, again aligned with changes in thrust at the same time and loss of ice on the high-speed camera. This is again explained by ice shedding.
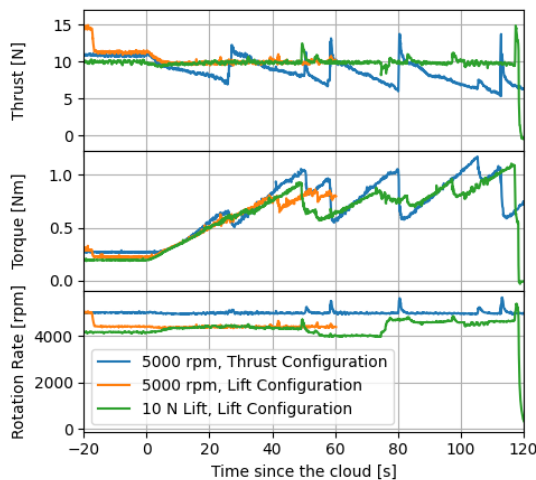
Fig. 3   *Thrust and torque development for the experiment at 1.5 g/m³ at −10 °C.*

In Fig. 4, the ice on the propeller is shown before and after the ice-shedding event after 58 seconds of ice accretion in the 5000 rpm thrust configuration case. A large portion of the ice on the rotor is missing from the after picture.

a)

b)
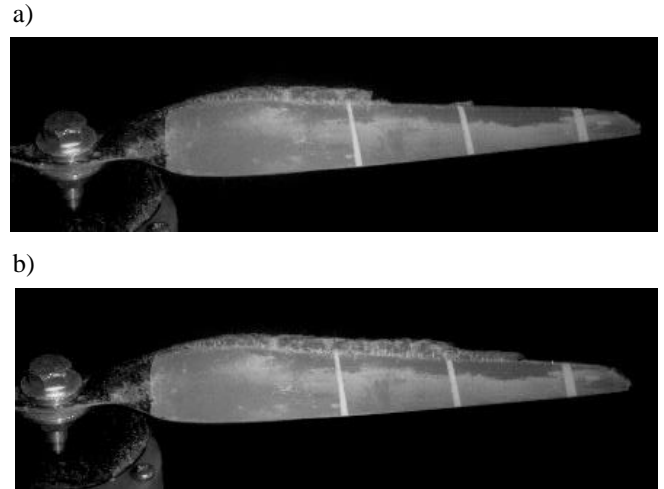
Fig. 4   *Ice on the propeller a) before and b) after an ice shedding event with a LWC of 1.5 g/m³ at −10 °C with a rotation rate of 5000 rpm and in thrust configuration.*

The change in the performance of the rotor in thrust configuration for different LWCs can be seen in Fig. 5. Here, it is shown that the gradient of the performance degradation decreases with a reduced LWC. The reduction in thrust occurs at a similar gradient compared to the higher LWC, while the increase in torque of the rotor happens at a lower rate at the lower LWC. The observed ice-shedding events are also not as significant as the ice-shedding events observed at the higher LWC. The thrust and torque values reached before the ice shedding events start are similar to those values measured with the higher LWC. This behaviour leads to a lower mean thrust value and a higher torque value.
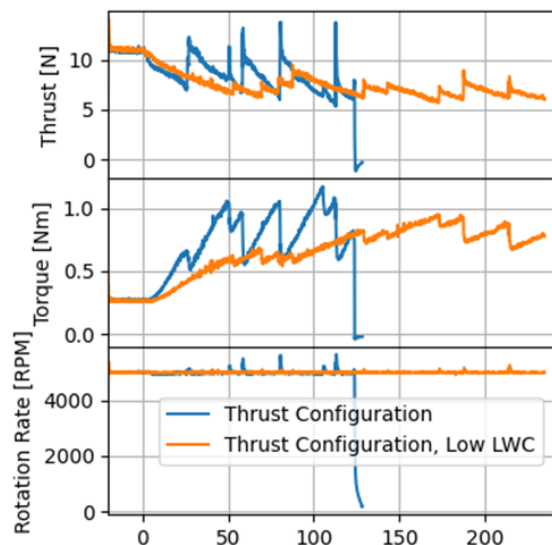
Fig. 5   *Thrust and torque development for the experiment at 1.5 g/m³ at −5 °C.*

In Fig. 6, the first ice shedding event on a blade for the experiments shown in Fig. 5 after 30 s for the high LWC and 60 s at the low LWC. At the higher LWC, more ice has accumulated on the propeller prior to the ice-shedding event. The ice shape that has formed is more complex, with a development of feathers and lobster tails, while at the low LWC, the ice shape does show less variance.
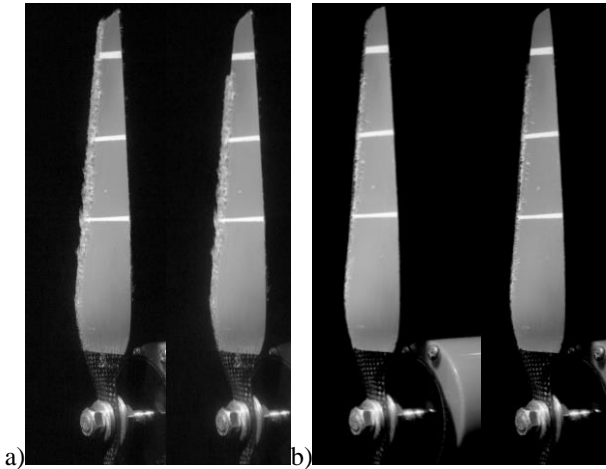
Fig. 6   First Ice shedding on a blade for the experiment at 1.5 g/m³ at -5 °C in thrust configuration at a) high or b) low LWC. One picture is before, and one after the ice-shedding.

The dependency of the performance degradation on the thrust and torque values for the lift configuration is shown in Fig. 7. This plot shows the thrust and torque values for an experiment performed at 4400 rpm. A third line is displayed, which shows the measured thrust and torque for the low LWC, where the time axis is reduced by the difference in the LWC, thus indicating the performance relative to the total amount of water collected by the rotor. This line is very close to the performance degradation by the high LWC, indicating that the performance degradation of the rotor is most strongly associated with the total amount of water collected.
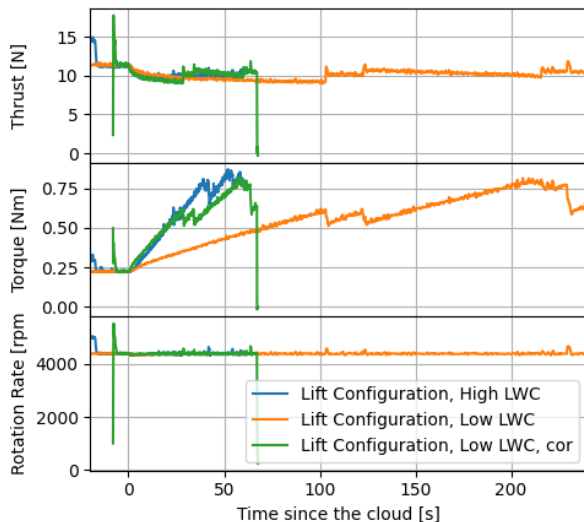
Fig. 7   Performance degradation in lift configuration at -10 °C, with a LWC of 0.56 g/m³ and 1.8 g/m.³.

In Fig. 8, the ice shapes, as captured by the photogrammetry method, are shown for the lift configuration at 4400 rpm. Tyhe ice shape at −5 °C is significantly more complex than at −10 °C. It displays multiple small features that change in chordwise and radial directions. The ice shape at −10 °C is more uniform and displays only a slight radial variation, a few small scale features. The difference in the ice shapes can also be seen on the cross-section taken at 75% of the radius. The ice shape at −5 °C has more minor variations resembling horns, representing the small radiuswise features. The ice shape at -10 °C is a more uniform ice block. Additionally, the icing extend is smaller at −10 °C on the top and bottom surfaces.
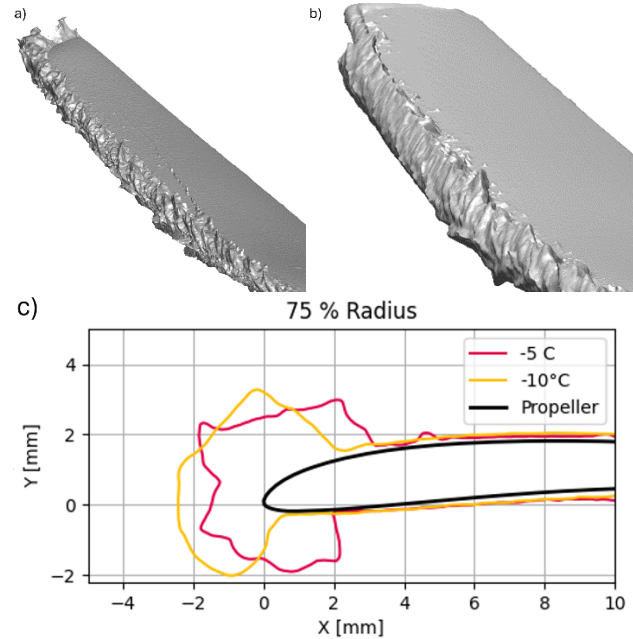
Fig. 8   Ice shapes at 4400 rpm and in lift configuration after 60 s of ice accretion at the low LWC a) at −5 °C, b) at −10 °C, and c) a cross section.

IV. DISCUSSION

One of the considerable challenges of testing the performance of rotors in an IWT is the possible blockage of the wind tunnel by the rotor. In this experiment, diameter of the rotor is 54% of the width of the testing section, which means that the performance of the rotor affected by the rotor, compared to the free stream. The restricted test section size will affect both configurations, where the lift configuration is likely more affected [23].

The work aimed to test the rotor in comparable conditions, both in thrust and lift configurations. Therefore, the rotation rate was fixed to achieve 10 N of thrust in both configurations. This increase in the rotation rate for the thrust configuration seems to have increased the ice accretion rate on the rotor, which leads to a larger performance degradation. This is especially visible in the change in the torque of the rotor.

The icing has only a very limited influence on the thrust of the rotors in lift configuration. This effect could be caused by multiple reasons, one being the difference in the local angle of attack of the rotor blades relative to the inflow, which leads to different impingement pattern and thus ice shapes. Especially the large ice accretion on the trailing edge could increase the lift the rotor is generating on the cost of increased drag. The

difference could also be due to the reduced ice accretion on the lift configuration rotor close to the tip. If less ice is accumulated on the tip, this could reduce the impact the icing has on the thrust generated by the rotor. This behaviour is consistent with findings in other research [9,10], but it could be caused by the proximity of the walls of the wind tunnel. The proximity of the walls could influence the flow patterns around the rotor, especially by redirecting the wake of the rotor to remain inside the wind tunnel confinement. This could increase the measured lift compared to a free stream situation. Further research needs to be done, to evaluate if the reason for this behaviour is due to the ice accumulation, or caused by the experimental setup.

A second observation of the experiments is that the speed of the performance degradation is proportional to the LWC at $-10\,°C$. This is significant for the developments of models for the behaviour of UAV rotors in icing conditions. This is likely caused by a very high freezing fraction on the rotor, even at the high LWC condition, and thus might not be accurate for very high LWCs or high temperatures.

The rotor in the thrust condition at $-5\,°C$ has less severe ice-shedding events at low LWC compared to the high LWC. They occur earlier in the ice accretion process, but once the ice shedding has led to a steady performance level , the performance degradation is similar to the high LWC. The difference could be caused by a change from a glaze ice to a mixed ice condition. A different ice regime could lead to an ice with less cohesion, and the voids in the ice shape would enable the more frequent shedding of small ice blocks. This would be caused by the increase in ice adhesion at lower temperatures with a simultaneous decrease in cohesion. This hypothesis is supported by the ice shapes observed in the high-speed camera images during the ice accretion process, which show different ice morphologies at the first ice shedding.

V. Conclusions

Icing on the rotors of UAVs is a significant issue that must be addressed to operate them safely in icing conditions. The influence of the ice accumulation on the aerodynamic performance is such that the power required to run the propeller may increase by more than 300%. Thus, a safe flight of the UAV is not be guaranteed if a UAV enters icing conditions. The experiments have shown a significant difference between the performance degradation seen in a lift or a thrust configuration, where in a lift condition the thrust generated by the rotor stays rather constant. In a thrust configuration the thrust of the rotor will decrease during the ice accretion. Significant areas of research for future evaluation are the ice-shedding behaviour and its influence on the rotor performance, as well as the numerical and experimental analysis of the effects of the wind tunnel walls on the ice accumulation on UAVs to verify the findings of this work.

References

[1] Shakhatreh, H.; Sawalmeh, A.H.; Al-Fuqaha, A.; Dou, Z.; Almaita, E.; Khalil, I.; Othman, N.S.; Khreishah, A.; Guizani, M. 486 Unmanned aerial vehicles (UAVs): A survey on civil applications and key research challenges. Ieee Access 2019

[2] Siquig, R. Impact of Icing on Unmanned Aerial Vehicle (UAV) Operations; Naval Environmental Prediction Research Facility: Monterey, CA, USA, 1990.

[3] Cao, Y.; Tan, W.; Wu, Z. Aircraft icing: An ongoing threat to aviation safety. Aerospace Science and Technology, 2018

[4] Bragg, M., Broeren, A., and Blumenthal, L., "Iced-airfoil aerodynamics," Progress in Aerospace Sciences, Vol. 41, No. 5, p. 323–362, 2005

[5] Szilder, K. and Yuan, W. In-flight icing on unmanned aerial vehicle and its aerodynamic penalties. In Proceedings of the Progress in 497 Flight Physics, Vol. 9, pp. 173–18, 2017

[6] Hann, R., Johansen, T.A. Unsettled Topics in Unmanned Aerial Vehicle Icing. SAE International, SAE EDGE Research Report EPR2020008, 2020

[7] Müller, N.C.; Hann, R., UAV Icing: A Performance Model for a UAV Propeller in Icing Conditions. In AIAA AVIATION Forum; AIAA, 2022

[8] Kozomara, D.; Neubauer, T.; Puffing, R.; Bednar, I.; Breitfuss, W. Experimental investigation on the effects of icing on multicopter UAS operation. In AIAA AVIATION FORUM 2021; AIAA, 2021

[9] Yan, S., Opazo, T., Palacios, J., Langelaan, J. W., & Germain, L. D. "Experimental evaluation of multi-rotor UAV operation under icing conditions." Annual Forum Proceedings-AHS International. Vol. 2018. American Helicopter Society, 2018

[10] Seddon, J.n M., and Simon N.. Basic helicopter aerodynamics. John Wiley & Sons, 2011

[11] Conlisk, A. T. "Modern helicopter rotor aerodynamics." Progress in aerospace sciences Volume 37, Issue 5 Pages 419-476, 2001

[12] Hann, R. & Johansen, T. A. UAV Icing: The Influence of Airspeed and Chord Length on Performance Degradation. Aircraft Engineering and Aerospace Technology 93, 832–841. ISSN: 1748-8842, 1748-8842, 2021

[13] Liu, Y., Li, L., Chen, W., Tian, W., and Hu, H., "An experimental study on the aerodynamic performance degradation of a UAS propeller model induced by ice accretion process," Experimental Thermal and Fluid Science, Vol. 102, 2019

[14] Müller, N.C.; Hann, R., UAV Icing: A Performance Model for a UAV Propeller in Icing Conditions. In AIAA AVIATION 2022 Forum; AIAA, 2022

[15] Müller, N. C., and Hann, R., "UAV Icing: 3D simulations of propeller icing effects and anti-icing heat loads" SAE Technical Paper 2023-01-1383, 2023,

[16] Tiihonen, M.; Jokela, T.; Makkonen, L.; Bluemink, G.J. VTT icing wind tunnel 2.0. In Proceedings of the Winterwind International Wind Energy Conference, 2016

[17] 1580 Test Stand Tyto Robotics. [Online]. Available: https://www.tytorobotics.com/products/series-1580-test-stand-bundle, Accessed 9.4.2024

[18] Phantom HighSpeed, VEO710L. [Online]. Available: https://phantomhighspeed.my.site.com/PhantomCommunity/s/detail/a1p3m000003lj4dAAA Accessed 9.4.2024

[19] Hann, R., Müller, N., Lindner, M., and Wallisch, J., "UAV Icing: Experimental Validation Data for Predicting ice Shapes at Low Reynolds Numbers," SAE Technical Paper 2023-01-1372, 2023

[20] SAE International, "ARP5905 Calibration and Acceptance of Icing Wind Tunnels," Aerospace Recommended Practice ARP5905, 2015

[21] Mejzlik Shop, Propeller 15x5 CCW 2B MC. [Online]. Available: thttps://shop.mejzlik.eu/propeller-15x5-ccw-2b-mc/ Accessed 9.4.2024

[22] Ghirardelli, M.; Kral, S.T.; Müller, N.C.; Hann, R.; Cheynet, E.; Reuder, J. Flow Structure around a Multicopter Drone: A Computational Fluid Dynamics Analysis for Sensor Placement Considerations. Drones 2023

In-Situ Cloud Particle Measurements on an UAV

Ville A. Kaikkonen[1], Eero O. Molkoselkä[2], Harri J. Juttula[1], Anssi J. Mäkynen[2]

[1] Unit of Measurement Technologies, University of Oulu, Finland
[2] Optoelectronics and Measurement Techniques Research Unit, University of Oulu, Finland

ville.kaikkonen@oulu.fi, eero.molkoselka@oulu.fi, harri.juttula@oulu.fi, anssi.makynen@oulu.fi

Abstract— **Cloud particle measurements have been typically carried out with specialized manned aircraft, limiting the measurement opportunities only for those parties having large enough resources. Hence, new tools are being developed to be used on small-scale unmanned aerial vehicles (UAVs) to make the measurements available for a larger user group and to increase the amount of cloud particle data collected around the globe. Lensless digital holographic imaging enables fast sampling rates together with lightweight construction, making it an appealing design choice for cloud particle sensor implementation on small-scale UAVs. The relative low air speeds of the small-scale UAVs also enable a dense spatial sampling of clouds. In this paper, we present a prototype of an UAV-mounted cloud particle sensor and results from the first test flights in varying weather conditions flown in 2023 on Muonio, Finland. With the sensor, cloud particles in the size range from 5 μm to 1 mm can be imaged and measured. Result presented are from the first flight campaign in September 2024 from Muonio, Finland. The flights were done using an X-UAV Talon UAV, which could perform typically 30 min flights and the maximum altitudes reached were 2 km ASL. Cloud particle measurement using the UAV cloud particle sensor from a cloud event with changing phase from liquid to ice is presented and discussed.**

Keywords— ***Unmanned aerial vehicle, cloud microphysics, digital holography, atmospheric icing, liquid water content, particle size distribution***

I. INTRODUCTION

Low-level clouds play an important part in Earth's radiation balance and there is still large uncertainty on the magnitude of their effect on global warming, and new methods are needed to make more precise climate models [1]. On the other hand, low level clouds and fog affect daily many human traffic by causing low visibilities and during cold weather conditions they also cause atmospheric icing affecting renewable energy production and UAV aviation. Additionally, in densely populated areas, the traditional, high cost and complex, methods to observe cloud properties using manned airplanes and helicopters are limited, and hence balloon-borne measurements and devices to measure cloud properties using small-scale UAVs have been demonstrated [2],[3].

The UAV cloud particle sensor developed at the University of Oulu is a standalone measurement system designed to be used with small-scale UAVs. It consists of a digital holographic imaging sensor, onboard control computer (Raspberry Pi 4 model B), a removable SSD drive and a battery. The computer controls the hologram recording and saves the captured holograms to the onboard SSD, which is to be removed and the data to be post processed after the landing.

In this article, we present the use of a novel, lightweight sensor for measurement of cloud particles in mixed-phase clouds.

II. MATERIALS AND METHODS

The measurement system consisted of a holographic imaging probe and its control hardware and software (University of Oulu) and of an UAV plane (Finnish Meteorological Institute). Next, the cloud particle measurement system is presented.

A. UAV Cloud Particle Sensor

The holographic image sensor used to sample cloud particles is based on in-line holographic imaging. The in-line geometry is simplest realisation of the holographic imaging, where only a monochromatic light source and a camera sensor are needed as main parts. The advantage of holographic imaging is the possibility to construct imaging devices without any, often heavy, optics. The simplicity of the technology also makes it possible to construct robust, lightweight imaging devices.

The sensor has an open fork-style structure, where the cloud particles move between the laser and camera in an open space with the airflow. When the particles have travelled inside the laser cone, they scatter the light forward and form a hologram via interference of light on the camera sensor Fig. 1. The movement of the particles in the hologram are frozen by operating the laser in pulsed mode. The camera sensor outputs digitized grayscale holograms, from which shadow images of cloud particles and other airborne particles can be generated via back propagation of the captured light field (hologram). The properties of clouds are then calculated based on these individual particle shadow images on a known measurement volume in respect to time. The image information enables image-based detection of the cloud-phase (i.e. liquid, ice or mixed).
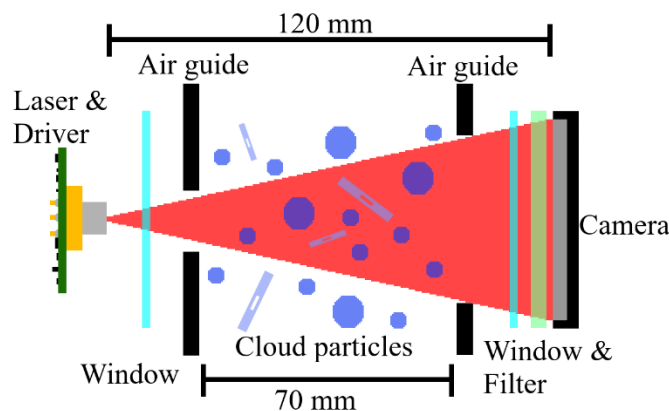
Fig. 1 An illustration of the holographic imaging geometry including the main dimensions and optical components. The cloud particle sizes are exaggerated for better visual access.

The holograms are exposed using a pulsed 660 nm center-wavelength laser diode as the point-like light source, the pulse length used was 25 ns. The holograms are digitized using a grayscale USB3-camera having a 12-megapixel resolution (Sony IMX304). The sampling volume recorded in a single hologram is 2 cm³, and maximum stable sampling rate has been found to be 10 Hz, resulting in a sampling rate of 20 cm³/s.

The sensor head presented in this work was designed to operate in in-situ measurement liquid clouds, hence it has low heating power (6 W per side) in the laser and camera housings, the heating is only to prevent condensation on the protective windows of the sensor when flying in warm clouds. It would be quite straightforward to increase the heating power of the sensor heads to meet power levels required for anti-icing operation, but then the battery energy capacities and thermal balancing needs more attention than with lower power levels.

After considering various lightweight single-board computers, the Raspberry Pi 4 was chosen as the on-board computer due to its USB3 chipset, which allows for the connection of both a high-speed camera and a Solid State Drive (SSD). A 1 TB SSD was selected to ensure sufficient storage capacity with good amount of headroom for recording holograms during an estimated 30-minute flight. An individual battery for the measurement system was used despite the increased total weight, as running the measurement from the UAV batteries might cause unwanted electrical behaviour due to high current peaks caused by the UAV propeller motor.

The measurement software is coded in Python. This software adjusts the camera settings for the measurement, initiates the image streaming, and stores the images in the BMP (bitmap) file format on the SSD [4]. A more detailed description of the sensor system can be found in [5].

B. Hologram reconstruction

The ICEMET Server, a rapid digital hologram processing and cloud particle analysis software, is developed using C++ and OpenCL. For the hologram analysis, version 1.14.0 of the software was employed. The ICEMET Server leverages GPGPU (General-Purpose Computing on Graphics Processing Units) for the resource-intensive task of hologram processing, necessitating a computer equipped with a graphics card. In this instance, the NVIDIA GeForce RTX 3080 was utilized.

In the first phase of the hologram processing, the background of the holograms are subtracted. This process removes all stationary objects from the hologram, such as particles stuck on the protective windows. Next, the pre-processed hologram is reconstructed in to multiple slices along the depth direction using angular spectrum light field propagation [7]. After this, the cloud particles are autofocused and binarized for size and shape feature extraction, and individual particle data is saved into a database together with the particle shadow images.

C. Particle size calibration

The UAV cloud particle sensor underwent calibration using monodisperse glass spheres (Whitehouse Scientific Ltd) spanning a size range from 5 µm to 156 µm. All the glass spheres, except for the 5 µm ones, were NIST-traceable. These glass beads were introduced into the measurement volume using a custom-made manual dispenser. The threshold employed during the particle image binarization phase in the analysis software was adjusted based on the calibration results. In Figure 2, we present a comparison of the measured median diameter values obtained by the UAV cloud particle sensor with the manufacturer-provided median values, along with their associated uncertainties.
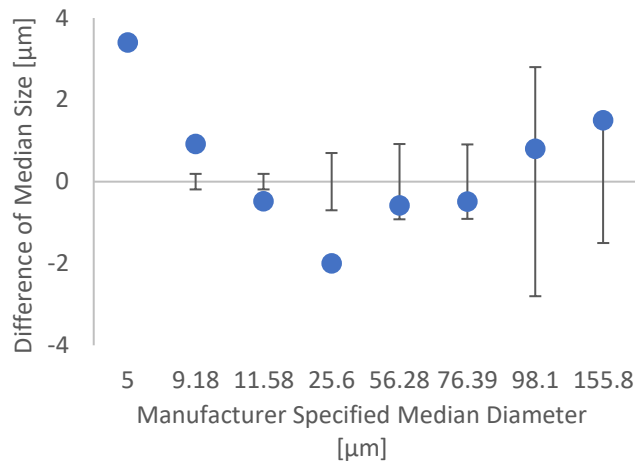
Fig. 2   A comparison of the median sizes of different monodisperse glass sphere samples, as measured by the manufacturer and the holographic cloud particle sensor. The manufacturer has specified 95% uncertainty limits for sizes ranging from 9.18 µm to 155.8 µm. These limits are shown as error bars for the individual sizes.

D. X-UAV Talon

As shown in Fig. 3, the X-UAV Talon, a fixed-wing UAV plane, was fitted with the UAV cloud particle sensor. The UAV can fly up to a weight of around 3 kg. It has a wingspan of 1718 mm and a body length of 1100 mm. When carrying an 800 g payload and maximum sized battery back, it can fly for approximately 20 to 30 minutes, depending on the batteries used. David Brus from the Finnish Meteorological Institute built and flew the UAV plane used in this flight campaign. The cloud measurement missions were carried out using an autopilot programmed with the ArduPilot software.

Fig. 3   Photo taken of the X-UAV Talon equipped with the UAV cloud particle sensor during the measurement campaign in Pallas.

III. Results

The first cloud in-situ measurements using the holographic sensor and the UAV were done in September 2023 in Muonio, Finland. In this paper, we present measurement results from a 20-minute flight made on 13th September. This flight started at 12:59 (UTC+00), take-off location and current weather conditions shown in Fig. 4. The flight took place near Pallasjärvi, the site co-ordinates are (68.02099611198969, 24.15342335823052), and the take-off altitude was 280 m ASL and temperature at the ground level +9°C.

The conditions for the flight were challenging, the harshest during the whole campaign week. We were under a raining cloud, and up in the cloud the temperature dropped below 0°C, causing condensation on the sensor's protective window surfaces. Nevertheless, we recorded cloud particle holograms during the approximately 1400 m ascent, corresponding altitude of 1650 m ASL before the heating capacity of the sensor heads was no longer enough to keep the sensors protective windows free from condensation at 13.07.31. The ambient temperature was measured to fell below 0°C at 13.06.40.

The sampling rate during this flight was 5.1 cm^3/s on average, the reason for lower than typical sampling was that just the SSD-drive used in this flight had a lower writing speed than the other two SSDs for an unknown reason. The writing speed was later tested, and similar behaviour was noted. It should be also noted, that in the data presented below are three periods where particle data is missing as raindrops had splashed on the protective windows. These splashes were detected in the hologram analysis phase and were marked and skipped in the analysis as unreliable frames. This is based on a rule that skips the holograms that have an unnaturally high number of detected objects on the hologram.

Despite the challenges with the SSD and the raindrops causing unwanted disturbance, the sampled data is unique in the way that it was the only measurement where could be seen the cloud phase transition from liquid to ice. Additionally, majority of the recorded ice crystals captured that week were captured during this flight.

Fig. 4   A frame capture from a video just after the take-off at 12:59 on Pallas, showing the rainy clouds and the X-UAV Talon on the left side.

A. Cloud particle data preparation

The results of the cloud particle analysis from this flight are presented in the Fig. 5. Even though the sensor can measure up to mm-size range particles, the upper limit on the liquid water content (LWC) and the median volume diameter (MVD) calculations is set to the commonly accepted cloud droplet largest size limit definition of 200 µm. The data presented is filtered so that the particle effective diameter is limited between 5 µm and 200 µm, and the ice crystals were filtered out based on roundness-filter (Heywood-criterion, upper limit of 1.2), some round ice crystals passed through the filter, but they were clearly a minority. Three different plots from the UAV cloud particle sensor data were made against to the time: droplet concentration, liquid water content and median volume diameter. In all these graphs a single sample point represents the data from one second sampling duration, corresponding on average to 5.1 cm^3 volume sampled per point. The last graph represents the flight altitude and ambient temperature measured using the flight controller data and external temperature and humidity sensor.

B. Cloud particle analysis results

From the three graphs, the different type of particles measured can be quite clearly distinguished. In the beginning, there are not too many particles measured, but the LWC and MVD have high values, caused mainly by the raindrops dropping through the measurement volume. Due to raindrops the MVD values are spread between 40 µm to 200 µm until the first cloud is reached approximately at 13:01:20 at altitude of approximately 600 m ASL, seen as the increase of droplet concentration together with a group of sampling points having a MVD just above 10 µm. Then at 13:02:32 a rain drop hits the protective windows and causes multiple holograms in a row to be discarded in the analysis software. After 40 s from the splash the window is again clean enough and a high LWC values are measured together with the MVD having value around 25 µm at altitude of approximately 1000 m ASL. The UAV passes again through a thin cloud layer around 1100 m ASL, but after that a thicker cloud layer approaches at approximately 1200 m ASL and the cloud continues continuously up to almost 1500 m ASL. In this cloud layer, a transition from liquid phase to mixed phase happens. The ambient temperature at the bottom of the cloud layer was measured to be +2°C and the temperature drops down to 0°C before reaching the top of this cloud layer. There were just a few individual crystals detected in the lower parts, but the ice crystal number increasing towards the top of this layer. After this thick cloud layer, in the last frames only ice crystals were measured until the condensation on the protective windows deteriorated the holograms and no more data could be retrieved from the rest of this flight.

The phase-changes were evaluated visually from the particle images, and marked as the yellow, green and blue bars on the graphs. A collection of cloud particle shadow images from the three different phases are presented in Fig. 6. As mentioned earlier, the sensor can measure also larger than 200 µm particles, the largest measured raindrop had a measured equivalent diameter of 0.77 mm, captured just after the take-off at 13:00:51 and the largest ice crystal had an equivalent diameter of 0.64 mm, captured 13:04:09 at altitude of just over 1100 m, shown in Fig. 7.
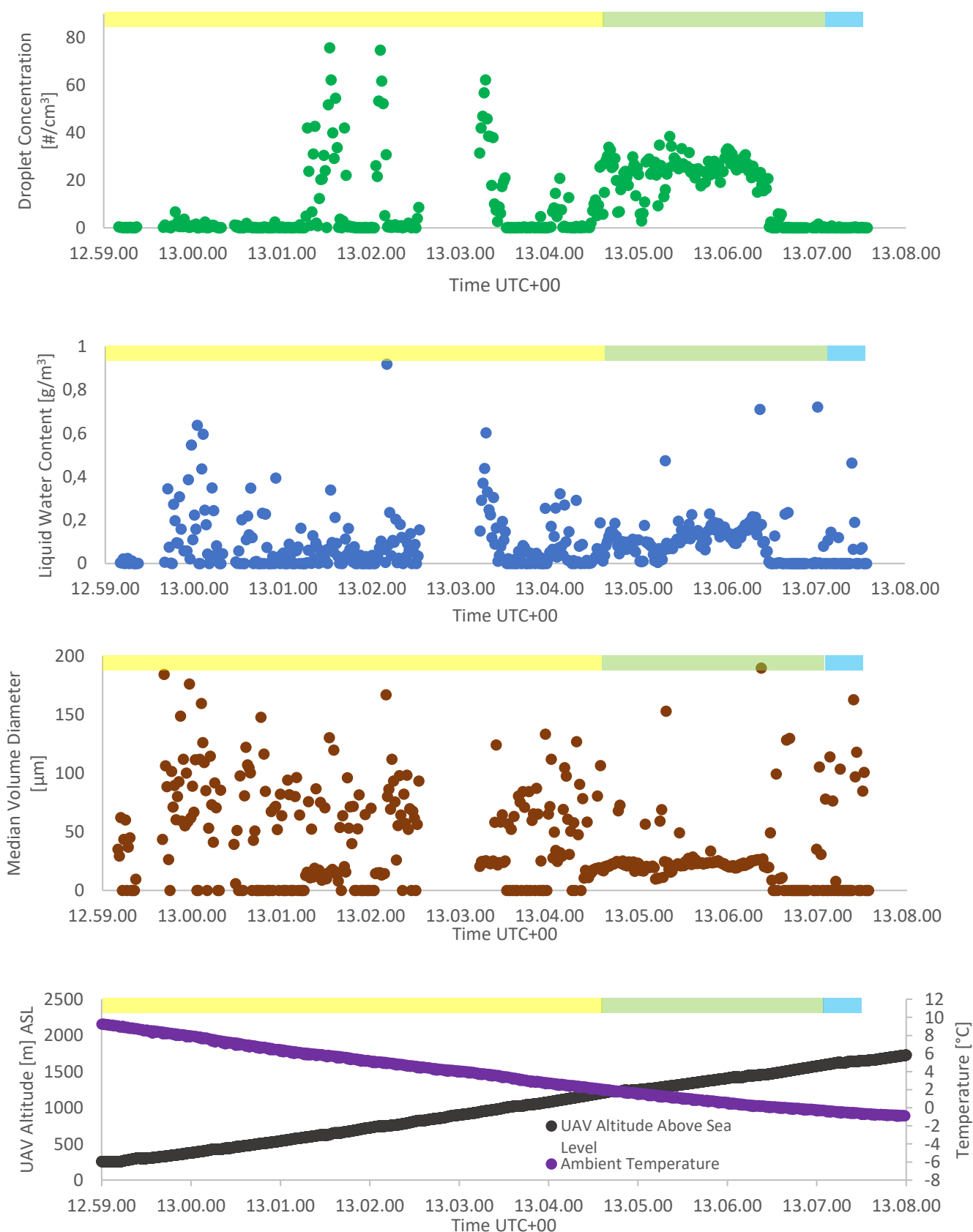
Fig. 5 The first three graphs present the measured droplet concentration, liquid water content and median volume diameter, plotted with one second resolution. At the last graph UAV altitude and ambient temperature measured with flight controller and a temperature sensor. The gaps in the droplet data points due to discarded holograms in the analysis phase. The colour-bars on the top of all the four graphs refer to visual classification based on the particle types in the sample points to three different cloud phases: liquid (yellow), mixed (green) and ice (blue).
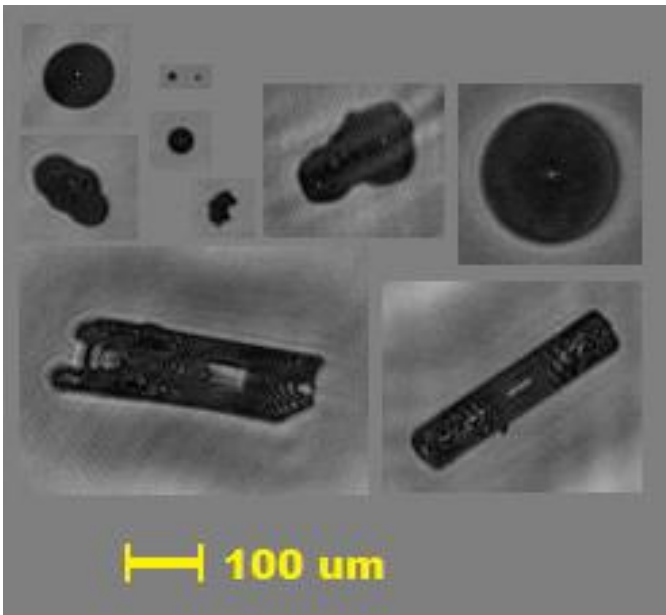
Fig. 6 Shadow image collage of different type of cloud particles, size ranges from 6 µm to 190 µm
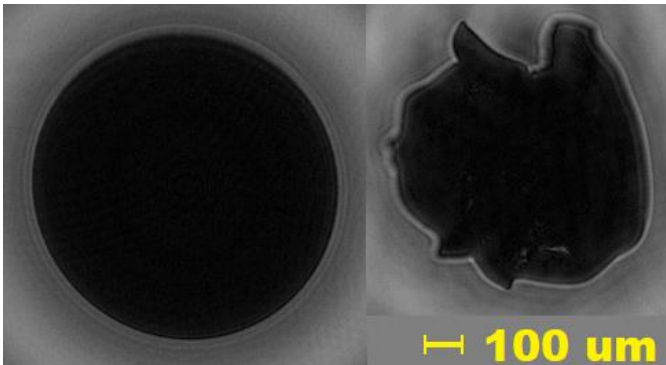
Fig. 7 The largest raindrop and ice crystal measured during the flight.

IV. CONCLUSIONS

A novel holographic cloud particle sensor was presented and results from a test flight in liquid, ice and mixed-phase conditions was presented. The results show the high potential of the sensor system to capture detailed and dense samples of cloud particles. Although the processing of the data is more computationally demanding than in light scattering cloud particle probes, there is an advantage for both visual inspection of the collected data, as well as possibility to utilize different type of image-based filtering and classification methods.

The resolving power of the measurement system could be improved by replacing the red laser diode with a suitable shorter wavelength laser diode, this would have a positive effect for the smaller particles located further away from the camera sensor. The UAV cloud particle sensor's sampling capability of warm liquid clouds has been demonstrated in previous studies, to make it suitable for measuring icing clouds, the system should be modified to have higher heating of the camera and laser housings. In future, automated particle image classification of liquid and ice particles will further broaden the applicability of this type of measurement system.

REFERENCES

[1] PCC: *Climate Change 2021: The Physical Science Basis. Contribution of Working Group I to the Sixth Assessment Report of the Intergovernmental Panel on Climate Change* [Masson-Delmotte, V., P. Zhai, A. Pirani, S.L. Connors, C. Péan, S. Berger, N. Caud, Y. Chen, L. Goldfarb, M.I. Gomis, M. Huang, K. Leitzell, E. Lonnoy, J.B.R. Matthews, T.K. Maycock, T. Waterfield, O. Yelekçi, R. Yu, and B. Zhou (eds.)]. Cambridge University Press, Cambridge, United Kingdom and New York, NY, USA, 2391 pp, 2021.

[2] Smith, Helen R., et al., "The Universal Cloud and Aerosol Sounding System (UCASS): a low-cost miniature optical particle counter for use in dropsonde or balloon-borne sounding systems." *Atmospheric Measurement Techniques*, vol 12.12, pp. 6579-6599, Dec. 2019.

[3] Ramelli, Fabiola, et al., "Using a holographic imager on a tethered balloon system for microphysical observations of boundary layer clouds." *Atmospheric Measurement Techniques*, vol. 13.2, pp. 925-939, Feb. 2020.

[4] (2024) GitHub [Online]. Available: https://github.com/molkoeero

[5] V. A. Kaikkonen, E. O. Molkoselkä, H. J. Juttula and A. J. Makynen, "UAV Cloud Particle Sensor," I2MTC 2024 - International Instrumentation and Measurement Technology Conference, accepted for presentation, May 20-23, 2024.

[6] J. P. Fugal, T. J. Schulz, and R. A. Shaw, "Practical methods for automated reconstruction and characterization of particles in digital in-line holograms," *Meas Sci Technol.*, vol. 20, no. 7, p. 075501, 2009

Technical Requirements for RPAS Operations in Cold Climates

Richard Hann[1,2], Kasper Trolle Borup[1]

[1] UBIQ Aerospace, Norway[1]
[2] Norwegian University of Science and Technology (NTNU), Department of Engineering Cybernetics, Norway

richard.hann@ubiqaerospace.com

Abstract— **Remotely piloted aerial systems (RPAS) face significant challenges from atmospheric in-flight icing, which can drastically impair their safety and functionality. The objective of this document is to describe the effects of icing on RPAS and to suggest comprehensive operational and technical requirements for the safe operations of RPAS in icing conditions. This holistic approach is designed to inform and guide aircraft designers, operators, and policymakers in addressing the challenges posed by icing in uncrewed aerial operations.**

Keywords— ***icing, ice protection systems, RPAS, UAV, UAS, drone, technical requirements, specifications, certification***

I. Introduction

Remotely piloted aerial systems (RPAS)[1], have become increasingly important for commercial and defence applications. A major concern for these aerial systems is atmospheric in-flight icing, a hazard encountered in environments with supercooled clouds or freezing precipitation. Flight in icing conditions presents a substantial safety hazard that limits the operational availability, flyability, range, and functionality of RPAS in cold weather [1].

Atmospheric in-flight icing is a meteorological phenomenon critical to safety and occurs when aircraft encounter supercooled liquid water in the atmosphere. This supercooled water, present as cloud droplets or precipitation (rain/drizzle), remains in a liquid state even below the freezing point. Upon colliding with an aircraft, these supercooled droplets freeze upon impingement. This leads to ice accretion on the aircraft's surfaces, building into various ice shapes. Atmospheric icing can occur globally, at any latitude, and at any time of the year – but is substantially more frequent at higher latitudes, in cold climate regions, and during cold seasons [2,3].

The accumulated ice can take several different ice shapes or ice morphologies, see examples in Fig. 1. Rime ice occurs at lower temperatures when droplets freeze instantly upon
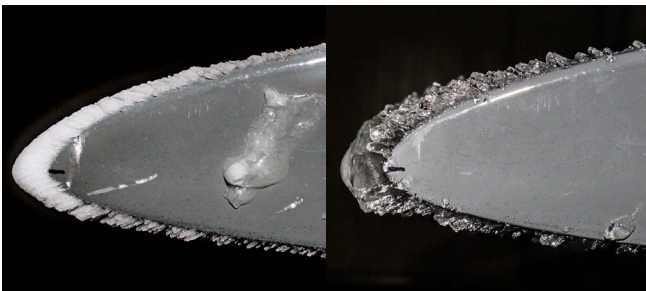
Figure 1: Rime ice (left) and glaze ice (right) ice shapes on a RPAS wing from icing wind tunnel experiments.

impact. Glaze ice forms in temperatures near freezing, where not all droplets freeze immediately. Mixed ice is a combination of glaze and rime ice, resulting from partial freezing of droplets and the formation of a liquid film.

II. Icing Effects

A growing body of research proves that icing severely impairs RPAS, e.g. [4–12]. Ice affects a larger number of components and, without suitable ice protection systems, can lead to a loss of the aircraft within minutes, see Tab 1.

A. Critical Effects

The following represents an assessment of negative icing effects on critical components, ranked by sensitiveness.

- **Airspeed sensor/pitot tube:** Ice accretion on the pitot tube, see Fig. 2, leads to blocked airspeed readings, resulting in erroneous data provided to the autopilot. This could cause inappropriate autopilot responses, such as stalls or nose-diving. Because of the exposed location and small size of the pressure holes, airspeed sensors are extremely sensitive to icing and can get blocked within seconds.

- **Propellers:** Icing on propellers rapidly and severely reduces thrust and increases power requirements. Experiments have shown a reduction of thrust by 75% percent and a power increase by 250% percent after only 100 seconds in moderate icing conditions [10]. Ice shedding due to centrifugal forces, see Fig. 3, can cause excessive vibrations and imbalances exceeding 10G, which can damage the propulsion system.
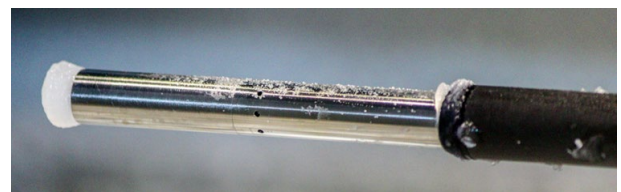
Figure 2: Ice accretion on a RPAS pitot tube.

Figure 3: Ice accretion on a RPAS propeller after several ice-shedding events, creating "steps" on the leading edge.

---

[1] Also called uncrewed aerial vehicles (UAVs), unmanned aerial vehicles, unmanned aerial systems (UAS), or drones.
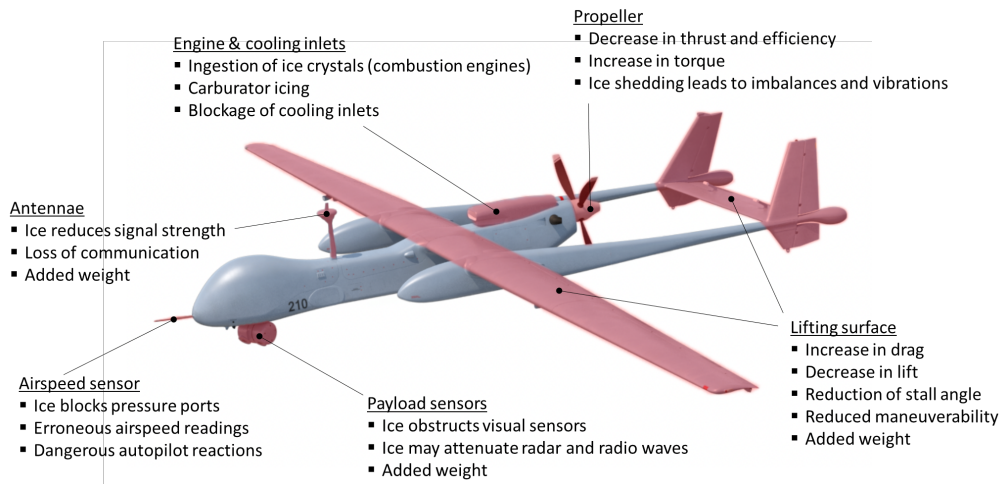
Figure 4: An overview of icing effects on different components of a typical tactical fixed-wing RPAS.

- **Lifting surfaces:** Ice accretion on wings and vertical/horizontal stabilizers alters the airfoil geometry and profile. This substantially increases drag, decreases lift, and reduces the stall margins. Simulations have shown a reduction of lift by 37%, an increase in drag by 107%, and a stall angle reduction of 4 degrees in severe icing conditions [7]. Also, ice reduces the effectiveness of control surfaces and thereby reduces manoeuvrability.

- **Autopilot:** Atmospheric icing can mislead the autopilot by altering the RPAS's flight performance, stability, and control. The autopilot system may struggle to accurately identify and adapt to these changes, increasing the risk of flight errors.

- **Antennae:** Icing on antennae can attenuate electro-magnetic and degrade signal quality and lead to communication loss. This is particularly critical for remotely-piloted RPAS, where reliable communication is essential for safe operation.

B. Secondary Effects

- **Carburetor icing:** In RPAS with piston engines, the carburetor can experience icing as the vaporization of fuel causes a drop in temperature, which, combined with high humidity, leads to ice formation inside the engine. This can obstruct the fuel/air mixture, resulting in engine power loss or shutdown.

- **Engine & cooling inlets:** Ice accretion on engine and cooling inlets can restrict critical airflow, leading to reduced combustion efficiency, potential engine stall, or mechanical failure due to overheating from inadequate heat dissipation.

- **Payload sensors:** Icing on payload sensors, such as cameras or radar domes, can obscure lenses and surfaces, leading to compromised data quality and reduced sensor accuracy.

Figure 4 gives an visual summery of all systems and components on a typical RPAS that can be affected by icing.

III. ICE PROTECTION SYSTEMS

Ice protection systems (IPS) in aviation are categorized as anti-icing or de-icing systems. Anti-icing systems continuously prevent any ice accretion on critical aircraft surfaces. De-icing systems allow for an uncritical amount of ice to accumulate, which is then removed periodically. Today, there are several concepts that can be used for ice protection [1]; most common are electro-thermal systems, which use electrical heat; pneumatic boots that mechanically break ice through inflatable membranes (e.g. rubber); freezing point depressant systems ("weeping wings") that disperse a de-icing fluid; and piccolo tubes that channel hot, high-pressure engine bleed air into critical areas (most commonly found on airliners). Furthermore, there are more advanced ice protection concepts that have low maturity but may be promising in the future. For example, icephobic coatings passively change material properties such that ice cannot form on surfaces or reduce ice adhesion. Also, electro-mechanical systems are under development which induce forces in form of displacement, generated by electric motors, to break and shed ice from aircraft with low energy requirements.

For RPAS, the absence of a pilot necessitates reliable ice detection systems to activate and deactivate ice protection systems as needed. It is crucial that these systems are lightweight, energy-efficient, and rapid at detecting an icing encounter. In addition, for continuous flight in icing conditions, detection systems need to be able to indicate the severity of icing and when the aircraft exists icing conditions.

IV. ICING ENVIRONMENTS

Icing environments describe icing conditions that aircraft can expect to encounter and are used for design and certification. Icing environments describe expected combinations of liquid water content, droplet sizes, and exposure times. In manned aviation, the civil aviation authorities have developed icing environments to be used for certification. These icing envelopes are described in several appendices of the certification standards [13,14]. For RPAS, typically, the following icing envelopes are considered relevant.

- **Appendix C, in-cloud icing:** There are two envelopes that describe typical icing conditions in two different types of clouds, see Fig. 5. The continuous maximum (CM) envelope describes icing in stratus clouds with liquid water contents 0.2-0.8 g/m³ and droplet sizes 15-40 microns over a 17.4 nm (32.2 km) extent. The intermittent maximum (IM) envelope describes icing in isolated cumulus clouds with liquid water contents 1.1-2.9 g/m³ and droplet sizes 15-50 microns in diameter over a 2.6 nm (4.8 km) extent.

Component	Criticality	Effects	Duration till critical effects
Airspeed sensor	Very high	Ice blocks the sensor, leading to erroneous airspeed readings and dangerous autopilot responses.	< 1 min
Propeller	High	Ice accretion leads to rapid and significant performance degradation, thrust reduction, and power requirement increase. Ice shedding causes vibrations exceeding 10G.	< 4 min
Lifting surfaces (wings, etc.)	Moderate to high	Ice changes wing geometry, leading to decreased lift, increased drag, and reduced stall angles. Also, adds weight and reduces maneuverability.	< 10 min
Autopilot	Moderate	Autopilots must adapt to icing-induced changes in flight performance, stability, and control. This includes identifying icing conditions and adjusting flight parameters accordingly.	< 10 min
Antennae	Low to moderate	Ice accretion on antennae increases weight and drag of the airframe. Ice can decrease signal strength and lead to communication loss.	< 10min

Table 1: Overview of component criticality and duration till effects reach a critical level.
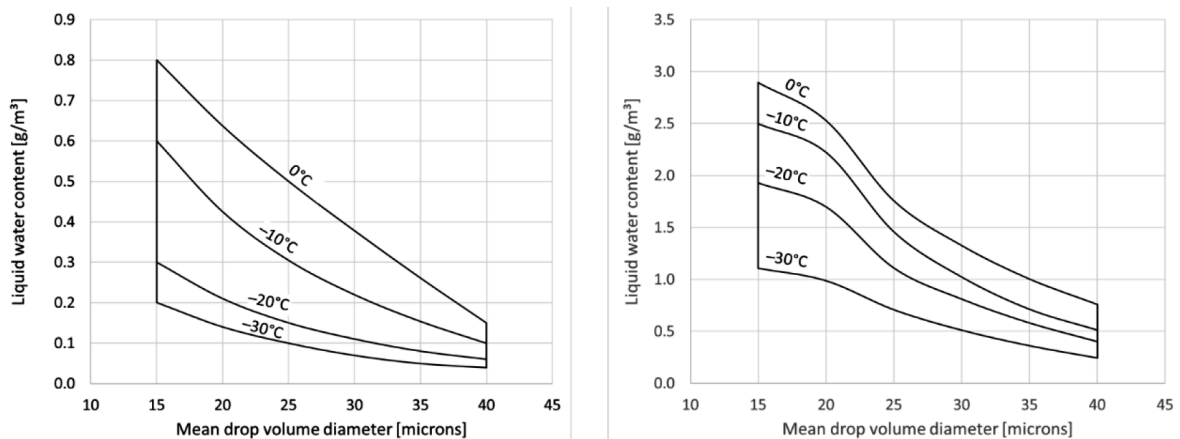
Figure 5: Meteorological icing environments as defined by the civil aviation authorities for Appendix C in-cloud icing. Continuous maximum icing in stratus clouds (left) and intermittent maximum icing in cumulus clouds (right), adapted from [14,15].

- **Appendix O, SLD icing:** More recently, two envelopes have been developed to account for supercooled large droplet icing (freezing precipitation), a very severe form of icing. There are two envelopes that describe freezing drizzle (FZDZ) and freezing rain (FZRA). These conditions are typically very severe and challenging to design for.

Note that these envelopes represent averages over a set distance, and actual conditions may fall outside these predefined ranges. Further research is essential to determine the most appropriate icing envelopes suited for different RPAS, tailored to their specific operational needs.

V. Ice Protection Systems

When addressing the operational and technical requirements for RPAS intended for operating in icing conditions, it is necessary to consider three distinct scenarios based on the aircraft's ice protection capabilities:

- **No ice protection system:** Aircraft without ice protection systems cannot operate in icing conditions, as ice accretions quickly com-promise performance and system integrity, potentially leading to loss of the aircraft. Operations must strictly avoid areas with any forecasted icing and avoid flight into visible moisture (e.g. clouds, fog, rain) in cold weather. This essentially translates to no flight beyond visual line of sight (BVLOS) in cold weather.

- **Inadvertent icing:** Aircraft are equipped with basic ice protection systems to handle unexpected, short-term icing. These systems provide a safety margin for exiting icing conditions inadvertently (unintentionally) encountered but are not intended for prolonged exposure to such environments.

- **Flight into known icing (FIKI):** Aircraft equipped with advanced ice protection systems, allowing for safe and continuous operations in known (forecasted) icing conditions. Such sophisticated systems enable the RPAS to handle a wide range of icing situations, thereby significantly broadening their operational capabilities and flexibility. Some severe icing conditions may still be outside the envelope for continuous operation.

In the following, two tables offer an overview of requirements for RPAS operating in these three icing scenarios. Table 2, outlines each case's risks, operational implications, and the required ice protection system components. Table 2, translates these aspects into recommendations for both operational and technical requirements. Applying the requirements from Tab. 2 in a design or an acquisition process ensures an outcome where RPAS capabilities match the desired operational requirements.

	No ice protection system	Basic ice protection system	Advanced ice protection system
Description	Aircraft have no ice protection capabilities and cannot operate in conditions with any risk of icing. Any icing encounter has a high likelihood of leading to a loss of aircraft.	Aircraft have a basic ice protection system that allows take-off in conditions that could result in an icing encounter. The basic protection system ensures the safe exit of any inadvertent icing encounters.	Aircraft have an advanced ice protection system that allows safe, continuous flight into known icing conditions.
Level of icing impact	High	Moderate	Low
Operational implications	▪ No flight beyond visual line of sight (BVLOS) when static ground air temperatures are below +5°C. ▪ Aircraft must avoid icing conditions entirely. ▪ Flight planning relies heavily on weather forecasts. ▪ Restrictions on operating in certain climates or seasons.	▪ Take off in conditions where icing could be present. ▪ Aircraft must immediately exit icing conditions if encountered. ▪ No sustained operations in icing environments.	▪ Continuous operations in a wide range of icing conditions, including moderate to severe icing. ▪ Limited operations into most severe conditions like freezing rain/drizzle (SLD).
Required ice protection elements	▪ None	▪ Ice detection system ▪ Protected pitot tube ▪ Protected propeller	▪ Ice detection system ▪ Protected pitot tube ▪ Protected propeller ▪ Protected lifting surfaces (wings, empennage) ▪ Protected antennae (optional) ▪ Protected payloads (optional)

Table 2: Summary of operational limitations of RPAS operating in icing environments depending on their ice protection system capabilities.

VI. SUMMARY

For RPAS operations in cold weather environments, the importance of adequate operational and technical requirements to ensure safe operation cannot be overstated. Suitable ice protection systems are crucial for guaranteeing the operational readiness and effectiveness of military and commercial RPAS in diverse and challenging conditions. Suitable ice protection systems enable key aspects of RPAS operations.

- **Mission readiness and safety:** Operations often require RPAS to operate in harsh, cold-weather environments where icing is a common hazard. Suitable ice protection systems ensures that aircraft can perform their missions in any cold weather without the risk of ice-related failures, which can compromise mission objectives and safety.

- **Operational flexibility and extended range:** Robust ice protection systems allow to operate across a wider range of environments and weather conditions. This flexibility allows for greater strategic and tactical options, ensuring that critical missions can be carried out under various circumstances without being limited by weather constraints.

- **Enhanced performance and reliability:** Advanced ice protection systems ensure that RPAS maintain optimal aerodynamic performance and system functionality even in icy conditions. This reliability is essential for critical missions where performance can directly impact mission success and the safety of ground forces relying on RPAS support.

- **Autonomy in operations:** Given the unmanned nature of RPAS, autonomous ice detection and protection capabilities are crucial. They enable RPAS to independently manage icing threats, reducing the need for ground intervention and allowing for more autonomous operation profiles.

In summary, the integration of effective ice protection systems in RPAS is a key factor in enhancing their operational effectiveness, safety, and reliability in cold weather conditions. This capability is essential not only for the successful execution of missions but also for maintaining the integrity and longevity of these valuable assets. A key factor in acquiring RPAS that provide value is setting the right requirements that reflect the operational requirements.

REFERENCES

[1] Hann, R., Johansen, T.A. (2020). Unsettled Topics in Unmanned Aerial Vehicle Icing. SAE International, SAE EDGE Research Report EPR2020008. doi.org/10.4271/EPR2020008.6

[2] Sørensen, K.L., Borup, K.T., Hann, R., Bernstein, B., Hansbø, M. (2021). UAV Atmospheric Icing Limitations: Climate Report for Norway and Surrounding Regions. Report. UBIQ Aerospace.

[3] Bernstein, B. C., Le Bot, C. (2009). An inferred climatology of icing conditions aloft, including supercooled large drops. Part II: Europe, Asia, and the globe. Journal of applied meteorology and climatology, 48(8), 1503-1526.

[4] Hann, R. (2020). Atmospheric Ice Accretions, Aerodynamic Icing Penalties, and Ice Protection Systems on Unmanned Aerial Vehicles. PhD Thesis NTNU2020:200, Norwegian University of Science and Technology.

[5] Wallisch, J., Hann, R. (2023). UAV Icing: Intercycle Ice Effects on Aerodynamic Performance. SAE International Conference on Icing of Aircraft, Engines, and Structures.

[6] Müller, N.C., Hann, R. (2023). UAV Icing: 3D simulations of propeller icing effects and anti-icing heat loads. SAE International Conference on Icing of Aircraft, Engines, and Structures.

[7] Lindner, M., Wallisch, J., Hann, R. (2023). UAV Icing: Numerical Simulation of Icing Effects on Wing and Empennage. SAE International Conference on Icing of Aircraft, Engines, and Structures.

[8] Heramarwan, H., Müller, N., Lutz, T., Hann, R. (2023). UAM Icing: Ice Accretion Simulations and Experiments of an eVTOL Rotor. SAE International Conference on Icing of Aircraft, Engines, and Structures.

[9] Hann, R. (2023). Numerical Simulation of In-Flight Icing of Unmanned Aerial Vehicles. In: Habashi, W.G. (eds) Handbook of Numerical Simulation of In-Flight Icing. Springer.

[10] Müller, N.C., Løw-Hansen, B., Borup, K.T., Hann, R. (2023). UAV icing: Development of an ice protection system for the propeller of a small UAV. Cold Regions Science and Technology, 213, 103938.

[11] Lindner, M., Wallisch, J., Hann, R. (2023). UAV Icing: Numerical Simulation of Icing Effects on Wing and Empennage. SAE International Conference on Icing of Aircraft, Engines, and Structures.

[12] Hann, R., Johansen, T.A. (2021). UAV icing: the influence of airspeed and chord length on performance degradation. Aircraft Engineering and Aerospace Technology, Vol. 93, No. 5.

[13] Hann, R., Hearst, R.J., Sætran, L.R., Bracchi, T. (2020). Experimental and Numerical Icing Penalties of an S826 Airfoil at Low Reynolds Numbers. Aerospace, 7(4), 46.

[14] Federal Aviation Administration FAA (2002), 14 CFR Parts 25 and 29, Appendix C, Icing Design Envelopes, DOT/FAA/AR-00/30.

[15] European Union Aviation Safety Agency EASA (2007). CS-25 Certification Specifications for Large Aeroplanes

Topic	Technical requirement	Scenario
General	The RPAS shall maintain performance and safety for the duration of an icing encounters. This duration is defined as the time from initial ice accumulation to the point where the UAV successfully exits the icing conditions.	All
General	The duration of an inadvertent icing encounter should be at least 5 min.	Inadvertent icing
General	The duration of an flight into known icing encounter should be at least 20 min.	Flight into known icing
General	The effectiveness of the ice protection system shall be demonstrated during flight tests into natural icing conditions.	All
General	The performance of an ice protection system (propeller or airframe) shall be demonstrated for critical design cases in icing wind tunnel tests.	All
General	Critical icing design cases should be identified from Appendix C (continuous maximum and intermittent maximum) for the airframe and propeller separately by means of simulation.	All
Ice detection	The RPAS shall be able to accurately detect the onset and presence of icing conditions. The time between entering icing conditions and detection shall be sufficient to allow the RPAS to safely exit the icing conditions. Detection duration should be less than 1 minute.	Inadvertent icing
Ice detection	The RPAS shall be able to accurately detect the onset and presence of icing conditions. The time between entering icing conditions and detection shall be sufficient to allow the RPAS to activate suitable ice protection systems. The detection duration should be less than 1 minute. In addition, the RPAS shall detect when icing conditions have been exited and estimate icing severity (ice accretion rate).	Flight into known icing
Airspeed sensor	The static pressure port shall always provide a data reading not affected by ice or air moisture condensation, which can form even flying outside clouds.	All
Airspeed sensor	Pitot tubes, which provide airspeed indication through the total pressure reading, shall be heated.	All
Propulsion	Ice accretions on propeller or rotor shall not result in hazardous vibrations, which can damage the propulsion system.	All
Propulsion	The propulsion system shall be protected against excessive performance loss due to icing for the duration of the icing encounter. Sufficient thrust and torque shall be are maintained to keep the RPAS airborne and manoeuvrable.	All
Propulsion	Ice shedding from an heated or unheated propeller shall not lead to excessive vibrations to damage the propulsion system.	All
Airframe	Ice accretions on the airframe shall not results in hazardous aerodynamic performance degradation during the duration of the icing encounter. This includes effects on li[, drag, moment, stall, and control surface effectiveness.	All
Airframe	For a de-icing system, it shall be shown that intercycle ice shapes are not resulting in hazardous aerodynamic performance degradation.	Flight into known icing
Airframe	The total weight of ice accretions accumulated during an icing encounter shall not result in hazardous weight changes.	All

Table 3: Recommendations for technical requirements of RPAS operating in icing conditions.

An Experimental Study on the Icing-Induced Performance Degradation of UAV Propellers

Anvesh Dhulipalla[1], Nianhong Han[1], Haiyang Hu[1] and Hui Hu[1]

[1] *Department of Aerospace Engineering, Iowa State University, Ames, Iowa 50014, USA*

Corresponding author, E-mail: huhui@iastate.edu

Abstract— **Unmanned Aerial vehicles (UAVs) pose a high risk of accidents due to icing in cold climatic regions. In this study, two field studies were conducted during different icing weather conditions in authorized airspace near Boone, IA, revealing the glaze ice formation on the propellers of a quadcopter. This ice formation resulted in a significant decrease in performance, and to understand the physics behind the reduction in performance, further study is conducted using a Digital Image Projection (DIP)--based 3D scanning system to quantify the 3D shape of the ice structure accreted over the propellers. The scanned propellers are 3D printed to study the effects of ice accretion on aerodynamic performances and wake characteristics. The wake characteristics of the rotating ice-accreted UAV propeller were addressed using the Particle Imaging Velocimetry (PIV) technique and the time-resolved measurements of aerodynamic forces and UAV propeller power consumption. Both "free-run" and "phase-locked" PIV measurements were performed on the propellers to provide instantaneous flow characteristics and the averaged flow measurements (e.g., mean velocity, vorticity, and turbulence kinetic energy) in the wake of the rotating propeller model. The glaze ice's typical formation of irregular structures can greatly disturb the spinning propeller's wake flow field, which generates much larger and more intricate vortices. This increases the turbulent mixing in the wake region, providing direct evidence in elucidating the significant increase in power consumption of the rotating propeller model.**

Keywords— ***PIV – Particle Image Velocimetry, DIP – Digital Image Velocimetry, UAV- Unmanned Aerial Vehicle, TKE – Turbulent Kinetic Energy, GPS – Global Positioning System, LWC – Liquid Water Content,***

I. INTRODUCTION

Unmanned Aerial Vehicles, or UAVs in short, represent one of the most significant breakthroughs in the aerospace community. Since UAVs can be controlled remotely or sometimes autonomously, they have been widely used for various applications, including agriculture, urban planning, cargo transport, wildlife conservation, healthcare, and search and rescue [1–5]. Compared to traditional manned aircraft, the cost and mortality reductions associated with deploying UAVs are also very appealing for military reconnaissance and surveillance. As a result, a collection of UAVs, such as Predator, Phoenix, and Global Hawk, have been used for achieving widespread military missions. With the fast-expanding UAV applications, the effects of adverse weather (e.g., rain, snow, and icing) on UAV flight performance must be examined carefully for safe and efficient UAV operations under such adverse weather [6–8].

Inflight icing is one of the most well-known aviation dangers threatening unmanned and manned airplanes flying in cold climates.[9–11]. Compared with large-sized, manned aircraft, small-sized UAVs are much more susceptible to inflight icing problems due to the lower cruising altitude associated with relatively warmer ambient temperatures and higher liquid water content (LWC) in the air, the slower flying speed to cause longer exposure time to icing conditions, and greater vulnerability to the damages of the electric sensors on-board [12,13]. The possible damage caused by inflight icing tends to render UAV operation unfeasible in cold weather. The commonly used UAV icing avoidance strategies either keep UAVs on the ground or modify their flight paths, greatly reducing UAV operational capability in cold climates [14].

Advancing the technology for safer and more efficient operation of UAVs in cold climates requires the development of novel and effective ice detection and anti-/de-icing strategies explicitly tailored for UAV icing protection. Doing so requires understanding the underlying physics pertinent to UAV icing phenomena. As reported in the recent study by Liu et al. [15], in comparison to the baseline case without any ice accretion over a UAV propeller blade, rime ice accretion was found to cause an increase of 15% in mean thrust force due to an increase in the effective chord length associated with the rime ice accretion. However, under the glaze icing condition, ice accretion decreased the mean value of the thrust force of the same propeller by 70%. The UAV propeller was found to consistently consume more power despite varied ice accumulation over the propeller blades [16]. Ice shedding during UAV flights can affect the performance of the system. The thrust fluctuations rose dramatically when ice shedding, potentially posing a flying safety hazard [17]. Due to the limited power availability of UAVs, compensating for the increased drag and decreased thrust would be impossible, which could result in a crash if not for manual operation to land the UAVs. A UAV's slow flying speed would also increase the exposure time of the UAV to icing conditions, which can severely damage the onboard sensors [18].

Numerous studies have also been conducted to develop anti-/de-icing systems for UAV icing protection. Most conventional anti-/de-icing methods for aircraft icing protection are thermal-based systems, i.e., use electrical heating or hot-air injection to heat massive surfaces of airframe surface, which are usually inefficient and energy-consuming. A hybrid anti-/de-icing technology by integrating the minimized surface heating to delaminate ice accretion in critical regions and hydro-/ice-phobic coatings with ultra-low ice adhesion strength and outstanding mechanical durability to reject ice accretion and water runback over the surfaces of blades was introduced by Gao et al., [19]. With a superhydrophobic surface (SHS) coating, there is a reduction in power consumption during the ice experiment. However, it was found that the propeller surface coated with SHS coating

has less frequency of ice shedding when compared to Stress localized surface (SLS) and slippery liquid-infused porous surface (SLIPS) coated propellers [20].

In the present study, a flight test campaign was conducted by flying a quadcopter UAV under atmospheric icing conditions. A substantial amount of ice was found to accreted over the surfaces of the UAV propeller blades, resulting in a dramatic increase in the power consumption for the iced UAV propellers. For a better understanding of the underlying physics behind the performance degradation, while the three-dimensional (3D) shape of an iced propeller was measured by using a Digital Image Projection (DIP)-based 3D profiler scanning system, an iced UAV propeller model was made by 3D printing the measurement results of the 3D profiler scanning system. The iced UAV propeller model was installed in a wind tunnel for a comprehensive experimental study to examine the effects of ice accretion on aerodynamic performances and wake characteristics of the iced UAV propeller. In addition to measuring the aerodynamic forces (i.e., thrust and drag forces) and power consumption characteristics of the iced UAV propeller as a function of the propeller rotation speed, the wake characteristics behind the rotating iced UAV propeller were also quantified by using a high-resolution Particle Imaging Velocimetry (PIV) system. The aerodynamic force and power consumption measurements were correlated with measured wake flow characteristics behind the rotating iced propeller to elucidate the underlying physics for a better understanding of the detrimental effects of the ice accretion on the performance of UAV propellers, which can be used to develop more effective and robust anti-/de-icing strategies to ensure safer and more efficient UAV operation under cold climates.

II. EXPERIMENTAL SETUP

A. Weather condition

The critical factor in this study is to observe the weather conditions and determine the timing of the flight. Calm weather is ideal for flying as it is safer and more accessible than rainy, windy, or snowy weather. When flying in calm weather, the aircraft experiences less drag, leading to a shorter take-off and landing distance and faster ground speed. Moreover, power usage is also less affected by calm weather. The ground station relies on software for full control and drone mission planning. The experimental investigation was conducted in an authorized air space at Agricultural Engineering and Agronomy Research Farm in Boone, IA, during the weather conditions shown in Table 1.

TABLE I. WEATHER CONDITIONS DURING THE FLIGHT TEST

Take off weight	3.37 lb
Date	03/15/2022, 8:55 am
Temperature	-3°C
Humidity	93 %
Wind Speed	3 mph
Weather Condition	FZFG (Freezing Fog)
Location	Boone, Iowa
Cloud condition	Overcast at 200 ft
Visibility	< 0.25 miles
LWC	0.05 g/m^3

B. Quadcopter Setup

1) *Avionics*: The Pixhawk 4 flight controller is an open-source flight controller that uses PX4 FMU (Flight Management Unit) software to control flights. The flight controller relies on various sensors to determine the vehicle's state, which is essential for stabilizing and enabling autonomous control. These sensors include a gyroscope, accelerometer, magnetometer (compass), barometer, and GPS or another positioning system. The system can determine several vehicle states like position/altitude, heading, speed, airspeed, orientation(attitude), rotation rates in different directions, and battery level. To connect with the controllers, such as electronic speed controllers and servos, the Pixhawk 4 uses pulse width modulation, which is connected to the controller board.

Fig. 1. The Assembled Quadcopter

2) *Propulsion: T*he quadcopter is powered by electric brushless DC motors (readytosky motors). These motors have a high torque of 190 g, operate at 920 Kv, and are paired with a 40A ESC and DJI 9-inch propellers. To meet the power requirements during windy or extreme icing conditions, a high discharge rate of 120C is recommended. The quadcopter uses a 5200mAh battery to provide the necessary RPM for all four motors.

3) *Communication and Tracking:* A radio module is utilized to enable long-range control of the UAS from a computer-based ground control station. This radio module can transmit and receive telemetry and control data for the aircraft and has an effective range of approximately 450 meters. The ground control station runs QgroundControl software, allowing us to control the UAS remotely. The GPS module provides navigation, altitude, and ground speed data, equipped with an LED indicator and a safety switch.

The loiter time for the icing experiment was fixed at 2 minutes at an altitude of 100 meters. Before taking off, we must ensure the drone is ready by calibrating its magnetometer, gyroscope, and compass. It is essential to consider the orientation of the battery and the placement of internal components during quadcopter assembly to minimize vibration metrics, as illustrated in Fig. 1.

C. 3D Scanning Setup

In the present study, a 3D scanning system based on the digital image projection (DIP) technique was used to measure the 3D shapes of the iced UAV propeller after the inflight icing test campaign. The DIP system is based on the principle of

structured light triangulation in a fashion like the stereo vision technique but replacing one of the cameras in the stereo pair with a digital projector [21]. A digital image with known pattern characteristics was projected onto the test object of interest (i.e., ice structures accreted over the surface of the UAV propeller for the present study). Due to the complex three-dimensional (3D) geometrical profiles of the test objects (i.e., the surface of the accreted ice structures), the projected digital patterns are deformed when observed from a perspective different from the projection axis. By comparing the distorted digital patterns (i.e., acquired images with ice structures accreted over the surface of the UAV propeller) with a reference digital pattern without the test objects on the reference surface, the 3D profile of the iced UAV propeller can be retrieved quantitatively. Further information about the technical basis and implementation of the DIP system is available from Zhang et al. [21]

D. PIV Setup

The propellers were then 3D printed and installed in a close- at Iowa State University for a comprehensive experimental study to examine the effects of ice accretion on aerodynamic performances and wake characteristics of the iced UAV propellers. The propeller was driven by a brushless motor (920Kv) powered by a DC power supply (VOLTEQ HY3050EX). The rotational speed of the propeller was measured by a tachometer (Monarch PLT200), which generates a pulse signal for each propeller's rotation. During the experiments, the rotational speed of the model was fixed at $n = 4000$ rpm. To mitigate the disturbance (Changes in rpm), an automatic rotational speed correction was formulated into the system using a proportional-integral-derivative algorithm (PID). A force measurement (ATI-IA Mini 45) and power consumption analysis have been performed on the 3D-printed baseline and iced propellers.
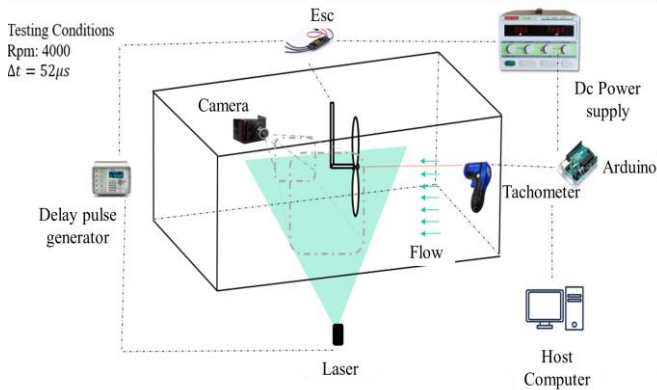
Fig. 2. Experimental Setup for PIV

During the experiments, in addition to measuring the aerodynamic forces (i.e., thrust and drag forces) and power consumption characteristics of the iced UAV propeller as a function of the propeller rotation speed, the wake characteristics behind the rotating iced UAV propeller were also quantified by using a high-resolution Particle Imaging Velocimetry (PIV) system, as shown in Fig. 2 For the PIV measurements, the flow was seeded with ~1 μm oil droplets by using a smoke generator. The illumination for the PIV measurements was provided by a double-pulsed Nd: YAG laser emitting two pulses of 200 mJ at 532 nm. A high-

resolution camera (Fast Cam mini WX) with an axis perpendicular to the laser sheet was used for PIV image acquisition. The digital camera and the double-pulsed Nd: YAG laser were connected to a workstation via a digital delay generator (Berkeley Nucleonics, Model 565), controlling the timing of the laser illumination and the image acquisition.

After acquiring PIV images, velocity vectors were obtained instantaneously using a cross-correlation technique between successive frames of particle image patterns in a 64×64-pixel interrogation window with an effective overlap of 50% in PIV image processing. Once the instantaneous velocity vectors (u_i, v_i) were determined, the vorticity (ω_z) could be calculated. The ensemble-average flow quantities, such as mean velocity and in-plane turbulence kinetic energy ($TKE = (0.5 * (u'^2 + v'^2)/u_\infty^2)$). Were obtained from the instantaneous PIV measurements. This study obtained a sequence of over 500 frames of instantaneous PIV image pairs to ensure the convergence of turbulence statistics of the PIV measurements. The measurement uncertainty level for the velocity vectors was estimated to be within 2%. In contrast, the uncertainties for the measurements of ensemble-averaged flow quantities, such as turbulent kinetic energy distributions, were around 5%. The "free-run" PIV measurements aimed to determine ensemble-averaged flow statistics in the propeller wake, including mean velocity, vorticity, and turbulence kinetic energy. To ensure that the measurements were meaningful, the image acquisition rate was set to a frequency that was not a harmonic frequency of the rotating frequency of the propeller model. "Phase-locked" PIV measurements were conducted to investigate the relationship between unsteady wake vortices and the position of the rotating propeller blades. The digital tachometer was used to detect the position of a pre-marked propeller blade, generating a pulse signal as it passed through the vertical PIV measurement plane. The pulse signal was input to the delay generator to trigger the digital PIV system and achieve "phase-locked" PIV measurements at different rotation phase angles of the pre-marked propeller blade. About 1000 instantaneous PIV measurements were taken at each pre-selected phase angle to calculate the phase-averaged flow velocity distribution in the wake of the propeller model.

III. RESULTS AND DISCUSSION

A. Ice Accretion on UAV Propellers

As the ice accumulated over the UAV surface during the flight, the battery's power level was consumed rapidly, resulting in a pilot intervention to manually override the mission to return to the launch point. However, If the ice build-up continues, and if allowed for sufficient time, all aerodynamic lift forces could be reduced, leading to an ultimate crash. The snapshots of the acquired images of the ice structures accreted over the propeller blades right after the UAV landed safely on the ground for the icing flight test campaign are shown in Fig. 3.

(a) Ice structure on suction side

(b) Ice structure on pressure side
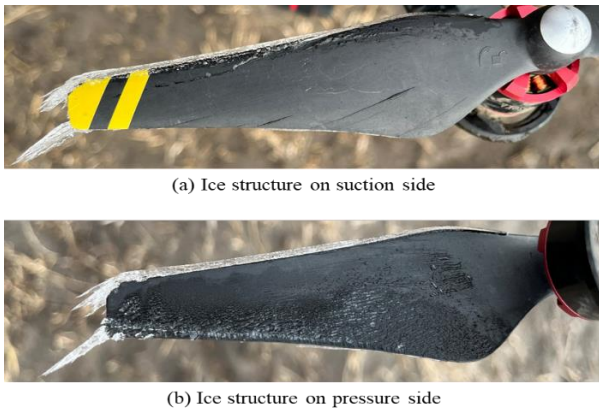
Fig. 3. Raw Images of ice accreted on the suction side and pressure side of the propeller after landing.

Since the airflow is relatively warm, it cannot transfer heat fast enough to remove all the latent heat of fusion released during the solidification process of the super-cooled water droplets when they hit the propeller blade. Only some super-cooled water droplets freeze upon impact, while the rest flows freely over the blade surface. The water that hits the blade is quickly carried away from the direct impingement zone by the boundary layer airflow and centrifugal force caused by the propeller's rotation. Consequently, while the ice layer on the blade surface extends further downstream, the unfrozen water is also pushed radially from the blade root to the tip due to the centrifugal force. Thus, the ice layer grows much faster on the outer edge of the propeller blade (near the blade tip) than on the inner edge (close to the blade root). Furthermore, due to the strong centrifugal force, some surface water separates from the ice accreting blade surface and forms icicle structures that protrude outward into the airflow. As more super-cooled water droplets impinge on the propeller blade, the ice accretion process over the blade surface becomes even more complex, resulting in irregular "lobster-tail-like" ice structures. It can be seen from the cross-sectional view of the scanned 3D objects in **Error! Reference source not found.** The glaze ice changes the shape of the leading edge and is very irregular; this aerodynamic shape transformation significantly affects the airfoil's lift and drag characteristics, reducing the propeller's efficiency.

Fig. 5 Shows the power consumption of the drone during the 80-second loiter time of the icing flight continuously increased from 220 Watts to 830 Watts. The area under the curve represents the average energy consumed, which is 404 Joules. The battery level became critical at around 130 seconds, so manual control was used to land the drone safely. During the descent, there is a sharp decrease in power consumption and an increase in altitude at around 140 seconds due to ice shedding, which causes a sudden change in mass. The autopilot (PID controller) reduces the throttle to maintain altitude, decreasing power consumption. Ice formation continues until landing. A non-icing weather flight's power consumption during loiter is constant at around 200 Watts, with a total energy consumption of 204 Joules, as shown in the top graph of Fig. 5. Therefore, the energy consumed by the icing flight is 93% higher than the non-icing weather flight. In electric motor-driven vehicles like quadcopters, the power provided to the aircraft is controlled by adjusting the current drawn to meet the power requirements. The no-icing flight was conducted during calm weather conditions. The weather data were obtained from the METARS report, and the power consumption data were provided in TABLE II.

TABLE II. WEATHER CONDITIONS AND POWER CONSUMPTION DATA FOR THE TEST FLIGHTS

Date	3/15/2022	03/25/2022
Temperature	26 °F	46 °F
Humidity	93 %	87 %
Wind speed	3 mph	7 mph
Power Consumed during ascent	272 (J)	258 (J)
Power Consumed during Loiter	404 (J)	205 (J)
Power Consumed during descent	620 (J)	185 (J)

Fig. 4. 3D Profile and cross-sectional views of an Ice accreted Propeller.
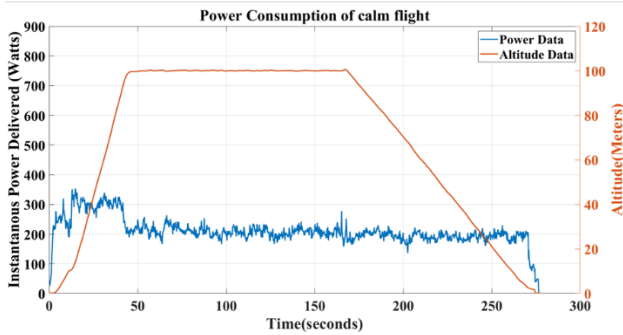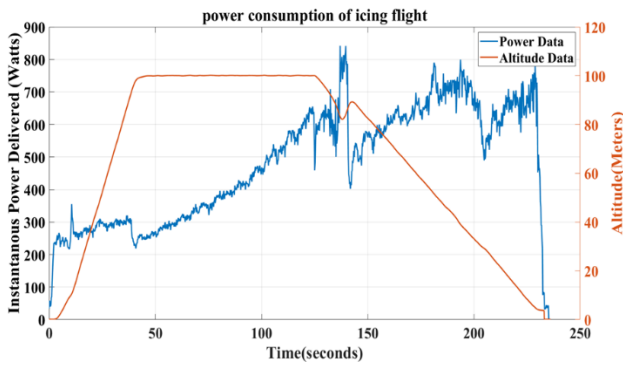
Fig. 5. Comparison of power consumption for the test cases with inflight icing and non-icing flight.

Based on the measurement result of the iced UAV propeller, a test model with the detailed features of the accreted ice structures over the UAV propeller was made of plastics using a rapid prototype machine (i.e., 3D printer). Fig. 6 Shows the pictures of the 3D-printed iced propeller model for the present study and a "clean" UAV propeller (i.e., without any ice accretion) as the comparison baseline. This quantitatively reveals the ice structures' characteristics accreted over the UAV propeller.
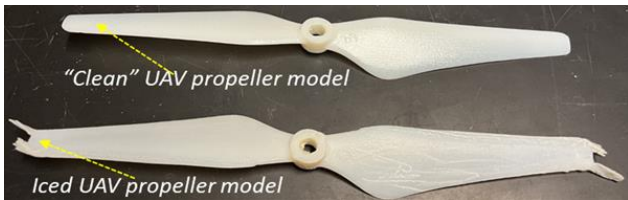
Fig. 6. 3D-printed UAV propeller models.

B. Thrust generation and power consumption of the baseline and iced propellers.

The aerodynamic forces acting on the propeller models at different rotational speeds were measured using a force transducer. Even though the measured thrust is equal for both propellers with the increased rotational speed, the power inputs required to drive the propellers acted differently. For the iced propeller, it can be seen from Fig. 7 That the required power input increases dramatically (as indicated by the blue line in (a)). Due to the iced propeller model's complex "lobster-tail-like" ice structures, the aerodynamic drag acting on the propeller would increase significantly compared to the baseline propeller model. As a result, a significantly higher amount of power (i.e., 25.2 to 73.2 Watts at 4000 rpm) was necessary to maintain the propeller's consistent rotational velocity.
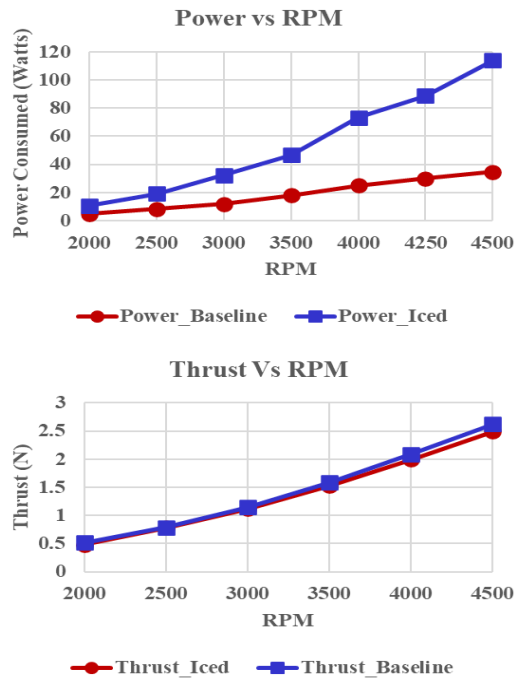
Fig. 7. Comparison of the power consumed and thrust generated by iced and clean propellers.

C. Averaged flow measurements in the wake flow field of clean and iced propellers.

The above results have demonstrated that the complex glaze ice structure could increase power consumption rapidly and may even lead to a complete reduction in thrust if the ice accumulation increases. The present study utilized averaged PIV measurements to uncover the underlying mechanisms behind the reduced performance of the UAS propeller model in icing conditions. Fig. 8 Shows the free-run PIV measurements in terms of combined averaged flow velocity distributions (a, b), vorticity distribution (c, d), and normalized in-plane turbulence kinetic energy distributions (e, f) in the wake of baseline and iced propellers. These measurements provided valuable, transient insights into the wake flow field of the propeller model with ice accumulation. The propeller model's temporally resolved wake flow structures under glaze ice accretion conditions suggest that the much larger, irregular ice shapes formed in such wet icing conditions can significantly contaminate the propeller wake flow field, which is responsible for the propeller performance degradation. As shown in Fig. 8(a), the velocity of the airflow is increased as the electrical energy from the motor is converted to kinetic energy by adding momentum to the flow. Along with the flow acceleration, the vortex channels are generated due to flow separation as the airflow passes through the rotating propellers. Fig. 8(c) shows that the blue region is due to the tip vortex. The wake flow field generated by a rotating propeller with large ice structures produces significantly larger and more complex vortex structures transported downstream, resulting in a turbulent mixing and highly distorted wake flow field as depicted in Fig. 8(d).
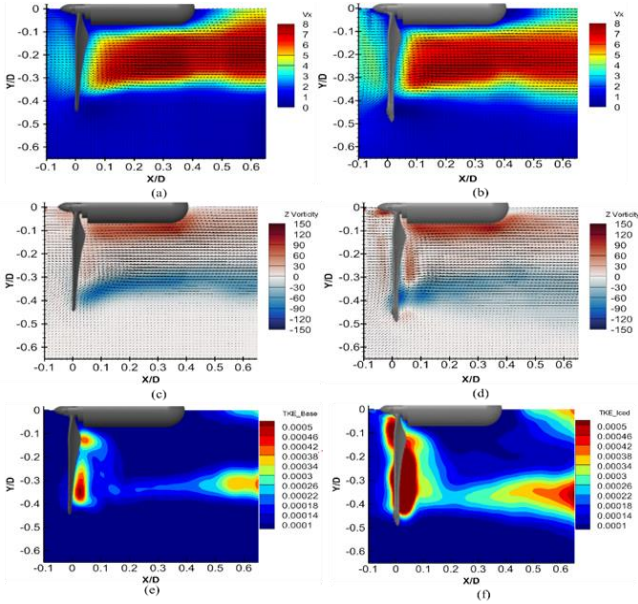
Fig. 8. Averaged flow statistics obtained from instantaneous PIV measurements in the wake of a rotating propeller (a, c, e) clean and (b, d, f) Iced. (ω=4,000RPM)

These larger vortex structures in the wake flow field rapidly increase drag force and greater structural vibrations. Moreover, the propeller wake width expands quickly due to generating these vortices, which can cause extensive flow disturbances to other components of the UAV in the propeller's wake. Whereas the TKE for the baseline propeller is observed to be relatively small compared to the iced propeller, indicating that the airflow for the baseline propeller is smooth with well-organized vortices.

To Quantitatively compare the wake characteristics of baseline and iced propellers, the transverse profiles of the mean flow velocity were extracted from the PIV measurement results at the downstream locations of X/D=0.15 and 0.60, respectively, as shown in Fig. 0. At X/D = 0.15 the velocity of the iced wake region produced by baseline and iced propeller were almost similar but as we go downstream to X/D=0.60 the wake velocity of the iced propeller is less than that of clean propeller because of the vortex shedding induced by accreted ice geometry as shown in Fig. 9(b).
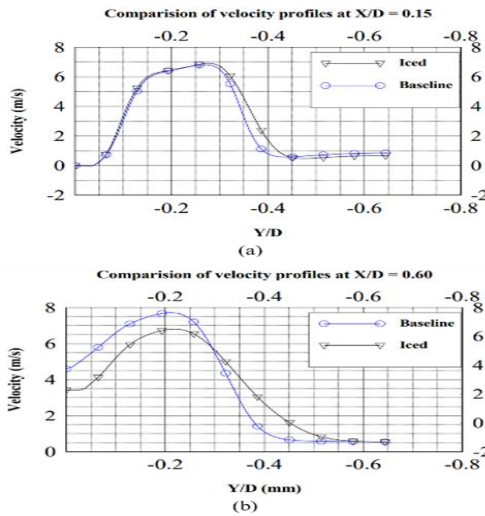
Fig. 9. Transverse velocity profiles in the wake region at (a) X/D=0.15, (b) at X/D=0.60.

D. Phase-locked PIV measurements of the wake flow field of baseline and iced propellers.

The formation of large and complex ice structures over the blade surfaces of a rotating propeller model under glaze icing conditions can create complex, large-scale vortex structures and significantly higher TKE in the wake flow field. This, in turn, leads to a significant reduction in the aerodynamic performance of the propeller model. To gain further insights into the wake evolution characteristics of the propeller model under glaze icing conditions, the present study used "phase-locked" PIV measurements to capture "frozen" images of the unsteady vortex structures in the wake flow field. These measurements helped to reveal the dependence of unsteady wake vortices on the rotation of the propeller blades more clearly and quantitatively. Fig. 10 illustrates the phase-averaged vorticity distributions in the wake of the clean propeller (a, c) and iced propeller (b, d) at phase angles of $\theta = 0°$ and $150°$. Where θ is the angle between the PIV measurement plane and the position of the propeller blade. As the phase angle increases, the propeller blade rotates out of the PIV measurement plane, and the vortices generated by the propeller are transported downstream in the wake flow field. In contrast to a clean propeller, the propeller with glaze ice accretion exhibits significantly larger vortices, primarily due to the presence of a lobster-tail-like structure at the tip. Furthermore, as these vortices travel downstream, the low-speed region increases in size due to the expansion and dissipation of the vortices.
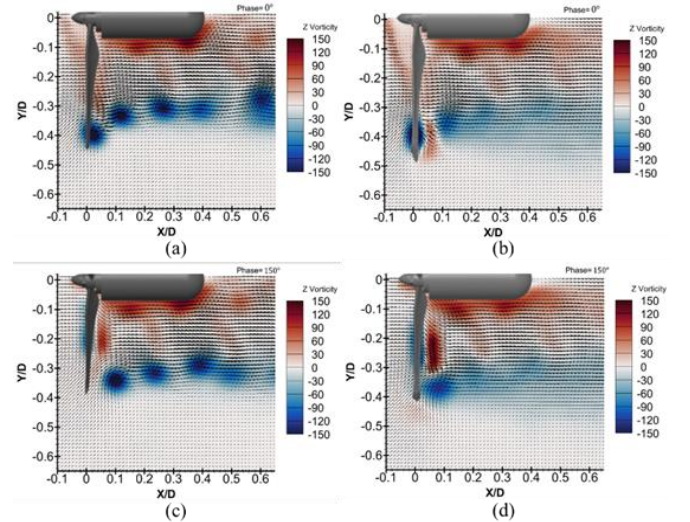
Fig. 10. Phase-locked vorticity distributions in the wake of clean (a, c) and iced (b, d) propeller models.

IV. CONCLUSIONS

An experimental study was conducted to investigate the detrimental effects of weather conditions on quadcopters. The study examined meteorological conditions and conducted flights in various weather conditions. The ice accumulation on the quadcopter's propellers was also investigated, revealing ice masses of 0.23 grams and 0.49 grams on different propellers. The difference in ice mass of 0.25 grams was attributed to ice shedding.

This study confirmed the presence of sharp horn-like glaze ice formation on the leading edge of iced propellers, while runback due to aerodynamic and centrifugal forces was responsible for trailing edge icing. The energy consumed during an icing flight was 98% higher than non-icing weather flight. Interestingly, comparing different propellers, the discarded ice mass was found to be responsible for sudden spikes in power consumption.

The Particle Imaging Velocimetry (PIV) technique was used to resolve ice-accretion-induced wake characteristics of a rotating UAS propeller. Time-resolved measurements of aerodynamic forces and power consumption of the UAS propeller model were also conducted. Both free-run and phase-locked PIV measurements were taken for clean and iced propeller models to provide both instantaneous flow characteristics and ensemble-averaged flow statistics, such as mean velocity, vorticity, and turbulence kinetic energy, in the wake of the rotating propeller model. Based on the results from the propeller with the glaze ice formation, the lobster-tail-like ice structures on the propeller are responsible for distortions in the wake flow field by generating complex vortex structures. The distribution turbulence kinetic energy (TKE) in the propeller's wake was significantly increased under glaze icing conditions. This provided direct evidence for the dramatic increase in power consumption of the rotating iced propeller model.

REFERENCES

[1] D. Tsouros, S. Bibi, P. S.- Information, and undefined 2019, "A review on UAV-based applications for precision agriculture," *mdpi.com*, 2019, doi: 10.3390/info10110349.

[2] G. Pajares, "Overview and Current Status of Remote Sensing Applications Based on Unmanned Aerial Vehicles (UAVs)," *Photogrammetric Engineering & Remote Sensing*, vol. 81, no. 4, pp. 281–329, Apr. 2015, doi: 10.14358/PERS.81.4.281.

[3] J. Revuelto *et al.*, "Intercomparison of UAV platforms for mapping snow depth distribution in complex alpine terrain," *Cold Regions Science and Technology*, vol. 190, p. 103344, Oct. 2021, doi: 10.1016/J.COLDREGIONS.2021.103344.

[4] M. Eckerstorfer, Y. Bühler, R. Frauenfelder, and E. Malnes, "Remote sensing of snow avalanches: Recent advances, potential, and limitations," *Cold Regions Science and Technology*, vol. 121, pp. 126–140, Jan. 2016, doi: 10.1016/J.COLDREGIONS.2015.11.001.

[5] S. Aggarwal *et al.*, "Aerial application of herding agents to advance in-situ burning for oil spill response in the Arctic: A pilot study," *Cold Regions Science and Technology*, vol. 135, pp. 97–104, Mar. 2017, doi: 10.1016/J.COLDREGIONS.2016.12.010.

[6] D. Bie, D. Li, J. Xiang, H. Li, Z. Kan, and Y. Sun, "Design, aerodynamic analysis and test flight of a bat-inspired tailless flapping wing unmanned aerial vehicle," *Aerospace Science and Technology*, vol. 112, 2021, doi: 10.1016/j.ast.2021.106557.

[7] R. L. Hawley and J. D. Millstein, "Quantifying snow drift on Arctic structures: A case study at Summit, Greenland, using UAV-based structure-from-motion photogrammetry," *Cold Regions Science and Technology*, vol. 157, pp. 163–170, Jan. 2019, doi: 10.1016/J.COLDREGIONS.2018.10.007.

[8] Q. Hu *et al.*, "A method for measuring ice thickness of wind turbine blades based on edge detection," *Cold Regions Science and Technology*, vol. 192, p. 103398, Dec. 2021, doi: 10.1016/J.COLDREGIONS.2021.103398.

[9] Y. Cao, W. Tan, and Z. Wu, "Aircraft icing: An ongoing threat to aviation safety," *Aerospace Science and Technology*, vol. 75, pp. 353–385, Apr. 2018, doi: 10.1016/j.ast.2017.12.028.

[10] D. I. Ignatyev, A. N. Khrabrov, A. I. Kortukova, D. A. Alieva, M. E. Sidoryuk, and S. G. Bazhenov, "Interplay of unsteady aerodynamics and flight dynamics of transport aircraft in icing conditions," *Aerospace Science and Technology*, vol. 104, p. 105914, Sep. 2020, doi: 10.1016/j.ast.2020.105914.

[11] V. Vercillo *et al.*, "Analysis and modelling of icing of air intake protection grids of aircraft engines," *Cold Regions Science and Technology*, vol. 160, pp. 265–272, Apr. 2019, doi: 10.1016/J.COLDREGIONS.2019.01.012.

[12] K. Szilder and S. McIlwain, "In-flight icing of UAVs – the influence of flight speed coupled with chord size," *Canadian Aeronautics and Space Journal*, vol. 58, no. 02, pp. 83–94, Aug. 2012, doi: 10.5589/q12-007.

[13] R. Hann and T. A. Johansen, "UAV icing: the influence of airspeed and chord length on performance degradation," *Aircraft Engineering and Aerospace Technology*, vol. 93, no. 5, pp. 832–841, 2021, doi: 10.1108/AEAT-06-2020-0127/FULL/HTML.

[14] B. Zhang, L. Tang, and M. Roemer, "Probabilistic Weather Forecasting Analysis for Unmanned Aerial Vehicle Path Planning," *Journal of Guidance, Control, and Dynamics*, vol. 37, no. 1, pp. 309–312, Jan. 2014, doi: 10.2514/1.61651.

[15] Y. Liu, L. Li, W. Chen, W. Tian, and H. Hu, "An experimental study on the aerodynamic performance degradation of a UAS propeller model induced by ice accretion process," *Exp Therm Fluid Sci*, vol. 102, pp. 101–112, Apr. 2019, doi: 10.1016/j.expthermflusci.2018.11.008.

[16] Y. Liu, L. Li, Z. Ning, W. Tian, and H. Hu, "Experimental investigation on the dynamic icing process over a rotating propeller model," *J Propuls Power*, vol. 34, no. 4, pp. 933–946, 2018, doi: 10.2514/1.B36748.

[17] N. Han, H. Hu, and H. Hu, "An Experimental Investigation on the Dynamic Ice Accretion Process over the Blade Surface of a Rotating UAV Propeller," in *AIAA SCITECH 2022 Forum*, Reston, Virginia: American Institute of Aeronautics and Astronautics, Jan. 2022. doi: 10.2514/6.2022-1538.

[18] H. Beaugendre, F. Morency, and W. G. Habashi, "FENSAP-ICE's Three-Dimensional In-Flight Ice Accretion Module: ICE3D," *https://doi.org/10.2514/2.3113*, vol. 40, no. 2, pp. 239–247, May 2012, doi: 10.2514/2.3113.

[19] L. Gao, Y. Liu, L. Ma, and H. Hu, "A hybrid strategy combining minimized leading-edge electric-heating and superhydro-/ice-phobic surface coating for wind turbine icing mitigation," *Renew Energy*, vol. 140, pp. 943–956, Sep. 2019, doi: 10.1016/j.renene.2019.03.112.

[20] N. Han, H. Hu, and H. Hu, "An Experimental Investigation to Assess the Effectiveness of Various Anti-Icing Coatings for UAV Propeller Icing Mitigation," *AIAA AVIATION 2022 Forum*, 2022, doi: 10.2514/6.2022-3964.

[21] K. Zhang, T. Wei, and H. Hu, "An experimental investigation on the surface water transport process over an airfoil by using a digital image projection technique," *Exp Fluids*, vol. 56, no. 9, pp. 1–16, Sep. 2015, doi: 10.1007/S00348-015-2046-Z/FIGURES/14.

Vibration of Suspended Cables with Active Control

László E. Kollár

Savaria Institute of Technology, ELTE Eötvös Loránd University, Budapest, Hungary

kl@inf.elte.hu

Abstract— **Active control is applied in order to attenuate vibration of conductors or cables. The motion of the chosen point at mid-span is observed, and the control system intervenes by moving the cable support axially in order to reduce the vibration amplitude at the observed point. This method of vibration control may successfully attenuate even high-amplitude vibrations that arise as a consequence of wind acting on transmission line conductors or on cable-stayed bridges or ice shedding from conductors. Time delay due to sampling in the digital control influences the efficiency of the method. Results show that the application of vibration control successfully reduces the initial great displacements that follow ice shedding from a conductor, but increasing sampling delay diminishes the effects of control.**

Keywords— ***Cable, control, ice shedding, time delay, vibration***

I. INTRODUCTION

Cable structures are often exposed to dynamic loads under extreme weather conditions due to wind or ice shedding. These loads are associated with high-amplitude vibration and excessive dynamic forces that may damage the structure; therefore, effort should be made to develop solutions for reducing the undesired consequences of vibration. Typical applications of such structures with suspended cables are overhead transmission lines with conductors, and cable-stayed bridges.

The most common method to overcome wind-induced vibration is the utilization of passive, semi-active or active vibration dampers. Passive dampers have been applied for decades [1], [2]; but more recently, active vibration control methods have also been proposed [3]. Another method of active vibration damping is the application of an actuator at one of the suspension points of the cable and controlling its displacement. The motion of a chosen point of the cable is observed, and the control system determines a response that results in the vertical or the axial motion of cable support, so that the vibration amplitude of the observed point of the cable is reduced [4]-[6]. Such method may successfully attenuate even high-amplitude vibrations. The high-amplitude wind-induced vibration is the so-called galloping, but ice shedding from transmission line conductors also results in high rebound height followed by decaying free vibration when the reduction of the initial high jump should be achieved by the application of active control.

Vibration following ice shedding from transmission line conductors has been studied for decades both experimentally [7] and numerically [8]. Researchers made great effort to estimate the conductor rebound height after ice shedding including the proposal of simple formulae even in more recent developments [9] with further modifications [10], [11]. Most recently, data-driven models were also developed to predict rebound height [12] and to study the dynamics of multi-span lines following ice shedding [13]. Method for attenuation of vibration following ice shedding was considered in the recent research of the author, and the effects of time delay that always occurs in digital control due to sampling were studied [14], [15]. Results showed that a vibration absorber could effectively reduce vibration amplitude at a specific position along the cable where it was placed; however, control with great enough time delay might even increase the amplitude.

The present research focuses on the application of active vibration control of suspended cables considering issues that arise in digital control. The method is tested on a transmission line model to attenuate vibration following ice shedding from a conductor. The main benefit from the development of this control method is to protect the structure, avoid damage, and thereby increase its lifetime and extend its range of operation under severe ambient conditions.

II. NONLINEAR MODEL OF SMALL-SAG SUSPENDED CABLES

The linear theory of small-sag suspended cables has been studied for decades. Reference [16] developed the linear theory of free vibrations of a suspended cable considering in-plane and out-of-plane motions. The linearized dynamic response of a flat-sag cable was also discussed in [17], together with a nonlinear theory of vibration. Nonlinear models have been developed in [4]-[6], which take into account coupling between the in-plane and out-of-plane motions and the displacement of the support points. The cable motion is decomposed into two parts. The quasi-static motion considers the displacement of the cable due to the support movement; whereas the dynamic motion involves the modal motion of a cable with fixed ends.
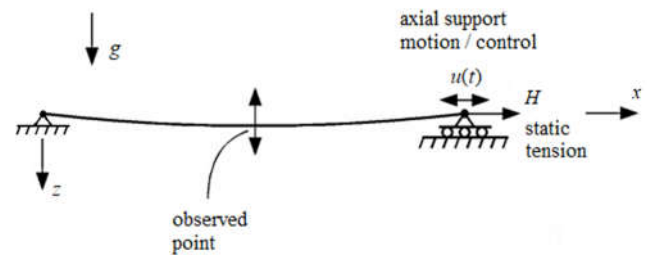
Fig. 1   Control of cable vibration by axial support motion

The cable model of the present study is based on the above developments, and considers axial support motion at one of the suspension points where the control is applied as shown in Fig. 1. The coordinate system is chosen so that *x*, *y* and *z* denote the longitudinal (or axial), transverse and vertical directions, respectively. The parameters and equations used in the model are described in Sections II.A and II.B, and further details can be found in [5].

A. Quasi-Static Motion

Support movement is assumed in the right end of the cable in the axial direction only. Correspondingly, the following

boundary conditions are applied with the equations describing the quasi-static motion:

$$u_q(0,t) = u_a(t) = 0 \qquad \text{and} \qquad u_q(L,t) = u_b(t)$$
$$v_q(0,t) = v_q(L,t) = 0 \tag{1}$$
$$w_q(0,t) = w_q(L,t) = 0$$

where u and w are the longitudinal (or axial) and vertical components of the in-plane motion, and v is the transverse horizontal component of the motion. The subscript q refers to quasi-static motion, and L is the span length. Then, the equations of the quasi-static motion are expressed as follows

$$u_q(x,t) = \frac{E_q}{E} u_b(t) \left[\frac{x}{L} + \frac{\lambda^2}{4} \left(\frac{x}{L} - 2\left(\frac{x}{L}\right)^2 + \frac{4}{3}\left(\frac{x}{L}\right)^3 \right) \right]$$
$$v_q(x,t) = 0 \tag{2}$$
$$w_q(x,t) = -\frac{E_q A}{H} \frac{u_b(t)}{L} w_s(x)$$

The parameter w_s describes the static profile of the cable

$$w_s = \frac{H}{\mu g} \left[\cosh \frac{\mu g L}{2H} - \cosh \frac{\mu g}{H}\left(\frac{L}{2} - x\right) \right],$$

the parameter λ was defined in [16] and [17]

$$\lambda^2 = \left(\frac{8d}{L}\right)^2 \frac{EA}{H\left(1 + 8\left(\frac{d}{L}\right)^2\right)},$$

and the effective axial modulus was introduced in [5]

$$E_q = \frac{1}{1 + \frac{\lambda^2}{12}} E.$$

The symbol E denotes the Young's modulus of the cable, μ is its mass per unit length, d is the sag, and g stands for gravitational acceleration. The cross section of the cable can be calculated as $A = \mu/\rho$ if the cable density ρ is known, and the horizontal component of cable tension is determined from $H = \mu g L^2/8d$.

B. Dynamic Motion

The dynamic motion is described by the modal components with the longitudinal component neglected for small sags.

$$u_d(x,t) \approx 0$$
$$v_d(x,t) = \sum_n y_n(t) \phi_n(x) \tag{3}$$
$$w_d(x,t) = \sum_n z_n(t) \psi_n(x)$$

The coordinates y_n and z_n are the amplitudes of the out-of-plane and in-plane modes, respectively. The out-of-plane mode shapes ϕ_n and the in-plane mode shapes ψ_n can be given as follows

$$\phi_n(x) = \sin\frac{n\pi x}{L} \qquad \text{and} \qquad \psi_n(x) \approx \sin\frac{n\pi x}{L} \tag{4}$$

Then, the following equations can be derived for the coordinates y_n and z_n for mode n

$$\mu_{c,n}\left(\ddot{y}_n + 2\zeta_{y,n}\omega_n\dot{y}_n + \omega_n^2 y_n\right) + S_n y_n\left(T_q + T_d\right) = F_{y,n} \tag{5a}$$

$$\mu_{c,n}\left(\ddot{z}_n + 2\zeta_{z,n}\omega_n\dot{z}_n + \omega_n^2 z_n\right) + S_n z_n\left(T_q + T_d\right)$$
$$+ \Lambda_n T_d - \alpha_{c,n}\ddot{u}_b = F_{z,n} \tag{5b}$$

The quasi-static tension and dynamic tension can be written in the form

$$T_q = h_u u_b \qquad \text{with} \qquad h_u = \frac{E_q A}{L}$$
$$T_d = \sum_n \left[h_{1,n} z_n + h_{2,n}\left(y_n^2 + z_n^2\right) \right]$$

The excitation applied to the cable is considered by the modal forces, $F_{y,n}$ and $F_{z,n}$. Further parameters in the governing equations (5) are constant vectors and matrices that can be calculated from the cable parameters [5].

The cable motion is obtained by the superposition of the quasi-static and dynamic motions

$$u(x,t) = u_q(x,t)$$
$$v(x,t) = v_d(x,t) \tag{6}$$
$$w(x,t) = w_q(x,t) + w_d(x,t)$$

C. Control with time delay

Control is applied at the right end of the suspended cable. Different control strategies have been proposed in the literature [4], [5]. A simple proportional control is applied here, in which the displacement at the support is proportional to the displacement of the observed point obtained in the dynamic motion

$$u_b(t) = P w_d(x_i, t) \tag{7}$$

where x_i is the location of the observed point, and P is the control gain. Practically, only the total displacement w can be measured, but the displacement w_q can be calculated, and thus, the displacement w_d can be obtained.

The time delay is considered in the model by keeping the control u constant during k consecutive time steps in the numerical integration, i.e. $\tau = k\Delta t$, where τ is the time delay, Δt is the time step. Then the control can be written as follows

$$u_b(t) = P w_d(x_i, t_j) \qquad t \in \left[t_j, t_j + \tau \right) \qquad j = 0,1,2,\dots$$

III. SMALL-SCALE MODEL OF A TRANSMISSION LINE

The model described in Section II was implemented using the software Matlab. Parameters are defined so that they correspond to the laboratory model of a one-span section of a transmission line in the Savaria Institute of Technology, ELTE Eötvös Loránd University, Budapest. The line parameters are listed in Table 1.

TABLE I. PARAMETERS OF THE TRANSMISSION LINE MODEL

Parameter	Unit	Value
Span length, L	m	16.62
Mass per unit length, μ	kg/m	0.061
Cross section of conductor, A	mm²	7.6
Young's modulus, E	GPa	60
Sag, d	m	0.305

Vibration control is applied to attenuate vibration initiated by ice shedding that may be modelled in laboratory by load

removal. The scenario simulated involved 7 concentrated loads in the middle 40% of the span with constant distances between them. The mass of each of these loads was 0.8 kg, which means that each of them weighed 7.848 N. The initial displacement in this load case was reported 0.095 m in [18]. The sketch of the initial set-up with the concentrated loads is shown in Fig. 2. Then, these loads are removed at the initial time instance, $t = 0$ s, which is followed by vibration. The vibration control is applied in the present model to reduce the maximum displacement during this vibration.

Fig. 2 Sketch of the initial (before load removal) set-up of the simulated scenario

Excitation force does not act during vibration following ice shedding, but the vibration is initiated by the removal of the load that ice represented on the conductor or cable. Therefore, the modal forces $F_{y,n} = F_{z,n} = 0$. The point where the motion is observed is located in the middle of the span, i.e. $x_i = L/2$. The first goal with the model developed was to study the effects of time delay, because it gave information whether the digital control was successful with taken the sampling delay into account. Correspondingly, other details were simplified in these simulations as follows. The sag-induced inertia was neglected, although it becomes significant when the axial acceleration of the support is great enough. Furthermore, only the first three vibration modes were considered.

IV. RESULTS AND DISCUSSION

The model described in Section II was applied first to simulate the load removal scenario from the experimental set-up as outlined in Section III. The total displacement of the cable is the sum of displacements of the three mode shapes considered. Since the second mode shape has a node at mid-span, the displacement is zero in that vibration mode at that position. Thus, the total displacement is composed from those in the first and third vibration modes. The initial displacements in both of these vibration modes were assumed to be the half of the initial displacement 0.095 m. The values of modal damping $\zeta_{y,n}$ and $\zeta_{z,n}$ were assumed to be equal to 0.08. Simulation results were compared to those reported in [18], which were validated by comparing the rebound height with experimental observations. The vertical displacement in the dynamic motion is plotted in Fig. 3. Note that there is no quasi-static motion in this case, since the support was not allowed to move. The displacements in the first three vibration modes are represented by the dashed and dotted curves in Fig. 3, and the sum of them, i.e. the total displacement, can be seen in the solid curve.

Note that the zero value in Fig. 3 denotes the unloaded position of the cable at mid-span in static equilibrium. Also note that the coordinate system is defined so that the direction of the z axis is positive downward as shown in Fig. 1. Therefore, the increased sag due to the load occurs as a positive initial displacement in Fig. 3.
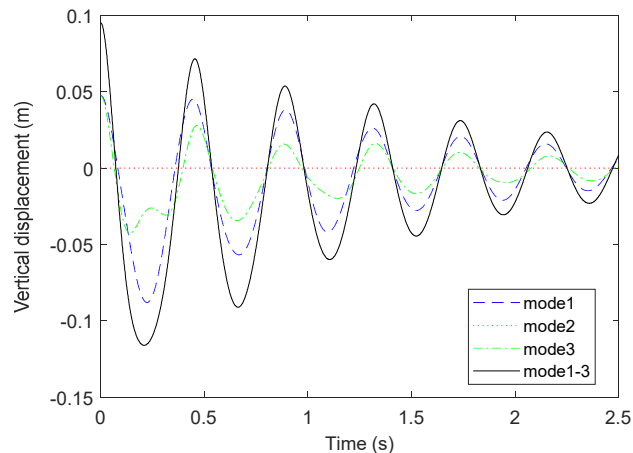
Fig. 3 Vertical displacement after load removal, displacements in first three vibration modes (mode1, mode2, mode3) and total displacement (mode1-3) with no support motion

The parameters characterizing the vibration are compared with those obtained in the numerical simulations of [18]. These parameters are the maximum rebound height above the loaded position, the decay described by the ratio of amplitudes in the 6th cycle (after the completion of 5 cycles) and in the first cycle, and the period. The comparison is shown in Table 2. Discrepancies up to 15% can be observed when the modal damping in the vertical direction $\zeta_{z,n}$ was chosen to be 0.08. Modal damping in the transverse direction $\zeta_{y,n}$ had no effect on the vertical motion.

TABLE III. COMPARISON OF VIBRATION CHARACTERISTICS OBTAINED BY THE PRESENT MODEL AND IN [18]

Parameter	Present model	Model of [11]	Discre-pancy
Maximum rebound height above loaded position (m)	0.21	0.2	5%
Decay (reduction ratio of amplitudes after 5 cycles)	0.22	0.25	-14%
Period (s)	0.43	0.4	7.5%

The application of control at the right support of the cable contributes to reducing the peaks in the vibration due to ice shedding. The control gain $P = 0.1$ was assumed in the following simulations. Fig. 4(a) depicts the motion at the right support where the control is applied together with the axial and vertical components of the resulting quasi-static motion of the cable at mid-span. The vertical component of the quasi-static motion at mid-span is also shown in Fig. 4(b) in order to compare it with the vertical component of the dynamic motion and with the resulting vertical motion of the cable at mid-span, which is the sum of the quasi-static and dynamic motions. Results show that the maximum rebound height may be reduced by an order of magnitude by the application of control at the cable support. Finding the most efficient control gain and control strategy is the subject of further research, which may further attenuate the vibration. However, sampling delay was not considered so far, which diminishes the effects of control.
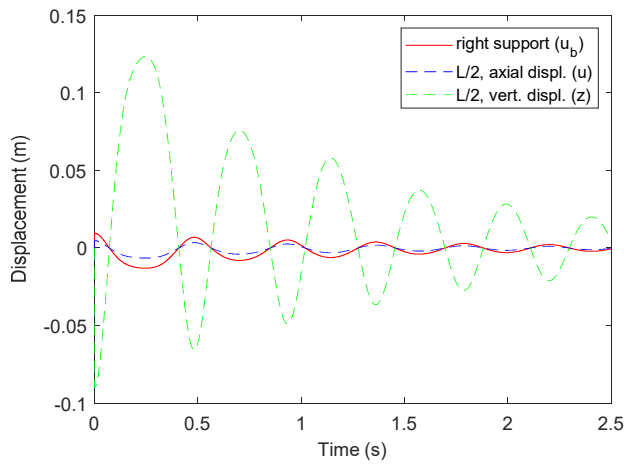
(a)
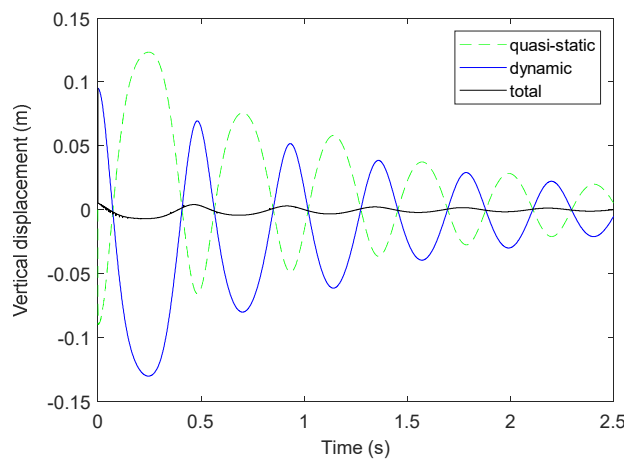
(b)

Fig. 4   Motion with control at right support; (a) Quasi-static motion at right support (u_b) and at mid-span ($L/2$) in axial (u) and vertical (z) directions; (b) Vertical displacements in quasi-static and dynamic motions, and the sum of them (total)

Sampling delay of 20 ms was considered in the present simulations. It means that the motion of right support cannot be represented by a smooth curve as the solid one in Fig. 4(a). The position of the right support does not change between two sampling, in other words, it is constant during 20 ms, and then it changes abruptly according to the new sample taken. Consequently, the vertical displacement at mid-span would change during each 20 ms time interval according to a controlled position of the support, which is a response to a cable position measured in the past. Then, at the end of this time interval, new sample is taken, the support position is changed abruptly, and the cable at mid-span also changes its position abruptly. This phenomenon leads to a motion that is represented by the sawtoothed curve in Fig. 5.

Fig. 5 compares three curves that describe the vertical motion of the cable at mid-span without control, with control neglecting sampling delay, and with control and sampling delay of 20 ms. Control with time delay significantly increases the maximum rebound height compared to that obtained without considering time delay. However, the maximum displacement is still reduced about one fourth of the value obtained without control. The extent of this reduction depends
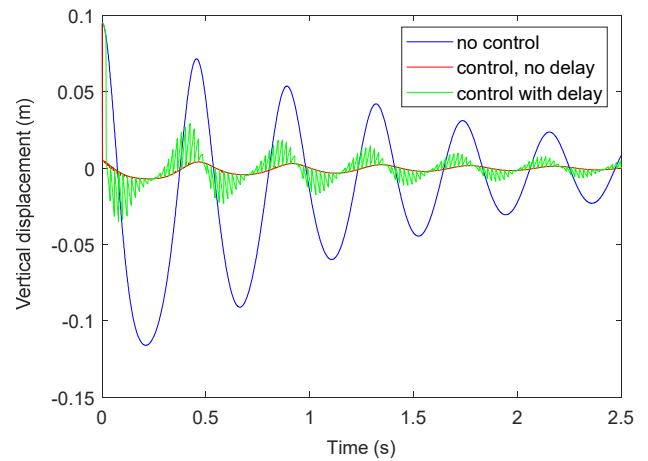
Fig. 5   Comparison of vertical displacements without control, with control neglecting sampling delay, and with control considering sampling delay of 20 ms

on the value of time delay, whose examination is the subject of ongoing research. These results demonstrate that further effort should be taken in order to develop the vibration control with time delay.

V. Conclusions

A method was applied to control vibration of suspended cables or conductors by moving one of the supports axially considering time delay due to sampling, which is always present in digital control. The motion of the cable at mid-span was observed, and the action of the control resulted in the reduction of the vertical displacement of the cable. The method was applied for the simulation of ice shedding under laboratory conditions. Theoretically, the vibration control may reduce the maximum rebound height by an order of magnitude, but increasing sampling delay diminishes the effects of control and requires quick changes in the displacement of the support point, which is associated with high acceleration peaks. Such problems may cause limitations in the implementation of the control, and requires further investigation.

Future research involves improvement of the model, development of the control strategy, and validation by laboratory experiments. The model can be improved by several aspects including the consideration of sag-induced inertia that becomes important for the high acceleration peaks that occur in the digital control with sampling delay. The modal damping ratios were estimated in the present model, which may also be improved by calculating them from experimental observations. The consideration of more than three vibration modes in the theoretical model would result in the more accurate prediction of the motion. The control will further be studied by scrutinizing the effects of control gain, different control strategies, and time delay due to sampling. The control is expected to reduce displacement along the cable; therefore study of the dynamics of the cable at points other than the observed one should also be considered. Model developments may be verified by laboratory experiments, and then the validated model will also be applied for full-scale transmission lines or cable-stayed bridges.

REFERENCES

[1] H. Wagner, V. Ramamurti, R. Sastry, K. Hartmann, "Dynamics of stockbridge damper," *J Sound Vib.*, vol. 30(2), pp. 207–220, 1973.

[2] J. Vecchiarelli, I. G. Currie, D. G. Havard, "Computational analysis of aeolian conductor vibration with a stockbridge-type damper," *J Fluids Struct.*, vol. 14, pp. 489–509, 2000.

[3] X. Wang, B. Yang, S. Guo, W. Zhao, "Nonlinear convergence active vibration absorber for single and multiple frequency vibration control," *J Sound Vib.*, vol. 411, pp. 289–303, 2017.

[4] Y. Fujino, P. Warnitchai, B. M. Pacheco, "Active Stiffness Control of Cable Vibration," *Transactions of the ASME*, vol. 60, pp. 948-953, 1993.

[5] Y. Achkire, "Active Tendon Control of Cable-Stayed Bridges," PhD thesis, Active Structures Laboratory, Université Libre de Bruxelles, Belgium, May 1997.

[6] A. Preumont, *Vibration Control of Active Structures*, 2nd ed., New York, NY, USA: Kluwer Academic Publishers, 2002.

[7] V. T. Morgan, D. A. Swift, "Jump height of overhead-line conductors after the sudden release of ice loads," *Proc. IEE.* vol. 111(10), pp. 1736–1746, 1964.

[8] A. Jamaleddine, G. McClure, J. Rousselet, R. Beauchemin, "Simulation of ice shedding on electrical transmission lines using ADINA," *Comput. Struct.* vol. 47(4/5), pp. 523–536, 1993.

[9] B. Yan, K. Chen, Y. Guo, M. Liang, Q. Yuan, "Numerical simulation study on jump height of iced transmission lines after ice shedding," *IEEE Trans. Power Deliv.* vol. 28(1), pp. 216–225, 2013.

[10] C. Wu, B. Yan, L. Zhang, B. Zhang, Q. Li, "A method to calculate jump height of iced transmission lines after ice-shedding," *Cold Reg. Sci. Technol.* vol. 125, pp. 40–47, 2016.

[11] G. Huang, B. Yan, N. Wen, C. Wu, Q. Li, "Study on jump height of transmission lines after ice-shedding by reduced scale modeling test," *Cold Reg. Sci. Technol.* vol. 165, 102781, 2019.

[12] X. Long, X. Gu, C. Lu, Z. Li, Y. Ma, Z. Jian, "Prediction of the jump height of transmission lines after ice-shedding based on XGBoost and Bayesian optimization," *Cold Reg. Sci. Technol.* vol. 213, 103928, 2023.

[13] K. Wu, B. Yan, H. Yang, Q. Liu, J. Lu, M. Liang, "Characteristics of multi-span transmission lines following ice-shedding," *Cold Reg. Sci. Technol.* vol. 218, 104082, 2024.

[14] Y. Meng, L. E. Kollár, "Dynamic analysis of electrical vibration absorbers for suspended cables," *Proc IMechE Part C: J Mechanical Engineering Science*, vol. 235(24), pp. 7445-7455, 2021.

[15] L. E. Kollár, "Ice-shedding-induced vibration of conductors with active vibration control," *Cold Regions Science and Technology*, vol. 196, 103504, 2022.

[16] H. M. Irvine, T. K. Caughey, "The linear theory of free vibrations of a suspended cable," *Proc R Soc Lond* A, vol. 341, pp. 299-315, 1974.

[17] H. M. Irvine, *Cable Structures*, Cambridge, MA, USA: The MIT Press, 1981.

[18] M. Ammar, L. E. Kollár, "Modelling Cable Vibration Following Load Removal." In: Okada, M. (eds) *Advances in Mechanism and Machine Science. IFToMM WC 2023. Mechanisms and Machine Science*, vol. 149. Springer, Cham., 2024.

A structured panorama of electromechanical ice protection systems

Y. Rafik[1,3], M. Budinger[1], V. Pommier-Budinger[2], H. Polaert[3]

[1] *Institut Clément Ader (ICA), University of Toulouse, INSA, ISAE-SUPAERO, MINES ALBI, UPS, CNRS, 31055 Toulouse, France*

[2] *Fédération ENAC ISAE-SUPAERO ONERA, University of Toulouse, 31400 Toulouse, France*

[3] *Safran Nacelles, Route du Pont 8 - 76700 Gonfreville l'Orcher, France*

Abstract- **The objective of this paper is to provide an overview and analysis of recent research aimed at improving mechanical-based Ice Protection Systems (IPS) and increasing their technological readiness based on academic papers, industrial products and technology patents. Ice properties and indicators for de-icing evaluation are presented first. The study classifies mechanical IPS according to excitation type. The paper describes also possible actuation systems.**

Keywords - Ice protection systems, Electromechanical de-icing, De-icing criteria, Actuators

1   INTRODUCTION

Icing is considered one of the greatest threats to flight safety. Several solutions have been developed to prevent ice accumulation on aircraft. These solutions can be divided into two categories: anti-icing solutions and de-icing solutions, and in terms of their mode of action (chemical, mechanical, or biological). Anti-icing solutions are designed to prevent the formation of ice and are used continuously when the aircraft is flying in icing conditions. De-icing solutions are used periodically to remove ice from the airframe after it has begun to accumulate.

The most commonly used solution is the bleed-air anti-icing system. This system drives heat from the engine and assigns it to each segment within the slats through a supply line. The heat then ejects from the sprout of a flute-shaped tube (piccolo tube) within the slats to heat the leading edge skin of the wing [1]. Thus, the engine design is oversized to provide thermal energy while maintaining aircraft propulsion. Another solution for anti-icing using thermal energy is to generate heat with electrical heat mats. This solution is referred to as electro-thermal anti-icing. Thermal solutions are reliable but require high power [2].

This article focuses on de-icing solutions. The paper first presents the ice properties and the indicators used to eval-

uate de-icing. Then it provides a classification of mechanical IPS as a function of the type of excitation. Finally, the possible electromechanical actuation systems for inducing deformations, shocks or vibrations leading to de-icing are described and analyzed.

2   MECHANICAL DE-ICING CRITERIA

2.1   *Ice properties*

Ice is considered a brittle material and can take many forms. In the literature, atmospheric ice has been divided into three categories: glaze ice (transparent and compact), rime ice (whitish and porous) and mixed ice (in between glaze and rime). Mechanical systems have more difficulty de-icing low-density ice because rime ice stores less elastic energy for a given amount of strain.

2.2   *Ice fracture*

Mechanical de-icing involves the initiation and propagation of cohesive and adhesive fractures in the ice (Figure 1). To properly size electromechanical deicing systems, it is necessary to define ice fracture criteria. In [3], the authors have established such criteria. The articles identify three key parameters for ice fracture propagation: cohesive tensile strength of the ice, adhesive shear strength of the ice/substrate interface, and critical energy release rate of the ice/substrate interface. The energy release rate G is an energetic indicator of the mechanical de-icing expressed in J/m^2. It represents the amount of strain energy in the ice per unit area. In the case of a beam, the formula for G is:

$$G = -\frac{1}{b}.\frac{\Delta U}{\Delta a} = \frac{1}{b}.\frac{U_i - U_{i-1}}{ai + 1 - a_i} \qquad (1)$$

with b the width of the beam, a_i the length of the crack and U_i the elastic strain energy of the structure at step i [4] of the fracture process.

To propagate the fracture, G must exceed a critical value G_c [5]. G_c depends mainly on the type of interface. It may decrease if a coating is applied to the substrate.
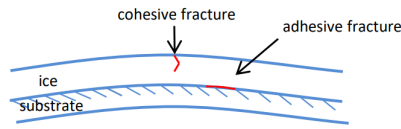
Figure 1: Cohesive and adhesive fractures [3]

The specific deicing mechanism depends on the size of the block of ice, its characteristics, and the properties of the substrate ([6]).

2.3 De-icing indicators

As mentioned earlier, one way to evaluate the performance of a deicing system is to compute the energy release rate G in the ice. To objectively compare de-icing systems using normalized metrics, it is better to calculate performance indicators such as G/U. This indicator represents the energy release rate normalized by the total strain in the structure. It indicates a system's ability to produce energy in the ice for a given total energy in the structure. It should be as high as possible. For example, Figure 2 shows the evolution of the G/U indicators computed for a single flexural or extensional mode as a function of the evolution of the adhesive fracture. The indicators show that the flexural modes have a strong capacity to initiate a fracture but cannot protect a complete surface using a single resonant mode.
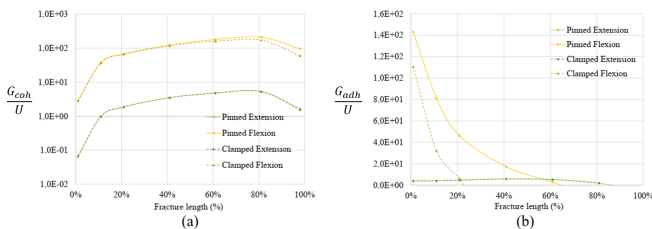
Figure 2: G/U indicators computed for a beam under different boundary conditions and types of modes [4]

3 CLASSIFICATION AND ANALYSIS OF DIFFERENT EXCITATION METHODS FOR MECHANICAL DE-ICING SYSTEMS

3.1 Static excitation

Static solutions consist of "slowly" inducing deformations in the structure. The deformation is transmitted to the ice, which accumulates strain energy. When a critical displacement is reached, cohesive fractures occur within the ice and adhesive fractures occur at the ice/airfoil interface. These fractures eventually lead to ice shedding.

Static solutions include pneumatic de-icing, which uses elastic boots attached to the airfoil to create deformations in the ice (Figure 6). Another static solution is to use shape memory alloy (SMA) materials. The transformation energy is typically applied by external heating or direct resistive heating of the SMA material itself [7].
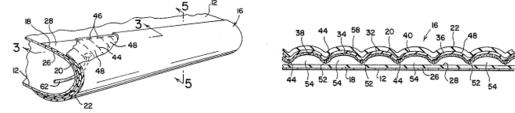
Figure 3: Pneumatic De-icers - Goodrich [8]

The primary disadvantage of static methods is the creep effect that occurs when ice is deformed slowly [9]. The creep effect decreases the stress in the ice for a given strain, thus reducing the strain energy for a given displacement. To compensate for this effect, larger displacements are applied. In the case of pneumatic boots, the deformation of the boots is significant enough to generate non-negligible drag on the airfoil.

3.2 Impact

Another way to create deformation in the ice is to apply an impact to the structure. This is the case for the Sonic Pulse Electro-Expulsive Deicer (SPEED), which was developed in collaboration with NASA Lewis and ARPA's SBIR program [7] and led to a patent in 2000 [10]. The system employs electromagnetic actuators to generate impacts on the airfoil, effectively removing the ice [10].

The copper coils located behind the wings act as actuators. Powered by a pulsed current, they deform and impact the skin of the structure, generating an acceleration that causes the ice accumulated above the actuators to detach and fall.

This solution requires little energy compared to thermal solutions, but it has some drawbacks. The skin and the actuators are exposed to repeated impacts, which can affect their lifetime. Therefore, this solution is more suitable for small aircraft, such as the CS-23, which have very limited power capacity but fewer de-icing cycles than larger aircraft. To generate impacts, the actuators need high pulse currents in an inductive load. Capacitive storage banks are therefore necessary and could penalize the mass balance of the solution.

3.3 Vibrations

Recently, there has been a growing interest in resonant solutions [4, 11, 12, 13] These solutions based on vibrations use actuators to excite the skin at a given frequency corresponding to a resonance of the structure. The amplification at resonance allows the generation of high dis-

placements with a low force as shown in Figure 4. Currently, resonant solutions are not used on aircraft. However, previous work has shown promising results, and despite its early development, industrial companies are actively investigating resonant solutions and filing patents [14, 15, 16, 17, 12, 13, 18].
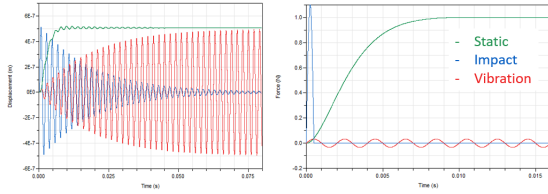
Figure 4: Displacements induced by different excitations and effort requirements [19]

The vibration modes are classified into two categories: flexural modes, which involve out-of-plane displacements, and extensional modes, which involve in-plane displacements. The flexural modes begin with a higher G/U, making the initiation of the fracture easier, but the energy release rate decreases significantly after 60% of the adhesive propagation (Figure 2). In flexural modes, the strain energy is concentrated around the antinodes, where the cohesive fracture is typically initiated. Around the nodes, the strain energy density decreases. Delaminating the entire surface using a flexural mode is thus complicated. However, a method has been proposed by [17] to improve the strain energy distribution. It reduces the density of strain energy around the node and increases it around the antinodes, allowing delamination with only one flexural mode. Extensional modes have a higher fracture initiation cost, but the value of G/U is fairly constant. The main challenge with these modes is the parasitic flexural displacement that occurs with the addition of actuators and is exacerbated for geometries with curvature (e.g. leading edges). Gastaldo et al. worked on a way to reduce the level of parasitic bending displacements by optimizing the thickness of the substrate or positioning the actuators in a specific way (Figure 5) [18].
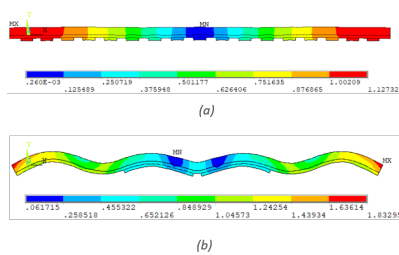
Figure 5: Modal shapes of extensional mode for (a) architectured substrate (16kHz) (b) reference substrate (13kHz) [18]

4 EVALUATION OF THE POSSIBLE ACTUATION SYSTEMS FOR ELECTROMECHANICAL IPS

4.1 Pneumatic actuation systems for static excitation

Pneumatic boots: By far, the most popular static solution is the pneumatic boot (Figure 6). They have been used on a wide variety of aircraft, mostly regional and smaller aircraft that have less power available for de-icing systems because most of the power generated is used for propulsion. The boots are inflated with air, which, in general aviation, comes from an engine-driven pump in aviation. In most cases, for pneumatic de-icing systems, aircraft are equipped with a turbine engine and the air is bled from the engine itself.

The main drawback of this system is its durability: boots are generally made of fabric-reinforced synthetic rubber such as neoprene, which has low resistance to erosion and impact. Boots can be repaired locally with patches, but the number of repairs is limited. The typical life expectancy of deicing boots is 3 - 10 years with proper care (www.goodrichdeicing.com). Another flaw of this system is the non-negligible drag induced by the boots. Since there is creep in the ice, a high displacement must be produced to shed the ice. The boots significantly increase the drag when inflated.

Figure 6: Pneumatic de-icing solution - Safran Aerosystems / Boots system closeup

Pneumatic bags and a metallic leading edge: Palacios [20] has also studied the pneumatic system to protect helicopter rotor blades from ice buildup. In this system, the metallic skin of the blade itself is deformed under pneumatic pressure to expel the ice. This system takes advantage of centrifugal forces by using them to generate the pneumatic pressure, thus avoiding using a pump. The tests of this system were carried out in a wind tunnel and coatings were tested on an instrumented rotor system to measure the ice shedding (Figure 7). The results were positive. However, the system has not yet been implemented in a real helicopter. Ice creep requires the use of high strain rates to avoid excessive deformation of the metal substrate.

Figure 7: Wind tunnel model with pneumatic deicing prototype / Side view of undeployed and deployed system / Ice adhesion strength rotor system [20]

4.2 Electromagnetic actuation systems for impact

Deformation induced by Eddy currents: A well-suited actuator for impact solutions is the electromagnetic actuator. These actuators use Lorentz force to generate displacements. Impacts can be produced with high current peaks.

Those actuators are far from being used in an aircraft, but some research presented promising results of electromechanical de-icing systems based on actuators using eddy currents to generate deformations. Jiang et al. [21] investigated various architectures using a stress-based finite element method to accurately predict de-icing test results. Endres et al. [22] also worked on a similar de-icing system as shown in Figure 8. The Electro Impulse De-Icing (EIDI) system operates on the same principle.

Figure 8: Example of electro-impulse de-icing system prototype [22]

Deformation induced by mechanical impact: Cox&Co produces low-power ice protection systems based on impacts. Their Electro-Mechanical Expulsion Deicing System (EMEDS) is used in a wide range of aircraft, from business jets (Hawker 4000) to larger aircraft (US Navy P-8 Poseidon, Figure 9). A millisecond-duration high current electrical pulse delivered to the actuators causes the actuators to change shape rapidly. The actuators impact the erosion shield causing it to flex and vibrate.

Figure 9: EMEDS solution - Cox&Co (www.coxandco.com)

The EMEDS system is sometimes combined with thermal anti-icing at the front of the airfoil to break up the ice into two blocks, making it easier to remove. Unlike the pneumatic system, EMEDS does not increase drag, and the displacement in the event of an impact is less

due to the absence of a creep effect in the ice. The system takes advantage of the high accelerations produced by the actuators, and the inertial effect helps to remove the ice. The system is also less susceptible to erosion due to its metallic outer surface.

The main disadvantage of the EMEDS system is its heavy power supply. The added mass of the power supply cannot be ignored when compared to the mass of the actuators. To generate high accelerations, the actuators require high currents, which means that the electrical power supplied by the aircraft needs to be adapted to meet the required current.

4.3 Electromechanical actuation systems for vibration

Electrodynamic shaker: Electromagnetic actuators can also be used to generate vibrations. The DeICE-UT project conducted a study on the de-icing of wind turbines and developed a solution using shakers (electromagnetic actuators) that generate low-frequency vibrations combined with other actuators (SH transducers in Figure 10) that generate ultrasonic waves to protect the wind turbines from ice build-up. Electromagnetic actuators are well-suited for low frequencies. However, their main shortcoming is the impedance of the coil, which results in reactive power proportional to frequency. After 2-3 kHz, the reactive power increases compared to the active power used to produce the displacement. This reactive power does not count in the consumption, but the electrical supply should be adjusted, increasing the total mass of the system.

Figure 10: DeICE-UT project - De-icing on wind turbines (www.deice-ut.eu)

Rotative shaker: Another way to generate vibrations with electromagnetic actuators is to use rotating electric motors in combination with unbalanced masses. The excitation frequencies are less than 1 kHz. Aero Ice Free (AIF) combines this type of actuator with composite leading edges for general aviation and UAS de-icing (Figure 11).

Figure 11: AeroIceFree - Rotative shakers / Patent [23]

4.4 Piezoelectric actuation systems for vibration

Piezoelectric actuators are particularly well suited for vibration solutions. They have a wider frequency range compared with the electromagnetic actuators, from a few kHz up to 200 kHz in some applications.

Patchs: Two kinds of piezoelectric patch transducers can be found on the market: bulk ceramics, which are fragile flat transducers available in various thicknesses and shapes, and piezocomposites, which are made of bulk ceramics prestressed in a resin (figure 12. The advantage of piezocomposites is that they allow a certain amount of flexure in the transducers. This allows them to be bonded to curved surfaces. They can also withstand higher stresses than bulk ceramics (50 MPa versus 25 MPa) [24] . However, they only come in certain sizes, which can be a problem if a specific size is needed to ensure good coupling of the transducers to the structure. De-icing systems based on vibrations excited by piezoelectric actuators are still in the early stages of development. Recently, some results from theses [4] and French DGAC projects [25] have shown promising results with successful de-icing tests on aluminum or CFRP NACA profiles made under laboratory conditions (ice deposition made with a wind tunnel) [19]. For the time being, the identified limit of the actuators is their resistance to shocks: up to 10-15J for some technologies of piezocomposite actuators [26], which is lower than the solutions presented above.
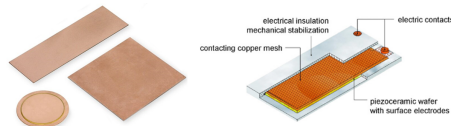
Figure 12: Bulk ceramics and piezocomposites (PI DuraAct)

Prestressed actuators: One way to increase the shock resistance of piezoelectric actuators is to apply compressive stress as in prestressed actuators. They consist in bulk ceramics stacked and prestressed with a screw (Figure 13). They have been studied for deicing in [27]. On the industrial side, Pytheas Technology also worked on a de-icing system based on prestressed actuators and patented it in 2023 [28].
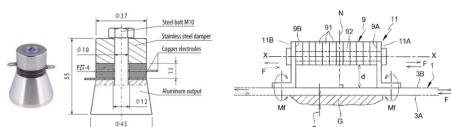
Figure 13: Actuator studied in [27] / Patent for de-icing system using prestressed piezo actuators [28]

5 CONCLUSION

Mechanical de-icing solutions are low-energy solutions that can be divided into three categories depending on the type of excitation: static, impact and vibration. Static or low-frequency solutions have very low energy consumption but require significant structural deformation due to ice creep. Impact solutions are characterized by high impulse forces that require an appropriate power supply. They share a weak aerodynamic effect with vibratory solutions. Vibratory solutions require lower forces when used at resonance of the structure, but require wide bandwidth actuators such as piezoelectric actuators and a good understanding of ice fracture mechanisms to optimize the de-icing efficiency. The question of the durability of the piezoelectric actuators is also an open question that requires further study.

REFERENCES

[1] F. Zhang, et al., Reliability analysis of bleed air anti-icing system based on subset simulation method, Applied Thermal Engineering 115 (2017) 17–21.

[2] O. Meier, et al., A handbook method for the estimation of power requirements for electrical de-icing systems, DLRK, Hamburg 31 (2010).

[3] M. Budinger, et al., Electromechanical resonant ice protection systems: energetic and power considerations, AIAA Journal 59 (7) (2021) 2590–2602.

[4] V. Palanque, Design of low consumption electromechanical de-icing systems, Ph.D. thesis, Université de Toulouse; ISAE-Supaero (2022).

[5] V. Palanque, et al., Cohesive strength and fracture toughness of atmospheric ice, Cold Regions Science and Technology 204 (2022) 103679.

[6] G. Gastaldo, et al., Stress and energy release rate influence on ice shedding with resonant electromechanical de-icing systems, in: ICAS 2022-33rd Congress of the International Council of the Aeronautical Sciences, 2022.

[7] Z. Goraj, An overview of the deicing and anti-icing technologies with prospects for the future, in: 24th international congress of the aeronautical sciences, Vol. 29, Citeseer, 2004.

[8] P. W. Kageorge, Pneumatic deicers with inextensible threads, uS Patent 4,687,159 (Aug. 18 1987).

[9] M. Mellor, et al., Effect of temperature on the creep of ice, Journal of Glaciology 8 (52) (1969) 131–145.

[10] J. J. Gerardi, et al., Electro-magnetic expulsion de-icing system, uS Patent 6,102,333 (Aug. 15 2000).

[11] V. Pommier-Budinger, et al., Electromechanical resonant ice protection systems: initiation of fractures with piezoelectric actuators, AIAA Journal 56 (11) (2018) 4400–4411.

[12] M. Budinger, et al., Electromechanical resonant ice protection systems: analysis of fracture propagation mechanisms, AIAA Journal 56 (11) (2018) 4412–4422.

[13] J. Palacios, et al., Ultrasonic de-icing of wind-tunnel impact icing, Journal of Aircraft 48 (3) (2011) 1020–1027.

[14] P. Gonidec, et al., Method for supplying electric power to an ultrasonic nacelle de-icing and anti-icing, uS Patent 11,492,128 (Nov. 8 2022).

[15] T. Le Docte, Piezoelectric de-icing of an air inlet, uS Patent 8,793,970 (Aug. 5 2014).

[16] T. Strobl, et al., Device and method for deicing and/or preventing ice formation and profile element and aircraft having such a device, uS Patent 10,442,540 (Oct. 15 2019).

[17] A. Bourhis, et al., De-icing element liable to be exposed to ice, uS Patent App. 18/316,334 (Nov. 16 2023).

[18] G. Gastaldo, et al., Full instantaneous de-icing using extensional modes: The role of architectured and multilayered materials in modes decoupling, Ultrasonics (2024) 107264.

[19] Y. Rafik, et al., Models and indicators for actuators sizing of resonant electromechanical ice protection systems, in: Recent Advances in Aerospace Actuation Systems and Components (R3ASC), 2023.

[20] J. Palacios, et al., Ice testing of a centrifugally powered pneumatic deicing system for helicopter rotor blades, Journal of the American Helicopter Society 60 (3) (2015) 1–12.

[21] X. Jiang, et al., Studies on the electro-impulse de-icing system of aircraft, Aerospace 6 (6) (2019) 67.

[22] M. Endres, et al., Experimental study of two electro-mechanical de-icing systems applied on a wing section tested in an icing wind tunnel, CEAS Aeronautical Journal 8 (2017) 429–439.

[23] A. Gornik, Systems and methods for applying deformations to a structural surface, uS Patent 10,173,781 (Jan. 8 2019).

[24] M. Gall, et al., Integrity of piezoceramic patch transducers under cyclic loading at different temperatures, Smart Materials and Structures 18 (10) (2009) 104009.

[25] Y. Rafik, et al., Resonant electromechanical ice protection systems: test results on naca profiles, in: More Electric Aircraft, Toulouse, France, Feb. 7-8, 2024.

[26] G. Gastaldo, et al., Proposition of a new qualification impact test for aerospace smart structures, in: ICAS 2022-33rd Congress of the International Council of the Aeronautical Sciences, 2022.

[27] V. Daniliuk, et al., Ultrasonic de-icing of wind turbine blades: Performance comparison of perspective transducers, Renewable Energy 145 (2020) 2005–2018.

[28] F. Mosca, et al., De-icing system for a mechanical part, comprising at least one piezoelectric actuator, wO 2023/222549 A1 (May 8 2023).

Development of Anti-/De-Icing System based on Active Thermography

Adeel Yousuf, Hassan Abbas Khawaja, Muhammad Shakeel Virk

UiT – The Arctic University of Norway

yousuf.adeel@uit.no, hassan.a.khawaja@uit.no, muhammad.s.virk@uit.no

Abstract— **Ice accretion remains a pervasive challenge for infrastructure in cold climates, posing threats to both human safety and machine operability. Addressing this issue, our work introduces an innovative, automated ice detection/mitigation system leveraging active infrared thermography. This technology enables the detection of ice on low-temperature surfaces exhibiting thermal contrast. The system integrates low-cost thermal infrared cameras and gridded-gradient heaters to remotely operate and mitigate the identified ice patches. The operational workflow begins with the system mapping the region of interest, identifying iced surface patches within its field of view. Subsequently, the system makes calculated decisions to initiate mitigation measures for the detected regions. The evaluation of the system encompasses key factors such as heat transfer, power converter efficiency, and dynamic switching behaviour. The study explores the impact of two heating techniques: continuous power heating and modified pulsed power heating, conducting a comparative analysis to discern their respective efficacy. This research not only introduces an effective solution for ice detection and mitigation but also contributes valuable insights into optimizing the efficiency and performance of such systems. By addressing the challenges posed by ice accretion, our work aims to enhance the safety and functionality of onshore and offshore infrastructure in cold climatic regions.**

Keywords— ***System design, ice protection, infrared, electrothermal, remote sensing***

I. INTRODUCTION

Icing is a natural phenomenon in cold regions especially Arctic regions and ice accretion on onshore, offshore, and airborne structures poses grave damage to them in terms of system operation; consequences may lead to irreversible losses in terms of human and machine safety [1,2]. In most of the cases where exposure to cold weather is prolonged, avoiding the icing situation is simply not an option and therefore different techniques are adopted to prevent the ice (anti-icing system) or melt the ice (de-icing system). Overall system comprising an ice detection and mitigation strategy is called an ice protection system. Multiple techniques exist in literature or in practice that propose different technologies manifesting the laws of optics, physics, and chemistry to detect and prevent/melt the ice [3-6]. These techniques leverage each other's pros and cons to solve application-specific problem at hand.

Upon carefully conducted literature review and up to the best knowledge of authors an automated, energy efficient ice protection system could not be found in application. This paper presents the ongoing work conducted in this regard to achieve the desired objectives of economic, reliable and remotely operated autonomous system. Direct/indirect ice detection strategies were studied [7,8] and active Infrared Thermography (IRT) was shortlisted for its non-destructive remote sensing and wide area scan capabilities. Previous works also exist to support the proposition that long wave infrared (LWIR) cameras can detect and differentiate the fresh water and saline ice [9-12]. For the ice mitigation part, electrothermal heating is chosen to be implemented for it is comparatively efficient than other existing strategies. This system also serves as excitation technique for active thermography. Since the work is ongoing, the conceptual design and supporting preliminary heat transfer simulations are presented in the following section.

II. METHODOLOGY

System design is divided into three phases: (i) conceptual design – that presents the big picture of overall system (ii) preliminary heat transfer simulation mandatory to study thermal behaviour of heating system (iii) hardware design.

A. Conceptual Design

A conceptualised economical ice protection system is shown below in Figure 1 in which arrowheads with numbering show the sequence of operation. Starting off with an LWIR camera that focuses on the target surface prone to icing (ship deck here), the camera captures incident thermal radiation emitted by the target and the environment and sends output thermogram to the controller. Based on the decision (ice/no ice), it will send signals to energize/de-energize the transducers/relays for heating only at the locations where ice is detected. For this, a gridded heated surface comprised of small heating elements is proposed that can attain a gradient heating pattern. For research phase, remote image processing shall also be incorporated into the system. In this setup the controller shall send captured images to a cloud server from where they can be downloaded through an image processing software such as MathWorks® MATLAB. Additionally, the inclusion of supervisory control for emergency operations ensures the overall system's reliability and fail-safe operation.

One of the most significant challenges in IRT is expensive operational setup and equipment, particularly the infrared camera. The heavy cost hinders field study of icing on structures as it adds to the maintenance costs of camera in case of mishap or malfunction [1]. So, to address this issue low cost LWIR FLIR® Lepton on-chip cameras are suggested. The camera resolution is 80×60 and costs around only $250. To assess if such a low-end camera can detect ice or not, a simple experiment was conducted for comparative study between FLIR® Lepton and FLIR® T1030SC cameras; both are LWIR cameras featured with uncooled microbolometer, later one being 768×1024 in resolution and costing approx. $50000. The experiment comprised of an ice cube of known

dimensions placed over a high emissive (~0.85) PET sheet supporting 75W, 230V heater (see Figure 2).

1) Image acquisition
2) Uploading images to the server
3) Downloading images for remote image processing
4) Processed image decision (ice/no ice)
5) Reading decisions from the cloud server
6) Activation/deactivation of corresponding transducers
7) Energize/de-energize relays
8) Switching ON/OFF embedded heaters in the surface and supplying controlled heating
9) Supervisory control for emergency operation/system failure

Fig. 1   Conceptual design of proposed ice detection and mitigation system [13].

Fig. 2   Ice cube placed on PET sheet for infrared thermography analysis of low- and high-resolution images [13].

The ice cube was observed with both the cameras and their results were subjected to image processing in which goal was to segment the ice edges. Closing morphological operation was performed along with Canny edge detection technique to successfully achieve the desired result. It was observed that both the cameras were able to capture and detect the ice after image processing. However, from the accuracy point of concern, FLIR® T1030SC camera is more accurate than the Lepton, which is why the difference of 2°C in mean temperature is apparent (see Figure 3).

Lepton (80×60) – edge detected image
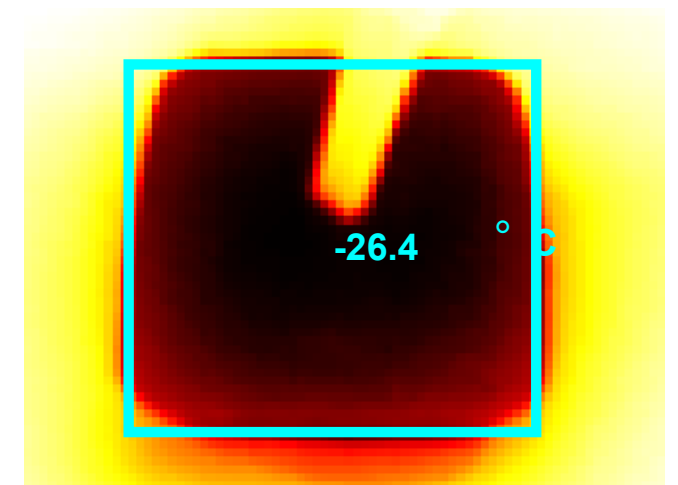
Lepton (80×60) – average temperature of segmented region

T1030SC (768×1024) – edge detected image

314
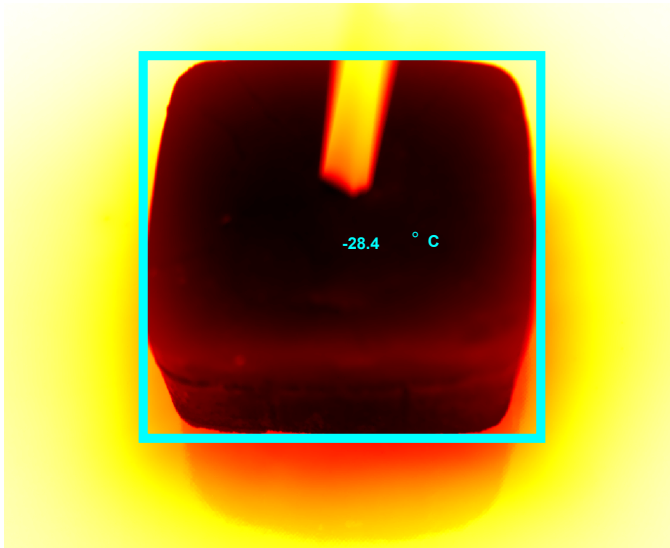
T1030SC (768×1024) – average temperature of segmented region

Fig. 3   Final results after applying morphological operations on thermal IR images [13].

B. Simulation

For ice mitigation system the idea of gridded, gradient heating elements is presented, according to which the target surface will be accompanied by multiple adhesive heaters. For energy saving heaters at only those locations will be switched on that experience icing. This concept is first simulated in software before proceeding for actual hardware design.

For this purpose, a two-dimensional aluminium surface (100cm×50cm) with subzero temperature regions (representing ice) is simulated in MATLAB®. Corresponding parameters for aluminium sheet and heaters are taken into account and Finite Difference Method (FDM) is applied to solve 2D heat equation. Boundary conditions are 258K for air temperature whereas the temperature for iced region is taken as 253K in the initial conditions. For illustration, figure 4 below shows 4 out of 18 heaters of equal dimensions (10cm×10cm) activated for studying heat transfer. Heating is activated at t = 5s. This case is chosen to mimic a condition when icing will only need to be removed at these particular heater locations. Pattern at t = 4s shows the temperature diffusion across the perimeter of iced region.

Figure 5 below displays contour plots after the heaters are activated. It is assumed that heat transfer is only taking place through conduction without any heat loss and heaters turn ON in step function pattern (with constant 400K temperature assumed). Temperature evolution seeks to achieve thermal equilibrium over aluminium sheet. Simulation is run here for 500s; if ran for an extended time that stage can be observed in a contour plot with uniform temperature of 400K over whole surface.

C. Hardware Design

As a part of hardware design implementation electronic assembly including two Lepton IR cameras are planned to be fixed in a waterproof polycarbonate plastic box with IP67 rating. Lepton cameras feature 50° horizontal field of view (FOV) so two cameras can cover an extended view. A 3D
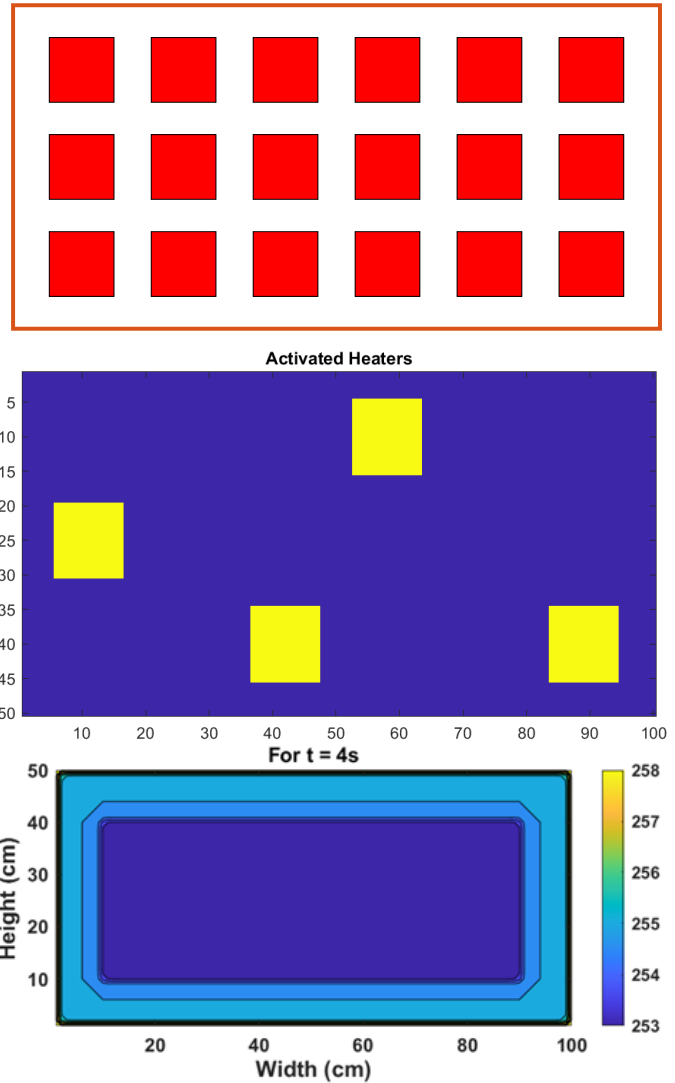
Fig. 4   Eighteen gridded heaters over aluminium surface and considering 4 out of 18 activated heaters for simulation. Last image shows thermal pattern at t = 4s in the presence of ice when heaters are not yet activated.

printed casing is developed for them that houses camera module and germanium window for the camera lens. germanium is chosen for its high transmission rate for LWIR. The box is also supposed to house cable connections for controller and relay modules for the activation of heaters. Figure 6 shows a 3D printed camera housing; a red-shaded exposure can be seen in front of one of the cameras, it is the installed Germanium window.

A thin aluminium target surface (100cm×50cm×0.05cm) is prepared for electrothermal heating supplied with 18 gridded adhesive heaters (in a matrix of 3×6). Since aluminium itself is highly shiny, its one side facing the cameras is polished with black acrylic spray which has a high emissivity value (~ 0.9) as shown in Figure 7. This step is important to perform as otherwise reflected radiation can deceive thermal camera.

Final results are expected to arrive after the complete implementation of remaining system that include communication between controller and software. The hardware setup shall be tested in laboratory as well as on the field.

315
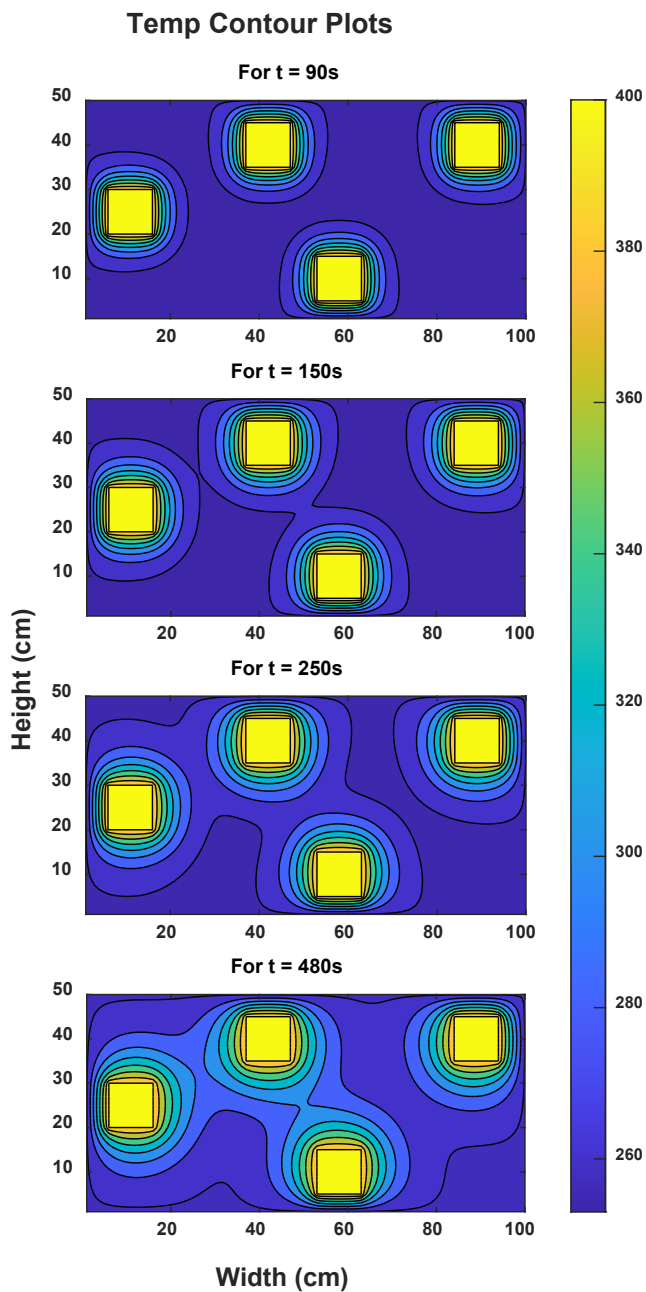
Fig. 5   Heating pattern for activated heaters.
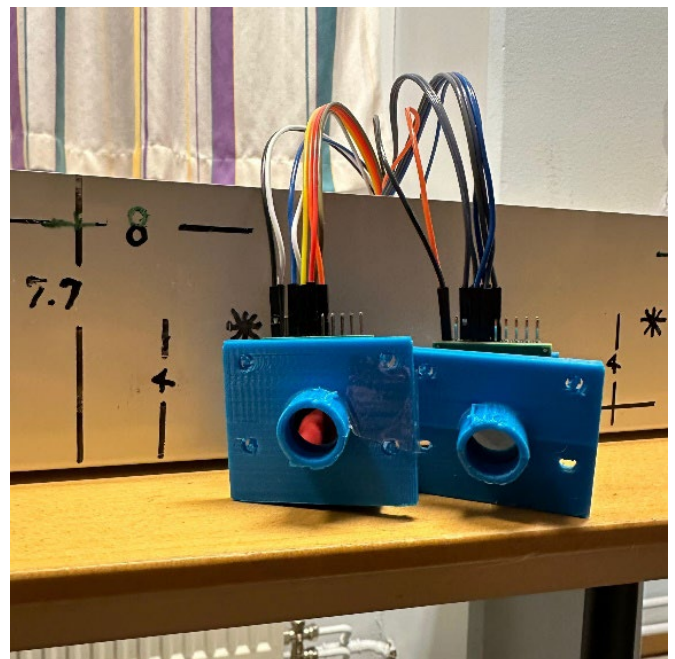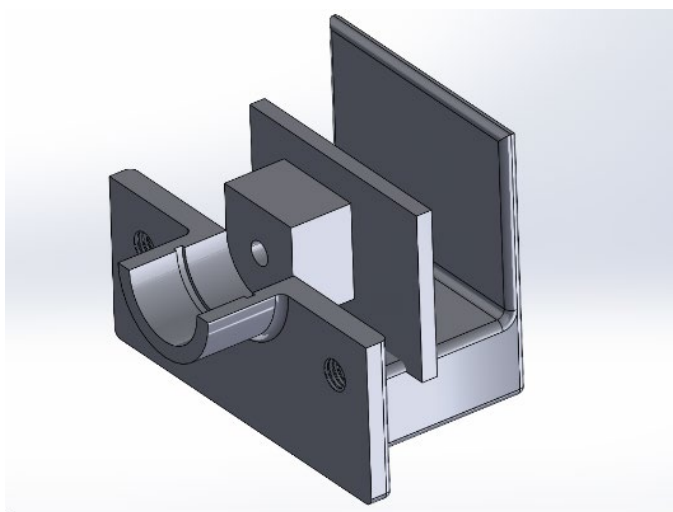
Fig. 6   3D printed FLIR® Lepton camera housing.
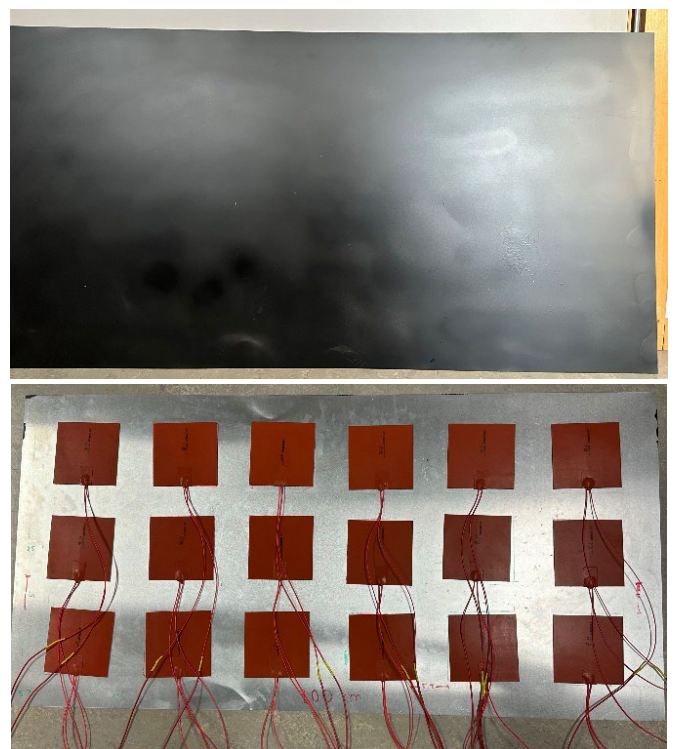
Fig. 7   Polished side and heaters side of aluminium sheet.

III. Conclusion

Build-up of ice on structures poses risks to structures in aviation, energy, transport, and marine sectors. In this regard, a conceptual ice protection system based on active infrared thermography as its ice detection module and electrothermal heating as its ice mitigation module is presented. The work is underway and currently showcases heat transfer simulations and completed hardware setup. Final results are awaited till the completion of whole setup. The work addresses the ice accretion challenge faced by different surfaces and structures in cold climate regions and aims to automation with cost-effectiveness and energy efficiency.

316

REFERENCES

[1] A. Yousuf, H. Khawaja, and M. S. Virk, "A review of infrared thermography applications for ice detection and mitigation," Cold Regions Science and Technology, vol. 218, no. 104058, 2024.

[2] C. C. Ryerson, "Ice protection of offshore platforms," Cold Regions Science and Technology, vol. 65, no. 1, pp. 97-110, 2011.

[3] M. S. Virk, M. Y. Mustafa, and Q. Al-Hamdan, "Atmospheric ice accretion measurement techniques," The International Journal of Multiphysics, vol. 5, no. 3, pp. 229-241, 2011.

[4] H. Xue, H. A. Khawaja. "Review of the Phenomenon of Ice Shedding from Wind Turbine Blades," The International Journal of Multiphysics, vol.10, no. 3, pp. 265–276, 2016.

[5] K. Wei, Y. Yang, H. Zuo, and D. Zhong, "A review on ice detection technology and ice elimination technology for wind turbine," (in English), Wind Energy, vol. 23, no. 3, pp. 433-457, 2020.

[6] T. Rashid, H. A. Khawaja, and K. Edvardsen, "Review of marine icing and anti-/de-icing systems," Journal of Marine Engineering & Technology, vol. 15, no. 2, pp. 79-87, 2016.

[7] J. Y. Jin and M. S. Virk, "Seasonal weather effects on wind power production in cold regions- a case study," International Journal of Smart Grid and Clean Energy, vol. 8, no. 1, 2019.

[8] Z. Andleeb, H. A. Khawaja, M. Moatamedi. "Multiphysics based Analysis of Materials for Roads in Cold Regions to Prevent Ice Adhesion and Low-Temperature Crack Developments," The International Journal of Multiphysics, vol.16, no. 4, pp. 437-447, 2022.

[9] T. Rashid, H. A. Khawaja, and K. Edvardsen, "Determination of Thermal Properties of Fresh Water and Sea Water Ice using Multiphysics Analysis," The International Journal of Multiphysics, vol. 10, no. 3, pp. 277-290, 2016.

[10] T. Rashid, H. A. Khawaja, and K. Edvardsen, "Ice Detection of Pure and Saline Ice Using Infrared Signature," Sensors & Transducers, vol. 206, no. 11, pp. 82-87, 2016.

[11] T. Rashid, H. Lang, M. Taimur, N. Chiodarelli, M. Volder, K. Edvardsen, H. A. Khawaja, "Roll to Roll coating of carbon nanotube films for electro thermal heating," Cold Regions Science and Technology, vol. 182: no. 103210, 2021.

[12] T. Rashid, H. A. Khawaja, K. Edvardsen, "Measuring Thickness of Marine Ice Using IR Thermography," Cold Regions Science and Technology, vol. 158, pp. 221 – 229, 2018.

[13] A. Yousuf, H. A. Khawaja, and M. S. Virk, "Conceptual design of cost-effective ice detection system based on infrared thermography," Cold Regions Science and Technology, vol. 215, no. 103941, 2023.

Simulating Aircraft Wheel-Road Interactions in Winter with Multi-Tool Analysis (MTA)

María Loaiza Osorio[1], Jean-Denis Brassard[1], Gelareh Momen[1], and Jean Perron[2]

[1] *Anti-icing Materials International Laboratory (AMIL), University of Quebec at Chicoutimi, Canada*
[2] *Department of Applied Sciences, University of Quebec at Chicoutimi, Canada*

mllosorio@etu.uqac.ca, jdbrassa@uqac.ca, gelareh_momen@uqac.ca, j1perron@uqac.ca

Abstract— **Ground operations, encompassing taxiing, takeoff, and landing, play a vital role in aviation safety. The interaction between an aircraft's tires and the runway is particularly crucial during landings, with approximately 50% of flight accidents occurring during this phase, often leading to overruns or excursions. A significant contributing factor to these incidents is maintaining adequate braking efficiency. Runways must provide sufficient friction levels to facilitate the safe movement of airplanes. This research aims to develop an innovative tool to measure friction at an established speed. The Multi-tool Analysis machine (MTA) utilizes a rounded rubber actuated by a pneumatic cylinder with variable pressure, simulating the interaction between aircraft wheels and a runway contaminated by icing precipitation. Our overarching objective is to significantly contribute to the broader field of frictional analysis, offering a valuable resource for researchers and practitioners alike.**

Keywords—***Friction; Runway De-icing Products; Ice adhesion; Runway excursion; Concrete.***

I. INTRODUCTION

During a flight, various phases demand distinct attention and sensitivity, designating certain stages as critical. These critical phases necessitate precise adherence to procedures, thoughtful decision-making, and optimal conditions to ensure the safety and success of the overall flight operation. Ground operations, such as taxiing, takeoff, and landing, fall into this category [1]. The importance of friction between an aircraft's tires and the runway pavement is particularly pronounced during the critical landing phase. Given that about 50% of flight accidents occur during this phase, with the majority resulting in overruns or runway excursions, low braking efficiency significantly contributes to these incidents [2, 3]. Expanding our perspective beyond aviation, the anti-slip characteristics of runways significantly contribute to safety. Runways must provide sufficient friction levels to support airplanes' safe movement [4].

In 2021, Canada adopted the Global Reporting Format (GRF) to enhance flight safety and comply with the International Civil Aviation Organization's (ICAO) call for regulated and enhanced reporting methods for runway surface conditions, leading to this initiative [5].

Laboratory methodologies for testing friction and simulating the challenging conditions of runways during winter are pivotal fields of study that address this condition and the issues it represents for the safety and economic aspects of passengers, airport operators, and manufacturers.

Currently, the laboratory testing device that correlates most with the GRF is the British Pendulum Test (BPT) [6]. However, this test outputs the results in its own representation, the British Pendulum Number (BPN), making comparison with the coefficient of friction (µ) established in the range and the results from other equipment complicated.

Based on the crucial significance of advancing frictional studies, this research is dedicated to creating an apparatus for precise friction measurement. The focus of our investigation centers on developing and implementing an innovative device, leveraging the capabilities of the Multi-Tool Analysis machine (MTA). The objective is to introduce a tool that enhances the accuracy of friction measurement and addresses the challenges posed by traditional methodologies. By integrating advanced technology and experimental precision, we aim to contribute to the broader field of frictional analysis and provide a valuable resource for researchers and practitioners alike.

This study will meticulously examine the MTA's calibration and fundamental operation, with particular emphasis on comparing and validating its friction data results within the ranges stipulated by the Canadian Runway Index (CRFI) under both dry and icy conditions. By conducting rigorous experiments, our goal is to thoroughly comprehend its performance.

Furthermore, as a pivotal component of this study, we made a first approach and proposed a mathematical model for the MTA apparatus. This mathematical framework provides insights into the tribological interactions, laying the groundwork for future validation and enhanced predictive capabilities.

II. MATERIALS AND METHODS

The Multi-tool Analysis device simulates the interaction between aircraft wheels and a runway contaminated by icing precipitation and measures friction at an established speed within a range of 0.5 mm/sec to 74.0 mm/sec using a rounded rubber actuated by a pneumatic cylinder with variable pressure, see Fig. 1. In this study, we measure the friction of standard concrete samples previously cleaned and dried at room temperature.
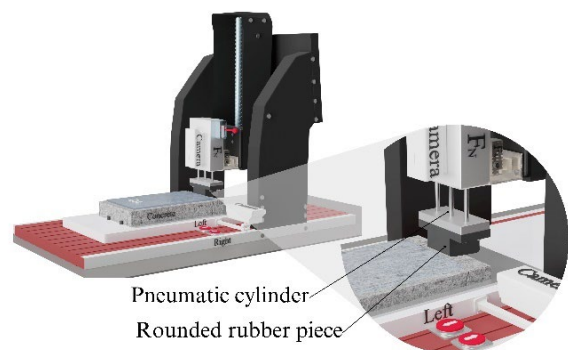
Fig 1   Multi-Tool Analysis machine (MTA) close-up with parts

The MTA setup was employed to assess friction levels on a concrete surface, maintaining a controlled temperature at -5°C within the snow chamber at the Anti-Icing Materials International Laboratory (AMIL) of the UQAC. The concrete specimens under evaluation, measuring 10 cm × 20 cm × 5 cm, were chosen for their ability to closely replicate the surface properties found on typical Canadian airport runways, including roughness and absorption characteristics.

Before exposure to icy conditions, the concrete samples underwent cleaning and drying processes. Subsequently, the specimens were placed in the cold room of the AMIL, where a temperature of -5°C ± 0.1 was maintained. Once the samples reached the target temperature, they were subjected to freezing drizzle for 30 minutes, with a mean volumetric diameter (MVD) of approximately 320 µm, which generates an ice thickness rate of about 5 to 8 mm/h. To ensure the concrete and ice temperatures stabilized at -5 ± 0.5 °C, allowing for the dissipation of latent heat generated during icing, a minimum interval of 1 hour was required between the icing process and initiating the friction test. Following this preconditioning, the iced concrete specimens underwent individual evaluation using the MTA.

Fig. 2: Concrete samples after icing in the cold room

The rounded rubber piece was tested in the 3D optical profilometer to assess its surface roughness. This machine utilizes white light interferometry with a simple recipe setup for topography measurement. Data analysis was performed using Profilm3D software, and parametric and statistical estimates of waviness and roughness heights were conducted following the International Organization for Standardization ISO 4287-1997 guidelines. Testing utilized 20x and 50x magnification lenses, with measured area dimensions of 1 x 0.84 mm and 0.4 x 0.34 mm, roughness values of recycled rubber respectively [7, 8].

A total of 80 tests were conducted, with the testing procedure divided into two conditions: dry and icy. We utilized ten concrete samples, allocating 5 for dry and 5 for icy conditions. Each sample underwent testing at four pressure levels: 10, 20, 40, and 80 PSI, with two repetitions for each pressure. All tests were conducted at -5°C (icing and testing).

III. RESULTS

A. 3D profilometry

We opted for 100% recycled vulcanized rubber for the rubber piece, as it balances cost-effectiveness, performance, and sustainability in replicating friction between aircraft wheels and concrete surfaces. This decision was made to mimic the technical conditions of aircraft tire carcasses and address economic considerations, especially given that this is our inaugural use of this machine for measuring friction in this specific scenario [9].

For safety reasons, components like tire tread carcasses are typically made of natural rubber in aircraft applications. Natural rubber has a smoother surface than recycled rubber, mainly because it contains fewer additives, impurities, or contaminants. The surface roughness of natural rubber is usually between 0.1 and 1 µm (Rq), while recycled rubber can range from 6 to 55 µm [10, 11].

Fig. 2 displays the surface roughness image generated by the 3D optical profilometer. Since this device is engineered to measure small surface regions, six measurements were conducted on the rubber sample. The mean surface roughness values for the lenses 20x and 50x were 25.2 ± 4 and 31.56 ± 11 µm, respectively. This indicates the variability of the surface roughness of the rubber along its area.
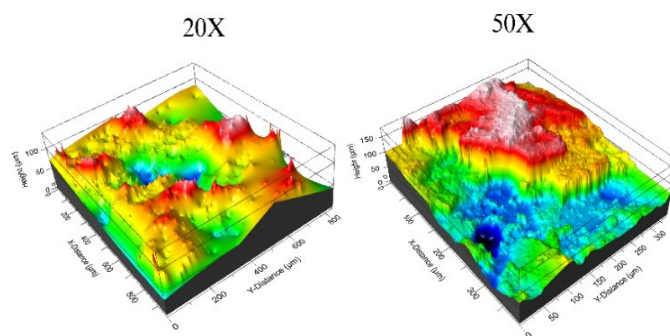
Fig. 3   3D profilometry view of the rubber piece

B. MTA Friction with Concrete

On the other hand, the results of the MTA friction tests are divided by dry and icy conditions, allowing us to observe the correlation between these conditions in terms of the increasing friction tendency with the increment of pressure. During testing, this logical correlation was acquired, confirming the device's correct operation.

Figure 4 illustrates the average values of each test, plotted against the applied normal force, along with their corresponding friction values. Each data point represents the average of 10 tests. For concrete subjected to icy conditions (blue), the increase in friction value commences at 40 PSI. Friction values remained consistent at 10 PSI and 20 PSI. Conversely, for dry concrete (orange) tests, the proportional relationship between friction and normal force was evident across all four pressure levels examined.
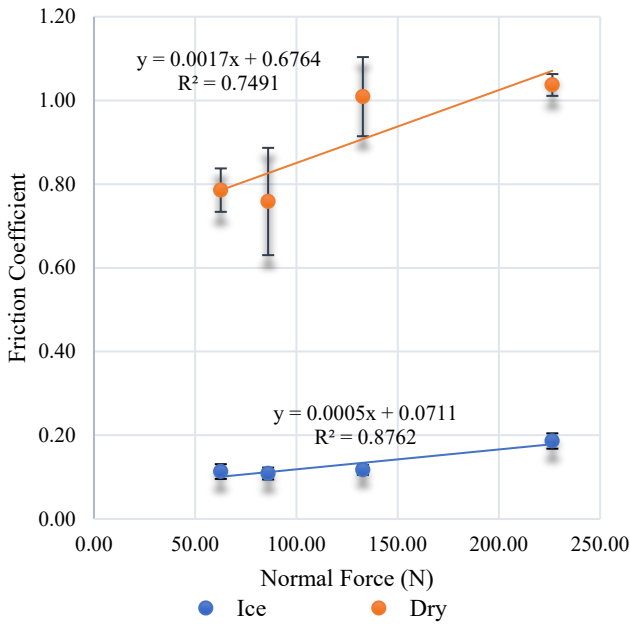
Fig. 4: Friction results for dry an ice concrete sample

To confirm the accuracy of the friction values obtained under the two distinct conditions, we employed the Canadian Runway Friction Index (CRFI), see Table 1. This standardized approach to assessing runway conditions enables us to effectively evaluate friction levels on Canadian runways. The CRFI provides a range for dry runways of >0.4 and icy conditions of <0.19 [12].

TABLE I. COMPARISON BETWEEN THE CRFI RANGE AND MTA FRICTION RESULTS

Condition	Pressure (PSI)	Normal Force (N)	Friction μ	Standard deviation	CRFI [5]
Ice	10	62.63	0.11	0.02	<0.19
	20	86.03	0.11	0.01	
	40	132.81	0.12	0.01	
	80	226.39	0.19	0.02	
Dry	10	62.63	0.79	0.05	>0.4
	20	86.03	0.76	0.13	
	40	132.81	1.01	0.09	
	80	226.39	1.04	0.03	

This data represents the averages of the friction test results, accompanied by their respective standard deviations, all of which were not greater than 0.02 for ice and 0.13 for dry conditions. Furthermore, all values fall within the CRFI range, indicating a favorable response of the apparatus under various testing conditions.

C. Mathematical Model

To complement our study and analysis of the MTA friction device, we have developed two main initial approaches for the mathematical modeling of the phenomena. These models focus on simulating the coefficient of friction between two sliding surfaces. The first approach assumes that the coefficient of friction is not a function of speed, utilizing the Coulomb law of friction. In the second approach, we consider the fluid effect, where the coefficient of friction is highly dependent on speed, employing the concept of the Liquid-Like Layer (L-LL) or Laplace pressure. Additionally, we have explored the option of a hybrid model combining aspects of both approaches for the case where the coefficient of friction exhibits a slight dependency on speed. This model could be helpful for the industry for predicting the μ based on observations and thus support efficiency and security on the runway.

IV. CONCLUSIONS

The Multi-Tool Analysis machine, with its friction tool, correlates with the CRFI range for ice and dry conditions, aligning with the scope proposed in this regulation. This allows us to confirm using this new methodology for simulating aircraft wheel interactions with the runway during taxiing and measuring friction values under different conditions.

This device offers significant advantages and contributes to current laboratory developments in friction measurement devices under winter conditions, addressing a significant gap in laboratory methodologies. Its main benefits include:

- Measurement of any flat surface
- Easy interchangeability of the rubber attachment with other attachments, such as an ice scraper, to simulate different scenarios
- Simple testing procedure with short execution time
- Cost-effective
- Compatibility with various types of contaminants, including winter precipitations and Runway De-icing Products
- Repeatability of tests with a standard deviation of approximately 16% for dry conditions and 9% for ice conditions

V. FUTURE STUDIES

The following steps for this project involve testing for additional contaminants such as snow, water, and RDPs, both in liquid and solid form. By doing so, this tool can become a practical methodology for manufacturers to assess the performance of their products before real-life outdoor operations.

REFERENCES

[1]   *Federal Aviation Administration, Aviation Instructor's Handbook (FAA-H-8083-9)* in *Chapter 9: Techniques of Flight Instruction.*

[2]   Jiang, B. and H. Wang, *An integrated analytical model for friction characteristics of aircraft tire on wet runway pavement.* Tribology International, 2023. **185**: p. 108501.

[3]   Daidzic, N.E. and J. Shrestha, *Airplane landing performance on contaminated runways in adverse conditions.* Journal of Aircraft, 2008. **45**(6): p. 2131-2144.

[4]   Wambold, J.C., et al., *International PIARC experiment to compare and harmonize texture and skid resistance measurements*. 1995: PIARC.

[5]   Canada, T., *Advisory Circular (AC) No. 300-019: Global Reporting Format (GRF) for Runway Surface Conditions*, O. Transport Canada: Ottawa, Canada, Editor. 2021.

[6]   Brassard, J.-D., et al., *Assessment of Runway Surface Conditions by British Pendulum Testing under the Global Reporting Format Winter Conditions.* Applied Sciences, 2022. **12**(19): p. 9646.

[7]   *ISO 4287: 1997, International Organization for Standardization 4287: Geometrical Product Specifications (GPS), Surface texture: Profiling method – Terms, definitions and surface texture parameters.*

[8]   Cntech. *Profilm3 Optical Profiler*. 2009; Available from: https://www.cntech.co.uk/p/profilm3d-optical-profiler.

[9]   De, S.K. and J.R. White, *Rubber technologist's handbook.* Vol. 1. 2001: iSmithers Rapra Publishing.

[10]   Sethuraj, M.R. and N.T. Mathew, *Natural rubber: biology, cultivation and technology*. 2012: Elsevier.

[11]   Ido, T., et al., *Sliding friction characteristics of styrene butadiene rubbers with varied surface roughness under water lubrication.* Tribology International, 2019. **133**: p. 230-235.

[12]   Canada, T., *Advisory Circular (AC) No. 300-019*, G.R.F.G.f.R.S. Conditions, Editor. 2021.

Numerical investigations on aero-engine icing characteristics at mixed phase conditions

Haifeng Qi [1], Shinan Chang [1,*], Xiaowei Zhu [1], Yinglin Yang [1], Zuojun Shen [1], Jingwu He [1]

[1] *School of Aeronautic Science and Engineering, Beihang University, China*

qhf@buaa.edu.cn, sn_chang@buaa.edu.cn, xiaoweizhu@buaa.edu.cn, yangyl@buaa.edu.cn, shenzuojun@buaa.edu.cn, hejingwu@buaa.edu.cn

Abstract—**Ice crystal/mixed phase icing in aero-engine will cause engine surge, stalling, thrust reduction, and even stop in extreme cases, which seriously endangers flight safety. In this paper, the characteristics of mixed phase ice accretion in aero-engines are numerically studied. The air flow field model, mixed phase trajectory model, impact model, sticking model and ice accretion model are established. The effect of different melting rate (LWC/TWC) on aero engine icing is analyzed and discussed. The results show that with the increase of the melting rate, the ice thickness of the nacelle, the nosecone and the fan pressure side surface increased significantly. The icing of the fan and the IGV is mostly concentrated on the pressure side, and there is only a small amount of icing on the suction side. When the fan span is 90% and the melting rate is 0.05, 0.15, and 0.25, the maximum icing amount on the fan surface is 1.56, 3.85, and 5.71mm, respectively. Furthermore, when the melting rate is 0.3, the ice area of 90% span of the bypass surface increases by 40.2% compared to 30% span. Finally, in the design of engine anti-icing, it is necessary to focus on the effect of icing on the surface of each component on the engine performance.**

Keywords—***Mixed phase, Aero-engine icing, Numerical simulation, Melting rate, Phase transformation***

I. INTRODUCTION

With the rapid development of the aerospace industry, civil aircraft and large transport aircraft pay more attention to economy, safety and comfort. When the aircraft flies through cloud at subsonic speeds (Ma < 1), supercooled water droplets (SCWD) in the cloud can hit the windward surface of the aircraft/engine parts and freeze [1-2]. Nevertheless, unlike the icing of SCWD hitting the surface of aircraft/engine components, there have been many incidents of aero-engine loss of thrust at altitudes above 7 km since the 1990s. After a series of investigations, it was found that the thrust loss was mostly caused by the icing of ice crystals inside the engine, and the icing conditions were significantly different from the icing of supercooled water droplets, which aroused great concern in the aviation industry [3-4].

When the aircraft is cruising at high altitude, the engine will suck in a lot of ice crystals. Under the action of the high-temperature internal flow of the engine, the ice crystals will partially melt and form the mixed phase. The mixed phase particles further form a liquid water film on the surface of internal engine structures such as compressor blades, and subsequently inhaled ice crystals adhere to these wet surfaces and cool the surface to below freezing. As the ice crystals continue to suck in, eventually the internal structure of the engine will be covered by ice. Different from the icing on the outside of the engine caused by the impact of SCWD, ice crystal icing (ICI) may occur in the whole low-pressure

compressor to high-pressure compressor primary stator blade area [5-6].

Nevertheless, the simulated aero-engine ICI test has the characteristics of high cost, long period and poor universality. Therefore, numerical simulation method has become an important means to study ICI. Villedieu et al. [7] used the Lagrange method to establish mathematical models for ice crystal shape, heat and mass transfer, adhesion, fragmentation and rebound during ice crystal impact. Meanwhile, Trontin et al. [8] carried out numerical simulation on ice crystal and mixed phase icing, considering the influence of ice crystal erosion effect. Norde et al. [9] used Euler method to calculate particle trajectories, established ice crystal impact and erosion models, and improved the classical Messinger thermodynamic model of icing based on the characteristics of mixed phase heat and mass transfer processes. The results show that this method can accurately predict the thickness and shape of ice. Jiang et al. [10] calculated and analyzed the movement process of ice crystals in the inner channel of turbofan engine. The result shows that the liquid water mass fraction of 20μm ice crystal at adhesion position is 10.22% while liquid water mass fraction of 100μm ice crystal at the compressor outlet is just 2.1% and there will be no ice accretion inside the compressor. Bu et al. [11] took the ice crystal adhesion effect into consideration and conducted numerical studies on the surface icing of NACA 0012 airfoil under frost and glaze ice conditions respectively. The results show that the ice crystal adhesion effect has a great influence on the amount of ice and the shape of ice under the mixed phase.

Based on the above research, the research on aero engine icing is relatively scarce, and more research work on engine icing is needed. Therefore, a numerical study of aero-engine mixed phase icing is carried out in this paper. In addition, sensitivity parameters of aero-engine icing (icing time, melting rate) are analyzed in order to provide necessary data support for aero-engine anti-icing design under different mixed phase icing conditions.

II. MODEL DEVELOPMENT

A. Aero-engine system description

Aero-engine is highly complex and precise thermal machinery, as the heart of the aircraft, is not only the power of aircraft flight, but also an important driving force to promote the development of aviation. Every important change in the history of human aviation is closely related to the technological progress of aero-engine.

The icing inside the aero engine is mainly due to the suction effect of the engine operation, so that the ice crystals/mixed phases in the high altitude are sucked into the

environment above the freezing point inside the engine. The temperature of the ice crystals increases gradually during the movement of the internal channel of the engine, and some of the ice crystals melt to produce mixture phase of ice water. The mixture phase impacts and wets the internal structural surfaces of the aero-engine, cooling the surfaces, and then the inhaled ice crystals adhere to these wetted and cooled surfaces, gradually forming ice accretion on the surface. Nevertheless, due to the relatively small size of the components in the engine channel, once the surface icing phenomenon occurs, it is more likely to cause the uneven flow field inside the engine, resulting in engine speed loss, power decline, surge. Meanwhile, ice shedding can also cause compressor blade damage, and even lead to serious accidents such as engine stalling and stopping in high-altitude cruise state.

Therefore, this paper mainly studies mixed phase icing of the aero-engine, as shown in Fig. 1. Fig. 1(b) shows the corresponding mesh of each component. Meanwhile, the mesh is refined in the ice-sensitive areas, such as the lip of the aero-engine nacelle and the leading edge of the fan. After the verification of mesh independence, the number of selected mesh is about 1.93 million. The rotation speed of the nosecone and fan is set to 2000r/m.
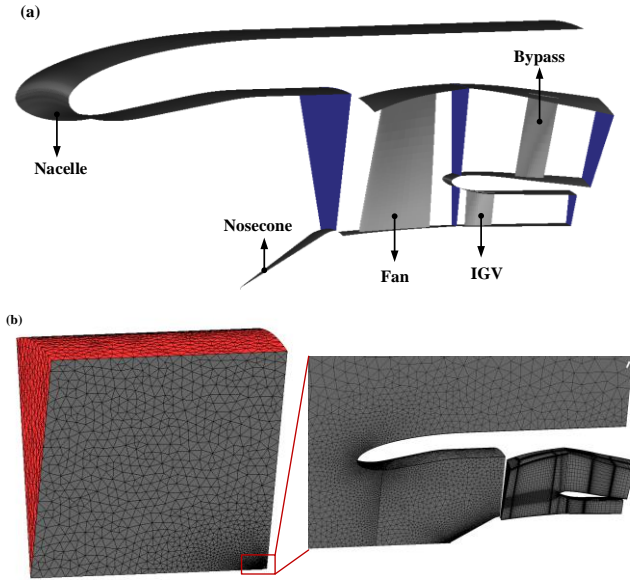
Fig. 1. Aero-engine model. (a) Aero-engine components. (b) Aero-engine components mesh.

B. Model development

The solution of air flow field is based on the conservation equations of mass, momentum and energy. The specific calculation equation can be obtained as follows:

$$\frac{\partial \rho_a}{\partial t} + \nabla\left(\rho_a \boldsymbol{u_a}\right) = 0 \tag{1}$$

$$\frac{\partial\left(\rho_a \boldsymbol{u_a}\right)}{\partial t} + \nabla\left(\rho_a \boldsymbol{u_a u_a}\right) = -\nabla p + \nabla \cdot \tau + \rho_a \boldsymbol{g} \tag{2}$$

$$\frac{\partial\left(\rho_a E_a\right)}{\partial t} + \nabla\left(\rho_a \boldsymbol{u_a} H_a\right) = \nabla\left(k_a\left(\nabla T_a\right) + \boldsymbol{u_a}\tau\right) + \rho_a \boldsymbol{g u_a} \tag{3}$$

Whereas, for rotating parts, the effect of rotation speed needs to be considered in the relative reference frame. For the energy equation, the velocity vector needs to be replaced by the velocity vector in the relative reference frame for

calculation. For the momentum equation, the influence of Coriolis force ($\boldsymbol{F_{cor}}$) and centrifugal force ($\boldsymbol{F_{cen}}$) should be considered in the source term. Therefore, the momentum equation is calculated as follows:

$$\frac{\partial\left(\rho_a \boldsymbol{u_r}\right)}{\partial t} + \nabla\left(\rho_a \boldsymbol{u_r u_r}\right) = \nabla \sigma_r + \rho_a \boldsymbol{g} + \boldsymbol{F_{cor}} + \boldsymbol{F_{cen}} \tag{4}$$

where Coriolis force and centrifugal force are calculated as follows:

$$\boldsymbol{F_{cor}} = -2\rho\left(\boldsymbol{n} \times \boldsymbol{u_r}\right) \tag{5}$$

$$\boldsymbol{F_{cen}} = -\rho \boldsymbol{n} \times \left(\boldsymbol{n} \times \boldsymbol{r}\right) \tag{6}$$

The solution for the motion of ice crystal particles is also based on the mass, momentum and energy equations, which are calculated as follows:

$$\frac{\partial \alpha}{\partial t} + \nabla\left(\alpha \boldsymbol{u_p}\right) = 0 \tag{7}$$

$$\frac{\partial\left(\alpha \boldsymbol{u_p}\right)}{\partial t} + \nabla\left(\alpha \boldsymbol{u_p u_p}\right) = \frac{C_D \, \text{Re}_p}{24K}\alpha\left(\boldsymbol{u_a} - \boldsymbol{u_p}\right) + \frac{\alpha}{Fr^2}\left(1 - \frac{\rho_a}{\rho_p}\right) \tag{8}$$

$$\frac{\partial\left(\alpha T\right)}{\partial t} + \frac{\partial\left(\alpha T \boldsymbol{u_p}\right)}{\partial x} = \alpha\left(\dot{q}_{conv} + \dot{s}_{rad} + \dot{q}_{evap/cond} + \dot{q}_{freeze/melt}\right) \tag{9}$$

Similarly, for rotating components, the Coriolis force and centrifugal force need to be added to the source term of the momentum equation.

The mixed phase sticking model proposed by Trontin et al. [8] is adopted in this paper. This mixed phase sticking model mainly depends on the melting rate η (LWC/TWC) of the ice crystal, the mass fraction of the impacting droplet (Y_d), and the mass fraction of the impacting ice crystal (Y_{ic}). The sticking coefficient (ε) can be expressed as follows:

$$\varepsilon = \max\left(\varepsilon_{ic}, \ \varepsilon_d\right) \tag{10}$$

Ice crystal sticking coefficient (ε_{ic}) and droplet sticking coefficient (ε_d) are obtained as follows:

$$\varepsilon_{ic} = \left(K_{ic} - 2\right)\left(\frac{\text{LWC}}{\text{TWC}}\right)^3 + \left(3 - 2K_{ic}\right)\left(\frac{\text{LWC}}{\text{TWC}}\right)^2 + K_{ic}\left(\frac{\text{LWC}}{\text{TWC}}\right) \tag{11}$$

$$\varepsilon_d = K_d\left(Y_d + \frac{\text{LWC}}{\text{TWC}}Y_{ic}\right) \tag{12}$$

where the mass fraction of the impacting particle is calculated as follows:

$$Y_{ic} = \frac{\dot{m}_{imp,ic}}{\dot{m}_{imp,ic} + \dot{m}_{imp,d}} \tag{13}$$

$$Y_d = 1 - Y_{ic} \tag{14}$$

Finally, the thermodynamic model of Shallow-Water icing considering the initial water film flow is adopted. Shallow-Water icing model (SWIM) is based on the motion of surface water film [12-13]. When the mixture phase impacts the aero-engine surface, a thin liquid film is formed. The liquid film may runback under the shear stresses created by the airflow. Moreover, under the influence of thermodynamics, the water film will freeze, evaporate and sublimate. The SWIM calculates heat and mass transfer during icing and liquid water runback by determining the thickness of water film on the surface nodes of aero-engines [14]. For the SWIM,

the equations for mass, momentum, and energy can be calculated as follows:

$$\rho_f\left[\frac{\partial h_f}{\partial t}+\nabla\left(\boldsymbol{u}_f h_f\right)\right]=u_a\cdot\mathrm{LWC}\cdot\beta-\dot{m}_{evap}-\dot{m}_{ice} \quad (15)$$

$$\boldsymbol{u}_f=\frac{h_f}{2\mu_f}\boldsymbol{\tau}_a-\frac{h_f^2}{3\mu_f}\rho_f\boldsymbol{a} \quad (16)$$

$$\rho_f\left[\frac{\partial h_f c_f\tilde{T}}{\partial t}+\nabla\left(\boldsymbol{u}_f h_f c_f\tilde{T}\right)\right]=\left[c_f\left(T_a-\tilde{T}\right)+\frac{\|\boldsymbol{u}_p\|^2}{2}\right]u_a\cdot\mathrm{LWC}\cdot\beta$$
$$-0.5\dot{m}_{evap}\left(L_{evap}+L_{sub}\right)+\left(L_{fusion}-c_{ice}\tilde{T}\right)\dot{m}_{ice}$$
$$+\sigma\varepsilon\left(T_a^4-\tilde{T}^4\right)-k_h\left(\tilde{T}-T_{ice,rec}\right) \quad (17)$$

It can be found that there are three unknowns in the mass and energy equations, which are the thickness of the water film, the equilibrium temperature of the air, water film, ice and wall surface, and the amount of icing. Therefore, additional constraints are required during the solution process. The specific constraints are as follows:

$$h_f\geq 0,\ \dot{m}_{ice}\geq 0,\ h_f\tilde{T}\geq 0,\ \dot{m}_{ice}\tilde{T}\leq 0 \quad (18)$$

III. ANALYSES OF SIMULATION RESULTS

In order to evaluate the effect of melting rate on aero-engine icing, the melting rate η are introduced. The melting rate of ice crystals ranges from 0.05 to 0.30. The pressure and temperature of the air are 41kPa and 250.15K, respectively. And the Mach number of the flight is 0.4. The relative humidity and icing time are selected as 65% and 180s respectively.
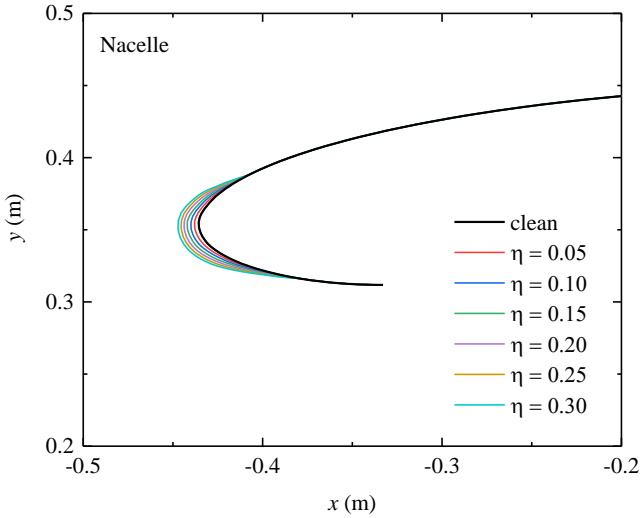
Fig. 2. Prediction of nacelle surface ice shape at different melting rate.

Under different melting rates, the ice thickness of the nacelle surface is shown in Fig. 2. It can be seen from the figure that with the increase of melting rate, the ice thickness on the surface of the nacelle increases significantly. This is because with the increasing of LWC, the thickness and wetting range of the liquid film increase, and more ice crystals can be attached to the frozen surface for heat transfer and ice accumulation. With the continuous decrease of LWC, although the erosion effect of ice crystals is weakened, at the same time, the thickness of liquid film on the frozen surface becomes smaller, which is not enough to adhere to more ice

crystals, resulting in gradual decrease in the total amount of ice. And the ice thickness of the stagnation point of the nacelle with melting rate of 0.30 is 4.90 times that of the nacelle with melting rate of 0.05.

Consequently, it can be concluded that if the mixed phase/ice crystal ice accumulation reaches the maximum ice thickness, there must be enough ice crystal content to ensure that the ice crystal through the phase transformation heat to make the ice surface temperature drop below the freezing point, and there must be enough liquid water content to adhere to the ice crystal on the ice surface for heat transfer.
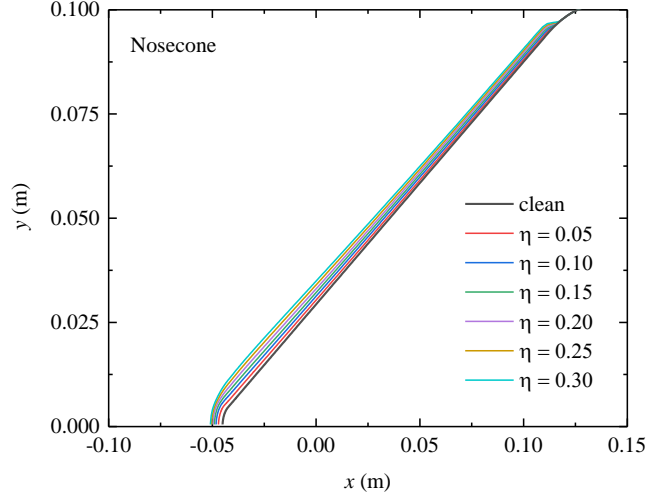
Fig. 3. Prediction of nosecone surface ice shape at different melting rate.

Fig. 3 shows the variation of ice thickness on the nosecone surface at different melting rates. It can be seen that the melting rate has a significant effect on the amount of ice on the nosecone surface. When the melting rate was 0.05 and 0.30, the maximum amount of ice on the nosecone surface was 1.98 and 5.82mm, respectively. With the increase of melting rate, the ice thickness on the nosecone surface increased. In addition, the icing growth rate at the tip of the nosecone was significantly greater than that at other parts. This is because with the increase of LWC, there will be partial overflow after impacting the nosecone surface, and the linear velocity of the nosecone tip is small, resulting in higher growth rate of icing at the nosecone tip.
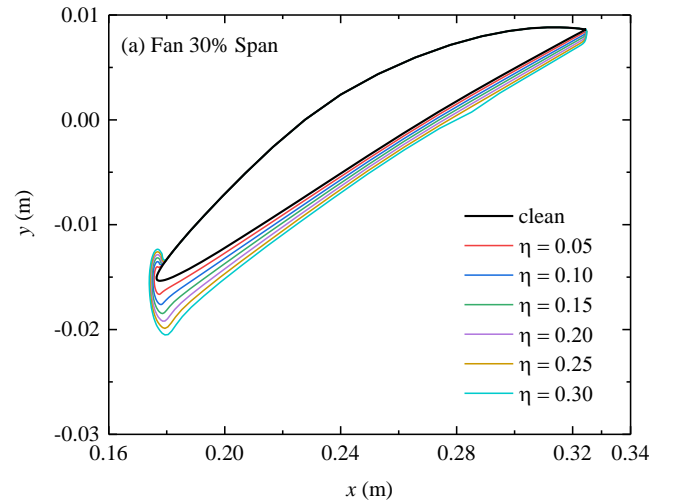
(a) Fan 30% Span.
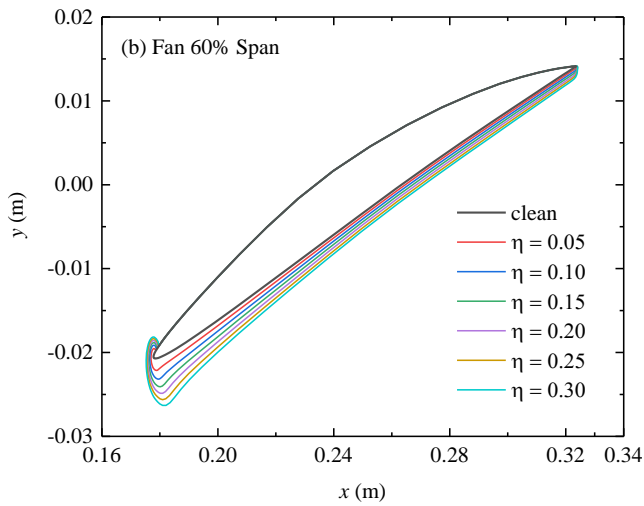
(b) Fan 60% Span.
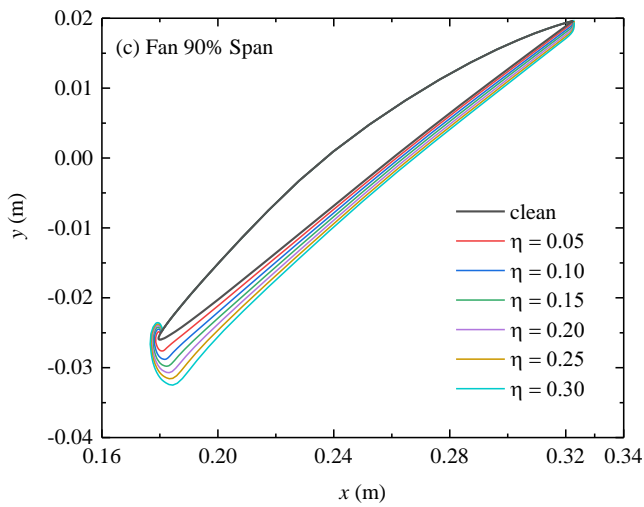
(c) Fan 90% Span.

Fig. 4. Prediction of fan surface ice shape at different melting rate.

The change of icing amount on fan surface is shown in Fig. 4. It can be observed from the figure that under the same fan span, with the increase of melting rate, the ice accumulation thickness on the pressure side of the fan increases. At the same melting rate, the amount of icing on the pressure side of the fan increases with the increase of fan span. When the melting rate is 0.30 and the fan span is 30%, 60% and 90%, the maximum icing amount on the fan surface reaches 5.42, 6.26 and 6.59mm, respectively. Furthermore, the maximum amount of ice on the fan surface at melting rates of 0.05, 0.15, and 0.25 at fan span of 90% is 1.56, 3.85, and 5.71mm. At the same time, it can be seen from the figure that there is no obvious icing on the suction side of the fan. Therefore, in the anti-icing design of the fan surface, the icing on the suction side does not need to be considered, but the leading edge of the suction side needs to be considered.
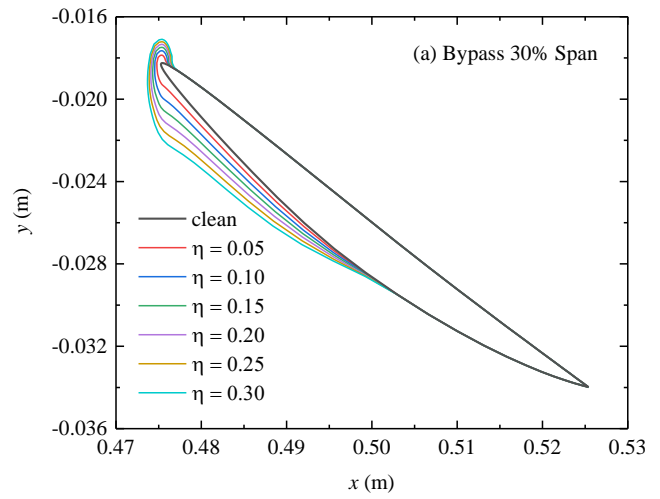
(a) Bypass 30% Span.
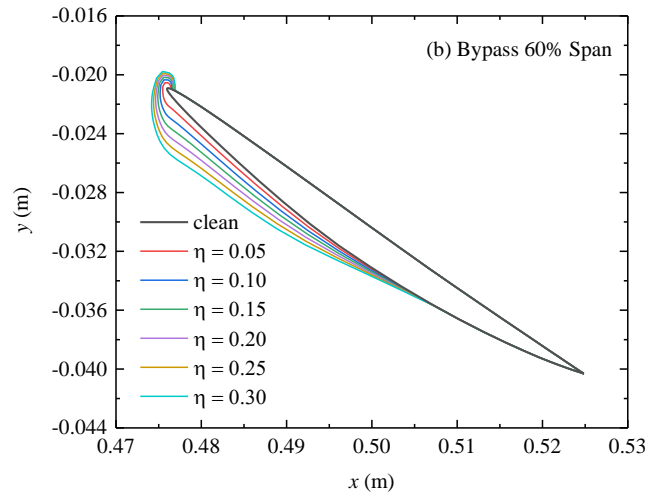
(b) Bypass 60% Span.
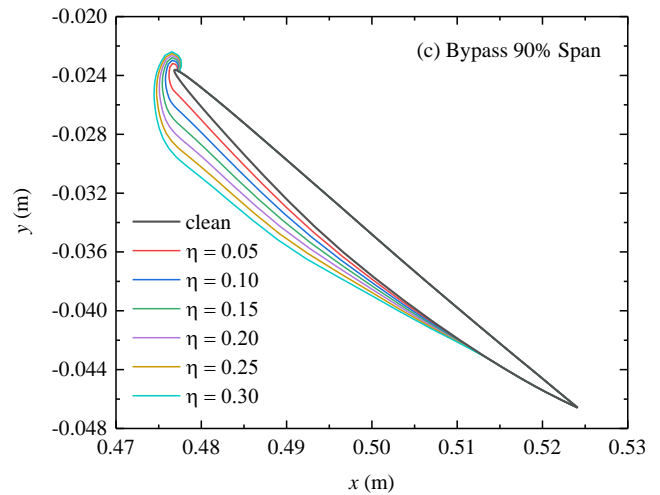
(c) Bypass 90% Span.

Fig. 5. Prediction of bypass surface ice shape at different melting rate.

Fig. 5 shows the predicted ice shape of the bypass surface. It can be seen that the icing on the bypass surface is mostly concentrated on the windward side, and there is a small amount of icing on the leading edge of the leeward side. This is due to the fact that the collection coefficient of the mixed phase on the windward side is significantly higher than that on the lee side. As the melting rate increases, the ice thickness on

the windward side of the bypass surface also increases. On the windward side of the bypass surface, the icing amount near the leading edge is the most. When the bypass surface span is 90% and the melting rate is 0.3, the icing thickness reaches 3.82mm.

In addition, with the increase of bypass surface span, the ice area on the windward side increases. When the melting rate is 0.3, the ice area of 90% span of the bypass surface increases by 40.2% compared to 30% span. This is due to the effect of fan rotation, so that more of the mixed phase hits the windward side of the bypass surface. At different spans, the ice growth rate near the bypass front is relatively high, but the change is not significant at other locations.

Not only the by-pass surface, but also the surface of the IGV will be affected by the fan rotation. Fig. 6 shows the variation of ice thickness on the IGV surface. It can be seen that the icing is mainly concentrated on the pressure side, while only a small part of the leading edge of the suction side is frozen. When the span is 30%, there is no obvious icing on the IGV surface. For the pressure side, the icing thickness of the IGV surface increases with the increase of melting rate. Meanwhile, with the increase of the surface span of the IGV, the icing thickness also increases. When the melting rate is 0.3, the maximum ice thickness of the leading edge with surface span of 30%, 60% and 90% is 0.1, 1.26 and 2.41mm, respectively.
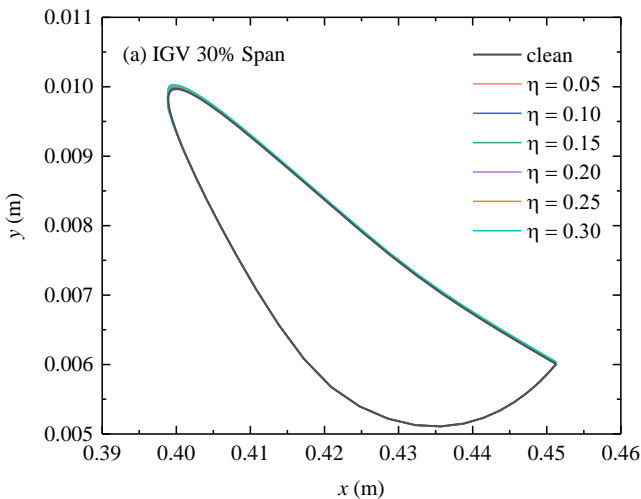
(a) IGV 30% Span.
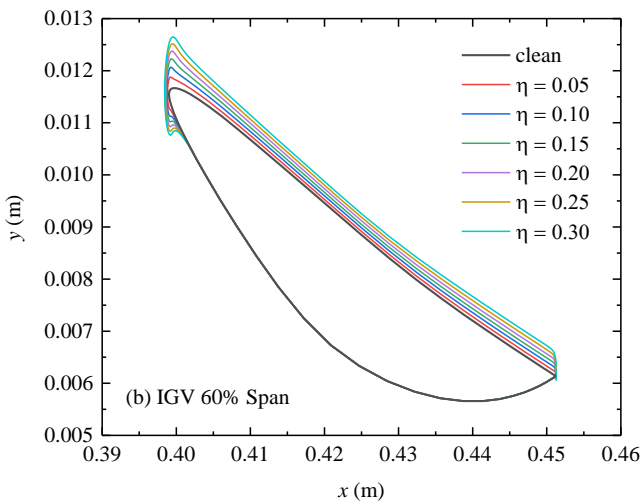
(b) IGV 60% Span.
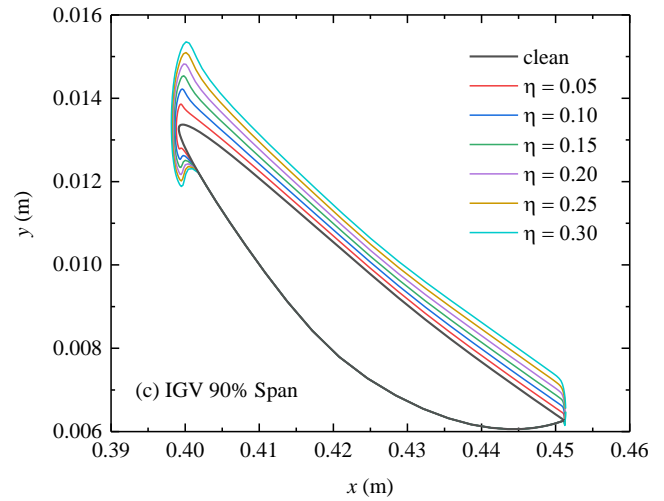
(c) IGV 90% Span.

Fig. 6. Prediction of IGV surface ice shape at different melting rate.

Compared with the icing on the bypass surface in Fig. 5, the icing on the IGV surface is less. This is mainly related to the fan geometry. The mixed phase around the fan is gradually deviated by the centrifugal force generated by the fan rotation and the Coriolis force, and more of the mixed phase hits the windward side of the bypass surface through the fan. Therefore, in the design of anti-icing, it is necessary to pay attention to the pressure side and leading edge of the blade.

IV. CONCLUSIONS

The aero-engine ice accretion model is established in this paper, which includes air flow field model, mixed phase trajectory model, mixed phase impact model, mixed phase sticking model and mixed phase ice accretion model. The effect of different melting rate (LWC/TWC) on aero-engine icing is analyzed. The conclusions are shown as follows:

（1）With the increase of melting rate, the ice thickness of nacelle surface, nosecone surface and fan pressure side surface increased significantly.

（2）The icing of the fan is mainly concentrated on the pressure side of the fan, and there is a small amount of icing on the leading edge of the suction side of the fan. The icing area of suction side decreases with the increase of fan span.

（3）When the fan span is 90% and the melting rate is 0.05, 0.15 and 0.25, the maximum icing amount on the fan surface is 1.56, 3.85, and 5.71mm, respectively. Moreover, when the melting rate is 0.3, the ice area of 90% span of the bypass surface increases by 40.2% compared to 30% span.

REFERENCES

[1] Qun Dang, Mengjie Song, Xuan Zhang, et al. Modelling study on freezing process of water droplet on inclined cold plate surface with droplet dynamic behavior considered[J]. International Journal of Heat and Mass Transfer, 2022, 197: 123327.

[2] Haifeng Qi, Shinan Chang, Yinglin Yang, et al. Numerical investigations on aero-engine icing characteristics at mixed phase conditions[J]. Applied Thermal Engineering, 2024, 238: 122044.

[3] Chen Guang. Discussion on GEnx engine icing[J]. International Aviation, 2014, 2: 72-73.

[4] Linchuan Tian, Linkai Li, Haiyang Hu, et al. Experimental Study of Dynamic Ice Accretion Process over Rotating Aeroengine Fan Blades[J]. Journal of Thermophysics and Heat Transfer, 2023, 37(2): 353-364.

[5] Yuan Qinghao, Fan Jiang, Bai GuangChen. Review of Ice Crystal Icing in Aero-engines[J]. Journal of Propulsion Technology, 2018, 39(12): 2641-2650.

[6] Yasir A. Malik, Lokman Bennani, Stephan Bansmer, et al. Experimental and numerical investigation of accretion inception and heat transfer physics in ice crystal icing[J]. International Journal of Heat and Mass Transfer, 2023, 214: 124364.

[7] P. Villedieu, P. Trontin, R. Chauvin. Glaciated and mixed phase ice accretion modeling using ONERA 2D icing suite[C]. 6th AIAA Atmospheric and Space Environments Conference, 2014. DOI:10.2514/6.2014-2199.

[8] P. Trontin, G. Blanchard, P. Villedieu. A comprehensive numerical model for mixed-phase and glaciated icing conditions[C]. 8th AIAA Atmospheric and Space Environments Conference, 2016. DOI:10.2514/6.2016-3742.

[9] E Norde, der Weide Van, E. T. A, H. W. M Hoeijmakers. Eulerian method for ice crystal icing in turbofan engines[J]. AIAA Journal, 2018, 56(1): 1-13.

[10] Jiang Feifei, Dong Wei, Zheng Mei, et al. Phase change heat transfer characteristic of ice crystal ingested into turbofan engine[J]. Journal of Aerospace Power, 2019, 34(03): 567-575.

[11] Bu Xueqin, Li Hao, Huang Ping, et al. Numerical simulation of mixed phase icing on two-dimensional airfoil[J]. Acta Aeronautica et Astronautica Sinica, 2020, 41(12): 124085.

[12] Y. Bourgault, H. Beaugendre, W. G. Habashi. Development of a Shallow-Water Icing Model in FENSAP-ICE[J]. Journal of Aircraft, 2000, 37(4): 640-646.

[13] Lavoie, Pierre, Pena, et al. Comparison of thermodynamic models for ice accretion on airfoils[J]. 2018, 28(5): 1004-1030.

[14] Ren Yongpeng, Shen Lianyang, Wang Zhongyi, et al. Calculation of Blade-profile Icing and Analysis of Flow Field[J]. Advances in Aeronautical Science and Engineering, 2020, 11: 636-644.

An Experimental Investigation on the Characteristics of Dynamic Ice Accretion Process over Rotating Aeroengine Fan Blades

Linchuan Tian[1], Linkai Li[1], Haiyang Hu[1], Ramsankar Veerakumar[1], Hui Hu[1]

[1] Iowa State University, Ames, Iowa, USA

Tlc19910604@sjtu.edu.cn, linkaili@nuaa.edu.cn, haiyangh@iastate.edu, rveeraku@uwyo.edu, huhui@iastate.edu

Abstract—**An experimental campaign was conducted to quantify the dynamic ice accretion process over the rotating aero-engine fan blade model and the corresponding icing-induced performance degradation. The experiments were conducted in a unique Icing Research Tunnel at Iowa State University (ISU-IRT) with a scaled CFM-56 spinner-fan model under both the glaze and rime icing condition. The growth and shedding details of the ice layer and the unsteady water runback behaviours were quantitatively measured by using a Digital Image Projection (DIP) based 3D scanning technique and high-speed imaging system, presenting a 3D ice structure on the blades as a function of the time. In addition, two static pressure transducers were applied to measure the static pressure ratio between the fan entrance and exit. The ice structures accreted on the fan blades were found to significantly change the designed geometry of the blades and the flow path, especially near the root region, where lower centrifugal force exists, under both glaze and rime icing conditions. While the runback icing phenomenon was found only on the relatively warmer glaze icing condition, presenting an unpredictable 'pin-like' ice structure on the high span region (≥50% span). The iced aero-engine fan was found to have a continuous efficiency drop during the dynamic icing process, especially under the glaze icing condition. Such performance degradation is correlated with the acquired snapshots of the dynamic ice accretion images and measured 3D ice structures to elucidate the underlying physics pertinent to aero-engine fan icing.**

Keywords— ***Aero-engine fan; Icing; Performance degradation; Digital Image Projection Technique; 3D ice structure***

I. INTRODUCTION

Aircraft icing has been extensively recognized as one of the most severe hazards in aviation industry, which jeopardize the safety operations of aircraft in cold weather [1–4]. When airborne, supercooled water droplets (SWD in short), existing in clouds and fog, impact the exposed cold surfaces of an aircraft, and the freezing process of the supercooled water droplets forms complex ice shapes. Ice accretion usually takes place on all the exposed cold frontal surfaces of the aircraft, like airfoil wings, propellers, as well as windshields. The ice accretion on the aircraft can dramatically degrade the aerodynamic design and off-design performance by altering the streamlined shape of the key components and thus increasing the drag while decreasing the lift of those components. This effect also occurs on the key components of the aero-engine, such as nacelle, spinners, and fan blades, which can also cause detrimental effects on each suffered components and the general performance of the aero-engine [5,6]. The current research has found that the icing events on cold surfaces of rotating aero-engine spinner [7] and fan

blades can induce an imbalance in the rotator system, leading to serious mechanical vibrations [8]. Meanwhile, the ice shedding, especially for the large ice chunk, from the iced components of the aero-engine could damage the downstream engine casing, compressor cascade, and other engine components, which can further result in "power-loss" accidents such as stall, surge, and flameout [9]. While some extensive studies have been performed in recent decades on aircraft icing physics to develop more effective and efficient anti-/de-icing strategies [10–12], the majority of the present researchs only put emphasis on ice accretion and the prediction of the icing process over aircraft wings. Limited research work can be found in the literature, which focused on aero-engine icing phenomena [13–17]. The underlying physics of the dynamic ice accretion process on the rotating engine fan is much more complicated when compared to that on fixed aircraft wings due to its special 3D design geometry of the blades, i.e., twisted and curved blades, and unique internal flow aerodynamic environment, such as the pressure gradient and the centrifugal forces associated with the rotation motion.

Almost all the previous studies on this aero-engine fan blade icing were conducted based on numerical simulations. Das [18,19] conducted a series of numerical studies to simulate the dynamic ice accretion on the aero-engine fan blade model of a high bypass ratio turbofan engine under various icing conditions. Hutchings et al. [20] integrated various icing simulations to characterize the ice-accumulation-induced shape changes of aero-engine fan blades and examined the degradation of their performance. They demonstrated that in the test case, which corresponds to the maximum ice layer thickness (near 8% chord length of the blade), the icing-induced pressure loss was tripled, and the inhaled airflow rate of the engine fan was reduced by 15% compared with the no-ice condition. Bidwell et al. [21] also simulate and study the dynamic ice accretion process on Energy Efficient Engine (E3) with NASA's LEWICE3D software. It was found that the droplet sizes, i.e., the large droplets, would result in an increased impingement rate on the aero-engine fan blades. More recently, Dong et al. [22] have numerically examined the ice accretion process on rotating aero-engine fan blades. To characterize the accumulated ice structures on the fan blades, the profiles of the iced blade from root to tip positions as a function of the SWD impingement time was carefully examined. Although the numerical studies listed above improved our understanding of the dynamic ice accretion process on rotating aero-engine fan blades, comprehensive experimental investigations are still highly

desirable to explore further insight into the underlying physics pertinent to aero-engine icing phenomena. The experimental studies will also help to establish a quantitative measurement database to validate and verify the aero-engine icing numerical simulations and unsteady heat transfer modelling.

In the present study, comprehensive experimental campaigns to quantitatively characterize the dynamic icing process over the rotating aero-engine fan blades' surface and its performance degradation under various icing conditions were conducted in an icing research tunnel at Iowa State University (ISU-IRT). A scaled aero-engine fan model with a transparent casing for visualization (CFM-56) was chosen to be exposed to typical wet glaze icing and dry rime conditions. During the experiment, a high-resolution and high-speed imaging system cooperated with a phase-locking technique was used to reveal the details of dynamic ice accretion process. A novel technique, called digital image projection (DIP) based 3D-scanning technique was also utilized to quantify the 3D ice shapes development over the surfaces of rotating aero-engine fan blades as a function of the supercooled water droplet impingement time. The static pressure ratio was also quantitatively measured simultaneously to study the icing-induced performance degradation. The objective of the present study is to characterize the dynamic ice accretion details and the detrimental effects of such dynamic icing process on the aero-engine fan; and to gain a deep understanding of the aero-engine icing phenomena, which is essential for the future fine-design of effective and robust anti-/de-icing strategies, especially for the aero-engine icing mitigation.

II. EXPERIMENTAL SETUP AND TEST MODE

1. Introduction of the icing research tunnel used for the present study.

As clearly shown schematically in Fig.1, the experimental investigation was performed in the Icing Research Tunnel at Iowa State University (i.e., ISU-IRT in short). The ISU-IRT has a transparent acrylic-panel-covered test section, with a geometry of 400 mm in width, 400 mm in height, and 2,000 mm in length. It has the capacity to generate an icing environment with a maximum wind speed (i.e., $V\infty$) up to 60 m/s and a tunnel temperature (i.e., $T\infty$) as cold as -25 °C. A water spray system, including arrays of 9 pneumatic atomizing spray nozzles (IKEUCHI-BIMV-8002), was installed at the beginning of the contraction section to inject adjustable micro-sized water droplets into the test section. The liquid water content (LWC) level in the free-stream flow at a freezing temperature inside ISU-IRT can be fine-controlled from 0.1 g/m3 to 6.0 g/m3 by adjusting the pressure regulators of both the air and water pipe connected to the atomizer/spray nozzles. Based on the measurement results of LaVision's ParticleMasterTM system, the size of the water droplets exhausted from the atomizers/spray nozzles ranges from 10 to 100 μm with a mean volume diameter (MVD) of about 20 μm[23]. At certain given testing conditions for the icing study, the temperature inside the test section of ISU-IRT was calibrated (measured using thermocouples) to be quite uniform and stable before the experimental study, usually with the temperature fluctuations being less than ±1.0 oC. In summary, ISU-IRT is capable of simulating various inflight

icing phenomena over a wide range of icing conditions (i.e., from extremely wet glaze icing conditions to very dry rime icing). By leveraging ISU-IRT and the novel test systems, extensive research has been conducted in recent years to study various icing phenomena, such as aircraft icing, aero-engine icing, UAV/UAM/UAS icing, bridge cable icing, automobile icing, wind turbine icing, power transmission cable icing [16,24–27].
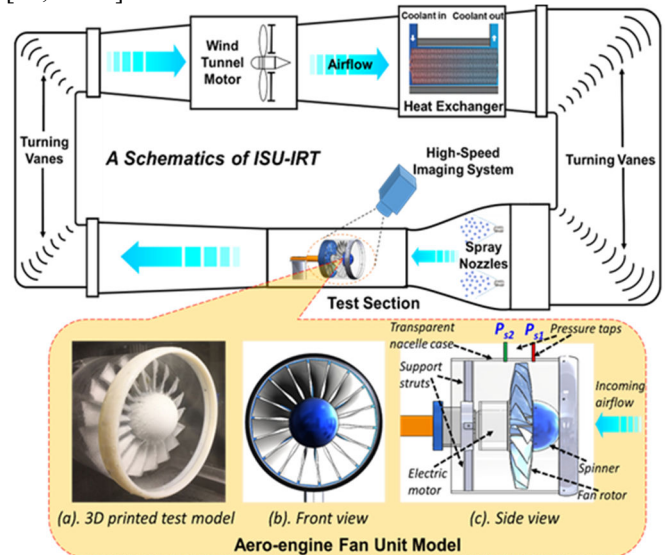
Fig. 1   Schematic of ISU-IRT and the test model.

2. The spinner-fan model used in the present study.

As also illustrated in Fig.1, an aero-engine model was designed and installed in the middle of the transparent test section of ISU-IRT during the icing test. Within the aero-engine model, the fan blades and an elliptical spinner was sketched based on a Boeing 18-inch aero-engine test rig, which was described in Ganz et al. (Ganz et al., 1998), with a scale ratio of 1:2.3. Figure 2 demonstrates the schematic shape of a single fan blade used in the present study with a chord length of C = 34 mm (50% span). The hub/tip ratio is designed as 0.402, with the aspect ratio chosen to be 1.65. A total of 18 fan blades are mounted circumferentially on a rotating disk with an outer diameter of 200 mm, which has a tip solidity of 1.035 and the hub solidity of 2.214 for the rotating aero-engine fan model in the present study. An elliptical-shaped spinner, which has a maximum base diameter of Ds = 80 mm and length of Ls = 40 mm, was used in this spinner-fan model. The spinning was applied to ensure a smooth entrance of the free stream airflow into the rotating fan blade section. The design rotor pitch at 25%, 50%, and 75% are 18mm, 24mm, and 34mm, separately. A nacelle was assembled by a cylindrical plexiglass duct, a rounded lip ring, and four support structures outside of the spinner-fan model. The gap between the inner wall of the nacelle case and the tips of the fan blades was set to be 1.0 mm.
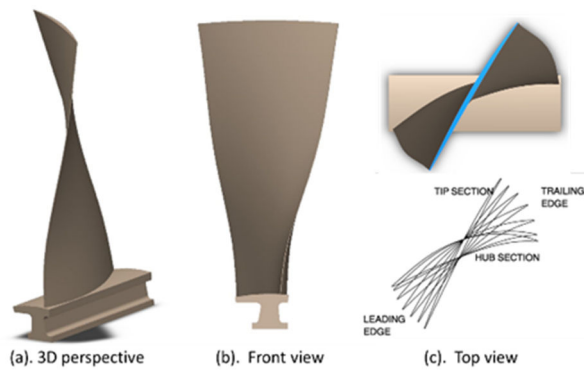
Fig. 2　Schematic of the fan blade used in the present study.

Most of the components of the aero-engine model, except the nacelle case (made of transparent Plexiglas tube), were manufactured by using a 3D printer (i.e., Connex 500 3D printer) with hard-plastic material (i.e., VeroWhitePlus, Stratasys, Inc), with a thermal conductivity near 0.45 W/(m·K). The parts were built and hardened layer-by-layer with a fine-resolution of about 25 μm. After 3D printing, the outer surfaces of each single fan blades, as well as the elliptical spinner, were further wet polished with fine sandpaper (i.e., up to 2000 grit) to achieve a very smooth, glossy finish. Moreover, in order to reduce the effects of the ice accretion over the rotating spinner on the performance of the engine fan blade, a commercially available Superhydrophobic coating (i.e., Neverwet by Rust-Oleum®) was sprayed over the spinner surface.

In the present study, the spinning fan blade model was installed on a brushless motor (Scorpion, SII-4020-420KV) which is powered by a direct current power supply (BK PRECISION, 1692). A Proportional-Integral-Derivative (PID) feedback control module (programmed on Arduino), an electrical speed controller (ESC, Scorpion, Commander 15V 60A), along with the data acquisition system (NI, USB-6218 and self-programmed MATLAB code) was used to monitor and maintain the constant angular rotation speed of the aero-engine fan blade model during the entire experiment of the dynamic ice accretion.

As demonstrated by the previous research, in-flight icing can be either dry rime ice or wet glaze ice, depending on various conditions (e.g., aircraft velocity, temperature, and humidity) [28–30]. In the present study, the rime and glaze ice accumulation over the rotating fan blade surfaces were achieved by changing both the ambient temperature and incoming free stream flow liquid water content (LWC) levels with a constant flow velocity of 15 m/s. More specifically, to achieve the aerodynamic similarity, the scaled model using the same advance ratio of 1.8 with the prototype one, with a 15 m/s incoming flow velocity and angular velocity of 2500 rpm (revolution per minute). While the icing condition is chosen based on the FAR Appendix C to Part 25, which discribes the typical glaze and rime icing condition the aero-engine may encounter during operating in cold and humid environment. The working parameters is then determined as V∞ = 15 m/s, T∞ = -15 ℃, and LWC = 0.50 g/m3 used in the rime icing experiment; while the corresponding variables become V∞ = 15 m/s, T∞ = -5 ℃, and LWC = 2.0 g/m3 for the glaze icing experiment. During the experiments, each trial of the icing experiments is designed to end after a total amount of 1.0 kg

of water (i.e., Mwater = 1.0kg) was sprayed into the test section of ISU-IRT. Since the LWC level in the incoming airflow for the glaze icing case (i.e., LWC =2.0 g/m3) is 4 times higher than that in the rime icing case (i.e., LWC =0.50 g/m3), the duration of the glaze icing experiments (i.e., total duration of ~150 seconds) is only 25% of the rime icing experiments (i.e., total duration of ~600 seconds) to achieve a fair comparison.

3. Measurement system used for the icing experiments.

In the current study, a high-speed and high-resolution imaging system (two FASTCAM MINI WX cameras, maximum pixel resolution of 2048×2048) along with two Nikon lenses (50 mm 1.8D and 105 mm NIKKOR 1.4E ED) were mounted in the test section. One was mounted to record the side view of the whole engine fan, and one was mounted above the test section to focus on one single blade at the top and mid-section of the fan. During the experiment, the phase-locked imaging technique was used for image acquisition, which is based on the combined use of a digital tachometer (MONARCH, PLT 200) and the synchronizer, generating the pulsed signal per rotation cycle to trigger the imaging system. The illumination system includes a pair of 200W studio light-emitting diode (LED) lights and one 50 W LED lights to provide a uniform, low-flicker illumination for image acquisition. A comprehensive image processing procedure was applied to enhance the image quality with Gaussian filtering, background removal, and image adjustment.

It is well known that the aero-engine fan plays a prominent role in the aero-engine system, which guides and maximizes the flow of the air passing through the downstream components. In Fig.1, the zoom-in model shows that two rows of pressure taps were applied on the nacelle of the model to simultaneously measure the pressure changes of the airflow between the inlet and outlet of the aero-engine fan, with the distance of one chord and 1.5 times chord length, separately. A digital pressure sensor array (Scanivalve, DSA-3217), with a pressure range of 10-inch H2O and ± 0.2% static accuracy, was used for the pressure measurements. The pressure measurement results would be used to characterize the performance degradation during the dynamic icing process.

Most importantly, a novel digital image projection (DIP in short) based 3D scanning technique was applied to achieve "in-situ" 3D geometry measurements of the ice structures. The DIP technique is based on the working principle of structured light triangulation, similar to the stereo version measurement technique, where one camera is replaced with a digital projector. During the measurement, the projector would project a pattern, i.e., the mesh or triangle pattern, onto the surface of interest on the test model (i.e., engine fan blades for the present study). After the ice accumulates on the surface, the pattern would be distorted as compared with the ice-free pattern. By comparing the distorted pattern with the reference one (ice-free pattern), and using the pre-calibration matrix, the 3D profile of the iced test model can be quantitatively acquired. More detailed information about the DIP measurement and calibration are available in previously published articles (Hu et al., 2023a; Veerakumar et al., 2020; Zhang et al., 2015). It should be noted that such a non-intrusive, high-resolution measurement technique could reveal the details of the iced model without damaging the

fragile ice structure, compared with the expensive and labor intense test methods, like hand tracing and mold-and-casting method.

To measure the uncertainty of the 3D scanning system, a test plate with a row of roughness hemisphere elements of different sizes was custom designed and used for pre-calibration. The measurement accuracy of the used DIP-based 3D scanning system can be estimated by quantitatively comparing the scanned results with the actual dimensions of the hemisphere elements. Based on the calibration results, the measurement error of the system is less than 1%. The ice profile obtained from each spanwise location of the 3D model would be used to analyze the dynamic icing process, droplets behavior, ice structure, and the design geometry change of the rotating engine fan model during icing events. During the data processing, the ice accumulated onto the blades was scaled with the related geometry of the blades to emphasis the change of designed geometry of the aero-engine fan blades. The ice, i.e., accumulated along the streamwise, would be nondimensionalized by the chord length at the 50% span (34 mm) to suggest the geometry change during the icing event at each time step. While the dimensionless ice thickness, which describe the ice accumulated along the circumferential direction, would be used to describe the geometry of the flow path (S1) change, by dividing the pitch at each spanwise, i.e., 34 mm of 75% span, 24 mm of 50% span and 18 mm of 25% span.

III. EXPERIMENTAL RESULTS AND DISCUSSIONS

1. The dynamic icing process under the glaze icing condition

The high-speed images to reveal the dynamic ice accretion over the spinning fan blade model are shown in Fig.3. Images were captured from two different views, the global view and the zoomed-in view. It can be seen that there are two significant icing stages under the glaze ice accretion process. At the initial stage, when the total impinged water droplets and contact area are relatively small, the supercooled water droplets (SWD), carried by the incoming flow, would impinge and freeze onto the aero-engine fan blades, forming a thin ice film. Such ice rough covers half of the blades and the stagnation point near the leading edge (LE) within only 30s icing duration time. While the rest of the ice-free region was found to have less direct impinged supercooled water droplets due to the twist and curved geometry of the blades and also the overlap of two blades under such mounting angle. With more SWD impinged onto the fan blades, the surface of the blades became much rougher, and a large ice layer was found on the leading edge. More importantly, the trace of radial water runback can be clearly seen from the blades, and the pin-like icicles, grow from the stagnation point near the LE for a 120s icing duration time. As described by Liu and Hu (Liu and Hu, 2018), under the relatively warmer ambient condition close to the freezing point and larger LWC levels, the airflow would not be able to remove the released latent heat of fusion from the solidification process of the SWD. As a result, some portion of the impinged supercooled water droplets would still remain in their liquid state. Driven by the aerodynamic force and centrifugal force, the unfrozen droplets would move in both streamwise and spanwise directions and form an unpredictable ice structure, as shown in Fig.3(c). A boundary

(Fig. 3 a dashed red line) was clearly found between the iced and ice-free part, which determines the thermal balance point where the unfrozen supercooled water droplets can reach before latent heat was fully removed, driven by the aerodynamic force.
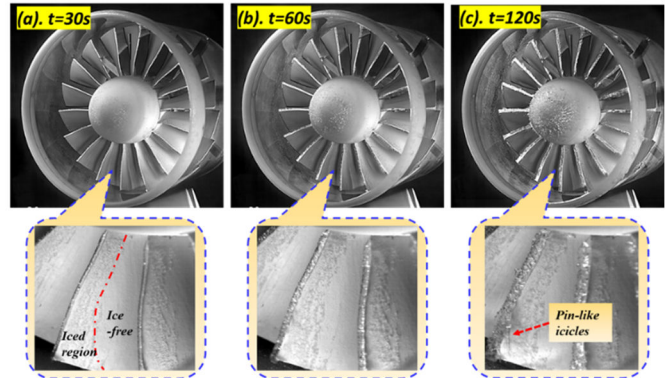
Fig. 3   Acquired dynamic ice accretion images of the rotating fan blades under the glaze icing condition of V_∞ = 15 m/s, $T\infty$ = -5.0 ℃, LWC=2.0 g/m3 and n=2500 rpm.

To acquire more details of the dynamic icing process, the DIP-based 3D scanning technique was used to quantify the 3D ice structure. Figure 4 (a)-(c) presents the time-resolved 3D ice structures of the aero-engine fan under the dynamic glaze icing condition. Obviously, both the suction side and pressure side present an interesting ice topology alone with different dimensions, with the local LWC, centrifugal force, and aerodynamic force difference.

For the suction side, the directly impinged supercooled water droplets only focus on a small part near the LE at the initial stage with a thin ice chunk built on it. The trace of runback icing and shedding phenomena (dashed black line region) are clearly seen at the tip region of the suction side from the 30s to 120s, where evolves from iced to ice-free condition. Those would indicate that the high-centrifugal force at the tip region would help the aero-engine fan to remove the ice and achieve self-cleaning. Lower than this span level, however, the centrifugal force is not sufficient enough to remove the ice layer, only presenting a runback icing phenomenon along both the span and stream direction without obvious ice shedding.

As shown in Figure 4, the pressure side presents a different icing topology. It is because no directly impinged SWD can be found at this region for the high span level, only with a few runback water droplets freezing at this place, with a relatively clean surface at the high span level of the pressure side. While most of the ice can be found at the root region, which suggests that the directly impinged area, local collection efficiency, and freezing rate should be much higher than the suction side at the same span. The ice covers almost the whole pressure side, not limiting to a narrow region close to the LE. The mounting angle, the geometry of the blade, and the solidity of the fan could be the reason for the local LWC difference. The middle part of the blades at the pressure side would also be influenced by both the icing and runback icing phenomenon, with a thick ice layer and the trace of runback icing presented in this region. Such icing structures at different span levels would cause the asymmetric geometry change and hence the non-uniform ice mass accumulation. For each span level, the flow path between the two blades (34, 24, 18 mm rotor pitch at 75%,

50%, 25% span) would change in an unpredictable manner, especially with the runback icing phenomenon, which would essentially change the working environment of the aero-engine fan.

The ice layer develops from the stagnation point of the LE, also presenting different icicles along the spanwise of the fan blade model. As also illustrated in Fig.4, the supercooled water droplets would freeze once impinging onto the stagnation point and form a thin layer near the LE at the initial stage. With more droplets impinging onto it, the unfrozen supercooled water droplet would form the radial runback from the stagnation line but in a different structure. The tip region (h>75% span) is still relatively clean, only with a few irregular and unpredictable icicles, since the centrifugal force level at this region would drive the SWD to move to the tip or directly blow off. Lower than this region (25%<h<75%), a 'pin-like' ice structure would grow near the stagnation line, which has the radical runback but without the obvious ice shedding phenomenon. While lower than the middle part(h<25%), there is almost no radical runback icing phenomenon due to the lowest centrifugal force level.
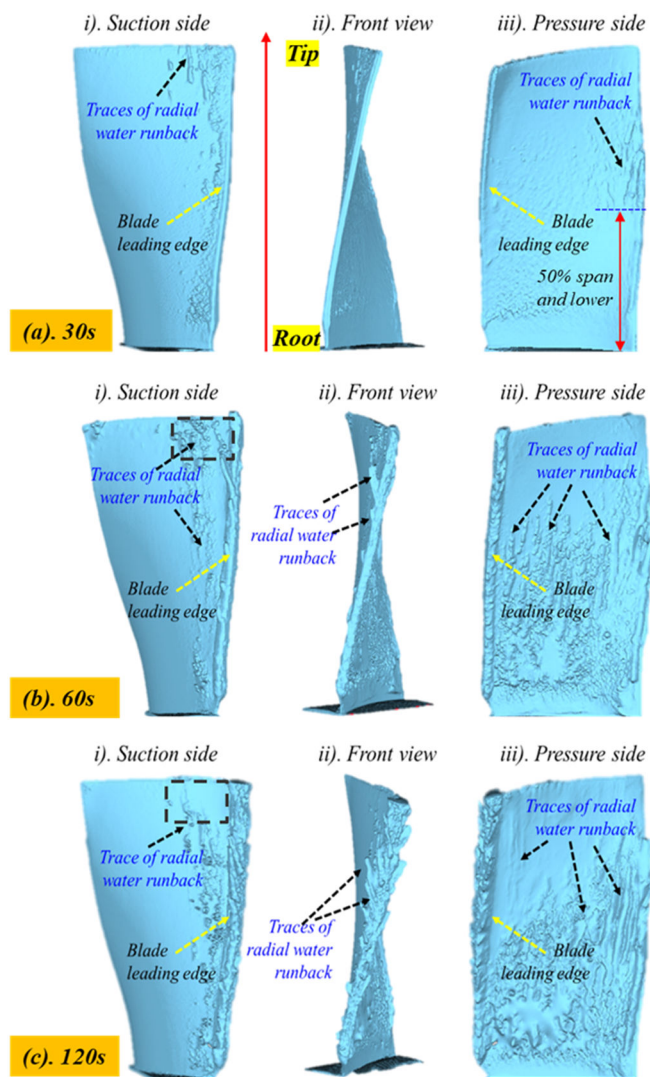
Fig. 4   Time-sequenced DIP measurement results to reveal the 3D shapes of the ice structures accreted over the fan blades under the glaze icing condition.

For the relatively warm and humid situation, the large ice chunk built from the stagnation point at LE would be the main threat to the aero-engine safety and stability, which would significantly distort the incoming flow condition and boundary layer flow development. Most importantly, such ice structure is usually unpredictable, determined by local unsteady heat transfer, ice adhesion, and centrifugal force. Considering that the aero-engine fan would rotate at high speed, which would facilitate the self-shedding of the ice structure at the high span region when encountering the icing events, the ice at both the stagnation point and the root region of the fan blades would be the main threat which requires the external force to achieve ice-free condition. Further study may consider the surface wettability effect on the dynamic icing process.

In general, all those data would indicate that the icing problem over the rotating blades is much more complicated than the stationary components, such as aircraft wings and the stator of the engine (Veerakumar et al., 2020; Zhang et al., 2015). The centrifugal force and its distribution characteristics from root to tip would change the local icing process, presenting 'clean tip,' 'radical runback middle,' and 'non-radical runback root' three special parts. Those are closely related to the local unsteady heat transfer, ice adhesion, and centrifugal force level. Such icing events would significantly distort the design geometry and the flow path of the engine fan and thus affects the inflow condition, i.e., the incoming flow velocity triangle and the boundary layer flow development. More studies are required to design highly efficient anti-/de-icing strategies tailored for the aero-engine fan, especially focusing on the root region, where the aerodynamic force and centrifugal force have less contribution in self-cleaning.

To quantitatively analyze the local icing details, the ice profile extracted from the DIP results at different time steps is also presented below. As clearly shown in Fig.5, for the high-span region, i.e., 75% spanwise, both the suction and pressure side are much cleaner due to the droplets blowing off or ice shedding. For 120s glaze ice accretion, the chord length increases from 2%, 4% to 10% at the time steps of the 30s, 60s, and 120s, in a non-linear trend, due to the linear LE increase and non-linear TE increase. As discussed above, few SWD would directly impinge at the tip region, and such non-linear ice growth at TE is mainly from the runback icing. In addition to the geometry change, the flow path between the two blades also changes with the icing process. Given the 34mm rotor pitch at the 75% span, such asymmetric icicle at the LE and TE would cause the flow path shrink of 17.6% and 4.4%, separately, for 120s icing duration time, which would significantly distort the boundary layer flow development and even the outflow condition.

While for the middle part (50% span), which takes most of loads of the engine fan, would also suffer from the dynamic icing process. For the LE, the ice chunk would cause 8.8% chord length increase and a 16.7% flow path shrink. The maximum ice thickness at the pressure side shifts to 90% chord length from the LE, with 8.3% flow path shrink. The maximum ice thickness at the TE increased ~24% compared with the 75% span, with the ice contaminating the whole pressure side, which would cause the design thickness distribution of blades to be unpredictable due to the icing and potential runback icing phenomenon.

The problem is even worse at the root region, where the low centrifugal force cannot drive the unfrozen SWD to move in the radial direction. As a result, the directly impinged SWD would freeze at or near this region, which means a high collection and high freezing rate at the root region. Clearly seen from the Fig.5, lower fluidity of the SWD at the root region would contribute to a worse icing condition, where more ice would accumulate at the aero-engine root, especially near the TE, where the aerodynamic force contributes more to the runback icing along the streamwise. A thick ice layer was found on the pressure side, which caused ~7.8% chord length increase and the flow path shrink ~ 18% at LE and 11.1% at the TE. Such icicles at the naturally narrow root region may even have detrimental effects on the engine fan, causing the potential flow blockage phenomenon.
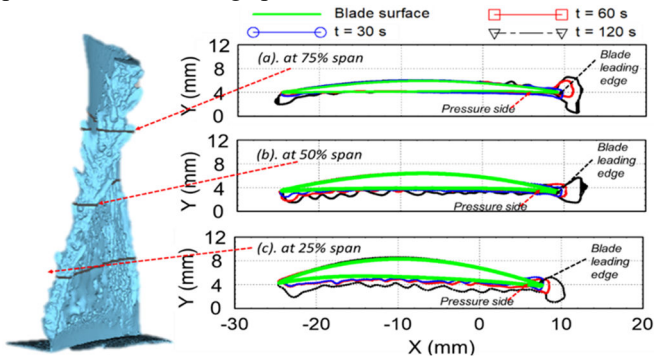
Fig. 5   Ice profile development of the iced fan blades at each spanwise under the glaze icing condition.

To determine performance degradation during the dynamic icing process, with such icicles considered to significantly change the surface roughness and blade's geometry (Gao and Cai, 2017), the incremental pressure ratio is applied in this paper. It is well known that the fan rotor of an aero-engine contributes to adding pressure energy to the airflow inhaled by the aero-engine. A higher increment for the airflow pressure across the fan rotor would not only suggest a greater thrust generated by the bypass airstream but also indicate a higher compression ratio of the engine core and, thereby, a higher combustion efficiency of the engine. To further study the aerodynamic performance during the dynamic icing process, the pressure increment ratio, which characterizes the ability of the aero-engine fan to pressurize the airflow when passing through it, was applied. During the experiment, the tested model was set to rotate at the constant angular speed of 2500 rpm, and the static pressure ratio would be simultaneously measured through the pressure transducer connected to the pressure taps located one and a half chord length from both the inlet and outlet of the fan rotor, as shown schematically in Fig.1.

In the present study, the dimensionless parameter, named the pressure increment coefficient, is then introduced to describe the performance degradation based on the static pressure measured during the dynamic icing process, which is defined as:

$$C_{\Delta P} = \frac{P_{s2} - P_{s1}}{\frac{1}{2} \times \rho_{air} \times V_\infty^2} \times 100\% \qquad (1)$$

where $C_{\Delta p}$ represents the ability of the engine fan to pressurize the air when passing through it, the P_{s2} and P_{s1} are

the static pressure measured one and a half chord length from the engine fan outlet and inlet, separately. The ρ_{air} and the V_∞ are the incoming airflow density and velocity. To better illustrate the effects of the icing process on the performance of the spinner-fan model used in the present study, the pressure increments coefficients measured during the icing experiments were normalized by the corresponding value under ice-free condition, which is defined as:

$$C_{\Delta P,ratio} = \frac{C_{\Delta P,iced}}{C_{\Delta P,ice-free}} \times 100\% \qquad (2)$$

where $C_{\Delta p}$, ice-free is the pressure increment coefficient of the "clean" spinner-fan model measured before starting the icing experiment. Therefore, the $C_{\Delta P,ratio}$ would be used to quantify the aero-engine performance change between the design point and the iced condition. Figure 6 shows the pressure increment ratio change during the glaze icing condition. As clearly shown in Fig.6, the icing process would continuously degrade the performance of the aero-engine fan since the engine fan adds and converts less pressure energy to the airflow. More importantly, it is found that the pressure increment ratio would drop sharply under the glaze icing condition. Within 120s icing duration time, the aero-engine fan exhibits a drastic drop in static pressure ratio from its design point to a condition where the fan cannot pressurize the airflow but ends up depressurizing it. Such phenomenon would usually be related with the rotating stall. Considering the designed flow path (S1) change, where the iced blades would form a convergent flow path, the airflow would lose the pressure energy and convert to the kinetic energy. In addition to the ice induce the flow path change, the iced blades would also induce the large flow separation, especially with the large ice chunk build on the LE, where boundary layer flow development is sensitive to LE geometry. Finally, both the structure change and aerodynamic environment change contributes to the such pressure increment drop and even the negative pressure increment. Considering the icing characteristics during the glaze ice accretion process, both the unpredictable ice chunk from the stagnation points near the LE and the thick ice layer at the root region would be a threat to the aero-engine safety and stability. It is believed that the ice chunk can be removed by leveraging the high-centrifugal force of the aero-engine fan, while the root region cannot achieve the same ice-free condition with a lower centrifugal force level. In general, such a condition can be regarded as the failure of the aero-engine fan, which is unacceptable and requires a tailored anti-/de-icing strategy to achieve ice mitigation, especially for the root region where the ice layer cannot be automatically shed off.

In summary, under the glaze icing condition, the airflow was not cold enough to dissipate the released latent heat of fusion quickly. As a result, the supercooled water droplets would partially freeze on the surface when impinging onto it. The unfrozen droplets would move in both streamwise and spanwise, driven by the aerodynamic force and centrifugal force. Under an increasing centrifugal force environment, the radial runback icing phenomenon starts at a boundary near 50% spanwise. Above this boundary, the centrifugal force would dominate the droplets' behaviour, and the runback icing develops along the radial direction, especially near the stagnation line of the LE. The aerodynamic force would dominate the runback icing characteristics for regions at the

root region (less than 25% spanwise), where the runback icing phenomenon develops only along the streamwise. As a result, most of the supercooled water droplets would freeze at this region, especially near the trailing edge, which is usually ignored from the view of the engineer, considering that the overall high centrifugal force of the rotation components of the engine would achieve self-cleaning of the ice. However, the root region contributes to most of the ice mass accumulation of the engine fan blades. Under such icing events, the inflow/outflow condition, i.e., velocity triangle and flow path area, would be distorted with the ice layer development, causing performance degradation. In addition to the aerodynamic considerations, the mechanical vibration due to the non-uniform ice mass distribution at blades also would be a threat to the aero-engine fan safety and stability, which may have some detrimental effects on the flow, such as flow blockage, stall, and even flameout of the aero-engine.
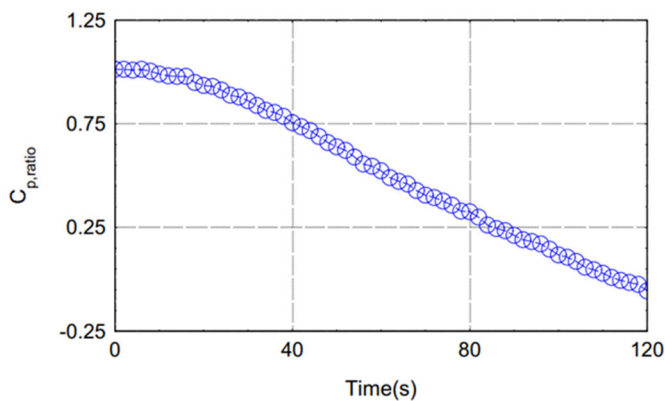
Fig. 6   Ice proPressure incremental ratio change during the glaze ice accretion process.

2.   The dynamic icing process under the glaze icing condition

For the cold and dry rime icing condition, however, the supercooled water droplets would present a different behaviour after impinging onto the cold surface of the aero-engine fan blades. Figure 7 shows the dynamic icing process using the high-speed imaging system, capturing both the global view and the zoom-in view. As shown in Fig.7, the ice rough at the initial stage presents a milky-white opaque appearance due to the existence of air bubbles/pockets trapped between the rime ice grains. Also, more iced regions can be seen on the blades in this case, not limited to a narrow region along the leading edge of the blades, due to a higher ice adhesion under lower ambient temperature. With more SWD impinging onto the surface, less runback icing is observed at all spanwise, only with the accreted ice layer conforming to the original profile of the fan blades. The ice layers accreted on the blades were found to increase monotonically even with more supercooled droplets impinging onto it. The surfaces of the iced fan blades became much rougher but with no observable 'pin-like' ice strcuture among the blades with 480s icing duration time. As described in Liu and Hu (2018), the heat dissipation speed is much fast when operating under cold rime icing condition, where most of supercooled droplets would freeze immediately once impinging onto the surface even driven by the same aerodynamic environment compared with the glaze icing condition. In this case, the ice layer would

follow the design geometry, usually called a streamline-like ice structure.
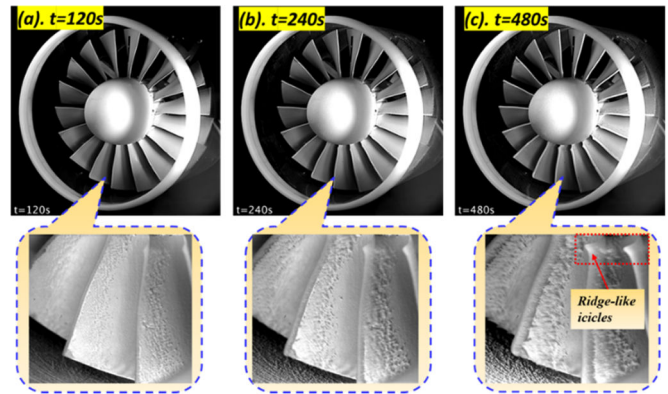
Fig. 7   Acquired ice accretion images of the rotating fan blades under the rime icing condition of V_∞ = 15 m/s, T_∞ = -15.0 ℃ and LWC=0.5 g/m^3 and n=2500 rpm

Figure 8 gives some of the typical ice profiles extracted from the 3D ice structure captured from DIP-based 3D scanning results at different time steps of the dynamic icing process. As shown in Fig.8 (a), a thin layer similar to the case of glaze icing formed at the initial icing stage but with more icing area. However, there is no observable trace of runback icing in both spanwise and streamwise. On the suction side, a more iced surface area can be found with a relatively thick ice layer, even at the tip region, which is ice-free under the glaze icing condition. Less ice shedding that occurs under the rime icing condition would be the main reason for such difference. The same, or even higher aerodynamic/centrifugal force, due to the increasing wind area of the iced fan blades, still cannot shed the ice layer, due to the high ice adhesion at such ambient temperature. With more supercooled water droplets impinging onto the iced surface, the cold air can still quickly remove the released latent heat of fusion. Thus, a thicker ice layer can be found on the 240s and 480s icing duration time. More important, the LE has no "pin-like" ice structure, as seen in the glaze ice condition. The ice layer simply grows from a thin layer to a relatively thicker one but with a small 'ridge-like' structure found on the root region, shown in Fig.8 (a) marked with the red dashed line.
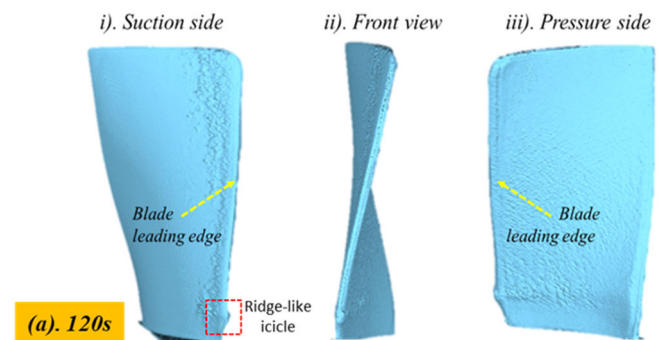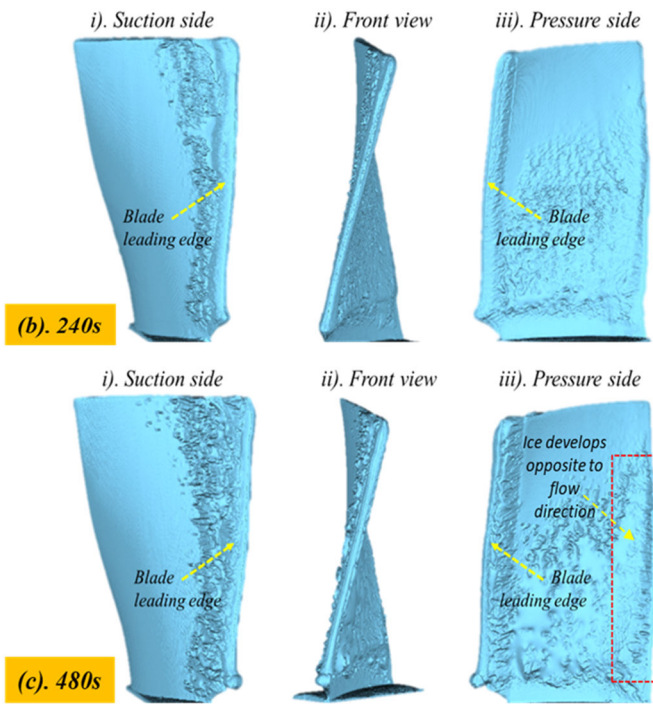
Fig. 8   Ice profile development of the iced fan blades at each spanwise under the rime icing condition.

For the pressure side, the ice layer develops from a thin film to a thicker one but in a different icing topology. Compared with the glaze icing condition, no runback water rivulets can be traced from the results; instead, an observable ice layer grows in the direction opposite to the flow on both the LE and TE, which may be determined by the bounce-off of the supercooled water droplets and the fast-freezing characteristics under rime icing condition. More study is required. Besides, it is obvious that most of the ice mass would still accumulate onto the root region of the pressure side, with a large ice layer built during 480s icing duration time, due to the low centrifugal force level and larger ice adhesion under the rime icing condition.

The ice built on the stagnation point shows a different trend with the glaze icing condition. At the 480s, the ice layer at the stagnation point presents a linear increase rate without observable radical runback icing, even at the tip region. Clearly, the fast removal of latent heat of fusion and higher ice adhesion of rime ice changes the dynamic icing process, where the centrifugal force at the same span level would not be sufficient to drive the supercooled water droplets to move or to shed the ice layer already built. Thus, a more regular but larger ice chunk can be found at the stagnation point, which essentially changes the design geometry of the aero-engine fan blades.

To determine the details of the rime ice among the blades, the profile was also extracted from the 3D ice structure measured with DIP-based 3D scanning results. As shown in Fig.9, the tip region, i.e., 75% span, has a more iced area, especially near the LE, on both the pressure side and suction side compared with the glaze icing condition. As mentioned above, the high ice adhesion strength of the rime ice keeps it firmly attached to the surface even under high aerodynamic and centrifugal forces. The overall thicker ice layer would be found at the whole span but with a few ices shedding from the blades since the ice profile near LE shrinks from 240s to 480s

at the tip region. The situation is more interesting when it comes to the ice accretion at the stagnation point. In general, the ice layer development follows the design profile and grows in a direction opposite to the flow. There is a clear asymmetric ice structure built on the LE with the 'horn-like' geometry at the front, which suggests the stagnation point shift to the marked point from its designed one. Such changes would affect its wind area, the water collection coefficient, and the design velocity triangle. With such a 'horn-like' ice structure built at the LE, there would be 15.7% chord length increase, and 8.8% flow path shrink at LE. While a thinner ice layer at the TE, due to a few indirect impingements of SWD and less runback icing, would only cause ~2.3% flow path change.

For the mid-section, the blades would present a relatively clean suction side but with a rougher pressure side compared with the higher span. The 'horn-like' ice structure built near the LE enlarges the chord length by 16.1%, also causing 12.3% geometric flow path to shrink. While the ice layer at the pressure side would develop from a thin layer to a thick one, with the maximum ice thickness located near 86% chord of the blades, which would cause the general surface roughness change and 8.3 flow path change near the TE.

The root region still contributes to most of the ice mass accumulation on the blades. The high ice adhesion of rime ice dominates the icing process at the root region, where most of the supercooled water droplets would directly freeze once impinging onto the surface. Both the stagnation points at the LE and the pressure side have a thick ice layer built on them. The ice layer on the root region significantly distorts the original geometry of the blades, which changes the chord length, the maximum thickness of the blades, and even thickness distribution. In detail, 14% chord length increase and 11% and 13.9% flow path shrink at LE and TE, separately. Clearly, the designed velocity triangle of the airflow changes with the dynamic icing process, which may result in a worse inflow condition for the downstream components, such as the inlet guide vane and the lower-pressure compressor.
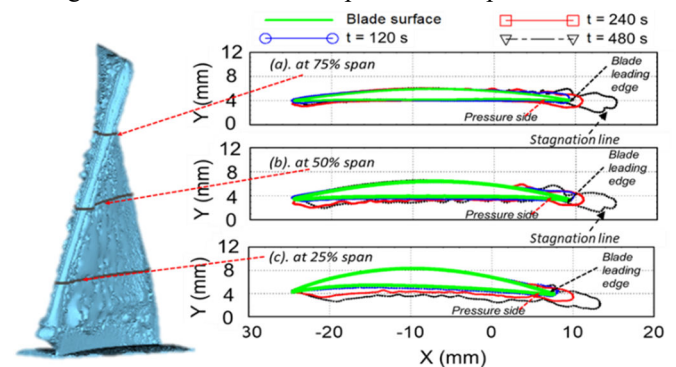
Fig. 9   Ice profile development of the iced fan blades at each spanwise under the rime icing condition.

Considering the similarity between the glaze and rime icing condition, the dynamic ice accretion process would deform the design geometry and the flow path of the aero-engine fan, which would jeopardize the performance and stability, and even pose a threat to the downstream components due to the change in designed velocity triangle. However, the different ambient conditions would induce a change in the icing process when the engine fan works under the glaze and the rime icing conditions. Under a more dry and

cold rime icing condition, the ice would accumulate following the design profile of the blades, with less runback icing. As a result, the ice layer under rime icing is smoother and predictable, causing less detrimental effects on the aero-engine fan. However, the lower temperature would reduce the fluidity of the supercooled water droplets, resulting in a worse working environment on the root region. As a result, such change would deform the boundary layer flow development when airflow passes through the root region with an even narrow flow path. Those would be a challenge for the engineer when designing the flow path since it is hard to apply the active anti-/de-icing strategy on a rotating aero-engine fan blade, especially at the narrow root region.

To determine the performance degradation during the dynamic icing process, the incremental pressure ratio is then applied to analyze the performance degradation during the rime icing condition. As shown in Fig.10, the results present a similar performance degradation trend. However, the engine fan can still guide and add pressure energy to the airflow only at a lower efficiency within 480s icing duration time. These results would suggest that the glaze ice accreting is harmful. More interestingly, the pressure increment ratio has a short increase when the rime ice starts to accumulate on the engine fan blades. A similar phenomenon was reported by Shin [31], where the roughness caused by the rime ice build-up at the initial stage of the accumulation process act as a "turbulator" and promotes a fast transition of the laminar boundary flow over the fan blades, which results in the improved aerodynamic performance of the aero-engine fan model. In addition, the rime ice accumulation usually follows the design geometry, which increases the effective chord length of the blades, which also contributes to the increase of the lift force on the iced blades in the initial stage. However, the penalty due to ice accretion overpowers the benefit when more supercooled water droplets impinge onto the iced fan blades. As a result, the efficiency of the ice aero-engine fan would drop during the icing condition.

Based on these test results, the rime icing would also cause performance degradation but with less penalty due to the much smoother ice layer and thus less interference with the airflow. These results are found to agree with the research findings reported by Li and Liu [17] when studying the dynamic icing process of the spinner-fan model and the propeller blades. That the glaze ice is considered to be more dangerous than the rime ice, which significantly distorts the designed geometry and, thus, the boundary layer flow development, which is found to degrade the aero-engine fan's performance. Compared with the glaze icing process, which is much more complicated due to the partial freezing characteristics of the supercooled water droplets and the runback icing phenomenon, the rime ice accretion process is more predictable and less harmful. However, with the understanding of the general performance degradation during the dynamic icing process, the connection between the initial rough ice, runback icing to the inflow, outflow condition, and boundary layer flow development is still unknown. Such results would suggest that a more fundamental study is still required to understand better the icing physics pertinent to the aero-engine fan icing, which would also contribute to the

design of the highly efficient anti-/de-icing strategies tailored for the aero-engine fan.
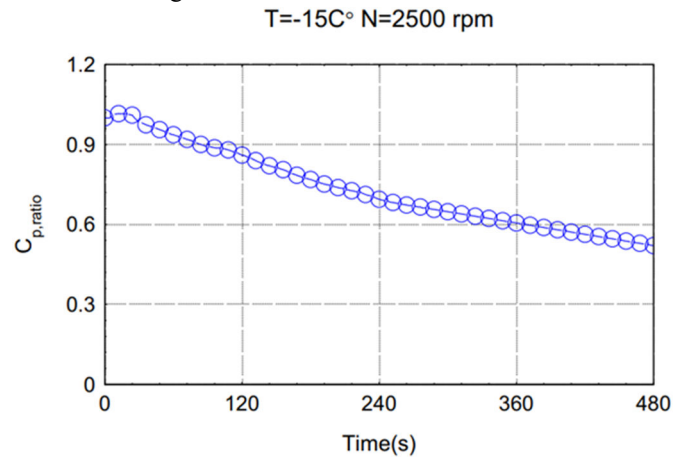
Fig. 10 Pressure incremental ratio change during rime ice accretion process,

IV. CONCLUSION

In the present study, an experimental campaign was conducted to quantify the 3D ice structures over a rotating aero-engine fan and the corresponding performance degradation during the icing process. Based on the time-resolved high-speed images and 3D scanned ice shape, it was found that the local LWC and collection efficiency is different with the pressure side and suction under both glaze and rime icing condition. The root region at the pressure side has the largest local LWC while the tip region, especially at the pressure side, has few directly impinged SWD, due to its geometry effect, i.e., the curved, twisted 3D geometry and mounting angle. The directly impinged supercooled water droplets would fast cover both the pressure and a narrow of the suction side with an ice chunk built from the stagnation point near the LE. However, there is a significant difference between the glaze and rime icing conditions.

Under the glaze icing condition, the supercooled water droplets would not freeze immediately upon impingement onto the model; instead, some portion of those droplets would form a runback water rivulet driven by the aerodynamic and centrifugal force. The linear distribution of centrifugal force along the spanwise contributes to different ice morphologies along the span. At 75% span, due to high centrifugal force, both the pressure side and suction side of the blades were found to be much cleaner due to the less direct impingement of SWD and potential ice shedding phenomenon. However, the direct impingement of supercooled water droplets and radial runback icing phenomenon would form an irregular and unpredictable ice chunk near the stagnation point at the LE, which would shrink ~17.6% flow path and enlarge 10% chord length of its design geometry. At 50% and 25% spans, the centrifugal forces are lower, which results in less radial runback icing but a more iced area on the surface of the blades, especially at the pressure side. The high local LWC and collection rate of SWD on the root region would significantly deform the designed flow path, with an 11% shrink in the cross-sectional area of the flow path, which would eventually affect the boundary flow development and the inflow condition of the downstream components. The pressure increment ratio measurement indicates that the aero-engine fan would quickly lose its ability to guide and compress the

air within 120s of icing. The engine fan would still rotate at design speed but does not pressurize the flow. Instead, the aero-engine fan would depressurize the airflow when passing through it, with a 2% pressure decrement.

The rime icing condition is less detrimental to the performance of the aero-engine compared with the glaze icing condition, where even more ice was found to be accumulated on both the pressure and suction side of blades due to the increasing ice adhesion strength under a lower ambient temperature. Under such conditions, there were fewer runback icing phenomena observed even at the tip region, i.e., above 75% span. The supercooled water droplets would quickly freeze at the point of impingement, forming an ice layer that follows the design geometry of the blade. It is found that most of the ice would accumulate on the root region of the pressure side, with a generally thicker ice layer compared with the glaze icing condition, which caused the geometric cross-section area to reduce by more than 13.9%. Such a dynamic icing process was still found to have a less detrimental effect on the aerodynamic performance compared to the glaze icing condition, with a 60% efficiency drop for a total time of 480s icing duration time. In addition, there was even an increase in efficiency at the very initial stage due to the increase of the effective chord length and the transition of the boundary layer flow. In summary, both the glaze and rime icing process would cause the performance degradation of the aero-engine fan. More detailed studies are still required to better understand the underlying icing physics, which would help the design of efficient and robust anti-/de-icing strategies tailored for the aero-engine fan when encountering different icing conditions.

REFERENCES

[1] Bragg, M. B., Broeren, A. P., and Blumenthal, L. A., "Iced-Airfoil Aerodynamics," *Progress in Aerospace Sciences*, Vol. 41, No. 5, 2005, pp. 323–362. https://doi.org/10.1016/J.PAEROSCI.2005.07.001

[2] Campbell, S. E., Broeren, A. P., and Bragg, M. B., "Sensitivity of Aircraft Performance to Icing Parameter Variations," *Journal of aircraft*, Vol. 44, No. 5, 2007, pp. 1758–1760.

[3] BRAGG, M. B., GREGOREK, G. M., and LEE, J. D., "Airfoil Aerodynamics in Icing Conditions," *Journal of Aircraft*, Vol. 23, No. 1, 1986, pp. 76–81. https://doi.org/10.2514/3.45269

[4] Cao, Y., Tan, W., and Wu, Z., "Aircraft Icing: An Ongoing Threat to Aviation Safety," *Aerospace Science and Technology*, Vol. 75, 2018, pp. 353–385. https://doi.org/https://doi.org/10.1016/j.ast.2017.12.028

[5] Hu, H., Tian, L., and Hu, H., "Experimental Investigation on Ice Accretion Upon Ice Particle

Impacting onto Heated Surface," *AIAA Journal*, 2023, pp. 1–13. https://doi.org/10.2514/1.J062425

[6] Li, L., Liu, Y., Tian, L., Hu, H., Hu, H., Liu, X., Hogate, I., and Kohli, A., "An Experimental Study on a Hot-Air-Based Anti-/de-Icing System for Aero-Engine Inlet Guide Vanes," *Applied Thermal Engineering*, Vol. 167, 2020, p. 114778. https://doi.org/https://doi.org/10.1016/j.applthermaleng.2019.114778

[7] Li, L., Liu, Y., and Hu, H., "An Experimental Study on Dynamic Ice Accretion Process over the Surfaces of Rotating Aero-Engine Spinners," *Experimental Thermal and Fluid Science*, Vol. 109, No. February, 2019, p. 109879. https://doi.org/10.1016/j.expthermflusci.2019.109879

[8] Schulze, W. M., "Aircraft Engine Inlet Cowl Anti-Icing System," US Patent: US5088277A, 1988.

[9] Linke-Diesinger, Andreas., "Systems of Commercial Turbofan Engines: An Introduction to Systems Functions," Springer, 2008.

[10] Zhou, W., Liu, Y., Hu, H., Hu, H., and Meng, X., "Utilization of Thermal Effect Induced by Plasma Generation for Aircraft Icing Mitigation," *AIAA Journal*, Vol. 56, No. 3, 2018, pp. 1–8. https://doi.org/10.2514/1.J056358

[11] Huang, X., Tepylo, N., Pommier-Budinger, V., Budinger, M., Bonaccurso, E., Villedieu, P., and Bennani, L., "A Survey of Icephobic Coatings and Their Potential Use in a Hybrid Coating/Active Ice Protection System for Aerospace Applications," *Progress in Aerospace Sciences*. Volume 105, 74–97. https://doi.org/10.1016/j.paerosci.2019.01.002

[12] Gray, L., "Review of Aircraft Deicing and Anti-Icing Fluid Storm Water Runoff Control Technologies," 2013.

[13] Mcgovern, R. K., Bulusu, K. V, Antar, M. a, and John, H., "One-Dimensional Model of an Optimal Ejector and Parametric Study of Ejector Efficiency," *25th International Conference on Efficiency, Cost, Optimization and Simulation of Energy Conversion Systems and Processes*, 2012, pp. 1–10.

[14] Reddy, E. S., Abumeri, G. H., Murthy, P. L. N., and Chamis, C. C., "Structural Tailoring of Aircraft Engine Blade Subject to Ice Impact Constraints," 1992. https://doi.org/10.2514/6.1992-4710

[15] Hamed, A., Das, K., and Basu, D., "Numerical Simulations of Ice Droplet Trajectories and Collection Efficiency on Aero-Engine Rotating Machinery," No. January, 2012, pp. 1–10. https://doi.org/10.2514/6.2005-1248

[16] Li, L., Liu, Y., Tian, L., Hu, H., Hu, H., Liu, X., Hogate, I., and Kohli, A., "An Experimental Study on a Hot-Air-Based Anti-/de-Icing System for Aero-Engine Inlet Guide Vanes," *Applied Thermal Engineering*, 2020. https://doi.org/10.1016/j.applthermaleng.2019.114778

[17] Li, L., Liu, Y., and Hu, H., "An Experimental Study on Dynamic Ice Accretion Process over the Surfaces of Rotating Aero-Engine Spinners," *Experimental Thermal and Fluid Science*, 2019.

https://doi.org/10.1016/j.expthermflusci.2019.10987 9

[18] Das, K., Hamed, A., Basu, D., and Mechanics, E., "Ice Shape Prediction for Turbofan Rotating Blades," 2006.

[19] Das, K., "Numerical Simulations of Icing in Turbomachinery," University of Cincinnati, 2006.

[20] Hutchings, R., "Effects of Supercooled Water Ingestion on Engine Performance," 2011.

[21] Bidwell, C. S., "Particle Trajectory and Icing Analysis of the E 3 Turbofan Engine Using LEWICE3D Version 3," 2012. https://doi.org/10.4271/2011-38-0048

[22] Dong, W., Zhu, J. J., Wang, R., and Chen, Y., "Numerical Simulation of Icing on the Rotating Blade," 2015.

[23] Hu, H., Al-Masri, F., Tian, L., and Hu, H., "Experimental Study of Dynamic Icing Process on a Pitot Probe Model," *Journal of Thermophysics and Heat Transfer*, 2023, pp. 1–12. https://doi.org/10.2514/1.T6782

[24] Gao, L., Liu, Y., and Hu, H., "An Experimental Investigation on the Dynamic Glaze Ice Accretion Process over a Wind Turbine Airfoil Surface," *International Journal of Heat and Mass Transfer*, Vol. 149, 2020, p. 119120. https://doi.org/10.1016/J.IJHEATMASSTRANSFER .2019.119120

[25] Liu, Y., Ma, L., Wang, W., Kota, A. K., and Hu, H., "An Experimental Study on Soft PDMS Materials for Aircraft Icing Mitigation," *Applied Surface Science*, 2018. https://doi.org/10.1016/j.apsusc.2018.04.032

[26] Liu, Y., Chen, W., Peng, Y., and Hu, H., "An Experimental Study on the Dynamic Ice Accretion Processes on Bridge Cables with Different Surface Modifications," *Journal of Wind Engineering and Industrial Aerodynamics*, Vol. 190, No. April, 2019, pp. 218–229. https://doi.org/10.1016/j.jweia.2019.05.007

[27] Peng, Y., Veerakumar, R., Liu, Y., He, X., and Hu, H., "An Experimental Study on Dynamic Ice Accretion and Its Effects on the Aerodynamic Characteristics of Stay Cables with and without Helical Fillets," *Journal of Wind Engineering and Industrial Aerodynamics*, Vol. 205, 2020, p. 104326. https://doi.org/10.1016/j.jweia.2020.104326

[28] Politovich, M. K., "Predicting Glaze or Rime Ice Growth on Airfoils," *JOURNAL OF AIRCRAFT*, Vol. 37, No. 1. https://doi.org/10.2514/2.2570

[29] Papadakis, M., Rachman, A., Wong, S., Yeong, H., and Bidwell, C. S., "Water Droplet Impingement on Simulated Glaze , Mixed , and Rime Ice Accretions," *Nasa/Tm-2007-213961*, No. October, 2007.

[30] Liu, Y., Bond, L. J., and Hu, H., "Ultrasonic-Attenuation-Based Technique for Ice Characterization Pertinent to Aircraft Icing Phenomena," *AIAA Journal*, 2017. https://doi.org/10.2514/1.J055500

[31] Shin, J., "Characteristics of Surface Roughness Associated with Leading-Edge Ice Accretion," *Journal of Aircraft*, Vol. 33, No. 2, 1996, pp. 316–321. https://doi.org/10.2514/3.46940

Enhancing Runway De-icing Product Application Through Airport Traffic Simulation

Claire Charpentier[1], Jean-Denis Brassard[1], Mario Marchetti[2], Gelareh Momen[1]

[1] *Anti-icing Materials International Laboratory / Université du Québec à Chicoutimi Canada*
[2] *University of Gustave Eiffel in Paris France*

claire.charpentier1@uqac.ca Jean-Denis1_Brassard@uqac.ca mario_marchetti@univ-eiffel.fr Gelareh_Momen@uqac.ca

Abstract— **Canada's harsh winter conditions have a major impact on airports maintenance. Runways must be de-iced or anti-iced to ensure the safety of all users. To achieve this, a combination of mechanical tools (typically for snow contamination) and chemical products in liquid or solid forms (for ice contamination) is used. While standardized tests exist to evaluate runway de-icing performance, they prove ineffective for products primarily used for prevention, such as anti-icing solutions.**

Hence, maintenance teams face a critical need to understand the performance and limitations of products under field-like conditions. This knowledge is essential for optimizing the usage of de-icing and anti-icing solutions in real-world scenarios.

In a field study it was observed that solid products are spread in a given quantity and sometimes covered with a fine mist of liquid products to ease the ice melting. What's more, the teams pass by several times with the spreading trucks to crush the solid to help the ice melt process. This mechanical activation is therefore essential in the process of developing a conclusive laboratory test.

The innovation of the airport traffic simulator addresses this need, allowing the precise replication of field conditions in a laboratory scale. It also enables safety tests to be carried out on different products and quantities under different conditions, whether de-icing or anti-icing, simulating winter precipitations, thanks to a dedicated climatic chamber in which it is used. Furthermore, the ability to complete the set-up with additional tools is also a significant advantage. The implementation of a thermal camera enables infrared thermography analysis of the sample. A visual camera is also attached to the unit, enabling the test to be monitored from outside the climatic chamber. The adjustment of the wheel-pavement contact pressure can simulate different types of vehicle such as cars, spreader trucks. In the context of the device, a cycle corresponds to a certain number of crushes with the wheel, a measurement time (thermal camera and Raman spectrometer) and submission to precipitation.

The device is modular and flexible. It allows the control of several important parameters to determine the effectiveness of the products, and thus enables a representative simulation of airport operating conditions. This set-up can be adapted in the future for a wide range of projects and problems to ensure user safety while optimizing costs and the environmental impact generated by de-icing and anti-icing products. Furthermore, this system can be adapted to implement and to test different types of pavement materials and surface roughness on which motorized traffic is present.

Keywords— ***Airport Traffic Simulator, anti-icing, de-icing, runway de-icing product, ice, winter operations, airport runway.***

I. Introduction

Runway contamination by ice is a major problem for northern airports. Slippery runways impact everyone's safety [1] [2], forcing runway technicians to apply tons of solid and liquid products to help the ice melt and removal [3], thus ensuring the safe landing and take-off of aircraft and the passage of all vehicles. To help professionals, standardized tests [4-6] are used to quantify the de-icing performance of the products involved in the process. However, a comparison between these tests and real-world operations reveals that the tests utilize more than 10 times the amount of products typically used in practice, as illustrated in Figure 1.

Fig. 1 Montreal Airports actual application rate for anti-icing purpose over a concrete pavement

In fact, in standardized tests, the equivalent of 282.5g/m^2 if we consider the 5 g stated, is applied on the substrate, compared to an average of 25.65g/m^2 in real-world condition. This high application rate distorts the results obtained, since the products are saturated and may not fully react.

On the second hand, during an airport winter test campaign conducted in the winter 2023, it was revealed that runway technicians had got into the habit of rolling over the RDP in their vehicles, crushing it to activate it mechanically (Fig. 2). By observing the passage of a truck over a treated runway, using a thermal camera, we saw that the mechanical activation of the products
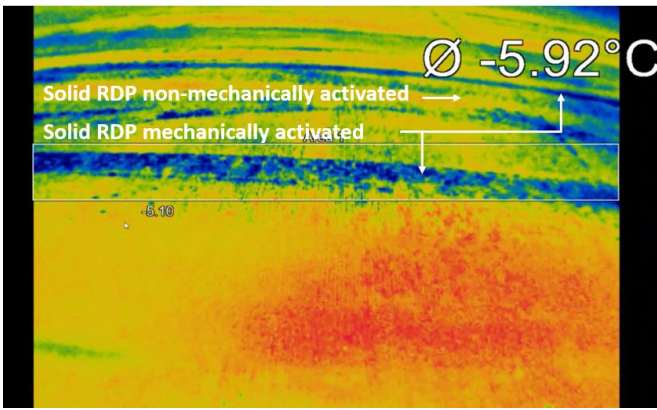
Fig. 2 truck rolled over solid RDP dispersing liquid RDP

cause a sharp drop in temperature proving that the product is more reactive and thus efficient, [7, 8].

Actual methods developed in laboratory are then not fully representative of the real-life operation and show that a new method is needed. The aim of the research carried out was to present a new tool that accurately reproduce the phenomenon of melting of RDP: the airport traffic simulator (ATS).

II. METHODOLOGY

A. Airport Traffic Simulator

The ATS simulates the passage of a vehicle wheel over a treated sample. Here, the sample is a block of concrete reproducing airport runway. The ATS is controlled by a computer outside the cold chamber in which it is installed. The cold room is also computer-monitored, to control temperature and wind conditions.

The ATS therefore consists of a moving table with an approximately speed of 0.10 km/h as presented on Fig. 3 with a slot for placing the test sample. The wheel, free to rotate upon back and forth movement of the table/sample, used on the assembly, is a solid wheel, without grooves, as the grooves create zones where the product is not crushed.

Two pistons are placed on either side of the wheel to inject compressed air to simulate a load. Loads can range from 0 to 5,000 lbs. In the test presented here, the load was set at 5,000 lbs to simulate the passage of a spreader truck over the sample.
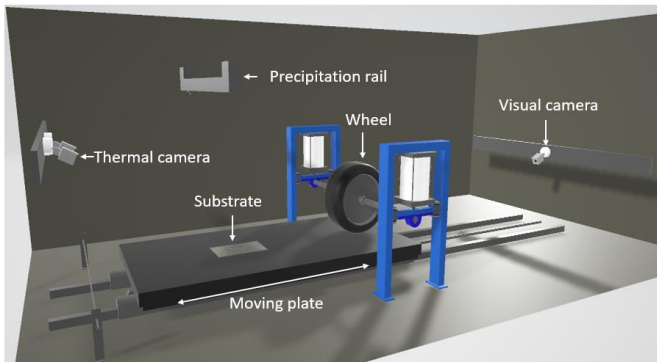
Fig. 1 : Airport Traffic Simulator (ATS) schematics.

Two cameras are positioned on the assembly to visually validate the experiment, and one thermal camera is also present to record temperature during the test.

The ATS is located under a precipitation rail with a nozzle to simulate freezing drizzle precipitation, for anti-icing studies,

if needed. In the test presented here, precipitation took place beforehand, so the behavior of the RDP is observed in de-icing.

B. Protocol

In order to validate the ATS, we compare the behavior of mechanically and non-mechanically activated RDPs. Thus, the solid RDP are currently used by Montréal Airports, it consists of solid sodium formate (NaFo) and liquid/aqueous potassium acetate (KAc).

The concrete substrates were iced under a precipitation of freezing drizzle median volumetric diameter of 320 micron, for 10 minutes at -10 °C. Following the precipitation, the substrate was left in the chamber for 2 hours to allow the ice to finish solidified and temperature return to the test temperature, the substrate was then weighed with a ±0.1 g precision balance to determine the initial ice mass.

The substrates were then submitted to de-icing on the ATS and 0.5 g of solid RDP and 0.35 g of liquid is sprayed onto the block to match application rates encountered in airports.

For the mechanically activated RDP, the substrates were submitted to the STA wheel every 5 minutes, with crushing at time 0 minutes, 5, 10, 15, 20, 25 and 30 minutes and ice melting measurement at 5, 10 and 30 minutes like in the ice melting standard. On the other hand, non-mechanically activated RDP is left in the chamber for 5, 10 and 30 minutes.

To enhance data collection and gain a deeper understanding of product performance, a thermal camera (Optris Pi450i) and its corresponding software (Optris PIX Connect) were employed in this procedure. The device used a microbolometer frame plane array (FPA) detector of uncooled 382 x 288 pixels. The distance between the camera lens and the target was of nearly 40 cm. The camera was installed into the climatic chamber and turned on at least 30 minutes before starting any measurements. A mirror made of reflective crumpled aluminium foil was placed in the FOV of the camera to make a radiative environment correction.

At the end of the test times, the concrete sample is collected, and the brine and remaining solid salt are gently removed using compressed air adjusted at 103 kPa (15 psi). The block is then reweighed on the same balance to evaluate the mass of melted iced.

The procedure is repeated with 3 samples for each test.

III. RESULTS AND ANALYSIS

The results will be presented along three axes: visual appearance, comparison of the mass of ice melted during the tests and finally the variation in minimum temperature during the test for mechanically activated and non-mechanically activated samples.

A. Visual comparison

The visual comparison is made between two sample: one mechanically activated after 30 minutes test and non-mechanically activated after 30 minutes test. The results are presented on Fig. 4. The analogy is made after compressed air removed brine, which stop the melting.

340

Mechanically activated sample after 30 min

Non-mechanically activated sample after 30 min
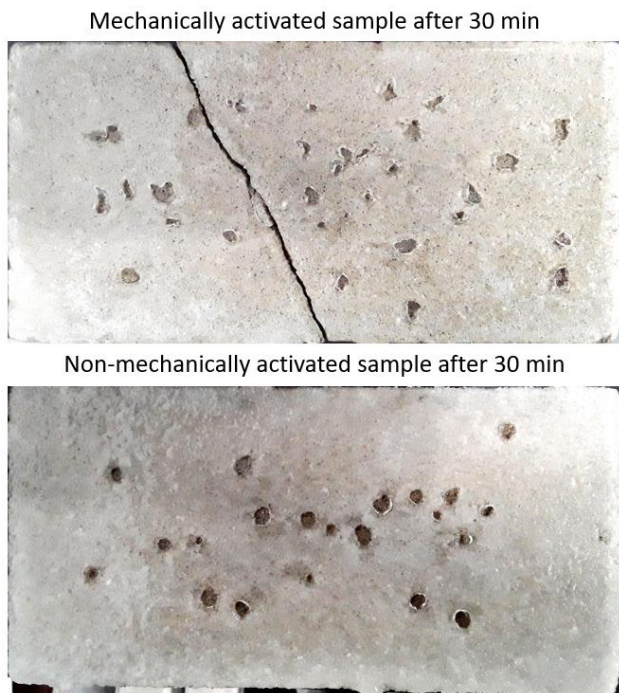
Fig. 4 Visual comparison of mechanically and non-mechanically activated samples after 30 minutes

In Fig. 4, it is important to note that the mechanically activated concrete block is broken in two. This is due to the wheel load applied to the block, yet it has no effect on the study as each piece of the block was recovered. At first view, the shape of the melting is different. The ice is thinner when mechanically activated. The way ice is penetrated in the first case show that the crushed salt allows an irregular ice melting, more from the shape of an ellipse. However, in the case of the non-activated, the RDP grains are directly penetrated in ice and basically the ice melting stop when the concrete is reached, In the case of the activated, the RDP seems to create more brine which is more active, even when the concrete is reached. In this case, the de-icing continued in the form of undercutting.

B. Ice melted comparison

A comparison of the mass of ice melted is made using the data collected during the 5, 10 and 30-minute like in the standard tests and are presented on Fig. 5. The standardized test has been added to show the relevance of using the same application rates as airports for studies. In fact, this one obviously shows greater ice melting since the quantity of product is greater but it is notable to indicate that the amount of ice melting is not 11 times higher than the present test. Also, mechanically activated RDP is much more effective than non-mechanically activated RDP.
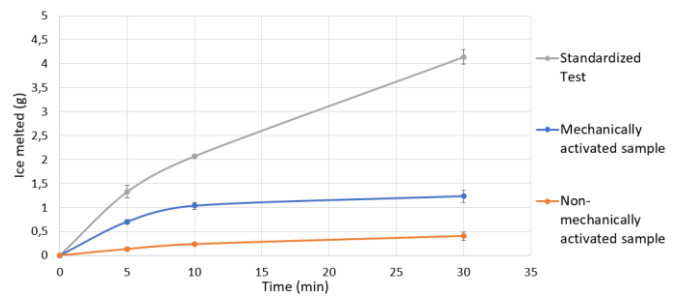
Fig. 5 Ice melted by standardized, mechanically and non-mechanically activated samples

The solid RDP was reduced to a powder and then mixed with ice and brine to activate it. As a result, it becomes 3 times more effective at melting ice after 5 minutes and 5 times more effective after 10 minutes. After 30 minutes, the mass of melted ice is 4 times higher than the non-activated. Based on this data, the melting rates can be calculated and presented on Fig 6.
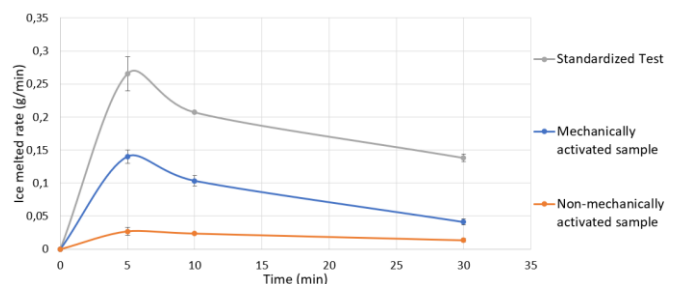
Fig. 6 Ice melted rate by standardized, mechanically and non-mechanically activated samples

Fig. 6 shows the rate of ice melting in g/min to highlight the RDP's melting capacity as a function of time, in order to validate the hypothesis. It should be noted that the ice melting rate of the standardized test is not 11 times greater than that of the presented test. Thus, the increase in product does not proportionally influence ice melting. It is thus notable that the mechanically activated solid RDP is more efficient throughout the test, with a significant peak in efficiency of 0.14 g/min ±0.01 g/min after 5 minutes, compared to the non-mechanically activated RDP which also reaches its peak of efficiency at 5 minutes but therefore the value is only 0.03 g/min +-0.01 g/min. This is due to the fact that, at this point in the trial, the RDP is in powder form and therefore dissolves greatly in the brine. Gradually, the brine loses its RDP concentration, leading to a reduction in product efficacy.

In the case of non-mechanically activated solid RDP, the trend curve appears to be more linear, since solid RDP dissolves very slowly in the brine. It eventually loses its effectiveness, as the liquid RDP is no longer effective.

C. Thermal comparison

Comparing the evolution of minimum temperature over the course of the test as presented on Fig. 7, is complex. Indeed, the temperature curve of the mechanically activated RDP remains complex to elaborate, as the thermal camera does not follow the block throughout the test, as the plate moves, taking the block to be crushed under the wheel. Data is therefore collected after each pass under the wheel. Nevertheless, important data emerge from this study.
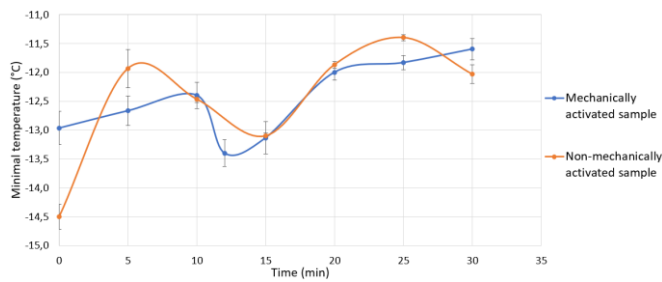
Fig. 7 Minimum temperature of mechanically and non-mechanically activated samples during the test

Fig. 7 shows that the non-mechanically activated RDP has a very low minimum temperature right from the start of the test, due to the application of the liquid RDP. This is not the case for activated RDP, as the concrete block cannot be placed under the thermal camera when the products are applied.

The minimum temperature of the mechanically activated RDP is -13.4 °C on average ±0.23 °C and is reached after 12 minutes. This corresponds to the end of the maximum efficiency reached by the RDP. The minimum temperature then seems to increase, following a quasi-linear trend.

The non-mechanically activated RDP reaches its minimum temperature (eluting the temperature at time 0) at 15 minutes. The minimum temperature then increases linearly, before decreasing again after 30 minutes. This can be explained by the fact that, as the solid RDP is not crushed, it partially melts in the brine, then disintegrates, restoring efficiency to the reaction. However, the efficiency is quickly halted by the fact that the grain has ice penetrated and is therefore no longer in contact with the ice, but simply with the concrete.

It can therefore be observed that mechanically activated solid RDP is more effective than non-mechanically activated solid RDP.

IV. Conclusions

The airport traffic simulator shows that the setup provides more representative results than non-activated RDP. It can effectively simulate the crushing of solid RDP on an airport runway, providing experimental results that are closer to the reality of the problem of winter contamination of airport runways. It clearly shows that by having a more representative methods help to better characterize the RDPs.

This new tool has a significant potential in the evaluation of the application rates, the furthers steps with the STA involve anti-icing test in order to establish a clear protocol to assess the application rates.

Such tools will be useful for both airports and RDP manufacturers to improve their process.

References

[1] A. Klein-Paste, "Runway Operability under Cold Weather Conditions. Tire-pavement friction creation by sand particles on iced pavements, and non-contacting detection of sand particles on pavements," *NTNU,* 2007.

[2] A. Klein-Paste, "Airplane braking friction on dry snow, wet snow or slush contaminated runways," *Cold Regions Science and Technology,* 2017/02/20/ 2017, doi: https://doi.org/10.1016/j.coldregions.2017.02.004.

[3] H. Lissner, M. Wehrer, M. Jartun, and K. U. Totsche, "Degradation of deicing chemicals affects the natural redox system in airfield soils," *Environmental Science and Pollution Research,* vol. 21, no. 15, pp. 9036-9053, 2014/08/01 2014, doi: 10.1007/s11356-013-2096-9.

[4] *AS6170 Ice Melting Test Method for AMS1431 and AMS1435 Runway Deicing/Anti-icing Products*, Aerospace Standard AS6170, SAE International, 2021.

[5] *AS6211 Ice Penetration Test Method for AMS1431 and AMS1435 Runway Deicing/Anti-icing Products*, Aerospace Standard AS6211, SAE International, 2021.

[6] *AS6172 Ice Undercutting Test Method for AMS1431 and AMS1435 Runway Deicing/Anti-icing Products*, Aerospace Standard AS6172, SAE International, 2021.

[7] C. Charpentier, J.-D. Brassard, M.-M. Tremblay, and G. Momen, "A Refined Procedure for Evaluating the Airport Runway De-icing Products Performance."

[8] C. Charpentier, J.-D. Brassard, G. Momen, and J. Perron, "Development of a dynamic ice penetration model for runway deicing products through performance experimental characterization," *Cold Regions Science and Technology,* p. 103932, 2023.

Meteorological Parameters Effect on Atmospheric Icing - A Field Experimentation Study

Xingbo Han+, Muhammad Virk, Jan-Arne Pettersen, Øyvind Søraas, Hamza Asif, Marius Wang & Morten Monland

Arctic Technology & Icing Group, UiT- The Arctic University of Norway.

xingbo.han@uit.no, muhammad.s.virk@uit.no, jan-arne.pettersen@uit.no

Abstract— **In cold regions, atmospheric icing on ground structures can give rise to a range of safety and operational challenges. Optimal implementation of the preventative measures against icing lies in the timely and precise monitoring of the meteorological icing events. Meteorological variables such as wind speed, atmospheric temperature, airborne liquid water content (LWC) and the distribution of airborne super cooled water droplets size (MVD) collectively influence the initialization and progression of the atmospheric icing events. These environmental factors exhibit inter-dependency. This research work describes a field monitoring of these environmental parameters and resultant icing events by using a state-of-the-art field ice monitoring station installed by UiT researchers in arctic circle of northern Norway. This field ice monitoring station is installed at 1006 m a.s.l on a mountain top in Narvik exposed to severe icing events. This icing station consists of various advance sensors such as heated anemometers, ice load monitors, HoloOptic, ICEMET, ICETROLL and heated web camera. The data from these sensors is collected to a data logger and being transfer to UiT webserver using 4G communication. This study investigates that how the change in the above listed environmental parameters effect the resultant accreted ice load, intensity and the inter-dependency of each other. The research work describes the results of some recorded icing events and corresponding meteorological parameters during winter 2022/2023 and tries to build the relationship between normal environmental parameters (wind velocity, relative humidity, and temperature) with the difficult-to-obtain droplet parameters (MVD and LWC). These filed experiments results will help to improve the existing ice physics models and validation of numerical or lab experimentation with the actual field icing events. The findings of this research can also be employed to estimate and compute the distribution of water droplet sizes and the concentration of airborne liquid water content in situations where measurement equipment is constrained.**

Keywords— ***Atmospheric icing, Meteorological parameter, Field measurements, Ice load*, MVD, LWC**

I. INTRODUCTION

In cold climate regions around the globe, icing on structures is a safety hazard for many industries. For example, power transmission lines icing can cause an increase in line load, wire torsion and fracture, insulator ice flashover discharge, tower collapse, etc. [1], resulting in large-scale power outages and huge economic losses. Since the recording of power line icing disasters in 1954, there have been various types of transmission line icing accidents [2]. Relevant reports have been made in regions such as China[3], Canada[4], Japan[5], Norway, Sweden and the United States[6]. In order to study the physics of ice accretion and propose corresponding mitigation methods, extensive research has been conducted. The ice accretion process on structures is relatively complex, with different icing types. The environmental & geometric factors such as the size and shape of the structure, wind speed, temperature, LWC (Liquid water content) and water droplet size distribution in the air[7] effect the ice accretion process.

Research on icing mechanisms started early, and in different icing models, the decisive factors for icing vary. In 1953, Imai[8] proposed that the rate of conductor icing is determined by environmental temperature, wind speed, and conductor diameter. Building upon this, in the Makkonen[9-10] model, icing on conductors is considered to be formed by the collision, capture, and freezing of water droplets on the conductor surface. The size of water droplets and the liquid water content in the air are also identified as key factors determining the rate of conductor icing. Finstad[11-12] defined the Mean Volume Diameter (MVD) of water droplets to study variations in collision coefficients of different-sized droplets on the conductor surface. Based on wind tunnel experiments and finite element software simulations, Jian Zhang et al[13-14]. pointed out that the water droplet collision coefficient on the conductor surface is a crucial factor affecting icing growth. Under the same environmental conditions, the water droplet collision coefficient can increase several times when the MVD increases from 10 μm to 40 μm. Additionally, according to the research of Sokolov Pavlo et al[15-16]., even with the same MVD, differences in water droplet size distribution can lead to variations in water droplet collision efficiency and icing rate on the surface of cylindrical objects. Therefore, the ISO 12494[17] standard document summarizes general guidelines for determining ice loads on structural surfaces, indicating that numerical values and analytical models for icing calculations require LWC and MVD in the air as model inputs.

However, measuring LWC and MVD is not straightforward, the rotating multi-cylinder method[18] is commonly used to indirectly measure LWC and the MVD in the air near the ground surface under icing conditions. This method involves measuring the differences in icing rates on various cylinders of different diameters. Jones Kathleenf et al[19]. investigated the characteristics of water droplet size distribution using this method. However, experimental results indicate that as icing time increases, the final diameters of different diameter cylinders tend to be the same. Therefore, it is necessary to ensure that there are always differences in cylinder diameters, and the sensor measurement accuracy should be sufficient to capture the differences in icing rates between the cylinders. Additionally, In addition, holographic imaging technology is also employed for measuring MVD and LWC[20-21], such as pioneering work done by Silverman and Thompson[22], and modern digital holographic airborne cloud measurement system realized by Fugal[23], but this method also requires

heating equipment to ensure that the measurement device is not affected by icing, and relevant equipment is not cheap.

To better integrate the current icing models with the engineering applications, considering the practical difficulty in obtaining some environmental parameters under icing conditions, exploring a simple and economical method to obtain MVD and LWC has become a new research direction. In fact, MVD and LWC are not entirely independent of environmental parameters such as wind speed, temperature, and relative humidity. An increase in relative humidity in the air is a necessary condition for increasing LWC, while an increase in wind speed can also facilitate the movement of large droplets of supercooled water to the surface of structures, forming ice accretion. Due to the ease of obtaining parameters such as wind speed, temperature, and relative humidity using conventional meteorological sensors, establishing a correspondence between MVD, LWC, and these parameters can facilitate the achievement of the aforementioned goal. This paper conducts real-time monitoring of various parameters involved in icing events under natural conditions, analyzes the patterns of parameter variations, attempts to fit calculation formulas for MVD and LWC, and validates them through experimental data.

II. DESIGN OF EXPERIMENTS

The field icing experiments were carried out at 1006 m above sea level, at 68 degrees north in the arctic circle of norther Norway. This station is installed by UiT researchers. A state of art fields ice monitoring station comprises of various meteorological sensors and icing sensors is used. Wind speed, wind direction, atmospheric temperature, relative humidity, and pressure are measured using a heated multi-purpose weather sensor. Liquid water content and droplet size measurements are carried out using ICEMET sensor[20-24]. Accreted ice load and icing intensity is measured using two ice load monitors (IL1 & IL2) and T-44 HoloOptic sensor. Additional ICETROLL sensor is installed for comparison of ice load from Ice load monitors. A video camera with heated lenses is installed to monitor the icing event. Figure 1 shows the field ice monitoring station used in this study.
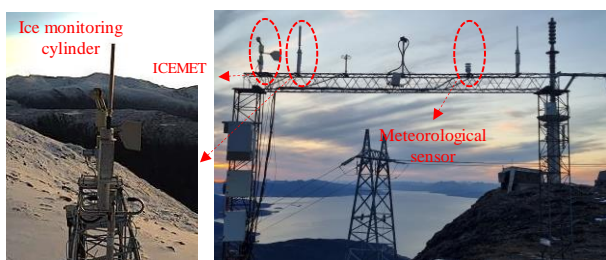
Fig. 1　Field ice monitoring station setup

III. LWC AND MVD DURING THE ICING EVENT

The field experiments employed three cylinders with a diameter of 30 mm (as per ISO12494) each as ice accretion monitors. These cylinders were connected in series with tension sensors, allowing real-time collection of ice mass data. The specific parameters of the three ice monitoring cylinders are shown in Table I.

TABLE I.　BASIC PARAMETERS OF ICE CYLINDER

Name	Diameter /mm	Length h/m	Installation method	Rotation situation
Ice Load Monitor (IL1)	30	0.5	Vertical up	Freely
Ice Load Monitor (IL2)	30	0.5	Vertical up	Freely
ICETROLL	30	1.0	Vertical Down	Forced (2 r/min)

By monitoring the ice mass on the cylinders, we can determine the start and end times of icing events. As shown in Figure 2, driven by an electric motor, the Icetroll cylinder rotates at a speed of 2 rpm, therefore the influence of ice accretion on the connection between the cylinder and tension sensors is avoided, resulting in relatively stable ice mass data that can serve as a fundamental reference. Analysis of the ice mass data from December 2022 reveals three periods during which the ice mass on all three cylinders simultaneously increased, indicating three icing events. The specific times are listed in Table II.

The data recorded by the ICEMET sensor for Liquid Water Content (LWC) and Median Volume Diameter (MVD) are shown in Figure 2, 3 & 4. By comparing the timing of the three icing events as shown in Figure 2, the following observations can be made:

TABLE II.　THE START AND END TIME OF THE ICING EVENTS

Name	Start time	End time	Duration/ h
Icing event 1	2022/12/05 05:21:00	2022/12/06 11:25:00	30
Icing event 2	2022/12/14 09:40:00	2022/12/15 23:21:00	37.5
Icing event 3	2022/12/21 05:29:00	2022/12/25 00:13:00	90.5

1) During the time intervals of the three icing events, LWC rapidly increased, and the duration of this increase corresponded directly to the period of ice accretion growth on the cylinders.

2) Over the recorded one-month period, there were a total of 8 time intervals where LWC exhibited a rapid increase (with LWC peaks reaching at least 0.025 g/m^3). However, only during time intervals No. 2, No. 3, and No. 6 LWC maintained relatively high values for an extended period, ultimately leading to three distinct icing events.

3) Under non-icing conditions, LWC values were close to 0 g/m^3, remaining below 0.025 g/m^3.

4) Comparing the data for LWC and MVD reveals that as LWC increases, MVD also increases correspondingly. However, there is not a strong correlation between the magnitudes of increase in LWC and MVD. This means that when LWC is relatively low, some water droplets in the air can still have diameters ranging from 30 μm to 40 μm. For example, during the time interval between No. 2 and No. 3, LWC was relatively low, yet the MVD value was comparatively high.
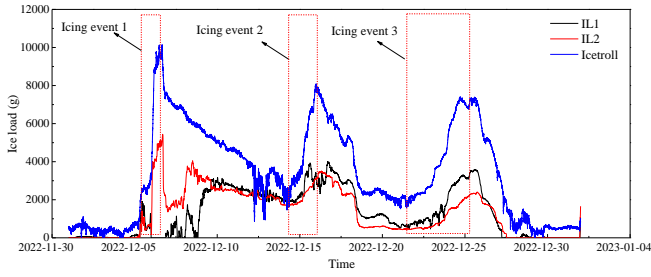
Fig. 2　Ice load on the cylinders
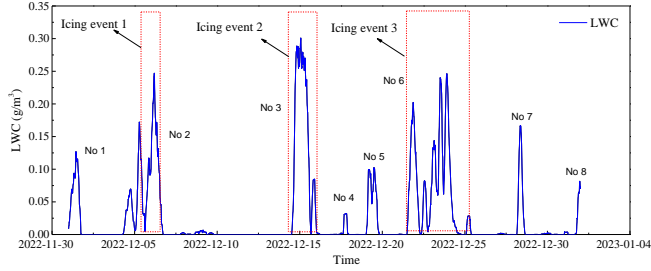
Fig. 3　The LWC data during the icing events
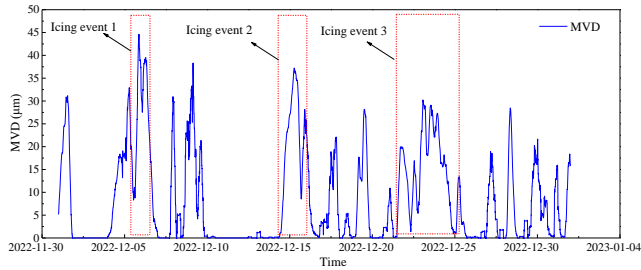
Fig. 4　The MVD data during the icing events

IV. IMPACT OF METEOROLOGICAL PARAMETERS ON MVD AND LWC

Based on the above analysis, it is evident that ice accretion occurs only during periods when both LWC and MVD rapidly increase. Wind speed (V in m/s), relative humidity (RH in %), and temperature (T in ℃) data were collected at a sampling frequency of 1 sample/min from October 18th to December 31st, 2022, at the location of the icing experimental station. The relationship between various meteorological parameters and LWC was plotted, as shown in Figure 5.

It can be observed that during the observation period, the majority of LWC data points (LWC > 0.1 g/m³) fall within the range of relative humidity RH > 80%, wind speed V < 20 m/s, and temperatures ranging from -10℃ to 4℃, with most MVD data points also increasing to 10 μm or above under similar conditions. Furthermore, LWC demonstrates a good correspondence with MVD (with a correlation coefficient R = 0.70). This roughly delineates the meteorological parameter range for ice accretion occurrence. Several points regarding the influence of each parameter on LWC and MVD include:

1) Relative humidity (RH) has a significant impact on LWC, with LWC increasing gradually only when RH exceeds 80%. When relative humidity is below 80%, regardless of other environmental conditions, LWC remains close to 0. Since LWC and MVD exhibit a high correlation coefficient (R = 0.8),

it is possible to derive mathematical formulas by fitting LWC to RH and MVD to LWC.

$$LWC = -0.0019+9.875\times10^{-6}\times\exp(0.10076\times RH) \quad (1)$$

$$MVD=36.416\times\left(LWC-1.874\times10^{-6}\right)^{0.14}　(RH>80\%) \quad (2)$$

2) Extracting all data points with RH > 80% and plotting scatter plots of LWC at different wind speeds and temperatures reveals that within the range of wind speeds from 0 to 13 m/s, LWC increases with increasing wind speed. However, when wind speeds exceed 13 m/s, LWC begins to decrease and remains below 0.1 g/m³. Therefore, it can be inferred that under conditions of high air humidity, an increase in wind speed within a certain range may facilitate an increase in the liquid water content in the air. This could be because higher wind speeds allow the airflow to carry more liquid water droplets through the ICEMET sensor, resulting in an increase in the collected LWC values. However, excessively high wind speeds (V > 13 m/s) may not favor the formation and concentration of liquid water droplets.

3) Similarly, within the RH > 80% range, temperature also exhibits certain regularities in its influence on LWC. Within the temperature range of T = -12℃ to 0℃, LWC initially increases and then decreases with increasing temperature. However, when the temperature exceeds 0℃ (0℃ to 4℃), LWC begins to increase gradually again. For higher temperatures, due to a lack of data, further discussion is not conducted here. Based on the observed patterns of temperature and wind speed affecting LWC, adjustments were made to Equation (1), resulting in Equation (3). As shown in Figure 7, using December data to validate the equation, the average error for LWC is 0.03 g/m3, and the average error for MVD is 6.87 μm.

$$
\begin{aligned}
LWC = &\left[-0.0019+9.875\times10^{-6}\times\exp(0.10076\times RH)\right] \\
&\times\left|-0.0066V^2+0.1336V+0.6140\right| \\
&\times\left|\frac{-1.5755T+0.0942}{T^2+2.903T+4.71}-0.5\right| \\
&(0\le V\le20\text{ m/s},-12℃\le T\le0℃)
\end{aligned}
\quad (3)
$$
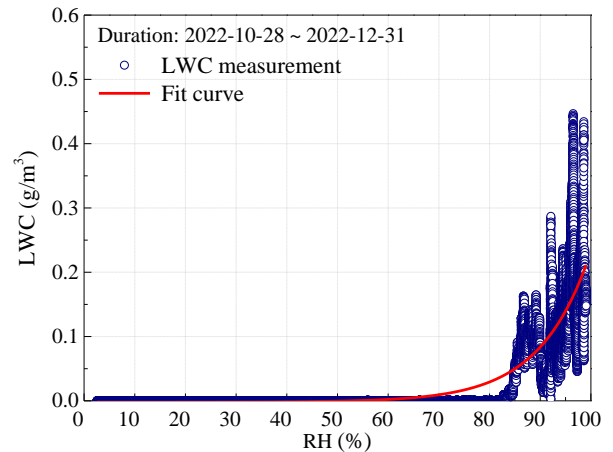
(a) The fitting curve of LWC
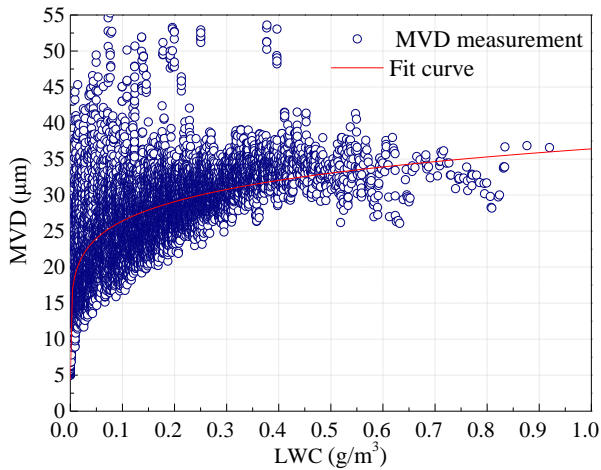
(a) The fitting curve of MVD

Fig. 5   Fitting curves of LWC and MVD
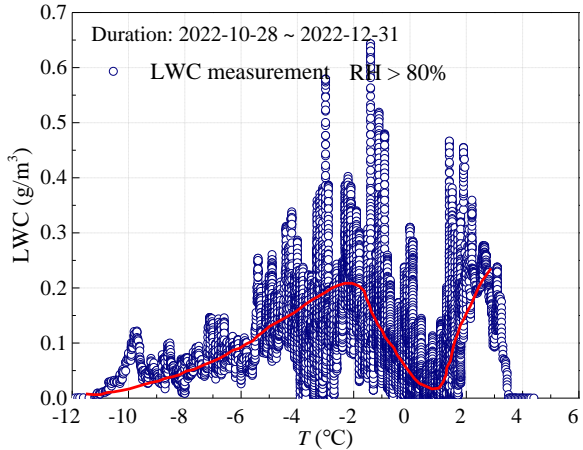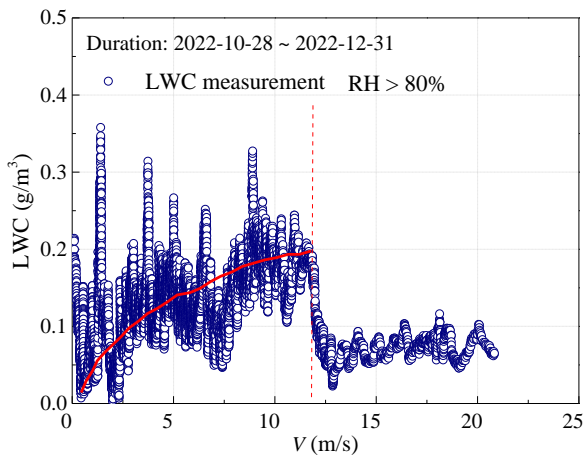
Fig. 6   Effect of meteorological parameters on LWC
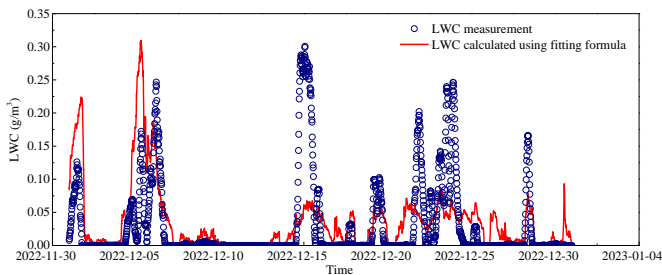
Fig. 7   Comparison between measurement and fitting formula data

V. PREDICTION USING MACHINE LEARNING

If fitting formulas are used to obtain LWC and MVD, although the errors are within an acceptable range, the limited data for fitting may hinder continuous optimization of the formulas. Therefore, this study attempts to explore the use of machine learning to predict LWC and MVD, aiming to continuously optimize prediction models as data volume increases.

As shown in Figure 8, a BP neural network based on the particle swarm optimization algorithm is employed to train a relationship model NET(V, T, RH) ~ (LWC, MVD) between general meteorological parameters and LWC and MVD. The neural network consists of 3 nodes in the input layer, 9 nodes in the hidden layer, and 1 node in the output layer. Meteorological data from October 18th to November 30th, 2022, are used for model training. The training and testing results are shown in Figure 9, indicating a good fit of the model to the data with a correlation coefficient R > 0.8.

To further test the model's accuracy in predicting LWC and MVD, validation is conducted using data from December 2022. As illustrated in Figure 10, the predicted LWC and MVD values are satisfactory, with an average prediction error of 0.02 g/m³ for LWC and 2.58 μm for MVD.

NET(V, T, RH) ~ (LWC, MVD)
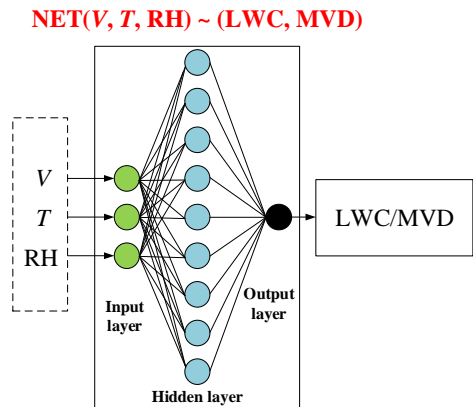
Fig. 8   BP neural network based on PSO algorithm

346

Test: R=0.81698
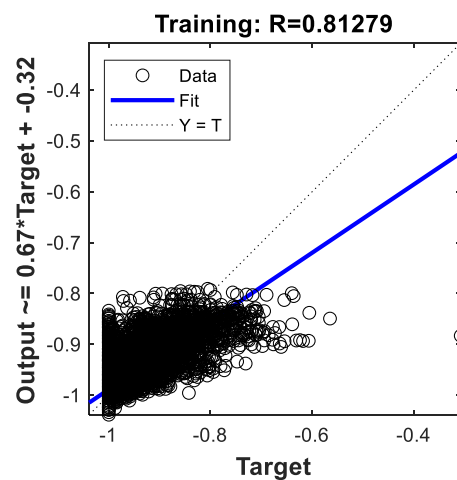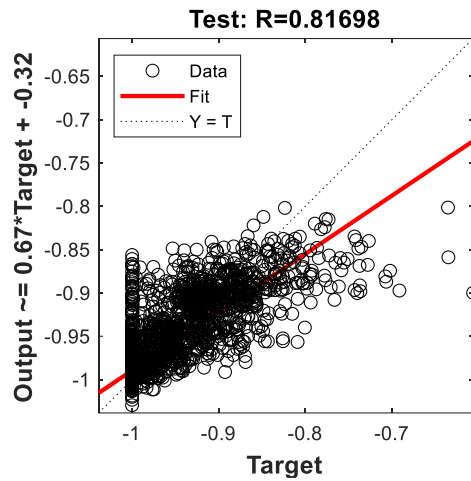
Fig. 9 Model training and test results

(a) LWC prediction
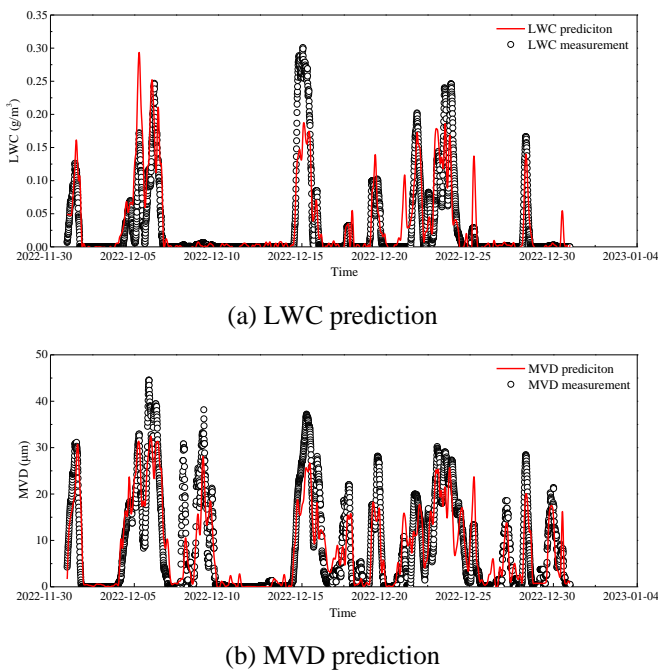
(b) MVD prediction

Fig. 10 Model prediction results

VI. CONCLUSION

Continuous icing mass data on the cylinders can reveal the timing of ice accretion events' onset and termination. There exists a good correspondence between the two parameters of liquid water content (LWC) and median volume diameter (MVD) in the air and the occurrence of ice accretion events. When both LWC and MVD increase to certain values (LWC > 0.1 g/m3, MVD > 5 μm) and the environmental temperature is below 0 ℃, ice accretion can occur on the surface of cylindrical structures.

Based on the comparison of meteorological parameters, the changes in LWC and MVD parameters before and after icing events are not independent of parameters such as wind speed, environmental temperature, and relative humidity. Through fitting data from a total of 65 days before and after three icing events, it is evident that LWC only increases to above 0.1 g/m³ when the relative humidity is greater than 80%, meeting the requirements for icing. Within the range of wind speeds from 0 to 13 m/s, LWC initially increases and then decreases with increasing wind speed, while environmental temperatures between 0 ℃ and -12 ℃ also exhibit a trend of initially increasing and then decreasing LWC. Moreover, the correlation coefficient between LWC and MVD parameters reaches 0.8, and MVD can be derived from a fitting formula of LWC. Based on this pattern, formulas for calculating LWC and MVD were fitted, with average errors relative to measured values of 0.03 g/m³ and 6.87 μm, respectively.

By using a particle swarm algorithm-based BP neural network to establish a relationship model between environmental parameters and LWC and MVD (NET (V, T, RH) ~ (LWC, MVD)), the model's predictive performance surpasses that of fitting formulas. The average errors for LWC and MVD are 0.02 g/m3 and 2.58 μm, respectively.

REFERENCES

[1] Shu, L., Wang, S., Jiang, X., Hu, Q., Liang, J., Yin, P., Chen, J. Modeling of AC flashover on ice-covered composite insulators with different shed configurations. IEEE Transactions on Dielectrics and Electrical Insulation, 2014, 21, (6), pp. 2642-2651.

[2] Hu, J., Lan, B., Xu, K., Jiang, X., Zhang, Z., Shi, B., Yang, H., Wu, Y. Artificial icing and AC flashover tests on glass insulators with silicone acrylate resin hydrophobic coatings. IEEE Transactions on Dielectrics and Electrical Insulation, 2016, 23, (2), pp. 1038-1047.

[3] Lei, Y., Meng, Z., Jiang, X., Hu, J., Zhang, Z. DC ice-melting and temperature variation of optical fibre for ice-covered overhead ground wire. IET Generation, Transmission & Distribution, 2016, 10, (2), pp. 352-358.

[4] Volat, C., Farzaneh, M., Mhaguen, N. Improved FEM models of one- and two-arcs to predict AC critical flashover voltage of ice-covered insulators. IEEE transactions on dielectrics and electrical insulation, 2011, 18, (2), pp. 393-400.

[5] Matsuda, H., Komuro, H., Takasu, K. Withstand voltage characteristics of insulator string covered with snow or ice. IEEE transactions on power delivery, 1991, 6, (3), pp. 1243-1250.

[6] Charneski, M. D., Gaibrois, G. L., Whitney, B. F. Flashover Tests of Artificially Iced Insulators. IEEE power engineering review, 1982, PER-2, (8), pp. 17-18.

[7] Jiang, X., Dong, B., Chao, Y., Zhang, Z., Hu, Q., Hu, J., Shu, L. Diameter correction coefficient of ice thickness on conductors at natural ice observation stations. IET Gener. Transm. Distrib, 2014, 8, (1), pp. 11-16.

[8] Imai, I. Studies on Ice Accretion. Researches on Snow and Ice, 1954, 1, pp. 35-44.

[9] Makkonen, L. Models for the Growth of Rime, Glaze, Icicles and Wet Snow on Structures. The Royal Society, 2000, 358, (1776), pp. 2913-2939.

[10] Makkonen, L., Lozowski, E. Fifty years of progress in modelling the accumulation of atmospheric ice on power network equipment. Proceedings of the 11th International Workshop on Atmospheric Icing of Structures, Canada, 2005,

[11] Finstad, K. J. On the Median Volume Diameter Approximation for Droplet Collision Efficiency. 1988,

[12] Finstad, K. J., Lozowski, E. P., Gates, E. M. A Computational Investigation of Water Droplet Trajectories. Journal of atmospheric and oceanic technology, 1988, 5, (1), pp. 160-170.

[13] Zhang, J., Makkonen, L., He, Q. A 2D Numerical Study on the Effect of Conductor Shape on Icing Collision Efficiency. Cold Regions Science and Technology, 2017, 143, pp. 52-58.

[14] Zhang, J., He, Q., Makkonen, L. A Novel Water Droplet Size Parameter for Calculation of Icing on Power Lines. Cold Regions Science and Technology, 2018, 149, pp. 65-70.

[15] Sokolov, P., Virk, M. S. Analytical parametrizations of droplet collision efficiency on cylinders – A review study. Cold Regions Science and Technology, 2018, 155, pp. 314-326.

[16] Sokolov, P., Virk, M. S. Droplet distribution spectrum effects on dry ice growth on cylinders. Cold Regions Science and Technology, 2019, 160, pp. 80-88.

[17] ISO 12494:2001(E), 2001. Atmospheric icing of structures. International Organization for Standardization, Geneva, CH.

[18] Knezevicil, D., Kindf, R. J. Determination of Median Volume Diameter (MVD) and Liquid Water Content (LWC) by Multiple Rotating Cylinders. 2014,

[19] Jones, K. F., Thompson, G., Claffey, K. J., Kelsey, E. P. Gamma Distribution Parameters for Cloud Drop Distributions from Multicylinder Measurements. Journal of Applied Meteorology and Climatology, 2014, 53, (6), pp. 1606-1617.

[20] Kaikkonen, V. A., Molkoselkä, E. O., Mäkynen, A. J. A rotating holographic imager for stationary cloud droplet and ice crystal measurements. Optical Review, 2020, 27, (2), pp. 205-216.

[21] Tiitta, P., Leskinen, A., Kaikkonen, V. A., Molkoselkä, E. O., Mäkynen, A. J., Joutsensaari, J., Calderon, S., Romakkaniemi, S., Komppula, M. Intercomparison of holographic imaging and single-particle forward light scattering in situ measurements of liquid clouds in changing atmospheric conditions. Atmospheric measurement techniques, 2022, 15, (9), pp. 2993-3009.

[22] Silverman, B. A., Thompson, B. J., Ward, J. H. A Laser Fog Disdrometer. Journal of applied meteorology (1962), 1964, 3, (6), pp. 792-801.

[23] Fugal, J. P., Shaw, R. A., Saw, E. W., Sergeyev, A. V. Airborne digital holographic system for cloud particle measurements. Appl Opt, 2004, 43, (32), pp. 5987-5995.

[24] Molkoselka, E. O., Kaikkonen, V. A., Makynen, A. J. Measuring Atmospheric Icing Rate in Mixed-Phase Clouds Using Filtered Particle Data. IEEE Transactions on Instrumentation and Measurement, 2021, 70, pp. 1-8.

A Timeline Study of Freezing Rain Events in Toledo Ohio Using Toledo Express Airport Weather Station [1955 to 2023]

Ahmed Abdelaal [1], *Kathleen Jones* [2], *Douglas Nims* [3]

[1] *State University of New York Polytechnic Institute, Utica, NY, USA*
[2] *Hanover NH USA*
[3] *University of Toledo, Toledo, OH, USA*

ahmed.abdelaal@sunypoly.edu.edu, *kathyjones@alum.mit.edu*, *douglas.nims@utoledo.edu*

Abstract— **Climate change is scientifically evident and is expected to cause changes in the frequency and severity of weather events including freezing rain. Freezing rain is a serious problem that affects different types of structures such as overhead lines, communication towers, and bridges. An increase in the frequency or severity of atmospheric icing events due to climate change poses a safety hazard to the public in addition to economic loss. Here, we investigate freezing rain events in Toledo, Ohio, USA, using 68 years of weather data at the Toledo airport for the period of record: February 1955 to December 2023. Results of the data analysis show that the annual mean temperature increases coupled with an increase in total annual precipitation and a decrease in annual mean wind speed. Although the frequency and duration of freezing rain events decrease, the intensity increases with greater hourly ice thickness rates. This study provides important insights into the impact of climate change on freezing rain events. Additional locations will be investigated in future studies to examine the changes in the freezing rain events and weather parameters to obtain more comprehensive conclusions.**

Keywords— ***climate change, freezing rain, ice thickness, severe events.***

I. INTRODUCTION

Climate change is one of the most serious challenges that is faced by the world today. This affects the probability of extreme weather events such as extreme precipitation [1] which in turn may affect the occurrence of atmospheric icing events including freezing rain. Freezing rain can occur when a warm air layer exists between the subfreezing layers at the cloud base and the earth's surface. This causes the snow precipitation starting at the cloud base to melt and then cool near the earth's surface with a high potential of freezing on structures. Freezing rain has caused extensive damage to utility power lines [2,3,4] and telecommunication towers [5], in addition to disrupting traffic on bridges due to ice shedding [6,7,8]. Therefore, changes in the severity and frequency of such events may have significant consequences on the safety and operation of these structures.

In this study, historical weather data were used to investigate the changes in the weather parameters. The data were used to calculate the uniform radial ice thickness using a simple model for ice accretion in freezing rain [9]. Linear regression was used to obtain the trend of the parameters with time. These linear relations were extrapolated to the future to project the values of these parameters using these historical data. Since weather data and changes to them are location-specific, this study focuses only on one location, which is the city of Toledo in Ohio in the United States.

II. LOCATION, ICE THICKNESS MODEL, AND WEATHER DATA

A. LOCATION

Fig. 1 A) Google map images of the city of Toledo in Ohio showing the location of the VGCS bridge, B) a zoom-in image of the VGCS bridge, C) an image of the VGCS bridge crossing the Maumee River [image source: FIGG Bridge Group], and D&E) ice accreting on the bridge cables during the 2011 ice event.

Toledo is located in northwest Ohio and is part of the Great Lakes region (western end of Lake Erie). Historically, Toledo has experienced several freezing rain events that affected many structures including the Veteran's Glass City Skyway (VGCS) Bridge. The VGCS bridge is a large single-pylon cable-stayed bridge that carries a total of six lanes of traffic (three lanes in each direction) with an average of 50,000 vehicles passing daily. Since the opening of the VGCS bridge in 2007, it experienced several icing events that led to the partial or full closure of the bridge due to ice shedding from the cables. One of the major events occurred in 2011 in which nearly 13 mm of ice accumulated on the bridge cables and persisted on the bridge cables for three days leading to a full closure of the bridge [6,7,8,10]. Although bridge closure is not

convenient for travellers, it is required for their safety from falling ice which can lead to vehicle damage, accidents, injuries, and death. Fig. 1 shows the location of Toledo and the VGCS bridge and images of ice accretion on the bridge during the ice event in 2011.

B. ICE THICKNESS MODEL

In this work, the simple model for ice accretion from freezing rain [9] was used to calculate the hourly equivalent radial ice thickness as follows:

$$R_{eq(H)} = \frac{1}{\pi \rho_i} [(P\rho_w)^2 + (3.6VW)^2]^{1/2} \times dt \qquad [1]$$

where:

$R_{eq(H)}$ is the hourly equivalent radial ice thickness (mm),

ρ_i is the ice density (taken to be 0.9 g/cm³),

P is the hourly precipitation rate (mm/hr),

ρ_w is the water density (1 g/cm³),

V is the wind speed (m/s),

W is the liquid water content of the rain-filled air (g/m³) which is calculated using [11]: $W = 0.067P^{0.846}$, and

dt is the time step used to compute the ice thickness from the accretion rate which is 1 hour for this calculation.

The total ice thickness $R_{eq(T)}$ is then calculated by adding the hourly increments for the hours that freezing rain is reported as follows:

$$R_{eq(T)} = \sum_{j=1}^{N} R_{eq(H)_j} \qquad [2]$$

The calculation of the ice accretion starts when freezing rain begins with $T \leq 0°C$ and ends after when freezing rain ends and the temperature exceeds $0°C$.

C. HISTORICAL WEATHER DATA

In order to perform the ice thickness calculations, sub-daily data (preferably hourly data) should be available at or near the locations of interest. The required data needed for the ice thickness algorithm are air temperature, wind speed, precipitation rate, and precipitation type. These measurements are available at the Automated Surface Observing System (ASOS) stations that are located typically at airports. These stations generally had human observers before they were commissioned as ASOS stations [12].

For this work, the Toledo Express Airport station data were used to analyze the weather parameters and calculate the ice thickness. The data are available hourly from 1955, except from 1965 to 1972 when the weather parameters were measured every hour but archived electronically only every third hour. These records are gradually being filled in from the paper records. Although hourly precipitation amount data are available at the station, the values may be affected by the freezing of the precipitation gauges during cold weather. Therefore, the daily precipitation that is available was prorated to each hour based on weighting factors that are set to each precipitation type and intensity as stated in [12]. For the period from 1965 to 1972, the hours with the known values were used to fill in temperature, wind speed, and precipitation type for the missing hours, assuming they did not change. The

precipitation amounts were divided equally between the three hours for the same period.

III. METHODOLOGY

The annual variations of temperature, wind speed, and precipitation, in addition to the variation in these weather parameters and calculated ice thickness during freezing rain events each winter were analyzed. In order to determine the trend of the weather data, the Hodrick and Prescott filter [13] (HP Filter) was used. The HP filter is a well-known filter in economics and was used in some climate studies as well such as [14] [15]. The filter is used to decompose the time series variable data (y_t) into a trend component (g_t) and a cyclical component(c_t) [13a] as follows:

$$y_t = g_t + c_t \qquad [3]$$

The components are determined by obtaining the minimum of the quadratic loss function:

$$min_{\{g_t\}} \left\{ \sum_{t=1}^{T} c_t^2 + \lambda[(g_{t+1} - g_t) - (g_t - g_{t-1})]^2 \right\} \qquad [4]$$

The parameter λ is a positive number that penalizes the variability in the trend components with respect to the cyclical component, namely the smoothing parameter. The resulting trend is smooth for large λ values and wiggly for lower values [14]. Several studies suggested different values for annual data such as 400 [16,17], 100 [18], 10 [19], and 6.25 [20]. In this work, $\lambda = 100$ was used for the HP filter calculations in order to have a smoother trend without losing the details of the data.

In the annual data analysis, the mean annual hourly temperature and wind speed as well as the total annual precipitation were calculated. This was done for the data starting from 1956 since the data archive started in February 1955. For the freezing rain events per winter season calculations, the events for each winter were extracted beginning in September and ending in April, labelling the winter by the start year. A linear regression analysis was performed using the HP-filtered data to determine the trend (positive or negative) and to determine the linear equation. These results were then extended until the end of the century to determine the expected linear changes in these parameters. A Python code was developed to conduct all of these analyses. The results are shown in the next section.

IV. RESULTS AND DISCUSSION

The first part of the analysis focuses on investigating the annual changes in temperature, wind speed, and precipitation, while the second part focuses on the freezing rain data analysis. The HP filter results are only shown for the mean annual temperature, mean annual wind speed, and total precipitation data, but these were applied to all the results shown below.

A. Annual Data Analysis

1) Mean Temperature

The mean annual temperature was obtained by calculating the mean of the hourly temperatures available throughout the year. Then, these data were filtered using the HP filter to

obtain the trend, which was then used in the linear regression. Fig. 2(A) shows the HP filter results for the annual temperature data from 1956 until 2022, and Fig. 2(B) shows the linear regression of the HP filter trend with the confidence interval which is extended to project the mean temperature through 2100.

(A)   (B)

(C)   (D)

(E)   (F)
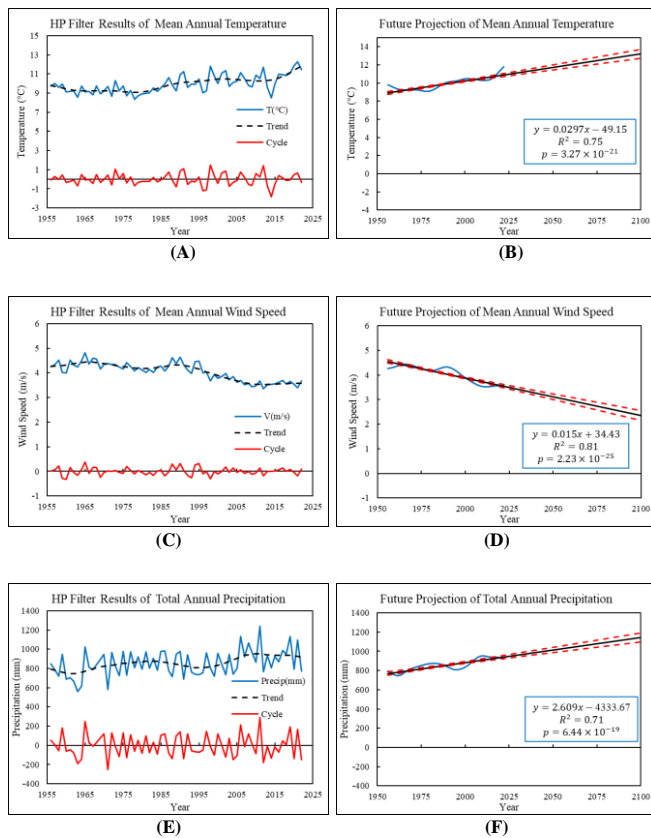
Fig. 2   Images on the left side show the HP filter results of the annual (A) mean temperature, (C) mean wind speed, and (E) total precipitation data, where the blue line is the raw data, the dashed black line is the trend, and the red line is the cyclical component from the HP filter results. Images on the right side show the linear regression results of the trend component (blue line) of the HP-filtered data, where the confidence interval is shown by the dashed red lines for (B) mean temperature, (D) mean wind speed, and (F) total precipitation.

As can be seen in Fig. 2(B), the annual mean temperature trend shows an increase of 2°C from 1956 to 2022. If this rate of increase continues, the annual mean temperature by the end of the century will reach 13°C with an increase of 4°C. This is a significant temperature change and could affect all the weather events that occur in this area. The p-value is a statistical method to validate a hypothesis against observed data in which a probability of 0.05 or lower is generally considered statistically significant. As shown in the figure, the p-value is less than 0.05, confirming the hypothesis that the temperature is correlated with time and rejecting the null hypothesis.

2) Mean Wind Speed

Similarly, the mean annual wind speed was calculated using the hourly wind speed data that were available throughout the year. The raw data was filtered using the HP

filter and linear regression was calculated from the trend of the filtered data. Fig. 2(C) shows the HP filter results for the annual mean wind speed from 1956 to 2022, and Fig. 2(D) shows the linear regression results and future projections to 2100.

As shown in Fig. 2(D), the annual mean wind speed trend is negative, leading to lower wind speeds. The mean wind speed decreased by nearly 1 m/s since 1956 and if the current rate continues, the annual mean wind speed will drop by nearly 2.2 m/s by the end of the century. The p-value for this correlation was much lower than 0.05, rejecting the null hypothesis.

3) Total Precipitation

For the precipitation, the annual total was calculated by summing the daily precipitation for the year (starting January 1st and ending by December 31st). It should be noted that this is for all types of precipitation. Fig. 2(E) shows the HP filter results for the annual precipitation. Fig. 2(F) shows the linear regression of the annual total precipitation with time indicating a significant increase in precipitation from 1956 to 2022. This will lead to an increase of nearly 45% in precipitation by the end of the century if this rate continues.

B. Freezing Rain Events Analysis

In this section, the results of the freezing rain regression analysis for each winter are presented. The analysis includes the mean of the freezing rain (Z) temperature, Z wind speed, hourly ice thickness increment, the total ice thickness, the number of hours with Z precipitation, and the sum of the Z precipitation. Fig. 3 shows the results of the HP filter trend for these parameters and the projection of the values to the end of the century using the linear regression of the HP trend.

1) Mean Z Temperature

The mean Z temperature was calculated using the temperature during the hours when freezing rain was reported. As can be seen in Fig. 3(A), the mean Z temperature trend shows an increase from −1.8 to −1.3°C from 1955 until 2022. This trend indicates that the mean Z temperature will reach −0.8°C by the end of the century.

2) Mean Z Wind Speed

As observed in the annual mean wind speed, the mean Z wind speed has been decreasing with time as shown in Fig. 3(B). The trend of the mean wind speed dropped by nearly 10% which would lead to a 1.1m/s drop in wind speed by the end of the century if the rate persists. The drop in mean Z wind speed is lower than the drop in annual mean wind speed.

3) Total Z Precipitation

The total Z precipitation was obtained by summing the precipitation during the Z hours for each winter. Although the total annual precipitation shows a significant positive trend as shown in Fig. 2(F), the total Z precipitation has shown a negative trend in Fig. 3(C). The trend of the total Z precipitation has decreased by 42% and will reach a total of 1.6 mm by the end of the century if the current trend continues. This could be an indicator that the probability of freezing rain events is lower in the future and a lower number of events is expected.
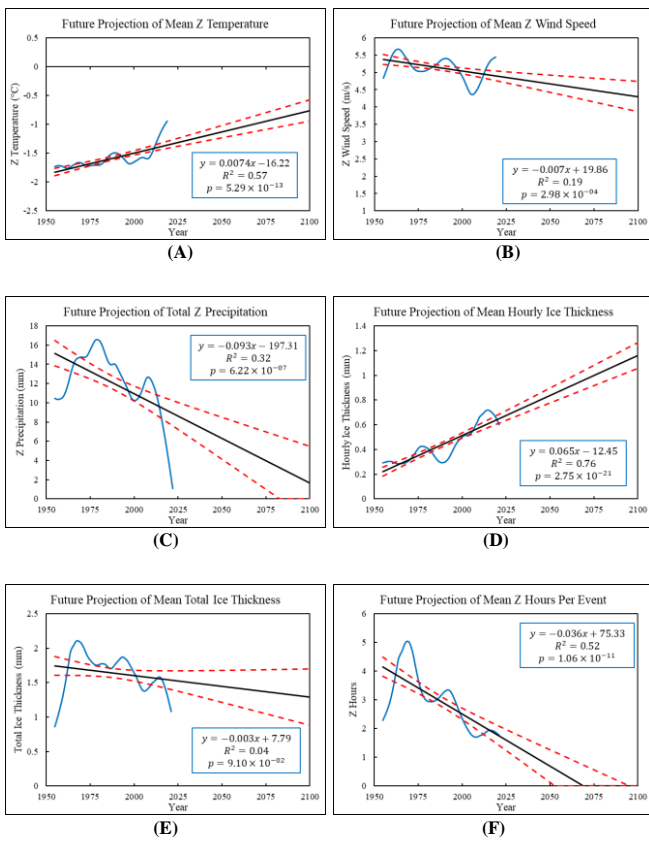
Fig. 3 The linear regression results of the trend component (blue line) of the HP filtered data where the confidence interval is shown by the dashed red lines for (A) mean Z temperature, (B) mean Z wind speed, (C) total Z precipitation, (D) hourly ice thickness increment during Z hours, (E) mean event total ice thickness, and (F) the mean Z hours per event.

4) Mean Hourly Ice Thickness During Z Hours

The annual mean hourly ice thickness increment during Z hours was calculated by averaging all the hourly ice thickness increments during Z hours for all Z events throughout the winter. As can be seen in Fig. 3(D), this trend is positive in the linear regression results. The mean hourly ice thickness would increase by 1 mm from 0.2 mm in 1955 by the end of the century given the current increasing rate.

5) Mean Total Ice Thickness per Event

The mean winter event total ice thickness was obtained by calculating the mean of the event total ice thicknesses of all Z events that winter. As shown in Fig. 3(E), the mean total ice thickness trend is negative. However, it should be noted that the p-value for this hypothesis is greater than 0.05 which means the null hypothesis is not rejected. In this case, the results of other statistically significant parameters will be used for deriving the conclusion.

6) Mean Z Hours per Event

The mean winter Z hours per event was calculated by obtaining the mean of the number of Z hours of all events for that winter. As can be seen in Fig. 3(F), it has a negative trend, reaching 0 by 2070. Given that the total Z precipitation is decreasing, the Z hours would be decreasing at a higher rate to cause an increase in the hourly ice thickness. Although the results of the Z temperature, Z precipitation, and hourly ice

thickness support these results, it is difficult to have a solid conclusion about the elimination of freezing rain events from a location considering the variability in climate conditions. However, these results show that freezing rain events tend to be shorter but more intense over the years.

V. CONCLUSIONS

This study investigates changes that occur to the annual weather parameters (mean temperature, mean wind speed, and total precipitation), in addition to the freezing rain events weather parameters (mean Z temperature, mean Z wind speed, total Z precipitation, mean hourly ice thickness increment, mean total event ice thickness, and mean event Z hours) in Toledo, Ohio in the United States. The data were smoothed using the HP filter and linear regression analyses of the resulting filtered parameters were conducted. From these analyses, it was found that the annual mean temperature and total precipitation showed positive trends which are consistent with typical climate change patterns. The mean wind speed showed a negative trend.

Regarding winter freezing rain, the mean Z temperature showed a positive trend while the mean Z wind speed had a negative trend, which matches the annual changes. However, the total winter Z precipitation showed a negative trend which did not match the annual precipitation positive trend. The results also showed a decreasing trend in the mean event Z hours which led to higher hourly ice thickness increments which would lead to lower total ice thickness per event. Although the mean total ice thickness results were not statistically significant due to a high p-value (>0.05), the previous conclusion matched the observed trend. This is an indication that freezing rain events are expected to be shorter and less frequent, but more intense. Overall, this study shows the possible effects of climate change on freezing rain events in Toledo.

REFERENCES

[1] Intergovernmental Panel on Climate Change (IPCC), *Climate change 2013: The physical science basis. Contribution of Working Group I to the Fifth Assessment Report of the Intergovernmental Panel on Climate Change, Cambridge University Press, Cambridge, UK,2014.*

[2] K. Savadjiev and M. Farzaneh, "Modeling of icing and ice shedding on overhead power lines based on statistical analysis of meteorological data," *IEEE Transactions on Power Delivery*, vol. 19, no. 2, p. 715-721, 2004, doi: https://doi.org/10.1109/TPWRD.2003.822527.

[3] T. Ishihara and S. Oka, "A numerical study of the aerodynamic characteristics of ice-accreted transmission lines," *Journal of Wind Engineering and Industrial Aerodynamics*, vol. 177, p. 60-68, 2018, doi: https://doi.org/10.1016/j.jweia.2018.04.008.

[4] B. Liu, K. Ji, X. Zhan, et al., "Experimental and numerical analysis of overhead transmission lines vibration due to atmospheric icing," in *2017 Prognostics and System Health Management Conference (PHM-Harbin)*, p.1-4, 2017, doi: https://doi.org/10.1109/PHM.2017.8079288.

[5] N. D. Mulherin, "Atmospheric icing and communication tower failure in the United States," *Cold Regions Science and Technology*, vol. 27, no. 2, p. 91-104, 1998, doi: https://doi.org/10.1016/S0165-232X(97)00025-6.

[6] D. K. Nims, V. Hunt, A. Helmicki, and T.-M. Ng, "Ice prevention or removal on the veteran's glass city skyway cables final report," Ohio Department of Transportation Office of Research and Development, State Job Number 134489, 2014.

[7] C. Mirto, A. Abdelaal, D. Nims, et al., "Icing management on the Veterans' Glass City Skyway stay cables," Transportation Research Record: *Journal of the Transportation Research Board*, vol. 2482, no. 1, p. 74-81, 2015, doi: https://doi.org/10.3141/2482-10.

[8] A. Abdelaal, D. Nims, K. Jones, and H. Sojoudi, "Prediction of ice accumulation on bridge cables during freezing rain: A theoretical modeling and experimental study," *Cold Regions Science and Technology*, vol. 164, p. 102782, 2019, doi: https://doi.org/10.1016/j.coldregions.2019.102782.

[9] K. Jones, "A simple model for freezing rain ice loads," *Atmospheric Research*, vol. 46, no. (1-2), p. 87–97, 1998.

[10] A. Abdelaal et al., "Investigation of using icephobic coatings on a cable stayed bridge," in *IWAIS 2015. Proceedings of the 16th International Workshop on Atmospheric Icing of Structures*, 2015.

[11] A. C. Best, "The size distribution of raindrops," *Quarterly Journal of the Royal Meteorological Society*. vol. 75, p. 16–36, 1949.

[12] K. Jones, R. Thorkildson, N. Lott, "The Development of a U.S. climatology of extreme ice loads," National Climatic Data Center technical report, 2002.

[13] R. Hodrick, E. Prescott, "Postwar U.S. Business Cycles: An empirical investigation," *Journal of Money, Credit and Banking*, vol. 29, no. 1, pp. 1-16, 1997, doi: https://doi.org/10.2307/2953682.

[14] A. Blöchl, G. Flaig, "The Hodrick-Prescott filter with a time-varying penalization parameter. an application for the trend estimation of global temperature," *Center for Economic Studies and Ifo Institute (CESifo) Working Paper*, no. 4577, *Munich,* 2014.

[15] F. Giancaterini, A. Hecq, C. Morana, "Climate Change Time-Reversible?", *Econometrics,* vol. 36, no.10, 2022, doi: https://doi.org/10.3390/econometrics10040036.

[16] I. Correia, J. Neves, and S. Rebelo, "Business cycles from 1850–1950: New facts about old data," *European Economic Review*, vol. 36, no. 2-3, p. 459–467, 1992, doi: https://doi.org/10.1016/0014-2921(92)90103-4.

[17] T. Cooley, L. Ohanian, "The cyclical behavior of prices," *Journal of Monetary Economics*, vol. 28, no. 1, p. 25–60, 1991, doi: https://doi.org/10.1016/0304-3932(91)90024-I.

[18] D. Backus and K. Patrick, "International evidence on the historical properties of business cycles," *The American Economic Review* vol. 82, no. 4, pp. 864–888, 1992.

[19] M. Baxter, R. King, "Measuring business cycles: Approximate band-pass filters for economic time series," *The Review of Economics and Statistics* vol. 81, no. 4, p.573–593, 1999.

[20] M. Ravn and H. Uhlig, "On adjusting the Hodrick-Prescott Filter for the frequency of observations," *The Review of Economics and Statistics*, vol. 84, no. 2, p.371-80, 2002.

An Experimental Study of Dynamic Ice Accretion Process on Wind Turbine Blades

Harsha Sista[1], Haiyang Hu[1], Linyue Gao[1], Hui Hu[1]

[1] Dept. of Aerospace Engineering, Iowa State University, Ames, Iowa, USA. Email: huhui@iastate.edu

Abstract—**The accretion of ice on the surface of a wind turbine blade causes a drastic reduction in the aerodynamic performance and as a result, the power output, in addition to posing a safety hazard. To quantify this phenomenon, an experimental study was conducted in the Iowa State University Icing Research Tunnel (ISU-IRT) to understand the dynamic ice accretion process and resultant aerodynamic performance degradation specifically experienced by offshore wind turbines at higher Liquid Water Content (LWC) levels. Four different LWC values were tested for both glaze and rime ice conditions each, to cover the possible spectrum of typical icing conditions. A high-speed imaging camera was used to capture the dynamic ice accretion process, while a Digital Image Projection (DIP) technique was used to perform the 3D qualification of the ice accretion characteristics. Two highly sensitive multi-axis force and moment transducers were used to measure the lift and drag forces acting upon the airfoil. A high-resolution Particle Image Velocimetry (PIV) system was also synchronized with the aerodynamic force measurements to characterize the behaviors of the turbulent airflows over the ice accreting airfoil model.**

Keywords— **Anti/De-icing, Wind Turbines, High-speed imaging, Digital Image Projection, Particle Imaging Velocimetry**

I. INTRODUCTION

While winters are supposed to be the best season for wind energy harvesting due to the generally higher wind speeds and increased air density with the decreasing temperature, icing represents the most significant threat to the integrity and efficiency of wind turbines in cold climates. It has been found that even a light icing event, such as frost, could produce enough surface roughness on turbine blades to reduce their aerodynamic efficiency considerably, resulting in substantial power reduction of the wind turbines. For wind farm sites with significant ice, icing-induced power output losses are found to reach over 20% of annual energy production [1,2]. In the case of extreme icing, it may not be possible to start wind turbines, with subsequent loss of all the possible power production for long periods. One notable example is the massive turbine shutdown after a severe storm blasted Texas in February 2021. Frozen turbines were blamed as being partially responsible for the weeks-long blackout that affected millions of Texans.

Recently, offshore wind turbine installation has become the target of a higher volume of research because of its distinct advantages over its onshore counterpart: stronger offshore winds can result in greater productivity, the turbine size can be significantly larger, and offshore wind parks can be installed closer to major cities, reducing the transmission line length to deliver the power [3]. Therefore, the challenges of increased installation cost, higher repair charges, and the difficulty of year-round access to the site due to changing weather conditions can be balanced by conducting research into decreasing the downtime of these turbines [4].

Ice accretion follows either glaze ice or rime ice formation, influenced by the geometry of the body, surface type, airspeed, temperature, liquid water content (LWC) and droplet size [5]. For glaze ice formation, impinging droplets do not freeze immediately, some of the water is able to run back and eventually freezes. In the rime ice process, impinging supercooled droplets are at a much colder temperature (usually below -10°C), and the size of droplets are smaller. Freezing of droplets happens immediately after impingement. Therefore, during glaze ice formation, formed ice have complicated shapes, while rime ice formation follows the shape of the blade airfoil.

Ice mitigation techniques such as hot air injection, resistive heating, pneumatic boots, hydrophobic coatings are used in wind turbine industry. Among all techniques, heating is the most efficient method for wind turbine which faces harsh icing conditions [6,7]. These anti-icing systems for wind turbines are mostly adopted from aircraft applications because basic concept and purpose are the same. However, icing conditions that wind turbine encounter are not exactly the same with aircraft icing conditions [8]. The electro-thermal strategy proposed by Gao et al. [9] is based on resistive heating and specifically designed for wind turbine blades.

In the present study, a comprehensive experimental investigation was conducted to investigate the dynamic ice accreting process over the surfaces of typical wind turbine blades and quantify the resultant aerodynamic performance degradation of the turbine blades during the dynamic ice accreting process. This was done using high-speed imaging, digital image projection, load cells, and particle image velocimetry.

II. EXPERIMENTAL SETUP

The experimental study was performed in the unique Icing Research Tunnel available at Iowa State University (i.e., ISU-IRT in short), which is a newly refurbished, multifunctional icing research tunnel. As shown schematically in Figure 1, ISU-IRT has a test section with four optically transparent side walls and dimensions of 2.0m in length x 0.4m in width x 0.4m in height. It has a capacity of generating a maximum wind speed of 60 m/s and airflow temperature down to - 25ºC. An array of pneumatic atomizers/spray nozzles (H. Ikeuchi and Co., Flat Spray BIMV Series Nozzles) were installed at the entrance of the contraction section of ISU-IRT to generate the droplets. The ISU-IRT is currently capable of generating LWC up to 5.0 g/m3. The LWC can be adjusted by changing the air and water pressure and the supplied flow rate. By using ISU-IRT, extensive icing and anti-/de-icing studies have been carried out in recent years for various engineering applications. Further information about the ISU-IRT can be found in Gao et al. [8].
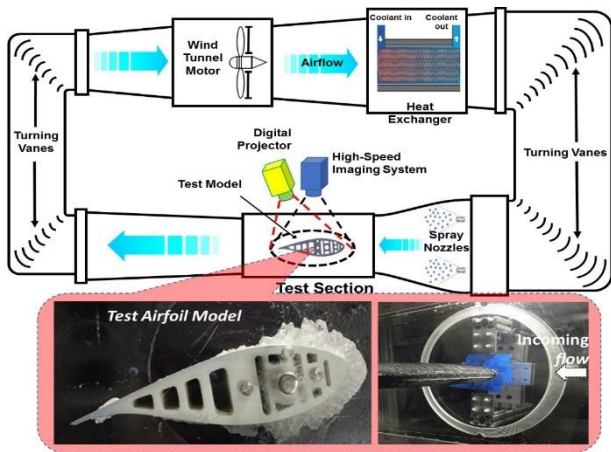
Fig. 1 Schematic of the ISU-IRT.

The airfoil model used in the experimental study is the DU91-W2-250 airfoil profile, which is widely used for wind turbine blade design due to its favourable aerodynamic performance and structural properties [9], [10]. The turbine blade model is 0.15m in airfoil chord length (i.e., C ¼ 0.15 m) and 0.40m in spanwise length. It was manufactured using a 3D printing rapid-prototyping machine. The surface of the model was sanded by using a series of progressively finer sandpapers, from 220 grit to 2000 grit, to achieve a smooth finish with a characteristic roughness of about 20-25µm [7]. Following that, several coatings of a primer were applied to prepare the surface for an all-weather spray-on enamel coating that is widely used to protect the surface of wind turbine blades (RustoleumTM, Flat Protective Enamel, white in color). The blade was mounted using three stainless-steel rods and set at an Angle of Attack of 5.0 degrees (i.e., AOA=5.0), which coincides with the angle at which the airfoil model has its maximum lift-to-drag ratio. To simulate typical Glaze icing conditions experienced by offshore wind turbines, the initial testing parameters were set to V = 40 m/s, T = -5 $^{\circ}$C. Two high-sensitivity multi-axis force-moment transducers (ATI-IA Mini 45) were mounted at either end of the blade model to capture the aerodynamic degradation by measuring the lift and the drag forces.

In addition, a high-resolution PIV system was also used to achieve flow field measurements to quantify the turbulence airflow over the airfoil surface of the turbine blade model during the dynamic ice accreting process. Fig. 2 shows the schematic of the experimental setup used for PIV measurements. For the PIV measurements before and after the ice accretion process, the incoming airflow was seeded with ~ 1 mm oil droplets by using a smoke generator, while the airborne supercooled water droplets were used as the tracer particles for the PIV measurements during the ice accretion process. It should be noted that, since the supercooled water droplets suspended in the incoming airflow have a mean volume diameter (MVD) of ~20 mm, the corresponding Stokes number of the water droplets was estimated to be about 1.0 (i.e., St z 1.0), indicating a reasonable dynamic response of the droplets to follow the incoming airflow. The illumination of for the PIV measurements was provided by a double-pulsed Nd: YAG laser (i.e., New Wave, Gemini PIV 200) adjusted on the second harmonic and emitting two pulses

of 200 mJ at the wavelength of 532 nm. A set of convex and concave cylindrical lenses along with optical mirrors were used to generate a laser sheet to illuminate the PIV tracers in the vertical plane passing through the middle span of the test model. The thickness of the laser sheet in the measurement region was set to be about 1.0 mm. A high-resolution 16-bit digital camera (2 K pixels x 2 K pixels, PCO2000, CookeCorp) was used for PIV image acquisition with the axis of the cameras perpendicular to the laser sheet. The digital camera and the double-pulsed Nd: YAG laser were connected to a workstation (host computer) via a digital delay generator (Berkeley Nucleonics, Model 565), which controlled the timing of the laser illumination and the image acquisition. Figure 2 shows the schematic of the PIV setup in the Icing Research Tunnel:
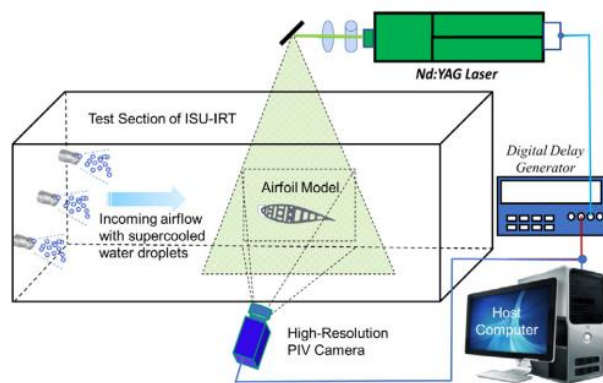
Fig. 2 Schematic of the PIV Setup in the ISU-IRT.

III. RESULTS AND DISCUSSION

The high-speed imaging system captures the dynamic ice accretion process over the airfoil, out of which a slice is extracted and studied at various time instants to demonstrate the time evolution. Figure 3 shows the dynamic ice accretion process for the Glaze icing condition at V = 40 m/s and T = -5°C at four different Liquid Water Contents: (a) LWC = 0.5 g/m3, (b) LWC = 1.0 g/m3, (c) LWC = 2.0 g/m3 and (d) LWC = 4.0 g/m3, with a runtime of 600s, 300s, 150s and 75s respectively:

From Figure 2(a), we can observe that for LWC = 0.5 g/m3 and a runtime of 600 seconds, the glaze ice structure accretes rapidly on the leading edge, but there is not much runback. There is an initial stage of runback, where the impinged water does not instantly freeze. However, this process does not last long because the LWC is low, meaning that the latent heat of fusion is removed quickly by heat transfer, although still not instantaneously. Following this, the ice directly begins accumulating on the leading edge, increasing the leading-edge ice thickness. The accreted ice has a clear and glassy structure, indicating that the ice formed is Glaze ice. From Figure 2(b), we can observe that for LWC = 1.0 g/m3 and a runtime of 300 seconds, the glaze ice structure again forms majorly over the leading edge, with not much runback. The initial stage of runback is slightly greater, which decreases the ice thickness on the surface of the airfoil. In addition, the leading-edge ice thickness at the end of the process is lesser than case (a), showing that the ice is spread over more of the airfoil surface.

However, a higher LWC value is needed to observe consistent runback spread across the airfoil. From Figure 2(c), we can observe that for LWC = 2.0 g/m3 and a runtime of 150 seconds, the runback process is much more clearly visible, indicating that the latent heat of fusion is insufficiently dissipated by heat transfer, causing the droplets to remain in the liquid state for longer periods of time. This causes the liquid droplets to runback in the direction of the air stream and combine with other droplets to form rivulet structures that are roughly evenly spaced along the spanwise direction. Once the runback freezes into clear, glassy structures, the leading-edge ice thickness starts increasing but is much lesser than in the previous cases.
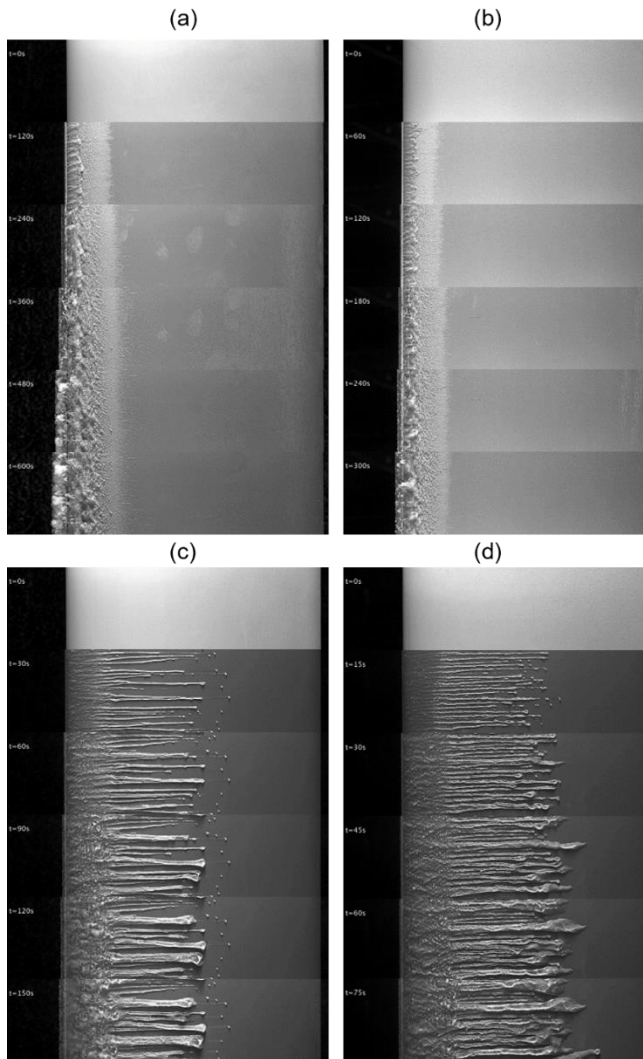
Fig. 3. Dynamic Ice Accretion Process on the wind turbine blade model for Glaze Ice at V = 40 m/s, T = -5 ° C at (a) LWC = 0.5 g/m3 (b) LWC = 1.0 g/m3 (c) LWC = 2.0 g/m3 (d) LWC = 4.0 g/m3.

From the image given in Fig. 2(d), we can observe that for LWC = 4.0 g/m3 and a runtime of 75 seconds, the glaze ice structure is almost completely in the form of runback, indicating that the latent heat of fusion for this case is much higher than the heat transfer is capable of dissipating. Therefore, the runback reaches more than 50% of the chord length, and the small rivulets merge into larger, thicker structures closer to the trailing edge. Since most of the ice distribution is in the form of runback, the leading-edge ice thickness does not grow much throughout the process. In

addition, since the time period for this case is only 75s, not all the ice that is pooled near the end of the runback structures changes into ice. Therefore, we can see that as the LWC increases, the latent heat of fusion generated by the icing process also increases, resulting in a greater region of runback and a lesser leading-edge ice thickness.

The iced model was then transported to a cooling chamber where the Digital Image Projection (DIP) technique was used to obtain a 3D scan of the resultant ice shape, which gives a qualitative representation of what the ice accretion looks like in different cases. Figure 4 compares the four Glaze ice cases:
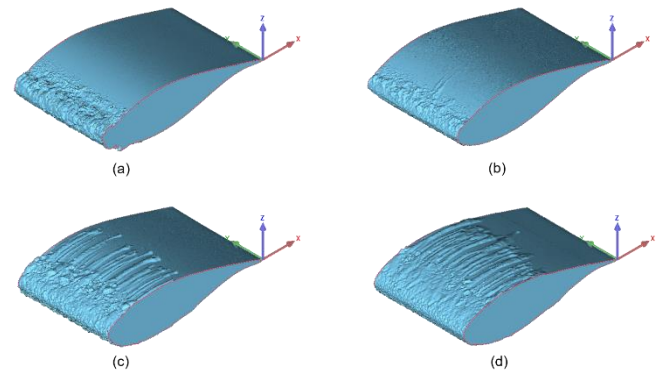
Fig. 4 3D Shape of the accreted ice on the wind turbine blade model for Glaze Ice at V = 40 m/s, T = -5 °C at (a) LWC = 0.5 g/m3 (b) LWC = 1.0 g/m3 (c) LWC = 2.0 g/m3 (d) LWC = 4.0 g/m^3.

Figure 4 shows us how the runback increases with an increase in the LWC for glaze ice. There are no rivulets for case (a), and only two small rivulets in an otherwise uniform structure are observed for case (b), indicating that LWC = 1.0 g/m3 is a transition case. For case (c) and case (d), we can see runback rivulet formation, and it is interesting to note that the rivulet structures are spread fairly evenly in the spanwise direction, indicating a uniform ice accretion process. In addition, the change in the leading-edge ice thickness for the four different cases can also be clearly observed from the 3D scan results.

Lift and drag are the two most important forces to consider when it comes to the aerodynamic performance of airfoils. To quantify the manner in which these forces are affected by icing events, the lift and drag forces were measured on the mounted turbine blade using two force-moment transducers as described in section 2. The coefficients of lift and drag, which are calculated from the measured lift and drag forces, are normalized by the respective values measured when the airfoil was ice free on the y-axis. Once the spray system is engaged, there is a rapid decrease in the lift force and a rapid increase in the drag force in the initial stages of the experiment. The rate of decrease of lift tapers off towards moderation as time goes on while and rate of increase of drag is more volatile. This initial effect, which can be observed for all cases, is explained by the formation of an initial rough ice structure which changes the geometry of the airfoil and disturbs the attached flow, possibly causing it to separate. The graphs diverge in terms of the magnitude of this decrease, and the rate at which the decrease happens, which can be explained by the icing structure characteristics corresponding to each case.

356
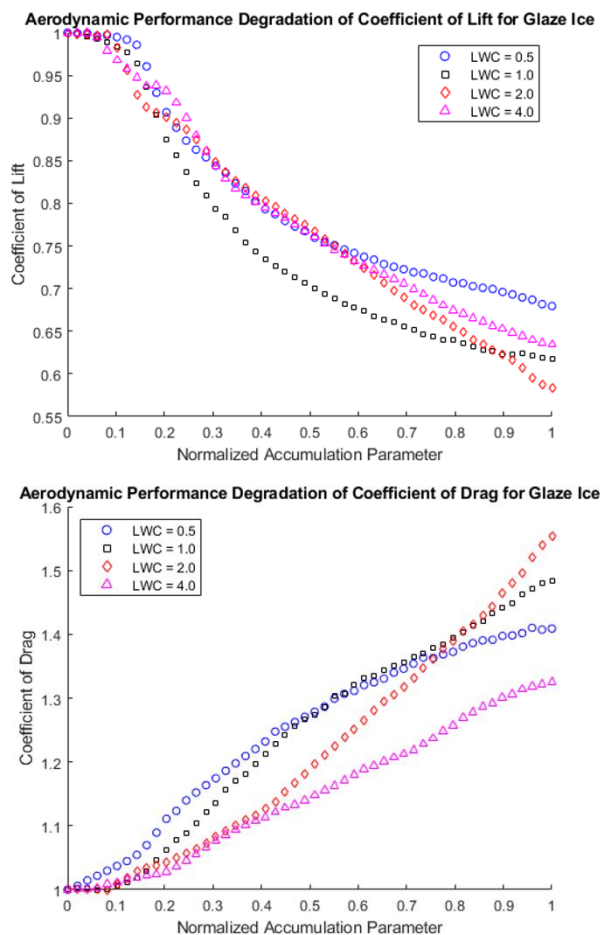
Fig. 5 Aerodynamic Performance Degradation of the airfoil due to the dynamic glaze ice accretion process in terms of (a) Coefficient of Lift and (b) Coefficient of Drag

In Figure 9(a), the coefficient of lift follows the trend: LWC 0.5>LWC 4.0>LWC 1.0> LWC 2.0 while in Figure 9(b), the coefficient of drag follows the trend: LWC 2.0>LWC 1.0> LWC 0.5> LWC 4.0. The degradation of lift and increase in drag depends on multiple factors: the change in shape at the leading edge of the airfoil and the change in surface roughness of the accreted ice structure. From Figure 4, we can see that case (c) has both ice formation on the leading edge, and significant rivulet formation. Therefore, the degradation in terms of lift and drag is the worst for this case (~40% and ~55% respectively). This case is followed by LWC = 1.0 g/m3, which has no rivulet formation, but the change in leading edge geometry due to the accreted ice is significant. It is interesting to note that for LWC = 0.5 g/m3, the leading-edge ice thickness is greater, but the aerodynamic performance degradation is lesser. This can be explained by the greater increase in the effective chord length of the iced airfoil, not considering which would increase the value of the coefficients of lift and drag. When it comes to LWC = 4.0 g/m3, leading-edge ice thickness is much smaller, and most of the degradation in the latter part of the graph is caused by the rivulets, leading to the amount of drag being much lesser than the other three (~30% degradation), even though the lift is comparable (~35% degradation).

To characterize the instantaneous flow field around the airfoil during the ice accretion process, the high-resolution PIV system described in section 2 was used. LWC = 1.0 g/m³ was selected, and the experimental runtime was set to 200s.
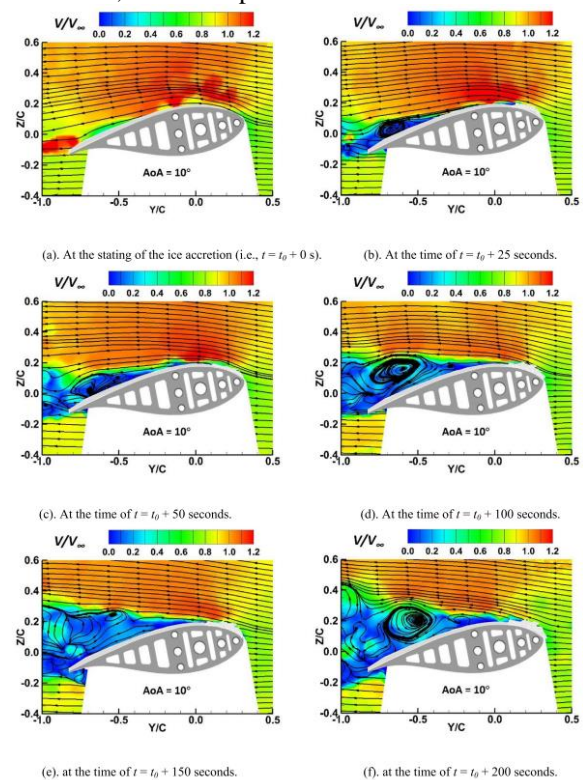
Fig. 5 Instantaneous PIV measurement results to reveal the dynamic changes of the airflow over the ice accreting surface of the turbine blade model as a function of the ice accretion time.

The incoming velocity contours in the no ice condition in Figure 5(a) follow the profile of the airfoil as it is before the stall angle. Shortly after the ice accretion process starts, e.g., at the time of t = 25 s, while evident ice structures were found to accrete over both upper and lower surfaces of the test model, the irregular-shaped ice structures accreted over the suction-side airfoil surface would affect the development of the boundary layer flow over the test surface significantly, resulting in the flow separation over the airfoil surface near the airfoil trailing edge, as revealed clearly in Fig. 5(b). As the time goes by, with more super-cooled water droplets impinging onto the airfoil surface, the irregular-shaped ice structures accreted over the test model were found to grow up rapidly, extruding further into the incoming airflow. As a result, the flow separation zone formed over the airfoil surface was found to expand further upstream and become bigger and bigger, as shown clearly from the PIV measurement results in Fig. 5(c) and (d). In addition to the formation of the large-scale flow separation, unsteady vortex structures were also found to be generated and shedding periodically from the ice accreting airfoil surface. With a continuous growth of the ice structures over the test model at later time of the ice accretion process, e.g., after the time of t = 150 s, while generation and shedding of unsteady vortex structures from the ice accreting airfoil surface became much more obvious, the large-scale flow separation zone over the airfoil surface was found to become so big that almost cover the entire upper surface of the test model, as shown clearly in Fig. 5(e)&(f). It indicates that, the airflow over the test model, which was originally in an attached flow regime, as shown clearly in Fig. 5(a), would

become in airfoil stall state, due to the significant ice accretion over the airfoil surface. The formation and expansion of the large-scale flow separation zone over the airfoil surface as induced by the ice Fig. 5. Acquired snapshot images to reveal the dynamic ice accreting process over the pressure-side surface (i.e., lower surface) of the turbine blade model. accretion would cause a dramatic degradation on aerodynamic performance of the turbine blade model (i.e., significant lift decreasing and rapid drag increasing), which was confirmed quantitatively from the aerodynamic force measurement results to be presented in next section.

IV. Conclusions

In this study, a comprehensive experimental investigation was conducted to understand the glaze ice accretion process over wind turbines, in both onshore and offshore conditions. The dynamic ice accretion process for each case was captured using a high-speed imaging camera, and a Digital Image Projection (DIP) based 3D scanning system was used to qualitatively visualize the ice structure formed for each case. The leading-edge ice thickness was found to be an important parameter through this part of the study, with a decreasing trend emerging with an increase in the LWC.

To quantify the effect such ice accretion had on the aerodynamic performance of the wind turbine airfoil, force-moment transducers were used to measure the lift and drag as the experiment was performed. This time series of data was converted to the coefficients of lift and drag and normalized and plotted in terms of the normalized accumulation parameter. This ensured that we could perform a comparison of the degradation of lift and increase of drag as the ice accretion process took place. For glaze ice, the leading-edge ice thickness and the effect of rivulet formation combined to influence the aerodynamic performance of the wind turbine airfoil.

The PIV measurements revealed clearly that the streamlines of the incoming airflow would conform well to the smooth, streamlined airfoil profile of the turbine blade model before starting the ice accretion process. After starting the ice accretion process, due to the rapid ice accretion to form irregular-shaped ice roughness structures over the airfoil surface, especially for those accreted near the airfoil leading edge, the streamlined profile shape of the test model was found to be deformed substantially. The development of the boundary layer airflow over the airfoil surface was found to be affected significantly. Induced by the ice accretion, the incoming airflow was found to separate from the ice accreting airfoil surface, causing the formation of a large-scale flow separation zone sitting over the upper surface of the test model. As the ice accretion time goes by, with the continuous growth of the complicated ice structures accreted over the test model, the separation point of the incoming airfoil was found to move further upstream, resulting in the continuous expansion of the large-scale flow separation zone over the airfoil surface during the dynamic ice accretion process. Meanwhile, more and more unsteady vortex structures were also found to be generated and shed from the ice accreting airfoil surface. The rapid expansion of the large-scale flow separation zone formed over the airfoil surface induced by the dynamic ice accretion was found to cause a dramatic degradation for the aerodynamic performance of the turbine blade model.

Therefore, this study sheds light on the dynamic ice accretion process on a wind turbine blade, and qualitatively and quantitatively characterizes the effect of such ice accretion on the aerodynamic performance.

References

1. F. Lamraoui, G. Fortin, R. Benoit, J. Perron, and C. Masson, "Atmospheric icing impact on wind turbine production," Cold Reg Sci Technol, vol. 100, pp. 36–49, Apr. 2014, doi: 10.1016/J.COLDREGIONS.2013.12.008.

2. F. Feng, S. Li, Y. Li, and W. Tian, "Numerical simulation on the aerodynamic effects of blade icing on small scale Straight-bladed VAWT," Phys Procedia, vol. 24, pp. 774–780, Jan. 2012, doi: 10.1016/J.PHPRO.2012.02.115.

3. S. P. Breton and G. Moe, "Status, plans and technologies for offshore wind turbines in Europe and North America," Renewable Energy, vol. 34, no. 3, pp. 646–654, Mar. 2009, doi: 10.1016/J.RENENE.2008.05.040.

4. G. van Bussel, G. van Bussel, M. Zaaijer, and M. Sc, "Reliability, Availability and Maintenance aspects of large-scale offshore wind farms, a concepts study Characterisation and modeling of active and passive airfoil add-on's View project Reliability, Availability and Maintenance aspects of large-scale offshore wind farms, a concepts study," 2001, Accessed: May 01, 2022. [Online]. Available: https://www.researchgate.net/publication/239589238

5. Parent, O. and Ilinca, A., "Anti-icing and de-icing techniques for wind turbines: Critical review," Cold Reg. Sci. Technol. 65(1):88–96, 2011, doi:10.1016/j.coldregions.2010.01.005.

6. Gent, R.W., Dart, N.P., and Cansdale, J.T., "Aircraft icing," Philos. Trans. R. Soc. London A Math. Phys. Eng. Sci. 358(1776), 2000.

7. Lehtomäki, V., "Wind Energy in Cold Climates Available Technologies - report," 2016.

8. Fakorede, O., Ibrahim, H., Ilinca, A., and Perron, J., "Experimental Investigation of Power Requirements for Wind Turbines Electrothermal Anti-icing Systems," Wind Turbines - Design, Control and Applications, InTech, ISBN 978-953-51-2496-2, 2016, doi:10.5772/63449.

9. Gao, L., Liu, Y., Zhou, W., and Hu, H., "An experimental study on the aerodynamic performance degradation of a wind turbine blade model induced by ice accretion process," 2019, doi:10.1016/j.renene.2018.10.032.

10. L. Gao, Y. Liu, L. Ma, and H. Hu, "A hybrid strategy combining minimized leading-edge electric-heating and superhydro-/ice-phobic surface coating for wind turbine icing mitigation," Renewable Energy, vol. 140, pp. 943–956, Sep. 2019, doi: 10.1016/J.RENENE.2019.03.112.

11. W. A. Timmer and R. P. J. O. M. van Rooij, "Summary of the Delft University Wind Turbine Dedicated Airfoils," Journal of Solar Energy Engineering, vol. 125, no. 4, pp. 488–496, Nov. 2003, doi: 10.1115/1.1626129.

12. R. P. J. O. M. van Rooij and W. A. Timmer, "Roughness Sensitivity Considerations for Thick Rotor Blade Airfoils," Journal of Solar Energy Engineering, vol. 125, no. 4, pp. 468–478, Nov. 2003, doi: 10.1115/1.1624614.

A Novel, Plasma-Based Anti-/De-icing System for Wind Turbine Icing Protection

Harsha Sista[1], Cem Kolbakir[1], Haiyang Hu[1], Xianglan Bai[1], Hui Hu[1]

[1] *Dept. of Aerospace Engineering, Iowa State University, Ames, Iowa, USA. Email:* huhui@iastate.edu

Abstract—**Wind turbine icing is a significant threat to the development, expansion, and integrity of wind turbines in cold weather. Ice accretion on wind turbines is found to cause a significant detrimental effect in terms of aerodynamic performance and energy production. To combat this, a novel, plasma-based anti-/de-icing System for Wind Turbine Icing Protection is developed. A Dielectric barrier discharge (DBD) based plasma system is used since it has been shown to effectively combat wind turbine icing. A comprehensive parametric testing campaign is conducted to investigate the effects of various DBD plasma actuation parameters on its thermodynamic characteristic. An infrared (IR) thermal imaging system is used to quantitatively measure the temperature distributions over the test plate under various test conditions. DBD plasma actuators are embedded over the surface of a DU91-W2-250 wind turbine blade model, and a series of experiments were conducted by using the Icing Research Tunnel available at Iowa State University (i.e., ISU-IRT) to evaluate the anti-/de-icing performance of the system for wind turbine icing mitigation. Dynamic anti-icing process was recorded by a high-speed imaging system, and an IR thermal camera was used to map the temperature distributions over the surface of the wind turbine blade model during the anti-/de-icing processes.**

Keywords— *Plasma, Anti/De-icing, Wind Turbines, Parametric Study, Dielectric Barrier Discharge*

I. INTRODUCTION

The number of wind farms in cold climate regions is increasing rapidly due to high wind sources. However, in these cold climate regions, ice formation is a concern. Ice forms on wind turbine blades, which affects its aerodynamic performance. Dangerous changes on aerodynamic loads may cause increased stress and vibrations [1], which may result in structural failures. As aerodynamic performance worsens, energy output from wind turbine degrades. Harvested energy may decrease up to 50% [2]. Furthermore, wind turbine icing is a serious hazard to wind farm employees and people passing by. During severe icing conditions, the operation must be stopped for long periods in order to assure safety [3].

Ice accretion follows either glaze ice or rime ice formation, influenced by the geometry of the body, surface type, airspeed, temperature, liquid water content (LWC) and droplet size [4]. For glaze ice formation, impinging droplets do not freeze immediately, some of the water is able to run back and eventually freezes. In the rime ice process, impinging supercooled droplets are at a much colder temperature (usually below -10°C), and the size of droplets are smaller. Freezing of droplets happens immediately after impingement. Therefore, during glaze ice formation, formed ice have complicated shapes, while rime ice formation follows the shape of the blade airfoil.

Ice mitigation techniques such as hot air injection, resistive heating, pneumatic boots, hydrophobic coatings are used in wind turbine industry. Among all techniques, heating is the most efficient method for wind turbine which faces harsh icing conditions [5,6]. These anti-icing systems for wind turbines are mostly adopted from aircraft applications because basic concept and purpose are the same. However, icing conditions that wind turbine encounter are not exactly the same with aircraft icing conditions [7]. The electro-thermal strategy proposed by Gao et al. [8] is based on resistive heating and specifically designed for wind turbine blades.

In recent years, plasma actuators, invented for the use of flow control, have shown capability for anti-icing applications. Dielectric barrier discharge (DBD) plasma actuators generally consist of two electrodes asymmetrically separated by a dielectric layer. A schematic of a plasma actuator can be seen in figure 1. Reviews of DBD plasma actuators as active flow control devices can be found at [9,10]. Two common types of DBD plasma actuators are studied for flow control and anti-icing application, alternating current driven AC-DBD and nanosecond pulse driven NS-DBD. Both have the same arrangement, but working mechanisms are different. AC variant induces near wall jet, whereas NS variant induces local compression wave [11–13]. Both types of plasma actuators induce thermal effect, which favors anti-icing purpose. It was shown that plasma actuators can be used on aircraft surfaces as anti-icing device [14,15] and would be as effective as electro-thermal heating films [16].
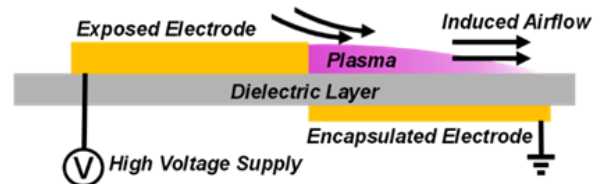
Fig. 1   Schematic of a DBD Plasma Actuator.

This study focuses on plasma based anti-icing for wind turbine blades. First, a parametric study is carried out on a flat plate to reveal the thermodynamic characteristics of DBD plasma actuators. DBD Plasma actuators will be examined under different operation (applied voltage, frequency, and power input). Later plasma actuators were employed on wind turbine blades, and its performance was tested under icing conditions pertinent to wind turbine icing.

II. EXPERIMENTAL SETUP

The experiments on NACA 0012 airfoil model were performed in the unique Icing Research Tunnel available at Aerospace Engineering Department of Iowa State University (i.e., ISU-IRT). A Schematic of the ISU-IRT is shown in Figure 2. The ISU-IRT is a multifunctional icing research

tunnel with a test section of 2.0 m in length × 0.4 m in width × 0.4 m in height with four side walls being optically transparent. FLIR IRW-4C infrared inspection window placed in the top panel of the test section. Above the window, FLIR A615 infrared (IR) camera was mounted. ISU-IRT has the capacity of generating a maximum wind speed of 100m/s and an airflow temperature down to −25 °C. An array of 9 pneumatic atomizer/spray nozzles are installed at the entrance of the contraction section of the icing tunnel to inject micro-sized water droplets (10 ~ 100μm in size) into the airflow. By manipulating the water flow rate through the spray nozzles, the liquid water content (*LWC*) in ISU-IRT could be adjusted (i.e., *LWC* ranging from 0.1 g/m^3 to 5.0 g/m^3). In summary, ISU-IRT can be used to simulate atmospheric icing phenomena over a range of icing conditions (i.e., from dry *rime* to extremely wet *glaze* ice conditions). Further information about ISU-IRT is available in Waldman et al. [17].
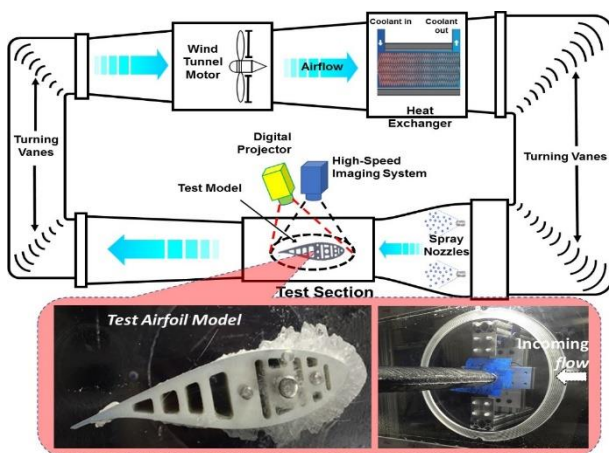
Fig. 2   Schematic of the ISU-IRT.

Schematics of the flat plate model is shown in Figure 3. A plasma actuator was employed on an acrylic glass plate. The surface of the plate was covered ~70 µm thick adhesive copper tape as the ground electrode, and 0.4 mm thick PVC film was attached on the whole surface as a dielectric layer. An exposed ~70 µm thick copper electrode was placed at the edge of the ground electrode. Length of the exposed electrode is ~95 mm. In this symmetric planar [18] configuration, the active electrode is on one side of the dielectric layer (exposed to the air) with a sheet electrode on the other side. The exposed electrode was subjected to high voltage. The encapsulated sheet electrode was connected to the ground.
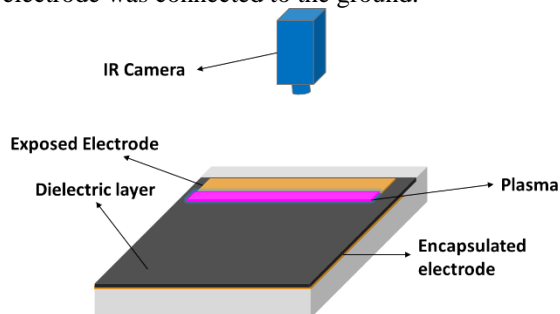
Fig. 3   Plasma actuator on a flat plate.

A DU91-W2-250 airfoil model was used in this study, which was made of a hard plastic material and manufactured by using a rapid prototyping machine (i.e., 3-D printing) that builds 3-D models layer-by-layer with a resolution of about 25 microns. The blade model has a chord length of c = 150 mm, which spanned the width of the test section. Supported by a stainless-steel rod, the blade was mounted at its quarter-chord and oriented horizontally across the middle of the test section. Schematic of the experimental model is shown in Figure 4. 15% of the blade surface of the model from the leading edge was covered with ~70 µm thick copper tape as the ground electrode and the whole surface of the blade model is covered with five layers of PCV dielectric layer. The thickness of the dielectric layer was ~ 0.4 mm. Lastly, 3 mm wide active electrodes were positioned at the leading edge of the airfoil. Exposed electrodes cover 5% of the chord on the suction side of the airfoil, while 10% is covered on the pressure side. The angle of attack is manually adjustable from the side wall of the test section using a digital inclinometer and was set to 5º.
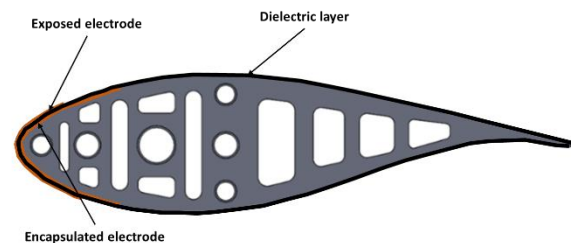
Fig. 4   Cross section of the DU 91-W2-25- airfoil model.

Schematics High voltage has been supplied to the plasma actuators by Nanjing Suman Co. CTP-200K high voltage AC generator. A variable autotransformer has been used to regulate the input power. Current measurements were obtained from a Pearson Current Monitor model 2877, and The voltage and current across the actuator were monitored by Tektronix MDO3104 mixed domain oscilloscope.

The power consumption of plasma actuators was calculated using:

$$P = \frac{1}{T}\int_0^T V(t) \times I(t)dt$$

Where *V(t)* and *I(t)* are the instantaneous voltage and current applied on the plasma actuators, and T is the total measurement time which contains about eight AC periods. Power consumption during the wind tunnel experiment was adjusted to *30W* with an autotransformer. The corresponding power density is *P$_d$=5.0 kW/m^2*.

III. RESULTS AND DISCUSSION

In the first part of the study, heating of dielectric layer surface by a DBD plasma actuator was investigated on a flat plate in quiescent air under different operating parameters (i.e. voltage and frequency). The surface temperature was measured with an IR imaging system. Figure 5 shows the typical surface temperature map during the plasma actuation. It can be seen from the figure that the highest temperature region was observed at the edge of the exposed electrode and the temperature can increase up to 50 °C for V=5kV f=7kHz. As we move further away from the exposed electrode, the temperature gradually decreases.
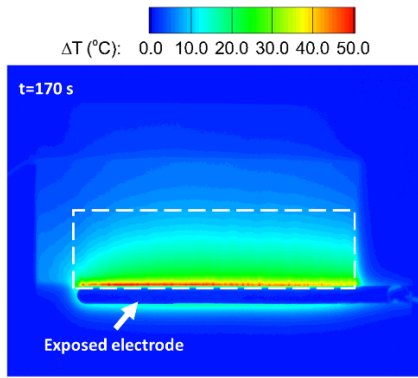
Fig. 5 Thermal image of the flat plate during AC-DBD plasma actuation at V = 5kV, f -= 7 KHz.

Surface temperature of the flat plate was measured for several voltage and frequencies of AC-DBD plasma actuation. Figure 6 and Figure 7 show the average surface temperature increase in time. In Figure 6, it can be seen that at low voltage input, surface temperature does not increase as much as in higher voltage cases and arrives at steady state in less than 20 seconds. At higher voltage input (5kV), the temperature increase is steeper and can reach more than 15°C as time goes on. On the other hand, it can be seen in figure 7 that, the influence of frequency is not too drastic as it was in comparison to voltage. Increasing the frequency from 5kHz to 7 kHz results in 8°C change in 180 seconds, where the voltage was 5kV.
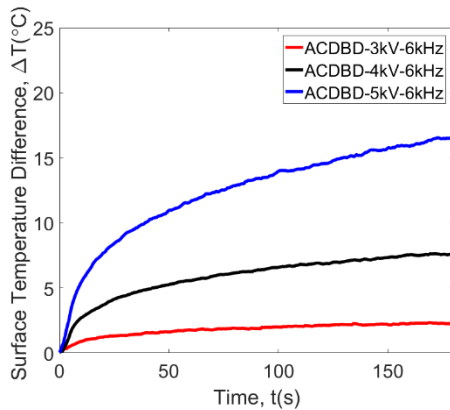
Fig. 6 Surface Temperature increase against time due to the influence of voltage.
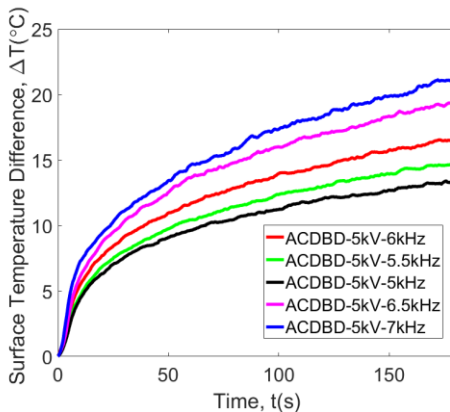
Fig. 7 Surface Temperature increase against time due to the influence of frequency.

As it was mentioned before, plasma-based anti-icing systems show great capabilities for aircraft icing mitigation. As high voltage is applied between electrodes, high electron field is generated. Electrons get accelerated and collide with neutrals and ions in the media. These collisions between electrons, ions, and neutrals result in thermal energy release and the source of gas heating [19–22].

In this part of this study, dynamic anti-icing process over a wind turbine blade model with plasma actuators was investigated. Plasma actuators were employed on DU91-W2-250 airfoil model, and anti-icing performance was explored under glaze icing conditions. Snapshots of wind turbine blade model with AC-DBD plasma actuators during the plasma actuation can be seen in figure 8.
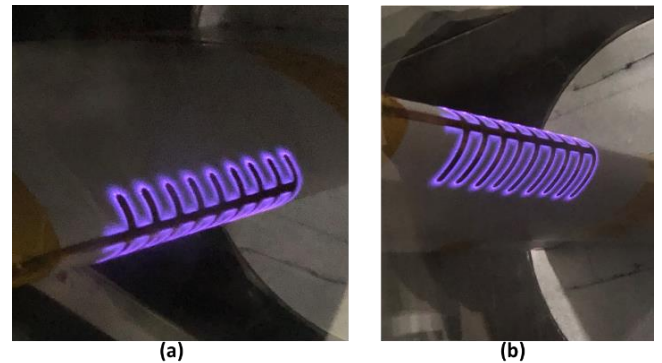
Fig. 8 (a) Upper and (b) lower surface of the leading edge with AC-DBD Plasma actuators in operation.

Figure 9 shows the dynamic ice accretion over a wind turbine blade model when plasma actuators were switched on (a) and kept off (b) under glaze icing conditions, i.e. $U=40m/s$, $T=-5°C$ and LWC = 1.0 g/m^3. Figure 10 shows the corresponding temperature maps during the plasma actuation. It can be seen clearly from figure 9 that in both cases, at the beginning of the icing process both blades are free of ice. After 10 seconds of icing process, thermal effect induced by plasma actuators prevent ice formation on the leading edge and water film was able to run back and freeze downstream of the airfoil, whereas for the case with no plasma actuation leading edge ice formation were observed. As the time goes on, it can be seen that after t=150 seconds of plasma actuation, all of the supercooled water droplets collected at the leading edge of the blade kept running back until they freeze and the ice rivulets get larger and larger at the downstream of the blade. On the other hand, for plasma off case, ice chunk became larger on the leading edge as more supercooled water droplets kept impinging and freezing at the leading edge of the blade.

Thermal energy generated by the actuators dissipated to the downstream of the airfoil as streaks due to the streamwise orientation of the actuators. As it is shown in figure 10(b) that impinging water droplets form thin water film and the temperature of the water film is higher than the initial surface temperature of the blade. it can be seen from figure 10(d), even after 150s of the icing process, water film temperature at the leading edge was still higher. Eventually, water film breaks up into rivulets and runback water was frozen and turned into ice.

361
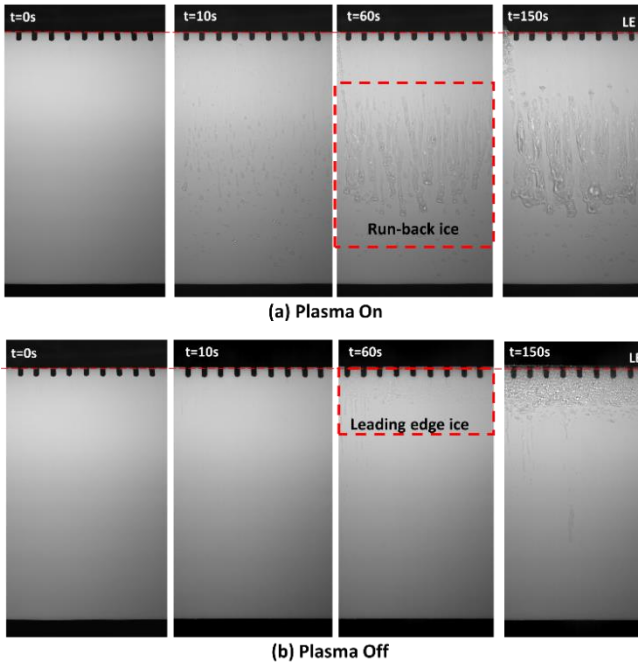
Fig. 9. Ice accretion process under glaze icing conditions at V = 40 m/s, T = -5°C and LWC = 1.0 g/m³ (a) Plasma on and (b) Plasma off
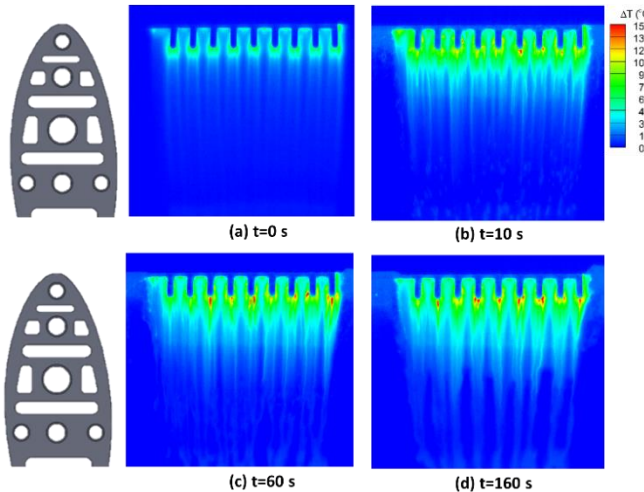
Fig. 10 Temperature map during the ice accretion process under glaze icing conditions at V = 40 m/s, T = -5°C and LWC = 1.0 g/m³ (a) t = 0s, (b) t = 10s, (c) t = 60s, and (d) t = 150s.

Nanosecond pulsed DBD plasma was also utilized for anti-icing applications, to obtain a comparison between the two types of plasma. Figure 11 shows the dynamic ice accretion over a wind turbine blade model when plasma actuators were switched on for (a) AC-DBD and (b) NS-DBD plasma at U=40m/s, T=-5°C and LWC = 1.0 g/m3. We observe that the runback region starts further back along the chord and is lesser in length for the NS-DBD plasma. This suggests that the pulsed application of the plasma does help in decreasing the total amount of ice accreted, since the leading edge is ice-free in both cases.

A Superhydrophobic (SHS) surface was also tested to see if the dynamic ice accretion characteristics differed because of the difference in the contact angle. Figure 12 shows the

dynamic ice accretion over a wind turbine blade model when plasma actuators were switched on for (a) AC-DBD and (b) NS-DBD plasma at U=40m/s, T=-5°C and LWC = 1.0 g/m3. Due to the contact angle being greater than 150 degrees, the droplets tend to roll off on impact, which causes much lesser ice accretion in the runback region. The airfoil remains relatively ice-free till around 240s, but as soon as the ice starts freezing on the surface, the hydrophobicity is not in the equation anymore, and further supercooled droplet impact will cause more freezing on the already present ice surface. In this case as well, we observe the runback region for the NS-DBD plasma case is lesser than that of the AC-DBD plasma case.
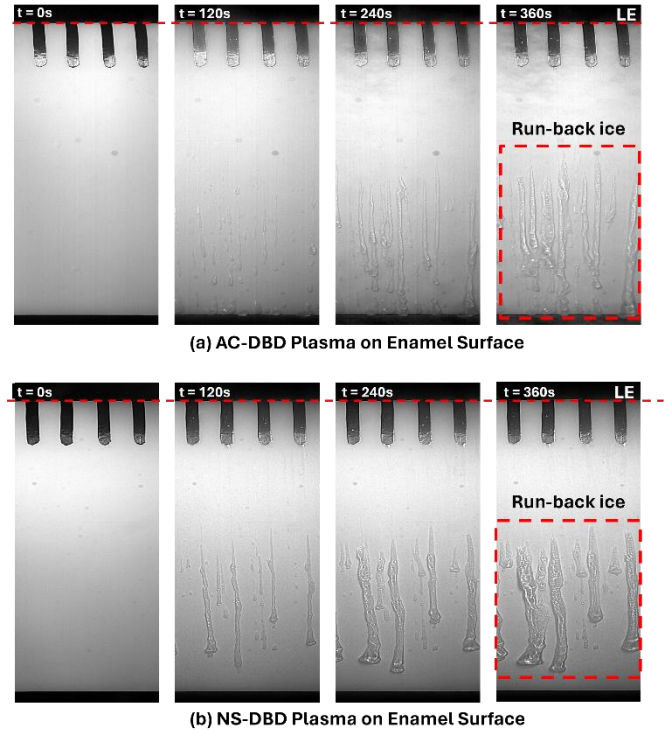
Fig. 11. Dynamic ice accretion on the turbine blade model with the plasma actuators switched on for (a) AC-DBD and (b) NS-DBD plasma at U=40m/s, T=-5°C and LWC = 1.0 g/m3.

IV. CONCLUSIONS

In this study, thermodynamic characteristics of DBD plasma were investigated parametrically. Effect of DBD plasma operation parameters, such as voltage and frequency on flat plate surface temperature was explored. Wind turbine blade model with plasma actuators manufactured. Anti-icing performance of the wind turbine blade was tested in ISU-IRT in glaze icing conditions and dynamic icing process was captured using high-speed imaging while IR thermal camera was used to map the temperature distributions over the surface.

It was shown in this study that, increasing voltage and frequency input to the DBD plasma actuators, result in an increase on dielectric surface temperature, due to higher power output. When DBD plasma actuators were employed on a wind turbine blade, thermal energy induced by plasma actuators successfully clear the leading edge of the blade by keeping supercooled water droplets at liquid state. Due to lower energy input, water rivulets turned into ice at

downstream of the airfoil before they were able the shed of from the blade completely.

The differences between AC-DBD plasma and NS-DBD plasma is also addressed in this study. The nanosecond pulsed DBD seems to be more efficient in minimizing the runback region across the chord of the airfoil. In addition, a superhydrophobic surface was also treated with plasma, and it was observed that the airfoil surface remained relatively ice-free for a much longer period of time due to the droplets rolling off the surface given its greater contact angle.

Plasma-based anti-icing systems offer great possibility to for wind turbine application. It has the potential to serve as dual-purpose system due to its capability of controlling the flow and inducing thermal energy to prevent ice formation.

REFERENCES

1. Dalili, N., Edrisy, A., and Carriveau, R., "A review of surface engineering issues critical to wind turbine performance," Nov. 2018, doi:10.1016/j.rser.2007.11.009.
2. Barber, S. and Wang, Y., "European Wind Energy Conference (EWEC 2010) The Impact of Ice Formation on Wind Turbine Performance and Aerodynamics Abstract," *Wind Energy* (Ewec), 2010.
3. Parent, O. and Ilinca, A., "Anti-icing and de-icing techniques for wind turbines: Critical review," *Cold Reg. Sci. Technol.* 65(1):88–96, 2011, doi:10.1016/j.coldregions.2010.01.005.
4. Gent, R.W., Dart, N.P., and Cansdale, J.T., "Aircraft icing," *Philos. Trans. R. Soc. London A Math. Phys. Eng. Sci.* 358(1776), 2000.
5. Lehtomäki, V., "Wind Energy in Cold Climates Available Technologies - report," 2016.
6. Fakorede, O., Ibrahim, H., Ilinca, A., and Perron, J., "Experimental Investigation of Power Requirements for Wind Turbines Electrothermal Anti-icing Systems," *Wind Turbines - Design, Control and Applications*, InTech, ISBN 978-953-51-2496-2, 2016, doi:10.5772/63449.
7. Gao, L., Liu, Y., Zhou, W., and Hu, H., "An experimental study on the aerodynamic performance degradation of a wind turbine blade model induced by ice accretion process," 2019, doi:10.1016/j.renene.2018.10.032.
8. Gao, L., Liu, Y., Kolbakir, C., Hu, H., Manelis, M., Weldon, J.A., and Naeve, N., "An Experimental Investigation on an Electric-Thermal Strategy for Wind Turbine Icing Mitigation," 2018, doi:10.2514/6.2018-3658.
9. Moreau, E., "Airflow control by non-thermal plasma actuators," *J. Phys. D. Appl. Phys.* 40(3):605, 2007.
10. Corke, T.C., Enloe, C.L., and Wilkinson, S.P., "Dielectric Barrier Discharge Plasma Actuators for Flow Control *," *Annu. Rev. Fluid Mech* 42:505–29, 2010, doi:10.1146/annurev-fluid-121108-145550.
11. Starikovskii, A.Y., Nikipelov, A.A., Nudnova, M.M., and Roupassov, D. V, "SDBD plasma actuator with nanosecond pulse-periodic discharge," *Plasma Sources Sci. Technol.* 18(3):34015, 2009, doi:10.1088/0963-0252/18/3/034015.
12. Nudnova, M., Kindusheva, S., Aleksahdrov, N., and Starikovskiy, A., "Rate of Plasma Thermalization of Pulsed Nanosecond Surface Dielectric Barrier Discharge," 2010, doi:10.2514/6.2010-465.
13. Roupassov, D. V, Nikipelov, A.A., Nudnova, M.M., and Yu Starikovskii, A., "Flow Separation Control by Plasma Actuator with Nanosecond Pulsed-Periodic Discharge," *AIAA J.* 47(1), 2009, doi:10.2514/1.38113.
14. Meng, X., Cai, J., Tian, Y., Han, X., Zhang, D., and Hu, H., "Experimental Study of Deicing and Anti-icing on a Cylinder by DBD Plasma Actuation," *47th AIAA Plasmadynamics and Lasers Conference AIAA*, 2016, doi:10.2514/6.2016-4019.
15. Zhou, W., Liu, Y., Hu, H., Hu, H., and Meng, X., "Utilization of Thermal Effect Induced by Plasma Generation for Aircraft Icing Mitigation," *AIAA J.* 56(3), 2018, doi:10.2514/1.J056358.
16. Liu, Y., Kolbakir, C., Hu, H., and Hu, H., "A comparison study on the thermal effects in DBD plasma actuation and electrical heating for aircraft icing mitigation," *Int. J. Heat Mass Transf.* 124:319–330, 2018, doi:10.1016/j.ijheatmasstransfer.2018.03.076.
17. Waldman, R.M. and Hu, H., "High-Speed Imaging to Quantify Transient Ice Accretion Process over an Airfoil," *J. Aircr.* 53(2):369–377, 2016, doi:10.2514/1.C033367.
18. Roth, J.R., Sherman, D.M., and Wilkinson, S.P., "Electrohydrodynamic Flow Control with a Glow-Discharge Surface Plasma," *AIAA J.* 38(7):1166–1172, 2000, doi:10.2514/2.1110.
19. Tirumala, R., Benard, N., Moreau, E., Fenot, M., Lalizel, G., and Dorignac, E., "Temperature characterization of dielectric barrier discharge actuators: influence of electrical and geometric parameters," *J. Phys. D. Appl. Phys.* 47(25):255203, 2014, doi:10.1088/0022-3727/47/25/255203.
20. Joussot, R., Hong, D., Rabat, H., Boucinha, V., Weber-Rozenbaum, R., and Leroy-Chesneau, A., "Thermal Characterization of a DBD Plasma Actuator: Dielectric Temperature Measurements using Infrared Thermography," *40th Fluid Dynamics Conference and Exhibit*, 2010, doi:10.2514/6.2010-5102.
21. Zhu, Y., Wu, Y., Cui, W., Li, Y., and Jia, M., "Numerical investigation of energy transfer for fast gas heating in an atmospheric nanosecond-pulsed DBD under different negative slopes," *J. Phys. D. Appl. Phys.* 46(49):495205, 2013, doi:10.1088/0022-3727/46/49/495205.
22. Conrads, H. and Schmidt, M., "Plasma generation and plasma sources," *Plasma Sources Sci. Technol* 9, 2000.

Inverse design of wind turbine blade section with CFD simulations under extreme weather conditions

Ibrahim Kipngeno Rotich[1,2*], László E. Kollár[2]

[1]Doctoral School of Environmental Sciences, ELTE Eötvös Loránd University, Budapest, Hungary
[2] Savaria Institute of Technology, ELTE Eötvös Loránd University, Budapest, Hungary,
Ibrahimrkipp@gmail.com, kl@inf.elte.hu

Abstract— With the increasing threat of climate change, wind energy is becoming one of the useful renewable energies in cold regions. However, ice accretion on wind turbines lowers aerodynamic performance (quantified by the lift-to-drag ratio, C_L/C_D), which worsens during irregular events such as winter storms. The aerodynamic performance degradation caused by icing on airfoils is numerically studied using the commercial software FENSAP-ICE. The study considers a range of atmospheric and physical conditions by varying the median volume diameter (MVD), liquid water content (LWC) and ambient temperature on 180-minute accretion time. Icing for a shorter period was found to have no negative effect or even slightly improved aerodynamic performance under some conditions. The cloud with MVD of 1000 µm was used to simulate ice accretion over a period of 60 minutes with varying LWC ranging from 0.01g/m³ to 0.1g/m³. The velocity distribution obtained from the iced airfoil was then used in the inverse design procedure. The target and designed airfoils were then subjected to in-cloud icing conditions. These conditions involved LWC of 0.1g/m³-1g/m³, MVD of 20µm-100µm, and air temperature of -4 °C and -17 °C over a 3-hour accretion period. The aerodynamic performance on the airfoil obtained by inverse design was found to be improved compared to the original airfoil, to a greater extent for -17 °C compared to -4 °C. The aerodynamic performance deteriorated with an increase in LWC and MVD after 180 minutes.

Keywords— *Airfoil, Aerodynamic performance, Inverse design, icing, numerical simulation.*

I. Introduction

Cold regions have challenges such as ice accretion due to seasonal conditions which lead to reduced wind energy performance and power output [1], [2], increased rotor loads [3], safety risks, limited or reduced access for maintenance activities, and cold weather shutdown that increases wear and tear [4]. Icing on wind turbines leads to approximately 20% annual power loss [5], [6]. Gao et al [7] studied ice accretion on an operational wind power farm and found out that icing contributed up to 80% power loss. Sahin & Farsadi [8] studied 5MW NREL turbine with different classifications on airfoil geometries under light icing which led to reduced power output. The results show a reduction of 9.27% in lift coefficient and a 48% increase in drag coefficient that causes alteration in aerodynamic performance. Gao & Hong [7] considered icing events ('pre-icing, operational-icing, stopped-icing, and post-icing') for evaluation on 2MW Eolos wind turbine which lasted for 51 hours and resulted in average 63% energy loss (25MWh). Stoyanov et al [8] examined icing mitigation i.e, tip-speed ratio derating and electrothermal anti-icing. The study found out that derating reduced accumulation of ice by 23% and daily power loss by 37% during icing. The

42 in-cloud icing occurrences per year were considered for the anti-icing strategy.

In cold regions, icing can occur up to 20% of the time during winter seasons, which justifies the need to have turbines which can operate during such extremes [9]. Some of the mitigation mechanisms employed involve the installation of heating and hydrophobic coatings. However, there is no clear solution to the performance improvement, which made it an active area of research. According to a study carried out by [10], numerical simulations showed an improvement in aerodynamic performance after a short period of ice accretion time under limited icing conditions. The aim of the present study is to apply an inverse design procedure to generate an airfoil shape that considers icing over a 60-minute period with varied conditions. The velocity distribution was obtained for an iced profile with slightly increased lift-to-drag ratio, C_L/C_D. The inverse design process involved this velocity distribution as target velocities to obtain a shape with higher lift-to-drag ratio.

II. Methodology

The methodology began with obtaining coordinates of an airfoil profile from airfoiltools.com [11]. ANSYS Fluent was used in creating meshed geometry and transferring a readable file to FENSAP ICE. The icing was then simulated for 60 minutes on NACA4418. The iced airfoil coordinates were then generated with increased chord length and meshed in ANSYS Fluent, but with slip conditions (to obtain shear velocities) on the boundary layer. This was aimed at generating target velocities to be used in MATLAB for the inverse design process.

A. *Computational domain*

ANSYS Fluent and FENSAP-ICE were used in the computational study. Geometry and meshing were prepared using ANSYS Fluent on a rectangular domain with 5 chord lengths from the leading edge to inlet, and 10 chord lengths behind the trailing edge. Triangular unstructured mesh was used in the domain with 1.05% growth rate which made a connectivity and meshes in the domain. The airfoil surface was divided into 1000 divisions to ensure sufficient grid resolution. To reduce the boundary layer effects and increase stability, no-slip condition was considered with 45 layers with an increase rate of 1.08% growth from first layer thickness calculated from y^+ value. The computational domain with mesh around the NACA4418 profile is shown in Figure 1. In the boundary conditions, inlet represented the inlet velocity conditions, airfoil surface with a spanwise length of 1 m acted as a wall with +0.1°C higher than the air temperature, and the outlet pressure was set to 0 Pa which assured numerical

stability by not interacting with unreal pressure gradients. The walls bounding the computational domain were represented as "symm" to ensure that external conditions were maintained.
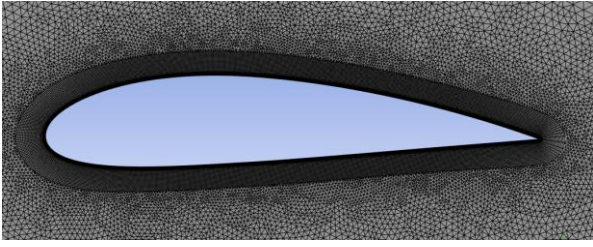
Figure 1: Unstructured triangular mesh around an airfoil on NACA4418.

The icing simulations were carried out using the software FENSAP-ICE 2023, which considered the turbulence models, the atmospheric conditions, the droplet parameters, and the physical conditions. The trajectories of the supercooled water droplets from the inlet are considered in the fluid flow, which predicts their collision on the airfoil surface. The continuous air and supercooled water droplet flows use the Eulerian-Lagrangian method in conserving continuity and momentum. The Bourgault icing model is used in determining the growth of ice by establishing conservation equations [12].

Ice accretion was considered during a relatively short period of time under the conditions listed in Table I. The shape of the airfoil with ice accretion obtained was then extracted with the coordinates generated and run again using the ANSYS Fluent. The velocities obtained near this shape were then used as target velocities in the inverse design procedure.

B. Inverse design

The modified Garabedian-McFadden iterative technique was used in the present study[13]. The velocity distribution obtained outside the boundary layer around the NACA0012 profile was used as the initial velocity distribution. The iterative procedure continued with number of iterations until the average error in the surface coordinate y of the airfoil reduced below a prescribed value. The coordinate position was determined by the equation below [13], [14].

$$\beta_0 \Delta y + \beta_1 \frac{d\Delta y}{dx} - \beta_2 \frac{d^2(y)}{dx^2} = V^2{}_{tar} - V^2{}_{pr}$$

Where V_{tar} and V_{pr} are target and actual velocities and β_0, β_1 and β_2 are numerical constants. When the actual velocities approach the target velocities, the change in the surface ordinate Δy tends to zero. After discretization, the equations can be organized in matrix form where the coefficient matrix is tridiagonal, and they are solved by the Thomas algorithm.

III. RESULTS AND DISCUSSION

A. Effect of rime ice conditions over a short period of time

Rime ice accretion over short time had a reduced impact on the airfoil shape, which does not change, or which may even increase the C_L/C_D. The velocity distribution around the iced airfoil is then applied in the inverse design process with the expectation that the modified shape can be used under some icing conditions without considerable aerodynamic performance degradation. The operating conditions used in this study for a shorter accretion time are described in Table I.

Operating conditions	
Airfoil	NACA4418
LWC (g/m^3)	0.1, 0.5, 1
Temperature (°C)	-20
Accretion time (min)	60
Velocity (m/s)	20
MVD (μm)	1000

Table I: Operating conditions used for ice accretion over a shorter time (60 min).

The results obtained after the shorter period of accretion time can be seen in Figure 2 that shows nearly constant aerodynamic performance for LWC of 0.01 g/m^3, 0.1 g/m^3 and 0.5 g/m^3. Based on the analysis, the maximum aerodynamic performance increased by 0.004 % for 0.01 g/m^3, 0.04% for 0.1 g/m^3 and 0.12% for 0.5 g/m^3 while 1 g/m^3 dropped by 11.44% from the 5th to 60th minute. The study shows that aerodynamic performance on an airfoil is greatly influenced by LWC, and ice shape complexities associated with it [15]. The association between thickness and LWC shows that there is a linearity in the growth, with an increase in LWC led to increased thickness on the leading edge [16]. Although the rime ice show smooth ice shape characteristics, increased LWC at higher accretion time showed a great drop in the aerodynamic performance due to shape variation and localized impingement causing airflow separation pattern to move towards the leading edge.
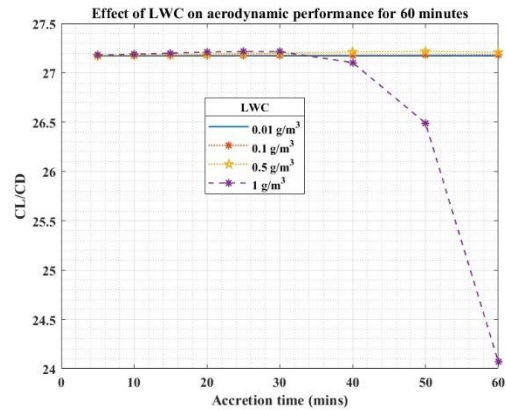
Figure 2: Aerodynamic performance over a shorter accretion time with varying LWC.

Based on the results obtained, it was observed that ice thickness varied greatly on the leading edge, which grew linearly with LWC. The ice thickness obtained for maximum C_L/C_D in this study was 45.31 mm (see Figure 3) and observed on 50th minute for 0.5g/m^3 with a C_L/C_D value of 27.2180. The chord length increases due to ice accretion, which influences geometric parameters, and in turn ice accretion, leading to significant aerodynamic implications and performance degradation.
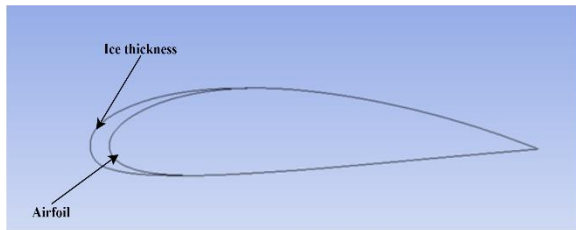
Figure 3: Ice thickness from "iced airfoil with maximum C_L/C_D" at 50th minute for 0.5 g/m³ (The chord length for an airfoil was 1-meter and ice thickness having 0.04531 meters)

The velocity distribution over an airfoil was obtained from the ANSYS Fluent applying slip conditions in order extract shear velocities over the iced airfoil that is depicted in Figure 3. The free stream velocity used was 20 m/s to get the velocity profile around the iced airfoil as shown in Fig. 4.
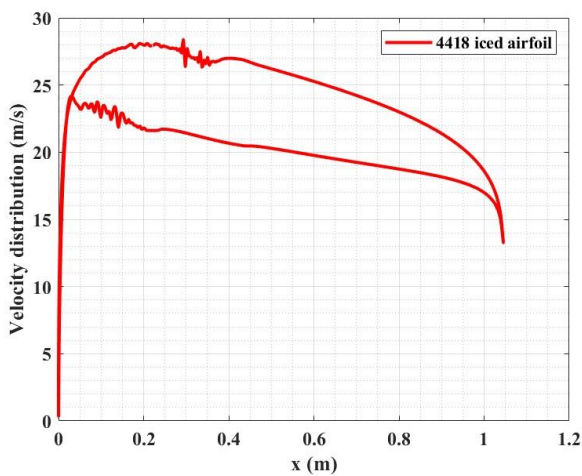
Figure 4: Target velocity at 20 m/s obtained from shear velocity distribution over iced airfoil by ANSYS Fluent.

The velocity distribution in Fig. 4 was applied in the inverse design process as target velocity distribution, and the inverse designed shape is shown in Fig. 5 by the curve "calculated". Note that although the velocity distribution around the iced airfoil is not smooth everywhere, the inverse design process provided a satisfactorily smooth shape.
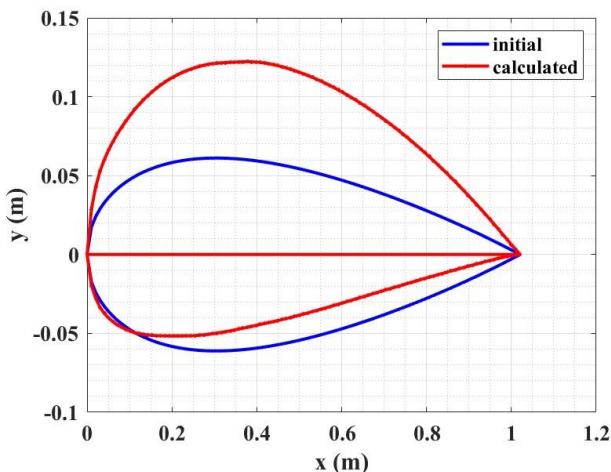
Figure 5: Inversed designed airfoil generated from target velocities plotted in Figure 4.

The aerodynamic performance of the airfoil with maximum C_L/C_D was examined on ANSYS Fluent with ambient temperature of 15 °C at density of 1.225kg/m³ with varying velocities. The aerodynamic performance was compared on bare, iced (short accretion time), and inverse designed airfoils. From the analysis, the highest improvement occurred at 6m/s with 11.14%. When velocity is increased, it shows a decreasing tendency such that at 30m/s, the difference between the C_L/C_D for different shapes is approximately 2.5% (Figure 6).
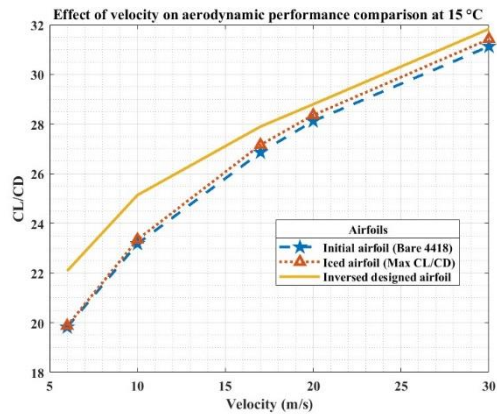
Figure 6: Aerodynamic performance at 15°C for the bare airfoil, iced airfoil (short accretion time), and inverse designed airfoil with varying velocity.

The icing study presented in Sections III.B and III.C is aimed at obtaining the aerodynamic performance with the inverse designed airfoil and comparing it with the results obtained for the iced airfoil for different air temperature, LWC and MVD. The icing conditions considered are described in Table II.

Operating conditions	
Airfoil	NACA4418
LWC (g/m³)	0.1, 0.5, 1
Temperature (°C)	-4, -17
Accretion time (mins)	180
Velocity (m/s)	20
MVD (μm)	20, 40, 60, 80 100

Table II: Operating conditions used in comparing aerodynamic performance of iced and inverse designed airfoil.

B. Impact of Temperature

The icing on the airfoil surface affects the aerodynamic performance due to shapes formed. Rime ice forms relatively smooth leading edge compared to glaze ice due to different collection efficiencies and freezing fractions [17]. The freezing fraction is lowered with increased temperature making unfrozen water film on the surface leading to runback which forms a "horny" shaped airfoil. The freezing fraction for rime ice is higher compared to glaze.

Comparing the leading-edge radius, the designed shape was streamlined/sharp compared to iced airfoil. Studies by [18], [19] show that disturbance at the leading edge had an impact

on the localised impingement of supercooled water droplets and led to an increased amount of ice accretion, which occurred for the inverse designed airfoil. The ice accretion generated for -4 °C increased the iced airfoil surface due to expansion in geometric configuration and droplet inertia.

C. Effect of MVD and LWC

The amount of water present in a cloud influences the rate of icing and mass of ice. High LWC leads to a higher ice accretion rate and increases the ice thickness [20]. When the LWC was kept constant and MVD increased, the thickness of ice on the leading edge increased. At -4 °C there is the formation of the horns which create disturbance of the flow over the surface. The disturbance leads to early separation moving towards the leading-edge increasing drag [21]. An increase in MVD increases the collision efficiency over the surface due to the inertial forces and gravity. Small droplets have higher chances to follow the air flow; thereby impacting less on the aerodynamic performance compared to higher droplets.

In Figure 7, the results presented show that increasing MVD led to decrease in aerodynamic performance for both airfoils. However, the irregularity on the iced airfoil surface, (that resulted in the velocity distribution shown in Figure 4) led to a slightly lower performance than the inverse designed one which had streamlined curvature on the leading edge. On the iced airfoil, the stagnation point moved slightly above from the initial un-iced airfoil. The inverse designed shape had a higher ratio C_L/C_D for most of the cases considered compared to the iced airfoil (see Figure 7).
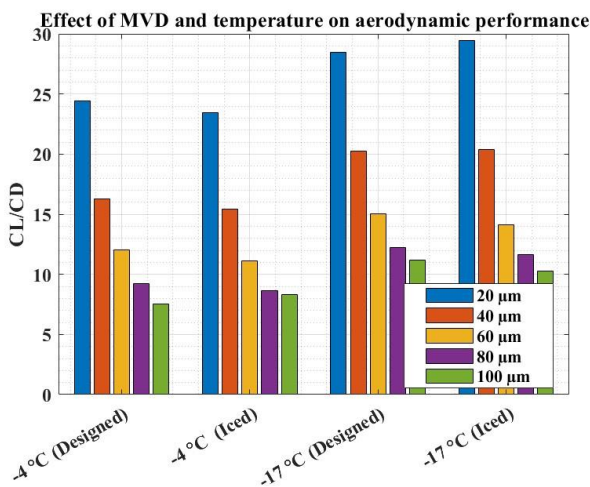
Figure 7: Effects of MVD and air temperature for iced and designed airfoils at 20m/s and 1g/m^3 after 180 minutes ice accretion.

The aerodynamic performance comparison was continued by maintaining constant MVD (20 µm) and velocity at 20 m/s while varying LWC ranging between 0.1g/m^3-1g/m^3. An increase in the LWC shows an increase in mass of water and increasing collection efficiency on the surface. The decrease in temperature led to an increase in the C_L/C_D. The inverse designed airfoil exhibits improved aerodynamic performance compared to the iced airfoil as it is represented in Figure 8. At -4 °C, the percentage improvement was 4.5 %, 0.98 % and 11.11 % for 0.1 g/m^3, 0.5 g/m^3 and 1 g/m^3, respectively, and for -17 °C, the improvement was 3.57 %, 2.26 % and 8.5 %

from iced to inverse designed airfoil for 0.1 g/m^3, 0.5 g/m^3 and 1 g/m^3, respectively (Figure 8).
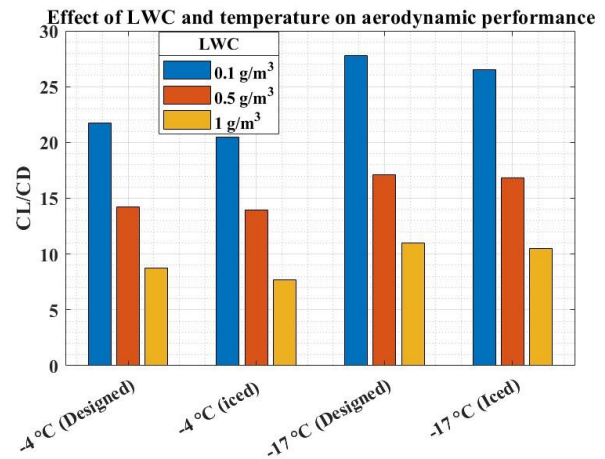
Figure 8: Effect of LWC and temperature on aerodynamic performance of iced and inverse designed airfoil at 20m/s and 20µm after 180 minutes ice accretion.

IV. CONCLUSIONS

The aerodynamic performance of NACA4418 was numerically modelled using FENSAP ICE software. The inverse design process was carried out with the velocity distribution obtained for iced airfoil with maximum C_L/C_D. The study used icing conditions with an MVD of 1000 µm and LWC of 0.5 g/m^3 which slightly improved aerodynamic performance up to the 50th minute and resulted in ice thickness of 45.31 mm at the leading edge. The target velocity distribution was generated from iced airfoil applying slip conditions in ANSYS Fluent, and then inverse design was applied using MATLAB. The aerodynamic performance from the iced and designed airfoil was compared by considering effects of physical parameters including MVD, LWC and air temperature for 180 minutes ice accretion. The MVD was varied between 20 µm to 100 µm and LWC from 0.1g/m^3 to 1 g/m^3. The study shows that an increase in MVD and in LWC led to reduction in C_L/C_D but was minimal for the inverse designed airfoil. The air temperature affects the airfoil shape on the leading edge, and consequently, the aerodynamic performance. Further research will involve experimental study about the effects of ambient conditions on aerodynamic performance carried out in an icing wind tunnel.

REFERENCE

[1]   P. Roberge, J. Lemay, J. Ruel, and A. Bégin-Drolet, "The effect of icing severity on wind turbine ice

protection systems efficiency," *Cold Reg Sci Technol*, vol. 207, p. 103774, Mar. 2023, doi: 10.1016/j.coldregions.2023.103774.

[2] I. K. Rotich and P. K. Musyimi, "Wind power density characterization in arid and semi-arid Taita-Taveta and Garissa counties of Kenya," *Clean Eng Technol*, p. 100704, Dec. 2023, doi: 10.1016/j.clet.2023.100704.

[3] C. Hochart, G. Fortin, J. Perron, and A. Ilinca, "Wind turbine performance under icing conditions," *Wind Energy*, vol. 11, no. 4, pp. 319–333, Jul. 2008, doi: 10.1002/we.258.

[4] M. Aizpurua-Etxezarreta, S. Carreno-Madinabeitia, A. Ulazia, J. Sáenz, and A. Saenz-Aguirre, "Long-Term Freezing Temperatures Frequency Change Effect on Wind Energy Gain (Eurasia and North America, 1950–2019)," *Sustainability*, vol. 14, no. 9, p. 5630, May 2022, doi: 10.3390/su14095630.

[5] J. Y. Jin and M. S. Virk, "Study of ice accretion and icing effects on aerodynamic characteristics of DU96 wind turbine blade profile," *Cold Reg Sci Technol*, vol. 160, pp. 119–127, Apr. 2019, doi: 10.1016/j.coldregions.2019.01.011.

[6] O. Yirtici, I. H. Tuncer, and S. Ozgen, "Ice Accretion Prediction on Wind Turbines and Consequent Power Losses," *J Phys Conf Ser*, vol. 753, p. 022022, Sep. 2016, doi: 10.1088/1742-6596/753/2/022022.

[7] L. Gao and J. Hong, "Wind turbine performance in natural icing environments: A field characterization," *Cold Reg Sci Technol*, vol. 181, Jan. 2021, doi: 10.1016/j.coldregions.2020.103193.

[8] M. Sahin and T. Farsadi, "The impacts of atmospheric icing on performance and behavior of a controlled large-scale wind turbine," *Journal of Renewable and Sustainable Energy*, vol. 15, no. 6, Nov. 2023, doi: 10.1063/5.0161724.

[9] Canada.ca, "Wind Energy in Cold Climates," Wind Energy. Accessed: Mar. 13, 2024. [Online]. Available: https://natural-resources.canada.ca/energy/energy-sources-distribution/renewables/wind-energy/wind-energy-cold-climates/7321

[10] I. Rotich and L. E. Kollár, "Numerical simulation of the performance of an asymmetrical airfoil under extreme weather conditions," *Mérnöki és Informatikai Megoldások*, vol. 3, no. 2, pp. 19–29, Dec. 2022, doi: 10.37775/EIS.2022.2.2.

[11] http://www.airfoiltools.com/, "NACA 4 digit airfoil generator (NACA 4418 AIRFOIL)." Accessed: Apr. 19, 2024. [Online]. Available: http://www.airfoiltools.com/

[12] Y. Bourgault, W. G. Habashi, J. Dompierre, and G. S. Baruzzi, "International journal for numerical methods in fluids a finite element method study of Eulerian droplets impingement models," 1999.

[13] J. Malone, J. Vadyak, and L. N. Sankar, "Inverse aerodynamic design method for aircraft components," *J. Aircr.*, vol. 24, pp. 8–9, 1987.

[14] L. E. Kollar and R. Mishra, "Inverse design of wind turbine blade sections for operation under icing conditions," *Energy Convers Manag*, vol. 180, pp. 844–858, Jan. 2019, doi: 10.1016/j.enconman.2018.11.015.

[15] R. Hann, R. J. Hearst, L. R. Sætran, and T. Bracchi, "Experimental and Numerical Icing Penalties of an S826 Airfoil at Low Reynolds Numbers," *Aerospace*, vol. 7, no. 4, p. 46, Apr. 2020, doi: 10.3390/aerospace7040046.

[16] H. Cheng, D. Zhao, N. L. Oo, X. Liu, and X. Dong, "Numerical Investigation on Intermittent Maximum Ice Accretion and Aerodynamic Performances of RG-15 Aerofoil at Low Reynolds Number," *Aerospace*, vol. 11, no. 1, p. 7, Dec. 2023, doi: 10.3390/aerospace11010007.

[17] Z. Xu, T. Zhang, X. Li, and Y. Li, "Effects of ambient temperature and wind speed on icing characteristics and anti-icing energy demand of a blade airfoil for wind turbine," *Renew Energy*, vol. 217, p. 119135, Nov. 2023, doi: 10.1016/j.renene.2023.119135.

[18] M. Morelli, L. Beretta, A. Guardone, and G. Quaranta, "Numerical Investigation of Ice Formation on a Wing with Leading-Edge Tubercles," *J Aircr*, vol. 60, no. 1, pp. 190–204, Jan. 2023, doi: 10.2514/1.C036888.

[19] L. Beretta, M. C. Morelli, A. Guardone, and G. Quaranta, "Numerical Investigation of Three-Dimensional Ice Formation on a Wing with Leading Edge Tubercles," in *AIAA SCITECH 2022 Forum*, Reston, Virginia: American Institute of Aeronautics and Astronautics, Jan. 2022. doi: 10.2514/6.2022-0707.

[20] Y. A. Malik, K. Köbschall, S. Bansmer, C. Tropea, J. Hussong, and P. Villedieu, "Ice accretion compositions in ice crystal icing," *Int J Heat Mass Transf*, vol. 220, p. 124910, Mar. 2024, doi: 10.1016/j.ijheatmasstransfer.2023.124910.

[21] P. Wang, L. Wang, X. Kong, D. Wu, and B. Huang, "Influence of relative thickness on static and dynamic stall characteristics and prediction of airfoils," *Ocean Engineering*, vol. 271, p. 113690, Mar. 2023, doi: 10.1016/j.oceaneng.2023.113690.

Wind Induced and Iced Response Analysis of the Terminal Tower Line System of Wind Farms under Strong Wind

Yupeng Liu[1], Yongcan Zhu[1], Shuai Wang[1], Xinbo Huang[1]

[1] Xi'An Polytechnic University, China

a799458669@163.com, 286844943@qq.com

Abstract— **In order to master the wind-induced and iced response characteristics of the terminal tower line system of wind farms under strong wind, taking a 35kV terminal tower line system of wind farms as the research object, the spatial finite element model of the terminal tower line system is established. The harmonic superposition method is used to simulate the fluctuating wind load time history of the terminal tower line system and superimpose the static wind pressure. The time-domain characteristics of wind-induced response of tower line system under wind load with different wind direction angles are analyzed. Compared with the wind-induced response of single tower, the variation laws of maximum displacement and stress of single tower and tower line system under different wind angles are explored, and the situation of conductor iced in practical application is also considered, and the most unfavorable wind direction angle is obtained. The results show that compared the tower line coupling effect has a great influence on the wind-induced vibration response of the tower line system, the displacement of the tower top increases obviously. The most unfavorable wind direction of terminal tower line system is perpendicular to the conductor layout direction. The influence of ice covering on the wind vibration response of terminal tower line system is great, and it is suggested to consider the influence of actual ice covering in the design.**

Keywords— *wind farms; terminal tower line system; fluctuating wind load; iced; wind-induced vibration response*

I. INTRODUCTION

In recent years, with the development of economy, countries all over the world pay more and more attention to the development and utilization of new energy. Among them, wind power plays an important role[1]. As the carrier of power transmission, transmission system is an extremely important engineering structure in the power energy system[2]. Since the transmission tower line system is often prone to roll instability failure under wind load, and the ice covering of conductors and towers will increase the possibility of such failure, the static stability analysis of the transmission tower line system can accurately determine the critical wind speed and tower failure units[3], which is of great significance for improving the wind resistance performance of the transmission tower and guiding the wind resistance reinforcement design of the transmission tower.

Luo Kelong et.[4] found that the acceleration response of the tower line system is smaller than that of the single tower, and the position of the dangerous cross section of the main material of the tower body changes after considering the coupling effect. Wang Dahai et.[5] found that the pylon coupling changed the dynamic characteristics of the transmission tower, and the most unfavorable wind direction of the system also changed. Sheng Jinma et.[6] analyzed that wind load has an important influence on tower stability. Yu Jiabao et.[7] found that under the action of strong wind, the inclined steel of transmission tower is more prone to dynamic instability than the main steel. However, there are few researches on terminal tower line system, and most of them do not consider the effect of ice covering on tower line system in actual situation.

In this paper, a T-junction tower in a 35kV transmission line in China is taken as the research object. Its terminal tower is hung on one side without the balance effect of the tension of the other side of the conductor, which makes the terminal tower subject to greater conductor force and more susceptible to wind and ice load. Moreover, there are few relevant studies, so it is very important to further study its stability.

Based on the harmonic superposition method, this paper uses Kaimal spectrum which changes along the height to simulate the fluctuating wind, and works out MATLAB program to simulate the wind load. Finite element software is used to analyze the stability of transmission towers under static wind load and fluctuating wind load, and B-R criteria and yield criteria are used to judge local instability[8-9]. This paper provides a reference for the transmission line technology design of T junction tower in wind farm.

II. MODEL

A. Finite element model of tower line system

In this paper, a T tower in a 35kV transmission line is taken as the research object. The main loop conductor is LGJ-240/30 steel core aluminum stranded conductor with a horizontal span of 200m; The branch conductor is LGJ-150/25 steel core aluminum stranded conductor, the horizontal span is 100m; The ground conductor is GJ-50; The insulator is U70B/146.

A four-tower three-conductor finite element model is established as shown in Figure 1, The main material of the tower body and cross arm is Q345 Angle steel,and other auxiliary materials is Q235 Angle steel. In the finite element calculation, the beam element of the tower is beam188, the insulator is BEAM188, and the power line is LINK10. The enlarged view of the terminal tower line system is shown in Figure 2.
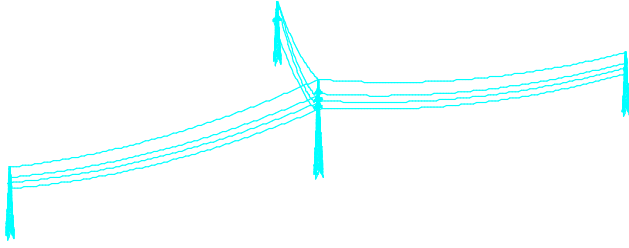
Fig. 1 A four-tower three-conductor finite element model
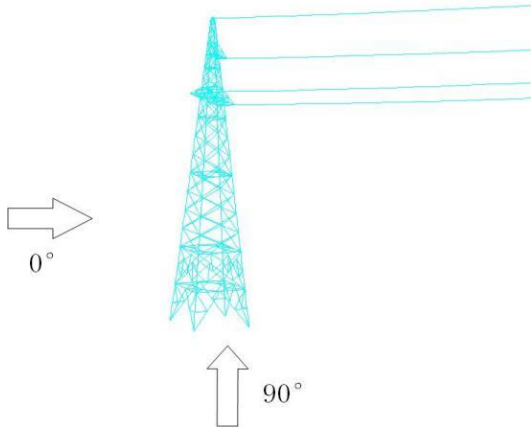
Fig. 2 The terminal tower line system

B. Wind load simulation

1) Static wind

When analyzing the stability of the transmission tower system under static wind, the nonlinear stability is analyzed by using the gradually increasing load method, considering the influence of both geometric and material nonlinearity, and the pseudo-static load calculated by the transmission tower is as follows:

$$W_S = W_0 \bullet \mu_Z \bullet \mu_S \bullet B_2 \bullet A_S \bullet \beta_Z \qquad (1)$$

$$W_0 = V^2 / 1600 \qquad (2)$$

Where: W_S and W_0 are the standard values of wind load and benchmark wind pressure; V is the wind speed at the base height; μ_z is the height change coefficient; μ_S is the wind load adjustment factor of transmission tower. β_Z is the body type coefficient; A_S is the calculated value of the projected area of the components on the windward side, η is the load reduction factor on the lee side of the tower, and B_2 is the increase factor of the ice wind load on the transmission tower.

The calculated pseudo-static load of the conductor is:

$$W_X = \alpha \bullet W_0 \bullet \mu_Z \bullet \mu_{SC} \bullet \beta_C \bullet d \bullet L_P \bullet B_1 \bullet sin^2\theta \qquad (3)$$

Where: α is the non-uniform coefficient of wind pressure; μ_{sc} is the size coefficient of the guide line. β_c is the wind load adjustment coefficient. d is the calculated outer diameter of the guide line, L_P is the horizontal distance, B_1 is the increase factor of the ice wind load on the guide line, and θ is the Angle between the wind direction and the guide line.

2) fluctuating wind

Harmonic superposition method is used to simulate fluctuating wind. Using the Kaimal spectrum that varies along height:

$$S(n) = \frac{200\, u^2 f}{n(1 + 50\, f)^{5/3}} \qquad (4)$$

Where: $S(n)$ is the power spectral density; u is the friction wind speed related to the ground roughness, $u = K\bar{v}(z)/\ln(z/z_0)$, $K \approx 0.4$, $\bar{v}(z)$ is the average wind speed, z is the height off the ground, z_0 is the ground roughness; f is similar coordinates, $f = nz\,/\,\bar{v}(z)$; n is the frequency.

The cross-spectral density function is:

$$S_{ij}(n) = \rho_{ij}\sqrt{S_{ii}(n)S_{jj}(n)} \qquad (5)$$

Where: $S_{ii}(n)$ and $S_{jj}(n)$ are self-spectral density functions, respectively.

The relevant parameters of pulsating wind simulation are as follows:

The average wind speed 'v' at 10m is 15m/s, and the ground roughness length 'z₀' is 0.15. The Kaimal constant is 0.4 and the exponential attenuation coefficient 'Cz' is 10, the time is 100s.

After simulation, the wind speed time history curve of each position is shown in Figure 3. It can be seen from Figure 4 that the simulated power spectrum is in good agreement with the target wind spectrum.
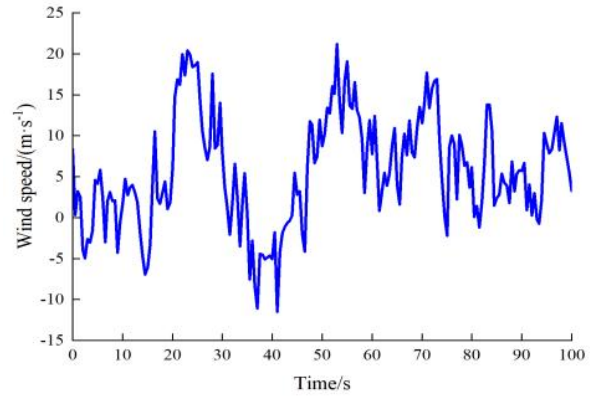
Fig. 3 Wind speed time history curve
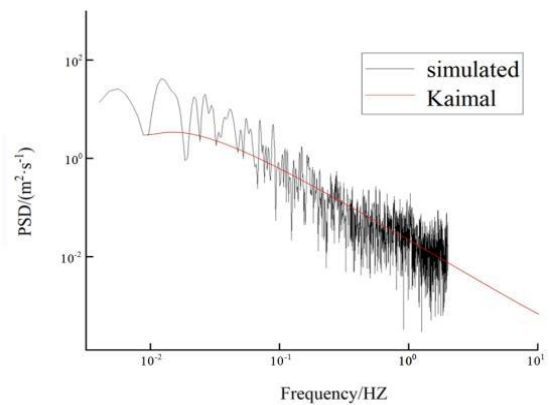
Fig. 4 Power spectrum fitting diagram

C. Ice load simulation

1) Ice load of the conductor

In order to facilitate the calculation of the icing load, it is generally considered that the icing is uniformly distributed along the conductor. The section of ice covered conductor is shown in Figure 5.

The additional force simulation method uses equal spacing concentrated forces to simulate the ice loading, where the mass M of each concentrated load is calculated as follows:

$$\begin{cases} m = \rho \pi b (D+b) \\ M = mL/n \end{cases} \quad (6)$$

Where: m is the mass of the ice covering on the conductor in unit length; ρ is the ice covering density; D is the outer diameter of the conductor; b is the ice thickness; L is the length of the conductor; n is the indicates the number of divided units.
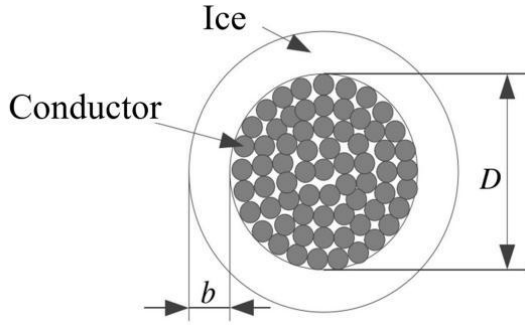
Fig. 5 Ice covered conductor section

The formula for calculating the ice gravity load per unit length of a line with a circular section is as follows:

$$q_1 = \pi \cdot b \cdot \alpha_1 \cdot \alpha_2 \cdot (d + b \cdot \alpha_1 \cdot \alpha_2) \cdot \gamma \cdot 10^6 \quad (7)$$

Where: q_1 is the ice covering gravity load per unit length; b is the basic ice thickness; d is the diameter of the circular overhead line; α_1 is the ice thickness correction parameter; α_2 is the height increasing coefficient of ice thickness; γ is the ice load, generally is 9kN/m^3

2) Ice load of the tower body

The tower body has a non-circular cross-section, and the formula for calculating the ice gravity load per unit area is:

$$q_1 = 0.6 \cdot b \cdot \alpha_2 \cdot \gamma \cdot 10^3 \quad (8)$$

III. COUPLING ANALYSIS OF WIND-INDUCED RESPONSE OF SINGLE TOWER AND TOWER LINE

A. Wind-induced response analysis of single tower and tower line under different directional angles

Based on the finite element model of single tower and tower line system, the wind load is applied by the method of nodal force, and the time history of wind vibration response at different wind angles is analyzed. The representative node of the top of the transmission tower is selected to extract and analyze the maximum displacement of the top of the single tower and the tower line system in the Z direction under different wind angles, as shown in the figure 6.

As can be seen from the figure, under different wind direction angles, the maximum displacement in Z direction of the single tower appears at 60°; under different wind

direction, the maximum displacement in Z direction of the tower line system appears at 90°. The reason is that when the wind direction is 90°, the wind direction changes from the direction along the line to the direction perpendicular to the line, the windward area of the line increases, and the plane coupling effect between the tower lines is amplified. At this time, the influence of tower line coupling effect on the transmission tower reaches the maximum, and the maximum displacement of the tower line system reaches the maximum in this direction, indicating that 90°wind direction is the most unfavorable wind direction in the analysis of wind-vibration response of tower line coupling system model.
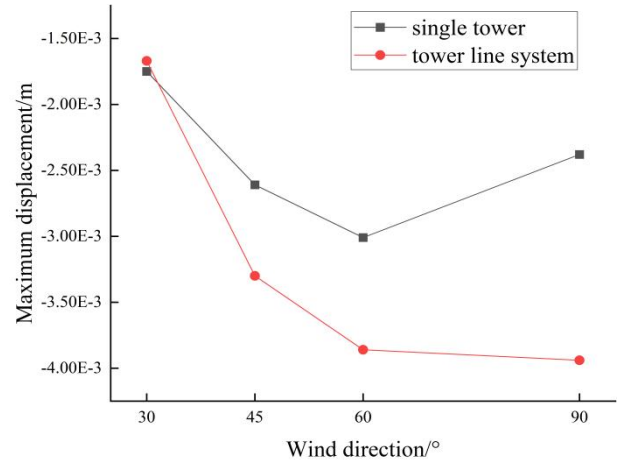
Fig. 6 The representative node of the top of single tower and tower line system under different wind angles

B. Comparison of operation conditions of single tower and tower line under the most unfavorable Angle

Based on the finite element model of the single tower and the tower line system, the time-history curve of the representative node of the top of single tower and tower line system under the most unfavorable wind angle of 90° is extracted, as shown in the figure 7.
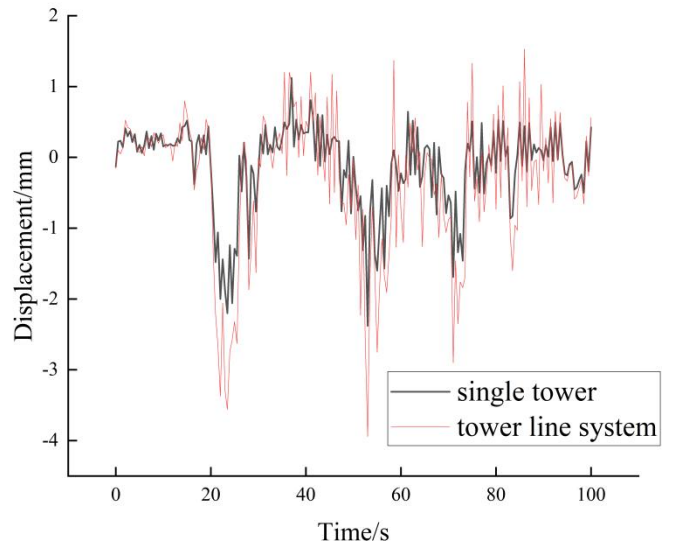
Fig. 7 The representative node of the top of single tower and tower line system under 90°

It can be seen from the figure 7 that under the most unfavorable wind direction of 90°, the displacement of the

top of the tower line system is larger than that of the single tower. The maximum displacement of the single tower is -2.38mm, and that of the tower line system is -3.94mm. The maximum displacement of the tower line system is 66% higher than that of the single tower. The reason is that the area under wind load increases due to the lines in the tower line coupling system, resulting in the mean displacement of the tower line system is greater than that of the single tower. It shows that the coupling effect of the tower line system has a great influence on the wind-vibration response of the tower line system, and the coupling effect of the tower line system should be considered in the study of transmission lines.

IV. STABILITY ANALYSIS OF ICE-COVERED TOWER LINE SYSTEM UNDER THE MOST UNFAVORABLE WIND ANGLE

A. Static analysis of tower line system with different ice thicknesses under designed maximum wind speed

In order to obtain the maximum ice cover thickness of transmission tower failure caused by the designed maximum wind load, the static stability analysis of the tower line system was carried out, and the wind pressure at each section of the tower was calculated and then loaded to the corresponding section of the finite element model for static stability analysis.

The ice thickness-displacement curve of the top point of the transmission tower is shown in the figure 8.
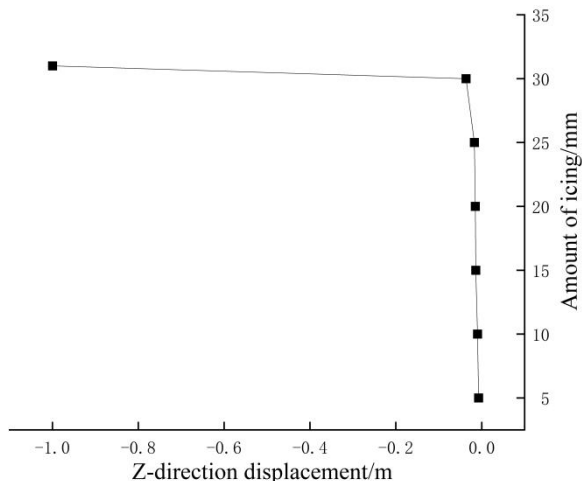
Fig. 8 Ice thickness-displacement curve at the top point of transmission tower

As can be seen from the figure 8, under the effect of 25m/s pseudo-static wind and 30mm ice cover thickness, the curve tends to be horizontal, and the structure has reached a state of instability according to the B-R criterion. In order to verify the instability, found that when 31mm ice cover thickness is applied, and large displacement occurs to confirm the structural instability.

B. Evaluation of wind resistance of tower line system with different ice thickness under designed maximum wind speed

Under the action of design wind load, there is the risk of buckling buckling and instability of transmission tower.

It causes local instability, causing structural damage and even toppling the tower under strong wind conditions. In order to be more intuitive and simplify the calculation, the compression ratio of transmission tower members is defined in this method as a judgment for evaluating the local instability of transmission tower members.

$$\eta = \frac{\sigma}{\delta_y} \tag{9}$$

Where: σ is the compressive stress of the member calculated under wind load, δ_y is the yield strength of the member steel.

The compression ratio of the transmission tower member corresponds to the state of the transmission tower at this time, as shown in the table I.

Tab. I The Voltage Yield Ratio of the Transmission Tower Corresponds to the State

η	The state of the tower
$\eta \leq 0.5$	The tower body is secure
$0.5 < \eta < 0.85$	It's necessary to strengthen the transmission tower Due to its high possibility of instability
$\eta \geq 0.85$	The tower body is unstable, and it needs to be replaced

As can be seen from Figure 9 of the stress cloud diagram, the maximum stress of the tower line system lies in the direction of the tower leg of the leeward side hanging line.
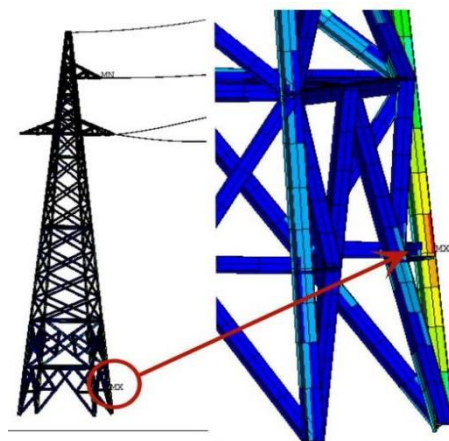
Fig. 9 The maximum stress of the tower line system

The maximum equivalent stress of the tower under different ice thicknesses was extracted, as shown in Figure 10.

As can be seen from Figure 10, when the ice thickness is 30mm, the maximum equal effect force of the transmission tower reaches 302MPa, while the material at the leg of the research tower body with the maximum force is Q345 and the yield strength is 345MPa. By comparison with Table 1, it can be seen that at this time, the transmission tower has a rod failure and is prone to collapse, which is consistent with the conclusion of B-R criteria.
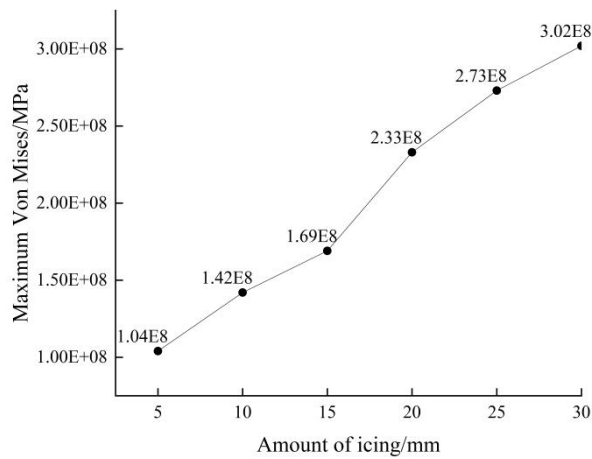
Fig. 10 The maximum equivalent stress of the tower under different ice thicknesses

To sum up, the first failure component of the terminal tower line system is located at the transmission line direction tower leg on the leeward side of the transmission tower. The collapse of the transmission tower is caused by the failure of local components at the tower leg, and this failure mode is caused by the instability of the compression member, which spreads from the local components to the whole transmission tower, and finally leads to the collapse accident induced by the instability of the whole structure of the transmission tower. The damage to the upper structure of the transmission tower leg is the most serious.

V. CONCLUSIONS

In this paper, a spatial finite element model of a T-connected four-tower three-line tower system in a 35kV wind farm is established, and the Kaimal spectrum and harmonic superposition method are used to simulate the pulsating wind. The ice-covered wind response of a single transmission tower and tower line system is analyzed, and the coupling between tower lines and the influence of ice cover on the wind-induced response of tower and tower in practical engineering is studied.

(1) Under wind load, the dynamic response of the pylon coupled system is stronger than that of a single tower, and the displacement response of the top of the pylon coupled system under the same wind direction Angle is greater than that of a single tower. 90° is the most unfavorable wind direction Angle, and the response of the pylon coupled system is the largest. Therefore, it is suggested that attention should be paid to the effect of the most unfavorable wind direction Angle in the structural design.

(2) Considering the influence of ice cover, the influence of different ice cover thicknesses on the tower line system is analyzed, and the effect of ice cover cannot be ignored in the design and operation of the terminal tower and the transmission tower in the middle section should have higher strength and stiffness.

(3) The maximum allowable ice thickness under the maximum design wind speed is obtained by using B-R criterion analysis, and the results are consistent with those obtained by using pressure rod instability or pull rod yield as the dynamic failure criteria of transmission tower members.

REFERENCES

[1] XIANG Zhengjian, WANG Lining, et. China's energy transition development under the great change[J]. International Petroleum Economics,2023,31(02)

[2] HUANG Xinbo, CAO Wen. Review of the disaster mechanism of transmission lines[J]. Journal of Xi'an Polytechnic University, 2017,31(05):589-605.

[3] WANG W M,LI H N,TIAN L. Progressive collapse analysis of transmission towerline system under earthquake[J]. Adv Steel Constr,2013,9:161-174.

[4] Analysis of Wind-Induced Response of a 500 kV Long-Span Transmission tower line System Crossing the Yangtze River[J]. Industrial Construction, 2022. 52(08):1-8.

[5] WANG Dahai, XIANG Xuzhi,et. Wind Tunnel Testing on Coupling Mechanism of Wind-induced Vibration of Transmission tower line[J]. System Power System Technology, 2022, 46(01).

[6] Jinma SHENG, et. Staric and dynamic stability analyses of new single-loop T-connection tower line system subjected to wind load[J]. Journal of Hefei University of Technology, 2022,45(04):464-468.

[7] YU Jiabao, ZHUO Yue, et. Analysis of Wind Vibration Response and Dynamic Instability of Large Crossing Transmission Tower Line System Between Islands[J]. Shandong Electric Power, 2024,51(01).

[8] TIAN L, MA R S,LI H N,et. Progressive collapse of power transmission tower line system under extremely strong earthquake excitations[J]. Int J Struct Stab Dyn,2016,16:1550030.

[9] LI X, LI H N, HUANG L Z. Nonlinear buckling analysis of collapsed steel tower for 220kV Guajing iced transmission line[J]. J Vib Shock,2009,28(5).

Equations of motion for supercoolded water droplets in atmospheric icing - an overview

Pavlo Sokolov[1], Muhammad S. Virk[1]

[1] *University of Tromsø – The Arctic University of Norway, Faculty of Engineering Science and Technology, Institute for Industrial Technology*

pavlo.sokolov@uit.no, muhammad.s.virk@uit.no,

Abstract— **Understanding the behavior of the supercoolded water droplets trajectories is crucial for correctly modeling atmospheric icing on structures. For a given spherical droplet in air, its behavior is governed by the equation of motion (EoM), known as Basset-Bousinnesq-Oseen (BBO) equation, for the flows at low Reynolds number, or, alternatively, the Maxey-Riley (MR) equation for the general case of a spherical particle suspended in a spatially nonuniform, time-dependent flow. Direct analytical and/or numerical evaluation of either equation is challenging due to presence of the term, which is singular under integration. This term represents the Basset force (also known as "history" term), which describes the force due to the lagging boundary layer development with changing relative velocity (acceleration) of bodies moving through a fluid. Generally, the Basset force can be disregarded during icing modeling, however its' importance when modeling arises when modeling atmospheric with low wind speeds, small droplet sizes and/or large characteristic dimensions of structures. Omission of the Basset force in such cases results is strongly underestimated mass of accreted ice. This paper discusses importance and the impact of the Basset term, along with overview of some selected analytical and numerical strategies which can be utilized in order to evaluate it.**

Keywords— **droplets motion; analytical; numerical; icing; Basset force**

I. Introduction

Atmospheric icing of structures is a hazardous phenomenon which may lead to many undesirable effects. The interest in modeling ice accretion on cylindrical objects primarily comes from preventing structural damage or collapse of objects such as overhead transmission lines or communication masts due to the accreted ice mass leading to dynamic instabilities. Ice mass accretion in these cases primarily comes from atmospheric icing such as in-cloud or precipitation icing. In studying these the prime interest lies in the parameterization of characteristics of the in-cloud droplet impingement on cylinders. The study of in-cloud icing is not a new scientific field, with some major milestones in terms of mathematical modeling of icing being works by Langmuir and Blodgett, 1944 [24], Cansdale and McNaugthon [5], Lozowski et al., 1979 [26], Stallabrass [42], Makkonen [29] and Finstad et al. [11]. The latter being independently verified by (Makkonen and Stallabrass [30] serves as a current benchmark model for atmospheric icing and it is part of governing standard ISO:12494 "*Atmospheric Icing of Structures*" [16]. The core of the Finstad et al. model uses a so-called "Median Volume Diameter approximation" (MVD) in order to parameterize the in-cloud droplet spectrum using this singular value, and an assumption that the cloud droplet distribution can be adequately represented by a uniform droplet distribution, where all the droplets have the same diameter, corresponding to cloud MVD. The verification of the concept was carried out by Finstad in their doctoral thesis [10], later expanded in paper of Finstad et al. [12] and based on the results of Makkonen and Stallabrass [30], it can be stated that the Finstad et al. model is applicable for the ranges of droplets overall collision efficiencies of $0.07 < E < 0.63$.

The main equation in the analytical modeling of atmospheric icing, which describes the rate of icing per unit time is given as [16]:

$$\frac{\mathrm{d}M}{\mathrm{d}t} = \alpha_1 \alpha_2 \alpha_3 wAv \tag{1}$$

In this equation, otherwise known as "*Makkonen model*" [31], A is the cross-sectional area of the object (with respect to the direction of the particle velocity vector, v), α_1 (also referred as E in literature and in here) is the collision efficiency, α_2 is the sticking efficiency, α_3 is the accretion efficiency. The correction factors α_1, α_2 and α_3 represent different processes that may reduce $\mathrm{d}M/\mathrm{d}t$ from its maximum value wAv. These correction factors vary between 0 and 1. Factor α_1 represents the efficiency of collision of the droplets, i.e. is the ratio of the flux density of the droplets that hit the object to the maximum flux density, which is a product of the mass concentration of the droplets, w, and the velocity, v, of the droplets with respect to the object.

Consequently, the collision efficiency α_1 is reduced from one, because small droplets tend to follow the air streamlines and may be deflected from their path towards the object, as shown in Fig. 1.
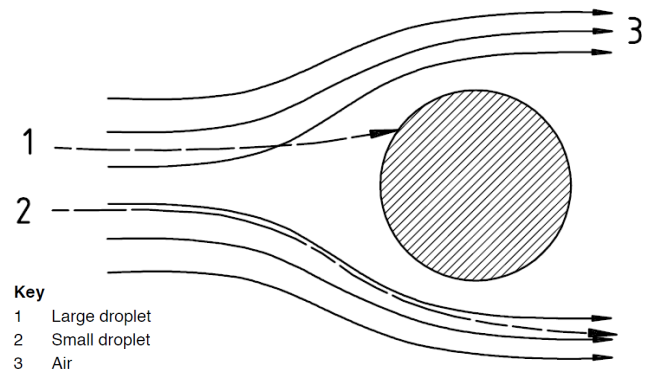
Fig. 1. Air streamlines & droplet trajectories around a cylindrical object [16].

In the broadest possible case of an arbitrarily given fluid flow, the "behavior" of water droplets can be explained using the definition of the Stokes number:

$$Stk = \frac{t_0 u}{L} \qquad (2)$$

where L is the characteristic length of the obstacle and t_0 is the relaxation time of the particle, which describes its exponential velocity decay due to influence of drag and it is defined as:

$$t_0 = \frac{\rho_p d_p^2}{18\mu_f} \qquad (3)$$

in which ρ_p is the particles density, d_p is the particle's diameter and μ_f is the absolute viscosity of the fluid. A particle with a low Stokes number follows fluid streamlines (perfect advection), while a particle with a large Stokes number is dominated by its inertia and continues along its initial trajectory, thus colliding with the object. As it can be seen from eqs. (2) and (3), larger particles, or those moving at higher velocities, will have higher Stokes number and thus – higher possibility of collision with the object, hence defining physical meaning of the collision efficiency.

However, in reality, the behavior of the droplet in actual flow is considerably more complicated than in this simplistic case, and the collision efficiency cannot simply be explained using only the definition of Stokes number, thus requiring the use of some sort of analytical and/or empirical formulations in order to calculate the overall collision efficiency. Presently, the overall collision efficiency formulation by Finstad et al. [11] is used in the ISO 12494 for calculation of α_1, which is itself is based on the earlier parameterization by Langmuir and Blodgett [24]. The key difference between these two models is a revision of droplet trajectories on a more modern machine, with more modern estimates of droplet drag coefficient, from experimental study of Beard and Pruppacher [3]. Moreover, Finstad simplified the elaborate scheme of Langmuir and Blodgett when it comes to correction of droplet's inertia parameter, due to non-Stokesian flow regime, which resulted in completely different parameterization for droplet collision efficiency [11].

In addition, the model is one of the more complete models featuring parameterizations of local collision efficiencies, droplets impact velocities and maximum impingement angles. Furthermore, the model provides the way of calculating the ice shapes on iced cylinder under assumption that developing ice layers will change the local collision efficiencies values and using variable ice density formulation of Makkonen [28], however, those calculations are absent from final published version [10], which made them somewhat preliminary in nature.

Finally, Finstad et al. [11] in their model discuss more complete droplet trajectory equations, following approach of (Oleskiw, 1982), which may be useful when potential flow approximation is not valid and viscous and boundary layer effects may be of importance. The model validation for cylinders and airfoils was done as part of doctoral thesis itself [10], subsequently, the validation for cylinders was independently carried out by Makkonen and Stallabrass [30], who recommended employing it over original Langmuir and Blodgett formulations in future studies. At present, this parameterization is the benchmark for calculation of droplet collision efficiencies on cylinders and it is an integral part of governing ISO standard – ISO 12494 *"Atmospheric Icing of Structures"* [16].

II. MATHEMATICAL OVERVIEW OF EXISTING ANALYTICAL THEORY OF ICING

The mathematical overview of the cloud impingement parameters calculations will start with the trajectory equations of the water droplet in the potential flow, as all analytical models which are based on the original Langmuir and Blodgett model, use or assume the same trajectory equations. These equations, in dimensionless form are given as [24]:

$$K v_x \frac{dv_x}{ds} = (C_D Re/24)(v_x - u_x) \qquad (4)$$

$$K v_y \frac{dv_y}{dy} = -(C_D Re/24)(v_y - u_y) \qquad (5)$$

$$dx/dt = -v_x \qquad (6)$$

$$dy/dt = v_y \qquad (7)$$

$$(Re/Re_\infty)^2 = (v_x - u_x)^2 + (v_y - u_y)^2 \qquad (8)$$

where the air velocity components for the potential flow around cylindrical objects are given as:

$$u_x = 1 + (y^2 - x^2)/(x^2 + y^2)^2 \qquad (9)$$

$$u_y = 2xy/(x^2 + y^2)^2 \qquad (10)$$

In the equations above, x and y are horizontal and vertical distances respectively, with origin taken from cylinder axis, where radius is equal to unity, quantities v_x and v_y denote horizontal and vertical component respectively of droplet velocity, u_x and u_y are horizontal and vertical component of air velocity respectively, Re_∞ denotes droplet's Reynolds number at freestream velocity, $(C_D Re/24)$ is the droplet drag coefficient, which is equal to unity, if Stokes law is obeyed; and greater than unity otherwise, and finally, K is the droplet's inertia parameter, defined as:

$$K = \frac{2\rho_p r_p^2 u}{9\mu_f C} = \frac{\rho_p d_p^2 u}{18\mu_f C} \qquad (11)$$

in which C is the characteristic length of the object, in case of cylinder $C = R$, where R is the cylinder radius. The droplet inertia parameter, K, can be recognized as the Stokes number from eq. (3), and, furthermore, with some manipulation it can be re-written as:

$$K = \frac{\rho_p d_p^2 u}{18\mu_f C} = \frac{t_0 u}{L} = \frac{\lambda_s}{L} \qquad (12)$$

The quantity $\lambda_s = t_0 u$ can be interpreted as the droplet's "range", i.e., the range which the droplet of the size d_p, released as projectile in the still air at velocity u would have before coming to rest, assuming Stokes' law is valid. If the Stokes flow is not valid, i.e., $(C_D Re/24) > 1$, the definition of the range parameter would not be valid, as higher droplet drag in ultra-Stokesian regime would reduce the actual value of droplet's range λ from that of λ_s for the case when Stokes' law is being valid. Therefore, a non-Stokesian drag correction factor must be introduced, defined as "range parameter" λ/λ_s

2 of 16

in [24]. Assuming Mach number much less than unity, the λ/λ_s ratio is calculated as:

$$\lambda/\lambda_s = \frac{1}{Re_\infty}\int_0^{Re_\infty}\frac{dRe}{(C_D Re/24)} \quad (13)$$

in which, the $(C_D Re/24)$ is the droplet drag coefficient as function of Re, and the integration variable Re is taken as relative droplet's Reynolds number with respect to the freestream. In their work, Langmuir and Blodgett used the following empirical fit for $(C_D Re/24)$:

$$(C_D Re/24) = 1 + 0.197 Re^{0.63} + 2.6 \times 10^{-4} Re^{1.38} \quad (14)$$

Having determined the λ/λ_s ratio, it is now possible to evaluate the "modified" inertia parameter K_0 with the λ/λ_s ratio included. Following Langmuir and Blodgett approach this is done as:

$$K_0 = (\lambda/\lambda_s)\left(K - \frac{1}{8}\right) + \frac{1}{8} \quad (15)$$

which is used in all subsequent calculations in Langmuir and Blodgett model [24], and this model derivatives in place of K. Upon closer inspection two potential issues are apparent.

First, is that the integral equation, from which the λ/λ_s ratio is obtained is not a straightforward calculation, usually requiring some approximations to it in order to be easily available, which may be valid only for certain ranges of droplet's Reynolds number Re. Some discussion about those approximations are given by, for example Ruff [40], Finstad [10], and Anderson [3]. Second, is that any sort of relation obtained as a result from the λ/λ_s integral calculation is intrinsically bound to the approximation for the droplet drag coefficient $(C_D Re/24)$ used, and thus, in return, depends on accuracy of experimental data and any parametric fits to it. The change of droplet drag coefficient $(C_D Re/24)$ parameterization was the major keystone of the works by [10] – [11], which, in essence, are a repeat of Langmuir and Blodgett calculations on more modern machine and with updated droplet drag coefficient expressions. For comparison purposes, these expressions are given as in [11]:

$$(C_D Re/24) = 1 + 0.102 Re^{0.955} \quad \text{for} \quad 0.2 \leq Re \leq 2.0$$

$$(C_D Re/24) = 1 + 0.115 Re^{0.802} \quad \text{for} \quad 2.0 \leq Re \leq 21.0$$

$$(C_D Re/24) = 1 + 0.189 Re^{0.632} \quad \text{for} \quad 21.0 \leq Re \leq 200.0$$

which are notably different from the empirical relations for $(C_D Re/24)$ used by Langmuir and Blodgett, and, as a result, part of the reason why the overall collision efficiency parameterization of Finstad et al., is markedly different from the rest of the models. Speaking about the overall collision efficiency parameterizations and the droplet impingement calculations, the cloud impingement parameters calculated in accordance with [10] are given as:

$$X(K,\phi) = \left[C_{X,1}K^{C_{X,2}}\exp\left(C_{X,3}K^{C_{X,4}}\right) + C_{X,5}\right] -$$
$$\left[C_{X,6}(\phi - 100)^{C_{X,7}} \times \left[C_{X,8}K^{C_{X,9}}\exp\left(C_{X,10}K^{C_{X,11}}\right) + C_{X,12}\right] \quad (16)$$

where X is either the overall collision efficiency E, the stagnation line collision efficiency β_0, the maximum impingement angle α_{max}, or the non-dimensional impact velocity V_0. The constants $C_{X,n}$ are listed in Table 1.

TABLE I. COEFFICIENT VALUES OF CLOUD IMPINGEMENT PARAMETERS [10].

Coefficient	$X = \beta_0$	$X = \alpha_{max}$	$X = E$	$X = V_0$
$C_{X,1}$	1.218	2.433	1.066	1.030
$C_{X,2}$	-6.70×10^{-3}	-4.70×10^{-3}	-6.16×10^{-3}	1.68×10^{-3}
$C_{X,3}$	-0.551	-0.375	-1.103	-0.796
$C_{X,4}$	-0.643	-0.576	-0.688	-0.780
$C_{X,5}$	-0.170	-0.781	-0.028	-0.040
$C_{X,6}$	3.05×10^{-3}	8.50×10^{-3}	6.37×10^{-3}	9.44×10^{-3}
$C_{X,7}$	0.430	0.383	0.381	0.344
$C_{X,8}$	2.220	1.757	3.641	2.657
$C_{X,9}$	-0.450	-0.298	-0.498	-0.519
$C_{X,10}$	-0.767	-0.420	-1.497	-1.060
$C_{X,11}$	-0.806	-0.960	-0.694	-0.842
$C_{X,12}$	-0.068	-0.179	-0.045	-0.029

In eq. (16) ϕ is the dimensionless Langmuir parameter, sometimes also referred as impingement parameter and is given as:

$$\phi = \frac{Re^2}{K} \quad (17)$$

Moreover, in order to calculate the cloud impingement parameters at following time steps, the accreted ice density and the iced diameter need to be obtained. The ice deposit diameter D_i of cylinder is calculated as [29]:

$$D_i = \left[\frac{4(M_i - M_{i-1})}{\pi\rho_i} + D_{i-1}^2\right]^{1/2} \quad (18)$$

where M is the accreted ice mass, per unit length, ρ is the ice density and subscript i indicates the time step. In analytical calculations the time step used is, $t = \omega/60$, where ω is the cylinder rotational speed in RPM. This is to ensure that the cylinder rotates at least $360°$ degrees along its longitudinal axis on each time step, in order to ensure that even ice deposit layer forms on the surface, in accordance with (Makkonen, 1984). The accreted ice density at any given time step is calculated as [29]:

$$\rho_i = 378 + 425\log_{10}(R_m) - 82.3\left(\log_{10}(R_m)\right)^2 \quad (19)$$

where, R_m is the Macklin density parameter, given as:

$$R_m = -\frac{V_0 d}{2t_s} \quad (20)$$

where d is the MVD in microns, V_0 is the impact velocity of the droplet in m/s and t_s is the surface temperature of the ice deposit in Celsius. In the case of dry growth, the surface temperature of the ice deposit can be obtained numerically as:

$$\frac{2}{\pi}Evw\left(L_f + c_w t_a - c_i t_s\right) =$$
$$h\left[(t_s - t_a) + \frac{kL_s}{c_p p_a}(e_s - e_a) - \frac{rv^2}{2c_p}\right] + \sigma\alpha(t_s - t_a) \quad (21)$$

where L_f and L_s are latent heats of fusion and sublimation respectively, c_w, c_i, and c_p are specific heats of water, ice and air respectively, p_a, e_s and e_a are air pressure, saturation water vapor pressures at surface and air temperatures respectively, h

is the overall heat transfer coefficient, $k = 0.62$, r is the recovery factor, with value of 0.79 being used for cylinder, t_s and t_a are surface and air temperatures in Celsius, σ is the Stefan-Boltzmann constant and $α = 8.1 \times 10^7$ K^3. More details on the terms of heat transfer and derivation of heat transfer equations are given in [29].

III. LIMITATIONS OF OVERALL COLLISION EFFICIENCY CALCULATIONS FOR LOW VALUES OF K

According to (Finstad et al. 1988a), they consider the lower limit of droplet inertia parameter being $K = 0.25$ in their model, below which Finstad et al. advise to recalculate the droplet trajectories using the appropriate drag coefficients for each droplet size in the spectra. All the previous discussion and formulae, which uses droplet diameter d_p in them, assume a median volume diameter (MVD) of the spectrum. MVD is such a value, for which half of the cloud droplet volume will be concentrated in droplets with larger or smaller diameters, respectively.

The usage of MVD originated from [24] and as later showed by [12] it is an ideal single-valued approximation for droplet spectra. The reason for this assumption is the difficulty, associated with measurements of distribution micron-sized droplets in nature. However, Jones et al. [19] has showed that MVD approximation may not always be valid and in natural conditions, such as on Mt. Washington in USA; and the use of a droplet distribution spectrum can yield significantly better results over a monodisperse distribution when comparing ice accretion data on a multicylinder device. In such cases, where overall collision efficiency has to be evaluated with the full droplet spectrum, with the cloud impingement parameters of full spectrum can be evaluated as:

$$K_{spec} = \sum w_i K_i \qquad (22)$$

$$X(K, \phi)_{spec} = \sum w_i X(K_i, \phi)_i \qquad (23)$$

where w_i is fractional weight of bin i, subscript i refers to a given parameter calculated for bin i, while subscript $spec$ shows the spectrum averaged values. The spectrum values are linearly dependent on the per-bin values, as spectrum values, $X(K, \varphi)_{spec}$ are obtained by summation of per-bin values $X(K_i, \varphi)_i$ using LWC fraction w_i as a weighting constant. Conversely, per bin values are dependent as square of bin's MVD, and independent of φ as it can be seen from the structure of it in eq. (17). Such dependence may result in a significant change of cloud impingement parameter values, when droplet distribution spectrum is changed, even in the case where different droplet distributions have matching MVD value of the entire spectrum.

Another common issue with the calculations of the could impingement parameters using the full droplet distribution spectrum is that the droplet spectra information is typically unavailable, especially for the icing in natural conditions. However, this can be circumvented to an extent, by using "synthesized" droplet distribution spectra, known as Langmuir distributions. The most commonly used Langmuir distributions are given in Table 2 in terms of diameter ratios. All Langmuir distributions have the same value of MVD along with 'distribution A' being monodispersed. These droplet distributions progressively get "wider" as the ratio of

diameters increases, meaning that for distributions with higher value of diameter ratios, the diameters of bins will become progressively smaller or larger, when compared with "preceding" distribution. For the droplet spectrum, each bin collision efficiency is calculated independently and then weighted using the LWC fraction, in order to obtain the overall collision efficiency of the entire spectrum.

TABLE II. LANGMUIR DISTRIBUTIONS.

LWC	B	C	D	E	F	G	H	J
0.05	0.56	0.42	0.31	0.23	0.18	0.13	0.10	0.06
0.1	0.72	0.61	0.52	0.44	0.37	0.32	0.27	0.19
0.2	0.84	0.77	0.71	0.65	0.59	0.54	0.50	0.42
0.3	1.00	1.00	1.00	1.00	1.00	1.00	1.00	1.00
0.2	1.17	1.26	1.37	1.48	1.60	1.73	1.88	2.20
0.1	1.32	1.51	1.74	2.00	2.30	2.64	3.03	4.00
0.05	1.49	1.81	2.22	2.71	3.31	4.04	4.93	7.34

The Langmuir distributions B–E were initially presented in [24] as a mathematical approximations of the droplet distribution spectra in fog and rising clouds on Mt. Washington observatory. Later, Howe [15] presented "wider" droplet distributions F – J, based on previous observations on Mt. Washington observatory, in order to adequately capture bimodal and trimodal droplet distributions, which are expected to happen in nature.

Speaking about ice accretion in natural conditions in the limit of the droplet inertia parameter $K \leq 0.25$, Fig. 2 shows the distribution of accreted ice masses compared to the calculated values of the droplet inertia parameter K for the icing site on Ålvikfjellet, Norway.
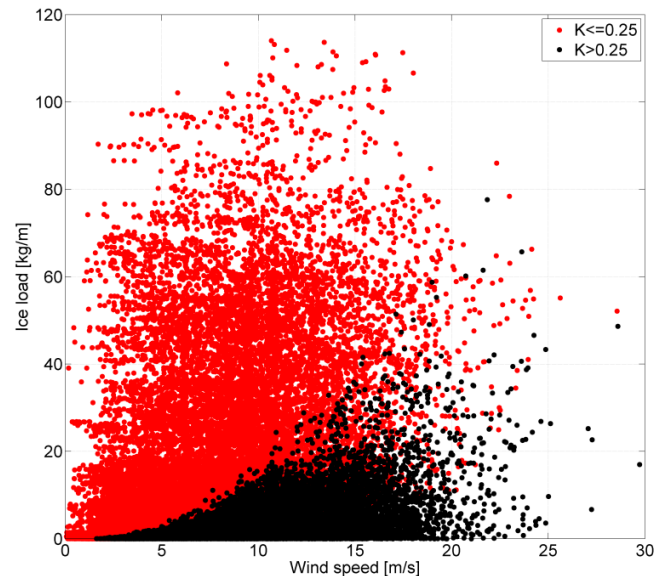
Fig. 2. Hourly data of modeled ice load and wind speed for the single conductor test span at Ålvikfjellet, 1085 m.a.s.l. Based on WRF data for the time period 1979 – 2017. Only points with LWC above 0.2 gm^{-3} are included. Red colors indicate when the Stoke's number falls below the critical limit of K ≤ 0.25. From Nygaard et al. [36].

As it can be seen from the Fig. 2, the majority of icing events on the Ålvikfjellet test span have values of the droplet inertia parameter $K \leq 0.25$, thus placing them outside the valid range of the analytical icing modeling methodology of ISO

12494. Thus, as per recommendation of Finstad et al. [11] one must calculate the cloud impingement parameters including full droplet distribution spectra along with all applicable drag terms. The effects of such modifications to the analytical modeling procedure of ISO 12494 will be showcased one-by-one.

IV. CALCULATIONS USING LANGMUIR SPECTRA

In order to showcase the effect of droplet distribution spectrum on the cloud impingement calculations, one known experimental case has been chosen from Sokolov and Virk [43]. The operating conditions for it are given in Table 3 and the calculated value of K is 0.3, which is very close to the current limit value.

TABLE III. OPERATING CONDITIONS.

Parameter	Value
Cylinder diameter (mm)	30
Air velocity (m/s)	4
Air temperature (°C)	−5
Icing duration (min)	30
LWC (g/m³)	0.4
Rotational speed (RPM)	5

In the calculations it is assumed that the circular cylinder is of the unit length and that the operating air pressure is equal to the one standard atmosphere. Furthermore, for this particular case, the information on the droplet distribution spectra is available. This droplet distribution spectrum is given in Figure 3 and Table 4.

TABLE IV. EXPERIMENTAL DISTRIBUTION.

Bin (µm)	Bounds (µm)	LWC fraction
5	0.61-5	0.0045
10	5 - 10	0.1138
15	10 - 15	0.1893
20	15 - 20	0.2902
25	20 - 25	0.1510
30	25 - 30	0.0935
35	30 - 35	0.0537
40	35 - 40	0.0419
45	40 - 45	0.0339
50	45 - 50	0.0277
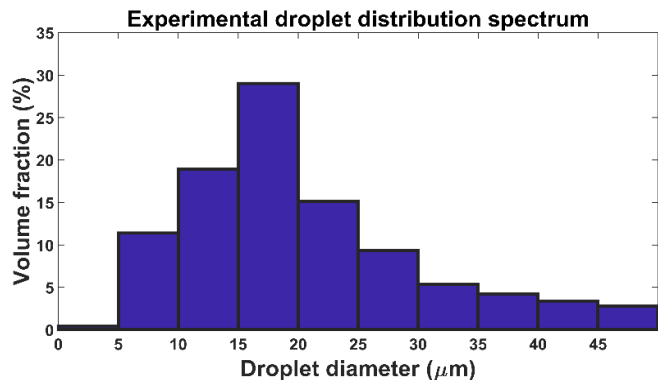
Fig. 3. Experimental distribution.

The calculated MVD of the experimental droplet distribution spectrum is 18.73 µm. Moreover, as it can be seen from expression for K in eqs. (11) and (12), in calculations with the distribution spectrum, each bin in it will have its own value of K, as function of dp_i, and, at least for some of these bins, the value of inertia parameter K_i can be below 0.25. In these cases, again, recalculation of droplet trajectories is needed, or alternatively, the values of overall and local collision efficiencies, impact velocities and maximum impingement angles can be constrained, i.e. $E = \beta_0 = v_0 = \theta = 0.01$, for $K_i \le 0.17$, as per [10], however, this approximation can only provide rough estimates, with another possibility being reading the values for those parameters from proper K and φ curves, as given by Finstad et al. [11]. For simplicity, the constraint of $X_i(K_i, \varphi)_i = 0.01$ for $K_i \le 0.17$ is used in the calculations, and the results of these calculations, in graphical form, are given in Fig. 4.

Stagnation line collision efficiencies for 30 mm cylinder

Spectrum averaged stagnation line collision efficiencies for 30 mm cylinder

Overall collision efficiencies for 30 mm cylinder

Spectrum overall collision efficiencies for 30 mm cylinder

Maximum impingement angles for 30 mm cylinder
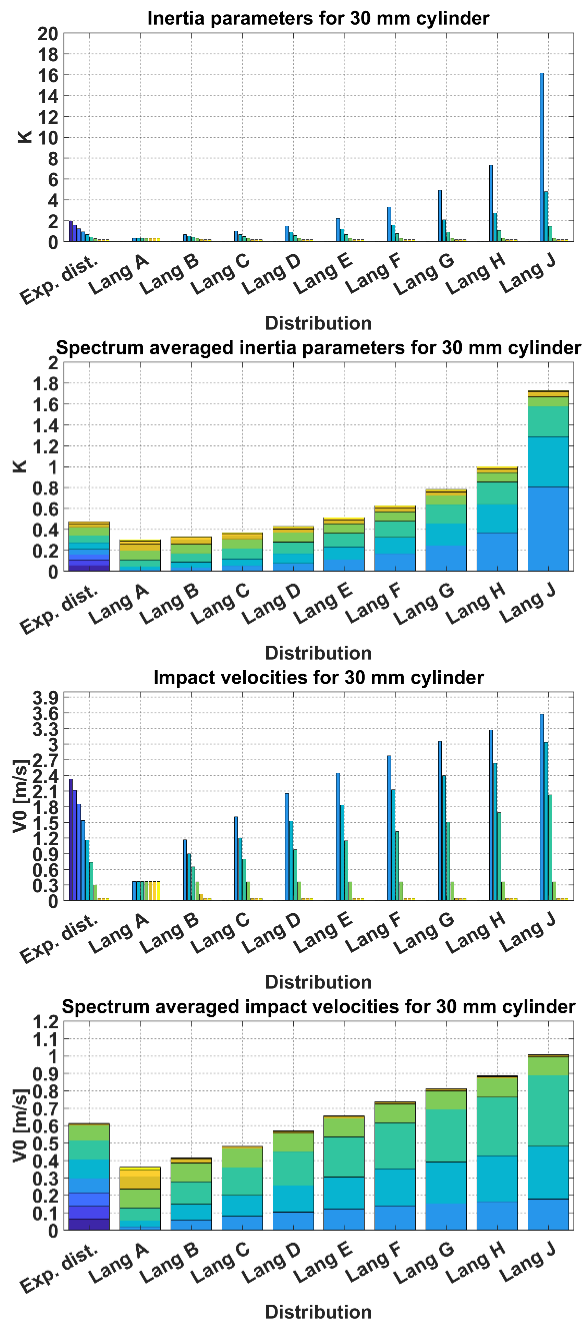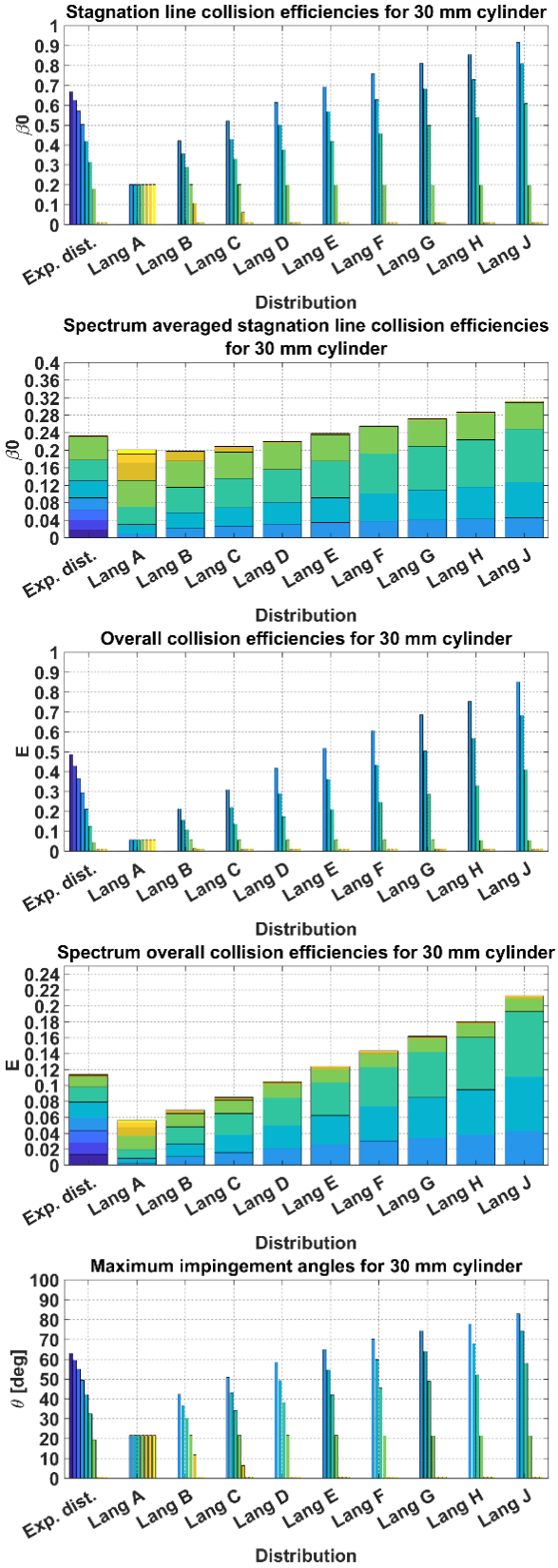
Fig. 4. The values of cloud impingement parameters in the analytical model on per-bin basis (left) and spectrum-averaged values (right).

Fig. 4 shows the values for inertia parameter (K), normalized impact velocities at stagnation line in m/s (V_0), stagnation line local collision efficiencies (β_0), maximum impingement angles (θ) and overall collision efficiencies (E), respectively for all distributions. The "*spectrum averaged*"

graphs present the spectrum averaged values of the respective parameter and how much each distribution contributes towards the average value with the exception of maximum impingement angles. The color code of Fig. 3 should be read as follows: each unique color represents a single bin from any given distribution used from Fig. 2 or Table 2. The right-hand side of Fig. 4, which shows the "spectrum-averaged" values in a "stacked" way "stacks" the individual values of each bin, weighted by its respective LWC in order to obtain the "spectrum-averaged" values, where again, each unique color represents the contribution of individual bin towards the final value of a given cloud impingement parameter.

As it can be inferred from Fig. 4 the primary reason different droplet distribution spectra affect the cloud impingement parameters is that they in an essence act as a significant increase in the value of the droplet inertia parameter K, with "wider" distributions providing the bigger increase. However, for bins with smaller diameters, the limit of $K_i = 0.17$ is quickly reached and for distribution D and above the three smallest bins are consistently below the constraint value, meaning that limits of $E = \beta_0 = v_0 = \theta = 0.01$ are enforced and there is virtually no distinction between them. Although, the change in parameters of interest between larger droplet diameters in said distributions, when compared to the MVD value of 18.73 microns is of considerably larger magnitude, which smooths the impact of the constrained values to a large extent.

V. THE "HISTORY TERM"

If even higher accuracy in cloud impingement calculations is needed, one must calculate the droplet trajectories for cases of interest. Moreover, in such cases the overall collision efficiency parameterization by Finstad et al. cannot be readily used, and one would need to find the value of E, based on the discussion in preceding section, or, following geometric interpretation of E, given by Finstad et al. [11].

As discussed previously, Finstad uses drag coefficient values reported by Beard and Pruppacher [4] over the original Langmuir and Blodgett empirical formulation for drag coefficient, while keeping the trajectories equations consistent with Langmuir and Blodgett [24]. Furthermore, Finstad et al., [11] argue that buoyancy and gravitational effects on drag can be ignored, however, the vorticity diffusion from accelerating droplets' surface and the induced mass increase of the droplet due to accelerating air in immediate surroundings are important factors of non-steady state drag term, and are represented in the model by so-called "history" term, following approaches of Pearcey and Hill [38] and Landau and Lifshitz [23], in the equations of motion of linearly accelerating particle in the flow. This term is defined as:

$$F = -\frac{18\rho_f}{(2\rho_p + \rho_f)d}\left(\frac{\mu}{\pi\rho_f}\right)^{\frac{1}{2}}\int_{-\infty}^{t}\frac{du(\tau)}{d\tau}\frac{d\tau}{\sqrt{t-\tau}} \qquad (24)$$

where ρ_p and ρ_f are particle and fluid densities, respectively, and $u(\tau)$ is droplet's absolute velocity. The "history term" aka. the Basset force and the history force is a kind of viscous force, which arises due to acceleration between continuous (fluid) and dispersed (particles, droplets) phases and the development of the boundary layer near the interfacial surface (*between the continuous and the dispersed phase*). The Basset

force describes the force due to the lagging boundary layer development with changing relative velocity (acceleration) of bodies moving through a fluid. Due to this lagging the relative velocities and the accelerations of bodies moving through a fluid at a time t depend on *all* previous changes in velocities and accelerations. In short, the current velocities and accelerations depend on the *history* of velocities and accelerations, hence why the name "history term". The Basset force is commonly neglected for practical reasons; however, it can be substantially important for particle motion when a high acceleration rate for the particle is encountered. The question is – how exactly important is the Basset force? Finstad et al., referring to Norment, suggest that history term becomes of importance in cases where:

$$N_A = d \left| \frac{du(\tau)}{d\tau} \right| \frac{1}{v^2} > 0.01 \qquad (25)$$

In which N_A is acceleration modulus. If the acceleration modulus threshold is exceeded, it needs to be incorporated into the trajectory equation. This trajectory equation, following Oleskiw [37] is in non-dimensional vector form, with added buoyancy and gravitational effects, reads as [37]:

$$\frac{d\bar{v}_p}{dt} = \frac{2\left(\rho_p - \rho_f\right)}{\left(2\rho_p + \rho_f\right)} \bar{g} - \frac{3\rho_f(C_D Re/24)}{4r_p\left(2\rho_p + \rho_f\right)} \left|\bar{v}_p - \bar{v}_f\right|\left(v_p - v_f\right)$$
$$- \frac{9\rho_f}{\left(2\rho_p + \rho_f\right)r_p} \sqrt{\frac{\mu_f}{\pi\rho_f}} \int_{-\infty}^{t} \frac{d\bar{v}_p}{d\tau} \frac{d\tau}{\sqrt{t - \tau}} \qquad (26)$$

where v_p is particle's (droplet's) velocity, r_p is the particles radius, v_f is the fluid (air) velocity and g is the gravitational acceleration. All quantities in this equation are non-dimensional and the first term on the right-hand side is the buoyancy and gravitational acceleration of the droplet, second term is the steady viscous drag, and the third term can be recognized as history term. The Langmuir and Blodgett and, by extension, Finstad droplet trajectory equations are the simplified version of the preceding equations, and these can be written as given in [36]:

$$\frac{d\bar{v}_p}{dt} = \frac{3\rho_f(C_D Re/24)}{8\rho_p R_p} \left|\bar{v}_p - \bar{v}_f\right|\left(v_p - v_f\right) \qquad (27)$$

where, R_p is particle radius. Finstad and Langmuir and Blodgett ignore the buoyancy and the gravitational acceleration of the droplet (as it is a very small value; for example, for a 20 μm diameter droplet the terminal velocity in air is about 1.2 mm/s [11]); along with the history term, as during the time of their publication [24] there was no way to approximate the history term. The reason for this is twofold.

First, the history term belongs to the group of integral equations called the Volterra integral equations. The Volterra integral equations concern themselves with solving for an unknown function x, while having a given function f. In the case of history term, the given function f is the droplet's accelerations while the unknown function x is the changes in the relative velocities due to the Basset force. It is not known how this unknown function x "looks" or "behaves" (which

properties it possesses). Second, the Basset force contains the term $\sqrt{t - \tau}$ in the denominator of the integrand. During the integration when $\tau \to t$ the denominator turns to zero and the integrand is singular under integration. Thus, it is not possible to integrate the history term in the "standard" way and some mathematical manipulations and approximations are needed.

Technically, the trajectory equation in eq. (26), is a simplified version of another equation, called the Basset-Boussinesq-Oseen equation (BBO equation). The Basset–Boussinesq–Oseen equation describes the motion of – and forces on – a small particle in unsteady flow at low Reynolds numbers. The BBO equation is written as:

$$\frac{\pi}{6}\rho_p d_p^3 \frac{dv_p}{dt} = \underbrace{3\pi\mu d_p\left(v_f - v_p\right)}_{\text{I}} - \underbrace{\frac{\pi}{6}d_p^3\nabla p}_{\text{II}} + \underbrace{\frac{\pi}{12}\rho_f d_p^3 \frac{d}{dt}\left(v_f - v_p\right)}_{\text{III}}$$
$$+ \underbrace{\frac{3}{2}d_p^2\sqrt{\pi\rho_f\mu} \int_{t_0}^{t} \frac{1}{\sqrt{t - \tau}}\left(v_f - v_p\right)d\tau}_{\text{IV}} + \underbrace{\sum_k F_k}_{\text{V}} \qquad (28)$$

The BBO equation is, in essence, is the Newton's second law, in which the left-hand side is the rate of change of the particle's linear momentum, and the right-hand side is the summation of forces acting on the particle. Or in other words – it is a conservation of momentum equation. The terms on the right-hand side are, respectively, the:

- I – Stokes' drag.
- II – Froude–Krylov force due to the pressure gradient in the undisturbed flow. The Froude–Krylov force is the force introduced by the unsteady pressure field generated by *undisturbed* waves. The Froude–Krylov force does, together with the diffraction force, make up the total non-viscous forces acting on a floating body in regular waves. The diffraction force is due to the floating body disturbing the waves.
- III – added mass. Added mass or virtual mass is the inertia added to a system because an accelerating or decelerating body must move (or deflect) some volume of surrounding fluid as it moves through it. Added mass is a common issue because the object and surrounding fluid cannot occupy the same physical space simultaneously. For simplicity this can be modeled as some volume of fluid moving with the object, though in reality *all* the fluid will be accelerated, to various degrees.
- IV – the history term aka. the Basset force.
- V – other forces acting on the particle, for example, gravity, etc.

The BBO equation describes is valid for any particle moving in any fluid, i.e., water droplet in air, sand particle in ocean, dust in air, etc. The issue with the BBO equation is term I, the Stokes drag. It makes it valid only for the droplet's Reynolds number $Re_d < 1$. A modification to the BBO equation, which makes it work with the flows, in which the droplet's Reynolds number $Re_d > 1$ is called a Maxey-Riley equation (MR equation). It describes the same physical phenomena as the original BBO equation, and it is given as Maxey and Riley [32] with original notation preserved:

$$m_p \frac{dV_i}{dt} = (m_p - m_F)g_i + m_F \frac{Du_i}{Dt}\bigg|_{\mathbf{Y}(t)} - \frac{1}{2}m_F \frac{d}{dt}\left\{V_i(t) - u_i[\mathbf{Y}(t), t] - \frac{1}{10}a^2\nabla^2 u_i\bigg|_{\mathbf{Y}(t)}\right\}$$

$$- 6\pi a\mu\left\{V_i(t) - u_i[\mathbf{Y}(t), t] - \frac{1}{6}a^2\nabla^2 u_i\bigg|_{\mathbf{Y}(t)}\right\} - 6\pi a^2\mu \int_0^t d\tau \left(\frac{d/d\tau\left\{V_i(\tau) - u_i[\mathbf{Y}(\tau), \tau] - \frac{1}{6}a^2\nabla^2 u_i\big|_{\mathbf{Y}(\tau)}\right\}}{[\pi v(t-\tau)]^{1/2}}\right) \quad (29)$$

The initial conditions are that the sphere is introduced at $t = 0$ and that there is no disturbance in the flow prior to this. The derivation of Maxey-Riley equation is based on a consistent treatment of the inertia and pressure gradient terms for a sphere in a nonuniform flow field. The inclusion of velocity gradients leads to modifications of the added mass terms, the Stokes drag, and the Basset history term due to curvature in the velocity profile; while in the low Reynolds number limit there is no force due to shear or particle spin. Besides the Faxen terms, the equation of motion differs from previous versions in the form of the fluid acceleration term $m_f \, Du_i/Dt$ as opposed to $m_f \, du_i/dt$. In general, the values of the values of these two derivatives, one following a fluid element and the other following the particle can differ substantially [32]. Due to its complicated nature, the MR equation is best viewed as providing the relative velocity of the particle in the fluid, and thus it is useful to define the quantity:

$$\mathbf{W}(t) = \mathbf{V}(t) - \mathbf{u}[\mathbf{Y}(t), t]$$

And thus, in terms of the relative velocity $\mathbf{W}$ the equation of particle motion is then [32]

$$\left(m_p + \frac{1}{2}m_F\right)\frac{dW_i}{dt} + 6\pi a^2\mu \int_0^t d\tau \frac{dW_i}{dt}[\pi v(t-\tau)]^{-1/2} + 6\pi a\mu W_i =$$

$$-m_p \frac{du_i}{dt} + m_F \frac{Du_i}{Dt} + (m_p - m_F)g_i + a^3\pi\mu\nabla^2 u_i + \frac{1}{20}a^2 m_F \frac{d}{dt}\left(\nabla^2 u_i \mid_{\mathbf{Y}(t)}\right) + \pi\mu a^4 \int_0^t d\tau \frac{d}{d\tau}\left(\nabla^2 u_i \mid_{\mathbf{Y}(t)}\right)$$

$$\times [\pi v(t-\tau)]^{-1/2} \quad (30)$$

The terms on the right-hand side in eq. (30) may be regarded as source terms for the relative velocity. Approximate results for $\mathbf{W}(t)$ may be derived depending on the accuracy required by the physical problem under consideration. In some instances, an estimate of particle velocity is only required to within some percentage of the fluid velocity scale U_0, in which case many terms are negligible. In other instances, the longer-term drift of the particle is required and the relative velocity has to be estimated to within a certain fraction of itself, or if the particle is settling under gravity, to within a fraction of the mean settling velocity. In this case many of the terms in eq. (30), such as fluid acceleration, is important. The accuracy to which $\mathbf{W}(t)$ is estimated will also determine the time scale over which the equation of motion can be applied, as errors accumulate in time and in an inhomogeneous flow the particle can eventually drift into regions of very different flow characteristics.

While the MR equation is the most complete equation for the droplet motion, the issues with its implementation for purposes of calculating droplet trajectories under the conditions of the atmospheric icing on structures remain. Chiefly of those is again the "history term" contained in the MR equation.

However, the problem of estimating the "history term", also referred as Basset force is not only limited to the field of atmospheric icing, and it extends to the multiphase flows in general. Therefore, significant amount of knowledge has been accumulated on the topic in the last 35 years, following the publication of the Finstad et al. model, since Tatom in 1988 [44] realized that the history term is equivalent to a half derivative of Riemann-Liouville type, which allowed researchers to more efficiently approach the problem, using the techniques developed for the fractional derivatives. The history term poses the main difficulty in a solution/numerical integration of MR equation. There are basically three issues with it: (i) the singularity of the kernel $K(t - \tau)$, (ii) the fact that MR equation is an implicit integro-differential equation due to the appearance of dv/dt on the right-hand side and (iii) the high computational costs for a numerical integration.

The first point (i) is the most involved one and can be addressed by a special quadrature scheme. The implicitness of (ii) is not a major issue and can be addressed rather easily as we will see. The last point (iii) stems from the necessity to recompute the history force – an integral over all previous time-steps – for every new time-step. Therefore, the computational costs grow with the square of the number of time-steps and can become quite substantial for long integration periods. This difficulty is inherent to the dynamics governed by the history force and cannot be addressed without further approximations. Note however that a higher order scheme reduces the number of necessary time-steps and therefore diminishes the problem of high computational costs indirectly.

Following the Moreno-Casas and Bombardelli [35], the broad classification of methods of approximating the "history terms" can be classed as follows:

- Modifying the kernel in the history term from eq. (24) in order to avoid singularity and make it applicable to use with finite Reynolds number.
- Numerical approximations to the history term, such as open-quadrature formulas, semi-derivative approaches, trapezoidal-based methods etc.
- Transforming the droplet trajectory equation, given in eq. (26) into higher-order Ordinary Differential Equation (ODE), explicit in velocity.

Out of these methods the most straight-forward approach is the modification to the kernel of the Basset force, as, for example done by Mei and Adrian [32]. This modified kernel,

called the "Basset kernel" is given as (original notation preserved):

$$K(t-\tau) = \left\{ (t-\tau)^{1/(2c_1)} + \left[\sqrt{\frac{\pi}{\nu}} \frac{|\vec{u_f} - \vec{u_p}|^3 (t-\tau)^2}{2\nu f_h} \right]^{1/c_1} \right\}^{-c_1} \quad (31)$$

$$f_h = \left[0.75 + c_2 \left(\frac{2a|\vec{u_f} - \vec{u_p}|}{\nu} \right) \right]^3 \quad (32)$$

where ν is the kinematic viscosity and $c_1 = 2$ and $c_2 = 0.105$.

However, there are two primary issues with the modified Basset kernel. First, Mei and Adrian [33] specify that their kernel is applicable to the droplet's Reynolds number $Re \approx 1$. Second, is the decay rate of the Basset kernel. The original "history term" has a decay rate proportional to the $t^{-1/2}$. In comparison, the Mei and Adrian kernel decays at much faster rate, being proportional to the t^{-2}. This means that the particle "history" becomes less dependent on the previous states as $t \to \infty$.

Another possible approach to the calculation of the "history term" is using transformation technique in order to transform the Volterra integrodifferential equation (which encodes the history term) into a higher order ODE. For example, Vojir and Michaelides [46] use an integrodifferential transformation, thus the droplet's equation of motion is converted into an explicit equation with respect to the particle relative velocity. This is accomplished by transforming the equation in the Laplace space, rearranging the resulting algebraic equation and transforming back into the time variable [34]. The resulting equation is a second-order differential equation in dimensionless form and reads as follows:

$$\frac{d^2 w_i}{dt^2} + \lambda \left(2c_1 - \frac{9\beta\lambda\Delta_H^2}{2} \right) \frac{dw_i}{dt} + \lambda^2 c_1^2 w_i = -\lambda(1-\beta)\frac{d^2 u_i}{dt^2} - \lambda^2(1-\beta)c_1 \frac{du_i}{dt} + \lambda^2(1-\beta)\Delta_H \sqrt{\frac{9\beta}{2\pi}} \int_0^t \frac{\frac{d^2 u_i}{d\tau^2}}{(t-\tau)^{0.5}} d\tau$$

$$+ \lambda\Delta_H \sqrt{\frac{9\beta}{2\pi t}} \times \left\{ \lambda(1-\beta)u'(0) - \lambda(1-\beta)G_i + c_1 \frac{w_{i0}}{2t} \right\} + \lambda^2(1-\beta)c_1 G_i + \lambda^2 w_{i0} \frac{9\beta\Delta_H^2}{2} \delta(t) + \lambda\Delta_H \sqrt{\frac{9\beta}{2\pi}} w_{i0}\delta^2(t) \quad (33)$$

where δ is the Dirac delta function, β is the ratio of the fluid-to-particle density, subscript i indicates the direction (x, y or z), w is the relative velocity calculated as $w_i = v_i - u_i$ and G_i is a non-dimensionalized gravitational acceleration. The eq. (33) is non-dimensionalized using the droplet characteristic time from eq. (3) and the characteristic velocity of the fluid U_0. Moreover, λ is the added mass term, $\lambda = 1/(1 + \frac{1}{2}\Delta_A\beta)$, with the Δ_A, Δ_H and c_1 being added mass, history and drag term coefficients, given as:

$$c_1 = 1 + 0.15 Re^{0.667} \quad (34)$$

$$\Delta_A = 2.1 - \frac{0.132 Ac^2}{(1 + 0.12 Ac^2)} \quad (35)$$

$$\Delta_H = 0.48 + \frac{0.5 Ac^3}{(1 + Ac)^3} \quad (36)$$

in which the particle Reynolds number Re and the acceleration number Ac are defined as:

$$Re = \frac{d|U_0 w_i|\rho_f}{\mu} \quad (37)$$

$$Ac = \frac{18\beta}{Re} \left| \frac{dw_i}{dt} \right| \quad (38)$$

In the eq. (33) the initial conditions for the velocity and the acceleration are:

$$w_i(0) = w_{i0} \quad (39)$$

$$\frac{dw_i}{dt}(0) = -\lambda c_1 w_{i0} - \lambda(1-\beta)u_i'(0)$$

$$+ \lambda(1-\beta)G_i - w_{i0}\lambda\Delta_H \sqrt{\frac{9\beta}{2\pi}}\delta(t) \quad (40)$$

The Dirac delta appears in the above equations always in conjunction with the initial relative velocity w_{i0} only. This is a manifestation of the fact that if the particle is introduced in the flow with a finite relative velocity at time $t = 0$, then an impulse acts upon it as a result of the fluid's reaction. In the case of zero initial relative velocity, which is of interest in most practical cases, the transformed equation becomes:

$$\frac{d^2 w_i}{dt^2} + \lambda \left(2c_1 - \frac{9\beta\lambda\Delta_H^2}{2} \right) \frac{dw_i}{dt} + \lambda^2 c_1^2 w_i = -\lambda(1-\beta)\frac{d^2 u_i}{dt^2} -$$

$$\lambda^2(1-\beta)c_1 \frac{du_i}{dt} + \lambda^2(1-\beta)\Delta_H \sqrt{\frac{9\beta}{2\pi}} \int_0^t \frac{\frac{d^2 u_i}{d\tau^2}}{(t-\tau)^{0.5}} d\tau$$

$$+ \lambda\Delta_H \sqrt{\frac{9\beta}{2\pi t}} \times \left\{ \lambda(1-\beta)u'(0) - \lambda(1-\beta)G_i + c_1 \frac{w_{i0}}{2t} \right\} \quad (41)$$

Equations (33) and (41) are explicit in w_i. Their numerical solution may be obtained by any standard numerical solution technique, explicit or implicit, and normally does not require iterations. They also have the additional advantage that the history integral term contains the second derivative of the fluid velocity only. Therefore, their solution requires less computational memory than other proposed methodologies, discussed previously. The disadvantage of the equations is that they are second-order differential equations and that they contain more terms than the other methods for computing the Basset force. In addition, it's not immediately clear, from a physical perspective, how to treat the term $d^2 u_i/d\tau^2$ in the integrand in the eqs. (33) and (41), as the fluid velocity components in eqs. (9) and (10) in the Finstad model only depend on the coordinates x and y.

When it comes to the numerical approximations of the "history term" most approaches have a few key similarities, namely, in order to circumvent the singularity problem,

numerical schemes need to be constructed to explicitly modify the integrand, or simply to change the upper limit of integration and separate the Basset term in two parts, while at the same time yielding solutions to the Basset integral with temporal accuracy larger than that obtained by the quadrature methods. One example of such approach is the numerical scheme of van Hinsberg et al. [47]. Van Hinsberg et al.

$$\int_{t_0}^{t} K(t-\tau)\frac{d}{dt}\left(f(\tau)\right)d\tau = \frac{4}{3}\frac{d}{dt}\left(f(t_0)\right)\sqrt{h} + \frac{d}{dt}\left(f(\tau_N)\right)\frac{\sqrt{h}\left(N-\frac{4}{3}\right)}{(N-1)\sqrt{N-1}+\left(N-\frac{3}{2}\right)\sqrt{N}}$$
$$+\sqrt{h}\sum_{k=1}^{N-1}\frac{d}{dt}\left(f(\tau_k)\right)\left(\frac{k+\frac{4}{3}}{(k+1)\sqrt{k+1}+\left(k+\frac{3}{2}\right)\sqrt{k}} + \frac{k-\frac{4}{3}}{(k-1)\sqrt{k-1}+\left(k-\frac{3}{2}\right)\sqrt{k}}\right) \quad (42)$$

where $f(\tau)$ is an arbitrary test function describing the relative velocity between the fluid and the particle, h is the time step for the computation and $\tau_k = t - kh$, with $k = 0, 1, 2, \ldots, N$.

While the approach, presented above, is rather straightforward, there is a few issues with it, or similar numerical scheme, when applied to the droplet trajectory calculations in the field of atmospheric icing on structures. First, the typical approximation for the $f(\tau)$ used is a simple polynomial or trigonometric expression, for example $f(\tau) = \tau^n/n$ or $f(\tau) = \cos(\tau)$ [35], [47]. The usage of such functions simplifies the resulting calculation procedure, for example in case of trigonometric function the result of the integration will be a Fresnel integral. Such simple approximation and their validation make sense for gravity or advection-driven flows, like channel flows, sediment flows, or settling particles for which these approximations were developed. However, the question remains how applicable these types of approximations for the atmospheric ice accretion, where the particle trajectory is governed by the balance of inertia and drag forces.

Daitche has proposed [8] a generalized numerical scheme to compute the history term integral to arbitrarily high degree of accuracy. Daitche in his scheme uses the dimensionless MRE of the following form [8]:

$$\frac{1}{R}\frac{dv}{dt} = \frac{Du}{Dt} - \frac{1}{S}(v-u) - \sqrt{\frac{3}{\pi}\frac{1}{S}}\int_{t_0}^{t}\frac{1}{\sqrt{t-\tau}}\left(\frac{dv}{dt}-\frac{du}{dt}\right)d\tau \quad (43)$$

The two dimensionless parameters are the density parameter

$$R = \frac{3m_f}{m_f + 2m_f}$$

and a ratio of the particle's viscous relaxation time and the characteristic time of the flow T

$$S = \frac{1}{3}\frac{a^2/\nu}{T}$$

Daitche considers the history force integral in the following form

$$\int_{t_0}^{t} K(t-\tau)\frac{d}{d\tau}f(\tau) + K(t-t_0)f(t_0) = \frac{d}{dt}\int_{t_0}^{t} K(t-\tau)f(\tau)d\tau \quad (44)$$

where $f(\tau) = v - u$. This form of history force integral features an additional term for the case of different initial velocity

between the phases. Therefore, the Maxey-Riley equation can be written in the following form, which is now also valid for initial conditions with $v(t_0) \neq u(t_0)$,

$$\frac{1}{R}\frac{dv}{dt} = \frac{Du}{Dt} - \frac{1}{S}(v-u) - \sqrt{\frac{3}{\pi}\frac{1}{S}}\frac{d}{dt}\int_{t_0}^{t}d\tau K(t-\tau)(v-u) \quad (45)$$

Note, that at this point the standard kernel of the history force is equal to a fractional derivative of the Riemann-Liouville type [8]:

$$\left(\frac{d}{dt}\right)^{1/2}f(t) \equiv \frac{1}{\sqrt{\pi}}\frac{d}{dt}\int_{t_0}^{t}\frac{1}{\sqrt{t-\tau}}f(\tau)d\tau \quad (46)$$

Thus, the numerical methods developed by Daitche can be also considered as higher order methods for the numerical computation of fractional derivatives and the solution of fractional differential equations. The general procedure of Daitche is to first split the integral into intervals of length h

$$\int_{t_0}^{t} K(t-\tau)f(\tau)d\tau = \sum_{i=0}^{n-1}\int_{\tau_i}^{\tau_{i+1}} K(t-\tau)f(\tau)d\tau \quad (47)$$

then to approximate $f(\tau)$ in every of the intervals with a polynomial and finally to compute the appearing integrals analytically. The order of the polynomial will determine the order of the scheme.

For the simplest case of a linear approximation leading to an order one scheme. By approximating $f(\tau)$ linearly in the interval $[\tau_i, \tau_{i+1}]$ [8]:

$$f(\tau) = f(\tau_i) + \frac{f(\tau_{i+1})-f(\tau_i)}{h}(\tau-\tau_i) + \mathcal{O}(h^2) \quad (48)$$

and

$$\int_{\tau_i}^{\tau_{i+1}} K(t-\tau)f(\tau)d\tau = \left(f(\tau_i) + \mathcal{O}(h^2)\right)\int_{0}^{h} K(t-\tau_i-\tau)d\tau$$
$$+ \frac{f(\tau_{i+1})-f(\tau_i)}{h}\int_{0}^{h}\tau K(t-\tau_i-\tau)d\tau \quad (49)$$

Summing up the terms for each of the intervals one obtains a formula for the whole integral, e.g. for the standard kernel

10 of 16

$$\int_{t_0}^{t} \frac{f(\tau)}{\sqrt{t-\tau}} d\tau = 2f(t_0)\sqrt{t-t_0} + \frac{4}{3} \sum_{i=0}^{n-1} \frac{f(\tau_{i+1}) - f(\tau_i)}{h}$$

$$\times \left((t-\tau_i)^{\frac{3}{2}} - (t-\tau_{i+1})^{\frac{3}{2}} \right) + \mathcal{O}(h^2)\sqrt{t-t_0} \qquad (50)$$

Note that no singular or diverging expressions appear. For this it is crucial to approximate only $f(\tau)$ with polynomials, but not the whole integrand. The quadrature scheme is linear in f and can thus be expressed as a weighted sum. Such a form is best suited for a numerical evaluation as modern processors/compilers can optimize this kind of operations rather well [8]. For further details and for general second- and third-order schemes, readers are advised to read the original source in full [8].

VI.   PRASATH ET AL. AND URIZARNA-CARASA ET AL.

In their work Prasath et al. [39], show that the Maxey-Riley equation in its entirety can be exactly mapped as a forced, time-dependent Robin boundary condition of the one-dimensional diffusion equation, and solved using the Unified Transform Method also known as Fokas method [13].

Prasath et al. obtain the exact solution for a general homogeneous time-dependent flow field and apply it to a range of physically relevant situations. In a particle coming to a halt in a quiescent environment, they show that the Basset history force speeds up the decay as stretched exponential at short time, while slowing it down to a power-law relaxation, $\sim t^{-3/2}$, at long time, which is consistent with the observations made by Mei and Adrian [33]. Moreover, in an example of a particle settling under gravity, Prasath et al. show that the particle tends to relax more slowly to its terminal velocity ($\sim t^{-1/2}$), whereas this relaxation would be expected to take place exponentially fast if the history term were to be neglected. An important example in their work is the growth of cloud drops is by the gravitational settling of larger drops through an environment of smaller droplets, and repeatedly colliding and coalescing with them. Using their solution, Prasath et al. estimate that the rate of growth rate of a cloud droplet can be gross overestimated when history effects are not accounted, which can be of an utmost importance when modeling atmospheric icing due to freezing rain. Finally, Prasath et al. solve exactly the particle motion in a plane in Couette flow and show that the location (and final velocity) to which a particle relaxes is different from that due to Stokes drag alone.

For a general flow, their approach makes possible a numerical scheme for arbitrary but smooth flows without increasing memory demands and with spectral accuracy. This scheme allows for a method to include the Basset history term in calculations up to spectral accuracy, without astronomical storage costs. Furthermore, their results indicate that the Basset history can affect dynamics significantly.

Most studies concerning particle dynamics in the low Stokes number limit include contributions from the Stokes drag, the second term on the right-hand side in the MR equation, but the Basset history integral is often neglected. The coefficient of this term is $\mathcal{O}(S^{1/2})$ relative to the Stokes drag, so it is nominally negligible at small Stokes number, but the factor it multiplies could cause the effect to become important in physical flows. A major hurdle in evaluating the Basset history integral is the continually increasing memory

cost associated in computing this term. The inclusion of the Basset history integral renders the MR equations to not represent a dynamical system, i.e., the future evolution of the particle motion depends not only on the current position and velocity, but also on the entire solution up to that time. Standard analytical techniques such as performing a Laplace transform are in general not useful in solving this system the full nonlinear equation. Moreover, even for the linear case, inverting the Laplace transform of a general function $G(t)$ with a kernel of the form $\sim 1/\sqrt{t}$ multiplied to it does not lead to an explicit function of t. Thus, the need arises to resort to quadrature schemes or approximations to the history kernel, as have been discussed and showcased in this paper previously.

Since these techniques approximate the history-kernel and are not aimed at obtaining the true asymptotic behavior, they neglect the aforementioned (and most bothersome) singular contributions at $t = 0$, which is a valid assumption when particles and fluid have the same initial velocity, which we emphasize, may not hold in many physical situations. By construction, the approximate schemes mentioned are polynomial order accurate. Instead, Prasath et al. do not approximate the history force kernel, they reformulate the equations of motion of the particle with the nonlocal history-dependence into a *local* problem for an extended dynamical system. In other words, they represent the entirety of the MR equation as a boundary condition to the one-dimensional diffusion equation. The extended dynamical system couples these three quantities in time [39]:

- the position of the particle,
- the velocity of the particle
- and the field satisfying the diffusion equation (which effectively contains the history term).

The reformulation allows for explicit solutions for spatially uniform fluid flows, with the additional benefit of being local. This allows for construction of numerical schemes that alleviate the issue of rising memory storage, due to necessity of storing all previous time steps from beginning. Since the effect of the Basset history integral is accounted for in terms of a dynamical variable, the method of Prasath et al. may also be employed in large simulations with restarts, which the first published method supporting a restart of simulations featuring Basset force in them.

Prasath et al. consider the MR equation in the following form in Lagrangian coordinates [39]:

$$\dot{\mathbf{y}} = \mathbf{v}(t) \qquad (51)$$

$$R\dot{\mathbf{v}} = \frac{D\mathbf{u}}{Dt} - \frac{1}{S}(\mathbf{v} - \mathbf{u}) - \sqrt{\frac{3}{\pi S}} \times$$

$$\left\{ \frac{1}{\sqrt{t}} \left(\mathbf{v}(0) - \mathbf{u}(0) \right) + \int_0^t \frac{(\dot{\mathbf{v}}(s) - \dot{\mathbf{u}}(s))}{\sqrt{t-s}} ds \right\} \qquad (52)$$

$$\beta \equiv \frac{\rho_p}{\rho_f}, \quad S \equiv \frac{1}{3} \frac{a^2/\nu}{T}, \quad R \equiv \frac{(1+2\beta)}{3} \qquad (53)$$

where $\mathbf{y}, \mathbf{v}$ are the vector position and velocity respectively of the particle, and $\mathbf{u}$ represents the (possibly spatially and temporally dependent) fluid velocity. Dots represent Lagrangian derivatives in time t and D/Dt represents the material derivative with respect to the fluid velocity; ρ_p, ρ_f are

11 of 16

the particle and fluid density, respectively, R is the effective density ratio including added-mass effects, and S the Stokes number (droplet inertia parameter), defined here as the ratio of particle relaxation timescale to flow timescale.

By utilizing the Fokas method, Prasath et al. modify the MR equation as the 1D diffusion equation on a half-line of '*pseudo*'-space x with a Dirichlet boundary condition given by $g_0(t)$ at $x = 0$ and let $q(x, t)$ be the variable that gets diffused. Note that x is a fictitious space, not to be confused with the physical space represented by y, hence why x is a pseudo-space. It is used only to establish the relationship between the Basset history integral and the Neumann boundary condition for the diffusion equation. This problem can be formulated in a time-interval $(0; T]$ as:

$$q_t = q_{xx}, \qquad x > 0, t \in (0, T],$$
$$q(x, 0) = 0, \qquad x > 0,$$
$$q(0, t) = g_0(t), \qquad t \in (0, T],$$

Subscripts here denote partial derivatives and the evolution of the variable $q(x, t)$ takes place in the $x - t$ plane in the domain $\mathcal{D}$. As common for problems posed on a semi-infinite domain, we assume the field $q(x, t)$ vanishes as $x \to \infty$ uniformly for all t.

The modified MR equation given by Prasath et al. in a reference frame moving with the particle as [39]:

$$\dot{y} = q(0, t) + u \qquad (54)$$

$$q_t(0, t) + \alpha\, q(0, t) - \gamma q_x(0, t) = f(q(0, t), y, t) \qquad (55)$$

$$\alpha = \frac{1}{RS}, \quad \gamma = \frac{1}{R}\sqrt{\frac{3}{S}},$$

$$f(q(0, t), y(t), t) = \left(\frac{1}{R} - 1\right)\frac{Du}{Dt} - q(0, t) \cdot \nabla u \qquad (56)$$

where $q(0, t) = v(t) - u(y(t), t)$ is the relative velocity of the particle. In this choice of reference frame, with the history term on the left-hand side. A forcing function f which is local in time, whereas in the original form of MR equation the forcing appears in a non-local manner. The $q(0, t)$ and $q_x(0, t)$ represent the Dirichlet and Neumann condition of a field satisfying the diffusion equation, there is now a need to consider the following boundary-value problem:

$$q_t = q_{xx}, \qquad x > 0, t \in (0, T],$$
$$q(x, 0) = 0, \qquad x > 0,$$
$$q_t(0, t) + \alpha\, q(0, t) - \gamma\, q_x(0, t) = f(q(0, t), y, t), \qquad t \in (0, T],$$
$$\dot{y} = q(0, t) + u(y(t)), \qquad t \in (0, T],$$
$$\lim_{t \to 0} q(0, t) = v_o$$
$$y(0) = y_0$$

The MR equation thus manifests itself as a non-linear modified Robin boundary condition to the diffusion equation. The $q(0, t)$ is not yet known on this axis, i.e., the particle velocity in the relative frame of reference, for which Prasath et al. derive an expression further in their work [39]. Higher order corrections in particle size, the Faxen correction, etc. can also be accommodated in the forcing expression, $f(q(0, t), y, t)$, however this is not accounted for in their work. Here u is a

known velocity field. In the general case, one would couple the MR equation with a fluid model (such as the Navier-Stokes equation) to simultaneously resolve particle locations and fluid velocities.

While Prasath et al. reformulation removes the integral term and memory effect and allows to use standard numerical techniques for partial differential equations to solve the MR equation. However, it requires dealing with an unbounded spatial computational domain. Prasath et al. also propose a numerical approach based on the integral form of the solution obtained by using Fokas's method [39]. An open-source reimplementation in Python of their numerical approach based on polynomial expansions was recently published by Urizarna-Carasa et al. [45]. However, their reformulation also opens up possibilities to apply other numerical techniques for partial differential equations to the MR equation. Recently, Jaganathan et al. [18] proposed another transformation of the closely related Maxey-Riley-Gatignol equation by embedding it into an extended state-space. This removes the non-locality in time and results in a dynamical system that can be solved with standard explicit numerical integrators.

To illustrate the opportunities offered by Prasath et al.'s reformulation, Urizarna-Carasa et al. [46] propose a finite difference method as solver for the MR equation. By modifying techniques developed by Koleva [22], Alshina et al., [2] and Fazio and Janelli [9] for solving initial-boundary value problems on infinite domains, they introduce a second and fourth order finite difference discretization. To efficiently deal with the nonlinearity at the boundary, Urizarna-Carasa et al. use implicit-explicit Runge-Kutta methods of order two and four, which avoid the need for an iterative nonlinear solver in every stage. Urizarna-Carasa et al. Python implementation of their finite difference approach [45], Prasath et al.'s algorithm [39] and Daitche's method [8], are to the author's knowledge, the only available algorithms that solve the MR equation without approximations to the kernel. Urizarna-Carasa et al. performed a comprehensive comparison of all three methods with respect to accuracy and computational efficiency for five different flow fields and particles of different size and density [46].

The reformulated MR equation in the [46] is exactly the same reformulated 1D diffusion equation of Prasath et al. with modified Robin boundary condition. The transformed MR equation is defined on a semi-infinite computational domain, which requires some caution when dealing with the right boundary condition. To discretize the MR equation in space, Urizarna-Carasa et al. propose two finite difference schemes [46]: the second order scheme by Koleva [22], based on the work Alshina et al. [2], and a novel fourth order approximation obtained by using compact finite differences for uniform grids proposed by Lele [25], and another technique based on the core idea in [9] to map equidistant nodes to the semi-infinite domain.

Urizarna-Carasa et al. [46] discretize the spatial domain with a quasi-uniform grid by defining a set of N uniform grid points $\xi_n = n/N$, $n \in \{0, 1, \ldots, N - 1\}$ in the interval $[0, 1)$. These are then mapped to $[0, \infty)$ via the logarithmic mapping:

$$x_n = x(\xi_n) = -c\ln(1 - \xi_n)$$

where c is a parameter that controls the distribution of nodes such that approximately half of the grid points are placed

within the interval [0, c] [9], [22]. Compared to the algebraic rule also proposed by Koleva and Fazio, the logarithmic rule produces a higher density of nodes around $x_0 = 0$. Since [46] aim is to approximate the boundary value $q(0, t)$, this is the region for which the highest accuracy is needed.

Discretizing the spatial derivatives in the MR equation together with expression for particle's velocity results in the semi-discrete system:

$$
\underbrace{\begin{bmatrix} \dot{q}(t) \\ \dot{y}(\mathrm{t}) \end{bmatrix}}_{=\dot{\eta}(t)} = \underbrace{\begin{bmatrix} & & & & & 0 & 0 \\ & A_s & & & & \vdots & \vdots \\ & & & & & 0 & 0 \\ 1 & 0 & 0 & \ldots & 0 & 0 & 0 \\ 0 & 1 & 0 & \ldots & 0 & 0 & 0 \end{bmatrix}}_{=A} \underbrace{\begin{bmatrix} q(t) \\ y(t) \end{bmatrix}}_{=\eta(t)}
$$
$$
+ \underbrace{\begin{bmatrix} v(q_0(t), y(t), t) \\ u(y(t), t) \end{bmatrix}}_{=\omega(q_0(t), \ y(t), \ t)} \tag{57}
$$

where the specific forms of $As \in \mathbb{R}^{N \times N}$ and $v(q_0(t), y(t), t) \in \mathbb{R}^N$ depend on whether the second or fourth order discretization is used [46]. Moreover,

$$
q(t) = \begin{bmatrix} q_0^{(1)}(t) & q_0^{(2)}(t) & q_1^{(1)}(t) & q_1^{(2)}(t) \ldots q_{N-2}^{(1)}(t) & q_{N-2}^{(2)}(t) \end{bmatrix}^T \tag{58}
$$

is a vector with both the horizontal and vertical components of the relative velocity at each node and

$$
\mathbf{q}(t) = \begin{bmatrix} q_0^{(1)}(t) & q_0^{(2)}(t) \end{bmatrix}^T \tag{59}
$$

Note that in a three-dimensional flow field one would have additional components $q_0^{(3)}(t)$, $q_1^{(3)}(t)$, etc.

The semi-discrete system in eq. (57) can be solved numerically by using a time stepping method. Urizarna-Carasa et al., [46] present the different time stepping schemes, such as: a second order implicit method (trapezoidal rule), a fourth order Diagonally Implicit Runge-Kutta (DIRK) method and Implicit-Explicit (IMEX) Runge-Kutta methods of order two and four.

The fully implicit Trapezoidal Rule applied to the semi-discrete system in eq. (57) yields (Urizarna-Carasa et al., 2024):

$$
\underbrace{\left(I - \frac{\Delta t}{2} A \right) \eta^{k+1}}_{= M_{left}} = \left(I + \frac{\Delta t}{2} A \right) \eta^k + \frac{\Delta t}{2} \left(\omega^k + \omega^{k+1} \right) \tag{60}
$$

where $\eta^k = \eta(t^k)$ and $\omega^k = \omega(q_0(t^k), y(t^k), t^k)$. Due to the ω^{k+1} term on the right-hand side this is an implicit system and requires a nonlinear solver [46]. They use the Newton-Krylov method LGMRES with M_{left} as preconditioner, implemented in the Newton-Krylov function of the `scipy.optimize` Python library. They take the solution of the explicit system

$$
\tilde{\eta}^{k+1} = (I + \Delta t A) \eta^k + \Delta t \omega^k \tag{61}
$$

as starting value for the Newton method.

As implicit time integrator Urizarna-Carasa et al. use the fourth order DIRK method ESDIRK4(3)6L[2]SA [21]. They follow a recommendation from Kennedy and Carpenter who recommend this method as the "*default method for solving stiff problems at moderate error tolerance*s" [21]. In ESDIRK methods, the first stage is explicit, but all other stages are implicit and require a nonlinear solver. As for the trapezoidal rule, they use the Python function `newton_krylov`. The previous stage is used as starting value.

In the semi-discrete system, only the ω term arising from the boundary condition is nonlinear. The A term is linear but stiff because of the discrete Laplacian. In order to avoid the overhead of having to use a fully nonlinear solver for every stage, Urizarna-Carasa et al. [46] propose to use an implicit-explicit Runge-Kutta method instead. This allows to treat the boundary term explicitly, thus avoiding a nonlinear solver per stage, while treating the stiff discrete Laplacian implicitly, which avoids a very harsh time step restriction. They use the second-order IMEX Midpoint rule by Ascher et al. [1] and the fourth order IMEX method combining the explicit ARK4(3)6L[2]SA–ERK and implicit ARK4(3)6L[2]SA–ESDIRK by Kennedy and Carpenter [21].

Urizarna-Carasa et al. [46] compare accuracy and computational cost of (i) the finite difference (FD) schemes described in their work in Section 2, (ii) the third-order direct numerical integrator proposed by Daitche [8] and (iii) their own implementation of Prasath's polynomial expansion method [13] for the reformulated problem in [39]. Urizarna-Carasa et al. [46] consider three flow fields where analytical solutions to the MR equation are available: a steady vortex, a quiescent flow and an unsteady but spatially homogeneous oscillatory background [39]. Additionally, they consider two unsteady and inhomogeneous flow fields where no analytic solution is known, the Bickley jet proposed by [41] with the parameters from [14] and an experimentally measured Faraday flow [6] – [7]. In the last two cases, they have measured the error against a high-resolution reference computed with Prasath et al.'s algorithm; and for each flow field, Urizarna-Carasa et al. investigate the accuracy of the methods when simulating trajectories of particles that are lighter ($R < 1$) or denser ($R > 1$) than the fluid or neutrally buoyant ($R = 1$) and cases with zero and non-zero initial relative velocity. Specifically, they use $R = 7/9$ where $\beta = 2/3$ and $R = 4/3$ where $\beta = 3/2$.

Urizarna-Carasa et al. [46] tested, Prasath et al.'s polynomial expansion, Daitche's direct integrator and their FD2 and FD4 methods for five different flow fields. For three of them, a quiescent flow, a steady, inhomogeneous vortex and a non-steady, homogeneous oscillating background, analytical solutions are available. For two unsteady, inhomogeneous fields, the Bickley jet and a Faraday flow interpolated from experimental data, and they compute a reference solution with Prasath et al.'s polynomial expansion approach with very high resolution.

Urizarna-Carasa et al. [46] numerical experiments suggest that:

1. Daitche's method is efficient for both zero and non-zero relative velocity and a good overall choice. However, it can become unstable for very small density ratios and Stokes numbers.
2. Prasath's polynomial expansion-based method is very accurate for both zero and non-zero relative velocity but computationally expensive.
3. The finite difference method of order two is efficient for both zero and non-zero initial relative velocity but, particularly in the latter case, Daitche's method is significantly more efficient.

4. The finite difference method of order four is efficient for zero initial relative velocity and could outperform both Daitche and FD2 + IMEX2 for the Faraday flow.

Daitche and FD2 + IMEX2 could both simulate 1 s trajectories in significantly less than one second runtime, illustrating their potential to provide solutions to the MRE in real-time. For the Faraday flow, for example, FD2 + IMEX2 could compute a 1 s trajectory with a relative discretization error of 7×10^{-5} in 8 ms. Urizarna-Carasa et al. suggest that an optimized implementation in a compiled language plus effective use of vectorization and multi-threading would make simulations even faster.

VII. DISCUSSION

The presented and discussed above analytical and numerical methods, such as methods and solutions by Daitche, [8], Prasath et al., [39], Urizarna-Carasa et al. [46] etc. allow for efficient handling of MR equation including the Basset history force in the numerical calculations. However, there are a few questions and items worth mentioning when it comes to applying these schemes to the multiphase flow conditions typical for atmospheric icing on structures.

First and foremost, the validation of all the presented scheme, be it for the cases of Couette flow, Faraday flow or Bickley jet were carried out in rather "quiescent" flow conditions. Generally, the issues with the present analytical and numerical solutions schemes in atmospheric icing of structures have issues with predicting the correct values of collision efficiencies for the values of droplet inertia parameter $K \leq 0.25$. For this value to arise the flow conditions should typically exhibit low wind speeds along with smaller droplet sizes. However, if the ice deposit growth significantly, or the structure being modeled has large characteristic dimensions at the start, the $K \leq 0.25$ situation can occur for high wind speed conditions, with fully turbulent flow. Thus, the question arises how well the presented scheme can handle such arbitrarily high wind speeds and/or particle diameters, bin terms of stability, convergence, total simulation time and memory usage.

Second, Urizarna-Carasa et al. [46] in their work show how strongly the initial conditions can affect the convergence of any tested scheme. While, in general, this should not be a major issue, questions still arise regarding compatibility of such calculations with the potential flow approximation, which was used to obtain the parametric fit of ISO 12494. In the authors opinion, if one has to resort to the full evaluation of the MR equation, including the Basset term, the better physical description of the general flow field is better. An example, for 2D general flows, would be using the exact analytical solutions of the Navier-Stokes equations as given by Ladyzhenskaya [20]. This combination should achieve highest physical accuracy without the need to implement (and test the performance) of different turbulence closure models.

Another potential question is the applicability of published models towards high values of density ratio parameter R. Most of the works cited here operate with neutrally buoyant and/or particle density ratios of approximately five, i.e. equivalent to a rock sinking in water. However, for typical icing event, the particle-to-fluid density ratio is of an order of $R = 700$–750, considerably higher than the one investigated by other authors, cited here. While Jaganathan et al. [17] claims that when it comes to the density ratio the Basset history force is as important as Stokes drag for marginally heavy ($R \sim 1$) particles, whereas it is negligible for particles much heavier than the fluid ($R \to \infty$), although the latter is valid only for a point particle.

Summarizing these comments, one can say that while there is a significant progress in handling of the Basset force has been accomplished, with some solutions even reaching spectral accuracy – i.e., the solution of Prasath et al. [39] for a neutrally-buoyant particles, there is still a verification gap present, particularly when it comes to the atmospheric icing on structures. In the authors' opinion, in order to address this knowledge gap, an experimental validation is needed, in which the particle trajectories have to be resolved. Such an experiment is well within reach for modern Particle Image Velocimetry (PIV) systems. Following the experimental work, analytical and numerical calculations of droplet trajectories using the MR equation with the Basset history term included. If the agreement between the experimental, analytical and numerical modeling will be adequate, a new derivation of the collision efficiency parameterization, in the similar spirit to the work of (Finstad, 1986) should be carried to finally answer the last remaining questions when it comes to the current state of affairs within the field of atmospheric icing on structures.

While there are no general guidelines as to how to carry such analysis, Jaganathan et al. [17] suggest the following:

- For short-duration simulations (small memory build-up), the quadrature approach with its scalable accuracy and nominal cost for short times is a reasonable choice.
- For kernels with fast decay (e.g. the kernel of [33]), window-based approaches are a computationally relieving alternative.
- For long-time and multi-particle simulations, where little can be said about the dynamics a priori, such as particles in turbulence, partial differential reformulation guarantees accuracy without growing-in-time computational costs.

VIII. CONCLUSION

In this paper the current state-of-affairs regarding analytical modeling and calculations of the cloud impingement parameters for the atmospheric ice accretion has been reviewed and discussed. The focus was on the mathematical model itself, its limitations and possible ways to overcome it. The main limitations of the current analytical icing parameterization of Finstad et al. are the underprediction of the accreted ice masses for the values of the overall collision efficiency $E < 0.10$ [16] and the breakdown of it for the values of the droplet inertia parameter $K \leq 0.25$ [11]. Finstad et al. recommend below this value to recalculate the droplet trajectories using full droplet distribution spectrum and all applicable drag terms. While the incorporation of the calculations with the full droplet distribution spectrum was performed successfully, even, to an extent, bypassing the limitation of unavailability of the droplet distribution spectra data in nature by using "synthesized" droplet distributions known as Langmuir distributions, example of which, along with the calculations are given in this paper.

When it comes to the inclusion of the full droplet drag terms there are additional issues the Finstad model and pertaining

calculations face. This primarily comes to the so-called "history term" which is a Volterra integrodifferential equation and is singular under integration. Several ways to overcome this has been investigated in literature, such as modified Basset kernels [33]; integro-differential transformation technique in order to transform the Volterra integrodifferential equation (which encodes the history term) into a higher order ODE, [48]; generalized quadrature scheme [8]; modified trazepoidal and window-based approaches [35], [47]; analytical solutions to MR equation by Prasath et al. [39] obtained using Fokas method to reformulate the problem; and Urizarna-Carasa et al. [46] numerical schemes expanding on the solution strategy of Prasath et al.

Especially, when it comes to latter mentioned works, they open possibility of deriving new parameterizations of the droplet impingement parameters up to and including the cases of $E < 0.10$ and $K \leq 0.25$, when coupled with more physically-complete description of the general flow field, such as the exact analytical solutions of the Navier-Stokes equations as given by Ladyzhenskaya [20]. This would allow one to effectively "solve" the atmospheric icing on structures, under the framework of ISO 12494. However, the exact implementation of these models for the multiphase flow in the atmospheric ice accretion on structures is most likely to be proven to be highly difficult. Not only the work of Finstad,[9] had to be essentially redone from scratch. Other important reasons include, but are not limited to, general lack of relevant experimental data, absence of studies which attempted to model the effect of Basset force for icing-related problems, lack of information about dependence of the particle-fluid relative velocity "correlation" for such types of problem, along with the strong dependence of it on the initial conditions, total flow time and the time step used in calculations.

REFERENCES

[1] Ascher, U. M., Ruuth, S. J., Spiteri, R. J. 1997. *Implicit-explicit Runge-Kutta methods for time-dependent partial differential equations, Applied Numerical Mathematics* vol. 25 pp. 151–167.

[2] Alshina, E.A., Kalitkin, N.N., Panchenko, S. 2002. Numerical solution of boundary value problems in unlimited area, *Matematicheskoe modelirovanie 14* (2002) 10–22.

[3] Anderson, D.N., 2004. Manual of Scaling Methods. NASA/CR—2004-212875

[4] Beard, K.V., Pruppacher, H.R., 1969. A Determination of the Terminal Velocity and Drag of Small Water Drops by Means of a Wind Tunnel. *Journal of Atmospheric Sciences* 26, 1066-1072. doi:10.1175/1520-0469(1969)026<1066:ADOTTV>2.0.CO;2

[5] Cansdale, J., McNaughtan, M., 1977. *Calculation of Surface Temperature and Ice Accretion Rate in a Mixed Water Droplet/ice Crystal Cloud.*

[6] Colombi, R., Rohde, N., Schlüter, M., von Kameke, A. 2022. Coexistence of inverse and direct energy cascades in Faraday waves, *Fluids 7* vol. 148.

[7] Colombi, R., Schlüter, M., v. Kameke, A. 2021 Three dimensional flows beneath a thin layer of 2d turbulence induced by faraday waves, *Experiments in Fluids* vol. 62 pp. 1–13.

[8] Daitche, A. 2013. Advection of inertial particles in the presence of the history force: Higher order numerical schemes, Journal of Computational Physics vol. 254 pp. 93–106.

[9] Fazio, R., Jannelli, A. 2014. *Finite difference schemes on quasi-uniform grids for BVPs on infinite intervals, Journal of Computational and Applied Mathematics* vol. 269 pp. 14–23.

[10] Finstad, Karen, J., 1986. Numerical and experimental studies of rime ice accretion on cylinders and airfoils. Ph.D. thesis. University of Alberta, Canada.doi:10.7939/R3N58CS1V.

[11] Finstad, K.J., Lozowski, E.P., Gates, E.M., 1988a. A computational investigation of water droplet trajectories. Journal of Atmospheric and Oceanic Technology, vol. 5, pp. 160-170. doi:10.1175/1520-0426(1988)005<0160:ACIOWD>2.0.CO;2

[12] Finstad, K.J., Lozowski, E.P., Makkonen, L., 1988b. On the median volume diameter approximation for droplet collision efficiency. *Journal of the Atmospheric Sciences* vol. 45, pp. 4008–4012.doi: 10.1175/1520-0469(1988)045<4008:OTMVDA>2.0.CO;2

[13] Fokas, A.S. 1997 A unified transform method for solving linear and certain nonlinear PDEs, *Proceedings of the Royal Society of London. Series A: Mathematical, Physical and Engineering Sciences* vol. 453 pp. 1411–1443.

[14] Hadjighasem, A., Karrasch, D., Teramoto, H., Haller, G. 2016. Spectral-clustering approach to Lagrangian vortex detection, *Physical Review E* vol. 93 063107.

[15] Howe, J.B. 1990. The rotating multicylinder method for the measurement of cloud liquid water content and droplet size. CRREL Report.

[16] ISO 12494:2001(E), 2001. *Atmospheric icing of structures. Standard. International Organization for Standardization. Geneva, CH*

[17] Jaganathan, D., Prasath, S.G., Govindarajan, R., Vasan., V. 2023a. The Basset–Boussinesq history force: its neglect, validity, and recent numerical developments. *Front. Phys.* 11:1167338. doi: 10.3389/fphy.2023.1167338

[18] Jaganathan, D., Govindarajan, R., Vasan, V. 2023b. Explicit runge-kutta algorithm to solve non-local equations with memory effects: case of the maxey-riley-gatignol equation. *arXiv:2308.09714.*

[19] Jones, K.F., Thompson, G., Claffey, K.J., Kelsey, E.P, 2014, Gamma Distribution Parameters for Cloud Drop Distributions from Multicylinder Measurements. *Journal of Applied Meteorology and Climatology*, vol. 53, pp. 1606 – 1617. doi: 10.1175/JAMC-D-13-0306.1

[20] Ladyzhenskaya, O.A. (1969) [1963], *The Mathematical Theory of Viscous Incompressible Flow, Mathematics and Its Applications, vol. 2 (Revised Second ed.),* New York; London; Paris; Montreux; Tokyo; Melbourne: Gordon and Breach, pp. xviii+224, MR 0254401, Zbl 0184.52603.

[21] Kennedy, C.A., Carpenter, M. H. 2016. Diagonally implicit Runge-Kutta methods for ordinary differential equations. A review, Technical Report.

[22] Koleva, M. N. 2005. Numerical solution of the heat equation in unbounded domains using quasi-uniform grids, in: *International Conference on Large-Scale Scientific Computing*, Springer, pp. 509–517.

[23] Landau, L., and E. M. Lifshitz, "*Fluid Mechanics,*" Pergamon Press, pp. 96-98, 1959.

[24] Langmuir, I., Blodgett, K., 1946. A Mathematical Investigation of Water Droplet Trajectories. Army Air Forces technical report 5418. Army Air Forces Headquarters, Air Technical Service Command.

[25] Lele, S.K. 1992. Compact finite difference schemes with spectral-like resolution, *Journal of computational physics* vol. 103 pp. 16–42.

[26] Lozowski, E.P., Stallabrass, J.R., Hearty, P.F., "The icing of an unheated, non-rotating cylinder in liquid water droplet-ice crystal clouds," National Research Council of Canada, Ottawa, CANADA, Mechanical Engineering Report LTR-LT-96, Feb. 1979.

[27] Lozowski, E.P., Stallabrass, J.R., Hearty, P.F., 1983a. The icing of an un-heated, nonrotating cylinder. part I: A simulation model. *Journal of Applied Meteorology* vol. 22, pp. 2053-2062 .doi:10.1175/1520-0450(1983)022<2053:265 TIOAUN>2.0.CO;2

[28] Lozowski, E.P., Stallabrass, J.R., Hearty, P.F., 1983b. The icing of an unheated, nonrotating cylinder. part II: Icing wind tunnel experiments. *Journal of Applied Meteorology* vol. 22, pp. 2063-2074. doi:10.1175/1520-0450(1983)022<2063:TIOAUN>2.0.CO;2

[29] Makkonen, L., 1984. Modeling of Ice Accretion on Wires. *Journal of Applied Meteorology*, vol. 23, pp. 929-939. doi:10.1175/1520-0450(1984)023<0929:MOIAOW>2.0.CO;2

[30] Makkonen, L., Stallabrass, J.R., 1987. Experiments on the cloud droplet collision efficiency of cylinders. J*ournal of Applied*

Meteorology vol. 26, pp. 1406-1411. doi:10.1175/1520 0450(1987)026<1406:EOTCDC>2.0.CO;2

[31] Makkonen, L., 2000. Models for the growth of rime, glaze, icicles and wet snow on structures. *Phil. Trans. R. Soc., Lond.* A 2000 358 2913-2939; DOI: 10.1098/rsta2000.0690. Published 15 Nov. 2000

[32] Maxey, M.R. and Riley, J.J., 1983. Equation of motion for a small rigid sphere in a nonuniform flwo. *Phy Fluids* 26:883–889.

[33] Mei, R., and Adrian, R.J., 1992. Flow past a sphere with an oscillation in the free-stream velocity and unstead drag at finite Reynolds number. *J Fluid Mech* 237:323-341.

[34] Michaelides, E.E., 1992. A novel way of computing the Basset term in unstead multiphase flow computations. *Physics of Fluids A: Fluid Dynamic*s 4, 1579; doi: 10.1063/1.858430

[35] Moreno-Casas, P.A., and Bombardelli, F.A., 2015. Computation of the Basset force: recent advances and environmental flow applications. *Envirion Fluid Mech*. DOI: 10.1007/s10652-015-9424-1.

[36] Nygaard, B.E.K., Byrkjedal, Ø., Iversen, E., Fredbo, M., Ágústsson, H., Welgaard, Ø., Gutman, I., Karlsson, T., Virk, M.S., Mc Innes, H., 2017. Development of a reliable modeling system for the calculation of rime ice loads on overhead transmission lines, in: *Proceedings of the 17th International Workshop on Atmospheric Icing of Structures*, Chongqing, China.

[37] Oleskiw, M.M., 1982. a Computer Simulation of Time-Dependent Rime Icing on Airfoils. Ph.D. thesis. University of Alberta, Canada.doi:10.7939/R3QR4NW8V.

[38] Pearcey, T and Hill, G.W., 1956. The accelerated motion of droplets and bubbles. *Aust. Jour. Phys.,* vol 9, pp. 19–30.

[39] Prasath, S.G., Vasan, V., Govindarajan, R. 2019. Accurate solution method for the Maxey–Riley equation, and the effects of Basset history, *Journal of Fluid Mechanics* vol. 868 pp. 428–460.

[40] Ruff, G.A., "Analysis and Verification of the Icing Scaling Equations," AEDC-TR-85-30, vol. 1 (rev), March 1986.

[41] Rypina, I., Brown, M. G., Beron-Vera, F. J., Koçak, H., Olascoaga, M. J., Udovydchenkov, I. 2007. On the Lagrangian dynamics of atmospheric zonal jets and the permeability of the stratospheric polar vortex, *Journal of the Atmospheric Sciences* vol. 64 pp. 3595–3610.

[42] Stallabrass, J.R., 1980. Trawler Icing: A Compilation of Work Done at N.R.C. (Givrage Des Chalutiers: Compilation Des Recherches Effectuees Au C.N.R.). Defense Technical Information Center.

[43] Sokolov, P., Virk, M. S. 2019. Droplet distribution spectrum effects on dry ice growth on cylinders. *Cold Regions Science and Technology* (ISSN 0165-232X), vol. 160, pp. 80 – 88, DOI: 10.1016/j.coldregions.2019.01.002

[44] Tatom, F. 1988. The Basset term as a semiderivative, *Applied Scientific Research* vol. 45 pp. 283–285.

[45] Urizarna-Carasa, J., Ruprecht, D., von Kameke, A., Padberg-Gehle, K. 2023. A Python toolbox for the numerical solution of the Maxey-Riley equation, *PAMM 22* e202200242.

[46] Urizarna-Carasa, J., Schlegel, L., Ruprecht, D. 2024. Efficient numerical methods for the Maxey-Riley equations with Basset history term. *arXiv:2403.13515v.*

[47] van Hinsberg, M.A.T., ten Thije Boonkkamp, J.H.M., Clercx, H.J.H., 2011. An efficient, second order method for the approximation of the Basset history force. J Comput Phys 230(4):1465–1478.

[48] Vojir, D.J., and Michaelides E.E., 1993. Effect of the History Term on the Motion of Rigid Spheres in a Viscous Fluid. *Int. J. Multiphase Flow*. Vol. 20, No. 3, pp. 547–556.

Experimental Investigation on Transient Heat Transfer in Supercooled Water during Recalescence

Masafumi Yamazaki[1], Joseph Gonzales[1], Hirotaka Sakaue[1]

[1] University of Notre Dame, Notre Dame, IN, USA

myamazak@nd.edu, jgonza21@nd.edu, hsakaue@nd.edu

Abstract— **Aircraft icing poses a threat to flight safety by inducing adverse aerodynamic effects. For recent aircraft, these effects are reduced by thermal icing-mitigation systems which consume a considerable amount of energy. For more efficient systems, an understanding of fundamental icing physics is necessary. When water freezes, there are two stages of solidification. One is the recalescence stage which takes place rapidly, on the order of 10 ms for a millimeter scale droplet. Due to its short time duration, investigation into icing physics during this stage is challenging. The transient heat transfer between freezing water and its contact surface is experimentally investigated using a luminescent technique. The temperature change on the contact surface was measured with the temperature-sensitive paint (TSP) and a high-speed camera at 4000 Hz. Images of the water undergoing a phase change was simultaneously measured at 1000 Hz.**

Keywords— *Aircraft icing, supercooled water, recalescence, luminescence*

I. Introduction

Since it was recognized in 1920s, aircraft icing has been a threat to safe aircraft operation [1]. It causes numerous adverse effects such as the degradation of aerodynamic performance and malfunction of flight instruments [2]. With great effort on the part of researchers, current aircrafts are equipped with icing mitigation devices. For these devices, thermal methods are the most common techniques for icing mitigation [3]. At the leading edge of wings, icing is prevented by applying heat from either exhaust gas (known as a bleed air system) or electrical heaters embedded underneath the leading-edge surface [4]. However, both methods require improvement in terms of their energy efficiency. The bleed air system utilizes 2.5 ~ 5.0 % of the core engine mass flow [5]. For electrical heaters, the power is provided by onboard generators [6]. Since energy is limited during flight, reduced energy consumption is ideal. With this in mind, most recent research aims to optimize relevant parameters such as heating temperature and the geometry of thermal systems based on conjugate heat transfer determined by computational fluid dynamics (CFD) simulations [3]. In order to calculate heat transfer at the surface of the wing, external air flow, supercooled water droplet impingement and resultant ice accretion, heat conduction through the skin, and internal flow are considered [4].

The heat transfer due to supercooled droplet impingement and ice accretion are calculated by aircraft icing simulations such as FENSAP-ICE and LEWICE. Those simulations first solve for the flow field around the wing, then calculate the trajectory of the droplets. Once the number, size, and velocity of the droplets impinging on segments of the wing are determined based on droplet trajectory, heat transfer on the surface of the wing is calculated using an energy balance model. In this phase, the messenger model is often used [7]. The messenger model treats the impinged droplets as water films and finds the amount of ice accreted in each segment, or section of the wing, as well as the amount of water that flows toward the trailing edge. Therefore, contributions of each individual supercooled droplet are not considered. Rather, such models only account for the aggregate icing behavior. To develop more precise models, a fundamental understanding of the freezing phenomena for a single supercooled droplet is necessary, and has been gaining attention [8].

The focus of recent investigations has been on determining the underlying physics behind droplet freezing. Droplet freezing can be divided into several stages in terms of temperature and phase transition [9]. Although the number and name of those stages differ depending on the field of study, there are two distinct stages: recalescence and secondary freezing [10]. The former is the time when the supercooled droplet turns into a mixture of water and ice [11]. The latter is when the mixture completely solidifies to become ice [12]. From an aircraft icing point of view, the heat transfer between droplets and the impinging surface is especially important during recalescence. Castillo et. al. measured the change of the temperature distribution on the surface of the droplet during recalescence on a substrate using an infrared camera [13]. By combining experimental results with numerical simulations, they concluded that most of the latent heat of fusion spread into the substrate, and only a part of it was released into the ambient air. They reported that the heat transfer from the droplet to the substrate was at least one order of magnitude larger than that to the ambient air. However, while the transient temperature distribution of the droplet surface has been experimentally observed, the transient temperature distribution of the substrate has still not been determined. The motivation of this research is to develop a measurement method which can measure temperature change in water as well as the contact surface simultaneously in a spatiotemporal manner. Based on the experimentally obtained temperature information in water and on the contact surface with the developed method, the transient heat transfer during the recalescence can be directly studied.

II. MEASUREMENT METHOD

A. Temperature and Phase Measurement in Water

During recalescence, there are temperature and phase changes occurring in water. Those changes take place in a

3-dimensional manner during the aircraft icing. Therefore, the requirements for an ideal measurement technique are 1) global rather than point measurement, 2) the ability to measure both temperature and phase, and 3) temporal resolution. Given those requirements, the use of a luminescent sensor was one of the promising candidate for temperature and phase change measurements during recalescence. Luminescent sensors are made by dissolving luminescent dye in water. When the luminescent water is excited by UV light, a part of the energy absorbed by the luminescent water is released as luminescence. With the appropriate selection for the luminescent dye, the intensity of the luminescence changes depending on temperature and phase in the case of water. In a recent study [14], a luminescent sensor that is capable of measuring temperature in both water and ice was developed. The luminescent sensor is used to measure the temperature and phase change when ice turns into water. Since the focus of this study is the recalescence, a new luminescent sensor was developed to have higher temperature sensitivity in water. The characterization of the developed luminescent sensor is given in Section III.

B. Temperature Measurement on Substrate

In order to address the transient heat transfer during the recalescence, the temperature measurement on the substrate is required in a spatiotemporal manner. In this work, a luminescent sensor, different from the kind used to measure temperature within the freezing water, was used to measure the temperature on the substrate. A luminescent dye with temperature sensitive luminescence was mixed into a coating. The coating was applied the opposite surface of the substrate from the one in contact with the luminescent water. In order to mitigate the temperature difference of the substrate between surfaces contacting the luminescent water and the coating, the aluminum foil was selected as the substrate. The temperature calibration of the coating is given in Section III.

C. Measurement Setup

Using the measurement techniques presented in the previous sections, the measurement setup was constructed as shown in Fig. 1. Aluminum foil was placed on a test stand and acted as the contact surface with the water. For the water temperature and phase change measurement, pyranine-based luminescent water was used. In order to capture the intensity change due to temperature and phase changes, images of excited luminescent water was recorded by a highspeed color camera. In this paper, the water was placed on the aluminum surface as a water film rather than a droplet. In this way, the propagation of the phase change of the water can be determined without the uncertainty caused by integration in the depth direction of recorded images. For the transient temperature distribution measurement on the substrate during the recalescence stage of freezing, Ruthenium-based temperature sensitive paint (TSP) was applied to the surface of the aluminum foil opposite the water film. Since the intensity of the emission of TSP changes with temperature, the substrate temperature can be measured from images captured by a high-speed camera.

In order to simulate the icing condition, the measurement setup was constructed inside an environment chamber. During the measurement, the temperature inside the environmental chamber was at -7.5 °C. At this temperature, the water film was supercooled. The luminescent water and TSP surface were excited by a 365 nm LED light and 445 nm laser, respectively. The luminescent response of the water was captured by a highspeed color camera at 1000 Hz and a highspeed camera recorded the TSP surface at 4000 Hz. Once the water film started freezing, a trigger signal was sent to two highspeed cameras to start recording at the same time. The phase change in the water film and temperature change of TSP were obtained from post image processing. In this way, the temperature and phase change of the water film as well as the temperature change on the substrate were measured simultaneously.
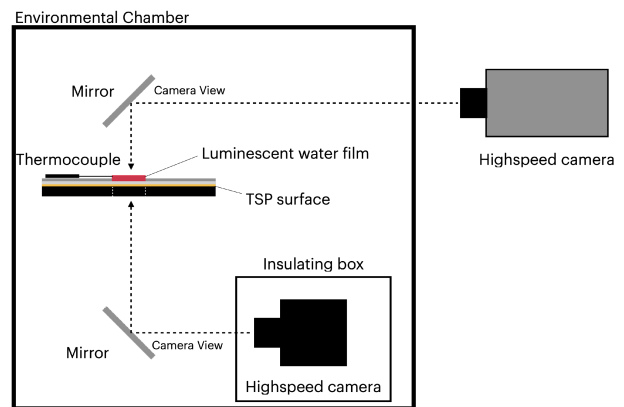
Figure 1. Schematic of experiment setup

III. Results and Discussion

A. Temperature Calibration of Luminescent Water

In order to measure the temperature of the luminescent water, the relationship between luminescence and temperature had to be determined. A film of luminescent water was placed on the aluminum foil substrate and the entire setup was placed in the environmental chamber. A thermocouple was inserted into the water film to measure the temperature. While the temperature in the environmental chamber was changed, the intensity of the emission from the luminescent water was captured by the highspeed color camera, which divided the intensity of the captured light into three color channels, red, green, and blue. The data was collected when the water film was in the liquid and solid phases separately. Fig. 2 shows the relationship between the intensity ratio of the luminescence and temperature measured by the thermocouple. For the intensity ratio, $\frac{I_R}{I_G}$, I_R and I_G are the intensity of the luminescence obtained from the red and green channels of the camera. The ratio decreased linearly with temperature in both the liquid and solid phases. The magnitude of the slope of the intensity ratio against temperature was higher for the solid phase. There are observable differences in the behavior of the intensity ratio is between the two phases, and Fig. 2 shows that the temperature can be measured by the luminescent water in both the liquid and solid phases.
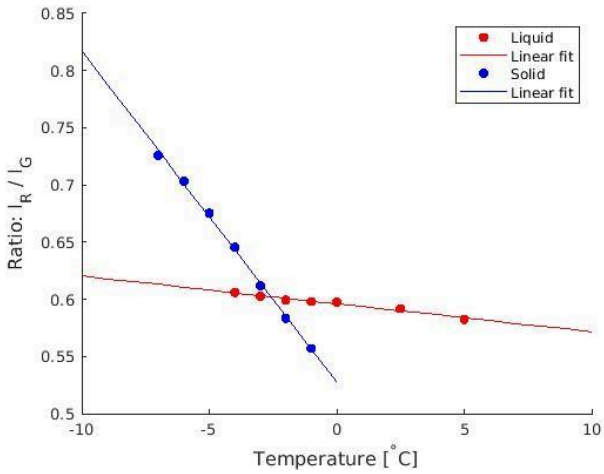
Figure 2. Temperature calibration of luminescent water

B. *Temperature Calibration of TSP*

Similar to the case of the luminescent water, the relationship between the luminescence from the TSP and temperature was also determined. To calibrate the TSP, the aluminum foil coated with the TSP was placed in the environmental chamber. The luminescence of the TSP was captured by the highspeed camera while the temperature inside the environmental chamber was changed. Fig. 3 shows the temperature calibration of TSP. Error bars are given as the measurement uncertainty of the thermocouple. The normalized intensity of the TSP decreased linearly as the temperature increased. Based on this relation between the intensity of the TSP and temperature, the temperature of the contact surface can be measured when it is coated with TSP.
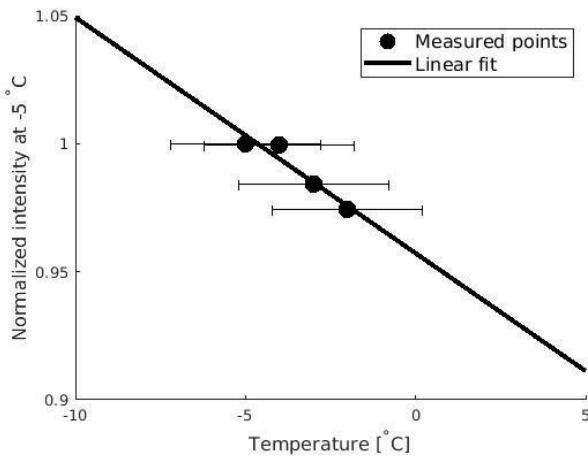
Figure 3. Temperature calibration of TSP

C. *Recalescence*

With the measurement setup shown in Fig. 1, images of the luminescent water film and the TSP on the contact surface during the recalescence were observed. Recalescence began when the temperature measured using the thermocouple was approximately -5 °C. The intensity of the luminescence near the tip of the thermocouple during recalescence was plotted as black dots superimposed on the temperature calibration plot (Fig. 2) and shown in Fig. 4. At the beginning of the recalescence, the intensity ratio was on the calibration line for the liquid phase. As the temperature increase during the recalescence, the intensity ratio changed along with the calibration line for the liquid. During the recalescence, it is thought that the liquid and solid phase coexist within the film. However, the effect of the existence of the solid phase in the film was not observed in the intensity ratio change of the luminescent water during the recalescence. This indicates that the luminescence of the luminescent water needs further calibration to account for the solid fraction, or the ratio of solid to liquid water in the mixture.
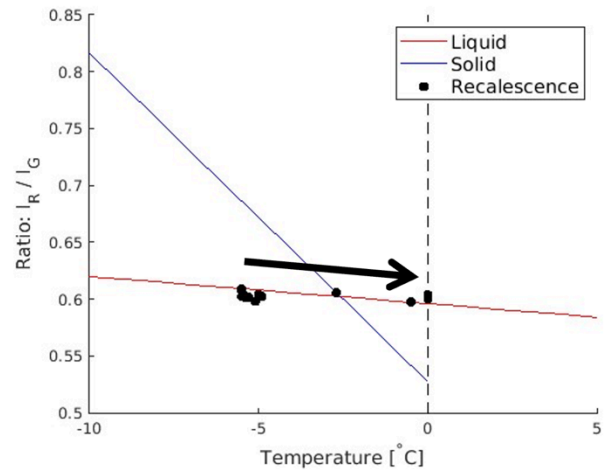
Figure 4. Intensity ratio of luminescent water during recalescence

Fig. 5 shows the raw image of TSP before the recalescence and Fig. 6 shows temperature maps obtained from raw images and the calibration line in Fig. 3 during the recalescence. In Fig. 6, $t = 0[s]$ is defined as the time when the thermocouple measured 0 °C, and the red point shows the position where the recalescence started. The recalescence started at the bottom left corner of the substrate and propagated to the rest of the surface. The temperature of the TSP showed -5 °C at the entire surface and 0 °C when the recalescence was completed. The propagation of the recalescence can be clearly tracked using the change in the area of the TSP that demonstrated a clear change in temperature.
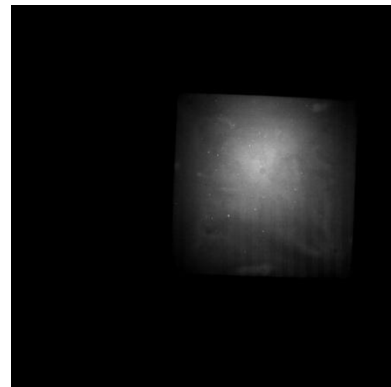
Figure 5. Raw image of TSP before recalescence
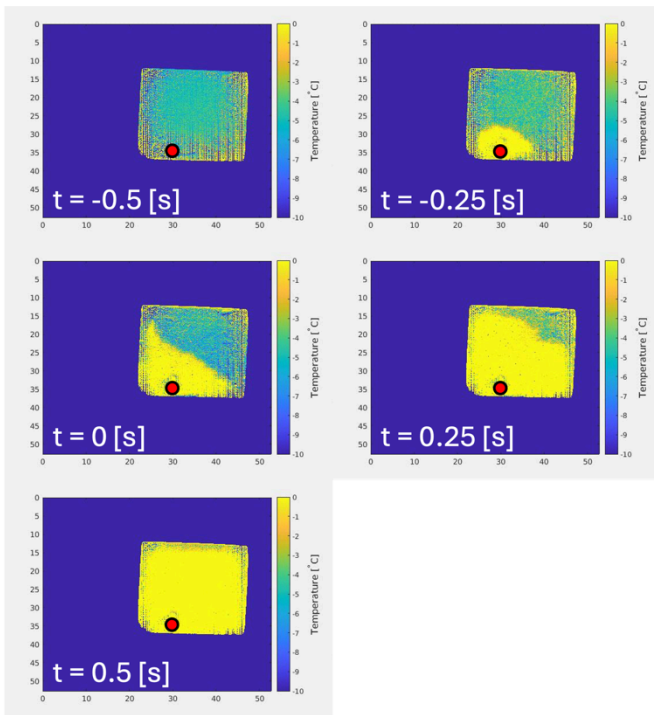
Figure 6. Temperature map of contact surface during recalescence

IV. CONCLUSIONS

In order to better study transient heat transfer during the recalescence of supercooled water, a measurement method using a combination of luminescent water and temperature-sensitive paint was developed. A TSP coated surface allowed for the measurement of the propagation front of recalescence in a spatially and temporally resolved manner. Using the methodology, the dynamics of freezing fronts, particularly how they respond to changes in temperature, geometry, and substrate properties, can be studied in more detail moving forward. The use of TSP alone, however, is limited to information at the surface in contact with the freezing water. In contrast, luminescent water allows for the measurement of temperature dynamics within a freezing film or bulk fluid. The luminescent water shown in this study demonstrated sensitivity to changes in temperature in both solid ice and liquid water, and is a promising candidate for measurements moving forward. Ideally, the luminescent water would allow for the visualization and quantitative measurement of simultaneous temperature and phase change dynamics during recalescence. However, because the luminescent water used in this work exhibits overlapping luminescent outputs for ice and supercooled water, the current measurement setup is unable to differentiate between the two forms to extract temperature information. Moving forward, the measurement technique will be improved in order to account for the solid fraction of a water-ice mixture, which can affect the luminescent output of the sensor. Once these calibrations have been completed, the luminescent water will be a much more effective sensor for studying freezing and recalescence dynamics.

REFERENCES

[1] P. J. Perkins, W. J. Rieke, "Aircraft icing problems—After 50 years," in *Proc. 31st Aerospace Sciences Meeting and Exhibit*, Reno, NV, USA, 11–14 Jan. 1993.

[2] M. G. Potapczuk, "Aircraft Icing Research at NASA Glenn Research Center," *J. Aerosp. Eng.,* vol. 26, pp. 260–276, 2013.

[3] M. P. C. Pellissier, W. G. Habashi, A. Peueyo, "Optimization via FENSAP-ICE of Aircraft Hot-Air Anti-Icing Systems," *J. Aircr.,* vol. 48, pp. 265–276, 2011.

[4] W. B. Wright, "An Evaluation of Jet Impingement Heat Transfer Correlations for Piccolo Tube Application," in *Proc. 42nd AIAA Aerospace Sciences Meeting and Exhibit*, Reno, NV, USA, 5–8 January 2004.

[5] K. E. Yeoman, "Efficiency of a Bleed Air Powered Inlet Icing Protective System," in *Proc. 32nd AIAA Aerospace Sciences Meeting and Exhibit*, Reno, NV, USA, 10–13 January 1994.

[6] L. Ding, S. Chang, M. Leng, "Transient characteristics of an electrothermal anti-icing process based on the improved messinger model," in *Proc. the 2016 IEEE International Conference on Aircraft Utility Systems (AUS)*, Beijing, China, 10–12 October 2016

[7] B. L. Messinger, "Equilibrium Temperature of an Unheated Icing Surface as a Function of Air Speed," *J. Aeronaut. Sci.*, vol. 20, pp. 29–41, 1953.

[8] J. Blake, D. Thompson, D. Raps, T. Strobl, "Simulating the freezing of supercooled water droplets impacting a cooled substrate," *AIAA J.*, Vol. 53, No.7, July 2015.

[9] J. P. Hindmarsh, A. B. Russell, X. D. Chen, "Experimental and numerical analysis of the temperature transition of a suspended freezing water droplet," *Int. J. Heat Mass Transf.*, vol. 46, pp. 1199–1213, 2003.

[10] S. Akhar, M. Xu, A. P. Sasmito, "Development and validation of a semi-analytical framework for droplet freezing with heterogeneous nucleation and non-linear interface kinetics," *Int. J. Heat Mass Transf.*, Vol. 166, 2021.

[11] J. P. Hindmarsh, D. I. Wilson, M. L. Johns, "Using magnetic resonance to validate predictions of the solid fraction formed during recalescence of freezing drops," *Int. J. Heat Mass Transf.*, 2005.

[12] M. Tembely, A. Dolatabadi, "A comprehensive model for predicting droplet freezing features on a cold substrate," *J. Fluid Mech.,* 2019.

[13] J. E. Castillo, Y. Huang, Z. Pan, J. A. Weibel, "Quantifying the Pathways of Latent Heat Dissipation during Droplet Freezing on Cooled Substrates," *Int. J. Heat Mass Transf.*, vol. 164, Jan 2021.

[14] J. Gonzales, H. Sakaue, "Novel optical temperature and phase change sensor based on the response of hydroxypyrene to sucrose in water ice," *Sensor Actuat. A-Phys.*, Vol. 344, 113711, Sep 2022.

Investigating Ice Nucleation and Heat Transfer Dynamics in Supercooled Liquid Water Using Thermography

Hassan Abbas Khawaja[1], Samaneh Keshavarzi[2], Adeel Yousuf[1], Manaf Muhammed[1],
Muhammad Shakeel Virk[1], Derek Harvey[2], Gelareh Momen[2]

[1] UiT – The Arctic University of Norway
[2] University of Quebec at Chicoutimi, Canada

hassan.a.khawaja@uit.no, skeshavarz@etu.uqac.ca, yousuf.adeel@uit.no, manaf.muhammed@uit.no,
muhammad.s.virk@uit.no, d2harvey@uqac.ca, gelareh_momen@uqac.ca

Abstract— **This study delves into the intricate interplay of thermography, ice nucleation, and heat transfer during the phase change from supercooled liquid water to crystallized ice. Utilizing high-resolution, high-speed infrared thermography, real-time temperature data is captured during ice nucleation events. By analysing these temperature profiles, valuable information about the dynamics of ice nucleation is revealed and presented. One of the key highlights of this study is the observation of nucleation under supercooled conditions. The evidence of how supercooled liquid water transforms into crystalline ice is provided, which sheds light on the underlying physics and mechanisms involved, like recalescence and phase change. This phase change process is significantly important in the context of cloud formation and freezing rain phenomena. The study may form the basis of developing a mathematical model for defining nucleation phase. These findings have practical implications across multiple industries and can aid in the development of more efficient anti-/de-icing systems, refrigeration systems, improved weather prediction models, and enhanced cryopreservation techniques. The study opens new avenues for further exploration in this field, ultimately advancing our understanding of these critical processes.**

Keywords— ***Ice Nucleation, Thermography, Heat Transfer Dynamics, Latent Heat***

I. INTRODUCTION

Ice nucleation is a key process in understanding ice accretion physics as most of the passive techniques use extending the nucleation time. The phenomena of ice nucleation and subsequent ice growth have paramount importance in various fields, including cold climate engineering, atmospheric science, cryopreservation, and refrigeration systems [1-5]. According to Classical Nucleation Theory (1928) nucleation involves the formation of the initial embryos of tiny stable solids from a supercooled or supersaturated mother phase (vapor or liquid phase). For freezing and ice growth to occur, an ice nucleus must reach a certain size called the critical size (r*) to be thermodynamically stable (Figure 1). Below this critical size, an ice nucleus is unstable and will be destroyed, reverting to the mother phase [1, 6]. Ice nucleation and its growth will happen under a thermodynamic driving force. However, according to modern study, the process of nucleation is dynamic and is also impacted by varying environmental factors [7]. In this regard homogenous and heterogenous nucleation are often studied that are characterized by absence

or presence of any external agent to create nucleation sites in water droplets, respectively [1, 8].
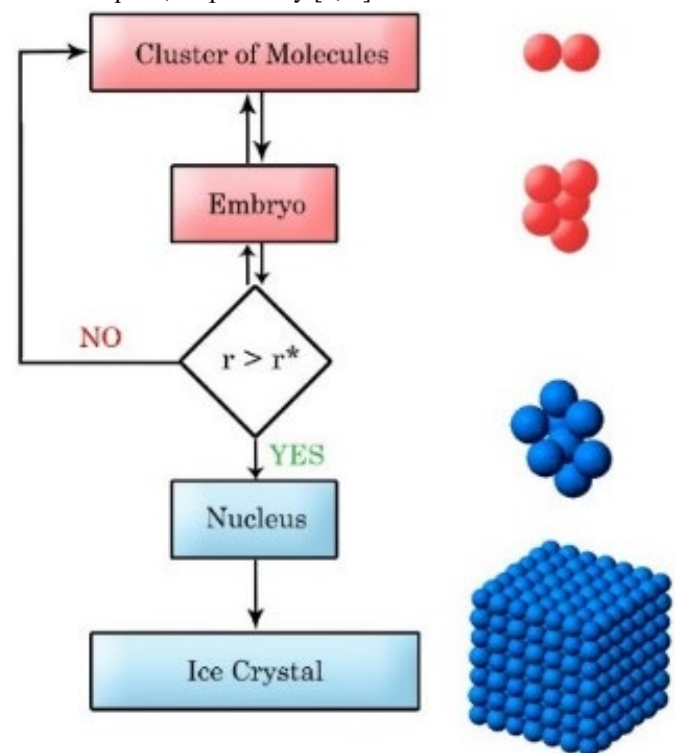
Fig. 1 A graphic representation of ice nucleation phenomenon according to Classical Nucleation Theory (CNT) [9]

Various experimental studies have been conducted to understand the formation of ice from water droplets. The studies focus on monitoring water droplet impact on cold substrates as it experiences freezing. The process concludes in four steps: supercooling, recalescence (nucleation), phase change, and ice cooling (see Figure 2). When droplet impinges a supercooled surface, a liquid-substrate interface is created by which conductive heat transfer takes place and droplet undergoes supercooling. During this stage the morphology of water droplet changes; its contact angle decreases with an increased droplet contact area. Treated hydrophobic surfaces make this contact angle large to create small interface with the solid substrate and hence take longer time for supercooling. Moreover, time duration of supercooling stage is dependent on drop size; smaller droplets comparatively get cooled faster

until nucleation initiation [10]. Once a thermal equilibrium is established at this liquid-substrate interface, droplet loses its latent heat and nucleation begins; this stage is termed as recalescence. During this stage an ice shell appears on the circumference of the droplet, rising from the droplet-substrate interface up till the top. It is an instantaneous step and not much literature is available that makes an in-depth analysis for it. After the evolution of latent heat temperature remains constant while phase change takes place, in which the water content inside the frozen shell starts solidifying gradually. A pointed tip is formed at the completion of solidification stage followed by ice cooling [10, 11].
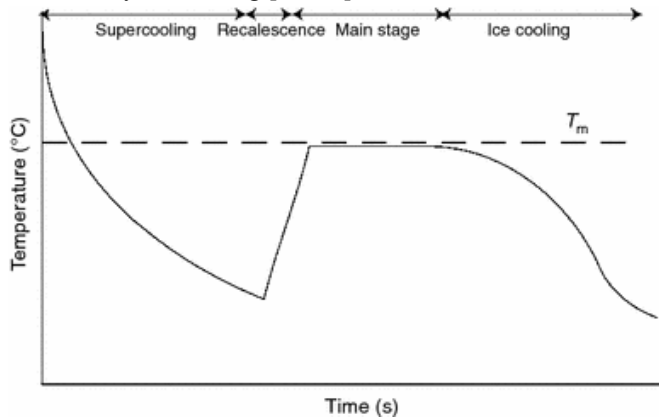
Fig. 2 Freezing process of a supercooled droplet takes place in four stages [7].

High speed infrared thermography can be used to study the phase change and track temperatures changes in water and ice [12-15]. There is also work in progress on the development of ice detection system based on the thermography [16-18]. There are basically two arrangements for IR camera in this context: taking a side view of droplet or taking a top-down view. Side view makes it possible to quantify conduction heat transfer between solid substrate and liquid droplet. Li and Liu [19] recorded top-down view temperature maps during droplet freezing using IR thermography to determine the onset of freezing in pure water droplets versus droplets containing anti-freezing agents. Alizadeh et al. [20] used top-down IR thermography along with highspeed visual imagery to study the impact of droplets impinging on hydrophilic, hydrophobic and superhydrophobic surfaces. Their studies revealed that drop-substrate contact area can delay nucleation by heat transfer as well as by reducing probability of heterogenous nucleation at the interface.

Tavakoli et al. [10] carried out infrared thermography of a droplet freezing experiment on hydrophilic and hydrophobic glass substrate. They used FLIR® A600 thermal camera to get a top-down view of water droplet and observed that this main drop surrounds itself on the top side by condensed micro drops that make an appearance of bumpy straight-line pattern, which is called 'recalescence front'. This front of condensed micro drops travels down the drop with the release of latent heat as the nucleation and solidification proceed. They postulated that solidification of main drop is triggered by these 'travelling' condensed micro drops surrounding it when they reach the main drop, and this way they deduced that nucleation front is activated from point of trijunction (formed by liquid-substrate interface, substrate-gas interface, liquid-gas interface). Castillo et al. [21] performed numerical simulations of

solidification stage (phase change stage) using the boundary conditions determined by IR temperature. For that purpose, they employed side-view IR thermography. They revealed that heat transfer rate between drop-substrate is greater than heat transfer between drop-ambient air, and same applies in case of latent heat release. Li et al. [22] used high-speed visual and infrared imaging to observe supercooled large droplets colliding with a hydrophilic and hydrophobic surface, and studied droplets impact, spreading and rebound.

Among all the four steps of droplet freezing, recalescence has not been studied in detail up to the best knowledge of authors, and since it is a split-second process thermocouples are not a reasonable choice for this purpose. High speed imaging is an efficient tool for high resolution studies. The current article highlights recalescence during the impinging water droplets on a cold aluminium substrate using high speed colour camera and a high-resolution long wave thermal infrared camera. The generated data from sequence file is analysed within MATLAB.

II. METHODOLOGY

Experimental design consists of a set of experiments involving ice nucleation which are carried out in cold room laboratory at UQAC – Université du Québec à Chicoutimi, Canada. Individual droplets are dropped using medical syringe with hypodermic needle on aluminium substrate maintained at -13℃ and observed for solidification.

The overall setup includes a small chamber supported by Peltier cooler and thermocouple, cold bath, high speed camera, infrared (IR) camera, aluminium substrate, data acquisition system, temperature and humidity sensors, and a vibration-free table. (Graphic setup of experiment with some actual visuals are shown in Figure 3). A thermally insulated and optically transparent double layer chamber placed on motionless table ensured that the parameters affecting ice nucleation were uniform during experiments in order to increase the accuracy of results and reproducibility of experiments. Its transparency facilitated in imaging the side view of freezing water droplet with Mikrotron MotionBLITZ EoSens Cube7 Mono high-speed camera. The camera offers 525 fps at 3MP resolution with capability to adjust framerate to 200,000 fps at lower resolutions. This feature enabled capturing fast motion sequences such as, water droplet freezing, quite reliably with sufficiently sharp details. LED lights were used to illuminate the scene for high-speed optical camera. Since the chamber walls were opaque for infrared analysis, an IR camera (T1030sc with 50μm close-up lens) was set at height for recording top view of the droplet. The chamber is also supported by temperature and humidity sensors that recorded the surrounding and in-chamber atmospheric parameters before and during the experiments. Prior to experiment the temperature of the aluminium substrate was measured with an IR camera and a thermocouple (K-type) which was then removed during the experiments.

The temperature of thermostatic bath was decreased to a desired value (-15°C) and aluminium substrate was placed over it. Once the temperature became stable water droplets of 10 μL/20 μL volume were dropped onto it with no frost formation. The freezing process onwards was recorded by both high-speed and IR cameras with side and top views, respectively.

By visual high-speed & IR cameras recordings all the four stages of cooling and freezing of water droplets are identified: supercooling – recalescence – solidification – ice cooling. Recalescence, which is an instant stage and happens in a split second can be easily monitored using high-speed camera at 1000 fps.

While working with the thermal camera it needed to be stopped after every 5 minutes due to its limitations. Visual camera, however, could snap a continuous video. For thermal infrared camera, before each recording it was made sure that the target (droplet) was well focused and not blurry, and correct temperature range was selected from camera settings. The sequence file generated by IR camera is analysed by FLIR® ResearchIR software. Circular region of interest (ROI) is sketched over the location of a singular droplet to measure average temperature change over it. Temporal data of this ROI is extracted and then analysed in MATLAB.
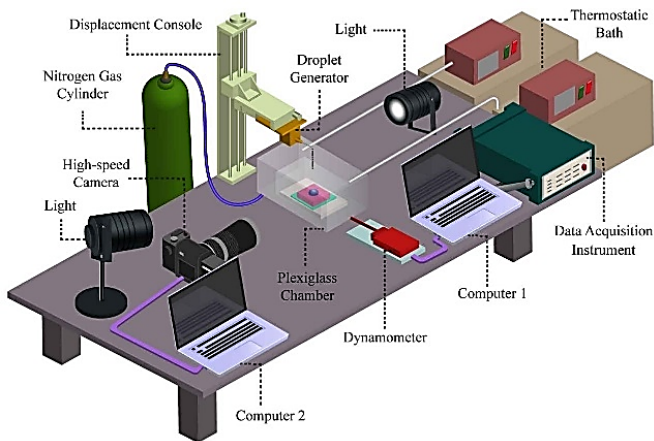
Fig. 3 Graphic representation of experimental setup for ice nucleation droplet test.

III. RESULTS AND DISCUSSION

Sequential temperature distribution against elapsed time during recalescence as observed through high-speed infrared imaging is presented below in Figure 4. Evolution of thermal gradient is clearly visible on droplet as it initiates from droplet-substrate-air interface. Immediately prior to recalescence at t = 0, the droplet is supercooled at about -8°C and then after t = 17ms a gradual conductive heat transfer takes place from the substrate and rises across the droplet height. The low temperature regions (blue coloured) remain in supercooled state while the crystallization front rises. This crystallization front is composed of ice-water mixture and covers the whole droplet. At about t = 85ms the crystallization process is completed, and droplet temperature is maintained at approx. 0°C.

IR camera covers the split-second transition at recalescence during which a visible, translucent ice front starts developing from liquid-substrate interface rising towards the tip making a dome shaped outer cover with liquid water inside. Such observations are also recorded by Keshavarzi et al [23] while studying ice nucleation process via high-speed imaging on hydrophobic and superhydrophobic surfaces. Visually this process is apparent through high-speed camera because ice and water have different refractive index (ice: 1.31, water: 1.33). Moreover, the air bubbles get trapped in ice shell giving it a translucent outlook [24]. The transparency of water droplet

fully disappears after the solidification (or phase transition event) in which the water content inside the shell solidifies gradually forming a cusp shape.
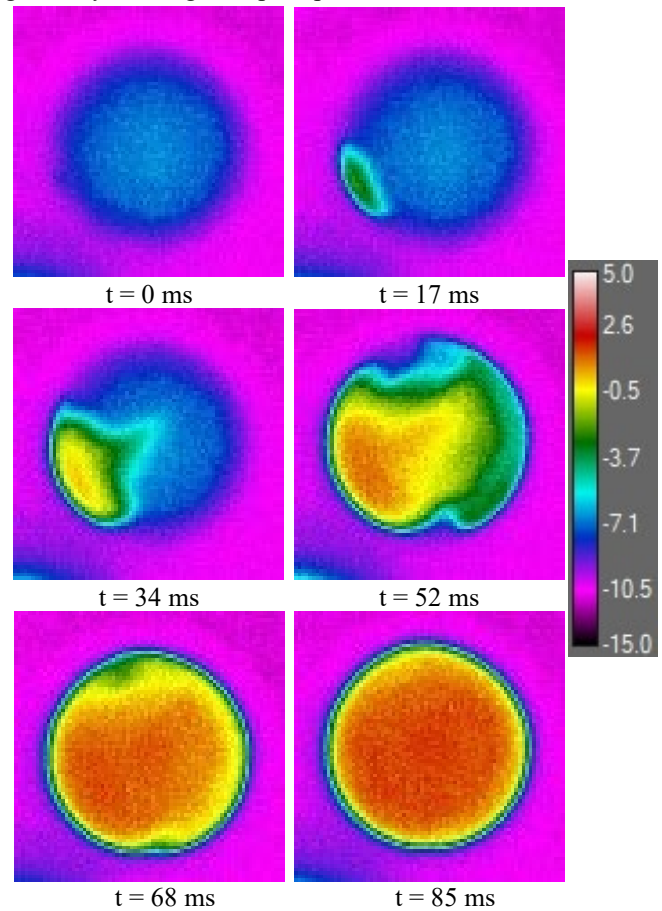
Fig. 4 Sequential infrared images of recalescence in sessile water droplet

IV. CONCLUSION

The paper discussed in detail the sequential process of freezing water droplet. utilizing the high-speed infrared thermography to study the freezing droplet on cold substrate. Supercooling can be better depicted in IR imagery whereas phase change is better analysed in visual high-speed camera. Utilizing high-resolution, high-speed infrared thermography, real-time thermal images were captured, and temperature data was analysed during ice nucleation events. By analysing these temperature profiles, we gained valuable information about the dynamics of ice nucleation. Our findings reveal the crucial role of nucleation sites, their distribution, and their impact on the overall heat transfer process. The overall knowledge contributes to a more comprehensive understanding of ice nucleation mechanisms and is a precursor to understanding the microphysics of surfaces undergoing ice accretion. The insights can be found useful in making hydrophobic coatings or treating those surfaces such that duration of supercooling and recalescence stages can be extended.

V. ACKNOWLEDGEMENT

REFERENCES

[1] [1] N. Maeda, "Brief overview of ice nucleation," Molecules, vol. 26, no. 2, 2021.

[2] M. S. Virk, M. Y. Mustafa, and Q. Al-Hamdan, "Atmospheric ice accretion measurement techniques," The International Journal of Multiphysics, vol. 5, no. 3, pp. 229-241, 2011.

[3] H. Xue, H. A. Khawaja. "Review of the Phenomenon of Ice Shedding from Wind Turbine Blades," The International Journal of Multiphysics, vol.10, no. 3, pp. 265–276, 2016.

[4] J. Y. Jin and M. S. Virk, "Seasonal weather effects on wind power production in cold regions- a case study," International Journal of Smart Grid and Clean Energy, vol. 8, no. 1, 2019.

[5] Z. Andleeb, H. A. Khawaja, M. Moatamedi. "Multiphysics based Analysis of Materials for Roads in Cold Regions to Prevent Ice Adhesion and Low-Temperature Crack Developments," The International Journal of Multiphysics, vol.16, no. 4, pp. 437-447, 2022.

[6] A. Goswami, I. S. Dalal, and J. K. Singh, "Seeding method for ice nucleation under shear," Journal of Chemical Physics, vol. 153, no. 9, 2020.

[7] M. A. Holden, J. M. Campbell, F. C. Meldrum, B. J. Murray, and H. K. Christenson, "Active sites for ice nucleation differ depending on nucleation mode," P Natl Acad Sci USA, vol. 118, no. 18, 2021.

[8] Z. Zhang and X.-Y. Liu, "Control of ice nucleation: freezing and antifreeze strategies," Chemical Society Reviews, vol. 47, no. 18, pp. 7116-7139, 2018.

[9] C. Long et al., "Micro/nano manufacturing aircraft surface with anti-icing and deicing performances: An overview," Nanotechnology Reviews, vol. 12, no. 1, 2023.

[10] F. Tavakoli, S. H. Davis, and H. P. Kavehpour, "Freezing of supercooled water drops on cold solid substrates: initiation and mechanism," Journal of Coatings Technology and Research, vol. 12, no. 5, pp. 869-875, 2015.

[11] A. G. Marin, O. R. Enriquez, P. Brunet, P. Colinet, and J. H. Snoeijer, "Universality of tip singularity formation in freezing water drops," Physical Review Letters, vol. 113, no. 5, 2014.

[12] T. Rashid, H. A. Khawaja, and K. Edvardsen, "Determination of Thermal Properties of Fresh Water and Sea Water Ice using Multiphysics Analysis," The International Journal of Multiphysics, vol. 10, no. 3, pp. 277-290, 2016.

[13] T. Rashid, H. A. Khawaja, and K. Edvardsen, "Ice Detection of Pure and Saline Ice Using Infrared Signature," Sensors & Transducers, vol. 206, no. 11, pp. 82-87, 2016.

[14] T. Rashid, H. Lang, M. Taimur, N. Chiodarelli, M. Volder, K. Edvardsen, H. A. Khawaja, "Roll to Roll coating of carbon nanotube films for electro thermal heating," Cold Regions Science and Technology, vol. 182: no. 103210, 2021.

[15] T. Rashid, H. A. Khawaja, K. Edvardsen, "Measuring Thickness of Marine Ice Using IR Thermography," Cold Regions Science and Technology, vol. 158, pp. 221 – 229, 2018.

[16] A. Yousuf, H. Khawaja, and M. S. Virk, "A review of infrared thermography applications for ice detection and mitigation," Cold Regions Science and Technology, vol. 218, no. 104058, 2024.

[17] T. Rashid, H. A. Khawaja, and K. Edvardsen, "Review of marine icing and anti-/de-icing systems," Journal of Marine Engineering & Technology, vol. 15, no. 2, pp. 79-87, 2016.

[18] A. Yousuf, H. A. Khawaja, and M. S. Virk, "Conceptual design of cost-effective ice detection system based on infrared thermography," Cold Regions Science and Technology, vol. 215, no. 103941, 2023.

[19] F. F. Li and J. Liu, "Thermal infrared mapping of the freezing phase change activity of micro liquid droplet," Journal of Thermal Analysis and Calorimetry, vol. 102, pp. 155-162, 2010.

[20] A. Alizadeh et al., "Dynamics of ice nucleation on water repellent surfaces," Langmuir, vol. 28, no. 6, 2012.

[21] J. E. Castillo, Y. Huang, Z. Pan, and J. A. Weibel, "Quantifying the pathways of latent heat dissipation during droplet freezing on cooled substrates," (in English), Int J Heat Mass Tran, vol. 164, 2021.

[22] H. Li, I. V. Roisman, and C. Tropea, "Influence of solidification on the impact of supercooled water drops onto cold surfaces," Experiments in Fluids, vol. 56, no. 6, 2015.

[23] S. Keshavarzi, A. E. b, K. Maghsoudi, and G. M. R. Jafari, "Ice nucleation on silicone rubber surfaces differing in roughness parameters and wettability: Experimental investigation and machine learning–based predictions," Cold Region Science & Technology, vol. 203, no. 103659, 2022.

[24] M. Song, C. Dang, T. Higashi, and E. Hihara, "Review of experimental data associated with the solidification characteristics of water droplets on a cold plate surface at the early frosting stage," Energy and Buildings, vol. 223, no. 110103, 2020.

Forecasting Ice Risk Due to Wet Snow on a Cable-Stayed Bridge Across the Firth of Forth, Scotland

Kristian Ingvaldsen[1], Bjørn Egil Nygaard[1], Steven Downie[2], Oliver Riches[2], Chris Tracey[3], Nick Forbes[3], Jason Cheetham[4]

[1] Kjeller Vindteknikk, Norconsult, Norway
[2] Arup, United Kingdom
[3]BEAR, Scotland
[4] Transport Scotland, Scotland

kristian.ingvaldsen@norconsult.com, bjorn.egil.nygaard@norconsult.com, steven.downie@arup.com, oliver.riches@arup.com, ctracey@bearscotland.co.uk, nforbes@bearscotland.co.uk, Jason.Cheetham@transport.gov.scot

Abstract— **This paper presents the development of a probabilistic forecast system that aims to predict the ice risk due to wet snow accumulation on a cable-stayed bridge ("Queensferry Crossing") across the Firth of Forth, Scotland. Since it opened to traffic in 2017, the bridge has been closed on three occasions due to ice falling from different bridge elements above road level and landing on the carriageway. This has forced the road authorities to do frequent patrols and visual inspections of the bridge during periods with winter precipitation to ensure that the towers/cables are ice-free, even though snowfall relatively rarely leads to ice accumulation. The goal of the development of a revised forecast system is therefore to reduce the number of unwarranted patrols (false alarms) to a minimum, limiting the need for visual inspections to periods with real risk of ice accumulation only. The forecast system has been developed by Norconsult (department Kjeller Vindteknikk) and Arup on behalf of BEAR/Transport Scotland.**

The revised system is based upon Global Forecast System (GFS) and Global Ensemble Forecast System (GEFS) data dynamically downscaled using the Weather Research and Forecasting model (WRF). The downscaled meteorological data are subsequently processed by an ice accretion model to yield hourly values of accumulated ice loads over the next 48 hours.

By downscaling a total of four global forecasts (GFS and three GEFS members) the system accounts for the uncertainties related to the future development of the present weather system. To further reduce the risk of false negative predictions, the system combines data from the nine closest model grid points and nine different vertical levels (spanning the vertical extent of the bridge towers) from each forecast, yielding a total of 324 ice load series on which to base the risk assessment. The system has not been thoroughly validated due to the lack of a sufficiently large observational dataset, however, the spread generated by the multi-member (ensemble) forecast combined with spatial aggregates across the model's three-dimensional grid (both horizontally and vertically) enables the system's sensitivity to be tuned continuously as more data becomes available.

The probabilistic ice risk forecast is updated every six hours and is visualized via a web-based platform. The system issues risk levels (low, moderate, high or severe) based on each forecast individually, as well as a total risk level based on all forecasts combined. A pilot version of the system has been operational for two winter seasons, and in its unvalidated state it has issued significantly less false alarms compared to current practice during its limited pilot period.

Keywords— ***Ice risk, wet snow, bridge operation, ensemble forecast***

I. INTRODUCTION

Queensferry Crossing (Figure 1) opened on the 30th of August 2017 and replaces the Forth Road Bridge as the primary carrier of road vehicles crossing the Firth of Forth between Fife to the North and Edinburgh to the south. The main section of Queensferry Crossing consists of a 1746 m long, three-tower cable stayed bridge, with towers extending from sea level to 210 m height.

Since the opening of the bridge there have been three events where the bridge has been closed due to observations of ice falling from the stay cables and towers onto the carriageway. During at least one of the events, falling ice pieces have also inflicted damage to passing cars (see Figure 2). A key component in risk management and safe operation of the bridge is reliable icing forecasts, together with real-time measurements on the bridge.

Figure 1: Aerial view of Queensferry Crossing. Photo: Transport Scotland

Due to the lack of a sufficiently accurate ice risk prediction system, the responsible road authorities have been forced to issue manual patrols of the bridge during all periods of predicted/observed snowfall to ensure safe operation of the bridge. Since snowfall typically only leads to ice accumulation during quite specific weather conditions, the current ice risk management practice has led to many unwarranted patrol hours. Even though the existing ice risk forecasting system is quite conservative, the system has also failed to capture some of the observed events. Such false negative predictions are typically related to small-scale precipitation showers which

are inherently difficult to predict. The objective of this study was therefore to develop a revised ice risk forecasting system that helps reduce the number of unwarranted patrols (false alarms) as well as false negative predictions. Another objective was to provide a robust decision-making system for reopening the bridge after a closure through predictions of instrumental icing as well as meteorological (active) icing periods. The revised forecasting system is based on state-of-the-art ice accretion models coupled with a regional numerical weather prediction model (WRF) and was developed by Norconsult (department Kjeller Vindteknikk) and Arup on behalf of BEAR/Transport Scotland.

The initial phase of the study involved the generation of a long-term historical meteorological (hindcast) dataset covering 20 years, providing statistical basis for a detailed climatological assessment of the frequency and severity of ice accretion locally. Furthermore, the hindcast dataset allowed the ice prediction system to be validated against the three documented cases, and subsequently tailored to optimize its representation of the local icing climatology. The optimization of the ice accretion model included the development of a procedure to account for subgrid-scale precipitation showers not directly represented by the numerical weather prediction model.

Figure 2: Windscreen damaged by an ice piece falling from the towers/stay cables of the Queensferry Crossing bridge. Photo: Graeme Stevenson

During the 2022-23 winter season, a pilot version of the revised forecasting system was made operational in the second phase of the study. The system then consisted of a single-member ice risk forecast with a lead time of 48 hours and updates every six hours. During the following winter season, the pilot system was extended to a four-member ensemble forecast yielding probabilistic ice risk predictions.

II. DATA AND METHODOLOGY

This section provides a brief overview of the data and methodology constituting the multilayered modelling chain, including descriptions of convective precipitation parametrization and ice risk assessments.

A. Hindcast Data

The hindcast dataset was generated using the Weather Research and Forecasting model (WRF) [1] with the ERA5 reanalysis dataset [2] as input. After validating a variety of different model configurations against the documented icing events, the simulation was setup with a horizontal resolution of 4 km x 4 km, 51 vertical levels to (ensure sufficiently

detailed representations of vertical temperature profiles) and no cumulus parametrization scheme. The hindcast simulation covered a 20-year period from 2001 to 2021 with hourly output of all meteorological variables needed for icing calculations.

B. Operational Forecast Data

The operational WRF forecasts were run with an identical configuration to that of the hindcast. During the first pilot winter (2022-23 winter season) a deterministic one-member forecast was set up with input from the Global Forecast System (GFS). The 48-hour forecasts were initiated every six hours providing updated input data to the ice accretion model. During the second pilot winter (2023-24 winter season) the forecast system was expanded with three members from the Global Ensemble Forecast System (GEFS) yielding a four-member probabilistic ensemble forecast on which to base the ice risk predictions.

C. Accounting for Subgrid-Scale Convective Precipitation

Not all precipitation types are resolved by the WRF model. Sudden snow showers originating from convective clouds are particularly difficult to predict in any numerical weather prediction model due to the sheer size of such clouds – most of them are simply too small to be resolved explicitly even by high-resolution model simulations. However, reports have clearly stated that some of the events that have led to the closure of Queensferry Crossing have been of precisely this nature. It was therefore crucial that the ice risk forecasting system could identify periods with increased probability of wet snow accretion due to convective precipitation – even though it is not explicitly predicted by weather model.

Although the size of a single convective cloud is too small for it to be resolved, the underlying weather conditions that enable the formation of such clouds is often far greater in scale, and thus easier to predict by the model.

A common way to investigate the *potential* for convective cloud formation is to calculate the so-called convective available potential energy (CAPE). Convective clouds are formed when moist air is allowed to rise freely in the atmosphere, which may only occur when the rising air is warmer (lighter) than the surrounding air. So even though the model is not able to predict the exact time, place, and intensity of specific small-scale precipitation showers, the model can predict whether such showers are likely to occur in a given region/time period. We may then use this information to add *potential precipitation* to the deterministic model using a simple function that yields the precipitation intensity as a function of CAPE, i.e. precipitation that could occur if a precipitation shower where to hit the location in question. Precipitation showers are also often accompanied by sudden temperature drops due to evaporative cooling and downdrafts of colder air from aloft. This is accounted for by also adjusting the temperature whenever "potential" precipitation showers are added into the model. The methodology was calibrated against measured precipitation and temperatures at Edinburgh Airport. Potential precipitation is subsequently translated to *potential wet snow* by serving it as input to the wet snow accretion model.

D. Determining the Ice Risk

Each 48-hour meteorological forecast is postprocessed through an ice accretion model yielding hourly time series of the total ice load on a reference ice collector due to wet snow. The predicted ice risk pertains until the simulated ice load is removed by either melting or sublimation. Should the ice risk pertain at the end of the 48-hour forecast period, the predicted ice load is carried over to the next forecast iteration to avoid that the period of elevated ice risk is ended prematurely. The ice accretion model applied in this project has been developed at Kjeller Vindteknikk through a series of R&D projects and is described in detail in [3].

The output from the weather prediction model (WRF) is available on a three-dimensional grid with a horizontal resolution of 4 km x 4 km and a vertical resolution that decreases with height (nine vertical levels in the lowest 200 m of the atmosphere). Data from the nine grid points closest to the bridge location (representing an area of 144 km^2 centered around the bridge) were all postprocessed with the ice accretion model to account for icing events that are slightly displaced in the model. Furthermore, data from all nine vertical levels that span the height of the bridge towers (210 m) were also processed, yielding a total of 81 hourly ice load series for each of the four 48-hour forecast members on which to base the risk assessment – all with the intension to minimize the false negative rate of the forecast system.

There is a vast number of ways in which the total of 324 ice load series could be combined to yield a single, probabilistic ice risk prediction, allowing the sensitivity of the forecast system to be tuned readily. In its current unvalidated state, the focus has been to keep the false negative rate at a minimum, accepting the consequence of a slightly elevated false alarm rate. Therefore, the number of ice load series per forecast member was reduced to nine by taking the maximum ice load value for each time step across the nine vertical levels (i.e. the height at which the ice accumulates is irrelevant for the risk). Furthermore, the ice load series were averaged with equal weights on all nine model grid points across the horizonal plane, making the location of the predicted icing event within the 144 km^2 area surrounding the bridge irrelevant to the ice risk as well. The ice risk level (*moderate*, *high*, or *severe*) was ultimately determined based on the size of the aggregated ice load (0.1 kg/m, 0.5 kg/m and 1.0 kg/m, respectively) from each forecast member (more severe icing events are generally associated with greater safety risks and increased model hit rates).

The predicted ice risk levels along with key meteorological parameters were made available to the bridge operators via a web-based data visualization platform.

III. RESULTS

This section presents key results from the hindcast study, as well as the operational ice prediction system during the two pilot winter seasons.

E. Findings From the Hindcast Study

The key takeaway from the hindcast study was that the model predicted ice accretion on the bridge towers during all of the documented events. The addition of potential precipitation during periods with increased probabilities of small-scale snow showers (see section C) enabled the model to reproduce one of the documented events that otherwise

would have been missed, while only accounting for 1.6 additional yearly icing events on average. The average number of yearly icing events for each risk level are summarized in Table 1 along with the typical duration of the events. Note that the estimated event durations derived from the model are likely conservative because the modelled ice loads often remain on the object (bridge) until all ice is melted or sublimated. In reality, however, the accreted wet snow is more likely to fall off the bridge (due to gravity, wind or other dynamic forces) which will help to shorten periods with elevated ice risks.

Due to the lack of continues measurements/observations during the hindcast period, the actual performance of the model in terms of true positive rate/false negative rate is not known.

Table 1: Yearly number of icing events and their typical durations for each risk level.

Risk level	Number of yearly events	Typical duration (p50)
Medium	6.9	9.0 hours
High	3.0	9.0 hours
Severe	1.5	14.0 hours

F. Findings From the Operational Pilot Study

There were no observations of ice accretion on the bridge made by the patrols during either of the two pilot winter seasons. Consequently, the true positive rate of the operational ice prediction system is not possible to quantify at this stage. For simplicity, all icing events predicted by the forecast system during the pilot period are therefore assumed to be false positives (false alarms).

Table 2 summarizes the number of icing events predicted by a single model member during the two pilot winter seasons (lead time of 6 – 12 hours). By comparing the values with those based on the long-term hindcast dataset (Table 1) we see that the first winter was about average while the second pilot season had significantly fewer icing events compared to the long-term average. The fact that the first pilot season had approximately the same number of predicted events as the hindcast simulation on average could imply that both the hindcast model and the operational model are conservative considering that there were no observed events during that particular winter. This (to be on the conservative side) was the intention behind the "multiple grid point approach", i.e. that each forecast member (or hindcast) considers a whole array of adjacent model grid points in both the vertical and horizontal to minimize the probability of false negative predictions. It could also be that the ice accretion model itself is conservative (i.e. that it overestimates the ice load even with "perfect" input data).

Table 2: Number of predicted icing events during the two pilot winter seasons.

Risk level	2022-23 winter	2023-24 winter
Medium	10	4
High	3	0
Severe	1	0

In general, the uncertainties related to weather forecasts increase with increasing lead time, i.e. the weather five hours from now is more predictable than the weather five days from now. As such, the spread between individual members in an ensemble forecast tend to increase with increasing lead time. As the lead time gets down to a few hours, the members should converge towards the true outcome. Figure 3 shows the number of false alarms (or hours of elevated ice risk in the predictions) as a function of forecast lead time for a single forecast and a four-member ensemble. In this figure, all instances (hours) with an ice load > 0 kg/m in either member is defined as a positive prediction (most conservative threshold possible). The results suggest that the addition of three extra members in the four-member ensemble yields an increase in false alarms of approximately 200 – 300 % (depending on lead time) compared to the single forecast.

We also see that the number of false alarms decreases with decreasing lead time. This is to be expected during a winter with no actual icing events, because, as mentioned above, the individual members of an ensemble tend to converge towards the true outcome as the lead time decreases.
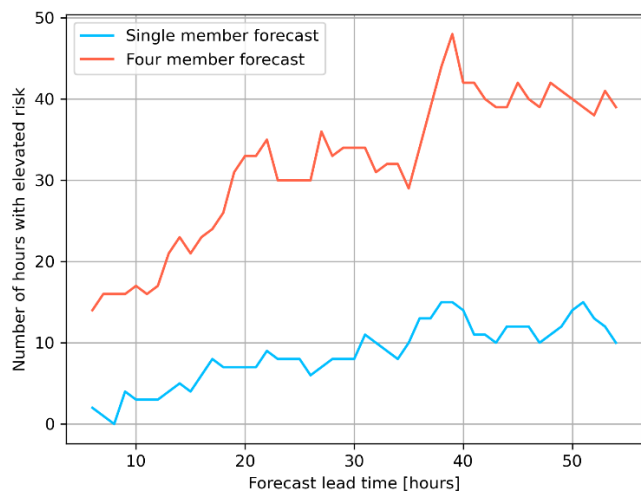
Figure 3: Number of false alarms (ice load > 0 kg/m in one or more members when no ice is observed) issued by a single-member (blue) and four-member ensemble model (red) as a function of forecast lead time during the second pilot season.

To get a better understanding of the patterns shown in Figure 3, Figure 4 shows the average ensemble spread (difference between the maximum and minimum values of the four members) in terms of temperature and precipitation (both of which are key parameters in the wet snow accretion model) as a function of forecast lead time. The two parameters show very different patterns, with the temperature spread increasing almost linearly with lead time, while the spread in precipitation intensity is more evenly distribution across all lead times (although slightly lower for lead times of 20 hours or less). Given the ice accretion model's sensitivity to both temperature and precipitation intensity, the ensemble spread is sufficiently large to impact the outcome of the ice accretion model even for lead times of a few hours. However, t

Furthermore, the fact that the spread in precipitation intensity is relatively constant with respect to lead time suggests that the parameter has relatively low predictability

(i.e. more precise input data does not significantly reduce the uncertainty). The total number of unique hours with predicted precipitation during the second pilot winter season increased by approximately 40 % when expanding from a single-member forecast to a four-member forecast, which further underlines the importance of ensemble predictions in applications where it is crucial to avoid false negatives.
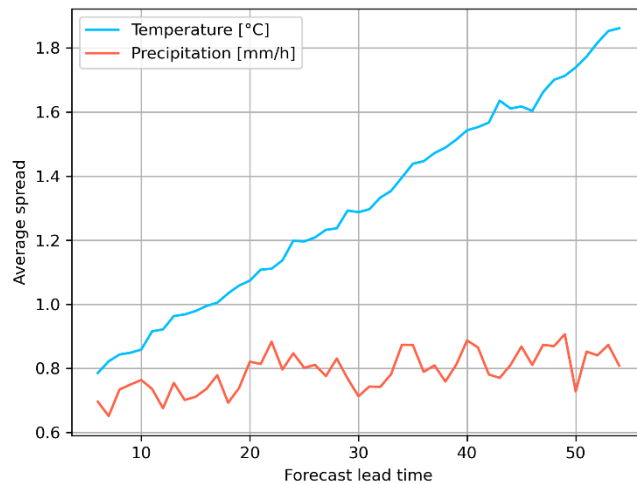
Figure 4: Average temperature and precipitation spread of the four-member ensemble system as a function of forecast lead time during the second pilot season.

IV. CONCLUSIONS

The primary goal of the advanced forecast system development was to significantly reduce the number of false positives (unnecessary patrols) without increasing the risk of false negatives. Secondary, closely related goals include providing a robust decision-making system for reopening the bridge after a closure and development of a data driven approach to learning from past incidents.

As there were no recorded instances of ice forming on the bridge over the pilot study period, no further evidence has been obtained regarding the risk of false negatives. However, it does appear clear that the number of false positives can be significantly reduced, even with a relatively conservative approach to setting of risk thresholds. This is true for both versions of the advanced system (single-member and four-member ensemble) even though the four-member ensemble system showed an increase in the number of false alarms of approximately 200 – 300 % compared to the single-member deterministic version (depending on lead time).

The introduction of a four-member ensemble prediction system during the second pilot season enables probabilistic ice risk predictions (i.e. "there is a 25 % chance of ice risk tomorrow at noon") which subsequently allows the balance between the system's true positive and false negative rates to be tuned to the desired sensitivity (within an interval determined by the overall skill of the model). This, however, requires the ensemble prediction system to be properly validated against observations of actual icing events.

REFERENCES

[1] W. C. Skamarock, J. B. Klemp, J. Dudhia, D O. Gill, Z. B. J. Liu and X. Y. Huang, "A description of the advanced research WRF model version 4.," Atmospheric Research, 2019

[2] H. Hersbach, "The ERA5 Atmospheric Reanalysis," in *AGUFM, NG33D-01.*, 2016.

[3] E. Thorsteins, B. E. Nygaard, K. Ingvaldsen and Á. J. Eliasson, "Wet snow icing modeling and comparison with field data," in *International Workshop on Atmospheric Icing of Structures (IWAIS)*, 2022.

An experimental investigation on the application of conductive heaters for anti/de-icing of railway switches

Arefeh Lotfi[1*], Adeel Yousuf[1] & Muhammad Shakeel Virk[1]

[1]*Arctic Technology & Icing Research Group, UiT – The Arctic University of Norway*
Arefeh.Lotfi@uit.no

Abstract—**Conductive heaters are the most prevailing types of heaters presently in the railway industry to mitigate the effect of ice on railway switches. Although they are easy and inexpensive to install, they use a significant amount of electricity. Some new technologies have been introduced to replace the conductive heater, but the conductive electrical heater is still the most favorable method. The objective of this research work is to get a scientific understanding of heat distribution in the rail in the condition of ice and measure variables such as time and power consumption of the heater in different situations. A series of lab-based experiments are conducted for *1) De-icing and 2) anti-icing (a)Pre-heating and b) Simultaneous heating)* condition. In the de-icing scenario, melting of the ice cube on the stock rail is observed. In the first scenario of anti-icing, rails are heated to the target temperature, and then water droplets are sprayed on them below freezing temperature. In the second anti-icing scenario, spraying and heating are started at the same time. Then, the heat distribution, heating time, and power consumption are discussed in these different scenarios. Experiments are conducted at two different temperatures of -2 °C and -20°C, and the target temperature of the rail is defined as +5 °C. The temperature on the railway switch is observed using thermocouples and Infrared cameras.**

Keywords— ***Railway, Switches, Anti-icing, De-icing, Conductive heater, Thermocouples, Infrared Camera.***

I. Introduction

Railway switches, also known as turnouts or points, are movable sections of tracks that allow trains to switch between the tracks. Ice and snow accumulation on these switches can hinder them from moving correctly, leading to hazardous operational issues and safety concerns. The efficiency of rail traffic is increased, and accident rates are dramatically reduced when switches are effectively protected from severe weather[1]. In this regard, the railway industry employs different methods of mitigating ice to prevent these issues, such *as hot air blowers, chemicals, gas heating, water heaters, etc[1-6]*.

One of the most important and common methods is using conductive electrical heaters. Electric heaters are installed on the railway switches to generate heat and prevent the formation of ice and the accumulation of snow. Maintaining a higher temperature on the switch components ensures the switches remain operational and allows trains to switch tracks smoothly. Regardless of the weather, the primary purpose of the switch point heating system is to melt snow and ice that could otherwise interfere with the optimal operation of the switch points. Each switch point heating system's operation should balance the needs based on the snow and ice melting process, weather circumstances (tunnels, inland, coastal, mountainous, etc.), wind and snow conditions, and energy efficiency[7].

In such ice mitigation system, heat is generated whenever a current passes through a resistive material. Compared to other heaters, this method uses practically the most straightforward technology, and its infrastructure is inexpensive. Also, electricity with standard parameters is required for this equipment. This heater's main component is a flat, oval resistor heater that is mounted on the stock rail foot. Depending on the type of turnout and the surrounding conditions, the heater's precise placement on the rail and the use of additional special equipment can vary[6]. The limited heat conduction efficiency in this condition necessitates a prolonged operation period for effective ice/snow-melting[8].

1 Sheath
2 Heating element
3 Connection pins
4 Insulation (magnesium oxide), highly compressed, seamless
5 End insulation

Figure 1. Example of conductive heater structure [2]

Although this device is simple in structure and easy to install, its old technology does not make it good enough in terms of electrical and thermal efficiency. The rail is larger than the heater, and there is a temperature difference with the air due to which the heat transfer rate to surroundings is high. As a result, the entire rail is heated by the heating device, which uses a lot of energy to heat the lengthy rail[9].

Throughout the years, it has been demonstrated that turnouts cannot be effectively heated by these resistive electric systems. In order to increase its effectiveness, researchers studied some modifications in the heater. The electric heating technique has been changed [1] by 1) expanding the area of contact between the heater and rail by converting the heating element's cylindrical to the flat form, 2) modifying the outer sheath material to make it resistant to most chemicals, water, and salt, 3) converting the embedded resistance wire's linear shape to a helical one, and 4) utilization of insulating material to conceal the heating element on the air-facing surface[10].

Also, new methods like contactless heaters and induction heating have been introduced to decrease the energy consumption of electrical heaters. Induction heating for railway switches was introduced and tested in Poland in 1978/1979 on some selected switches and stations for the first time. In this design, rails were heated with eddy currents induced inside the rails. Wires for heating were insulated, and they weren't in contact with the rails in a galvanic way. Through the years, this method evolved, and researchers have done studies to complete this concept and make up for the flaws[1, 6, 8, 9, 11, 12]. Although these studies claimed that the induction method has a better performance than the conduction method, especially in some specific frequencies, it seems that using them has some difficulties, and the rail industry is still using the conductive method. So, this study focuses on the real-world heating mechanism and aims to get a better understanding of the process of anti-icing and deicing and power consumption using the industry-preferable method.

II. METHODOLOGY

This lab-based experimental study mainly focuses on the anti/deicing of railway switches. In the de-icing mode, ice is allowed to build up on the surface to a predetermined point before being removed, while in the anti-icing mode, ice development is prevented from starting [13]. So, in these experiments de-icing is introduced by trying to melt ice cubes, and anti-icing is defined as spraying of water on the heated surface.

To study the railway switch heating process, a pair of rails (*stock rail, moving rail*) from the switch area were located in a cold room chamber of UiT. The rails and heaters used in this study are obtained from the Norwegian rail authorities to meet the current industrial demands & standards. In this cold room lab, the environmental temperature can be simulated until the temperature of -25°C. An electrical resistive heater is attached to the stock rail using four clamps. Ballasts and soil are placed under the rails to make the condition as realistic and as accurate as possible.

Figure 2. The experiment setup

In this experiment, the UIC 54 rail has been used to study the heat distribution along the rail. On both rails, thermocouples were installed at three sections of rails to record the temperature distribution. A control device is designed to control the heater using a temperature controller and some resistances. Also, this device can read the power consumption by a power meter. Moreover, the temperature data from thermocouples are recorded using an automated data logger system. An IR camera, model FLIR A615, is used to record the heat distribution of the rail cross-section during experiments. IR control software V4.59 is used to process image sequences.

First, two ice cubes were placed on the desired location along the stock rail foot in the de-icing step to monitor the melting process. This experiment has been repeated twice. The first scenario involves an environment temperature of -2ºC, whereas the second scenario has been done at -20ºC. The final temperature on the rail, which is controlled by an automated sensor in the middle of the stock rail, is defined as +5, so the heater is on until the temperature reaches this threshold.

Figure 3. Location of ice cubes on the rail for de-icing study.

One of these ice cubes is almost in the middle of the rail between two clamps, and the other one is close to the clamp that holds the heater. The objective is to evaluate the impact of ice placement along the rail in relation to its distance from the clamps.

In the next phase, a spray bar system is used to simulate the anti-icing method. This experiment has been done for an environment temperature of -2 ºC in two conditions. In the first scenario, the rail is kept at the target temperature (+5 ºC) and then sprayed with water droplets, while in the other scenario, heating and spraying water start at the same time.

Figure 4. Anti-icing experiment.

So, all the scenarios of this experiment is defined according to the following table:

Table 1. Scenarios' definition

Room temperature (ºC)	Rail Temperature (ºC)	Ice mitigation method	
-2	+5	De-icing	
-20	+5		
-2	+5	Anti-icing	With pre-heating
-2	+5	Anti-icing	Heating and spraying at the same time

III. RESULTS & DISCUSSION

A. De-icing

During the de-icing experiment, two ice cubes were placed along the foot of the rail, as shown in Figure 5. The initial temperature of ice cubes 1 and 2 in the atmospheric temperature of -2 ºC, respectively, shows -4.1 ºC and -3.8 ºC according to the infrared images. These numbers in the environment of -20 ºC show -21.5 ºC and -20.7 ºC. At the temperature of -2 ºC, the first ice starts melting almost 5 minutes after heating, and at -20 ºC, it takes 30 minutes for the first ice to start melting.
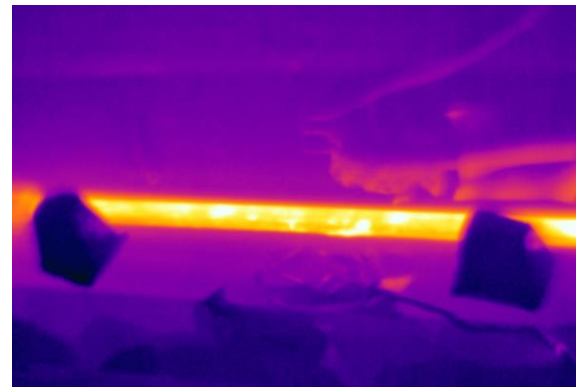
Figure 5. Melting of ice cubes and rail heater temperature distribution- image from IR camera.

In both scenarios (-2 ºC, -20 ºC), the ice cube 1, which is closer to the clamp, started melting earlier. According to this result, it seems that the foot of the rail does not transfer a similar amount of heat to both rails, and the presence of clamps has a role in transferring the heat to the rail. Clamps can make better contact between the heater and the rail according to higher force at the location and increase the contact surface to transfer heat.

Figure 6. Ice cubes during melting

Table 2 presents melting time and electrical power used for each scenario. Figures 7 and 8 show plots of these numbers, allowing easy observation of the result.

Table 2. Time and power of melting in de-icing scenarios

	Environment temperature (ºC)	Time to melt (min)	Power (kWh)
Ice 1	-2	30	0.2
Ice 2		42	0.27
Ice 1	-20	42	0.66
Ice 2		57	0.8

According to Figure 7, the line slope for -2 ºC and -20 ºC is very close. This means that the behavior of ice cubes regarding the melting time in different temperatures is similar. The melting time of cube 1 at -2 ºC is 1.4 times greater than that of cube 2, and this ratio at -20 ºC is 1.36. which means that roughly the melting time of the location near clamps is 1.4 times faster than the middle part. Also, ice cube 1 melts 1.4

times later when it is at -20 ℃ rather than -2 ℃, while the difference in melting time for cube 2 at -20 ℃ and -2 ℃ is 1.36 times. According to these results, it seems that the difference in melting time between these two different rail locations is almost as great as the difference when the temperature difference is 18 ℃, which means that the relation of the location of ice cube 1 to ice cube 2 regarding the melting time is equal to melting time of ice cube 1 at temperature -2 ℃ to cube 1 at -20 ℃.
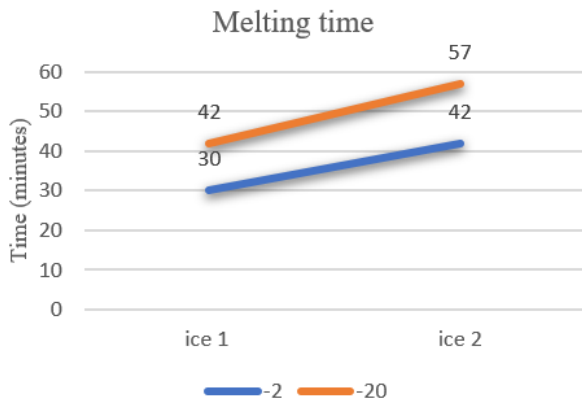
Figure 7. Comparison of melting time
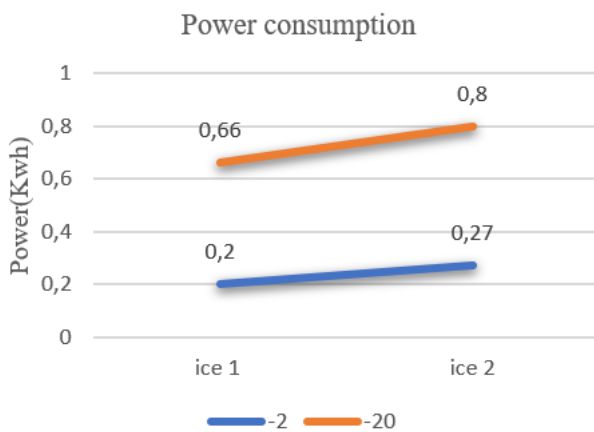
Figure 8. Comparison of power consumption

Regarding the power consumption in these two scenarios, at the temperature of -2 ℃, cube 2 consumes 1.35 times power greater than ice 1, while at -20 ℃, this ratio is 1.21. In ice cube 1, power consumption is 3.3 higher when the temperature reduces from -2 ℃ to -20 ℃, and in the location of ice cube 2, the ratio of power in these two temperatures is 2.96.
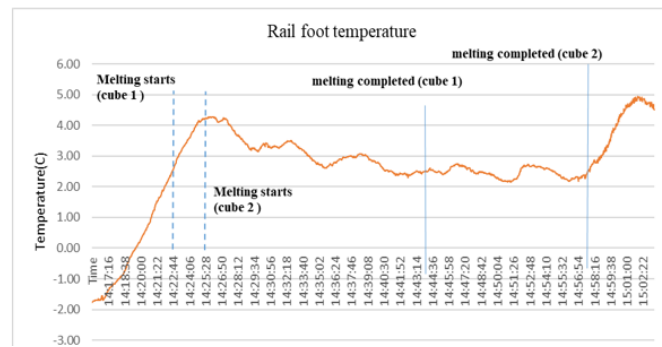
Figure 9. Variation of rail foot temperature recorded from the thermocouple at room temperature -2 ℃
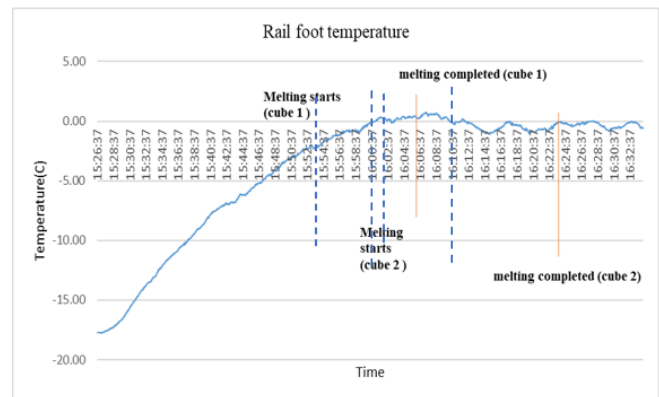
Figure 10. Variation of rail foot temperature recorded from the thermocouple in room temperature -20 ℃

Figures 9 and 10 show the temperature of the foot of the rail, where the thermocouple is almost between the two ice cubes. When the heater is on, the heat gradually transfers from the heater to the foot of the rail, and the temperature of this part starts increasing. Some of this heat is used to increase the temperature of ice cubes. Figures show that when both ice cubes start melting, the temperature of the foot begins decreasing, while after completing the melting process, the rail foot temperature starts increasing. The reason can be the heat that ice needs to change its phase from solid to liquid.

B. Anti-icing

The anti-icing experiment is done in an environment with a temperature of -2 ℃ in two different conditions. In the first scenario, heating is started until the rail temperature reaches +5 ℃, then water spraying is started. In the second scenario, in the same condition, heating and spraying start together.

Figure 11. The anti-icing experiment
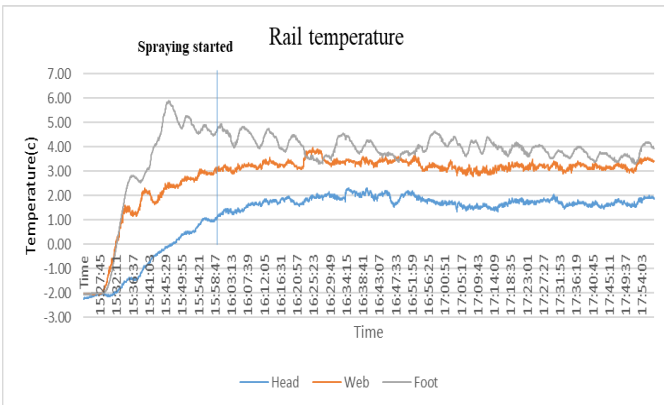
Figure 12. Temperature of stock rail recorded from thermocouples during anti-icing with pre-heating
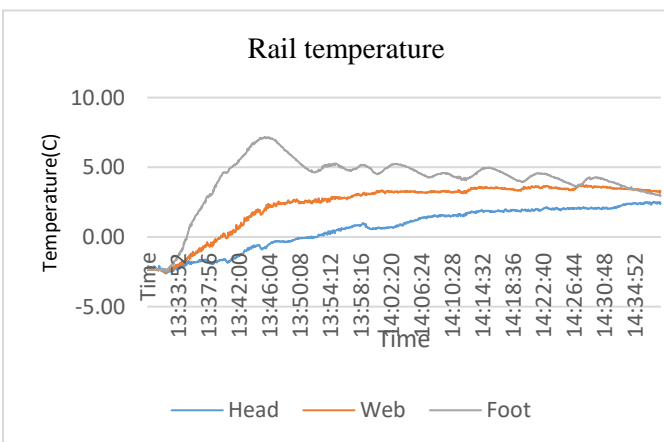
Figure 13. Temperature of stock rail from thermocouples during anti-icing without pre-heating

In a pre-heating scenario, rails used 0.17 kWh to keep heating for one hour during spraying, while without pre-heating, this power consumption is 0.35 kWh. Also, the time for reaching the target temperature is two times greater when there is no preheating. So, according to the results, the time and power to reach the target temperature and the power to keep this temperature for one hour can be doubled when there is no pre-heating.

Table 3. Time and power consumption in the anti-icing experiment

Room temperature	Anti-icing method	Power to reach +5C rail (	Time to reach +5	Power For one hour
-2	Pre-heating	0.10	6	0.17
-2	No pre-heating	0.20	12	0.35

C.   CONCLUSION

In this lab-based experimental study, the process of de-icing and anti-icing on a railway switch is observed. The de-icing scenario mainly compares the process of ice melting at different locations on the rail foot. In the area closer to the clamps, the melting happens faster and requires less power than in the area in the middle of two clamps. Anti-icing scenarios show that in a close switch state, it is more efficient to have a pre-heating before precipitation in order to keep the rail temperature at a target temperature. Results presented the time and power needed to reach the target temperature and also to keep the temperature for one hour, which is two times greater when pre-heating is not used.

Acknowledgment

REFERENCES

1. Elżbieta, S., et al., *Application of 3D Simulation Methods to the Process of Induction Heating of Rail Turnouts*, in *Infrastructure Design, Signalling and Security in Railway*, P. Xavier, Editor. 2012, IntechOpen: Rijeka. p. Ch. 12.
2. Fastrax, *ENGINEERED SNOW CLEARING PRODUCTS FOR RAIL APPLICATIONS*, Thermon, Editor.
3. *PRODUCT CATALOG*, r. company, Editor. 2007, www.railsco.com.
4. Omer, R., et al., *Evaluation and Optimization of Winter Snow and Ice Control Operations for Railway Platforms*. 2013, Transportation Planning & Development: Toronto

5. *Good Practice Guide- De-icing Agents for On Station Use*. 2006, Association of Train Operating Companies.

6. Żelazny, R., P. Jabłoński, and T. Szczegielniak, *Operation of the Prototype Device for Induction Heating of Railway Turnouts at Various Operating Frequencies.* Energies, 2021. **14**(2): p. 476.

7. *Lavspenning/Sporvekselvarme - TS Switch point heating system*. Tekniske spesifikasjoner 03/04/2024]; Available from: https://trv.banenor.no/ts/Lavspenning/Sporvekselv arme_-_ _TS_Switch_point_heating_system#Fixed_or_flexibl e_heating_elements_fixed_to_the_web_of_rails.

8. Oh, H., et al. *A Study on High-Frequency Induction Heating System for Railway Turnout*. in *2019 IEEE 13th International Conference on Power Electronics and Drive Systems (PEDS)*. 2019.

9. Oh, H.-S., et al., *A study on de-icing for railway turnouts using 250kHz-200W-class induction heating system.* AIP Advances, 2019. **9**(12).

10. *Technology Review of Autonomous Rail Switch Heating System- "Blue Point"*. April 23, 2021, NIBE Element Railway Solutions.

11. Flis, M., *Energy efficiency analysis of railway turnout heating system with a melting snow model heated by classic and contactless heating method.* Archives of Electrical Engineering, 2019. **68**(3): p. 511-520.

12. Szychta, E. and L. Szychta, *Comparative Analysis of Effectiveness of Resistance and Induction Turnout Heating.* Energies, 2020. **13**(20): p. 5262.

13. Lotfi, A. and M.S. Virk, *Railway operations in icing conditions: a review of issues and mitigation methods.* Public Transport, 2023. **15**(3): p. 747-765.

Local environmental loads for railway overhead contact line system design

Maria Enger Hoem[1], Bjørn Egil Nygaard[1], Gabor Horvath[2]

[1] *Kjeller Vindteknikk (Part of Norconsult), Norway*
[2] *Analysis and Special Structures, Norconsult, Norway*

maria.hoem@norconsult.com, bjorn.egil.nygaard@norconsult.com, gabor.horvath@norconsult.com

Abstract— **Overhead contact line support structures are designed to withstand static and environmental loads. Traditionally, the environmental loads used in structural design of railway masts and cross-span structures are based on reference values found in national annexes to international standards. These reference values are defined for large areas which does not necessarily capture the local terrain effects sufficiently. In this paper we present how modelled historical meteorological data along the railway line is used to obtain site-specific wind and ice loads. And furthermore, how these environmental loads contribute to optimized design with respect to reduction in structural steel and concrete and corresponding reduction in equivalent CO2 emissions.**

Trønderbanen and Meråkerbanen, two railways covering 120 km and connecting Trondheim in Norway and Storlien in Sweden, have historically been run by diesel but are now in transition of becoming electric. This specific railway is quite winding, and the reference loads are relatively high which results in large steel mast dimensions. The calculation of site-specific environmental loads confirms relatively high 50-year wind gust values, while the ice loads are reduced compared to the reference values. Furthermore, an assessment of the concurrent wind and ice loads shows a lower probability compared to the predefined load cases proposed in the standards. The comparison of the combined load cases to actual occurrence of combined loads are illustrated visually through scatterplots. When taking the site-specific environmental loads into account, it turns out that it is mainly the static loads of the overhead contact line system that determines the strength capacity, and the environmental loads become less important.

Keywords— **Environmental loads, combination loads, ice modelling, electric railway, reduced CO2 emissions**

I. Introduction

In order to create more modern and environmentally friendly railways some previously non-electrified lines are being rebuilt to run on electric power instead of fossil fuels. One such railway line is the 120 km long stretch between Trondheim in Norway and Storlien in Sweden, which will be rebuilt for World Ski Championship 2025 held in Trondheim [1], see map in Fig 2. The World Ski Championship 2025 has the ambition to be the most sustainable of all time, and most transportation from and to the championship is planned by the railway.

A railway overhead contact line system must be built along the tracks to supply the electric motor with electricity through the pantograph on the train – which means that overhead contact line support structures must be designed and built. Traditionally, environmental loads for design of structures such as masts are taken directly from national annexes of international standards.

For the Electrification of Trønderbanen and Meråkerbanen (ETM) project [2] the reference values for wind and ice loads taken directly from the standards yield large environmental loads on the masts. This makes the mast design challenging due to the strict requirements of maximal horizontal deflection of the overhead contact line system, due to both static and environmental loads.

These reference values for wind and ice are set to represent large areas and will often miss local effects that may influence the wind and icing conditions radically. However, with the use of model data with fine resolution that captures the local terrain effects better, site-specific environmental loads can be analysed.

II. Design challenges of overhead contact line support structures

The overhead contact line is what supplies the electric railway with electric power. Its structural integrity directly impacts safety, reliability, and operational efficiency. A picture of an overhead contact line system is shown in Fig 1.
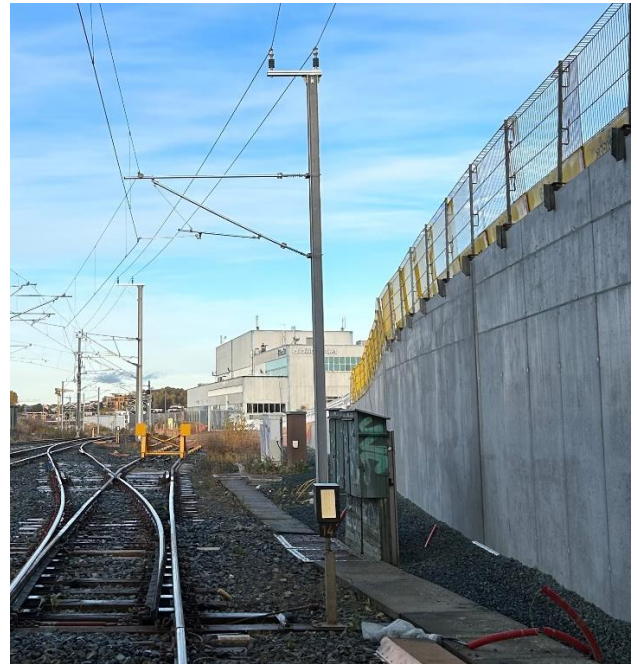
Fig 1: Photograph of one of the overhead contact line support structures at ETM. The upper two lines are autotransformer wires. On the horizontal boom there is the catenary wire at the top and the contact wire at the bottom.

Fig 2: Map of location Vikhammar (blue dot) which is located along the fjord Trondheimsfjorden in Trondheim, Norway. From Kartverket.

Bane NOR Technical Regulations works as a governing standard for designing, constructing, and dimensioning railway facilities in Norway. It collects the norms of railway technical disciplines, such as for overhead contact line system [3].

There are strict requirements to the dimensioning of the masts. The total deflection of the contact line due to static loads must not exceed 37 mm (12 mm from the mast and 25 mm additional from de deflection of the foundation) The total deflection of the contact line due to environmental loads must not exceed 63 mm (should not exceed 18 mm due to deflection of the mast and should not exceed 45 mm due to the deflection and rotation of the foundation). To ensure that the contact line never goes under the pantograph the strict limitations written in Bane NOR technical regulations must be hold.

This particular railway section is following the complex coastline from Trondheim to Hell. With all the curves of the track and the high tension in the lines the structural loads are relatively large alone, and the strict requirements due to both static and environmental loads made it difficult to design the masts. Large steel mast dimensions were needed after the initial calculations.

III. INPUT DATA AND METHOD

A. Reference values for environmental loads.

The technical regulations are following the European standard EN 50119 for railway installations, or as Norwegian version NEK 900 [4]. NEK 900 states that for overhead contact line systems load cases combining wind and ice should be considered as defined in The Norwegian electrotechnical standard for overhead electrical lines exceeding AC 1 kV (NEK445) [5] which is the translation of EN 50341-1 plus the Norwegian annex (NEK EN).

The NEK 445 refers to both wind and ice loads. Reference wind loads are to be taken from the Eurocode EN 1991-1-4

with Norwegian annex [6]. ISO 12494 for atmospheric icing [7] is listed as resource for ice calculations.

The Norwegian appendix to Eurocode EN 1991-1-4 gives a reference wind speed for Trondheim municipality of 26 m/s at 10 m height above ground. With terrain category 2, suitable for areas with low vegetation like bushes and small trees, the 50-year gust value becomes 39.7 m/s.

A reference ice load of 40 N/m is given for this area in NEK445. However, NEK 445 also states that the reference values should only be applied in cases where no other site-specific data are available. Therefore, instead of using reference values, high-resolution meteorological hindcast data is used to calculate the local wind loads, ice loads and the combination of these.

B. Hindcast data.

Meteorological hindcast data has been widely used in recent years to improve assessment of local wind and ice loads on structures. In this project, the hindcast data is generated using the Weather Research and Forecasting model (WRF) [8] with ERA5-T reanalysis dataset as input. Two datasets are combined, one coarser long-term dataset, and one high-resolution shorter-term dataset as summarized in Table I.

TABLE I. WRF-DATA SETUP

Simulation name	WRF3km	WRF1km
Horizontal resolution	3 km x 3 km	1 km x 1 km
Time period	1991-2020	2005
Input dataset	ERA5	FNL
Nr of vertical levels	32	32
Boundary layer scheme	MYNN	YSU
Microphysics scheme	Thompson-Eidhammer	ETA Ferrier

The high-resolution dataset is used to correct the wind speed and wind direction of the coarser dataset to better capture local terrain effects. The long-term correction method

is described in Liléo et al. [9]. The long-term corrected data series consists of hourly data for a 29-year period.

C. Calculation of wind and ice loads

There are three load cases that is evaluated when considering environmental loads on structures defined in NEK 445:

1) Wind actions without icing.
2) Ice load without wind (weight of the ice).
3) A combination of extreme wind and less extreme (nominal) ice load.

From the hindcast data, hourly ice loads are calculated. Wind and ice loads are then used in extreme value calculations with the methods described in the following sections.

1) Wind:

Extreme wind is calculated based on modelled timeseries of wind speed and the set of formulas given in the wind standard (NS-EN 1991-1-4) for calculating wind gusts. Based on the wind speed for the strongest storms and the surface roughness, the turbulence intensity and corresponding gust factor are determined separately for each sector.

Extreme wind analysis is carried out on the timeseries. Gumbel-Lieblein's methodology [10], [11], [12], which is a recognized method for calculating extreme wind, has been used. The methodology assesses the distribution of annual maxima of wind speed.

2) Ice:

With proximity to the fjord and low terrain elevation, icing due to supercooled cloud droplets or freezing rain can be neglected, and wet snow is the remaining icing type that should be considered when calculating design loads.

Wet snow occurs during snowfall at temperatures just above freezing. In such cases, the snowflakes will contain a certain amount of liquid water, which makes them sticky and easily attaches to lines. The icing rate increases with increased wind speed. Accumulation of wet snow on a horizontal line can be modelled based on information about precipitation, wind, temperature, and humidity as described in Thorsteins et al. (2022) [13]. Since wet snow only occurs under very special weather conditions, despite a longer time series (29 years), there will be relatively few episodes to base the extreme value calculation on. To increase the statistical basis, calculations have been carried out with an ensemble methodology consisting of a series of icing calculations for the same model point where the temperature is changed with values varying between -2 and 2 °C. Furthermore, a 50-year wet snow load is estimated for each of the 40 realizations. Dimensioning wet snow load is based on the median in this distribution.

In some cases, dry snow can form on the line if the line is already covered with a layer of ice (wet snow). Such cases are typically linked to periods with falling temperatures and low wind speeds (<~5 m/s) after periods with wet snow icing. This phenomenon is therefore most prominent in areas with forest and areas with generally low wind speeds near the ground.

A statistical analysis is used to determine the extreme values. The extreme value analysis is called Peaks-Over-Threshold (POT) and involves fitting the events that exceed a high limit with a theoretical probability distribution. In the POT analysis, the exceedances are fitted to a generalized Pareto distribution. Once the distribution is best fitted to the data, return periods can be determined, with corresponding return values. The code used for the extreme value calculation is documented in Coles [14].

D. Combination of wind and ice

The load case with a combination of wind and ice loads, i.e., wind pressure on the iced line, should be calculated according to the guidelines given in chapter 4.6.1 in NEK 445. This means that the wind forces should be calculated based on gusts with low probability in combination with ice load with a high probability. When the icing type is wet snow, the extreme wind speed used should be multiplied by wind speed reduction factor, Bi, equal to 0.7. A scaling of the wind speed with 0.7 corresponds to a scaling of the wind pressure with 0.49. See overview of the load cases in Table II, where ρ_{air} is air density, FG is wind gust, D_{wire} is the diameter of the line, IM is ice mass, g is gravity, Bi is wind reduction factor, and ID is the ice diameter calculated from ice load of specified return period and an ice density of 600 kg/m³ for wet snow.

TABLE II. LOAD CASES FROM NEK 445

Load case	Formula
1	$F_{wind} = 0.5 \cdot \rho_{air} \cdot FG_{50}^2 \cdot D_{wire}$
2	$F_{ice} = IM_{50} \cdot g$
3	$F_{comb2} = 0.5 \cdot \rho_{air} \cdot (FG_{50} \cdot B_i)^2 \cdot ID_3$
4	$F_{comb1} = 0.5 \cdot \rho_{air} \cdot (FG_3 \cdot B_i)^2 \cdot ID_{50}$

In chapter 4.6 in NEK 445 it is described that the load case with combined wind and ice loads can be omitted on the advice of a meteorologist. Since the data from WRF3km is given with 1-hour resolution for the entire period from 1989 to 2023, the actual simultaneity of wind and ice on the lines can be analysed. Hourly values of the combination load are calculated, and based on these time series, a site-specific wind speed reduction factor can be calculated. In some cases, the probability of strong wind occurring at the same time as there is ice on the lines is very low. Consequently, the load caused by extreme gusts may be greater than the load caused by a combination of wind and ice on the lines, and the combined load case will not be the dimensioning load case in the structural design calculations.

IV. SITE SPECIFIC ENVIRONMENTAL LOADS

Hindcast data are extracted from the model datasets for six points along the ETM-project track from Trondheim to Hell, representing six individual segments subject to detailed climatological analyses. For each location ice and wind loads are calculated and extreme values are estimated as described previously. The loads are also decomposed into the relevant line directions.

Modelled 50-year ice loads, in form of wet snow, vary from 24.0 N/m to 39.2 N/m for the six locations. Which means all are below the reference value of 40 N/m (approximately 4.1 kg/m) from the standard.

A reference wind speed of 26 m/s is given for this region in the Norwegian annex to Eurocode 1-4, which for terrain category 2 yields a 50-year wind gust value of 39.7 m/s at 10 m height. The modelled 50-year wind gusts for the six locations are all higher than this wind speed and varies from 40.3 m/s to 44.6 m/s. The high wind speeds are explained by the vicinity to open water bodies and local exposure to onshore winds.

Using hourly model data for wind and ice, hourly values of wind pressure on iced conductors are calculated. The analysis shows that the 50-year values of wind force on iced conductors range from 13.9 N/m to 21.2 N/m for the six locations. In comparison, if these values were to be calculated from the pre-defined load cases (3 and 4 in Table II), and reference values of wind and icing obtained from relevant standards, the value would be 28.6 N/m and apply for all locations. The difference is mainly explained by lower ice loads, and lower probability of simultaneous wind and icing. When calculating site specific factors for wind speed reduction, Bi values range from 0.49 to 0.69 for the six locations, which are all lower than the standard value of 0.7.

Since Bane NOR Technical Requirements states that environmental loads for mast dimensioning should be based on 10-year return values, extreme value analysis is performed for several return periods including 50 years, 10 years and 3 years to cover all four of the defined load cases.

A plot of extreme wind for different return periods is shown in Fig 3 where the blue crosses are the highest wind gust for each year, and the solid black line is the fitted Gumbel distribution for return period estimation.
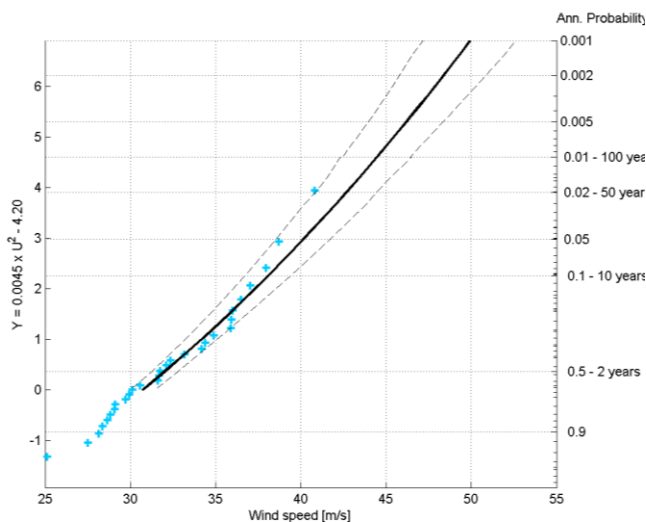
Fig 3: Extreme wind analysis of modelled wind gusts at 10 m height at Vikhammar. The thick black line show the Gumbel-Lieblein fit to the annual wind gust maxima (blue plus-signs) from the timeseries where the WRF1km are synthesized with WRF3km.

V. CONCLUSIONS

Calculation of local environmental loads has had a great impact on the structural design of railway masts, cross-span structures and their foundations for the ETM project. The model data confirmed that the line is exposed to severe weather events partly due to the close vicinity to the coastline. However, the detailed analysis of simultaneous wind and icing gave reduced design loads through site-specific wind reduction factors obtained from the model timeseries.

E. Increased understanding of combination load calculations.

To better understand and communicate the analysis of the load cases defined in NEK 445 used for structural design, a plot of the load cases which includes horizontal loads is developed. This include load case 1, 3 and 4 described earlier, while load case 2 is a vertical load.

An example of such scatter plot is shown in Fig 4 for Vikhammar, a location where the railway track is close to the coastline and exposed to onshore winds. Hourly modelled data decomposed to the relevant line direction are plotted as small blue circles with its value for wind load at the x-axis and its ice load value on the y-axis. The highest wind force occurs at small ice loads (less than 7 N/m), while the highest ice loads occur with wind force less than 10 N/m.

From the hourly values of ice load and wind speed, a 50-year wind force on iced conductor is estimated to 21.2 N/m as shown with the dashed blue line.

The three load cases for horizontal loads listed in Table II are also plotted using the modelled data. Load case 1, 3, and 4 are shown with pink, red and green dots respectively. Here the 3-year wind gust is taken as 0.76 times the 50-year value, the icing diameters are calculated assuming a specific wet snow density of 600 kg/m^3, a 25 mm conductor diameter and a wind speed reduction factor (Bi) of 0.7 as given in the standard.

Lastly, the light blue dot is the resulting combination load defined as load case 3 from NEK 445, but with the use of reference values for 50-year wind gust and 50-year ice load from the standards.

For Vikhammar, the 50-year combined load calculated from hourly modelled values is 21.2 N/m, while the combination load based on standard values is 28 N/m. This gives a reduction of 7 N/m, which is a 25 % reduction, when using site-specific modelled data. The results were similar for all six locations along the railway, however significantly larger reductions were identified in more sheltered segments of the line [2].
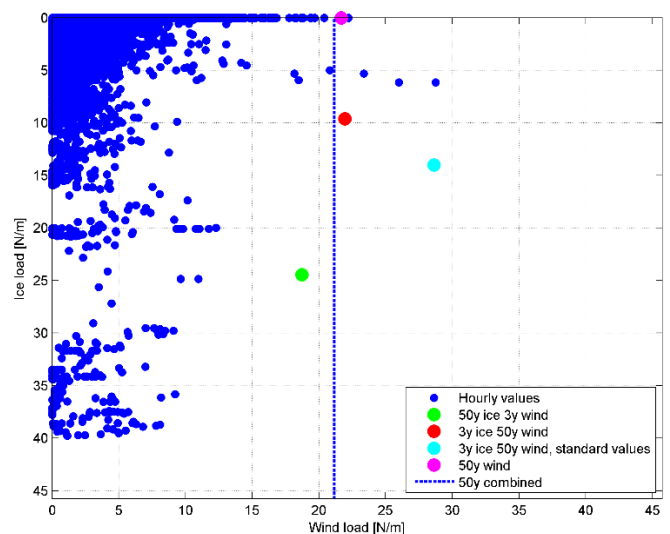
Fig 4:   Calculated loads at Vikhammar. Small blue dots are hourly values of ice and wind loads (including 40 temperature perturbations). Blue dashed line marks 50-year combination load calculated from the hourly data. Pink dot marks 50-year modelled wind force without icing. Red dot marks combination load of 50-year wind and 3-year ice, while green dot marks combination load of 3-year wind and 50-year ice, all from modelled data. Light blue dot marks combination load based on reference values from standards. All values are given as horizontal loads per meter line [N/m] for a line of 25 mm thickness at 10 m height above ground.

F. Reduced steel amounts and C02 emissions

The masts for the overhead contact line support system are HEB steel beams for the freestanding masts and HEM steel beams for the tension masts. The relevant sizes are HEB200 (nominal weight of 61.3 kg/m) to HEB280 (nominal weight of 103 kg/m) and HEM260 (nominal weight of 172.7 kg/m) [3].

There are about 2500 steel masts planned to be installed along the railway line. Mast dimensions are larger when the structure is calculated with the use of standard reference values compared to the use of site-specific values. Also, when using local loads there are more possibilities of local optimization of the mast design. Nearly every mast along the line is optimized through automated calculations, contributing to a more environmental friendly and economical design with less material usage while still upholding the necessary structural capacity of the system.

The amount of steel is reduced with approximately 133 tons when using site specific environmental loads in the mast design. This corresponds to a reduction in CO2 emissions of 335 tons.

REFERENCES

[1] (2024) Trønderbanen on the SJ website. [Online]. Available: https://www.sj.no/en/strekning/tronderbanen-2/

[2] M.E. Hoem and B.E. Nygaard, "Trønder- og Meråkerbanen – Klimalaster for jernbanelinjer", Norconsult, Tech. Rep. KVT/2022/R017/MEH, 2022.

[3] (2024) Kontaktledning/Prosjektering og Bygging/Fundamenter, master og åk, [Online], Available: https://trv.banenor.no/wiki/Kontaktledning/Prosjektering_og_Byggin g/Fundamenter,_master_og_%C3%A5k

[4] *Electric railway installations,* Norwegian electrotechnical standard NEK 900:2014, 2014.

[5] *Overhead electrical lines exceeding AC 1 kV*, Norwegian electrotechnical standard NEK 445:2016, 2016.

[6] *Eurocode 1: Actions of structures – Part 1-4: General actions – Wind actions*, NS-EN 1991-1-4:2005+NA:2009, 2009.

[7] *Atmospheric icing of structures*, ISO 12494:2017, 2017

[8] (2024) Weather Research & Forecasting Model (WRF) [Online]. Available: https://www.mmm.ucar.edu/models/wrf

[9] S. Liléo, E. Berge, O. Undheim, R. Klinkert and R.E. Bredesen, "Long-term correction of wind measurements. State-of-the-art, guidelines and future work", Elforsk, Tech. Rep. 13:18, 2013.

[10] E. Gumbel, "Statistics of extremes", Columbia University Press, 1958.

[11] J. Lieblein, "Efficient methods of extreme-value methodology", National Bureau of Standards, NEA-CSNI-R, 1976.

[12] R. Harris, "Gumbel re-visited – a new look at extreme value statistics applies to wind speeds", Journal of Wind Engineering and Industrial Aerodynamics, vol. 59(1), pp 1-22, 1996.

[13] E. Thorsteins, B.E. Nygaard, K. Ingvaldsen and Á.J. Elíasson, "Wet snow icing modelling and comparison with field data", in Proc. IWAIS, 2022

[14] S. Coles, "An introduction to statistical modelling for extreme values", Springer, 2001.

Energy production optimization from biomass wood chips used in the Arctic region

Tomi Abioye[1], Espen Johannessen[2], Geanette Polanco[2], Thu Minh Huynh Thi[3], Hung Thanh Nguyen[1]

[1] UiT the Arctic University of Norway - IVT. Faculty. – Department of Industrial Technology. Norway
[2] UiT the Arctic University of Norway - IVT. Faculty. – Department of Building, Energy and Material Technology. Norway
[3] Ho Chi Minh City University of Technology and Education – Faculty of Vehicle and Energy Engineering. Vietnam

abioyetomi@gmail.com, espen.johannssen@uit.no, Geanette.polanco@uit.no, thuhtm@hcmute.edu.vn, hung.thanh.nguyen@uit.no

Abstract— **Constraints on accessibility and use of energy to support human activities' development and permanence in the Arctic regions are more severe due to the extreme weather characteristics in the area. Nevertheless, the compromise to align with the European's plan of reduction of greenhouse gas emissions is the same as in any other region or country [1] [2] [3]. Therefore use of solid biomass as source of green energy then is also expected there [3]. Heat and power can then be generated from biomass wooden chips by combustion which is a thermochemical conversion process that provides room heating, heated water, or any other functionality [4] [5]. It is known that biomass wooden chips usually contain higher moisture content and lower heating values than fossil fuels like coal or petroleum [6]. Nevertheless, they can be produced locally as it is the case of biomass wooden chips from crushed Norway spruce (Picea abies) a common biomass source in Narvik, Norway. As the moisture content in biomass wooden chips plays an important role in the combustion efficiency and heat exchange performance [7] [8], it is proposed in this work that the moisture content in these biomass wooden chips tends to be in frozen conditions which reduces the energy efficiency of the power generation process [9] [10]. Low atmospheric temperatures impose an additional constraint in the gas flow kinematics involves in the heat exchange process due to the thermal gradient. Technological advancements and development on the design of the overall biomass energy production systems will contribute not only to the reduction of greenhouse but to increase the sustainability of the system adapted to cold climate conditions [11]. In this study, energy management will be analysed by exploring the impact of moisture content and conditions in biomass feed on a commercial boiler equipped with a water district heating heat exchanger through simulation that discharges to the atmosphere. Analysis will focus on two-sections of the process, the combustion (combustion products and their characteristics) and the heat transfer process between the combustion products and the surroundings. The findings indicate that an increase in moisture content of the biomass as expected gives higher heat loss to the evaporation phase change, while simultaneously decreasing the heat exchange from the combustion to the district heated water. However, there exists an optimal moisture content for each the atmospheric temperature conditions.**

Keywords—***Energy optimization, Biomass wood chips, Arctic region, renewable energy, Picea abies.***

I. INTRODUCTION

The use of central heating systems to heat public spaces and rooms can be traced back to the 4th century BC in Greece and later became popular in palaces, large villas and homes of upper class and wealthy Roman merchants [4]. Hot air and smoke were generated from furnaces or fireplaces and used to heat up the rooms directly above and other rooms through ducts in the wall. In the late 19th century, the advancement of technologies associated with steam boilers, cast iron processing and the manufacture of quality copper provided an avenue for the development of hydronic central heating systems where water or steam is used for heat transfer in heating systems. By the year 2011, several state-of-the-art technologies like oil fired boilers, wood and biomass furnaces and solar fireplaces could be used to ensure a thermally comfortable and safe environment for inhabitants at a reasonable rate, especially with the technological strides made in control and automation engineering which made heating systems more intelligent and able to operate with the use of sensors to meet several operational requirements [4]. The need to achieve not only efficient energy production processes but at the same an environmentally friendly imposes an extra constraint in the how the energy production systems are used.

The use of biomass as source of energy presents a good potential balance between the energy produced and exhaust products generated after the current use that involved the burning of biomass. Biomass is a relatively cheap energy source with less greenhouse gas impact, and it is nearly CO2 neutral. Biomass can be produced from natural sources like wood waste, grasses, and fast-growing energy crops which are generally ubiquitous and industrial sources like liquid manure and biodiesel [1]. However, biomass potential of supplying renewable energy can be limited by expertise, management capacity in building, an efficient and sustainable biomass supply network, and the level of advancement of bioenergy systems [12].

Bioenergy is generated from biomass that can be transformed to solid, liquid, and gaseous biofuels which is eventually used for production of heat, power, and fuel for transportation. Recently, there has been an increased use of biomass as a substitute for conventional fossil fuels [6]. However, biomass mostly have higher moisture content and lower heating values which makes them differ significantly from conventional fossil fuels like coal or petroleum [6].

In the Arctic region the energy production encounters the additional challenges such as for example long winters. Winter conditions include low temperature but also humidity values that vary between different ranges that in other zones. Holding and development of human activities in this area depends on having an energy security in the Arctic [13]. The use of local sources is biomass is also a key aspect of a sustainable energy production. Then it is proposed here that the study will be carry out considering system Norway Spruce (Picea abies), as the mean source for the wood biomass.

Norway Spruce is a highly adaptable tree including to the Arctic conditions and where it is a fast-growing spruce.

II. MOISTURE

Moisture content affects the net calorific value and the rate of biomass consumption. A high moisture content in biomass causes the combustion process to release less heat because much of the energy is used to evaporate water.

The moisture content also determines how the combustion of biomass in the furnace should be regulated so that the efficiency of the furnace is improved, and emissions are brought to a minimum. The moisture content can be measured through direct or indirect methods. Several measurement techniques exist for determining moisture content. Direct methods involve the measurement of moisture content through the direct analysis of the biomass wood chips while the indirect methods perform measurements on the flue gases that are formed [14].

A. Factors that Affect Moisture Content Measurement

One of the high complexity aspects of studying the moisture effects on biomass burning processes reside on the fact that individual properties of biomass change with the moisture content. The degree to which the moisture content measurements are affected depends on which properties in the wood is measured. Usually, the measured properties are affected by the characteristics of the wood. In general, the fiber saturation point of the wood is reached at approximately 23% moisture content. Above the fiber saturation point, water molecules are less tightly bound to the wood, and this affects some of the measured properties.

Another factor that greatly influences the measurement result is the temperature of the biomass. This is because many properties of water and wood as well as the relationship between these properties are affected by temperature. A few degrees temperature change above the freezing point of the biomass leads to small changes in the wood and water properties. These changes are small when compared with the changes that occur when the water turns into ice. There is a great difference between the properties of ice and liquid water because the molecules in ice become more tightly bound together with less opportunity to move and this affects both their mechanical and electrical properties. Also, the properties of ice can sometimes be like those of wood which makes it difficult to distinguish them.

To address the effect of the variation of the moisture content in the biomass wood chips on the efficiency of the energy production process. a fixed set of moisture on the Spruce Norway will be evaluated.

III. HEATING SYSTEMS

A. Heating systems based on Wood and Pellet Burning Stoves

Some heating systems used in the heating of buildings, burn biomass in stoves to radiate heat directly into the rooms or burn the biomass in a boiler which is connected to a water circuit that supplies thermal energy in the form of hot water in insulated pipes for the provision of heat [15]. Wood burning stoves with regulated air flow can provide efficiency reaching around 75%. Wood burning stoves provide a high heating effect for a short period of time which results in sudden temperature increment. However, pellet burning stoves are more efficient, about 85% efficient and provide a means for automatic pellet ignition and pellet feeding. Automatic pellet feeding from storage allows for continuous operation of the pellet stoves for a long period depending on the size of the stove and on the surrounding temperature. Usually pellet stoves have thermostats that switch them on and off and a computer system to adjust the feed rate of pellets. A regular room stove provides heating to the surrounding through forced-air ventilation while others have a boiler for heating water that circulates to heat radiators in other rooms [4].

There are few disadvantages of wood biomass heating systems, including: the requirement of a storage area and the incomplete combustion of wood produces dangerous emissions including particulate matter, carbon monoxide, nitrogen oxides, sulphur oxides and volatile organic compounds [4].

The design of a biomass combustion system and its operating parameters are dependent on the properties of the biomass that will be used. Properties like the moisture content, heating value and composition of minor constituents such as chlorine, sulfur and nitrogen are important to consider when designing a biomass combustion system. These unique biomass properties can provide certain advantages and pose several challenges to the combustion process. A very good understanding of the physical and chemical processes that occur during biomass combustion can contribute to a more efficient and improved heating system [6].

The most common types of combustion chambers have air supplied through three channels. The first channel provides air supply during the ignition of fuel, after which the channel closes. The second source is used to supply the primary air that flows around the fuel to maintain combustion. The third air channel is used to supply air needed for secondary combustion [16].

B. Combustion Reactions in the Furnace

Several physical and chemical processes occur simultaneously when fuel burns in a combustion chamber. Some of these processes are drying and heating of fuel, separation of volatile matter, flaming combustion of pyrolysis products and combustion of the solid combustible residue [17].

Once biomass is subjected to heat in the presence of oxygen, several processes begin to occur simultaneously in the combustion chamber. Firstly, heat transfer occurs at the surface of the biomass through conduction and the temperature in the biomass continues to rise until the pyrolysis temperature is reached. When the pyrolysis temperature is reached then thermal decomposition of the biomass starts and heat is transferred inside the biomass through conduction and through the pores by convection. Close to the end of the pyrolysis process after volatiles are released, the homogeneous reactions occur, and the char ignites [18]. The increase in the heating rate and quantity of biomass and the decrease in biomass porosity results in higher volatile and char ignition temperature [18]. The thermal decomposition of biomass during a combustion reaction is usually separated into two phases:

Phase 1:

$$Solid \rightarrow Char + Gas \qquad (1)$$

Phase 2:

$$Char \rightarrow Gas + Ash \qquad (2)$$

The governing equations of the phenomena occurring during the combustion fulfil the main statement of conservation of mass (eq. 3), as well as conservation of energy (eq. 4). Additionally, as the process involves several compounds that will be broke down in individual chemical elements (species), then a transport equation for each species (eq. 5) is required to model the local mass fraction of each species.

The continuity equation:

$$\frac{\partial(\rho_f W_i)}{\partial x} = 0 \qquad (3)$$

Momentum equation:

$$\frac{\partial}{\partial x_i}\left(\rho_f W_i W_j\right) = \frac{\partial}{\partial x_i}\left(\mu_{eff}\frac{\partial W_j}{\partial x_i}\right) - \frac{\partial p}{\partial x_j} \qquad (4)$$

Species transport equation:

$$\frac{\partial}{\partial x_i}(\rho W_i Y_k) = \frac{\partial}{\partial x_i}\left[\rho\left(D_{m,k} + \frac{\mu_{eff}}{\rho\sigma_t}\right)\frac{\partial Y_k}{\partial x_i}\right] + R_k \qquad (5)$$

Where ρ is the density, W is the mass flow, μ_{eff} is the effective dynamic viscosity, p is the pressure, Y is the mass fraction of the species k, D_m is the mass diffusivity, σ_t is the shear stress, and R_k is the net rate of production of species.

The rate of reaction of the thermal decomposition of biomass is governed by the first-order Arrhenius law. Combustion is one of the thermo-chemical processes through which biomass can be used to produce energy by the application of heat and in the presence of oxygen. About 90% of the total renewable energy generated from biomass is produced through the process of combustion [5]. Biomass furnaces can combust several types of biomasses like wood, dry leaves, hard vegetable shells and rice husks [5].

In combustion, biomass is mixed with oxygen in a high temperature environment to form carbon dioxide, water vapour and heat.

$$BM + O_2 + (H_2O)_{liq} \rightarrow CO_2 + (H_2O)_{gas} + q \qquad (6)$$
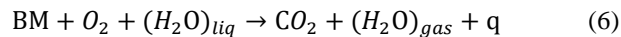
where BM is biomass and q is heat.

An approximate chemical equation for the combustion of biomass is given below:

$$CH_{1.44}O_{0.66} + 1.03O_2 + (H_2O)_{liq} \rightarrow$$
$$CO_2 + 0.72H_2O + q \qquad (7)$$
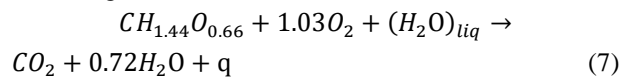
Combustion in biomass occurs due to the exothermic reaction between the biomass and oxygen. The main products released from combustion are H_2O and CO_2. Also, due to the preexisting water content in the biomass before combustion, water (gas) is released along with the hot fumes [19].

The heat produced depends majorly on the type of biomass used but can also be influenced by many other factors. Majority of biomass contain a fraction of carbon below 50%, and a greater portion of the remaining being oxygen which causes a lower high heating value (HHV) about 20 MJ/kg biomass [5] [20]. The combustion of biomass is an exothermic process where chemical energy is released and is converted into either mechanical or electrical energy [5].

Wood composition is normally done by listing the compound present in it. The number of different compounds reported varies. Fig. 1 shows the characterisation of the Norway spruce using a composition of 4 compounds, such as cellulose, lignin, galactoglucomannans (GGM) and Xylan [21]. It is also important to mention that these characteristics differs for different ages of the tree, as it is shown in Table I [22].
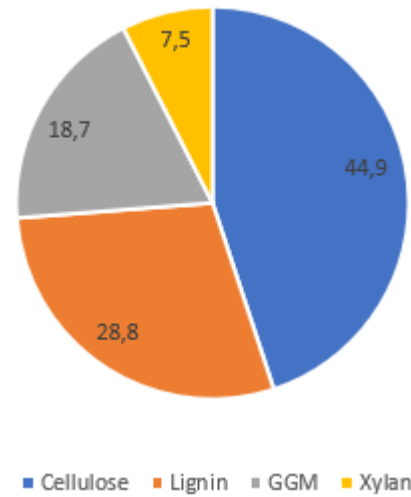
Fig. 1   Composition of Norway Spruce.

TABLE I. PROXIMATE AND ULTIMATE ANALYSIS OF SPRUCE WOOD

Element	Cellulose [%]	Lignin [%]
Juvenile wood	38.1 - 40.3	28.0 - 30.8,
Mature wood	40.2 - 42.7	26.1% - 28.2

Biomass is characterized by its ultimate and proximate analysis where the ultimate analysis reports the weight percent of carbon, hydrogen, nitrogen, sulfur, and ash given on as received, dry ash free or dry basis and the proximate analysis that reports the moisture content, volatile matter, and fixed carbon. The ultimate analysis and heating value of Norway spruce wood, obtained from local sources in Trondheim, is shown in the Table II.

PROXIMATE ANALYSIS			
Moisture[a]	Volatile matter[b]	Fixed carbon[b]	Ash[b]
6.23	86.34	13.43	0.23

ULTIMATE ANALYSIS					
C[b]	H[b]	O[b]	N[b]	S[b]	HHV (MJ/kg)
50.1	6.2	43.52	0.07	0.05	20.45

HHV: higher heating value. [a]wt%. [b]wt%, dry basis.

TABLE II. THE AMOUNT OF MAIN CHEMICAL COMPOUNDS

IV. PROCESS DESCRIPTION

The model of the energy production process presented in Fig. 2 includes 4 zones, the drying zone, pyrolysis zone, combustion/Cracking zone and cooling zone [23]. The model has been developed in Aspen Plus. In the drying zone the temperature is about >150 ºC and at this temperature the water vapor is cleared. The biomass material will evaporate, and dry biomass is formed, water vapor enters after evaporation. In the pyrolysis zone will occur the thermal decomposition reactions that break long chains (hemicellulose, cellulose, and lignin) in biofuels into non-condensable gases (H_2, CO, CO_2., and others), gaseous hydrocarbons, hydrocarbons liquid (acetic acid, aromatic hydrocarbons, ketones, oxygen-containing compounds, furan compounds, phenol, and guaiacol). The pyrolysis zone temperature ranges from 150-700 ºC. the combustion will take place in the burning/cracking zone, when oxygen encounters the products that leave the pyrolysis zone.
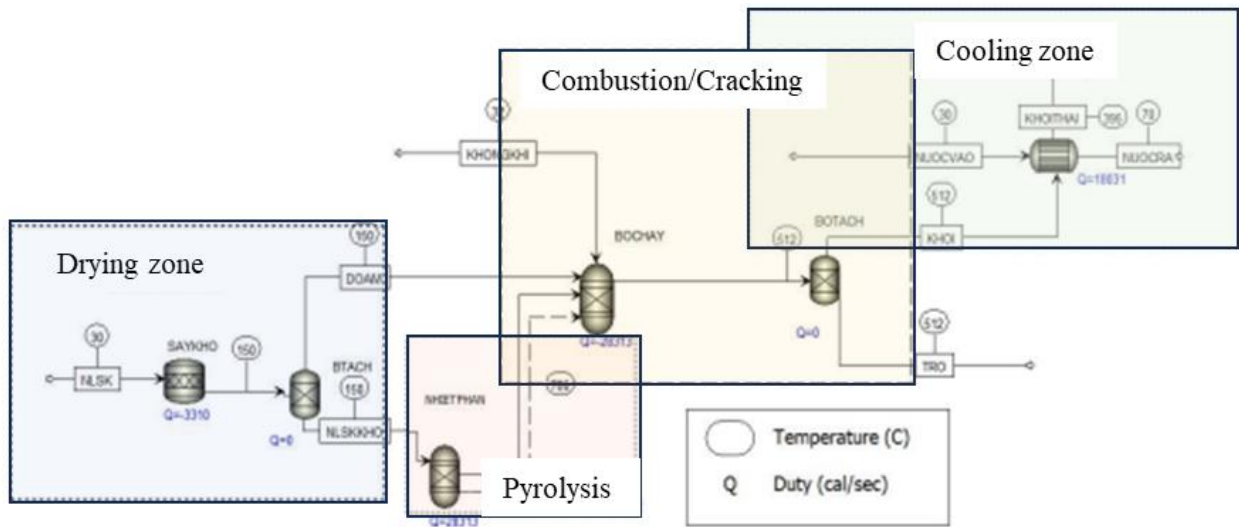
Fig. 2   Aspen Plus Energy production model.
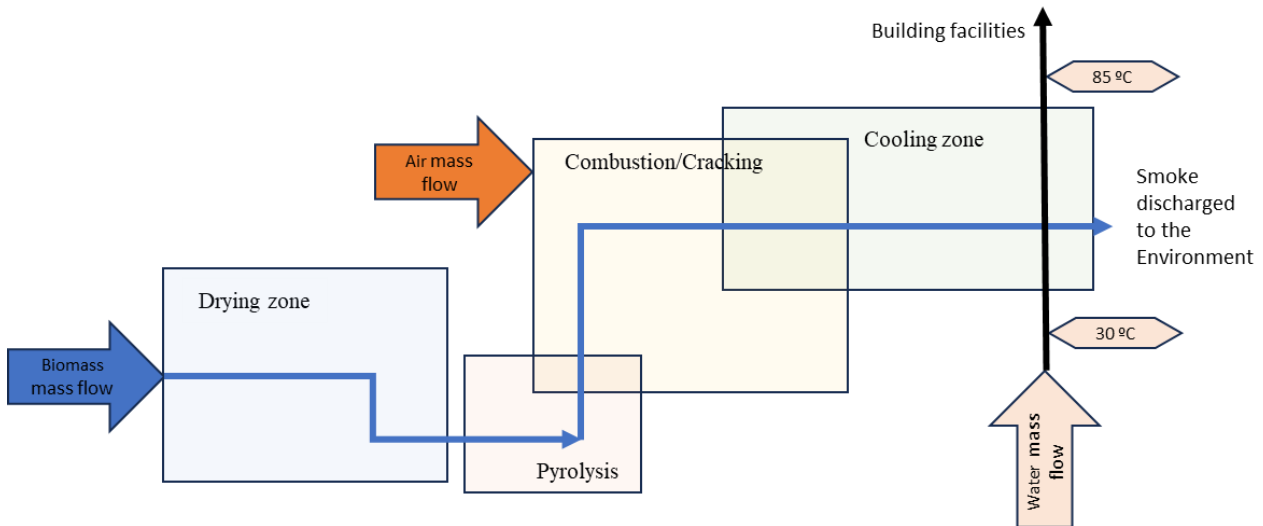
Fig. 3   Location of the main flows and temperature set as constant in the model.

.

The products formed in the pyrolysis zone will continue to participate in chemical reactions to create into the main gases H_2, CO, and CO_2. Last zone identified as the cooling zone, contains the main heat exchange process between the combustion products and the water that heated up for further uses in the building.

A. Simulation data

Table III contains the values of the main variables required in every simulation. Location of those variables in the model can be observed in Fig. 3. To evaluate the effects of the moisture contains under the Arctic regions conditions a set of 12 simulations were set by using three different temperatures (-15, -10, -5 and 0ºC) and three moisture content (15, 25 and 35%).

TABLE III. Model data

Variable in the process	Value
Air mass flow [kg/hr]	500
Biomass mass flow [kg/hr]	30
Water mass flow [kg/hr]	1000
Temperature Water in [ºC]	30
Temperature Water out [ºC]	85

B. Evaluation criterion

The model and the simulation conditions were set following data from our own measurement of moisture content, and sone data taken from commercial equipment. In this paper the variable selected to evaluate the correlation between the ambient temperature and the moisture content was the exhaust temperature of the smoke, which is discharged to the

417

environment. Nevertheless, a comprehensible discussion of some section of the process will be discussed.

V. RESULTS

Fig. 4 and Fig. 5 comprise the behaviour of the exhaust temperature for the evaluated matrix of ambient temperature and moisture content.

Fig. 4 shows an inverse linear proportionality between the exhaust temperature and the moisture content. It can be expressed by eq. 7. The constant values for the corresponding moisture content are summarized in Table IV.
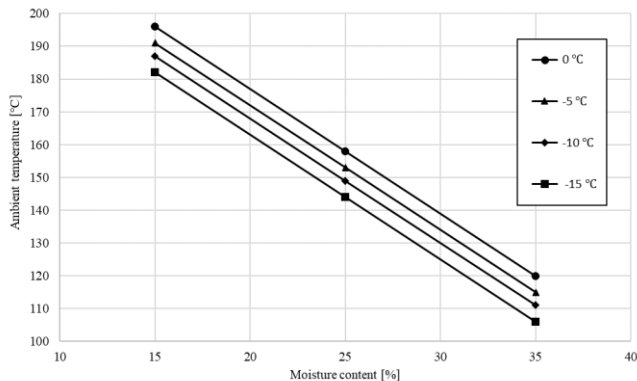
Fig. 4 Exhaust smoke temperature as function of moisture content.

$$T_{exhaust} = -3.8 \, \text{MC} + T_{const\_MC} \tag{7}$$

TABLE IV. CONSTANT VALUE FOR THE LINEAR FUNCTION OF EXHAUST TEMPERATURE AND THE MOISTURE CONTENT

Ambient temperature [ºC]	T_{const_MC} [ºC]
0	253
-5	248
-10	244
-15	239

Fig. 5 shows a linear proportionality between the exhaust temperature and the moisture content. It can be expressed by eq. 8. The constant values for the corresponding moisture content are summarized in Table V.
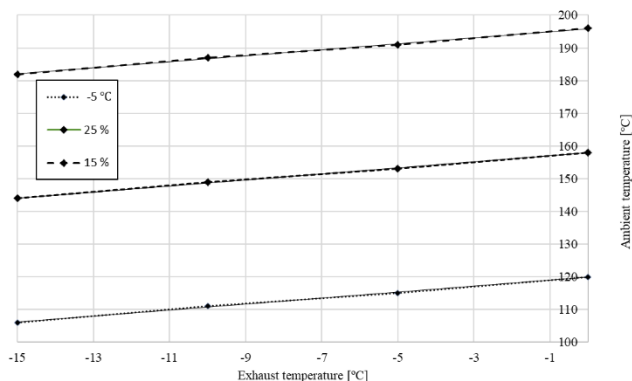
Fig. 5 Exhaust smoke temperature as function of ambient temperature.

$$T_{exhaust} = 0.92 \, T_{Amb} + T_{Cont\_Amb} \tag{8}$$

TABLE V. CONSTANT VALUE FOR THE LINEAR FUNCTION OF EXHAUST TEMPERATURE AND THE MOISTURE CONTENT

Moisture content [%]	T_{Cont_Amb} [ºC]
15	195,9
25	157,9
35	119,9

Under the conditions set for the simulations this trend in the exhaust temperature can be translated to the condition after the combustion and before the heat exchanger. The enthalpy difference before and after the heat exchanger will keep a constant value, which means that the influence of the ambient temperature in the combustion temperature will be also inversely proportional, however as enthalpy is not a linear proportionality. Same type of argument can be applied to the ambient temperature effect, obtaining a non-linear proportionality between the exhaust temperature and the ambient temperature.

VI. CONCLUSIONS

The effects of the moisture content inside the wooden was simulated by the developed model for different ambient temperatures, obtaining the conclusion that the operation of the energy production system will be in fact affected by the ambient temperature in combination with the moisture content of the wood located in situ. These effects are in fact a combination of opposite effect from the moisture content (inverse proportionality effect) and the ambient temperature (proportionality effect). The effect of both studied variables was identified as linear proportionalities for the exhaust temperature.

REFERENCES

[1] A. Midilli, I. D. and M. Ay, "Green energy strategies for sustainable development," *Energy Policy,* vol. 34, no. 18, pp. 3623-3633, 2006.

[2] C. Whittaker, W. Macalpine, N. E. Yates and I. Shield, "Dry Matter Losses and Greenhouse Gas Emissions From Outside Storage of Short Rotation Coppice Willow Chip," *BioEnergy Research,* vol. 9, no. 1, pp. 288-302, 2016.

[3] S. E. Ibitoye, R. M. Mahamood, T.-C. Jen and C. Loha, "An overview of biomass solid fuels: Biomass sources, processing methods, and morphological and microstructural properties," *Journal of Bioresources and Bioproducts,* vol. 8, no. 4, pp. 333-360, 2023.

[4] G. Martinopoulos, K. T. Papakostas and A. M. Papadopoulos, "Martinopoulos, G., K.T. Papakostas, and A.M. Papadopoulos, A comparative review of heating systems in EU countries, based on efficiency and fuel cost. Renewable and Sustainable Energy Reviews, 2018. 90: p. 687-699.," *Renewable and Sustainable Energy Reviews,* vol. 90, pp. 687-699, 2018.

[5] A. Tursi, "A review on biomass: importance, chemistry, classification, and conversion," *Biofuel Research Journal,* vol. 6, no. 2, pp. 962-972, 2019.

[6] M. Hupa, O. Karlström and E. Vainio, "Biomass combustion technology development - It is all about chemical details," *Hupa, M., O. Karlstrom, and E. Vainio, Biomass combustion technology development - It is all about chemical details. Proceedings of the*

Combustion Institute, 2017. 36(1): p. 113-134., vol. 36, no. 1, pp. 113-134, 2017.

[7]   G. Haarlemmer, "Simulation study of improved biomass drying efficiency for biomass gasification plants by integration of the water gas shift section in the drying process," *Biomass and Bioenergy,* vol. 81, pp. 129-136, 2015.

[8]   J. Mižáková, J. Pitel', A. Hošovský, I. Pavlenko, M. Ochowiak and S. Khovanskyi, "Biomass Combustion Control in Small and Medium-Scale Boilers Based on Low Cost Sensing the Trend of Carbon Monoxide Emissions," *Processes, 2021. 9(11).,* vol. 9, no. 11, 2021.

[9]   L. Fridh, S. Volpé and L. Eliasson, "A NIR machine for moisture content measurements of forest biomass in frozen and unfrozen conditions," *International Journal of Forest Engineering,* vol. 28, no. 1, pp. 42-46, 2017.

[10]   E. Ilbahar, C. Kahraman and S. Cebi, "Location selection for waste-to-energy plants by using fuzzy linear programming," *Energy,* vol. 234, 2021.

[11]   A. Biniek-Poskart, M. Sajdak, M. Skrzyniarz, J. Rzącki, A. Skibiński and M. Zajemska, "The Application of Lignocellulosic Biomass Waste in the Iron and Steel Industry in the Context of Challenges Related to the Energy Crisis," *Energies,* vol. 16, no. 18, p. 6662, 2023.

[12]   S. Silveira, L. Andersson and A. Lebedys, "Opportunities to boost bioenergy in Lithuania," *Biomass and Bioenergy,* vol. 30, no. 12, pp. 1076-1081, 2006.

[13]   "Energy security in the Arctic: Policies and technologies for integration of renewable energy," Arctic Portal, 2024. [Online]. Available: https://arcticportal.org/. [Accessed 02 2024].

[14]   O. Abioye, "Design of a process control system for combustion regulation by moisture content measurements in Biomass feed," M. Eng. thesis, UiT The Arctic University of Norway. Department of Industrial Engineering, Narvik, May 2023.

[15]   T. Vonžodas, "Research of factors influencing the burnout quality inside a biomass combustion chamber," *Mechanics,* vol. 23, no. 1, 2017.

[16]   H. e. a. Hartmann, "Low Emission Operation Manual for Chimney Stove Users," 2012.

[17]   T. Koyuncu and Y. Pinar, "The emissions from a space-heating biomass stove," *Biomass and Bioenergy,* vol. 31, no. 1, pp. 73-79, 2007.

[18]   X. Liang and J. Kozinski, "Numerical modeling of combustion and pyrolysis of cellulosic biomass in thermogravimetric systems," *Fuel,* vol. 79, no. 12, pp. 1477-1486, 2000.

[19]   J. C. Wurzenberger, S. Wallner, H. Raupenstrauch and J. G. Khinast, "Thermal conversion of biomass: Comprehensive reactor and particle modeling," *AIChE Journal,* vol. 48, no. 10, pp. 2398-2411, 2002.

[20]   G. Beggio, Biomass gasification, pyrolysis and torrefaction - Practical design and theory, 3rd ed., Detritus, 2018.

[21]   N. Giummarella, G. Henriksson, L. Salmén and M. Lawoko, "On the effect of hemicellulose removal on cellulose-lignin interaction," *Nordic Pulp & Paper Research Journal,* vol. 32, no. 4, pp. 539-546, 2017.

[22]   I. ˇCabalová, M. Bélik, V. Kuˇcerová and T. Jurczyková, "Chemical and Morphological Composition of Norway Spruce Wood (Picea abies, L.) in the Dependence of Its Storage," *Polymers,* vol. 13, 2021.

[23]   V. K. Trong and V. T. Hau, "Technical simulation the effects of fuel moisture biomass in boiler operations with Aspen Plus software," BEng. Thesis. Ho Chi Minh City University of Technology. Thermal Engineering Technology Department, Ho Chi Minh City, July 2023.

Application of two wet snow models based on weather station data in Germany

Bodo Wichura[1], Gregor Meusel[2], Maren Böltes[3]

[1] German Meteorological Service, Climate and Environment Consultancy Potsdam
[2] GEO-NET Umweltconsulting GmbH, Hannover
[3] Freie Universität Berlin, Meteorological Institute

bodo.wichura@dwd.de, meusel@geo-net.de, m.boeltes@fu-berlin.de

Abstract— **The severe wet snow event in the Münsterland area (northwest part of Germany) in November 2005 was surveyed for IWAIS 2009 by Wichura and Makkonen [1] and the simple wet snow accretion model of Makkonen [2] was applied to reconstruct the evolution of the accretion process in time. As a result of the analysis, the simple wet snow accretion model was modified by Makkonen and Wichura [3, referred as MW]. The spatial distribution of the frequency of atmospheric icing (wet snow as well as in-cloud icing and freezing rain) in Germany was analysed on the basis of weather station data evenly distributed over the territory of Germany by a paper for IWAIS 2013 [4].**

In the present paper, the spatial distribution of wet snow loads is analysed using data of 73 weather stations evenly distributed over the territory of Germany for the period 1971-2000. The analysis was carried out on the basis of two wet snow accretion estimation approaches: First, the simple wet snow accretion model in the modified version of MW. Second, the classical wet snow accretion model, generally described in ISO 12494 [5], using the parameterizations of Ducloux and Nygaard [6, referred as DN].

The results show that the simple wet snow accretion model performs well in lowlands and low mountain range areas, but it does not in coastal areas, in mountain ridge areas as well as in high mountain regions. The reason for this result is that the visibilities as well as the observations (ww-codes) from hourly ground SYNOP messages are the input parameters for the simple wet snow load model: Using these parameters only, meteorological situations, when snow fall and fog occur simultaneously, result in too low visibilities and (much) too high wet snow accretion intensities.

The application of the classical wet snow accretion model to the Münsterland event shows comparable results as with the simple wet snow model if the vertical velocity of the snowflake is slightly modified. As the data requirements of the classical wet snow accretion model, in particular hourly precipitation measurements, are hard to fulfil from SYNOP messages and under conditions of snow fall, 6- or 12-hourly precipitation data are used as well for the analysis of historical data in the time series 1971-2000, depending on data availability. The results show that the classical wet snow accretion model performs well for the whole territory of Germany. The analysis of 50-years return values of wet snow loads show a good agreement with values according to the National Annex of EN 50341-1:2012 [7].

Keywords— ***icing, accretion, wet snow, exceptional snowfall, actions on structures***

I. INTRODUCTION

Atmospheric icing is a complex phenomenon involving multiple physical processes affected by large variations over time and space, and significantly influenced by topography. Atmospheric icing is classified according to two different formation processes, precipitation icing (including freezing rain and wet snow) and in-cloud icing (also called rime/glaze, including fog; cf. [5], [8]).

Atmospheric icing can represent a risk to human life and activities and may have several economic implications. For instance, icing events can damage power lines, affecting both the economic activities and the human comfort [1]. Furthermore, icing events can damage renewable energy systems (wind turbines or solar panels) or decrease their efficiency. Finally, they may have an impact on the operational reliability of scientific equipment (e.g. for meteorological instruments, cf. [8]).

The goal of the study is to analyse the spatial distribution of wet snow loads in Germany on the basis of two wet snow accretion estimation approaches: First, the simple wet snow accretion model in the modified version of MW. Second, the classical wet snow accretion model, generally described in [5], using and modifying the parameterizations DN. The paper continues the studies that have been carried out for the wet snow event in the Münsterland area in 2005 [1] and for the analysis of spatial and temporal distribution of wet snow events in Germany [9].

II. DATA AND METHODOLOGY

A. Data

In this paper the spatial distribution of of wet snow loads is analyzed using weather station data of 74 meteorological stations evenly distributed over the territory of Germany. The data basis is almost the same as it was used in [4].

The study was elaborated using the hourly ground SYNOP messages as primary data in order to accomplish an accurate identification of wet snow accretion conditions from homogeneous data sets.

All hourly ground SYNOP messages (ww-codes from WMO-table 4677) which report icing, that means all messages regarding the occurrence of precipitation icing (wet snow) were analyzed.

For a detailed analysis using hourly SYNOP messages it was necessary to select those meteorological stations that fulfill the following criteria (see [10]):

- during the period from 1971 to 2000 the stations provided continuously SYNOP messages with information about the state of the weather (ww-codes from table 4677),
- the stations are representative from the point of view of the geographic position and
- the final number of stations and their spatial distribution allow a correct evaluation of wet snow characteristics for Germany.

Fulfilling these criteria, 74 stations were selected for the evaluation of wet snow events. Five of these stations are situated at altitudes higher than 1000 m and 54 of them are situated at altitudes lower than 500 m. The locations of the selected 74 stations in Germany are plotted in Fig. 1.

The data set included hourly values of air temperature, of dew point temperature, of wind direction and wind velocity, of horizontal visibility and of SYNOP messages (ww-codes from table 4677). Furthermore, total precipitation sums for intervals of mostly 6- or 12-hours are additionally included to the dataset in order to apply the DN model.

Fig. 1. Locations of weather stations in Germany whose SYNOP messages were analysed

B. Detection of Wet Snow events

The following ww-codes from table 4677 codes in hourly ground SYNOP messages were used to detect the wet snow events:

- snow and sleet during the preceding hour before observation (ww = 22, 23),
- snow and sleet showers during the preceding hour before observation (ww = 26),
- drifting snow (ww=38, 39),
- rain (with or without drizzle and/or ice grains) with snow (ww=68, 69),
- snow of various intensity, with or without breaks during the observation interval (ww = 70 - 75),
- snow and sleet showers of various intensity during the observation interval (ww = 83 - 86).

When analysing meteorological observations of snowfall, a criterion needs to be applied to select the wet snow events from all observations of snowfall.

This was done based on theory [see 2, 3, 11] so that wet snow is considered to occur when there is snow fall and the wet bulb temperature is greater than -0.2°C.

C. The MW model by Makkonen and Wichura (2010)

The following description of the MW model is directly taken from [3]. A wet snow model that uses visibility V_m [in m] as input parameter for the calculation of intensity I [gm^{-2}s^{-1}] of wet snow accretion per unit cross sectional area was presented by [2]. The model has been modified by MW to the use of two simple equations

$$I = 2100 \ [V_m]^{-1.29} \qquad daytime \qquad (1)$$
$$I = 2100 \ [0.5V_m]^{-1.29} \quad nighttime$$

When simulating time-dependent growth of a snow load on a cable the evolution of the snow mass M [gm^{-1}] accreted during a time-step i of duration $\Delta\tau$ on a conductor is calculated in using I, the snow deposit diameter D [m] and the density of the wet snow deposit ρ_i:

$$M_i = M_{i-1} + I_i D_{i-1} \Delta\tau \qquad (2)$$
$$D_i = \left[\frac{4(M_i - M_{i-1})}{\pi \rho_i} + D_{i-1}^2 \right]^{1/2}$$

According to the ISO reference collector - i.e. a cylinder of the diameter D_0 slowly rotating around its axis and its mass accretion can be considered as having a cylindrical growth - an initial diameter $D_0 = 0.03$ m is used for both models.

A relationship between snow density ρ_i (in kg m^{-3}) on a collector (an overhead cable, for instance) and wind velocity u_i (in ms^{-1}) a time-step i is used:

$$\rho_i = k + 20u_i \qquad (3)$$

The constant $k = 100 \ \text{kg} m^{-3}$ is used [see 3 for more details]. The wet snow load is considered to disappear when the wet bulb temperature is greater than +5.0 °C or when, for more than 24 h, no accretion (according to the model's accretion criteria) occurred and the wet bulb temperature is greater than +0.0 °C.

D. The DN model by Ducloux and Nygaard (2014)

The following description of the DN model is directly taken from [6]. Wet snow loads can be calculated on the basis of the classical equation given in the [5].

$$\frac{dM}{dt} = \eta_1 \eta_2 \eta_3 wAV \qquad (4)$$

dM is the linear mass density of snow accreted on the ISO reference collector during a small time dt; $\eta_1 \eta_2 \eta_3$ is the product of the collision, sticking and accretion efficiency factors; w is the mass concentration of snowflakes in the atmosphere; A is the cross-sectional area per unit length of the ISO reference collector with respect to the direction of the particle velocity vector V. Its linear mass density dM during a small time-step i of duration $\Delta\tau$, with ρ_i (constant density of accreted snow during dt) is determined according to the equation

$$\frac{dM}{dt} = \frac{\pi \rho_i}{2} D \frac{dD}{dt} \qquad (5)$$

Combining Eqs. (4) and (5) and considering e as the snow thickness of the accretion ($D = D_0 + 2e$) and $A = D \cdot 1\text{m}$ leads to e_i and M_i during a time-step i of duration $\Delta\tau$

$$e_i = e_{i-1} \frac{\eta_1 \eta_2 \eta_3 w_i V_i}{\pi \rho_i} \Delta \tau \tag{6}$$

$$M_i = M_{i-1} \frac{\pi \rho_i}{4} (\{D_0 + 2e_i\}^2 - \{D_0 + 2e_{i-1}\}^2)$$

η_1 describes the collision efficiency factor. For wet snow, it is assumed that all snowflakes collide with the collector and it is set to is set to $\eta_1 = 1$.

η_2 is the sticking efficiency factor and can be estimated using the snowflake velocity V_i. V_i is classically composed of the wind velocity U_i and the terminal velocity V_t (vertical velocity) of the snowflakes according to

$$\eta_2 = \frac{1}{\sqrt{V_i}} \tag{7}$$

$$V_i = \sqrt{U_i^2 + V_t^2}$$

[6] used a value of $V_t = 1.7$ ms^{-1}. This was used in our study initially but is revised to $V_t = 2.0$ ms^{-1} in accordance with [12], see results for more details.

The accretion efficiency factor η_3 can be considered as a trigger if wet snow accretion occurs or not. $\eta_3 = 1$ means that wet snow accretion starts and/or continues and $\eta_3 = 0$ means that wet snow cannot accrete. In addition to the the wet bulb temperature criterion (wet bulb temperature is greater than -0.2°C) two criteria for relative humidity RH can be defined, depending on air temperature T_a:

$$RH_{low} = 96 \cdot exp(-0.2 \cdot T_a) \tag{8}$$

$$RH_{up} = 39 \cdot (7.2 - T_a)^{0.5}$$

If the measured relative humidity is within the two limits and if $T_a \leq +2°C$, then wet snow is possible and $\eta_3 = 1$.

In order to calculate the snow mass concentration w_i at time-step i, the precipitation intensity P_i (in mm s^{-1}) and V_t are used

$$w_i = \frac{c_i P_i}{V_t} \tag{9}$$

Values of P_i, needed to be estimated approximately as they are available as 6- or 12-hourly sums of precipitation in historical data sets only. For model application, it is assumed that the precipitation fell continuously during the whole accumulation period (6- or 12-hours) and the sums of precipitation were split evenly into hourly values of P_i.

The factor c_i defines a correction factor due to wind velocity for P_i. The catch ratio CR_i of rain gauges for snow (or mixed precipitation) depends on wind velocity U_i, and P_i needs to be corrected in order to estimate the "true" value for precipitation. The CR_i [%] for mixed precipitation on a Hellmann precipitation gauge [see 13], which is used in Germany, is applied, as in [6]. The wind velocity U_i used for the calculation of CR_i must be offset by a factor of 0.7 (70%), as the wind velocity at 10 m height above ground is higher than the wind velocity at the precipitation gauge, which is located at a height of approx. 2 m.

The catch ratio CR is calculated as

$$CR_i = 96.63 + 0.41(0.7U_i)^2 - 9.84(0.7U_i) \tag{10}$$
$$+ 5.95T_{a\,i}$$

$$c_i = \frac{100}{CR_i}$$

In contrast to [6], snow density ρ_i (in kg m^{-3}) is estimated by equation (3). The wet snow load is considered to disappear when there are no new wet snow deposits for more than 5 consecutive hours. This is the original criterion that was used by [6], whereas they proposed to elaborate another criterion for mountainous regions. Nevertheless, results show that the criterion does not lead to unrealistic values and it was therefore retained.

E. Extreme value analysis

An extreme value analysis of wet snow mass results estimated with the DN model was carried out. Annual (block) maxima of resulting wet snow mass values were used to analyse the data on the basis of the Fisher-Tippett extreme distribution, type I (distribution function F(x), "Gumbel"-distribution)

$$F(x) = exp\left\{-exp\left(-\frac{(x-a)}{b}\right)\right\} \tag{11}$$

The R-package *in2extRemes* [14] was used to estimate 50 years return values of wet snow loads from M. The estimation of parameters a and b in equation (11) was carried out by the Maximum-Likelihood-Method implemented in *in2extRemes*.

If the yearly block maxima contain zero values (due to no wet snow event for the corresponding year), the calculation of the return values must be adjusted. This can be done by examining only the non-zero block maxima for the time series that include zero block maxima values, but for a modified (smaller) return period (corresponding to $F(M_{m\_y})$, which corresponds to the 50 years return period in the extreme value calculation with non-zero block maxima $F(M_{50y})$.

$$F(M_{50y}) = F_0 + (1 - F_0)F(M_{m\_y}) \tag{12}$$

$$F(M_{m\_y}) = \frac{F(M_{50y}) - F_0}{1 - F_0}$$

F_0 is the percentage of years with zero block maxima values in the full time series.

III. RESULTS

A. *The MW model by Makkonen and Wichura (2010)*

Absolute maximum values of wet snow mass, calculated by the MW model are shown in Fig. 2. The results show that some of the absolute maxima are clearly too high. Even if it is assumed that 10-50 kgm^{-1} could theoretically be possible, these absolute maximum values are being exceeded markedly. Red markers in Fig. 2 show unrealistic MW results with high wet snow masses greater than 50 kgm^{-1}. Those values occur at 23 of the 74 stations examined.

The largest absolute maximum is calculated for station Brocken, a highly exposed station in the middle of Germany. In 1997, wet snow accretion of 91792 kgm^{-1} was determined by the model.

Overall, it is noticeable that all unrealistic high model results are estimated at mountain or exposed stations (including exposition at coast of Baltic sea for station Arkona). More realistic results are estimated for stations in the northern German lowlands and between the central low mountain ranges and the Alps.

Unrealistic high model results can be explained by equation (1), in which (only) the visibility V_m is used to estimate the intensity I of wet snow accretion. If V_m becomes (extremely) small, the value for the wet snow load becomes (very) large.
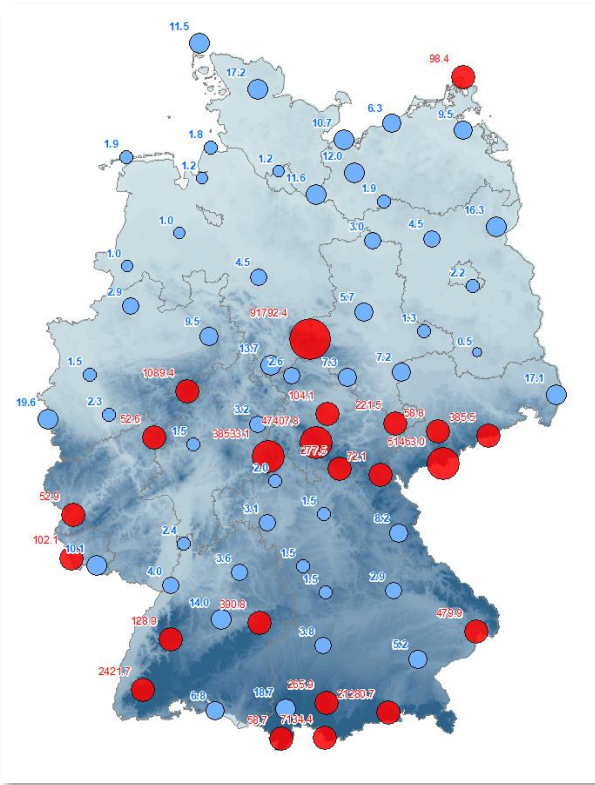
Fig. 2. Absolute maximum values of wet snow mass [kgm^{-1}], calculated by the MW model. Red markers show unrealistic high model results (wet snow mass greater than 50 kgm^{-1}).

At times when the maxima, shown in Fig. 2, occurred, values of V_m of about 100 metres were observed, which were even reduced to 50 metres during night-time.

The strength of the model, in which only one parameter needs to be observed, turns into its weakness in such cases. The reason for small values of visibility (and the resulting unrealistic high values of wet snow mass) may be the presence of fog along with snowfall during observation. Fog must be reported by the observer if visibility is less than 1000 m. On the other hand, light snowfall is to be reported by the observer for visibilities greater than or equal to 4000 m, moderate snowfall for visibilities between 1000 m and 4000 m and heavy snowfall for visibilities below 1000 m. As the definitions of fog and heavy snowfall are equivalent in terms of visibility, "cases" of heavy snowfall - and therefore heavy wet snow depositions - can result even from observations of weather conditions with fog and light snowfall. This is due to the fact, that the detection of wet snow events was done only by using the ww-codes from SYNOP messages and the subsequent calculation of intensity I was only based on visibility V_m. Any additional observation and/or measurement that could be used to avoid the use of observations of visibility during periods of simultaneous occurrence of fog could help to improve the model results.

B. The DN model by Ducloux and Nygaard (2014)

Since both the observations of snow loads [see 1] as well as model results from [3] are available for the Münsterland event in 2005, the data from this event were initially compared with the model results according to the DN model. The analysis of wet snow deposition photos from the Münsterland event

indicated a maximum mass of wet snow accretion of 5±2 kgm^{-1} [1, 3].

Fig. 3 shows that the maximum value of wet snow mass estimated by the original setup (blue line) of the DN model is significantly larger than result according to [3, red line]. The range of observed values (black rectangle) is met by the blue line, but only at the very edge of the rectangle that is defined by the uncertainties of the analysis [see 1]. The (overall) maximum wet snow mass estimated by the original model setup is 8.5 kgm^{-1} and is therefore far outside the error interval of the observed value.
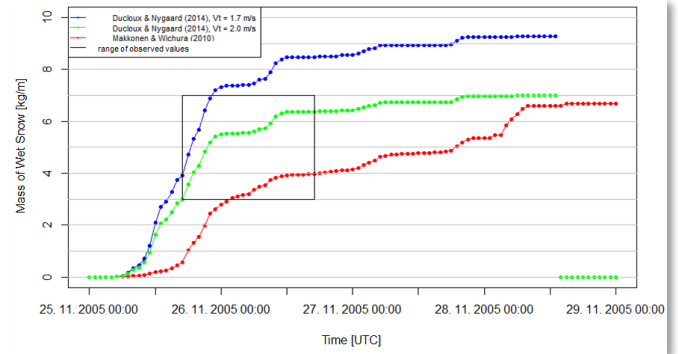
Fig. 3. Comparison of calculated wet snow deposits with the range of observed values (rectangle marked in black) for the Münsterland event [see 1]. The red line shows the results of the MW model, the blue and green lines show the results of the model by Ducloux and Nygaard [6], using terminal velocities V_t of 1.7 ms^{-1} and 2.0 ms^{-1}, respectively.

The setup of the DN model is therefore modified by adjusting terminal velocity V_t (vertical velocity) of the snowflakes. According to [12], V_t is 2.0±0.8 ms^{-1}. For this reason, V_t is adjusted to 2.0 ms^{-1} in our modified setup and Fig. 3 shows the improvement of results.
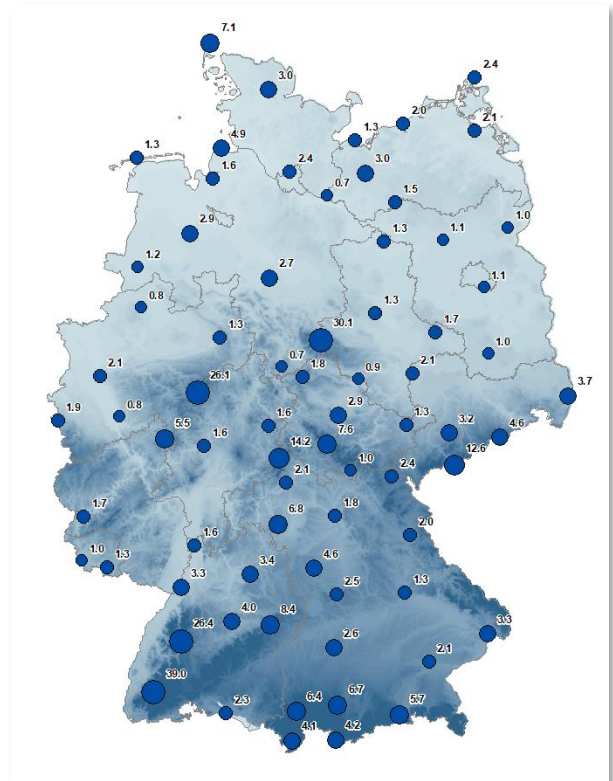
Fig. 4. Absolute maximum values of wet snow mass [kgm^{-1}], calculated by the DN model.

By modification of V_t to 2.0 ms^{-1} the final (overall) maximum value of wet snow mass is 7.0 kgm^{-1} and it varies from 3.0 to 6.4 kgm^{-1} during the time interval of observations (black rectangle). These results confirm the optimised DN model results applying a modified V_t.

Absolute maximum values of wet snow mass, calculated by the DN model are shown in Fig. 4. The results show clearly better results for maximum wet snow masses for Germany even in mountainous or exposed regions. As expected from results of the MW model, the highest maxima are estimated for mountainous regions. At four stations the maximum values of wet snow mass are higher than 20 kgm^{-1}, at the stations Brocken (30.1 kgm$^{-1}$ at 1142 m a.s.l.), Kahler Asten (26.1 kgm^{-1} at 839 m a.s.l.), Freudenstadt (26.4 kgm^{-1} at 797 m a.s.l.) and Feldberg/Schw. (39.0 kgm^{-1} at 1486 m a.s.l.). At these stations, in particular the high wind velocities lead to higher wet snow loads, compared to other locations.

The reason why the modelled maximum values of wet snow mass in the Alpine region are generally not so high could be the lower number of events and the shorter duration of events due to the generally lower temperatures and consequently a lower number of wet snow conditions in the Alpine region. The comparison of the number of events at stations Zugspitze (4.2 kgm^{-1} at 2960 m a.s.l.) and Feldberg/Schw. with only 498 events and 830 events, respectively, illustrates this finding.

List auf Sylt (7.1 kgm^{-1} at 26 m a.s.l.) and Cuxhaven (4.9 kgm^{-1} at 5 m a.s.l.), two of the 20 largest maxima, are located in the north-west of Germany, near the coast of North Sea at low altitudes. The fact that larger events are also modelled there, although the stations are located in the lowlands, is consistent with the observations of the power grid operators and their experiences of damages due to wet snow accretions in the past.

Fig. 5 shows a comparison of absolute maximum values of wet snow mass [kgm^{-1}], calculated by both models (MW and DN). It illustrates again that by both models realistic and comparable results are estimated for stations in the northern German lowlands and between the central low mountain ranges and the Alps. Model results are generally not comparable to each other in mountainous or exposed regions.

Fig. 6 shows the 50-year return values of wet snow mass calculated from yearly block maxima values of DN model results. The results are realistic for the whole area of Germany. The only station that with 50-year return value of wet snow mass that is higher than 20 kgm^{-1}, is Feldberg/Schw. (22.4 kgm^{-1} at 1486 m a.s.l.). At two stations Brocken (14.6 kgm^{-1} at 1142 m a.s.l.) and Kahler Asten (10.1 kgm^{-1} at 839 m a.s.l.) results are higher than 10 kgm^{-1}, at all other stations lower 50-year return values of wet snow mass are analysed. The result for the station Münster/Osnabrück (0.37 kgm^{-1} at 47 m a.s.l.) is significantly lower than the value of 1.77 kgm^{-1} that would result from extreme value analysis of the yearly MW block maxima values by Maximum-Likelihood-Method implemented in *in2extRemes* [14]. This result is most likely due to the different data basis, analysing the time interval from 1949 to 2009 in [3] and from 1971 to 2000 herein (i.e. the Münsterland event is not part of the dataset analysed here).
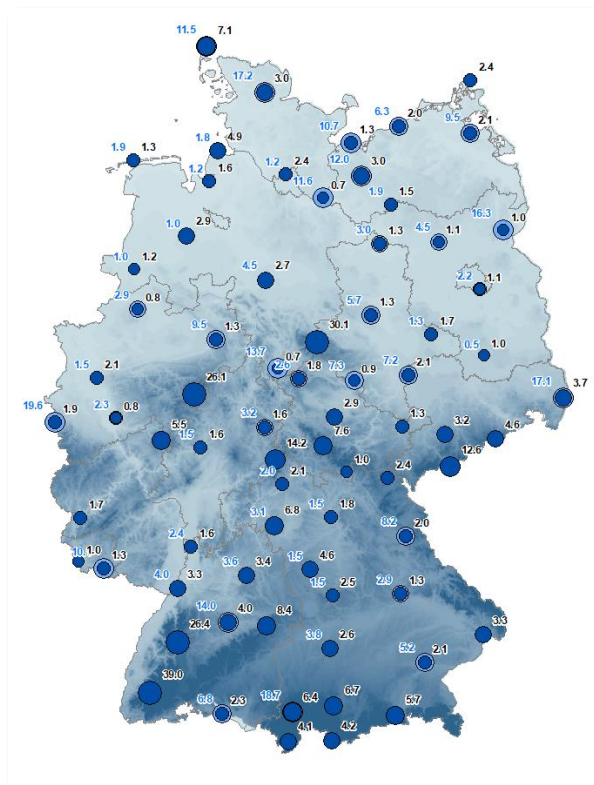

Fig. 5. Comparison of absolute maximum values of wet snow mass [kgm^{-1}], calculated by the both models, MW and DN. Stations with unrealistic high model results (red markers from Fig. 2) are not shown.
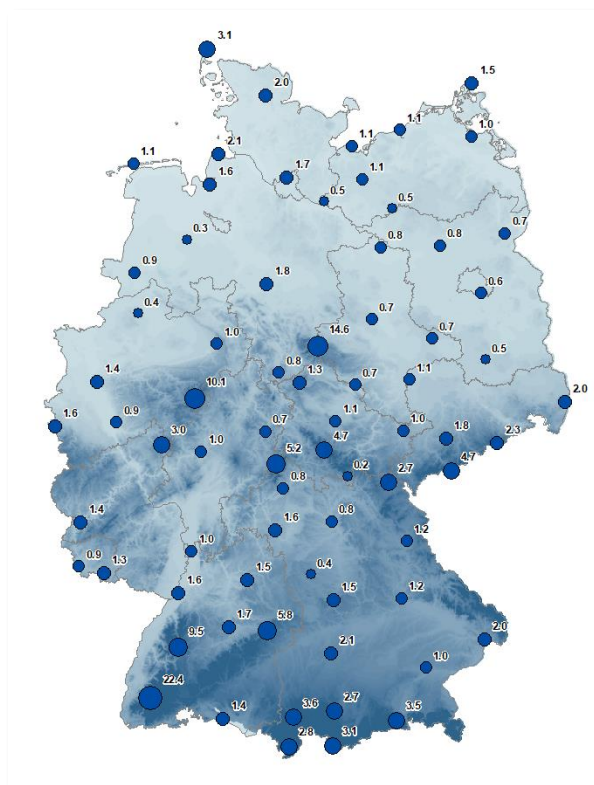

Fig. 6. 50-year return values of wet snow mass [kgm^{-1}] calculated from yearly block maxima values of DN model results.

In order to compare the 50-year return values of wet snow mass calculated from yearly DN block maxima values, they are plotted in Fig. 7 in the map of National Annex of EN 50341-1:2012 [7]. Fig. 7 shows the good agreement of DN model results with the values according to [7]. The 50-year return values of wet snow mass estimated with the DN model correspond to the respective ice load zones. In many cases, the 50-year return values of wet snow mass analysed by DN model correspond even to higher ice load zones from [7] which means that the zoning is on the safe side, at least for wet snow loads.
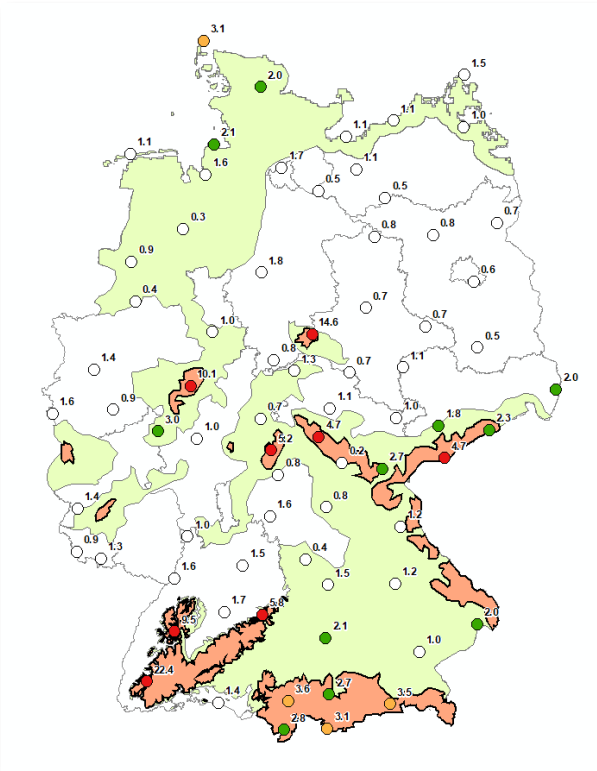

Fig. 7. Results from Fig. 6 plotted in the map of National Annex of EN 50341-1:2012 [7]. White area filling/points indicate regions/results for ice load zone 1. Light green area filling and green points indicate regions/results for ice load zone 2, light red area filling and red points correspond to ice load zones 3 and 4 (Zone 4 is not resolved).

IV. CONCLUSIONS

The paper shows that in some regions of Germany the MW model results are clearly too high. Most unrealistic high MW model results are estimated at mountain or exposed stations. More realistic results are estimated for stations in the northern German lowlands and between the central low mountain ranges and the Alps. The reason for small values of visibility (and the resulting unrealistic high values of wet snow mass) may be the presence of fog along with snowfall during observation. The strength of the model, in which only one parameter needs to be observed, turns into its weakness in such cases.

After modification of the DN model setup (adjusting the terminal velocity V_t of the snowflakes to 2.0 ms^{-1}) the results are in good agreement with the observations from the Münsterland event. The DN model results show for all stations in Germany clearly better results for maximum wet snow mass even in mountainous or exposed regions.

The 50-year return values of wet snow mass calculated from yearly DN block maxima show realistic results for the whole area of Germany. The results are compared to National Annex of EN 50341-1:2012 [7] and show the good agreement with ice load zone map in [7].

REFERENCES

[1] B. Wichura and L. Makkonen, "Evaluation of a Wet Snow Accretion model for the Münsterland event in November 2005," presented at the 13th International Workshop on Atmospheric Icing of Structures (IWAIS 2009), Andermatt, September 8 to 11, 2009, 2009.

[2] L. Makkonen, "Estimation of wet snow accretion on structures," *Cold Regions Science and Technology,* vol. 17, no. 1, pp. 83-88, 1989.

[3] L. Makkonen and B. Wichura, "Simulating wet snow loads on power line cables by a simple model," *Cold Regions Science and Technology,* vol. 61, no. 2-3, pp. 73-81, 2010, doi: http://dx.doi.org/10.1016/j.coldregions.2010.01.008.

[4] B. Wichura, "The Spatial Distribution of Icing in Germany Estimated by the Analysis of Weather Station Data and of Direct Measurements of Icing," in *Proceedings of the 15th International Workshop On Atmospheric Icing Of Structures (IWAIS 2013)*, St. John's, Newfoundland and Labrador, September 8-11, 2013 2013: Compusult Ltd., pp. 303-309.

[5] ISO 12494, "Atmospheric icing of structures," International Organization for Standardization, Geneva, 2017.

[6] H. Ducloux and B. E. Nygaard, "50-year return-period wet-snow load estimation based on weather station data for overhead line design in France," (in English), *Natural Hazards and Earth System Sciences,* vol. 14, no. 11, pp. 3031-3041, 2014, doi: DOI 10.5194/nhess-14-3031-2014.

[7] *Freileitungen über AC 1 kV - Teil 2-4: Nationale Normative Festlegungen (NNA) für Deutschland (basierend auf EN 50341-1:2012)*, DIN EN 50341-2-4:2019-09, Berlin, 2019.

[8] S. Fikke *et al.*, "COST Action 727: Atmospheric Icing on Structures; Measurements and data collection on Icing : State of the Art," vol. 75, ed. Zürich: Publication of MeteoSwiss, 75, 2006, p. 110.

[9] D. Nikolov and B. Wichura, "Analysis of spatial and temporal distribution of wet snow events in Germany," presented at the 13th International Workshop on Atmospheric Icing of Structures (IWAIS 2009), Andermatt, September 8 to 11, 2009, 2009.

[10] A. Manea, I. Ralita, A. Dumitrescu, A. Sommerfeld, and B. Wichura, "Analysis of spatial and temporal distribution of freezing rain events in Romania and Germany," presented at the 13th International Workshop on Atmospheric Icing of Structures (IWAIS 2009), Andermatt, September 8 to 11, 2009, 2009.

[11] L. Makkonen, "The heat balance of wet snow," *Meteorological Magazine,* vol. 110, p. 82, 1981.

[12] S. E. Yuter, D. E. Kingsmill, L. B. Nance, and M. Löffler-Mang, "Observations of precipitation size and fall speed characteristics within coexisting rain and wet snow," *Journal of applied meteorology and climatology,* vol. 45, no. 10, pp. 1450-1464, 2006.

[13] B. Goodison, P. Louie, and D. Yang, "WMO solid precipitation intercomparison. Final Report," *World Meteorol. Org., Instruments and Observing Methods Rep,* vol. 67, 1998.

[14] E. Gilleland and R. Katz, "in2extRemes: Into the R package extRemes. Extreme value analysis for weather and climate applications," in "NCAR TECHNICAL NOTES," NCAR, Boulder, Colorado, 2016, vol. NCAR/TN-523+STR.

Icing Transmission Line Image Dehazing Based on Adaptive Low Frequency Attenuation

Ye zhang[1*], Pengchao Zhai[1], Jinghao Shang[2], Xinbo Huang[1], Botao Li[1]

[1] Xi'an Polytechnic University, the School of Electronics and Information, Xi'an, China
[2] Xi'an Microelectronics Technology Institute, Xi'an, China

zhangye@xpu.edu.cn, 1639479797@qq.com, sjhnjust@163.com, huangxb1975@163.com, 962033407@qq.com

Abstract—**The clarification of icing images assumes a pivotal role in ensuring subsequent feature extraction and condition diagnosis of transmission line icing images captured in adverse weather conditions. This work proposes a simple and adaptive single-image dehazing algorithm. Firstly, the input image is decomposed into three channels to obtain a single-channel grayscale image. Secondly, low-frequency adaptive attenuation and high-frequency sharpening enhancement are applied to the grayscale image, and the processed components are combined to reconstruct the dehazed image. Finally, comprehensive grayscale equalization is performed based on the dehazed image, and the three-channel images, after individual processing, are merged to produce the enhanced icing image of the transmission line post-dehazing. To enhance efficacy, a more precise and spatially adaptable adaptive attenuation factor is formulated. Several transmission line icing images acquired at different distances, backgrounds, and targets were evaluated and compared to classical dehazing methods such as MSRCR, Dark Channel Prior, KIM, and DehazeFormer. Experimental results demonstrate that this method generally surpasses other methods in terms of robustness and applicability.**

Keywords—***Iced transmission line, image dehazing, low frequency attenuation, image enhancement***

I. INTRODUCTION

Transmission lines are integral components of the power grid infrastructure, facilitating the transmission and protection of the electricity supply—a crucial element in the stable progression of the national economy and the welfare of the population. Unfortunately, since most of these transmission lines are installed in harsh outdoor environments, the problem of transmission line icing, caused by severe winter conditions characterized by heavy ice and snow, can have a significantly detrimental impact on the reliable operation of the power grid [1]-[3]. Recently, computer vision technology has been widely utilized in the field of power systems, offering improved solutions for the problem of icing [4]-[6]. However, images of iced transmission lines captured amid winter precipitation, including rain, snow, and haze, often face challenges such as color distortion, obscured edge features, and the lack of intricate details [7]-[9]. These challenges can significantly impede the identification and status analysis of transmission line icing. Therefore, it is essential to focus on researching and developing an effective dehazing method for icing images, allowing for the extraction of morphological features from different types of icing. This effort enhances the recognition of icing patterns in images and contributes to the reliable operation of transmission lines in snowy environments.

At present, the techniques employed for single image dehazing predominantly encompass image enhancement, image restoration, and deep learning approaches. Sun et al. [10] used dark channel prior and fast weighted guided filtering to dehaze real-time images. The experimental results demonstrated its good defogging ability while preserving more image details. Zhang et al. [11] proposed a multi-scale retinex with color restoration (MSRCR) of multi-channel convolution (MC) to defog a single image. KIM et al. [12] formulated a cost function that consists of the contrast term and the information loss term to maximize contrast for dehazing with minimal loss of information. BermanTali et al. [13] proposed an algorithm based on a nonlocal prior, and introduced a haze-line, a line in RGB space that each color cluster in a sharp image becomes, to restore a haze-free image. Zhang and Wang et al. [14] developed a multi-level fusion module and a Residual Mixed-convolution Attention Module (RMAM) with an attention block, with these two modules, the method achieved dehazing end-to-end.

While these methods have effectively addressed dehazing, the distinctive nature of transmission line images, characterized by complex and variable backgrounds often containing sky areas, presents a challenge for traditional dehazing algorithms. Zhang et al. [15] employed the Gaussian function model to simulate the grayscale distribution of the image, aiming to enhance the defogging of transmission line images. Peng and Chen et al. [16] introduced a dehazing algorithm based on the dark channel prior assumption and multi-directional transformation, effectively reducing color distortion in transmission line images post-dehazing. Liu and Jia et al. [17] presented an enhanced pyramid network for transmittance map calculation and an improved U-net network for atmospheric light value estimation, resulting in the generation of more realistic deblurred transmission line images. Preserving key information in the image post-dehazing is essential to facilitate subsequent analysis of surface texture characteristics and grayscale distribution among different icing types.

In this paper, we present a novel method for dehazing and enhancing iced transmission line images based on adaptive low-frequency attenuation. Our approach aims to improve the quality of hazy transmission line icing images that suffer from issues such as low definition, insufficient illumination, and low contrast.

The principal contributions of this paper can be outlined as follows, encompassing a three-fold endeavor:

1.Introduction of a novel dehazing technique that incorporates low-frequency attenuation for dehazing purposes, coupled with high-frequency sharpening to enhance the detail information within the images.

2. Introduction of an adaptive attenuation factor characterized by spatial adaptability, thereby enhancing the effectiveness of the dehazing process.

3. Extensive experiments and analysis demonstrate that the proposed method can achieve satisfactory dehazing effects for hazy images in various transmission line icing scenarios.

II. PROPOSED METHOD

The proposed method consists of three primary phases. Firstly, it involves isolating the R, G, and B channels from the input image, followed by applying low-pass filtering to the grayscale representations of these channels to extract their respective low-frequency components. Subsequently, the high-frequency components are obtained by subtracting the low-frequency counterparts from the original image for each channel. Secondly, the dehazing process primarily targets the low-frequency components. This is achieved by introducing attenuation factors and employing mask operations to remove the haze components within these components while simultaneously applying sharpening to the high-frequency components. Finally, a global gray equalization procedure is applied to the image, and the processed low-frequency and high-frequency components are then combined. The comprehensive workflow of our proposed method is visually illustrated in Fig. 1.
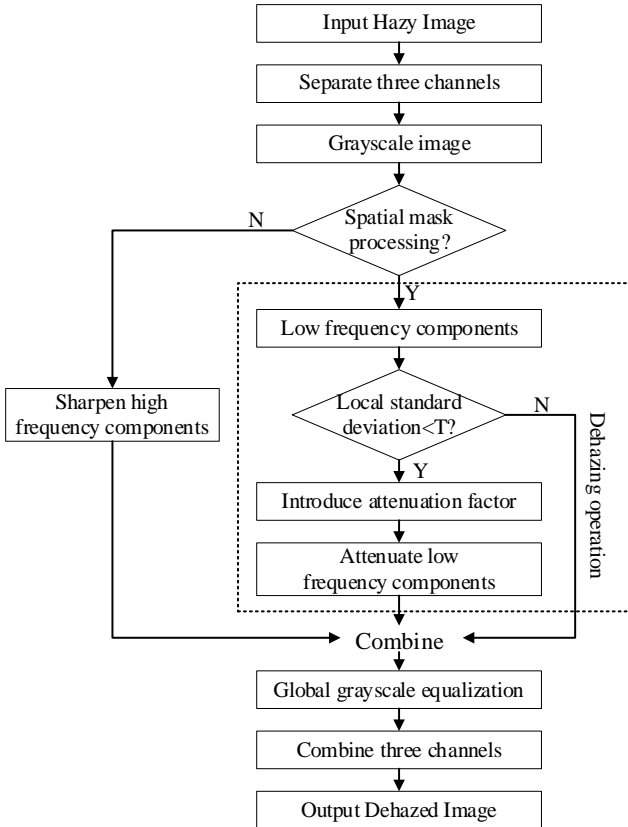

Fig. 1 Flow chart of the proposed image dehazing algorithm.

A. Dehaze modeling

In consideration of the aforementioned, we have developed a particular image dehazing model, presented as follows:

$$W(i,j) = \lambda * L(i,j) + f * H(i,j) \qquad (1)$$

Where $L(i,j)$ and $H(i,j)$ represent the low and high-frequency components, respectively, λ denotes the introduced attenuation factor with spatial adaptation, f is the operator used for high-frequency sharpening, and the processed image is represented as $W(i,j)$. Therefore, low frequency attenuation is a pixel-level operation, which can effectively avoid the block effect caused by traditional algorithms [18].

The low-frequency components of the image can be acquired through spatial domain mask operation. We employ a median filter mask template to process specific pixels, following this procedure: Initially, the pixel under consideration serves as the center of the template. Subsequently, the pixels within the template window are statistically sorted based on their gray values, and the middle gray value is chosen to replace the gray value of the central pixel of the template. The entire image is then traversed based on the template center to complete the processing of all pixels. The definition of the mask template window is as follows: $G(i,j)$ represents the gray value of a pixel in the original image, with (i,j) denoting the center window size $(2w+1) \times (2w+1)$, where w is an integer, as long as the number of rows and columns are odd, the template windows can also be defined as rectangles. The low-noise low-frequency component $L(i,j)$ that retains the edge detail information of the image can be obtained by median filtering [19], which is defined as follows:

$$L(i,j) = median\{G(i+\Delta i, j+\Delta j)\} \qquad (2)$$

For the high-frequency component of the image, it can be obtained by subtracting the low-frequency component from the original image, as demonstrated below:

$$H(i,j) = A(i,j) - L(i,j) \qquad (3)$$

where $A(i,j)$ is the original image. We opted for the Laplacian of Gaussian (LoG) operator to enhance the high-frequency components isolated from the image.

The LoG operator first utilizes Gaussian filtering to mitigate image noise and subsequently employs Laplacian filtering for edge detection. It is designed to find the optimal filter for edge detection based on the image's signal-to-noise ratio, thereby reducing image noise while enhancing edge sharpness to a minimum [20]. Thus, utilizing the LoG operator for convolution with the separated high-frequency components enables the acquisition of high-frequency sharpening components while preserving the edge features of the image as much as possible. The commonly used two-dimensional LoG operator template is depicted in Fig. 2.

$$\begin{bmatrix} 0 & 0 & -1 & 0 & 0 \\ 0 & -1 & -2 & -1 & 0 \\ -1 & -2 & 16 & -2 & -1 \\ 0 & -1 & -2 & -1 & 0 \\ 0 & 0 & -1 & 0 & 0 \end{bmatrix}$$

Fig. 2 LoG operator convolution kernel

B. Low Frequency Adaptive Attenuation Factor Construction

To achieve a more effective dehazing effect, it is imperative to construct a more accurate attenuation factor λ. The mask template is depicted in Fig. 3.
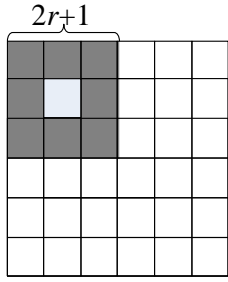
Fig. 3 Attenuation factor template operation

Set the size of the original image $A(i,j)$ as $m \times n$, take the pixel (i,j) in the low-frequency component $L(i,j)$ as the center, and calculate the local mean $m(i,j)$ and the local standard deviation $\sigma(i,j)$ for the local area of size $(2r+1) \times (2r+1)$ to obtain the local information of the low-frequency component. The $m(i,j)$ is given as

$$m(i,j) = \frac{1}{(2r+1)^2} \sum_{k=i-r}^{i+r} \sum_{s=j-r}^{j+r} L(k,s) \tag{4}$$

and the $\sigma(i,j)$ is represented as

$$\sigma^2(i,j) = \frac{\sum_{k=i-r}^{i+r} \sum_{s=j-r}^{j+r} \left[L(k,s) - m(i,j) \right]^2}{(2r+1)^2} \tag{5}$$

Moreover, the global pixel gray mean value is defined as

$$G_m = \frac{1}{m \times n} \sum_{i=0}^{m} \sum_{j=0}^{n} A(i,j) \tag{6}$$

According to the above local information, the attenuation factor λ is defined as follows:

$$\lambda = \frac{G_m}{\sigma(i,j)} \tag{7}$$

Therefore, substituting a and the LoG operator into formula (1), the definition of the low-frequency attenuation image dehazing model is:

$$W(i,j) = \frac{G_m}{\sigma(i,j)} * L(i,j) + \text{LoG} * H(i,j) \tag{8}$$

The attenuation factor λ defined according to the above method, exhibits spatial adaptability and effectively attenuates the low-frequency components with precision. As per equation (6), we know that G_m is a constant, so λ is inversely proportional to the local standard deviation. In areas where image features undergo significant changes, such as edges, the local standard deviation is large, resulting in a relatively small value of λ. Consequently, the attenuation of the low-frequency component diminishes, preserving edge information. Conversely, in hazy regions of the image, where the local standard deviation is small, λ assumes a relatively large value, accurately attenuating the low-frequency haze component. During specific operations, we can predefine a threshold value T based on real-time haze density. When the local standard deviation falls below the threshold T, an effective attenuation factor can be generated.

C. Global Contrast Enhancement

The conventional global grayscale equalization technique enhances image visual appeal by boosting contrast, yet it tends to sacrifice edge details and other critical information. Conversely, local grayscale equalization tends to homogenize pixel grayscales within each window, resulting in noticeable block effects [21][22]. Our proposed spatially adaptive attenuation factor exclusively influences the low-frequency components of the image, thereby mitigating the risk of over-enhancement associated with image blocking and noise. This method effectively enhances image clarity post-dehazing while attenuating the haze component. Subsequently, applying global grayscale equalization to the dehazed grayscale image is essential to enhance overall contrast.

For a digital image, the histogram precisely records the statistical relationship between all gray levels and the probability of occurrence of each gray level. Even after low-frequency dehazing, the image often suffers from low contrast, primarily due to its distribution within a limited quantization range on the grayscale histogram. Gray equalization primarily aims to broaden the distribution of gray levels in the dehazed image, ensuring a more even spread. This process enhances the gray dynamic range of the image and subjectively improves its brightness and visual appearance. By evenly distributing pixels across each gray level, the contrast of the image is subjectively enhanced. Despite contrast enhancement, the image remains grayscale. Therefore, to obtain a color dehazed image with improved clarity and contrast, the processed images of the R, G, and B channels need to be merged.

III. EXPERIMENTAL RESULTS

The experimental environment of this paper is Windows 10 version 64-bit operating system, including Intel Core i5 3.3 GHz, Memory 8 GB, the software is MATLAB and Halcon. We compare the proposed dehazing algorithm with four commonly used dehazing algorithms, including the Dark Channel Prior (DCP) proposed by He[23] et al., the Optimized Contrast Enhancement (OCE) proposed by KIM[24] et al., and MSRCR algorithm proposed by Jiang[25] et al., and DehazeFormer proposed by Song[26] et al..

A. Qualitative Analysis

The issue of icing and haze affecting transmission line images primarily stems from the harsh outdoor conditions. Therefore, we conducted experimental verification using line images collected from the field. We categorized the instance images into two groups: long-range images and close-range images to assess the efficacy of the proposed algorithm. Both types of images were uniformly resized, with the long-range images adjusted to 640 pixels × 480 pixels and the close-range images to 320 pixels × 240 pixels.

In these selected representative images, the backgrounds comprise high-altitude views, forests, land, and varying concentrations of haze, while the main targets include wires and insulators. Qualitative analysis primarily focuses on visual quality comparison. A successful dehazing enhancement effect is indicated by the processed image effectively removing noise and haze compared to the original image, while significantly enhancing edge detail information without color distortion or false contours.

The results of the long-range image analysis are depicted in Fig. 4. From the experimental findings, it is observed that MSRCR exhibits a favorable effect on composite insulator snow-covered images characterized by distinct color features in the third group. However, noticeable halo phenomena and pseudo-color noise are evident in the fourth group of results. DCP demonstrates poor processing efficacy in the sky area. For instance, in the second group of image processing results, evident halo phenomena are observed in the wire area, pseudo-color blocks appear in the sky area, and the overall image appears darker. OCE displays relative stability in processing the latter three groups, effectively removing haze from the image while enhancing contrast. Nevertheless, due to the relatively low impurity content in the atmosphere during misty weather, the parameter estimation method in OCE to compensate for hazy images is only locally effective. For instance, in the first set of results, a distinct black halo is observed in the area of the wire against the snowy background. DehazeFormer demonstrates a favorable overall dehazing effect on the first set of images; however, noticeable distortion phenomena are observed in the sky area in the processing results of the fourth set of images.

As depicted in Fig. 5, the dehazing results of close-range images illustrate remarkable achievements by the five methods; however, variations persist in the processing outcomes of different methods. The processing results of DCP and OCE exhibit similarities, both resulting in an overall reduction in image brightness, leading to darker images and some loss of edge detail information. For instance, the results of groups 6, 7, and 9 appear darker than the original image, and the wire part in the lower right corner of the second group of results shows a loss of detail. DehazeFormer demonstrates a good overall dehazing effect on the first group of images, yet significant distortion is observed in the processing results of the fourth group of images.

Furthermore, achieving color fidelity in dense haze weather proves challenging for the results of DCP and OCE. In the 8th group of results, an over-enhanced pseudo-color is evident in the background noise, while a pseudo-color block effect is observed in the upper-right sky area of the 10th group of DPC results. MSRCR struggles to dehaze the 8th group of images but remains relatively stable for other processing results, showcasing its unique enhancement feature with color recovery. However, this method exhibits significant dependency on scale parameters, leading to color distortion in individual results at the same scale, as observed in groups 1 and 9. Additionally, the time consumption of MSRCR increases linearly with the number of scales, making it the most time-consuming among the four algorithms tested. DehazeFormer effectively restores detailed image information in situations with light haze, such as the 5th and 6th groups. However, when processing heavily hazed images, serious color temperature imbalances occur, resulting in color temperature deviations in the 1st, 3rd, and 7th groups of images, presenting a red color temperature different from its original state and leading to the loss of image details. Moreover, color distortion and mosaic phenomena occur in the processing of images in the 9th and 10th groups.

From the qualitative analysis of the dehazing results of the two types of transmission line icing images, it is evident that the proposed method exhibits greater robustness in dehazing on-site images of iced transmission lines in various environments. Additionally, it enhances the contrast between the foreground and background of the image and effectively strengthens edge and detail information. Moreover, the low-frequency dehazing with spatial adaptability not only prevents over-enhancement of image noise by traditional dehazing algorithms but also eliminates blocking phenomena in the image. Furthermore, the proposed method corrects grayscale distribution bias, achieves color fidelity, and enhances contrast, thereby effectively enhancing dehazing in images of iced transmission lines.
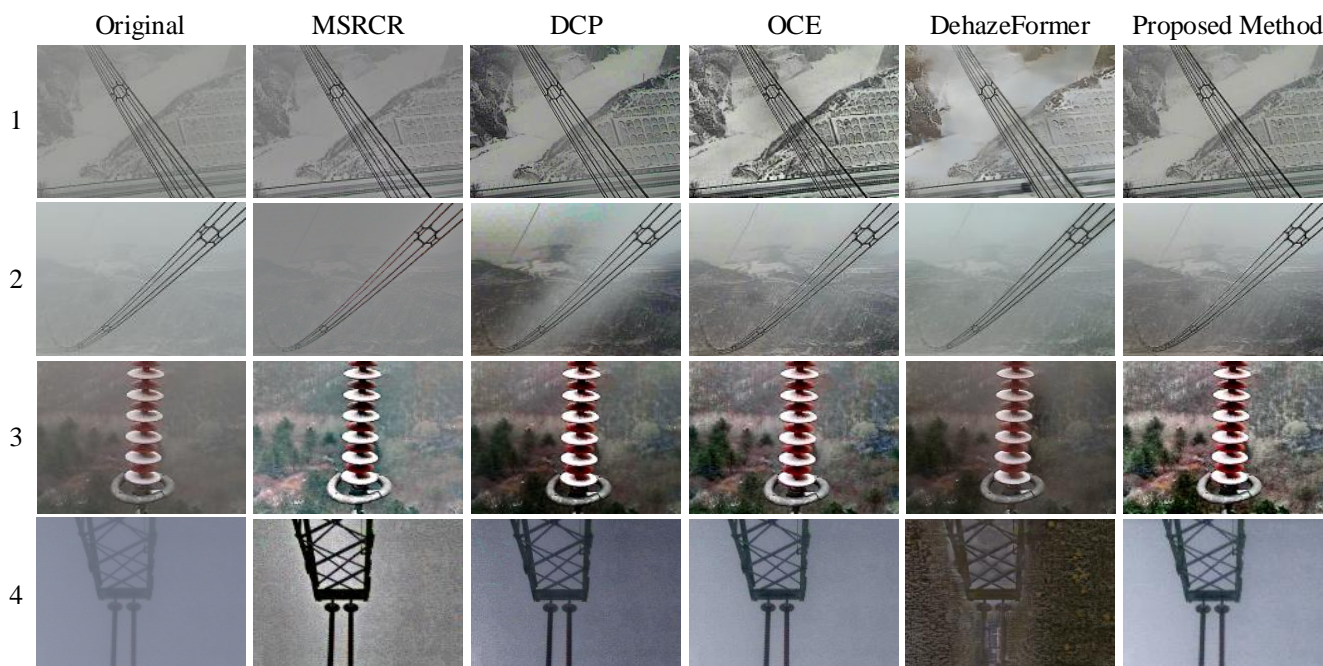
Fig. 4 Qualitative analysis results of dehazing processing of long-range images
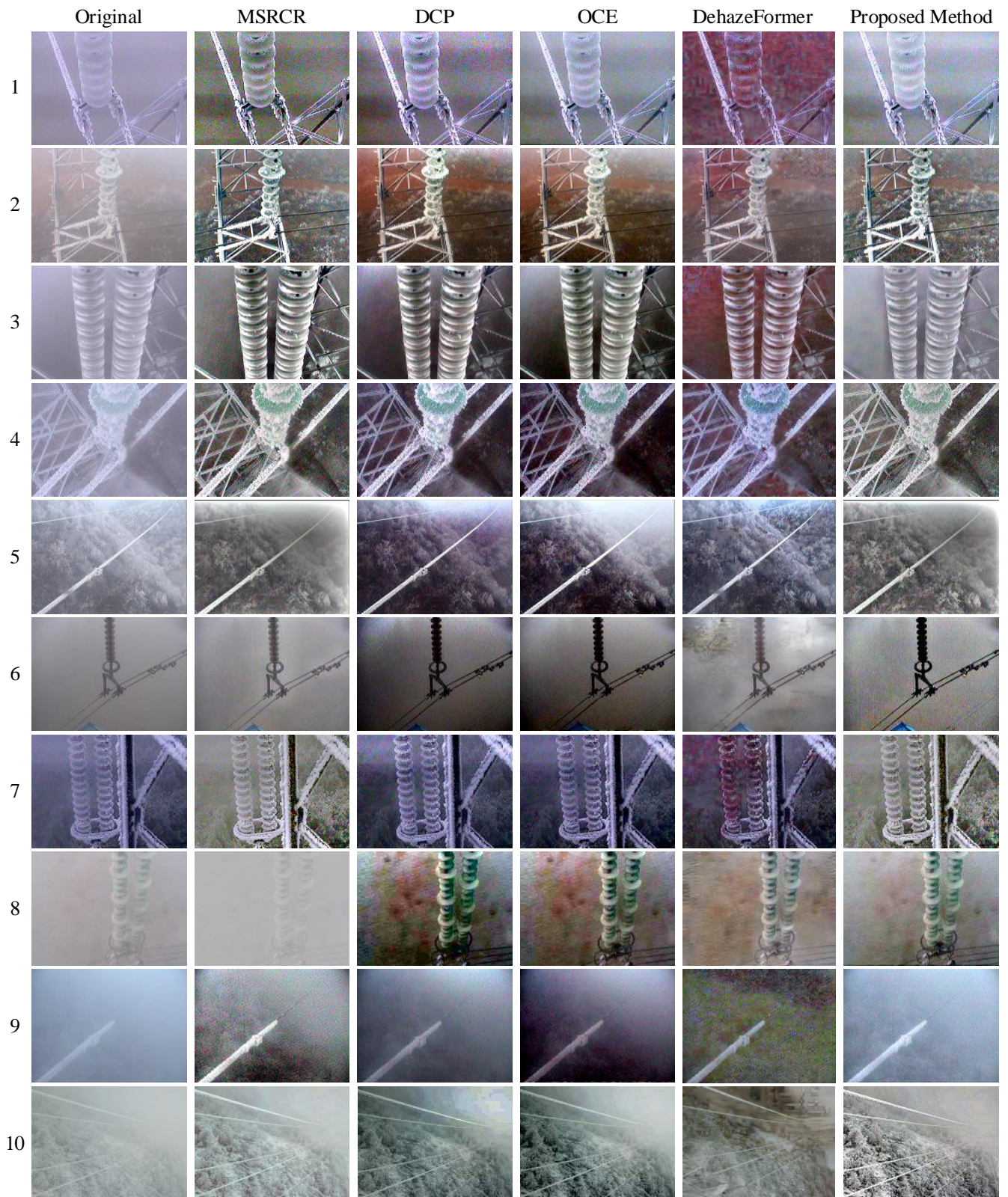
Fig. 5 Qualitative analysis results of dehazing processing of close-range images

B. Quantitative Analysis

To quantitatively analyze the performance of different image dehazing algorithms, we calculate the average gray value, standard deviation, and average gradient of the processed images, respectively, for evaluation [27]. Let F denote the image after dehazing to be evaluated, where the size of the image is $m \times n$, and $F(i, j)$ represents the gray value at pixel point (i, j) of the image.

The average gray value μ reflects the average brightness of the image, with a higher value indicating greater image brightness. It is defined as follows:

$$\mu = \frac{1}{m \times n} \sum_{i=1}^{m} \sum_{j=1}^{n} F(i,j) \qquad (9)$$

The standard deviation σ represents the deviation of the gray value of each pixel in the image from the mean. The larger the standard deviation of the image, the greater the dispersion of its gray levels, and the better the image quality, which is given as

$$\sigma = \sqrt{\frac{1}{m \times n} \sum_{i=1}^{m} \sum_{j=1}^{n} \left(F(i,j) - \mu \right)^2} \qquad (10)$$

The average gradient ∇G represents the detail contrast and texture changes of the image, the larger the value, the clearer the picture, which is represented as

$$\nabla G = \frac{\sum_{i=1}^{m} \sum_{j=1}^{n} \sqrt{\Delta x F(i,j)^2 + \Delta y F(i,j)^2}}{m \times n} \qquad (11)$$

Where $\Delta x F(i,j)$ and $\Delta y F(i,j)$ represent the first-order difference of pixel (i,j) in the x and y directions, respectively.

Using the above three image quality evaluation indicators, we quantitatively analyze the dehazing effect of the experimental result images in Fig. 4 and Fig. 5. The results are presented in Table I and Table II. The larger the σ value and the ∇G value in the calculation result, the closer the μ value is to 128, the better the image enhancement effect, and the more in line with the visual characteristics of the human eye [28][29].

TABLE I. QUANTITATIVE ANALYSIS RESULTS OF DEHAZING PROCESSING OF LONG-RANGE IMAGES

Number	Original			MSRCR			DCP			OCE			DehazeFormer			Proposed Mothed		
	μ	σ	∇G	μ	σ	∇G	μ	σ	∇G	μ	σ	∇G	μ	σ	∇G	μ	σ	∇G
1	144	22	11	132	29	20	123	40	20	139	40	26	153	36	14	142	57	45
2	163	27	7	132	20	10	121	47	13	140	43	19	152	32	8	141	42	22
3	108	26	5	128	44	20	83	53	18	106	55	32	78	35	7	97	50	24
4	135	9	2.7	131	50	31	102	27	11	150	34	13	59	20	11	132	30	8
Average	137	21	6	130	35	20	107	41	15	133	43	22	110	30	10	**127**	**44**	**24**

TABLE II. QUANTITATIVE ANALYSIS RESULTS OF DEHAZING PROCESSING OF CLOSE-RANGE IMAGES

Number	Original			MSRCR			DCP			OCE			DehazeFormer			Proposed Mothed		
	μ	σ	∇G	μ	σ	∇G	μ	σ	∇G	μ	σ	∇G	μ	σ	∇G	μ	σ	∇G
1	160	18	11	166	39	24	131	48	31	149	39	24	97	36	23	126	47	24
2	165	25	5	124	54	15	99	58	16	107	60	15	112	37	11	124	53	25
3	158	24	6	149	30	15	104	58	16	99	62	17	99	46	14	126	56	10
4	160	28	12	126	52	24	104	66	33	83	66	34	107	52	29	126	61	25
5	159	37	9	134	45	12	102	58	18	105	69	21	111	51	17	128	52	25
6	134	19	5	138	22	9	77	40	12	86	46	12	140	34	9	133	41	7
7	97	36	19	129	48	20	87	48	27	80	49	29	73	45	29	131	44	33
8	165	10	2	179	3	8	102	38	9	107	34	7	132	19	6	133	43	13
9	165	26	2	167	32	7	109	40	5	83	52	7	89	25	28	129	51	18
10	170	17	3	171	26	8	105	39	8	146	50	9	116	27	10	131	54	16
Average	153	24	7	148	35	14	102	49	18	105	53	18	107	37	17	**129**	**50**	**20**

From the results, it can be observed that the proposed method achieves the best scores in both the μ and the ∇G: the μ value of the two types of image processing results are 127 and 129, respectively, which are closest to the optimal value, indicating optimal improvement in brightness and detail enhancement. The average values of σ and ∇G are both twice the value of the original image, indicating that the method has also achieved the best results in terms of image contrast and sharpness.

Quantitative analysis demonstrates that the method is highly effective in dehazing and denoising transmission line icing images, as well as enhancing image edges and improving image contrast. It exhibits wide applicability and robustness to haze weather.

IV. Conclusions

A dehazing enhancement method suitable for icing images of transmission lines is proposed in this paper. The key contribution is introduced an adaptive attenuation factor with spatial adaptability.

Its main benefits are: (1) Achieving superior haze removal performance compared to traditional methods such as DCP, OCE, MSRCR, and the state-of-the-art deep learning-based method DehazeFormer. (2) Effectively preserving important edge detail information during dehazing, facilitating subsequent segmentation analysis of icing areas.

Experimental results demonstrate the effectiveness and wide applicability of the proposed method for dehazing enhancement in various transmission line icing image scenarios. By spatially adaptively attenuating low-frequency components, it surpasses traditional uniform processing approaches and deep models in improving the clarity and details of severely hazy images, thereby making ice features more discernible and benefiting downstream tasks.

However, the proposed method has two limitations. Firstly, it does not perform well in dehazing when dealing with hazy images captured on-site under low lighting and with changing backgrounds. Secondly, when haze is accompanied by rain or snow, the method struggles to avoid interference from rain and snow lines in the image during dehazing. These limitations can potentially be addressed by implementing better image preprocessing techniques and establishing background templates. In the future, further optimization and improvement of the algorithm's robustness and application range will be necessary.

References

[1] X. Wang, Z. Yan, Y. Zeng, et al., "Research on correlation factor analysis and prediction method of overhead transmission line defect state based on association rule mining and RBF-SVM." *Energy Reports*, vol. 7, pp. 359–368, Elsevier BV, 2021.

[2] A. Mukherjee, P. K. Kundu, A. Das. "Transmission Line Faults in Power System and the Different Algorithms for Identification, Classification and Localization: A Brief Review of Methods." *Journal of The Institution of Engineers (India): Series B*, Springer Science and Business Media LLC, 2021.

[3] L. Li, D. Luo, W. Yao. "Analysis of transmission line icing prediction based on CNN and data mining technology." Soft Computing, *Springer Science and Business Media LLC*, 2022, 26(16): 7865–7870.

[4] M. Kreutz, A. A. Alla, A. Eisenstadt, et al. "Ice Detection on Rotor Blades of Wind Turbines using RGB Images and Convolutional

Neural Networks." *Procedia CIRP*, Elsevier BV, 2020, 93: 1292–1297.

[5] Q. Hu, X. Xu, D. Leng, et al., "A method for measuring ice thickness of wind turbine blades based on edge detection," *Cold Regions Science and Technology*, vol. 192, Elsevier BV, pp. 103398, 2021.

[6] J. Chatterjee, M. T. Alvela Nieto, H. Gelbhardt, et al. "Domain-invariant icing detection on wind turbine rotor blades with generative artificial intelligence for deep transfer learning." *Environmental Data Science*, vol. 2, Cambridge University Press (CUP), 2023.

[7] M. Kaur, D. Singh, V. Kumar, et al. "Color image dehazing using gradient channel prior and guided L0 filter." *Information Sciences*, vol. 521, Elsevier BV, pp. 326–342, 2020.

[8] S. Cheng, B. Yang. "An efficient single image dehazing algorithm based on transmission map estimation with image fusion." *Engineering Science and Technology, an International Journal*, vol. 35, Elsevier BV, pp. 101190, 2022.

[9] X. Yan, G. Wang, P. Lin, et al. "Underwater image dehazing using a novel color channel based dual transmission map estimation." *Multimedia Tools and Applications*, vol. 2023, Springer Science and Business Media LLC.

[10] F. Sun, S. Wang, G. Zhao, et al. "Single-image dehazing based on dark channel prior and fast weighted guided filtering." *Journal of Electronic Imaging*, vol. 30, no. 02, SPIE-Intl Soc Optical Eng, 2021.

[11] W. Zhang, L. Dong, X. Pan, et al. "Single Image Defogging Based on Multi-Channel Convolutional MSRCR." *IEEE Access*, vol. 7, Institute of Electrical and Electronics Engineers (IEEE), pp. 72492–72504, 2019.

[12] J.-H. Kim, W.-D. Jang, J.-Y. Sim, et al. "Optimized contrast enhancement for real-time image and video dehazing." *Journal of Visual Communication and Image Representation*, vol. 24, no. 3, Elsevier BV, pp. 410–425, 2013.

[13] D. Berman, T. Treibitz, S. Avidan. "Single Image Dehazing Using Haze-Lines." *IEEE Transactions on Pattern Analysis and Machine Intelligence*, vol. 42, no. 3, Institute of Electrical and Electronics Engineers (IEEE), pp. 720–734, 2020.

[14] X. Zhang, T. Wang, W. Luo, et al. "Multi-Level Fusion and Attention-Guided CNN for Image Dehazing." *IEEE Transactions on Circuits and Systems for Video Technology*, vol. 31, no. 11, Institute of Electrical and Electronics Engineers (IEEE), pp. 4162–4173, 2021.

[15] F. Zhang, W.-G. Wang, Y.-B. Zhao, et al. "Automatic diagnosis system of transmission line abnormalities and defects based on UAV." *2016 4th International Conference on Applied Robotics for the Power Industry (CARPI)*, IEEE.

[16] T. Peng, Z. Chen, S. Gong, et al. "Visual Power Line Inspection Via Multi-direction Transform." *2019 IEEE Innovative Smart Grid Technologies - Asia (ISGT Asia)*, IEEE.

[17] J. Liu, R. Jia, W. Li, et al. "Image Dehazing Method of Transmission Line for Unmanned Aerial Vehicle Inspection Based on Densely Connection Pyramid Network." *Wireless Communications and Mobile Computing*, vol. 2020, Hindawi Limited, pp. 1–9.

[18] S.-C. Pei, T.-Y. Lee. "Effective image haze removal using dark channel prior and post-processing." *2012 IEEE International Symposium on Circuits and Systems*, IEEE.

[19] K. Verma, B. K. Singh, A. S. Thoke. "An Enhancement in Adaptive Median Filter for Edge Preservation." *Procedia Computer Science*, vol. 48, Elsevier BV, pp. 29–36, 2015.

[20] C. Qin, Q. Liu. "Pellet ore image segmentation based on improved watershed algorithm." *Journal of Wuhan University of Science and Technology*, vol. 38, no. 02, pp. 134-137, 2015.

[21] W. Wang, X. Yuan, X. Wu, et al. "Dehazing for images with large sky region." *Neurocomputing*, vol. 238, Elsevier BV, pp. 365–376, 2017.

[22] J. Shi, K. Yang. "An Improved Method of Removing Fog and Haze Effect From Images." *Proceedings of the 2016 4th International Conference on Machinery*, Materials and Information Technology Applications, Atlantis Press, 2016.

[23] K. He, J. Sun, X.-O. Tang. "Single image haze removal using dark channel prior." *2009 IEEE Conference on Computer Vision and Pattern Recognition*, IEEE, 2009.

[24] J.-H. Kim, W.-D. Jang, J.-Y. Sim, et al. "Optimized contrast enhancement for real-time image and video dehazing." J*ournal of*

Visual Communication and Image Representation, vol. 24, no. 3, Elsevier BV, pp. 410–425, 2013.

[25] B. Jiang, G. A. Woodell, D. J. Jobson. "Novel multi-scale retinex with color restoration on graphics processing unit." *Journal of Real-Time Image Processing*, vol. 10, no. 2, Springer Science and Business Media LLC, pp. 239–253, 2014.

[26] Y. Song, Z. He, H. Qian, et al. "Vision Transformers for Single Image Dehazing." *IEEE Transactions on Image Processing*, vol. 32, Institute of Electrical and Electronics Engineers (IEEE), pp. 1927–1941, 2023.

[27] P. Wang, S. Wang, Y. Zhang, et al. "Multispectral Image under Tissue Classification Algorithm in Screening of Cervical Cancer." *Journal of Healthcare Engineering*, vol. 2022, Hindawi Limited, pp. 1–9, 2022.

[28] L. Li, Q. Ye, J.-P. Liu, et al. "A fog simulation method based on depth estimation." *Progress in Laser and Optoelectronics*, vol. 60, no. 10, pp. 82-88, 2023.

[29] Y. Sun, Z. Zhao, D. Jiang, et al. "Low-Illumination Image Enhancement Algorithm Based on Improved Multi-Scale Retinex and ABC Algorithm Optimization." *Frontiers in Bioengineering and Biotechnology*, vol. 10, Frontiers Media SA, 2022.

Wet snow accumulation – Study of an event in 2019

Árni Jón Elíasson[1], Egill Thorsteins[2], Sigurjón Páll Ísaksson[2]

[1] Landsnet, Reykjavík, Iceland
[2] Efla Consulting Engineers, Reykjavík, Iceland

arnije@landsnet.is, egill.thorsteins@efla.is, sigurjon.pall.isaksson@efla.is

Abstract— **Northern part of Iceland has historically been getting severe wet snow events. Between 1972-2023, there have been nine such events. The last event occurred on 10.–11. Dec. 2019, when wet snow accretion combined with strong wind resulted in failures of 61 towers in 66-132 kV lines and failure of more than 120 wooden poles in 11-33 kV distribution lines.**

The paper presents a study on the event in Dec. 2019. The weather leading to the wet snow accumulation is described. Results of an in-situ inspection of the accumulated wet snow on conductors of transmission and distribution lines in the affected area are presented. A hindcast simulation of the event is performed to estimate hourly weather parameters in a 2km x 2km grid (WRF model). The simulated data are subsequently used as input for a cylindrical wet snow accretion model. The measured and simulated wet snow loading are analysed in relation to the weather during the event. The weather in Dec. 2019 is also compared to similar historically wet snow cases in the area.

Keywords—*Wet snow accumulation, WRF, icing model, field measurements, drifting snow, sticking efficiency, ice shedding.*

I. Introduction

Severe wet snow icing is generally rare in most countries. It is, however, relatively frequent in many parts of Iceland, and the northern part has historically been experiencing frequent and significant wet snow events. The icing database (IceDat) [1] shows that between 1972 and 2023, nine such events led to severe damage to the overhead lines in the area. The last event occurred on 10.–11. December 2019, when wet snow accretion was combined with strong wind and resulted in failures of 61 towers in 66-132 kV lines and failure of more than 120 wooden poles in 11-33 kV distribution lines. In a new 220 overhead line in the area, one of the conductors was sagging down to the ground due to heavy wet snow ice load and conditions of unbalanced ice, i.e., where the neighboring spans had less ice load.

The weather was bad during and shortly after the accumulation event in December 2019, and traveling to the icing sites was challenging. It was thought manageable to arrive into the field to make appropriate observations and measurements of the icing before the workforce arrived, and traces of the icing were destroyed. Making valuable measurements in the areas with the most severe icing was thus possible.

Landsnet (grid owner) operates many automatic load cells in transmission lines and test spans all around the country. Unfortunately, wet snow accumulation did not occur on any measurement sites with load cells in the area during this event. Thus, direct and continuous measurements are not available.

II. The Atmospheric Situation

On 9. Dec. 2019, a low-pressure system formed south of the country. It deepened quickly, about 23 hPa in 24 hours from 9. Dec.:12 to 10. Dec. :12. It went north along the east coast and then south over the country on the east side. The low-pressure system was deepest at 949 hPa at 12. Dec. :00 a short distance southeast of the country [2]. The precipitation was very heavy in the northern part of the country. Precipitation measurements were unreliable in the weather due to strong wind, but Fig. 1 shows a weather forecast of the precipitation from the Met Office based on a HARMONIE-AROME model.
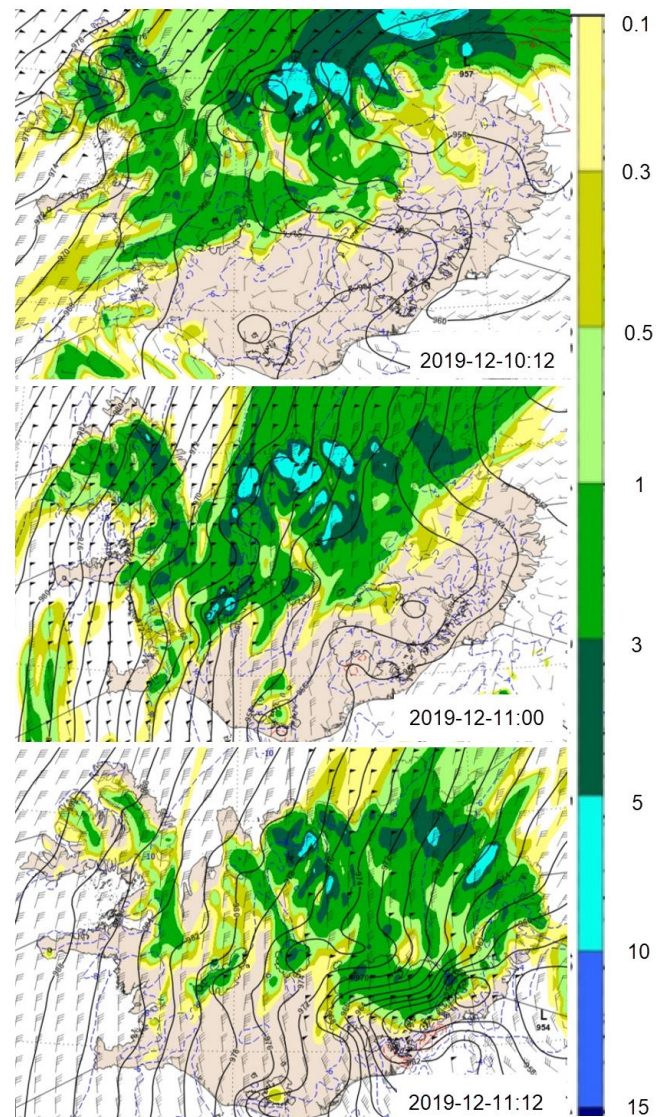

Fig. 1 Precipitation (mm/hour) predicted by the Met Office (Harmonie-Arome model) during 24 hours between 2019-12-10:12 to 2019-12-11:12.

The precipitation prediction in the lowlands near the coast is in many places in the range of 3-5 mm/hour for part of the period and later in the range of 1-3 mm/hour. Precipitation increases in the nearby mountains with increased altitude.

Measurements of temperature, wind, atmospheric pressure and relative humidity are available from many automatic weather stations in the area. Ten measuring sites close to the coast were selected to be most representative for the wet snow study; see location in Fig. 2. Nine measuring sites are at altitudes between 4-32m a.s.l., and the highest is at 103m a.s.l.

Fig. 3 shows the variation of the wet-bulb temperature (Tw) for the ten measuring stations, i.e., the average value and the range identified with a maximum and minimum value at any station for a given hour. Prerequisites for wet snow accumulation are often defined as Tw between 0°C and 1.2°C. Thus, favorable temperature conditions for wet snow accumulation start around 2019-12-09:20 and last to 2019-12-11:03, i.e., around 32 hours. Wind speed was relatively high in the event. Measurements from the selected automatic weather stations are in Fig. 4. The average exceeded 20 m/s for 16 hours, and the peak wind for a single measuring site was 35 m/s. The accumulation time in the field seems to have started at 10. December between 0 and 6 and lasted until 2 am 11. December.
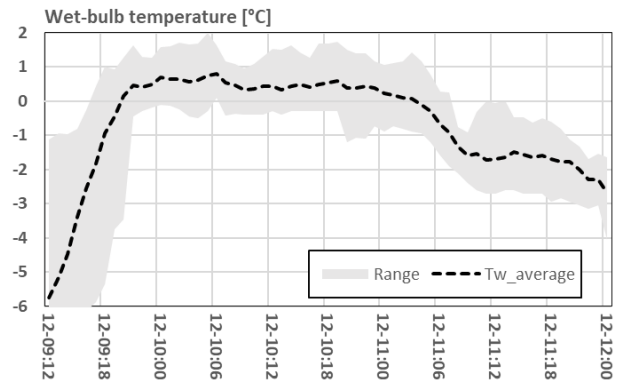

Fig. 3 Wet bulb temperature at ten automatic measuring stations.
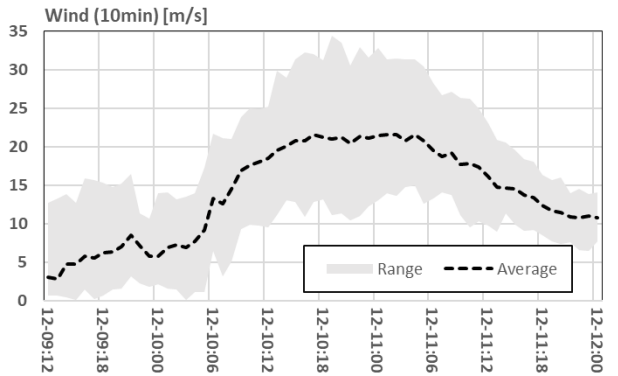

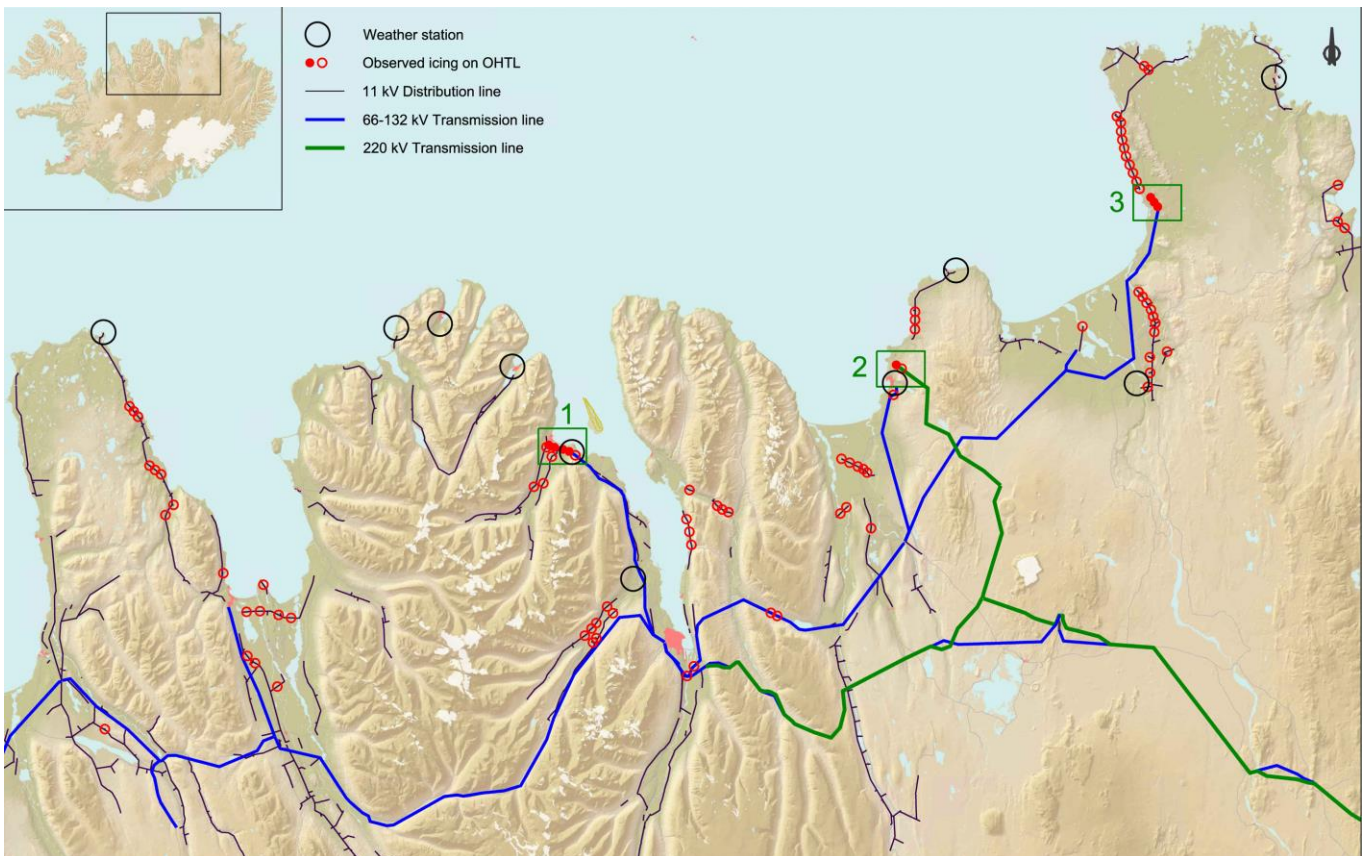Fig. 4 Measured wind speed [m/s] (10. min on the hour) in 9 automatic weather stations.

Fig. 2 Observed icing on overhead lines in the icing event 09-11 Dec. 2019. Location of ten weather station and location of the three areas used in study.

435

III. MEASUREMENTS AND FIELD INVESTIGATION

Severe wet snow accumulation was on many overhead lines in the northern part of the country during 10.-11. December 2019, resulting in many outages and failures. Fig. 2 shows the overhead lines where wet snow icing was observed. In the following, three areas are presented and examined in more detail; two of them had a severe failure of 66/132 kV wooden towers and the third experienced high ice load on a few spans in a newly built 220 kV line, resulting in an outage but no tower failure. These three locations are marked in Fig. 2; they were chosen because they have important overhead lines in the grid and were inspected, especially after the storm. The three selected areas are all near the coastline and at an altitude between 5 and 100 m. There was also a lot of damage to 11 kV lines, but inspection of damage and icing was not as detailed as of the transmission lines.

Time for field inspection and measurements on undisturbed traces of icing is often minimal, as there is an urgent need to repair and restore the transmission lines. Therefore, it is often only possible to carry out limited measurements on weight and diameter, and visual assessment and photography are the best options.

In some cases, it may also be challenging to evaluate icing that represents the accumulation by a single value. Ice accumulation sometimes varies along the span, being less at suspension points due to increased rotational stiffness. Furthermore, in extreme wet snow icing, the accumulation can slide to the centre of spans and even be affected by a snow drift when the conductor sags to or near the ground. For this reason, it is not possible to only look at the largest measurements when assessing icing representing accumulation on a freely rotating cylinder.

A. Area 1 - Dalvík (66/132kV DA1)

DA1 is a transmission line with H-frame wooden towers built for 132 kV but operated on 66 kV. Severe wet snow accumulated between 10.-11. Dec. 2019, in the last 4 km of the line, near the village of Dalvík. The first outage occurred 10. Dec: 20:26, but the line was re-energized. A permanent outage occurred 11. Dec. at 07:59, inspection revealed total collapse of all 31 towers on a 3.7 km long section. Fig. 5 shows the location of failed towers, and Fig. 6 to Fig. 10 shows the failed section and examples of the icing. Icing inspection was performed 12. December 13:00-16:00 and the typical ice diameter was measured as 10-17 cm (equivalent diameter).

Two ice samples were taken; the unit weight was 13.1 kg/m and 16.8 kg/m, and the density was 0,76 g/cm^3 in both cases. Icing accumulation was generally larger in the middle of the spans and less near suspension points. Most of the iced and failed towers in DA1 were in the range of 5-40 m a.s.l. The end of the icing section, at Hámundarstaðaháls, was at a higher altitude or 90-100 m.a.s.l. Fig. 10 shows the icing at that location. An automatic weather station at the same location (Hámundarstaðaháls) shows that the wet-bulb temperature at this location was slightly below zero, see Fig. 23.

Fig. 5 The iced section of DA1, red circles show broken poles. Blue arrow shows direction of accumulation on poles.

Fig. 6 Failed section in DA1.

Fig. 7 Icing on conductors next to failed tower.

Fig. 8 Measurement in DA1. Ice mass = 16.8 kg/m and density = 0.76 g/cm^3.

Fig. 9   Measurement of ice diameter 14 cm.

Fig. 10 Icing at Hámundarstaðaháls, elevation ~70 m a.s.l. Crane holding conductors above road crossing after failure.

DA1 was erected in 1985; there were seven wet snow icing events known on the failed section with the highest ice load in the range of 5 to 8 kg/m. This was the first failure of the line due to icing in 34 years.

B. Area 2 – Húsavík (220kV TR1)

220kV TR1 consists of steel towers constructed in 2017. Severe wet snow accumulation occurred on the last spans of TR1, near Húsavík, in the wet snow icing event 10. December 2019. Fig. 11 shows the iced section, which is ca. 60m a.s.l. The accumulation was most severe in the last span next to the substation, and the conductor sagged to the ground due to unbalanced ice, see Fig. 12. It resulted in a line outage (on 10. Dec. at 20:01) and burned conductor strands. Ice load was estimated as 15 kg/m before it was mechanically removed from the conductors. The accumulation continued and resulted in approx. 9 kg/m on earth wires that had not got complete ice removal as the conductors, see Fig. 13. Icing inspection took place 13. December between 14-16:30.

Fig. 11   The iced section of TR1, red circle, shows a damaged conductor. Blue arrows show the direction of icing on towers.
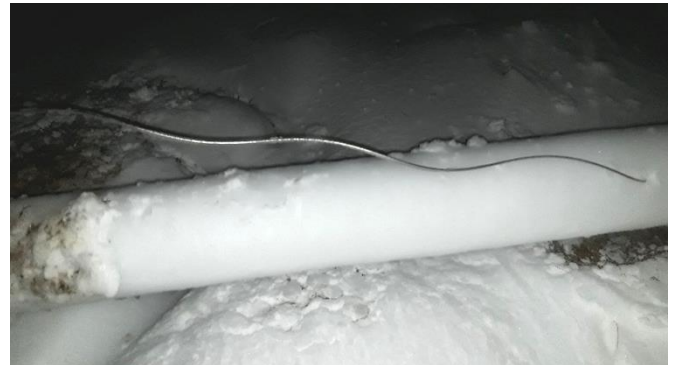

Fig. 12 Conductor sagged to the ground, ice mass estimated 15 kg/m. Photo Dec. 10th, at 21.

Fig. 13   Icing on the last span of TR 1. Earth wire sagged below conductors after the ice was removed from the conductors. The icing on earth wire is ~ 9 kg/m.

C. Area 3 – Kópasker (66/132kV KS1)

KS1 is a H-frame wood tower line built for 132 kV but operated on 66 kV. Wet snow accumulation started on the 10. Dec. on the last 2.5 km of the line, 15 towers next to village Kópasker. The first line outage occurred at 12, and at 13, it was informed that ten towers were broken. Three towers failed later. Line inspection took place 13. December. It was evaluated that the equivalent icing was generally in the 5 to 12 kg/m range.

In spans that had not sagged to the ground, there was generally considerably less ice mass next to the tower compared to the middle of the span. This results from different rotational stiffness and sliding of the wet snow along the span to the lowest point. A spiral form had formed at one location, indicating the accumulation sliding along the conductor, see Fig. 19. Conductors had, in some places, sagged to the ground, and the ice diameter at those locations was around 23 cm (20-25 cm); a part of that icing is due to drifting snow next to the ground.

When conductors sag down to 2-3 m from the ground, an increased accumulation can often be noticed due to the drifting snow effect. The same may be seen in ice keels on wood pole towers. KS1 was erected in 1985, and three wet snow icing events were previously known on this line section with a maximum ice load of 2 kg/m. This event was the first failure of the section.
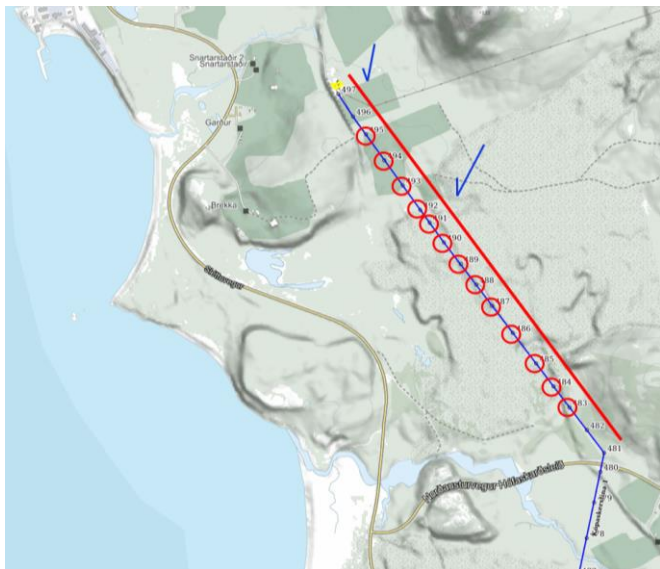

Fig. 14 The iced section of KS1, red circles show broken poles. Blue arrow shows direction of accumulation on poles.

Fig. 15 Ice diameter is much less at suspension points than in the middle of the span and close to the ground.

Fig. 16 Icing on KS1. When the conductors come close to the earth, there is an extra accretion because of drifting snow.

Fig. 17 Measurement of ice mass and ice density in KS1. Ice mass 14.8 kg/m and density 0.68 g/cm^3.

Fig. 18 Large ice diameter. Accumulation is influenced by drifting snow near the ground.

Fig. 19 Spiral form of icing due to sliding of accumulation.

IV. Hindcast simulation and Icing model

Icing models, using results from weather models as input, have been used to evaluate and quantify wet snow icing for many years [3], [4], [5] and [6]. Using this event to evaluate how well the icing model can predict and quantify the icing is valuable. The model setup in [4] is used here as a reference.

A Numerical simulations of the atmospheric flow

The study uses atmospheric hindcast data that is prepared with the Weather Research and Forecasting model (WRF), where cloud microphysics, including the generation of precipitation particles through autoconversion, is handled by the Thompson scheme [7] which features the modifications made to wet snow predictions as described in [8].

The hindcast data has a horizontal resolution of 2km x 2km with 51 vertical levels. The model is forced by the ERA-5 reanalysis dataset from the European Centre for Medium-Range Weather Forecasts (ECMWF).
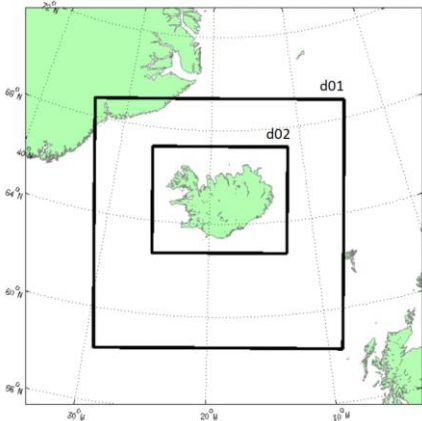

Fig. 20   Model domain setup showing the two nested domains of the WRF simulation. The horizontal grid spacing is 8km x 8km (d01) and 2km x 2km (d02) for the outer and innermost domains.

The spatial grid resolution of 2km x 2km enables good representations of atmospheric flow in large- and medium-scale terrain complexity. However, the resolution is insufficient to capture local terrain complexity where the topographic length scale has a similar dimension to the model grid (or smaller). The study uses results in the lowest height level, ~20 m height.

B Wet snow icing model

The wet snow accumulation model applied in the study is founded on the well-known cylindrical icing model [9].

$$\frac{dM}{dt} = \alpha_1 \cdot \alpha_2 \cdot \alpha_3 \cdot w \cdot V_N \cdot D$$

where α_1 is the collision efficiency, α_2 is the sticking efficiency, α_3 is the accretion efficiency, w is water content (kg/m^3), D is the effective accretion dimension (m) perpendicular to the object, V_N is the velocity of the particles perpendicular to the object (m/s).

The critical part of the model is how the sticking efficiency is evaluated (α_2). Here, it is based on the assumption in [10] but further related to wet-bulb temperature (Tw) by using the freezing fraction (SR) and Tw relation in [5], resulting in sticking factor depending on Tw and wind speed as in Fig. 21. Water content (w) was calculated using hourly precipitation

(RR1h) and fallspeed of snow particles depending on SR according to [5]. Ice ablation is modeled using thermodynamic criteria, and a description of other parameters, such as α_1, α_3, density, and influence of graupel, was used as implemented in [5].
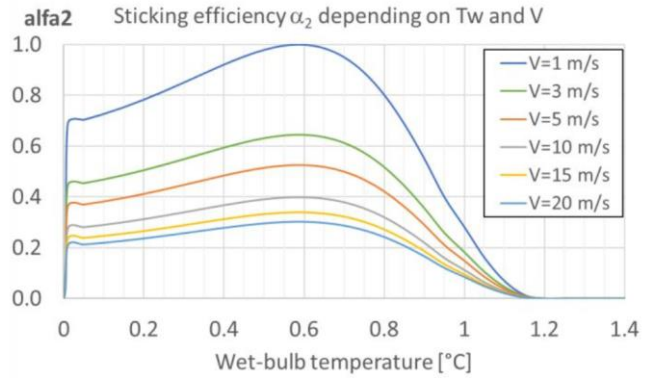

Fig. 21   Sticking factor α_2 depending on wet-bulb temperature and wind speed.

The wet snow icing model is very sensitive to Tw, as seen in Fig. 21, and a modest temperature shift can significantly affect the predicted accumulation. The sticking efficiency in the model is most effective when the wet-bulb temperature is between 0<Tw<1.0 with a peak value around Tw=0.6°C. The sticking factor drops to zero near 1.2°C since it assumes that high liquid water content (LWC) in incoming snowflakes will lead to immediate ice shedding. It is worth noticing that the sticking efficiency can be improved since the ice shedding is here modeled separately, and its influence should thus not be included in it, i.e., α_2 should not go to zero at Tw=1.2°C. It is only correct at the initial stage of accumulation. Snowflakes with high LWC can accumulate onto existing accumulation if the total LWC of the accumulation is less than the critical LWC for ice shedding.

C Area 1 – Dalvík. Results of icing model

Calculated wet snow ice load in WRF model points near the failed section of 66/132kV DA1 are shown in Fig. 22 (red values). Field observation indicates the maximum ice load as 15 kg/m and varied between 8 to 15 kg/m in the iced section. Calculated ice load varies in the area, but points nearest to DA1 have no or limited calculated ice load and thus severely underestimate the reality.

Fig. 23 shows the input to the icing model in the three most representative WRF points and a comparison to measured values of Tw and wind. The underprediction is mainly related to wet-bulb temperature, which is largely outside the effective accumulation range in the icing model when accumulation took place. Tw in the WRF model deviates from the average in the measurements part of the time; it is below in the beginning and later higher. There is an automatic weather station nearby, Hámundarháls, at 103m a.s.l. This station is in the lower range of the Tw measurements but gives reasonable confidence that the average measurements are representative here at sea level in altitudes 0 to 20m. Wind speed at measuring site Hámundarháls is relatively low compared to other measuring sites. Wind speed predicted by the WRF model in points P1, P2 and P3 is somewhat higher than measured at Hámundarháls.
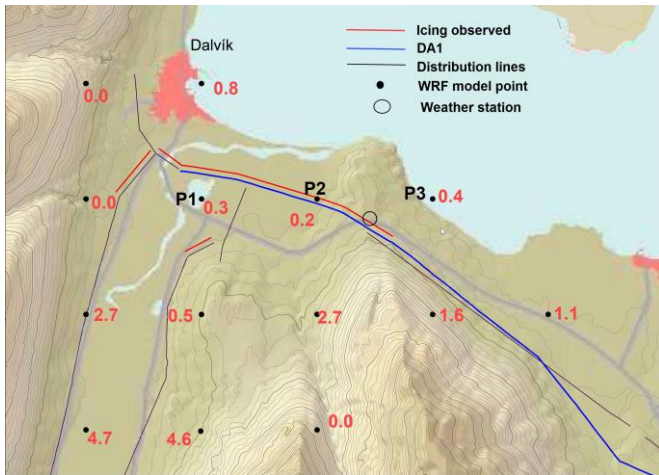
Fig. 22   Results of icing model (kg/m) in WRF model points in area 1. Location of DA1 and weather station (Hámundarháls). Red lines show where icing occurred.
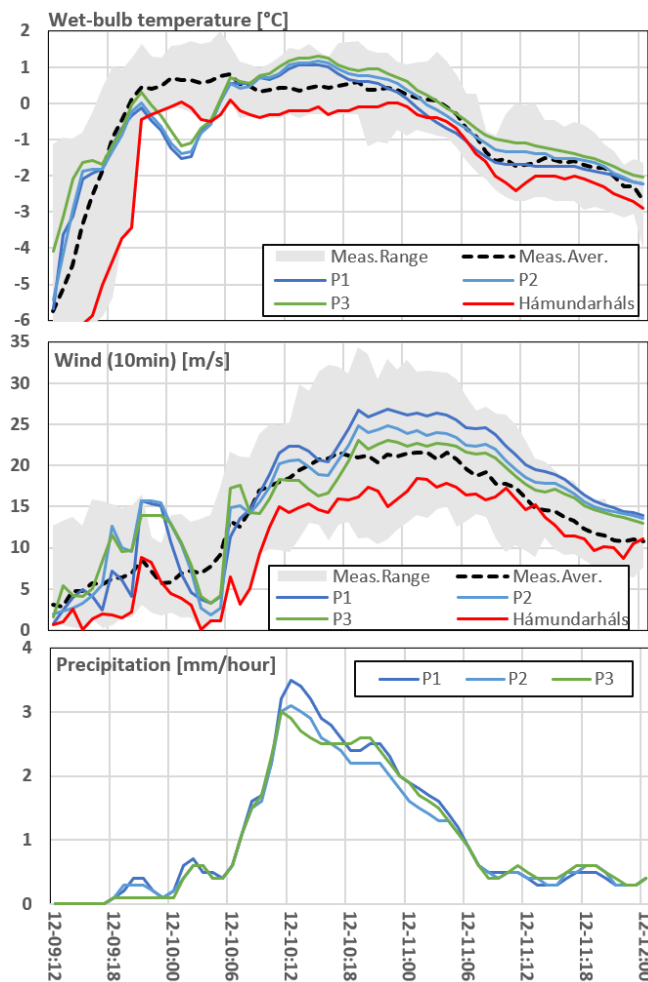

Fig. 23 Measurements and WRF data (P1, P2, P3) in area 1. Hámundarháls is a nearby weather station.

The icing model was also analysed for the three points (P1, P2, P3) by using the measured average wet-bulb temperature instead of the value from the WRF hindcast simulation. It resulted in a large difference in ice load, see Table I. The calculated ice load using Tw from measurements is in better compliance with the field measurements, although they are slightly too high.

Point	Tw from WRF model	Tw from measurements
P1	0.3 kg/m	20.2 kg/m
P2	0.2 kg/m	15.3 kg/m
P3	0.4 kg/m	16.3 kg/m

Model points P1 to P3 are in the height range of 1-7m a.s.l.

D   Area 2 – Húsavík. Results of icing model

Calculated wet snow ice load in WRF model points near 220kV TR1 are shown in Fig. 24. Field observation indicates the ice load was highest 15 kg/m on the last span (60 m a.s.l) and rapidly decreasing with increasing terrain height in other spans. The calculated ice load varies in the area, point P1 should be the most representable, and it has only 0.3 kg/m. Point P2 is nearby, and it has 6.4 kg/m. Overall, the calculations underestimate the reality somewhat.
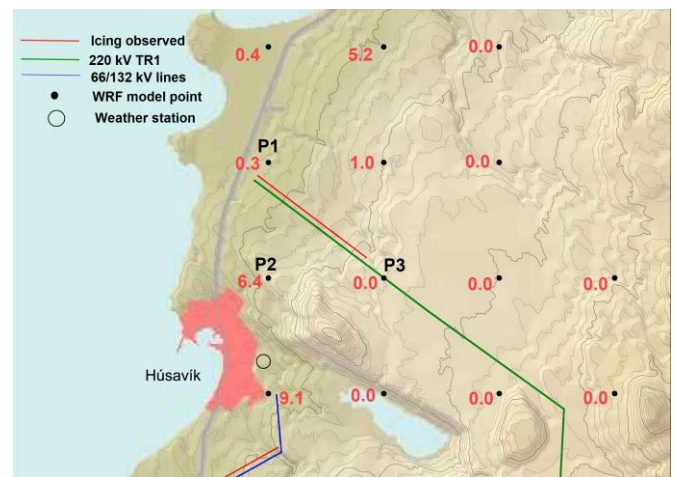

Fig. 24   Results of icing model (kg/m) in WRF model points in area 2. Red line shows icing zone.

Fig. 25 shows the input to the icing model in the three most representative WRF points (P1, P2, P3) and a comparison to measured values of Tw and wind. The underprediction is mainly related to wet-bulb temperature, which is largely outside the effective accumulation range in the icing model, especially in the measurements at the beginning of the accumulation. A nearby weather station at Húsavík has Tw close to the average of measurements. This station is located in a sheltered area concerning wind speed, as may be seen since it is at the lower end of the wind speed range. Unsurprisingly, measured wind at Húsavík is lower than at the site of TR1.
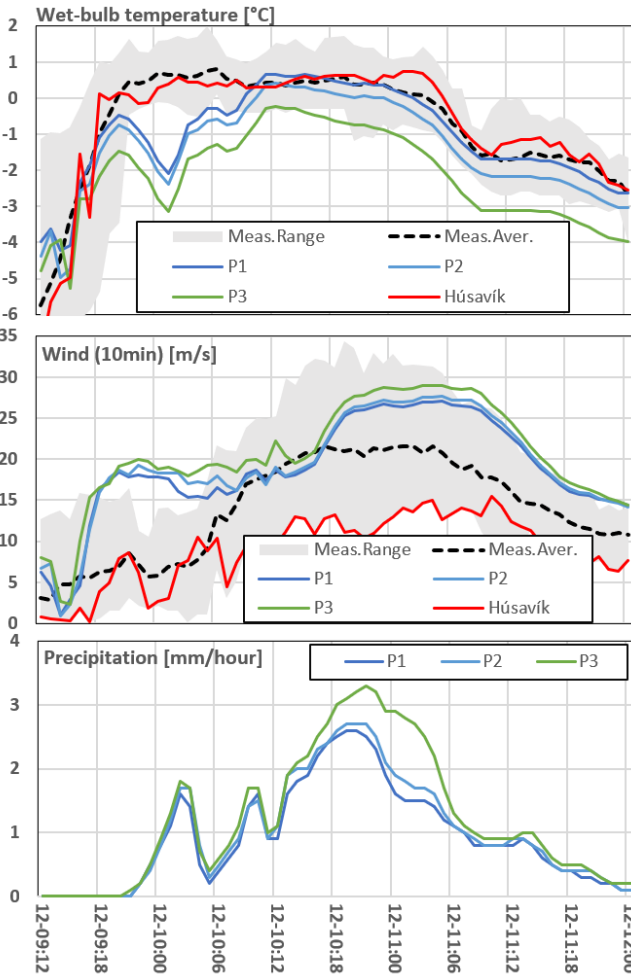
Fig. 25 Measurements and WRF data (P1-P3) in area 2. Húsavík is a nearby measuring site.

The icing model was also analysed for the three points using the measured average wet-bulb temperature instead of the value from the WRF hindcast simulation. It resulted in a much higher ice load, as Table II shows.

TABLE II. AREA 2 - ICE LOAD [KG/M]. RESULTS FROM TWO DIFFERENT DATA SETS OF T_w.

Point	Tw from WRF model	Tw from measurements
P1	0.3 kg/m	(3.8) 13.4 kg/m [1]
P2	6.4 kg/m	17.8 kg/m
P3	0 kg/m	(22.8 kg/m) [2]

[1] Point P1 has two icing values since the model had ice shedding during the accumulation due to high LWC. The first value is with the ice shedding, and the second is without it.

[2] The altitude of the WRF model point P3 is 220m a.s.l. and therefore, it is inappropriate to use Tw from measurements close to sea level without calibration.

E   Area 3 – Kópasker. Results of icing model

Calculated wet snow ice load in WRF model points near the failed section of 66/132kV KS1 are shown in Fig. 26. Field observation indicates the ice load was highest 12 kg/m in a few spans but otherwise in the range of 5-12 kg/m. Calculated

ice load varies in the area, but points near the failed KS1 predict only ~2 kg/m, which underestimates the reality.

Fig. 27 shows the input to the icing model in the most representative WRF points (marked with red) and a comparison to measured values of Tw and wind. The underprediction is mainly related to wet-bulb temperature, which is initially outside the effective accumulation range.
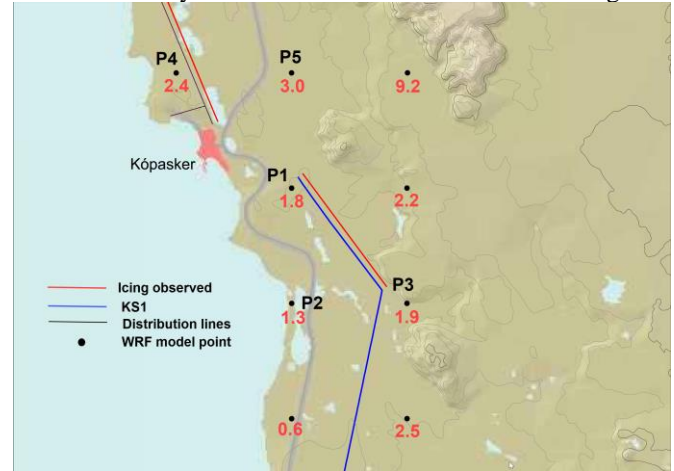

Fig. 26 Results of icing model (kg/m) in WRF model points in area 3. Red lines show where icing occurred.
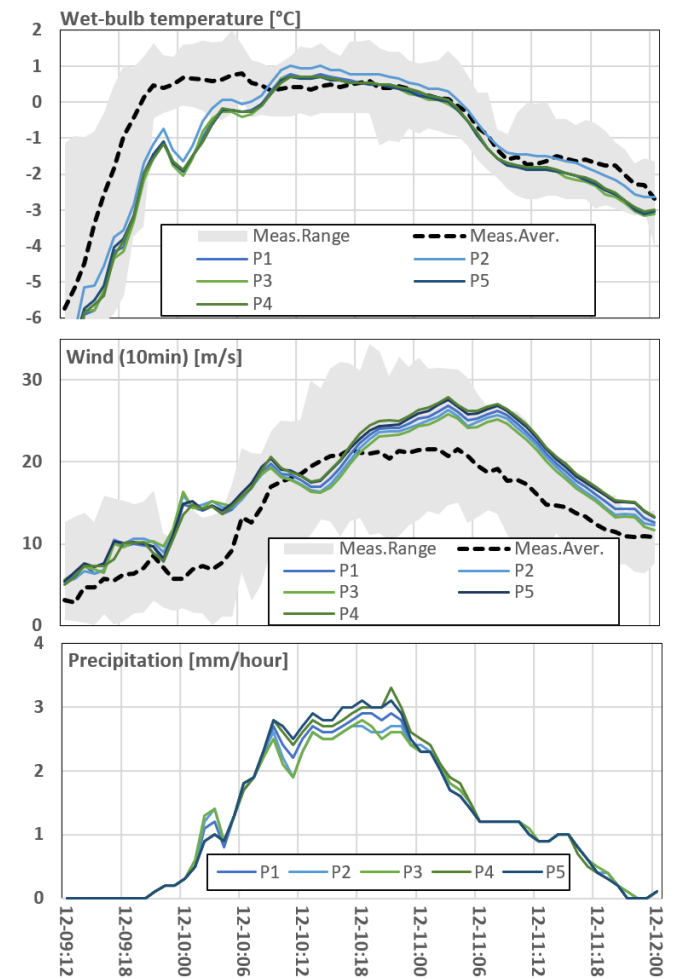

Fig. 27 Measurements and WRF data (P1-P5) in area 3.

The icing model was also analysed for the five points by using the measured average wet-bulb temperature instead of the value from the WRF hindcast simulation, see Table III. It

441

resulted in a much higher ice load that somewhat overestimates the actual loading.

TABLE III. AREA 3 - ICE LOAD [KG/M]. RESULTS FROM TWO DIFFERENT DATA SETS OF Tw.

Point	Tw from WRF model	Tw from measurements
P1	1.8 kg/m	16.8 kg/m
P2	1.3 kg/m	14.4 kg/m
P3	1.9 kg/m	16.6 kg/m
P4	2.4 kg/m	17.3 kg/m
P5	3.0 kg/m	18.4 kg/m

Model points P1 to P5 are in the height range of 9-38 m a.s.l.

F   Results of icing analysis

Table IV summarizes the results for the three areas in the study. Values presented as field observation and measurements evaluate icing on conductor mid-span without the influence of ice sliding and drifting snow. The given range shows the variation within the main icing area.

TABLE IV. COMPARISON OF OBSERVATION AND ICING MODEL

	Unit	Area 1	Area 2	Area 3
Field observation and measurement	[kg/m]	8 - 15	15	5 - 12
Ice model with WRF input data	[kg/m]	0.2-0.4	0-6.4	1.3-3.0
Ice model with WRF input data but Tw from measurements (average)	[kg/m]	15.3-20.2	13.4-17.8	14.5-18.4

The analysis concludes that the icing model, in combination with input data from the WRF hindcast simulation, severely underestimates the actual icing in all areas. The main reason for the underestimation is that the accuracy of the wet-bulb temperature in the WRF simulation is slightly inaccurate, and a modest temperature shift greatly influences the results.

Very different results come when the icing is calculated as before, but using the average of the measured wet-bulb temperature and temperature instead of the WRF temperature. The results align with observed icing but somewhat overestimate the actual icing. It is not possible to conclude if the overestimation is due to input parameters or from the model itself. The icing model includes a reduction factor for the sticking efficiency, depending on the amount of graupel at the accumulation time; see paragraph IV-b. If the restriction is removed, it leads to somewhat higher icing values.

A reduction factor is introduced for the sticking efficiency, depending on the amount of graupel during wet snow events.

Overall, the results show how sensitive the model is to the wet-bulb temperature. It is challenging to accurately predict the ice load at individual sites during an icing event using a numerical simulation of the atmospheric flow. The whole event on a larger scale may be well predicted, but a slight shift in temperature may shift the wet snow icing area. A reasonable approach to improve the icing model results is to make a sensitivity analysis by performing many analyses and shifting the temperature slightly in each analysis; see the perturbation approach in [5] and [6].

The cylindrical icing model was used in the calculation, and it assumes a circular icing shape and a slowly rotating conductor. It would be interesting to include the rotational stiffness of the conductor and non-circular ice shape, as can be found in the icing model in [11] and [12], and compare its effect on the results.

V. SUMMARY AND CONCLUSIONS

Severe wet snow events in northern Iceland are rather frequent, with nine events occurring in 51 years. The last event, from December 2019, is described in the paper. What characterizes the accumulation in the event in December 2019 is: Maximum ice load ~15 kg/m, length of accumulation period 16-20 hours, wind speed 15-30 m/s, precipitation 0.3-3.0 mm/hour and water content 0.3-0.6 g/cm^3.

Field investigation and measurement were performed in the areas with the most severe icing. Unfortunately, there were no measuring sites with load cells in the regions with severe accumulation. Ice accumulation generally varied along the span, being less at suspension points. In extreme icing, the conductor sagged to or near the ground and was sometimes affected by a snow drift.

Icing calculations were made for three areas with severe icing accumulated on overhead lines. The input parameters for the icing model came from atmospheric simulations (WRF). Data from ten automatic weather stations were used to assess the weather conditions in the event and the accuracy of the WRF simulation. Overall, the WRF simulation was assessed to be reasonably good; there were some differences in the wet-bulb temperature.

The icing model initially used WRF data as input to the icing model, which resulted in limited wet snow loading, and the reason was the sensitivity of the icing model to a slight deviation of the wet-bulb temperature. Very different results were obtained when the wet-bulb temperature was replaced with the average of measurements. The results aligned with observed icing but somewhat overestimated the actual icing. It is impossible to conclude if the overestimation is due to input parameters, e.g., to high wind or precipitation, or from the model itself.

Overall, the results show how sensitive the model is to the wet-bulb temperature, and it is challenging to get the requested accuracy in a numerical simulation without calibration with direct measurement.

REFERENCES

[1]   Á. J. Elíasson, S. P. Ísaksson and E. Þorsteins, "Registration of observed icing on overhead lines in Iceland," in *IWAIS 2019*, Reykjavík, 2019.

[2] Guðrún Nína Petersen, "Ísingarveður á aðventu 10.-11 desember 2019," Veðurstofa Íslands (VÍ 2020-003), Reykjavik, 2020.

[3] Á. J. Elíasson, H. Ágústsson and G. M. Hannesson, "Wet-snow accumulation - A study of two severe events in complex terrain in Iceland," in *IWAIS 2013*, 2013.

[4] Á. J. Elíasson, S. P. Ísaksson, H. Ágústsson and E. Þorsteins, "Wet snow icing - Comparing simulated accretion with observational experience," in *IWAIS 2015*, Uppsala, 2015.

[5] E. Thorsteins, B. E. Nygaard, K. Ingvaldsen and Á. J. Elíasson, "Wet snow icing modeling and comparison with field data," in *IWAIS 2022*, Montreal, 2022.

[6] B. E. Nygaard, L. Carlshem, J. Bartsch, L. Lee and H. Ágústsson, "Development of a 50-year return value ice load map," in *IWAIS 2019*, Reykjavik, 2019.

[7] G. Thompson, R. P. Field and R. a. W. Hall, "Explicit forecasts of winter precipitation using an improved bulk microphysics scheme. Part II: Implementation of a new snow parameterization," *Mon. Wea. Rev.,*, vol. 136, pp. 5095-5115, 2008.

[8] E. C. Iversen and G. T. a. B. E. Nygaard, "Improvements to melting snow behavior in a bulk microphysics scheme," *J. Atmos. Res.,* vol. 253, pp. 105471, 2021., 2021.

[9] L. Makkonen, "Models for the growth of rime, glaze, icicles and wet snow on structures," *Philos Trans Royal Soc London Series A: Math Phys Eng Sci,* p. 2913–2939, 2000.

[10] B. E. K. Nygaard, H. Ágústsson and K. Somfalvi-Toth, "Modeling Wet Snow Accretion on Power Lines: Improvements to Previous Methods Using 50 Years of Observations," *Journal of Applied Meteorology and Climatology,* pp. 2189-2203, 2013.

[11] K. Ueno, Y. Eguchi, T. Nishihara, S. Sugimoto and H. Matsumiya, "Development of snow accretion simulation method for electric wires in consideration of snow melting and shedding," in *IWAIS 2015*, Uppsala, 2015.

[12] K. Ueno and T. Nishihara, "A snow accretion simulation method considering precipitation types based on the liquid water fraction of falling snowflakes," in *IWAIS 2017*, China, 2017.

[13] Á. J. Elíasson, G. M. Hannesson and E. Þorsteins, "Wet Snow Icing – Analysis of Field Measurements 1999-2016," in *IWAIS 2017*, China, 2017.